AFIT/DS/ENG/95-07

BINARY GAS MIXTURE ANALYSIS WITH AN INTERDIGITATED GATE ELECTRODE FIELD EFFECT TRANSISTOR (IGEFET) MICROSENSOR

DISSERTATION

Presented to the Faculty of the School of Engineering

of the Air Force Institute of Technology

Air University

In Partial Fulfillment of the

Requirements for the Degree of

Doctor of Philosophy

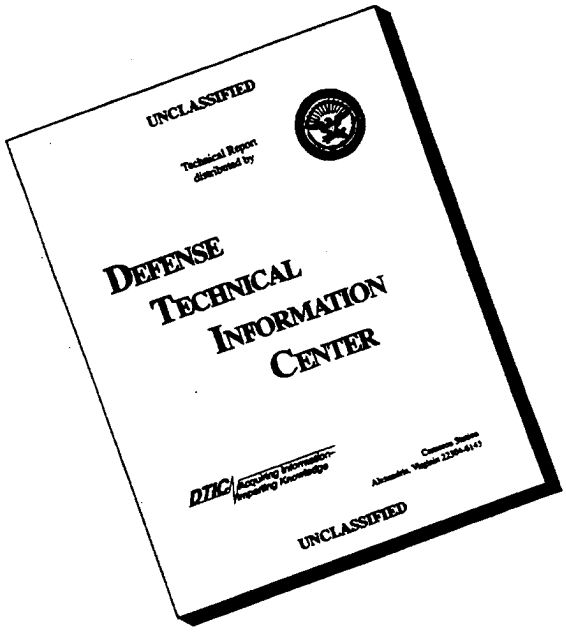
John M. Wiseman, BSEE, MSEE

December 1995

19960327 005

Approved for public release; distribution unlimited

DISCLAIMER NOTICE



THIS DOCUMENT IS BEST QUALITY AVAILABLE. THE COPY FURNISHED TO DTIC CONTAINED A SIGNIFICANT NUMBER OF PAGES WHICH DO NOT REPRODUCE LEGIBLY.

AFIT/DS/ENG/95-07

BINARY GAS MIXTURE ANALYSIS WITH AN INTERDIGITATED GATE ELECTRODE FIELD EFFECT TRANSISTOR (IGEFET) MICROSENSOR

John Michael Wiseman, B.S.E.E., M.S.E.E.

Approved:

Edward S. Kolesar — Oct. 25, 1995

*Edward S. Kolesar, Chairman (Adjunct Professor)

27 Oct 95

Matthew Kabrisky

30 Oct 95

Victor M. Bright

Oct 26, 1995

Major Paul H. Ostdiek

Oct 26, 1995

Milton E. Franke

Robert A. Calico, Jr.
Dean, School of Engineering

* Currently the W. A. Moncrief Professor of Engineering, Texas Christian University, Department of Engineering, 2000 South University Drive, Fort Worth, TX 76129.

Preface

As in any other significant undertaking, the accomplishments and results of this research could not have been achieved without the invaluable assistance of many individuals. I would especially like to thank my advisor, Dr. Edward Kolesar, for his technical guidance and helpful suggestions. His unfailing support and encouragement made the completion of this effort possible. I would also like to thank the members of my Dissertation Committee, Dr. Matthew Kabrisky, Dr. Victor Bright, Major Paul Ostdiek, and Dr. Milton Franke for their interest and careful review of this work. I thank Dr. John Lavoie of EG&G Mound Applied Technologies (Miamisburg, OH 45343-0987) and Dr. Johnathan Kiel of the Armstrong Aerospace Medical Research Laboratory (AL/OEDR, Brooks AFB, TX 78235-5301) for sponsoring this research.

I would also like to express my appreciation to previous students at AFIT who have conducted IGEFET research and whose contributions provided the foundation for this research. I would particularly like to thank Capt Tom Jenkins for his design work on the IGEFET microsensor. Also, I would like to thank Capt Clay Howe for the long days and nights sacrificed to initially screen the candidate gases for detection with the IGEFET microsensor. I would like to thank Don Smith and Bill Trop of the AFIT Electronics and Materials Cooperative Laboratory for their assistance with the laboratory equipment. I also thank Barry McDermott of Wright Laboratory (WL/AAWA, Wright Patterson AFB, OH 45433) whose support and encouragement were invaluable in the completion of this dissertation.

Finally, I wish to express my deepest appreciation to my parents and family for their love and support. I thank my parents, Bill and Ann, for standing by me when I made mistakes and encouraging me to strive for the highest goals. I am truly grateful to my wife, Sylvia, and my children, Julie and Katrina, for their love, patience, and encouragement.

John Michael Wiseman

Table of Contents

Preface iii

Table of Contents iv

List of Figures viii

List of Tables xlviii

List of Symbols liv

Abstract lxii

I. Introduction I-1

- Background I-1
- Problem Statement I-5
- Scope I-5
- Plan of Development I-6

II. Literature Review of the Metal-Substituted Phthalocyanine Compounds--Electrical and Gas Adsorption Properties II-1

- Adsorption Dependence on the Structure of the Phthalocyanine Crystals and Films II-3
- Electrical Properties of the Phthalocyanines II-18
  - Energy Band Theory II-20
  - Hopping Model of Conduction II-24
  - AC Conductivity II-28
  - Phthalocyanine Electrical Properties II-30
    - AC Electrical Conduction in the Phthalocyanine Compounds II-35
    - Metal Electrode/Phthalocyanine Contact Studies II-36
- Gas Adsorption Studies on the Phthalocyanine Compounds II-39
  - Adsorption Isotherms II-40
  - Heats of Adsorption II-43
  - Adsorption Kinetics II-44
- Summary II-47

III. Literature Review of Multicomponent Gas Analysis III-1

- Correlation III-2
- Cluster Analysis III-3
- Multiple Regression Analysis III-5
  - ***K***-matrix Method III-5

P-matrix Method III-7
Principal Component Analysis III-9
Neural Networks III-14
Summary III-18

IV. Fundamental IGEFET Microsensor Characterization IV-1

IGEFET Microsensor Design IV-1
Sensor Physical Characterization IV-2
Scanning Electron Microscopy IV-2
Transmission Electron Microscopy and Transmission Electron Diffraction IV-13
Infrared Spectroscopy IV-19
Baseline Sensor Electrical Characterization IV-44
Instrumentation System IV-53
Uncoated Sensor Characterization IV-60
DC Resistance of the Interdigitated Gate Electrode Structure IV-62
Impedance of the Interdigitated Gate Electrode Structure IV-62
Transfer Function Gain and Phase Delay of the IGEFET Sensor IV-92
Coated Sensor Characterization IV-68
Direct Current Resistance of the MPc-Coated Interdigitated Gate Electrode Structure IV-75
Transfer Function Gain and Phase Delay of the MPc-Coated IGEFET Sensor IV-79
Summary IV-98

V. Interdigitated Gate Electrode Finite-Difference Model V-1

Finite-Difference Modeling V-2
Finite-Difference and Gauss-Seidel Iteration Methods with Successive Over-Relaxation V-2
Derivation of a General Finite-Difference Formula for an Inhomogeneous, Lossy Dielectric System V-5
Interdigitated Gate Electrode Finite-Difference Model Implementation V-12
Finite-Difference Model Algorithm V-12
Finite-Difference Grid and Boundary Conditions V-16
Admittance Parameter Calculations V-34
Finite-Difference Model Implementation V-39
Finite-Difference Model Results V-42
Finite-Difference Model Verification V-57
Comparison with Published Data V-57
Experimental Measurements V-62
Semi-Infinite Thick Coatings V-64
Tantalum Oxide Thin Films V-66
Alternative Semi-Empirical Lumped-Element Circuit Model of the Interdigitated Gate Electrode Structure V-72
Summary V-82

VI. IGEFET Gas Sensitivity and Selectivity Analysis VI-1

Experimental Approach VI-1
Gas Generation and Delivery System VI-2
Test Protocol VI-4
Data Reduction and Analysis Approach VI-6
Normalization of the IGEFET Electrical Response. VI-6
Feature Vector Formation from the DC Resistance Measurements VI-7
Feature Vector Formation from the IGEFET Transfer Function Gain Measurements VI-22
Feature Vector Formation from the IGEFET Transfer Function Phase Measurements VI-37
Feature Vector Formation with Conductance Parameters Extracted from the IGEFET Transfer Function Gain/Phase Measurements VI-59
Principal Component Analysis and Multivariate Regression Implementation. VI-79
Gas Analysis Using the IGE Structure Normalized DC Resistance Response VI-85
Gas Analysis Using the IGEFET Transfer Function Gain Response VI-90
Gas Analysis Using the IGEFET Transfer Function Phase Response VI-100
Gas Analysis Using the Conductance Parameters Extracted from the IGEFET Transfer Function Response VI-106
Summary of the Gas Analyses VI-106

VII. Conclusions and Recommendations VII-1

Bibliography Bib-1

Appendix A. Principal Component Analysis of a Multicomponent Non-Linear System A-1

Appendix B. The Design of an Active Microsensor Utilizing Conventional CMOS Processing and Phthalocyanine Thin Films B-1

Theory of Operation B-3
Design Implemented B-4
Spice Simulation File B-5

Appendix C. Analysis of the MPc Infrared Absorption Spectra C-1

Appendix D. Evaluation of Experimental Measurement Techniques D-1

Evaluation of the AC Impedance Measurements D-1
Evaluation of the Time- and Frequency-Domain Square-Wave Response Measurements D-5
Summary D-8

Appendix E. Detailed Instrumentation Schematics E-1

Appendix F. Supporting Data: Baseline Characterization of the MPc-Coated Microsensor F-1

Appendix G. Derivation of the Equivalent Capacitance and Conductance of a Metal-Phthalocyanine-Metal Parallel Plate Capacitor with Schottky-Barrier Contacts ... G-1

Appendix H. Finite-Difference Equations for Nodes Along Vertical Interfaces H-1

Appendix I. Finite-Difference Model Source Code and Example Output I-1

Appendix J. Preliminary Experiments to Establish the Challenge Gas Exposure Cycle J-1

Appendix K. Supporting Data: DC Resistance Response of the MPc-Coated Microsensor to Challenge Gas Exposure K-1

Appendix L. Least-Squares Curve Fit Parameters Used to Form Feature Vectors and Examples of Feature Vectors Used for the Gas Analyses L-1

Appendix M. Supporting Data: Gain Response of the MPc-Coated IGEFET Microsensor to Challenge Gas Exposure M-1

Appendix N. Supporting Data: Phase Response of the MPc-Coated IGEFET Microsensor to Challenge Gas Exposure N-1

Appendix P. PCA and Multivariate Regression MathCad Code P-1

List of Figures

Figure I-1. Fundamental Interdigitated Gate Electrode Field Effect Transistor (IGEFET) Design (17). I-4

Figure II-1. Chemical Structure of the Metal-Substituted Phthalocyanine Compounds (26). II-2

Figure II-2. Chemical Structure of Copper Phthalocyanine (CuPc) (38). II-5

Figure II-3. Chemical Structure of Nickel Phthalocyanine (NiPc) (43). II-6

Figure II-4. Chemical Structure of Cobalt Phthalocyanine (CoPc) (39). II-7

Figure II-5. Stacking of the Planar Phthalocyanine Molecules within the Crystal Structure (42) II-8

Figure II-6. The α- and β-Phases of the Planar Phthalocyanines (26, 38). II-9

Figure II-7. Favorable Locations within a Metal-Substituted Phthalocyanine Structure for Charge Transfer Interactions. Charge Transfer Interactions are Favored Inside the Inner Circle and Outside the Outer Circle (26). II-11

Figure II-8. Infrared Spectrum for α-Phase Copper Phthalocyanine (73). II-13

Figure II-9. Infrared Spectrum for α-Phase Nickel Phthalocyanine (74). II-14

Figure II-10. Infrared Spectrum for α-Phase Cobalt Phthalocyanine (49). II-15

Figure II-11. IR Spectra of PbPc Films: a) As Prepared; After Exposure to b) 416 ppm NO_2, c) 1248 ppm NO_2, d) 2920 ppm NO_2, and e) After Bakeout. Arrows Mark the 1360 cm^{-1} Absorption Peak (90). II-19

Figure II-12. Formation of Energy Bands Caused By Splitting of the Atomic Energy Levels as the Interatomic Spacing Decreases (95). II-22

Figure II-13. Schematic Energy Band Representations of: (a) an insulator, (b) a semiconductor, and (c) a conductor (95). II-22

Figure II-14. Davis-Mott Energy Band Model (97). II-25

Figure III-1. A Dendrogram Illustrating the Results of a Cluster Analysis of 11 Different Vapors. The 11 Vapors are Indicated by the Acronyms at the Bottom of the Diagram (164). III-4

Figure III-2. Vector Representation of a Binary Gas Mixture's Composition where the Vector Component Axes are the Measured Responses From Three Different Conductivity Sensors (20). G and G_0 are the Sensor Conductivity in the Challenge and Carrier Gas, Respectively. p_{CO} and p_{CH_4} are the Partial Pressures of Carbon Monoxide and Methane, Respectively. III-8

Figure III-4. A Typical Artificial Neural Network. Eight Inputs (X_i) are Applied to the Eight Nodes of the Input Layer. The Interconnections Weights (w) are Adjusted During Training (177). III-16

Figure IV-1. IGEFET Revision 4 (Rev. 4) Microsensor IC Design. IV-4

Figure IV-2. Scanning Electron Micrograph of a Cross-Sectioned IGEFET Revision 4 Microsensor Showing the Interdigitated Gate Electrode Structure and the Degree of Oxide Undercutting Beneath the IGE Structure. IV-7

Figure IV-3. Diagram of the Cross-Sectioned Interdigitated Gate Electrode (IGE) Structure Revealed by the Scanning Electron Micrograph shown in Figure IV-2. Average Dimensions: A=860 nm, B=550 nm, C=300 nm, D=1200 nm, and E=260 nm. IV-9

Figure IV-4. Scanning Electron Micrograph of a Cross-Sectioned Interdigitated Gate Electrode Structure after Vacuum Deposition of a 1700 Å Thick Copper Phthalocyanine (CuPc) Thin Film. IV-10

Figure IV-5. Scanning Electron Micrograph of a Cross-Sectioned Interdigitated Gate Electrode Structure (Revision 3 Design) after Vacuum Deposition of a 8500 Å Thick Copper Phthalocyanine (CuPc) Thin Film. IV-11

Figure IV-6. Scanning Electron Micrograph of a Cross-Sectioned Interdigitated Gate Electrode Structure after Vacuum Deposition of a 30,000 Å Thick Copper Phthalocyanine (CuPc) Thin Film. IV-12

Figure IV-7. Transmission Electron Micrograph of a 500 Å Thick Copper Phthalocyanine (CuPc) Thin Film Sublimed onto a Carbon Grid. IV-14

Figure IV-8. Transmission Electron Micrograph of a 1000 Å Thick Nickel Phthalocyanine (NiPc) Thin Film Sublimed onto a Carbon Grid. IV-14

Figure IV-9. Transmission Electron Micrograph of a 700 Å Thick Cobalt Phthalocyanine (CoPc) Thin Film Sublimed onto a Carbon Grid. IV-14

Figure IV-10. Transmission Electron Diffraction Pattern of a 500 Å Thick Copper Phthalocyanine (CuPc) Thin Film Sublimed onto a Carbon Grid. IV-15

Figure IV-11. Transmission Electron Diffraction Pattern of a 1000 Å Thick Nickel Phthalocyanine (NiPc) Thin Film Sublimed onto a Carbon Grid. IV-15

Figure IV-12. Transmission Electron Diffraction Pattern of a 700 Å Thick Cobalt Phthalocyanine (CoPc) Thin Film Sublimed onto a Carbon Grid. IV-15

Figure IV-13. Transmission Electron Diffraction Pattern of a 500 Å Thick Copper Phthalocyanine (CuPc) Thin Film Sublimed onto a Carbon Grid after Heat Treatment at 350° C for 30 minutes in a Nitrogen Ambient. IV-17

Figure IV-14. Tranmission Electron Diffraction Pattern of a 500 Å Thick Copper Phthalocyanine (CuPc) Thin Film Sublimed onto a Carbon Grid after Heat Treatment at 350° C for 15 minutes in a Nitrogen Ambient. IV-17

Figure IV-15. Transmission Electron Diffraction Pattern of a 1000 Å Thick Nickel Phthalocyanine (NiPc) Thin Film Sublimed onto a Carbon Grid after Heat Treatment at 350° C for 15 minutes in a Nitrogen Ambient. IV-17

Figure IV-16. Transmission Electron Diffraction Pattern of a 700 Å Thick Cobalt Phthalocyanine (CoPc) Thin Film Sublimed onto a Carbon Grid after Heat Treatment at 350° C for 15 minutes in a Nitrogen Ambient. IV-17

Figure IV-17. Infrared Spectrum of the 6600 Å Thick Copper Phthalocyanine (CuPc) Thin Film Sublimed onto a Sodium Chloride Substrate. IV-20

Figure IV-18. Infrared Spectrum of the 7700 Å Thick Copper Phthalocyanine (CuPc) Thin Film Sublimed onto a Sodium Chloride Substrate. IV-21

Figure IV-19. Infrared Spectrum of the 7100 Å Thick Nickel Phthalocyanine (NiPc) Thin Film Sublimed onto a Sodium Chloride Substrate. IV-22

Figure IV-20. Infrared Spectrum of the 6500 Å Thick Nickel Phthalocyanine (NiPc) Thin Film Sublimed onto a Sodium Chloride Substrate. IV-23

Figure IV-21. Infrared Spectrum of the 5300 Å Thick Cobalt Phthalocyanine (CoPc) Thin Film Sublimed onto a Sodium Chloride Substrate. IV-24

Figure IV-22. Infrared Spectrum of the 5800 Å Thick Cobalt Phthalocyanine (CoPc) Thin Film Sublimed onto a Sodium Chloride Substrate. IV-25

Figure IV-23. Infrared Spectrum of the Sodium Chloride IR Substrate. IV-26

Figure IV-24. Infrared Absorption Peaks of the 6600 Å and 7700 Å Thick Copper Phthalocyanine (CuPc) Thin Films Compared to the Published Reference Peaks (Normalized with Respect to the 1120 cm^{-1} Peak) (73). IV-27

Figure IV-25. Infrared Absorption Peaks of the 6500 Å and 7100 Å Thick Nickel Phthalocyanine (NiPc) Thin Films Compared to the Published Reference Peaks (Normalized with Respect to 1120 cm^{-1} Peak) (74). IV-27

Figure IV-26. Infrared Absorption Peaks of the 5300 Å and 5700 Å Thick Cobalt Phthalocyanine (CoPc) Thin Films Compared to the Published Reference Peaks (Normalized with Respect to 1120 cm^{-1} Peak) (49). IV-28

Figure IV-27. Infrared Spectrum of the 6600 Å Thick Copper Phthalocyanine (CuPc) Thin Film after Heat Treatment at 350°C for 30 minutes in a Nitrogen Ambient. IV-30

Figure IV-28. Infrared Spectrum of the 7100 Å Thick Nickel Phthalocyanine (NiPc) Thin Film after Heat Treatment at 350°C for 30 minutes in a Nitrogen Ambient. IV-31

Figure IV-29. Infrared Spectrum of the 5700 Å Thick Cobalt Phthalocyanine (CoPc) Thin Film after Heat Treatment at 350°C for 30 minutes in a Nitrogen Ambient. IV-32

Figure IV-30. Infrared Spectrum of the 6600 Å Thick Copper Phthalocyanine (CuPc) Thin Film Sublimed onto a Sodium Chloride Substrate after Exposure to 770 ppm NO_2 for 46 hours. IV-34

Figure IV-31. Infrared Spectrum of the 7100 Å Thick Nickel Phthalocyanine (NiPc) Thin Film Sublimed onto a Sodium Chloride Substrate after Exposure to 770 ppm NO_2 for 46 hours. IV-35

Figure IV-32. Infrared Spectrum of the 5800 Å Thick Cobalt Phthalocyanine (CoPc) Thin Film Sublimed onto a Sodium Chloride Substrate after Exposure to 770 ppm NO_2 for 46 Hours. IV-36

Figure IV-33. Infrared Spectrum of the Sodium Chloride IR Substrate after Exposure to 770 ppm NO_2 for 46 hours. IV-38

Figure IV-34. Infrared Spectrum of the 6600 Å Thick Copper Phthalocyanine (CuPc) Thin Film Sublimed onto a Sodium Chloride Substrate after Exposure to 770 ppm NO_2 for 46 hours and Subsequent Purging at 150°C for 1.5 hours in a Nitrogen Ambient. IV-39

Figure IV-35. Infrared Spectrum of the 7100 Å Thick Nickel Phthalocyanine (NiPc) Thin Film Sublimed onto a Sodium Chloride Substrate after Exposure to 770 ppm NO_2 for 46 hours and Subsequent Purging at 150°C for 1.5 hours in a Nitrogen Ambient. IV-40

Figure IV-36. Infrared Spectrum of the 5800 Å Thick Cobalt Phthalocyanine (CoPc) Thin Film Sublimed onto a Sodium Chloride Substrate after Exposure to 770 ppm NO_2 for 46 hours and Subsequent Purging at 150°C for 1.5 hours in a Nitrogen Ambient. IV-41

Figure IV-37. Comparison of the Normalized Infrared Absorption Peaks for the 6600 Å Thick Copper Phthalocyanine (CuPc) Thin Film for the Pre-Exposed, 770 ppm NO_2 Exposed, and the Purged Conditions (Normalized with Respect to the 1120 cm^{-1} Peak).. ..... IV-42

Figure IV-38. Comparison of the Normalized Infrared Absorption Peaks of the 7100 Å Thick Nickel Phthalocyanine (NiPc) Thin Film for the Pre-Exposed, 770 ppm NO_2 Exposed, and the Purged Conditions (Normalized with Respect to the 1120 cm^{-1} Peak). IV-42

Figure IV-39. Comparison of the Normalized Infrared Absorption Peaks of the 5800 Å Thick Cobalt Phthalocyanine (CoPc) Thin Film for the Pre-Exposed, 770 ppm NO_2 Exposed, and the Purged Conditions (Normalized with Respect to the 1120 cm^{-1} Peak). IV-43

Figure IV-40. Infrared Spectrum of the 7100 Å Thick Copper Phthalocyanine (CuPc) Thin Film Sublimed onto a Sodium Chloride Substrate after Exposure to 3700 ppm NH_3 for 3 hours. IV-45

Figure IV-41. Infrared Spectrum of the 6500 Å Thick Nickel Phthalocyanine (NiPc) Thin Film Sublimed onto a Sodium Chloride Substrate after Exposure to 3700 ppm NH_3 for 3 hours. IV-46

Figure IV-42. Infrared Spectrum of the 5300 Å Thick Cobalt Phthalocyanine (CoPc) Thin Film Sublimed onto a Sodium Chloride Substrate after Exposure to 3700 ppm NH_3 for 3 hours. IV-47

Figure IV-43. Infrared Spectrum of the 7700 Å Thick Copper Phthalocyanine (CuPc) Thin Film Sublimed onto a Sodium Chloride Substrate after Exposure to 3700 ppm NH_3 for 3 hours and Subsequent Purging at 150° C for 1.5 hours in a Nitrogen Ambient. IV-48

Figure IV-44. Infrared Spectrum of the 6500 Å Thick Nickel Phthalocyanine (NiPc) Thin Film Sublimed onto a Sodium Chloride Substrate after Exposure to 3700 ppm NH_3 for 3 hours and Subsequent Purging at 150° C for 1.5 hours in a Nitrogen Ambient. IV-49

Figure IV-45. Infrared Spectrum of the 5300 Å Thick Cobalt Phthalocyanine (CoPc) Thin Film Sublimed onto a Sodium Chloride Substrate after Exposure to 3700 ppm NH_3 for 3 hours and Subsequent Purging at 150° C for 1.5 hours in a Nitrogen Ambient. IV-50

Figure IV-46. Comparison of the Normalized Infrared Absorption Peaks of the 7700 Å Thick Copper Phthalocyanine (CuPc) Thin Film for the Pre-Exposed, 3700 ppm NH_3 Exposed, and the Purged Conditions (Normalized with Respect to the 1120 cm^{-1} Peak). IV-51

Figure IV-47. Comparison of the Normalized Infrared Absorption Peaks of the 6500 Å Thick Nickel Phthalocyanine (NiPc) Thin Film for the Pre-Exposed, 3700 ppm NH_3 Exposed, and the Purged Conditions (Normalized with Respect to the 1120 cm^{-1} Peak). IV-51

Figure IV-48. Comparison of the Normalized Infrared Absorption Peaks of the 5300 Å Thick Cobalt Phthalocyanine (CoPc) Thin Film for the Pre-Exposed, 3700 ppm NH_3 Exposed, and the Purged Conditions (Normalized with Respect to the 1120 cm^{-1} Peak). IV-52

Figure IV-49. Electrical Instrumentation System for the IGEFET Microsensor Characterization. IV-54

Figure IV-50. Closed-Loop Temperature Control System. IV-50

Figure IV-51. Instrumentation Configuration for Measuring the Interdigitated Gate Electrode (IGE) Structure's DC Resistance. IV-51

Figure IV-52. Instrumentation Configuration for Measuring the Interdigitated Gate Electrode (IGE) Structure's Input (Electrode-to-Ground) Impedance. IV-52

Figure IV-53. Instrumentation Configuration for Measuring the Interdigitated Gate Electrode (IGE) Structure's Through (Inter-Electrode) Impedance. IV-52

Figure IV-54. Instrumentation Configuration for Measuring the IGEFET Transfer Function Gain and Phase Delay. IV-61

Figure IV-55. Instrumentation Configuration for Measuring the IGEFET Time- and Frequency-Domain Square-Wave Response. IV-61

Figure IV-56. Bias Voltage Dependence of the Uncoated Interdigitated Gate Electrode (IGE) Structure's DC Resistance for IGEFET Sensing Elements 1, 2, and 3. Microsensor Maintained at 150° C in a Dry Air Ambient. IV-63

Figure IV-57. Bias Voltage Dependence of the Uncoated Interdigitated Gate Electrode (IGE) Structure's DC Resistance for IGEFET Sensing Elements 4, 5, and 6. Microsensor Maintained at 150° C in a Dry Air Ambient. IV-63

Figure IV-58. Bias Voltage Dependence of the Uncoated Interdigitated Gate Electrode (IGE) Structure's DC Resistance for IGEFET Sensing Elements 7, 8, and 9. Microsensor Maintained at 150° C in a Dry Air Ambient. IV-64

Figure IV-59. Average Interdigitated Gate Electrode (IGE) Structure's DC Resistance for each Microsensor Sensing Element. Average Composed of DC Resistance Measurements From Eight Microsensors Maintained at 30° C in a Dry Air Ambient. IV-64

Figure IV-60. Temperature Dependence of the Uncoated Interdigitated Gate Electrode (IGE) Structure's DC Resistance for IGEFET Sensing Elements 7, 8, and 9. Microsensor Maintained in a Dry Air Ambient. Bias Voltage=10 V. IV-65

Figure IV-61. Temperature Dependence of the Uncoated Interdigitated Gate Electrode (IGE) Structure's DC Resistance for IGEFET Sensing Elements 4, 5, and 6. Microsensor Maintained in a Dry Air Ambient. Bias Voltage=10 V. IV-65

Figure IV-62. Bias Voltage Dependence of the Uncoated Interdigitated Gate Electrode (IGE) Structure's DC Resistance for IGEFET Sensing Elements 7, 8, and 9. Microsensor Maintained in a Dry Air Ambient. Bias Voltage=10 V. IV-66

Figure IV-63. Magnitude of the Uncoated Interdigitated Gate Electrode (IGE) Structure's Input and Through Impedance for IGEFET Sensing Element 3. Microsensor Maintained in at 30° C in a Dry Air Ambient. IV-67

Figure IV-64. Phase of the Uncoated Interdigitated Gate Electrode (IGE) Structure's Input and Through Impedance for IGEFET Sensing Element 3. Microsensor Maintained at 30° C in a Dry Air Ambient. IV-67

Figure IV-65. Bode Plot of the Uncoated Interdigitated Gate Electrode (IGE) Structure's Through Capacitance for IGEFET Sensing Element 3 at Three Different Temeperatures. Microsensor Maintained in a Dry Air Ambient. IV-70

Figure IV-66. Bode Plot of the Uncoated Interdigitated Gate Electrode (IGE) Structure's Though Dissipation for IGEFET Sensing Element 3 at Three Different Temperatures. Microsensor Maintained in a Dry Air Ambient. IV-70

Figure IV-67. Uncoated Interdigitated Gate Electrode (IGE) Structure's Through Capacitance for all Nine IGEFET Sensing Elements at Three Different Temperatures. Microsensor Maintained in a Dry Air Ambient. Measurement Frequency=20 KHz. IV-71

Figure IV-68. Uncoated Interdigitated Gate Electrode (IGE) Structure's Input Capacitance for all Nine IGEFET Sensing Elements at Three Different Temperatures. Microsensor Maintained in a Dry Air Ambient. Measurement Frequency=20 KHz. IV-71

Figure IV-69. Bode Plot of the IGEFET Amplifier's Transfer Function Gain and Phase Delay. Measurement Temperature=150° C. Microsensor Maintained in a Dry Air Ambient. IV-72

Figure IV-70. Bode Plot of the Uncoated IGEFET Microsensor's Transfer Function Gain and Phase Delay. Measurement Temperature=30° C. Microsensor Maintained in a Nitrogen Ambient. IV-74

Figure IV-71. Bias Voltage Dependence of the Interdigitated Gate Electrode (IGE) Structure's DC Resistance for Several IGEFET Sensing Elements Coated with a 3 μm Thick Copper Phthalocyanine (CuPc) Film. Microsensor Maintained at 30° C in a Nitrogen Ambient. IV-76

Figure IV-72. Bias Voltage Dependence of the Interdigitated Gate Electrode (IGE) Structure's DC Resistance for Several IGEFET Sensing Elements Coated with a 3 μm Thick Copper Phthalocyanine (CuPc) Film. Microsensor Maintained at 70° C in a Nitrogen Ambient. IV-76

Figure IV-73. Bias Voltage Dependence of the Interdigitated Gate Electrode (IGE) Structure's DC Resistance for Several IGEFET Sensing Elements Coated with a 3 μm Thick Copper Phthalocyanine (CuPc) Film. Microsensor Maintained at 100° C in a Nitrogen Ambient. IV-77

Figure IV-74. Temperature Dependence of the Interdigitated Gate Electrode (IGE) Structure's DC Resistance for IGEFET Sensing Elements Coated with a 0.2 μm Thick Copper Phthalocyanine (CuPc) Film. Microsensor Maintained in a Dry Air Ambient. Bias Voltage=10 V. IV-77

Figure IV-75. Temperature Dependence of the Interdigitated Gate Electrode (IGE) Structure's DC Resistance for IGEFET Sensing Elements Coated with a 0.5 μm Thick Copper Phthalocyanine (CuPc) Film. Microsensor Maintained in a Dry Air Ambient. Bias Voltage=10 V. IV-78

Figure IV-76. Temperature Dependence of the Interdigitated Gate Electrode (IGE) Structure's DC Resistance for IGEFET Sensing Elements Coated with a 1.0 μm Thick Copper Phthalocyanine (CuPc) Film. Microsensor Maintained in a Nitrogen Ambient. Bias Voltage=10 V. IV-78

Figure IV-77. Average Interdigitated Gate Electrode (IGE) Structure's DC Resistance for IGEFET Sensing Elements Coated with Copper Phthalocyanine (CuPc) Films with Different Thicknesses. Microsensor Maintained at 30° C in a Dry Air Ambient. The Horizontal Bars Represent the Maximum and Minimum Resistance of Three IGEFET Sensors Possessing the Same CuPc Film Thickness. IV-80

Figure IV-78. Bias Voltage Dependence of the Interdigitated Gate Electrode (IGE) Structure's DC Current for IGEFET Sensing Elements Coated with a 0.2 μm Thick Copper Phthalocyanine (CuPc) Film. Microsensor Maintained at 150° C in a Dry Air Ambient. IV-80

Figure IV-79. Bias Voltage Dependence of the Interdigitated Gate Electrode (IGE) Structure's DC Current for IGEFET Sensing Elements Coated with a 0.5 μm Thick Copper Phthalocyanine (CuPc) Film. Microsensor Maintained at 150° C in a Dry Air Ambient. IV-81

Figure IV-80. Bias Voltage Dependence of the Interdigitated Gate Electrode (IGE) DC Current For IGEFET Sensing Elements Coated with a 1.0 μm Thick Copper Phthalocyanine (CuPc) Film. Microsensor Maintained at 150° C in a Dry Air Ambient. IV-81

Figure IV-81. Extended Range Bias Voltage Dependence of the Interdigitated Gate Electrode (IGE) Structure's DC Current for the IGEFET Sensing Elements Coated with a 0.2 μm Thick Copper Phthalocyanine (CuPc) Film. Microsensor Maintained at 150° C in a Dry Air Ambient. IV-82

Figure IV-82. Extended Range Bias Voltage Dependence of the Interdigitated Gate Electrode (IGE) Structure's DC Current for the IGEFET Sensing Elements Coated with a 0.5 μm Thick Copper Phthalocyanine (CuPc) Film. Microsensor Maintained at 150° C in a Dry Air Ambient. IV-82

Figure IV-83. Extended Range Bias Voltage Dependence of the Interdigitated Gate Electrode (IGE) Structure's DC Current for the IGEFET Sensing Elements Coated with a 1.0 μm Thick Copper Phthalocyanine (CuPc) Film. Microsensor Maintained at 150° C in a Dry Air Ambient. IV-83

Figure IV-84. Bode Plots of the Sensor Transfer Function's Gain for an IGEFET Coated with a 3200 Å Thick Copper Phthalocyanine (CuPc) Film at Several Different Temperatures. Microsensor Maintained in a Dry Air Ambient. ... IV-84

Figure IV-85. Bode Plot of the Sensor's Transfer Function Phase for an IGEFET Coated with a 3200 Å Thick Copper Phthalocyanine (CuPc) Film at Several Different Temperatures. Microsensor Maintained in a Dry Air Ambient. ... IV-84

Figure IV-86. Bode Plots of the Sensor's Transfer Function Gain for an IGEFET Coated with a 4300 Å Thick Nickel Phthalocyanine (NiPc) Film at Several Different Temperatures. Microsensor Maintained in a Dry Air Ambient. IV-85

Figure IV-87. Bode Plot of the Sensor's Transfer Function Phase for an IGEFET Coated with a 4300 Å Thick Nickel Phthalocyanine (NiPc) Film at Several Different Temperatures. Microsensor Maintained in a Dry Air Ambient. IV-85

Figure IV-88. Bode Plot of the Sensor's Transfer Function Gain for an IGEFET Coated with a 5100 Å Thick Cobalt Phthalocyanine (CoPc) Film at Several Different Temperatures. Microsensor Maintained in a Dry Air Ambient. IV-86

Figure IV-89. Bode Plot of the Sensor's Transfer Function Phase for an IGEFET Coated with a 5100 Å Thick Cobalt Phthalocyanine (CoPc) Film at Several Different Temperatures. Microsensor Maintained in a Dry Air Ambient. IV-86

Figure IV-90. Nyquist Plot of the Sensor's Transfer Function for an IGEFET Coated with a 3200 Å Thick Copper Phthalocyanine (CuPc) Film at Several Different Temperatures. Microsensor Maintained in a Dry Air Ambient. IV-88

Figure IV-91. Nyquist Plot of the Sensor's Transfer Function for an IGEFET Coated with a 4300 Å Thick Nickel Phthalocyanine (NiPc) Film at Several Different Temperatures. Microsensor Maintained in a Dry Air Ambient. IV-88

Figure IV-92. Nyquist Plot of the Sensor's Transfer Function for an IGEFET Coated with a 5100 Å Thick Cobalt Phthalocyanine (CoPc) Film at Several Different Temperatures. Microsensor Maintained in a Dry Air Ambient. IV-89

Figure IV-93. Temperature Dependence of the Sensor's Relative Permittivity Determined From the Finite-Difference Model and the Measured Gain/Phase at 106 Hz for the IGEFET Sensors Coated with 3200 Å Copper Phthalocyanine (CuPc), 4300 Å Nickel Phthalocynanine (NiPc) and 5100 Å Thick Cobalt Phthalocyanine (CoPc) Films. Microsensor Maintained in a Dry Air Ambient. IV-89

Figure IV-94. Frequency Dependence of the Sensor's Relative Permittivity Determined From the Chapter V Finite-Difference Model and the Measured Gain/Phase of an IGEFET Coated with a 3200 Å Thick Copper Phthalocyanine (CuPc) Film at Three Different Temperatures. Microsensor Maintained in a Dry Air Ambient. IV-90

Figure IV-95. Frequency Dependence of the Sensor's Relative Permittivity Determined From the Chapter V Finite-Difference Model and the Measured Gain/Phase of an IGEFET Coated with a 4300 Å Thick Nickel Phthalocyanine (NiPc) Film at Three Different Temperatures. Microsensor Maintained in a Dry Air Ambient. IV-90

Figure IV-96. Frequency Dependence of the Sensor's Relative Permittivity Determined From the Chapter V Finite-Difference Model and the Measured Gain/Phase of an IGEFET Coated with a 5100 Å Thick Cobalt Phthalocyanine (CoPc) Film at Three Different Temperatures. Microsensor Maintained in a Dry Air Ambient. IV-91

Figure IV-97. Model of a Metal Electrode-Phthalocyanine Thin Film-Metal Electrode Parallel Plate Capacitor. a) Physical Model where DG is the Driven Gate Electrode, FG is the Floating Gate Electrode, and MPc is the Metal Phthalocyanine Thin Film; b) Electrical Model where C_s is the Schottky Barrier Capacitance; C_b is the Thin Film Bulk Capacitance, and G_b is the Thin Film Bulk Conductance; c) Simplified Equivalent Electrical Circuit where C_{eq} is the Equivalent Capacitance, and G_{eq} is the Equivalent Conductance (187). IV-93

Figure IV-98. Temperature Dependence of the Equivalent Conductance of the Metal Electrode-Phthalocyanine Thin Film-Metal Electrode Parallel Plate Capacitor Model at Three Different Frequencies as the Result of the Thermal Activation of the Phthalocyanine Film's Conductance. IV-94

Figure IV-99. Temperature Dependence of the Equivalent Capacitance of the Metal Electrode-Phthalocyanine Thin Film-Metal Electrode Parallel Plate Capacitor Model at Three Different Frequencies as the Result of the Thermal Activation of the Phthalocyanine Film's Conductance. IV-94

Figure IV-100. Frequency Dependence of the Sensor's Loss Factor Determined From the Chapter V Finite-Difference Model and the Measured Gain/Phase of an IGEFET Coated with a 3200 Å Thick Copper Phthalocyanine (CuPc) Film at Three Different Temperatures. Microsensor Maintained in a Dry Air Ambient. IV-96

Figure IV-101. Frequency Dependence of the Sensor's Loss Factor Determined From the Chapter V Finite-Difference Model and the Measured Gain/Phase of an IGEFET Coated with a 4300 Å Thick Nickel Phthalocyanine (NiPc) Film at Three Different Temperatures. Microsensor Maintained in a Dry Air Ambient. IV-96

Figure IV-102. Frequency Dependence of the Sensor's Loss Factor Determined From the Chapter V Finite-Difference Model and the Measured Gain/Phase of an IGEFET Coated with a 5100 Å Thick Cobalt Phthalocyanine (CoPc) Film at Three Different Temperatures. Microsensor Maintained in a Dry Air Ambient. IV-97

Figure IV-103. Arrhenius Plot of the Sensor's Loss Factor Determined From the Chapter V Finite- Difference Model and the Measured Gain/Phase at 106 Hz of IGEFET Sensors Coated with a 3200 Å Copper Phthalocyanine (CuPc), 4300 Å Nickel Phthalocyanine (NiPc), and 5100 Å Cobalt Phthalocyanine (CoPc) Thick Films. Microsensor Maintained in a Dry Air Ambient. IV-97

Figure V-1. Typical Finite-Difference Node in a Homogeneous Region with Equidistant Neighbors (190). V-3

Figure V-2. General Finite-Difference Node on a Dielectric Interface (190). V-6

Figure V-3. General Finite-Difference Node Illustrating the Lumped-Element Circuit Analog (190). V-6

Figure V-4. Geometry of a Discretized Admittance Element between Nodes 0 and 2 (190). a) Three-Dimensional Illustration of Admittance Element. b) Simplified Two-Dimensional Representation of Admittance Element. V-8

Figure V-5. Geometry of the Lower Discretized Admittance Element along an Interface (190). V-9

Figure V-6. Geometry of the Upper Discretized Admittance Element along an Interface (190). V-11

Figure V-7. Finite-Difference Model Algorithm for Computing the IGEFET Transfer Function (TF). Y_1 and Y_2 are the Calculated Two-Port Admittance Parameters Multiplied by the Meander Length. Y_L is the Load Capacitance. V-13

Figure V-8. Pseudo-Planar Finite-Difference Model (W is the Electrode Width, FT is the Film Thickness, OxH is the Oxide Thickness, EH is the Electrode Height, and ESep is the Inter-Electrode Space. Applied Potentials are in Volts). V-14

Figure V-9. Planar Finite-Difference Model (W is the Electrode Width, FT is the Film Thickness, OxH is the Oxide Thickness, EH is the Electrode Height, and ESep is the Inter-Electrode Space. Applied Potentials are in Volts). V-15

Figure V-10. Physical Model for a 1 μm Thick Film Deposited over 1 μm Thick Electrodes. V-19

Figure V-11. Meander (shaded region) Created by Folding the Inter-Electrode Space Around the Interdigitated Electrodes. (L is the Electrode Length, W is the Electrode Width, ESep is the Inter-Electrode Separation, and m_L is the Meander Length Measured with respect to the Center of the Inter-Electrode Gap). V-19

Figure V-12. Variable Number of Nearest Neighbors (N. N.) for Nodes at the Interface of Two Vertical Grid Regions with Different Grid Resolutions. V-23

Figure V-13. Nodes Requiring the Development of Modified Forms of Equation V-15 (See Appendix H). V-23

Figure V-14. Percent Gain Change in the IGE Structure's Transfer Function as a Function of the Upper Boundary Position for Various Relative Permittivity Values. (EH=1.2 μm, OxH=0.9 μm, UC=0.3 μm, FT=0.2 μm, ESep=10 μm, Vertical Resolution=1 μm). V-26

Figure V-15. Percent Gain Change in the IGE Structure's Transfer Function as a Function of the Upper Boundary Position for Different Relative Permittivity Values. (EH=1.2 μm, OxH=0.9 μm, UC=0.3 μm, FT=0.2 μm, ESep=10 μm, Vertical Resolution=1 μm). V-26

Figure V-16. Percent Gain Change in the IGE Structure's Transfer Function as a Function of Upper Boundary Position and Film Thickness. (EH=1.2 μm, OxH=0.9 μm, UC=0.3 μm, ϵ_F=100+0j, ESep=10 μm, Vertical Resolution=1 μm). V-27

Figure V-17. Contour Plot of the Potential Distribution Within an IGE Structure Coated with a 0.3 μm Thick Film. (The Equi-Potential Lines are Spaced at 0.05 V Intervals. EH=1.2 μm, OxH=0.9 μm, UC=0.3 μm, ϵ_F=1-20j, ESep=10 μm, Vertical Resolution=0.1 μm). V-27

Figure V-18. Contour Plot of the Potential Distribution Within an IGE Structure Coated with a 1.2 μm Thick Film. (The Equi-Potential Lines are Spaced at 0.05 V Intervals. EH=1.2 μm, OxH=0.9 μm, UC=0.3 μm, ϵ_F=1-20j, ESep=10 μm, Vertical Resolution=0.1 μm). V-28

Figure V-19. Contour Plot of the Potential Distribution Within an IGE Structure Coated with a 1.7 μm Thick Film. (The Equi-Potential Lines are Spaced at 0.05 V Intervals. EH=1.2 μm, OxH=0.9 μm, UC=0.3 μm, ϵ_F=1-20j, ESep=10 μm, Vertical Resolution=0.1 μm). V-28

Figure V-20. Contour Plot of the Potential Distribution Within an IGE Structure Coated with a 3.5 μm Thick Film. (The Equi-Potential Lines are Spaced at 0.05 V Intervals. EH=1.2 μm, OxH=0.9 μm, UC=0.3 μm, ϵ_F=1-20j, ESep=10 μm, Vertical Resolution=0.1 μm). V-29

Figure V-21. Contour Plot of the Potential Distribution Within an IGE Structure Coated with a 3.5 μm Thick Film. (The Equi-Potential Lines are Spaced at 0.05 V Intervals. EH=1.2 μm, OxH=0.9 μm, UC=0.3 μm, ϵ_F=1-2j, ESep=10 μm, Vertical Resolution=0.1 μm). V-29

Figure V-22. Contour Plot of the Potential Distribution Within an IGE Structure Coated with a 3.5 μm Thick Film. (The Equi-Potential Lines are Spaced at 0.05 V Intervals. EH=1.2 μm, OxH=0.9 μm, UC=0.3 μm , ϵ_F=1-100j, ESep=10 μm, Vertical Resolution=0.1 μm). V-30

Figure V-23. Calculated Gain for a IGE Structure Coated with a 3.5 μm Thick Film as a Function of the Maximum Relative Residue and Vertical Grid Spacing (EH=1.2 μm, OxH=0.9 μm, UC=0.3 μm , ϵ_F=1-2j, ESep=10 μm). V-33

Figure V-24. Two-Port Admittance Parameter Model. V-36

Figure V-25. Surface Integral Paths (S_1 and S_2) around the Interdigitated Electrodes. (Applied Potentials are in Volts).. ..... V-36

Figure V-26. Discretized Surface Integral at a Typical Finite-Difference Node. V-38

Figure V-27. Discretized Surface Integral at the Intersection of a Gaussian Surface with a Line of Symmetry. V-38

Figure V-28. π-Equivalent Model of the Interdigitated Gate Electrode Structure. V-40

Figure V-29. Gain/Phase Response Calculated from the Pseudo-Planar Model of the IGE Structure Coated with a Semi-Infinitely Thick Film (ϵ' and ϵ'' are the Relative Permittivity and Loss Factor of the Semi-Infinitely Thick Film). V-43

Figure V-30. Gain/Phase Response Calculated By Lee's Model (Infinitely Thin Electrode Approximation) for an IGE Structure Coated with a Semi-Infinitely Thick Film (190). (ϵ' and ϵ'' are the Relative Permittivity and Loss Factor of the Semi-Infinitely Thick Film). V-43

Figure V-31. Gain/Phase Response Calculated with the Pseudo-Planar Model for the Geometry of the IGEFET Sensor Design (Table V-1) Coated with a Semi-Infinitely Thick Film (ϵ' and ϵ'' are the Relative Permittivity and Loss Factor of the Semi-Infinitely Thick Film). V-45

Figure V-32. Effect of an Oxide Undercut on the Gain/Phase Response of an IGE Structure Coated with a Semi-Infinitely Thick Film Possessing a Relative Permittivity of Unity. V-46

Figure V-33. Contour Plot of the Potential Distribution Within an Uncoated "Ideal" IGE Structure. (The Equi-Potential Lines are Spaced at 0.05 V Intervals. EH=1.2 μm, OxH=0.9 μm, UC=0.3 μm, ϵ_F=1-0j, ESep=10 μm, Vertical Resolution=0.1 μm). V-47

Figure V-34. Contour Plot of the Potential Distribution Within an Uncoated IGE Structure Possessing a 0.5 μm Oxide Undercut. (The Equi-Potential Lines are Spaced at 0.05 V Intervals. EH=1.2 μm, OxH=0.9 μm, UC=0.3 μm, ϵ_F=1-2j, ESep=10 μm, Vertical Resolution=0.1 μm). V-47

Figure V-35. Effect of an Oxide Undercut on Gain/Phase Response of an IGE Structure Coated with Semi-Infinitely Thick Films with Three Different Values of Relative Permittivity. V-48

Figure V-36. Gain/Phase Response of the IGE Structure Coated with a 0.2 μm Thick Film (ϵ' and ϵ'' are the Film's Relative Permittivity and Loss Factor). V-49

Figure V-37. Gain/Phase Response of the IGE Structure Coated with a 1.2 μm Thick Film (ϵ' and ϵ'' are the Film's Relative Permittivity and Loss Factor). V-50

Figure V-38. Gain/Phase Response of the IGE Structure Coated with a 4.5 μm Thick Film (ϵ' and ϵ'' are the Film's Relative Permittivity and Loss Factor). V-51

Figure V-39. Effect of Film Thickness on the Gain/Phase Response of an IGE Structure Coated with a Film Whose Relative Permittivity is 10. ..... V-53

Figure V-40. Magnitude of the Calculated Y_{11} and Y_{12} Admittance Parameters for Different Film Loss Factors (Film Thickness = 1.2 μm and Relative Permittivity = 5). V-54

Figure V-41. Phase of the Calculated Y_{11} and Y_{12} Admittance Parameters for Different Film Loss Factors (Film Thickness = 1.2 μm and Relative Permittivity = 5). V-54

Figure V-42. Real and Imaginary Parts of the Calculated Y_{11} Admittance Parameter for Different Film Loss Factors (Film Thickness = 1.2 μm and Relative Permittivity = 5). The Admittance Parameters are Normalized With Respect to the Permittivity of Free Space, ϵ_0, and are on a Per-Unit Length Basis. If ϵ_0 is Given in Farads/cm, then the Admittance is Expressed on a Per-Unit cm Basis. V-55

Figure V-43. Real and Imaginary Parts of the Calculated Y_{12} Admittance Parameter for Different Film Loss Factors (Film Thickness = 1.2 μm and Relative Permittivity = 5). The Admittance Parameters are Normalized With Respect to the Permittivity of Free Space, ϵ_0, and are on a Per-Unit Length Basis. If ϵ_0 is Given in Farads/cm, then the Admittance is Expressed on a Per-Unit cm Basis. V-55

Figure V-44. Distributed Inter-Electrode Admittance (Y_{ie}) Circuit Model of the Interdigitated Gate Electrode Structure. Y_i are (n-1)-Distributed Admittances with i = 2 Through (n-1). Y_{EG} is the Electrode-to-Ground Admittance Beneath the Driven-Gate (DG) Electrode and the Floating-Gate (FG) Electrode. V-56

Figure V-45. Equivalent Distributed Inter-Electrode Admittance (Y_{ie}) Circuit Model of the Interdigitated Gate Electrode Structure. The Y_i Admittance Elements in Figure V-42 have been Reduced to the Equivalent Y_e Admittance. Y_{EG} is the Electrode-to-Ground Admittance Beneath the Driven-Gate (DG) Electrode and the Floating-Gate (FG) Electrode. V-58

Figure V-46. Electrode to Ground Capacitance , C_1, Calculated with the FTE Model Compared to Lee's Data (190). V-60

Figure V-47. IGE Sensor Transmission Line Model. C_T, C_L, and C_X - Field Oxide, Load, and Ambient Interelectrode Capacitances, R_A and C_A- Film Resistance and Capacitance (181). V-61

Figure V-48. Transfer Function of the IGE Structure Coated with a 300 Å Thick PEO Film Exposed to Five Dewpoints (°C) (Plus:3.6; Cross:5.4; Circle:8.5; Square:12.7; and Triangle:14.8). Solid Curve-Calculated Response (181). V-63

Figure V-49. Effect of the (C_T/C_A)-Ratio On the "Bowing" of the Sensor's Transfer Function Calculated by Garverick (181). V-63

Figure V-50. Loss Factor Frequency Dependence of Uncured EPON 828 Epoxy Measured with Two Different IGEFETs along with Data Reported by Lee (190). V-67

Figure V-51. Transfer Function of a Fully Cured EPON828-Coated IGEFET. V-68

Figure V-52. Transfer Function Gain of the Tantalum Oxide Coated IGEFET Sensor. V-68

Figure V-53. Moisture Response of the Tantalum Oxide Coated IGEFET Sensor Transfer Function's Gain. V-71

Figure V-54. Moisture Response of the Tantalum Oxide Coated IGEFET Sensor Transfer Function's Phase. V-71

Figure V-55. Moisture Response of the Parallel Plate Capacitor's Tantalum Oxide Dielectric Relative Permittivity. V-73

Figure V-56. Moisture Response of the Parallel Plate Capacitor's Tantalum Oxide Dielectric Loss Factor. V-73

Figure V-57. Lumped-Element Circuit Model of the Interdigitated Gate Electrode Structure. Y_{IE} is the Inter-Electrode Admittance, and Y_{EG} is the Electrode-to-Ground Admittance. G_1, G_2 are the Conductances and C_1, C_2 are the Capacitances Associated with Two Separate Relaxation Processes which Combine to Form the Inter-Electrode Admittance. G_{EG} is the Electrode-to-Ground Conductance and C_{EG} is the Electrode-to-Ground Capacitance. V-74

Figure V-58. Bode Plot of the Sensor Transfer Function's Gain For an IGEFET Coated with a 3200 Å Thick Copper Phthalocyanine (CuPc) Film at 170°C. Microsensor Maintained in a Dry Air Ambient. V-77

Figure V-59. Bode Plot of the Sensor Transfer Function's Phase For an IGEFET Coated with a 3200 Å Thick Copper Phthalocyanine (CuPc) Film at 170°C. Microsensor Maintained in a Dry Air Ambient. V-77

Figure V-60. Nyquist Plot of the Sensor's Transfer Function For an IGEFET Coated with a 3200 Å Thick Copper Phthalocyanine (CuPc) Film at 170 °C. Microsensor Maintained in a Dry Air Ambient. V-78

Figure V-61. Arrhenius Plot of the G_1 Conductance Obtained From Least-Square Fitting the Measured Gain/Phase of IGEFET Sensors Coated with 3200 Å Copper Phthalocyanine (CuPc), 4300 Å Nickel Phthalocyanine (NiPc), and 5100 Å Cobalt Phthalocyanine (CoPc) Thick Films. Microsensor Maintained in a Dry Air Ambient. V-80

Figure V-62. Arrhenius Plot of the G_2 Conductance Obtained From Least-Square Fitting the Measured Gain/Phase of IGEFET Sensors Coated with 3200 Å Copper Phthalocyanine (CuPc), 4300 Å Nickel Phthalocyanine (NiPc), and 5100 Å Cobalt Phthalocyanine (CoPc) Thick Films. Microsensor Maintained in a Dry Air Ambient. V-80

Figure VI-1. Gas Generation and Delivery System. VI-3

Figure VI-2. Challenge Gas Exposure Cycle for the IGEFET Microsensor Gas Analysis. VI-5

Figure VI-3. CuPc-Coated IGE Structure DC Resistance Before, During, and After Exposure to 1000 ppb NO_2. P1 is a 16 minute (min), 100° C Purge, P2 is a 16 minute, 100° C Exposure, P3 is a 16 minute, 100° C Purge, P4 is a 3 hour, 170° C Purge, and P5 is a 45 minute Cool to 100° C Purge. (Film Thickness = 0.32 μm.) VI-8

Figure VI-4. CuPc-Coated IGEFET Transfer Function Gain Before and After Exposure to 400 ppb NO_2. (Film Thickness = 0.32 μm. Temperature = 100° C.) VI-9

Figure VI-5. CuPc-Coated IGEFET Transfer Function Phase Before and After Exposure to 400 ppb NO_2. (Film Thickness = 0.32 μm. Temperature = 100° C.) VI-9

Figure VI-6. CuPc-Coated IGE Structure Normalized DC Resistance Response for Several NO_2 Exposures. (Film Thickness = 0.32 μm. Temperature = 100° C.) VI-10

Figure VI-7. NiPc-Coated IGE Structure Normalized DC Resistance Response for Several NO_2 Exposures. (Film Thickness = 0.43 μm. Temperature = 100° C.) VI-10

Figure VI-8. CoPc-Coated IGE Structure Normalized DC Resistance Response for Several NO_2 Exposures. (Film Thickness = 0.51 μm. Temperature = 100° C.) VI-11

Figure VI-9. CuPc-Coated IGE Structure Normalized DC Resistance Response for Several NH_3 Exposures. (Film Thickness = 0.32 μm. Temperature = 100° C.) VI-13

Figure VI-10. NiPc-Coated IGE Structure Normalized DC Resistance Response for Several NH_3 Exposures. (Film Thickness = 0.43 μm. Temperature = 100° C.) VI-13

Figure VI-11. CoPc-Coated IGE Structure Normalized DC Resistance Response for Several NH_3 Exposures. (Film Thickness = 0.51 μm. Temperature = 100° C.) VI-14

Figure VI-12. CuPc-Coated IGE Structure Normalized DC Resistance Response to Binary Gas Mixtures Containing 200 ppm NH_3 and Various NO_2 Concentrations. (Film Thickness = 0.32 μm. Temperature = 100° C.) VI-14

Figure VI-13. NiPc-Coated IGE Structure Normalized DC Resistance Response to Binary Gas Mixtures Containing 200 ppm NH_3 and Various NO_2 Concentrations. (Film Thickness = 0.43 μm. Temperature = 100° C.) VI-15

Figure VI-14. CoPc-Coated IGE Structure Normalized DC Resistance Response to Binary Gas Mixtures Containing 200 ppm NH_3 and Various NO_2 Concentrations. (Film Thickness = 0.51 μm. Temperature = 100° C.) VI-15

Figure VI-15. Possible Interactions of a NO_2 and NH_3 Binary Gas Mixture with the Metal-Phthalocyanine (MPc) Surface. a) NO_2 and NH_3 Exchange Process, b) NH_3 Adsorption on an Available Site, c) NO_2 Adsorption on an Available Site, d) Reactive Process, e) NH_3 Exchange Process. VI-16

Figure VI-16. CuPc-Coated IGE Structure Normalized DC Resistance Response to Repeated 100 ppb NO_2 Exposures. (Film Thickness = 0.32 μm. Temperature = 100° C.) VI-18

Figure VI-17. CuPc-Coated IGE Structure Normalized DC Resistance Response to Repeated 50 ppm NH_3 Exposures. (Film Thickness = 0.32 μm. Temperature = 100° C.) VI-18

Figure VI-18. CuPc-Coated IGE Structure Normalized DC Resistance Response to Repeated Exposures to Binary Mixtures Containing 50 ppm NH_3 and 100 ppb NO_2. (Film Thickness = 0.32 μm. Temperature = 100° C.) VI-19

Figure VI-19. Concentration Dependence of the MPc-Coated IGE Structure Normalized DC Resistance Response to Nitrogen Dioxide. (Temperature = 100° C.) VI-19

Figure VI-20. Concentration Dependence of the MPc-Coated IGE Structure Normalized DC Resistance Response to Ammonia. (Temperature = 100° C.) VI-21

Figure VI-21. Normalized DC Resistance Feature Vector Formation Process. VI-23

Figure VI-22. Bode Plots of the CuPc-Coated IGEFET Transfer Function Gain Response for Several NO_2 Exposures. (Film Thickness = 0.32 μm. Temperature = 100° C.) VI-24

Figure VI-23. Bode Plots of the NiPc-Coated IGEFET Transfer Function Gain Response for Several NO_2 Exposures. (Film Thickness = 0.43 μm. Temperature = 100° C.) VI-24

Figure VI-24. Bode Plots of the CoPc-Coated IGEFET Transfer Function Gain Response for Several NO_2 Exposures. (Film Thickness = 0.51 μm. Temperature = 100° C.) VI-25

Figure VI-25. Bode Plots of the Baseline Transfer Function Gain of the MPc-Coated IGEFET Sensing Elements. (Temperature = 100° C.) VI-27

Figure VI-26. Comparison of the Transfer Function Gain Response of the Three MPc-Coated IGEFET Sensing Elements to a 100 ppb NO_2 Exposure. (Temperature = 100° C.) VI-27

Figure VI-27. Bode Plots of the CuPc-Coated IGEFET Transfer Function Gain Response for Several NH_3 Exposures. (Film Thickness = 0.32 μm. Temperature = 100° C.) VI-28

Figure VI-28. Bode Plots of the NiPc-Coated IGEFET Transfer Function Gain Response for Several NH_3 Exposures. (Film Thickness = 0.43 μm. Temperature = 100° C.) VI-28

Figure VI-29. Bode Plots of the CoPc-Coated IGEFET Transfer Function Gain Response for Several NH_3 Exposures. (Film Thickness = 0.51 μm. Temperature = 100° C.) VI-29

Figure VI-30. Bode Plots of the CuPc-Coated IGEFET Transfer Function Gain Response to a Binary Gas Mixture Containing 200 ppm NH_3 and Various NO_2 Concentrations. (Film Thickness = 0.32 μm. Temperature = 100° C.) VI-29

Figure VI-31. Bode Plots of the NiPc-Coated IGEFET Transfer Function Gain Response to a Binary Gas Mixture Containing 200 ppm NH_3 and Various NO_2 Concentrations. (Film Thickness = 0.43 μm. Temperature = 100° C.) VI-30

Figure VI-32. Bode Plots of the CoPc-Coated IGEFET Transfer Function Gain Response to a Binary Gas Mixture Containing 200 ppm NH_3 and Various NO_2 Concentrations. (Film Thickness = 0.51 μm. Temperature = 100° C.) VI-30

Figure VI-33. Time Dependence of the CuPc-Coated IGEFET Transfer Function Gain Response for Several NO_2 Exposures. (Approximate Frequency = 100 Hz. Film Thickness = 0.32 μm. Temperature = 100° C.) VI-32

Figure VI-34. Time Dependence of the NiPc-Coated IGEFET Transfer Function Gain Response for Several NO_2 Exposures. (Approximate Frequency = 100 Hz. Film Thickness = 0.43 μm. Temperature = 100° C.) VI-32

Figure VI-35. Time Dependence of the CuPc-Coated IGEFET Transfer Function Gain Response for Several NH_3 Exposures. (Approximate Frequency = 44 Hz. Film Thickness = 0.32 μm. Temperature = 100° C.) VI-33

Figure VI-36. Time Dependence of the NiPc-Coated IGEFET Transfer Function Gain Response for Several NH_3 Exposures. (Approximate Frequency = 44 Hz. Film Thickness = 0.43 μm. Temperature = 100° C.) VI-33

Figure VI-37. Time Dependence of the CuPc-Coated IGEFET Transfer Function Gain Response to Binary Gas Mixtures Composed of 200 ppm NH_3 and Various NO_2 Concentrations. (Approximate Frequency = 44 Hz. Film Thickness = 0.32 μm. Temperature = 100° C.) VI-34

Figure VI-38. Time Dependence of the NiPc-Coated IGEFET Transfer Function Gain Response to Binary Gas Mixtures Composed of 200 ppm NH_3 and Various NO_2 Concentrations. (Approximate Frequency = 44 Hz. Film Thickness = 0.32 μm. Temperature = 100° C.) VI-34

Figure VI-39. Concentration Dependence of the MPc-Coated IGEFET Transfer Function Gain Response for Several NO_2 Exposures. (Approximate Frequency = 100 Hz. Time Slice = 9.5 min. Temperature = 100° C.) VI-35

Figure VI-40. Concentration Dependence of the MPc-Coated IGEFET Transfer Function Gain Response for Several NO_2 Exposures. (Approximate Frequency Interval = 800 -12000 Hz. Time Slice = 9.5 min. Temperature = 100° C.) ... VI-35

Figure VI-41. Concentration Dependence of the MPc-Coated IGEFET Transfer Function Gain Response for Several NH_3 Exposures. (Approximate Frequency = 44 Hz. Time Slice = 9.5 min. Temperature = 100° C.) VI-36

Figure VI-42. Concentration Dependence of the MPc-Coated IGEFET Transfer Function Gain Response for Several NH_3 Exposures. (Approximate Frequency Interval= 800-4000 Hz. Time Slice = 9.5 min. Temperature = 100° C.) VI-36

Figure VI-43. Gain Response Feature Vector Formation Process. VI-38

Figure VI-44. Bode Plots of the CuPc-Coated IGEFET Transfer Function Phase Response for Several NO_2 Exposures. (Film Thickness = 0.32 μm. Temperature = 100° C.) VI-40

Figure VI-45. Bode Plots of the NiPc-Coated IGEFET Transfer Function Phase Response for Several NO_2 Exposures. (Film Thickness = 0.43 μm. Temperature = 100° C.) VI-40

Figure VI-46. Bode Plots of the CoPc-Coated IGEFET Transfer Function Phase Response for Several NO_2 Exposures. (Film Thickness = 0.51 μm. Temperature = 100° C.) VI-41

Figure VI-47. Bode Plots of the CuPc-Coated IGEFET Transfer Function Phase Response for Several NH_3 Exposures. (Film Thickness = 0.32 μm. Temperature = 100° C.) VI-41

Figure VI-48. Bode Plots of the NiPc-Coated IGEFET Transfer Function Phase Response for Several NH_3 Exposures. (Film Thickness = 0.43 μm. Temperature = 100° C.) VI-42

Figure VI-49. Bode Plots of the CoPc-Coated IGEFET Transfer Function Phase Response for Several NH_3 Exposures. (Film Thickness = 0.51 μm. Temperature = 100° C.) VI-42

Figure VI-50. Bode Plots of the CuPc-Coated IGEFET Transfer Function Phase Response to a Binary Gas Mixture Containing 200 ppm NH_3 and Various NO_2 Concentrations. (Film Thickness = 0.32 μm. Temperature = 100° C.) VI-44

Figure VI-51. Bode Plots of the NiPc-Coated IGEFET Transfer Function Phase Response to a Binary Gas Mixture Containing 200 ppm NH_3 and Various NO_2 Concentrations. (Film Thickness = 0.43 μm. Temperature = 100° C.) VI-44

Figure VI-52. Bode Plots of the CoPc-Coated IGEFET Transfer Function Phase Response to a Binary Gas Mixture Containing 200 ppm NH_3 and Various NO_2 Concentrations. (Film Thickness = 0.51 μm. Temperature = 100° C.) VI-45

Figure VI-53. Time Dependence of the CuPc-Coated IGEFET Transfer Function Phase Response for Several NO_2 Exposures. (Approximate Frequency Interval = 100-500 Hz. Film Thickness = 0.32 μm. Temperature = 100° C.) VI-47

Figure VI-54. Time Dependence of the NiPc-Coated IGEFET Transfer Function Phase Response for Several NO_2 Exposures. (Approximate Frequency Interval = 100-500 Hz. Film Thickness = 0.43 μm. Temperature = 100° C.) VI-47

Figure VI-55. Time Dependence of the CuPc-Coated IGEFET Transfer Function Phase Response for Several NH_3 Exposures. (Approximate Frequency = 100 Hz. Film Thickness = 0.32 μm. Temperature = 100° C.) VI-48

Figure VI-56. Time Dependence of the NiPc-Coated IGEFET Transfer Function Phase Response for Several NH_3 Exposures. (Approximate Frequency = 100 Hz. Film Thickness = 0.43 μm. Temperature = 100° C.) VI-48

Figure VI-57. Time Dependence of the CuPc-Coated IGEFET Transfer Function Phase Response to Binary Gas Mixtures Composed of 200 ppm NH_3 and Various NO_2 Concentrations. (Approximate Frequency = 44 Hz. Film Thickness = 0.32 μm. Temperature = 100° C.) VI-49

Figure VI-58. Time Dependence of the NiPc-Coated IGEFET Transfer Function Phase Response to Binary Gas Mixtures Composed of 200 ppm NH_3 and Various NO_2 Concentrations. (Approximate Frequency = 44 Hz. Film Thickness = 0.43 μm. Temperature = 100° C.) VI-49

Figure VI-59. Time Dependence of the CuPc-Coated IGEFET Transfer Function Phase Response upon Repeated Exposure to a Binary Gas Mixture Composed of 50 ppm NH_3 and 100 ppb NO_2. (Approximate Frequency = 106 Hz. Film Thickness = 0.32 μm. Temperature = 100° C.) VI-50

Figure VI-60. Time Dependence of the CuPc-Coated IGEFET Transfer Function Phase Response upon Repeated Exposure to a Binary Gas Mixture Composed of 50 ppm NH_3 and 100 ppb NO_2. (Measured in a Second Experiment One Month Later. Approximate Frequency = 106 Hz. Film Thickness = 0.32 μm. Temperature = 100° C.) VI-50

Figure VI-61. Time Dependence of the CuPc-Coated IGEFET Transfer Function Phase Response upon Repeated Exposure to a 400 ppb NO_2 Challenge Concentration. (Approximate Frequency = 200 Hz. Film Thickness = 0.32 μm. Temperature = 100° C.) VI-52

Figure VI-62. Bode Plots of the NiPc-Coated IGEFET Transfer Function Phase Response at Selected Time Intervals During the First Exposure to a Binary Gas Mixture Composed of 200 ppm NH_3 and 100 ppb NO_2. Film Thickness = 0.43 μm. Temperature = 100° C. VI-54

Figure VI-63. Bode Plots of the NiPc-Coated IGEFET Transfer Function Phase Response at Selected Time Intervals During the Second Exposure to a Binary Gas Mixture Composed of 200 ppm NH_3 and 100 ppb NO_2. (Film Thickness = 0.43μm. Temperature = 100° C.) VI-54

Figure VI-64. Bode Plots of the NiPc-Coated IGEFET Transfer Function Phase Response at Selected Time Intervals During the Third Exposure to a Binary Gas Mixture Composed of 200 ppm NH_3 and 100 ppb NO_2. (Film Thickness = 0.43μm. Temperature = 100° C.) VI-55

Figure VI-65. Interaction of an NO_2 and NH_3 Binary Gas Mixture with the Surface and Intercrystallite Space of an MPc Film. VI-55

Figure VI-66. Concentration Dependence of the MPc-Coated IGEFET Transfer Function Phase Response to NO_2. (Approximate Frequency Interval = 200-600 Hz. Time Slice = 9.5 min. Temperature = 100° C.) VI-57

Figure VI-67. Concentration Dependence of the MPc-Coated IGEFET Transfer Function Phase Response to NO_2. (Approximate Frequency Interval = 10-38 KHz. Time Slice = 9.5 min. Temperature = 100° C.) VI-57

Figure VI-68. Concentration Dependence of the MPc-Coated IGEFET Transfer Function Phase Response upon NH_3. (Approximate Frequency = 106 Hz. Time Slice = 9.5 min. Temperature = 100° C.) VI-58

Figure VI-69. Concentration Dependence of the MPc-Coated IGEFET Transfer Function Phase Response upon NH_3. (Approximate Frequency Interval= 5-9 KHz. Time Slice = 9.5 min. Temperature = 100° C.) VI-58

Figure VI-70. Phase Response Feature Vector Formation Process. VI-60

Figure VI-71. Conductance Parameter Feature Vector Formation Process. VI-62

Figure VI-72. Comparison of the Spreadsheet Model and the Levenberg-Marquardt Non-Linear Least-Squares Curve Fit Methods for a Bode Plot of the CuPc-Coated IGEFET Transfer Function Gain After a 4000 ppb NO_2 Exposure. (Temperature = 100° C.) VI-65

Figure VI-73. Comparison of the Spreadsheet Model and the Levenberg-Marquardt Non-Linear Least-Squares Curve Fit Methods for a Bode Plot of the CuPc-Coated IGEFET Transfer Function Phase After a 4000 ppb NO_2 Exposure. (Temperature = 100° C.) VI-65

Figure VI-74. Comparison of the Spreadsheet Model and the Levenberg-Marquardt Non-Linear Least-Squares Curve Fit Methods for a Bode Plot of the NiPc-Coated IGEFET Transfer Function Gain After a 4000 ppb NO_2 Exposure. (Temperature = 100° C.) VI-66

Figure VI-75. Comparison of the Spreadsheet Model and the Levenberg-Marquardt Non-Linear Least-Squares Curve Fit Methods for a Bode Plot of the NiPc-Coated IGEFET Transfer Function Phase After a 4000 ppb NO_2 Exposure. (Temperature = 100° C.) VI-66

Figure VI-76. Comparison of the Spreadsheet Model and the Levenberg-Marquardt Non-Linear Least-Squares Curve Fit Methods for a Bode Plot of the CoPc-Coated IGEFET Transfer Function Gain After a 4000 ppb NO_2 Exposure. (Temperature = 100° C.) VI-67

Figure VI-77. Comparison of the Spreadsheet Model and the Levenberg-Marquardt Non-Linear Least-Squares Curve Fit Methods for a Bode Plot of the CoPc-Coated IGEFET Transfer Function Phase After a 4000 ppb NO_2 Exposure. (Temperature = 100° C.) VI-67

Figure VI-78. Comparison of the Spreadsheet Model and the MathCad Non-Linear Least-Squares Curve Fit Method for a Bode Plot of the CuPc-Coated IGEFET Transfer Function Gain Prior to Exposure. (Temperature = 100° C.) VI-68

Figure VI-79. Comparison of the Spreadsheet Model and the MathCad Non-Linear Least-Squares Curve Fit Method for a Bode Plot of the CuPc-Coated IGEFET Transfer Function Phase Prior to Exposure. (Temperature = 100° C.) VI-68

Figure VI-80. Bode Plots of the CuPc-Coated IGEFET Transfer Function Gain Before and After a 4000 ppb NO_2 Exposure. The Solid Lines Represent the Spreadsheet Model Curve Fits to Equation (V-31). (Temperature = 100° C.) VI-71

Figure VI-81. Bode Plots of the CuPc-Coated IGEFET Transfer Function Phase Before and After a 4000 ppb NO_2 Exposure. The Solid Lines Represent the Spreadsheet Model Curve Fits to Equation (V-34). (Temperature = 100° C.) VI-71

Figure VI-82. Bode Plots of the NiPc-Coated IGEFET Transfer Function Gain Before and After a 4000 ppb NO_2 Exposure. The Solid Lines Represent the Spreadsheet Model Curve Fits to Equation (V-31). (Temperature = 100° C.) VI-72

Figure VI-83. Bode Plots of the NiPc-Coated IGEFET Transfer Function Phase Before and After a 4000 ppb NO_2 Exposure. The Solid Lines Represent the Spreadsheet Model Curve Fits to Equation (V-34). (Temperature = 100° C.) VI-72

Figure VI-84. Bode Plots of the CoPc-Coated IGEFET Transfer Function Gain Before and After a 4000 ppb NO_2 Exposure. The Solid Lines Represent the Spreadsheet Model Curve Fits to Equation (V-31). (Temperature = 100° C.) VI-73

Figure VI-85. Bode Plots of the CoPc-Coated IGEFET Transfer Function Phase Before and After a 4000 ppb NO_2 Exposure. The Solid Lines Represent the Spreadsheet Model Curve Fits to Equation (V-34). (Temperature = 100° C.) VI-73

Figure VI-86. Bode Plots of the CuPc-Coated IGEFET Transfer Function Gain Response to Repeated 4000 ppb NO_2 Exposures. The Solid Lines Represent the Gain Response Derived from the Spreadsheet Model Curve Fits of the Pre-Exposed and Exposed CuPc-Coated IGEFET Transfer Function Gain Data to Equation (V-31). (Temperature = 100° C.) VI-74

Figure VI-87. Bode Plots of the CuPc-Coated IGEFET Transfer Function Phase Response to Repeated 4000 ppb NO_2 Exposures. The Solid Lines Represent the Phase Response Derived from the Spreadsheet Model Curve Fits of the Pre-Exposed and Exposed CuPc-Coated IGEFET Transfer Function Gain Data to Equation (V-34). (Temperature = 100° C.) VI-74

Figure VI-88. Bode Plots of the NiPc-Coated IGEFET Transfer Function Gain Response to Repeated 4000 ppb NO_2 Exposures. The Solid Lines Represent the Gain Response Derived from the Spreadsheet Model Curve Fits of the Pre-Exposed and Exposed NiPc-Coated IGEFET Transfer Function Gain Data to Equation (V-31). (Temperature = 100° C.) VI-75

Figure VI-89. Bode Plots of the NiPc-Coated IGEFET Transfer Function Phase Response to Repeated 4000 ppb NO_2 Exposures. The Solid Lines Represent the Phase Response Derived from the Spreadsheet Model Curve Fits of the Pre-Exposed and Exposed NiPc-Coated IGEFET Transfer Function Gain Data to Equation (V-34). (Temperature = 100° C.) VI-75

Figure VI-90. Bode Plots of the CoPc-Coated IGEFET Transfer Function Gain Response to Repeated 4000 ppb NO_2 Exposures. The Solid Lines Represent the Gain Response Derived from the Spreadsheet Model Curve Fits of the Pre-Exposed and Exposed CoPc-Coated IGEFET Transfer Function Gain Data to Equation (V-31). (Temperature = 100° C.) VI-76

Figure VI-91. Bode Plots of the CoPc-Coated IGEFET Transfer Function Phase Response to Repeated 4000 ppb NO_2 Exposures. The Solid Lines Represent the Phase Response Derived from the Spreadsheet Model Curve Fits of the Pre-Exposed and Exposed CoPc-Coated IGEFET Transfer Function Gain Data to Equation (V-34). (Temperature = 100° C.) VI-76

Figure VI-92. Concentration Dependence of the MPc-Coated IGEFET Normalized G_1 Conductance Parameter Response to Nitrogen Dioxide. (Temperature = 100° C.) VI-78

Figure VI-93. Concentration Dependence of the MPc-Coated IGEFET Normalized G_2 Conductance Parameter Response to Nitrogen Dioxide. (Temperature = 100° C.) VI-78

Figure VI-94. Principal Component Analysis Process. VI-82

Figure VI-95. Prediction Error of the NO_2 Concentration for 15 Challenge Gas Exposures as a Function of the Number of Eigenvectors Used in the Calibration. VI-86

Figure VI-96. Comparison of the Known (as Generated) and Predicted NO_2 Concentration for 15 Challenge Gas Exposures. Analysis Performed with the Normalized DC Resistance Data Using 4 Eigenvectors in the Calibration. VI-86

Figure VI-97. Prediction Error of the NH_3 Concentrations for 15 Challenge Gas Exposures as a Function of the Number of Eigenvectors Used in the Calibration. VI-87

Figure VI-98. Comparison of the Known (as Generated) and Predicted NH_3 Concentration for 15 Challenge Gas Exposures. Analysis Performed with the Normalized DC Resistance Data Using 2 Eigenvectors in the Calibration. VI-87

Figure VI-99. NO_2, NH_3, and Total Prediction Error For 27 Binary Gas Mixtures as a Function of the Number of Eigenvectors Used in the Calibration. VI-88

Figure VI-100. Comparison of the Known (as Generated) and Predicted NO_2 Concentration for 27 Binary Mixture Exposures. Analysis Performed with the Normalized DC Resistance Data Using 9 Eigenvectors in the Calibration. VI-88

Figure VI-101. Comparison of the Known (as Generated) and Predicted NH_3 Concentration for 27 Binary Mixture Exposures. Analysis Performed with the Normalized DC Resistance Data Using 9 Eigenvectors in the Calibration. VI-89

Figure VI-102. Comparison of the Known (as Generated) and Predicted NO_2 Concentration for 27 Binary Mixture Exposures. Analysis Performed with the Normalized DC Resistance Data Using 7 Eigenvectors in the Calibration. VI-91

Figure VI-103. Comparison of the Known (as Generated) and Predicted NH_3 Concentration for 27 Binary Mixture Exposures. Analysis Performed with the Normalized DC Resistance Data Using 7 Eigenvectors in the Calibration. VI-91

Figure VI-104. Comparison of the Known (as Generated) and Predicted NO_2 Concentration for 11 Binary Mixture Exposures. Analysis Performed with the Normalized DC Resistance Data Using 7 Eigenvectors in the Calibration. VI-92

Figure VI-105. Comparison of the Known (as Generated) and Predicted NH_3 Concentration for 11 Binary Mixture Exposures. Analysis Performed with the Normalized DC Resistance Data Using 7 Eigenvectors in the Calibration. VI-92

Figure VI-106. Prediction Error of the NO_2 Concentration for 15 Challenge Gas Exposures as a Function of the Number of Eigenvectors Used in the Calibration. Analysis Performed with the Gain Response Data. VI-93

Figure VI-107. Comparison of the Known (as Generated) and Predicted NO_2 Concentration for 15 Challenge Gas Exposures. Analysis Performed with the Gain Response Data Using 5 Eigenvectors in the Calibration. VI-93

Figure VI-108. Prediction Error of the NH_3 Concentration for 15 Challenge Gas Exposures as a Function of the Number of Eigenvectors Used in the Calibration. Analysis Performed with the Gain Response Data. VI-94

Figure VI-109. Comparison of the Known (as Generated) and Predicted NH_3 Concentrations for 15 Challenge Gas Exposures. Analysis Performed with the Gain Response Data Using 4 Eigenvectors in the Calibration. VI-96

Figure VI-110. NO_2, NH_3, and Total Prediction Error for 27 Binary Gas Mixtures as a Function of the Number of Eigenvectors Used in the Calibration. Analysis Performed with the Gain Response Data. VI-96

Figure VI-111. Comparison of the Known (as Generated) and Predicted NO_2 Concentration for 27 Binary Mixture Exposures. Analysis Performed with the Gain Response Data Using 9 Eigenvectors in the Calibration. VI-97

Figure VI-112. Comparison of the Known (as Generated) and Predicted NH_3 Concentration for 27 Binary Mixture Exposures. Analysis Performed with the Gain Response Data Using 9 Eigenvectors in the Calibration. VI-97

Figure VI-113. Comparison of the Known (as Generated) and Predicted NO_2 Concentration for 11 Binary Mixture Exposures. Analysis Performed with the Gain Response Data Using 9 Eigenvectors in the Calibration. VI-98

Figure VI-114. Comparison of the Known (as Generated) and Predicted NH_3 Concentration for 11 Binary Mixture Exposures. Analysis Performed with the Gain Response Data Using 9 Eigenvectors in the Calibration.. . . . . VI-98

Figure VI-115. Time Dependence of the CuPc-Coated IGEFET Transfer Function Gain Response upon Repeated Exposure to the Binary Gas Mixture Composed of 50 ppm NH_3 and 100 ppb NO_2. . . . . VI-99

Figure VI-116. Prediction Error of the NO_2 Concentration for 15 Challenge Gas Exposures as a Function of the Number of Eigenvectors Used in the Calibration. Analysis Performed with the Phase Response Data. VI-101

Figure VI-117. Comparison of the Known (as Generated) and Predicted NO_2 Concentration for 15 Challenge Gas Exposures. Analysis Performed with the Phase Response Data Using 3 Eigenvectors in the Calibration. VI-101

Figure VI-118. Prediction Error of the NH_3 Concentration for 15 Challenge Gas Exposures as a Function of the Number of Eigenvectors Used in the Calibration. Analysis Performed with the Phase Response Data. VI-102

Figure VI-119. Comparison of the Known (as Generated) and Predicted NH_3 Concentrations for 15 Challenge Gas Exposures. Analysis Performed with the Phase Response Data Using 3 Eigenvectors in the Calibration. VI-102

Figure VI-120. NO_2, NH_3, and Total Prediction Error for 27 Binary Gas Mixtures as a Function of the Number of Eigenvectors Used in the Calibration. Analysis Performed with the Phase Response Data. VI-103

Figure VI-121. Comparison of the Known (as Generated) and Predicted NO_2 Concentration for 27 Binary Mixture Exposures. Analysis Performed with the Phase Response Data Using 4 Eigenvectors in the Calibration. VI-103

Figure VI-122. Comparison of the Known (as Generated) and Predicted NH_3 Concentration for 27 Binary Mixture Exposures. Analysis Performed with the Phase Response Data Using 4 Eigenvectors in the Calibration. VI-104

Figure VI-123. Comparison of the Known (as Generated) and Predicted NO_2 Concentration for 11 Binary Mixture Exposures. Analysis Performed with the Phase Response Data Using 4 Eigenvectors in the Calibration. VI-104

Figure VI-124. Comparison of the Known (as Generated) and Predicted NH_3 Concentration for 11 Binary Mixture Exposures. Analysis Performed with the Phase Response Data Using 4 Eigenvectors in the Calibration.. . . . . VI-105

Figure VI-125. Prediction Error of the NO_2 Concentration for 15 Challenge Gas Exposures as a Function of the Number of Eigenvectors Used in the Calibration Set. Analysis Performed with the Conductance Parameters Extracted from the IGEFET Transfer Function Gain and Phase Data. VI-107

Figure VI-126. Comparison of the Known (as Generated) and Predicted NO_2 Concentration for 15 Challenge Gas Exposures. Analysis Performed with the Conductance Parameters Extracted from the IGEFET Transfer Function Gain and Phase Data Using 4 Eigenvectors in the Calibration. VI-107

Figure B-1. Schematic of the IGEFET Two-Stage CMOS Differential Amplifier. B-2

Figure C-1. Percent Error in the Infrared Absorption Spectra of the Deposited Copper Phthalocyanine Film Relative to the Sadtler Reference Spectra. (Sample 1: Film Thickness-6600 Å. Sample 2: Film Thickness-7700 Å. Infrared Spectra Normalized with Respect to 1120 cm^{-1} Peak) C-2

Figure C-2. Percent Error in the Infrared Absorption Spectra of the Deposited Nickel Phthalocyanine Film Relative to the Sadtler Reference Spectra. (Sample 1: Film Thickness-6500 Å. Sample 2: Film Thickness-7100 Å. Infrared Spectra Normalized with Respect to 1120 cm^{-1} Peak.) C-3

Figure C-3. Percent Error in the Infrared Absorption Spectra of the Deposited Cobalt Phthalocyanine Film Relative to the Published Reference Spectra. (Sample 1: Film Thickness-5300 Å. Sample 2: Film Thickness-5700 Å. Infrared Spectra Normalized with Respect to 1120 cm^{-1} Peak.) C-4

Figure C-4. Percent Change in the Infrared Absorption Spectra of the Deposited 6600 Å Copper Phthalocyanine Thin Film Relative to the Sadtler Reference Spectra for the Pre-Exposed, 770 ppm NO_2 Exposed, and the Purged Conditions. (Infrared Spectra Normalized with Respect to 1120 cm^{-1} Peak.) C-6

Figure C-5. Percent Change in the Infrared Absorption Spectra of the Deposited 7100 Å Nickel Phthalocyanine Thin Film Relative to the Sadtler Reference Spectra for the Pre-Exposed, 770 ppm NO_2 Exposed, and the Purged Conditions. (Infrared Spectra Normalized with Respect to 1120 cm^{-1} Peak.) C-7

Figure C-6. Percent Change in the Infrared Absorption Spectra of the Deposited 5800 Å Cobalt Phthalocyanine Thin Film Relative to the Published Reference Spectra for the Pre-Exposed, 770 ppm NO_2 Exposed, and the Purged Conditions. (Infrared Spectra Normalized with Respect to 1120 cm^{-1} Peak.) C-8

Figure C-7. Percent Change in the Infrared Absorption Spectra of the Deposited 7700 Å Copper Phthalocyanine Thin Film Relative to the Sadtler Reference Spectra for the Pre-Exposed, 3700 ppm NH_3 Exposed, and the Purged Conditions. (Infrared Spectra Normalized with Respect to 1120 cm^{-1} Peak.) C-9

Figure C-8. Percent Change in the Infrared Absorption Spectra of the Deposited 6500 Å Nickel Phthalocyanine Thin Film Relative to the Sadtler Reference Spectra for the Pre-Exposed, 3700 ppm NH_3 Exposed, and the Purged Conditions. (Infrared Spectra Normalized with Respect to 1120 cm^{-1} Peak.) C-10

Figure C-9. Percent Change in the Infrared Absorption Spectra of the Deposited 5300 Å Cobalt Phthalocyanine Thin Film Relative to the Published Reference Spectra for the Pre-Exposed, 3700 ppm NH_3 Exposed, and the Purged Conditions. (Infrared Spectra Normalized with Respect to 1120 cm^{-1} Peak.) C-11

Figure D-1. Magnitude of the Input and Through Impedances as a Function of Frequency for an Epoxy-Coated Interdigtated Gate Electrode (IGE) Structure at Different Cure Times. (Temperature = 30° C, Nitrogen Ambient.) D-2

Figure D-2. Phase of the Input and Through Impedances as a Function of Frequency for an Epoxy-Coated Interdigtated Gate Electrode (IGE) Structure at Different Cure Times. (Temperature = 30° C, Nitrogen Ambient.) D-2

Figure D-3. Computed and Measured Transfer Function Gain for an Epoxy-Coated IGEFET at 10, 20, and 30 minute Cure Times. The Transfer Function Gain was Computed from the AC Impedance Measurements. The AC Impedance and the IGEFET Transfer Function Gain/Phase Measurements were Collected in Separate Experiments fromTwo Different Epoxy-Coated IGEFET Sensors. (Epoxy- EPON 828 Mixed with the Versamide V-40 Curing Agent, Temperature = 30° C, Nitrogen Ambient.) D-4

Figure D-4. Time-Domain Square-Wave Response of an IGEFET Coated with a 0.2 μm Thick Cobalt Phthalocyanine (CoPc) Thin Film Before (Purge) and After Exposure to 1000 ppb NO_2. The Input Square-Wave Signal is Provided as a Reference. (Temperature = 150° C) D-6

Figure D-5. Time-Domain Square-Wave Response of an IGEFET Coated with a 1 μm Thick Cobalt Phthalocyanine (CoPc) Thin Film Before (Purge) and After Exposure to 1000 ppb NO_2. The Input Square-Wave Signal is Provided as a Reference. (Temperature = 150° C) D-6

Figure D-6. Frequency-Domain Square-Wave Response of an IGEFET Coated with a 0.2 μm Thick Cobalt Phthalocyanine (CoPc) Thin Film Before (Purge) and After Exposure to 1000 ppb NO_2. The Harmonic Content of the Input Square-Wave Signal is Provided as a Reference. (Temperature = 150° C) D-7

Figure D-7. Frequency-Domain Square-Wave Response of an IGEFET Coated with a 1 μm Thick Cobalt Phthalocyanine (CoPc) Thin Film Before (Purge) and After Exposure to 1000 ppb NO_2. The Harmonic Content of the Input Square-Wave Signal is Provided as a Reference. (Temperature = 150° C) D-7

Figure D-8. Computed and Measured Transfer Function Gain of an IGEFET Coated with a 0.2 μm Thick Cobalt Phthalocyanine (CoPc) Thin Film Before (Purge) and After Exposure to 1000 ppb NO_2. The IGEFET Transfer Function Gain was Computed from the Frequency-Domain Square-Wave Response Data. (Temperature = 150° C) D-9

Figure D-9. Computed and Measured Transfer Function Gain of an IGEFET Coated with a 1 μm Thick Cobalt Phthalocyanine (CoPc) Thin Film Before (Purge) and After Exposure to 1000 ppb NO_2. The IGEFET Transfer Function Gain was Computed from the Frequency-Domain Square-Wave Response Data. (Temperature = 150° C) D-9

Figure E-1. Detailed Electrical Schematic for the IGEFET Microsensor Electrical Measurements. The Numbers within the Test Chamber are the IC Package Bond Pad Pin Numbers. DG - Driven Gate Electrode, FG - Floating Gate Electrode, V_{out} - Output Signal, V_{bias} - Bias Voltage, V_{ss} - Negative Supply Voltage, V_{dd} - Positive Supply Voltage, V_{off} - Offset Voltage, Col - Column, AMP - Sensor Amplifier. E-2

Figure E-2. Detailed Electrical Schematic for the Interdigitated Gate Electrode (IGE) Measurements. DG - Driven Gate Electrode, FG - Floating Gate Electrode, Col - Column, SW - Switch. All Unused Connections of Test Chamber #2 were Grounded. E-3

Figure E-3. Detailed Electrical Schematic for the Closed-Loop Temperature Regulation of the IGEFET Microsensors in both Test Chambers. Col - Column. E-4

Figure F-1. Temperature Dependence of the Interdigitated Gate Electrode (IGE) Structure's DC Resistance for IGEFET Sensing Elements Coated with a 0.2 μm Thick Nickel Phthalocyanine (NiPc) Film. Microsensor Maintained in a Dry Air Ambient. Bias Voltage=10 V. F-2

Figure F-2. Temperature Dependence of the Interdigitated Gate Electrode (IGE) Structure's DC Resistance for IGEFET Sensing Elements Coated with a 0.5 μm Thick Nickel Phthalocyanine (NiPc) Film. Microsensor Maintained in a Dry Air Ambient. Bias Voltage =10 V. F-2

Figure F-3. Temperature Dependence of the Interdigitated Gate Electrode (IGE) Structure's DC Resistance for IGEFET Sensing Elements Coated with a 1.0 μm Nickel Phthalocyanine (NiPc) Film. Microsensor Maintained in a Dry Air Ambient. Bias Voltage=10 V. F-3

Figure F-4. Temperature Dependence of the Interdigitated Gate Electrode (IGE) Structure's DC Resistance for IGEFET Sensing Elements Coated with a 0.2 μm Cobalt Phthalocyanine (CoPc) Film. Microsensor Maintained in a Dry Air Ambient. Bias Voltage=10 V. F-3

Figure F-5. Temperature Dependence of the Interdigitated Gate Electrode (IGE) Structure's DC Resistance for IGEFET Sensing Elements Coated with a 0.5 μm Cobalt Phthalocyanine (CoPc) Film. Microsensor Maintained in a Dry Air Ambient. Bias Voltage=10 V. F-4

Figure F-6. Temperature Dependence of the Interdigitated Gate Electrode (IGE) Structure's DC Resistance for IGEFET Sensing Elements Coated with a 1.0 μm Cobalt Phthalocyanine (CoPc) Film. Microsensor Maintained in a Dry Air Ambient. Bias Voltage=10 V. F-4

Figure F-7. Average Interdigitated Gate Electrode (IGE) Structure's DC Resistance for IGEFET Sensing Elements Coated with Nickel Phthalocyanine (NiPc) Films with Different Thicknesses. Microsensor Maintained at 30° C in a Dry Air Ambient. The Error Bars Represent the Maximum and Minimum Resistance of Three IGEFET Sensors Possessing the Same NiPc Film Thickness. No Error Bars are Plotted for the 0.2 μm Film Thickness, since only a Single Data Point was Available.. ..... F-5

Figure F-8. Average Interdigitated Gate Electrode (IGE) Structure's DC Resistance for IGEFET Sensing Elements Coated with Cobalt Phthalocyanine (CoPc) Films with Different Thicknesses. Microsensor Maintained at 30° C in a Dry Air Ambient. The Horizontal Bars Represent the Maximum and Minimum Resistance of Three IGEFET Sensors Possessing the Same CoPc Film Thickness. F-5

Figure F-9. Bias Voltage Dependence of the Interdigitated Gate Electrode (IGE) Structure's DC Current for IGEFET Sensing Elements Coated with a 0.2 μm Thick Nickel Phthalocyanine (NiPc) Film. Microsensor Maintained at 150° C in a Dry Air Ambient. F-6

Figure F-10. Bias Voltage Dependence of the Interdigitated Gate Electrode (IGE) Structure's DC Current for IGEFET Sensing Elements Coated with a 0.5 μm Thick Nickel Phthalocyanine (NiPc) Film. Microsensor Maintained at 150° C in a Dry Air Ambient. F-6

Figure F-11. Bias Voltage Dependence of the Interdigitated Gate Electrode (IGE) Structure's DC Current for IGEFET Sensing Elements Coated with a 1.0 μm Thick Nickel Phthalocyanine (NiPc) Film. Microsensor Maintained at 150° C in a Dry Air Ambient. F-7

Figure F-12. Bias Voltage Dependence of the Interdigitated Gate Electrode (IGE) Structure's DC Current for IGEFET Sensing Elements Coated with a 0.2 μm Thick Cobalt Phthalocyanine (CoPc) Film. Microsensor Maintained at 150° C in a Dry Air Ambient. F-7

Figure F-13. Bias Voltage Dependence of the Interdigitated Gate Electrode (IGE) Structure's DC Current for IGEFET Sensing Elements Coated with a 0.5 μm Thick Cobalt Phthalocyanine (CoPc) Film. Microsensor Maintained at 150° C in a Dry Air Ambient. F-8

Figure F-14. Bias Voltage Dependence of the Interdigitated Gate Electrode (IGE) Structure's DC Current for IGEFET Sensing Elements Coated with a 1.0 μm Thick Cobalt Phthalocyanine (CoPc) Film. Microsensor Maintained at 150° C in a Dry Air Ambient. F-8

Figure F-15. Extended Range Bias Voltage Dependence of the Interdigitated Gate Electrode (IGE) Structure's DC Current for IGEFET Sensing Elements Coated with a 0.2 μm Thick Nickel Phthalocyanine (NiPc) Film. Microsensor Maintained at 150° C in a Dry Air Ambient. F-9

Figure F-16. Extended Range Bias Voltage Dependence of the Interdigitated Gate Electrode (IGE) Structure's DC Current for IGEFET Sensing Elements Coated with a 0.5 μm Thick Nickel Phthalocyanine (NiPc) Film. Microsensor Maintained at 150° C in a Dry Air Ambient. F-9

Figure F-17. Extended Range Bias Voltage Dependence of the Interdigitated Gate Electrode (IGE) Structure's DC Current for IGEFET Sensing Elements Coated with a 1.0 μm Thick Nickel Phthalocyanine (NiPc) Film. Microsensor Maintained at 150° C in a Dry Air Ambient. F-10

Figure F-18. Extended Range Bias Voltage Dependence of the Interdigitated Gate Electrode (IGE) Structure's DC Current for IGEFET Sensing Elements Coated with a 0.2 μm Thick Cobalt Phthalocyanine (CoPc) Film. Microsensor Maintained at 150° C in a Dry Air Ambient. F-10

Figure F-19. Extended Range Bias Voltage Dependence of the Interdigitated Gate Electrode (IGE) Structure's DC Current for IGEFET Sensing Elements Coated with a 0.5 μm Thick Cobalt Phthalocyanine (CoPc) Film. Microsensor Maintained at 150° C in a Dry Air Ambient. F-11

Figure F-20. Extended Range Bias Voltage Dependence of the Interdigitated Gate Electrode (IGE) Structure's DC Current for IGEFET Sensing Elements Coated with a 1.0 μm Thick Cobalt Phthalocyanine (CoPc) Film. Microsensor Maintained at 150° C in a Dry Air Ambient. F-11

Figure H-1. Geometry of a Node Along the Vertical Interface Above and Below the Driven-Gate Electrode. F-11

Figure H-2. Geometry of the Node at the Upper Corner of the Vertical Interface Above the Driven-Gate Electrode. F-11

Figure J-1. MPc-Coated IGE Structure Normalized DC Resistance Response to a 100 ppb NO_2 Challenge Gas Exposure at 150° C. A- Begin 100 ppb NO_2 Exposure. B- Begin Dry Air Purge. J-2

Figure J-2. MPc-Coated IGE Structure Normalized DC Resistance Response for Several NO_2 Challenge Gas Exposures Following Pre-conditioning of the Microsensor with a 1000 ppb NO_2 Exposure for 1 hour. A- Begin 1000 ppb NO_2 Exposure. B- Begin Dry Air Purge. C- Begin 15 minute, 100 ppb NO_2 Exposure. D- Begin 15 minute, 200 ppb NO_2 Exposure. E- Begin 15 minute, 400 ppb NO_2 Exposure. Temperature-150° C. J-2

Figure J-3. MPc-Coated IGE Structure Normalized DC Resistance Response for Several NO_2 Challenge Gas Exposures Following Pre-conditioning of the Microsensor with a 1000 ppb NO_2 Exposure for 1 hour. A- Begin 1000 ppb NO_2 Exposure. B- Begin Dry Air Purge. C- Begin 15 minute, 100 ppb NO_2 Exposure. D- Begin 15 minute, 200 ppb NO_2 Exposure. E- Begin 15 minute, 300 ppb NO_2 Exposure. F- Begin 15 minute, 400 ppb NO_2 Exposure. Temperature-170° C. J-4

Figure J-4. MPc-Coated IGE Structure Normalized DC Resistance Response for Several NO_2 Challenge Gas Exposures Following Pre-conditioning of the Microsensor with 1000 ppb NO_2 for 1 hour. A- Begin 1000 ppb NO_2 Exposure. B- Begin Dry Air Purge. C- Begin 15 minute, 100 ppb NO_2 Exposure. D- Begin 15 minute, 100 ppb NO_2, 100ppm NH_3 Exposure. Temperature-170° C. J-4

Figure J-5. MPc-Coated IGE Structure Normalized DC Resistance Response to a 15 minute, 100 ppb NO_2 Challenge Gas Exposure at170° C. J-6

Figure J-6. CuPc-Coated IGE Structure Normalized DC Resistance Response for Several NO_2 Challenge Gas Exposures. A- Begin 15 minute, 100 ppb NO_2 Exposure with Subsequent Dry Air Purge. B- Begin 15 minute, 400 ppb NO_2 Exposure with Subsequent Dry Air Purge. Temperature-170° C. J-6

Figure J-7. CuPc-Coated IGE Structure Normalized DC Resistance Response for Several NO_2 Challenge Gas Exposures. A- Begin 15 minute, 100 ppb NO_2 Exposure with Subsequent Dry Air Purge. B- Instrument Re-calibration and Response Re-normalization. C- Begin 15 minute, 400 ppb NO_2 Exposure with Subsequent Dry Air Purge. Temperature-170° C. J-7

Figure J-8. MPc-Coated IGE Structure Normalized DC Resistance Response to a 15 minute, 100 ppb NO_2 Challenge Gas Exposure at 40° C with a Subsequent Dual-Temperature Dry Air Purge. A-Begin 100 ppb NO_2 Challenge Gas Exposure. B- Begin 30 minute, Dry Air Purge at 40° C. C- Begin Approximately 13 hour, Dry Air Purge at 170° C. D- Begin Cooling to 40° C. J-8

Figure J-9. Effect of Different Purge Temperatures on the MPc-Coated IGE Structure Normalized DC Resistance Response to a 15 minute, 100 ppb NO_2 Challenge Gas Exposures at 40° C. A-Begin 100 ppb NO_2 Challenge Gas Exposure with a 60 minute, Dry Air Purge at 40° C. B- Begin Approximately 15 hour, Dry Air Purge at 85° C. C- Begin Cooling to 40° C. D- Begin Approximately 15 hour, Dry Air Purge at 170° C. J-8

Figure K-1. CuPc-Coated IGE Structure Normalized DC Resistance Response to Binary Gas Mixtures Containing 100 ppb NO_2 and Various NH_3 Concentrations. (Film Thickness = 0.32 μm. Temperature = 100° C.) K-2

Figure K-2. NiPc-Coated IGE Structure Normalized DC Resistance Response to Binary Gas Mixtures Containing 100 ppb NO_2 and Various NH_3 Concentrations. (Film Thickness = 0.43 μm. Temperature = 100° C.) K-2

Figure K-3. CoPc-Coated IGE Structure Normalized DC Resistance Response to Binary Gas Mixtures Containing 100 ppb NO_2 and Various NH_3 Concentrations. (Film Thickness = 0.51 μm. Temperature = 100° C.) K-3

Figure K-4. CuPc-Coated IGE Structure Normalized DC Resistance Response to Binary Gas Mixtures Containing 425 ppb NO_2 and Various NH_3 Concentrations. (Film Thickness = 0.32 μm. Temperature = 100° C.) K-3

Figure K-5. NiPc-Coated IGE Structure Normalized DC Resistance Response to Binary Gas Mixtures Containing 425 ppb NO_2 and Various NH_3 Concentrations. (Film Thickness = 0.43 μm. Temperature = 100° C.) K-4

Figure K-6. CoPc-Coated IGE Structure Normalized DC Resistance Response to Binary Gas Mixtures Containing 425 ppb NO_2 and Various NH_3 Concentrations. (Film Thickness = 0.51 μm. Temperature = 100° C.) K-4

Figure K-7. CuPc-Coated IGE Structure Normalized DC Resistance Response to Binary Gas Mixtures Containing 1000 ppb NO_2 and Various NH_3 Concentrations. (Film Thickness = 0.32 μm. Temperature = 100° C.) K-5

Figure K-8. NiPc-Coated IGE Structure Normalized DC Resistance Response to Binary Gas Mixtures Containing 1000 ppb NO_2 and Various NH_3 Concentrations. (Film Thickness = 0.43 μm. Temperature = 100° C.) K-5

Figure K-9. CoPc-Coated IGE Structure Normalized DC Resistance Response to Binary Gas Mixtures Containing 1000 ppb NO_2 and Various NH_3 Concentrations. (Film Thickness = 0.51 μm. Temperature = 100° C.) K-6

Figure K-10. CuPc-Coated IGE Structure Normalized DC Resistance Response to Binary Gas Mixtures Containing 50 ppm NH_3 and Various NO_2 Concentrations. (Film Thickness = 0.32 μm. Temperature = 100° C.) K-6

Figure K-11. NiPc-Coated IGE Structure Normalized DC Resistance Response to Binary Gas Mixtures Containing 50 ppm NH_3 and Various NO_2 Concentrations. (Film Thickness = 0.43 μm. Temperature = 100° C.) K-7

Figure K-12. CoPc-Coated IGE Structure Normalized DC Resistance Response to Binary Gas Mixtures Containing 50 ppm NH_3 and Various NO_2 Concentrations. (Film Thickness = 0.51 μm. Temperature = 100° C.) K-7

Figure K-13. CuPc-Coated IGE Structure Normalized DC Resistance Response to Binary Gas Mixtures Containing 400 ppm NH_3 and Various NO_2 Concentrations. (Film Thickness = 0.32 μm. Temperature = 100° C.) K-8

Figure K-14. NiPc-Coated IGE Structure Normalized DC Resistance Response to Binary Gas Mixtures Containing 400 ppm NH_3 and Various NO_2 Concentrations. (Film Thickness = 0.43 μm. Temperature = 100° C.) K-8

Figure K-15. CoPc-Coated IGE Structure Normalized DC Resistance Response to Binary Gas Mixtures Containing 400 ppm NH_3 and Various NO_2 Concentrations. (Film Thickness = 0.51 μm. Temperature = 100° C.) K-9

Figure K-16. Concentration Dependence of the CuPc-Coated IGE Structure Normalized DC Resistance Response to Nitrogen Dioxide (NO_2). Error Bars Indicate the Maximum and Minimum Normalized Resistances in a Data Set which Included the Responses Measured From Two IGEFET Sensor Elements After Triplicate Exposures to the Challenge Gas. (Film Thickness = 0.32 μm. Temperature = 100 ° C.) K-9

Figure K-17. Concentration Dependence of the NiPc-Coated IGE Structure Normalized DC Resistance Response to Nitrogen Dioxide (NO_2). Error Bars Indicate the Maximum and Minimum Normalized Resistances in a Data Set which Included the Responses Measured From Two IGEFET Sensor Elements After Triplicate Exposures to the Challenge Gas. (Film Thickness = 0.43 μm. Temperature = 100 ° C.) K-10

Figure K-18. Concentration Dependence of the CoPc-Coated IGE Structure Normalized DC Resistance Response to Nitrogen Dioxide (NO_2). Error Bars Indicate the Maximum and Minimum Normalized Resistances in a Data Set which Included the Responses Measured From Two IGEFET Sensor Elements After Triplicate Exposures to the Challenge Gas. (Film Thickness = 0.51 μm. Temperature = 100 ° C.) K-10

Figure K-19. Concentration Dependence of the CuPc-Coated IGE Structure Normalized DC Resistance Response to Ammonia (NH_3). Error Bars Indicate the Maximum and Minimum Normalized Resistances in a Data Set which Included the Responses Measured From Two IGEFET Sensor Elements After Triplicate Exposures to the Challenge Gas. (Film Thickness = 0.32 μm. Temperature = 100 ° C.) K-11

Figure K-20. Concentration Dependence of the NiPc-Coated IGE Structure Normalized DC Resistance Response to Ammonia (NH_3). Error Bars Indicate the Maximum and Minimum Normalized Resistances in a Data Set which Included the Responses Measured From Two IGEFET Sensor Elements After Triplicate Exposures to the Challenge Gas. (Film Thickness = 0.43 μm. Temperature = 100 ° C.) K-11

Figure K-21. Concentration Dependence of the CoPc-Coated IGE Structure Normalized DC Resistance Response to Ammonia (NH_3). Horizontal Bars Indicate the Maximum and Minimum Normalized Resistances in a Data Set which Included the Responses Measured From Two IGEFET Sensor Elements After Triplicate Exposures to the Challenge Gas. (Film Thickness = 0.51 µm. Temperature = 100 °C.) K-12

Figure M-1. Bode Plots of the CuPc-Coated IGEFET Transfer Function Gain Response After a 16 minute Exposure to a Binary Gas Mixture Containing 100 ppb NO_2 and Various NH_3 Concentrations. (Film Thickness = 0.32 µm. Temperature = 100° C.) M-2

Figure M-2. Bode Plots of the NiPc-Coated IGEFET Transfer Function Gain Response After a 16 minute Exposure to a Binary Gas Mixture Containing 100 ppb NO_2 and Various NH_3 Concentrations. (Film Thickness = 0.43 µm. Temperature = 100° C.) M-2

Figure M-3. Bode Plots of the CoPc-Coated IGEFET Transfer Function Gain Response After a 16 minute Exposure to a Binary Gas Mixture Containing 100 ppb NO_2 and Various NH_3 Concentrations. (Film Thickness = 0.51 µm. Temperature = 100° C.) M-3

Figure M-4. Bode Plots of the CuPc-Coated IGEFET Transfer Function Gain Response After a 16 minute Exposure to a Binary Gas Mixture Containing 425 ppb NO_2 and Various NH_3 Concentrations. (Film Thickness = 0.32 µm. Temperature = 100° C.) M-3

Figure M-5. Bode Plots of the NiPc-Coated IGEFET Transfer Function Gain Response After a 16 minute Exposure to a Binary Gas Mixture Containing 425 ppb NO_2 and Various NH_3 Concentrations. (Film Thickness = 0.43 µm. Temperature = 100° C.) M-4

Figure M-6. Bode Plots of the CoPc-Coated IGEFET Transfer Function Gain Response After a 16 minute Exposure to a Binary Gas Mixture Containing 425 ppb NO_2 and Various NH_3 Concentrations. (Film Thickness = 0.51 µm. Temperature = 100° C.) M-4

Figure M-7. Bode Plots of the CuPc-Coated IGEFET Transfer Function Gain ResponseAfter a 16 minute Exposure to a Binary Gas Mixture Containing 1000 ppb NO_2 and Various NH_3 Concentrations. (Film Thickness = 0.32 µm. Temperature = 100° C.) M-5

Figure M-8. Bode Plots of the NiPc-Coated IGEFET Transfer Function Gain Response After a 16 minute Exposure to a Binary Gas Mixture Containing 1000 ppb NO_2 and Various NH_3 Concentrations. (Film Thickness = 0.43 µm. Temperature = 100° C.) M-5

Figure M-9. Bode Plots of the CoPc-Coated IGEFET Transfer Function Gain Response After a 16 minute Exposure to a Binary Gas Mixture Containing 1000 ppb NO_2 and Various NH_3 Concentrations. (Film Thickness = 0.51 μm. Temperature = 100° C.) M-6

Figure M-10. Bode Plots of the CuPc-Coated IGEFET Transfer Function Gain Response After a 16 minute Exposure to a Binary Gas Mixture Containing 50 ppm NH_3 and Various NO_2 Concentrations. (Film Thickness = 0.32 μm. Temperature = 100° C.) M-6

Figure M-11. Bode Plots of the NiPc-Coated IGEFET Transfer Function Gain Response After a 16 minute Exposure to a Binary Gas Mixture Containing 50 ppm NH_3 and Various NO_2 Concentrations. (Film Thickness = 0.43 μm. Temperature = 100° C.) M-7

Figure M-12. Bode Plots of the CoPc-Coated IGEFET Transfer Function Gain Response After a 16 minute Exposure to a Binary Gas Mixture Containing 50 ppm NH_3 and Various NO_2 Concentrations. (Film Thickness = 0.51 μm. Temperature = 100° C.) M-7

Figure M-13. Bode Plots of the CuPc-Coated IGEFET Transfer Function Gain Response After a 16 minute Exposure to a Binary Gas Mixture Containing 400 ppm NH_3 and Various NO_2 Concentrations. (Film Thickness = 0.32 μm. Temperature = 100° C.) M-8

Figure M-14. Bode Plots of the NiPc-Coated IGEFET Transfer Function Gain Response After a 16 minute Exposure to a Binary Gas Mixture Containing 400 ppm NH_3 and Various NO_2 Concentrations. (Film Thickness = 0.43 μm. Temperature = 100° C.) M-8

Figure M-15. Bode Plots of the CoPc-Coated IGEFET Transfer Function Gain Response After a 16 minute Exposure to a Binary Gas Mixture Containing 400 ppm NH_3 and Various NO_2 Concentrations. (Film Thickness = 0.51 μm. Temperature = 100° C.) M-9

Figure M-16. Time Dependence of the CuPc-Coated IGEFET Transfer Function Gain Response for Several NO_2 Concentrations. (Approximate Frequency = 800-12000 Hz. Film Thickness = 0.32 μm. Temperature = 100° C.) M-9

Figure M-17. Time Dependence of the NiPc-Coated IGEFET Transfer Function Gain Response for Several NO_2 Concentrations. (Approximate Frequency = 800-12000 Hz. Film Thickness = 0.43 μm. Temperature = 100° C.) M-10

Figure M-18. Time Dependence of the CuPc-Coated IGEFET Transfer Function Gain Response for Several NH_3 Concentrations. (Approximate Frequency = 800-12000 Hz. Film Thickness = 0.32 μm. Temperature = 100° C.) M-10

Figure M-19. Time Dependence of the NiPc-Coated IGEFET Transfer Function Gain Response for Several NH_3 Concentrations. (Approximate Frequency = 800-12000 Hz. Film Thickness = 0.43 μm. Temperature = 100° C.) M-11

Figure N-1. Bode Plots of the CuPc-Coated IGEFET Transfer Function Phase Response After a 16 minute Exposure to a Binary Gas Mixture Containing 100 ppb NO_2 and Various NH_3 Concentrations. (Film Thickness = 0.32 μm. Temperature = 100° C.) N-2

Figure N-2. Bode Plots of the NiPc-Coated IGEFET Transfer Function Phase Response After a 16 minute Exposure to a Binary Gas Mixture Containing 100 ppb NO_2 and Various NH_3 Concentrations. (Film Thickness = 0.43 μm. Temperature = 100° C.) N-2

Figure N-3. Bode Plots of the CoPc-Coated IGEFET Transfer Function Phase Response After a 16 minute Exposure to a Binary Gas Mixture Containing 100 ppb NO_2 and Various NH_3 Concentrations. (Film Thickness = 0.51 μm. Temperature = 100° C.) N-3

Figure N-4. Bode Plots of the CuPc-Coated IGEFET Transfer Function Phase Response After a 16 minute Exposure to a Binary Gas Mixture Containing 425 ppb NO_2 and Various NH_3 Concentrations. (Film Thickness = 0.32 μm. Temperature = 100° C.) N-3

Figure N-5. Bode Plots of the NiPc-Coated IGEFET Transfer Function Phase Response After a 16 minute Exposure to a Binary Gas Mixture Containing 425 ppb NO_2 and Various NH_3 Concentrations. (Film Thickness = 0.43 μm. Temperature = 100° C.) N-4

Figure N-6. Bode Plots of the CoPc-Coated IGEFET Transfer Function Phase Response After a 16 minute Exposure to a Binary Gas Mixture Containing 425 ppb NO_2 and Various NH_3 Concentrations. (Film Thickness = 0.51 μm. Temperature = 100° C.) N-4

Figure N-7. Bode Plots of the CuPc-Coated IGEFET Transfer Function Phase Response After a 16 minute Exposure to a Binary Gas Mixture Containing 1000 ppb NO_2 and Various NH_3 Concentrations. (Film Thickness = 0.32 μm. Temperature = 100° C.) N-5

Figure N-8. Bode Plots of the NiPc-Coated IGEFET Transfer Function Phase Response After a 16 minute Exposure to a Binary Gas Mixture Containing 1000 ppb NO_2 and Various NH_3 Concentrations. (Film Thickness = 0.43 μm. Temperature = 100° C.) N-5

Figure N-9. Bode Plots of the CoPc-Coated IGEFET Transfer Function Phase Response After a 16 minute Exposure to a Binary Gas Mixture Containing 1000 ppb NO_2 and Various NH_3 Concentrations. (Film Thickness = 0.51 μm. Temperature = 100° C.) N-6

Figure N-10. Bode Plots of the CuPc-Coated IGEFET Transfer Function Phase Response After a 16 minute Exposure to a Binary Gas Mixture Containing 50 ppm NH_3 and Various NO_2 Concentrations. (Film Thickness = 0.32 μm. Temperature = 100° C.) N-6

Figure N-11. Bode Plots of the NiPc-Coated IGEFET Transfer Function Phase Response After a 16 minute Exposure to a Binary Gas Mixture Containing 50 ppm NH_3 and Various NO_2 Concentrations. (Film Thickness = 0.43 μm. Temperature = 100° C.) N-7

Figure N-12. Bode Plots of the CoPc-Coated IGEFET Transfer Function Phase Response After a 16 minute Exposure to a Binary Gas Mixture Containing 50 ppm NH_3 and Various NO_2 Concentrations. (Film Thickness = 0.51 μm. Temperature = 100° C.) N-7

Figure N-13. Bode Plots of the CuPc-Coated IGEFET Transfer Function Phase Response After a 16 minute Exposure to a Binary Gas Mixture Containing 400 ppm NH_3 and Various NO_2 Concentrations. (Film Thickness = 0.32 μm. Temperature = 100° C.) N-8

Figure N-14. Bode Plots of the NiPc-Coated IGEFET Transfer Function Phase Response After a 16 minute Exposure to a Binary Gas Mixture Containing 400 ppm NH_3 and Various NO_2 Concentrations. (Film Thickness = 0.43 μm. Temperature = 100° C.) N-8

Figure N-15. Bode Plots of the CoPc-Coated IGEFET Transfer Function Phase Response After a 16 minute Exposure to a Binary Gas Mixture Containing 400 ppm NH_3 and Various NO_2 Concentrations. (Film Thickness = 0.51 μm. Temperature = 100° C.) N-9

Figure N-16. Time Dependence of the CuPc-Coated IGEFET Transfer Function Phase Response for Several NO_2 Concentrations. (Approximate Frequency = 10-38 KHz. Film Thickness = 0.32 μm. Temperature = 100° C.) N-9

Figure N-17. Time Dependence of the NiPc-Coated IGEFET Transfer Function Phase Response for Several NO_2 Concentrations. (Approximate Frequency = 10-38 KHz. Film Thickness = 0.43 μm. Temperature = 100° C.) N-10

Figure N-18. Time Dependence of the CuPc-Coated IGEFET Transfer Function Phase Response for Several NH_3 Concentrations. (Approximate Frequency = 5-9 KHz. Film Thickness = 0.32 μm. Temperature = 100° C.) N-10

Figure N-19. Time Dependence of the NiPc-Coated IGEFET Transfer Function Phase Response for Several NH_3 Concentrations. (Approximate Frequency = 5-9 KHz. Film Thickness = 0.43 μm. Temperature = 100° C.) N-11

List of Tables

Table I-1. Sensitivity and Selectivity of Different Microsensor Technologies. I-3

Table II-1. Chemical, Physical, and Electrical Properties of Copper Phthalocyanine (CuPc), Nickel Phthalocyanine (NiPc), and Cobalt Phthalocyanine (CoPc). II-4

Table II-2. Calculated Crystal Plane Spacings of CuPc, NiPc, and CoPc (53). II-9

Table II-3. Infrared Absorption Frequencies of the α- and β-Phase Metal-Substituted Phthalocyanine Compounds (49). II-16

Table II-4. Electrical Mobilities of Several Phthalocyanine Compounds. II-32

Table II-5. Electrical Conduction Activation Energies of Several Phthalocyanine Compounds II-34

Table II-6. Electrical Properties of Au/ZnPc/M devices. RR= Rectification Ratio and V_{oc}= Open Circuit Photovoltage. Irradiation Conditions: 10mW/cm^2 (130). II-38

Table III-1. Effect of the Eigenvector Number on the IND and frac$_i$ Criteria along with the Standard Error of Prediction (SEP) for the Infrared Absorption Analysis of Pseudocumene/*p*-xylene Mixtures (173). III-13

Table III-2. Comparison of Different Multivariate Statistical Analysis Techniques with Respect to Properties of Sensing Application. III-19

Table IV-1. Geometrical Dimensions of the Revision 4 IGEFET Microsensor Design. IV-3

Table IV-2. 64-Pin DIP Wire Bond Function Summary (Continued on the next page). IV-5

Table IV-2. 64-Pin DIP Wire Bond Function Summary (Continuation from Previous Page). IV-6

Table IV-3. α-Phase Copper Phthalocyanine Crystal Plane Spacings. IV-16

Table IV-4. α-Phase Nickel Phthalocyanine Crystal Plane Spacings. IV-16

Table IV-5. α-Phase Cobalt Phthalocyanine Crystal Plane Spacings. IV-16

Table IV-6. β-Phase Cobalt Phthalocyanine Crystal Plane Spacings Following a 15 minute, 350° C Heat Treatment in Nitrogen. IV-18

Table IV-7. Metal-Dependent Absorption Band of Sublimed MPc Films. IV-44

Table IV-8. Uncoated Interdigitated Gate Electrode Structure Capacitances. IV-69

Table V-1. Critical Dimensions of the Interdigitated Gate Electrode Structure. V-16

Table V-2. Variation in the Calculated Gain for Various Model Geometries (continued on next page). V-31

Table V-2. Variation in the Calculated Gain for Various Model Geometries (continued from preceding page). V-32

Table V-3. Comparison of the Finite-Difference Model using Finite Thickness Electrodes (FTE) with Lee's Model (190). V-60

Table V-4. Comparison of Calculated and Measured Electrical Parameters of an Uncoated IGEFET Sensor. V-65

Table V-5. Comparison of EPON 828 Epoxy Material Parameters Extracted From the Finite-Difference Model and Data Reported By Lee (190). V-67

Table V-6. Measured and Calculated Gain Response of IGEFET Sensors Coated with Tantalum Oxide Thin Films. V-70

Table V-7. Least-Squares Calculated Lumped-Element Circuit Model Parameters for a CuPc-Coated IGEFET Sensor at Three Different Temperatures V-78

Table V-8. Least-Squares Calculated Lumped-Element Circuit Model Parameters for a NiPc-Coated IGEFET Sensor at Three Different Temperatures. V-79

Table V-9. Least-Squares Calculated Lumped-Element Circuit Model Parameters for a CoPc-Coated IGEFET Sensor at Three Different Temperatures. V-79

Table V-10. Activation Energies for the Inter-Electrode Model Conductances for the Three Different Phthalocyanine Thin Films. V-81

Table VI-1. IGEFET Sensing Element MPc Film Coating Type and Thickness. VI-5

Table VI-2. Minimum Least-Squares Error Resulting from Fitting the MPc-Coated IGEFET Transfer Function Gain and Phase Data with the Spreadsheet Model using Fixed Values for the Inter-Electrode Capacitances (C_1 and C_2). (Challenge Gas Concentration = 4000 ppb NO_2. Temperature = 100° C.) VI-64

Table VI-3. Dependence of the Levenberg-Marquardt Non-Linear Least-Squares CurveFit Upon the Initial Guess for the Fit Parameters. (Data Fitted was the CuPc-Coated IGEFET Transfer Function Gain Measured Prior to Challenge Gas Exposure at 100° C.) VI-69

Table VI-4. Spreadsheet Model Parameters Used to Fit the MPc-Coated IGEFET Transfer Function Gain/Phase Data Before and After Exposure to Various NO_2 Challenge Gas Concentrations (Temperature = 100° C.) VI-77

Table VI-5. Calibration Gas Concentrations for Single Component and Binary Gas Mixture Analyses. VI-81

Table VI-6. NO_2 and NH_3 Component Concentrations within the Single Component and Binary Mixture Calibration and Test Sets. (Brackets Indicate Concentration). VI-84

Table VI-7. Prediction Error (%) in the Predicted Gas Concentrations Obtained from the Four Analyses with each Type of Measureed Data. VI-109

Table C-1. Percent Error in the Measured Infrared Absorption Spectra of the Metal-Substituted Phthalocyanine (MPc) Thin Films Relative to Published Reference Spectra. C-5

Table J-1. MPc-Coated IGE Structure Normalized DC Resistance Response to the Nitrogen Dioxide (NO_2) Challenge Gas Exposures when Re-Normalized after Instrument Re-Calibration. J-7

Table L-1. Least-Squares Fit Parameters for the CuPc-Coated IGE Structure's Normalized DC Resistance Response as a Function of the NO_2 Challenge Gas Concentration. (Data Fitted to an Equation of the Form: $C=AR_N^{\alpha} + B$. R^2-Correlation Coefficient) L-2

Table L-2. Least-Squares Fit Parameters for the NiPc-Coated IGE Structure's Normalized DC Resistance Response as a Function of the NO_2 Challenge Gas Concentration. (Data Fitted to an Equation of the Form: $C=AR_N^{\alpha} + B$. R^2-Correlation Coefficient) L-2

Table L-3. Least-Squares Fit Parameters for the CoPc-Coated IGE Structure's Normalized DC Resistance Response as a Function of the NO_2 Challenge Gas Concentration. (Data Fitted to an Equation of the Form: $C=AR_N^{\alpha} + B$. R^2-Correlation Coefficient) L-3

Table L-4. Calibration Vectors Formed From the Normalized DC Resistance Data for Single Component Nitrogen Dioxide Challenge Gas Exposures. L-4

Table L-5. Typical Test Vectors Formed From the Normalized DC Resistance Data for Single Component Nitrogen Dioxide Challenge Gas Exposures. L-5

Table L-6. Least-Squares Fit Parameters for the CuPc-Coated IGE Structure's Normalized DC Resistance Response as a Function of the NH_3 Challenge Gas Concentration. (Data Fitted to an Equation of the Form: $C=AR_N + B$. R^2-Correlation Coefficient) L-6

Table L-7. Least-Squares Fit Parameters for the NiPc-Coated IGE Structure's Normalized DC Resistance Response as a Function of the NH_3 Challenge Gas Concentration. (Data Fitted to an Equation of the Form: $C=AR_N + B$. R^2-Correlation Coefficient) L-6

Table L-8. Least-Squares Fit Parameters for the CoPc-Coated IGE Structure's Normalized DC Resistance Response as a Function of the NH_3 Challenge Gas Concentration. (Data Fitted to an Equation of the Form: $C=AR_N + B$. R^2-Correlation Coefficient) L-7

Table L-9. Calibration Vectors Formed From the Normalized DC Resistance Data for Single Component Ammonia Challenge Gas Exposures. L-8

Table L-10. Typical Test Vectors Formed From the Normalized DC Resistance Data for Single Component Ammonia Challenge Gas Exposures. L-9

Table L-11. Calibration Vectors Formed From the IGE Structure's Normalized DC Resistance Response to Binary Gas Mixtures of Ammonia and Nitrogen Dioxide. L-10

Table L-12. Typical Test Vectors Formed From the IGE Structure's Normalized DC Resistance Response to Binary Gas Mixtures of Ammonia and Nitrogen Dioxide. L-11

Table L-13. Least-Squares Fit Parameters for the CuPc-Coated IGEFET Transfer Function Gain Response as a Function of the NO_2 Challenge Gas Concentration. (Data Fitted to an Equation of the Form: $\log(C) = AG_N + B$) L-12

Table L-14. Least-Squares Fit Parameters for the NiPc-Coated IGEFET Transfer Function Gain Response as a Function of the NO_2 Challenge Gas Concentration. (Data Fitted to an Equation of the Form: $\log(C)=AG_N + B$) ... L-13

Table L-15. Calibration Vectors Formed From the IGEFET Transfer Function Gain Response Data for Single Component Nitrogen Dioxide Challenge Gas Exposures. L-14

Table L-16. Typical Test Vectors Formed From the IGEFET Transfer Function Gain Response Data for Single Component Nitrogen Dioxide Challenge Gas Exposures. L-15

Table L-17. Least-Squares Fit Parameters for the CuPc-Coated IGEFET Transfer Function Gain Response as a Function of the NH_3 Challenge Gas Concentration. (Data Fitted to an Equation of the Form: $\log(C) = AG_N + B$) L-16

Table L-18. Least-Squares Fit Parameters for the NiPc-Coated IGEFET Transfer Function Gain Response as a Function of the NH_3 Challenge Gas Concentration. (Data Fitted to an Equation of the Form: $\log(C)=AG_N+B$) ... L-17

Table L-19. Calibration Vectors Formed From the IGEFET Transfer Function Gain Response Data for Single Component Ammonia Challenge Gas Exposures. ... L-18

Table L-20. Typical Test Vectors Formed From the IGEFET Transfer Function Gain Response Data for Single Component Ammonia Challenge Gas Exposures. ... L-19

Table L-21. Calibration Vectors Formed From the IGEFET Transfer Function Gain Response to Binary Mixtures of Ammonia and Nitrogen Dioxide. ... L-20

Table L-22. Typical Test Vectors Formed From the IGEFET Transfer Function Gain Response to Binary Mixtures of Ammonia and Nitrogen Dioxide. ... L-21

Table L-23. Least-Squares Fit Parameters for the CuPc-Coated IGEFET Transfer Function Phase Response as a Function of the NO_2 Challenge Gas Concentration. (Data Fitted to an Equation of the Form: $C = AP^{\alpha} + B$. R^2-Correlation Coefficient) ... L-22

Table L-24. Least-Squares Fit Parameters for the NiPc-Coated IGEFET Transfer Function Phase Response as a Function of the NO_2 Challenge Gas Concentration. (Data Fitted to an Equation of the Form: $C=AP^{\alpha} + B$. R^2-Correlation Coefficient) ... L-23

Table L-25. Calibration Vectors Formed From the IGEFET Transfer Function Phase Response Data for Single Component Nitrogen Dioxide Challenge Gas Exposures. ... L-24

Table L-26. Typical Test Vectors Formed From the IGEFET Transfer Function Phase Response Data for Single Component Nitrogen Dioxide Challenge Gas. ... L-25

Table L-27. Least-Squares Fit Parameters for the CuPc-Coated IGEFET Transfer Function Phase Response as a Function of the NH_3 Challenge Gas Concentration. (Data Fitted to an Equation of the Form: $C = AP^{\alpha} + B$. R^2-Correlation Coefficient) ... L-26

Table L-28. Least-Squares Fit Parameters for the NiPc-Coated IGEFET Transfer Function Phase Response as a Function of the NH_3 Challenge Gas Concentration. (Data Fitted to an Equation of the Form: $C=AP^{\alpha} + B$. R^2-Correlation Coefficient) ... L-27

Table L-29. Calibration Vectors Formed From the IGEFET Transfer Function Phase Response Data for Single Component Ammonia Challenge Gas Exposures. ... L-28

Table L-30. Typical Test Vectors Formed From the IGEFET Transfer Function Phase Response Data for Single Component Ammonia Challenge Gas Exposures. L-29

Table L-31. Calibration Vectors Formed From the IGEFET Transfer Function Phase Response to Binary Mixtures of Ammonia and Nitrogen Dioxide. L-30

Table L-32. Typical Test Vectors Formed From the IGEFET Transfer Function Phase Response to Binary Mixtures of Ammonia and Nitrogen Dioxide. L-31

Table L-33. Least-Squares Fit Parameters for the Conductance Parameters Extracted From the MPc-Coated IGEFET Transfer Function Gain/Phase Measurements as a Function of the NO_2 Challenge Gas Concentration. (Data Fitted to an Equation of the Form: $C = AG_N^{\alpha} + B$. R^2-Correlation Coefficient) L-32

Table L-34. Calibration Vectors Formed From the Conductance Parameters Extracted From the MPc-Coated IGEFET Transfer Function Gain/Phase Measurements for Single Component Nitrogen Dioxide Challenge Gas Exposures. L-32

Table L-35. Typical Test Vectors Formed From the Conductance Parameters Extracted From the MPc-Coated IGEFET Transfer Function Gain/Phase Measurements for Single Component Nitrogen Dioxide Challenge Gas Exposures. L-33

List of Symbols

Symbols

α	Convergence Factor
ϵ	Permittivity
ϵ^*	Complex Permittivity
ϵ_F	Film Permittivity
ϵ_r	Relative Permittivity
ϵ''	Loss Factor
ϵ'	Relative Permittivity
μ	Mobility
μ_{hop}	Hopping Mobility
μ_n	Electron Mobility
μ_p	Hole Mobility
ν_d	Average Drift Velocity
ν_{ph}	Phonon Frequency
σ	Electrical Conductivity
σ_{hop}	Hopping Conductivity
τ	Relaxation Time
τ_c	Mean Free Time Between Collisions
ϕ	Phase
χ	Electric Susceptibility
χ'	Real Part of Electric Susceptibility
χ''	Imaginary Part of Electric Susceptibility
ψ	Wave Function

ω	Angular Frequency
A	Cross-Sectional Area
AC	Alternating Current
AFIT	Air Force Institute of Technology
BF_3	Boron Trifluoride
c	Speed of Light
C	Capacitance
C_{eq}	Equivalent Capacitance
CHEMFET	Chemically-Sensitive Field-Effect Transistor
C_i	Input Capacitance
Co	Cobalt
CoPc	Cobalt Phthalocyanine
C_t	Through Capacitance
Cu	Copper
CuPc	Copper Phthalocyanine
d	Electrode Separation
DC	Direct Current
DES	Diethyl Sulfide
DFP	Diisopropyl Fluorophosphonate
DG	Driven-Gate Electrode
DIMP	Diisopropyl Methylphosphonate
DIP	Dual-In-line Package
DMMP	Dimethyl Methylphosphonate
E	Electric Field

E_F	Fermi Energy
E_g	Energy Gap
EH	Electrode Height
F(E)	Fermi-Dirac Distribution Function
FG	Floating-Gate Electrode
f_L	Frequency Limit for Equipotential Approximation
FT	Film Thickness
FTE	Finite Thickness Electrode
G	Conductance
G_{eq}	Equivalent Conductance
GPIB	General Purpose Interface Bus
h	Planck's Constant
h	Node Spacing
H_2Pc	Unsubstituted Phthalocyanine
HBr	Hydrobromic Acid
HCl	Hydrochloric Acid
I	Current
IC	Integrated Circuit
IGE	Interdigitated Gate Electrode
IGEFET	Interdigitated Gate Electrode Field-Effect Transistor
IR	Infrared
J	Current Density
k	Wave Vector
k_B	Boltzmann Constant

KBr	Potassium Bromide
KC	Known Concentration
ℓ	Element Length
L	Electrode Length
M	Metal
m_L	Meander Length
m_n	Effective Electron Mass
MOS	Metal-Oxide-Semiconductor
MOSFET	Metal-Oxide-Semiconductor Field-Effect Transistor
MOSIS	Metal Oxide Semiconductor Implementation System
m_p	Effective Hole Mass
MPc	Metal-Substituted Phthalocyanine
n	Electron Density
n	Iteration Count
N. N.	Nearest Neighbors
$N(E)$	Density of States
N_2H_2	Hydrazine
NaCl	Sodium Chloride
N_C	Effective Density of States in the Conduction Band
n_f	Number of Fingers on Driven Gate Electrode
NH_3	Ammonia
n_i	Intrinsic Carrier Concentration
Ni	Nickel
NiPc	Nickel Phthalocyanine

NO_2	Nitrogen Dioxide
n_v	Number of Vertical Nodes in Finite-Difference Grid
N_V	Effective Density of States in the Valence Band
OxH	Oxide Height
p	Hole Density
P/R	Chamber Pressure to Deposition Rate Ratio
PC	Predicted Concentration
PCA	Principal Component Analysis
PCR	Principal Component Regression
PEO	Polyethylene Oxide
PLS	Partial Least-Squares
PtPc	Platinum Phthalocyanine
q	Electric Charge
R	Hopping Distance
R	Resistance
R'	Finite-Difference Model Node Voltage Calculation Relative Residue
S	Surface Integration Path
SAW	Surface Acoustic Wave
SC	Single Component
SC	Single Crystal
SCLC	Space-Charge-Limited Current
SEM	Scanning Electron Microscopy
SEP	Standard Error of Prediction
t	time

T	Temperature
TED	Transmission Electron Diffraction
TEM	Transmission Electron Microscopy
TF	Thin Film
TOL	Toluene
UC	Oxide Undercut
$u_k(x)$	Arbitrary Periodic Function of x
v	Carrier Velocity
V	Potential
V	Voltage
V_{bias}	Bias Voltage
V_{dd}	Positive Supply Voltage
V_{fg}	Floating-Gate Electrode Voltage
V_{offset}	Offset Voltage
V_{out}	Output Voltage
V_{ss}	Negative Supply Voltage
W/H	Electrode Width to Oxide Height Ratio
W	Electrode Width
$W(E)$	Mobility Thermal Activation Energy
Y	Admittance
Z_{input}	Input Impedance
$Z_{through}$	Through Impedance

Units of Measure

µm	Micrometer
cm	Centimeter
cm^{-1}	Wavenumber
dB	Decibel
eV	Electron Volt
F	Farad
GHz	Gigahertz
Hz	Hertz
K	Kelvin
kcal	Kilocalorie
KHz	Kilohertz
kJ	Kilojoules
MΩ	Megaohm
MHz	Megahertz
min	Minutes
ml	Milliliter
mm	Millimeter
nm	Nanometer
Pa	Pascal
pF	Picofarad
ppb	Parts-per-billion
ppm	Parts-per-million
V	Volts

Å	Angstrom
°	Degrees
°C	Degrees Centigrade

Abstract

Single component and binary gas mixtures of nitrogen dioxide (NO_2) and ammonia (NH_3) were analyzed with a microsensor composed of an array of Interdigitated Gate Electrode Field Effect Transistor (IGEFET) sensor elements coated with copper-, nickel-, and cobalt-phthalocyanine thin films. Improvements in the IGEFET microsensor design and operation facilitated simultaneous measurement of the direct current (DC) and alternating current (AC) electrical response of the metal-substituted phthalocyanine (MPc) films to challenge gas exposure. A finite-difference model of the interdigitated gate electrode (IGE) structure confirmed the fundamental operation of the IGEFET microsensor. Principal component analysis (PCA) and multilinear regression were applied to features identified in the measured response of the IGE structure's DC resistance, as well as the IGEFET transfer function's gain and phase, to gas mixtures containing 100-4000 parts-per-billion (ppb) NO_2 and 20-400 parts-per-million (ppm) NH_3. The extracted features were normalized to minimize the effect of baseline drift. The individual gas components were discriminated on the basis of the opposite changes (sign change) they induced in the MPc-coated IGEFET sensor's electrical properties, the different gas sensitivities manifested by the MPc films, the time dependence of the electrical changes upon gas exposure, and the different gas sensitivities of the frequency components within the MPc-coated IGEFET transfer function. The predicted concentrations were generally within 50% of the known concentrations for all of the gas analyses. The single component analysis of each test gas using the normalized DC resistance response data yielded the smallest error (14% for ammonia and 26% for nitrogen dioxide). The error in the predicted single component gas concentrations were significantly larger (typically 40%) when the analyses were conducted with the IGEFET transfer function's gain and phase response. For the binary gas mixture analysis, the smallest error in the predicted gas concentrations (approximately 25% for each component) was achieved with the gain response data. The phase response data was the least effective measurement for predicting the gas component concentrations. An alternative approach to the analysis of the IGEFET transfer function data was investigated; this technique utilized a lumped-element circuit model that accounts for most of the variation observed in the transfer function gain and phase Bode plots. When the NO_2 analysis was performed with the conductance parameters extracted from the lumped-element circuit model, the predicted gas concentration error was significantly less than the error obtained with the gain and phase response features, and was equivalent to the error obtained with the normalized DC resistance.

BINARY GAS MIXTURE ANALYSIS WITH AN INTERDIGITATED GATE ELECTRODE FIELD EFFECT TRANSISTOR (IGEFET) MICROSENSOR

I. *Introduction*

Background

The measurement and detection of chemical species and the control of chemical reactions have widespread applications. Of particular interest to the military, is a capability for monitoring toxic and corrosive chemical compounds (1, 2). Two important classes of environmentally-sensitive compounds are chemical warfare nerve agents and the oxides of nitrogen. Chemical warfare nerve agents, such as the organophosphorus compounds, are extremely toxic to personnel and may have an ancillary effect on electronic equipment. Additionally, the oxides of nitrogen are known to evolve from the detonation material in stockpiled munitions as they age, and this compound causes the corrosion of the munition's firing mechanism (3). The traditional methods for monitoring gas vapors, such as gas chromatography, mass spectrometry, and optical spectrometry (4), require expensive and bulky instrumentation which is unsuitable for field applications. Therefore, field sampling and subsequent transfer to an analytical laboratory for remote processing is often necessary. Consequently, remote analysis involves considerable delays in the identification and quantification of the hazardous compounds. Therefore, the need for real-time continuous monitoring of toxic or corrosive gases directly at the application site has motivated the development of inexpensive and miniaturized chemical microsensors.

In the field, chemical microsensors must be capable of detecting low concentrations of the target gas in an ambient environment where potential interferences can be at much higher concentrations. For example, the decomposition of certain explosives produce, in addition to the nitrogen oxides, potential interferents, such as, methanol, carbon monoxide, and water (5). Thus, candidate chemical microsensors must be both selective and sensitive to the specific gas of interest.

In general, the fundamental principle of operation of chemical microsensors is to observe a change in some physical, chemical, or electrical property of a chemically-selective coating that interacts with the chemical species to be detected. Therefore, the chemical microsensor's selectivity is a function of the measured property (e.g., film mass, electrical conductivity, infrared absorbance, etc.) and the

strength of the interaction with the detectant species. Microsensors which measure a physical property affected by a relatively non-specific physicochemical interaction (e.g., physisorption) with a chemical species generally lack selectivity and reproducibility. For example, the coated bulk-wave piezoelectric quartz crystal microbalance (6-9) and the surface acoustic wave gas microsensor (10-13) detect mass changes in the sensor's coating upon the sorption of any gas. In contrast to simple mass changes, modulation of the coating's electrical impedance requires a much stronger (chemical bond strength) and specific interaction (chemisorption) involving charge transfer between the coating and the sorbed species. Therefore, a microsensor whose operating principle is based upon electrical impedance changes should demonstrate a high degree of selectivity. Microsensor technologies which rely on electrical impedance changes include the notch filter (14), the chemiresistor (15), and the chemically-sensitive field-effect transistor (CHEMFET) (16). Table I-1 summarizes the sensitivity and selectivity of several popular microsensor technologies.

One type of CHEMFET sensor is the Interdigitated Gate Electrode Field Effect Transistor (IGEFET). In the IGEFET, a chemically-sensitive film is intimately interfaced with an interdigitated gate electrode structure that is connected to the gate contact of a conventional Metal-Oxide-Semiconductor Field-Effect Transistor (MOSFET). Figure I-1 illustrates the fundamental IGEFET physical structure. The IGEFET sensor's operation is based upon the sensitivity of the field effect transistor's output current to changes in the molecular structure or chemical composition of the thin film that covers the interdigitated gate electrode; the molecular and compositional changes occur as the result of an electronic interaction with an adsorbed gas. The electronic interaction of the gas with the chemically-sensitive film is manifested as a change in the film's electrical impedance.

In a recent investigation (18), the well-known organic p-type semiconductor, copper phthalocyanine (CuPc), was utilized as the IGEFET chemically-sensitive coating in a novel approach for unambiguously distinguishing two challenge gases: nitrogen dioxide (NO_2) and diisopropyl methylphosphonate (DIMP). In this approach, the gas-induced impedance perturbations measured when the IGEFET was excited with a voltage pulse, were manifested as a change in the temporally-dependent output potential (voltage) of the IGEFET. The IGEFET's specificity feature was realized by computing a normalized difference Fourier transform magnitude spectrum of the IGEFET's output voltage. This signal processing scheme revealed spectral features which unambiguously distinguished the nitrogen dioxide and diisopropyl methylphosphonate challenge gas responses.

To further enhance the selectivity of the IGEFET, a microsensor has been proposed which incorporates an array of IGEFET sensing elements coated with different metal-substituted phthalocyanine

Table I-1. Sensitivity and Selectivity of Different Microsensor Technologies.

Sensor Technology	Thin-Film Material	Gas Detected	Property Measured	Detection Limit	Selectivity	References
Quartz Crystal Microbalance	Copper Salts	DIMP	Frequency Shift	1 ppb	DIMP 39.4 Hz/ppm Ammonia 0.02 Hz/ppm Chloroform 0.11 Hz/ppm	7
Surface Acoustic Wave Device	H_2Pc	Nitrogen Dioxide	Frequency Shift	500 ppb	Nitrogen Dioxide 4.9 Hz/ppm Ammonia -0.3 Hz/ppm Toluene 0.5 Hz/ppm	11
	PbPc	Nitrogen Dioxide	Frequency Shift	5 ppb	Nitrogen Dioxide 800 Hz/ppm No Competing Gases Reported	12
Notch Filter	Copper and Cuprous Oxide	DIMP	% Conductance Change	100 ppb	DIMP 3.5% at 1 ppm Hydrogen -1.5% at 1×10^6 ppm Oxygen 3.5% at 1×10^6 ppm	14
Chemiresistor	CuPc	Nitrogen Dioxide	% Conductance Change	3 ppb	Nitrogen Dioxide 1200% at 0.5 ppm Fluorine 100% at 0.25 ppm Ammonia 0% at 0.5 ppm	15
	NiPc	Nitrogen Dioxide	% Conductance Change	3 ppb	Nitrogen Dioxide 422% at 0.5 ppm Fluorine 0% at 0.25 ppm Ammonia 0% at 0.5 ppm	15
	CoPc	Nitrogen Dioxide	% Conductance Change	3 ppb	Nitrogen Dioxide 536% at 0.5 ppm Fluorine 25% at 0.25 ppm Ammonia 0% at 0.5 ppm	15
CHEMFET	PbPc	Nitrogen Dioxide	Threshold Voltage Shift	<20 ppb	Nitrogen Dioxide 440 mV at 20 ppb Relative Humidity- 150 mV in 50% RH/50 ppb NO_2	16

DIMP-Diisopropyl Methylphosphonate, H_2Pc-Metal-Free Phthalocyanine, PbPc-Lead Phthalocyanine, CuPc-Copper Phthalocyanine, NiPc-Nickel Phthalocyanine, CoPc-Cobalt Phthalocyanine, RH-Relative Humidity, NO_2-Nitrogen Dioxide

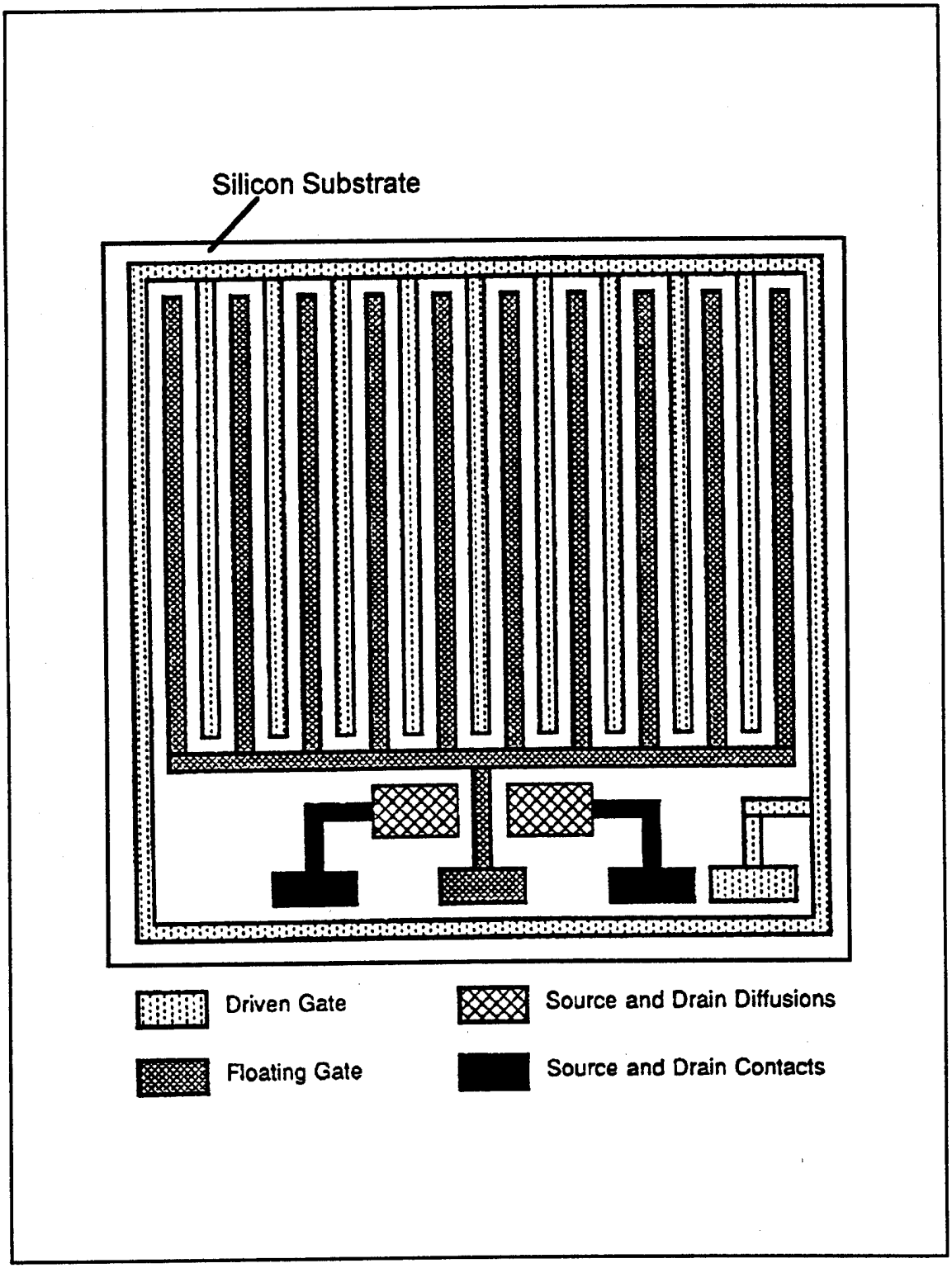


Figure I-1. Fundamental Interdigitated Gate Electrode Field Effect Transistor (IGEFET) Design (17).

(MPc) thin films (21). Optimally, each sensing element would generate a unique response to the detectant gas, and therefore, increase the information available for identification and quantification. A similar approach, in combination with pattern recognition techniques, has been employed for multicomponent gas analysis with SAW devices (19), chemiresistors (20), and piezoelectric quartz crystal micro-balances (4).

Three evolutionary designs of IGEFET microsensors have been accomplished which incorporate arrays of either nine or ten independent sensing elements (21, 22, 23). These prototype designs have been experimentally evaluated, and their best features have recently been integrated into a revised design of the IGEFET microsensor (24) that was used in this research.

Problem Statement

Although a unique IGEFET microsensor response spectral envelope has been demonstrated for individual gases, it remains to be shown that the IGEFET can be utilized to analyze a gas mixture. The purpose of this research was to investigate the utility of the electrical response of an array of IGEFET sensing elements coated with three different metal-substituted phthalocyanines to analyze binary gas mixtures.

Scope

This research effort analyzed the direct current (DC) and alternating current (AC) electrical characteristics of metal-substituted phthalocyanine thin films (upon gas adsorption) to determine the individual component gas concentrations in a binary challenge gas mixture. Copper phthalocyanine (CuPc), nickel phthalocyanine (NiPc), and cobalt phthalocyanine (CoPc) served as the gas sensitive films deposited on the array of IGEFET sensing elements. These three metal-substituted phthalocyanines were selected for this research because of their demonstrated gas sensitivity (21). The binary gas mixtures analyzed were composed of various concentrations of nitrogen dioxide (NO_2) and ammonia (NH_3). A sensor capable of analyzing ammonia and nitrogen dioxide mixtures has application in environmental pollution studies. These two gases were selected for the binary gas mixture analysis after screening the electrical response of the metal-substituted phthalocyanine films to several different gases. The other gases screened were boron trifluoride (BF_3) and three organophosphorus compounds, including diisopropyl fluorophosphonate (DFP), diisopropyl methylphosphonate (DIMP), and dimethyl methylphosphonate (DMMP). The screening of the candidate gases was accomplished in collaboration with Captain Clay Howe, and the results are reported elsewhere (25). Binary gas mixture analysis with

these two gases was facilitated by the opposite changes (sign change) they induced in the metal-substituted phthalocyanine's electrical properties. Since MPc films are p-type semiconductors (26), electron accepting gases, such as nitrogen dioxide, that adsorb on the MPc surface cause an increase in the effective hole concentration and, therefore, cause an increase in the conductivity. In contrast, electron donating compounds, such as ammonia, reduce the effective hole concentration and the conductivity. In order to correlate the IGEFET microsensor's performance with the changes in the phthalocyanine's electrical characteristics, the interdigitated gate electrode electrical response was simulated for various electrode geometries and sensor coating complex electrical permittivities using a finite-difference method. The metal-substituted phthalocyanine thin film's morphology and chemical structure, as well as the environmental parameters that influence the IGEFET microsensor's response, were also characterized.

Plan of Development

Chapter II reviews the current literature which pertains to the properties of the metal-substituted phthalocyanines. The morphology and chemical structure of the phthalocyanines, and their gas adsorption and electrical properties are comprehensively discussed. Chapter III reviews and discusses the statistical analysis approaches that are appropriate for analyzing gas mixtures, with an emphasis on those studies involving chemiresistor sensors. Chapter IV describes the IGEFET microsensor and the baseline characterization of the IGEFET and the metal-substituted phthalocyanine film properties. Chapter V presents a finite-difference model that explains the electrical response of the IGEFET. The results of the single component and binary gas mixture analyses are presented in Chapter VI. Chapter VII summarizes the significant contributions of this research and recommends topics for further investigation.

II. *Literature Review of the Metal-Substituted Phthalocyanine Compounds Electrical and Gas Adsorption Properties*

Phthalocyanine and its metal derivatives possess favorable chromatic, thermal, optical, and electrical properties which has lead to their use in a wide variety of applications, including catalysts, colorants, lasers, lubricants, blood substitutes, color photography, and xerography (27). The metal-substituted phthalocyanine compounds are based on the structure shown in Figure II-1. The substitution of different metals (M) in the structure influences the physico-chemical properties of the phthalocyanine compounds.

The large number of applications and the versatility inherent in the ability to substitute various metal ions (M) in the phthalocyanine molecule has motivated extensive research into their chemical, physical, and electrical properties. Several extensive reviews and books dedicated to collecting and summarizing the large body of literature generated on the phthalocyanine compounds have been published (26, 28-31). The extensive literature focused on the phthalocyanine compounds has undoubtedly contributed to its adoption as a model compound in the study of molecular crystals and organic semiconductors. Reviews of molecular crystals and organic semiconductors usually include some discussion of the properties of the phthalocyanine compounds (32-37). One application for the phthalocyanine compounds, which has attracted increasing interest, is their use as the chemically-sensitive component in gas microsensors. This interest primarily stems from the high sensitivity of the phthalocyanine compound's electrical properties upon gas adsorption. In a recent review article, Wright provides a thorough discussion of gas adsorption and its effect on the electrical properties of the phthalocyanine compounds (26).

In this research, the change in the electrical properties of metal-substituted phthalocyanine thin films upon the sorption of a gas is capitalized upon as the basis for quantitative gas detection. Therefore, the purpose of this chapter is to review both the electrical and gas adsorption properties of the phthalocyanine compounds. To accomplish this objective, this chapter begins with a discussion of the structure of the metal-susbstituted phthalocyanine compounds and the effects of structural variation on the gas adsorption properties. Following this introduction to the phthalocyanine compound's structure, their electrical properties, including a description of the prevalent models of charge transport in these materials, are discussed. The final section of this chapter describes the experimental results characterizing gas adsorption on the phthalocyanine compounds.

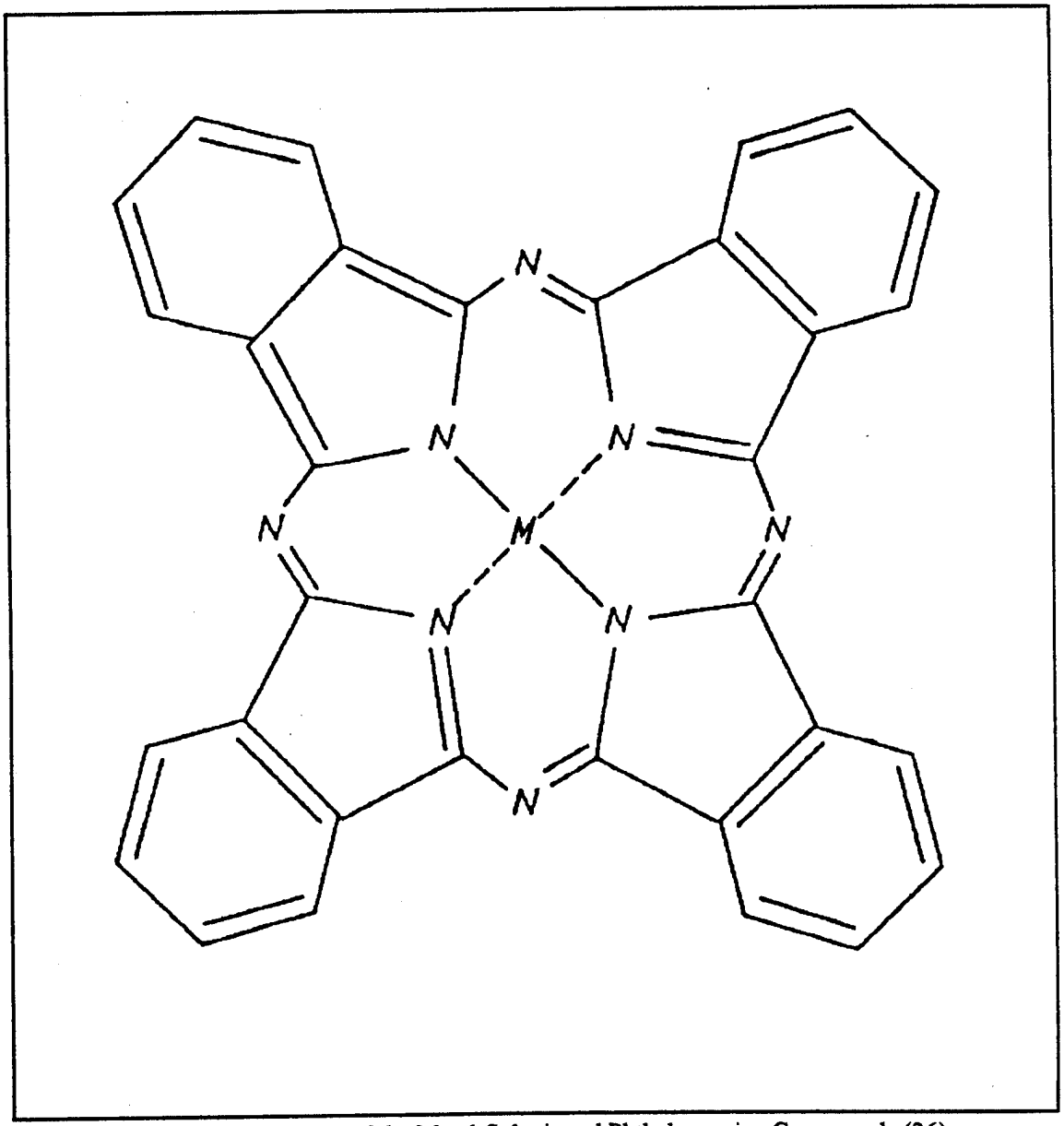


Figure II-1. Chemical Structure of the Metal-Substituted Phthalocyanine Compounds (26).

Adsorption Dependence on the Structure of the Phthalocyanine Crystals and Films

The structure of the metal-substituted phthalocyanine compounds, shown in Figure II-1 is characterized by the macrocyclic ring and the presence of a central metal ion (M). Over 70 different metal-substituted phthalocyanine compounds are known (37), and descriptions of many of the structures have been published (26). The structure of the three metal-substituted phthalocyanines used in this research, copper phthalocyanine (CuPc), nickel phthalocyanine (NiPc), and cobalt phthalocyanine (CoPc), are shown in Figures II-2 through II-4 (38, 39), and Table II-1 summarizes some of their important chemical, physical, and electrical properties. In unsubstituted phthalocyanine (H_2Pc), and in most of its metal complexes (MPc), the macrocyclic ring is planar to within 0.3 Å (37). Out-of-plane metal complexes may form when the metal atom is too large, as is the case for lead (40, 41), to fit into the cavity centered between the four central nitrogen atoms. The macrocyclic ring, common to all phthalocyanine compounds, generates an extensive delocalized π-electron system within the molecule. The π-electron system represents a highly polarizable electron cloud which is presumed to dominate the morphological, electrical, and gas adsorption properties of the phthalocyanine compounds. The intermolecular forces between these large polarizable molecules in the solid state are predominately attractive dispersive forces and short-range repulsive forces (26, 32). These forces permit different polymorphic structures with similar overall lattice energy. X-ray diffraction studies by Robertson (42) and Brown (38) on metal-free (H_2Pc), nickel (NiPc), copper (CuPc), and platinum (PtPc) phthalocyanine compounds demonstrated a monoclinic crystal structure in which the planar molecules are arranged in a characteristic "herring bone" arrangement of molecular stacks, as shown in Figure II-5. The stacking axis corresponds to the b-crystal axis. The interplanar spacings for CuPc, NiPc, and CoPc determined from diffraction studies are listed in Table II-2. There are two common polymorphs of the planar phthalocyanine compounds, named the α- and β-phases. As illustrated diagrammatically in Figure II-6, the two polymorphs differ by the angle made between the stacking axis and the normal to the molecular plane, which is approximately 25° for the α-phase and 45° for the β-phase (26, 38). The β-phase is more stable compared to the α- phase (26). Infrared spectroscopy (49) and differential scanning calorimetry (50, 51) have been used to follow the α-phase to β-phase transition. Sidorov reported that the complete conversion of α-phase CuPc and NiPc thin films to the β-phase required heating in vacuum at 280-300° C for 2 hours and for more than 5 hours, respectively (49). Differential scanning calorimetry results confirmed a phase transition temperature near 280° C for CuPc, NiPc, and CoPc. However, with CuPc a slow conversion to the β-phase may also occur at a temperature near 190° C (50, 51).

Table II-1. Chemical, Physical, and Electrical Properties of Copper Phthalocyanine (CuPc), Nickel Phthalocyanine (NiPc), and Cobalt Phthalocyanine (CoPc).

Property	CuPc	NiPc	CoPc	References
Chemical Formula	$C_{32}H_{16}N_8Cu$	$C_{32}H_{16}N_8Ni$	$C_{32}H_{16}N_8Co$	44
Molecular Weight	576	571	571	45
Crystalline Form	monoclinic	monoclinic	monoclinic	45
Melting Point (°C)	Do Not Melt			46
Sublimation Point (°C)	300 (10^{-7} Torr Vacuum) to 500 (1 atmosphere)			48
Density (g/cc)	1.61	1.59	1.53	45
Solubility	Soluble in Concentrated Sulfuric Acid Insoluble in Water			46
Resistivity (Ω·cm) 295K, 10^{-4} Torr, Single Crystal	1.2×10^{10} to 6.2×10^{13}	1×10^{10} to 4×10^{13}	9×10^{9} to 6.7×10^{12}	26
Relative Permittivity	2.4 to 5.1	-	-	47

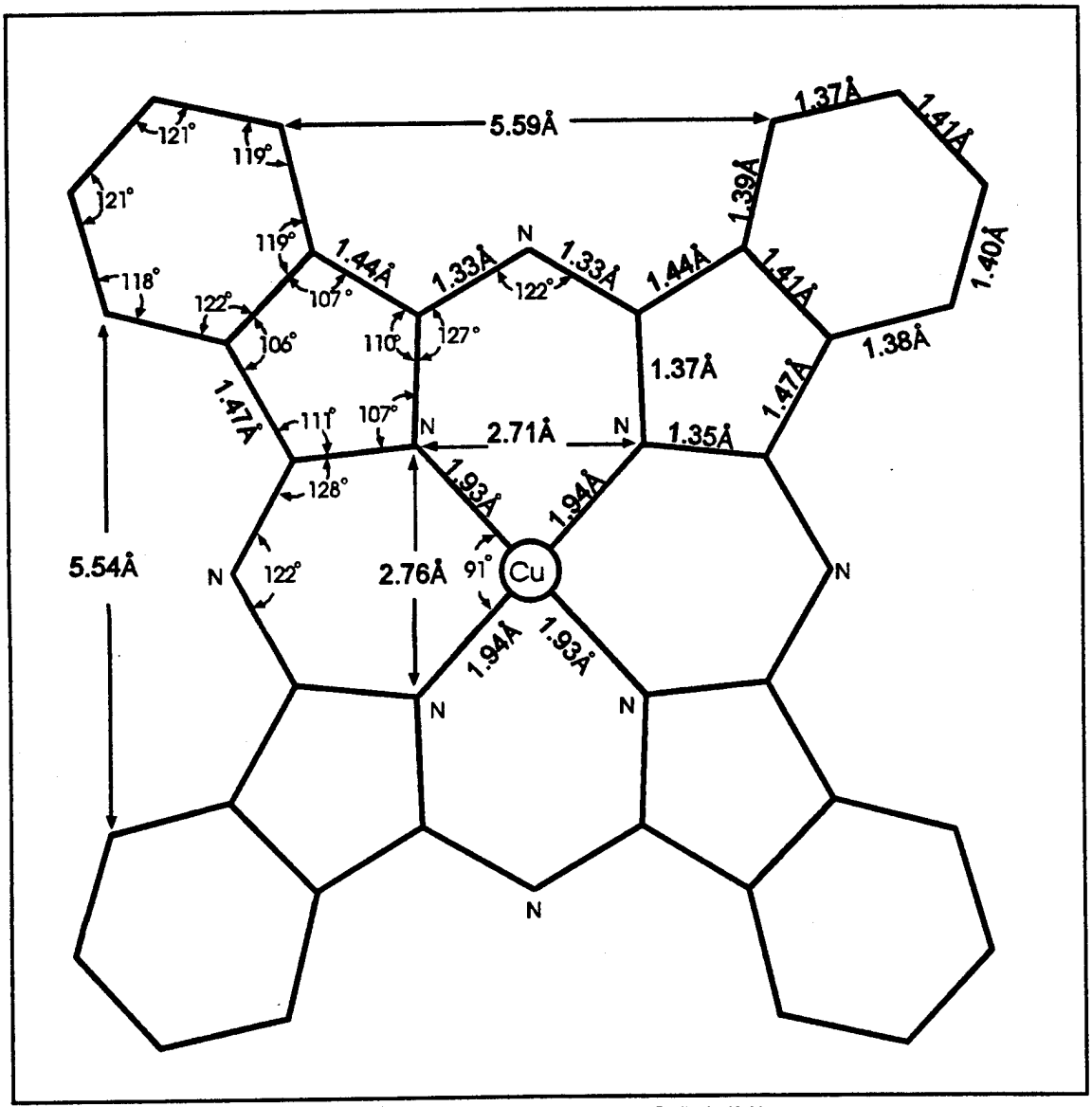


Figure II-2. Chemical Structure of Copper Phthalocyanine (CuPc) (38).

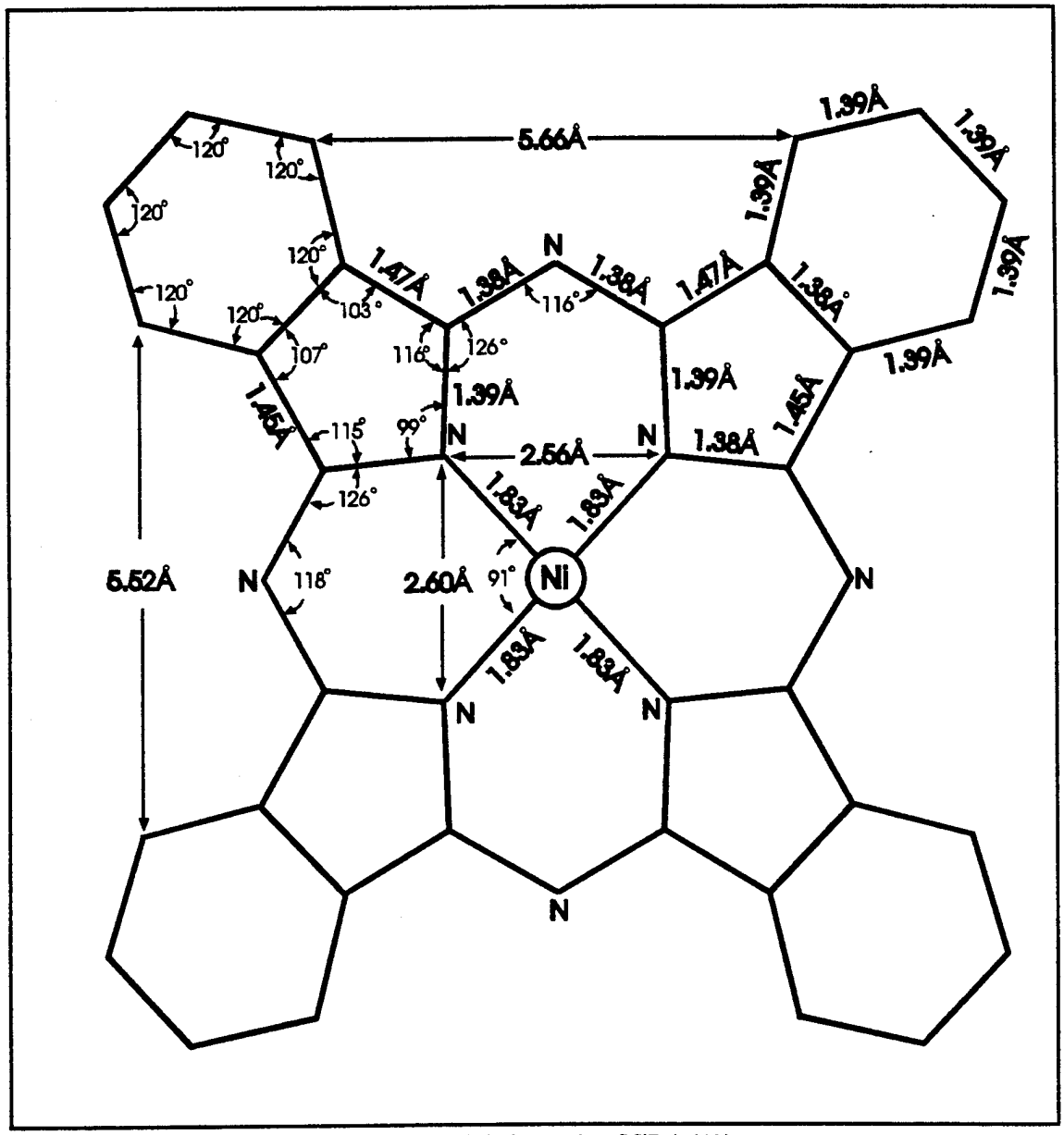


Figure II-3. Chemical Structure of Nickel Phthalocyanine (NiPc) (43).

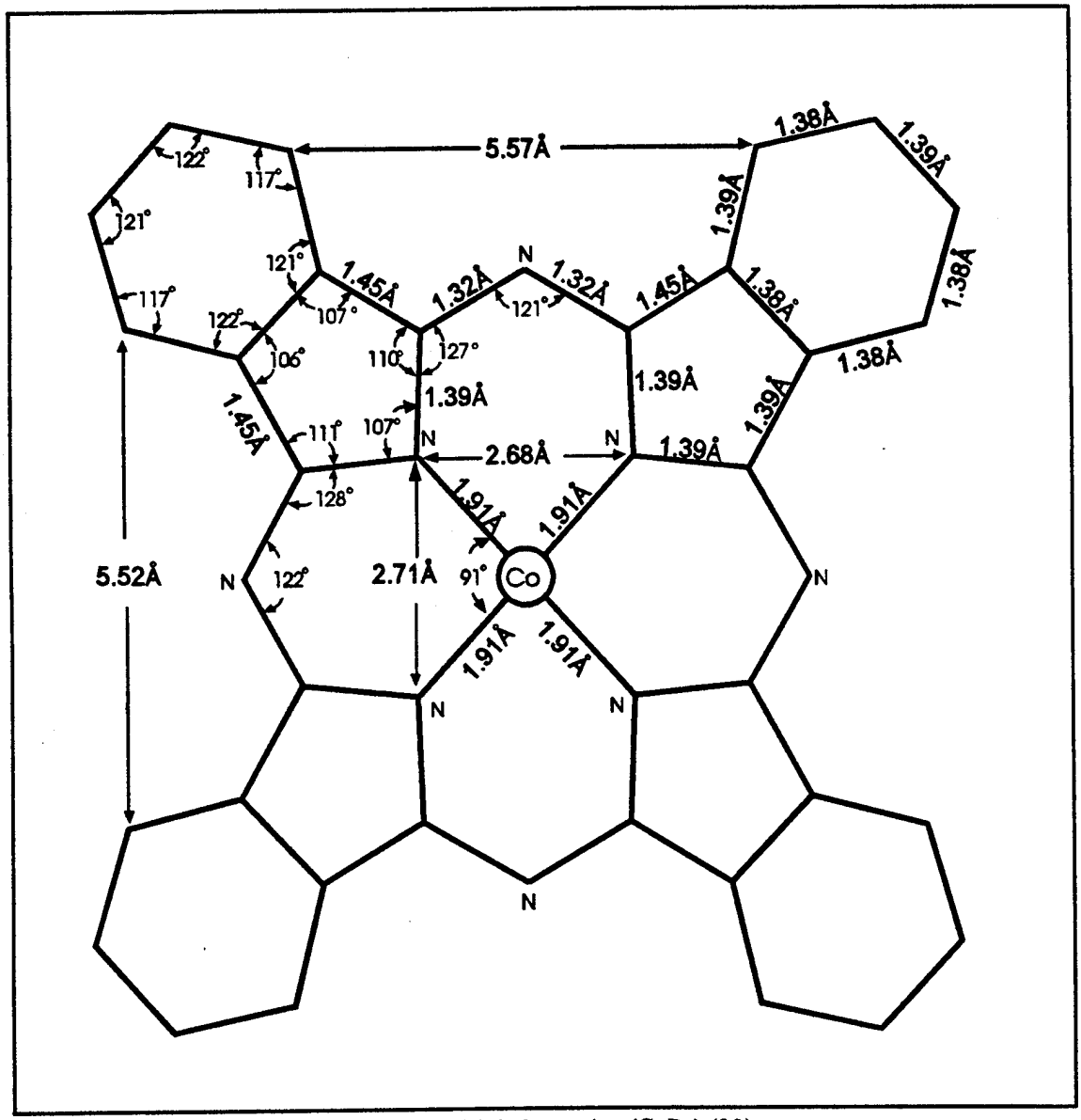


Figure II-4. Chemical Structure of Cobalt Phthalocyanine (CoPc) (39).

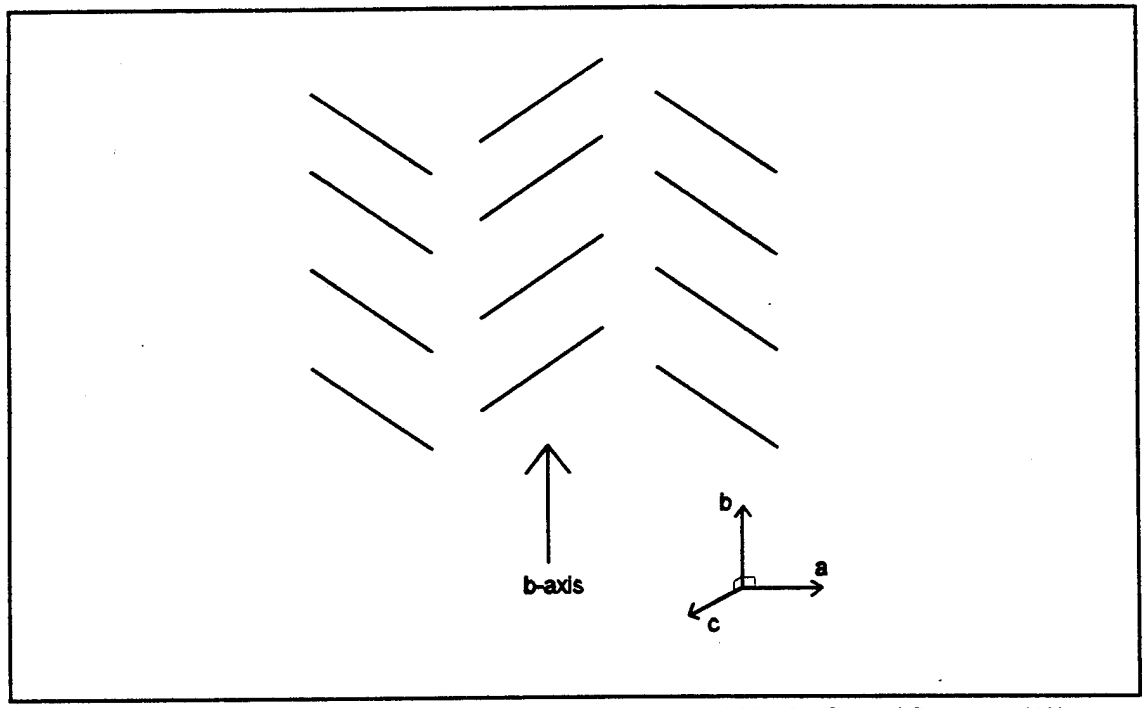


Figure II-5. Stacking of the Planar Phthalocyanine Molecules within the Crystal Structure (42).

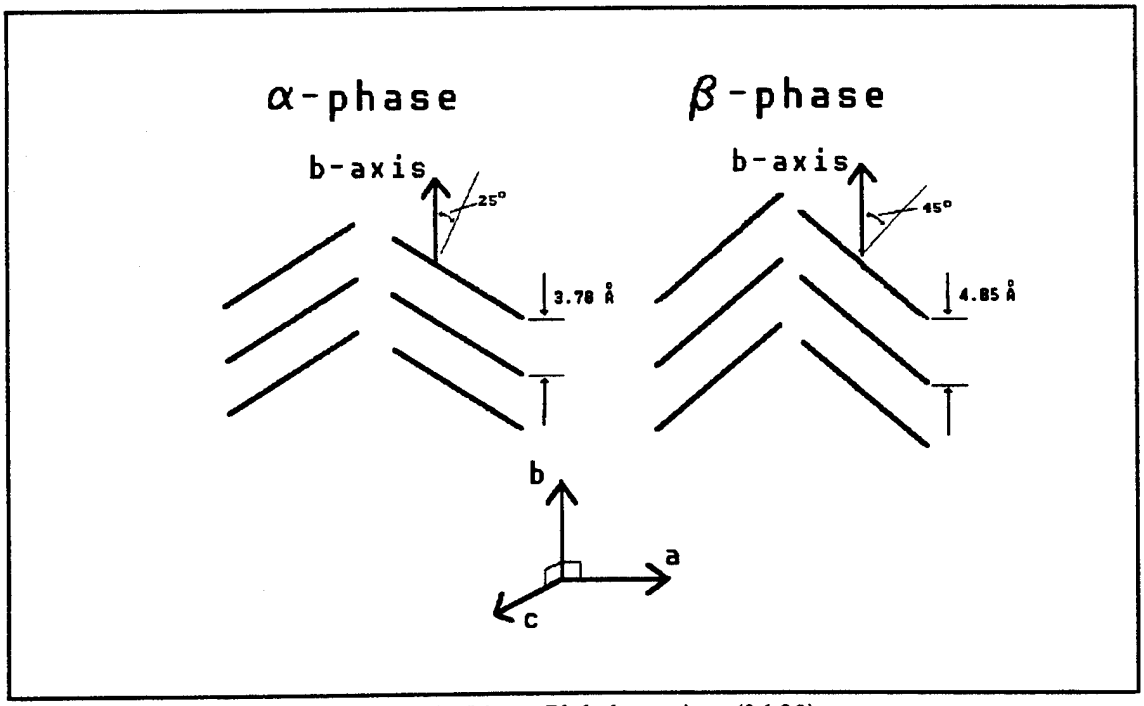


Figure II-6. The α- and β-Phases of the Planar Phthalocyanines (26,38).

Table II-2. Calculated Crystal Plane Spacings of CuPc, NiPc, and CoPc (53).

Miller Indices	Interplanar Spacing (Å)		
	CuPc	NiPc	CoPc
(200)	12.96	13.07	12.94
(002)	11.96	12.13	12.04
(202)	8.76	8.54	8.80
(400)	6.48	6.54	6.47
(004)	5.98	6.07	6.02
(402)	5.68	5.54	5.69
(600)	4.32	4.34	4.31

The structural properties of importance in gas adsorption is the large delocalized π-electron system, the presence of hetero-atoms (nitrogen), and the central metal ion. The highly-polarizable electron cloud of π electrons results in strong van der Waals interactions with adsorbate molecules. Furthermore, the low ionization energy of these electrons make the phthalocyanine compounds good electron donors which favors charge-transfer interactions with electron acceptor gases. Charge-transfer interactions are also favored by the high polarization energy of the phthalocyanine compounds. The polarization energy, defined as the difference between the gas phase ionization energy and the energy required to remove an electron from the bulk of the solid phase, stabilizes the products of a charge-transfer process (26). Small differences in the ionization and polarization energies are observed for different metal-substituted phthalocyanines (26). The presence of the nitrogen atoms in the phthalocyanine structure results in a non-uniform electron distribution within the π-electron system. Theoretical calculations of the charge distribution (52) suggest that the divalent metal ions accept a substantial portion of the electrons, leaving only a small effective positive charge on the ions. The nitrogen atoms and the outermost carbon atoms also gain a larger share of the electrons at the expense of the inner carbon atoms. Based on these calculations, two adsorption sites on the molecule that favor charge-transfer interactions are proposed; one site at the center and the other site at the extreme outside edge, as shown in Figure II-7 (26).

Although the extensive single crystal structure information is necessary for understanding the properties of the phthalocyanine compounds, it is insufficient for characterizing gas adsorption on a phthalocyanine thin film surface. The surfaces of phthalocyanine thin films present a range of different gas adsorption sites corresponding to the different crystal faces, edges, and corners. These sites are not considered in the ideal crystalline bulk analyses. Inclusion of surface heterogeneity leads to a distribution of adsorption interaction energies and determines an effective surface energy for each available adsorbing gas molecule. For example, adsorption onto the center of phthalocyanine molecules within a stack may be blocked by neighboring phthalocyanine molecules. This situation leaves only the outer edges of the molecule free for adsorbing gases. In contrast, the phthalocyanine molecule at the end of a stack has a significant portion of its surface available for adsorption. Since the film properties may differ significantly from either single crystal or amorphous morphologies, and since gas microsensors use phthalocyanine compounds primarily in the form of thin films, numerous studies have been performed to characterize their structural properties.

The need for thin film characterization has been acknowledged with a large number of scanning electron microscopy (SEM) and transmission electron diffraction (TED) studies that have yielded

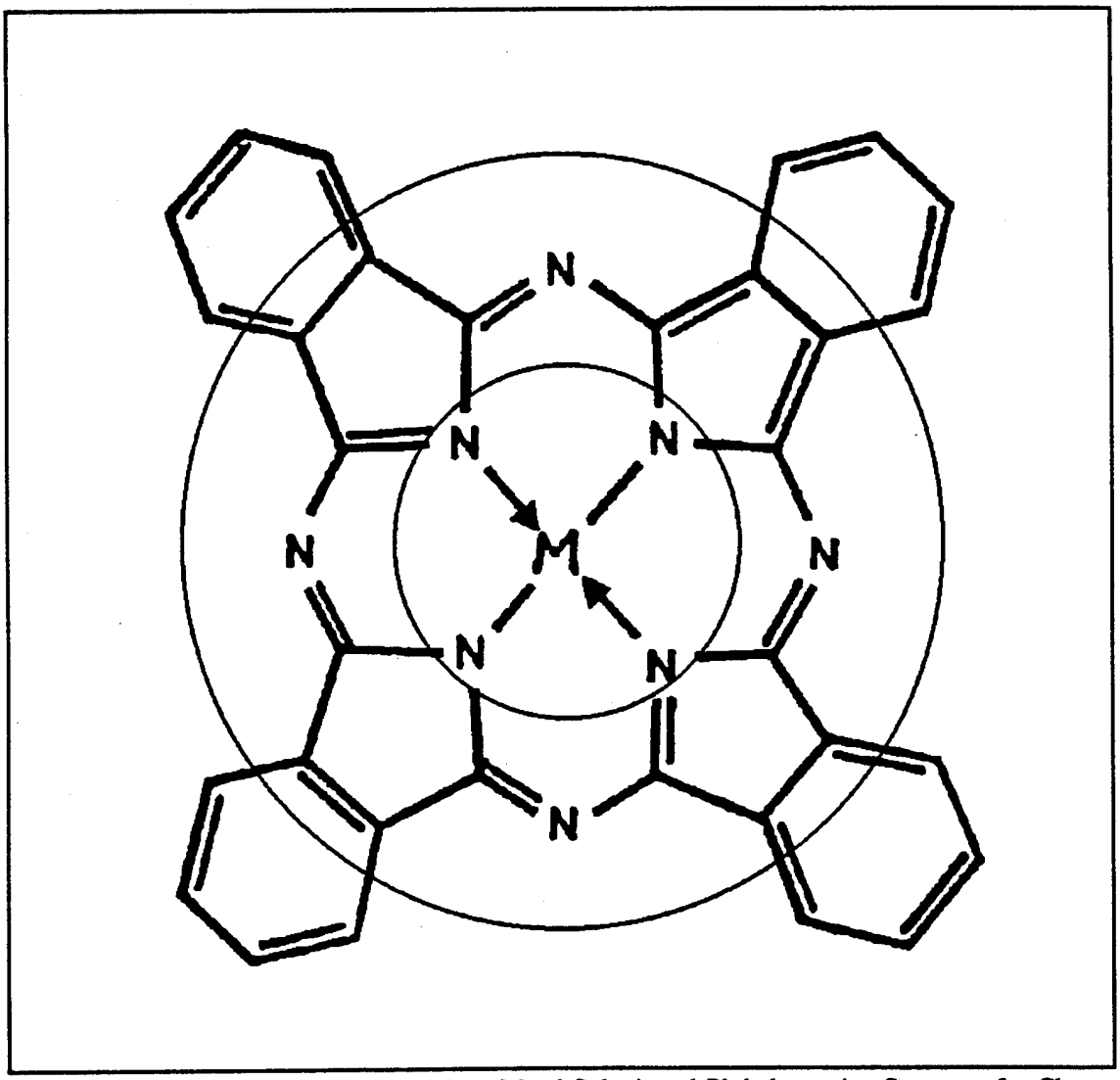


Figure II-7. Favorable Locations within a Metal-Substituted Phthalocyanine Structure for Charge Transfer Interactions. Charge Transfer Interactions are Favored Inside the Inner Circle and Outside the Outer Circle (26).

information on morphology, crystal structure, orientation of crystallites within a film, and lattice imaging (53-68). The results of these studies have shown that the phthalocyanine thin films are sensitive to the conditions of film growth and to subsequent thermal and chemical treatment. Phthalocyanine films are usually prepared via vacuum thermal sublimation of the powder onto a substrate. The structure of the thin films depends on the following conditions during growth: substrate temperature (53, 68, 69, 70), substrate material (55, 56, 63), sublimation rate (47), sublimation temperature (26), and background pressure (47). The film characteristics also depend on the type of metal ion present in the phthalocyanine compound being deposited. According to Wright, the substrate temperature has a more significant effect on the film structure compared to the substrate material (26). Sublimation at low pressure onto substrates maintained at room temperature yields the meta-stable α-phase (71), which may be converted to the β-phase with a subsequent heat treatment (50, 51, 54, 58, 59, 72) or solvent treatment (66). Wright's conclusion concerning these studies was (26):

> All these studies of the factors influencing the structure of phthalocyanine films serves to emphasize the need to control and specify the conditions of film preparation and subsequent treatment in all studies involving adsorption onto film surfaces and the consequent effects on electrical properties. Ideally such control and specification should be accompanied by characterization of the structure and morphology of these films as well as their surface chemical composition to ensure that results are strictly comparable between investigators.

The structure and morphology of the phthalocyanine thin films and their effect on gas adsorption properties have been studied by infrared spectroscopy (49, 73-92). The published spectra of α-phase CuPc, NiPc, and CoPc thin films deposited on potassium bromide (KBr) substrates (IR windows) are shown in Figures II-8 through II-11, inclusive (49). As a result of the different crystal structures, the phthalocyanine compounds and their polymorphs have been identified by their infrared spectra (49, 73-82). Table II-3 compares the optical absorption frequencies[1] of CuPc, NiPc, and CoPc in the two different crystalline forms. The optical absorption changes in the infrared spectra have been used to identify the thermally induced α-to-β transition (49) and the adsorption of water (83, 84, 86), pyridine (84, 86), ammonia (84, 87), hydrazine (84, 87), phenol (84, 86), methanoic acid (86), ethanoic acid (83), HCl (83), HBr (83), nitric oxide (88, 89), and nitrogen dioxide (90, 91, 92). Sidorov and Kotlyar

---

[1]In the field of infrared spectrophotometry, optical absorption frequencies are often reported in wavenumbers (cm^{-1}). A frequency expressed in wavenumbers can be converted to units of ordinary frequency (s^{-1}) by multiplying by the speed of light.

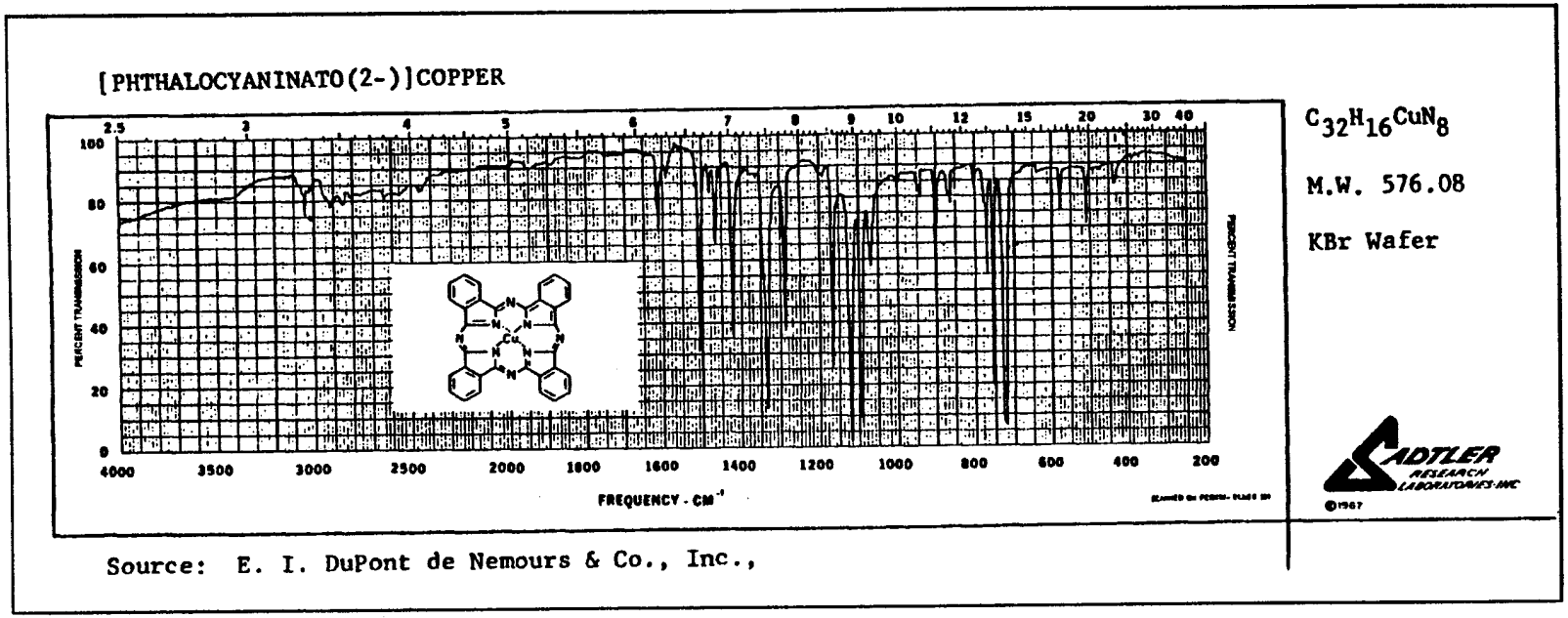


Figure II-8. Infrared Spectrum for α-Phase Copper Phthalocyanine (73).

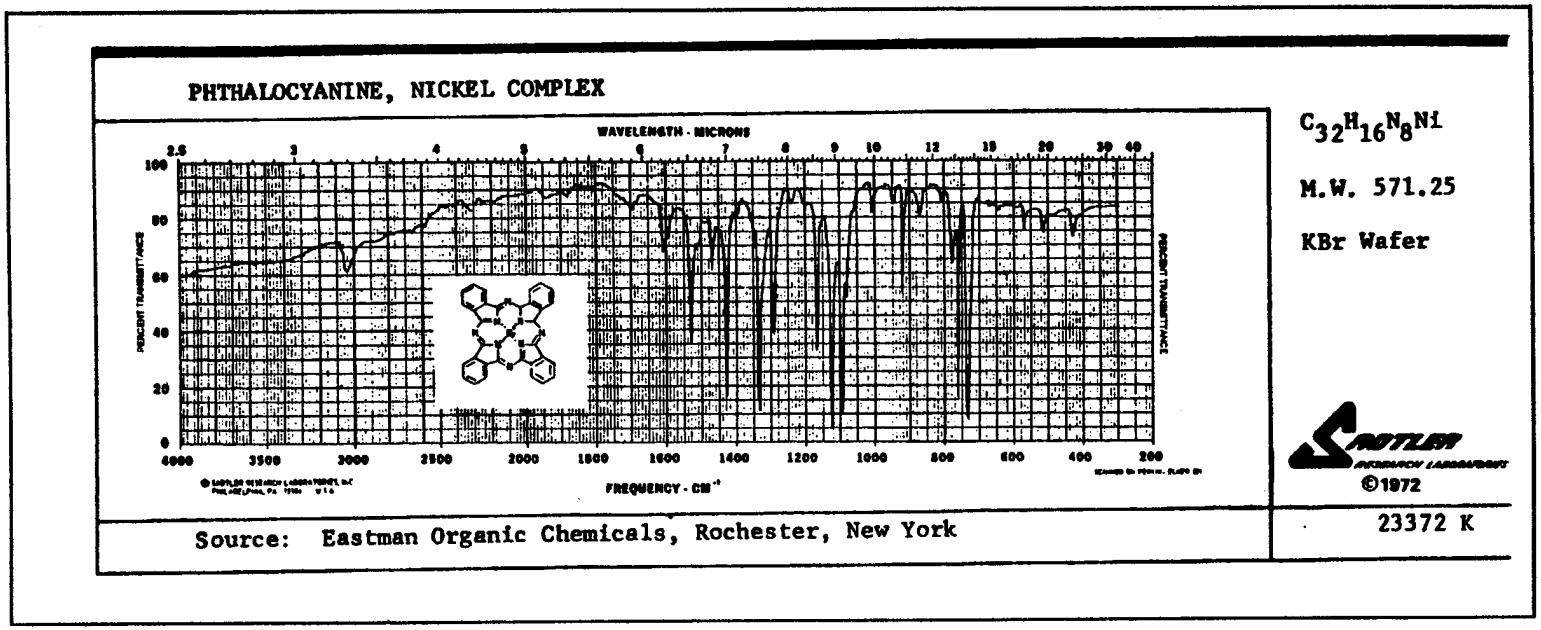


Figure II-9. Infrared Spectrum for α-Phase Nickel Phthalocyanine (74).

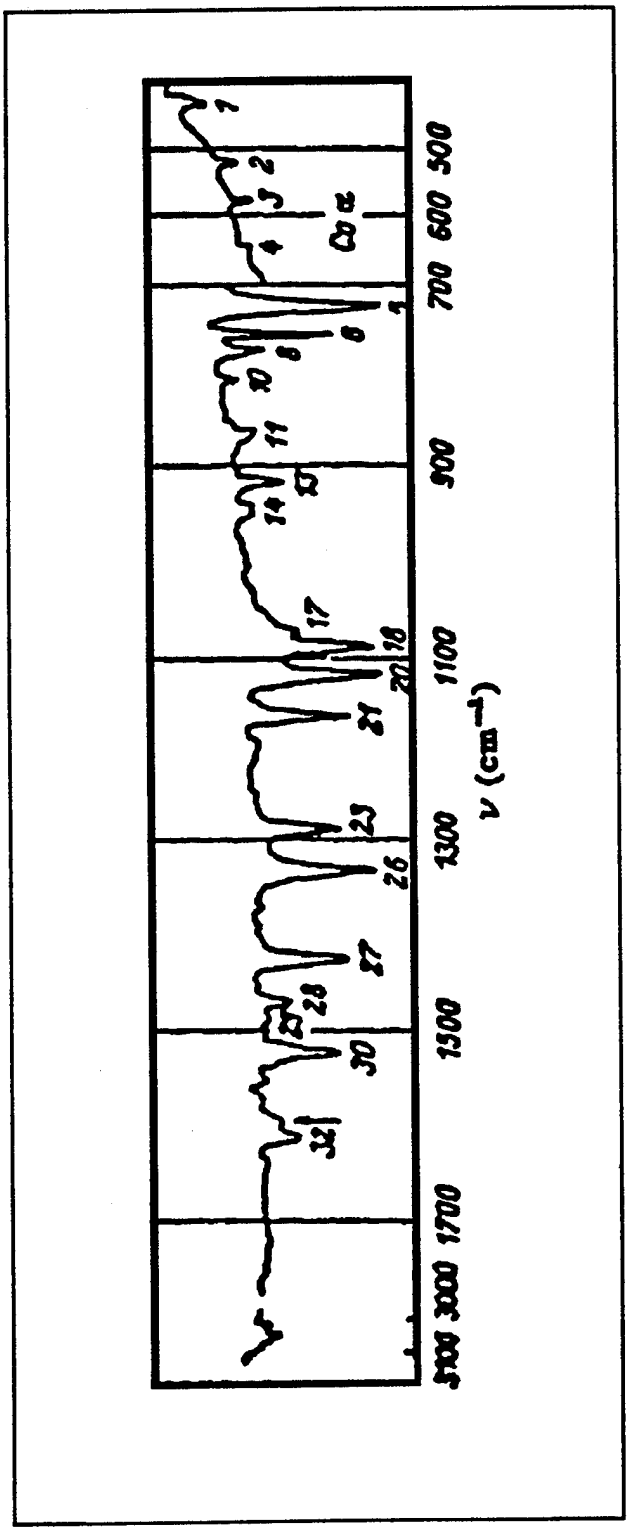


Figure II-10. Infrared Spectrum for α-Phase Cobalt Phthalocyanine (49).

Table II-3. Infrared Absorption Frequencies of the α- and β-Phase Metal-Substituted Phthalocyanine Compounds (49).

No.	Metal-Substituted Phthalocyanine Compounds and their Crystalline Phase						No.						
	CuPc		NiPc		CoPc			CuPc		NiPc		CoPc	
	α	β	α	β	α	β		α	β	α	β	α	β
1	434	436	435	436	434	436	16	-	957	-	956	-	956
2	507	507	520	520	520	520	17	1068	1067	1078	1078	1075	1078
3	575	575	575	575	575	575	18	1092	1089	1091	1089	1092	1089
4	643	641	646	645	645	645	19	-	1100	-	1100	-	1102
5	722	730	726	734	726	734	20	1121	1123	1122	1123	1121	1123
6	754	754	756	756	756	756	21	1165	1164	1165	1165	1165	1165
7	769	-	772	773	772	-	22	-	1174	-	1173	-	1174
8	-	780	-	780	-	780	23	1287	1287	1291	1291	1291	1291
9	802	802	806	804	805	805	24	1334	1334	1335	1335	1334	1334
10	864	-	862	-	863	-	25	1420	1419	1430	1428	1428	1427
11	870	-	867	-	868	-	26	1466	1465	1472	1471	1471	1471
12	-	877	-	877	-	877	27	1480	1480	1493	1493	1487	1487
13	900	900	917	917	915	915	28	1507	1506	1536	1536	1526	1525
14	940	-	940	-	940	-	29	1591	1589	1600	1598	1597	1597
15	949	949	948	948	948	948	30	1611	1609	1612	1611	1612	1611

reported that the rate of phase transformation was greatly influenced by the type of the central metal atom (49). The central metal atom also affected the adsorption of acidic gases (85). Whereas the magnesium, zinc, and iron phthalocyanine compounds interacted with HCl and HBr, the copper and metal-free phthalocyanine compounds would only interact with the more reactive HBr molecules. The interaction between these acids and the phthalocyanine compounds was attributed to a charge-transfer reaction with the central nitrogen atoms of the phthalocyanine ring. In a companion paper, Sidorov reported similar results for the adsorption of water on the Be and Mg phthalocyanine compounds (83). However, water adsorption was not observed on the Zn, Cu, Fe, Co, and Ni phthalocyanine compounds. Sauvage and Backer found that phenol, pyridine, and formic acid was adsorbed only on the α-phase, and not the β-phase of manganese phthalocyanine (86). These results were explained on the basis that the β-phase possesses a more compact structure. In the same study, they also found that exposure of MnPc to water and ethanol weakly perturbed its IR spectrum. For example, water exposure produced a weak peak at 1066 cm^{-1}, a shoulder at 1654 cm^{-1}, and enhancement of the intensities of all peaks. The latter change was interpreted as a splitting of the 1078 cm^{-1} band in the MnPc spectrum. The peak at 1654 cm^{-1} corresponded with a strong absorption band due to water at 1650 cm^{-1}. However, definite assignment was not made since this band was not removed upon subsequent heat treatment at 150 °C. These perturbations have been subsequently considered to be the result of minor structural changes, and not due to gas adsorption. Furthermore, the overall enhancement of all peak intensities suggested that the MnPc molecular stacking had become "looser", allowing the MnPc molecules to vibrate "more freely". Steinbach and Zobel studied the adsorption of hydrazine (N_2H_2) and ammonia (NH_3) on the phthalocyanines (87). FePc, which catalyzes the decomposition of hydrazine to ammonia and nitrogen, adsorbed hydrazine in both the α- and β-phase. Decomposition of the FePc-N_2H_2 complex produced α-FePc. In contrast to hydrazine adsorption, only the β-phase of FePc would adsorb ammonia. Furthermore, exposure of β-MnPc, β-CuPc, and β-ZnPc to either hydrazine or ammonia did not produce any observable changes in their IR spectra. Similar to the adsorption of ammonia on FePc, nitric oxide only adsorbs on β-phthalocyanines, and this result was attributed to the fact that the α-phase was more compact, and therefore, the central metal atom is less accessible for interaction with NO (89). This interpretation conflicts with Sauvage and Backer's assertion that the β-phase possesses a more compact structure. Electron microscopy studies have revealed that the molecular separation along the b-axis is smaller for the α-phase phthalocyanines (60). Sauvage and Backer do not support their interpretation with any X-ray or electron microscopy studies. The disappearance of the IR bands characteristic of the β-phase was interpreted as evidence of the bulk absorption of NO.

Several investigators have studied NO_2 adsorption on phthalocyanine thin films. Honeybourne and Ewen found that the exposure of α-H_2Pc to 10^3 Pa NO_2 in air (9900 ppm) caused extensive broadening of the infrared spectra (90). When the exposed sample was heated to 150° C, bands associated with irreversible nitration appeared at 1525, 1365, and 840 cm^{-1} (90). However, Sadaoka et al. found that β-CoPc and β-CuPc exposed at room temperature to 50 torr NO_2 developed new IR bands which were removed upon heating (91). CoPc infrared bands due to the adsorption of NO_2 were observed at 1590 (nitrosyl or bidentate nitrato), 1510 and 1005 (monodentate nitrato), 1460 (nitrito), 1400 and 1050 (NO_3^-) and 1265 (NO_2^-) cm^{-1}. In contrast, CuPc only had two bands associated with NO_2 adsorption: a band at 1460 cm^{-1} and another band at 1333 cm^{-1} which was also observed prior to NO_2 exposure. The exposed samples were heated stepwise to 300° C at 50° C intervals. After 10 minutes of heating in vacuo per step, the infrared spectrum was recorded. In the CuPc sample, the bands at 1460 and 1333 cm^{-1} disappeared upon heating to temperatures below 100° C, in agreement with the results of the thermal desorption experiments to be discussed later. In contrast, heating to 100° C had little effect on bands attributed to NO_2 adsorbed onto CoPc at room temperature. However, all the bands had disappeared upon heating to 250° C. Schoch and Temofonte reported the adsorption of NO_2 on NiPc and PbPc films deposited on NaCl substrates (92). As shown in Figure II-11, they found that the change in the IR spectra resulting from NO_2 adsorption on the phthalocyanine compounds was reversible, except for a band at 1360 cm^{-1}. This band, along with a small peak at 840 cm^{-1}, formed in the IR spectra of the uncoated (that is, no phthalocyanine thin film coating) NaCl substrate upon exposure to NO_2. Reversible spectral changes were observed over the band spanning 1600-1800 cm^{-1} due to NO_2 trapped in the film, and an extremely broad absorption over most of the mid-IR range resulting from free carriers created by charge transfer with the phthalocyanine ring. Schoch and Temofonte also estimated an optical detection limit of 100 ppm NO_2, which is much greater than the electrical detection limit of 1-10 ppb NO_2. They proposed that the anisotropy of the film's crystallites accounts for the difference in the electrical and optical detection limits. According to Schoch and Temofonte, the electrical conductivity is measured parallel to the needle axis, where the electrical conductivity resulting from NO_2 adsorption is greater compared to the other directions. In contrast, the optical measurements are averaged over all possible orientations throughout the bulk of the film.

Electrical Properties of the Phthalocyanines

Charge transport within the phthalocyanine compounds has generally been interpreted in accordance with two broad conduction models. The first is solid-state physics energy band theory, whose

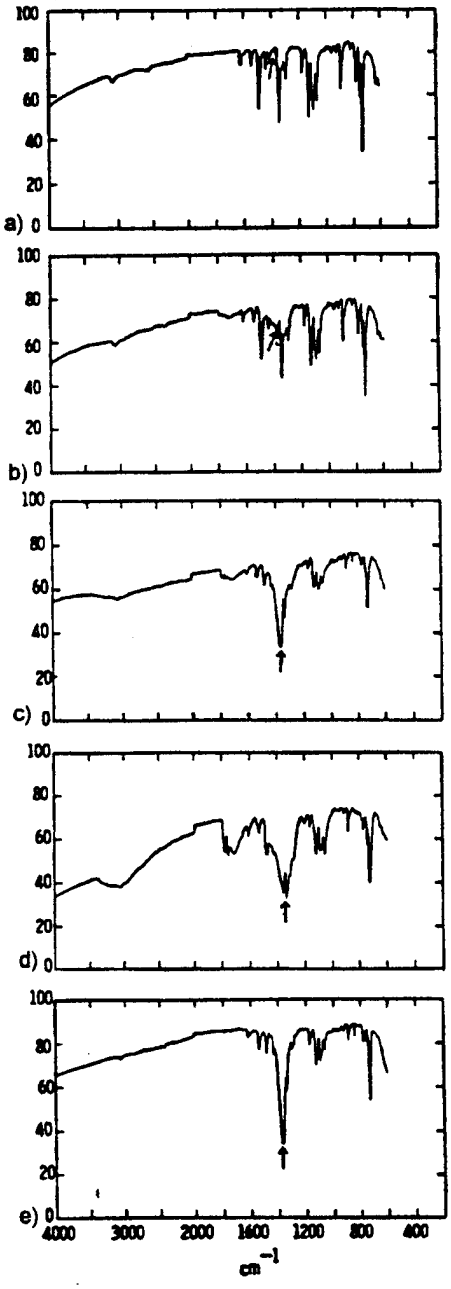


Figure II-11. IR Spectra of PbPc Films: a) As Prepared; After Exposure to b) 416 ppm NO_2, c) 1248 ppm NO_2, d) 2920 ppm NO_2, and e) After Bakeout. Arrows Mark the 1360 cm^{-1} Absorption Peak (92).

development is based upon the regular periodicity of atoms in a crystalline material. Charge transport in single crystal phthalocyanine compounds has been interpreted utilizing this model. However, in polycrystalline phthalocyanine thin films, conduction is modeled in terms of charge carriers hopping between localized states formed within the band gap of the material. The formation of these localized states results from the increased disorder in the film. These models have usually been applied to the analysis of DC electrical measurements. However, additional insight into the charge transport mechanisms can be obtained from the AC electrical properties of these materials. This section begins with a description of the two charge transport models and a discussion of the AC conductivity based upon these models. Following this general theoretical development, the theoretical and experimental data concerning charge transport in several phthalocyanine thin film candidates are reviewed. This review includes a discussion of the junction properties of phthalocyanine/metal electrode contacts.

Energy Band Theory. The fundamental premise of energy band theory is the crystalline structure of the material (93, 94). When atoms or molecules condense into a crystalline structure, a long-range periodic potential is defined by the atoms located at the crystal lattice sites. Kronig and Penney developed a model to determine the energy bands formed in a crystalline material. Their model considered a single electron within a lattice described as an infinite periodic one-dimensional square-well potential. In the one-electron approximation, Bloch had shown earlier that the wave function of a single electron in a periodic potential, $\psi_k(x)$, must have the form:

$$\psi_k(x) = u_k(x) \exp(-jkx) \qquad \text{(II-1)}$$

where $u_k(x)$ is a periodic function of x, k is the wavevector of a plane wave, and j equals $\sqrt{-1}$. Assuming a wave function of this form, Kronig and Penney's solution of Schrodinger's wave equation revealed a band structure where physically realizable wave functions are possible for only certain k values. This mathematical result can be interpreted in physical terms as allowed and forbidden energy bands.

Although the exact solution has not been realized, similar results have been obtained using approximate methods for actual crystals. One approach is the tight-binding approximation which assumes that the wave functions of adjacent atoms only interact to a small extent and, therefore, the crystal wave function is strongly influenced by the wave functions of the isolated atoms. That is, the electrons are "localized" to a particular molecule. As the isolated atoms condense to form the crystalline solid, the Coulomb interaction between the atomic cores and the overlap of the electron distributions

cause the discrete atomic energy levels to split into bands. The formation of the energy bands is illustrated in Figure II-12. The width of these bands is a function of the overlap of the atomic orbitals.

Solids may be generally classified into three groups: insulators, semiconductors and conductors. The energy band diagrams for each of these classes are illustrated in Figure II-13. The conduction and valence bands are defined according to their degree of electron occupancy. The conduction band is the lowest energy, empty or partially-filled band. The valence band is the highest energy, completely filled band. The energy band separating the conduction and valence bands is called the bandgap, E_g. In an insulator, the bandgap energy is large which reduces the probability of an electron acquiring sufficient energy to transition to an energy level in the conduction band. Since the conduction band is devoid of carriers, insulators are poor electrical conductors. In a semiconductor, the bandgap energy is not as large, and electrons are more readily promoted to the conduction band. An electron which is promoted to the conduction band leaves a hole (vacancy) in the valence band. Both the electron and hole will conduct an electrical current under the influence of an externally applied electric field. In a conductor, the highest energy band is partially filled or overlaps the valence band, and therefore, there is no electron energy transition barrier.

The carrier concentration in a material is determined by the energy state distribution for charge carriers and the probability of occupancy of each energy state. The energy state distribution is known as the density of states, *N(E)*. The probability that an electron occupies a state with energy, E, is given by the Fermi-Dirac distribution function, *F(E)*. The electron density in the conduction band, n, is obtained by integrating from the bottom of the conduction band ($E_C = 0$) to the top of conduction band, E_{top} (95):

$$n = \int_{E_C}^{E_{top}} N(E)F(E)dE \qquad \text{(II-2)}$$

where the Fermi-Dirac distribution function, *F(E)*, is given by (95):

$$F(E) = \frac{1}{1 + \exp\left[(E - E_F)/k_B T\right]} \qquad \text{(II-3)}$$

where E_F is the Fermi energy level, k_B is Boltzmann's constant, and T is the absolute temperature in degrees Kelvin. When the Fermi energy level is more than $3k_BT$ below the conduction band edge, the

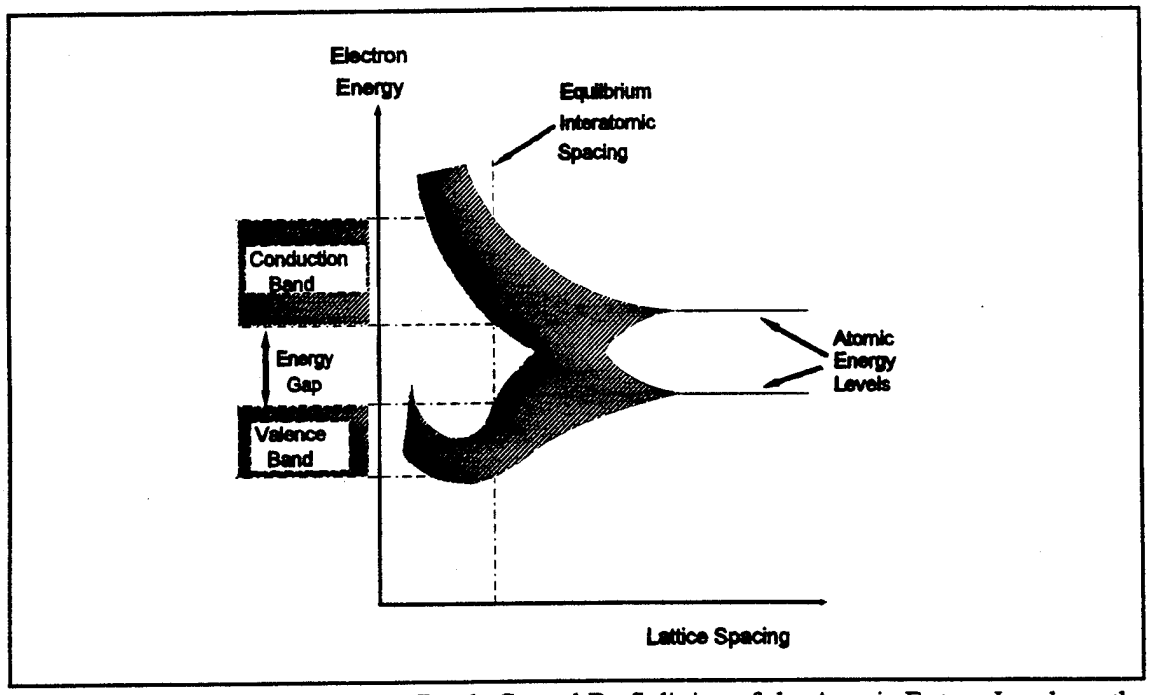


Figure II-12. Formation of Energy Bands Caused By Splitting of the Atomic Energy Levels as the Interatomic Spacing Decreases (95).

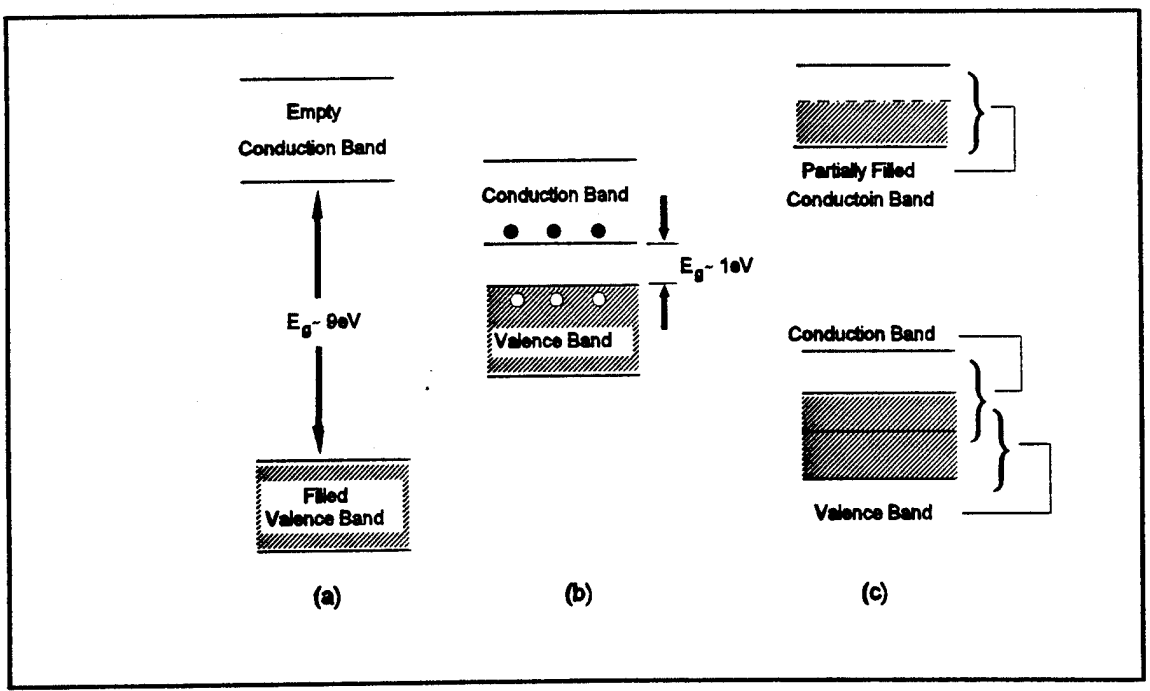


Figure II-13. Schematic Energy Band Representations of: (a) an insulator, (b) a semiconductor, and (c) a conductor (95).

Fermi-Dirac distribution function, *F(E)*, can be approximated by the Maxwell-Boltzmann distribution. Using this approximation, the electron density, n, is given by (95):

$$n = N_C \exp\left[-\frac{E_C - E_F}{k_B T}\right] \tag{II-4}$$

where N_C, the effective density of states in the conduction band, is equal to (95):

$$N_C \equiv 2\left[\frac{2\pi m_n k_B T}{h^2}\right]^{3/2} \tag{II-5}$$

where m_n is the effective electron mass, and h is Planck's constant. A similar expression for the hole density, p, in the valence band is given by (95):

$$p = N_V \exp\left[-\frac{E_F - E_V}{k_B T}\right] \tag{II-6}$$

where N_V, the effective density of states in the valence band, is equal to (95):

$$N_V \equiv 2\left[\frac{2\pi m_p k_B T}{h^2}\right]^{3/2} \tag{II-7}$$

where m_p is the effective electron mass. Applying the law of mass action, the intrinsic carrier concentration, n_i, in a semiconductor is given by:

$$n_i = \sqrt{N_C N_V}\, \exp\left[-\frac{E_g}{2k_B T}\right] \tag{II-8}$$

where E_g is the energy gap between the valence and conduction bands. Conduction in a material depends not only upon the concentration of free carriers, but also on their mobility. Electrons moving within a material collide with lattice atoms, impurity atoms, and other scattering centers. The average time between collisions is called the mean free time between collisions, τ_c. Upon the application of an external electric field, E, the electrons acquire an average drift velocity, v_d, given by (95):

$$v_d = \frac{q\tau_c}{m_n} E \tag{II-9}$$

where q is the charge on an electron. The proportionality constant between the drift velocity and the applied electric field, E, is defined as the mobility, μ. The mobility depends on the carrier type, and it is generally much greater for electrons compared to holes. In addition, the mobility depends on temperature, where higher temperatures increase lattice scattering, but decrease impurity scattering.

The applicability of energy band theory to describe electrical conduction in a material needs to be questioned when the degree of localization of the charge carrier to a particular atom/molecule is large. The localization is a function of the degree of atomic/molecular orbital overlap between nearest-neighbors within the lattice. For large orbital overlap, energy band theory is more appropriate. Large orbital overlap requires the presence of long-range order over distances of 10^5 to 10^8 Å within the material (96). As a result of the large overlap, the electronic wavefunction is distributed across several adjacent atoms/molecules, and the charge carrier is delocalized. Thus, the mean free path and the corresponding mobility of the charge carrier are large. Estimates of the charge carrier mobility required for energy band theory to be applicable are on the order of 1 $cm^2/V \cdot s$ (37, 96). A mobility of 1 $cm^2/V \cdot s$ corresponds to a mean free path comparable to the lattice spacing (96). When the extent of orbital overlap is small, a localized state model, where conduction occurs through a hopping mechanism, is more appropriate.

Hopping Model of Conduction. The energy band structure of crystalline materials is a direct consequence of the long-range periodic structure. In polycrystalline and amorphous materials, this long-range order is lost, but the local structure retains a short-range order similar to the local structure of crystalline materials. The loss of long-range order within the material leads to the formation of localized states (97). However, since the short-range order is retained, the concept of the density of states developed for crystalline materials is also applicable to noncrystalline solids (97). The existence of localized states is consistent with the tight-binding approximation for calculating band structures (37). Similar to crystalline materials, hopping conduction in noncrystalline materials is closely tied to the energy band structure and the density of energy states.

Davis and Mott postulated a model based on the formation of localized states at the normal band edges and the formation of a band near the Fermi energy level within the bandgap (97). The localized states at the band edges form tails which extend a few tenths of an eV into the forbidden energy gap. The Davis-Mott energy band diagram is shown in Figure II-14 where E_C and E_V denote the energy levels at the edges of the conduction and valence energy bands, respectively, E_F denotes the Fermi energy level, and the shaded regions represent the continuum of localized energy states. The extent to which the tails extend into the bandgap are denoted by E_A and E_B. The energy levels, E_C and E_V, denote the sharp

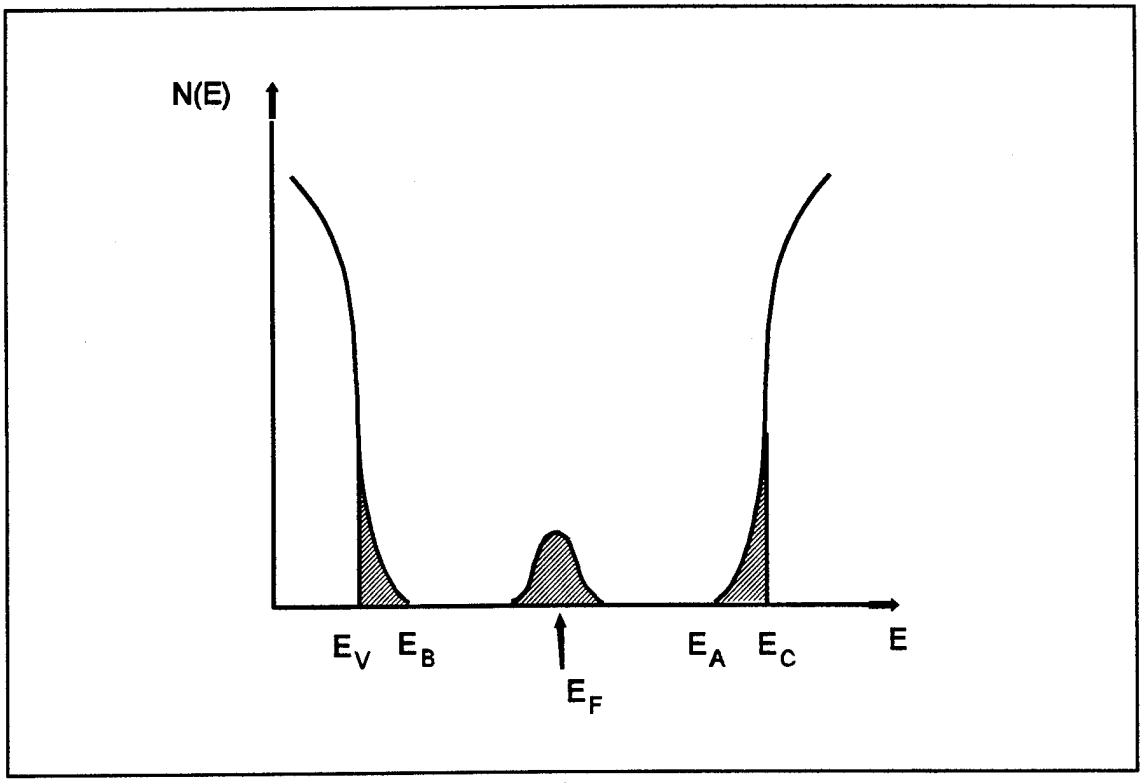


Figure II-14. Davis-Mott Energy Band Model (97).

transitions from the localized states within the tails to the extended states within the valence and conduction bands. An abrupt decrease (by several orders of magnitude) in the carrier mobility accompanies the transition from the extended to the localized states (97). Since localized states exist between E_C and E_V, and conduction within the localized states is severely mobility limited, the energy interval between E_C and E_V is referred to as a mobility gap rather than an energy gap (96).

Three different charge transport mechanisms are possible within the Davis-Mott model (97). In an analogous manner to conduction in a crystalline material, charge transport may occur in the extended states. Charge transport may also occur between localized states by a thermally-activated energy exchange between charge carriers and phonons. The third mechanism for charge transport within the Davis-Mott model is phonon-assisted charge carrier tunneling between localized states near the Fermi energy level.

Assuming a thermally-activated hopping process, the mobility is expected to be of the form (97):

$$\mu_{hop} = \mu_0 \exp\left[-W(E)/k_B T\right] \qquad \text{(II-10)}$$

where μ_{hop} = hopping mobility

$W(E)$ = mobility thermal activation energy.

The pre-exponential, μ_0, is given by (97):

$$\mu_0 = (1/6)\,\nu_{ph}\, q\, R^2/(k_B T) \qquad \text{(II-11)}$$

where ν_{ph} = phonon frequency,

q = fundamental unit of charge

R = hopping distance.

The phonon frequency depends upon the extent of molecular orbital overlap (37). A similar expression for the hopping mobility can be derived by using a thermally-activated hopping probability and the lattice constant to establish the hopping diffusion constant, and then applying the Einstein relation to obtain the mobility (37, 97).

According to Nagels, Mott considered two separate cases for conduction within the localized states depending upon whether the states were located in the band tails or in a band near the Fermi energy

level. For conduction within the band tails, Mott assumed a fixed hopping distance, and a density of states function which varied with energy to some positive integer power, s, to derive the following expression for electron conduction (97):

$$\sigma_{hop} = \frac{\sigma_0}{k_B T}\left(\frac{kT}{\Delta E}\right)^s C \exp\left[-(E_A - E_F + W)/k_B T\right] \qquad \text{(II-12)}$$

where $\sigma_0 = (1/6)\nu_{ph} q^2 R^2$

W = energy difference between localized states

$\Delta E = E_C - E_A$

and the constant, C, is given by:

$$C = s! - (\Delta E/k_B T)^2 \exp(-\Delta E/k_B T)\left[1 + s(k_B T/\Delta E) + s(s-1)(k_B T/\Delta E)^2 + \ldots\right]. \qquad \text{(II-13)}$$

If electrical conduction is occurring through sites separated by a fixed hopping distance, and whose energies are located within a band of localized states near the Fermi energy level, the hopping conductivity is given by (97):

$$\sigma_{hop} = \sigma_0 N(E_F) \exp(-2\alpha R) \exp(-W/k_B T) \qquad \text{(II-14)}$$

where α is a parameter representing the decay rate of the wavefunction at a hop site.

According to Nagels, once Mott had derived the hopping conductivity for sites separated by a fixed hopping distance, he then postulated the need for a variable range hopping mechanism. Mott argued that, as the temperature decreases, the number and energy of the phonons decreases. Therefore, phonon assisted hops between a given energy state, to a state with a much higher energy, becomes less likely compared to hops between more widely spatially separated sites with similar energy states. This situation gives rise to a distribution of hopping distances and the so called variable range hopping mechanism. Mott then derived the following expression for variable range hopping between sites with energies close to the Fermi energy level (97):

$$\sigma_{hop} = \sigma_0(T) N(E_F) \exp\left[-A/T^{1/4}\right] \qquad \text{(II-15)}$$

where the hopping distance, and, therefore σ_0, are now temperature dependent, and A is a constant. The expression for $\sigma_0(T)$ is given by (97):

$$\sigma_0(T) = \frac{q^2 \nu_{ph}}{2[8\pi\alpha k_B T N(E_F)]^{1/2}}. \qquad \text{(II-16)}$$

Although the $T^{1/4}$ dependence of $\ln(\sigma)$ has been widely observed, other experimental evidence suggests that these equations do not fully explain the observed electrical conduction mechanism (97). Departure from the model may, in part, be due to the simplifying assumptions made in the derivation of these equations. Mott's derivation neglected tunneling effects, electron-phonon interactions, and multiphonon processes, and he also assumed that the density of states is constant at the Fermi energy level.

AC Conductivity. Additional information concerning the mechanism responsible for electrical conduction can be obtained from the measurements of the AC conductivity. In the frequency range up to 10^8 Hz, conduction in the extended states does not depend on frequency (97). However, if the conduction is due to hopping between sites near the Fermi energy level, Austin and Mott (98) derived a formula relating the electrical conductivity to the angular frequency, ω, of an applied field that can be expressed as (97):

$$\sigma(\omega) = \frac{\pi}{3} q^2 k_B T [N(E_F)]^2 \alpha^{-5} \omega [\ln(\nu_{ph}/\omega)]^4 \qquad \text{(II-17)}$$

Since the derivative of $\ln(\sigma)$ with respect to $\ln(\omega)$ varies slowly over a wide range of frequencies, Equation (II-17) can be approximated as:

$$\sigma(\omega) \simeq const \cdot \omega^{s'} \qquad \text{(II-18)}$$

where the exponent, s', is defined as $d\ln(\sigma)/d(\omega)$, and is given by:

$$s' = 1 - \frac{4}{\ln(\nu_{ph}/\omega)}. \qquad \text{(II-19)}$$

According to Nagels, charge transport in the energy band tails should also obey Equation (II-17).

The conductivity's frequency dependence of a large number of materials obey Equation (II-18) over a wide frequency range with a value of $s' \approx 0.8$ (99-101). According to Johnsher, the large number of materials displaying this behavior encompasses all structural forms (single crystal, polycrystalline,

amorphous, glassy, and aggregates), all types of chemical bonds (covalent, ionic, and molecular), all possible types of polarizing species (dipoles, hopping electrons, and ions), and a wide range of geometrical configurations (bulk samples, thin films, even on the molecular scale, and intricate geometries) (101). The encompassing applicability of Equation (II-18) has served as the basis for criticism of the Austin-Mott model (97, 99). Furthermore, in some experiments where Equation (II-18) is obeyed, the Austin-Mott model fails to predict a reasonable value for the density of states (97).

An alternative development of Equation (II-18) is based upon a conduction model that considers hopping carriers in a polarizable medium (99). In this model, a carrier is thermally excited into an energy state that corresponds to the energy of a polarized empty state. The carrier then undergoes a tunneling transition into an empty polarized energy state. Through a relaxation process, the polarization energy is lost to the surroundings, and the carrier now occupies the new site. At equilibrium, the thermal energy gained by the carrier exactly balances the polarization energy lost to the surroundings following the transition to the new site. However, under the influence of an externally applied electric field, there is a net energy loss required for transitions that occur in excess of the equilibrium transition rate. This loss is proportional to the magnitude of the polarization, and it is independent of the rate at which the polarization is established.

The polarization is related to the applied electric field by a complex frequency-dependent quantity called the electric susceptibility, $\chi(\omega)$. The electric susceptibility may be expressed as:

$$\chi(\omega) = \chi'(\omega) - j\chi''(\omega) \qquad \text{(II-20)}$$

The imaginary part of the electric susceptibility, $\chi''(\omega)$, is defined as the dielectric loss, and it is related to the AC conductivity by the equation,

$$\sigma(\omega) = \epsilon_0 \omega \chi''(\omega) \qquad \text{(II-21)}$$

where ϵ_0 is the permittivity of free space. As discussed above, the energy loss is independent of frequency, but is proportional to the magnitude of the polarization and, therefore, the loss, $\chi''(\omega)$, must be proportional to the magnitude of $\chi(\omega)$. This observation implies that the loss is proportional to $\chi'(\omega)$. Furthermore, $\chi'(\omega)$ and $\chi''(\omega)$ are Hilbert transforms of each other (99, 102). The properties of Hilbert transforms require that the real and imaginary parts of $\chi(\omega)$ satisfy the following equations (99):

$$\chi''(\omega) = A \, \mathrm{sgn}\,(\omega) \, |\omega|^{n-1} \qquad \text{(II-22)}$$

and

$$\chi'(\omega) = A \tan(n\pi/2) |\omega|^{n-1} \qquad \text{(II-23)}$$

where

$$\text{sgn}(\omega) = \frac{|\omega|}{\omega}, \qquad \text{(II-24)}$$

A is a constant, and the exponent satisfies the condition, $0 < n < 1$. The conductivity expression obtained by combining Equations (II-21) and (II-22) possesses the same power law frequency dependence derived from the Austin-Mott model. While this approach considered hopping between two identical states separated by a fixed hopping distance, any real system will possess some distribution of energy states and hopping distances and, therefore, the loss must be summed over these distributions.

Phthalocyanine Electrical Properties. The electronic energy band structure of a few phthalocyanine compounds have been calculated. The calculated electronic structure of an isolated metal-free phthalocyanine molecule has served as the basis wavefunction in tight-binding calculations of the crystal band structure. (37). The crystal band structure is highly anisotropic with bandwidths along the b^{-1} direction of the reciprocal lattice ($\approx$ 0.2 eV for holes, and $\approx$ 0.6 eV for electrons (103)) approximately an order of magnitude greater than along the other two crystallographic axes. The bandwidth of an energy band is defined as the difference between the maximum and minimum allowed energy levels within the 1st Brillouin zone[2]. Therefore, a large bandwidth implies a smaller effective mass and greater mobility for the charge carrier. Calculations for the metal-free phthalocyanine cation and anion radicals revealed similar anisotropy in their band structures. The ionization potential and electron affinity were estimated from the calculated charge distribution to be 7.45 eV and 3.81 eV, respectively (104). Energy band structure calculations accomplished for platinum phthalocyanine (PtPc) again revealed a maximum bandwidth along the b^{-1} direction (105). However, in this case, the hole bandwidths (0.04-3.6 eV) were greater than the electron bandwidths (0.001-0.2 eV).

The mean square velocity of the charge carriers were calculated from the band structures of the phthalocyanine compounds. Assuming a constant mean free time for the charge carriers, the mobility will be proportional to the mean square velocity of the carriers. The carrier velocities calculated for

---

[2]This definition was inferred from the data and the corresponding discussion presented in reference (103).

metal-free phthalocyanine revealed that the electron mobility was greater than the hole mobility. However, the opposite result was reported for PtPc (105). As a result of the 5d-orbitals of the metal in PtPc, the hole band was much broader compared to that in the metal-free phthalocyanine, and the hole mobility was found to be greater than the electron mobility.

Numerous measurements of the charge carrier mobilities in the phthalocyanines have been performed, and they are summarized in Table II-4. The data in Table II-4 reveals that the carrier mobility in thin films is greatly reduced relative to the mobility in single crystals, and that the incorporation of a transition metal enhances the carrier mobility of metallated phthalocyanine relative to the metal-free variant. The greater structural disorder present in thin films is expected to increase the number of trapping and scattering centers and reduce the carrier mobility relative to that in single crystal materials. A decrease in the mobility may also be due to the incorporation of impurity atoms during film preparation (47). Gould performed space-charge-limited current measurements on thin films of CuPc prepared by vacuum sublimation at different ratios of chamber pressure-to-deposition rate (P/R). As the (P/R)-ratio increased, the mobility decreased, and the trapping concentration increased. He attributed these results to incorporation of nitrogen and oxygen impurity atoms from the ambient. The enhanced carrier mobility for the metallated phthalocyanines included in Table II-4 has also been observed with Hall mobility measurements in single crystal CuPc (115). The enhanced carrier mobility within CuPc was attributed to an interaction of the 3d-orbitals of the Cu atom with the π-electrons of the phthalocyanine ring, and to an out-of-plane interaction of the Cu atom with the nitrogen atoms located on phthalocyanine rings above and below it (115).

The charge carrier mobilities presented in Table II-4 for the single crystal phthalocyanines are consistent with the results of the energy band calculations. In order for an energy band model to be applicable, the product of the charge carrier relaxation time and the bandwidth must obey the Uncertainty Principle. The relationship between mobility and the relaxation time for a given direction is given by (104):

$$\mu = q \tau v^2 / k_B T \qquad \text{(II-25)}$$

where the carrier velocity, v, depends upon the shape of the energy bands (bandwidth) along a given direction of the reciprocal lattice. A lower limit for the mobility can be established given the calculated bandwidths and applying the Uncertainty Principle and Equation (II-25). This limit has been estimated to be approximately 1 $cm^2/V \cdot s$ (37). Experimentally determined mobilities of charge carriers within single crystal phthalocyanine compounds are of this order of magnitude. Since the mobilities in the thin

Table II-4. Electrical Mobilities of Several Phthalocyanine Compounds.

Phthalocyanine Compound	Crystalline State	Drift Mobilities	
		Magnitude ($cm^2/V \cdot s$)	Reference Number
H_2Pc	SC[1]	0.05-0.1	108
		μ_e~0.43-0.7, μ_h~0.24-0.56	107
		μ_e~1.4 μ_h~1.1 (373)	109
	TF[2]	10^{-2}-10^{-3}	110
CuPc	SC	7	111
	TF	10^{-4}	113
		0.02	114
		10^{-2}-10^{-4}	47
PbPc	SC	0.6-4.0	108

[1] SC - Single Crystal
[2] TF - Thin Film

films were two orders of magnitude less than 1 $cm^2/V \cdot s$, a hopping model may be more appropriate for discussing charge transport for these morphologies. Further support for the use of energy band theory to describe charge transport in single crystal phthalocyanine compounds has been motivated by the measurement of the mobility's temperature dependence. For temperatures spanning 290-600K, the mobility varies according to an equation of the form:

$$\mu = A T^{-n} \tag{II-26}$$

where A is a temperature-independent constant, n is equal to approximately 1.5, and T is the temperature in degrees Kelvin (107, 109, 112). This behavior suggests that charge transport is dominated by lattice phonon scattering (93).

The activation energy for electrical conduction in the phthalocyanine compounds has been measured (see Table II-5) and, in some cases, attributed to the bandgap energy of the semiconductor. However, care must be taken when interpreting activation energy measurements in terms of the bandgap, since the purity and crystallinity of the phthalocyanine samples is difficult to control (26). Barbe and Westgate (118) found that in metal-free phthalocyanine, electrical conduction was extrinsic for temperatures less than 360K, and intrinsic for higher temperatures. Below 360K, charge transport was dominated by a trapping level located 0.38 eV below the conduction band edge. Heilmeier and Harrison also found that conduction in CuPc single crystals under vacuum was extrinsic for temperatures below 373K, with an activation energy of 0.81 eV. When measured in an oxygen ambient, the activation energy was 0.81 eV over the entire temperature range. In phthalocyanine thin films, which are expected to have a greater density of traps, the observed activation energy was less than in single crystals.

The trap density in phthalocyanines has been measured with space-charge-limited current (SCLC) techniques and thermally-stimulated current measurements (47, 114, 118, 121). In a material where the charge transport is space-charge limited, the current obeys a power law dependence with respect to both applied voltage and film thickness. When discrete shallow traps are present in the film, the space-charge limited-current density is governed by (72):

$$J = 9/8\ \theta \epsilon \mu V^2/d^3 \tag{II-27}$$

where θ is the ratio of free to trapped carrier densities, μ is the charge carrier mobility, ϵ is the permittivity, V the applied voltage, and d the separation between electrodes. From the temperature dependence of the space-charge limited-current, the energy and the density of the trap states in single-crystal metal-free phthalocyanine were determined to be 0.38 eV and 5×10^{19} cm^{-3}, respectively, for

Table II-5. Electrical Conduction Activation Energies of Several Phthalocyanine Compounds.

Phthalocyanine Compound	Activation Energy (eV)	Reference Number
Metal-free	0.85	135
	1.12	116
	0.85	115, 117
	0.38 (<360K) 1.05 (>360K)	118
	0.62 (TF[1])	72
	0.80, 0.6, 0.80, 0.85 (TF)	119
Cu	0.79	135
	0.99	116
	0.81 (<373K) 1.03 (>373K)	115
	0.8	117
	1.0, 0.75, 0.75, 1.0 (TF)	119
Ni	0.74	135
	0.8	117
	0.95	116
	1.0, 0.7, 0.85, 0.95 (TF)	119
Co	0.6	135
	0.8	117
	0.45, 0.35, 0.5 (TF)	119
	0.44 (TF/air)	120

[1]TF - Thin Film
[2]If Not Tagged with TF, the Activation Energies are for Single Crystal

electrons, and 0.38 eV and 2×10^{12} cm^{-3} for holes (118). The density of hole trap states in thin films of metal-free phthalocyanine was four orders of magnitude greater than that measured in the single crystal (72). Space-charge-limited currents in CuPc thin films have been interpreted with a model possessing an exponential distribution of trap levels (47, 114). In this case, the current density is proportional to V^{l+1} and d^{2l+1}, where l is a temperature parameter characterizing the exponential trap distribution (47). The measured trap density depends upon the deposition conditions, and it varies between 5×10^{22} and 6×10^{24} cm^{-3}. The thermally-stimulated current measurements of the trap states in single crystal H_2Pc and PbPc agree well with the SCLC measurements with trap energies of 0.30 to 0.38 eV, and densities of 1×10^{13} to 2×10^{14} cm^{-3} (121).

AC Electrical Conduction in the Phthalocyanine Compounds. AC electrical conduction measurements have been used to further investigate charge transport in the phthalocyanine compounds. Eley and Parfitt measured the resistance of phthalocyanine powder samples with AC excitation to capacitively short the contact resistance between crystallites (122). In the 50 KHz to 1 MHz frequency range, the resistance decreased with increasing frequency, and approached a constant value for frequencies between 1 to 5 MHz. This high-frequency resistance value was interpreted with the aid of a simple circuit model for the crystal's electrical resistance.

Subsequent studies over a much wider frequency range indicated that the apparent tendency of the resistance to approach a constant value observed by Eley and Parfitt was an artifact of their limited frequency range (122, 123, 124). Measurements by Huggins and Sharbaugh revealed that the conductivity of H_2Pc continues to decrease with frequency up to 300 MHz (123). Abkowitz and Lakatos' (124) conductivity measurements at microwave frequencies on CuPc, H_2Pc, CoPc, and ZnPc were consistent with the results of Huggins and Sharbaugh. They found that the conductivity decreased from six to eight orders of magnitude from the DC value through the microwave frequencies. However, the relative magnitudes of the DC conductivities reported for these phthalocyanines was maintained at microwave frequencies with ZnPc>CoPc>CuPc>H_2Pc. Abkowitz and Lakatos also measured dielectric constants of 4.2 and 4.4 for H_2Pc and CuPc, respectively, at 34 GHz. Sakai et al. (125) measured the AC electrical properties of CuPc thin films in the frequency range spanning 30 Hz to 1 MHz. For frequencies above 1 KHz, the conductivity obeyed Equation (II-18), suggesting that charge transport is dominated by a hopping mechanism. Capacitance measurements were also consistent with this process, since the capacitance data fit the Kramer-Kronig transformation of Equation (II-18). The value of s' in Equation (II-18) required to fit the experimental data decreased from 0.8 at approximately 30° C to 0.4 at approximately 125° C. At frequencies less than 1 KHz, a frequency-independent DC conductivity

dominates. Sakai et al. attributed the DC conductivity to band conduction. Their activation energy measurements in vacuum indicated a bandgap for α-CuPc of 1.8 eV. In an oxygen ambient, the activation energy decreased to 0.5-0.7 eV, and the room temperature DC conductivity increased by a factor of 10^4. Despite these large changes in the DC electrical properties, little change was observed in the AC conductivity. Sakai et al. suggested that the rate at which the trap states created by adsorbed oxygen are filled and emptied was greater than the applied frequency and, therefore, oxygen should have little effect on the AC conductivity. Band conduction also became more dominant with increasing temperature. Thus, at high temperature, in an ambient with high oxygen concentration, the conductivity became less sensitive to the excitation frequency. Although Fendley and Johnsher observed similar behavior in CuPc, they postulated that the low-frequency behavior could be the result of a hopping process with a wide distribution of hopping time constants or, alternatively, it could be the result of interfacial barriers to the charge carriers (127). Nowroozi-Esfahani and Maclay (134) observed two polarization mechanisms in parallel plate capacitors with a CuPc thin film dielectric in the 10^2 to 10^6 Hz frequency range. The low-frequency polarization mechanism was voltage dependent and exhibited a loss peak (ω_p=500 Hz) only at zero bias. The high-frequency mechanism is relatively bias independent, with loss peaks occurring at 700, 800, and 650 KHz for -2, 0, +2 V, respectively. They also observed hysteresis in the capacitance as the voltage was varied. They interpreted their results in terms of a hopping conduction mechanism at high frequency, and they suggest that, at low frequencies, the dominant conduction process may involve interfacial polarization where charge carriers injected from the metal electrodes are trapped during the conduction process.

Metal Electrode/Phthalocyanine Contact Studies. DC conductivity studies have revealed that aluminum forms a blocking contact with metal phthalocyanine compounds. Vidadi et al. (128) found that the voltage dependence of the DC current in an Al-CuPc-Al sandwich structure can be explained by a Schottky barrier phenomena (95) at voltages less than 1.3 V. For voltages spanning 1.3-9 V, the contact resistance decreases, and the field assisted thermal emission of electrons from traps (Poole-Frenkel effect) within the bulk begins to dominate the observed current. The contact barrier height and trap depth calculated from their data were 0.75 eV and 0.56 eV, respectively. A Schottky effect was also reported by Fan and Faulkner (129) in studies of metal-free and zinc phthalocyanines sandwiched between a gold lower electrode and either an aluminum or indium surface electrode. In all cases, these sandwich structures or cells were rectifying. The rectification ratio was greatest with an indium surface electrode, and it was as high as 10^3 in cells with ZnPc. At higher voltages, the current became space-charge limited. The charge transport in cells possessing an indium electrode was

quantitatively explained in terms of a Schottky junction and energy band theory that incorporated an exponential distribution of traps. The results with Al electrodes were not as clear. Since Al has a greater work function than In, Al should have a lower barrier height to charge transport. However, the current in the Al cells was less than in the In cells. To explain this behavior, Fan and Faulkner postulated that the barrier was due to the formation of a thin aluminum oxide (Al_2O_3) layer. Although the thickness of the barrier was consistent with the thickness reported for naturally grown Al_2O_3 layers at room temperature, the barrier height of 1.27 eV was larger than previously reported for Al/Al_2O_3 systems.

In a subsequent study, Martin et al. (130) showed that the rectifying effect is due to the formation of a space-charge region when the ZnPc was exposed to oxygen during fabrication. Table II-6 shows the dark electrical properties of Au/ZnPc/M devices that were either entirely fabricated and tested under vacuum, or those that were exposed to air during fabrication. Rectifying behavior is correlated with exposure to air during fabrication. To eliminate the possibility that the rectifying behavior is the result of an oxide layer, an Al/Al_2O_3/ZnPc/ Au cell was studied. The cell was fabricated by first depositing the Al layer, exposing it to air to form the Al_2O_3 layer, and then completing the fabrication and testing entirely under vacuum. In this case, the rectification ratio was 1.0 at 0.5 V and 1.7 at 1.6 V, which indicates that the oxide layer was not responsible for the rectifying behavior. This observation was confirmed when a rectification ratio of 6100 at 1.5 V was observed in a Au/ZnPc/Au cell with a ZnPc film that was exposed to air during fabrication.

Alternating current measurements have also been used to study the phthalocyanine/metal electrode contact. Vidadi et al. (131) measured the temperature-frequency dependence of the capacitance and loss tangent of CuPc parallel plate capacitors. The capacitors were fabricated by the successive deposition of an aluminum electrode, CuPc film, and a second aluminum electrode without intermediate exposure to air. They found that the capacitance at 40° C was independent of frequency for the range spanning 100 Hz to 100 KHz. When the temperature was increased, the capacitance became increasingly more dispersive, decreasing with increasing frequency. This dispersive region shifted to higher frequency as the temperature was increased. The maximum capacitance value was independent of the film thickness. The loss tangent was frequency dependent and possessed a maxima that shifted to higher frequency as the temperature increased. These results were consistent with a simple circuit model that represented the phthalocyanine layer as a parallel RC network connected in series with capacitors representing Schottky barrier contacts. At low frequency and high temperature, the equivalent capacitance of this model is dominated by the two Schottky barrier contacts. At low temperature and high frequency, the equivalent capacitance is the series capacitance of the phthalocyanine bulk and two

Table II-6. Electrical Properties of Au/ZnPc/M devices. RR= Rectification Ratio and V_{oc}= Open Circuit Photovoltage. Irradiation Conditions: 10mW/cm^2 (130).

Metal (M)	ϕ_M (eV)	Vacuum		Air Exposed	
		RR (±0.5V)	V_{oc} (mV)	RR (±0.5V)	V_{oc} (mV)
Au	5.47	1.0	450	1.2	3.2
Cu	4.59	1.0	0	3.0	4.7
Cr	4.50	1.1	450	19.0	51
Al	4.41	1.0	420	82	144
In	4.12	0.5	100	39	57
Sm	2.7	1.0	230	-	72

Schottky barriers. Consistent with this model, Vidadi et al. reported that the minimum capacitance increased as the CuPc film thickness decreased. Based on their model, the Schottky barrier width and the CuPc permittivity were estimated to be 1000 Å and 3.2, respectively. Assuming the barriers formed as a result of localized states in the band gap, Vidadi et al. calculated a trap density of $3x10^{16}$ cm^{-3} with a trap depth of 0.54 eV.

Yasunaga and Shintaku (132) studied the AC electrical properties of degassed and oxygen doped lead phthalocyanine capacitors in the frequency range spanning 50 Hz to 1 MHz, and they obtained results similar to those reported by Vidadi et al. The effects of oxygen on the AC conductivity response were attributed to changes in the barrier capacitance and conductivity. The changes were related to a shift in the Fermi energy level towards the valence band within the lead phthalocyanine's bandgap. For the case of oxygen-free PbPc, the width of the band bending is small, and the corresponding barrier capacitance is large. That is, the Fermi energy level shifted when the PbPc was doped with oxygen, resulting in an increase in the band bending and, therefore, a corresponding decrease in the barrier capacitance.

A slightly more complex circuit model of the metallo-phthalocyanine/metal contact was postulated by Boudjema et al. (133) to account for the equivalent parallel conductance and capacitance of Au/MPc/M_2 capacitors measured over the extended frequency range of 10^{-3} to 10^5 Hz, with and without a superimposed DC bias. Two different MPc films, NiPc and ZnPc, were studied along with three different electrode metals, M_2 = Al, In, and Au. The conductance of the Au/NiPc/Au capacitors was nearly constant, and the capacitance increased by a factor of 5 at low frequencies. These results were not significantly altered by an applied DC bias. However, when a dissimilar metal is employed as the second electrode, the electrical behavior is dramatically affected. The conductance and capacitance become highly dispersive; both parameters varied by more than two orders of magnitude in the frequency range studied. Furthermore, the electrical properties are strongly affected by an external DC bias. The circuit model proposed to account for these experimental results has a series of three parallel RC networks corresponding to three regions within the phthalocyanine layer: a surface-charge layer, a space-charge region, and the bulk.

Gas Adsorption Studies on the Phthalocyanine Compounds

In general, gas adsorption studies are concerned with determining the nature of the adsorbed species and the adsorption sites, adsorption isotherms, heats of adsorption, and adsorption rates. This experimental data is then used to develop and justify theoretical models concerning the adsorption

processes. Similarly, experimental data of this nature is critical for understanding the adsorption of gases on phthalocyanine surfaces. The purpose of this section is to discuss gas adsorption on the phthalocyanine compounds with respect to the usual data collected in gas adsorption studies. Most of the discussion has been synopsized from Wright's review article, and the references contained therein. This section is divided into three sub-sections which discuss adsorption isotherms, heats of adsorption, and adsorption kinetics, respectively.

Adsorption Isotherms. The small surface area available in single crystals and thin films has made the direct measure of adsorption isotherms difficult and limited to powdered phthalocyanine compounds. According to Wright, adsorption isotherms on powdered β-CuPc have been measured for aliphatic and aromatic hydrocarbons, alcohols, esters, acids, and water (26). Unfortunately, since grain boundaries and lattice defects strongly influence the electrical properties of powdered phthalocyanines, adsorption studies on thin film and single crystal material are required for a complete analysis of the effects of adsorbed gases on the electrical properties of the phthalocyanine compounds (26). When the electrical conductivity was assumed to be proportional to the surface coverage, numerous studies have shown that NO_2 adsorption on phthalocyanine single crystals and thin films obeys the Freundlich isotherm (15, 135, 136, 137). Gutmann and Lyons claim, without justification, that this is a reasonable assumption (34). To help justify this assumption, the nature of electrical conductivity in single-crystal semiconductors will be considered. Since the surface properties of single crystals and thin films may differ substantially from bulk single-crystal properties, the following discussion is intended to illustrate that the surface conductivity of single crystals and thin films is linearly related to the surface impurity concentration (surface coverage). The purpose of the discussion is to show that a linear relationship between electrical conductivity and impurity concentration may be possible.

The electrical conductivity, σ, of a material depends on the number of charge carriers and their mobility, μ. In a semiconductor, two different carriers, electrons and holes, which may have different mobilities, are present. The electrical conductivity can be expressed as:

$$\sigma = (n \mu_n + p \mu_p) q \qquad \text{(II-28)}$$

where q is the fundamental unit of electronic charge, n is the electron density, p is the hole density, and μ_n and μ_p are the electron and hole mobilities, respectively. Assuming that the semiconductor is doped

with only electron acceptors (for example, NO_2) such that the total number of holes is dominated by the dopant concentration, then by the law of mass action ($n_i^2 = np$):

$$\sigma = (p\mu_p + \frac{n_i^2}{p}\mu_n)q \qquad \text{(II-29)}$$

where n_i is the intrinsic carrier concentration. For sufficiently large p, the second term is negligible, and the conductivity becomes directly proportional to the number of holes and, therefore, the acceptor dopant concentration. This analysis, however, ignores the effect of impurity scattering of the carriers by the Coulomb field of the ionized acceptor on the mobility. However, impurity scattering becomes important only at very high dopant concentrations (95). In gallium arsenide, the log(resistivity) is approximately linear with log(dopant concentration) over impurity concentrations spanning 10^{12} to 10^{20} impurities/cm^3. The log(resistivity) of silicon is linear with respect to log(dopant concentration) up to 10^{17} impurities/cm^3, and deviates slightly from linearity for dopant concentrations as large as 10^{21} impurities/cm^3. Although the preceding discussion supports the validity of assuming the proportionality between single crystal bulk conductivity and impurity concentration, it is based on the bulk properties of crystalline semiconductors, and is not applicable to the amorphous nature of phthalocyanine thin films. In fact, Wright remarks that the Freundlich dependence of the electrical conductivity on concentration is surprising since the isotherm relates log(surface coverage) to log(gas concentration), whereas the observed conductivity change is a function of the effective number of charge carriers and their mobilities (26). Wright argues that the activation energy for charge carrier generation and charge carrier mobility decreases with increasing surface coverage, and should shift the dependence of the gas modulated conductivity away from a simple Freundlich isotherm.

Although numerous studies have shown a Freundlich-type electrical conductivity dependence with respect to phthalocyanine thin films and NO_2 exposure concentration, the slope of the log(electrical conductivity) versus log(gas concentration) plot, which will be referred to as the Freundlich constant, varies considerably. Wright has collected the values of the Freundlich constants for the adsorption of NO_2 on a number of phthalocyanine compounds, along with the associated experimental conditions utilized by other investigators (26). The value of the constant spans the range 0.1 to 1.9. Values greater than unity have been interpreted as either molecular association (such as, the association of two NO_2 molecules to form N_2O_4) on the surface or diffusion into the bulk, whereas values less than unity indicate

occupation of multiple sites by each adsorbed species (138). The wide range of values for this constant, and the lack of any regular trend, was interpreted by Wright as (26):

> This probably reflects the absence of defined film preparation and treatment conditions, resulting in variable surface chemical and structural properties. The absence of any satisfactory model for the widely scattered results of Table 5 is disturbing, not only because it reflects the lack of understanding of the fundamental processes which are occurring, but also because the properties responsible for the variations may themselves change as the sensor films age ...

There is much less experimental data concerning the electrical conductivity (adsorption) isotherms of other gases. Sadaoka (137) reported Freundlich-type isotherms for nitrogen dioxide (NO_2), nitric oxide (NO), sulfur dioxide (SO_2), and oxygen (O_2) adsorption on metal-free phthalocyanine. Gas detection sensitivity was in the order: $NO_2 > NO > SO_2 > O_2$. Bott and Jones observed that the electrical conductivity of phthalocyanine thin films increased linearly upon exposure to increasing chlorine (Cl_2) concentrations (136). Since the film electrical conductances extrapolated to zero at zero Cl_2 concentration, the linear relationship is equivalent to a Freundlich-type conductivity isotherm, where the Freundlich constant is equal to one. Van Ewyk, in addition to demonstrating a Freundlich-type electrical conductivity isotherm for NO_2, investigated the effect of trifluoroborane (BF_3) on the conductivity of CuPc (135). Similar to NO_2, exposure of the phthalocyanine film to BF_3 increases the electrical conductivity. This effect was more rapid and saturated at lower concentrations compared to the NO_2 induced electrical conductivity changes. In contrast to the NO_2 conductance changes, the electrical conductance change was irreversible, suggesting a strong chemisorption process. As a result of the rapid electrical conductivity increase upon BF_3 exposure, an insufficient number of data points were obtained to establish an isotherm. However, the electrical conductivity response of perylene to NO_2 and BF_3 exposure obeyed a Freundlich-type isotherm. The electrical conductivity response of phthalocyanine to other gases does not always obey the Freundlich isotherm. One possible example is the ammonia-modulated electrical conductivity change induced in CuPc. Ammonia is an electron donor and, therefore, the electrical conductivity should be inversely proportional to the surface coverage (gas concentration). Szczurek and Lorenz observed a linear decrease in the electrical conductivity of CuPc upon exposure to NH_3 for pressures spanning 0.04 to 0.2 torr (139). In contrast to the results for Cl_2, since the slope is negative, this linear relationship cannot be cast into the form of a Freundlich isotherm. Although these results suggest that the isotherm is non-Freundlichian, the limited pressure range investigated, and the corresponding small changes in the conductance observed upon NH_3 adsorption, restricts the conclusions

that can be formulated concerning the electrical conductivity isotherm. According to Wright, the NH_3-modulated electrical conductivity response in the phthalocyanine compounds depends upon the initial electrical conductivity of the film and, therefore, is sensitive to trace quantities of other gases (26). For example, NH_3 had no effect on the phthalocyanine compounds when exposed in air, but the electrical conductivity increase normally induced in the phthalocyanine compounds when exposed to 50 ppb NO_2, was reduced nearly 50 percent when NH_3 was also present (140). Nevertheless, Szczurek and Lorenz were able to obtain reproducible responses by establishing a stable state in the phthalocyanine film prior to each NH_3 measurement (139).

Heats of Adsorption. Similar to the difficulty arising in the direct measurement of adsorption isotherms, heats of adsorption on phthalocyanine films, to date, have not been measured due to the limited surface area of the films. According to Wright, the adsorption isotherm studies on powdered β-CuPc discussed in the previous section were recorded at several temperatures, from which the heats of adsorption were determined (26). These heats of adsorption were generally small and often comparable to condensation heats. Chadwick, Dunning, and Wright determined a desorption energy of 76 kJ/mole for NO_2 from PbPc films (141). Wright emphasizes that, although this desorption energy is on the order expected for weak chemisorption, thermal desorption studies do not permit quantitative comparison between different materials. Comparison of the results of thermal desorption studies with other materials is hampered by the heterogeneous nature of the sublimed phthalocyanine films and the inability to ensure similar coverage prior to desorption (26).

Thermal desorption studies by Sadaoka et al. suggest two sites exist for the adsorption of gases on the phthalocyanine compounds (91, 142). The thermal desorption of oxygen, nitric oxide, and nitrogen dioxide on powdered β-phase metal-free, iron, cobalt, and copper phthalocyanines were monitored by measuring the appropriate peaks in the mass spectrum. The samples were heated to 150° C in vacuum prior to exposure to 20 to 200 torr of the gases at room temperature. The samples were then heated to 300° C at a constant rate of 10° C per minute. For oxygen, only a single desorption peak was observed for all the phthalocyanine compounds in the range of 50 to 100° C. Similar behavior was observed for the thermal desorption of NO and NO_2 from copper phthalocyanine (CuPc) and metal-free phthalocyanine (H_2Pc). In contrast, two peaks were observed, one in the range 50 to 100° C and the othe in the range spanning 100 to 250° C, for the desorption of NO and NO_2 from cobalt phthalocyanine (CoPc) and iron phthalocyanine (FePc). The desorption temperature indicated that the binding strength of the gases was on the order of 1.0 to 1.4 eV. The lower temperature peak was attributed to adsorption on the phthalocyanine macrocyclic ring, since this desorption peak was observed for all the

phthalocyanine compounds, whereas the higher temperature peak, which was observed in the spectra for FePc and CoPc, was ascribed to a stronger interaction with the central metal ion. The position of the higher temperature peak occurred at a higher temperature for NO_2 compared with NO, and was it considered to reflect the higher electron affinity of NO_2. However, the lower temperature peak occurred at the same position for both NO_2 and NO. As pointed out by Wright (26), the dependence of the desorption peaks on the adsorbate electron affinity should also have been reflected in the lower temperature desorption peak. From the position of the desorption peaks, Sadaoka's group calculated the adsorption site binding energies (142). The phthalocyanine-ligand binding energy was essentially the same for oxygen, nitric oxide, and nitrogen dioxide adsorption on CuPc and CoPc, with a value of approximately 1 eV (23 kcal/mole). The binding energy associated with the Co ion was 1.18 eV and 1.35 eV for NO and NO_2, respectively. The IR studies by Sadaoka's research team discussed earlier, support the results of these thermal desorption studies.

According to Wright (26), a comparison of Sadaoka's thermal desorption results with the studies by Contour et al. on the desorption of oxygen adsorbed onto powdered H_2Pc, FePc, and CuPc at low temperatures shows that the results of the thermal desorption studies depend on the temperature at which the adsorption was initially performed. When the adsorption of oxygen takes place at -160° C, no desorption peak was observed for H_2Pc, whereas desorption peaks at -140 and -115° C were observed with CuPc and FePc, respectively. When the adsorption temperature was raised, the amount of oxygen adsorbed was reduced, and the desorption peak shifted to higher temperatures.

Since these thermal desorption studies were performed on powdered samples, the results may not be transferable to the adsorption behavior on other surfaces. However, Sadaoka's group correlated the low temperature thermal desorption peak with the single peak observed in the electrical conductivity upon heating thin films similarly exposed to NO_2 at room temperature (91). This behavior was observed for H_2Pc (91), CoPc (91, 142), and CuPc (142), and it was interpreted as evidence against supporting a significant contribution to the electrical conductivity modulation from gases strongly adsorbed at the metal ion binding site. According to Wright, this interpretation is supported by the similar trends in the conductivity changes induced upon NO_2 exposure of single crystal H_2Pc and a host of other single crystal metal phthalocyanine compounds (26).

Adsorption Kinetics. A variety of kinetic responses have been observed for gas adsorption on the phthalocyanine compounds depending upon the adsorbate. In a study of NO_2 adsorption on single crystal β-CuPc, van Ewyk observed that the adsorption kinetics obeyed the Elovich equation when the NO_2 pressure was suddenly increased from 6 to 60 Pa at room temperature (135). Following the initial

100-second transient required for the gas to diffuse uniformly throughout the sample chamber, the electrical current increase was proportional to log(time) for approximately 30 minutes, after which equilibrium was obtained, and the current increase leveled-off. In contrast, Buchholz followed the kinetics of oxygen adsorption on CoPc by monitoring the intensity of the oxygen Auger peak relative to that of nitrogen as a function of time. The kinetic response was split into two regions: the initial response, indicating a linear adsorption rate of 5×10^{11} molecules/cm^2-s lasting for the first 5 minutes, which was followed by a slower uptake of oxygen that was attributed to oxygen diffusion into the bulk. According to Wright, Pack and Phelps observed oxygen adsorption kinetics which followed a (time)$^{1/2}$ relationship when PbPc was exposed for days to 10^3 Pa of oxygen (26). This relationship is consistent with oxygen diffusion into the PbPc bulk with a diffusion constant of 7×10^{-9} cm^2/s at 242° C and a diffusion activation energy of 1.4 eV. These effects were also readily reversed upon heating the sample in the absence of oxygen. Ionescu also studied the kinetics of oxygen adsorption on the phthalocyanines (143, 144, 145). In these studies, the current was monitored following exposure of metal-free and copper phthalocyanine to oxygen. When log(current) was plotted versus log(time), a straight line relationship was obtained. To explain their results, they derived a logarithmic relationship between the electrical current , I, and time, t, given by:

$$I(t) = A\, t^{\alpha} \qquad \text{(II-30)}$$

where A and α are constants. Below 140° C the value of α was approximately 0.5, which is consistent with a diffusion process; however, α decreased for temperatures above 140° C, suggesting a heat-induced structural change in the film. Their derivation was based on the rate of surface reaction in the case of a Langmuir-Hinschelwood mechanism for a single reactant, which is known to obey the Freundlich isotherm. Unfortunately, they did not demonstrate a Freundlich isotherm relationship between the electrical conductivity and the oxygen pressure. Unusual oxygen adsorption kinetics were also obtained by Langton and Day for iron phthalocyanine (146). They observed that a dark electrical conductivity variation with time followed a hyperbolic law. The kinetics were explained by postulating a process where oxygen adsorption involves two neighboring adsorption sites. Langton and Day also reported on the kinetics of carbon monoxide (CO) and nitric oxide (NO) adsorption. The kinetics of CO adsorption on iron phthalocyanine obeyed the Elovich equation, while the NO adsorption kinetics were complex and involved three distinct stages. Collins and co-workers conducted extensive studies of ammonia adsorption on the phthalocyanine compounds (147-149). The purity of the CuPc was shown to affect the kinetics and the magnitude of the electrical conductivity decrease upon exposure to

ammonia; with unpurified (as-supplied by the manufacturer) CuPc manifesting a much larger and faster conductivity decrease compared to a purified (by means of entrainer sublimation) CuPc sample (147). Although verification of the purity of these samples was not reported in this paper, other investigators have reported that a single entrainer sublimation procedure reduced the impurity concentration by over two orders of magnitude (151, 152). In addition, the phthalocyanine crystal structure was shown to affect the conductivity change upon exposure to ammonia (147, 148); the response of β-ZnPc was substantially larger and attained equilibrium more rapidly than α-ZnPc (149, 150). The adsorption kinetics for purified and unpurified CuPc did not follow any simple relationship (147). In contrast, the adsorption kinetics of ammonia adsorption on metal-free phthalocyanine obeyed the Elovich equation (147). These workers also observed adsorption kinetics upon exposure of purified CuPc to air. The conductivity decreased exponentially with time, and was shown to agree with a simple Langmuir model. The disagreement between these results and oxygen adsorption data obtained by Ionescu (143, 144, 145) was considered to be due to the difference between air and oxygen.

The electrical conductivity variation due to the exposure of a "clean" phthalocyanine surface to oxygen, and the variation observed upon NO_2 exposure of a phthalocyanine surface pre-exposed to air have been used to formulate an adsorption model for practical gas sensors (153). A "clean" surface which has been thoroughly degassed at low pressures, upon exposure to oxygen, rapidly forms a monolayer, typically in less than a minute at 10^{-4} Pa of oxygen pressure (153). However, NO_2 adsorption on the phthalocyanine compounds maintained in air is a much slower process. These results are interpreted in terms of a model where the NO_2 must displace existing oxygen molecules adsorbed onto the phthalocyanine surface from the atmosphere. NO_2 adsorption takes place on those sites from which oxygen is most easily displaced (153). Thus, NO_2 adsorption reaches equilibrium rapidly at low concentrations. Adsorption at higher concentrations requires the displacement of more strongly bound oxygen species, which is slower and less reversible. The kinetics of NO_2 adsorption on a given film were observed to vary as the film aged, and it was initially attributed to thermally induced structural changes (153). This conclusion, along with the proposed model, was later modified by Archer et al., to include the effects of gas exposure history (154). Prior gas exposure history was found to accelerate the response to NO_2 exposure due to the effect of residual, strongly bound NO_2. Similar to the earlier oxygen adsorption model, the exposure of a phthalocyanine thin film to NO_2 initially displaces the weakly bound oxygen. However, since the weakly bound oxygen molecules occupy sites which have the smallest sticking coefficients, the adsorption on these sites is correspondingly slow. As the surface coverage by NO_2 increases, lateral repulsions enhance the displacement of the more strongly bound

oxygen, and the adsorption rate increases. When the process is reversed, the more weakly-bound NO_2 molecules are displaced by oxygen. However, the strongly bound NO_2 is retained and subsequent exposure to NO_2 results in more rapid kinetics.

Summary

This chapter reviewed the electrical and gas adsorption properties of the phthalocyanine compounds. The structure and morphology of the phthalocyanine compounds were introduced and the effect of structural and morphological variation on their gas adsorption properties was discussed. Since a large number of preparation and handling factors have been shown to influence the structure and morphology of the phthalocyanine compounds, electrical and gas adsorption studies should be accompanied by a characterization of the phthalocyanine compound's physical structure and morphology. Charge transport in the phthalocyanine compounds was discussed in relationship to two conduction models: an energy band model and a charge carrier hopping model. Both the DC and AC electrical properties of the phthalocyanine compounds were presented. Finally, gas adsorption and its effect on the electrical conductivity was reviewed. The phthlalocyanine compounds are p-type semiconductors whose electrical conductivity is significantly altered by adsorption of electrophilic and electrophobic gases. Electrophilic (electron acceptor) gases, such as nitrogen dioxide, cause a large increase in the phthlaocyanine compound's electrical conductivity. In contrast, adsorption of electrophobic (electron donor) gases, such as ammonia, decrease the phthalocyanine compound's electrical conductivity. The relative sensitivity of the phthalocyanine compound's electrical conductivity to electrophilic and electrophobic gases varies with respect to its metal ion moiety. The differences in sensitivity, as well as the opposite electrical conductivity changes, are potential features that can be utilized in the analysis of a binary mixture of electrophilic and electrophobic gases.

III. *Literature Review of Multicomponent Gas Analysis*

The approach toward multicomponent gas analysis has primarily focused on calibrating an array of sensors with a set of mixtures of the detectant gases. In addition to multiple sensors, variable operating conditions for single sensors has been proposed for increasing the number of independent responses (20, 155, 156, 157). Following calibration, the concentration of the component gases in an "unknown" mixture are then determined through multilinear regression analysis. Clifford has described this approach for a selective gas detection and measurement system (158, 159). He proposed a general response equation for electrical conductance-type sensors in which the constants and the form of the terms are determined by a repetitive curve fitting procedure. To implement the procedure, the electrical resistance response is initially curve fitted for concentration variations of single component gases. Next, the resistance response due to various mixtures of the detectant gases is curve fitted. If an array of sensors is employed, each sensor is calibrated following this procedure. For certain systems, the general response equations may be linear, and standard pattern recognition algorithms, such as multilinear regression analysis, may be employed to determine the concentration of the component gases in an unknown mixture. For non-linear systems, non-linear regression analysis can be used to determine the component gas concentrations.

Accompanying the advance in computational power, multivariate statistical analysis techniques have become popular tools for the quantitative analysis of multicomponent systems. Multivariate analysis involves a set of general statistical methods which relate a set of independent variables (predictors) to a set of dependent variables (responses). The relationships between the predictors and the responses are typically established through a calibration process. These techniques are quite general and have been applied to non-linear systems, and to systems where the relationships between the predictors and responses are highly correlated (160). Since the statistical methods are independent of the particular parameters employed as predictor and response variables, they have been applied to multicomponent analysis with a wide variety of sensor technologies and analytical methods.

This Chapter reviews the following multivariate statistical analysis techniques that have been applied to gas sensing: correlation, cluster analysis, multiple regression analysis, principal component analysis, and neural networks. The first two techniques, correlation and cluster analysis, are used to identify the gas components present and to detect commonalities between the measured response patterns for different gases. These two techniques only provide qualitative information, and other methods must be used to determine gas concentrations. The other techniques, multiple regression analysis, principal

component analysis, and neural networks, provide both qualitative and quantitative information about the gas components. Multiple regression analysis determines the contributions of each predictor variable which minimizes the sum of the squared error between the predicted response and the measured response. Whereas multiple regression analysis attempts to establish the best response prediction for a given a set of predictor variables, principal component analysis investigates the internal correlation of the predictor variables. In its implementation, the principal component analysis technique determines a set of abstract features which account for the largest variance in a collection of predictor variables (161). These abstract features may then be utilized in multiple regression analysis or applied to an artificial neural network to classify or quantitatively predict component gas concentrations. Artificial neural networks employ an inherently parallel approach to achieve response prediction for a given set of predictor variables. The following sections describe each of these techniques in greater detail.

Correlation

The correlation technique, as applied to multicomponent gas analysis, is a process that is implemented to compare the sensor response pattern of an unknown gas, X, with the sensor response pattern of known calibration gases, X^s. This comparison is accomplished by defining an index, known as the correlation coefficient, that indicates the similarity between the different sensor response patterns. The correlation coefficient, ρ_{jkl}, is defined as (162):

$$\rho_{jkl} = \sum_{i=1}^{n} \left(\frac{x_{ijk} - \overline{x_{jk}}}{\sigma_i} \right) \left(\frac{x_{il}^s - \overline{x_l^s}}{\sigma_i^s} \right) \qquad \text{(III-1)}$$

where x_{ijk} is the response of sensor i to a test gas j at concentration k, x_{il}^s is the calibrated response of sensor i to standard gas l, $\overline{x_{jk}}$ is the average response for all the sensors to test gas j at concentration k, $\overline{x_l^s}$ is the average of the calibrated response for all the sensors to standard gas l, σ_i is the standard deviation of the test gas response data, and σ_i^s is the standard deviation of the calibration gas response data. In Equation (III-1), the sensor response data for the test and calibration gases are "auto-scaled" by subtracting the corresponding mean response (indicated by the bar) and dividing by the corresponding standard deviation. This "auto-scaling" is advantageous since it removes the bias introduced into an analysis when large variations in the sensor response values, which often occurs in gas sensing, are present (162). The correlation coefficient may vary from -1 for a perfect mismatch to +1 for an identical

sensor response pattern. In a successful analysis, there is typically a threshold value established for the correlation coefficient that ensures the correct identification of the gas present (163).

In addition to gas identification, if the response of each sensor in a sensor array are compared (auto-correlated) with the responses of the other sensors, the correlation method can also be used to identify collinearity between sensors in the sensor array. When two sensors are collinear, as indicated by a correlation coefficient with a value greater than 0.8 (162), they have essentially the same response to the gases evaluated. Therefore, the information provided by the two sensors is redundant. A high degree of collinearity, which is often observed between sensors with cross-sensitivities, can degrade the performance of multiple regression techniques (162). The principal component analysis technique, which represents the original data as linearly independent latent variables, can reduce the effects of collinearity (162).

Cluster Analysis

Cluster analysis is another common pattern recognition technique that is designed to identify groups or clusters in the sensor response patterns with different gases. Gases with similar chemical composition or possessing certain chemical functional groups may elicit similar sensor response patterns (164). These similar sensor response patterns group or cluster together within the n-dimensional vector space defined by the set of n-measurement variables (sensors). The object of cluster analysis is to group the sensor response patterns according to their proximity within the n-dimensional measurement space. The proximity of two sensor response patterns, i and j, is given by the general distance metric, d_{ij} (162):

$$d_{ij} = \left(\sum_{k=1}^{n} (x_{ik} - x_{jk})^N \right)^{1/N} \qquad \text{(III-2)}$$

where N is a positive integer, n is the number of elements in each sensor response pattern, x_{ik} is element k of sensor response pattern i, and x_{jk} is element k of sensor response pattern j.

The results of cluster analysis are commonly summarized in a dendrogram. Figure III-1 illustrates a dendrogram for an analysis of 11 different gases with an array of twelve surface acoustic wave devices (164). Each gas occupies a lone cluster at the base of the dendrogram. These isolated clusters are then merged together according to the similarity of their respective sensor response patterns. The vertical axis of the dendrogram in Figure III-1 represents the Euclidean distance (N=2 in Equation III-2) between the sensor response patterns obtained with each gas. Sensor response patterns which are

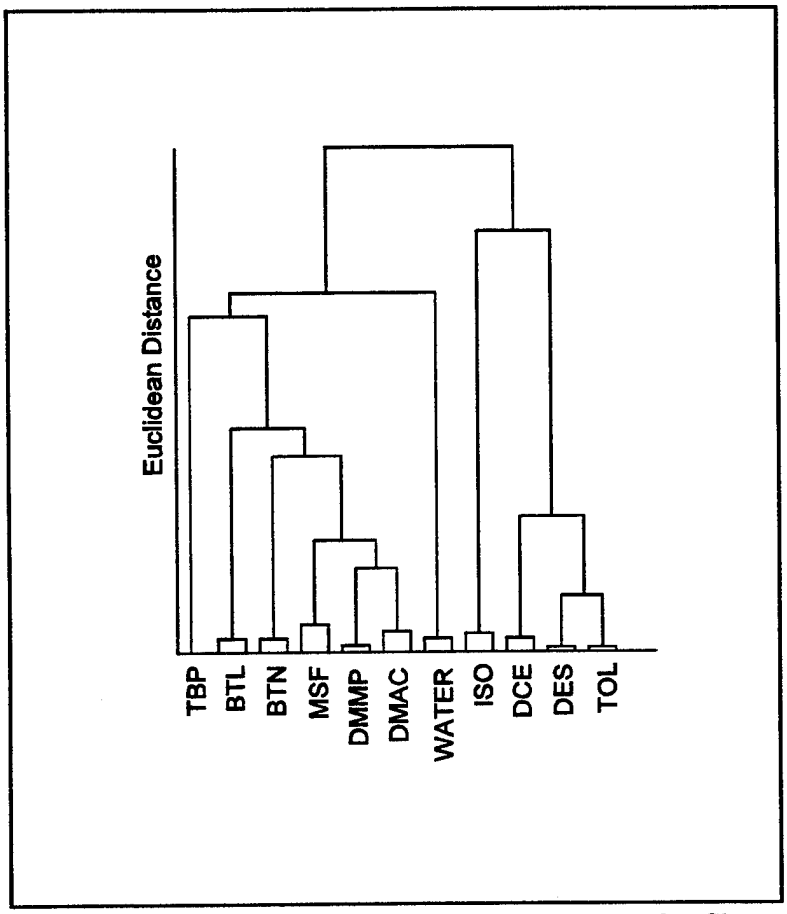


Figure III-1. A Dendrogram Illustrating the Results of a Cluster Analysis of 11 Different Vapors. The 11 Vapors are Indicated by the Acronyms at the Bottom of the Diagram (164).

close together in the n-dimensional vector space merge together low on the vertical axis, while those which are more distant, merge together near the top of the dendrogram. Thus, diethyl sulfide (DES) and toluene (TOL), which generate similar response patterns, merge low on the y-axis of the dendrogram. As the clusters are merged, the number of elements contained in the merged cluster increases. Since a cluster may contain several elements, several different approaches have been developed to determine the distance between clusters based upon the distance between: 1) the two closest elements of each cluster (referred to as single linkage or nearest neighbor), 2) the two farthest elements in each cluster (complete linkage or furthest neighbor), 3) the centroid of each cluster, and 4) the median of each cluster. According to Gardner and Bartlett (162), there is no accepted "best" method for merging clusters.

Cluster analysis provides classification information similar to that obtained with the correlation technique. Like the correlation technique, it can be used to identify collinearity between sensors. Since cluster analysis does not determine the concentration of gas components, it is often combined with other quantitative techniques, such as multiple regression and principal component analysis.

Multiple Regression Analysis

There are two basic approaches in the application of multiple regression analysis to multicomponent systems. These two approaches are referred to as classical least-squares (CLS) and inverse least-squares (ILS) (165), or as the ***K***-matrix and ***P***-matrix methods, respectively. Although transformed least-squares is specified as a separate multiple regression technique in the literature' it is essentially the application of either CLS or ILS to a mathematically transformed data set (163). The mathematical transformations are typically accomplished to cast the data into a linear form. Both the ***K***-matrix and ***P***-matrix methods require two conditions. The first condition requires the response to be equal to a linear combination of the predictor variables. A classic example is Beer's Law, which relates the measured optical absorption to the absorbing species concentration (166). The second condition requires the number of predictors, i, to be less than or equal to the number of responses, j ; that is, the number of equations must be greater than or equal to the number of unknowns. These two fundamental approaches are discussed in the following sub-sections.

K**-matrix Method.* In the ***K-matrix method, the responses, X_j , are measured for a set of m-independent calibration samples possessing known concentrations (predictors), C_i , of the component

gases. During calibration, the matrix equation shown below will be solved for the values of K_{ji} which minimizes the sum of the squared error. That is,

$$\boldsymbol{X} = \boldsymbol{KC} \tag{III-3}$$

where $\boldsymbol{X}$ is a $j \times m$ matrix of measured responses for each standard mixture, $\boldsymbol{C}$ is an $i \times m$ matrix containing the known concentrations, and $\boldsymbol{K}$ is a $j \times i$ matrix containing proportionality constants. Minimizing the squared error in the computed $\boldsymbol{K}$ matrix also minimizes the error in the calibration process, which may subsequently be used to predict the concentrations in the unknown samples. From least-squares regression analysis (167), the $\boldsymbol{K}$ matrix is given by (168):

$$\boldsymbol{K} = \boldsymbol{XC}^t\,(\boldsymbol{CC}^t)^{-1} \tag{III-4}$$

where the superscript, t, indicates the transpose operator. To determine the component concentrations in a mixture, the matrix Equation (III-3) can be solved for the unknown concentrations by premultiplying both sides of the equation by the inverse of the $\boldsymbol{K}$-matrix. That is,

$$\boldsymbol{C} = \boldsymbol{K}^{-1}\boldsymbol{X} \quad . \tag{III-5}$$

When $i = j$, the $\boldsymbol{K}$-matrix is square, and the inverse may be calculated. For an overdetermined system (with respect to the number of measured responses ($i > j$)), the $\boldsymbol{K}$-matrix is no longer square, and the solution of the matrix Equation (III-3) becomes

$$\boldsymbol{C} = \boldsymbol{MX} \tag{III-6}$$

where

$$\boldsymbol{M} = (\boldsymbol{K}^t\boldsymbol{K})^{-1}\boldsymbol{K}^t \quad . \tag{III-7}$$

There are two major disadvantages associated with applying the $\boldsymbol{K}$-matrix method to multicomponent analysis. First, to determine the component concentrations with this method, two matrix inverses must be calculated -- one during calibration, to determine the $\boldsymbol{K}$-matrix, and one during prediction, to determine the inverse of the $\boldsymbol{K}$-matrix or, when $\boldsymbol{K}$ is not square, the $\boldsymbol{M}$-matrix. The second disadvantage arises during the application of this method to non-linear systems. The presence of non-linearities produces multiple solutions when the inverse of the $\boldsymbol{K}$-matrix is attempted (168). For example, when the non-linear response is approximated as a power series with respect to the component concentrations, multiple solutions to the matrix equations are produced. In order to be useful, the correct

solution must be selected on the basis of physical significance (for example, solutions producing negative concentrations have no physical meaning, and they can be eliminated). However, cases may arise where the selection of the most relevant soution is difficult. In those cases where selection criteria for the most useful solution are not apparent, each solution may be evaluated on a trial-and-error basis for its relevancy in predicting the component gas concentrations. The problem of interpreting the usefuleness of multiple solutions is a possible explanation for the lack of publications which report on the application of the ***K***-matrix method to non-linear systems.

P-matrix Method. The ***P***-matrix method, in contrast to the ***K***-matrix method, defines the component concentrations as a function of the measured responses. This approach treats the measured responses for each mixture as a vector in an m-dimensional space. The "direction" of the vector corresponds to the chemical composition of the mixture, while the "length" of the vector is indicative of the sum of the concentrations of the various components. These two concepts are illustrated in Figure III-2 where the different axes represent the electrical conductivity of three independent sensors upon exposure to binary mixtures of carbon monoxide and methane (20).

The matrix formulation of this method can be expressed as (168):

$$\boldsymbol{C} = \boldsymbol{PX} \tag{III-8}$$

where C and X are the same matrices defined earlier in the ***K***-matrix approach, and P is given by least-squares multiple regression as:

$$\boldsymbol{P} = \boldsymbol{CX}^t(\boldsymbol{XX}^t)^{-1} \quad . \tag{III-9}$$

Thus, in contrast to the ***K***-matrix method, only a single matrix inversion is required to calculate the unknown component concentrations of a gas mixture. This approach has the added advantage that it can be readily adapted to accomplish non-linear analysis. That is, the elements of the response matrix, X, may now be non-linear functions of the measured responses. For example, the response matrix elements may represent the terms in a polynomial expansion of the concentrations, where the measured responses are the independent variables and the elements of the ***P***-matrix are the coefficients. Since the additional inversion performed in the ***K***-matrix method is not required, the non-linearities do not introduce multiple solutions.

The most serious limitation of the ***P***-matrix method, is that the number of standard mixtures must be greater than or equal to the number of measured responses used in the analysis. Since overdetermining the system with respect to the number of measured responses improves the reliability

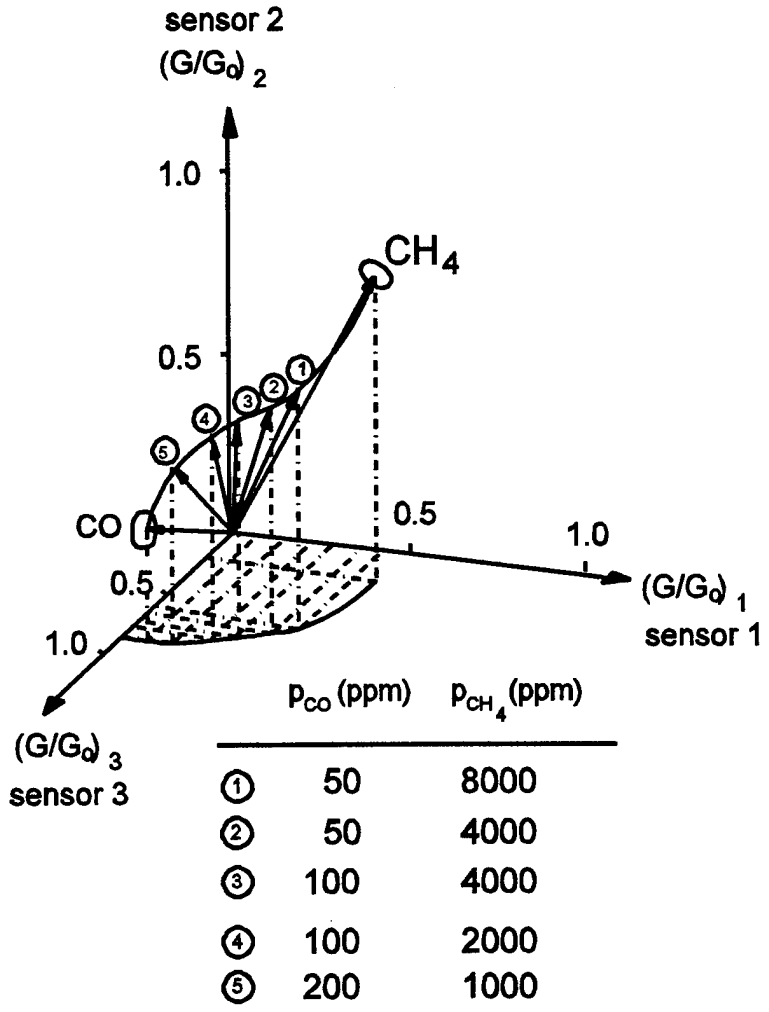


Figure III-2. Vector Representation of a Binary Gas Mixture's Composition where the Vector Component Axes are the Measured Responses From Three Different Conductivity Sensors (20). G and G_0 are the Sensor Conductivity in the Challenge and Carrier Gas, Respectively. p_{CO} and p_{CH_4} are the Partial Pressures of Carbon Monoxide and Methane, Respectively.

of the concentration estimates, a large set of measured responses is generally advantageous. However, the practical limitations associated with the preparation and handling of additional calibration samples restricts the number of measured responses that may be used in the analysis. In order to overcome this limitation of the ***P***-matrix method, the mathematical technique of principal component analysis (PCA) or principal factor analysis (PFA) has been developed (169, 170, 171).

Principal Component Analysis

PCA is a method for compressing the information content of a large data set into a smaller set of abstract features which account for the greatest variation in the data set (161). As stated earlier, the measured response data can be interpreted as a vector in an m-dimensional space, where m is the number of responses. The objective of PCA is to project this vector onto the vector space whose orthogonal coordinate axes account for the maximum variation in the data. Thus, PCA determines a set of vectors or abstract features which best represents the variation in the predictor data. However, these abstract features determined by PCA may not be optimal for predicting the dependent response (concentration). A closely related technique, called partial least squares (PLS), attempts to include predictive information in the computation of the abstract features (165). This enhancement is accomplished by modifying the PCA computation of the abstract features to include the concentration data. The PLS computational process yields abstract features which are not necessarily optimal for the predictor data, but they ideally have greater predictive ability compared to the PCA features. Although the following discussion will be limited to principal component analysis, much of the discussion is applicable to the PLS technique.

As shown in the theoretical development of PCA (170), the desired vector space is defined by the eigenvectors of the covariance matrix. The covariance matrix, $\boldsymbol{Z}$, is calculated as:

$$\boldsymbol{Z} = \boldsymbol{D}^{t}\boldsymbol{D} \qquad \text{(III-10)}$$

where $\boldsymbol{D}$ is the $j \times m$ matrix of measured responses for j standard mixtures. Although the $\boldsymbol{D}$ matrix is not necessarily square, the covariance matrix is square. The covariance matrix introduces a statistical bias in the analysis by weighting each data point in proportion to its absolute value (170). Thus, a greater statistical significance is placed on data points with large values. The bias introduced is desirable for measurements made with respect to an absolute standard, and the accuracy of each data point is the same (170).

An alternative representation, called the correlation matrix, places equal statistical bias on each column of data. The correlation matrix is computed similar to the covariance matrix, except that each

column vector of the data matrix is normalized with respect to its magnitude. This normalization procedure weights each column of data equally. Equal statistical biasing of the data is recommended when measurements are made with respect to an arbitrary reference, when each data column represents different properties having values which differ by several orders of magnitude, or when the experimental error is directly proportional to the measurement magnitude (170).

Eigenanalysis of either the covariance or correlation matrices will generate a set of eigenvectors. The number of eigenvectors contained in the set will be less than or equal to the number of measured responses, j. When the response data is highly correlated, fewer than j eigenvectors are required to describe most of the variance. For example, near infrared absorption spectrums, which may have thousands of data points, can typically be described with as few as 15 eigenvectors (172). Thus, data compression is achieved by projecting the data onto the space defined by those eigenvectors which account for most of the variance. That is,

$$\boldsymbol{F} = \boldsymbol{D}\boldsymbol{L}^{t} \tag{III-11}$$

where $\boldsymbol{L}$ is the reduced eigenvector matrix, and $\boldsymbol{F}$ contains the factor loadings which indicate the relative contribution of each eigenvector necessary to reproduce the data matrix. That is, the factor loadings are the coordinates of the data in the reduced eigenspace. Once the response data has been compressed through factor analysis, multiple regression analysis becomes possible. The regression analysis is performed using the factor loading matrix, $\boldsymbol{F}$, in place of the data matrix, $\boldsymbol{X}$, in Equation (III-9). A numerical example of PCA and multiple regression analysis of a multicomponent non-linear system is provided in Appendix A.

A number of criteria for eliminating eigenvectors have been described that are based on an examination of the corresponding eigenvalues (170). The j eigenvectors obtained from eigenanalysis can be divided into two classes: principal eigenvectors, which represent the real data, and secondary eigenvectors, which represent noise and components whose contribution to the measured response is small. Since the trace of a matrix is equal to the sum of its eigenvalues (167), the total variance in the original data is given by the sum of the eigenvalues. Thus, the magnitude of each eigenvalue indicates the relative importance of the corresponding eigenvector when accounting for the variance in the data (170, 173). When the eigenvectors are rank ordered according to the magnitude of the corresponding eigenvalues, it is found that, once the data is represented by a sufficient number of eigenvectors (those with the largest eigenvalues), the remaining eigenvalues become very small and do not vary significantly

A multicomponent infrared absorption study by Donahue provides an example of eigenvector selection based upon two different criteria. The two criteria are called the factor indicator function (IND) and $frac_i$. The eigenvectors are rank ordered according to the magnitude of the eigenvalues prior to application of both of these indicator functions. The empirical IND criteria is given by (170, 173):

$$IND = \left(\frac{\sum_{j=l+1}^{m} \lambda_j}{t(m-l)^5} \right)^{1/2} \qquad \text{(III-12)}$$

where λ_j is the jth eigenvalue; t is the number of rows in the data matrix; m is the number of mixtures; and l is the number of eigenvectors. For a set of m mixtures, principal component analysis produces m eigenvectors and m eigenvalues. The value of the IND function reaches a minimum when the correct number of eigenvectors are employed (170). The second criteria is defined by the equation (173)

$$\text{frac}_i = \frac{\lambda_i}{\sum_{j=i}^{m} \lambda_j} \qquad \text{(III-13)}$$

where λ_i is the ith eigenvalue in the set of eigenvalues arranged according to decreasing magnitudes, and the sum is over the ith eigenvalue and all the remaining eigenvalues. This function should reach a minimum when the variation in the eigenvalues becomes small. The eigenvector corresponding to the eigenvalue which minimizes the $frac_i$ function, and all the remaining eigenvectors, represents noise in the data. Thus, the appropriate number of eigenvectors is one less than that which minimizes the $frac_i$ function (173).

Unfortunately, these indicator functions may not converge on a minimum, or they may have multiple minima. The selection criteria fails when no minimum exists, and some of the other criteria which have been proposed (170) must be used to select the correct number of eigenvectors. Since the possiblility of multiple minima exists, the indicator function must be evaluated for all the eigenvalues obtained from the data set. If multiple minima are found to exist, choosing the minimum which occurs with the largest number of eigenvectors may provide a useful selection criteria.

The predictive capability of these indicator functions, as well as the effect of the number of eigenvectors included in the calibration process with respect to the accuracy of the predicted component

concentrations, has been evaluated in terms of the Standard Error of Prediction (SEP) through a cross-validation procedure. In this procedure, the error for an independent set of validation samples is measured as a function of the number of eigenvectors. For a single component, the SEP is given by (168, 173):

$$\text{SEP} = \left(\frac{\sum_{j=1}^{m} (c_{ij} - \hat{c}_{ij})^2}{m - 1} \right)^{1/2} \qquad \text{(III-14)}$$

where c_{ij} and $\hat{c}_{ij}$ are the actual and estimated concentrations for the ith component in the jth mixture, and m is the number of mixtures. The SEP for the total mixture is given by (168, 173):

$$\text{SEP} = \left(\frac{\sum_{i=1}^{n} \sum_{j=1}^{m} (c_{ij} - \hat{c}_{ij})^2}{n(m - 1)} \right)^{1/2} \qquad \text{(III-15)}$$

where n is the number of components.

The results of PCA on standard binary mixtures composed of pseudocumene and *p*-xylene are given in Table III-1, where the IND and the frac_i values for each eigenvector are presented along with the SEPs for each component and mixture. The IND and frac_i criteria, which reach a minimum with 6 and 7 eigenvectors, respectively, indicate that the optimum number of eigenvectors is 6. In this case, however, the SEP continued to decrease when more than 6 eigenvectors were utilized. The assumption implicit in the IND and frac_i indicators is that the eigenvectors with small eigenvalues represent the noise in the data. The decrease in the SEP for more than 6 eigenvectors suggests that this assumption is not entirely valid, and some signal content, in addition to the noise, is represented by the eigenvectors with small eigenvalues. In a similar analysis involving three component mixtures composed of pseudocumene, *p*-xylene, and *m*-xylene, the IND criteria did not have a minimum, while the frac_i criteria mainfested two similar minimums when 9 and 13 eigenvectors were utilized. The SEPs plateau with 7 eigenvectors, one less than the number predicted by the frac_i criteria. The SEP for component 3 decreases to a second plateau with 11 eigenvectors, again, one less than that predicted by the frac_i criteria, at which point, the SEPs of the two other components begin to decrease. Upon inspection of

Table III-1. Effect of the Eigenvector Number on the IND and $frac_i$ Criteria along with the Standard Error of Prediction (SEP) for the Infrared Absorption Analysis of Pseudocumene and *p*-xylene Binary Mixtures (173).

Number of Eigenvectors	IND x 10^5	$frac_i$	SEP $comp_1$	SEP $comp_2$	SEP total
1	8.03	0.994			
2	1.92	0.968	1.42	2.75	2.19
3	1.58	0.653	1.36	2.65	2.11
4	0.78	0.888	0.43	0.26	0.35
5	0.60	0.761	0.46	0.17	0.35
6	0.50	0.773	0.25	0.14	0.20
7	0.74	0.481	0.13	0.12	0.13
8	1.27	0.613	0.13	0.11	0.12
9	4.17	0.661	0.07	0.12	0.10
10			0.07	0.11	0.10

several data sets, the SEP for different components was found to reach its minimum with a different number of eigenvectors.

Neural Networks

Neural networks have only recently been applied to the analysis of multicomponent gas systems (174-177). In 1990, Nakamoto et al. was able to distinguish among five Japanese whiskeys with a neural network trained with data collected from an array of coated quartz crystal microbalance sensors (174). In a subsequent study, Gardner et al. was able to identify five different alcohols with a neural network trained with tin oxide chemiresistor data (175). Sommer et al. performed a quantitative analysis of methane and butane binary mixtures in air using neural networks trained with platinum pellistor measurements (176). The strong interaction of these gases on the platinum surface produces a highly non-linear pellistor response. Using two neural networks, each trained to identify only one of the two gases, the maximum concentration error was either 4 or 10 percent of the lower explosion limits (LELs) for methane and butane, respectively. The maximum concentration error is an alternative method for expressing the error in an analysis, and is always greater than the SEP. Similar concentration errors were obtained with a semi-empirical approach where the pellistor data was numerically fitted to a model which explicitly accounted for the reaction order and interaction effects. In another study, Gemperline et al. compared the capability of multivariate linear models (principal component regression and partial least squares) and artificial neural networks to analyze multicomponent systems possessing non-linear responses (177). Simulated and experimental spectroscopic data corresponding to multicomponent systems were evaluated. Non-linearities introduced into the simulated spectroscopic data sets for binary and ternary mixtures included stray light effects, concentration-dependent wavelength shifts, and concentration-dependent absorption bandwidth changes. The experimental data sets included two-component and five-component mixtures. Gemperline et al. found that the artificial neural network did not perform as well as PCR and PLS (manifested by a larger standard error of prediction (SEP)) when the input data set was highly correlated. They point out that the numerical analysis method of steepest descent, which is typically used to adjust the weights in a neural network, performs poorly with highly correlated data. However, if the input data set was orthogonalized in a manner similar to principal component analysis, the artificial neural network consistently produced slightly better results (smaller SEP values) compared to PCR and PLS. The PLS method also gave slightly better performance compared to PCR. Gemperline et al. concluded that PCR and PLS calibrations can produce good approximations to non-linear systems by including extra factors in the calibration model when low noise

data is available. They also demonstrated the potential for using artificial neural networks in gas analysis when principal components are utilized.

There are a wide variety of neural networks described in the literature. This brief review only discusses the type of neural networks utilized by the studies described above (176, 177). The reader is referred to the review article by Lippmann for a more general description of neural networks (178). In the studies relevant to the above disucussion, the neural networks were composed of three layers: a linear input layer, one hidden layer, and an output layer. Each layer consists of a set of nodes having one or more inputs and a single output, as shown in Figure III-3. The output from each node is computed by applying a predefined transformation or transfer function to the weighted sum of the inputs to the node. Classically, this pre-defined transformation is a hard-limiting, non-linearity such as a sigmoidal function (178). The neural network described by Sommer et al. used the sigmoidal Fermi distribution function as the node transfer function. Gemperline et al., however, evaluated several different node transfer functions. The input and output layer nodes were linear with their output equal to their input. The second layer (referred to as the hidden layer) was composed of a bias node with an output always equal to one, and with one to three nodes possessing either a linear or sigmoidal transfer function. A quadratic and a hyperbolic tangent transfer function were also evaluated, but prediction results with these transfer functions were not reported.

The neural network is trained (calibrated) by adjusting the weights according to the error observed between the network output, y, and the desired (correct), d, response (output) (179). Initially, the weights are assigned small random values, which are then adjusted while the training data set is repeatedly applied to the network inputs. The process by which the weights are adjusted is referred to as the back-propagation algorithm, because the error in the output is propagated back through the network to adjust the weights.

The back-propagation algorithm applies a gradient search to minimize the mean square error between the desired and the actual network outputs (179). The instantaneous gradient of the mean square error, ε^2, at a node with respect to the weight vector, W, is given by (179):

$$\nabla = \frac{\partial \varepsilon^2}{\partial W} \qquad \text{(III-16)}$$

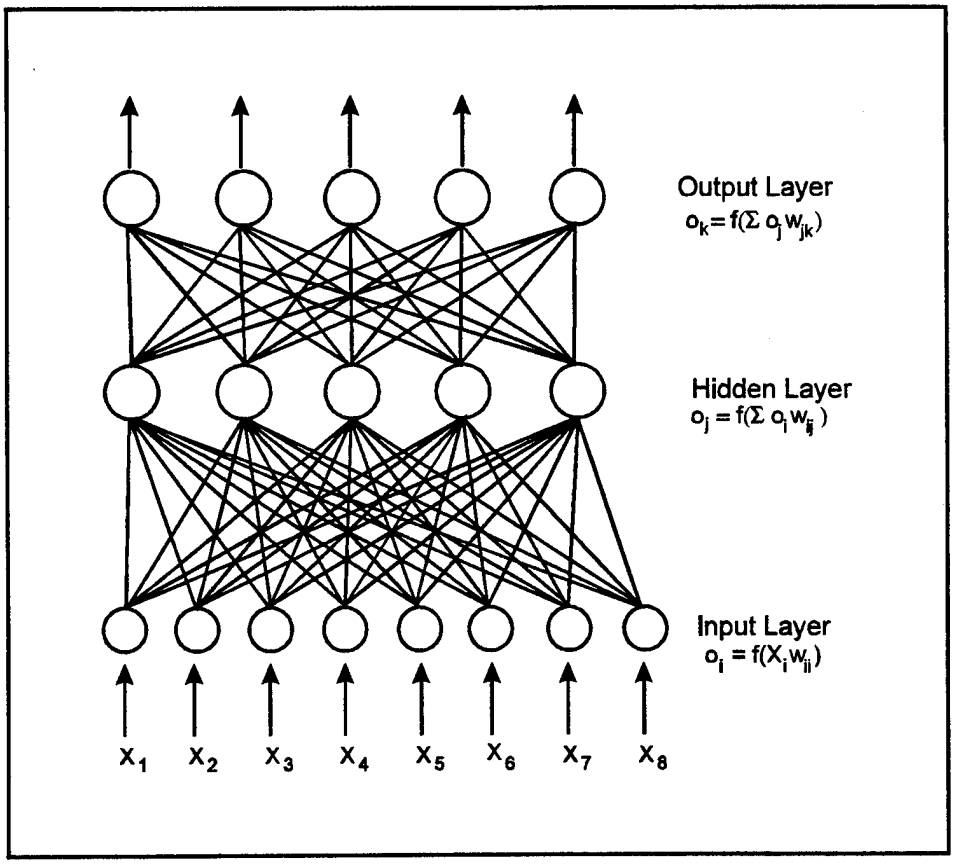


Figure III-3. A Typical Artificial Neural Network. Eight Inputs (X_i) are Applied to the Eight Nodes of the Input Layer. The Interconnections Weights (w) are Adjusted During Training (177).

where ε^2 is given by:

$$\varepsilon^2 = \sum_{j=1}^{N} (d_j - y_j)^2 . \qquad \text{(III-17)}$$

The weighted sum of the input vector X to a node is denoted by s, and it is given by:

$$s = W^T X . \qquad \text{(III-18)}$$

The gradient can be rewritten as:

$$\nabla = \frac{\partial \varepsilon^2}{\partial W} = \frac{\partial \varepsilon^2}{\partial s} \frac{\partial s}{\partial W} \qquad \text{(III-19)}$$

Since W and X are independent,

$$\frac{\partial s}{\partial W} = \frac{\partial W^T X}{\partial W} = X \qquad \text{(III-20)}$$

and, therefore,

$$\nabla = \frac{\partial \varepsilon^2}{\partial s} X . \qquad \text{(III-21)}$$

By defining the square error derivative, δ, associated with each node as:

$$\delta = -\frac{1}{2} \frac{\partial \varepsilon^2}{\partial s} , \qquad \text{(III-22)}$$

the gradient becomes:

$$\nabla = -2\delta X . \qquad \text{(III-23)}$$

Using the method of steepest descent (180), the weights, following application, k, of the training data set, are adjusted in the direction opposite to the gradient as follows:

$$W_{k+1} = W_k + \eta(-\nabla_k) = W_k + 2\eta \delta_k X_k . \qquad \text{(III-24)}$$

The parameter, η, is a gain term used to accelerate convergence. Equation III-24 is often modified to accelerate convergence by adding a third term which smooths the weight changes (178):

$$\boldsymbol{W}_{k+1} = \boldsymbol{W}_k + \mu(-\nabla_k) = \boldsymbol{W}_k + 2\mu\delta_k\boldsymbol{X}_k + \alpha(\boldsymbol{W}_k - \boldsymbol{W}_{k-1}). \quad \text{(III-25)}$$

The parameter, α, is referred to as the momentum. The expression for the square error derivative at each output node, δ_o, is given by (179):

$$\delta_o = \varepsilon \cdot f'(\boldsymbol{X}) \quad \text{(III-26)}$$

where f′ is the derivative of the transfer function associated with the node. At a hidden node, j, the expression for the square error derivative, δ_j, is given by (179):

$$\delta_j = \varepsilon_j \cdot f_j'(\boldsymbol{X}) \quad \text{(III-27)}$$

where

$$\varepsilon_j = \sum_k \delta_k W_{jk} \quad \text{(III-28)}$$

and *k* is over all nodes in the layers above node j.

Summary

This chapter discussed and summarized several multivariate statistical analysis techniques that have been applied to the analysis of the response of chemosensor arrays challenged with multicomponent gas mixtures. Table III-2 compares the suitability of each of the methods discussed in this chapter for accomplishing different sensor applications. With respect to this research, only those methods which are applicable to the analysis of multicomponent mixtures are acceptable candidates since binary gas mixtures are being investigated. In addition, the transfer characteristics of the Interdigitated Gate Electrode Field-Effect Transistor (IGEFET) microsensor were not likely to be linear and, therefore, an acceptable method for this research must also be capable of handling non-linearities. The response of the microsensor elements were also expected to be highly correlated since chemically similar films were deposited on the microsensor array. Thus, a principal component analysis technique combined with a *P*-matrix multiple regression analysis was selected for performing the gas analyses in this research. Although an artificial neural network is also a good candidate for this research, these networks have only recently been applied to multicomponent gas analysis, and are more complicated to implement compared to the well established PCA and multiple regression techniques.

Table III-2. Comparison of Different Multivariate Statistical Analysis Techniques with Respect to the Properties of Several Sensing Applications.

		Correlation	Cluster Analysis	Multiple Regression Analysis		Principal Component Analysis	Artificial Neural Networks
				K-Matrix	*P*-Matrix		
Task	Identification	X[1]	X	X	X	X	X
	Concentration Determination			X	X	X	X
Gas Mixture	Single Component	X	X	X	X	X	X
	Multicomponent			X	X	X	X
Transfer Characteristic	Linear	X	X	X	X	X	X
	Non-linear	X	X		X[2]	X[2]	X

[1]The X Symbol Means that the Technique is Applicable.
[2]With Appropriate Mathematical Transformation.

IV. *Fundamental IGEFET Microsensor Characterization*

The Interdigitated Gate Electrode Field-Effect Transistor (IGEFET) microsensor can be partitioned into two fundamental components: the integrated circuit (IC) and the chemically-sensitive thin film deposited on the surface of the interdigitated gate electrode (IGE) structure of each IGEFET sensing element. The combined properties of these two components determines the overall performance of the microsensor. The design of the integrated circuit determines, to a large extent, the fundamental electrical behavior of the microsensor. However, the chemically-sensitive film deposited on the surface of the interdigitated gate electrode and its interaction with gases can significantly influence the microsensor's electrical response. In this research investigation, three chemically-sensitive films, copper-, nickel-, and cobalt-phthalocyanine, were utilized. As discussed in Chapter II, the structure of the metal-substituted phtahalocyanine films signifcantly influences their gas adsorption and electrical properties. Therefore, to establish the basic operating characteristics of the IGEFET microsensor, both a physical and electrical characterization of the microsensor and the deposited metal-substituted phthalocyanine (MPc) films were conducted. The IGEFET microsensor and the deposited films were physically characterized using scanning electron microscopy (SEM). In addition, transmission electron microscopy (TEM) and infrared (IR) spectroscopy were used to further characterize the deposited MPc films. The microsensor, with and without the deposited MPc films, was characterized electrically with direct current (DC) and alternating current (AC) measurements of the sensor's electrical performance under a variety of experimental conditions. This chapter is organized into three sections. The first section introduces the microsensor design. The design overview is followed by the physical characterization of the microsensor and the deposited MPc films. The final section describes the electrical characterization of the microsensor.

IGEFET Microsensor Design

The IGEFET microsensor design used in this research was the fourth revision (Rev. 4) in the evolution of the IGEFET microsensor at the Air Force Institute of Technology (AFIT) (21, 22, 23). This particular revision of the IGEFET microsensor was designed by Capt Thomas Jenkins and fabricated by MOSIS (Metal Oxide Semiconductor Implementation System). An unpublished report prepared by Capt Jenkins provides a detailed description of the Rev. 4 design, and it is provided in Appendix B. The Rev. 4 design features an array of nine independent sensing elements. Each sensing element is composed of an interdigitated gate electrode (IGE) structure that is coupled to the non-inverting terminal of a

differential input amplifier. The interdigitated gate electrode was supported above an aluminum ground plane by a field oxide layer. The IGE structure was designed to have the dimensions provided in Table IV-1. The ground plane under each IGE structure was routed to a single output pad to form a single, continuous, metal ground plane common to all sensing elements. In contrast, the remaining sensing element connections were routed to separate bond pads, providing the capability to isolate and interrogate an individual sensing element's response with no impact on the performance of the other elements. The following external connections were available to each sensing element: driven-gate (DG) electrode, floating-gate (FG) electrode, bias voltage (V_{bias}), offset voltage (V_{offset}), output voltage (V_{out}), and the two power supply connections (V_{dd} and V_{ss}). In addition to the nine sensing elements, three test capacitors were included in the design for use in verifying the field oxide thickness. The IGEFET Rev.4 design sketched in Figure IV-1 shows the arrangement of the nine sensing elements, the three capacitors, the ground plane, and the wire bond configuration. The wire bond contact functions are provided in Table IV-2.

Sensor Physical Characterization

Three techniques were used to physically characterize the IGEFET microsensor and the phthalocyanine films. Scanning electron microscopy (SEM) was used to verify the IGEFET microsensor's structure and the morphology of the deposited phthalocyanine films. To lend further support to the SEM morphological studies and to estimate the crystallite size, transmission electron microscopy (TEM) of the phthalocyanine films was accomplished. Infrared (IR) spectroscopy was used to confirm the chemical composition and morphology of the MPc films, as well as to investigate the MPc gas adsorption properties.

Scanning Electron Microscopy. Although most of the sensor geometry was specified in the MOSIS design layout, the field oxide thickness and the electrode height of the interdigitated gate electrode structure were entirely dependent upon the MOSIS fabrication process. To measure the dimension of these structural features, an unpackaged IC die was cross-sectioned and imaged with SEM, as shown in Figure IV-2. Several measurements at different magnifications were averaged to obtain an oxide thickness of 0.9 μm and an electrode thickness of 1.2 μm. The oxide thickness measured between the bottom of a metal electrode and the top surface of the metal ground plane was consistent with the oxide thickness determined from the MOSIS supplied data and that determined from the on-chip test capacitor measurements. In addition to permitting measurement of the IGE field oxide thickness and electrode thickness, the cross-sectional images of the IGE structure revealed that the MOSIS etch process

Table IV-1. Geometrical Dimensions of the Revision 4 IGEFET Microsensor Design.

Number of IGEFET Sensor Elements	9
Number of Fingers in the Driven Electrode	35
Number of Fingers in Floating Electrode	34
Electrode Width (μm)	10
Electrode Separation (μm)	10
Overall Array Width (μm)	1370
Overall Array Length (μm)	1370

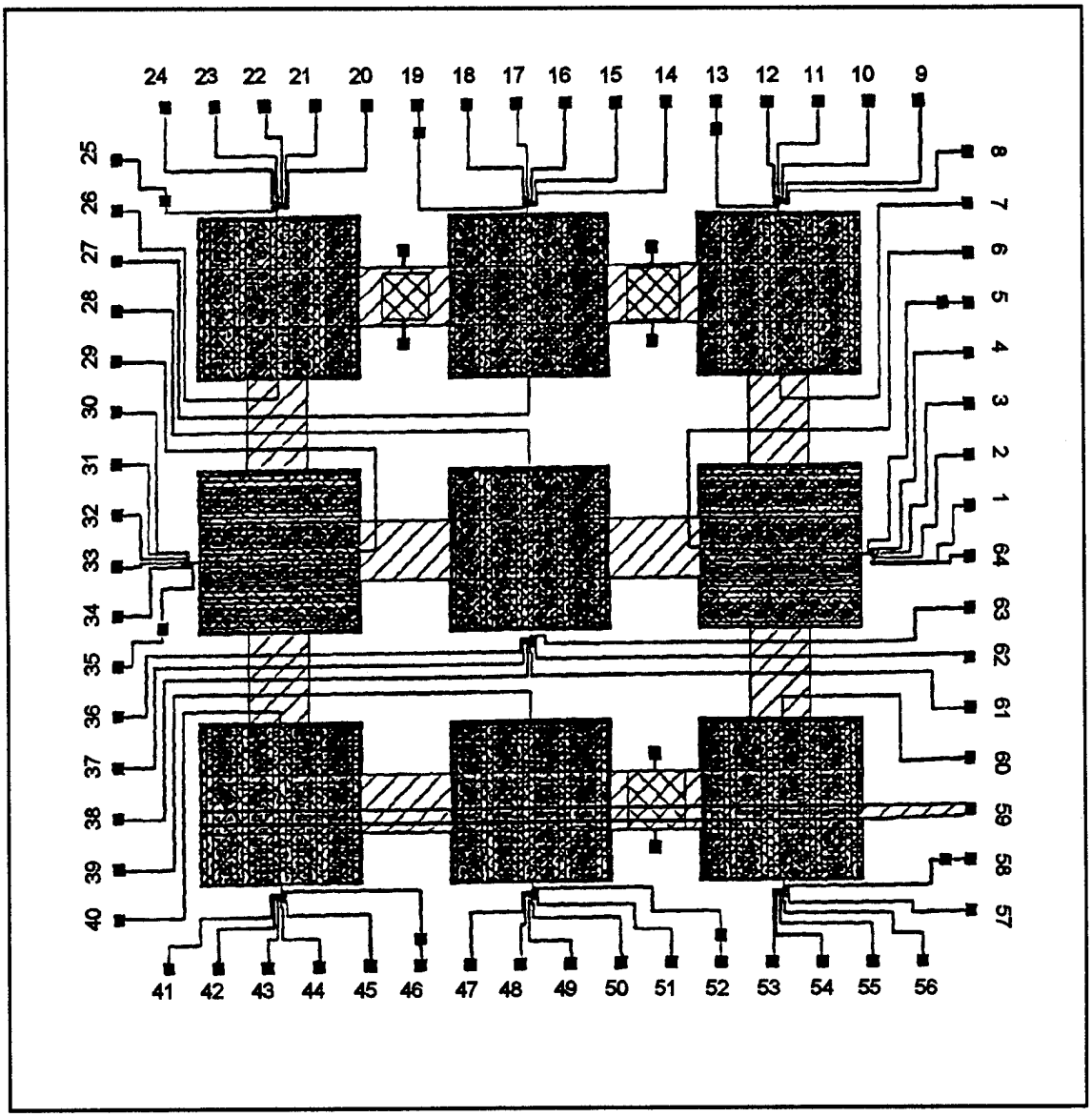


Figure IV-1. IGEFET Revision 4 (Rev. 4) Microsensor IC Design.

Table IV-2. 64-Pin DIP Wire Bond Function Summary (Continued on the next page).

Pin Number	Signal Name	Associated Microsensor	Pin Number	Signal Name	Associated Microsensor
1	V_{bias}	IGE#6	23	V_{out}	IGE#1
2	V_{ss}	IGE#6	24	V_{dd}	IGE#1
3	V_{out}	IGE#6	25	FG	IGE#1
4	V_{dd}	IGE#6	26	DG	IGE#1
5	FG	IGE#6	27	DG	IGE#2
6	DG	IGE#6	28	DG	IGE#5
7	DG	IGE#3	29	DG	IGE#4
8	V_{offset}	IGE#3	30	V_{offset}	IGE#4
9	V_{bias}	IGE#3	31	V_{bias}	IGE#4
10	V_{ss}	IGE#3	32	V_{ss}	IGE#4
11	V_{out}	IGE#3	33	V_{out}	IGE#4
12	V_{dd}	IGE#3	34	V_{dd}	IGE#4
13	FG	IGE#2	35	FG	IGE#4
14	V_{offset}	IGE#2	36	V_{offset}	IGE#5
15	V_{bias}	IGE#2	37	V_{bias}	IGE#5
16	V_{ss}	IGE#2	38	V_{ss}	IGE#5
17	V_{out}	IGE#2	39	DG	IGE#8
18	V_{dd}	IGE#2	40	DG	IGE#7
19	FG	IGE#2	41	V_{offset}	IGE#7
20	V_{offset}	IGE#1	42	V_{bias}	IGE#7
21	V_{bias}	IGE#1	43	V_{ss}	IGE#7
22	V_{ss}	IGE#1	44	V_{out}	IGE#7

Table IV-2. 64-Pin DIP Wire Bond Function Summary (Continuation from Previous Page).

Pin Number	Signal Name	Associated Microsensor	Pin Number	Signal Name	Associated Microsensor
45	V_{dd}	IGE#7	55	V_{ss}	IGE#9
46	FG	IGE#7	56	V_{out}	IGE#9
47	V_{offset}	IGE#8	57	V_{dd}	IGE#9
48	V_{bias}	IGE#8	58	FG	IGE#9
49	V_{ss}	IGE#8	59	Ground Plane	
50	V_{out}	IGE#8	60	DG	IGE#9
51	V_{dd}	IGE#8	61	V_{out}	IGE#5
52	FG	IGE#8	62	V_{dd}	IGE#5
53	V_{offset}	IGE#9	63	FG	IGE#5
54	V_{bias}	IGE#9	64	V_{offset}	IGE#6

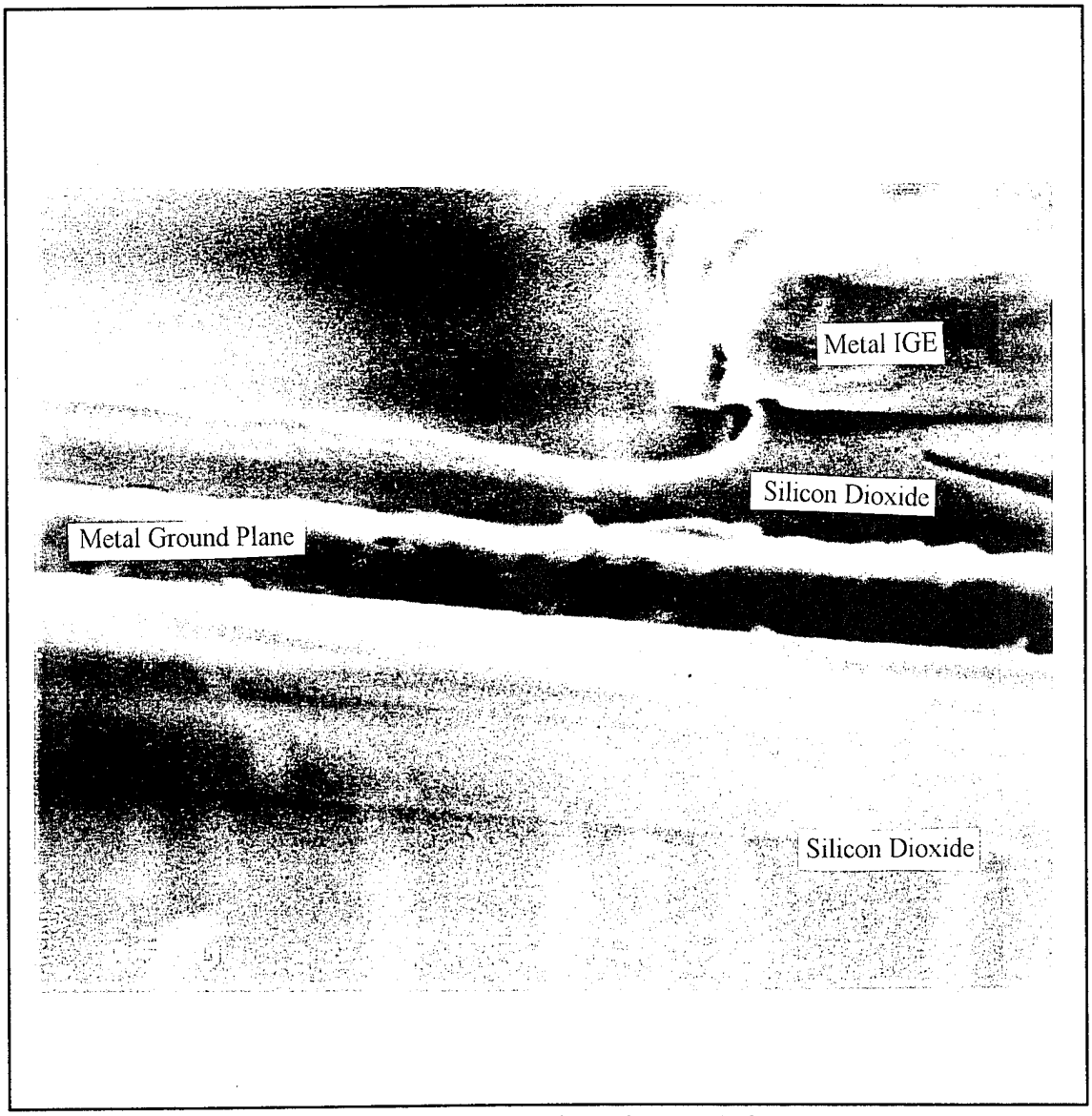


Figure IV-2. Scanning Electron Micrograph of a Cross-Sectioned IGEFET Revision 4 Microsensor Showing the Interdigitated Gate Electrode Structure and the Degree of Oxide Undercutting Beneath the IGE Structure.

used to remove the silicon dioxide from the region between the metal electrodes produced significant undercutting beneath the lower edge of the metal electrodes. Furthermore, the field oxide within the interelectrode spaces was etched to a level that was 3000 Å below the lower edge of the electrodes. A diagrammatic representation of the measured interdigitated gate electrode structure is shown in Figure IV-3. Although other IGE sensors reported in the literature are often assumed to possess the ideal structure, some degree of oxide undercutting is likely to be present. The 30 percent thinning of the field oxide between the metal electrodes was expected to significantly alter the microsensor's electrical behavior relative to that of an 'ideal' IGE structure. As a result, the field oxide undercut was partially accounted for in the finite-difference model of the IGE structure developed in Chapter V.

Cross-sectional SEM images of interdigitated gate electrode structures coated with copper-, nickel-, and cobalt-phthalocyanine films were used to evaluate the deposition of the MPc films onto the IGEFET microsensor. Since the film morphology observed in the SEM was nearly identical for all three films, most of the study was conducted with only the copper phthalocyanine (CuPc) film. Three CuPc films with different thicknesses were vacuum sublimed at a pressure of 10^{-6} torr onto three unpackaged IGEFET microsensors. The deposition rate, monitored with a calibrated piezoelectric quartz crystal film thickness detector, was maintained at approximately 3 Å/s. The vacuum sublimation technique used in this research to deposit the films has been described previously (25). The deposited CuPc film thicknesses were 1700 Å, 8500 Å, and 30,000 Å. These film thicknesses were chosen to provide examples of the IGE structure with an incompletely filled undercut, a nearly filled inter-electrode space, and a completely filled inter-electrode space. The cross-sectional images of the sensors with the three film thicknesses are shown in Figures IV-4 through IV-6. The columnar growth characteristic of the phthalocyanine films was apparent in all three samples. Although the deposited films appear to be uniform across the surface of the interdigitated gate electrodes, film growth within the undercuts was shadowed by the metal electrodes and by the film growth on the electrode's upper surface. This shadowing effect caused the formation of air gaps between the phthalocyanine deposited within the interelectrode space and the metal electrodes themselves. The discontinuity in the film was bridged when the film thickness was increased to 30,000 Å. Although the presence of an air gap might be expected to dominate the IGE structure's electrical behavior, deposition of a 2000 Å CuPc film caused a two order of magnitude decrease in the interdigitated gate electrode resistance (See Figures IV-59 and IV-77 presented later in this chapter). This result suggests that the film deposited in the inter-electrode space must contact the electrodes, at least in filamentary regions.

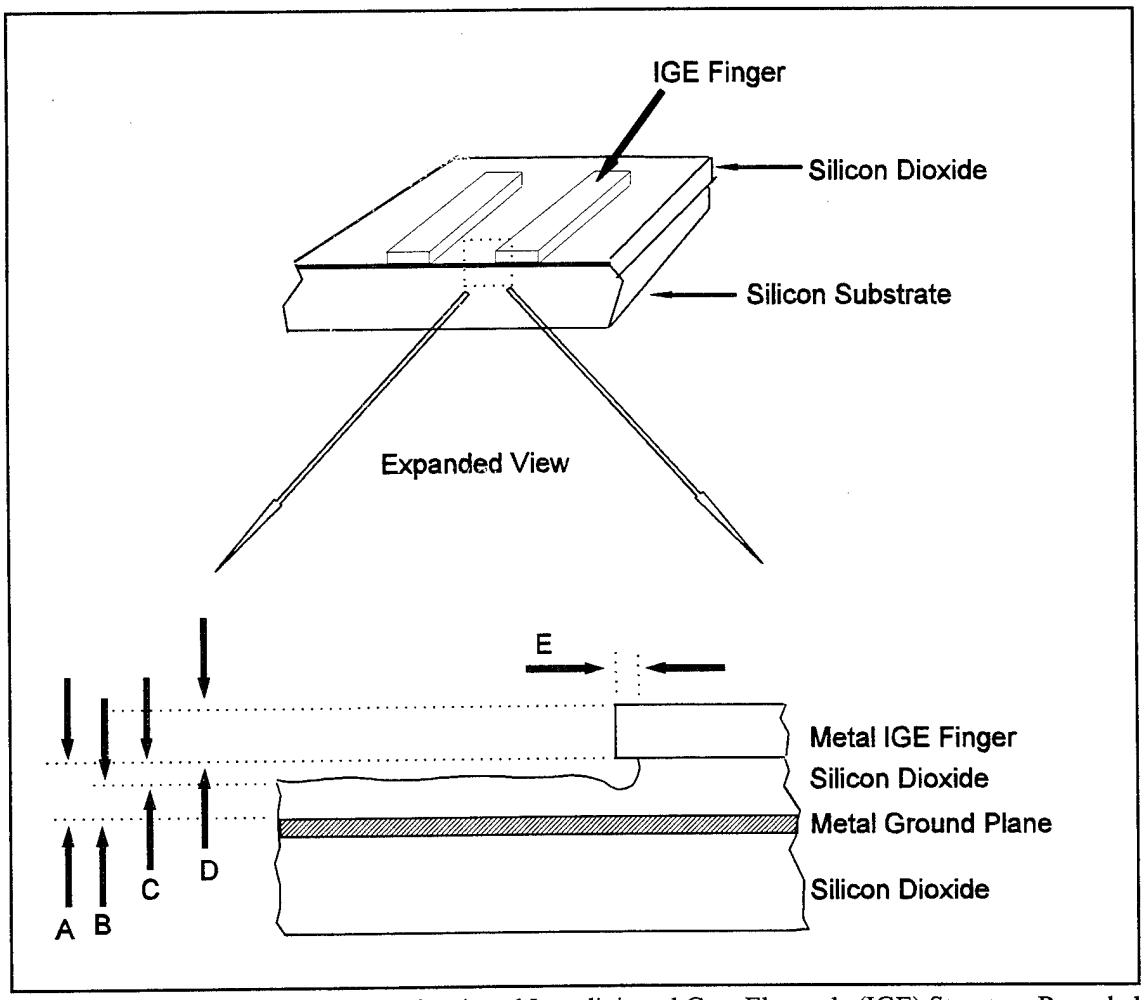


Figure IV-3. Diagram of the Cross-Sectioned Interdigitated Gate Electrode (IGE) Structure Revealed by the Scanning Electron Micrograph shown in Figure IV-2. Average Dimensions: A=860 nm, B=550 nm, C=300 nm, D=1200 nm, and E=260 nm.

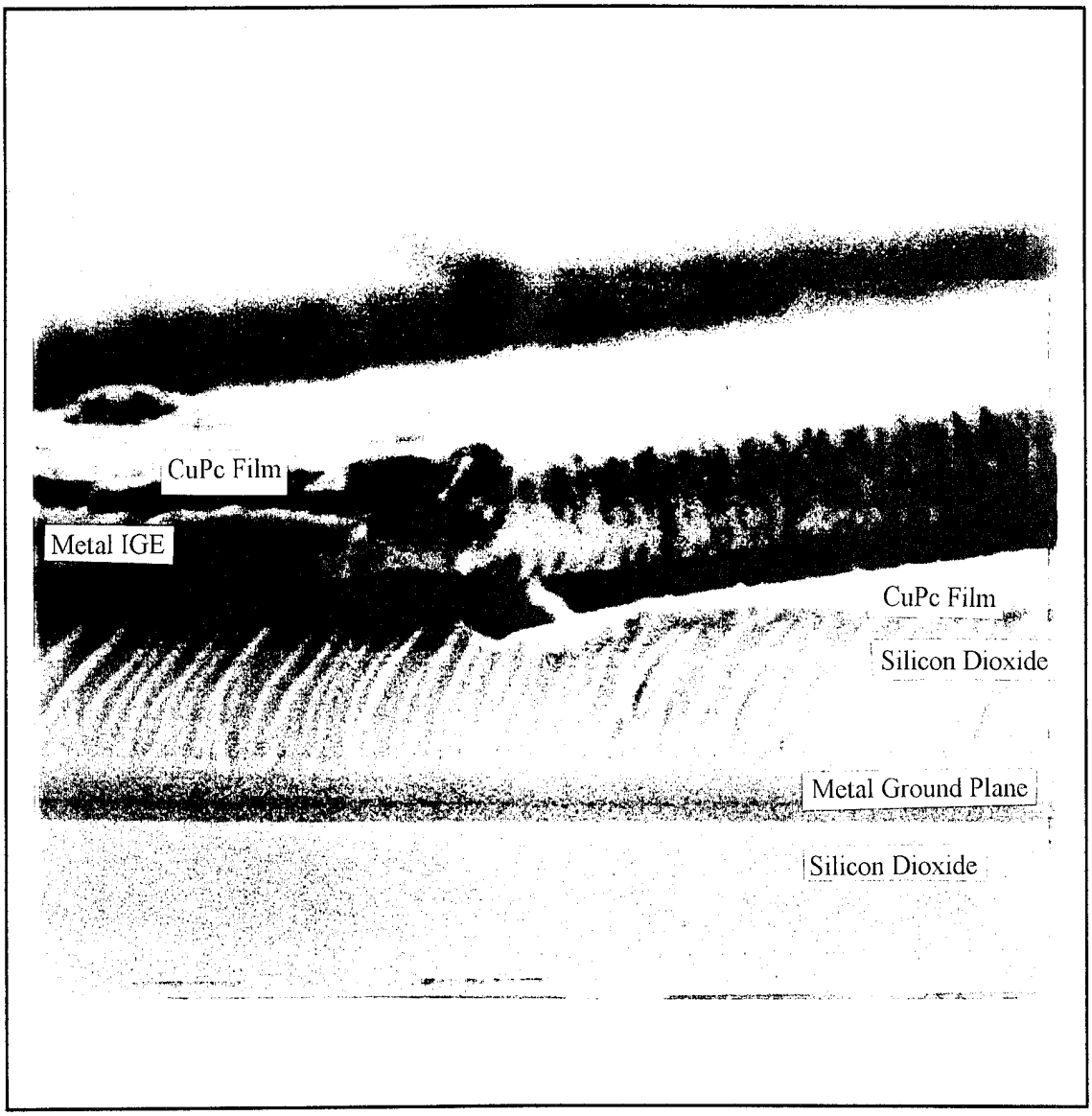


Figure IV-4. Scanning Electron Micrograph of a Cross-Sectioned Interdigitated Gate Electrode Structure after Vacuum Deposition of a 1700 Å Thick Copper Phthalocyanine (CuPc) Thin Film.

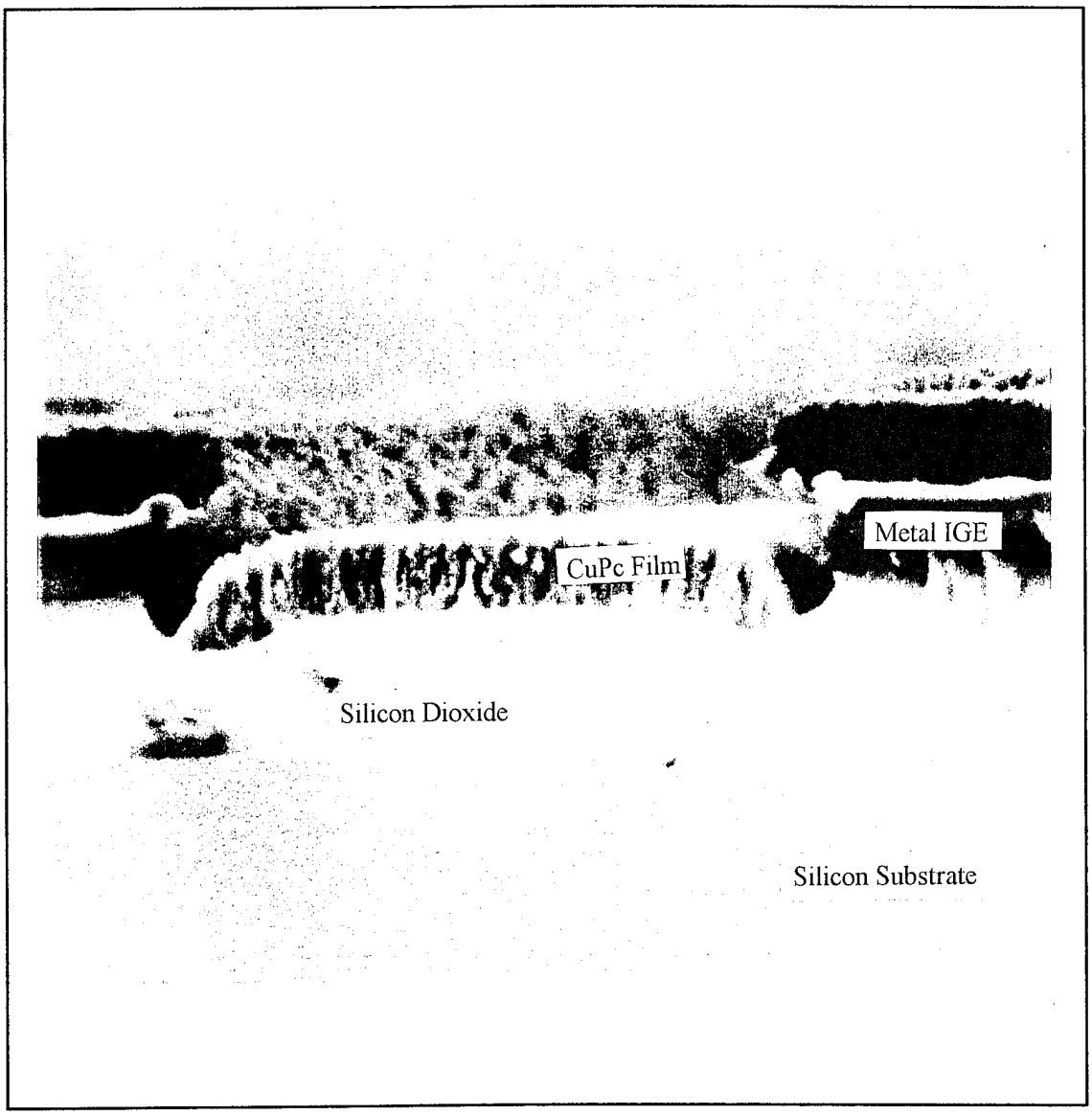


Figure IV-5. Scanning Electron Micrograph of a Cross-Sectioned Interdigitated Gate Electrode Structure (Revision 3 Design) after Vacuum Deposition of a 8500 Å Thick Copper Phthalocyanine (CuPc) Thin Film.

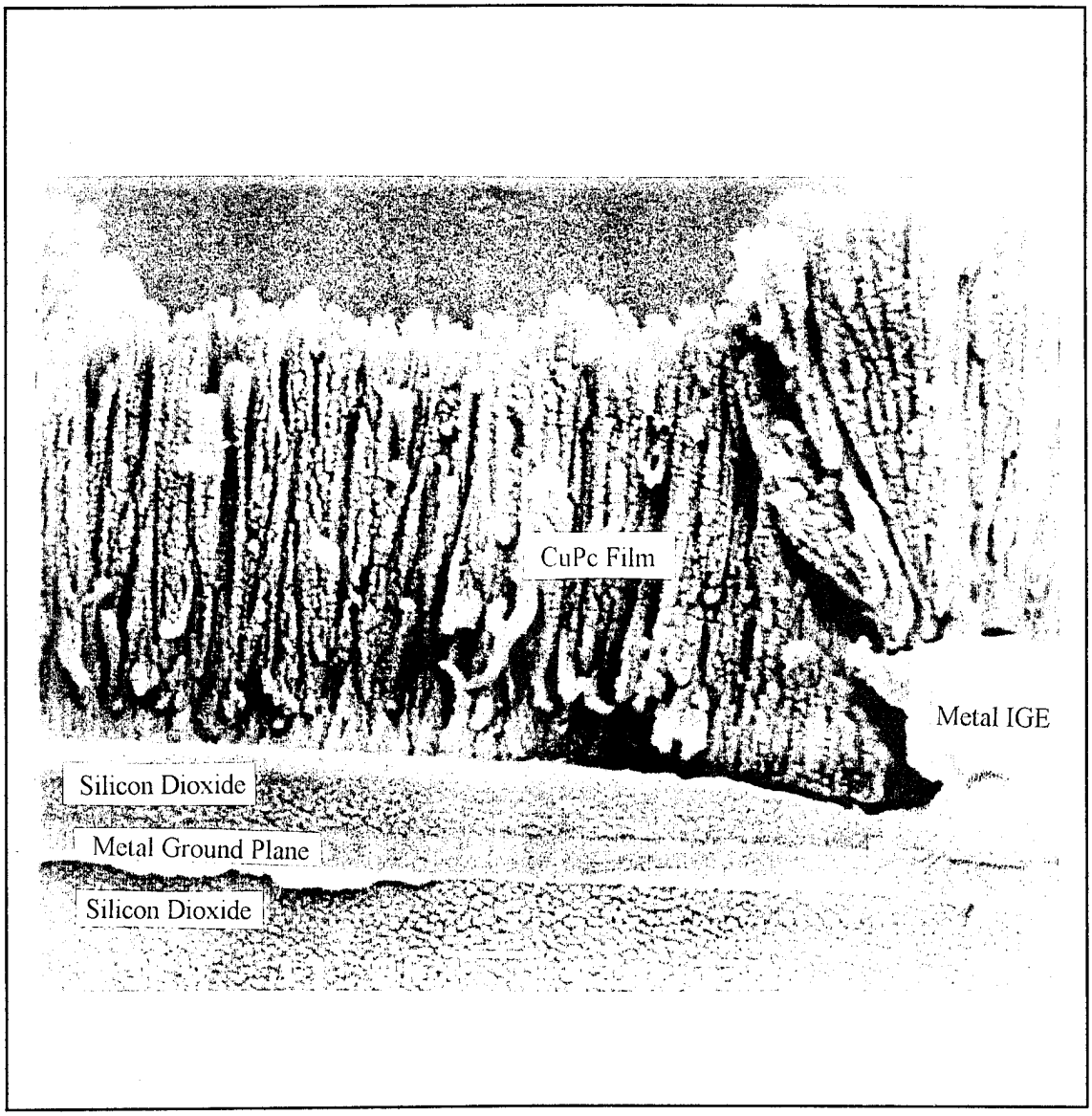


Figure IV-6. Scanning Electron Micrograph of a Cross-Sectioned Interdigitated Gate Electrode Structure after Vacuum Deposition of a 30,000 Å Thick Copper Phthalocyanine (CuPc) Thin Film.

Transmission Electron Microscopy and Transmission Electron Diffraction. To determine the crystalline phase of the columnar MPc films observed in the SEM, 500-1000 Å thick MPc films were vacuum sublimed at a pressure of 10^{-6} torr onto carbon grids for imaging with a transmission electron microscope (Transmission Electron Microscope, Model 2000FX, JEOL USA, Incorporated, Peabody, MA). Figures IV-7 through IV-9 show the polycrystalline nature of the sublimed CuPc, NiPc, and CoPc films. All three films are composed of a conglomeration of small crystallites which have an average radius of approximately 300 Å. In the microscope's electron beam diffraction mode, micrographs of the electron diffraction patterns generated by each film were captured (see Figures IV-10 through IV-12). The radius of the diffraction rings were measured with an optical loupe, and the crystal plane spacings were calculated using Bragg's Law. Comparison of the experimentally determined crystal plane spacings with those published, confirmed the identification of the α-phase crystalline structure for all three film types (see Tables IV-3 through IV-5).

Attempts to confirm thermal conversion to the β-phase using electron diffraction analysis were unsuccessful. Initially, when the MPc coated TEM grids were subjected to a 350° C heat treatment for thirty minutes in a nitrogen stream, the TEM grids were distorted, and the carbon film support ruptured. In the second attempt, the same heat treatment process was applied with a higher nitrogen flow rate. In this situation, the TEM grids maintained their physical integrity but all of the low-order diffraction rings characteristic of the phthalocyanine's large lattice constant were not observed. The electron diffraction pattern of a CuPc film following the 30 minute heat treatment is shown in Figure IV-13. The largest lattice spacing observed was less than 3 Å. Therefore, the electron diffraction pattern obtained likely represents the thermal decomposition product of the phthalocyanines. In contrast, the same heat treatment procedure was implemented to successfully convert α-phase MPc films deposited on NaCl substrates to the β-phase (discussed in the infrared spectroscopy section). In a final attempt to accomplish the thermal phase conversion process using electron diffraction analysis, the heat treatment time was reduced to 15 minutes. Although the resulting CuPc and NiPc electron diffraction patterns shown in Figures IV-14 and IV-15 were still clearly identified as the α-phase, the spots comprising the electron diffraction rings were more resolved, indicating a higher degree of crystallinity. However, the CoPc electron diffraction ring pattern was reduced to a small number of spots as shown in Figure IV-16. Although these spots could be correlated with the crystal spacings of β-phase CoPc as shown in Table IV-6, most of the low-order diffraction planes, including the 12.5 Å crystal spacing, were completely absent.

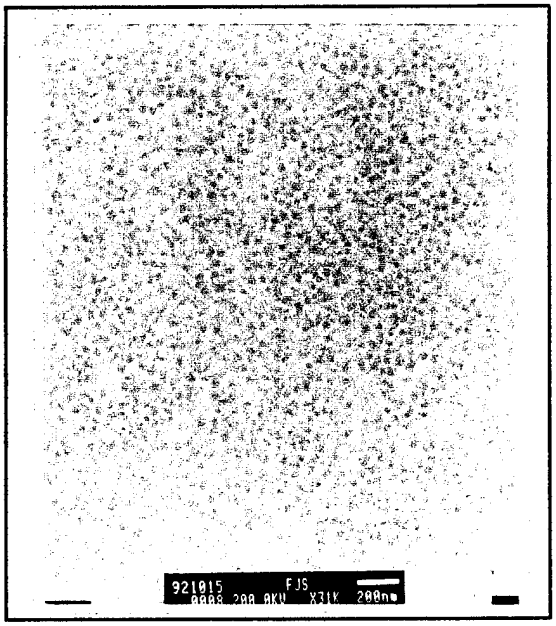


Figure IV-7. Transmission Electron Micrograph of a 500 Å Thick Copper Phthalocyanine (CuPc) Thin Film Sublimed onto a Carbon Grid.

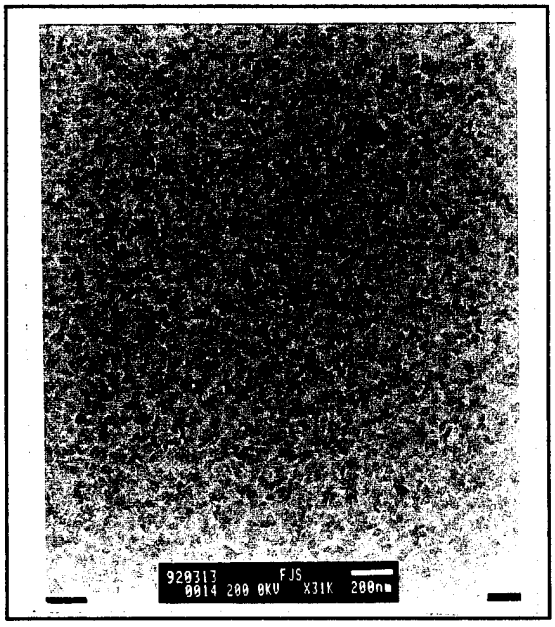


Figure IV-8. Transmission Electron Micrograph of a 1000 Å Thick Nickel Phthalocyanine (NiPc) Thin Film Sublimed onto a Carbon Grid.

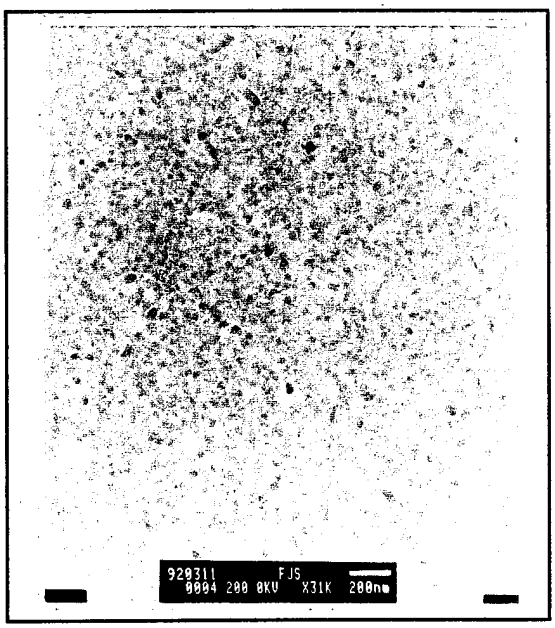


Figure IV-9. Transmission Electron Micrograph of a 700 Å Thick Cobalt Phthalocyanine (CoPc) Thin Film Sublimed onto a Carbon Grid.

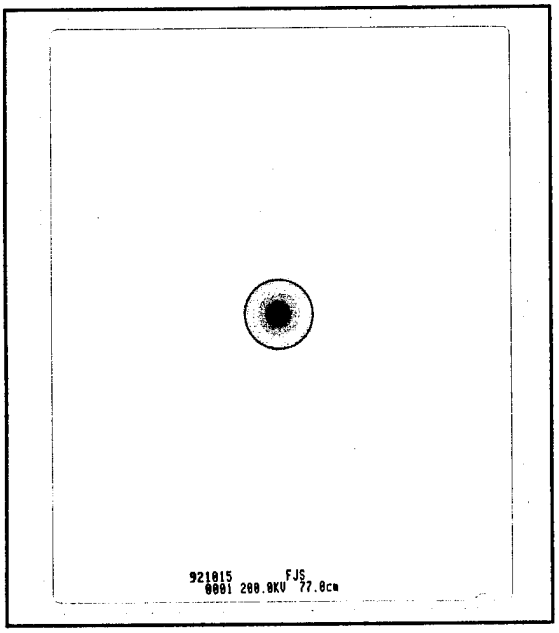


Figure IV-10. Transmission Electron Diffraction Pattern of a 500 Å Thick Copper Phthalocyanine (CuPc) Thin Film Sublimed onto a Carbon Grid.

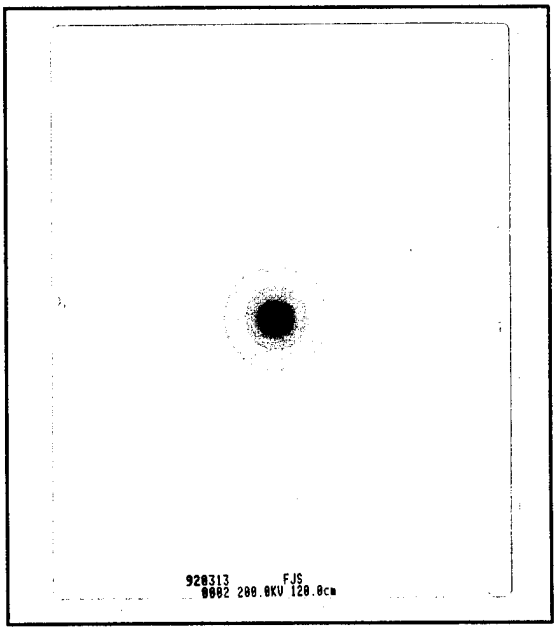


Figure IV-11. Transmission Electron Diffraction Pattern of a 1000 Å Thick Nickel Phthalocyanine (NiPc) Thin Film Sublimed onto a Carbon Grid.

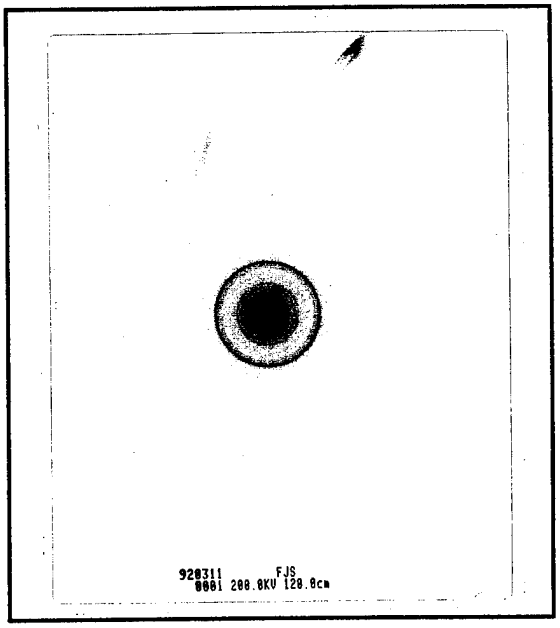


Figure IV-12. Transmission Electron Diffraction Pattern of a 700 Å Thick Cobalt Phthalocyanine (CoPc) Thin Film Sublimed onto a Carbon Grid.

Table IV-3. α-Phase Copper Phthalocyanine Crystal Plane Spacings.

Miller Index	Measured Radius (mm)	Calculated Spacing (Å)	Reported Spacing (56)	Error (%)
(200)	2.35	13.0	12.96	-0.3
(002)	2.55	11.9	11.96	0.5
(202)	3.40	9.0	8.76	-2.7
(400)	4.65	6.6	6.48	-1.9
(004)	5.10	6.0	5.98	-0.3
(402)	5.45	5.6	5.68	1.4
(600)	7.00	4.4	4.32	-1.9

Table IV-4. α-Phase Nickel Phthalocyanine Crystal Plane Spacings.

Miller Index	Measured Radius (mm)	Calculated Spacing (Å)	Reported Spacing (56)	Error (%)
(200)	2.30	13.0	13.07	0.5
(002)	2.50	11.9	12.13	1.9
(202)	3.45	8.6	8.544	-0.7
(400)	4.60	6.5	6.535	0.5
(004)	5.05	5.9	6.065	2.7
(600)	5.50	5.4	5.688	3.3
(006)	7.50	4.0	4.043	1.1
(110)	8.00	3.7	3.751	1.4

Table IV-5. α-Phase Cobalt Phthalocyanine Crystal Plane Spacings.

Miller Index	Measured Radius (mm)	Calculated Spacing (Å)	Reported Spacing (182)	Error (%)
(100)	2.4	12.4	12.4	0
(202)	3.4	8.7	8.79	1.0
(402)	5.4	5.5	5.60	1.8
(111)	8.1	3.7	3.69	-0.3
(112)	-	-	3.56	-
(312)	-	-	3.34	-
(800)	9.2	3.2	3.2	0

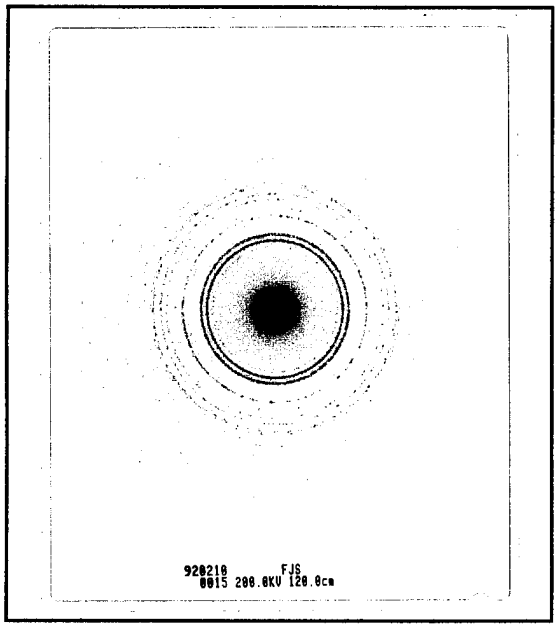


Figure IV-13. Transmission Electron Diffraction Pattern of a 500 Å Thick Copper Phthalocyanine (CuPc) Thin Film Sublimed onto a Carbon Grid after Heat Treatment at 350° C for 30 minutes in a Nitrogen Ambient.

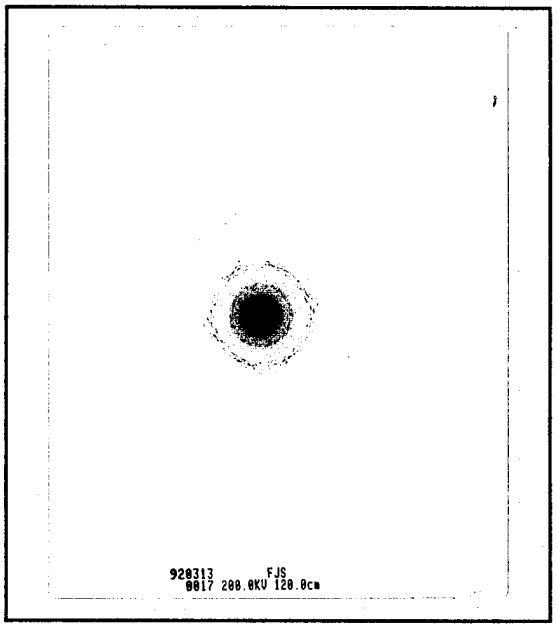


Figure IV-14. Tranmission Electron Diffraction Pattern of a 500 Å Thick Copper Phthalocyanine (CuPc) Thin Film Sublimed onto a Carbon Grid after Heat Treatment at 350° C for 15 minutes in a Nitrogen Ambient.

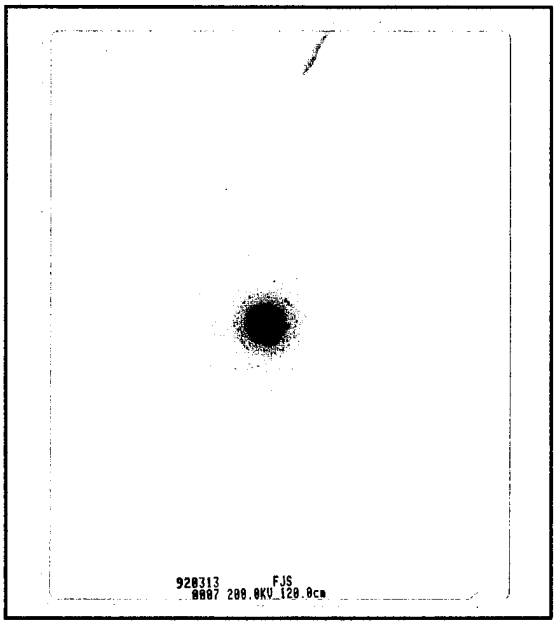


Figure IV-15. Transmission Electron Diffraction Pattern of a 1000 Å Thick Nickel Phthalocyanine (NiPc) Thin Film Sublimed onto a Carbon Grid after Heat Treatment at 350° C for 15 minutes in a Nitrogen Ambient.

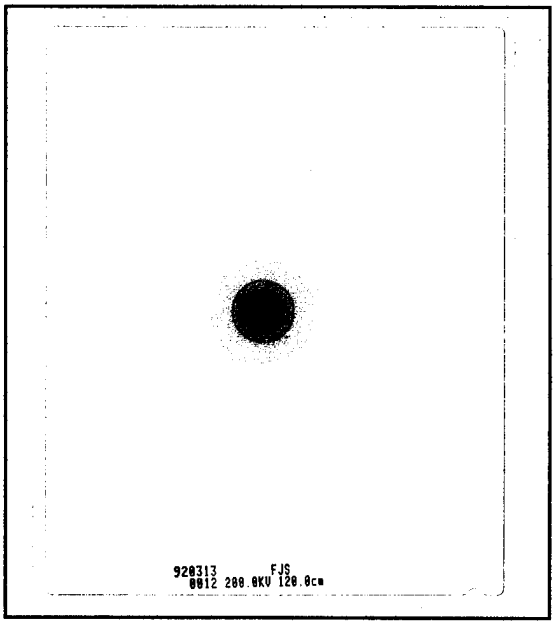


Figure IV-16. Transmission Electron Diffraction Pattern of a 700 Å Thick Cobalt Phthalocyanine (CoPc) Thin Film Sublimed onto a Carbon Grid after Heat Treatment at 350° C for 15 minutes in a Nitrogen Ambient.

Table IV-6. β-Phase Cobalt Phthalocyanine Crystal Plane Spacings Following a 15 minute, 350° C Heat Treatment in Nitrogen.

Miller Index	Measured Radius (mm)	Calculated Spacing (Å)	Reported Spacing (183)	Error (%)
(100)	-	-	12.50	-
(10$\bar{2}$)	3.05	9.6	9.55	-0.5
(002)	-	-	8.34	-
(20$\bar{2}$)	-	-	7.03	-
(200)	-	-	6.28	-
(102)	-	-	5.73	-
(30$\bar{2}$)	-	-	4.86	-
(10$\bar{4}$)	-	-	4.75	-
(30$\bar{4}$)	6.9	4.3	4.21	-2.1
(202)	-	-	4.11	-
(11$\bar{3}$)	-	-	3.84	-
(21$\bar{3}$)	8.0	3.7	3.72	0.5
(21$\bar{4}$)	8.7	3.4	3.38	-0.6
(31$\bar{4}$)	-	-	3.16	-
(400)	-	-	3.13	-
(21$\bar{5}$)	-	-	3.01	-
(31$\bar{5}$)	8.00	2.9	2.91	0.3

Infrared Spectroscopy. As discussed in Chapter II, the structure and morphology of the phthalocyanines and their gas adsorption properties have been studied by infrared (IR) spectroscopy. The published spectra for α-phase CuPc, NiPc, and CoPc are shown in Figures II-7 through II-9. The objective of this infrared study was two-fold: first, to confirm the chemical composition and morphology of the deposited films, and second, to study the interaction of these films with a set of candidate challenge gases. The candidate challenge gases screened included nitrogen dioxide (NO_2), ammonia (NH_3), boron trifluoride (BF_3), diisopropyl methylphosphonate (DIMP), dimethyl methylphosphonate (DMMP), and diisopropyl fluorophosphonate (DFP). From this set of gases, only NO_2 elicited a strong response in the phthalocyanine infrared spectra. Therefore, the discussion of the infrared spectral response to gas exposure is limited to the interaction of the phthalocyanines with NO_2 and NH_3, which was representative of the response observed with the remaining gases.

The phthalocyanines were vacuum sublimed at 10^{-6} torr onto one-inch diameter sodium chloride (NaCl) crystal substrates (IR windows). The deposition rate was maintained at 1-5 Å/s. To improve the resolution of the infrared spectra and to provide a larger surface area for the interaction of the films with the candidate gases, the phthalocyanine films were deposited on both sides of the IR windows. The film deposited on each side of the IR window was approximately 3500 Å thick, for a total thickness of approximately 7000 Å. The IR spectra of the deposited films measured with a Model 683 Infrared Spectrophotometer (Perkin-Elmer, Garden Grove, CA) are shown in Figures IV-17 through IV-22. The NaCl windows, which become opaque at small wave numbers, obscures the phthalocyanine spectra below 800 cm^{-1}. In contrast, the IR spectra shown in Figures II-7 through II-9 were generated from CuPc, NiPc, and CoPc films deposited onto potassium bromide substrates, which has a broader IR transmission bandwidth (from less than 200 cm^{-1} to greater than 4000 cm^{-1}) compared to sodium chloride (from approximately 800 cm^{-1} to 4000 cm^{-1}). The IR spectrum for the uncoated NaCl substrate (control reference) used in this investigation is shown in Figure IV-23, and it reflects the reduced bandwidth.

The measured IR spectra and the reference spectra presented in Chapter II were normalized to facilitate absorption peak intensity comparisons. These comparisons (see Figures IV-24 through IV-26) display the similarity between the experimentally deposited MPc films and the published spectra. An analysis of the normalized spectra provided in Appendix C revealed that the average error between the IR spectra of the deposited films and the reference spectra was on the order of 20 percent for CuPc and NiPc, and 45 percent for CoPc. Since a Sadtler reference spectra for CoPc was not available in the library, an alternative source for the CoPc spectra was utilized. To obtain the absorption peak intensities, it was necessary to fit a scale to this CoPc spectra. The greater IR spectra correlation error,

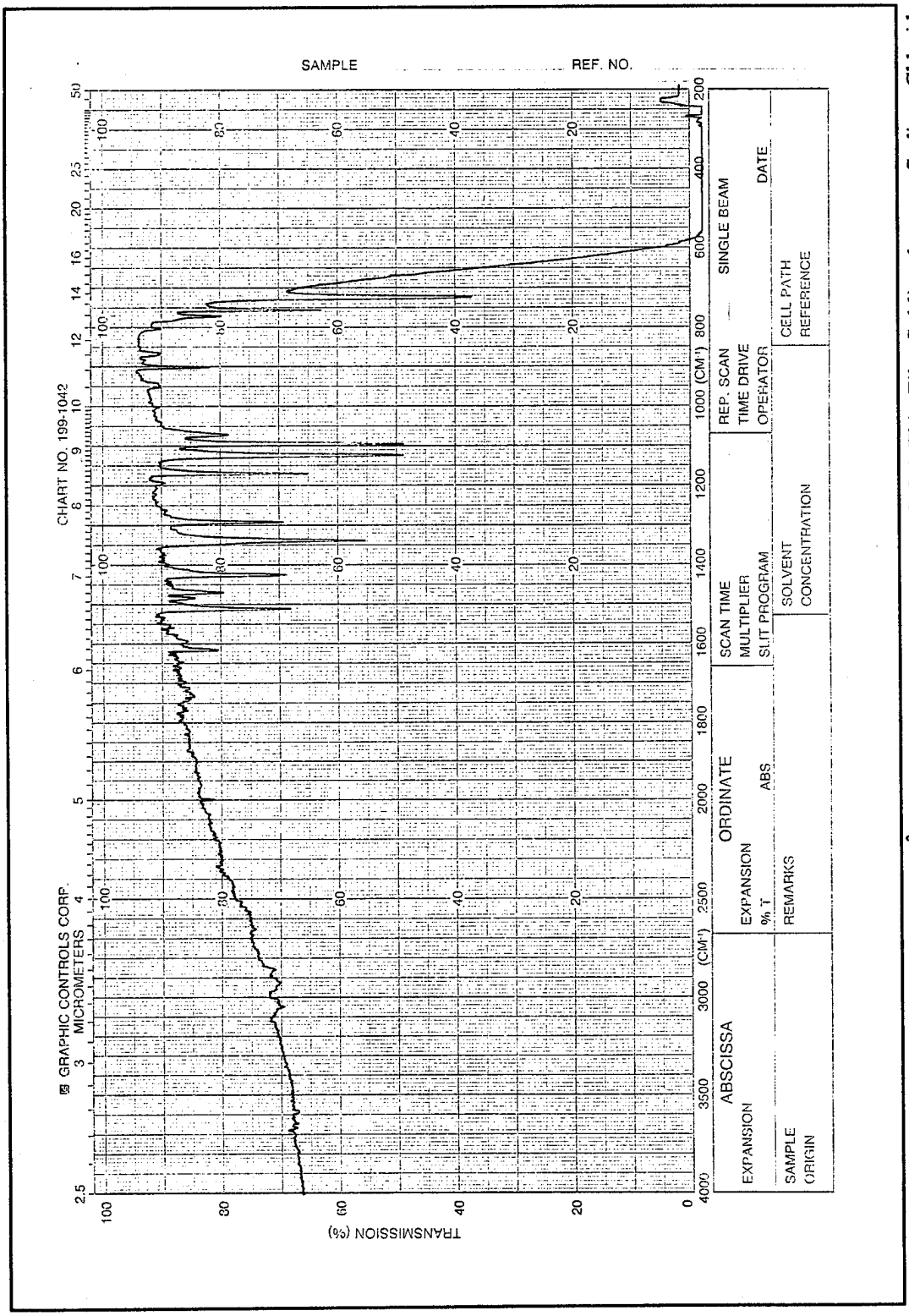


Figure IV-17. Infrared Spectrum of the 6600 Å Thick Copper Phthalocyanine (CuPc) Thin Film Sublimed onto a Sodium Chloride Substrate.

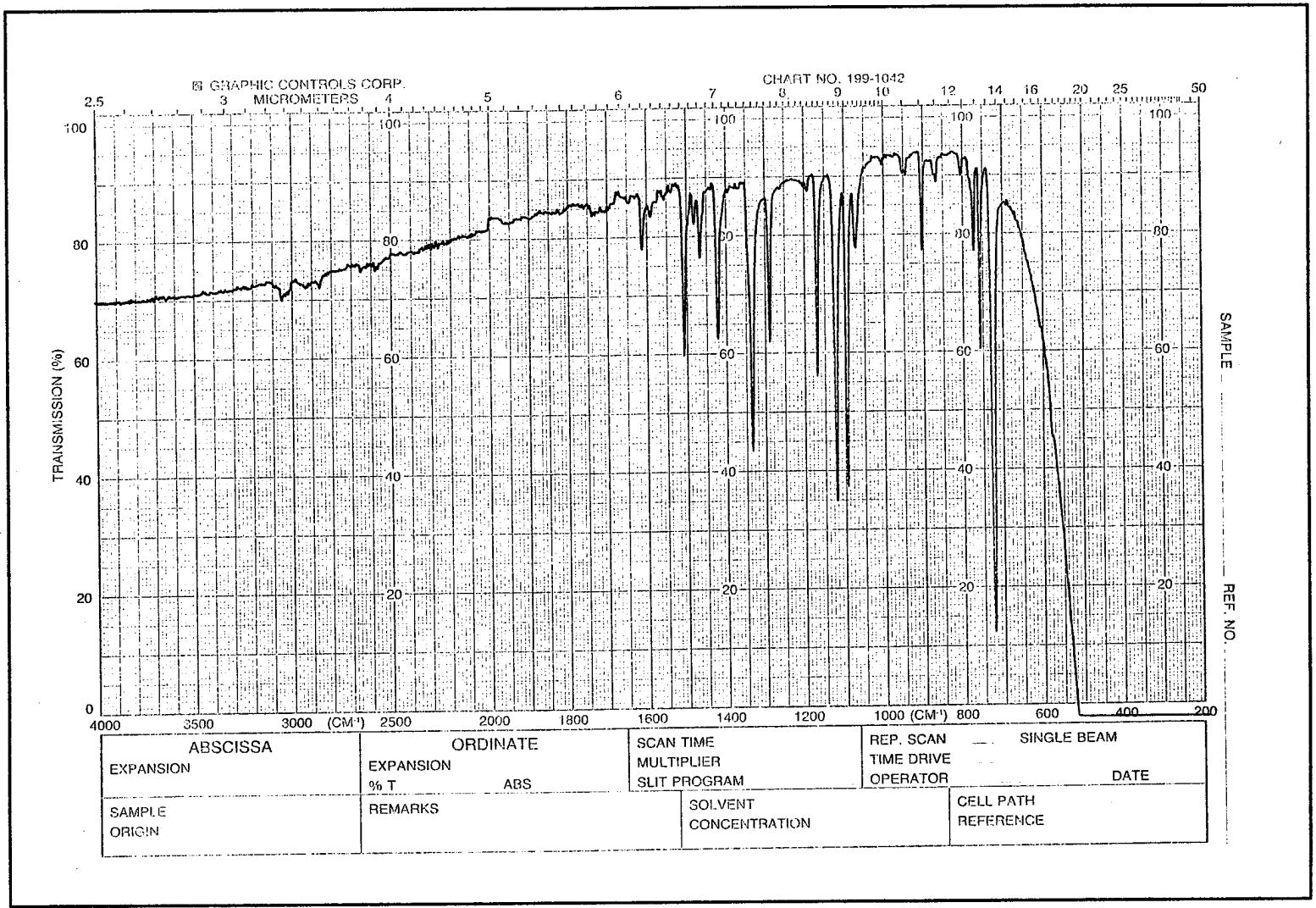


Figure IV-18. Infrared Spectrum of the 7700 Å Thick Copper Phthalocyanine (CuPc) Thin Film Sublimed onto a Sodium Chloride Substrate.

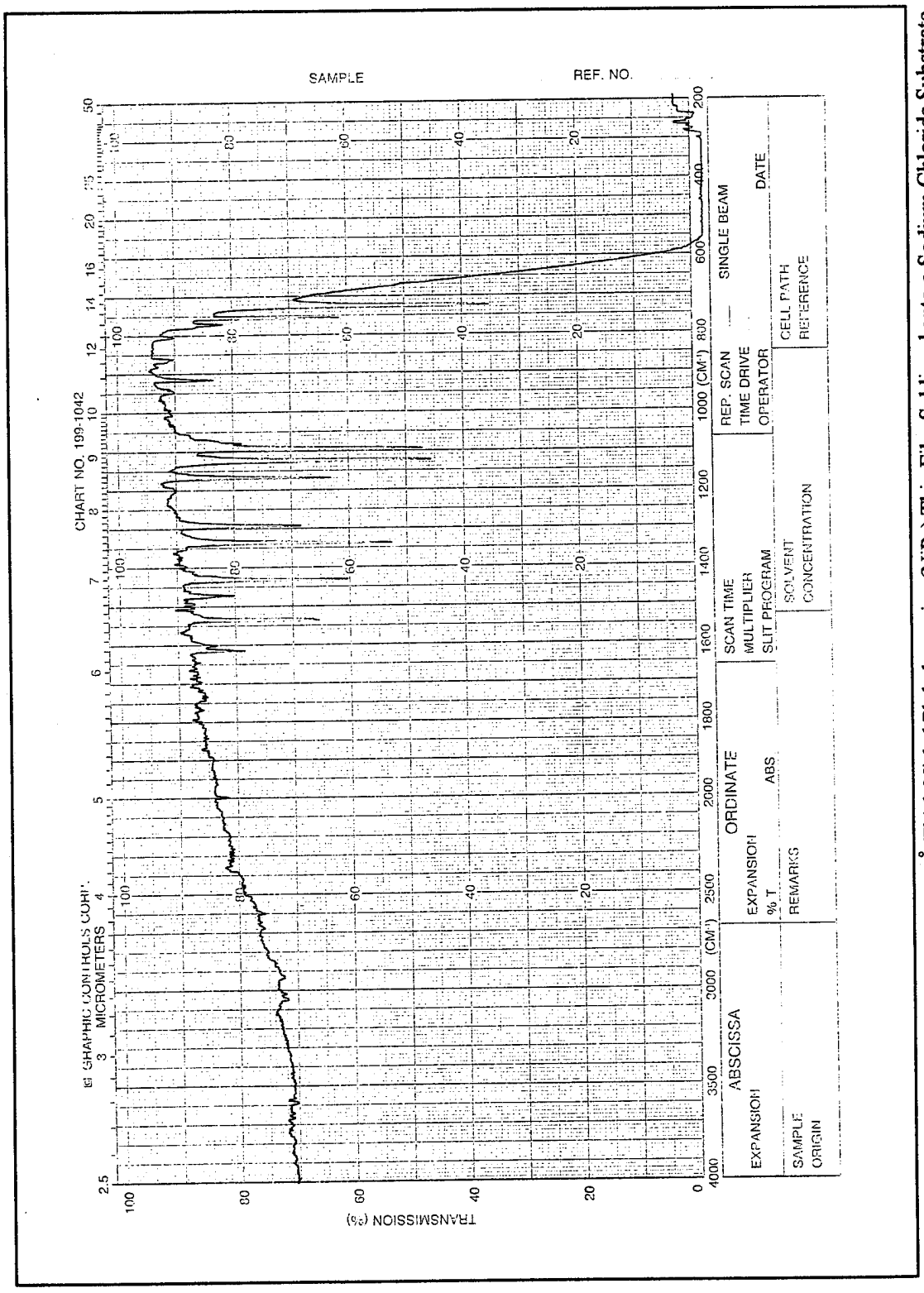


Figure IV-19. Infrared Spectrum of the 7100 Å Thick Nickel Phthalocyanine (NiPc) Thin Film Sublimed onto a Sodium Chloride Substrate.

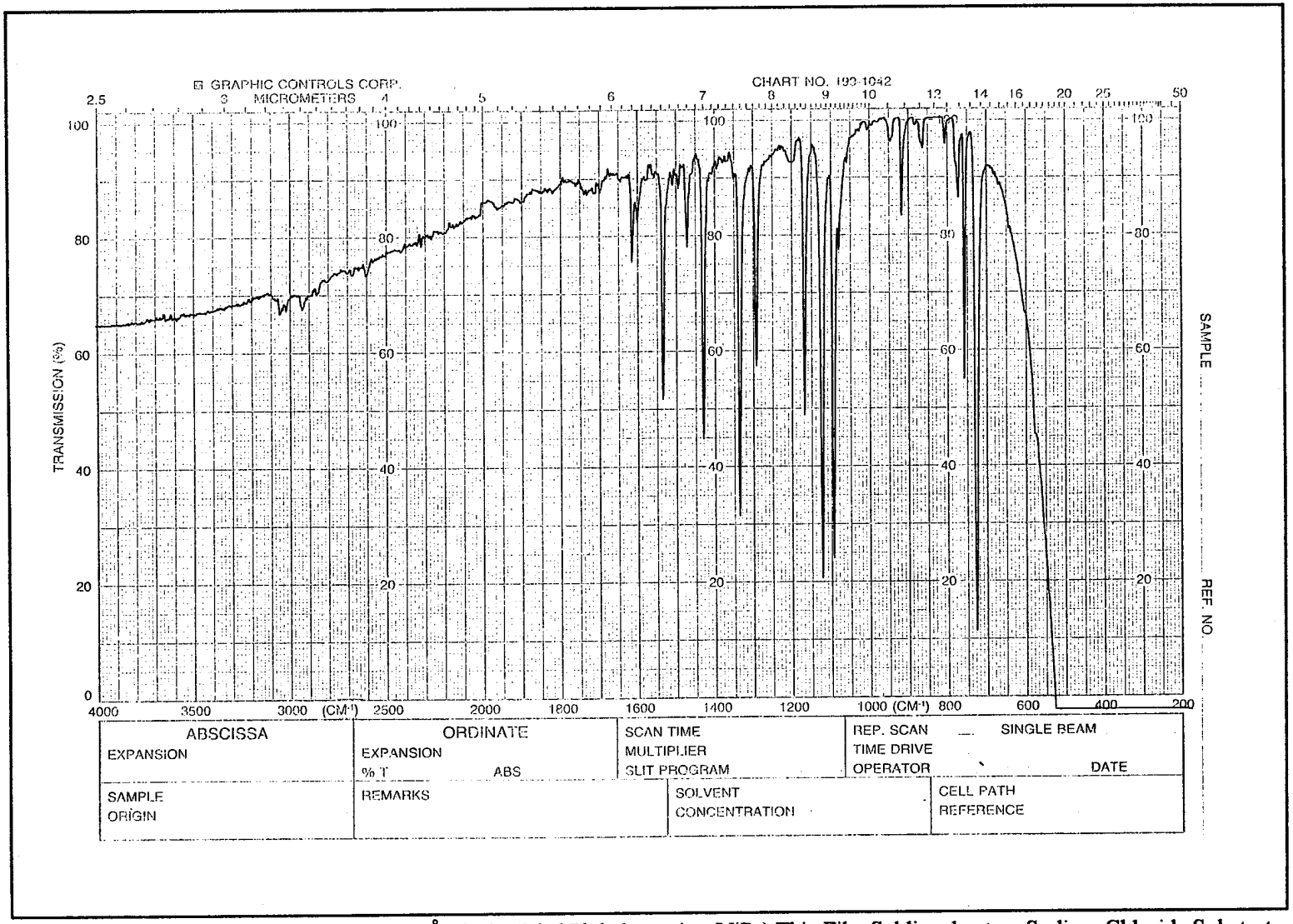


Figure IV-20. Infrared Spectrum of the 6500 Å Thick Nickel Phthalocyanine (NiPc) Thin Film Sublimed onto a Sodium Chloride Substrate.

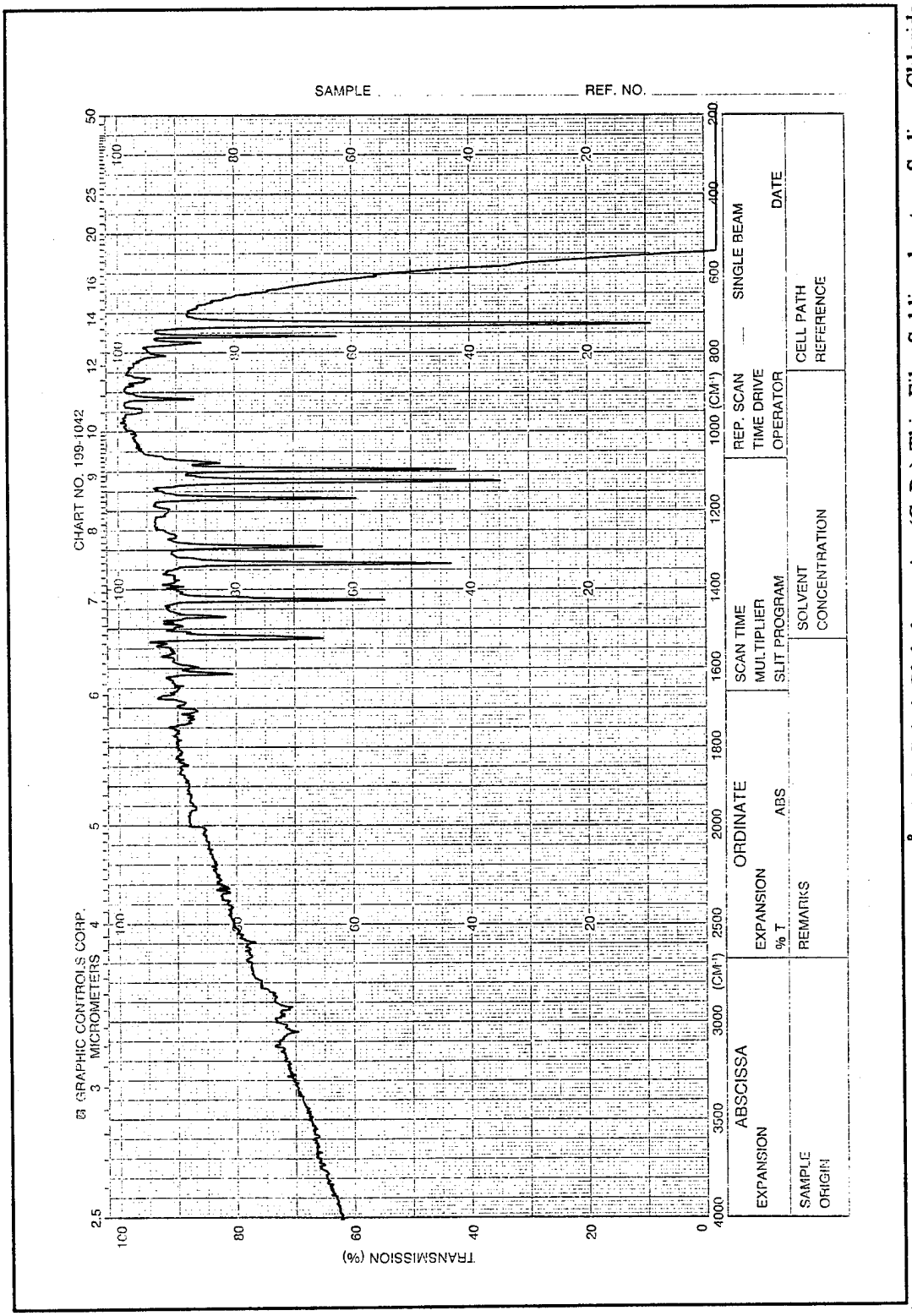


Figure IV-21. Infrared Spectrum of the 5300 Å Thick Cobalt Phthalocyanine (CoPc) Thin Film Sublimed onto a Sodium Chloride Substrate.

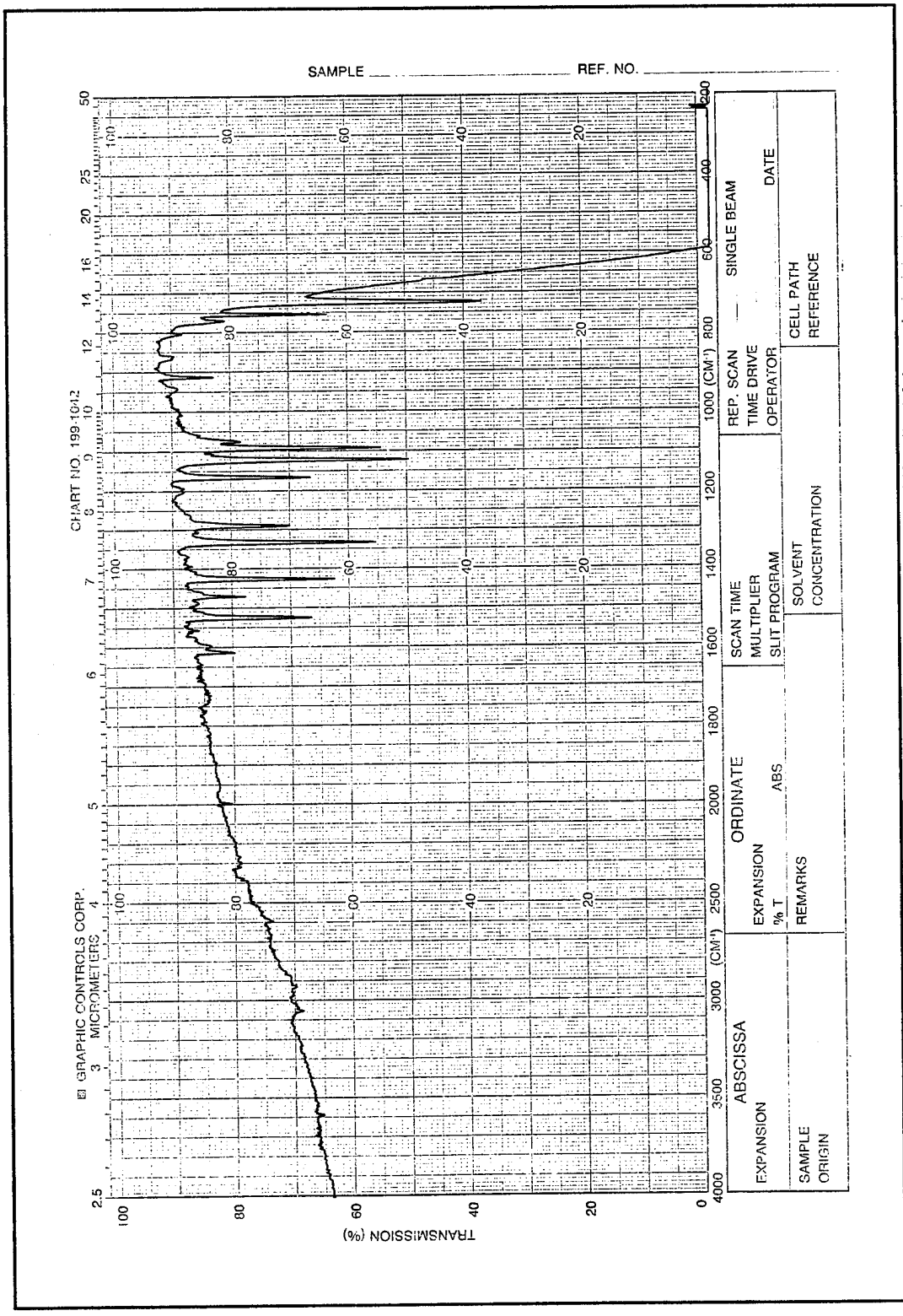


Figure IV-22. Infrared Spectrum of the 5800 Å Thick Cobalt Phthalocyanine (CoPc) Thin Film Sublimed onto a Sodium Chloride Substrate.

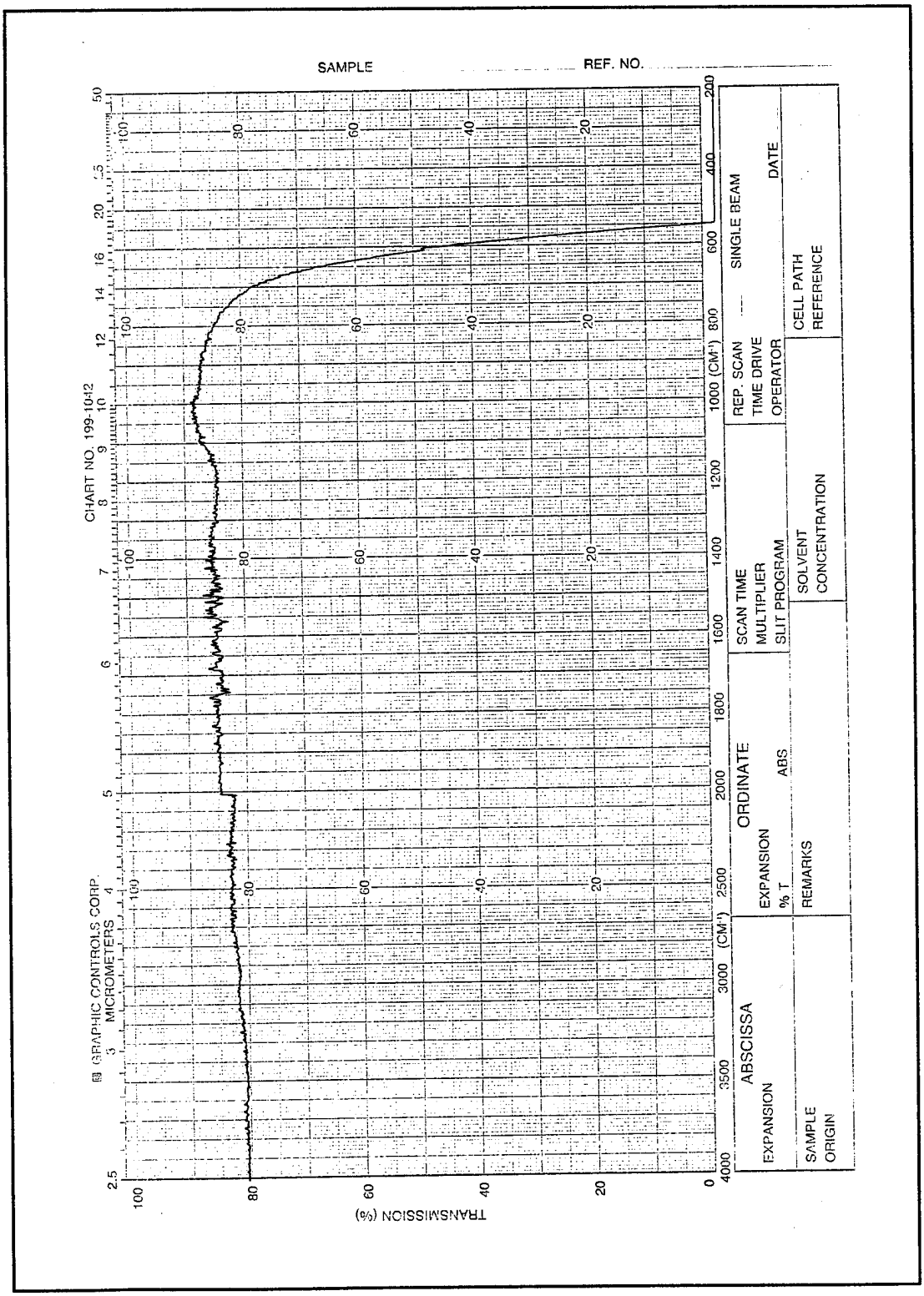


Figure IV-23. Infrared Spectrum of the Sodium Chloride IR Substrate.

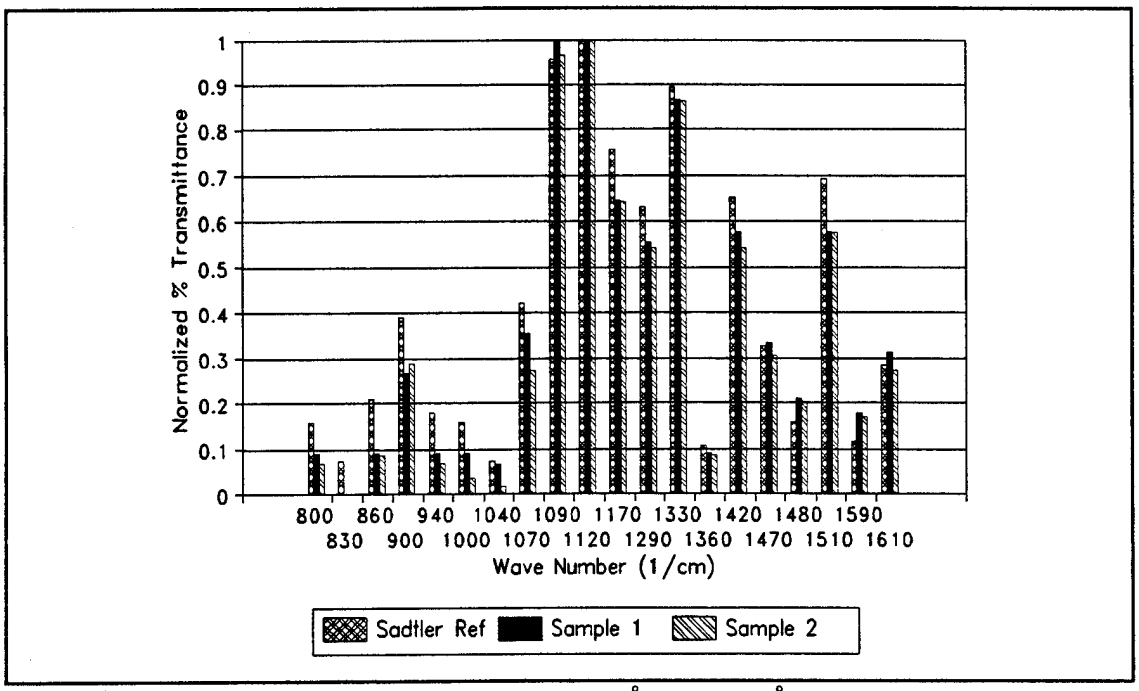


Figure IV-24. Infrared Absorption Peaks of the 6600 Å and 7700 Å Thick Copper Phthalocyanine (CuPc) Thin Films Compared to the Published Reference Peaks (Normalized with Respect to the 1120 cm^{-1} Peak) (73).

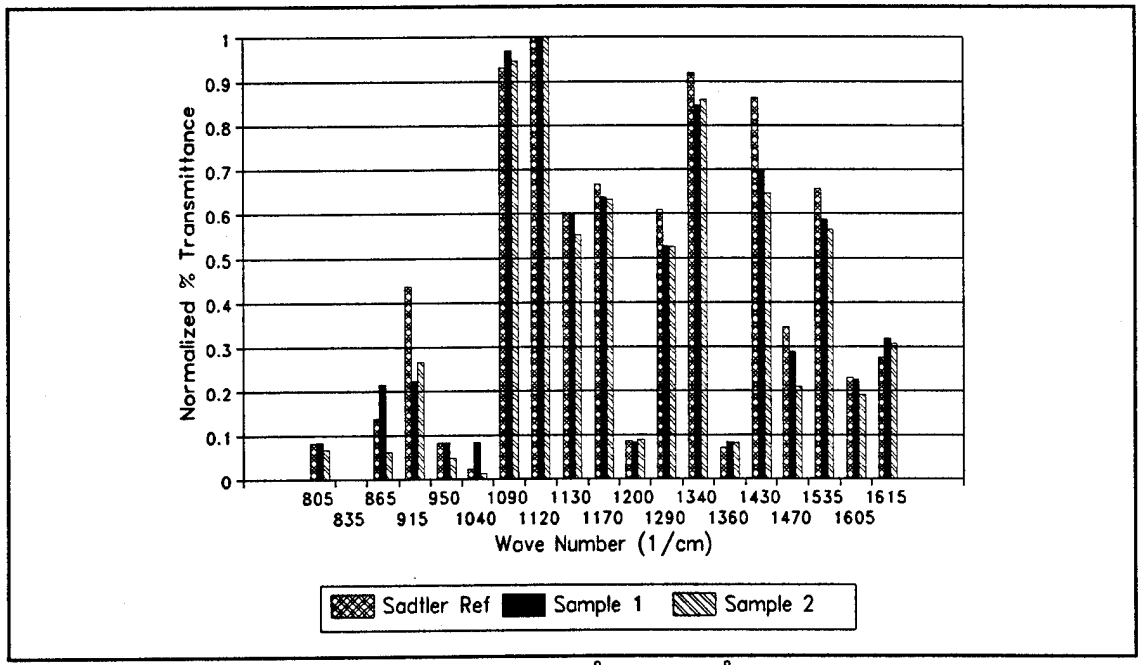


Figure IV-25. Infrared Absorption Peaks of the 6500 Å and 7100 Å Thick Nickel Phthalocyanine (NiPc) Thin Films Compared to the Published Reference Peaks (Normalized with Respect to 1120 cm^{-1} Peak) (74).

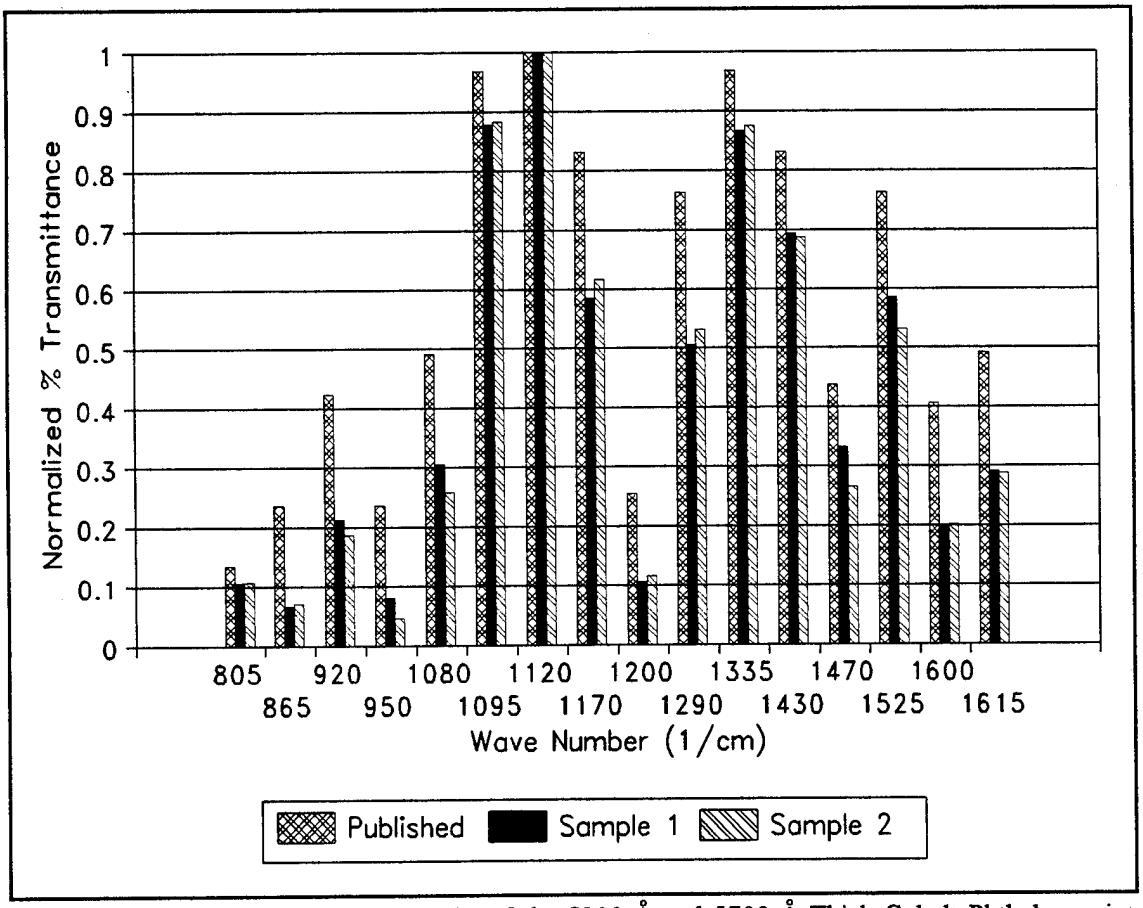


Figure IV-26. Infrared Absorption Peaks of the 5300 Å and 5700 Å Thick Cobalt Phthalocyanine (CoPc) Thin Films Compared to the Published Reference Peaks (Normalized with Respect to 1120 cm^{-1} Peak) (49).

indicative of the CoPc films, likely reflects the use of an alternative source for the CoPc spectra and the additional manipulations required to obtain the peak intensities. Nevertheless, a detailed comparison of the IR spectra of the deposited films with the published spectra presented in Chapter II unambigously identified the α-phase crystalline form of each phthalocyanine. Additionally, the α-phase phthalocyanine films deposited on the IR NaCl windows were thermally converted to the β-phase crystalline form using the heat treatment process described by Sadoaka (157). This treatment involved heating the MPc coated IR windows at 350° C for 30 minutes in a nitrogen ambient. The IR spectra of the heat treated MPc films are shown in Figures IV-27 through IV-29.

Careful comparison of the wavenumber position of the absorption peaks were used to identify each metallic phthalocyanine derivative and its crystalline phase. Table IV-7 lists the wavenumber locations of the characteristic MPc absorption peaks which shift to higher frequencies when the central metal atom is changed progressively from Cu, to Co, and finally, to Ni. Sidorov (49) observed an identical behavior with a larger group of MPc films and concluded that these absorption features "correspond to the vibrations of central atomic groups related to the central metal atom either by direct bonding or indirectly through a system of conjugated bonds". In contrast to the absorption bands associated with the metal atom, the location of absorption bands specific to a particular crystalline phase do not shift with respect to frequency with different central metal atoms. In particular, the heat treatment causes the formation of absorption bands indicative of the β-phase crystalline form at 879, 958, 1105, and 1178 cm^{-1}. The most prominent feature of the β-phase IR spectra is the band at 879 cm^{-1} with the other absorption features being of lower intensity or appearing as shoulders on adjacent bands. Sidorov reported that a doublet occurs at 725 cm^{-1} if the film is a mixture of the two phases. However, in this research, the thermal conversion to the β-phase crystalline form was complete since only a single band was observed at this frequency.

In addition to verifying the chemical composition and morphology of the deposited phthalocyanine films, changes in the infrared spectra confirmed NO_2 adsorption by the MPc films. The MPc coated IR NaCl windows were exposed at room temperature to a nitrogen ambient containing a 770 ppm NO_2 challenge gas concentration for approximately 46 hours. The gas concentration and exposure time were selected to insure saturation of the available adsorption sites and to maximize the change in the infrared spectra. As discussed in Chapter II, the IR detection limit for NO_2 adsorption on lead phthalocyanine is nearly five orders of magnitude greater than the electrical detection limit, and the adsorption properties of a film may be quite different compared to when it is exposed to ppb gas concentrations. The MPc infrared spectra following exposure to NO_2 (see Figures IV-30 through IV-32)

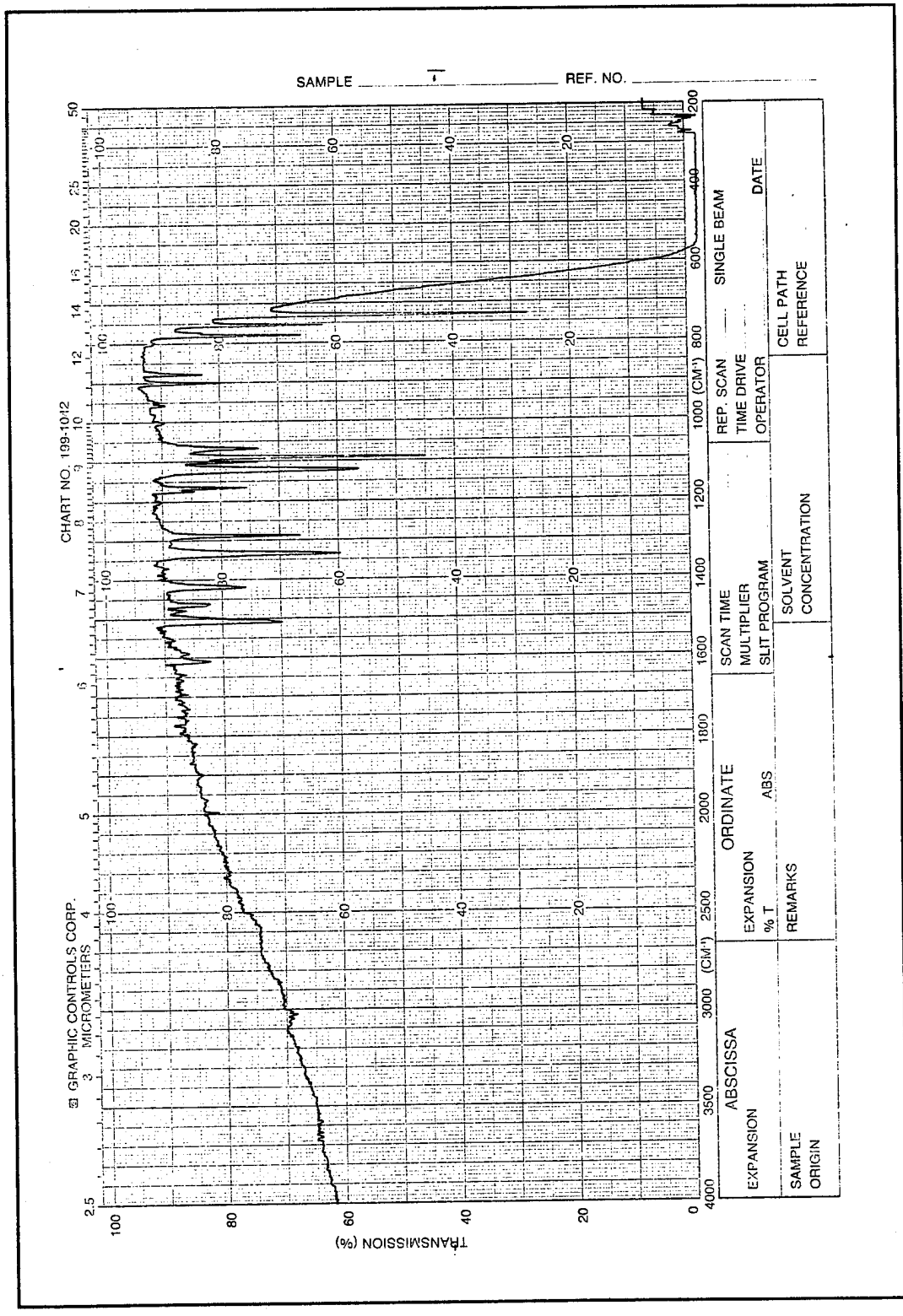


Figure IV-27. Infrared Spectrum of the 6600 Å Thick Copper Phthalocyanine (CuPc) Thin Film after Heat Treatment at 350°C for 30 minutes in a Nitrogen Ambient.

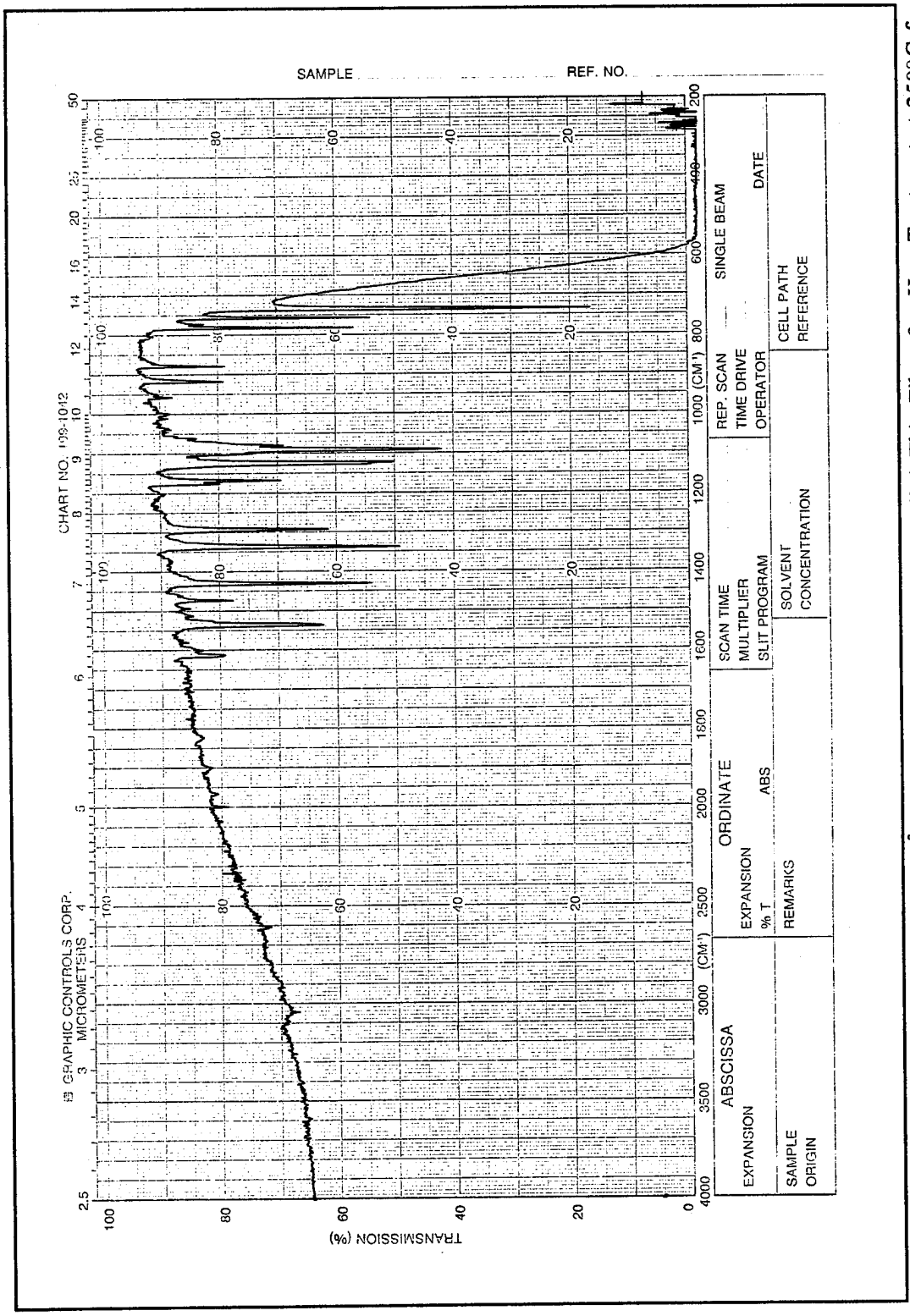


Figure IV-28. Infrared Spectrum of the 7100 Å Thick Nickel Phthalocyanine (NiPc) Thin Film after Heat Treatment at 350° C for 30 minutes in a Nitrogen Ambient.

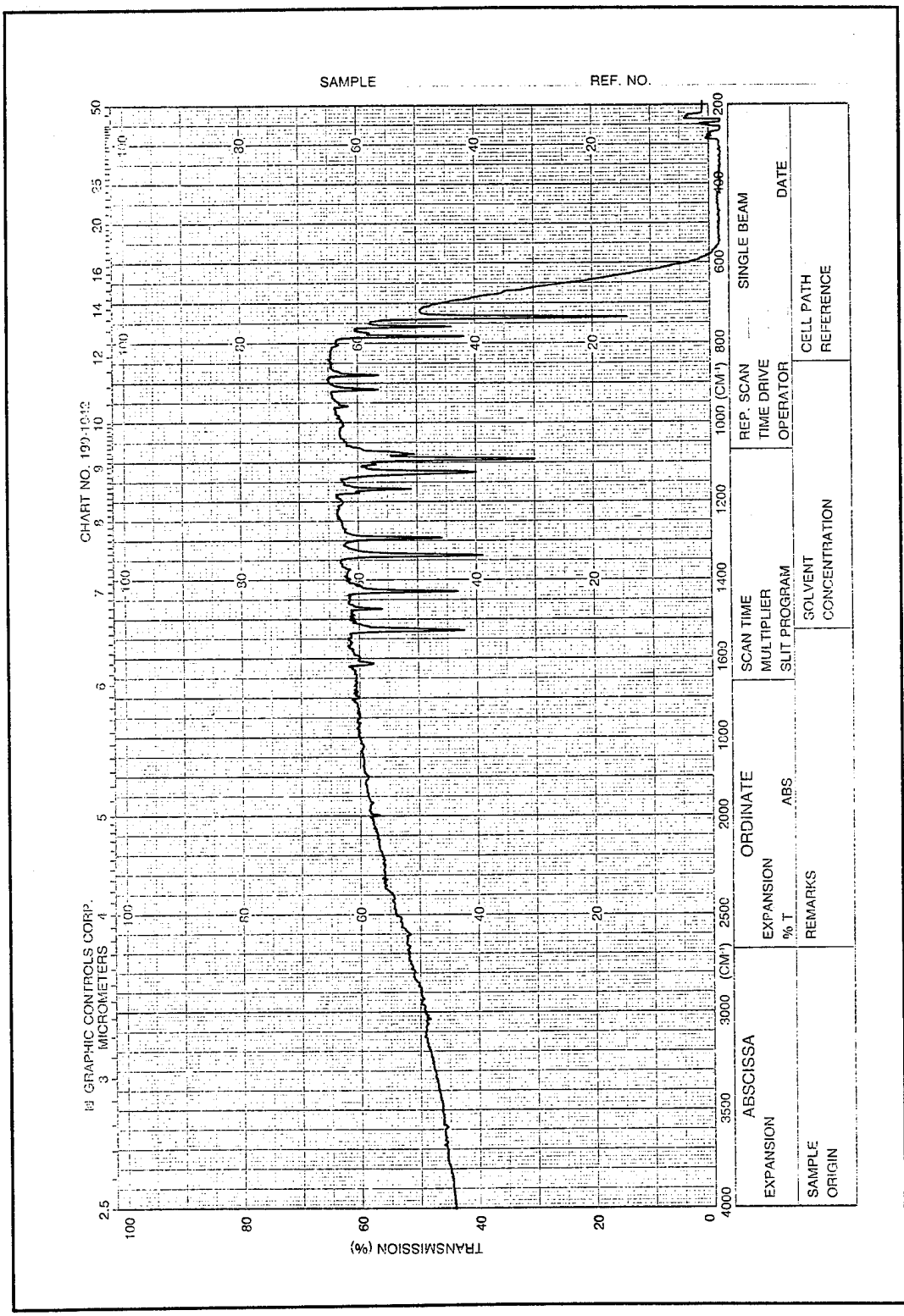


Figure IV-29. Infrared Spectrum of the 5700 Å Thick Cobalt Phthalocyanine (CoPc) Thin Film after Heat Treatment at 350°C for 30 minutes in a Nitrogen Ambient.

Table IV-7. Metal-Dependent Absorption Bands of Sublimed MPc Films .

Absorption Bands (cm^{-1})		
CuPc	CoPc	NiPc
903	915	918
1072	1075	1080
1289	1290	1293
1422	1428	1430
1468	1471	1470
1480	1487	1495
1507	1528	1535
1590	1597	1602

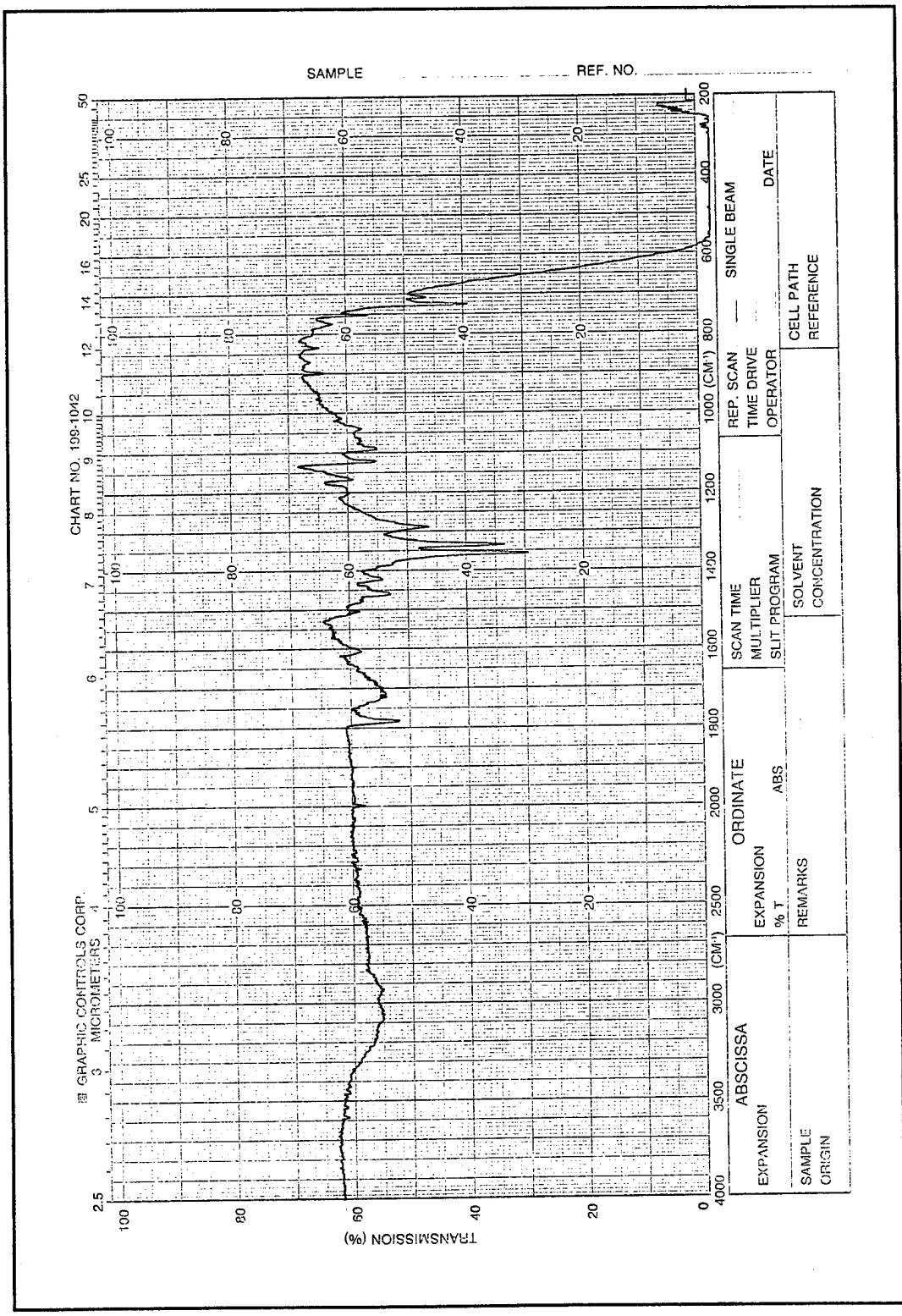


Figure IV-30. Infrared Spectrum of the 6600 Å Thick Copper Phthalocyanine (CuPc) Thin Film Sublimed onto a Sodium Chloride Substrate after Exposure to 770 ppm NO_2 for 46 hours.

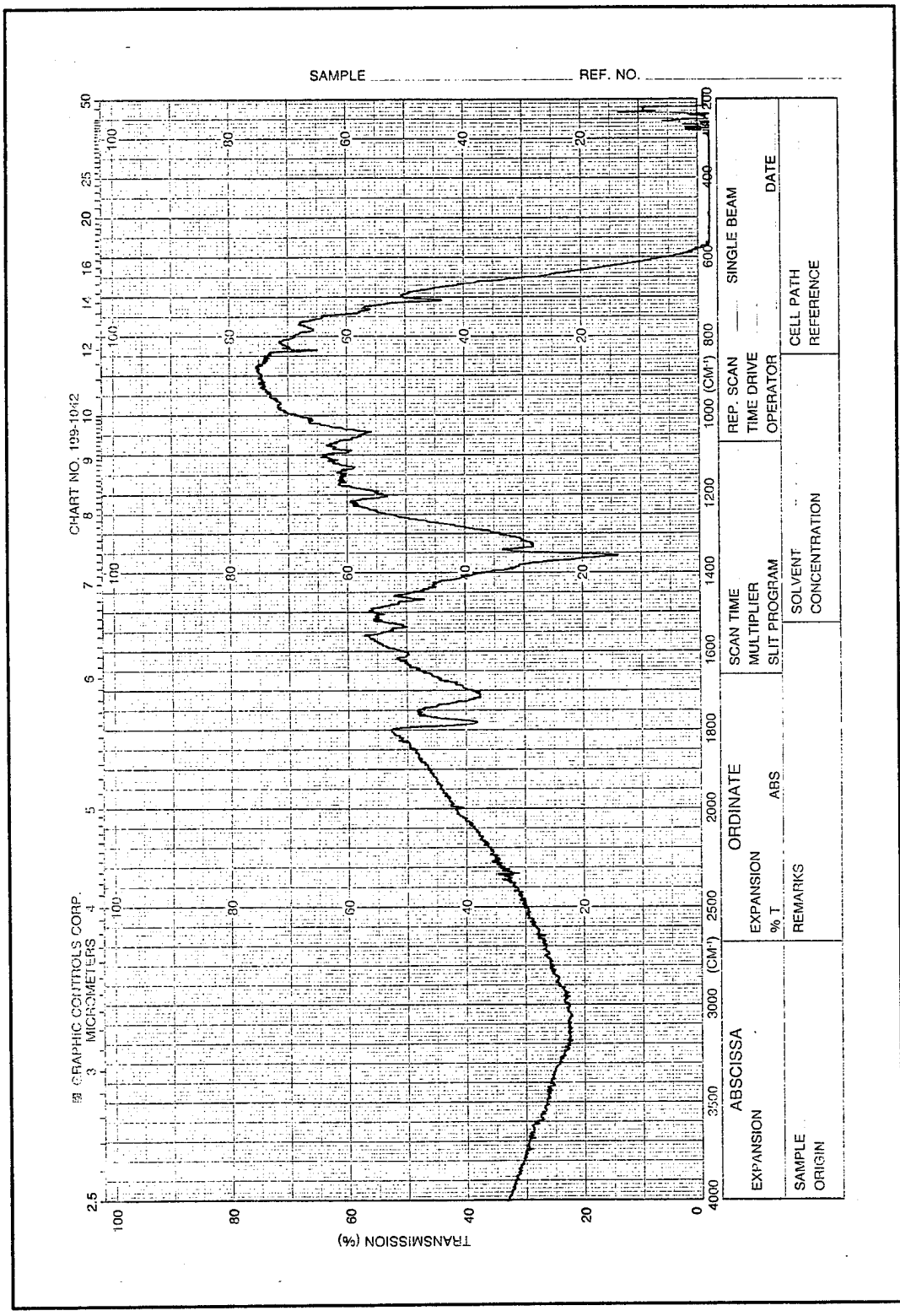


Figure IV-31. Infrared Spectrum of the 7100 Å Thick Nickel Phthalocyanine (NiPc) Thin Film Sublimed onto a Sodium Chloride Substrate after Exposure to 770 ppm NO_2 for 46 hours.

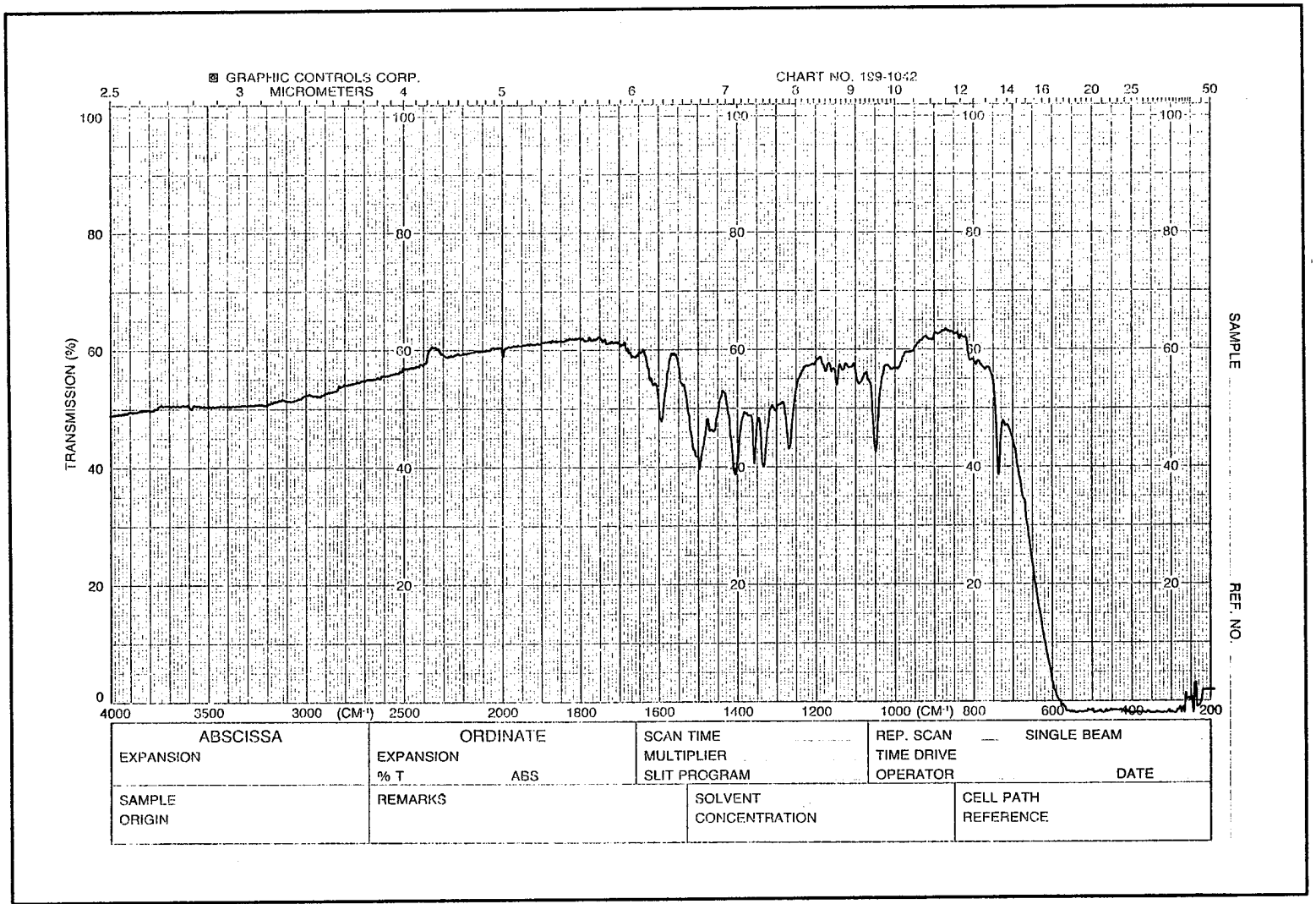


Figure IV-32. Infrared Spectrum of the 5800 Å Thick Cobalt Phthalocyanine (CoPc) Thin Film Sublimed onto a Sodium Chloride Substrate after Exposure to 770 ppm NO_2 for 46 Hours.

reveal a significant reduction in infrared transmission over the entire band compared to the IR spectra of the as-deposited samples (see Figures IV-19 through IV-21). Additionally, at least four new bands located near 835, 1040, 1360, and 1780 cm^{-1} were observed in the CuPc and NiPc IR spectra following NO_2 exposure. The infrared spectrum of an uncoated IR NaCl window after NO_2 exposure (see Figure IV-33) reveals that the NO_2 interaction with the salt substrate is responsible for the formation of the two bands located at 835 and 1360 cm^{-1}. The 1040 and 1360 band were also observed in the NO_2-exposed CoPc spectrum, but the other two bands were either obscured by the general increase in infrared absorption, or they were absent. The general increase in absorption across the mid-IR band, as well as the specific increases near 835, 1040, 1360, and 1780 cm^{-1}, following exposure of the MPc films to NO_2, are consistent with the IR spectral changes observed by Shoch and Temofonte for lead phthalocyanine upon NO_2 exposure (see Figure II-11).

Subsequent purging of the MPc-coated IR NaCl windows at 150° C for 1.5 hours in nitrogen to desorb the NO_2 resulted in the spectra shown in Figures IV-34 through IV-36. The normalized IR spectrum peak comparison between the pre-exposed, NO_2 exposed, and purged spectra are shown in Figures IV-37 through IV-39, and Appendix C contains an analysis of the percent change relative to the reference spectra observed for each film relative to the different experimental conditions. These two sets of figures reveal the extent to which the pre-exposed features of the IR spectra were recovered by the purge conditions. That is, they vary with the film type -- decreasing in order from CuPc, to NiPc, and finally, to CoPc. However, with all three film types, the bands near 835 and 1360 cm^{-1} were not removed by the purge process implemented at an elevated temperature. In fact, the band intensity at 1360 cm^{-1} for the NiPc sample increased following the purge, suggesting that the NO_2 originally bound to the phthalocyanine film diffuses toward the NaCl window upon heating. Other than these two bands, the IR spectra of the CuPc sample contained most of the pre-exposed features. Similarly, except for the distortion in the bands adjacent to the intense 1360 cm^{-1} band, most of the pre-exposed features of the as-deposited NiPc IR spectra were also recovered. Of the three film types, the smallest recovery of the pre-exposed IR spectral features was observed with the CoPc sample. The purge treatment of the CoPc sample reversed the general transmission decrease across the band caused by the NO_2 exposure. Furthermore, specific bands at 1050, 1270, 1400, and 1500 cm^{-1}, which formed as a result of the NO_2 exposure, were significantly reduced. Several of the pre-exposed bands located at 1090, 1120, 1160, 1290, 1430, 1470, and 1525 cm^{-1}, which were absent or of low intensity following the NO_2 exposure, were recovered by the purge treatment. In general, NO_2 is only partially (although significantly) desorbed from the MPc films under these test conditions. Since the challenge gas concentration and

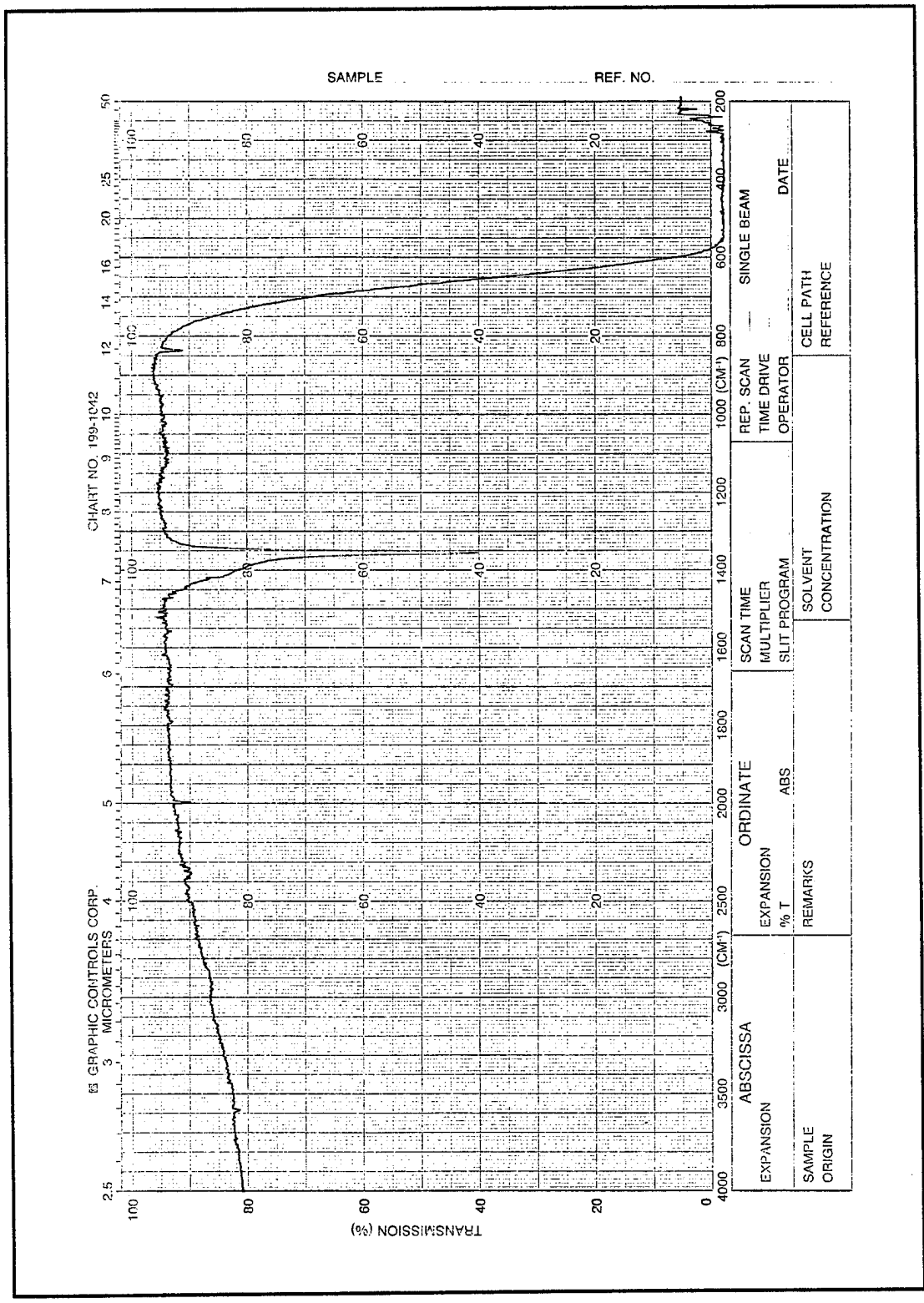


Figure IV-33. Infrared Spectrum of the Sodium Chloride IR Substrate after Exposure to 770 ppm NO_2 for 46 hours.

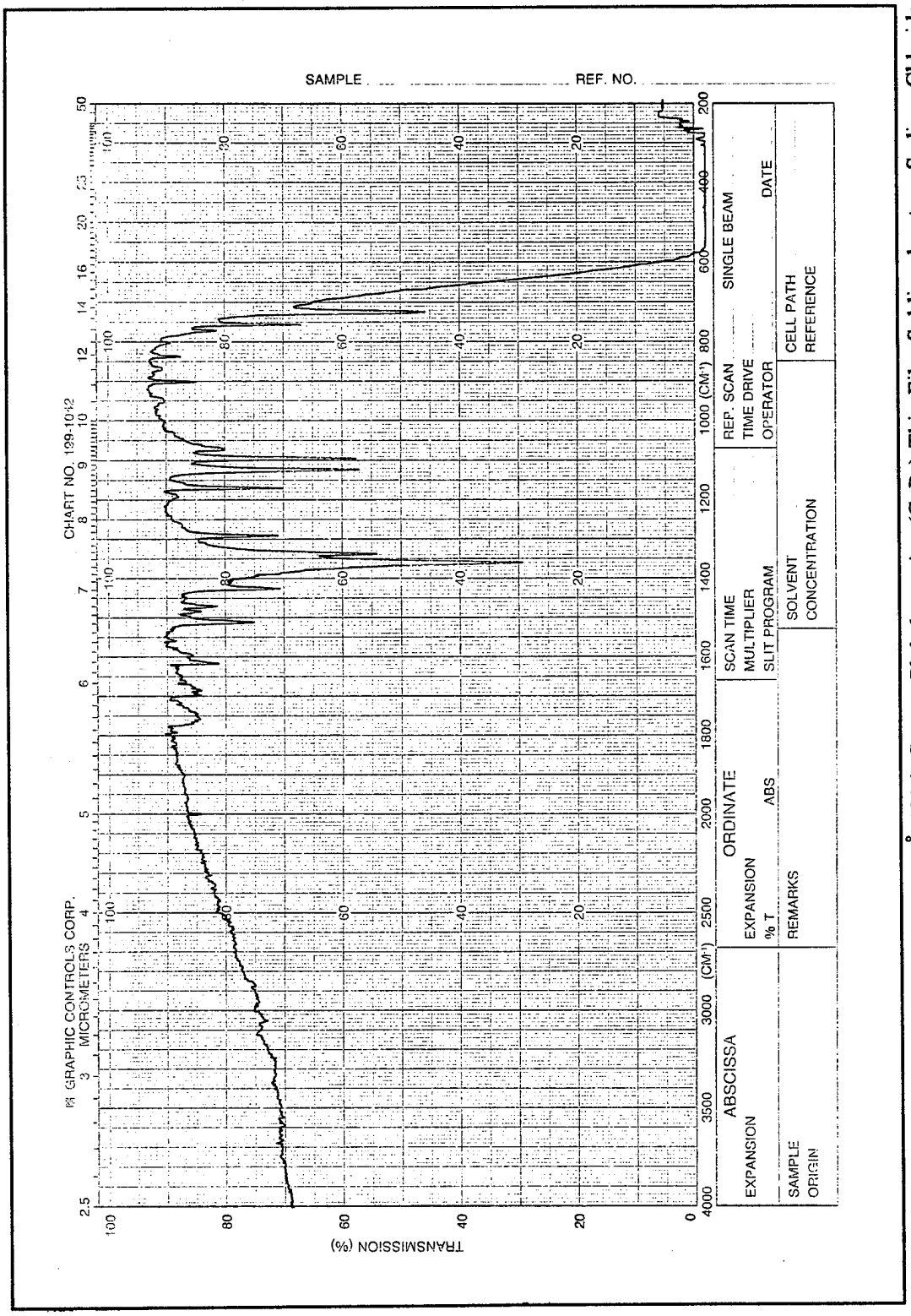


Figure IV-34. Infrared Spectrum of the 6600 Å Thick Copper Phthalocyanine (CuPc) Thin Film Sublimed onto a Sodium Chloride Substrate after Exposure to 770 ppm NO_2 for 46 hours and Subsequent Purging at 150° C for 1.5 hours in a Nitrogen Ambient.

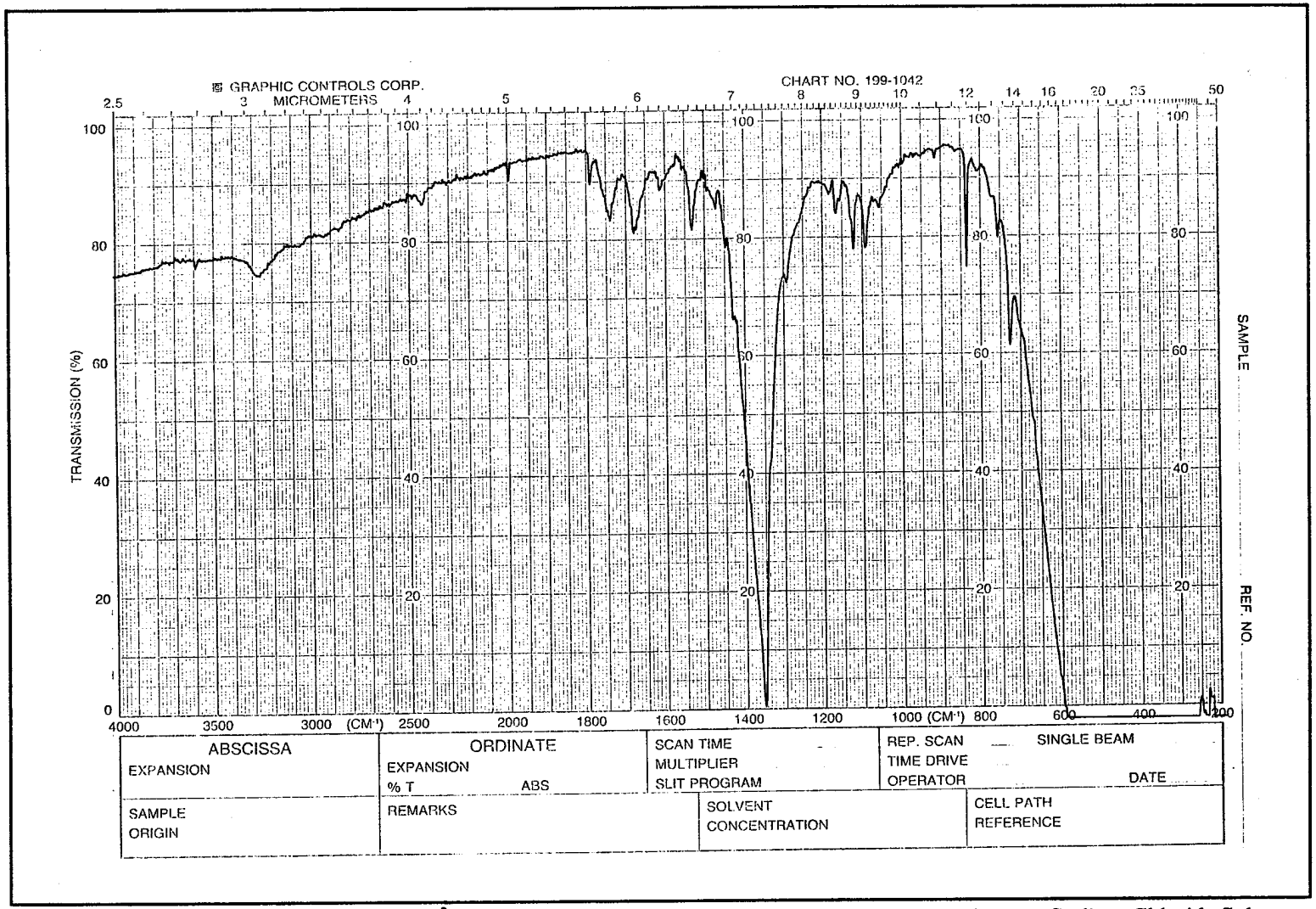


Figure IV-35. Infrared Spectrum of the 7100 Å Thick Nickel Phthalocyanine (NiPc) Thin Film Sublimed onto a Sodium Chloride Substrate after Exposure to 770 ppm NO_2 for 46 hours and Subsequent Purging at 150° C for 1.5 hours in a Nitrogen Ambient.

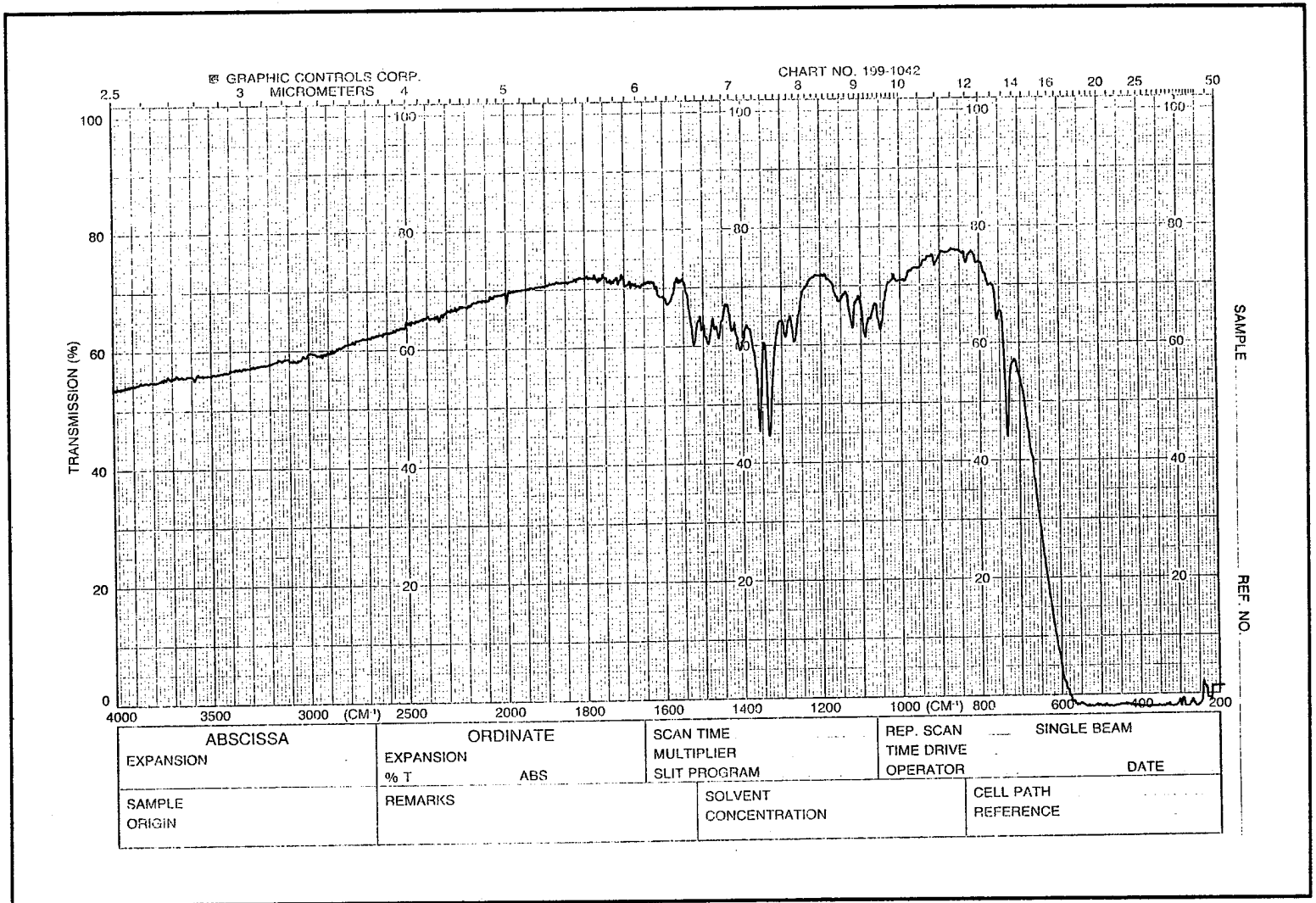


Figure IV-36. Infrared Spectrum of the 5800 Å Thick Cobalt Phthalocyanine (CoPc) Thin Film Sublimed onto a Sodium Chloride Substrate after Exposure to 770 ppm NO_2 for 46 hours and Subsequent Purging at 150° C for 1.5 hours in a Nitrogen Ambient.

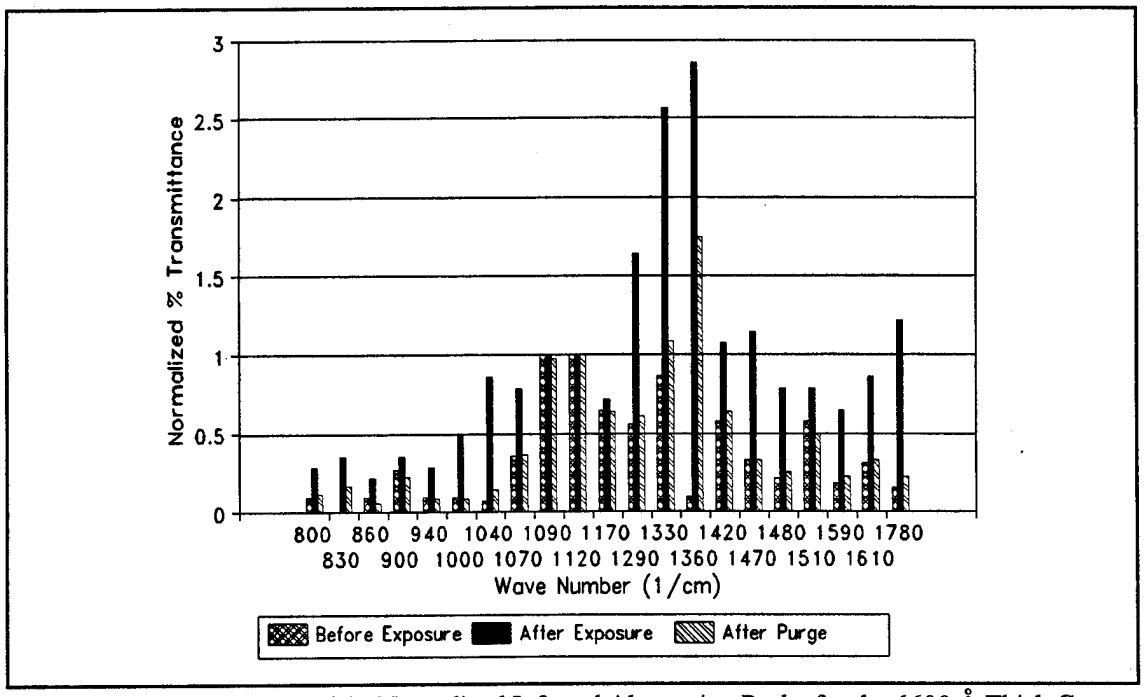


Figure IV-37. Comparison of the Normalized Infrared Absorption Peaks for the 6600 Å Thick Copper Phthalocyanine (CuPc) Thin Film for the Pre-Exposed, 770 ppm NO_2 Exposed, and the Purged Conditions (Normalized with Respect to the 1120 cm^{-1} Peak).

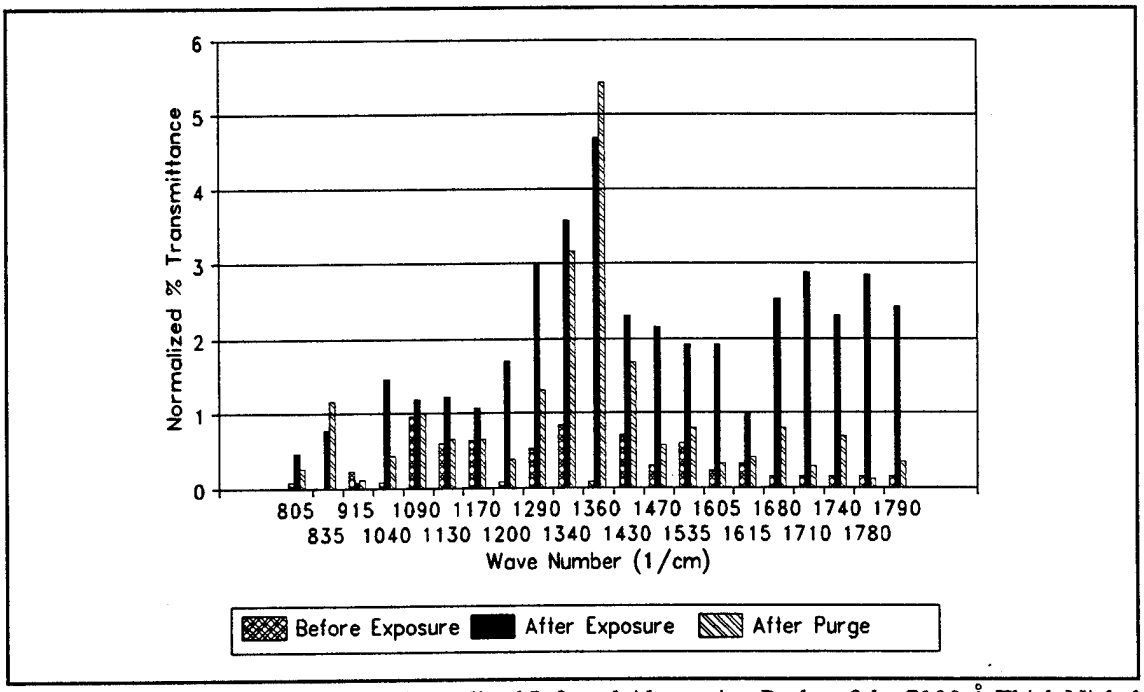


Figure IV-38. Comparison of the Normalized Infrared Absorption Peaks of the 7100 Å Thick Nickel Phthalocyanine (NiPc) Thin Film for the Pre-Exposed, 770 ppm NO_2 Exposed, and the Purged Conditions (Normalized with Respect to the 1120 cm^{-1} Peak).

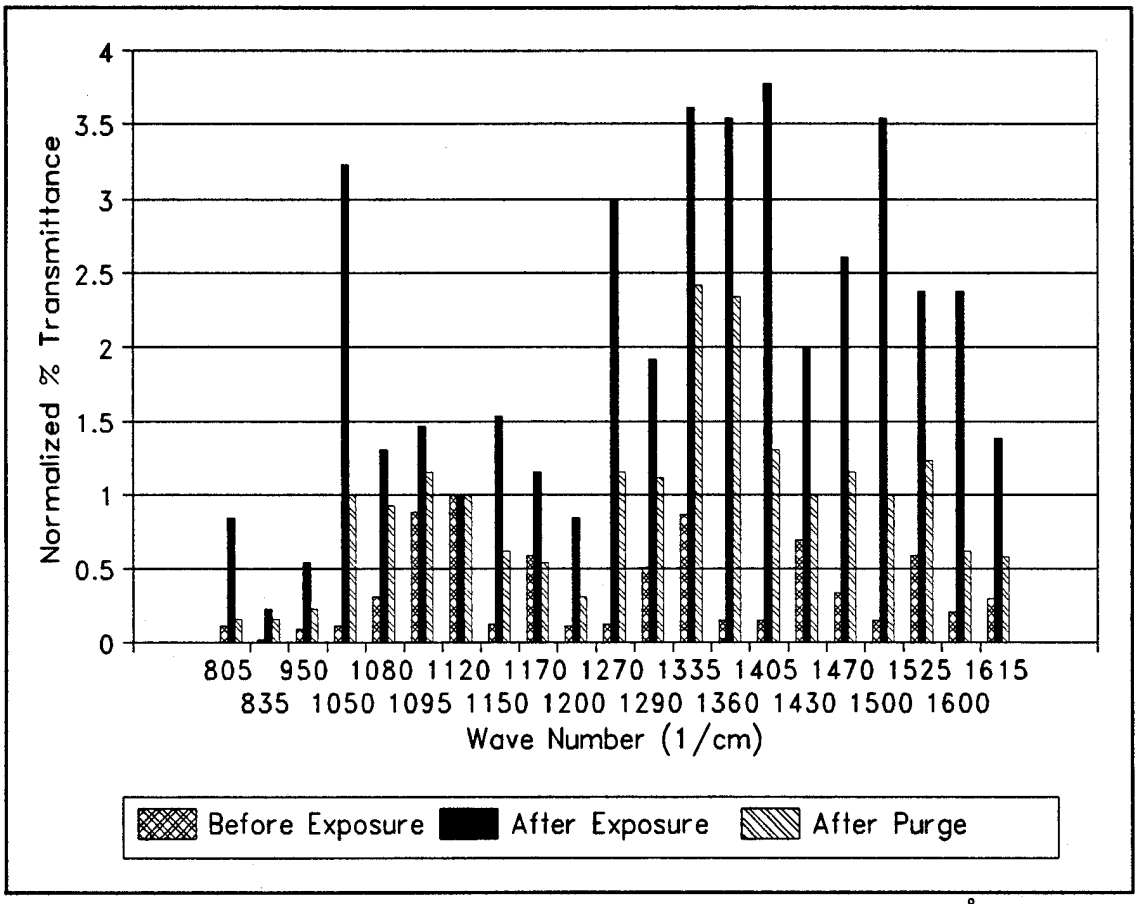


Figure IV-39. Comparison of the Normalized Infrared Absorption Peaks of the 5800 Å Thick Cobalt Phthalocyanine (CoPc) Thin Film for the Pre-Exposed, 770 ppm NO_2 Exposed, and the Purged Conditions (Normalized with Respect to the 1120 cm^{-1} Peak).

exposure time for the IGEFET's electrical operation were much less than those under which the IR samples were subjected to, this situation was anticipated to enhance the reversibility feature observed with the elevated temperature purge.

A similar procedure was used to investigate NH_3 adsorption on fresh MPc samples. Unfortunately, the results were not as dramatic as those for NO_2. The IR spectra of the MPc samples following exposure to a 3700 ppm NH_3 challenge gas concentration for approximately 3 hours (see Figures IV-40 through IV-42) do not reveal any significant change relative to the pre-exposed spectra shown earlier in Figures IV-18, IV-20, and IV-22. Since the NH_3 challenge gas exposure did not elicit an IR response, the subsequent purge at 150° C for 1.5 hours also yielded spectra essentially the same as the pre-exposed spectra (see Figures IV-43 through IV-45). The normalized peak comparisons (see Figures IV-46 through IV-48) and the analysis of the percent change in the pre-exposed, exposed, and purged IR spectra (see Appendix C) confirm the lack of significant IR spectrum changes of the MPc films to an NH_3 challenge. Although this lack of a significant IR spectrum change to NH_3 exposure could have resulted from desorption of the adsorbed gas as the sample was transported from the challenge gas exposure chamber to the infrared spectrophotometer (located in a separate building), other investigators have also reported no changes in the IR spectra of MPc films (with the exception of β-phase iron phthalocyanine) following NH_3 exposure (84, 87). However, the much more sensitive *in-situ* electrical measurements (see Chapter VI) clearly indicate the adsorption and desorption of NH_3 on the MPc-coated IGEFET sensors.

Baseline Sensor Electrical Characterization

While the physical characterization efforts confirmed the IGEFET sensor's physical dimensions, and the polycrystalline, α-phase morphology of the three phthalocyanine films, the purpose of the baseline sensor electrical characterization was to establish the operating envelope of the IGEFET sensors with and without MPc coatings.

Initially, a large set of electrical measurements was considered for monitoring the IGEFET sensor's electrical performance. This set included the IGE structure's DC resistance, the IGE structure's input (electrode-to-ground) and through (inter-electrode) AC impedances, the IGEFET sensor's time- and frequency-domain square wave response, and the IGEFET sensor's transfer function gain and phase. Although this complete set of electrical measurements was accomplished during the initial screening of the candidate challenge gases (see Chapter VI), it was subsequently reduced to facilitate a more rapid sampling period for each measurement type, while minimizing the challenge gas exposure time. The

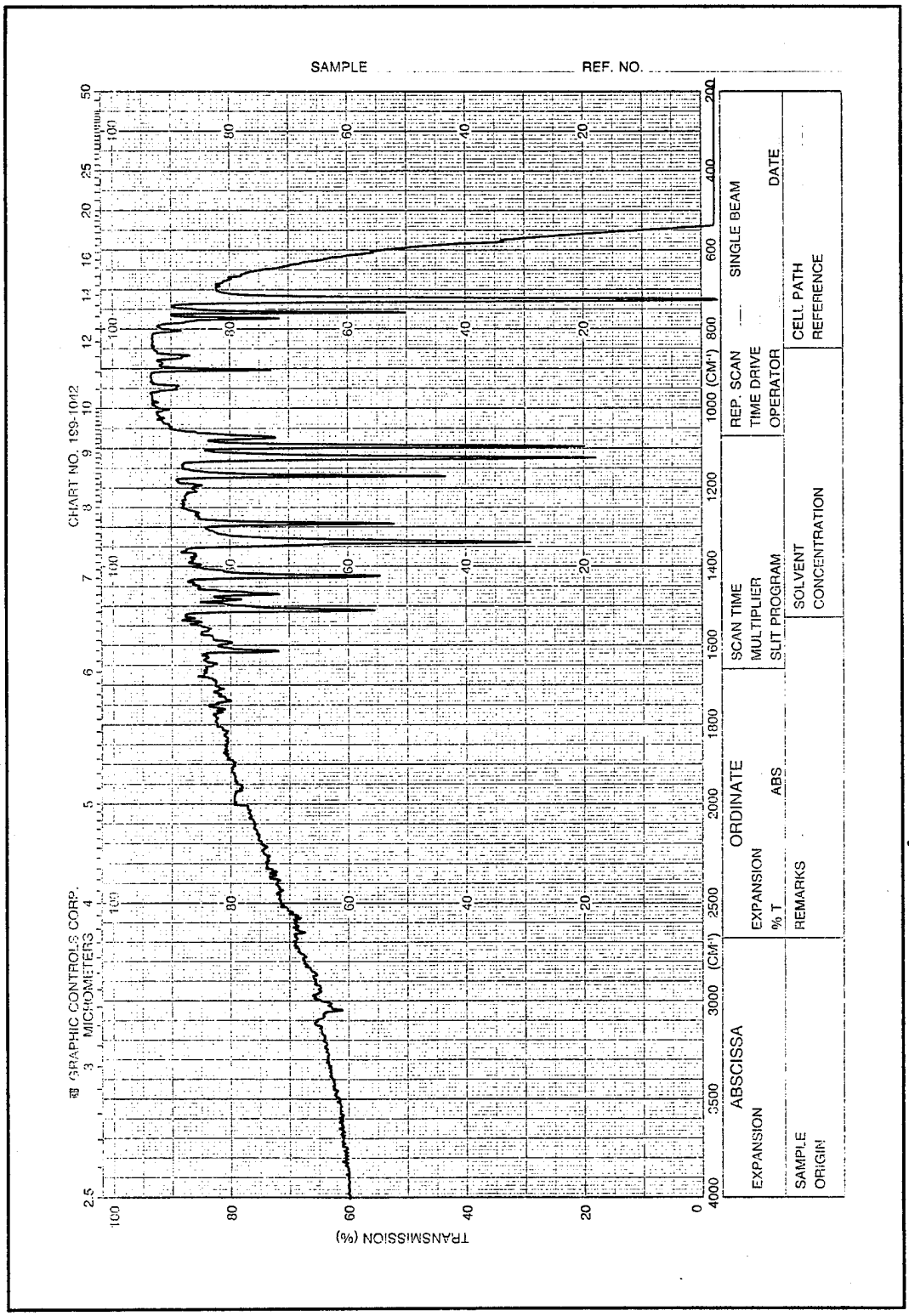


Figure IV-40. Infrared Spectrum of the 7100 Å Thick Copper Phthalocyanine (CuPc) Thin Film Sublimed onto a Sodium Chloride Substrate after Exposure to 3700 ppm NH_3 for 3 hours.

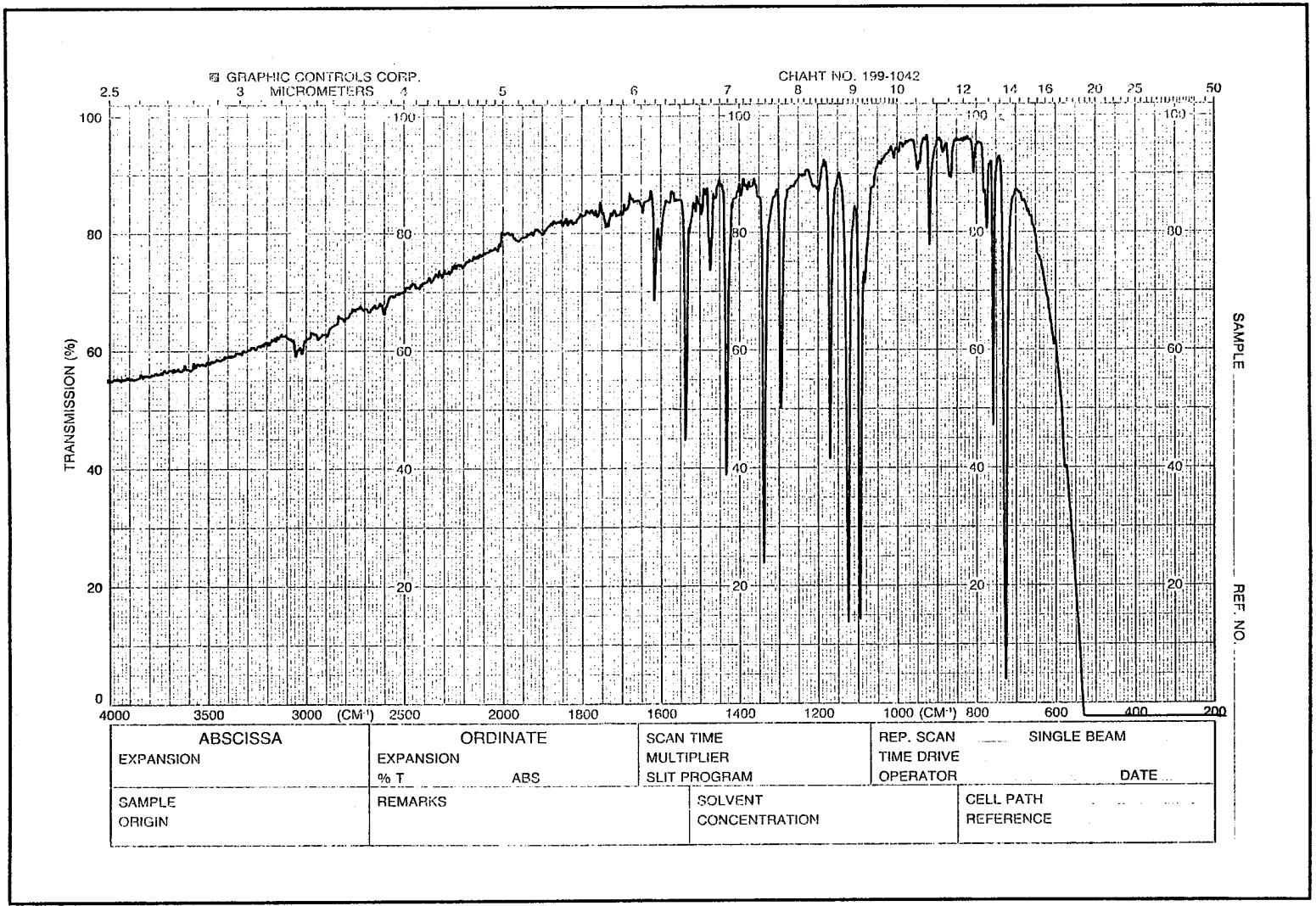


Figure IV-41. Infrared Spectrum of the 6500 Å Thick Nickel Phthalocyanine (NiPc) Thin Film Sublimed onto a Sodium Chloride Substrate after Exposure to 3700 ppm NH_3 for 3 hours.

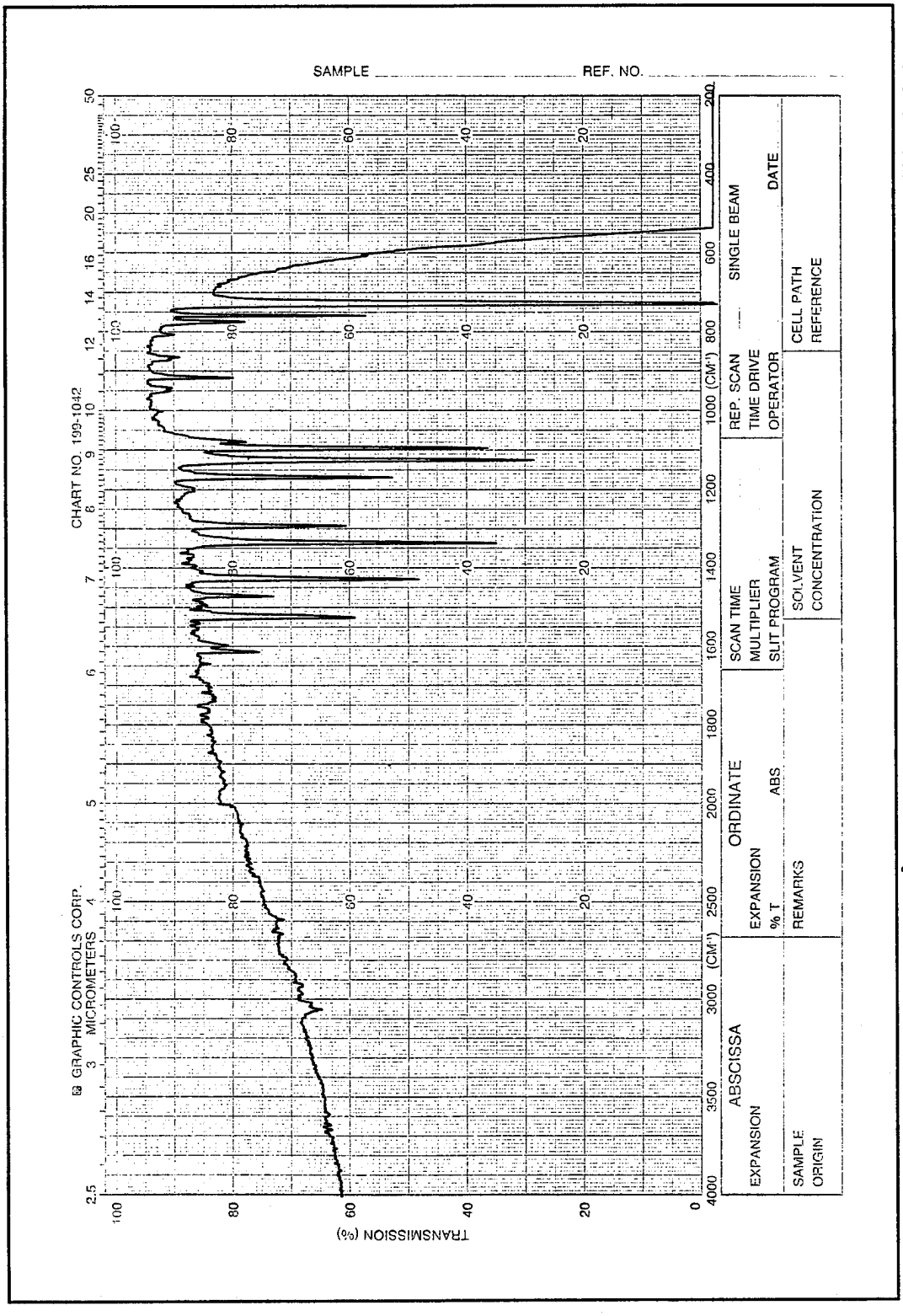


Figure IV-42. Infrared Spectrum of the 5300 Å Thick Cobalt Phthalocyanine (CoPc) Thin Film Sublimed onto a Sodium Chloride Substrate after Exposure to 3700 ppm NH_3 for 3 hours.

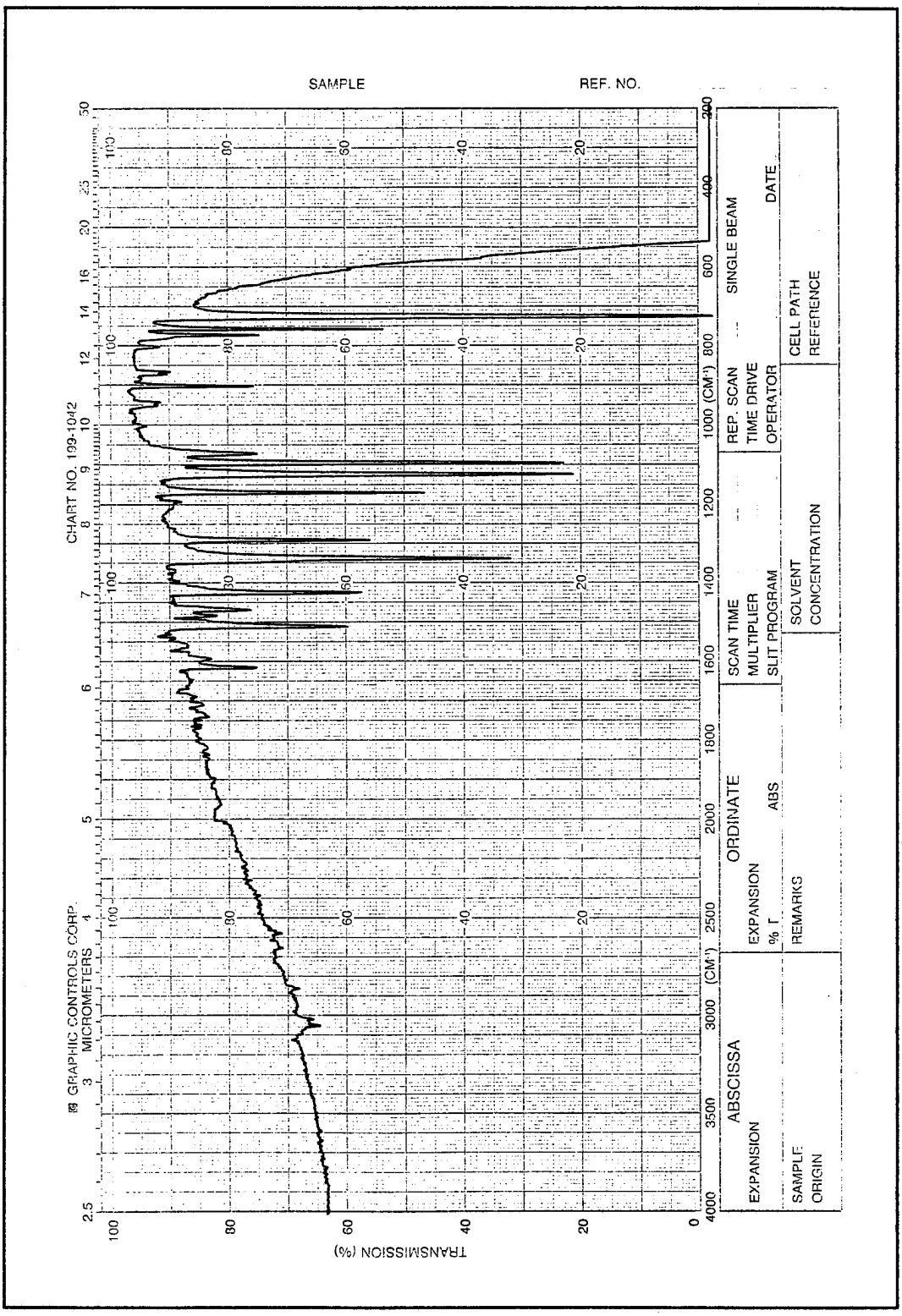


Figure IV-43. Infrared Spectrum of the 7700 Å Thick Copper Phthalocyanine (CuPc) Thin Film Sublimed onto a Sodium Chloride Substrate after Exposure to 3700 ppm NH_3 for 3 hours and Subsequent Purging at 150°C for 1.5 hours in a Nitrogen Ambient.

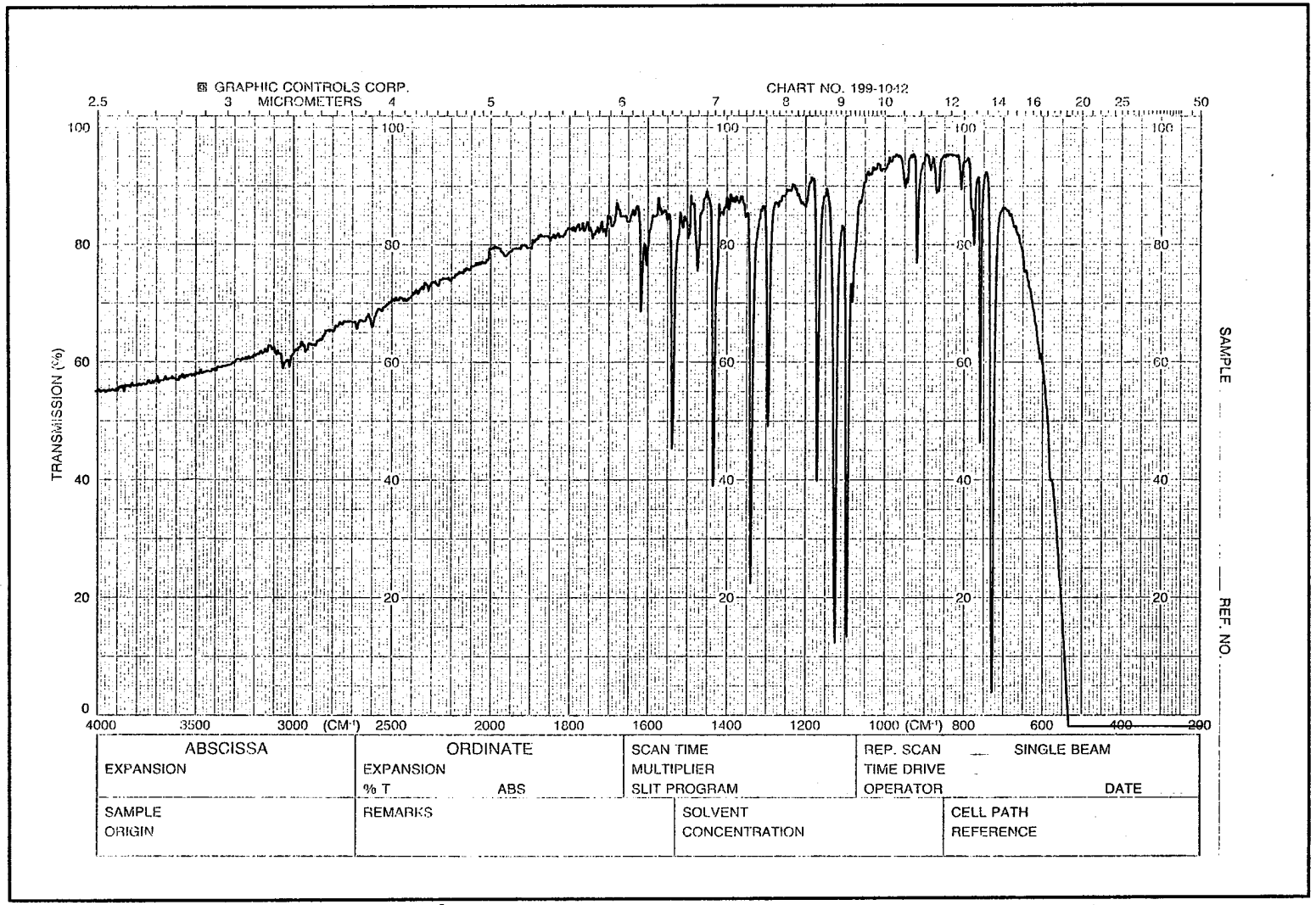


Figure IV-44. Infrared Spectrum of the 6500 Å Thick Nickel Phthalocyanine (NiPc) Thin Film Sublimed onto a Sodium Chloride Substrate after Exposure to 3700 ppm NH_3 for 3 hours and Subsequent Purging at 150° C for 1.5 hours in a Nitrogen Ambient.

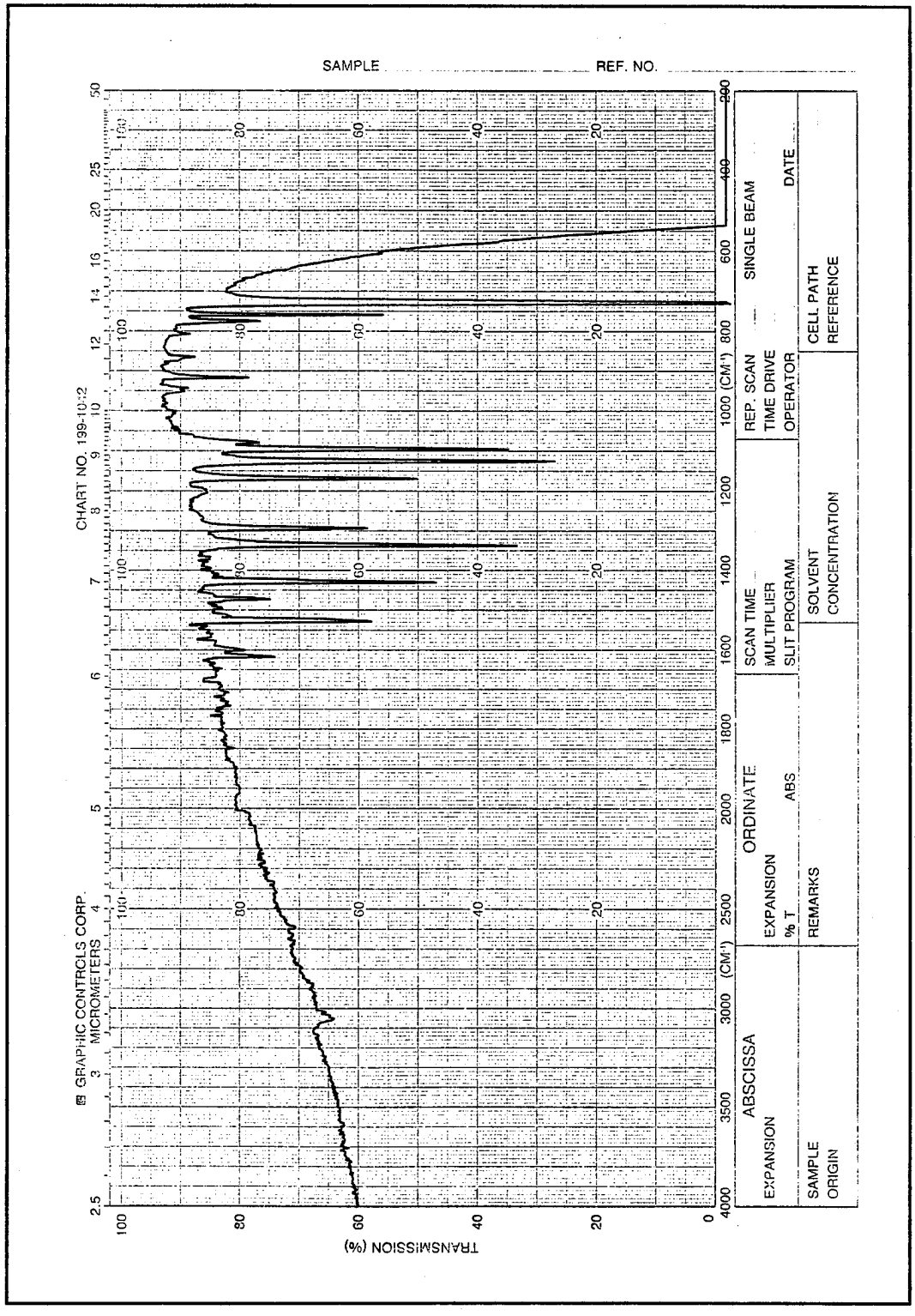


Figure IV-45. Infrared Spectrum of the 5300 Å Thick Cobalt Phthalocyanine (CoPc) Thin Film Sublimed onto a Sodium Chloride Substrate after Exposure to 3700 ppm NH_3 for 3 hours and Subsequent Purging at 150°C for 1.5 hours in a Nitrogen Ambient.

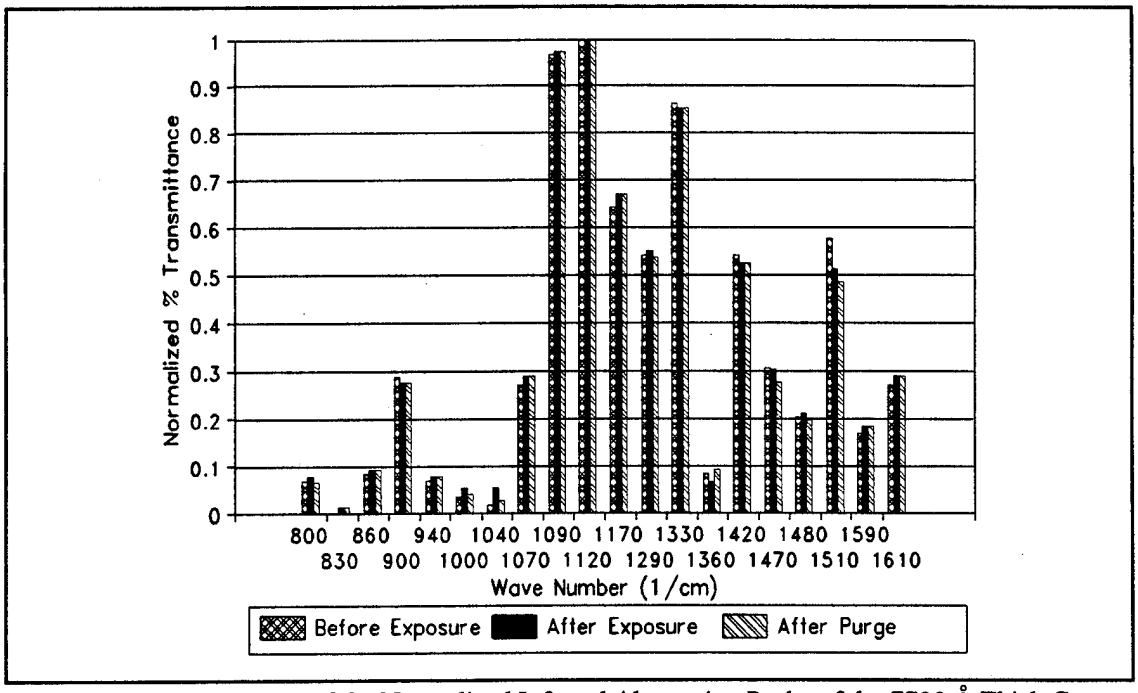


Figure IV-46. Comparison of the Normalized Infrared Absorption Peaks of the 7700 Å Thick Copper Phthalocyanine (CuPc) Thin Film for the Pre-Exposed, 3700 ppm NH_3 Exposed, and the Purged Conditions (Normalized with Respect to the 1120 cm^{-1} Peak).

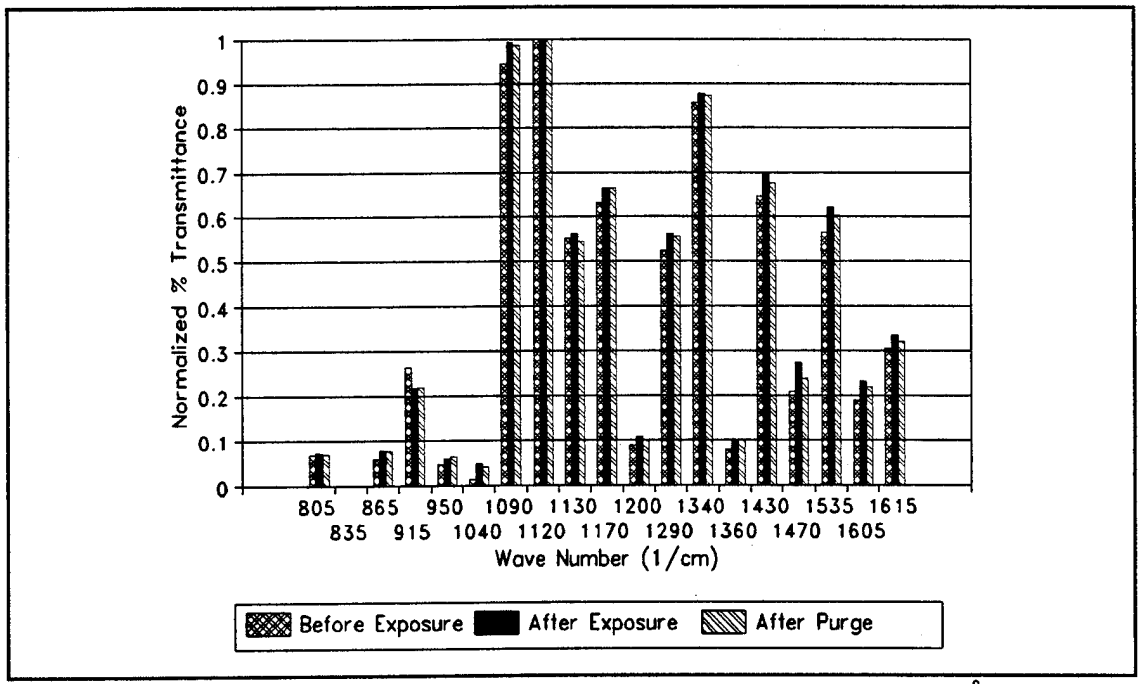


Figure IV-47. Comparison of the Normalized Infrared Absorption Peaks of the 6500 Å Thick Nickel Phthalocyanine (NiPc) Thin Film for the Pre-Exposed, 3700 ppm NH_3 Exposed, and the Purged Conditions (Normalized with Respect to the 1120 cm^{-1} Peak).

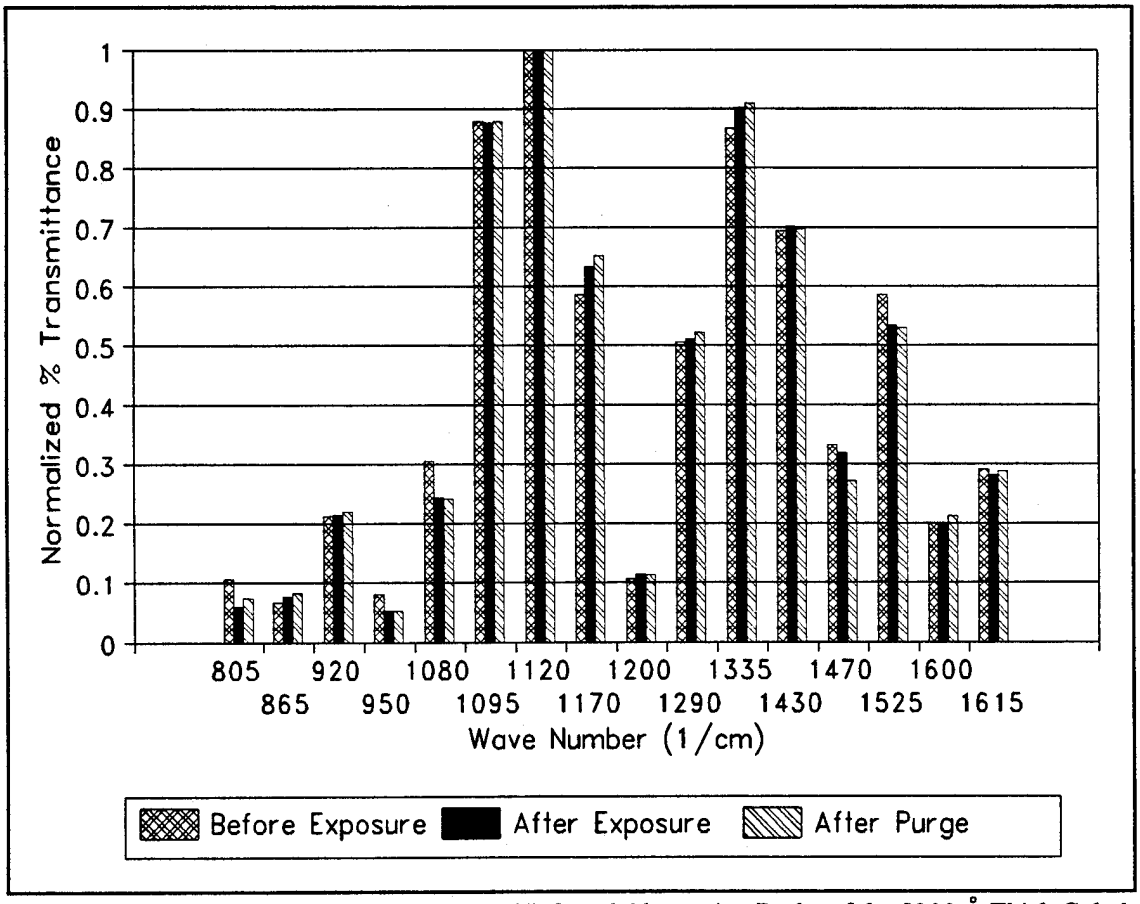


Figure IV-48. Comparison of the Normalized Infrared Absorption Peaks of the 5300 Å Thick Cobalt Phthalocyanine (CoPc) Thin Film for the Pre-Exposed, 3700 ppm NH_3 Exposed, and the Purged Conditions (Normalized with Respect to the 1120 cm^{-1} Peak).

subset of electrical measurements employed to monitor the effects of gas adsorption on the MPc-coated IGEFET sensors for the remainder of the research effort was composed of the IGE structure's DC resistance and the IGEFET sensor's transfer function gain/phase measurements. This measurement subset was selected on the basis of the preliminary experimental results (see Appendix D) which demonstrated that the information obtained from the other electrical measurements was either redundant to and/or more experimentally limited compared to the two selected electrical measurements.

The following discussion of the baseline sensor electrical characterization is divided into three sub-sections. The first sub-section describes the instrumentation system used to accomplish the complete set of electrical measurements. The second sub-section discusses the uncoated sensor's electrical properties and their dependence on several experimental parameters. The final sub-section describes the electrical properties of the MPc-coated IGEFET sensors.

Instrumentation System. The comprehensive set of electrical measurements collected on each of the nine IGEFET sensor elements mandated an instrumentation system that supported automated data acquisition. A dedicated personal computer (Model Z-248, Zenith Data Systems, St. Joseph, MI) equipped with a General Purpose Instrumentation Bus (GPIB) interface card (Model 01000-60300, Capital Equipment Corp., Burlington, MA) coordinated the data collection process using several different analytical instruments; it also provided closed-loop control of the microsensor's operating temperature. The general layout of the GPIB controlled instrumentation system shown in Figure IV-49 identifies the analytical instrumentation used to electrically characterize the devices under test. Two relay scanner frames (Model 603, Wavetek Corp, San Diego, CA and Model 706, Keithley Instruments, Cleveland, OH) equipped with a set of relay cards formed the switching matrix used to route the signal pathways from the instrumentation to the nine sensor elements in each of the IGEFET microsensors that were installed in the two test chambers. Detailed schematics of the instrumentation system are provided in Appendix E.

The GPIB control software, written in Pascal (Turbo Pascal, Borland International, Inc., Scotts Valley, CA), executed the test protocol for particular evaluations (see Chapter VI). In general, for all the test protocols, the GPIB software configured the instrumentation, monitored and controlled the IGEFET microsensor's temperature, sequenced the opening and closing of the switch relays for interrogation of the nine sensor elements on each IGEFET microsensor, maintained the experimental process time, downloaded data from the various instruments, and stored the data on magnetic media. The large data sets that were collected were formatted as binary records for efficient storage. The transfer function and impedance data were also scaled and converted to integer format to acheive a more

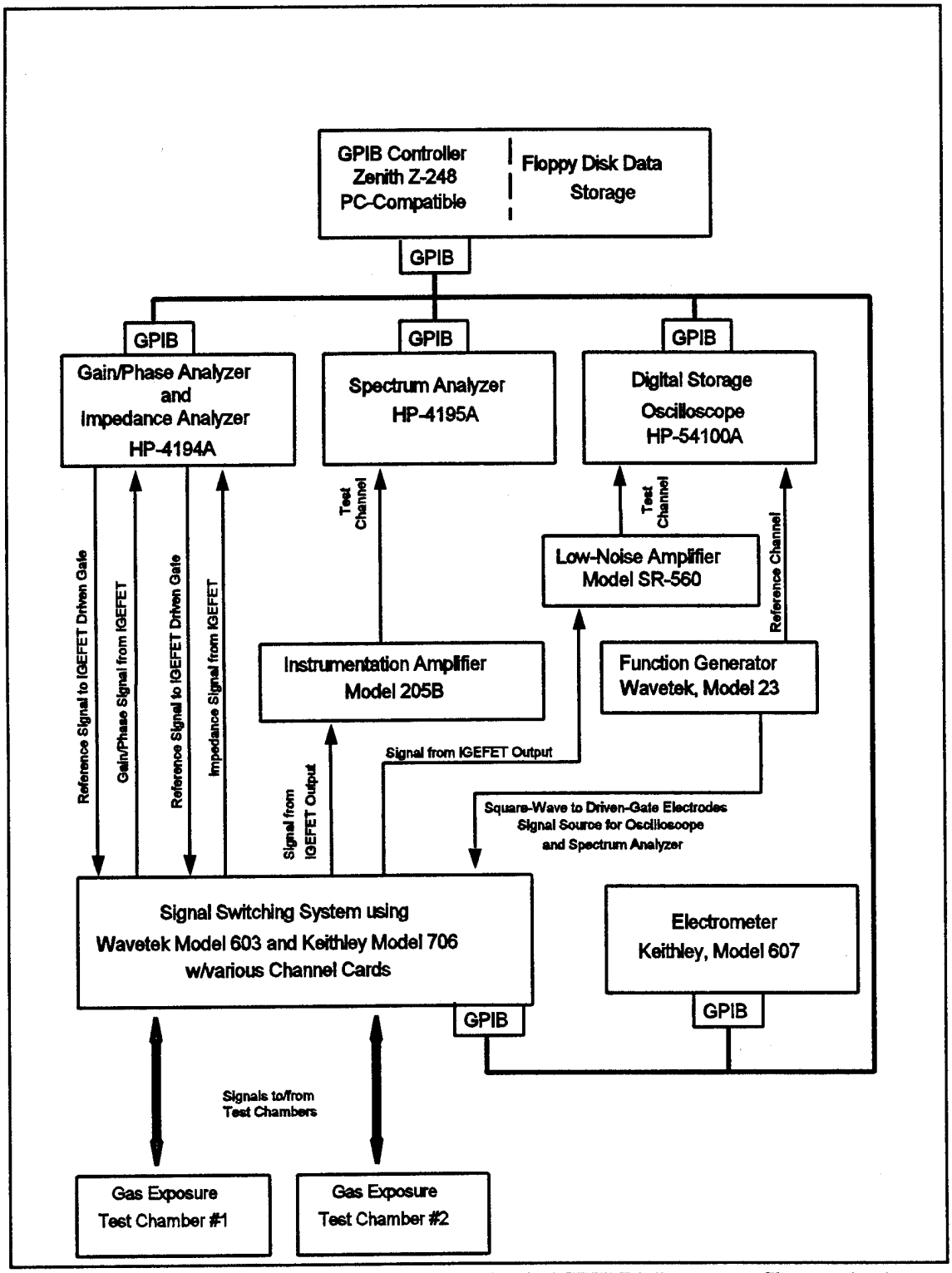


Figure IV-49. Electrical Instrumentation System for the IGEFET Microsensor Characterization.

dense storage capability. The storage of the data in this form necessitated additional software for extracting and converting the stored data into a text format for analysis.

The two sample chambers depicted in Figure IV-49 were specifically designed for the IGEFET microsensor performance characterization research (184) and modified for operation at temperatures up to 200° C (25). Each sample chamber was outfitted with a Type-K Thermocouple (model SA1-K, Omega Engineering, Stanford, CT) and a Kapton heater strip (model K005020C5, Watlow, St. Louis, MO) for control of the microsensor's temperature. The Kapton heater strip and the thermocouple were placed in intimate contact with the microsensor package by using a molded strip of spring steel. Insertion of the microsensor into the test socket compressed the spring steel strip, ensuring intimate contact of the heater strip and thermocouple with the IGEFET microsensor's package. Initially, the microsensor's temperature was controlled to within 2° C of the desired temperature by manual adjustment of the power supply voltage connected to the heater strips. To provide an automated elevated temperature purge capability, and to improve the long-term thermal stability, the open-loop method was replaced with a closed-loop control system capable of maintaining the long-term temperature to within 0.5° C. The closed-loop temperature control system is depicted in Figure IV-50. The Type-K thermocouples were connected to the instrumentation amplifier (model 205B, Trig-Tek Instrumentation, Anaheim, CA) through a thermocouple relay card (model 7057A, Keithley Instruments, Cleveland, OH) to provide a reference for electrometer measurement of the thermocouple voltage. The voltage measurement was converted to the microsensor temperature using a polynomial expression relating thermocouple voltage to temperature (185) programmed in the personal computer. The computation of the microsensor temperature accounted for the instrumentation amplifier gain which was set at 1000. If the measured temperature deviated more than 0.5° C. from the programmed desired temperature, the power supply (model 6624A, Hewlett Packard, Palo Alto, CA) voltage applied to the heater strip was adjusted appropriately in 0.05-V steps. The microsensor temperature measurements were made at approximately two-minute intervals. Although this temperature control system was excellent for tight temperature control, it was not optimal for controlling the large temperature adjustments used for elevated purge. The large temperature adjustments were accomplished by setting the power supply to a voltage previously determined to produce the desired purge temperature.

The two sample chambers were configured for two different categories of electrical tests. One of the sample chambers was configured solely for DC resistance and impedance measurements of the interdigitated gate electrode structure of each IGEFET sensor. The second chamber was configured to measure the IGEFET sensor's response (IGEFET sensor's transfer function gain/phase, and the IGEFET

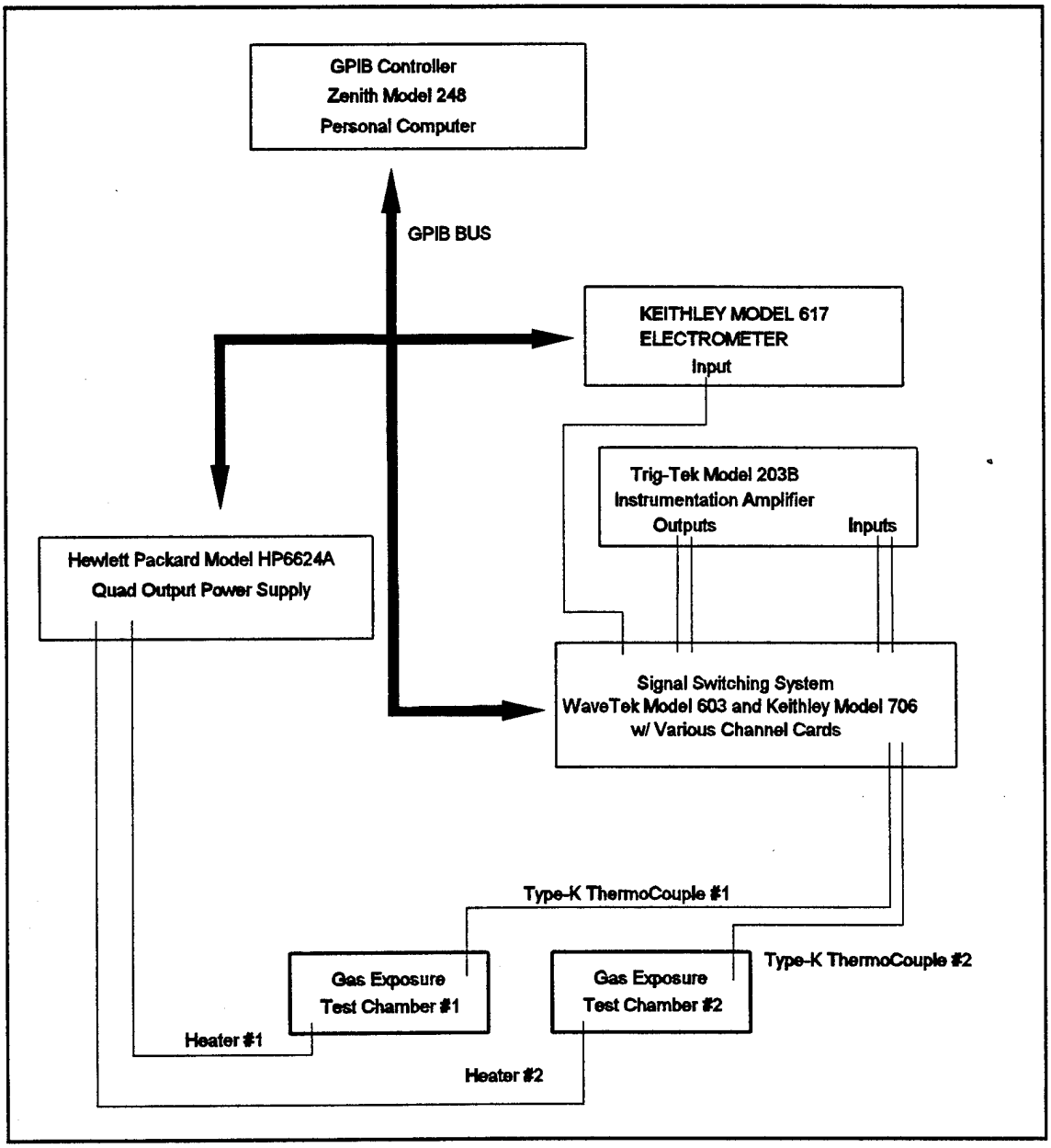


Figure IV-50. Closed-Loop Temperature Control System.

sensor's time- and frequency-domain square-wave response) at the differential amplifier output. These two test configurations were required since the floating-gate electrode bond wire necessary for electrical measurements of the interdigitated gate electrode structure of the sensor was removed to prevent capacitive loading of the IGEFET sensor's response.

The DC resistance of the IGE structure was measured with an electrometer (model 617, Keithley Instruments, Cleveland, OH) configured in the voltage/ampere (V/I) mode. The electrometer manufacturer recommends this mode for high resistance measurements to minimize the effects of leakage resistance and distributed capacitance (186). This operational mode permits the measurement of resistances on the order of 10^{16} ohms (186). The electrometer determines the resistance by measuring the current through the device under test relative to a fixed bias voltage. The simplified schematic in Figure IV-51 depicts the electrical connections between the test equipment and the IGEFET sensor. The electrometer's bias voltage was simultaneously applied to the driven gate electrodes of all nine IGEFET sensors. To measure the resistance of each interdigitated gate electrode structure, a low-current relay card (model 7158, Keithley Instruments, Cleveland, OH) installed in the Keithley scanner frame was closed to route the electrometer's input to a particular IGEFET microsensor's floating gate electrode. All other connections to the microsensor were grounded either through the low-current relay card or with coaxial shorting stubs placed on the sample chamber lead connectors.

Two different AC impedance measurements were made on the IGE structure: the input impedance and the through impedance. An impedance/gain-phase analyzer (model HP4194A, Hewlett Packard, Palo Alto, CA) that uses a four-wire measurement technique was configured as depicted in Figure IV-52 and IV-53 to accomplish the input and through impedance measurements, respectively. The input impedance is equivalent to the driven gate structure's electrode-to-ground impedance, and the through impedance is equivalent to the inter-electrode impedance. In the absence of any parasitic load capacitance, the combination of these two impedances determines the overall AC transfer function of the IGE structure (see Chapter V and Appendix D). Depending upon the particular analyzer mode, the impedance measurement was expressed either as an impedance, an admittance, or a capacitance and dissipation factor. The impedance measurements were recorded over the frequency range spanning 100 Hz to 1 MHz. Individual sensors were probed in a manner similar to the DC resistance measurements, with the exception that the test signal was applied only to the driven gate of the sensor under test. The signal pathways were routed through the same relay cards as for the DC measurements and, therefore, the DC resistance and AC impedance measurements were not collected simultaneously.

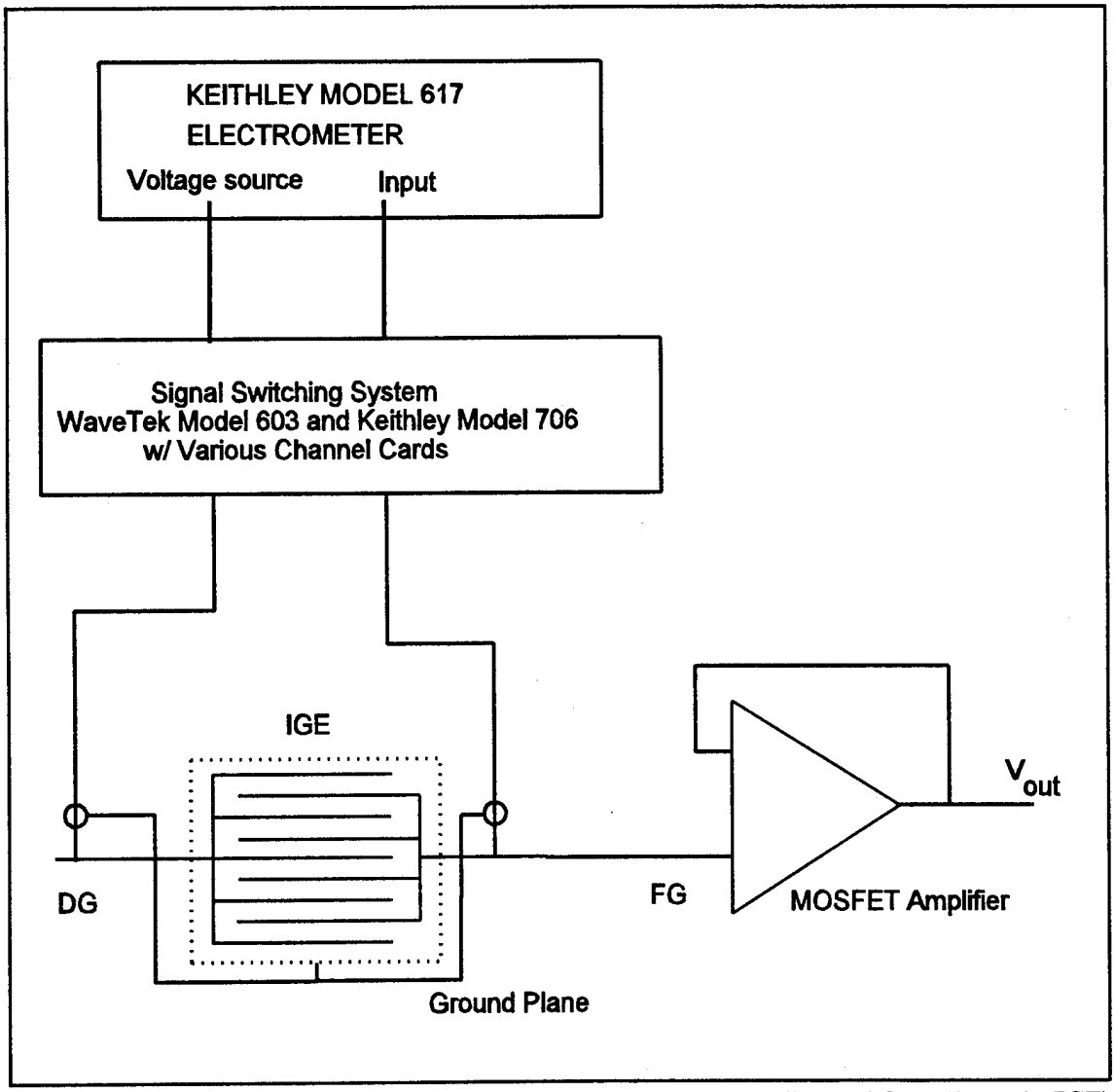


Figure IV-51. Instrumentation Configuration for Measuring the Interdigitated Gate Electrode (IGE) Structure's DC Resistance.

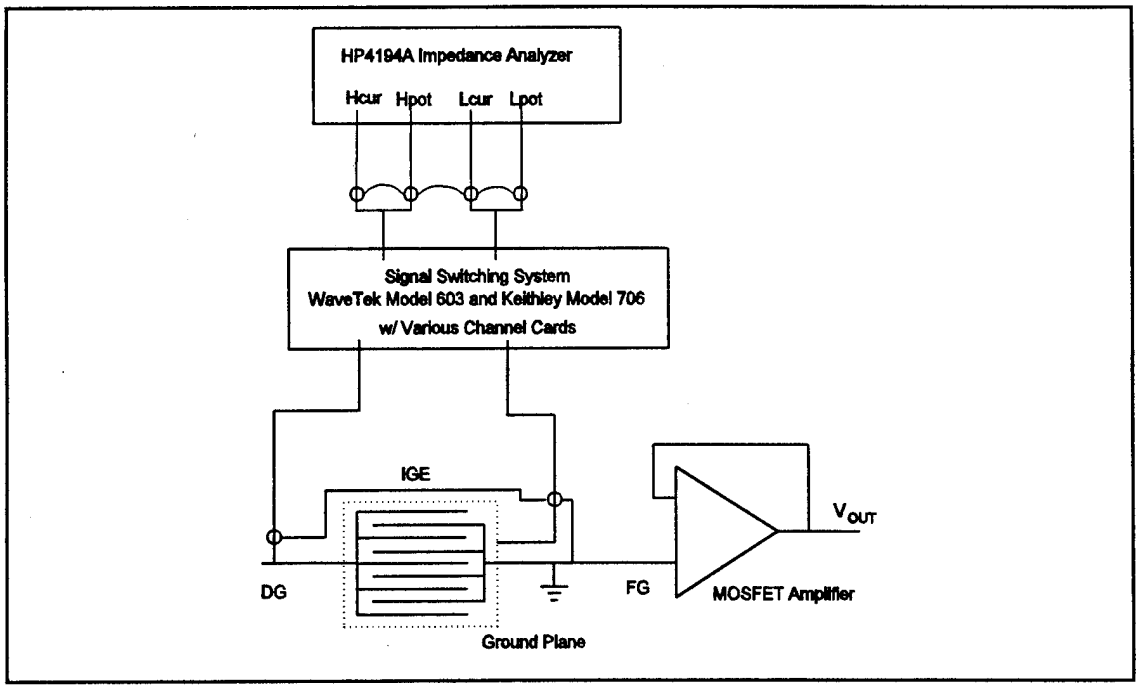


Figure IV-52. Instrumentation Configuration for Measuring the Interdigitated Gate Electrode (IGE) Structure's Input (Electrode-to-Ground) Impedance.

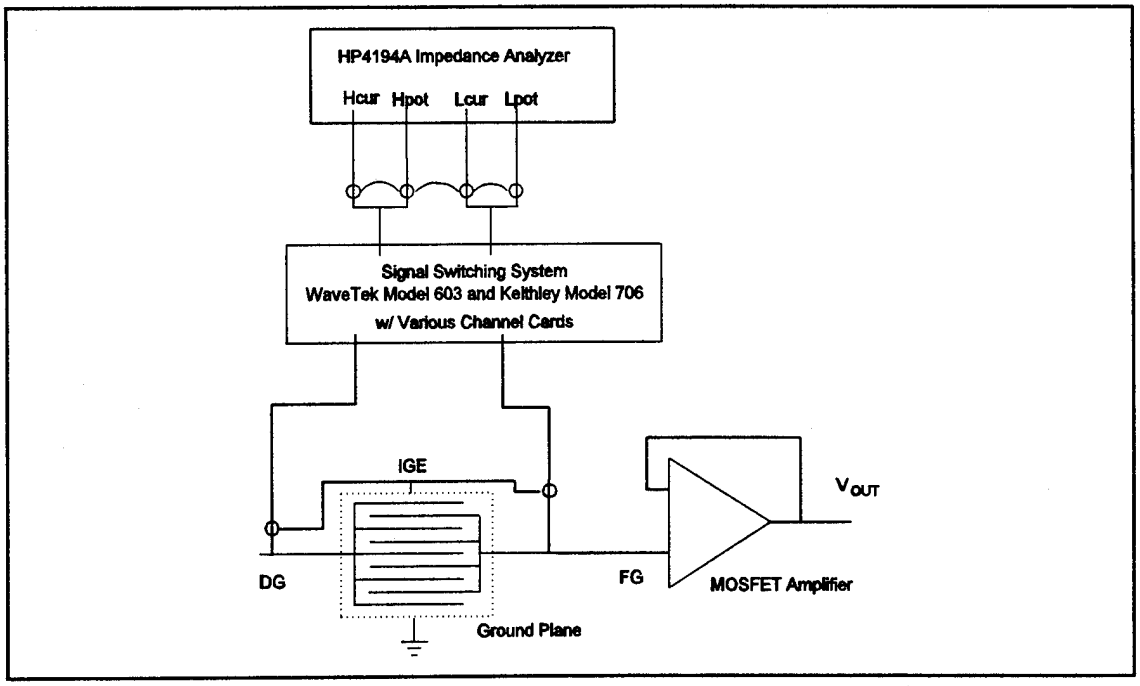


Figure IV-53. Instrumentation Configuration for Measuring the Interdigitated Gate Electrode (IGE) Structure's Through (Inter-electrode) Impedance.

In contrast to the IGE structure's DC resistance and AC impedance measurements described above, proper biasing of the IGEFET differential amplifiers was required to accomplish the IGEFET sensor response measurements, which included the IGEFET transfer function's gain/phase, as well as the IGEFET's time- and frequency-domain square-wave responses. Based upon the characterization of these amplifiers described by Howe (25), each IGEFET amplifier was configured as a voltage follower (unity gain) by shorting the amplifier output, V_{out}, to the inverting terminal of the differential amplifier, V_{offset}. The operating voltages were established with a precision power supply (model HP 6205B, Hewlett Packard, Palo Alto, CA) with the following values: V_{dd}=+5 V, V_{ss}=-5 V, V_{bias}= 0 V. Since the voltage follower configuration has unity gain, it permits the direct measure of the changes in the IGE structure's transfer function induced by the interaction of the MPc film with a challenge gas.

The IGEFET transfer function's gain and phase delay were measured with the impedance/gain-phase analyzer (model HP4194A, Hewlett Packard, Palo Alto, CA). The instrumentation configuration is depicted in Figure IV-54. The HP4194A was configured with a 1 MΩ input impedance and, therefore, did not require an instrumentation amplifier for impedance matching. The transfer function data was collected over the frequency range spanning 10 Hz to 1 MHz. The signal pathways to and from the HP4194A were routed through a set of matrix relay cards (model 7052, Keithley Instruments, Cleveland, OH) to the specific sensor under test.

The IGEFET microsensor's response to the square-wave excitation of the driven gate electrode was measured in the time and frequency domains. The instrumentation configuration is illustrated in Figure IV-55. A 50 Hz, 50% duty cycle square wave with a 2-V peak-to-peak signal amplitude from the function generator (model 23, WaveTek Corp., San Diego, CA) was simultaneously applied to the driven-gate electrodes of two IGEFET sensors and to one channel of a digitizing oscilloscope (model HP54100A, Hewlett Packard, Palo Alto, CA). The instrumentation amplifiers provided optimal coupling of the output from the two IGEFET amplifiers to the spectrum analyzer (model HP4195A, Hewlett Packard, Palo Alto, CA) and the second channel of the oscilloscope. The frequency spectrum of the applied square wave was recorded at the beginning of each experiment. The signal pathways between the instrumentation and the IGEFET sensors were routed through the same set of matrix relay cards used to route the gain/phase signals.

Uncoated Sensor Characterization. A series of measurements were performed to characterize the electrical behavior of the uncoated IGEFET sensor. This section presents and discusses the results of these measurements. First, the resistance measurements that characterize the DC response of the IGE structure will be discussed. This will be followed by a discussion of the results of the AC impedance

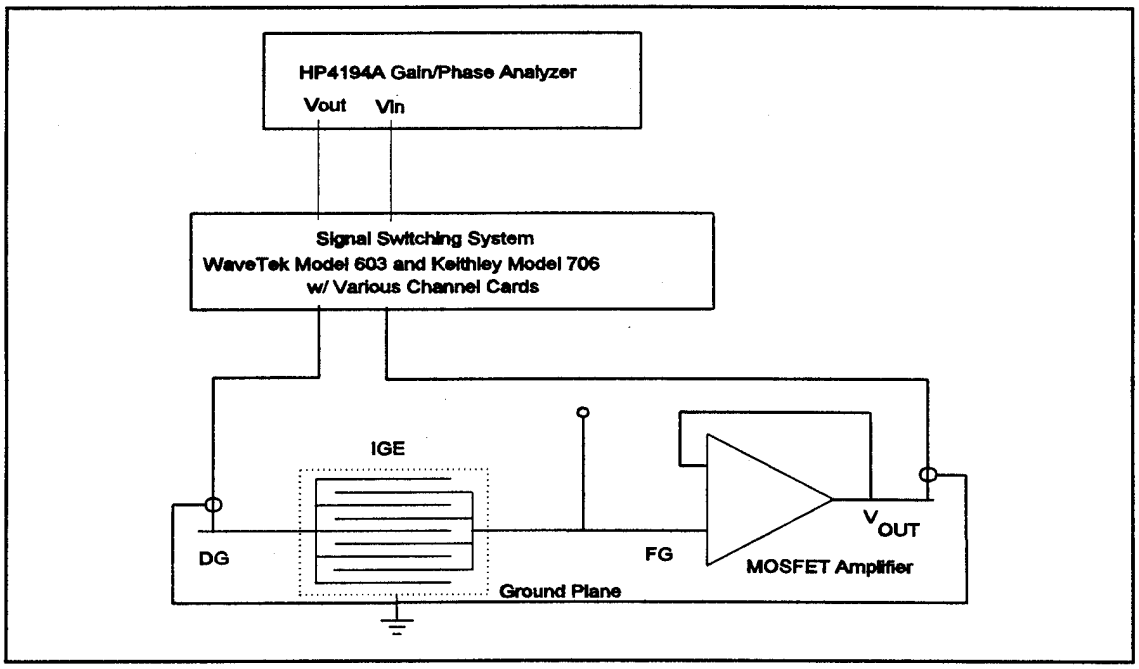


Figure IV-54. Instrumentation Configuration for Measuring the IGEFET Transfer Function Gain and Phase Delay.

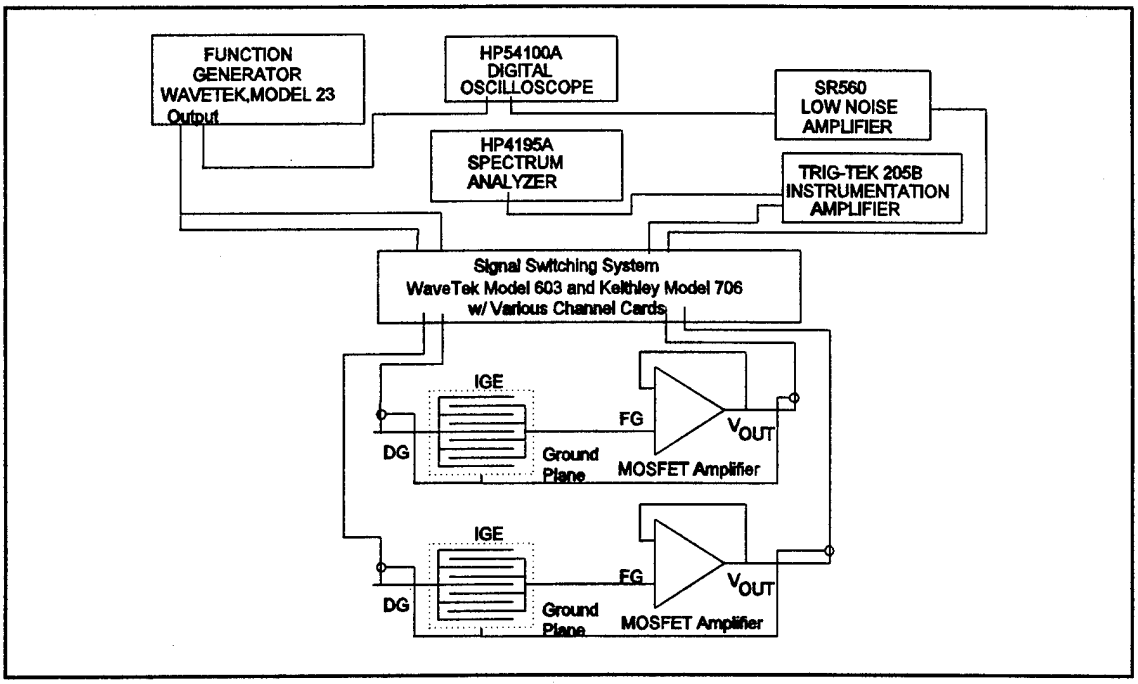


Figure IV-55. Instrumentation Configuration for Measuring the IGEFET Time- and Frequency-Domain Square-Wave Response.

measurements on the IGE structure and, finally, by a description of the IGEFET microsensor's transfer function gain/phase measurements.

DC Resistance of the Interdigitated Gate Electrode Structure. The IGE structure's DC resistance of each of the nine sensor elements was measured on 8 different microsensor IC's maintained at 30° C. Although a bias-voltage dependence was not observed for the uncoated IGE structure's DC resistances measured at 150° C (Figures IV-56 through IV-58), the optimum bias voltage for measuring the resistance of the MPc-coated IGE structures was determined to be 10 V (see the following section). Therefore, the uncoated IGE structure resistance measurements were also performed with a bias voltage of 10 V. Prior to inserting the microsensor IC package, an open test socket resistance greater than 10^{14} ohms was measured. Although the standard deviation of the IGE structure's resistance for each sensing element was typically less than 25%, the average resistance, as shown in Figure IV-59, varied considerably between sensor elements. Since only a single sensor design was accomplished, and then replicated to form the sensor element array, the wire bond arrangement and/or the external connections were considered the most likely source for the element-to-element IGE structure resistance variations. As stated earlier, the open test socket resistance measured for all nine sets of IGE structure connections was greater than 10^{14} ohms and, therefore, the resistance variability must arise within the packaged device. Inspection of the wire bond arrangement (see Figure IV-1) revealed that the driven- and floating-gate electrode bond pads of the elements possessing the smallest IGE structure resistances (elements 1, 6, and 9) were either adjacent to, or separated by, a single pad. Based upon this observation, the IGE strucuture's resistance variability was concluded to be the result of on-chip leakage paths between the driven- and floating-gate electrodes. Additional support for this conclusion was obtained from the IGE impedance measurements.

Since the IGEFET was expected to operate over a wide temperature range, the temperature dependence of the IGE structure's DC resistance was measured. Arrhenius plots (see Figure IV-60 through IV-62) of the DC resistance reveal a strong temperature dependence with an activation energy of approximately 0.57 ± 0.03 eV. Although the element-to-element resistance variation remains apparent in these plots, the temperature dependence of the various IGE elements is essentially the same.

Impedance of the Interdigitated Gate Electrode Structure. As described earlier in the instrumentation section, two impedance measurements were performed on the IGE structure: an input and through impedance measurement. Figure IV-63 and IV-64 depicts the magnitude and phase delay of the two impedance measurements for one IGE structure (element 3) maintained at 30° C. The input and through impedance phase delay of -90° over the entire measurement bandwidth indicates that both

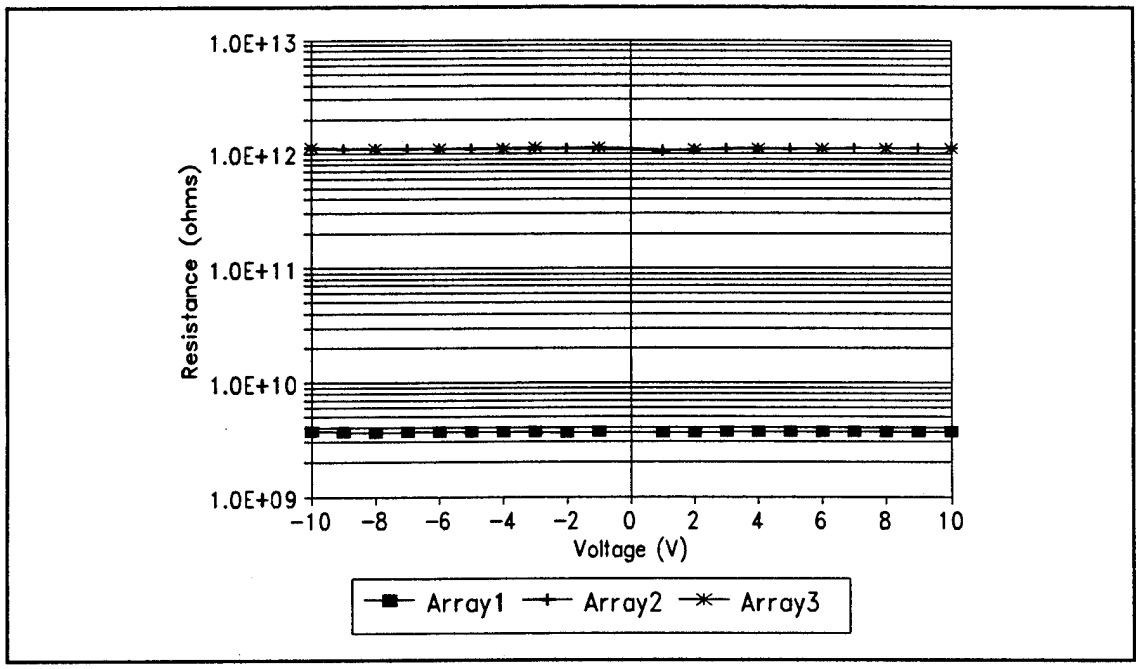


Figure IV-56. Bias Voltage Dependence of the Uncoated Interdigitated Gate Electrode (IGE) Structure's DC Resistance for IGEFET Sensing Elements 1, 2, and 3. Microsensor Maintained at 150° C in a Dry Air Ambient.

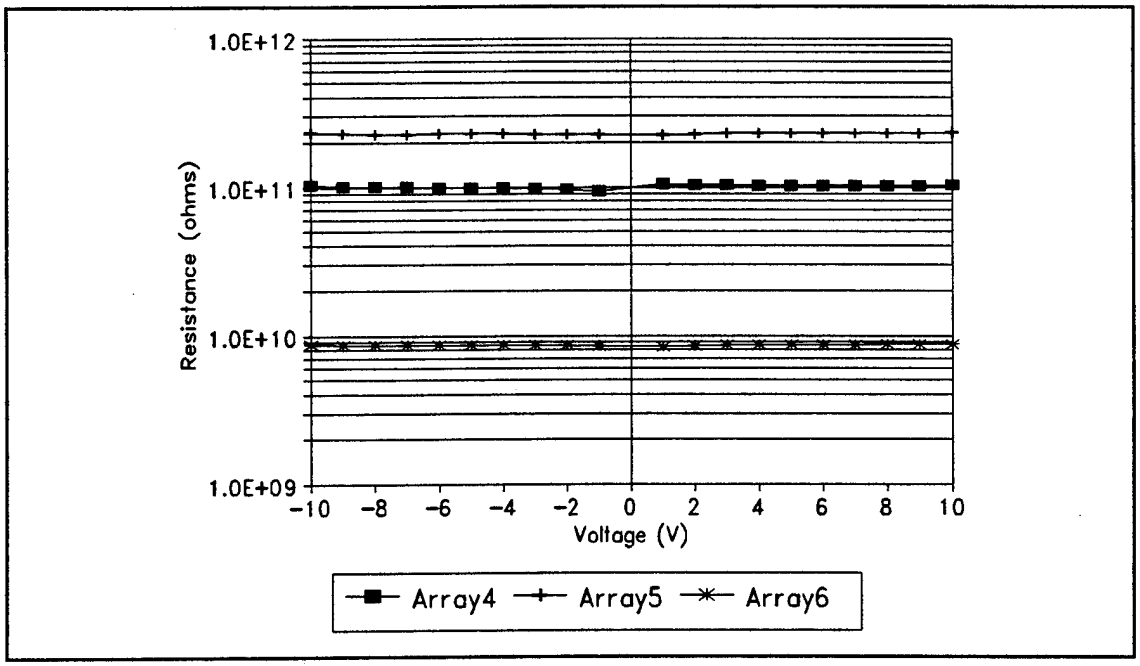


Figure IV-57. Bias Voltage Dependence of the Uncoated Interdigitated Gate Electrode (IGE) Structure's DC Resistance for IGEFET Sensing Elements 4, 5, and 6. Microsensor Maintained at 150° C in a Dry Air Ambient.

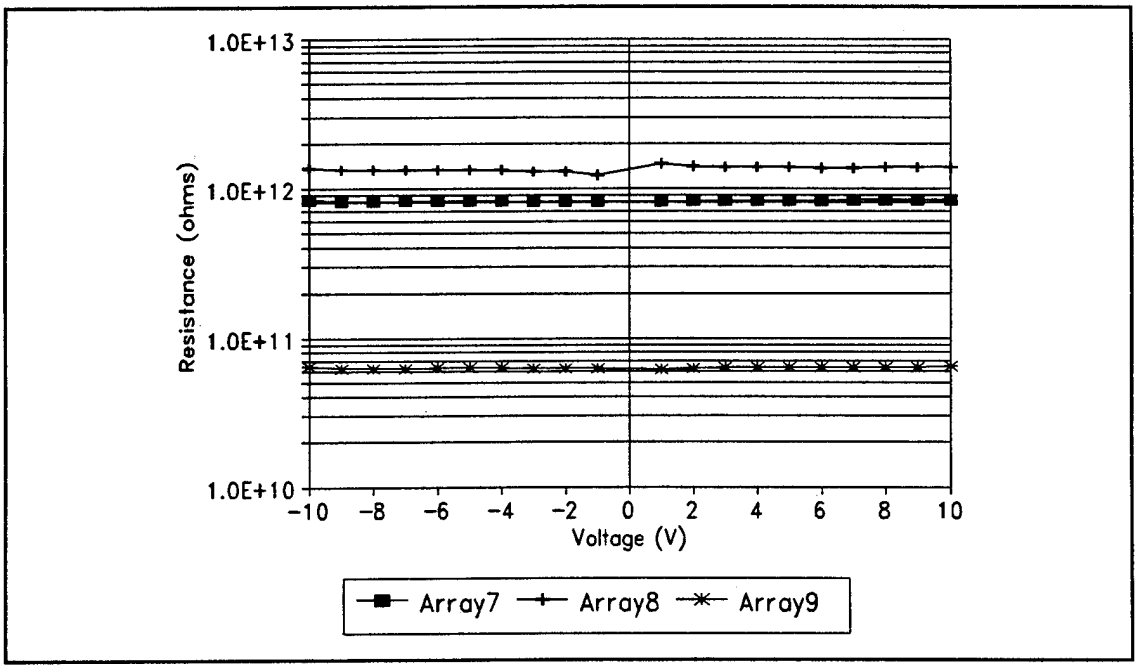


Figure IV-58. Bias Voltage Dependence of the Uncoated Interdigitated Gate Electrode (IGE) Structure's DC Resistance for IGEFET Sensing Elements 7, 8, and 9. Microsensor Maintained at 150° C in a Dry Air Ambient.

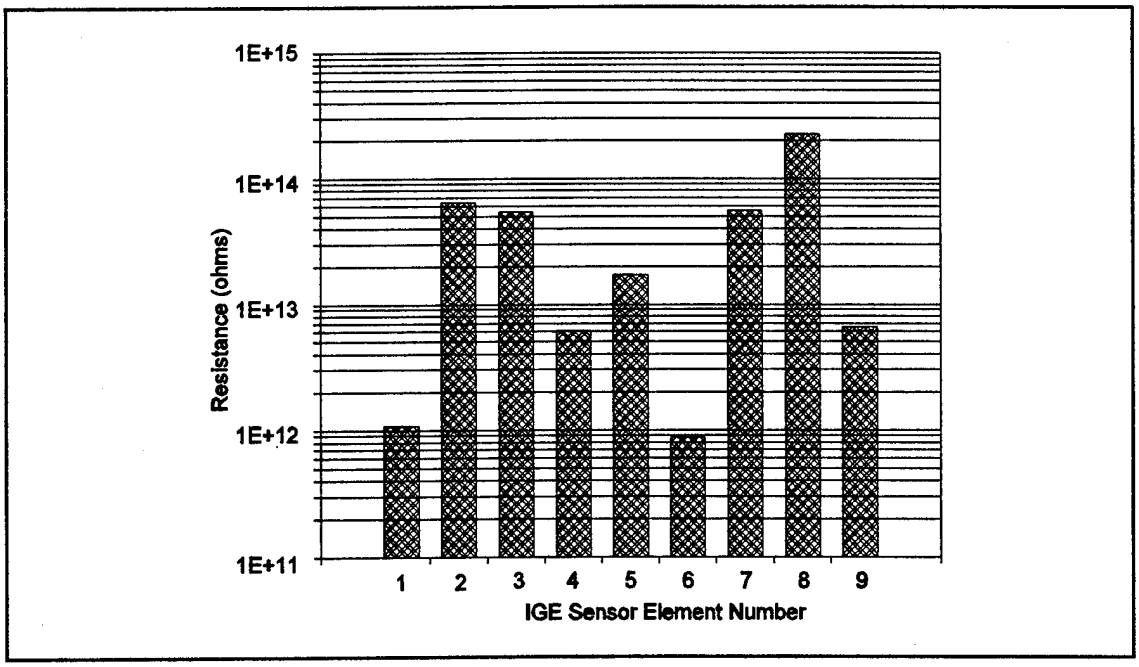


Figure IV-59. Average Interdigitated Gate Electrode (IGE) Structure's DC Resistance for each Microsensor Sensing Element. Average Composed of DC Resistance Measurements From Eight Microsensors Maintained at 30° C in a Dry Air Ambient.

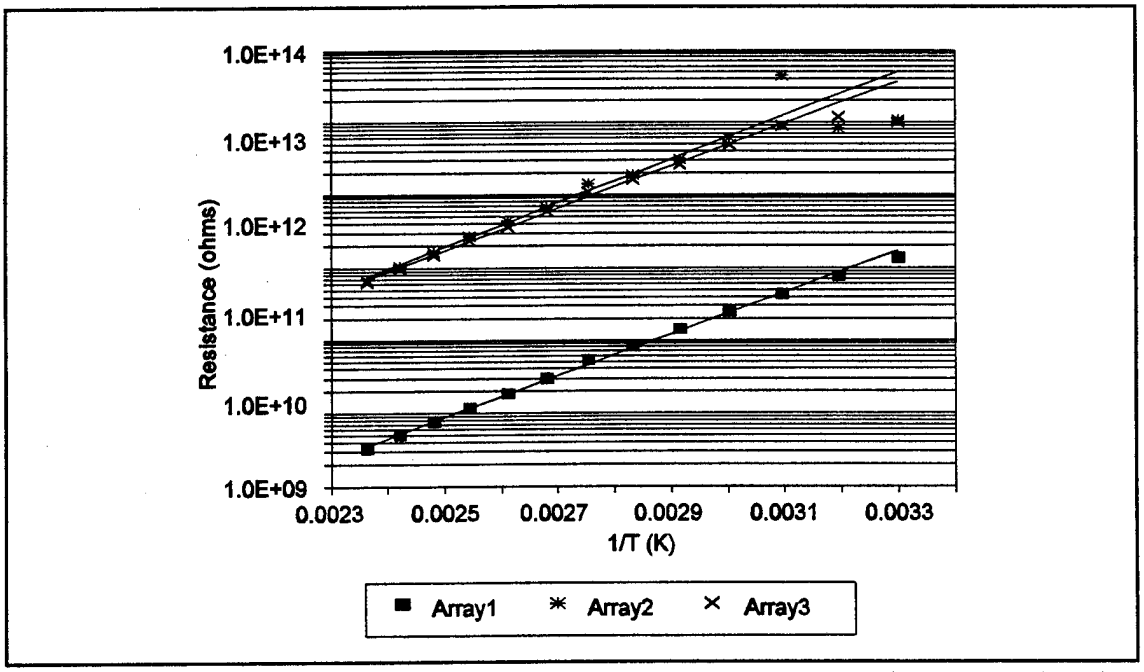


Figure IV-60. Temperature Dependence of the Uncoated Interdigitated Gate Electrode (IGE) Structure's DC Resistance for IGEFET Sensing Elements 7, 8, and 9. Microsensor Maintained in a Dry Air Ambient. Bias Voltage=10 V.

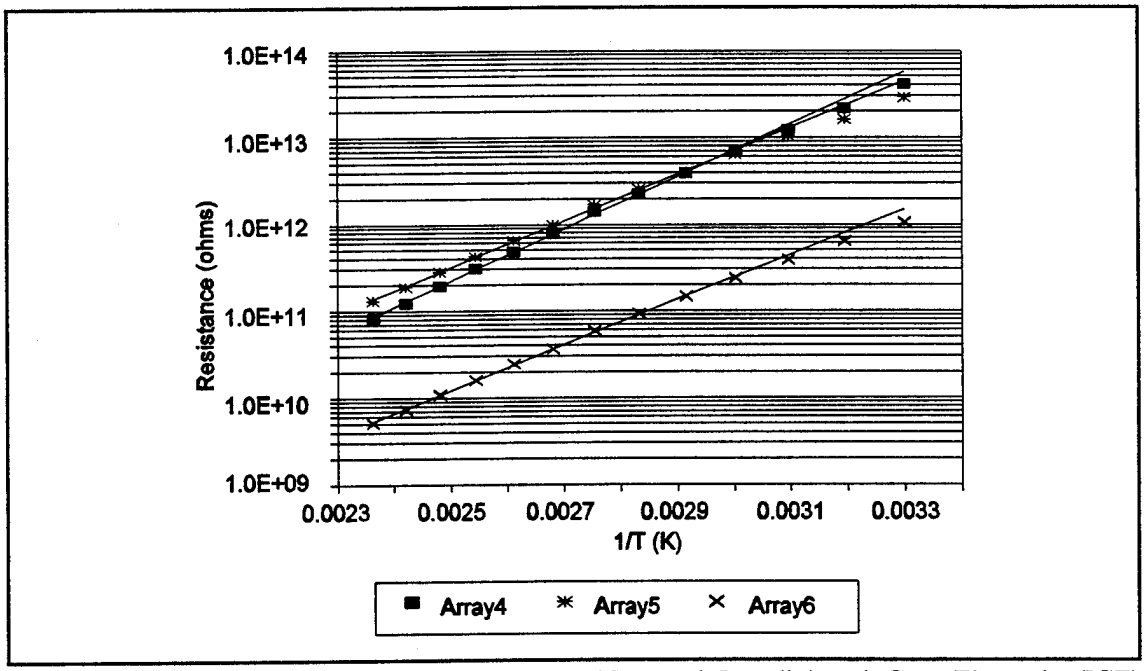


Figure IV-61. Temperature Dependence of the Uncoated Interdigitated Gate Electrode (IGE) Structure's DC Resistance for IGEFET Sensing Elements 4, 5, and 6. Microsensor Maintained in a Dry Air Ambient. Bias Voltage=10 V.

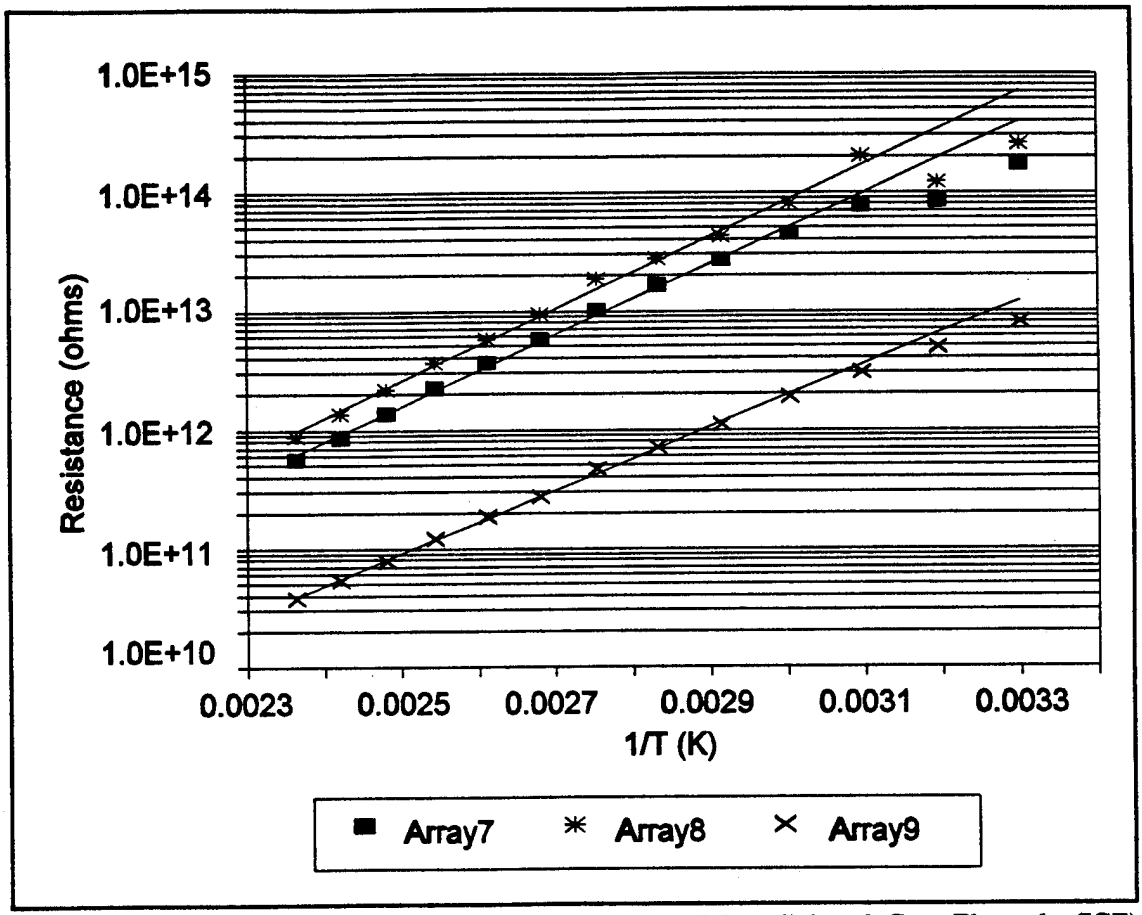


Figure IV-62. Bias Voltage Dependence of the Uncoated Interdigitated Gate Electrode (IGE) Structure's DC Resistance for IGEFET Sensing Elements 7, 8, and 9. Microsensor Maintained in a Dry Air Ambient. Bias Voltage=10 V.

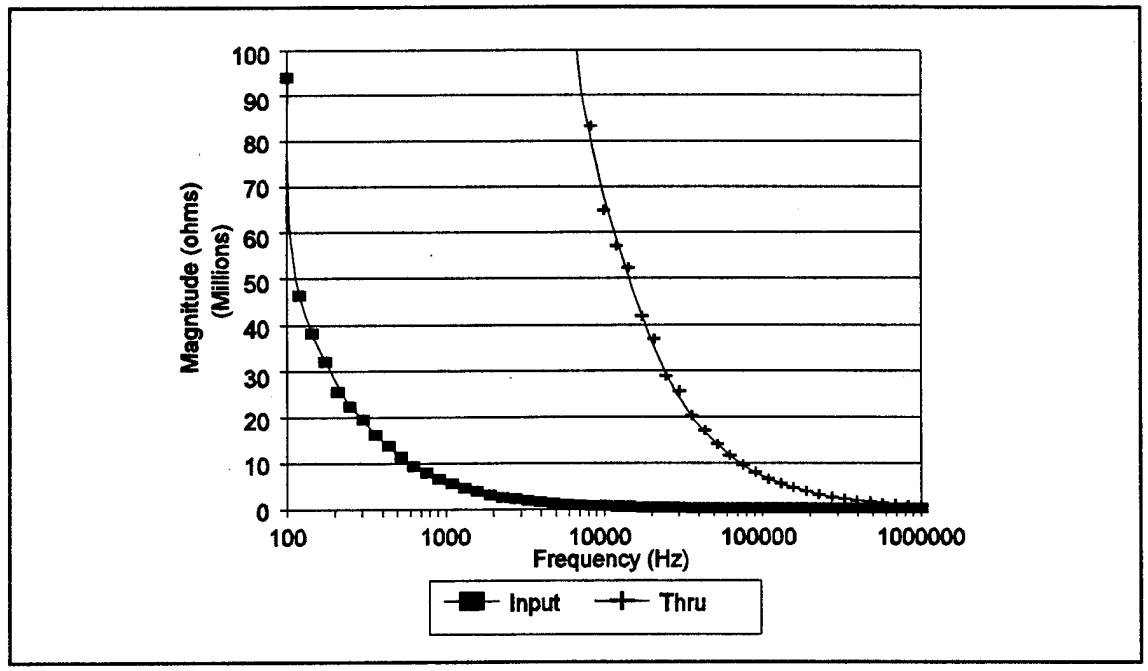


Figure IV-63. Magnitude of the Uncoated Interdigitated Gate Electrode (IGE) Structure's Input and Through Impedance for IGEFET Sensing Element 3. Microsensor Maintained in at 30° C in a Dry Air Ambient.

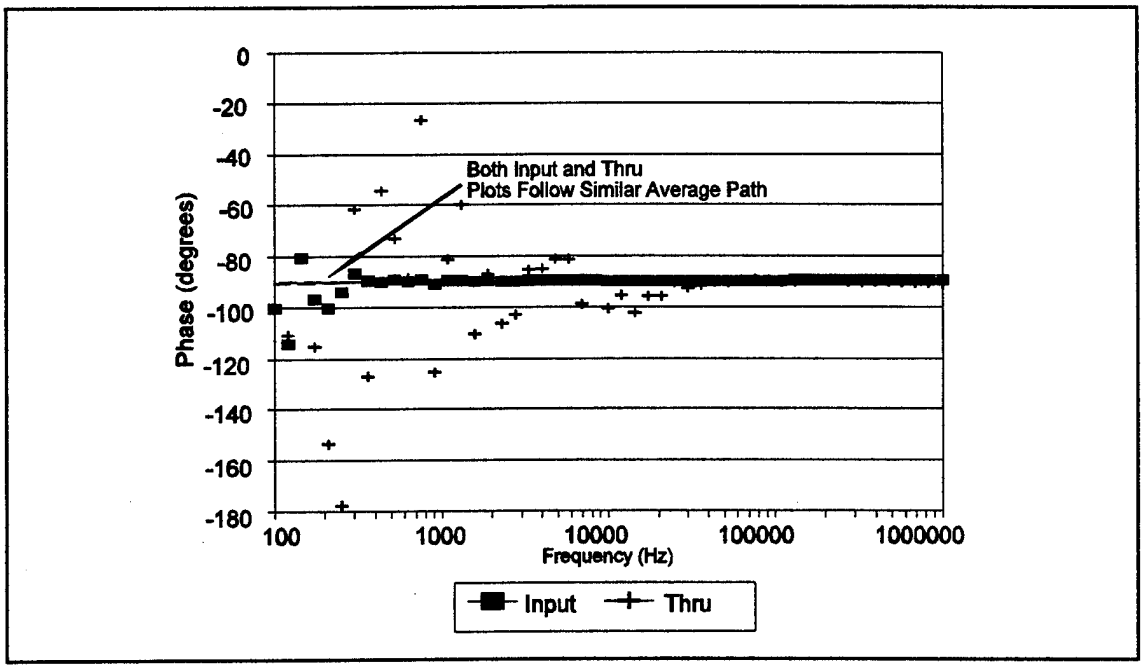


Figure IV-64. Phase of the Uncoated Interdigitated Gate Electrode (IGE) Structure's Input and Through Impedance for IGEFET Sensing Element 3. Microsensor Maintained at 30° C in a Dry Air Ambient.

impedances are primarily capacitive. These figures also illustrate a limitation of the impedance measurements. The largest impedance that can be reliably measured with the HP4194A impedance analyzer is limited to 100 MΩ. Although the input impedance magnitude remains less than 100 MΩ over the measurement bandwidth, the stability of the phase delay measurement is degraded for frequencies less than 400 Hz. In contrast, the magnitude of the through impedance, which has a capacitance that is two orders of magnitude less than the input impedance, exceeds the instrument's measurement capability for frequencies less than 10 KHz.

The input and through capacitances of the nine IGE elements on 8 different microsensors were measured with the impedance analyzer operating in the capacitance measurement mode. The results of these measurements are summarized in Table IV-8. The input capacitances of all nine IGE elements were the same with respect to an acceptable experimental error level. However, the through capacitances displayed the same variability that was observed with the DC resistance measurements. Therefore, except for the fact that the through capacitances were affected by the parasitic impedances stemming from the wire bond layout, the measured capacitances were in excellent agreement with the capacitances predicted by the finite-difference model of the uncoated IGE structure (see Chapter V).

For comparison with the observed temperature dependence of the IGE structure's DC resistance, the temperature dependence of the IGE structure's through and input impedance were measured. The through impedance was measured with the impedance analyzer in the capacitance/dissipation factor mode at three different temperatures: 30° C, 70° C, and 100° C. Unfortunately, instrument limitations restricted the reliable measurement of the through capacitance and dissipation factor, as shown in Figures IV-65 and IV-66, to frequencies greater than 2 KHz and 20 KHz, respectively. Considering this limitation, no significant change in the through capacitance and dissipation factor were observed at the different temperatures. Similar results were obtained with input impedance measurements at these temperatures. Figures IV-67 and IV-68 show the through and input capacitances for each of the nine IGE structures measured at 20 KHz at the three different temperatures.

Transfer Function Gain and Phase Delay of the IGEFET Sensor. Prior to removing the floating gate bond wire, the transfer function gain/phase of the IGEFET amplifier was measured with the gain/phase analyzer. To insure that the unity gain characteristics of the amplifier were unaffected by temperature, the amplifier's gain/phase measurement was performed on a microsensor maintained at 150° C. Figure IV-69 shows the amplifier's gain/phase response of three IGEFET sensor elements. It is apparent from Figure IV-69 that heating the microsensor to 150° C did not degrade the amplifier characteristics with a gain near unity (-0.1 dB) and zero phase delay.

Table IV-8. Uncoated Interdigitated Gate Electrode Structure Capacitances.

	Through Capacitance		Input Capacitance	
	Average	Standard Deviation	Average	Standard Deviation
IGE #	(pF)	(pF)	(pF)	(pF)
1	2.73	.033	22.5	1.21
2	.213	.0046	22.0	0.81
3	.216	.0052	21.8	1.09
4	.220	.0041	21.8	0.75
5	.211	.0036	22.2	0.98
6	3.38	.0090	22.7	1.16
7	.216	.0030	21.4	0.74
8	.214	.0038	21.7	0.80
9	.559	.0077	24.5	0.87

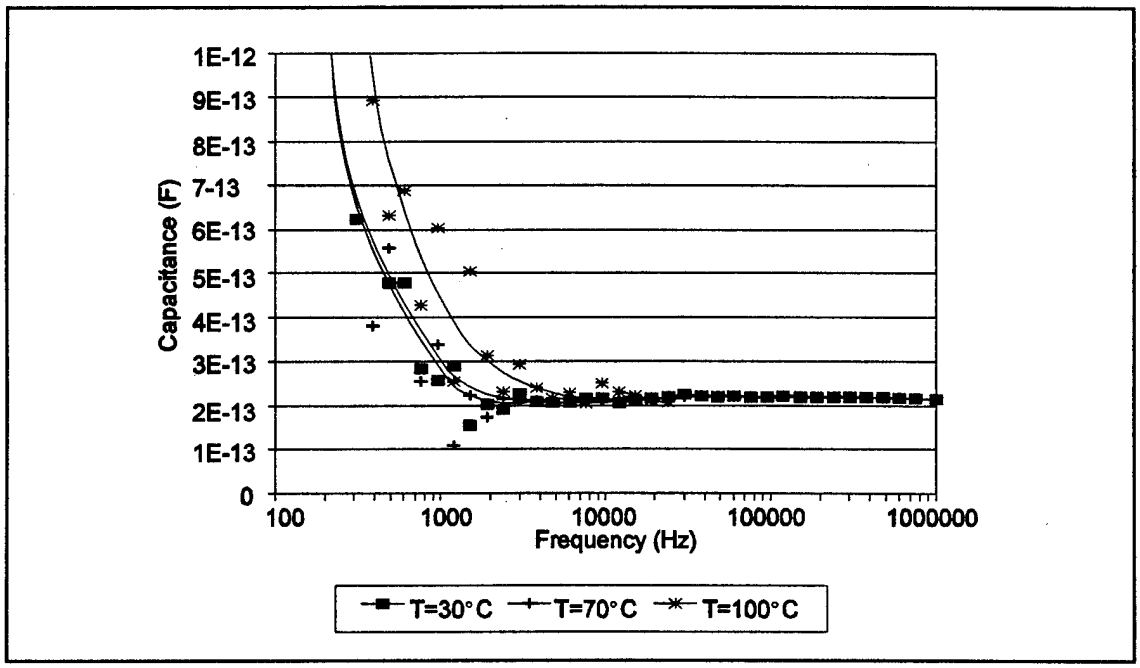


Figure IV-65. Bode Plot of the Uncoated Interdigitated Gate Electrode (IGE) Structure's Through Capacitance for IGEFET Sensing Element 3 at Three Different Temeperatures. Microsensor Maintained in a Dry Air Ambient.

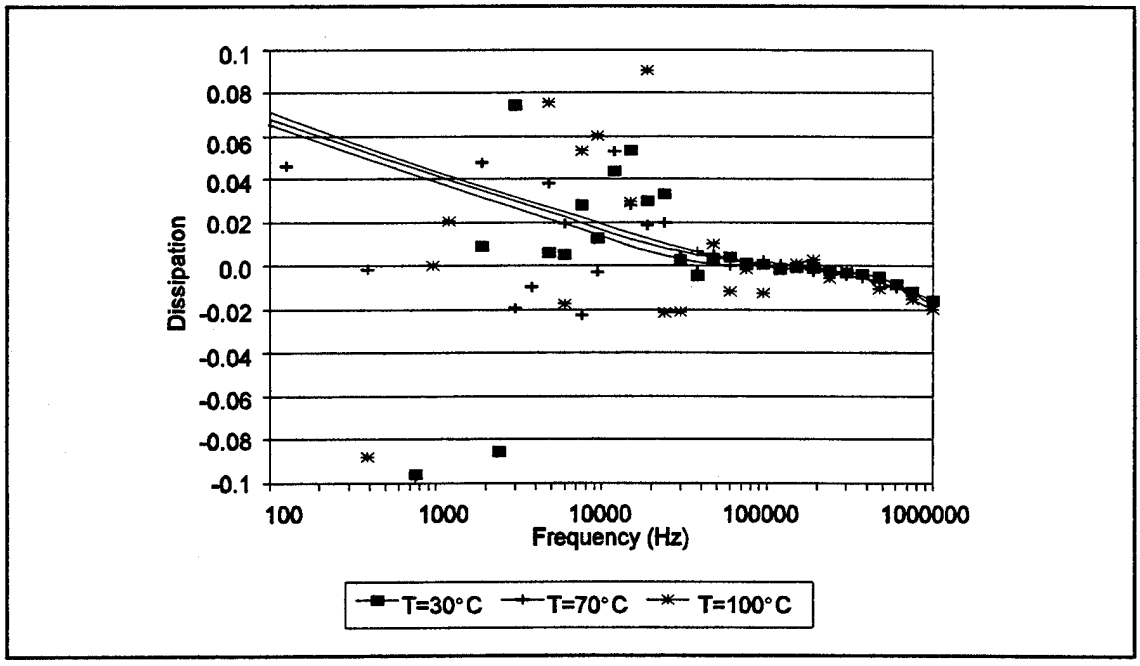


Figure IV-66. Bode Plot of the Uncoated Interdigitated Gate Electrode (IGE) Structure's Through Dissipation for IGEFET Sensing Element 3 at Three Different Temperatures. Microsensor Maintained in a Dry Air Ambient.

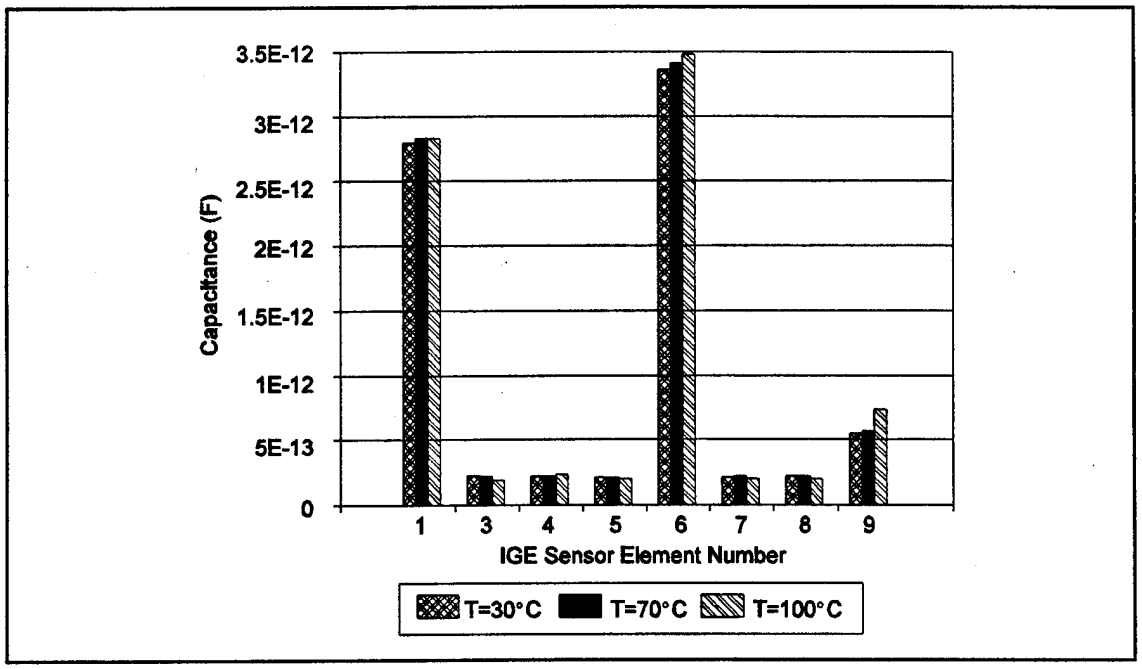


Figure IV-67. Uncoated Interdigitated Gate Electrode (IGE) Structure's Through Capacitance for all Nine IGEFET Sensing Elements at Three Different Temperatures. Microsensor Maintained in a Dry Air Ambient. Measurement Frequency=20 KHz.

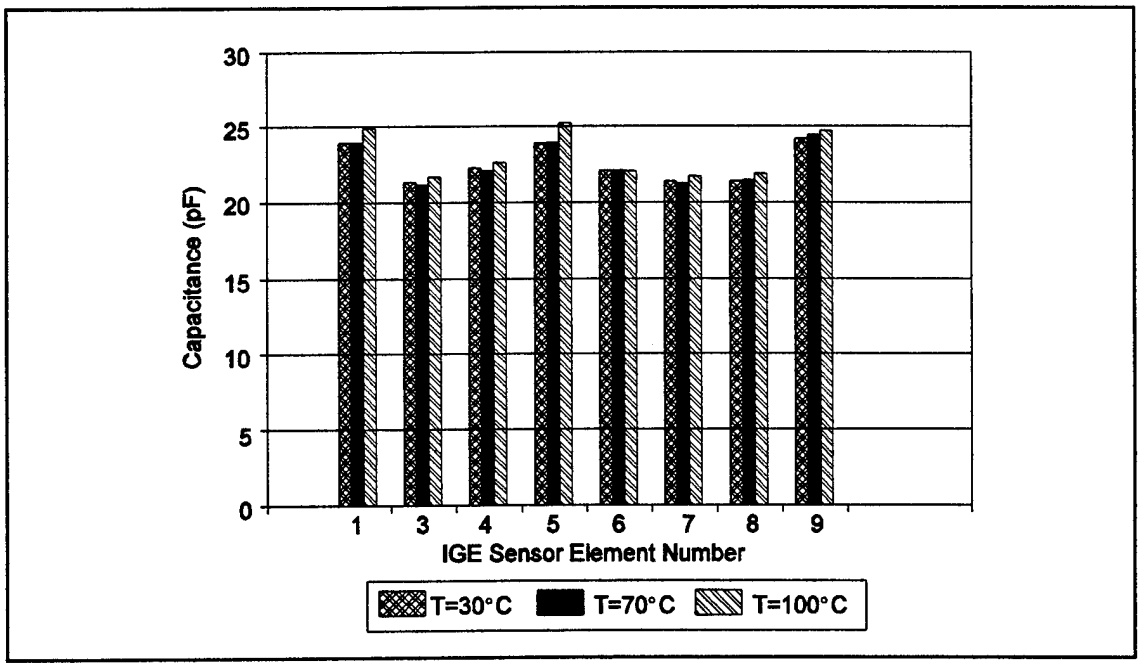


Figure IV-68. Uncoated Interdigitated Gate Electrode (IGE) Structure's Input Capacitance for all Nine IGEFET Sensing Elements at Three Different Temperatures. Microsensor Maintained in a Dry Air Ambient. Measurement Frequency=20 KHz.

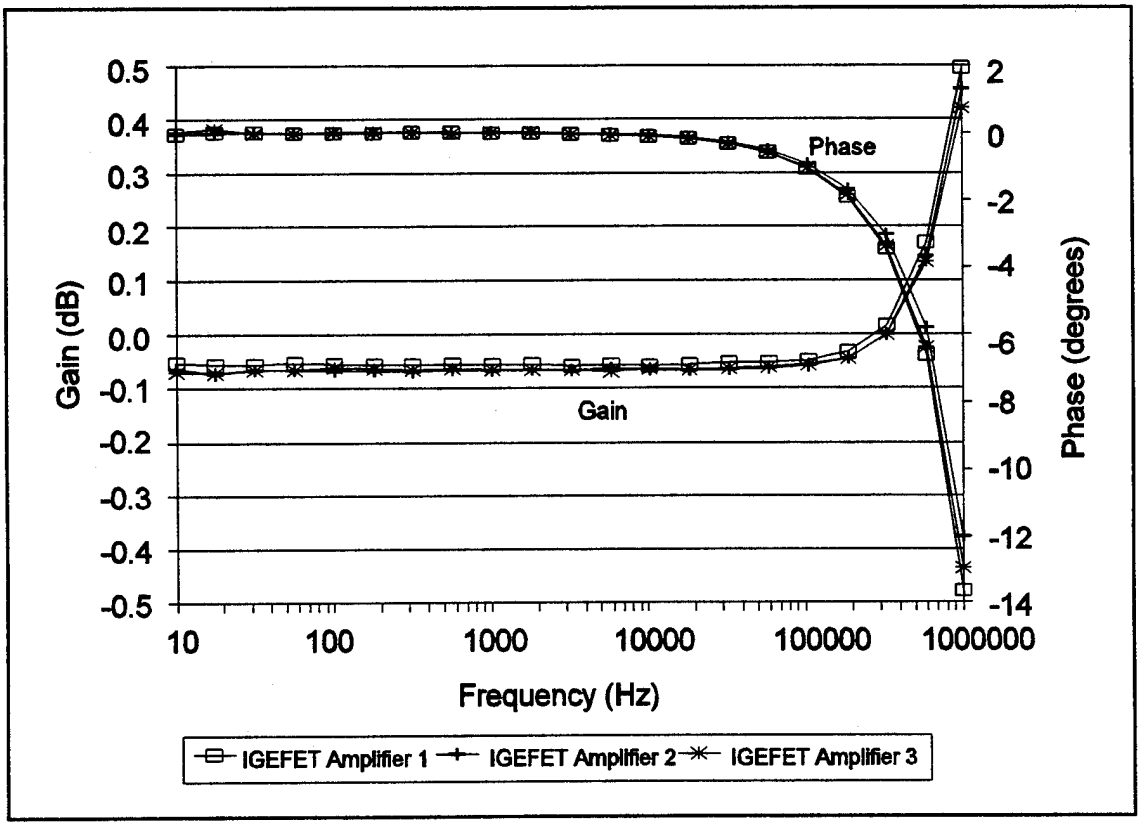


Figure IV-69. Bode Plot of the IGEFET Amplifier's Transfer Function Gain and Phase Delay. Measurement Temperature=150° C. Microsensor Maintained in a Dry Air Ambient.

The uncoated IGEFET sensor transfer function's gain and phase delay was measured after removing the floating gate electrode bond wire. The bond wire was removed to eliminate the capacitive loading effect on the IGE structure caused by the sensor package, test socket, and the coaxial cabling (approximately 1 foot in length) internal to the sample chamber. The parasitic capacitance-to-ground for the packaged device and the sample chamber alone was estimated to be 30 pF, and the external cabling to the instrumentation would likely add significantly more parasitic capacitance (>200 pF). A 0.8 pF parasitic capacitance was measured between adjacent pins on the package after removing the bond wires. The IGEFET sensor's gain measured at 30° C was uniform across the entire measured bandwidth (see Figure IV-70) with a value of -40.8 dB. Since the IGEFET amplifier was configured as a voltage follower, the measured IGEFET sensor's transfer function is equivalent to the IGE structure's transfer function. The IGE structure's transfer function can be considered to be a simple voltage divider between the through impedance and the input impedance (which, as a result of symmetry, is equivalent to the floating gate electrode-to-ground impedance). From the measured input (C_i) and through (C_t) capacitances listed in Table IV-8, and neglecting those affected by parasitic impedances, the transfer function's gain was calculated to be -40.4 dB, using the following equation:

$$\text{Gain (dB)} = 20 \log_{10}\left[\frac{C_i}{C_i + C_t}\right]. \qquad \text{(IV-1)}$$

This value of the transfer function's gain for the uncoated IGE structure is also in excellent agreement with the finite-difference model prediction for the uncoated IGE structure described in the next chapter. The measured phase delay was near 0°, except at high frequencies, where the phase delay rotation effect was introduced due to the amplifier characteristics. The lack of phase delay rotation is also consistent with the transfer function arising from a purely capacitive voltage divider configuration.

Coated Sensor Characterization. A series of measurements similar to those performed on the uncoated sensor were used to characterize the electrical behavior of the MPc-coated IGEFET sensor. For these measurements, MPc films with different thicknesses were vacuum sublimed in the standard manner onto the nine IGEFET elements of each microsensor tested. The film thicknesses and film types deposited onto the nine elements of a particular microsensor depended upon the particular test. The set of measurements performed on the MPc-coated devices included the DC resistance and transfer function gain and phase delay measurements. Although the DC resistance measurements presented below are restricted to the data obtained with CuPc films, similar results were also observed with both the NiPc

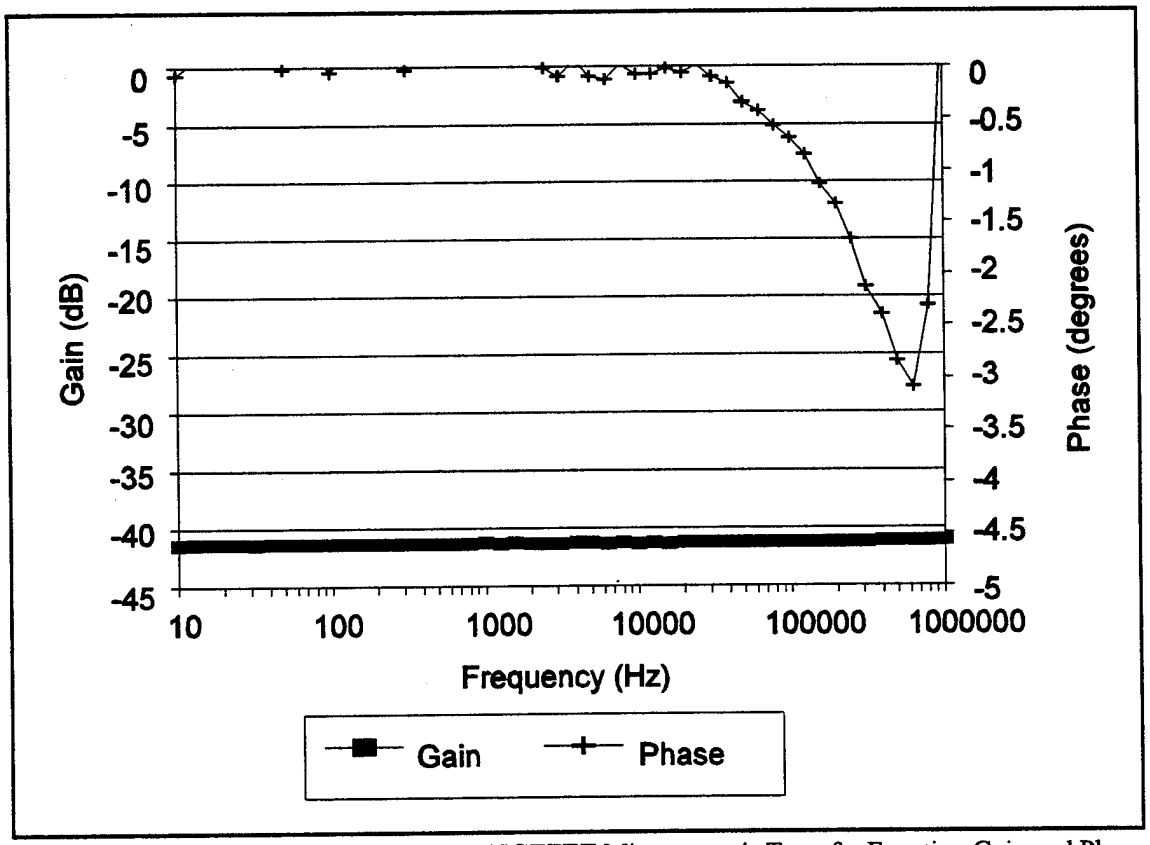


Figure IV-70. Bode Plot of the Uncoated IGEFET Microsensor's Transfer Function Gain and Phase Delay. Measurement Temperature=30° C. Microsensor Maintained in a Nitrogen Ambient.

and CoPc films (see Appendix F). The IGEFET sensor's transfer function measurements are presented for all three film types.

Direct Current Resistance of the MPc-Coated Interdigitated Gate Electrode Structure. The DC resistance of six IGE elements coated with a uniform 3 μm thick CuPc film was measured as a function of bias voltage at three different temperatures in a dry nitrogen ambient. A significant bias voltage dependence was observed in the measured DC resistance that decreased with increasing temperature (see Figures IV-71 through IV-73). Since the DC resistance-voltage dependence was minimized at all temperatures with a bias voltage of 10 V, this bias voltage was selected for all subsequent DC resistance measurements. The data in these figures also revealed that at 30° C, the parasitic leakage conductance, which had significantly reduced the uncoated resistance of IGE elements 1 and 6, was not dominating the resistance of these IGE structure elements that were coated with a 3 μm thick CuPc film. This suggests that the MPc film's conductance at this temperature was much greater than the leakage resistance paths. However, as the temperature was increased, the parasitic leakage paths were manifested by the lower resistance values for IGE elements 1 and 6 when measured with small bias voltages. Thus, the leakage conductance increased more rapidly with an increase in temperature compared to the conductance of the CuPc film.

The temperature dependence of the MPc-coated IGE structure's DC resistance was measured over the temperature range spanning 30-150° C. The microsensor for this test was coated with three CuPc film thicknesses: 2000 Å on elements 1-3, 5000 Å on elements 4-6, and 10000 Å on elements 7-9. The resistance measurements were made with a bias voltage of 10 V, and the microsensor was maintained in a dry air ambient. Arrhenius plots of the DC resistance for the three CuPc film thicknesses are shown in Figures IV-74 through IV-76. The activation energy for the CuPc films determined from these plots was 0.40 ±0.02 eV. Therefore, the DC resistance of the CuPc films decreases more slowly than the resistance of the uncoated sensor, which has a much larger activation energy (see the Uncoated Sensor Characterization section). The activation energies for NiPc and CoPc determined in similar experiments were 0.54±0.03 eV and 0.41±0.02 eV, respectively. Although the activation energy may be different in a nitrogen ambient, the more rapid increase in parasitic leakage conductance with temperature observed in dry air is consistent with the DC resistance measurements described above on the IGE elements coated with the 3 μm thick CuPc films.

Comparison of the data collected in the bias voltage and temperature dependency experiments revealed that the DC resistance of the IGE elements coated with the 3 μm thick CuPc film was greater than the resistance of the IGE elements coated with the thinner CuPc films. This result is a consequence

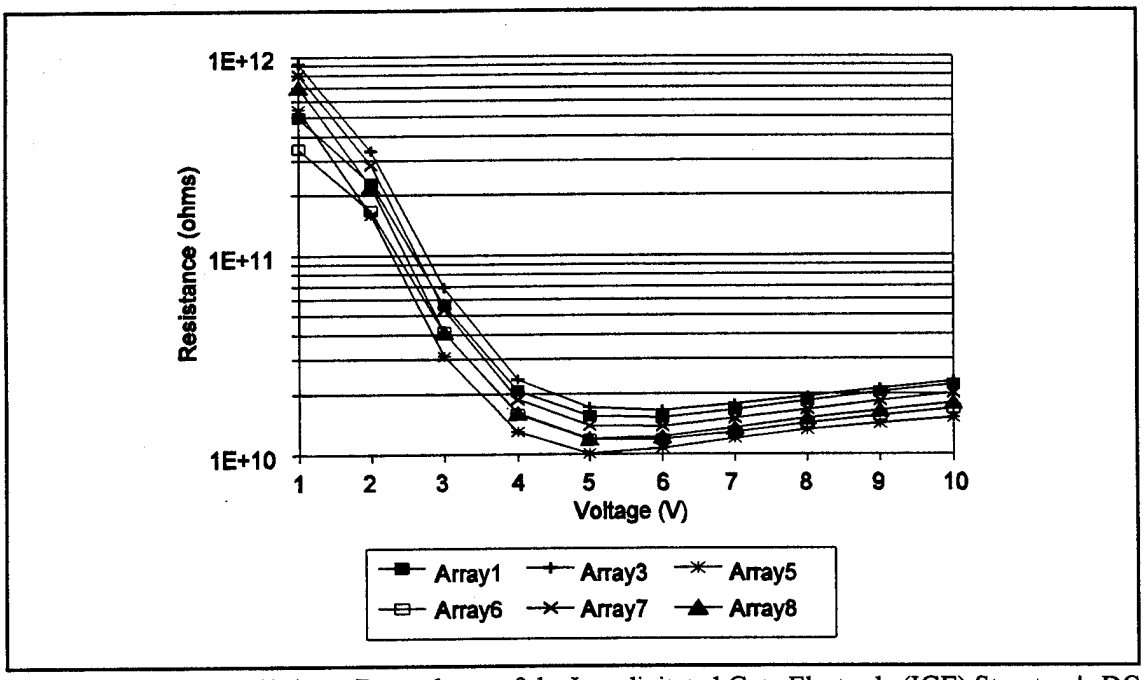


Figure IV-71. Bias Voltage Dependence of the Interdigitated Gate Electrode (IGE) Structure's DC Resistance for Several IGEFET Sensing Elements Coated with a 3 μm Thick Copper Phthalocyanine (CuPc) Film. Microsensor Maintained at 30° C in a Nitrogen Ambient.

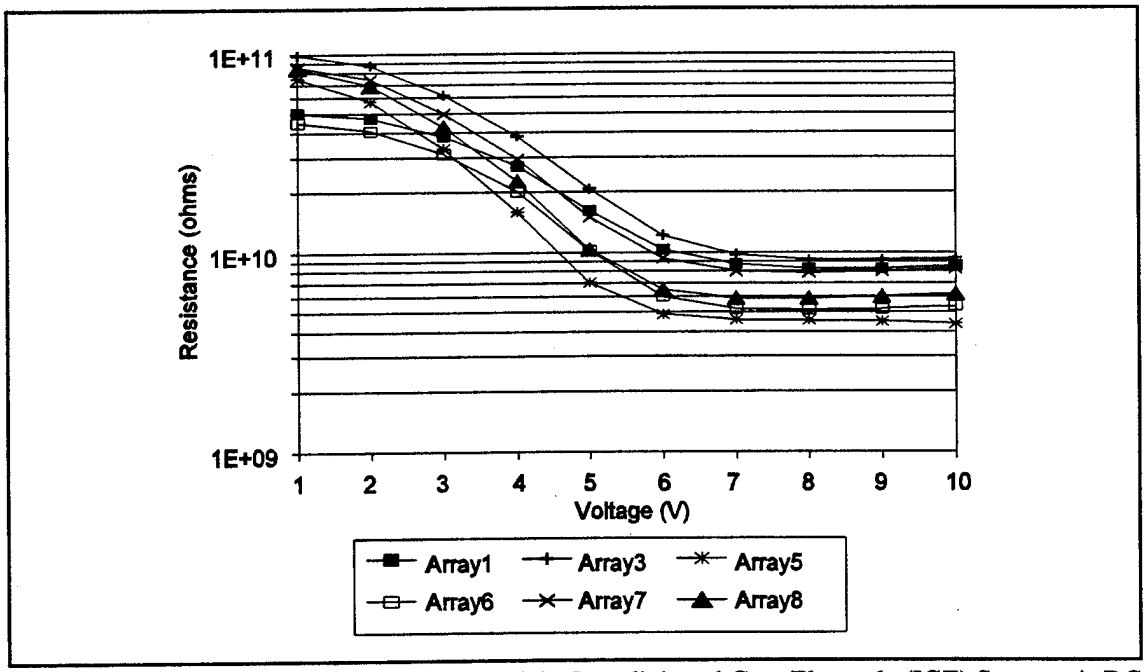


Figure IV-72. Bias Voltage Dependence of the Interdigitated Gate Electrode (IGE) Structure's DC Resistance for Several IGEFET Sensing Elements Coated with a 3 μm Thick Copper Phthalocyanine (CuPc) Film. Microsensor Maintained at 70° C in a Nitrogen Ambient.

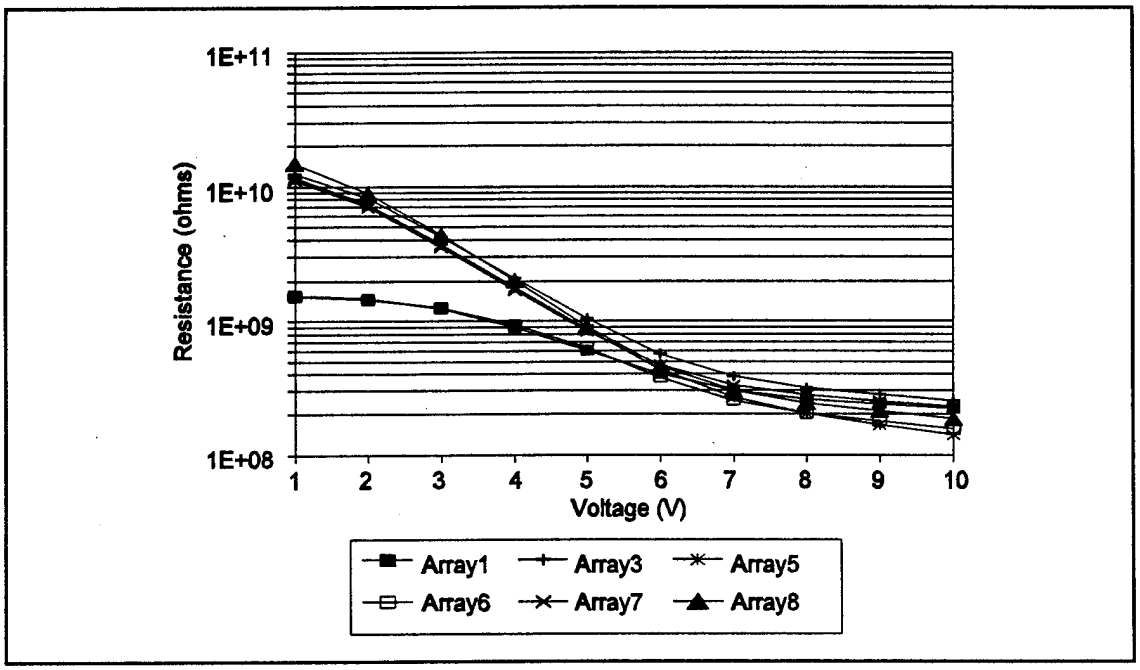


Figure IV-73. Bias Voltage Dependence of the Interdigitated Gate Electrode (IGE) Structure's DC Resistance for Several IGEFET Sensing Elements Coated with a 3 μm Thick Copper Phthalocyanine (CuPc) Film. Microsensor Maintained at 100° C in a Nitrogen Ambient.

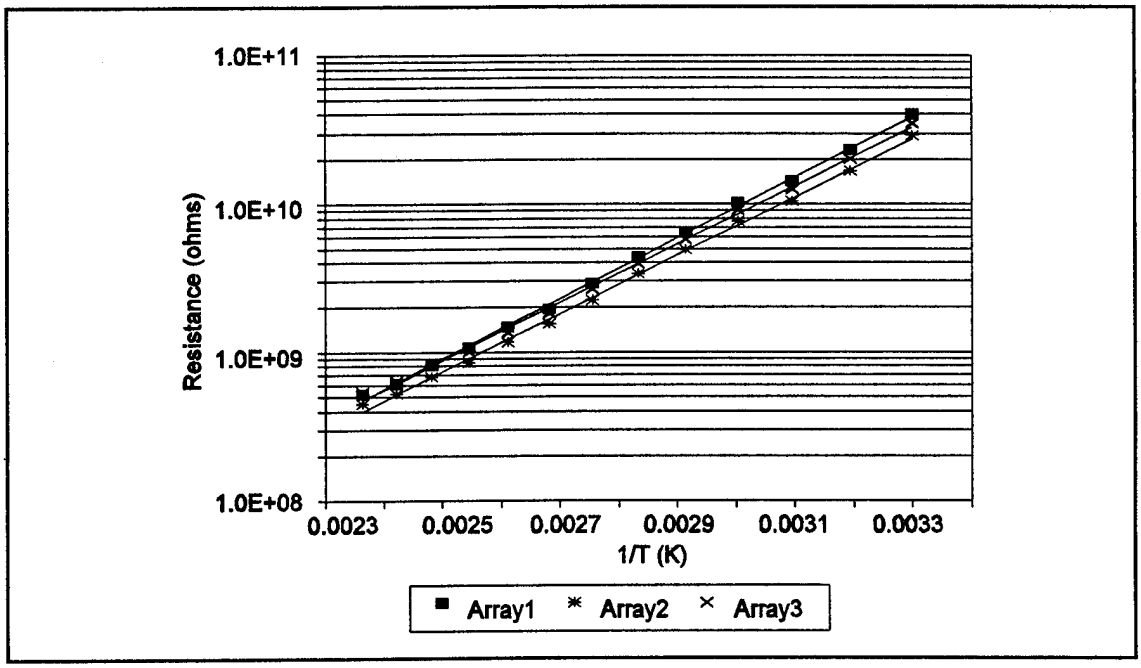


Figure IV-74. Temperature Dependence of the Interdigitated Gate Electrode (IGE) Structure's DC Resistance for IGEFET Sensing Elements Coated with a 0.2 μm Thick Copper Phthalocyanine (CuPc) Film. Microsensor Maintained in a Dry Air Ambient. Bias Voltage=10 V.

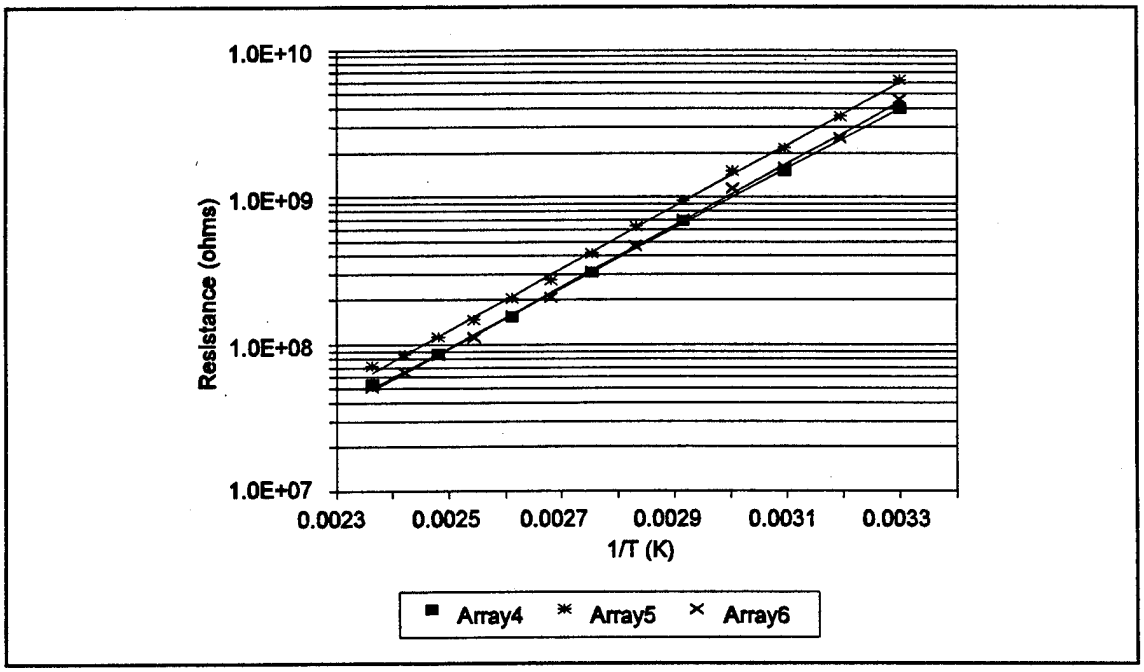


Figure IV-75. Temperature Dependence of the Interdigitated Gate Electrode (IGE) Structure's DC Resistance for IGEFET Sensing Elements Coated with a 0.5 μm Thick Copper Phthalocyanine (CuPc) Film. Microsensor Maintained in a Dry Air Ambient. Bias Voltage=10 V.

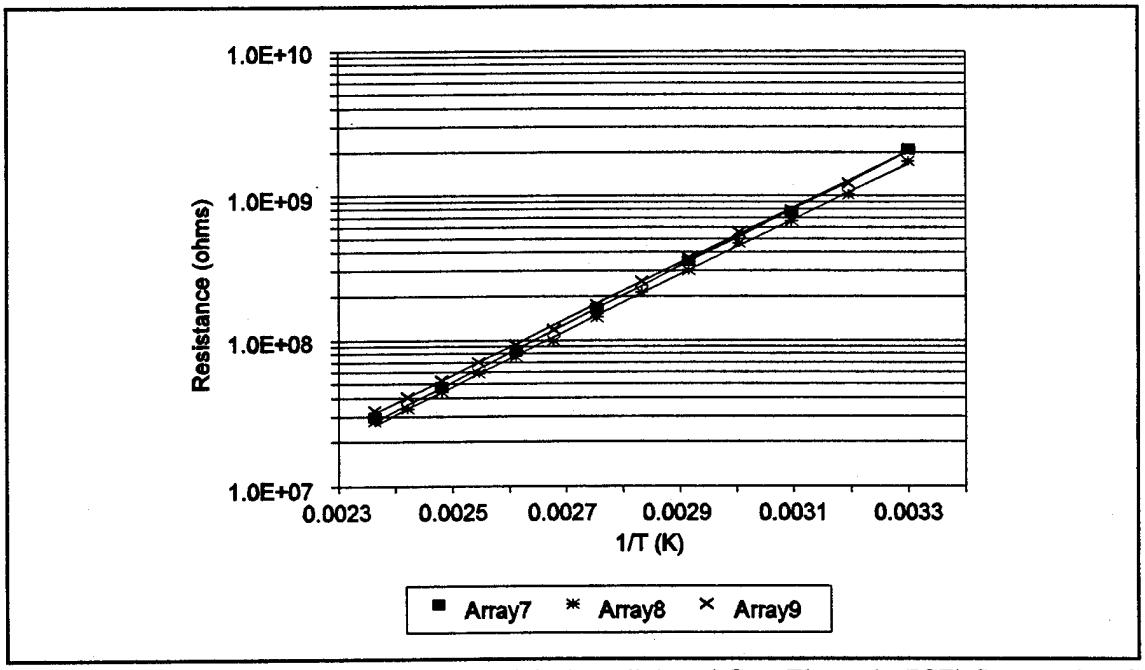


Figure IV-76. Temperature Dependence of the Interdigitated Gate Electrode (IGE) Structure's DC Resistance for IGEFET Sensing Elements Coated with a 1.0 μm Thick Copper Phthalocyanine (CuPc) Film. Microsensor Maintained in a Nitrogen Ambient. Bias Voltage=10 V.

of the different ambient environments in which the resistance measurements were conducted. The temperature dependent measurements were performed with the microsensor maintained in a dry air ambient and, therefore, the DC resistance of the MPc films were significantly reduced from interaction with oxygen (see Chapter II). Figure IV-77 plots the average DC resistance of the IGE strucutres coated with different film thicknesses measured at 30° C in the dry air ambient. As expected, the IGE structure's DC resistance decreased with increasing film thickness.

Additional bias voltage dependent measurements of the MPc-coated IGE structure's DC resistance were accomplished with the microsensor possessing the three film thicknesses maintained at 150° C in a dry air ambient. In the analysis of these experimental results, the measured DC resistance was converted to a current. Semi-logarithmic plots of the IGE structure's current as a function of the square root of the applied bias voltage (Figures IV-78 through IV-80) were observed to be linear for voltage values exceeding two volts, indicating a Schottky or Frenkel-Poole conduction mechanism (95). Given the symmetrical nature of the IGE structure, no rectification of the IGE current was detected when measured with bias voltage values spanning -10 to 10 V (Figures IV-81 through IV-83). At bias voltage values less than 2 V, Figures IV-78 through IV-80 reveal an increase in the current variation between the IGE elements with the same film thickness. This increased variation may again be attributed to the larger contribution of the leakage conduction current relative to the total measured current. The current in the IGE structure element 1 was consistently greater than the current in the other IGE structure elements possessing the same film thickness.

Transfer Function Gain and Phase Delay of the MPc-Coated IGEFET Sensor. The increased coupling between the interdigitated electrodes as the temperature was increased was also observed in the MPc-coated IGEFET sensor's transfer function. Figures IV-84 through IV-89 display the transfer function gain and phase delay Bode plots of an IGEFET microsensor coated with CuPc, NiPc, and CoPc films approximately 4000 Å thick. The CuPc, NiPc, and CoPc films were deposited on the IGEFET microsensor elements 1-3, 4-6, and 7-9, respectively. The response collected from the three sensors in each set were nearly identical and, therefore, only the data from the first element in each set is presented (the data from the other two sensors in each set is included in Appendix F). Although the deposited films increased the IGEFET sensor's gain at low frequencies, the high frequency gain was nearly the same as the uncoated sensor. This behavior suggests that the IGE structure's input and through capacitances are not significantly affected by the deposited films. The increase in the IGEFET sensor's gain at low frequencies stems from the increase in the inter-electrode coupling caused by the additional conductance through the MPc films. As the microsensor's temperature was raised, the film's

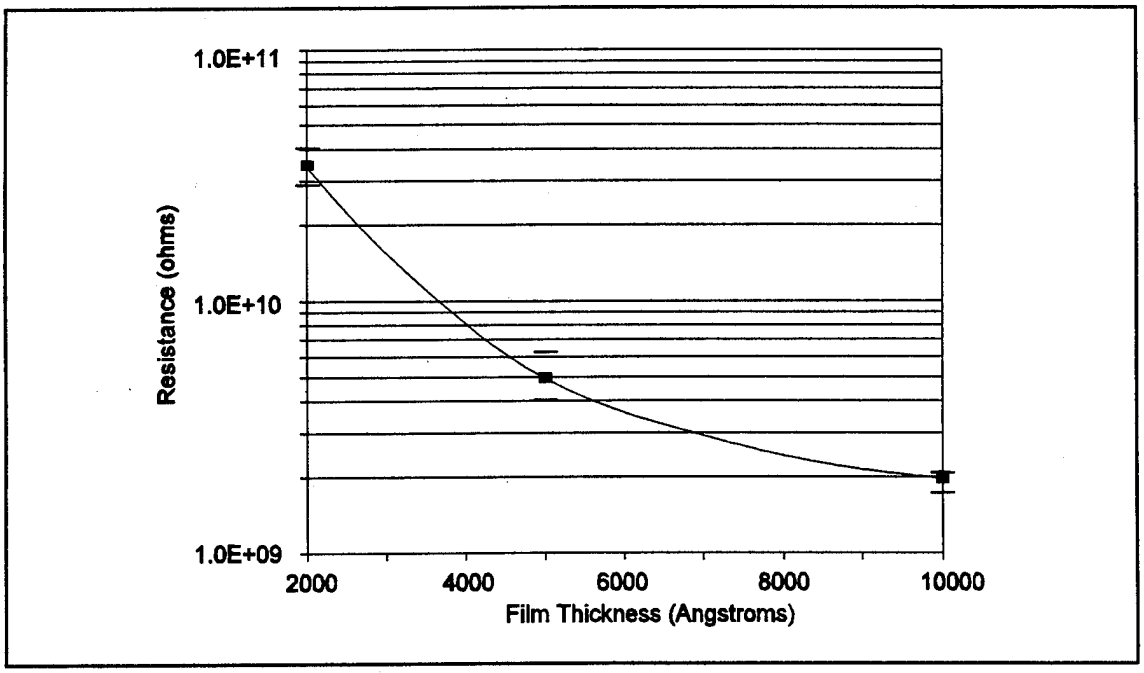


Figure IV-77. Average Interdigitated Gate Electrode (IGE) Structure's DC Resistance for IGEFET Sensing Elements Coated with Copper Phthalocyanine (CuPc) Films with Different Thicknesses. Microsensor Maintained at 30° C in a Dry Air Ambient. The Horizontal Bars Represent the Maximum and Minimum Resistance of Three IGEFET Sensors Possessing the Same CuPc Film Thickness.

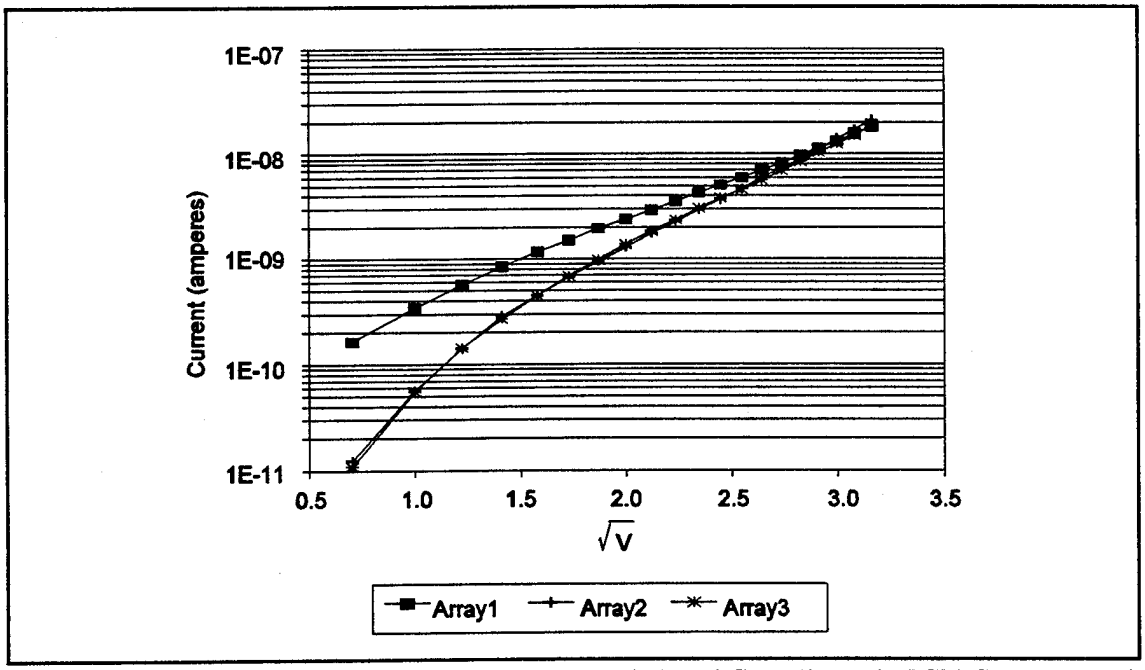


Figure IV-78. Bias Voltage Dependence of the Interdigitated Gate Electrode (IGE) Structure's DC Current for IGEFET Sensing Elements Coated with a 0.2 μm Thick Copper Phthalocyanine (CuPc) Film. Microsensor Maintained at 150° C in a Dry Air Ambient.

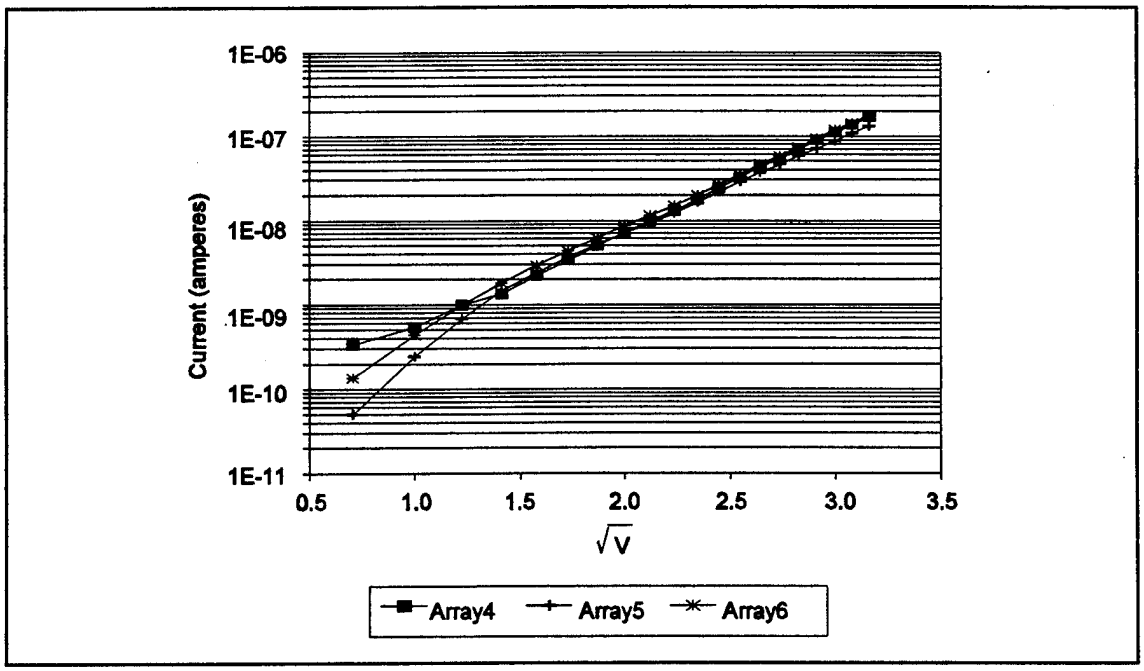


Figure IV-79. Bias Voltage Dependence of the Interdigitated Gate Electrode (IGE) Structure's DC Current for IGEFET Sensing Elements Coated with a 0.5 μm Thick Copper Phthalocyanine (CuPc) Film. Microsensor Maintained at 150° C in a Dry Air Ambient.

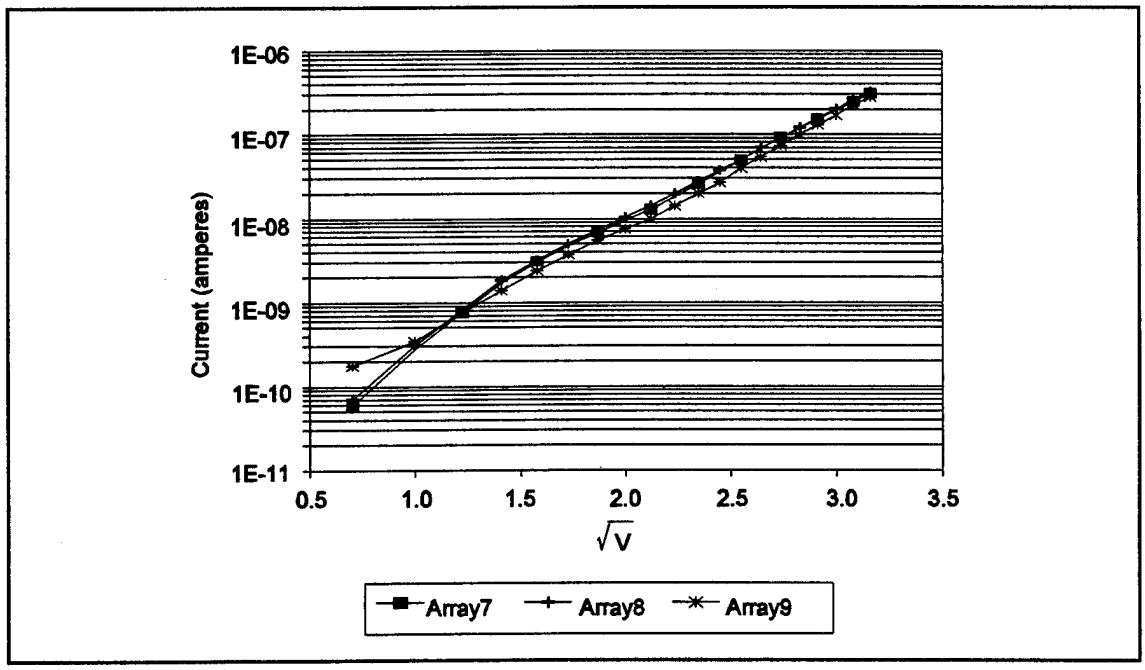


Figure IV-80. Bias Voltage Dependence of the Interdigitated Gate Electrode (IGE) DC Current For IGEFET Sensing Elements Coated with a 1.0 μm Thick Copper Phthalocyanine (CuPc) Film. Microsensor Maintained at 150° C in a Dry Air Ambient.

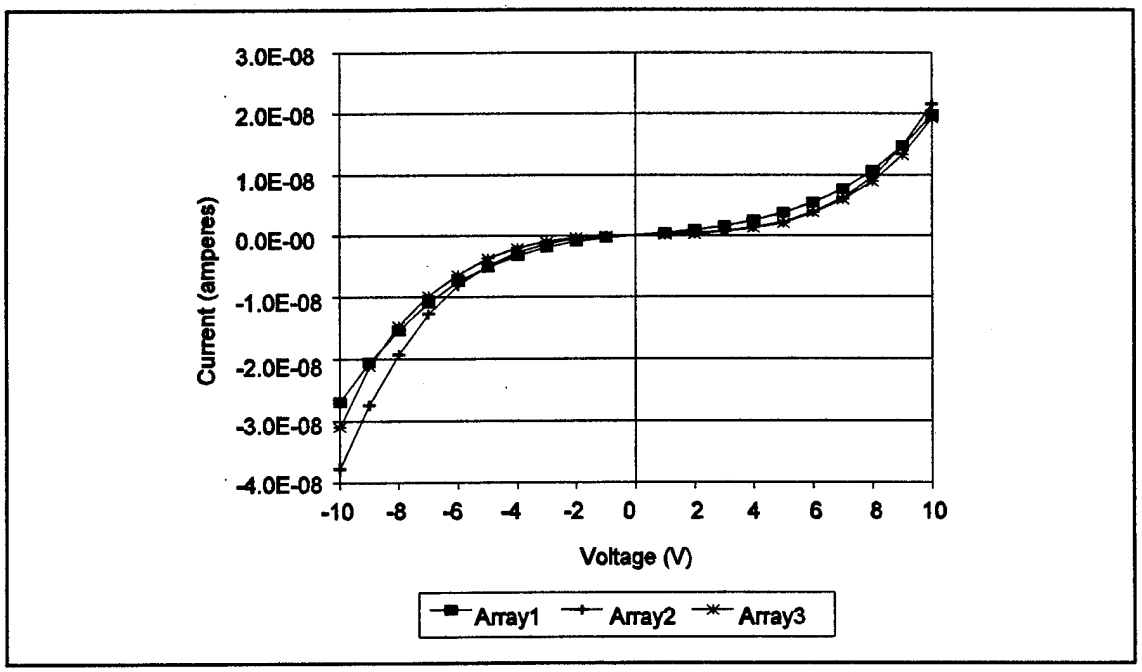


Figure IV-81. Extended Range Bias Voltage Dependence of the Interdigitated Gate Electrode (IGE) Structure's DC Current for the IGEFET Sensing Elements Coated with a 0.2 μm Thick Copper Phthalocyanine (CuPc) Film. Microsensor Maintained at 150° C in a Dry Air Ambient.

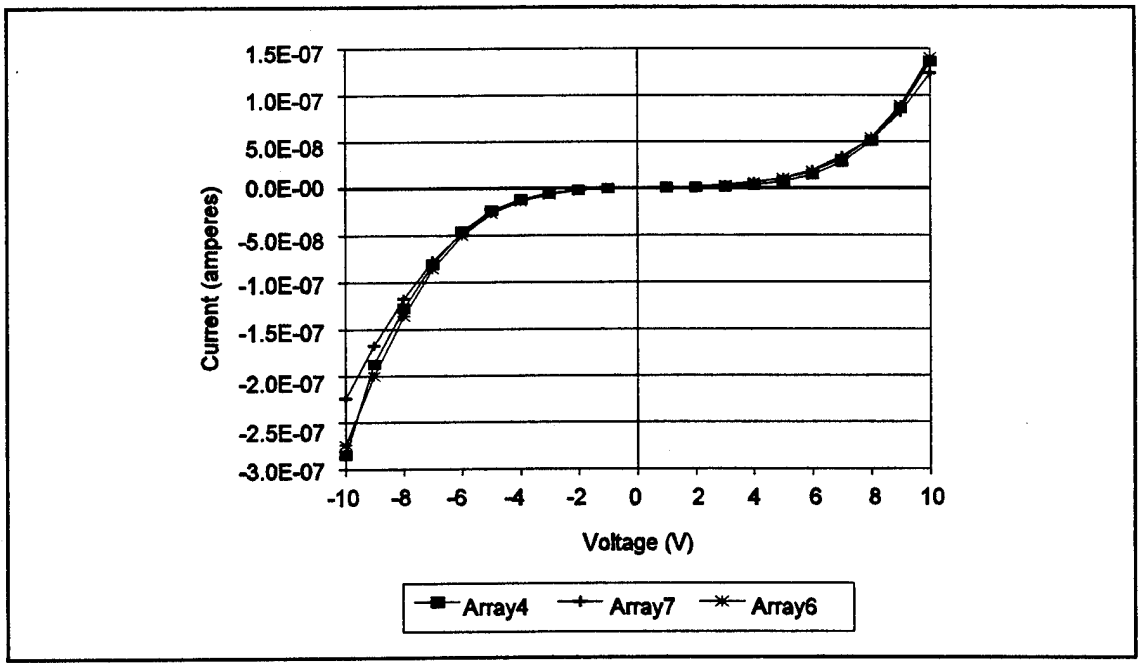


Figure IV-82. Extended Range Bias Voltage Dependence of the Interdigitated Gate Electrode (IGE) Structure's DC Current for the IGEFET Sensing Elements Coated with a 0.5 μm Thick Copper Phthalocyanine (CuPc) Film. Microsensor Maintained at 150° C in a Dry Air Ambient.

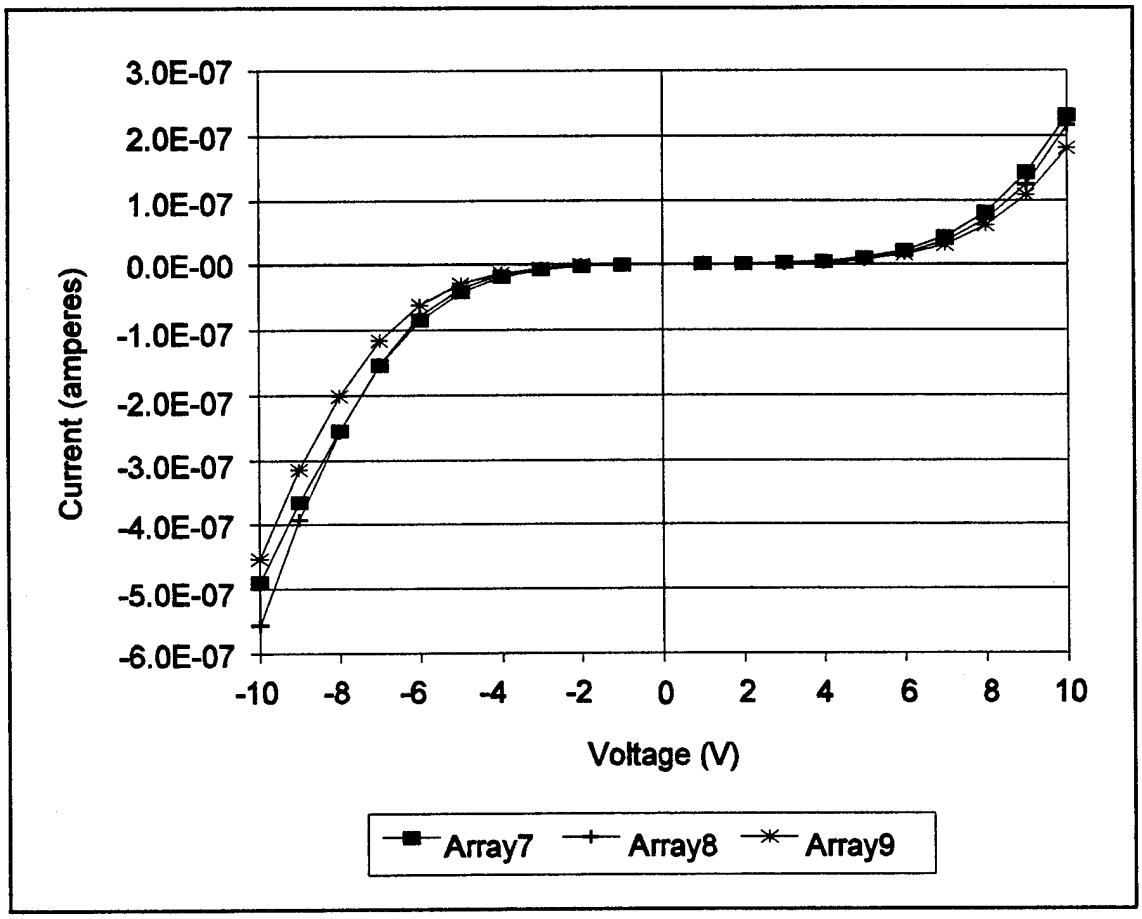


Figure IV-83. Extended Range Bias Voltage Dependence of the Interdigitated Gate Electrode (IGE) Structure's DC Current for the IGEFET Sensing Elements Coated with a 1.0 μm Thick Copper Phthalocyanine (CuPc) Film. Microsensor Maintained at 150° C in a Dry Air Ambient.

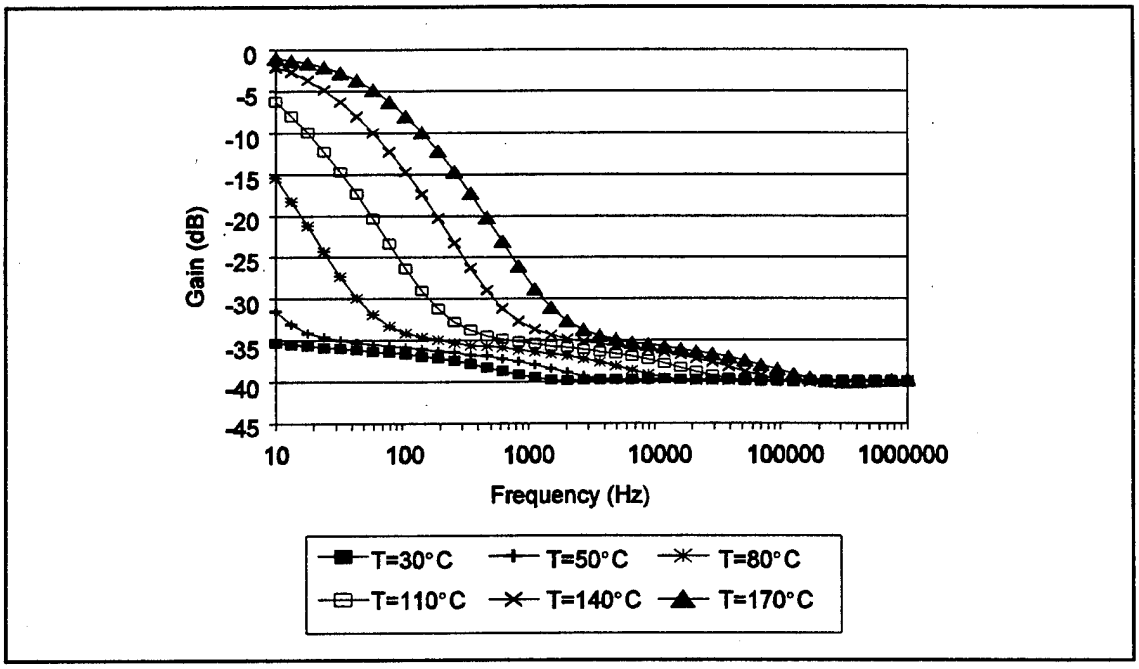


Figure IV-84. Bode Plots of the Sensor Transfer Function's Gain for an IGEFET Coated with a 3200 Å Thick Copper Phthalocyanine (CuPc) Film at Several Different Temperatures. Microsensor Maintained in a Dry Air Ambient.

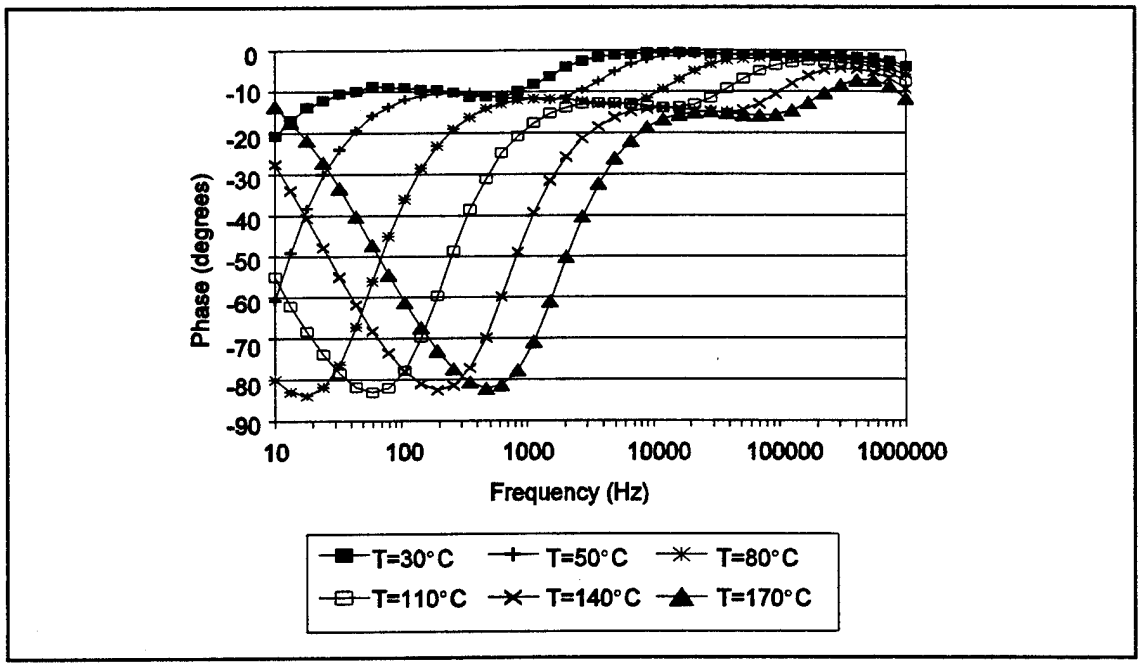


Figure IV-85. Bode Plot of the Sensor's Transfer Function Phase for an IGEFET Coated with a 3200 Å Thick Copper Phthalocyanine (CuPc) Film at Several Different Temperatures. Microsensor Maintained in a Dry Air Ambient.

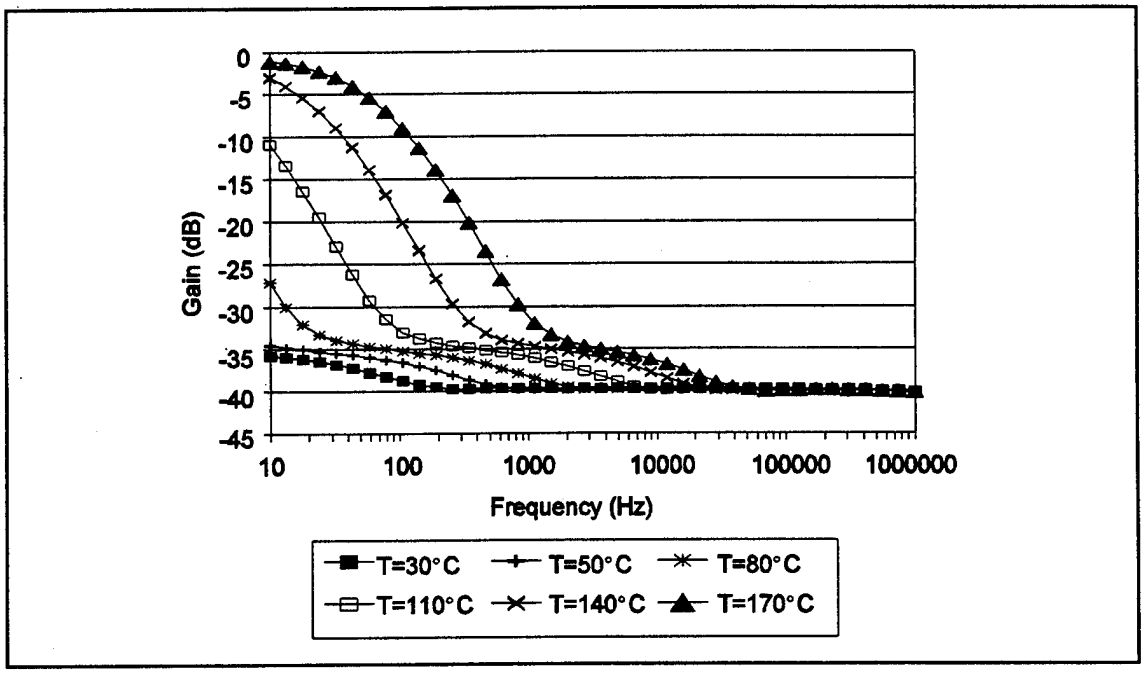


Figure IV-86. Bode Plots of the Sensor's Transfer Function Gain for an IGEFET Coated with a 4300 Å Thick Nickel Phthalocyanine (NiPc) Film at Several Different Temperatures. Microsensor Maintained in a Dry Air Ambient.

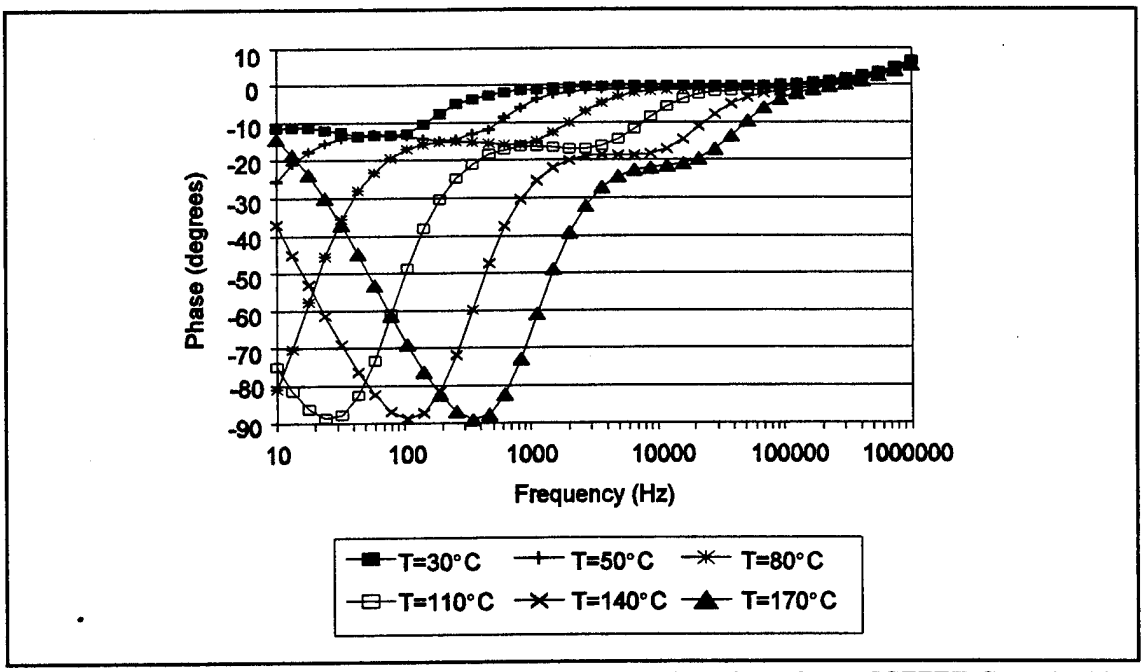


Figure IV-87. Bode Plot of the Sensor's Transfer Function Phase for an IGEFET Coated with a 4300 Å Thick Nickel Phthalocyanine (NiPc) Film at Several Different Temperatures. Microsensor Maintained in a Dry Air Ambient.

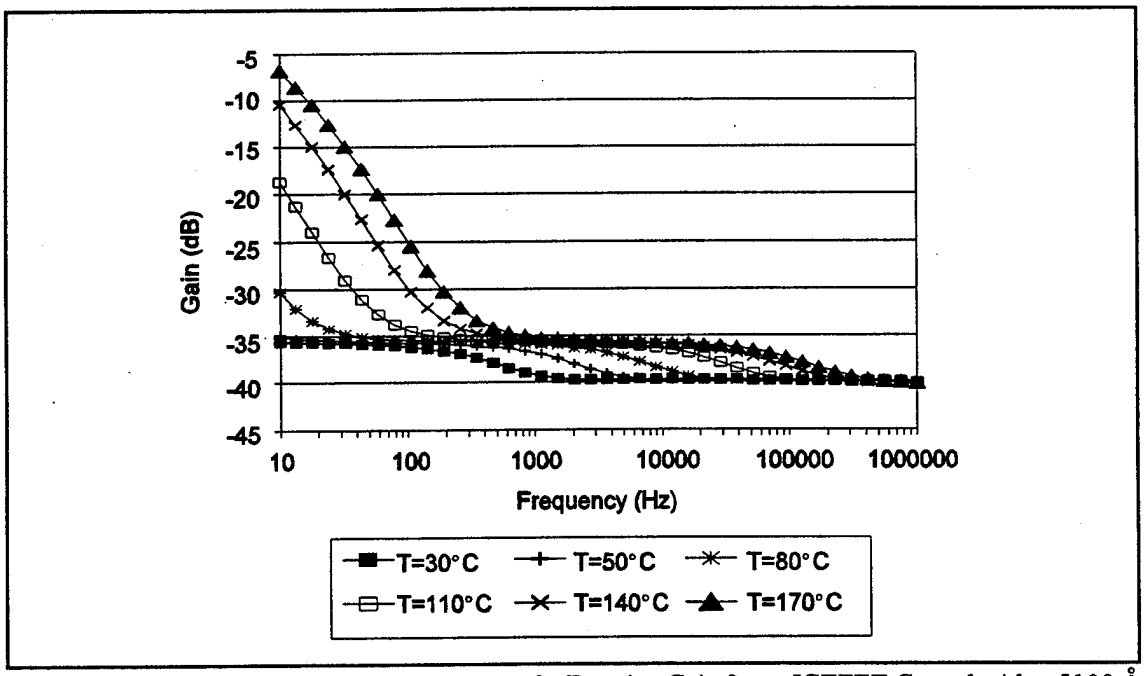


Figure IV-88. Bode Plot of the Sensor's Transfer Function Gain for an IGEFET Coated with a 5100 Å Thick Cobalt Phthalocyanine (CoPc) Film at Several Different Temperatures. Microsensor Maintained in a Dry Air Ambient.

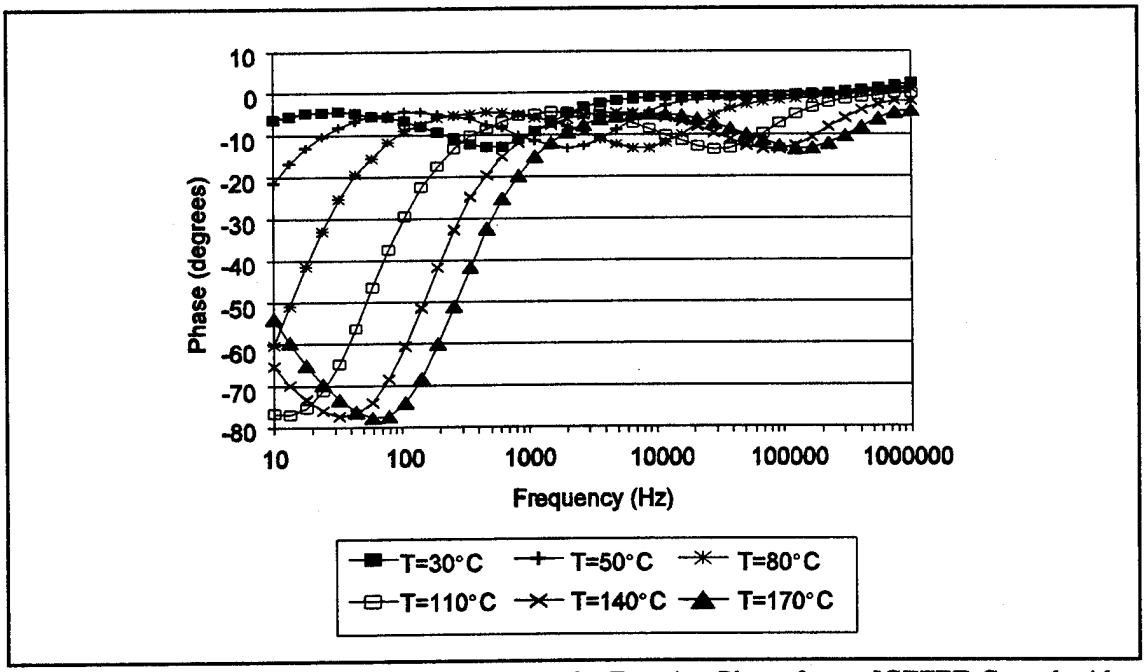


Figure IV-89. Bode Plot of the Sensor's Transfer Function Phase for an IGEFET Coated with a 5100 Å Thick Cobalt Phthalocyanine (CoPc) Film at Several Different Temperatures. Microsensor Maintained in a Dry Air Ambient.

conductance increased and, therefore, an increase in the sensor's gain was observed. At low frequencies and sufficiently high temperature, the driven- and floating-gate electrodes become "effectively" short circuited through the increased film conductance, and the sensor's gain approaches unity, while the phase delay approaches zero.

Although at 30° C, only a single minima in the IGEFET phase delay was observed, when the temperature was increased, a second low frequency minima was exposed. The two minima indicate the presence of two relaxation processes. For the CuPc-coated IGEFET, the minima revealed at the higher temperatures was located at a frequency 2.3 orders of magnitude lower than the high frequency minima. The frequency separation of the two minima remained constant in log space as the temperature was increased. While the magnitude of the low frequency minima also remained independent of temperature, the depth of the high frequency minima increased. In the Bode plot of the NiPc-coated IGEFET phase delay (Figure IV-87), which displays the smallest frequency separation between the two minima (2.0 orders of magnitude), the high frequency minima becomes a shoulder on the low frequency minima when the temperature was increased to 170° C. This change in the high frequency minima was accompanied by the largest increase in the phase delay (8.3° relative to the minima measured at 30° C). In contrast, in the Bode plot of the CoPc-coated IGEFET (Figure IV-89), which displays the largest separation between the two minima (3.4 orders of magnitude), the depth of the high frequency phase delay did not significantly change with temperature.

The difference in the temperature dependence of the two relaxation processes observed in the MPc-coated IGEFET transfer function are also reflected in the Nyquist plots of the gain/phase data (Figure IV-90 through IV-92). For all three films, the low-frequency IGEFET sensor gain/phase data measured at different temperatures traced the same contour (the frequency increases in a clockwise dierection along the contour). However, at high-frequency, the data for the CuPc and NiPc coated IGEFET sensors did not lie on a single contour. The IGEFET sensor's phase delay associated with the high-frequency relaxation process increased with temperature while the sensor's gain remained relatively constant.

Using the finite-difference model developed in the next chapter, the film permittivity and loss factor were determined from the measured gain/phase contours as a function of frequency and temperature. Figure IV-93 shows that the film permittivity corresponding to the gain/phase measured at 106 Hz increases exponentially as a function of temperature. Even larger increases in the film permittivity were observed at lower frequencies, as shown in Figures IV-94 to IV-96. Parallel plate capacitance measurements of copper (131) and lead (132) phthalocyanine reported in the literature

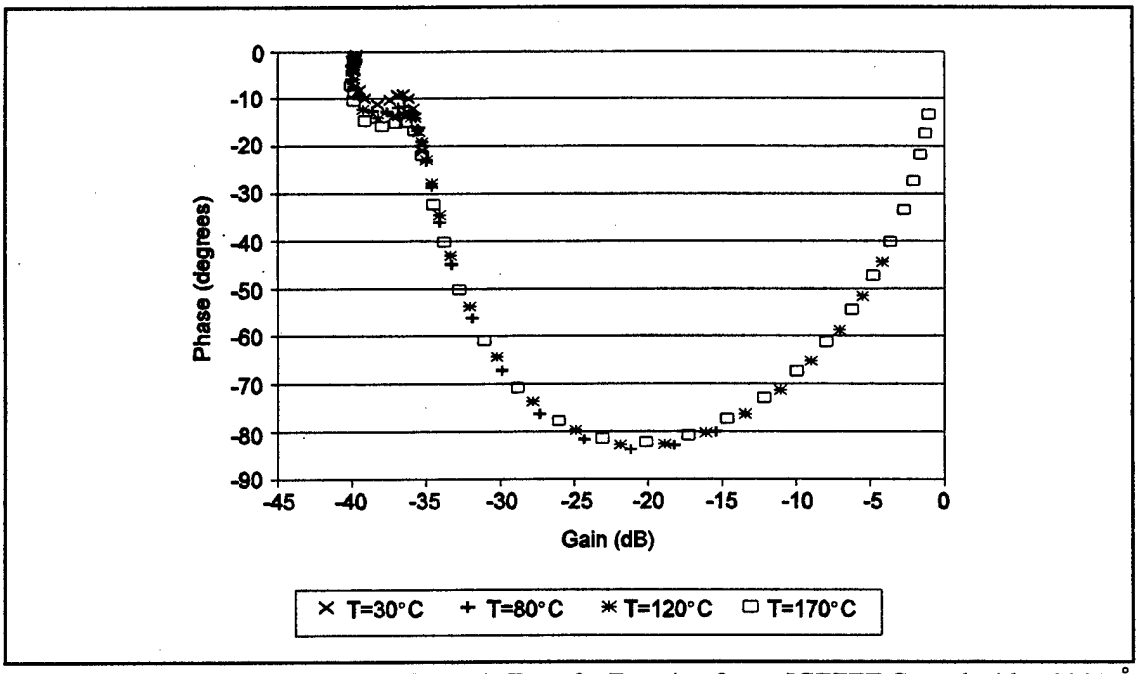


Figure IV-90. Nyquist Plot of the Sensor's Transfer Function for an IGEFET Coated with a 3200 Å Thick Copper Phthalocyanine (CuPc) Film at Several Different Temperatures. Microsensor Maintained in a Dry Air Ambient.

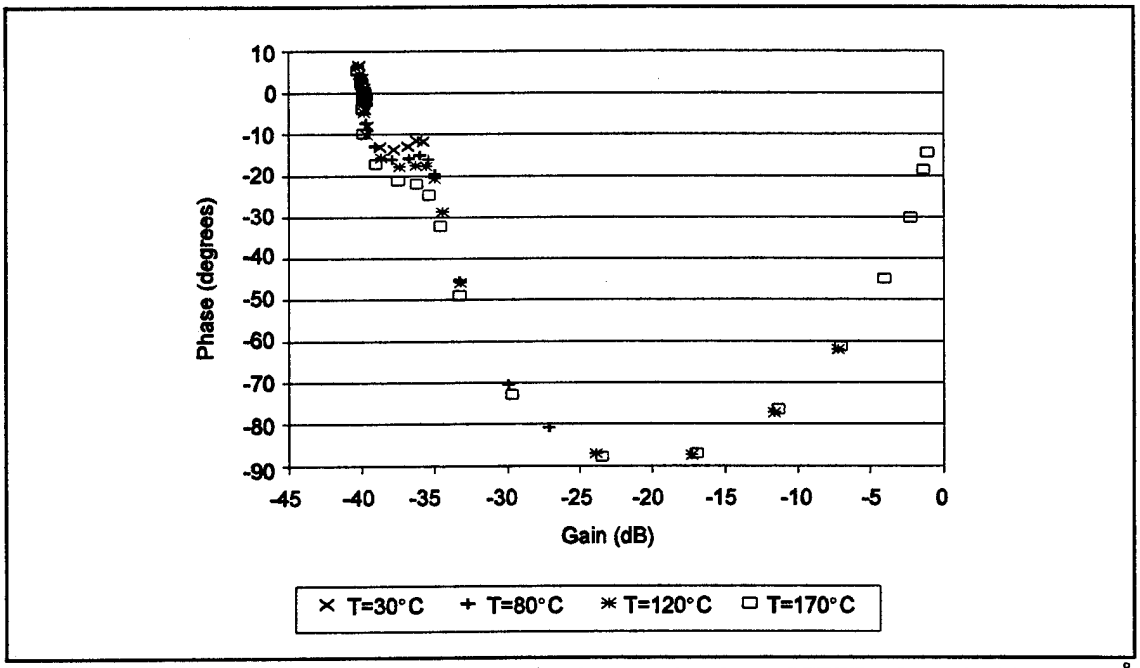


Figure IV-91. Nyquist Plot of the Sensor's Transfer Function for an IGEFET Coated with a 4300 Å Thick Nickel Phthalocyanine (NiPc) Film at Several Different Temperatures. Microsensor Maintained in a Dry Air Ambient.

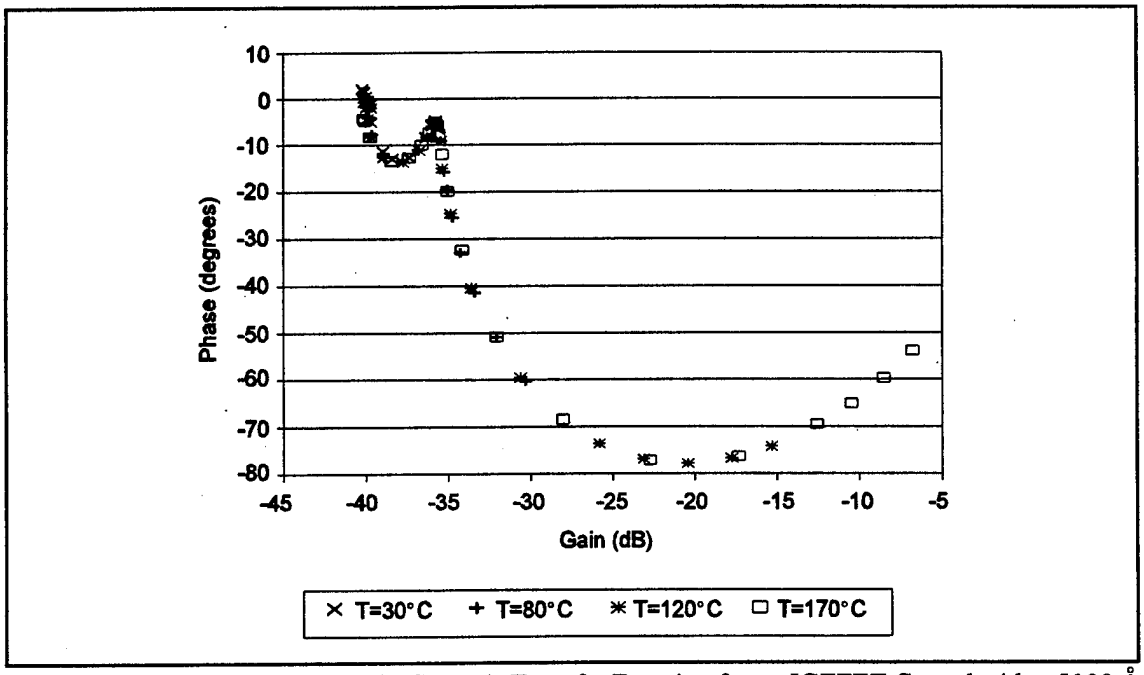


Figure IV-92. Nyquist Plot of the Sensor's Transfer Function for an IGEFET Coated with a 5100 Å Thick Cobalt Phthalocyanine (CoPc) Film at Several Different Temperatures. Microsensor Maintained in a Dry Air Ambient.

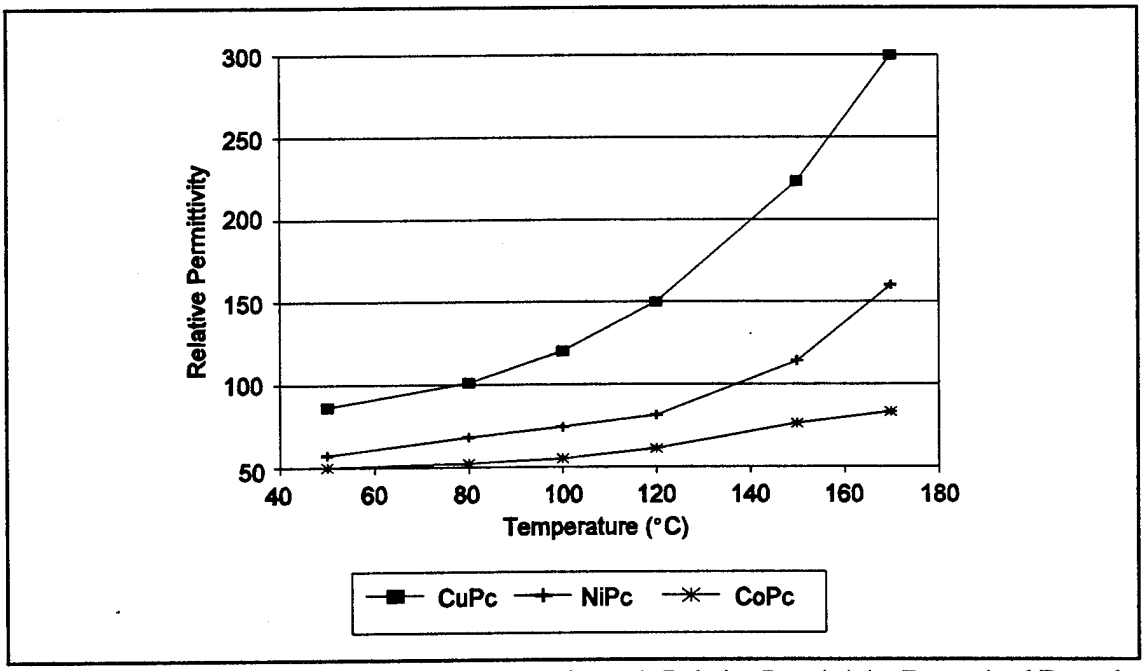


Figure IV-93. Temperature Dependence of the Sensor's Relative Permittivity Determined From the Finite-Difference Model and the Measured Gain/Phase at 106 Hz for the IGEFET Sensors Coated with 3200 Å Copper Phthalocyanine (CuPc), 4300 Å Nickel Phthalocynanine (NiPc) and 5100 Å Thick Cobalt Phthalocyanine (CoPc) Films. Microsensor Maintained in a Dry Air Ambient.

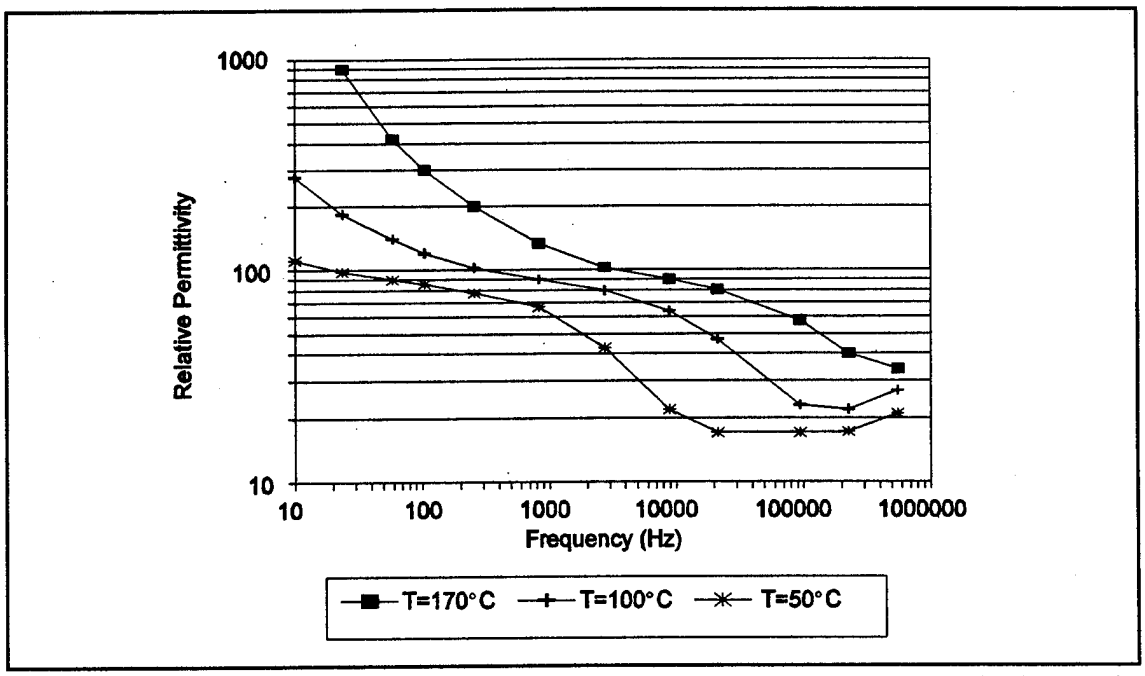


Figure IV-94. Frequency Dependence of the Sensor's Relative Permittivity Determined From the Chapter V Finite-Difference Model and the Measured Gain/Phase of an IGEFET Coated with a 3200 Å Thick Copper Phthalocyanine (CuPc) Film at Three Different Temperatures. Microsensor Maintained in a Dry Air Ambient.

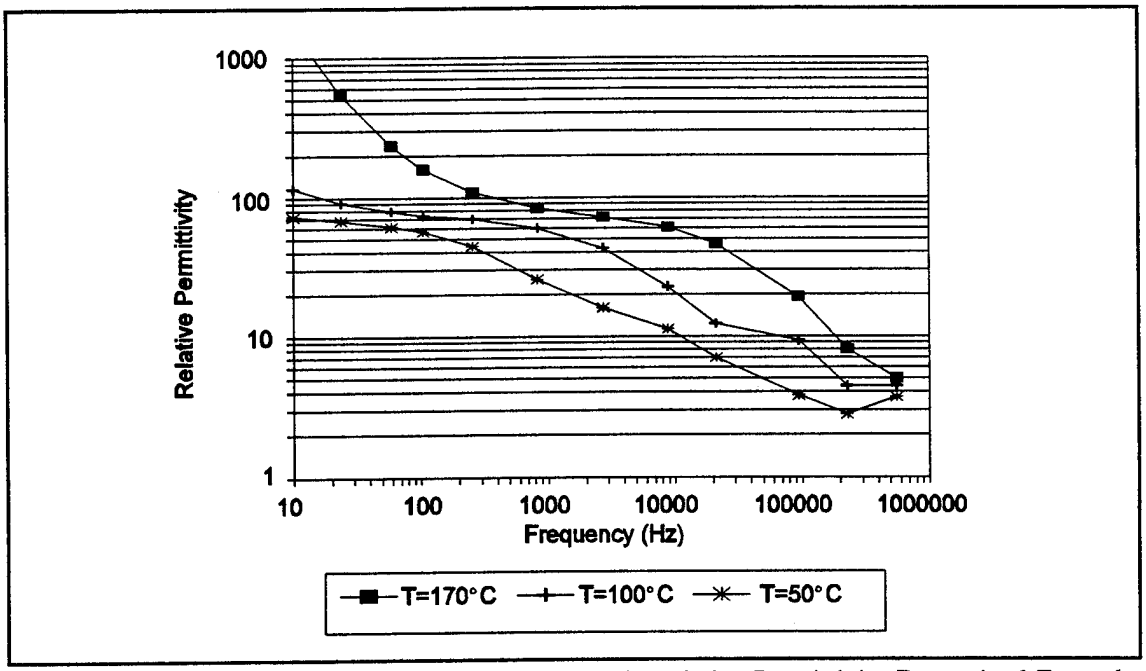


Figure IV-95. Frequency Dependence of the Sensor's Relative Permittivity Determined From the Chapter V Finite-Difference Model and the Measured Gain/Phase of an IGEFET Coated with a 4300 Å Thick Nickel Phthalocyanine (NiPc) Film at Three Different Temperatures. Microsensor Maintained in a Dry Air Ambient.

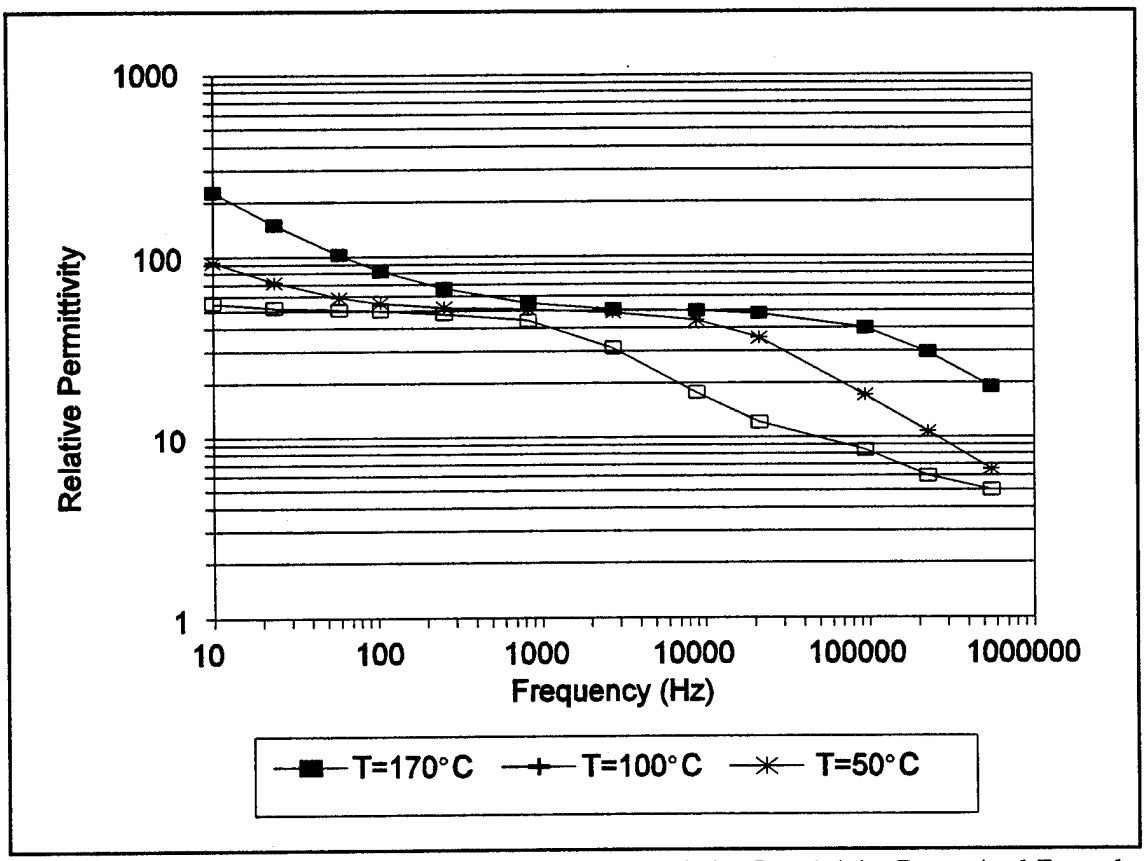


Figure IV-96. Frequency Dependence of the Sensor's Relative Permittivity Determined From the Chapter V Finite-Difference Model and the Measured Gain/Phase of an IGEFET Coated with a 5100 Å Thick Cobalt Phthalocyanine (CoPc) Film at Three Different Temperatures. Microsensor Maintained in a Dry Air Ambient.

demonstrated a similar frequency and temperature dependence with extraordinarily large capacitances at low-frequency and high temperature. However, as pointed out in these earlier studies, such large permittivities and capacitances can not be expected to arise from any bulk property of the phthalocyanine films. The parallel plate capacitor results were explained using a model developed by Simmons et al. (187) where the contact between the metal electrode and the phthalocyanine film forms a Schottky barrier. As shown in Figure IV-97, the metal electrode-phthalocyanine-metal electrode parallel plate capacitor was modeled as two Schottky barrier capacitances (C_s) connected in series with the parallel combination of the phthalocyanine film bulk conductance (G_b) and capacitance (C_b). The equivalent frequency-dependent conductance (G_{eq}) and capacitance (C_{eq}) of this network (Appendix G) are given by:

$$G_{eq} = \frac{\omega^2 G_b C_s^2}{4G_b^2 + \omega^2 (C_s + 2C_b)^2} \qquad \text{(IV-2)}$$

and

$$C_{eq} = \frac{2G_b^2 C_s + \omega^2 C_s C_b (C_s + 2C_b)}{4G_b^2 + \omega^2 (C_s + 2C_b)^2}. \qquad \text{(IV-3)}$$

The Schottky barrier capacitance and the phthalocyanine thin film capacitance were assumed to be temperature independent. However, the conductance in the phthalocyanine thin film is thermally activated. Figures IV-98 and IV-99 illustrate the variation in the equivalent capacitance and conductance with respect to temperature as a result of the thermal activation of the phthalocyanine film's conductance. At low temperatures (where G_b is small) and high-frequency, the equivalent capacitance reduces to:

$$C_{eq} = \frac{C_s C_b}{C_s + 2C_b}. \qquad \text{(IV-4)}$$

Furthermore, if $C_s \gg C_b$ then the equivalent capacitance is simply the film bulk capacitance. As the temperature is raised and G_b becomes appreciable relative to $\omega C_b(C_s + C_b)$, the equivalent capacitance will increase, and it will finally saturate at sufficiently high temperature with a value equal to C_s. This model accounts for the large permittivity at high temperature and low-frequency determined from the finite-difference model (see Chapter V) and gain/phase data (Figures IV-90 through IV-96). At low

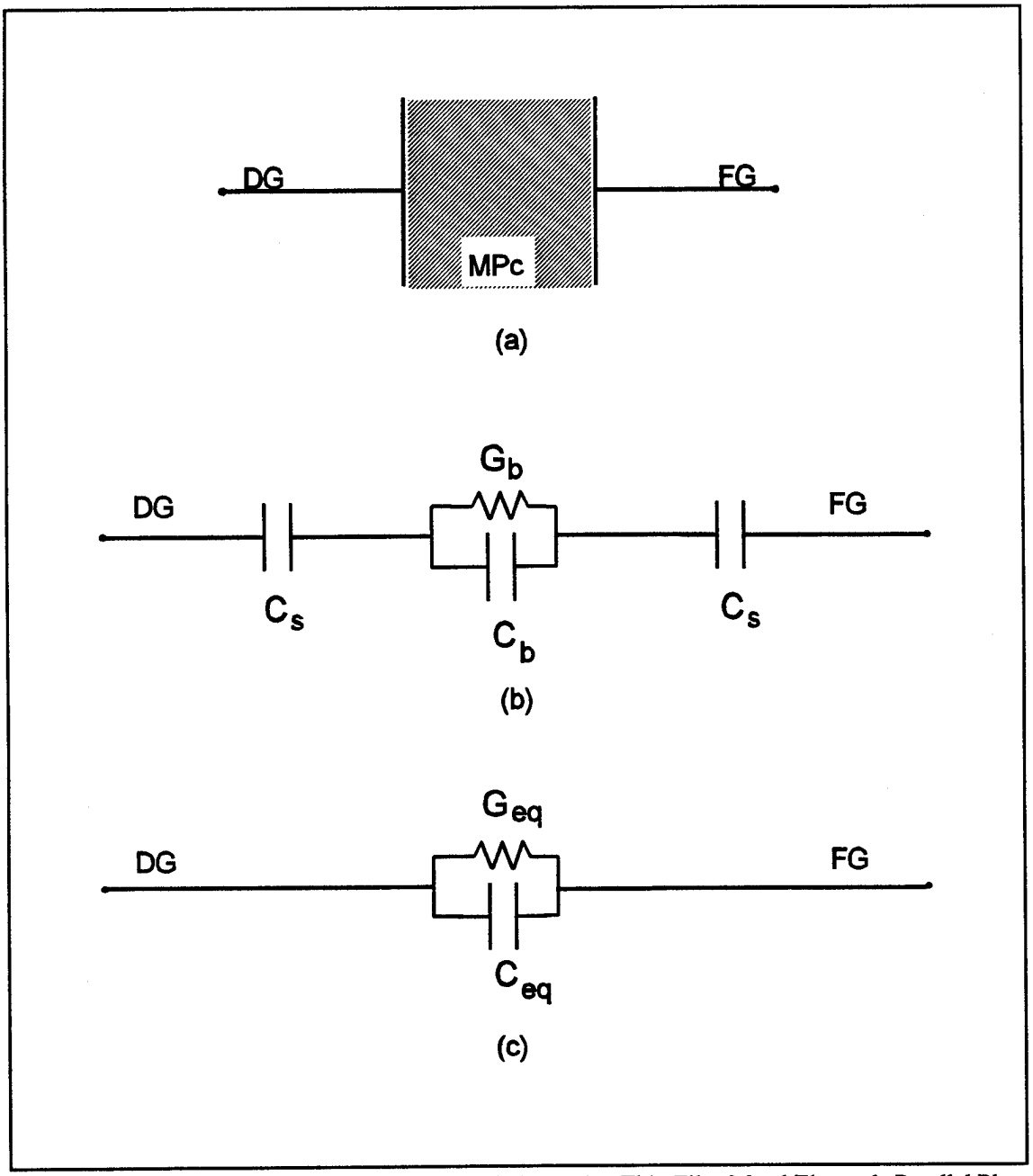


Figure IV-97. Model of a Metal Electrode-Phthalocyanine Thin Film-Metal Electrode Parallel Plate Capacitor. a) Physical Model where DG is the Driven Gate Electrode, FG is the Floating Gate Electrode, and MPc is the Metal Phthalocyanine Thin Film; b) Electrical Model where C_s is the Schottky Barrier Capacitance; C_b is the Thin Film Bulk Capacitance, and G_b is the Thin Film Bulk Conductance; c) Simplified Equivalent Electrical Circuit where C_{eq} is the Equivalent Capacitance, and G_{eq} is the Equivalent Conductance (187).

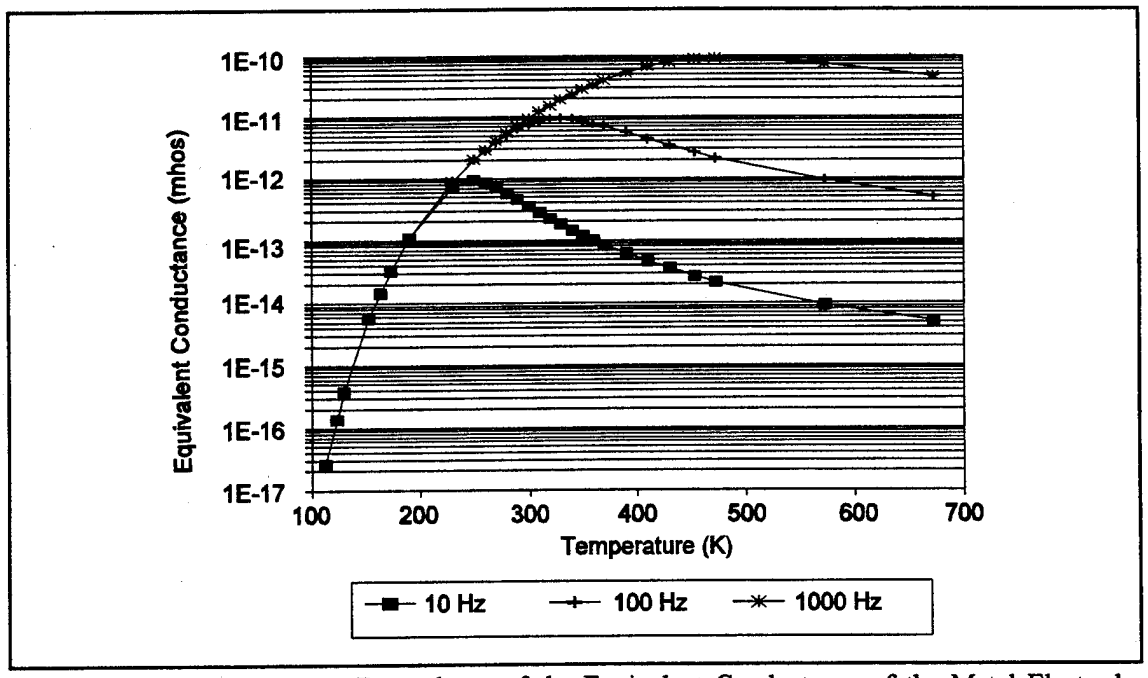


Figure IV-98. Temperature Dependence of the Equivalent Conductance of the Metal Electrode-Phthalocyanine Thin Film-Metal Electrode Parallel Plate Capacitor Model at Three Different Frequencies as the Result of the Thermal Activation of the Phthalocyanine Film's Conductance.

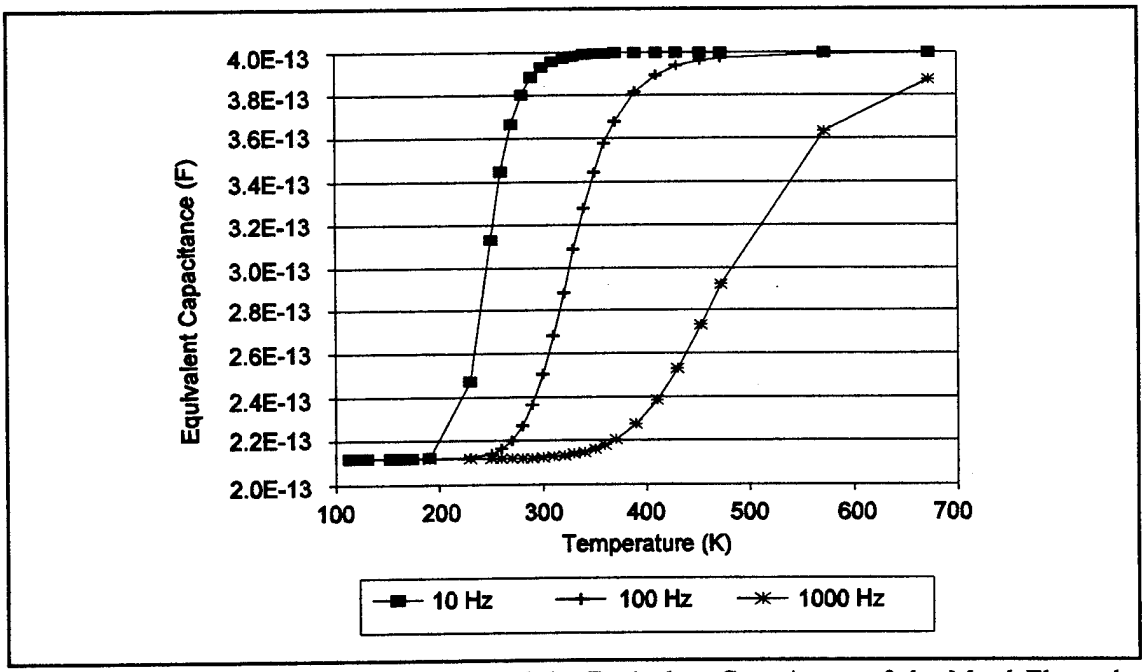


Figure IV-99. Temperature Dependence of the Equivalent Capacitance of the Metal Electrode-Phthalocyanine Thin Film-Metal Electrode Parallel Plate Capacitor Model at Three Different Frequencies as the Result of the Thermal Activation of the Phthalocyanine Film's Conductance.

temperature and high-frequency, the permittivity approaches a constant value of approximately 4 for the NiPc and CoPc coated IGEFETs, and a value of 20 for CuPc. A permittivity of 20 for the bulk CuPc film is significantly greater than the reported value of 3.2-3.6 (47,131). The Schottky barrier model is also supported by the voltage dependence of the current discussed earlier in this chapter (Figures IV-78 through IV-80). Unfortunately, the results at high-frequencies (above 90 KHz) can not be considered reliable for two reasons. First, the on-chip amplifier contributes a significant phase rotation above 90 KHz to the overall measured phase, as well as a small, but significant, increase in the gain (Figure IV-69). The second problem is that the gain/phase predicted by the finite-difference model is insensitive to changes in the complex permittvity for the given geometry and film properties. For example, the gain varies less than 1 dB (2.5%) for lossless dielectrics possessing a permittivity value in the range of 1 to 50. In contrast to the permittivity, the behavior of the loss factor was not consistent with the Schottky barrier model. Examination of Equation IV-2 indicates that, at high-frequency, the equivalent conductance reduces to a constant equal to the film conductance, and at low-frequency, the equivalent conductance is proportional to ω^2. Log-Log plots of the loss factor as a function of frequency (Figures IV-100 through IV-102) revealed a linear dependence at high temperature and low-frequencies. The slope of the line was independent of temperature and equal to -0.79, -0.87, and -0.78 for CuPc, NiPc, and CoPc, respectively. Since the loss factor is defined as $(\sigma/\omega\epsilon_o)$, the conductivity is proportional to $\omega^{0.2}$. At high-frequencies, the loss factor was constant and independent of temperature, which implies that the conductivity at high-frequencies becomes directly proportional to the frequency. Similar results have been reported by Sadaoka and Sakai where the conductivity of a CuPc film in an oxygen atmosphere was shown to be proportional to $\omega^{0.75}$ at frequencies above 100 KHz (91). Below 100 KHz, the conductivity was nearly frequency independent. Sadoaka and Sakai also showed that the observed behavior was dependent on the atmosphere in which the measurements were performed. The frequency dependence of the conductivity extended to frequencies less than 100 Hz when measured under vacuum. Sadoaka and Sakai, as well as other researchers who have observed similar behavior (127), concluded that the observed electrical properties are not the result of contact effects between the electrodes and the phthalocyanine thin films, but may be explained in terms of hopping charge transport between localized states or by a Maxwell-Wagner mechanism. Sadoaka and Sakai also proposed that the total conductivity is composed of a thermally activated DC component, which is relatively independent of frequency, and an AC component, which possesses a power law frequency dependence. Arrhenius plots of the loss factor measured at 106 Hz for each of the MPc films are shown in Figure IV-103. Except at low temperature, the CuPc and NiPc plots were linear with activation energies of 0.41 eV and 0.55 eV,

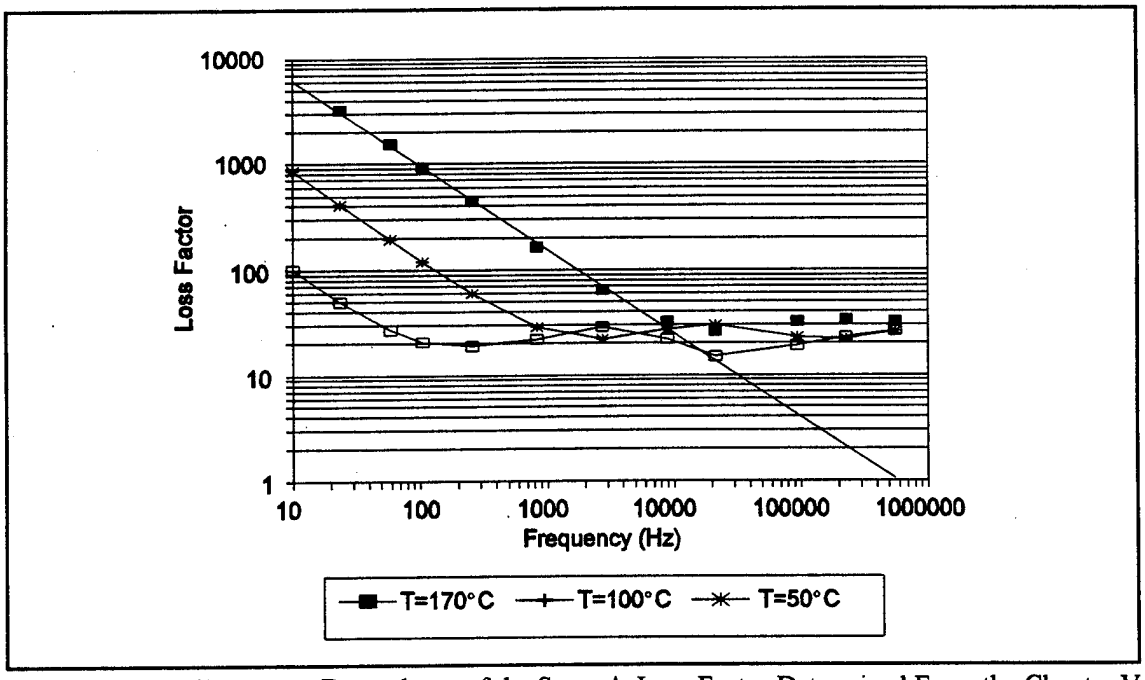


Figure IV-100. Frequency Dependence of the Sensor's Loss Factor Determined From the Chapter V Finite-Difference Model and the Measured Gain/Phase of an IGEFET Coated with a 3200 Å Thick Copper Phthalocyanine (CuPc) Film at Three Different Temperatures. Microsensor Maintained in a Dry Air Ambient.

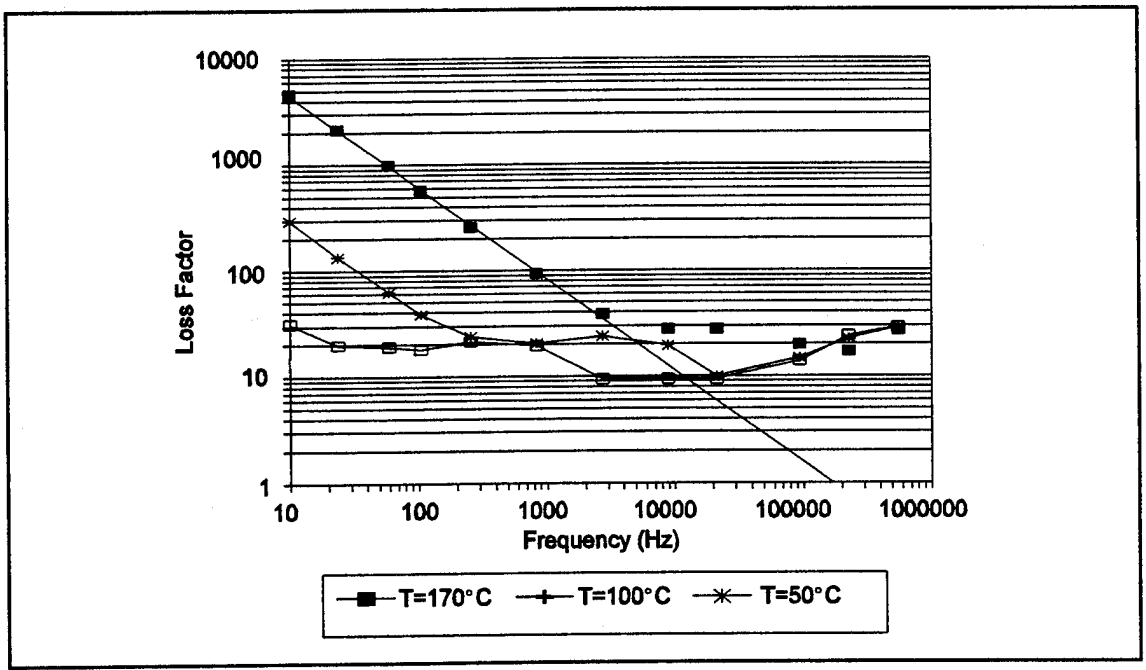


Figure IV-101. Frequency Dependence of the Sensor's Loss Factor Determined From the Chapter V Finite-Difference Model and the Measured Gain/Phase of an IGEFET Coated with a 4300 Å Thick Nickel Phthalocyanine (NiPc) Film at Three Different Temperatures. Microsensor Maintained in a Dry Air Ambient.

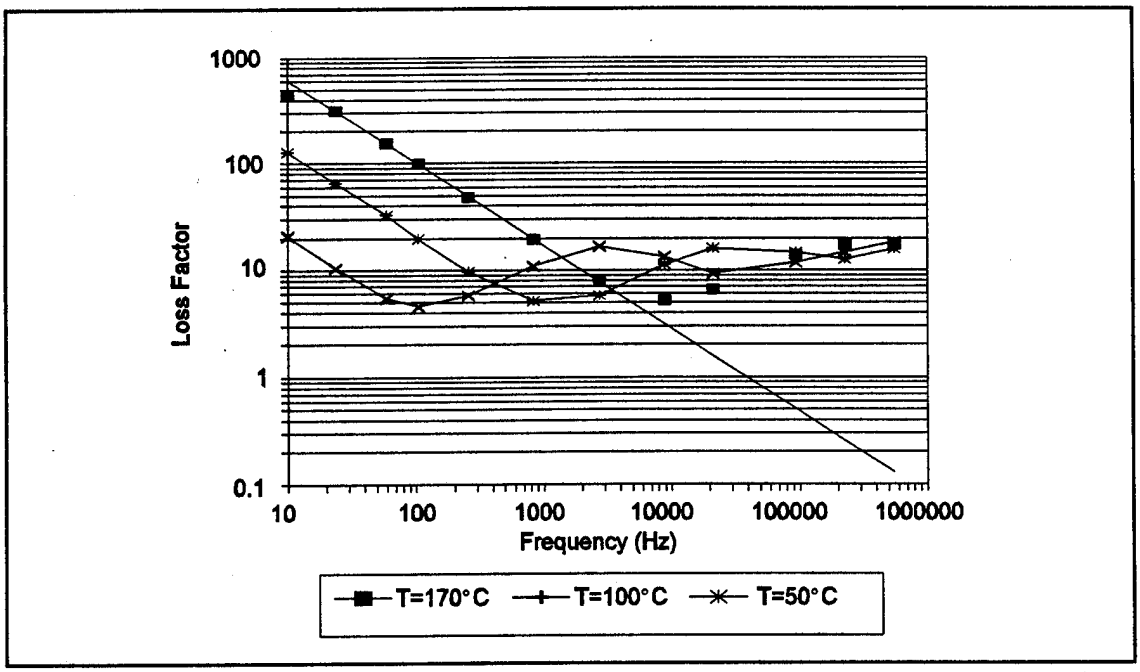


Figure IV-102. Frequency Dependence of the Sensor's Loss Factor Determined From the Chapter V Finite-Difference Model and the Measured Gain/Phase of an IGEFET Coated with a 5100 Å Thick Cobalt Phthalocyanine (CoPc) Film at Three Different Temperatures. Microsensor Maintained in a Dry Air Ambient.

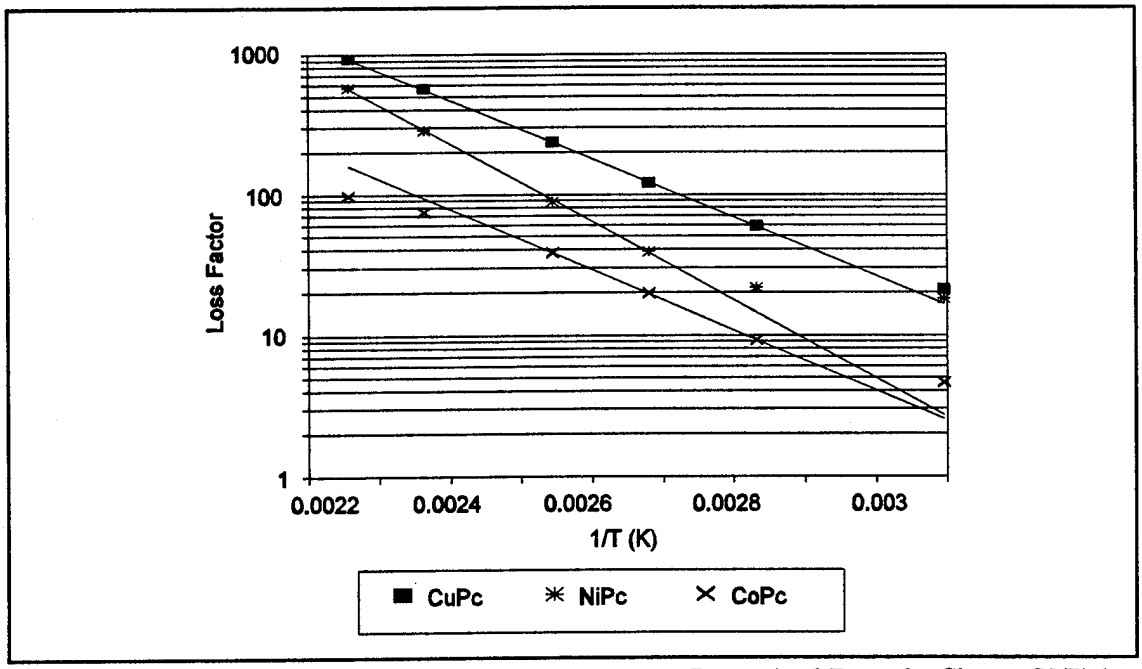


Figure IV-103. Arrhenius Plot of the Sensor's Loss Factor Determined From the Chapter V Finite-Difference Model and the Measured Gain/Phase at 106 Hz of IGEFET Sensors Coated with a 3200 Å Copper Phthalocyanine (CuPc), 4300 Å Nickel Phthalocyanine (NiPc), and 5100 Å Cobalt Phthalocyanine (CoPc) Thick Films. Microsensor Maintained in a Dry Air Ambient.

respectively. These activation energies are in excellent agreement with the 0.40 eV and 0.54 eV activation energies observed for CuPc and NiPc-coated IGEFETs determined from DC resistance measurements discussed earlier (Figures IV-74 and IV-75). In addition to the non-linearity at low temperature, the Arrhenius plot of the CoPc loss factor also deviated from linearity at high temperature. Over the linear portion of the plot, the activation energy determined from the slope was equal to 0.43 eV, and this value was consistent with the 0.41 eV activation energy determined from the DC resistance measurements (Figure IV-76).

Summary

This chapter presented the physical and electrical characterization of the IGEFET microsensor. After introducing the IGEFET microsensor design, the physical characterization of the microsensor and the deposited copper, nickel, and cobalt phthalocyanine films was discussed. Scanning electron microscopy confirmed the physical dimensions of the microsensor and the structure of the deposited MPc films. Transmission electron microscopy and infrared spectroscopy verified the chemical composition and the α-phase, polycrystalline morphology of the deposited films. In addition, infrared spectroscopy demonstrated the reversible adsorption of NO_2 on the metal phthalocyanine films.

Following the physical characterization, the electrical characterization of the uncoated and MPc-coated IGEFET microsensor was presented. To facilitate the electrical characterization, an automated instrumentation system was designed. This system facilitated the automated collection of the IGEFET structure's DC resistance and AC impedance, as well as the IGEFET microsensor's responses from each of the nine independent IGEFET elements. Using this instrumentation system, the electrical behavior of the uncoated and MPc-coated IGEFET microsensor were measured. The results from these measurements are listed below.

Uncoated IGEFET Electrical Characterization Results:

1) The IGE structure's DC resistance and impedance measurements identified leakage paths between the driven and floating gate electrodes which depended upon the IC's wire bond configuration. In addition, the measured resistance of the uncoated IGE structure was found to be highly temperature sensitive with an activation energy of 0.57 eV, but it was independent of the applied bias voltage.

2) The uncoated IGE structure's input and through impedances were shown to correlate with the uncoated IGEFET sensor's transfer function measurements and the finite-difference model predictions of the next chapter. However, the IGE impedance over a relatively wide frequency

range (100 Hz to 10 KHz) exceeds the measurement capability of the impedance analyzer and limits the usefulness of this measurement. Relative to the frequency range over which reliable measurements could be made, the uncoated IGE structure's impedances were temperature independent.

3) The temperature independence of the IGEFET sensor amplifier's transfer function was demonstrated.

MPc-Coated IGEFET Microsensor's Electrical Characterization Results:

1) The MPc-coated IGE structure's DC resistance was both voltage and temperature dependent. The variation in the IGE structure's DC resistance with voltage was minimized when the bias voltage was set at 10 V. Activation energies determined from the Arrhenius plots of the CuPc, NiPc, and CoPc coated IGE structure's DC resistance were 0.40, 0.54, and 0.41 eV, respectively.

2) The IGE structure's DC resistance decreased with increasing MPc film thickness. The MPc-coated IGE structure's DC resistance varied with the ambient atmosphere--the resistance being greater in a nitrogen ambient compared to dry air.

3) The logarithm of the DC current in the MPc-coated IGE structure increased linearly with the square root of the bias voltage for voltages greater than 2 V.

4) The MPc-coated IGEFET microsensor's transfer function was temperature sensitive. As the temperature increased, the sensor's gain at low frequencies increased. Bode plots of the phase at high temperatures revealed two minima in the transfer function's phase delay. The low-frequency minima simply shifted to higher frequency when the temperature was increased. The temperature dependence of the high-frequency phase minima varied with film type. With the CuPc and NiPc films, the phase delay at the high frequency minima increased. In contrast, the magnitude of the high-frequency minima observed with the CoPc film did not change significantly with temperature.

5) The temperature and frequency dependence of the permittivity and loss factor that was determined using the finite-difference model developed in Chapter V were consistent with the temperature and frequency dependence of the phthalocyanine thin film electrical properties reported in the literature. The large permittivity values observed at high temperature and low-frequency imply that the inter-electrode admittance in the finite difference model represents an

effective inter-electrode capacitance and conductance. The actual conduction mechanisms responsible for the effective inter-electrode admittance are not adequately modeled with a single parallel combination of a conductance and capacitance. This observation motivated the development of the alternative lumped-element circuit model discussed at the end of Chapter V.

V. *Interdigitated Gate Electrode Finite-Difference Model*

The IGEFET's interdigitated gate electrode (IGE) structure (see Figure I-1) is composed of pairs of driven- and floating-gate electrodes, which are supported above a solid metal ground plane with a silicon dioxide dielectric. The two gate electrodes are physically- and electrically-isolated from each other, and the floating-gate electrode is connected directly to the gate contact of the *in-situ* metal-oxide-semiconductor field-effect transistor (MOSFET). The primary geometrical features of the interdigitated gate electrode that influence its response are the electrode width and thickness, the electrode separation, and the thickness of the supporting dielectric. In operation, the interdigitated gate electrode is coated with a chemically-sensitive coating whose thickness and complex permittivity can significantly influence the IGEFET's response.

The effect of the interdigitated gate electrode geometry and the complex permittivity of the sensor coating on the IGEFET's performance were modeled using a finite-difference method to predict a functional sensor configuration and correlate the sensor's response with variations in the coating's complex dielectric constant. The model was verified by comparing its results with similar data published in the literature and with experimental measurements of the IGEFET's response when coated with films whose complex permittivity was established through independent parallel plate capacitor measurements.

Finite difference models for structures similar to the IGEFET interdigitated gate electrode have been developed (190, 191). Lee developed a finite-difference model for an interdigitated electrode structure coated with a semi-infinitely thick lossy dielectric (190). In this model, the electrodes were assumed to be infinitely thin. Since some IGEFET applications use very thin chemically-sensitive films, Lee's model must be modified to account for the finite electrode thickness and gas-sensitive films. Dang and Shigyo (191) have also developed a finite-difference model for this electrode structure that included the effect of finite thickness electrodes. However, their model was confined to semi-infinitely thick, lossless dielectrics.

The finite-difference model of the IGEFET's interdigitated gate electrode structure that was implemented in this research extends Lee's model to account for thin film coatings and finite thickness electrodes. This chapter is composed of three major sections. The first section reviews finite-difference modeling, with particular emphasis on the Gauss-Seidel iteration method with successive over-relaxation. The first section also summarizes Lee's development of a general, finite-difference formula for calculating the potential at nodes located at the boundary between two inhomogeneous lossy dielectrics. The second section discusses the finite-difference model of the interdigitated gate electrode

structure with finite thickness electrodes and thin dielectric film coatings. This section includes a discussion of the model results for four film geometries. The third section compares the model results with published reports and experimental data to establish the model's validity.

Finite-Difference Modeling

Finite-Difference and Gauss-Seidel Iteration Methods with Successive Over-Relaxation. As required by Gauss's Law, the solution of Poisson's equation specifies the potential distribution for a given set of boundary conditions. These boundary conditions are established by the particular geometry, set of materials, and applied potentials which describe the physical configuration under consideration. For the special case of a space-charge-free region, Poisson's equation reduces to Laplace's equation. Both Laplace's equation and Poisson's equation are elliptic partial-differential equations which are often difficult to solve analytically for complex boundary conditions. In these cases, the finite-difference method may be used to solve these equations numerically to yield the potential distribution that satisfies the specified boundary conditions.

To apply the finite-difference method, the structure to be analyzed is divided into a rectangular grid of nodes where the potential values are calculated. If we consider a typical node in a linear, homogeneous, space-charge-free region (see Figure V-1), it can be shown, using a truncated Taylor series expansion about the node, that the node potential, V_0, is given by the average of the potentials at its four surrounding nodes with an error that is proportional to the square of the node spacing (192):

$$V_0 = \frac{(V_1 + V_2 + V_3 + V_4)}{4} \quad . \tag{V-1}$$

Since an equation of this form applies to each node in the grid, a system of coupled linear equations are developed that describes the potential distribution. Typically, this system of equations is solved with iterative techniques. To implement this method, initial values are assigned to every node in the grid. Node-by-node, a new potential is calculated at every point using Equation (V-1). After a new node potential has been calculated for every point in the grid, the procedure is repeated until the potential at each node converges to a specific value. The node potential has converged to its actual value when the difference (referred to as the residual) between the most recently computed node potential and the node potential value from the preceding iteration is smaller than some acceptable error (called the convergence set point).

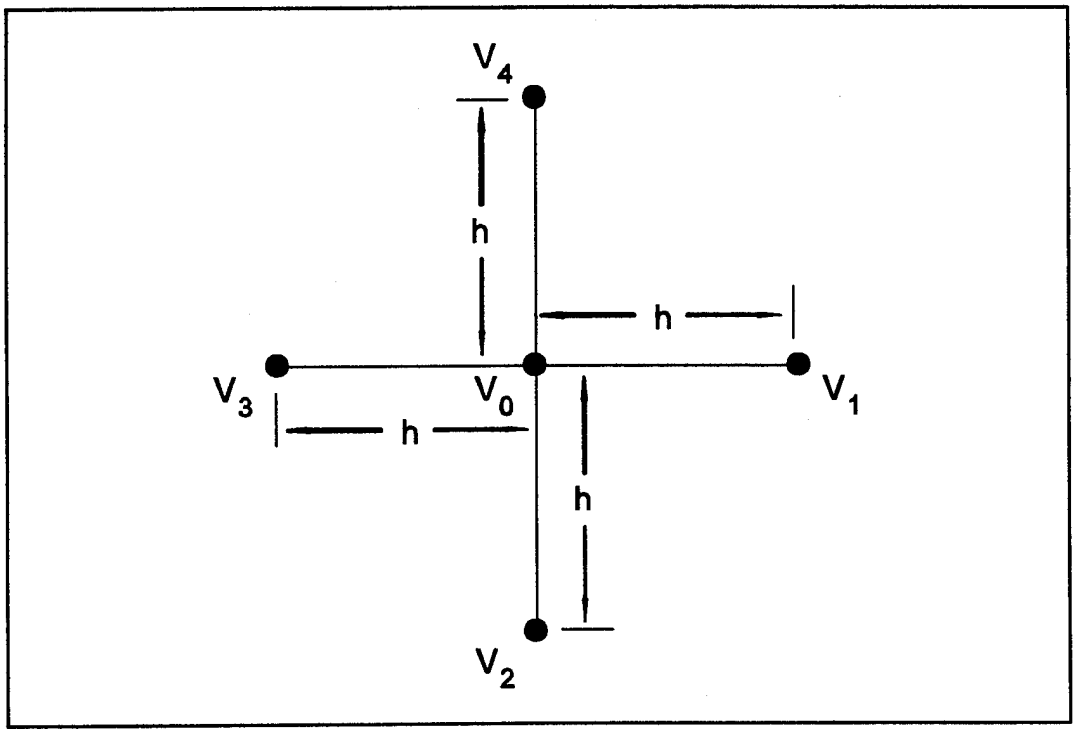


Figure V-1. Typical Finite-Difference Node in a Homogeneous Region with Equidistant Neighbors (190).

Although there are no precise methods, Lawrenson provides some general guidelines for defining an acceptable error (193). In order to gain confidence in the solution's accuracy, Lawrenson recommends evaluating the following features of the computed fields (193):

1) the symmetry of the field;
2) the fulfillment of boundary conditions;
3) the point-to-point potential variation; and
4) the formation and location of centers from which equipotential lines emanate.

According to Lawrenson, the features which require the greatest solution accuracy and, therefore, the greatest number of iterations, are items 3) (particularly near corners of the boundaries) and 4). Furthermore, if too large a mesh size is used, the above features will be unsatisfactory when the residuals are everywhere smaller than the convergence set point; that is, one or more of the numerical solution's features will deviate significantly from the characteristics that the exact solution would possess. For example, the potential in a homogenous region between two parallel plates maintained at two different potentials should vary monotonically in a direction perpendicular to the plates. In addition, the mesh size may be determined by repeated calculation with increasingly finer mesh resolution, until the solution variation is acceptable.

In the Gauss-Seidel iteration method, a single array is used to store the most recently updated node potential values. As soon as a new node potential has been computed, it replaces the old value in the array, and it is used in the subsequent calculations for the next node. Assuming the iteration cycle proceeds from the left to the right, and from the bottom to the top of the mesh, the node potential at the nth-iteration is given by:

$$V_0^n = \frac{(V_1^{n-1} + V_2^n + V_3^n + V_4^{n-1})}{4} \quad . \tag{V-2}$$

A simple modification to the Gauss-Seidel iteration method, which can significantly accelerate convergence, is known as the method of successive over-relaxation (193). In this technique, the new node potential is calculated as the sum of the old node potential and the product of a convergence factor, α, and an error term, or residual, R. That is,

$$V_0 = V_0^{n-1} + \alpha R^n \quad . \tag{V-3}$$

The residual for the nth-iteration is defined as:

$$R^n = \frac{(V_1^{n-1} + V_2^n + V_3^n + V_4^{n-1})}{4} - V_0^{n-1} \quad . \tag{V-4}$$

It can be shown that the Gauss-Seidel method converges more rapidly when $1 \leq \alpha \leq 2$. When $\alpha > 2$, the convergence process becomes unstable (193). If $\alpha < 1$, the process is under-relaxed and usually converges more slowly compared to when it is over-relaxed ($\alpha \geq 1$) (190).

Derivation of a General Finite-Difference Formula for an Inhomogeneous, Lossy Dielectric System. Whenever an electric field exists in an inhomogeneous region consisting of two lossy dielectrics whose time constants, ϵ/σ, are not equal, charge is induced at the interface between the two dielectrics. This interfacial charge must be taken into account to correctly calculate the potential distribution. Lee derived a general finite-difference formula for calculating the potential distribution in an inhomogeneous, lossy dielectric medium using two separate approaches (190). The first approach incorporated the interface charge density that was calculated directly from Maxwell's equations and used in the finite-difference formula that discretizes the continuous form of Poisson's equation. The second approach developed the finite-difference formula using a lumped-element circuit analogy. Since the derivation using the circuit model is particularly pertinent to the development of a method to account for an arbitrary load capacitance, it will be discussed, and the reader is referred to Lee (190) for the derivation achieved with Maxwell's equations.

Figure V-2 illustrates an arbitrary point on the interface between two dielectrics, either of which may be lossless or lossy. As shown, the separation between adjacent nodes is not necessarily equal. The unequal separations readily accommodate variable-sized finite-difference grids. The space around the central node can be discretized into admittance elements which couple the five nodes to form the circuit model of Figure V-3. The conductance and capacitance between two nodes in a homogeneous region are modelled with a resistor, G=1/R, and a capacitor, C, respectively. Additionally, along the interface, a resistor and a capacitor for each material must be included.

In general, the admittance of a circuit element is given by:

$$Y = (\sigma + j\omega\epsilon') \frac{A}{\ell} \tag{V-5}$$

where A is the element's cross-sectional area,

ℓ is the element's length,

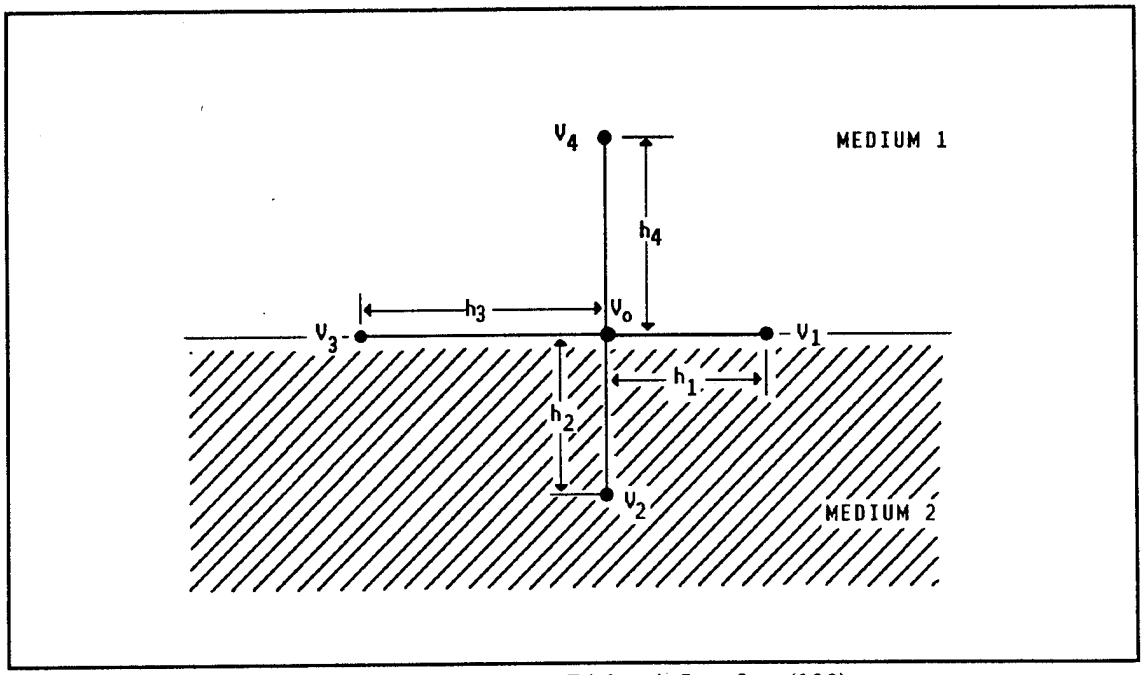


Figure V-2. General Finite-Difference Node on a Dielectric Interface (190).

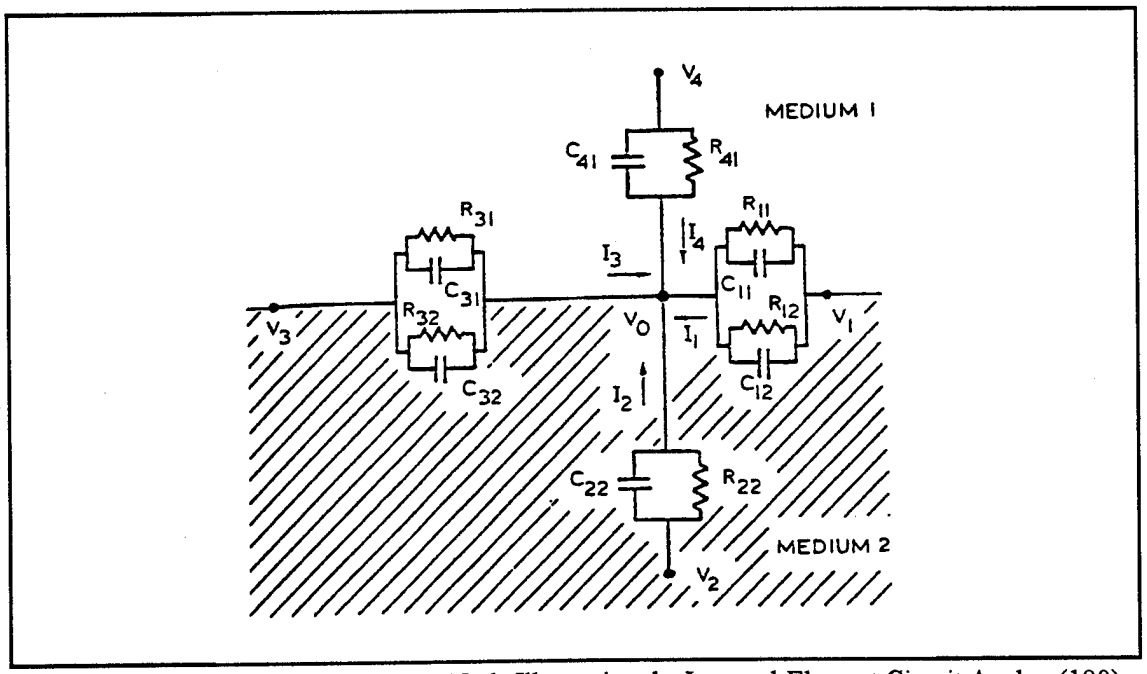


Figure V-3. General Finite-Difference Node Illustrating the Lumped-Element Circuit Analog (190).

σ is the material's conductivity,

ϵ' is the material's permittivity, and

ω is the radian frequency.

Equation (V-5) can be recast into a form emphasizing the complex nature of the dielectric's permittivity:

$$Y = j\omega\,(\epsilon' - j\epsilon'')\,A/\ell = j\omega\,\epsilon^{*}\,(A/\ell) \quad . \tag{V-6}$$

The calculation of the admittance between nodes depends on whether the node is located in either a homogeneous region or along the interface. In a homogeneous region, the admittance element's length is the distance between the nodes (h). Assuming a two-dimensional model, which is the case for the interdigitated electrode structure when the potential drop along the electrode's length is assumed to be negligible, the admittance may be calculated on a per-unit length basis; that is, the thickness (th) is assumed to be unity. The width (w) is taken to be one-half the perpendicular distance to the next row of nodes on one side, plus half the distance to the next row of nodes on the other side. For example, the admittance element, Y_2, between nodes 0 and 2 in Figure V-4 is[1]:

$$Y_2 = \epsilon_2^{*}(A/\ell) = \epsilon_2^{*}\left[\frac{(h_1/2 + h_3/2)}{h_2}\right] \cdot 1 \quad . \tag{V-7}$$

Y_2 is equivalent to the admittance of a parallel RC network (consisting of a resistance (R) in parallel with a capacitance (C)) since the material between nodes 0 and 2 has both conductivity and permittivity properties (permeability, and thus, inductance effects are usually negligible.

Along an interface, two different admittance elements must connect laterally adjacent nodes (one for each medium). For example, the admittance element for the upper half of the interfacial region between nodes 0 and 1 has the geometry of Figure V-5, and an admittance of:

$$Y_{11} = \epsilon_1^{*}\left[\frac{(h_4/2)}{h_1}\right] \cdot 1 \quad . \tag{V-8}$$

---

[1]As shown in Figure V-4a, the cross-sectional area of the admittance element (A) is given by the product of the admittance element's width (w) and the admittance element's thickness (th), which is assumed to be unity. With this assumption, the three-dimensional admittance element can then be represented by the two-dimensional admittance element, shown in Figure V-4b. The admittance element's length (ℓ) is equal to h_2.

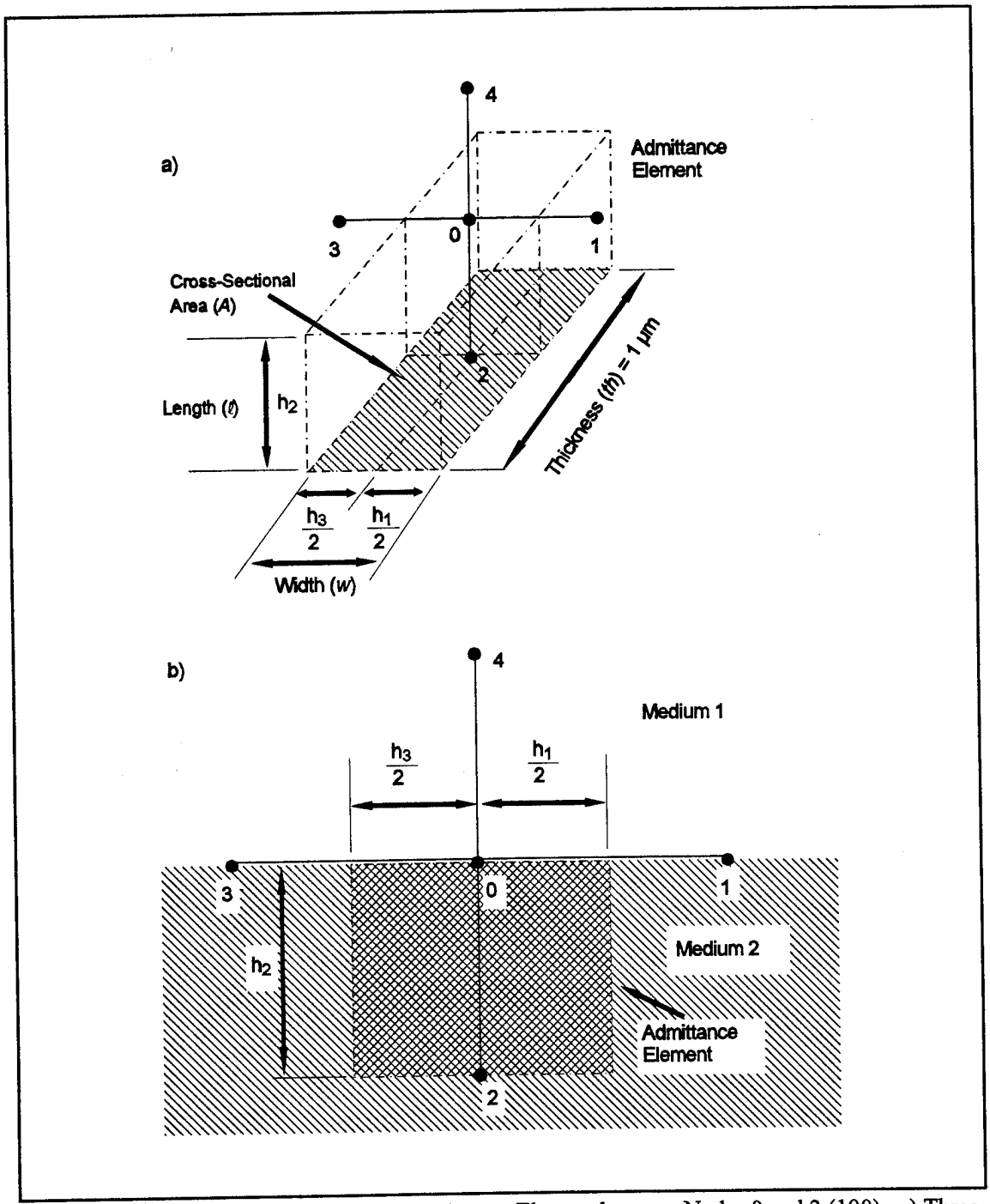


Figure V-4. Geometry of a Discretized Admittance Element between Nodes 0 and 2 (190). a) Three-Dimensional Illustration of Admittance Element. b) Simplified Two-Dimensional Representation of Admittance Element.

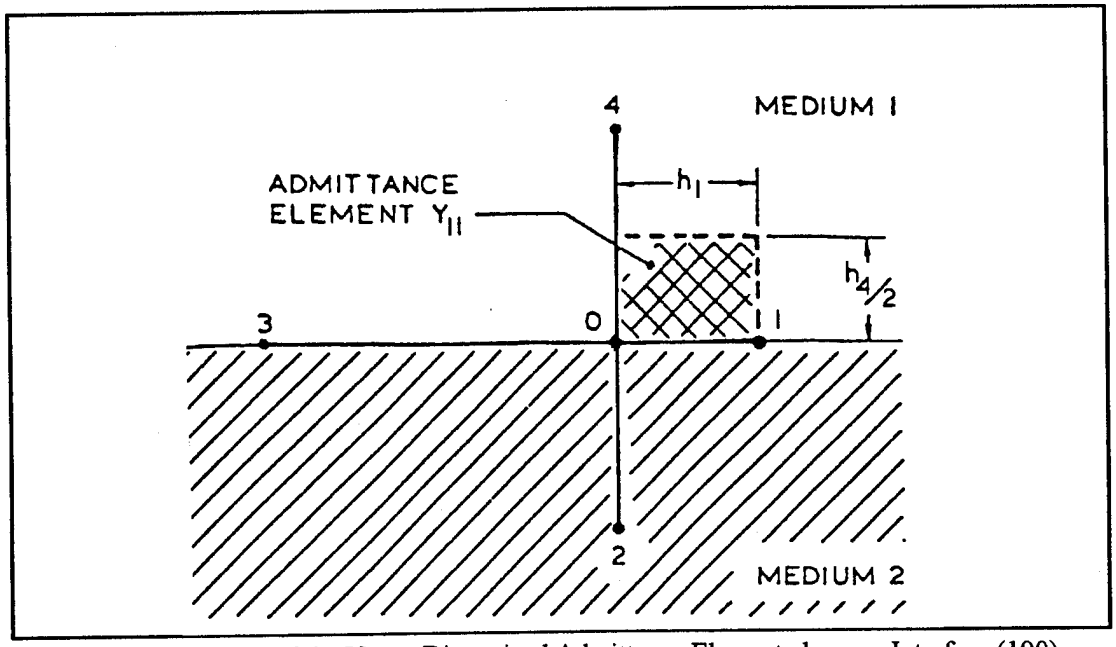


Figure V-5. Geometry of the Upper Discretized Admittance Element along an Interface (190).

Similarly, the admittance element for the lower half has the geometry of Figure V-6, and an admittance of:

$$Y_{12} = \epsilon_2^* \left[\frac{(h_2/2)}{h_1}\right] \cdot 1 \quad . \tag{V-9}$$

The total (net) admittance element of the circuit element connecting nodes 0 and 1 is obtained by algebraically adding Equations (V-8) and (V-9):

$$Y_1 = \left[\frac{(\epsilon_1^* h_4/2 + \epsilon_2^* h_2/2)}{h_1}\right] \cdot 1 \quad . \tag{V-10}$$

Similarly, the admittances for the remaining two elements connecting nodes 0 to 3, and 0 to 4 are:

$$Y_3 = \left[\frac{(\epsilon_1^* h_4/2 + \epsilon_2^* h_2/2)}{h_3}\right] \cdot 1 \tag{V-11}$$

and

$$Y_4 = \epsilon_1^* \left[\frac{(h_1/2 + h_3/2)}{h_4}\right] \cdot 1 \quad . \tag{V-12}$$

Applying Kirchoff's current law to node 0, using the current directions depicted in Figure V-3, implies:

$$I_1 + I_2 + I_3 + I_4 = 0 \tag{V-13}$$

where

$$I_n = Y_n (V_n - V_0). \tag{V-14}$$

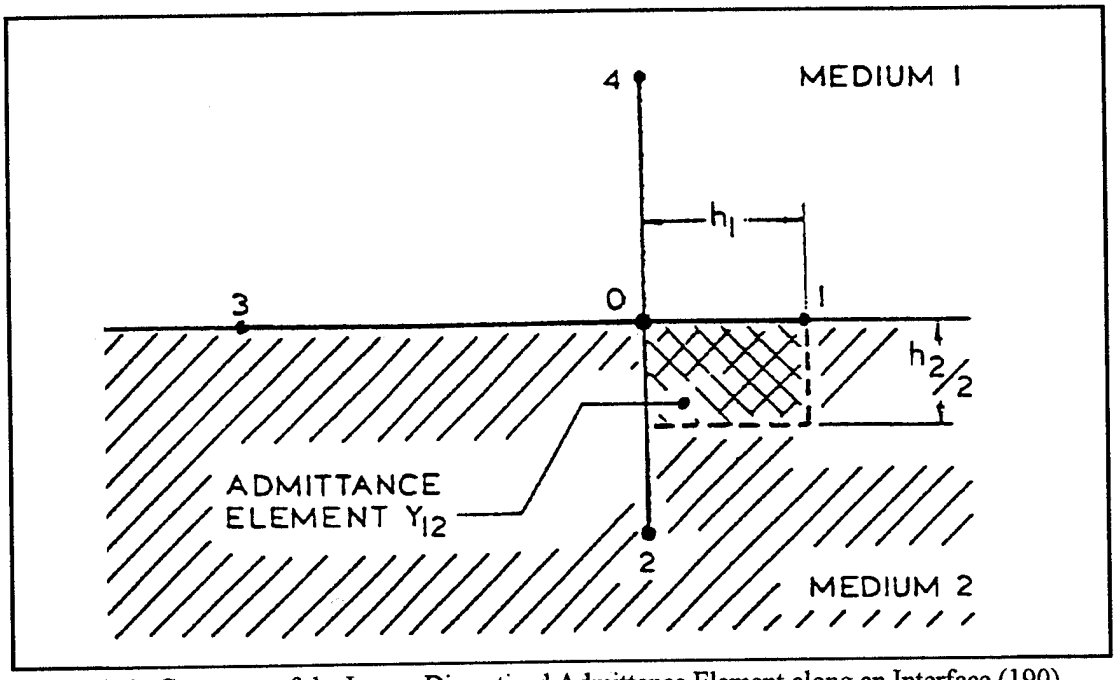


Figure V-6. Geometry of the Lower Discretized Admittance Element along an Interface (190).

Combining Equations (V-7) and (V-10 through V-14), and rearranging the terms to isolate V_0, the voltage at the center node, is obtained as:

$$V_0 = \frac{\dfrac{V_1}{h_1(h_1+h_3)} + \dfrac{\dfrac{\epsilon_2^*}{\epsilon_1^*}V_2}{h_2\left(\dfrac{\epsilon_2^*}{\epsilon_1^*}h_2+h_4\right)} + \dfrac{V_3}{h_3(h_1+h_3)} + \dfrac{V_4}{h_4\left(\dfrac{\epsilon_2^*}{\epsilon_1^*}h_2+h_4\right)}}{\dfrac{1}{h_1h_3} + \dfrac{1}{h_2h_4}\left[\dfrac{\dfrac{\epsilon_2^*}{\epsilon_1^*}h_4+h_2}{h_4+\dfrac{\epsilon_2^*}{\epsilon_1^*}h_2}\right]} \quad \text{(V-15)}$$

In the case where a square grid of nodes ($h_1 = h_2 = h_3 = h_4$) is employed, the potential distribution is calculated within a homogeneous region ($\epsilon_1^* = \epsilon_2^*$), and Equation (V-15) simplifies to:

$$V_0 = \frac{(V_1 + V_2 + V_3 + V_4)}{4} \quad \text{(V-16)}$$

which is identical to Equation (V-1).

Interdigitated Gate Electrode Finite-Difference Model Implementation

Finite-Difference Model Algorithm. The objective of the model was to determine the transfer function of the IGEFET's interdigitated gate electrode structure when coated with a dielectric thin film with arbitrary electrical conductivity and permittivity and connected to an arbitrary capacitive load (the *in-situ* MOSFET gate structure). The model algorithm which accomplished this objective is shown in Figure V-7. The algorithm begins with the calculation of the potential distribution of the intrinsic, or unloaded, interdigitated gate electrode structure with Equation (V-15) using the Gauss-Seidel iteration method with successive over-relaxation. Two separate models of the interdigitated gate electrode structure that are illustrated in Figures V-8 and V-9 were used, depending upon the film thickness. Gauss' Law is then applied to this potential distribution to determine the current in the driven- and floating-gate electrodes. By representing the interdigitated gate electrode structure as a two-port

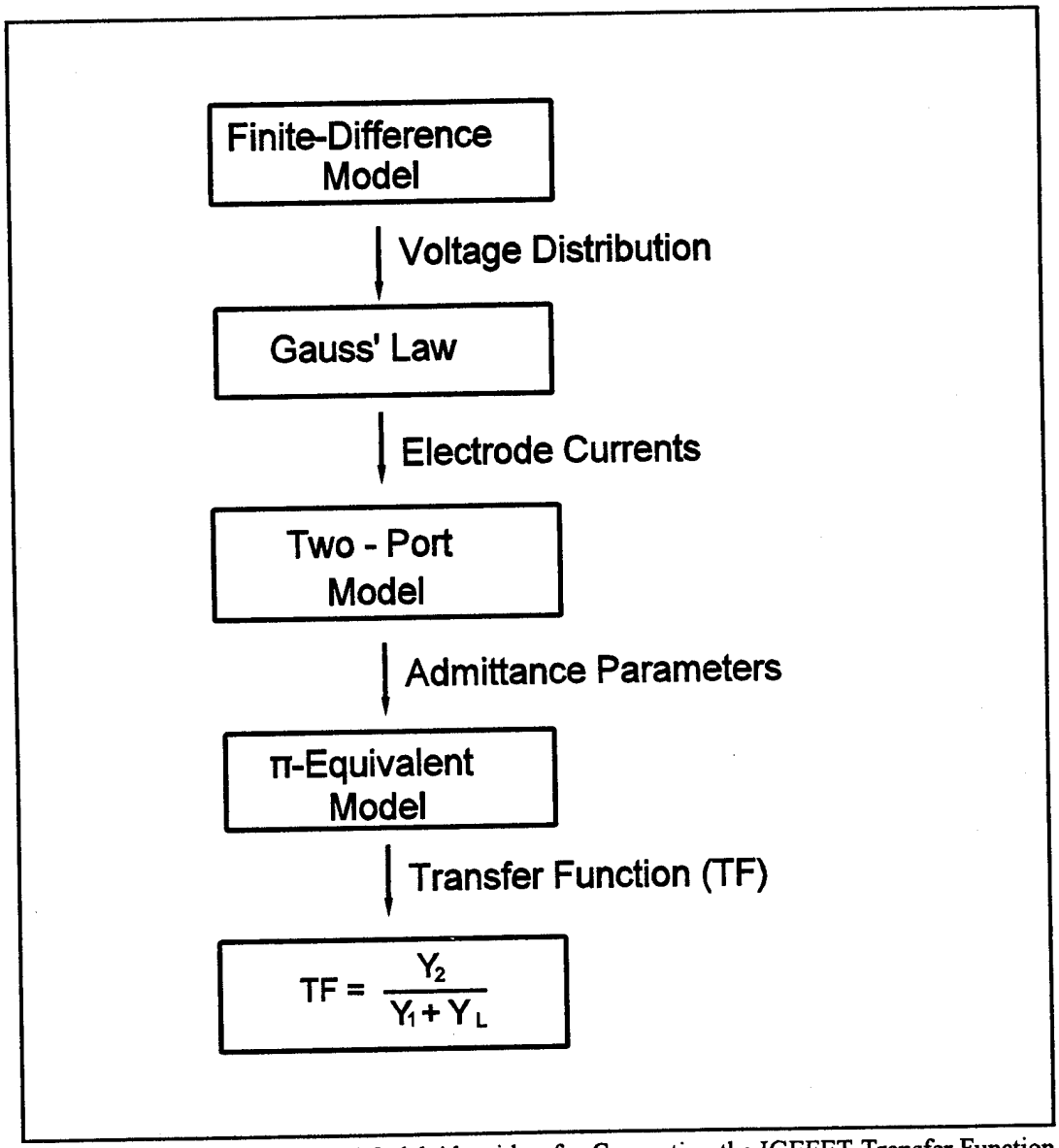


Figure V-7. Finite-Difference Model Algorithm for Computing the IGEFET Transfer Function (TF). Y_1 and Y_2 are the Calculated Two-Port Admittance Parameters Multiplied by the Meander Length. Y_L is the Load Capacitance.

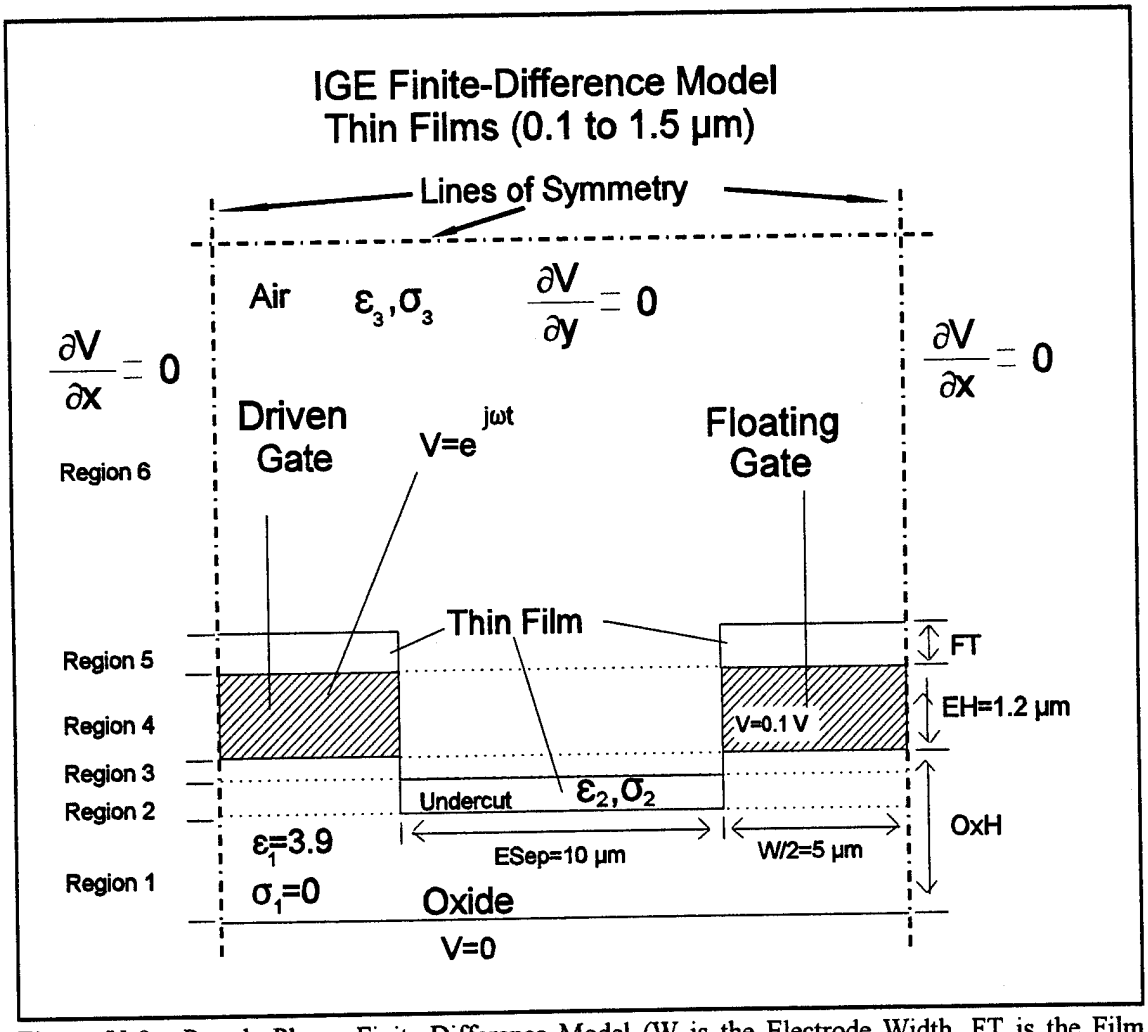


Figure V-8. Pseudo-Planar Finite-Difference Model (W is the Electrode Width, FT is the Film Thickness, OxH is the Oxide Thickness, EH is the Electrode Height, and ESep is the Inter-Electrode Space. Applied Potentials are in Volts).

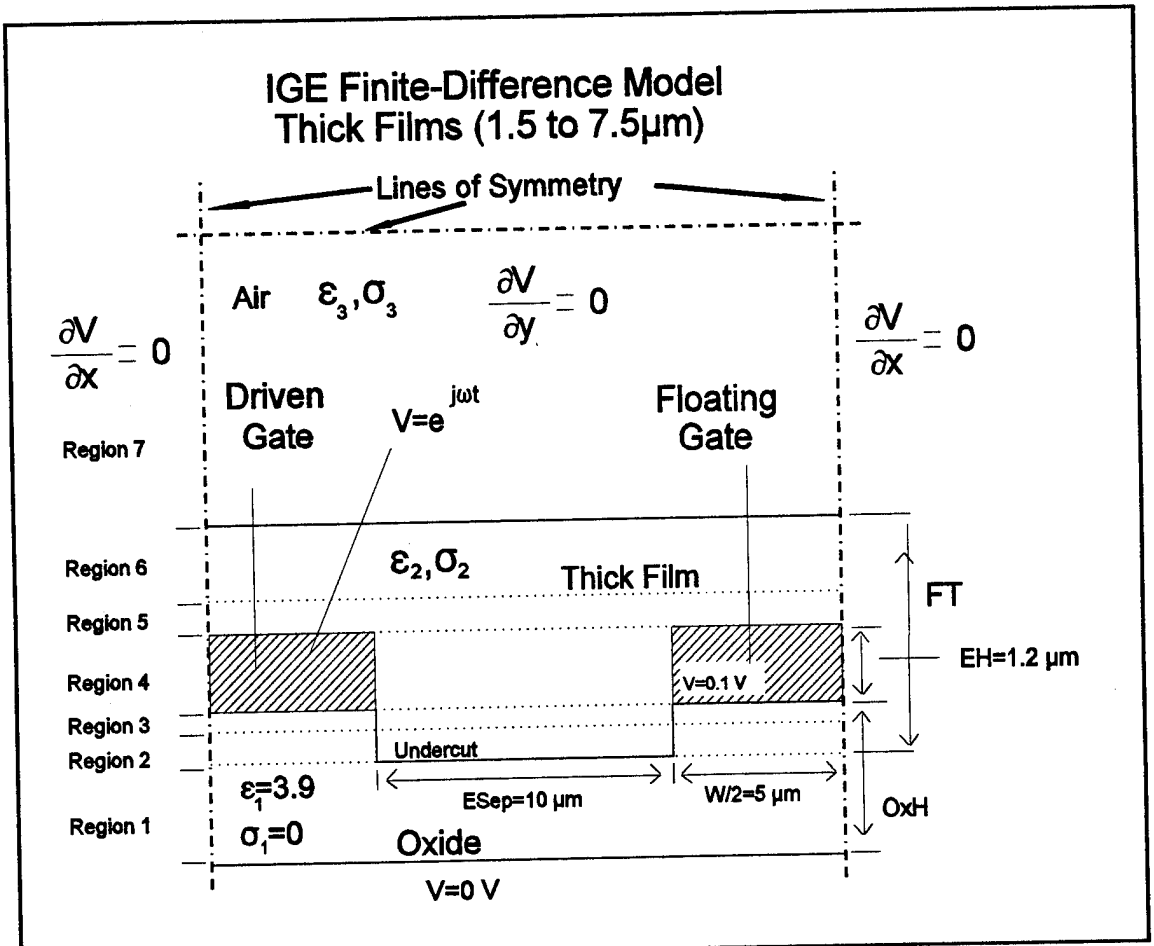


Figure V-9. Planar Finite-Difference Model (W is the Electrode Width, FT is the Film Thickness, OxH is the Oxide Thickness, EH is the Electrode Height, and ESep is the Inter-Electrode Space. Applied Potentials are in Volts).

network, the two-port admittance parameters can then be calculated from the driven- and floating-gate electrode voltages and currents. Finally, the transfer function of the interdigitated gate electrode structure coupled to an arbitrary load capacitance is calculated by analyzing the π-equivalent model of the two-port network (see Figure V-21).

Finite-Difference Grid and Boundary Conditions. The interdigitated gate electrode structure consists of pairs of physically- and electrically-isolated electrodes that are separated from a solid metal ground plane by a silicon dioxide dielectric layer. The critical physical dimensions of the IGEFET's interdigitated gate electrode structure are provided in Table V-1. These dimensions were confirmed by microscopic investigation (see Chapter IV). The oxide thickness was also confirmed from electrical measurements of on-chip test capacitors and from calculations based on the MOSIS supplied fabrication diagnostic data. The agreement between these two measurement techniques confirmed the validity of the micrographic measurements of the IGEFET features.

The choice of a suitable physical model of the interdigitated gate electrode structure depends on the thickness of the thin film coating deposited on the structure. From the scanning electron micrographs of the phthalocyanine-coated interdigitated electrodes, Jenkins inferred that the phthalocyanine films deposited by thermal evaporation conformally coated the electrodes (21). Thus, a phthalocyanine film thickness greater than the inter-electrode separation is required to planarize the film's surface. Since the MOSIS design rules do not permit an inter-electrode separation less than 4 μm, the thickness required to planarize the film over the inter-electrode space must be greater than 2 μm. For electrode configurations with a wider separation, an even thicker film is required. Films with a thickness of this magnitude are not desirable for at least two reasons: 1) films with a thickness greater than 1 μm will require multiple sublimations, and 2) the interaction of the test gases of interest with the film is predominantly a surface phenomenon (188). The films of interest in this research were typically less than 1 μm thick and, therefore, the model had to account for a nonplanar film surface. Despite the disadvantages associated with films having a thickness greater than 1 μm, several trial computations were performed with film thicknesses as large as 7.5 μm. To accommodate the thicker films, a second model was developed that treats the film as a planar surface where the inter-electrode space is completely filled. These two models, referred to as the pseudo-planar and planar models, respectively, are shown in Figures V-8 and V-9. The finite-difference grid partitioning these models are described below, following a discussion of some simplifying assumptions.

Since the phthalocyanine films conformally coat the electrodes (see Chapter IV), consideration was given to the film deposited on the sidewalls of the electrodes for the pseudo-planar model. The

Table V-1. Critical Dimensions of the Interdigitated Gate Electrode Structure.

Parameter	Value
Number of fingers in the driven electrode structure (nominal)	35
Number of fingers in the floating electrode structure (nominal)	34
Electrode width (μm) (nominal)	10
Electrode thickness (μm)	1.2 ± 0.2
Electrode length (μm) (nominal)	1340
Inter-Electrode Separation (μm) (nominal)	10
Overall array width (μm) (nominal)	1370
Overall array length (μm) (nominal)	1370
Oxide thickness (μm)	0.9 ± 0.1
Oxide undercut (μm)	0.3 ± 0.1

shaded region in Figure V-10 illustrates a 1 μm thick film which conformally coats a pair of 1 μm thick electrodes with a 10 μm separation. If the shaded region is approximated by a right triangle, the volume occupied on a per-unit length (that is, 1 μm) basis, is 0.5 μm^3. For a 1 μm length segment of the electrode, the total volume between the electrodes, as indicated in Figure V-10, is 20 μm^3. Because the shaded region occupies less than 5% of the inter-electrode volume, it may be neglected in a first-order consideration. In the proposed model for the IGE structure coated with films whose thickness is less than 1.5 μm, the dielectric coating will be modeled as three planar regions (hence, the name pseudo-planar model). As shown in Figure V-8, these three planar regions include the region within the inter-electrode space and the two regions directly above the electrodes.

Since the interdigitated gate electrode structure is physically periodic in its design, every other electrode can be treated as being at the same potential. Further, because the frequency of operation was sufficiently low (wavelength >> electrode length), each electrode can be treated as an equipotential region and, therefore, the analysis was restricted to two dimensions. Leal's analysis of an IGEFET's interdigitated electrode structure revealed that the frequency limit, f_L , for this approximation is given by (194):

$$f_L = \frac{c}{2\pi L\sqrt{\epsilon_r}} \qquad \text{(V-17)}$$

where c is the speed of light, L is the electrode length, and ϵ_r is the relative permittivity of the coating. The corresponding frequency limit for the interdigitated gate electrode structure with an electrode length, $L \approx 1340$ μm, and coated with CuPc, $\epsilon_r \approx 3.6$ (47), is greater than 10 GHz. Furthermore, since the interdigitated gate electrode structure is physically periodic in its design, and assuming that deviations from periodicity within the array and its perimeter are negligible, the model was further restricted to a pair of half-electrodes bounded by vertical planes of symmetry. Nevertheless, a non-symmetrical feature within the array is created at the corners where the inter-electrode space folds around the interdigitated electrodes. The folding of the inter-electrode space around the interdigitated electrodes forms a meander, (illustrated in Figure V-11) whose net length can be measured with respect to the center of the inter-electrode gap. With a 20 μm inter-electrode spacing (ESep), a 10 μm electrode width (W), and a 1000 μm length (L), the corners of the meander contribute less than 5 percent to the total meander length. For even narrower inter-electrode spacings, the contribution of the corners to the meander length decreases.

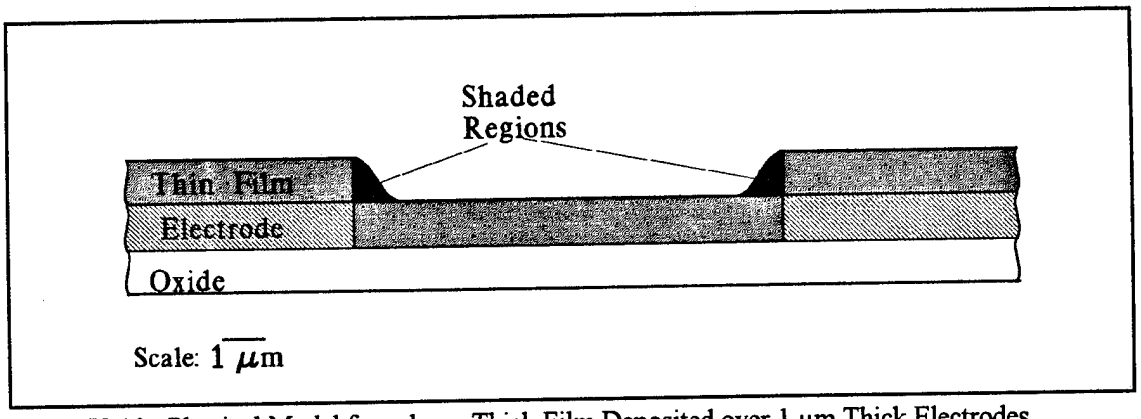


Figure V-10. Physical Model for a 1 μm Thick Film Deposited over 1 μm Thick Electrodes.

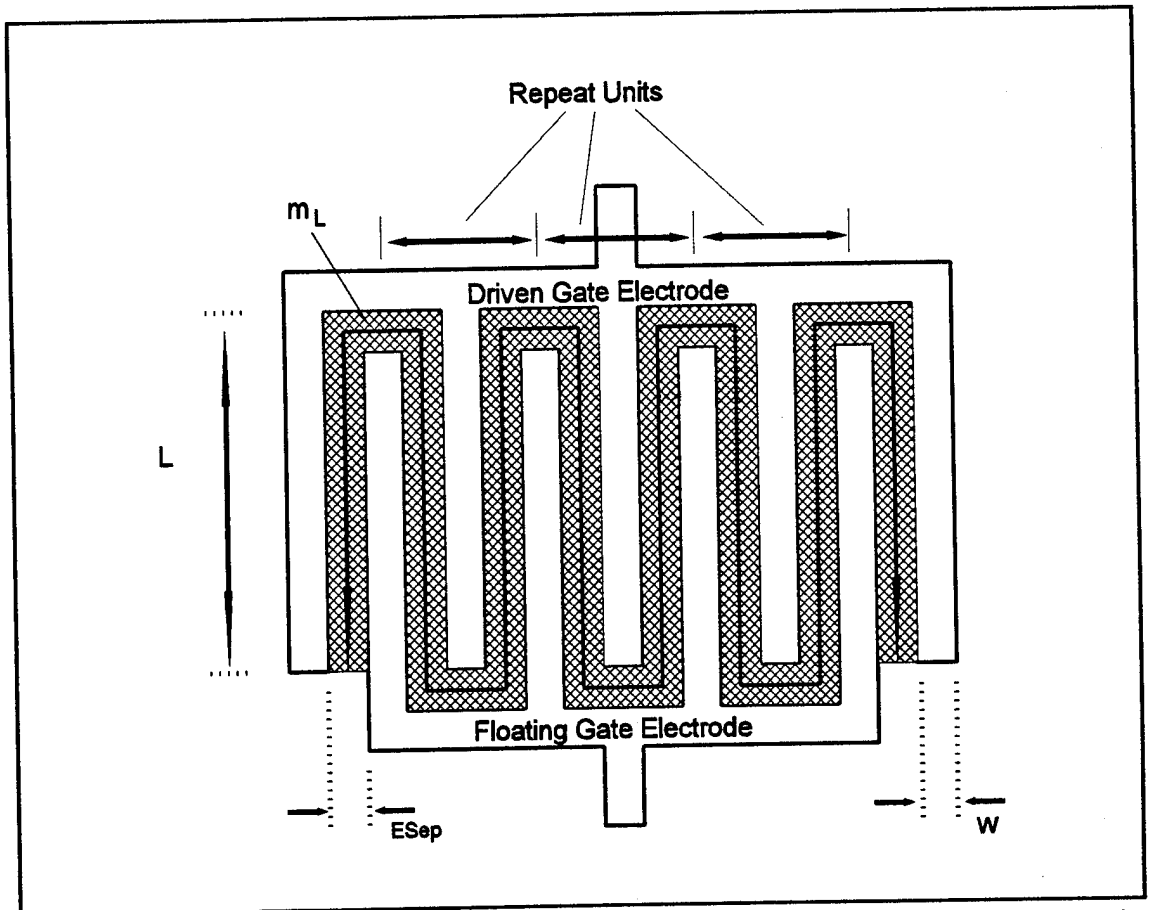


Figure V-11. Meander (shaded region) Created by Folding the Inter-Electrode Space Around the Interdigitated Electrodes. (L is the Electrode Length, W is the Electrode Width, ESep is the Inter-Electrode Separation, and m_L is the Meander Length Measured with respect to the Center of the Inter-Electrode Gap).

Although the deviation at the corners of the meander is independent of the number of fingers in the electrode array, the deviation from periodicity on the lateral sides of the array diminishes as the number of fingers increases. For the same electrode geometries discussed in the preceding paragraph, an array with 10 fingers on the driven-gate electrode and 9 fingers on the floating-gate electrode, the contribution of the lateral fingers to the meander is on the order of 10 percent. The contribution of the lateral sides to the meander length is dominated by the electrode length and the number of electrode fingers. For the current IGEFET geometry (see Table V-1) the lateral sides contribute less than 5 percent to the total meander length. Thus, the deviation from periodicity along the lateral sides of the array may be neglected. In support of this argument, Lee experimentally verified a similar model which neglected the deviations from periodicity around the perimeter of an interdigitated array possessing 10 fingers on the floating-gate electrode and 9 fingers on the driven-gate electrode (190). In Lee's array, the lateral sides contributed approximately 10 percent to the overall meander length.

The finite-difference grid employed to discretize the interdigitated gate electrode structure was divided into six vertical regions for the pseudo-planar model and seven vertical regions for the planar model. These regions correspond to boundaries between different materials or to changes in the resolution of the finite-difference grid. The model's accuracy and computation time depends on the number of nodes used to partition the interdigitated gate electrode structure. Areas with intense electric fields require closer node spacing (finer grid resolution) compared to those areas with small potential variations. However, in regions where the potential variations are small, fine node spacing is inappropriate because it significantly increases computation time and yields only a marginal improvement in accuracy. Since the potential changes most rapidly between the electrodes, and between the electrodes and the ground plane, a fine mesh was used in Regions 1-5 in both models. In contrast, a larger vertical spacing was chosen for the remaining regions in both models since less potential variation in these regions was expected (compared to Regions 1-5) and to avoid the computational burden associated with the large vertical dimensions of these regions.

Since no analytical method for determining the mesh sizes exists, the mesh sizes selected for Regions 1-3, 6, and 7 were based on the mesh sizes used by Lee (190). Except for the oxide undercut, Regions 1-3 have a vertical geometry similar to Lee's model. Lee used a vertical mesh dimension with n_V-vertical nodes and a spacing of OxH/(n_V-1), where OxH represents the oxide thickness. For modeling the IGEFET, n_V was equal to ten, and OxH was equal to 0.9 μm, yielding a vertical resolution of 0.1 μm. Similarly, Region 6 and Region 7 of the pseudo-planar and planar models, respectively, possess a vertical geometry identical to the second and third regions in Lee's model. Of the two regions in Lee's

model, the second region has the greatest vertical resolution (1 μm). In the current models, Region 6 (pseudo-planar model) and Region 7 (planar model) used a mesh containing 15 vertical nodes with a 1 μm vertical resolution. These parameters were computationally determined (by trial) to ensure: 1) sufficient mesh resolution and, 2) to establish the upper boundary's position, so that the Neumann boundary condition could be invoked with sufficient solution accuracy (the computational trials are discussed later in this section).

Region 4 and Region 5 in both models, as well as Region 6 for the planar model, contain the finite thickness electrodes and the thin film coating. Since the combined thickness of Regions 4 and 5 was less than 3 μm, the 1 μm vertical resolution of the equivalent mesh in Lee's model was noted to be unacceptable. Instead of the 1 μm resolution used by Lee, a 0.1 μm vertical resolution was assigned to these regions. The determination of this grid resolution for Regions 4 and 5 was based upon the grid resolution employed between the interdigitated electrodes and the ground plane, where the potential variation is large. In a recent study with a finite thickness interdigitated electrode model (195), this resolution produced results comparable to those reported by Lee. For the thick films studied in the planar model, maintaining the 0.1 μm vertical resolution for the entire film thickness would have resulted in an unnecessary computational burden. Therefore, a slightly larger resolution of 0.5 μm was assigned to Region 6 (planar model) which represents the portion of the film which extends beyond the 1.5 μm height located above the interdigitated electrodes.

The horizontal grid for all regions in both models was defined to have a total of 33 nodes with a horizontal resolution of 1 μm for nodes in the same columns as the electrodes, and a variable horizontal resolution for the node columns located within the inter-electrode space of ESep/20, where ESep is the inter-electrode separation. The selection of this number of nodes was again based on Lee's simulation, which had essentially the same horizontal geometry as the current model. However, this model accommodates a variable inter-electrode separation which spans 4-20 μm and, therefore, either the number of nodes or the resolution must be allowed to vary. For an inter-electrode separation and electrode width of 12.5 μm, Lee employed a mesh with a horizontal resolution on the order of 1 μm. Maintaining a ratio of 1 μm horizontal resolution relative to a 12.5 μm inter-electrode space, a 4 μm inter-electrode space requires a minimum horizontal resolution of approximately 0.3 μm. If the horizontal resolution is fixed at 0.3 μm, more than 66 nodes would be required to model the interdigitated electrodes with a 20 μm inter-electrode space. A more computationally efficient approach allows the resolution to vary. That is, a 1 μm minimum horizontal resolution for interdigitated electrodes with a maximum inter-electrode spacing of 20 μm requires 20 nodes. To minimize the number of

horizontal nodes required in the mesh, the horizontal resolution beneath the 5 μm wide half-electrodes was fixed at 1 μm. Thus, a total of 30 horizontal nodes are required to model the interdigitated electrode structure. Finally, three additional horizontal nodes are required to perform the simulation. Two of the additional nodes are required to implement the Neumann boundary conditions (discussed below), and the third node provides an origin (reference point).

In general, the fineness of the grid may be varied by changing either the horizontal or vertical spacing. Although the horizontal grid spacing can be allowed to vary between vertical regions, this flexibility requires the development of a different finite-difference formula at the interface of the two vertical regions to account for the mismatch in the number of nodes (190). Figure V-12 illustrates the mismatch between two vertical regions where the grid resolution in one vertical region is twice that of the other. At the interface, grid loci alternate between possessing four and five nearest neighbors (N. N.). Therefore, the same horizontal spacing was maintained in different vertical regions of the finite-difference grid.

The introduction of the oxide undercut and the pseudo-planar deposition of the dielectric film required the development of general finite-difference equations similar to Equation (V-15) for the vertical interfaces and corners indicated in Figures V-13. The equations corresponding to these interfaces are provided in Appendix H.

The potential distribution within this finite-difference grid can be uniquely determined for a given set of boundary conditions. Both Dirichlet and Neumann boundary conditions are imposed on the interdigitated gate electrode structure, as shown in Figures V-8 and V-9. A sinusoidal voltage, V = 1 - 0j volts, was applied to the driven-gate electrode in the analysis. The ground plane was assigned a voltage, V = 0 - 0j volts. Although in practice the floating-gate electrode is left floating and effectively connected to ground through a high impedance leakage path through the gate oxide and doped semiconductor, it is necessary to assign a particular voltage to the floating-gate electrode to establish a valid boundary condition to uniquely solve Poisson's equation. Assuming that the interdigitated gate electrode structure, along with the thin film coating, comprise a pseudo-linear system, assigning a voltage to the floating-gate electrode should not affect the calculation of the system's transfer function. In an earlier study (195), an arbitrary voltage applied to the floating-gate electrode was shown to only influence the convergence rate of the simulation. When the floating-gate electrode was grounded (V=0-0j volts), the solution converged after 1659 iterations. When a small voltage (0.001V) was applied to the floating-gate electrode, the number of iterations required to achieve convergence was reduced to 624. Increasing the applied voltage on the floating electrode to 0.1 V, and then to 0.9 V, did not enhance

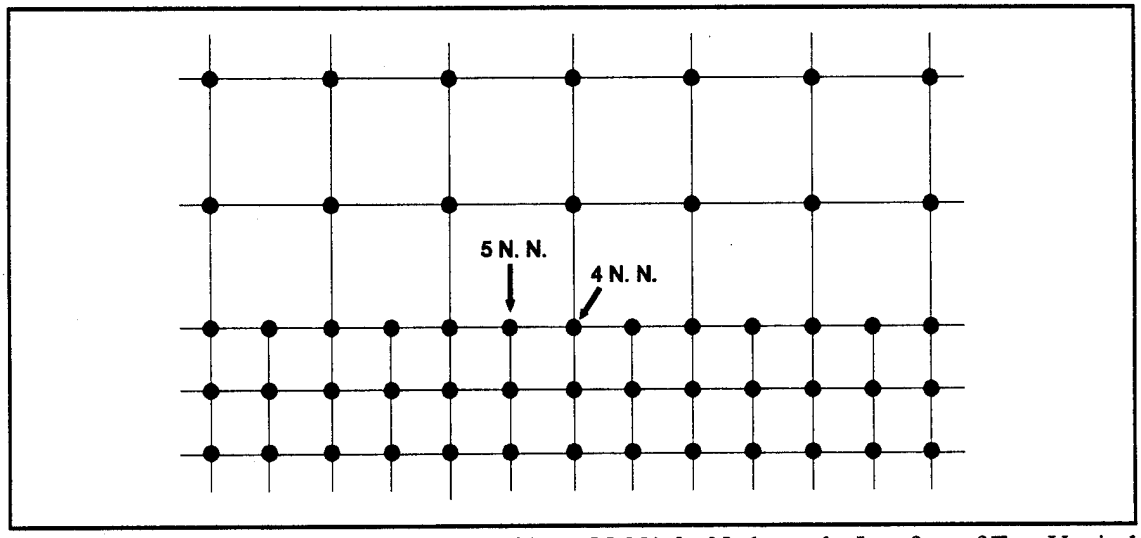


Figure V-12. Variable Number of Nearest Neighbors (N. N.) for Nodes at the Interface of Two Vertical Grid Regions with Different Grid Resolutions.

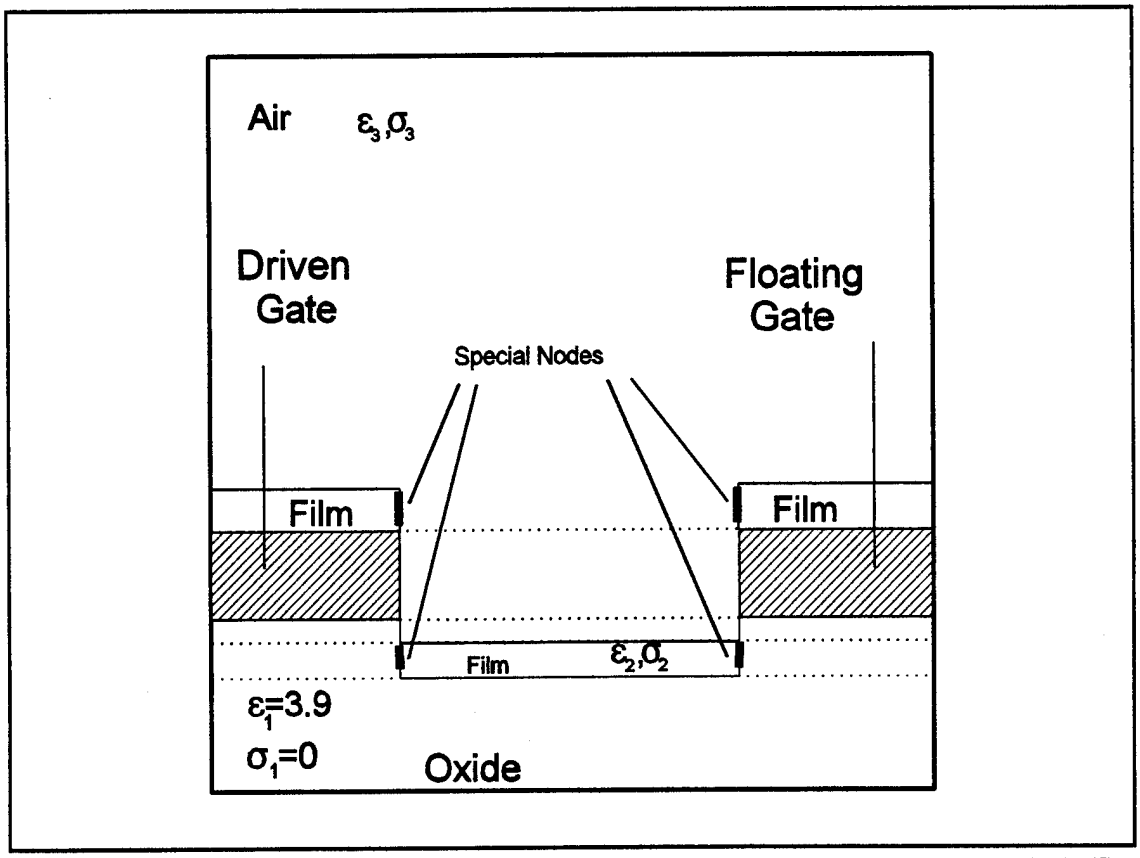


Figure V-13. Nodes Requiring the Development of Modified Forms of Equation V-15 (See Appendix H).

the convergence rate. Additional computational trials performed during this research demonstrated that a potential drop of 2.0 V, -0.1 V, and -0.9 V on the floating-gate electrode did not alter the computed gain/phase of the IGE structure, nor did they enhance the convergence rate. Based upon these results and the earlier study, a voltage of 0.1 V was assigned to the floating-gate electrode to establish the Dirichlet boundary condition at this electrode. It should be emphasized that, although the transfer function for a linear system is not affected by assigning a voltage to the floating-gate electrode, the electric field and potential distributions within the interdigitated electrode structure are significantly altered and will not represent the field distributions within the actual IGEFET microsensor. The applied voltage independence of the calculated interdigitated gate electrode structure's gain/phase contributes to the confidence in the model configuration and results.

Since the electrode structure is bounded by vertical lines of symmetry, the Neumann boundary condition is imposed, with the normal derivative of the potential equal to zero, or $\partial V/\partial x = 0$. The upper boundary condition is more difficult to specify because the region above the coated electrodes is semi-infinite, although it is modeled as a finite field. The semi-infinite boundary condition may also be modeled by the Neumann boundary condition ($\partial V/\partial y = 0$). The application of this Neumann boundary condition implies the existence of a mirrored set of conductors at a symmetrical distance with respect to the upper boundary, but if the line of symmetry is sufficiently far from the electrodes, the interaction of the electrodes with the mirrored conductors would be negligible, and the boundary at infinity is, correspondingly, adequately modeled (190).

The position of the upper boundary at which the Neumann boundary condition becomes valid was determined by repetitively performing the simulation as a function of the upper boundary's location. As the distance between the interdigitated electrodes and the upper boundary was increased (by increasing the number of vertical nodes in Region 6 (pseudo-planar model) or Region 7 (planar model) mesh), the solution variation in successive simulations decreased. The vertical grid resolution for both models in these regions was fixed at 1μm. Therefore, the number of vertical nodes in these regions determined the upper boundary position relative to the top surface of the deposited film. In order to neglect the film thickness, the calculations were performed with thin films (typically 0.2 μm thick). Although the modeled "deposited" film was thin, most of the calculations were performed with the complex permittivity of the top region matched to the complex permittivity of the "deposited" film. This configuration produced an effective semi-infinitely thick film above the interdigitated electrodes. The solution variation with respect to the upper boundary position was measured as the percent change in

the gain for a given upper boundary position relative to the gain calculated with the upper boundary position located at 20 μm (20 nodes).

Figures V-14 and V-15 illustrate the effect of the upper boundary position on the solution for various film complex permittivities. Increasing the magnitude of either the real or imaginary part of the complex permittivity requires that the upper boundary position be located at a greater distance from the interdigitated electrodes. These results are consistent with the expected increase of the electric field's penetration into the semi-infinite region above the electrodes as the complex permittivity increases. However, for thin films, a greater portion of the electric field will be confined within the thin film, and the upper boundary position may be lowered without significantly affecting the solution. This behavior was observed for a 1.2 μm thick film, as shown in Figure V-16. To ensure a valid Neumann boundary condition at the top of the grid, an upper boundary position of 15 μm, which produced less than a 2 percent change in the calculated gain for all cases evaluated, was selected for the remaining calculations.

To further investigate the validity of the selected model conditions, contour plots of the calculated potential distribution were examined. Figures V-17 through V-22 represent contour plots of the potential distribution within the interdigitated gate electrode structure for films of different thickness and complex permittivity. These plots were generated with a constant vertical resolution of 0.1 μm to avoid distortion of the potential field in the vertical direction. However, the horizontal resolution was not held constant across these plots: 1.0 μm resolution for nodes above and below the electrodes, and 0.5 μm resolution for nodes between the electrodes. The fine vertical resolution for the entire grid required the upper boundary position be reduced to 11-12 μm so that the data structure would not exceed the 64K byte data segment of the 80486-based computer. Modification of the vertical resolution and the upper boundary position had only a slight effect on the computed gain as shown in Table V-2. The finer vertical resolution caused a significantly longer computation time, and in general, required a stricter convergence condition (defined in a later sub-section entitled Finite-Difference Model Implementation). Figure V-23 shows that the maximum relative residue (defined in the Finite-Difference Model Implementation sub-section) must be reduced in order for the calculated gain to reach a stable value when the finer vertical grid resolution was used. Examination of Figures V-17 through V-22 reveals several features of the calculated potential distributions. In addition to satisfying the Neumann and Dirichlet boundary conditions, the equipotential lines beneath the electrodes approximate the potential distribution expected for infinite parallel plates. This behavior is consistent with the geometry of the interdigitated gate electrode structure (10 μm wide electrodes and 0.9 μm electrode-to-ground separation). As the film thickness was increased, the potential decayed more slowly as the distance from

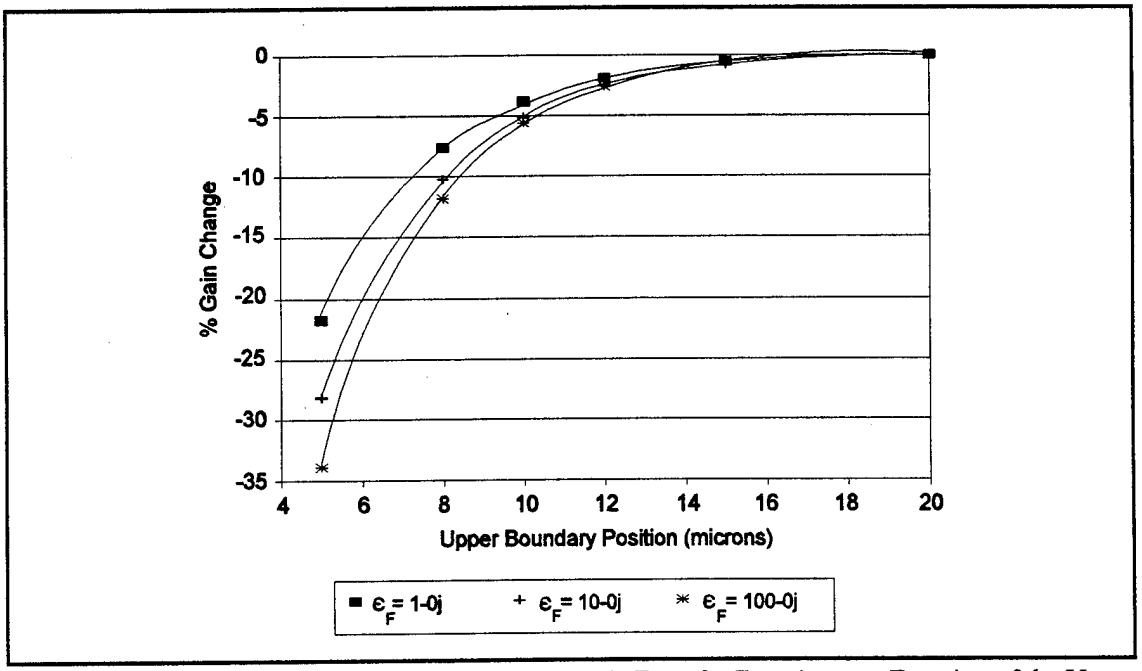


Figure V-14. Percent Gain Change in the IGE Structure's Transfer Function as a Function of the Upper Boundary Position for Various Relative Permittivity Values. (EH=1.2 μm, OxH=0.9 μm, UC=0.3 μm, FT=0.2 μm, ESep=10 μm, Vertical Resolution=1 μm).

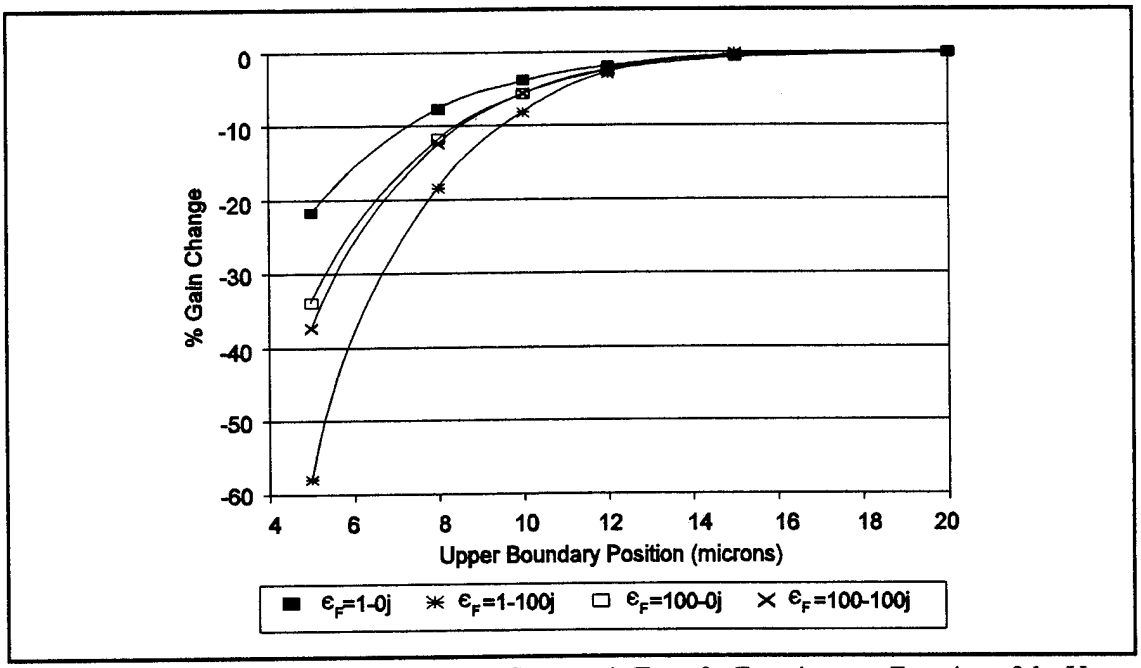


Figure V-15. Percent Gain Change in the IGE Structure's Transfer Function as a Function of the Upper Boundary Position for Different Relative Permittivity Values. (EH=1.2 μm, OxH=0.9 μm, UC=0.3 μm, FT=0.2 μm, ESep=10 μm, Vertical Resolution=1 μm).

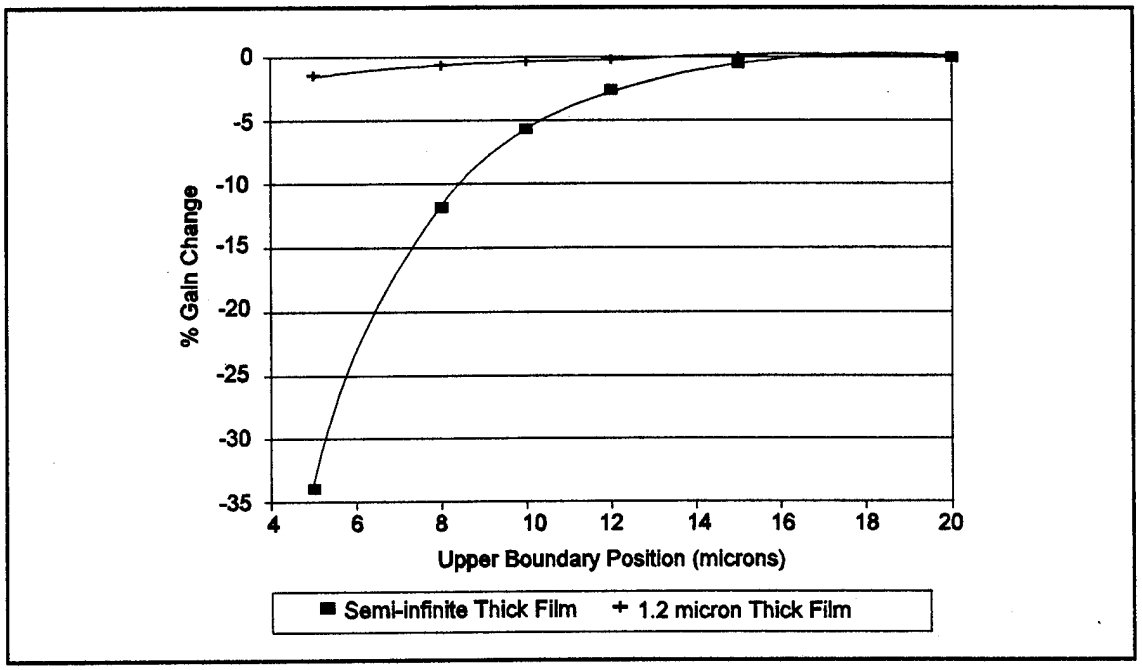


Figure V-16. Percent Gain Change in the IGE Structure's Transfer Function as a Function of Upper Boundary Position and Film Thickness. (EH=1.2 μm, OxH=0.9 μm, UC=0.3 μm, ϵ_F=100-0j, ESep=10 μm, Vertical Resolution=1 μm).

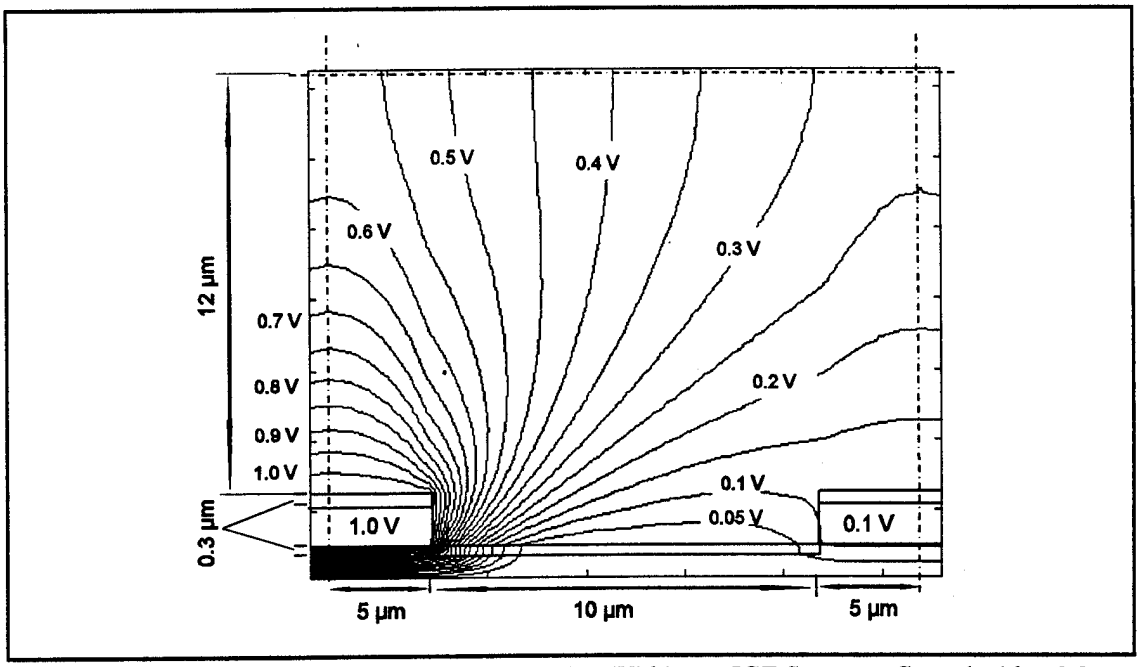


Figure V-17. Contour Plot of the Potential Distribution Within an IGE Structure Coated with a 0.3 μm Thick Film. (The Equi-Potential Lines are Spaced at 0.05 V Intervals. EH=1.2 μm, OxH=0.9 μm, UC=0.3 μm, ϵ_F=1-20j, ESep=10 μm, Vertical Resolution=0.1 μm).

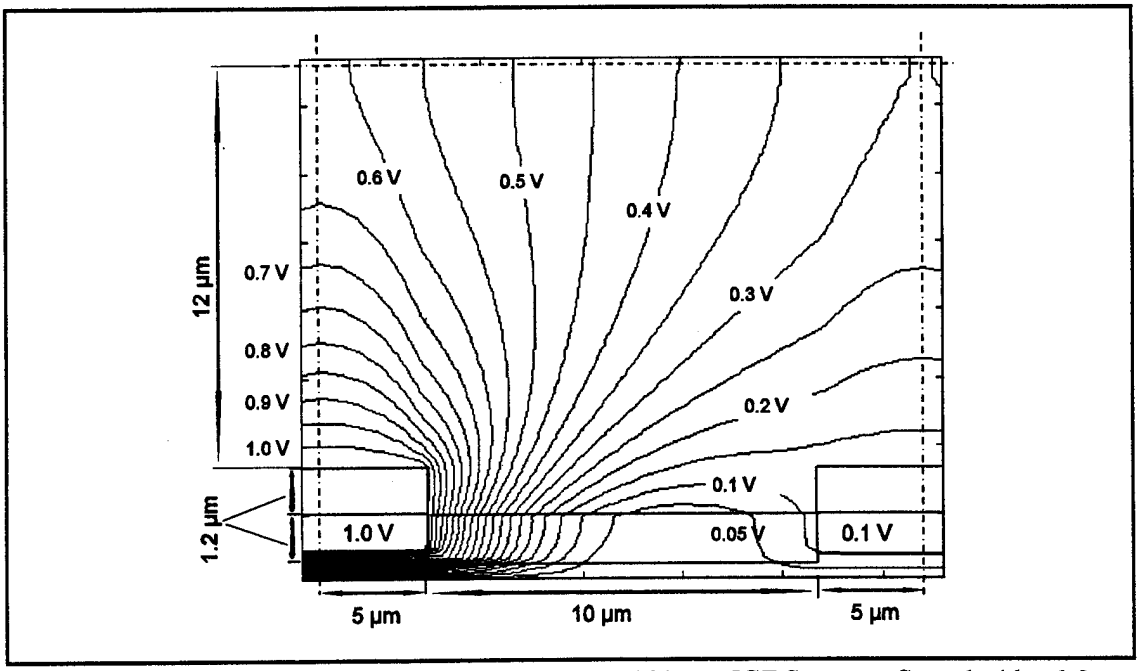


Figure V-18. Contour Plot of the Potential Distribution Within an IGE Structure Coated with a 1.2 µm Thick Film. (The Equi-Potential Lines are Spaced at 0.05 V Intervals. EH=1.2 µm, OxH=0.9 µm, UC=0.3 µm, ϵ_F=1-20j, ESep=10 µm, Vertical Resolution=0.1 µm).

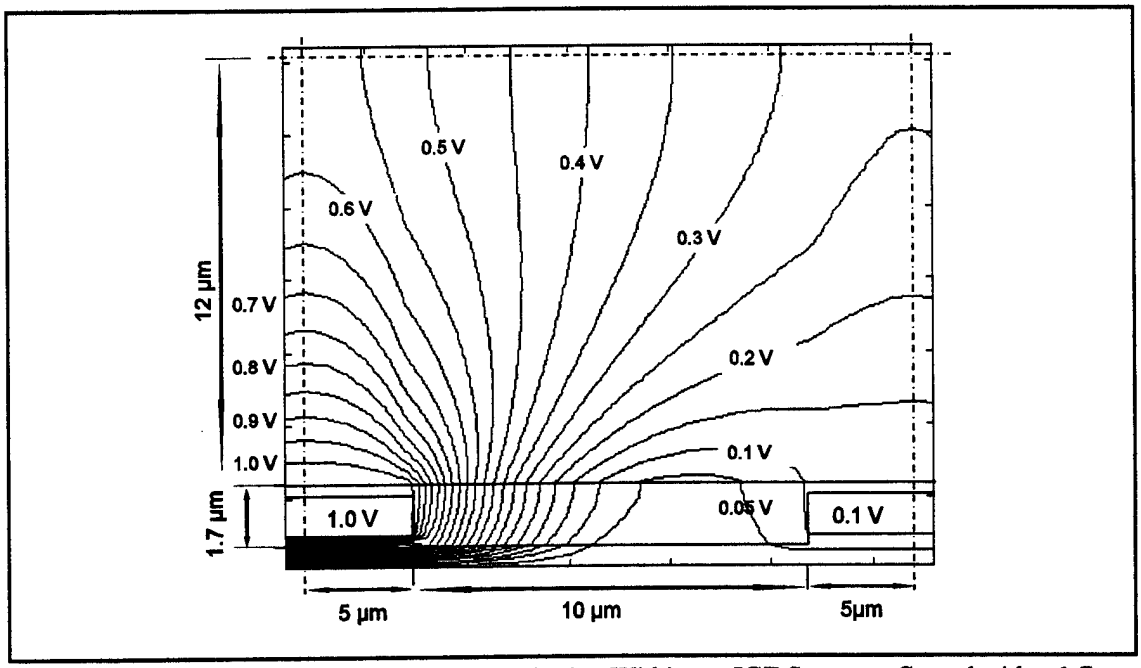


Figure V-19. Contour Plot of the Potential Distribution Within an IGE Structure Coated with a 1.7 µm Thick Film. (The Equi-Potential Lines are Spaced at 0.05 V Intervals. EH=1.2 µm, OxH=0.9 µm, UC=0.3 µm, ϵ_F=1-20j, ESep=10 µm, Vertical Resolution=0.1 µm).

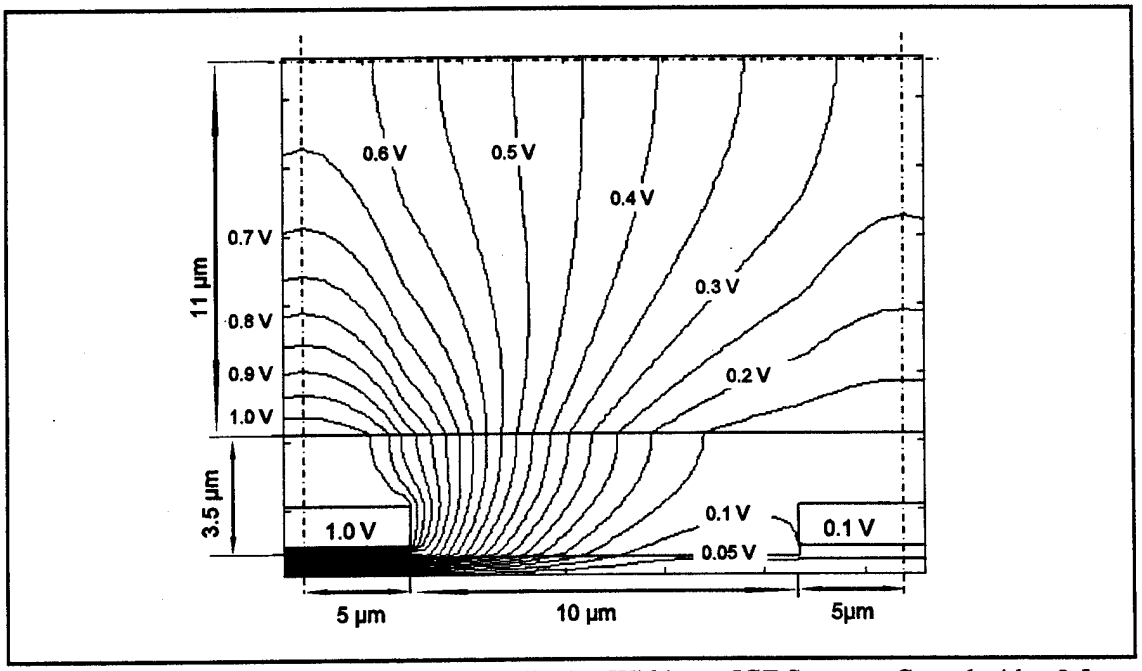


Figure V-20. Contour Plot of the Potential Distribution Within an IGE Structure Coated with a 3.5 µm Thick Film. (The Equi-Potential Lines are Spaced at 0.05 V Intervals. EH=1.2 µm, OxH=0.9 µm, UC=0.3 µm, ϵ_F=1-20j, ESep=10 µm, Vertical Resolution=0.1 µm).

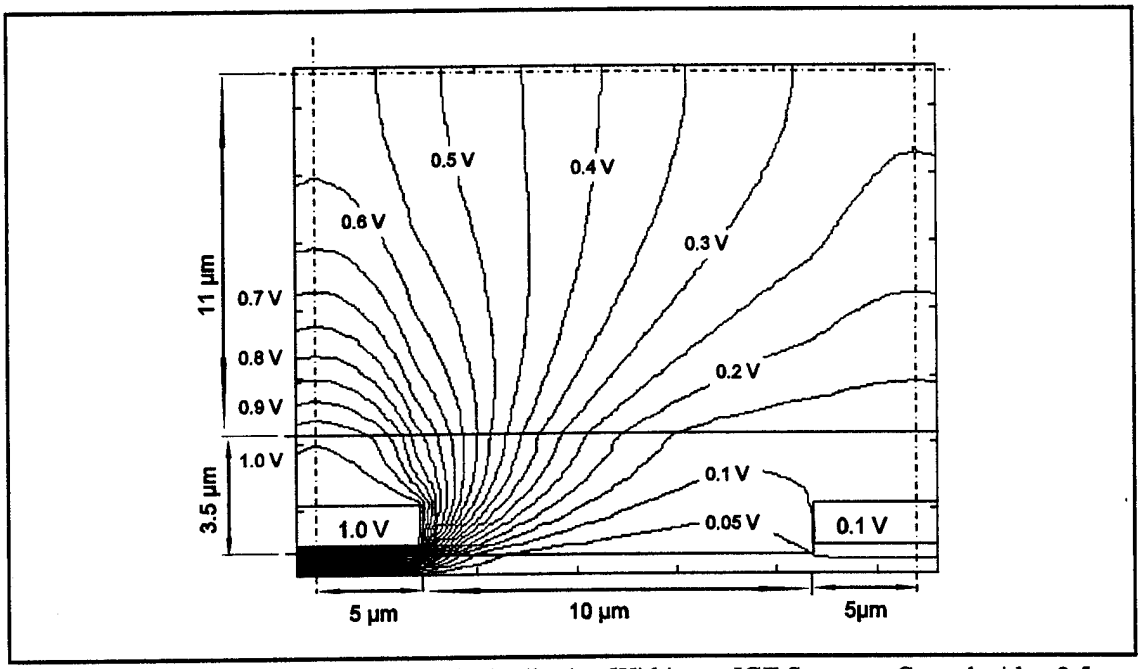


Figure V-21. Contour Plot of the Potential Distribution Within an IGE Structure Coated with a 3.5 µm Thick Film. (The Equi-Potential Lines are Spaced at 0.05 V Intervals. EH=1.2 µm, OxH=0.9 µm, UC=0.3 µm, ϵ_F=1-2j, ESep=10 µm, Vertical Resolution=0.1 µm).

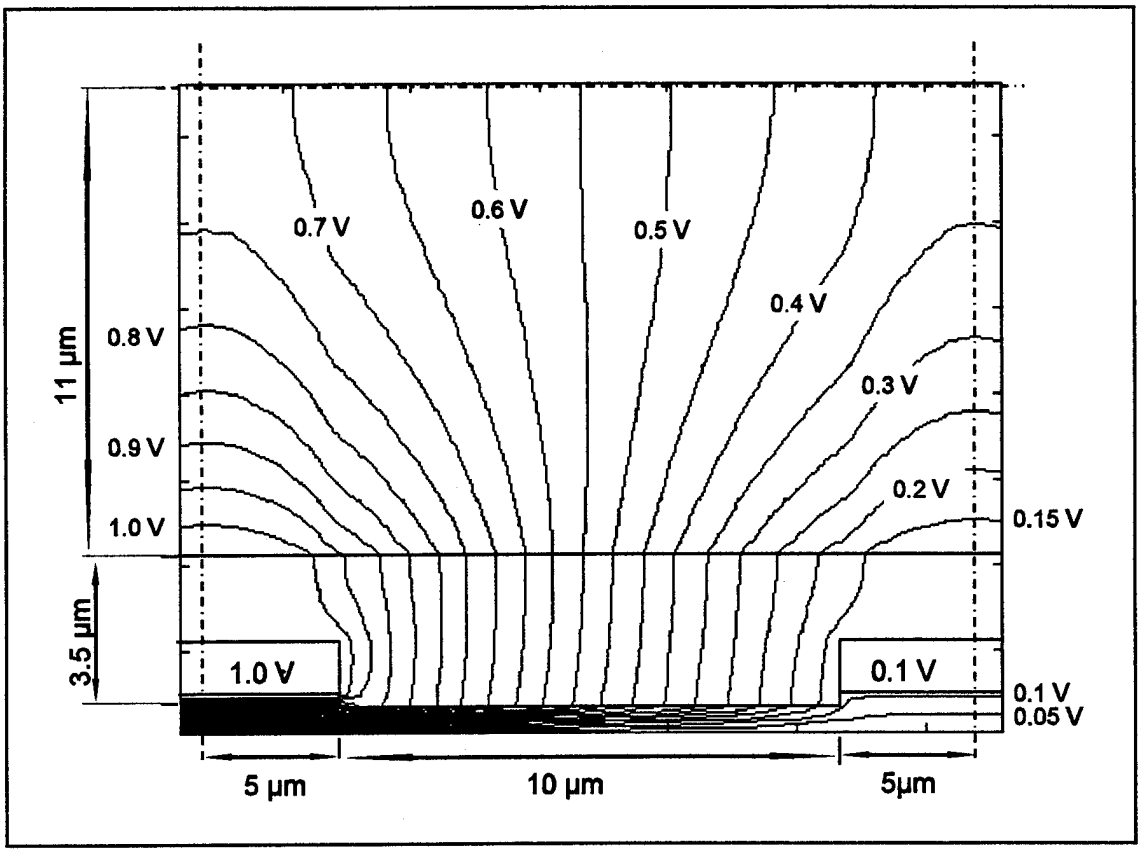


Figure V-22. Contour Plot of the Potential Distribution Within an IGE Structure Coated with a 3.5 µm Thick Film. (The Equi-Potential Lines are Spaced at 0.05 V Intervals. EH=1.2 µm, OxH=0.9 µm, UC=0.3 µm , ϵ_F=1-100j, ESep=10 µm, Vertical Resolution=0.1 µm).

Table V-2. Variation in the Calculated Gain for Various Model Geometries (continued on next page).

Deposited Film Thickness (μm)	Deposited Film Permittivity		Upper Boundary Position (μm)	Vertical Resolution (μm)	Maximum Relative Residue	Gain (dB)
	ϵ'	ϵ''				
0.3	1	20	12	0.1	10^{-5}	-40.7
				1.0	10^{-4}	-40.4
	20	10	15	0.2	$2 \cdot 10^{-5}$	-39.9
				0.5	10^{-4}	-39.7
				1.0	10^{-4}	-39.6
	20	100	12	0.1	10^{-5}	-43.0
				1.0	10^{-4}	-43.2
			15	0.2	10^{-5}	-43.8
				1.0	10^{-4}	-43.9
	20	1000	15	0.2	10^{-4}	-6.23
					10^{-5}	-6.22
				1.0	10^{-4}	-6.21
1.2	1	2	12	0.1	10^{-5}	-40.4
				1.0	10^{-4}	-40.4
	1	10	15	0.2	10^{-5}	-39.8
				1.0	10^{-4}	-39.8
	1	20	12	0.1	10^{-5}	-46.2
				1.0	10^{-4}	-46.5
	1	100	15	0.2	10^{-4}	-13.5
				1.0	10^{-4}	-13.4
	1	1000	15	0.2	10^{-5}	-0.648
				1.0	10^{-4}	-0.687
For all cases: Oxide Height = 0.9 μm; Electrode Height = 1.2 μm; Oxide Undercut = 0.3 μm.						

Table V-2. Variation in the Calculated Gain for Various Model Geometries (continued from preceding page).

Deposited Thickness (μm)	Deposited Film Permittivity		Upper Boundary Position (μm)	Vertical Resolution (μm)	Maximum Relative Residue	Gain (dB)
	ϵ'	ϵ''				
1.7	1	20	12	0.1	10^{-5}	-34.5
				1.0	10^{-4}	-34.9
			15	1.0	10^{-4}	-35.1
3.5	1	2	11	0.1	10^{-5}	-39.3
				1.0	10^{-4}	-39.3
	1	20	11	0.1	10^{-5}	-22.4
				1.0	10^{-4}	-22.4
			15	1.0	10^{-4}	-22.5
	1	100	11	0.1	10^{-5}	-5.19
				1.0	10^{-4}	-5.18
			15	1.0	10^{-4}	-5.19
For all cases: Oxide Height = 0.9 μm; Electrode Height = 1.2 μm; Oxide Undercut = 0.3 μm.						

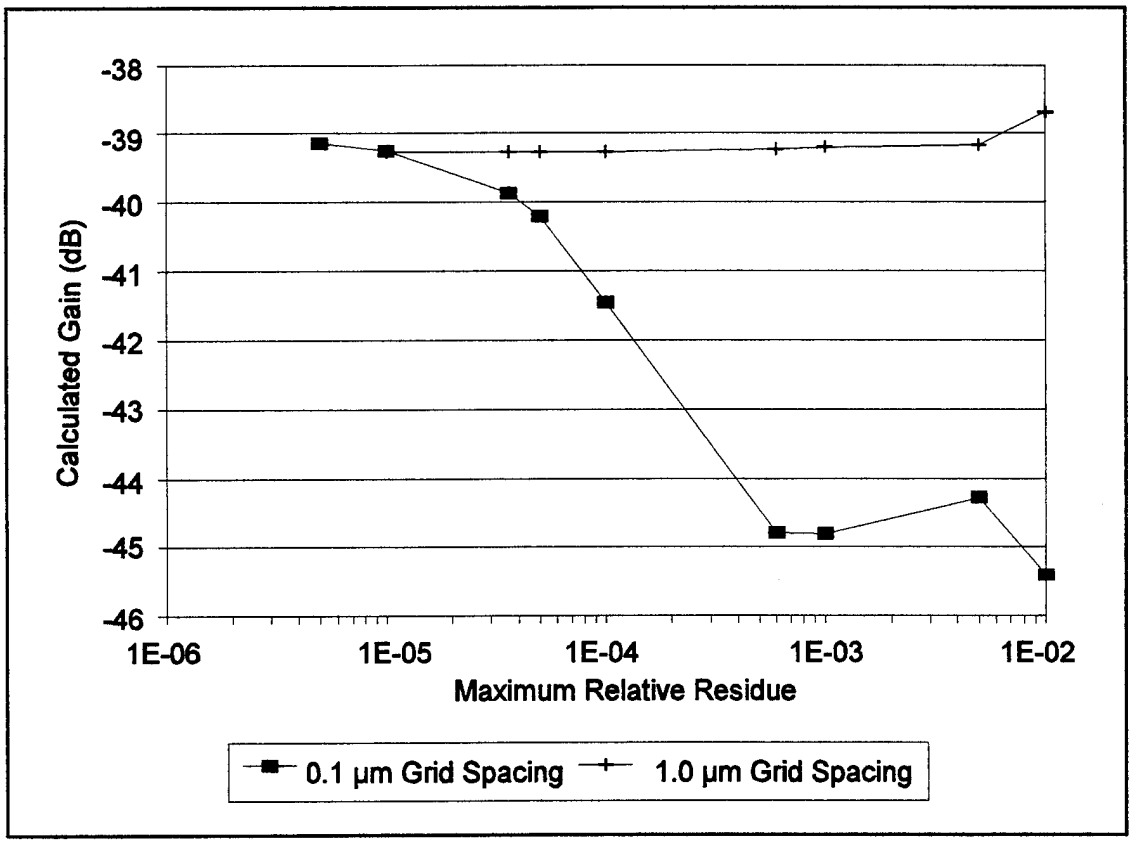


Figure V-23. Calculated Gain for a IGE Structure Coated with a 3.5 µm Thick Film as a Function of the Maximum Relative Residue and Vertical Grid Spacing (EH=1.2 µm, OxH=0.9 µm, UC=0.3 µm , ϵ_F=1-2j, ESep=10 µm).

the electrodes was increased. The rate that the potential decreased was the greatest in air, and the rate decreased with corresponding increases in the film's dielectric loss. Therefore, when the thin film coated IGE structure is operated as a gas sensor, a challenge gas which increases the thin film's conductivity will cause an increase in the coupling between the electrodes.

Admittance Parameter Calculations. The finite-difference calculation yields the potential distribution within the interdigitated gate electrode structure when a specific voltage is assumed on the driven and floating electrodes. To obtain the interdigitated gate electrode's transfer function, the two-port admittance parameters were extracted from the potential distribution. The admittance parameters were calculated from the applied terminal voltages, and the terminal currents were determined by applying Gauss' Law to the potential distribution from the finite-difference calculation. Once the admittance parameters were obtained, the transfer function was further modified to account for an arbitrary capacitive load (the effect of the *in-situ* MOSFET gate structure).

This approach assumes that the materials used to fabricate the interdigitated gate electrode, including the thin films deposited on the gate, form a linear, and time-invariant system. A sufficient condition for linearity is that the superposition principle is applicable; that is, the response of a system to the linear combination of two or more signals is equal to the sum of the responses produced by each signal applied separately (196). This condition implies that the transfer function of the system is independent of the magnitude of the excitation signal. Real systems, in general, are not perfectly linear. However, any continuous, differentiable function is linear over a range of sufficiently small input values. Thus, a non-linear system may be treated as a linear system provided the excitation signal is sufficiently small that the superposition principle applies. Correspondingly, a system is time-invariant if its response is independent of the time period over which it is being observed (102). In this study, since the change in the sensor's electrical properties results from a change in the chemical state of the thin film as its interacts with a gaseous environment, the system is not totally time-invariant. However, a time-invariant analysis can be used if the time required to perform any given measurement is short relative to the rate of change of the system's response. For the case where the film's chemical state is reversibly modified by gas exposure, the system may be allowed to attain equilibrium before making a measurement.

The admittance matrix equation for the interdigitated gate electrode's structure is given by:

$$\begin{bmatrix} I_1 \\ I_2 \end{bmatrix} = \begin{bmatrix} Y_{11} & -Y_{12} \\ -Y_{21} & Y_{22} \end{bmatrix} \begin{bmatrix} V_1 \\ V_2 \end{bmatrix} \qquad \text{(V-18)}$$

where the currents and voltages are complex and have the polarity shown in Figure V-24. Since the interdigitated gate electrode is symmetrical and reciprocal, ($Y_{11}=Y_{22}$ and $Y_{12}=Y_{21}$), the matrix equation can be rearranged as:

$$\begin{bmatrix} I_1 \\ I_2 \end{bmatrix} = \begin{bmatrix} V_1 & -V_2 \\ V_2 & -V_1 \end{bmatrix} \begin{bmatrix} Y_{11} \\ Y_{12} \end{bmatrix} \quad . \tag{V-19}$$

The two-port admittance parameters obtained by left multiplying both sides of Equation (V-19) with the inverse of the voltage matrix are:

$$Y_{11} = (-I_1V_1 + I_2V_2) / (-V_1^2 + V_2^2) \tag{V-20}$$

and

$$Y_{12} = (I_2V_1 - I_1V_2) / (-V_1^2 + V_2^2) \quad . \tag{V-21}$$

Consequently, if the terminal currents and voltages are known, the two-port admittance parameters can be determined. In this situation, the terminal voltages are known, since they are the voltages assigned to the driven- and floating-gate electrodes in the finite-difference calculation. The terminal currents were calculated by evaluating a Gaussian surface integral around the electrodes. Figure V-25 shows the Gaussian surfaces around the interdigitated gate electrodes. The currents obtained from this calculation should be independent of the integration path. This technique is commonly used in electrostatics to calculate the charge enclosed within a closed surface (197, 198). In the sinusoidal steady-state case, the field is complex, and the integration process yields the enclosed complex charge magnitude or current passing through the surface. The driven-gate current, I_1, and the floating-gate current, I_2, through the Gaussian surfaces are given by:

$$I_1 = \oint_{S_1} (\sigma + j\omega\epsilon') \bar{E} \cdot d\bar{S}_1 \tag{V-22}$$

and

$$I_2 = \oint_{S_2} (\sigma + j\omega\epsilon') \bar{E} \cdot d\bar{S}_2 \quad . \tag{V-23}$$

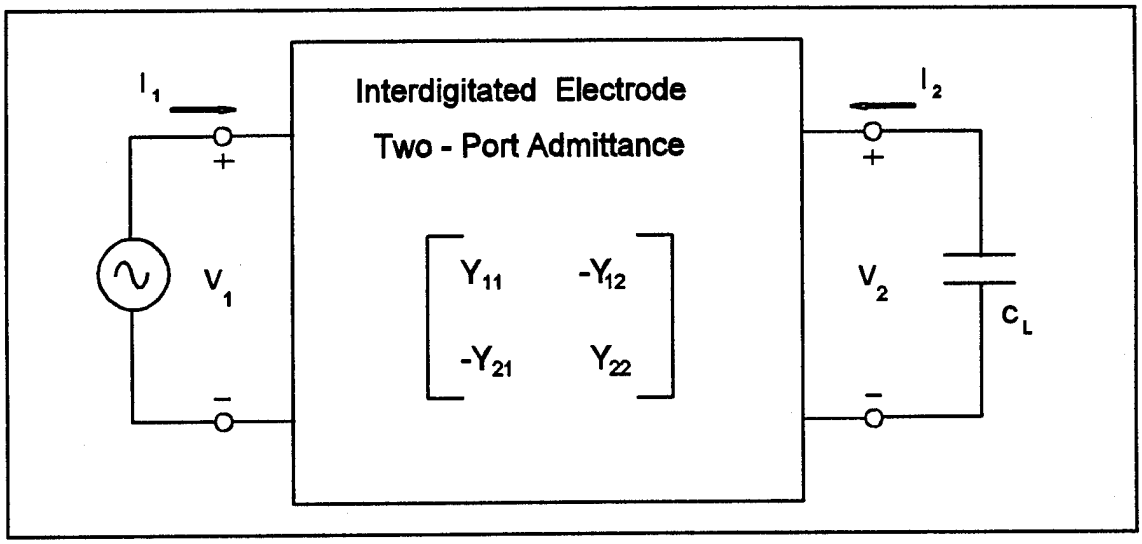


Figure V-24. Two-Port Admittance Parameter Model.

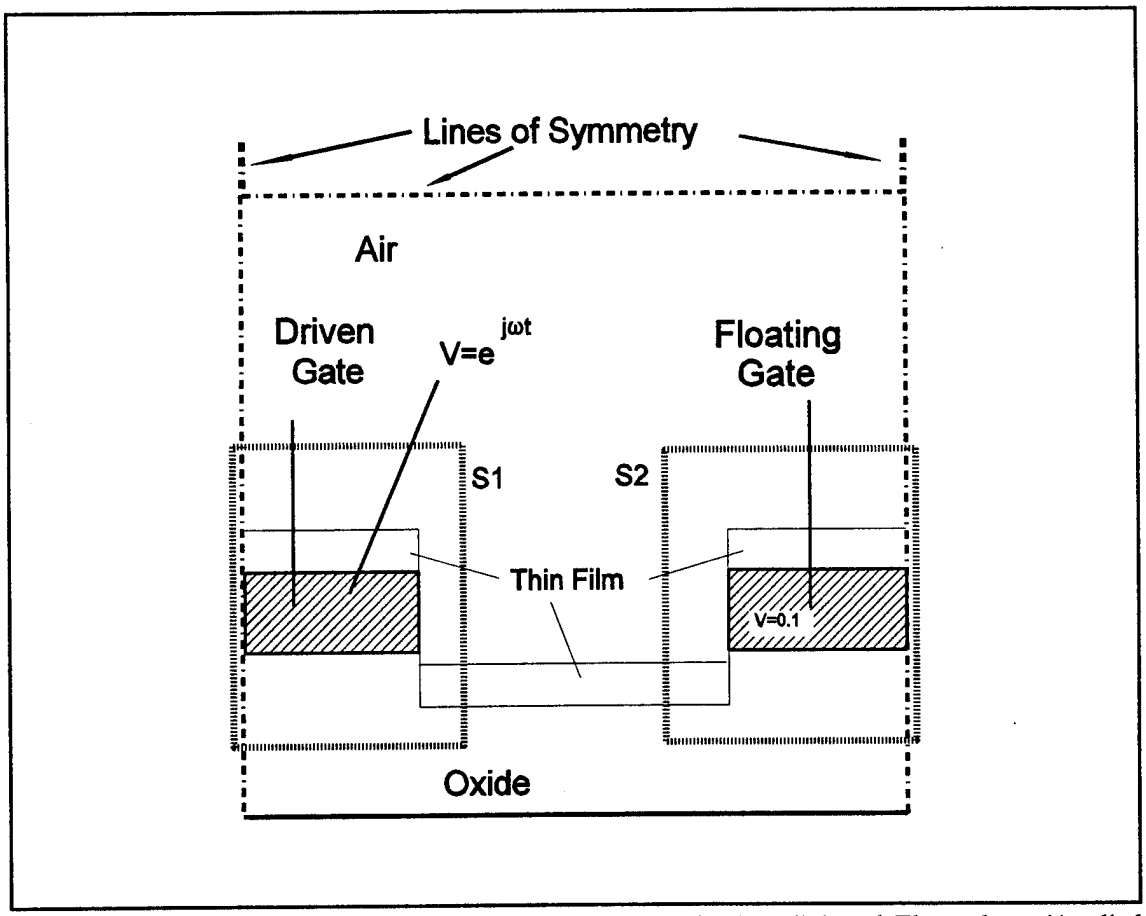


Figure V-25. Surface Integral Paths (S_1 and S_2) around the Interdigitated Electrodes. (Applied Potentials are in Volts).

These integrals were evaluated by summing the differential current elements passing through the Gaussian surface between two nodes, as shown in Figure V-26. Except at the intersection of the lines of symmetry with the Gaussian surface, the admittance elements connecting any two nodes along the integration path are the same as those used in formulating the finite-difference equations (Equations (V-7) and (V-10 through V-12)). The current element passing through the surface shown in Figure V-26 was then calculated using Ohm's Law:

$$I = \frac{[\, V(M,N) - V(M+1,N) \,]\,(\,\sigma + j\omega\epsilon'\,)\,(\,h_1/2 + h_3/2\,)}{h_4} \quad . \qquad \text{(V-24)}$$

For those nodes at the intersection of the integration path with the lines of symmetry, a smaller admittance element is enclosed, as shown in Figure V-27. It is unclear whether Lee accounted for these smaller admittance elements in his algorithm (190). Choosing the Gaussian surface to coincide with the lines of symmetry simplifies the integration since the potential gradient across the lines of symmetry is zero, and the current passing through the Gaussian surface along these lines is also zero. To perform the integration, Lee and other investigators (190, 198) simply summed the current elements along the path. Green (197), on the other hand, halved the first and last differential current components within each linear section of the summation. Green's method is equivalent to integration using the trapezoidal rule. Similar to Lee, this analysis effort applied a simple summation integration technique to obtain the total currents. The two-port admittance parameters calculated using these voltages and currents in Equations (V-20) and (V-21) were doubled, since the model considers only half electrodes. Furthermore, these admittances are expressed on a per-unit-length basis with respect to the interdigitated gate electrode structure.

The overall length of the electrode structure was accounted for by determining the total length of the meander structure formed by the folded space between the interlaced electrodes. The meander length, m_L, is measured with respect to the center of the inter-electrode space, as shown in Figure V-11. When the inter-electrode separation, ESep, and the electrode width (W) are equal, the meander length is given by:

$$m_L = (n_f - 2)(4\text{ESep} + 2\text{L}) + 2(\text{ESep} + \text{L}) \qquad \text{(V-25)}$$

where n_f is the number of fingers on the driven-gate electrode, and L is the electrode length. Applying Equation (V-25) to the array shown in Figure V-11, where $n_f = 5$, the meander length is equal to the sum of the three repeat units of length, 4ESep + 2L, and the two lengths, ESep + 2L, located on the lateral

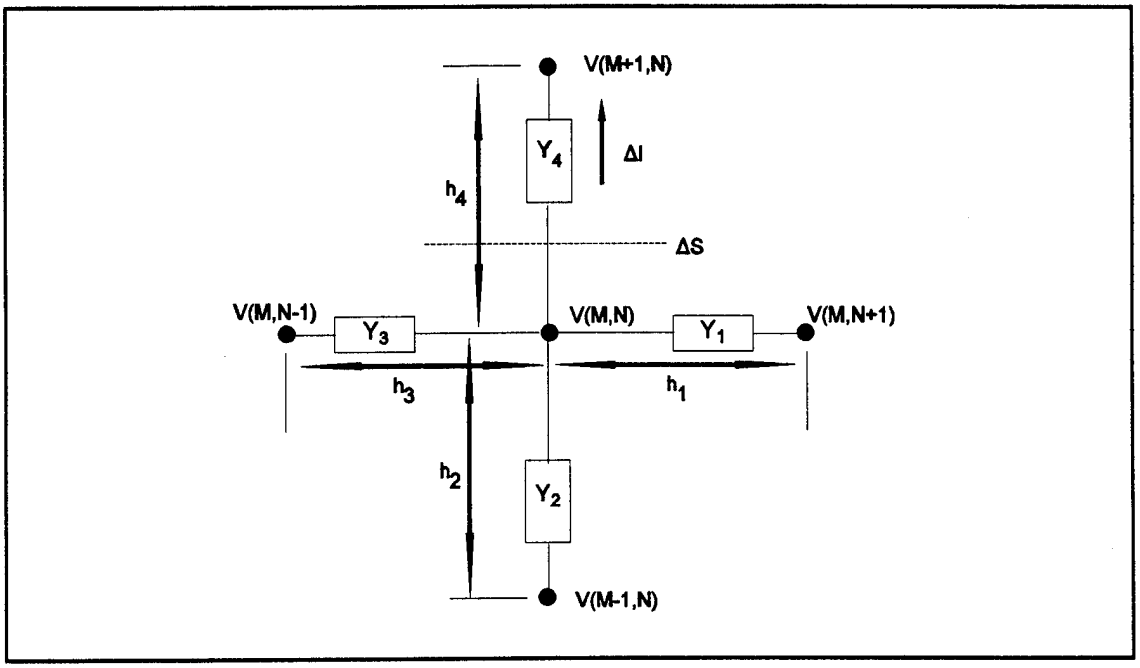


Figure V-26. Discretized Surface Integral at a Typical Finite-Difference Node.

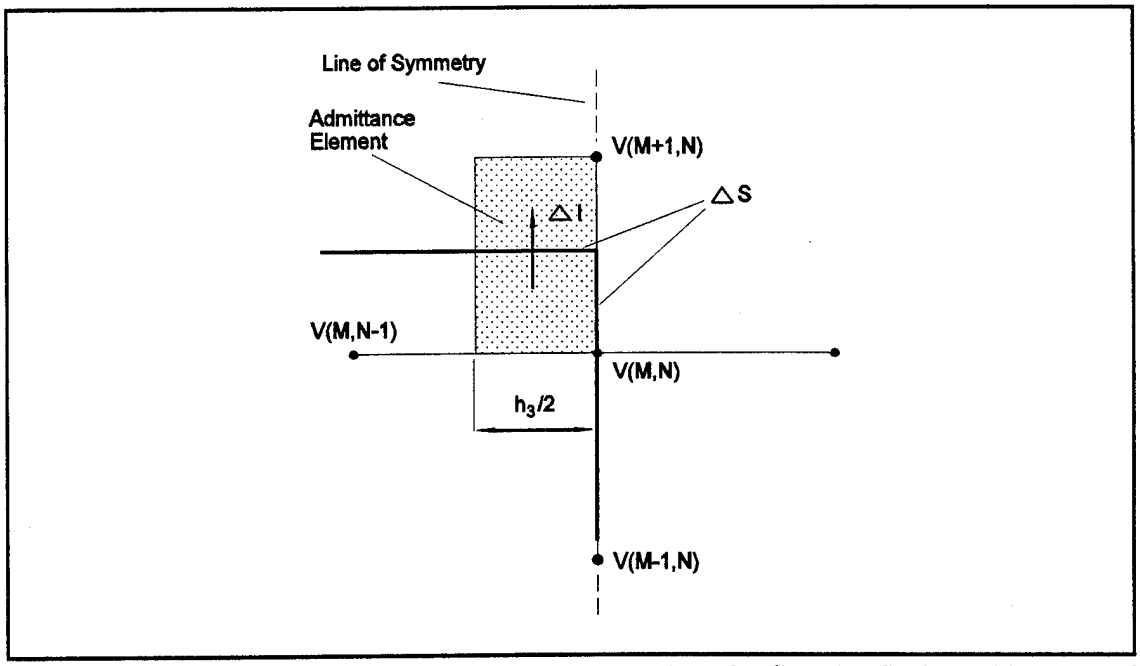


Figure V-27. Discretized Surface Integral at the Intersection of a Gaussian Surface with a Line of Symmetry.

edges of the array. The meander length, in part, determines the magnitude of the inter-electrode coupling, and the total electrode-to-ground capacitance. Lengthening the meander increases both the inter-electrode coupling and the capacitance to ground by the same proportion, and consequently, has no influence on the intrinsic or unloaded gain. However, an increased inter-electrode coupling and capacitance to ground will reduce the affect of any load capacitance (specifically, the in-situ MOSFET gate capacitance) on the interdigitated gate electrode's gain. Thus, although the meander length does not affect the intrinsic or unloaded gain of the interdigitated electrode structure; however, it does influence the effect of an external load. Accounting for half-electrodes along with the total meander length, yields the admittance parameters for the matrix equation and the π-equivalent model shown in Figure V-28.

Simple circuit analysis of the π-equivalent model implies that the intrinsic interdigitated gate electrode voltage transfer function is:

$$\frac{V_2}{V_1} = \frac{Y_{12}}{Y_{11}} \tag{V-26}$$

and with an arbitrary load, Y_L, the transfer function becomes:

$$\frac{V_2}{V_1} = \frac{Y_{12}}{Y_{11} + Y_L} \quad . \tag{V-27}$$

Since the load on the interdigitated gate electrode is primarily capacitive (the *in-situ* MOSFET's gate contact input capacitance and the interconnect capacitance), the model's simulation only considered capacitive loads for Y_L.

Finite-Difference Model Implementation. Each region within the finite-difference grid had an associated relaxation parameter. The user was able to select either fixed or variable relaxation parameters. If the variable option is utilized, the initial relaxation parameter setting for all three regions was 1.6. Although this value may not be the optimum selection for the relaxation parameter, an adequate convergence rate was consistently obtained. The Neumann boundary conditions require a zero normal gradient at the vertical lines of symmetry and along the upper boundaries in the Region 6 (pseudo-planar) and Region 7 (planar model) configurations (Figures V-8 and V-9) . The nodes in the finite-difference grid may be grouped into rows and columns. A column is defined by the set of vertical nodes corresponding to a particular horizontal node position. Likewise, a row is defined by the set of horizontal nodes for a particular vertical node position. Using these definitions, the two vertical lines of symmetry are modeled by columns 2 and 30. Since the number of rows in the finite-difference grid

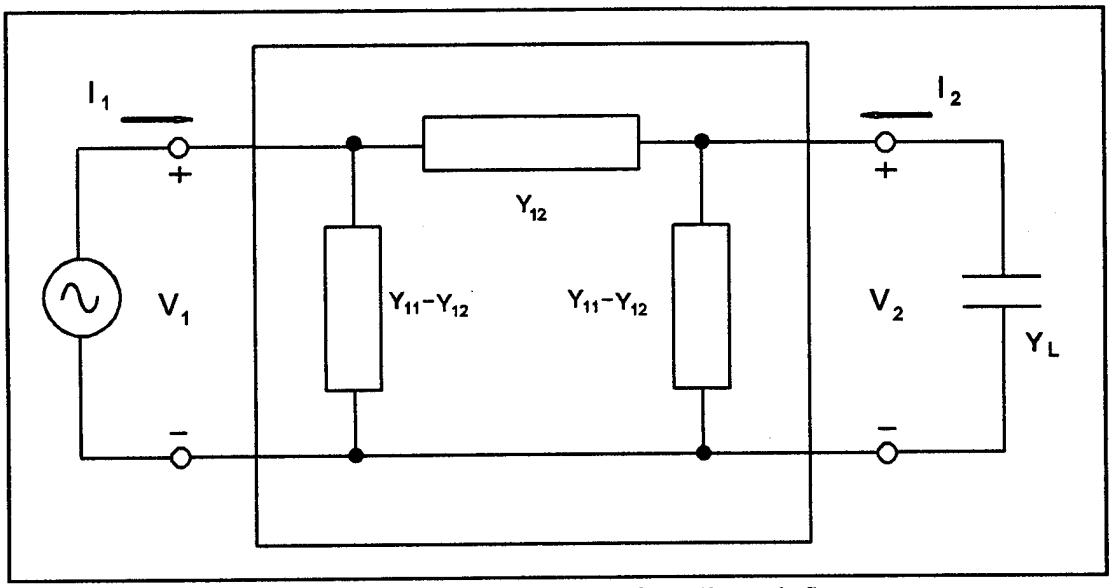


Figure V-28. π-Equivalent Model of the Interdigitated Gate Electrode Structure.

depends upon the thin film thickness, the line of symmetry at the upper boundary position can not be defined by an explicit row number. However, the line of symmetry at the upper boundary can be defined as the row just below the top row of the finite-difference grid. The Neumann boundary condition at the vertical lines of symmetry was achieved by reflecting the nodal potentials in columns 3 and 29 into columns 1 and 31, respectively. Similarly, the boundary condition along the upper edge of the top dielectric layer was simulated by reflecting the row of nodal potentials just below the line of symmetry into the row just above the line of symmetry. For a successful computation execution, the Gauss-Seidel iteration continues until the nodal potentials converge. Convergence occurred when the relative residue (defined below) was no greater than the specified convergence set-point everywhere in the finite-difference grid. Acceptable accuracy was achieved when the convergence set-point was equal to 10^{-4}. The effect of a capacitive load (Y_L) was accounted for by extracting the interdigitated electrode structure's two-port admittance parameters, and then adding the load capacitance to the output admittance term (Y_{11}). The model algorithm requires the following inputs: the complex permittivity of the top dielectric layer, the convergence set-point, the inter-electrode separation, the film thickness, the load capacitance, and the output file name. The model algorithm was coded in Turbo Pascal 5.0, and it was implemented on a 80486-based personal computer. The Pascal source code, a sample input, and the corresponding sample output are provided in Appendix I.

As stated earlier, the value of the relaxation parameter is critical for efficient convergence. In this algorithm, the values of the relaxation parameters were adjusted dynamically during the finite-difference calculation. The adjustment was based on the observed variation in the sum of the relative residues for each region that was produced during three successive iterations. The relative residue, R', is defined as the magnitude of the difference in the calculated potential for the two most recent iterations, normalized by the most recently calculated potential for that node; that is:

$$R' = \left| \frac{V^n - V^{n-1}}{V^n} \right|. \qquad \text{(V-28)}$$

After every third iteration, if the total relative residue increased, which indicated a diverging solution, the relaxation parameter was reduced by 0.02. Otherwise, if the total relative residue decreased, the relaxation parameter was increased by 0.01 to further accelerate convergence. Since it is more critical to prevent divergence, the relaxation parameter was reduced by a greater amount than it was increased.

The relaxation parameter was restricted to values between 1.2 and 1.9. Both the relaxation parameter adjustment increments, and the limits themselves, were the same as those used by Lee (190).

Finite Difference Model Results. For a given geometry, to calculate the gain/phase space over which the IGE structure's transfer function varies with the thin film's complex permittivity, the model calculates the gain/phase with either a constant permittivity or loss factor, while incrementing the other parameter over a finite range to generate the gain/phase contours. Gain/phase contours were generated for several different thin film thicknesses.

The gain/phase response of the IGE structure coated with a semi-infinitely thick film is shown in Figure V-29. With an uncoated IGE, the coupling between the electrodes and, therefore, the gain, are minimized. When a lossless semi-infinitely thick film is deposited on the IGE structure, the admittance parameters are purely capacitive, and the IGE structure's phase is zero. Thus, lossless dielectrics with permittivities greater than unity increase the IGE structure's gain without the introduction of a phase shift. If, however, the dielectric is lossy, the admittance parameters become complex, and the gain increase[2] is accompanied by a negative phase shift. When the loss factor becomes large, as in highly conductive films or for lossy dielectrics at low frequency, the electrodes are effectively short-circuited, and the IGE structure's gain approaches unity, and the phase shift approaches zero.

Lee's gain/phase calculations for a similar IGE structure (190) qualitatively confirms the IGE structure's gain/phase response predicted by the current model. Lee's results, shown in Figure V-30, are for an IGE structure with a 12.5 μm electrode separation and electrode width that was coupled to a load capacitance of 1.6 pF (in-situ MOSFET gate capacitance, Y_L). The wider electrode separation reduces the inter-electrode coupling and, therefore, reduces the gain. Furthermore, the load capacitance reduces the gain as predicted by Equation (V-27). For example, the minimum gain[3] computed with the current model decreases from -39.9 dB to -44.9 dB when the IGE structure is connected to a 1.6 pF load capacitance (Y_L). A more detailed comparison with Lee's model is presented in the following section.

The gain/phase contours with a semi-infinitely thick coating were repeated after establishing the particular geometrical features of the current IGEFET sensor (see Chapter IV and Table V-1). The most significant change in the IGE structure was the introduction of the oxide undercut within the inter-

---

[2]Since the model assumes linear, lossless and lossy dielectrics, the gain is always negative. Therefore, an increase in gain means the gain is becoming less negative. Similarly, a reduction in gain means the gain is becoming more negative.

[3]The minimum gain is the most negative gain computed along a gain/phase contour of constant relative permittivity, ϵ'. An increase in the minimum gain means the minimum gain becomes less negative.

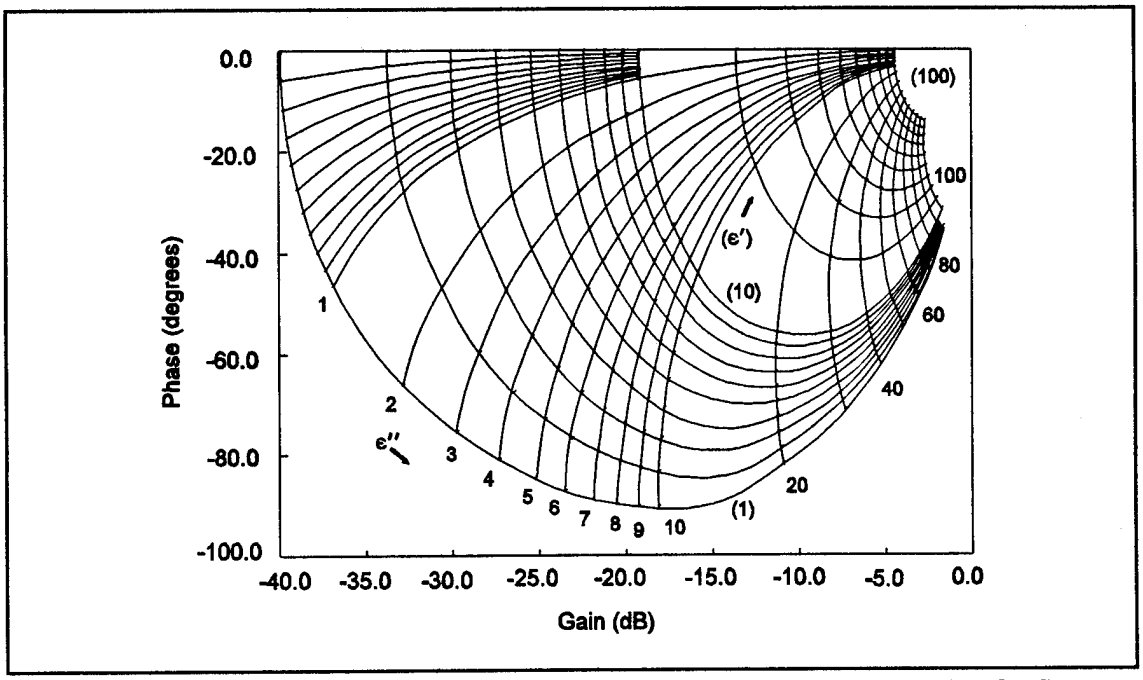


Figure V-29. Gain/Phase Response Calculated from the Pseudo-Planar Model of the IGE Structure Coated with a Semi-Infinitely Thick Film (ϵ' and ϵ'' are the Relative Permittivity and Loss Factor of the Semi-Infinitely Thick Film).

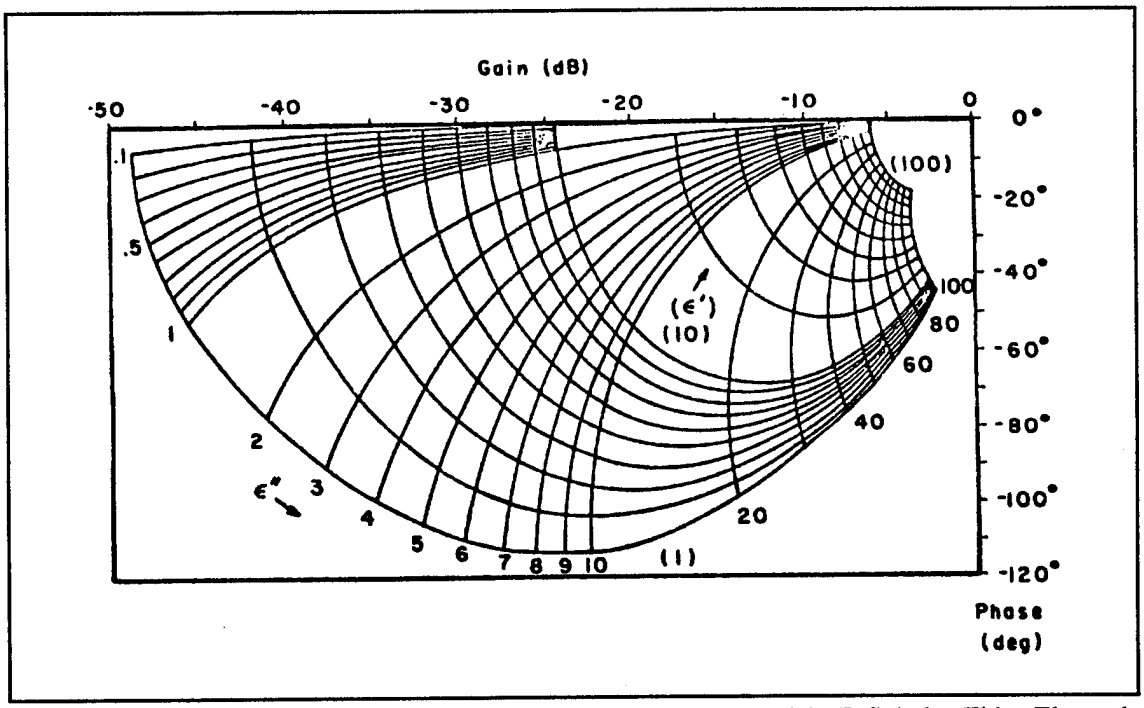


Figure V-30. Gain/Phase Response Calculated By Lee's Model (Infinitely Thin Electrode Approximation) for an IGE Structure Coated with a Semi-Infinitely Thick Film (190). (ϵ' and ϵ'' are the Relative Permittivity and Loss Factor of the Semi-Infinitely Thick Film).

electrode space (see Figures IV-2 and IV-3). The calculated gain/phase contours are shown in Figure V-31. While the increased electrode height was expected to increase the inter-electrode coupling, the effects of the decreased oxide thickness and the inclusion of the oxide undercut dominate and reduce the minimum gain. In addition to the decrease in minimum gain, these geometrical changes distort the gain/phase contours, particularly for small permittivities and moderate levels of loss.

The observed distortion in the gain/phase contours motivated an investigation of the effect of the oxide undercut on the IGE structure's transfer function. Figure V-32 shows the gain/phase contours for a semi-infinitely thick coating with a relative permittivity of unity deposited on an IGE structure possessing five different oxide undercuts. The introduction of the oxide undercut causes distortion in the gain/phase contours. Furthermore, the minimum gain increased with larger oxide undercuts. Contour plots of the potential distribution within an "ideal" IGE structure and within an IGE structure possessing a 0.5 μm oxide undercut are shown in Figures V-33 and V-34. Comparison of the potential at the points labeled A and B in Figures V-33 and V-34 indicates that the inter-electrode coupling is only slightly increased. However, the change in the potential distribution resulting from the oxide undercut near the bottom right corner of the driven-electrode signifcantly reduces the electrode-to-ground coupling. Therefore, the increase in the computed transfer function gain is primarily the result of the decrease in the fringe electrode-to-ground coupling. As depicted in Figure V-35, the gain increase resulting from the oxide undercut will only be observed when the IGE structure is coated with a film having a permittivity less than that of the oxide. If the permittivity of the film coating is greater than that of the oxide, the oxide undercut will have the opposite effect on the gain.

The IGE structure's transfer function gain/phase contours were calculated for several film thicknesses in the range spanning 0.2 μm to 7.5 μm. Figures V-36 through V-38 show the gain/phase contours for 0.2, 1.2, and 4.5 μm thick films. Two striking features of the gain/phase contours corresponding to the 0.2 and 1.2 μm thick films were the phase shifts between -180° and -360°, as well as the very large decrease in gain observed for certain values of the film's complex permittivity. As the film thickness increased, the value of the permittivity required to observe this behavior decreased. Phase shifts between -180° and -360° were not observed for film thicknesses greater than 1.7 μm. However, a film thickness greater than 3.5 μm was required to eliminate the observed decrease in gain with increasing loss. As the permittivity was increased, the film thickness at which the above behavior became observable decreased. Increasing the film thickness in excess of 3.5 μm caused the gain/phase contours corresponding to low permittivities and loss to be more sensitive to changes in the complex permittivity. For example, the gain of an IGE structure coated with a semi-infinitely thick dielectric film

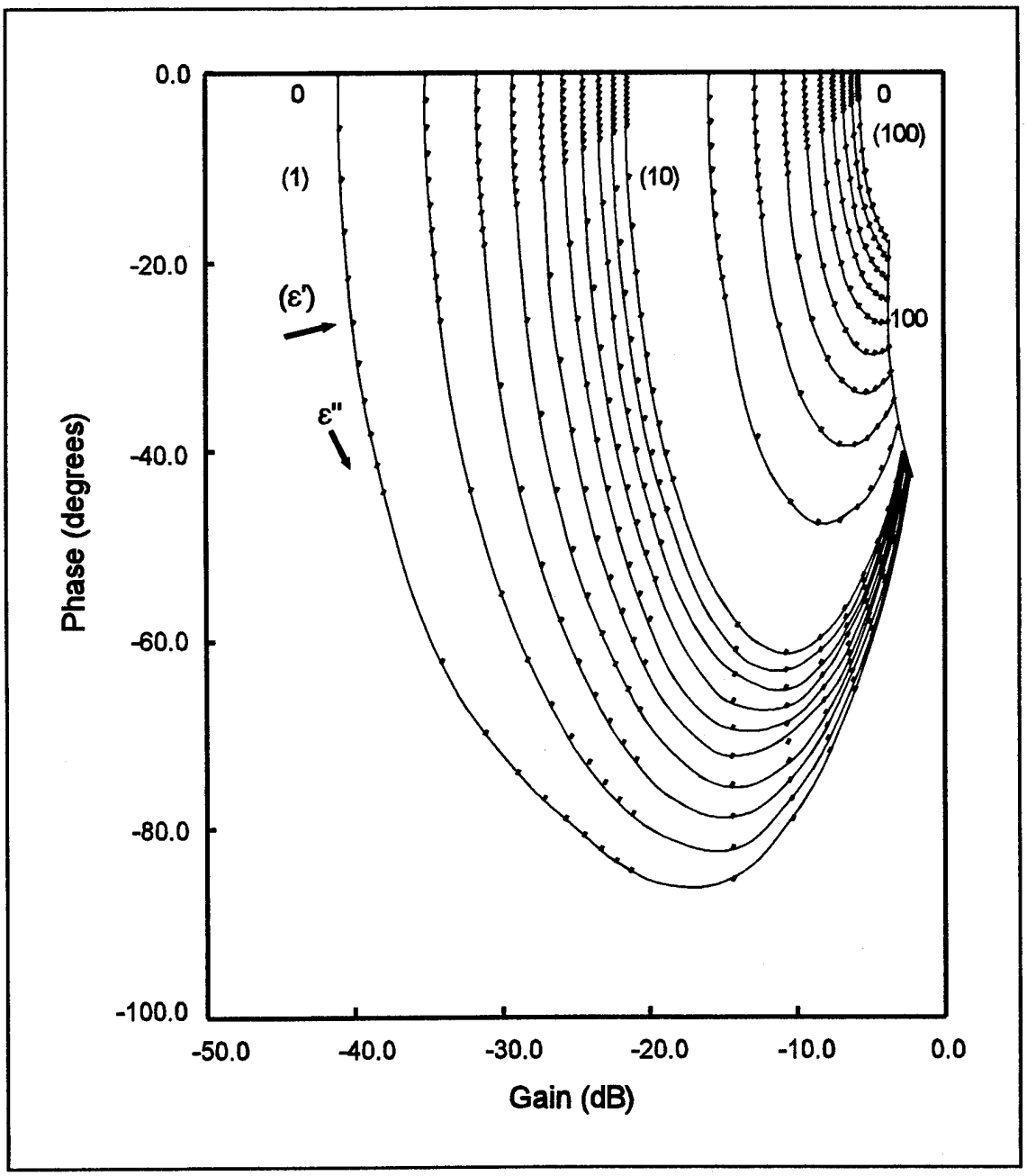


Figure V-31. Gain/Phase Response Calculated with the Pseudo-Planar Model for the Geometry of the IGEFET Sensor Design (Table V-1) Coated with a Semi-Infinitely Thick Film (ϵ' and ϵ'' are the Relative Permittivity and Loss Factor of the Semi-Infinitely Thick Film).

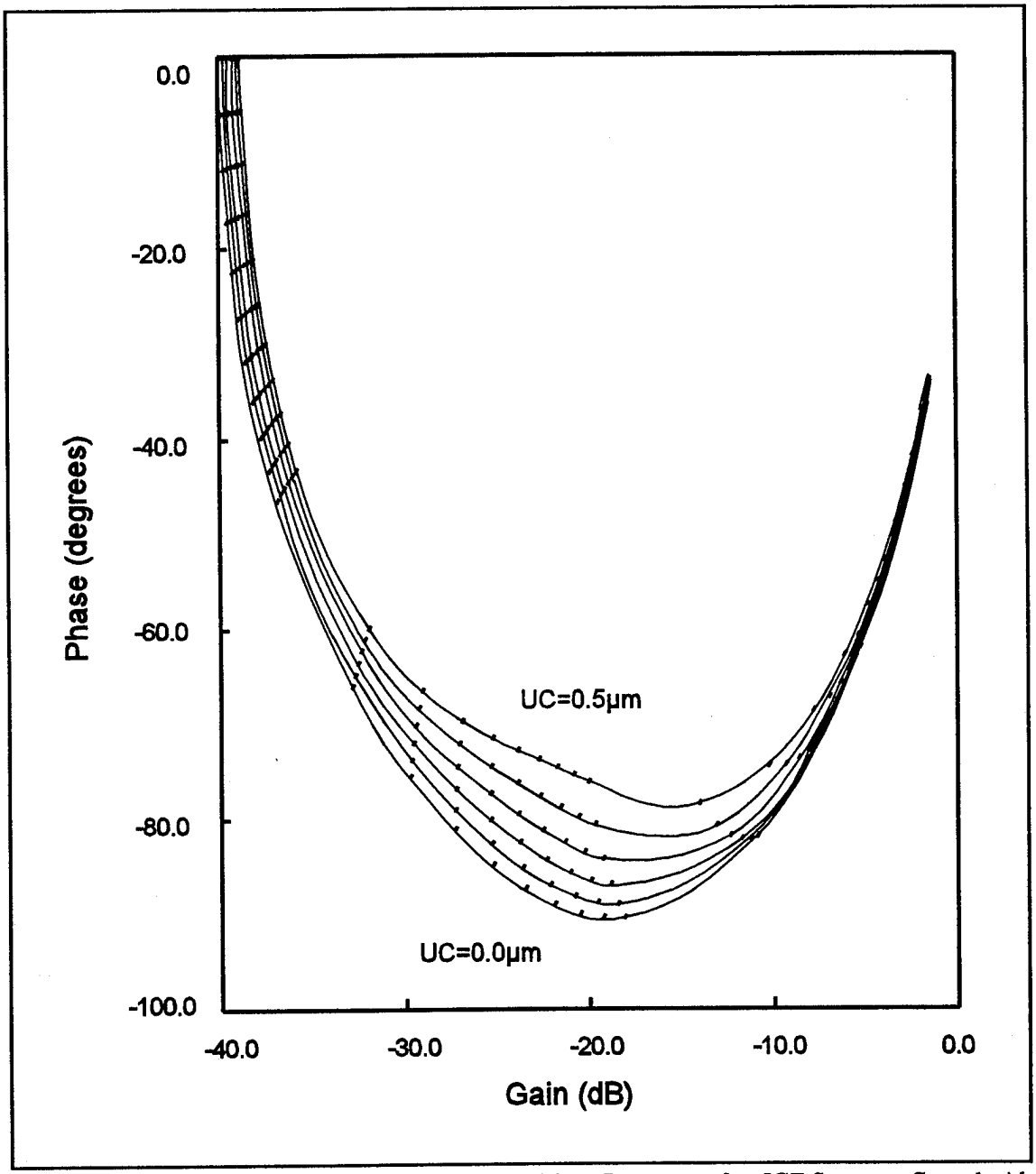


Figure V-32. Effect of an Oxide Undercut on the Gain/Phase Response of an IGE Structure Coated with a Semi-Infinitely Thick Film Possessing a Relative Permittivity of Unity.

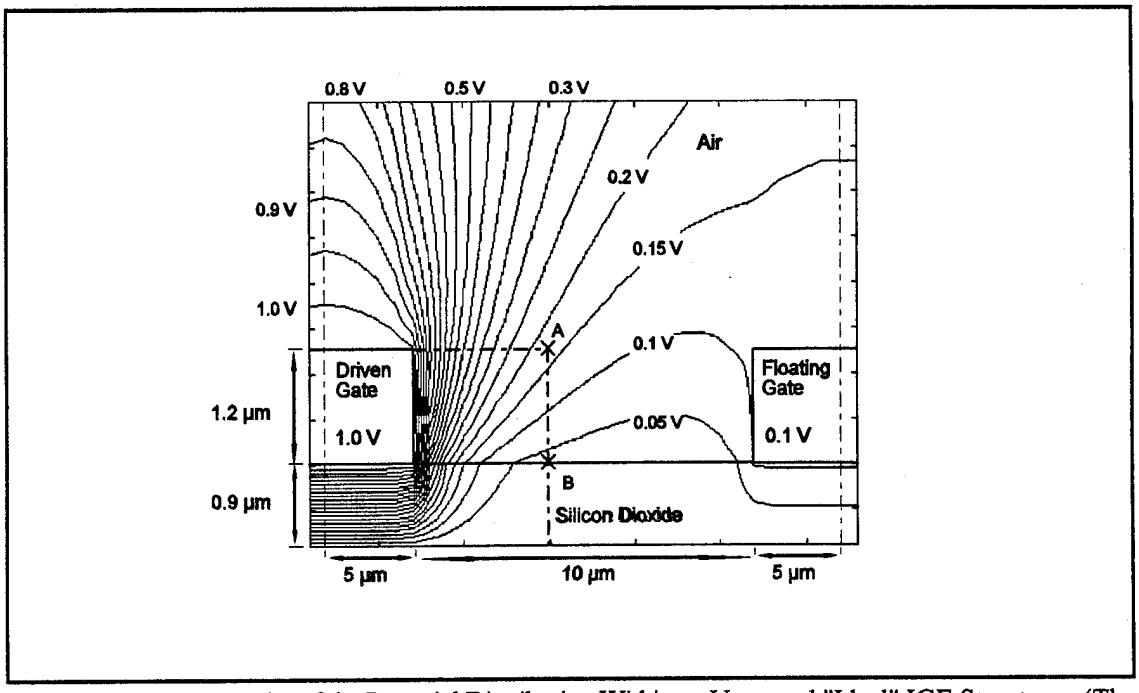


Figure V-33. Contour Plot of the Potential Distribution Within an Uncoated "Ideal" IGE Structure. (The Equi-Potential Lines are Spaced at 0.05 V Intervals. EH=1.2 µm, OxH=0.9 µm, UC=0.0 µm, ϵ_F=1-0j, ESep=10 µm, Vertical Resolution=0.1 µm).

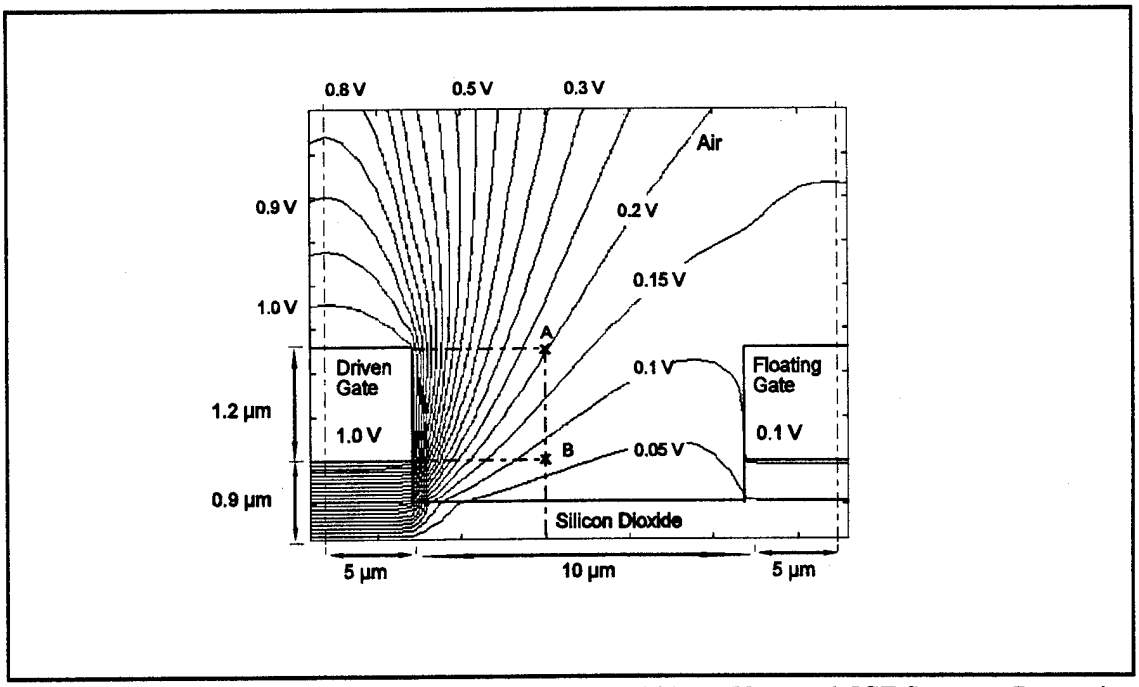


Figure V-34. Contour Plot of the Potential Distribution Within an Uncoated IGE Structure Possessing a 0.5 µm Oxide Undercut.. (The Equi-Potential Lines are Spaced at 0.05 V Intervals. EH=1.2 µm, OxH=0.9 µm, UC=0.5 µm, ϵ_F=1-0j, ESep=10 µm, Vertical Resolution=0.1 µm).

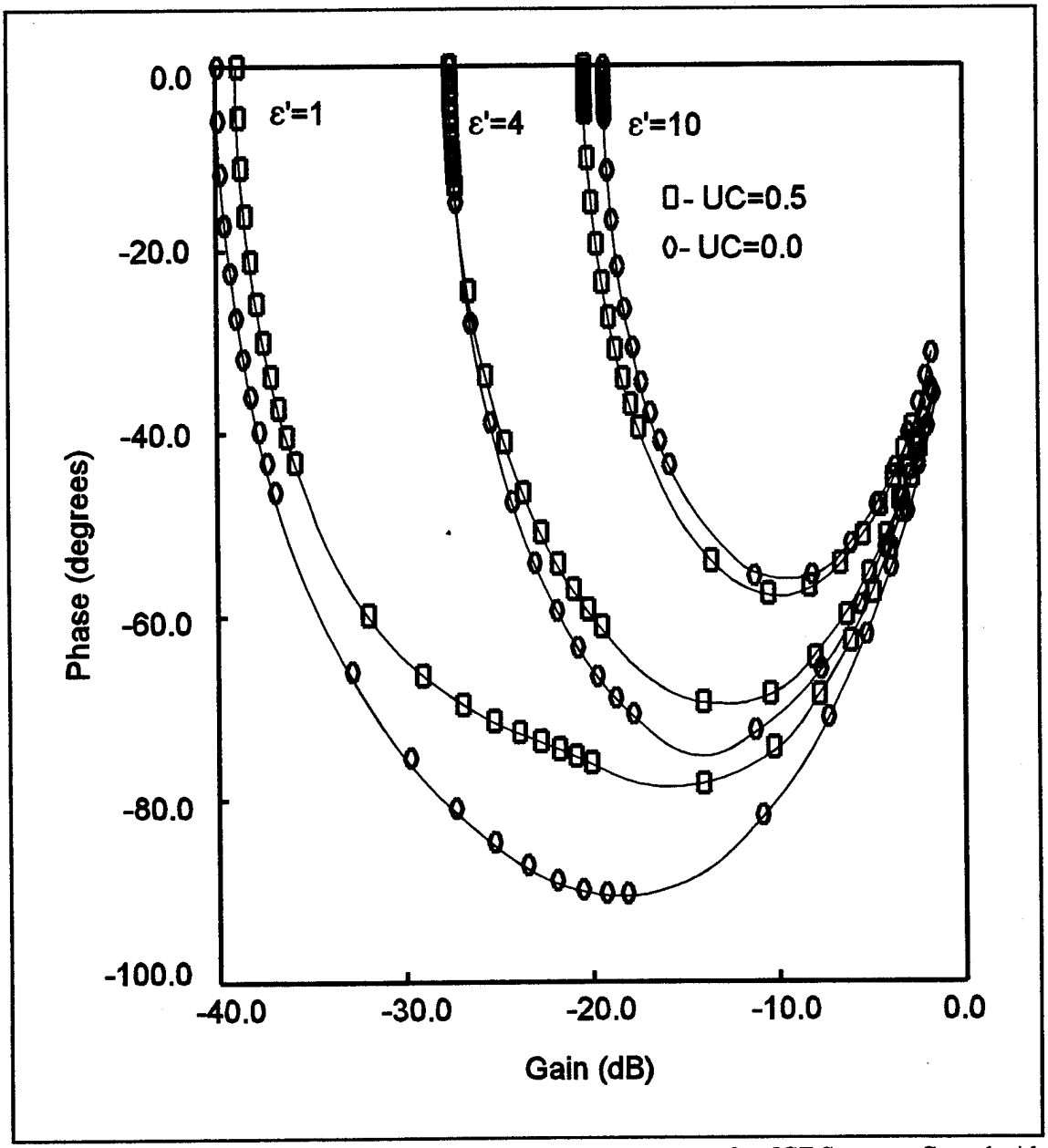


Figure V-35. Effect of an Oxide Undercut on Gain/Phase Response of an IGE Structure Coated with Semi-Infinitely Thick Films with Three Different Values of Relative Permittivity.

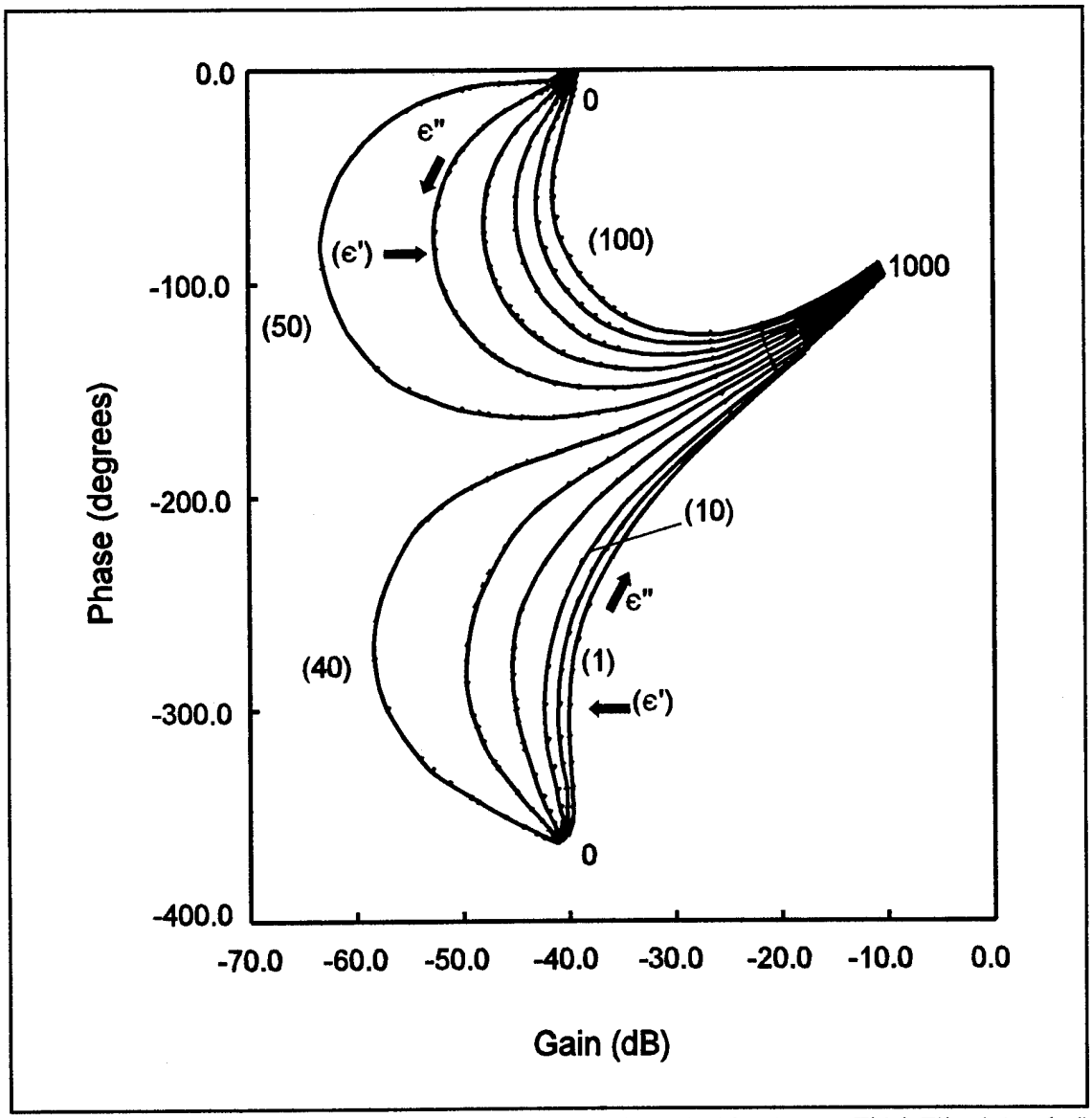


Figure V-36. Gain/Phase Response of the IGE Structure Coated with a 0.2 μm Thick Film (ε′ and ε″ are the Film's Relative Permittivity and Loss Factor).

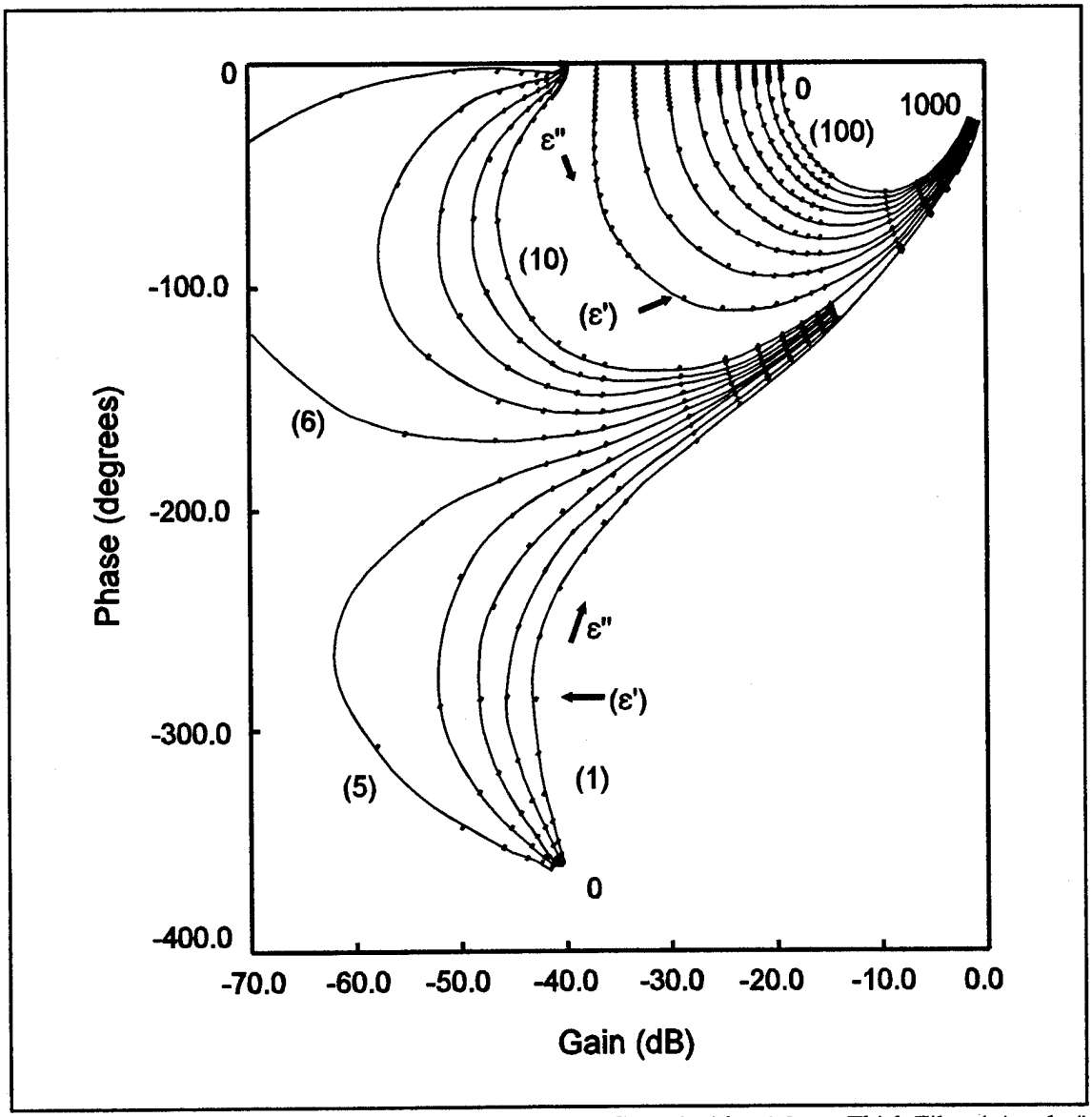


Figure V-37. Gain/Phase Response of the IGE Structure Coated with a 1.2 μm Thick Film (ϵ' and ϵ'' are the Film's Relative Permittivity and Loss Factor).

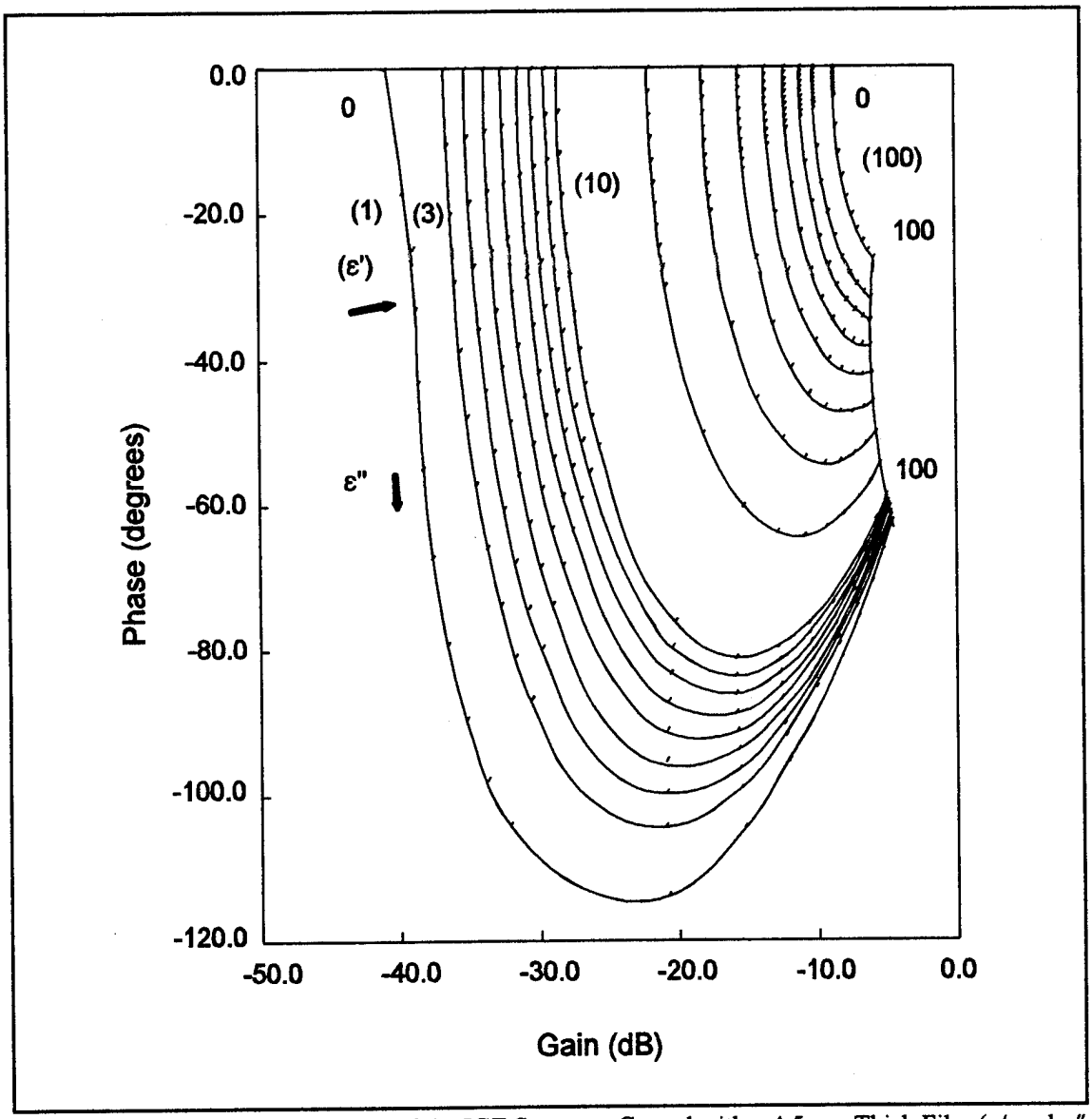


Figure V-38. Gain/Phase Response of the IGE Structure Coated with a 4.5 μm Thick Film (ϵ' and ϵ'' are the Film's Relative Permittivity and Loss Factor).

will increase more compared to the same IGE structure coated with a 3.5 μm thick film if the film's relative permittivity is increased from a value of 1 to a value of 2. Figure V-39 illustrates the effect of film thickness for a film possessing a relative permittivity of 10. The decrease in gain with increasing loss is the result of a more rapid increase in the fringe electrode-to-ground admittance relative to the increase in the inter-electrode admittance. The electrode-to-ground admittance roughly corresponds to the computed Y_{11} admittance parameter, and the inter-electrode admittance essentially corresponds to the computed Y_{12} admittance parameter. As shown in Figure V-40, for a 1.2 μm thick film with a relative permittivity of 5, Y_{11} initially increases much more rapidly than Y_{12}. This behavior causes the transfer function's gain to initially decrease as the loss is increased, leading to the "bowing" feature observed in the gain/phase contour in Figure V-37. Additionally, Figure V-40 reveals that the gain minimum observed in Figure V-37 for a loss factor of 20 corresponds to a minimum in the Y_{12} curve. A plot of the corresponding admittance's phase in Figure V-41 reveals that the phase shifts approximately -180° near this value of loss. The small values of the real part of this admittance parameter (Y_{12}) causes the phase oscillation for loss values between 18-30. Figures V-42 and V-43 show the real and imaginary parts of the two admittance parameters (Y_{11} and Y_{12}). At zero loss, the Y_{11} admittance parameter is purely capacitive. As the loss is increased, the increase in the conductance term is accompanied by an increase in the capacitive term. Similarly, the inter-electrode admittance is also purely capacitive at zero loss. However, the capacitance term decreases as the loss increases. At an approximate loss value of 20, the capacitance decreased to zero, and with further increases in the loss value, the admittance behaves inductively. This decrease in the imaginary term prior to any significant increase in the real term introduces the zero in the IGE transfer function. This behavior is not observed in films with thicknesses greater than 3.5 μm, since the increase in loss imparts an appreciable increase in the real part of the inter-electrode admittance before the imaginary term passes through zero. Although not apparent on this scale, the real part of Y_{12} becomes negative for loss values spanning 18 to 28. The regions of the gain/phase curves in Figures V-36 through V-39 where a phase shift greater than 180° is observed correspond to cases where the real part of Y_{12} is negative.

Negative values for the real part of the inter-electrode admittance (the conductance term) stem from the distributed nature of the finite-difference calculation. As discussed earlier, admittance elements composed of parallel combinations of conductances and capacitances couple each node in the finite-difference grid to the surrounding nodes (see Figure V-3). Modelling the inter-electrode admittance as a distributed network of conductances and capacitances, as shown in Figure V-44, imply that the conditions which give rise to a negative conductance term in the inter-electrode admittance may be

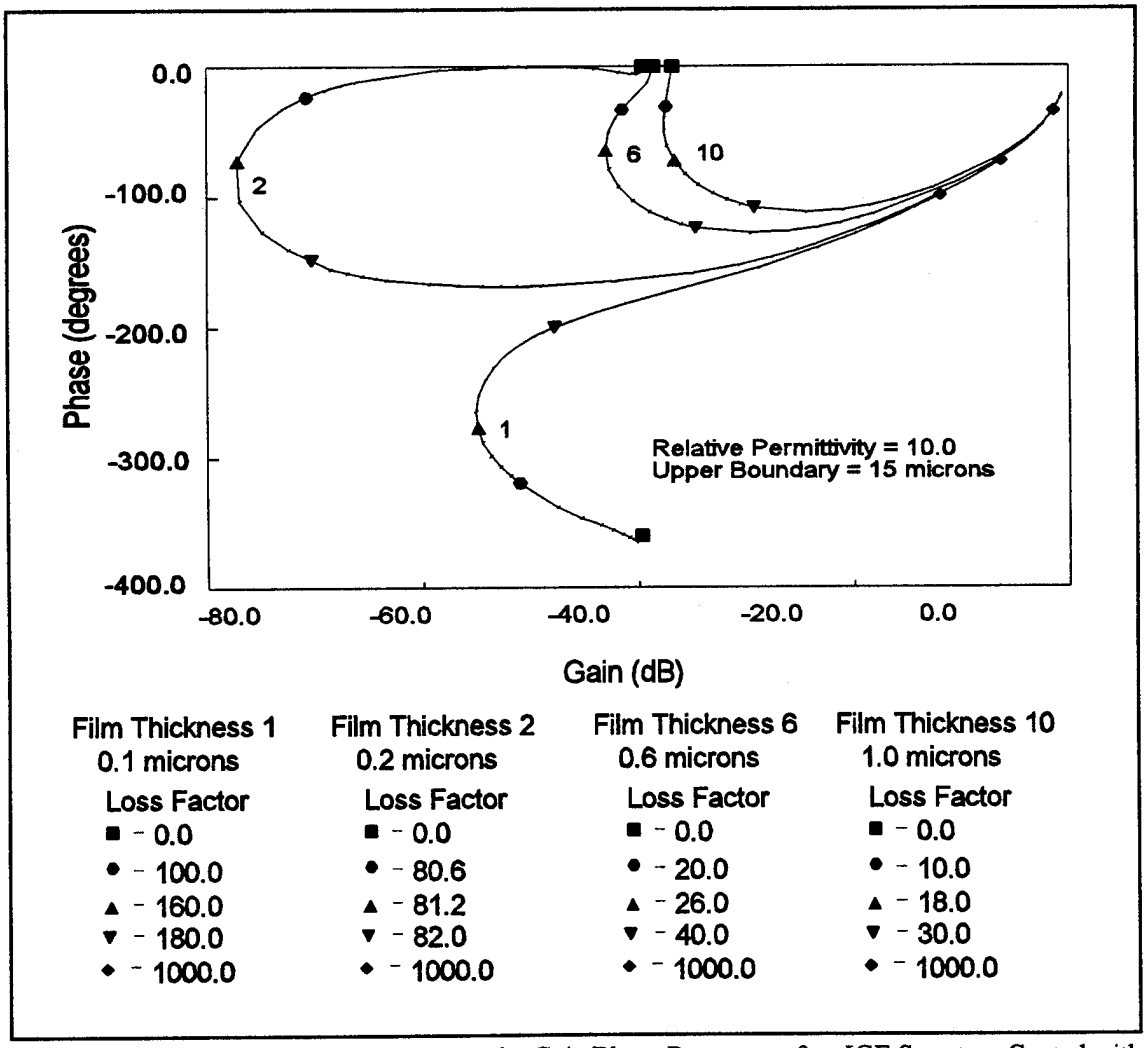


Figure V-39. Effect of Film Thickness on the Gain/Phase Response of an IGE Structure Coated with a Film Whose Relative Permittivity is 10.

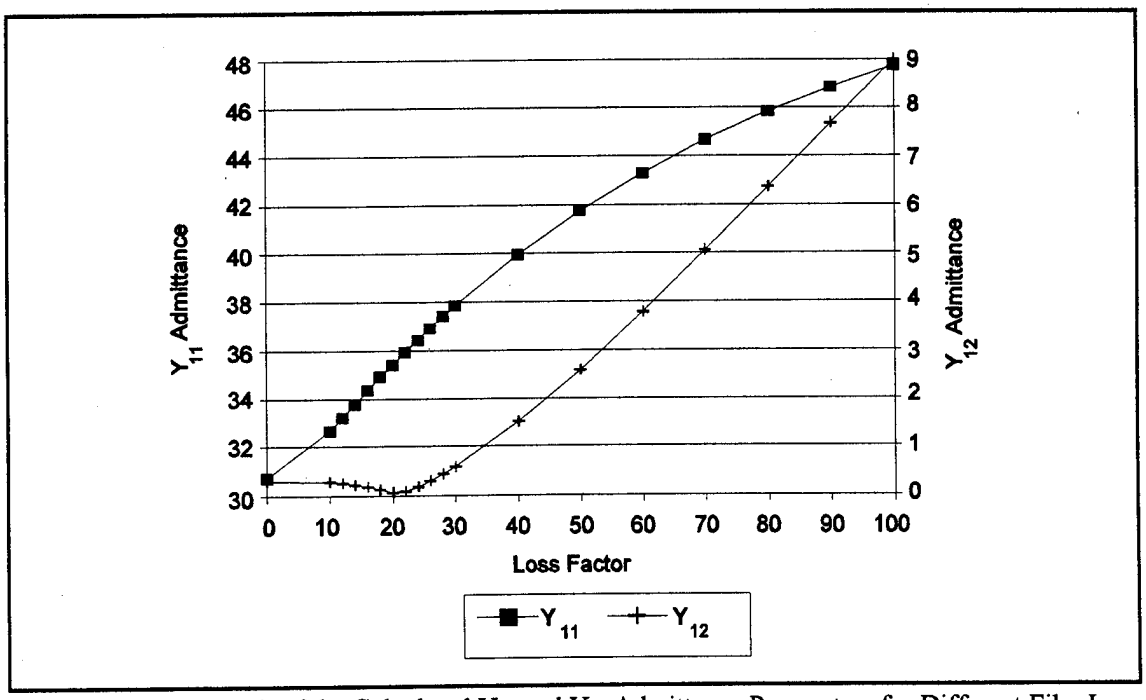


Figure V-40. Magnitude of the Calculated Y_{11} and Y_{12} Admittance Parameters for Different Film Loss Factors (Film Thickness= 1.2 μm and Relative Permittivity = 5).

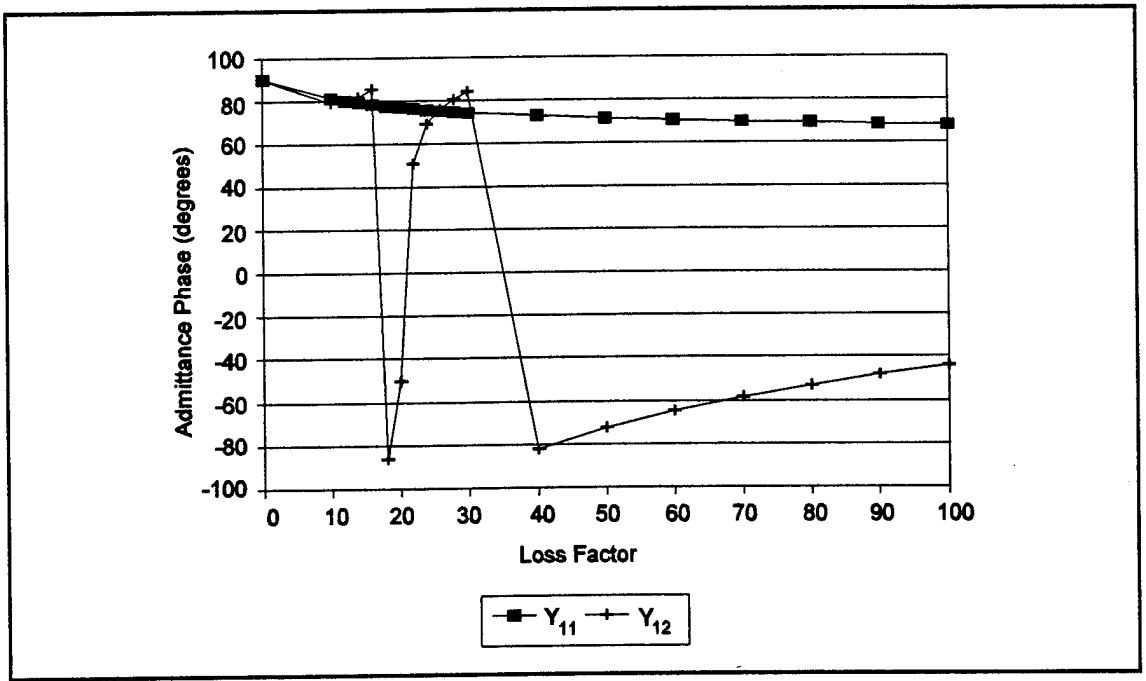


Figure V-41. Phase of the Calculated Y_{11} and Y_{12} Admittance Parameters for Different Film Loss Factors (Film Thickness= 1.2 μm and Relative Permittivity = 5).

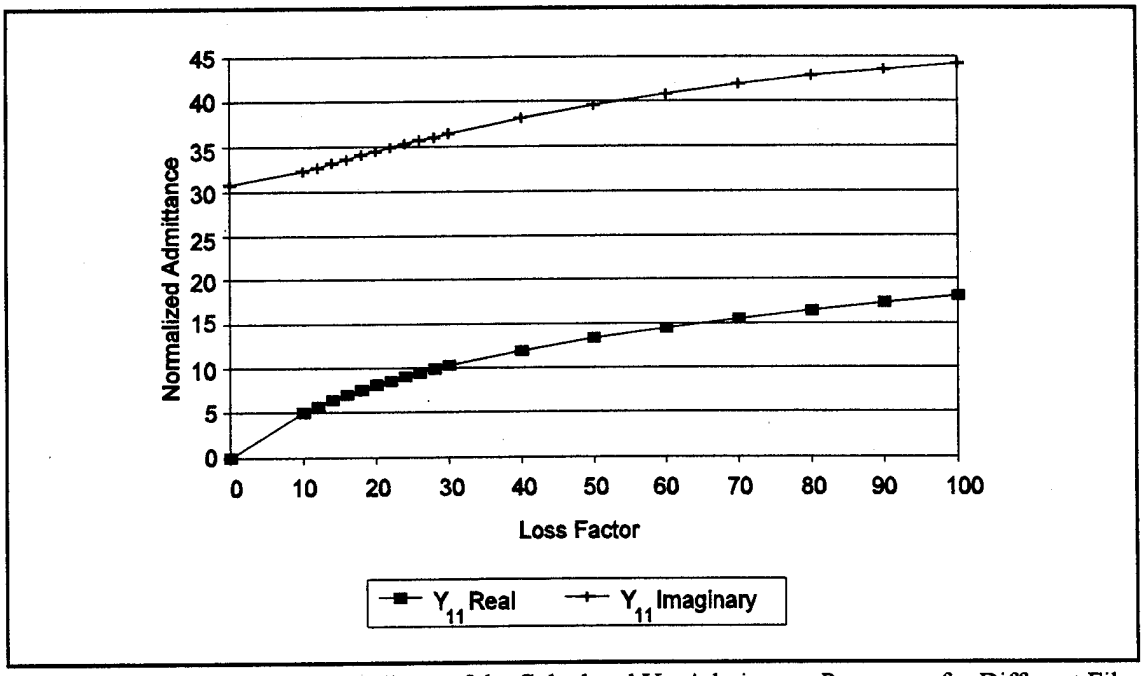


Figure V-42. Real and Imaginary Parts of the Calculated Y_{11} Admittance Parameter for Different Film Loss Factors (Film Thickness = 1.2 μm and Relative Permittivity = 5). The Admittance Parameters are Normalized With Respect to the Permittivity of Free Space, ϵ_0, and are on a Per-Unit Length Basis. If ϵ_0 is Given in Farads/cm, then the Admittance is Expressed on a Per-Unit cm Basis.

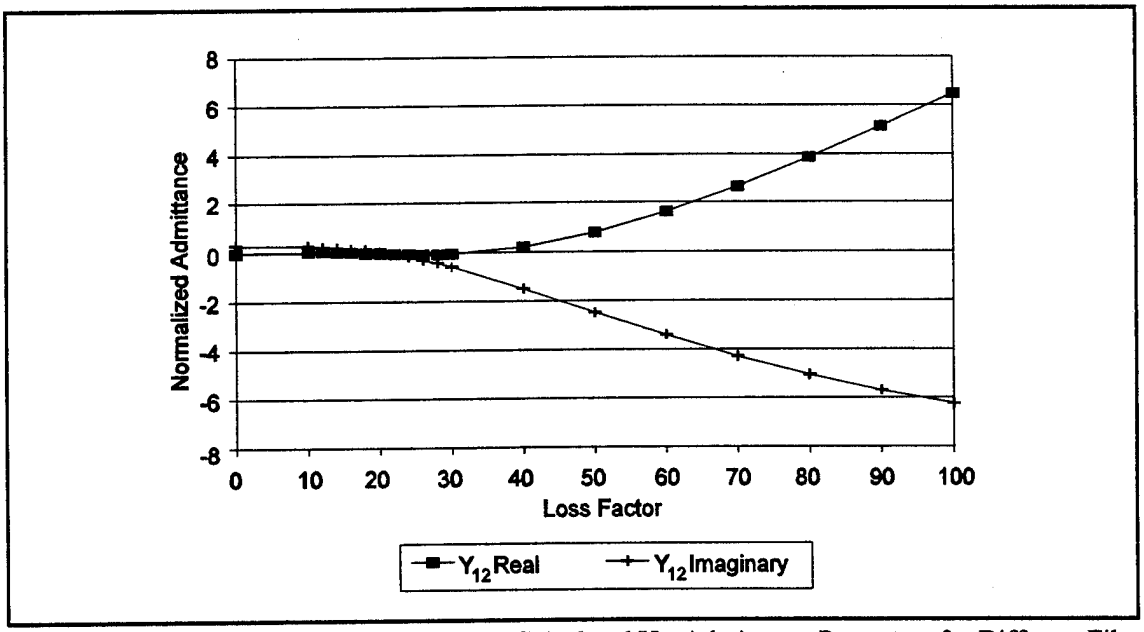


Figure V-43. Real and Imaginary Parts of the Calculated Y_{12} Admittance Parameter for Different Film Loss Factors (Film Thickness = 1.2 μm and Relative Permittivity = 5). The Admittance Parameters are Normalized With Respect to the Permittivity of Free Space, ϵ_0, and are on a Per-Unit Length Basis. If ϵ_0 is Given in Farads/cm, then the Admittance is Expressed on a Per-Unit cm Basis.

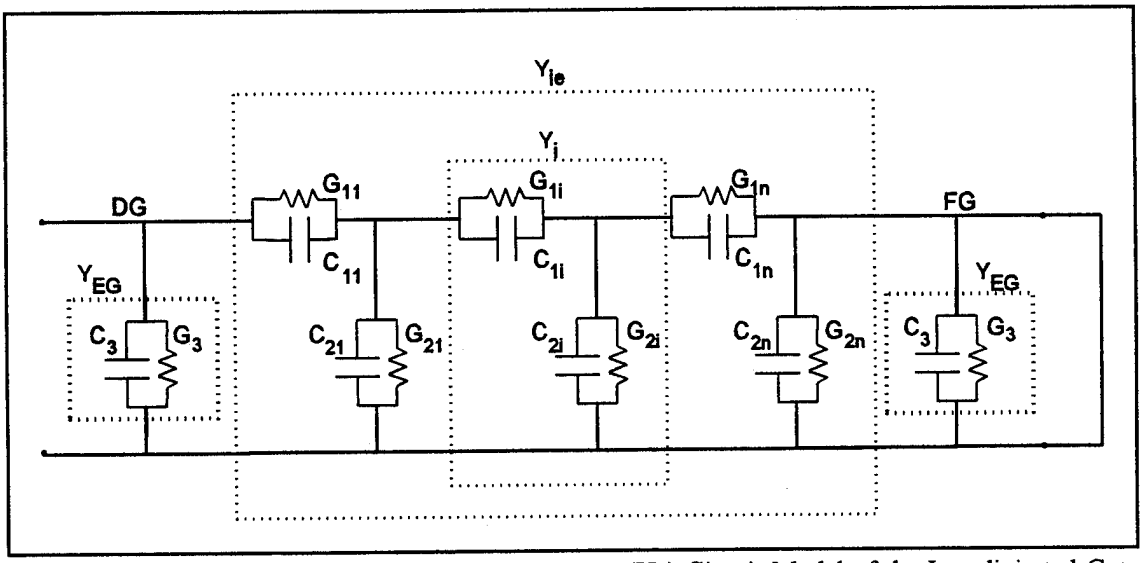


Figure V-44. Distributed Inter-Electrode Admittance (Y_{ie}) Circuit Model of the Interdigitated Gate Electrode Structure. Y_i are (n-1)-Distributed Admittances with i = 2 Through (n-1). Y_{EG} is the Electrode-to-Ground Admittance Beneath the Driven-Gate (DG) Electrode and the Floating-Gate (FG) Electrode.

derived. If the floating-gate electrode in Figure V-44 is grounded, the circuit can be simplified through a sequence of series and parallel impedance or admittance combinations to yield the circuit shown in Figure V-45. The inter-electrode admittance, Y_{ie}, of the circuit in Figure V-45 is given by:

$$Y_{ie} = \frac{(G_1 + j\omega C_1)(G_e + j\omega C_e)}{G_1 + G_e + j\omega(C_1 + C_e)} \tag{V-29}$$

where ω is the angular frequency, and G_e and C_e are the effective conductance and capacitance obtained by the sequence of series/parallel combinations, respectively. The real part of the inter-electrode admittance is negative whenever the cosine of the inter-electrode admittance phase ($\phi_{Y_{ie}}$) is negative. The inter-electrode admittance phase is given by:

$$\phi_{Y_{ie}} = \arctan\left[\frac{\omega(C_1G_e + G_1C_e)}{G_1G_e - \omega^2C_1C_e}\right] - \arctan\left[\frac{\omega(C_1 + C_e)}{G_1 + G_e}\right] \tag{V-30}$$

The cosine will be negative whenever $90° < \phi_{Y_{ie}} < 270°$. Since C_1, C_e, G_1, and G_e are all positive numbers, the second term in Equation (V-30) spans between 0° and 90° for all ω. Thus, if the first term is less than 0°, the above criteria for obtaining a negative real part of the inter-electrode admittance will be satisfied. The first term will be less than 0° whenever $\omega^2 > (G_1G_e)/(C_1C_e)$.

Finite-Difference Model Verification

The finite-difference model was verified using two different approaches. The first approach compared the model results with the previously published data of Lee (190) and Garverick (181, 199). Lee's research provides data on the sensor response with thick (semi-infinite) films. On the other hand, Garverick studied the IGE sensor response when coated with very thin films (300Å). The second approach for verifying the finite-difference model was to experimentally confirm the model's results by measuring the IGEFET sensor's electrical properties when coated with films possessing different complex permittivity and thickness values.

Comparison with Published Data. As previously discussed, Lee developed a finite-difference model to predict the transfer function of an interdigitated gate electrode sensor coated with a semi-infinitely thick film. Lee validated his model with experimental measurements of the transfer function of uncoated sensors possessing various geometries. The sensor capacitances and transfer function gain calculated with the current finite-difference model for the same sensor geometries were compared with

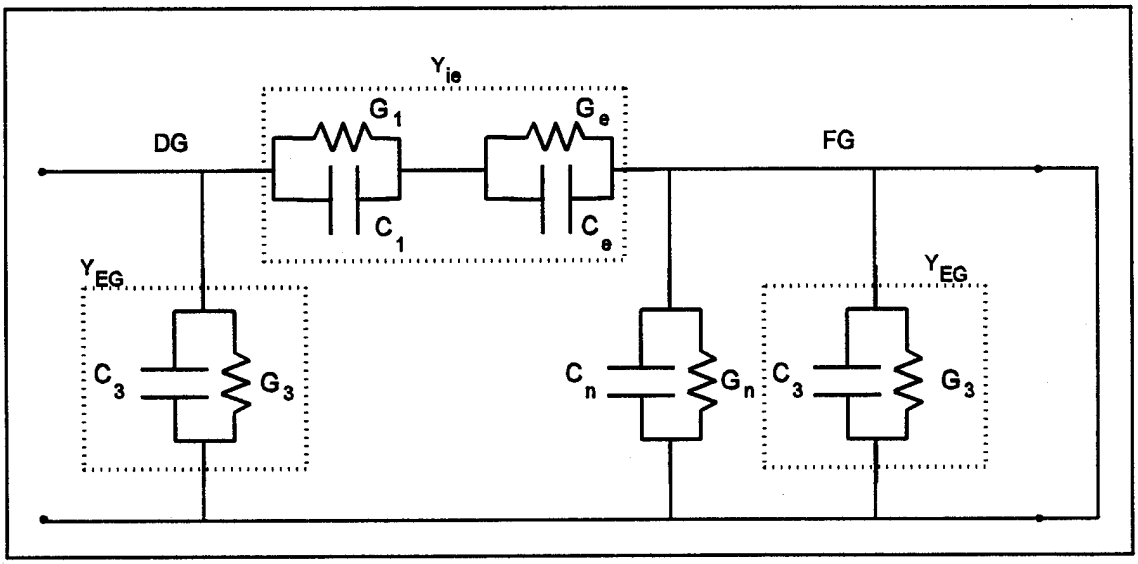


Figure V-45. Equivalent Distributed Inter-Electrode Admittance (Y_{ie}) Circuit Model of the Interdigitated Gate Electrode Structure. The Y_i Admittance Elements in Figure V-42 have been Reduced to the Equivalent Y_e Admittance. Y_{EG} is the Electrode-to-Ground Admittance Beneath the Driven-Gate (DG) Electrode and the Floating-Gate (FG) Electrode.

Lee's results. Lee calculated the uncoated sensor response for four different electrode width to oxide height, (W/H)-, ratios. To obtain different (W/H)-ratios, Lee varied the oxide height for a fixed electrode width of 12.5 μm. Table V-3 compares the results of the current finite-difference model (which will be referred to as the finite thickness electrode (FTE) model) with Lee's results for an uncoated sensor with four different (W/H)-ratios. Since the sensors were uncoated, the top dielectric is air with a complex permittivity of 1 - 0j and, therefore, the calculated model admittances, Y_{11} and Y_{12}, reduce to purely capacitive terms, C_{11} and C_{12} (expressed on a per-unit length basis). The model calculations were performed assuming a 1 μm electrode height and no oxide undercut.

The electrode-to-ground capacitance, C_{11}, is within 2.5 percent of the value reported by Lee for all (W/H)-ratios. This behavior indicates that the infinitely thin electrode approximation facilitates an accurate calculation of C_{11} for sensors possessing these geometries. The expected reciprocal relationship between the electrode-to-ground capacitance and the oxide height was observed as the (W/H)-ratio was increased (the oxide height decreased). The small deviation observed between the FTE model and Lee's model increases with decreasing oxide thickness, as shown in Figure V-46. Furthermore, the FTE model diverged from the ideal parallel plate capacitor behavior as the oxide height was decreased. Specifically, the inter-electrode capacitance, C_{12}, predicted by the FTE model was consistently larger than Lee's model. The larger inter-electrode capacitance is consistent with the larger fringe field associated with the finite thickness electrodes. Although the infinitely thin electrode approximation produces less than a 7 percent deviation with respect to the FTE result for a (W/H)-ratio of 5.8, the deviation increases to more than 20 percent with a (W/H)-ratio of 27.8. These errors in the calculated capacitances produce a maximum 2 dB difference in the sensor's transfer function gain predicted by the two models. Despite the small deviations in the calculated capacitances and transfer function gain introduced by the infinitely thin electrode approximation, the results obtained with the current finite-difference model are consistent with Lee's results and verify the model's predictions for thick films.

For thin films, the model's predictions were compared with the data published by Garverick (181). Garverick investigated the application of Lee's sensor for determining the sheet resistance of thin films as a function of the dewpoint. To obtain the sheet resistance, Garverick developed a semi-empirical transmission line model of the IGE sensor that is shown in Figure V-47. Using this model, a set of calibration curves were generated relating either the sensor's transfer function gain or phase to the sheet resistance. Generation of these curves required two simplifying assumptions: 1) the sheet resistance is the only model element that may vary with dewpoint, and 2) all model elements were non-dispersive. Garverick calculated the model elements C_T and C_L from the device geometry with the

Table V-3. Comparison of the Finite-Difference Model using Finite Thickness Electrodes (FTE) with Lee's Model (190).

	(W/H)-Ratio							
	27.8		14.7		7.5		5.8	
	FTE	Lee	FTE	Lee	FTE	Lee	FTE	Lee
C_{11} (pF/cm)	10.48	10.74	5.78	5.88	3.19	3.22	2.57	2.58
C_{12} (fF/cm)	34.7	28.0	36.6	31.0	41.4	37.0	44.9	42.0
Gain (dB)	-49.6	-51.6	-44.0	-45.7	-37.7	-38.7	-35.2	-35.7

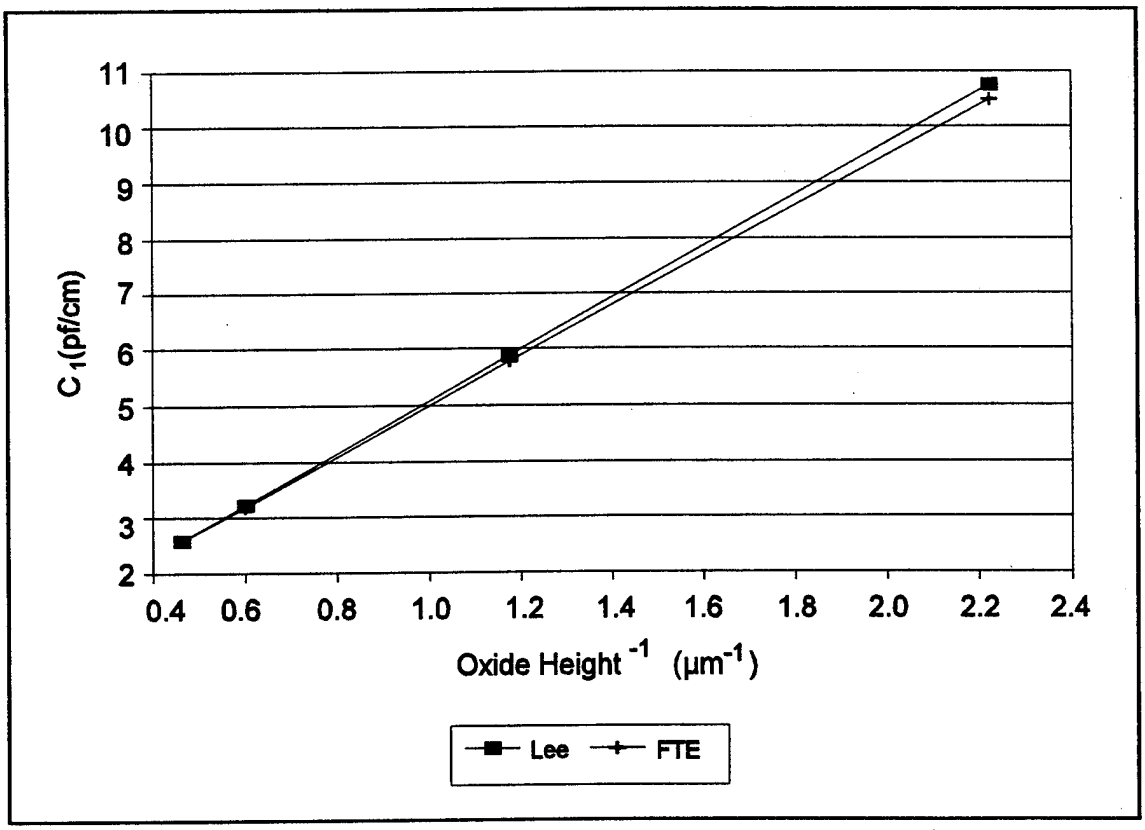


Figure V-46. Electrode-to-Ground Capacitance, C_1, Calculated with the FTE Model Compared to Lee's Data (190).

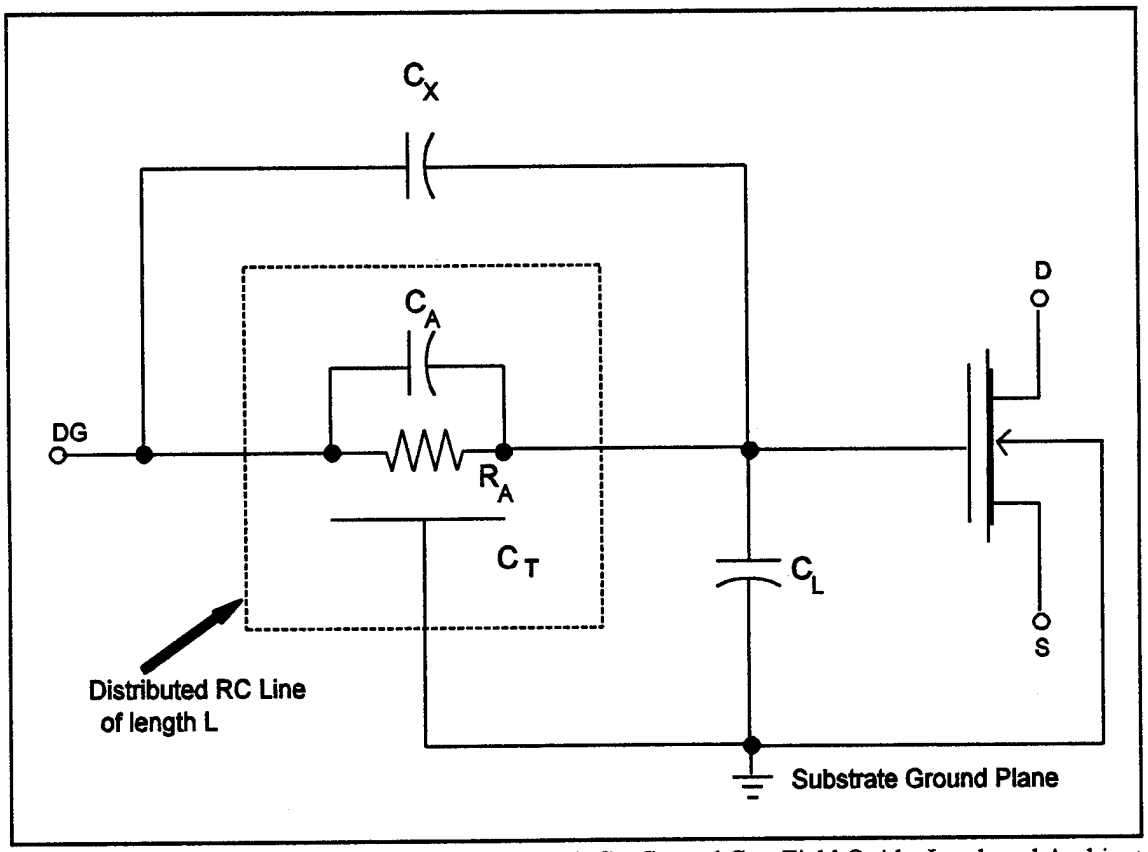


Figure V-47. IGE Sensor Transmission Line Model. C_T, C_L, and C_X - Field Oxide, Load, and Ambient Inter-Electrode Capacitances, R_A and C_A- Film Resistance and Capacitance (181).

assumption that the film's permittivity was equal to that of the oxide. For each value of C_A (or equivalently for each (C_T/C_A) ratio), R_A was incremented to trace each gain/phase contour. The value of C_X was chosen to satisfy the experimentally measured high frequency gain constraint. To demonstrate the ability to determine sheet resistance, the sensor was coated with a very thin polyethylene oxide (PEO) film (300Å) and exposed to air at several different dewpoints. The sensor's transfer function following moisture absorption by the PEO film was measured, and the sheet resistance was extracted from the calibration curves.

To verify the proposed IGEFET sensor finite-difference model thin film calculations, the gain/phase contours that are functions of the dewpoint (sheet resistance or loss) were qualitatively compared with Garverick's gain/phase contours. Garverick's data for a PEO-coated sensor exposed to five dew points is shown in Figure V-48. The solid curve in Figure V-48 represents the calibration curve for (C_T/C_A)=45. This data demonstrates that the sensor's transfer function may actually decrease for certain loss (dewpoint) values, as was observed with the proposed IGEFET sensor finite-difference model for films whose thickness was less than 4.5 μm (see Figures V-36 through V-39). As the (C_T/C_A)-ratio increased, Garverick showed that the "bowing" of the gain/phase contours increased, as shown in Figure V-49. This behavior is consistent with the proposed model results, where the maximum "bowing" in the gain/phase contours occurred when the imaginary part of the inter-electrode admittance, Y_{12}, (the inter-electrode capacitance term) passed through zero prior to the increase in the real part of Y_{12}, as shown in Figure V-43.

Experimental Measurements. As mentioned earlier, two approaches were chosen to validate the proposed IGEFET sensor model. The first approach, as just described, was to compare the model results with previously published data. The second approach confirmed the model results experimentally by measuring the current IGEFET sensor electrical properties when coated with films possessing different complex permittivity and thickness values. For thick films, the electrical properties of the uncoated sensor, and the sensor coated with a semi-infinitely thick epoxy film, were measured. The selection of an epoxy film for these experiments was based on past experience with this film in our laboratory (23, 195), and the availability of the previously published epoxy cure data measured by Lee (190) with an IGE structure sensor. Verification with thin films was accomplished by measuring the electrical properties of tantalum pentoxide thin films with three different thicknesses. The tantalum pentoxide films were also exposed to moisture to investigate the effect of loss on the sensor's transfer function.

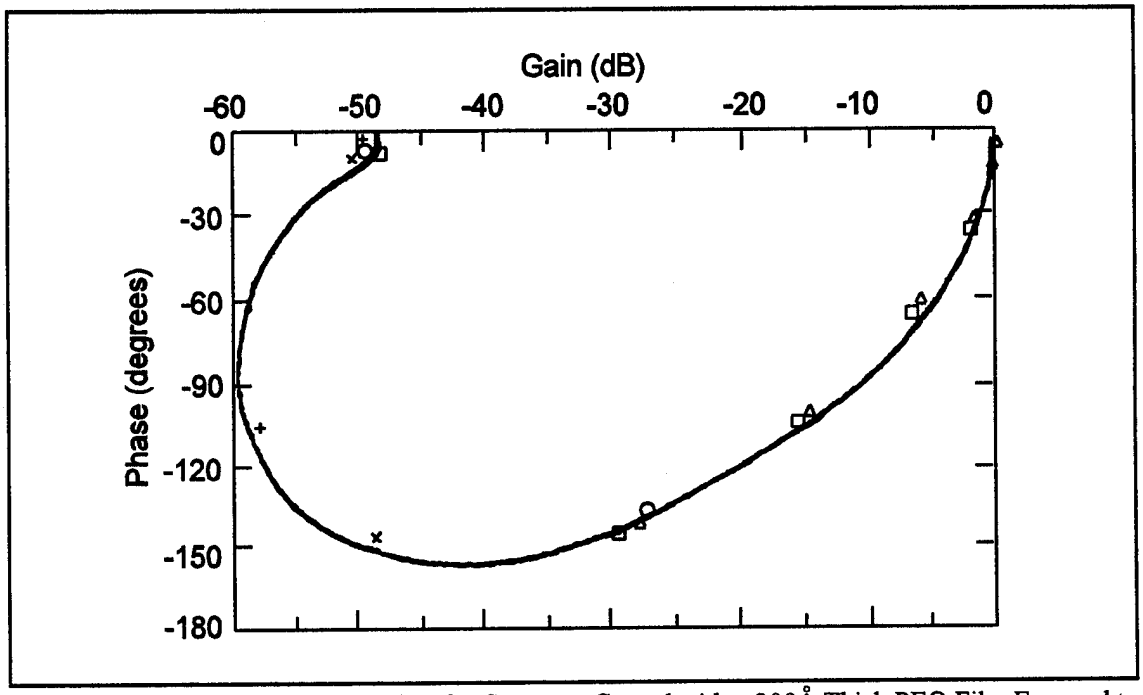


Figure V-48. Transfer Function of the IGE Structure Coated with a 300Å Thick PEO Film Exposed to Five Dewpoints (° C) (Plus:3.6; Cross:5.4; Circle:8.5; Square:12.7; and Triangle:14.8). Solid Curve-Calculated Response (181).

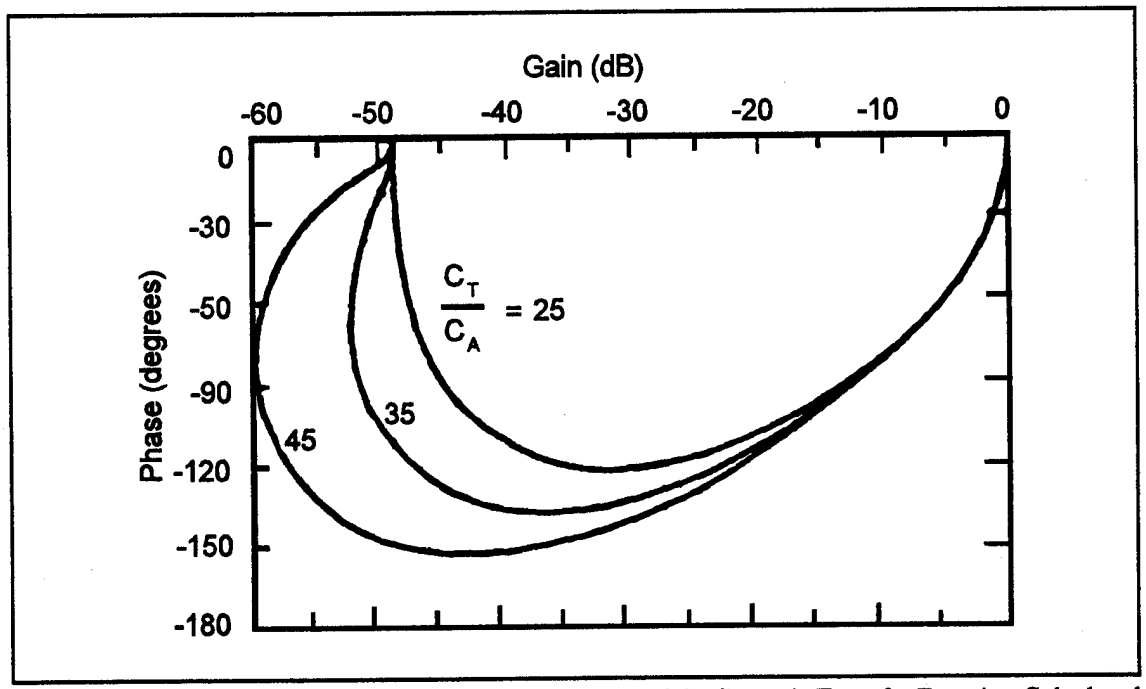


Figure V-49. Effect of the (C_T/C_A)-Ratio On the "Bowing" of the Sensor's Transfer Function Calculated by Garverick (181).

Semi-Infinite Thick Coatings. As a preliminary check on the proposed IGEFET sensor model, the response of the interdigitated electrode structure, prior to film deposition, was compared with the predicted response in Table V-4. The model calculations were performed given the current IGEFET geometry provided in Table V-1. The electrode-to-ground capacitance, C_1, and the inter-electrode capacitance, C_2, were measured with an HP4192A Low-Frequency Impedance Analyzer at 1 KHz (see Chapter IV). The sensor gain at 1 KHz was measured with an HP4194A Gain/Phase Analyzer (see Chapter IV). Initial measurements of the IGEFET sensor gain revealed significant variation between different microsensor elements. This variation was caused by parasitic capacitances between the driven-gate and floating-gate electrodes, and the floating-gate electrode-to-ground path. To eliminate these parasitic capacitances, the floating-gate electrode bond wire was removed. Table V-4 shows the measured gain for two IGEFET sensor elements before and after removal of the floating-gate bond wire. Before removal of the bond wire, the measured gain for neither of the sensors agreed with the -41.0 dB gain calculated with the model. The gain of sensor element 1 was greater than that predicted by the model, and this result indicates the presence of a parasitic capacitance causing greater coupling between the driven-gate and floating-gate electrodes. This behavior corresponds to the situation where the sensor's driven-gate and floating-gate bond pads are adjacent to each other in the integrated circuit package. For example, sensor element 6, which has adjacent locations for its driven-gate and floating-gate bond pads, behaved similarly. A second parasitic capacitance between the floating-gate electrode and ground was also identified, since the gain of sensor element 2 was less than that predicted by the model. A floating-gate electrode-to-ground parasitic capacitance effectively increases the load on the floating-gate, and according to Equation (V-27), reduces the transfer function gain. This parasitic capacitance is primarily due to the coaxial cable connected to the floating-gate within the test cell and the coaxial cable connecting the test cell to the instrumentation. After removal of the bond wire, which effectively eliminates these parasitic capacitances, the large variation between sensor elements was no longer observed, and the measured gain was in good agreement with the calculated gain. Table V-4 also reveals that the inter-electrode capacitance for sensor element 1 was nearly an order of magnitude greater than that predicted by the model and the measured value for sensor element 2. The electrode-to-ground capacitance was consistent across the sensor elements and was in good agreement with the model predictions. However, since the gain of both sensor elements calculated from the measured capacitances were significantly greater than the measured gain with the floating-gate electrode connected to its wire bond, the electrode-to-ground parasitic capacitance was compensated for by the impedance analyzer

Table V-4. Comparison of Calculated and Measured Electrical Parameters of an Uncoated IGEFET Sensor.

	Model	Sensor Element 1		Sensor Element 2	
		FG Bonded	FG Bond Removed	FG Bonded	FG Bond Removed
C_1 (pF)	22.7	22.0	---	21.9	---
C_2 (pF)	0.203	2.7	---	0.215	---
Calculated Gain (dB)	41.0	-19.2	---	-40.3	---
Measured Gain (dB)	---	-24.5	-40.2	-46.5	-40.9

calibration. For measurements using the gain/phase analyzer, the presence of the electrode-to-ground parasitic capacitance increased the load on the floating-gate electrode and decreased the measured gain.

Further support for the proposed IGEFET sensor model's validity with semi-infinitely thick films was obtained from the gain/phase measurements performed on IGEFETs coated with uncured and cured EPON 828 epoxy. Gain/phase measurements on two IGEFET sensors over the frequency range spanning 10 to 100 Hz, were used to determine the relative permittivity and bulk conductivity of uncured EPON 828 epoxy. Using the gain/phase measurements, the relative permittivity and the loss factor, which is defined as ($\sigma/\omega\epsilon'$), were extracted from the model calibration curves similar to Figure V-22. The bulk conductivity was obtained from a log-log plot of loss factor versus frequency, as shown in Figure V-50. If the conductivity is frequency independent, a log-log plot of the loss factor versus frequency will be linear with a slope of (-1), and it will have a y-intercept given by $\log(\sigma/\epsilon')$. The relative permittivity and bulk conductivity of the uncured epoxy were compared with the data reported by Lee in Table V-5. The relative permittivity of the cured epoxy was also determined using the proposed IGEFET sensor model and the corresponding gain/phase measurements. The EPON 828 epoxy was mixed with an equal amount of the Versamide V-40 curing agent, and the mixture was deposited on the IGEFET and allowed to cure overnight. The IGEFET sensor's gain/phase, shown in Figure V-51, was then measured and used to extract a cured permittivity of 3.3 from the calibration for a semi-infinite film shown in Figure V-24. The relative permittivity of the cured epoxy determined with parallel plate capacitor measurements was equal to 5. The difference in these permittivity values may reflect the difference in the curing and measurement conditions. The parallel plate capacitor structures were cured, and the capacitance was measured in the ambient laboratory air. In contrast, the epoxy deposited on the IGEFET was cured, and the gain/phase was measured under a dry nitrogen environment in the sample cell described in Chapter IV. Despite the large difference in permittivity measured with the parallel plate capacitor and the IGEFET, both permittivities were within the manufacturer specified permittivity value range for the cured epoxy (199).

Tantalum Oxide Thin Films. The finite-difference model predictions of the IGEFET sensor's electrical behavior when coated with thin films was experimentally verified with electrical measurements performed on tantalum oxide coated sensors. Three tantalum oxide films, 0.9 μm, 1.9 μm, and 3.9 μm thick, were deposited by sputtering them on to the nine sensor IGE arrays of the IGEFET Revision 3 design (23). The IGEFET sensor's gain corresponding to each film thickness are shown in Figure V-52. The sensor gain was computed from the IGE inter-electrode and electrode-to-ground capacitances measured with the HP4192A Low-Frequency Impedance Analyzer. These

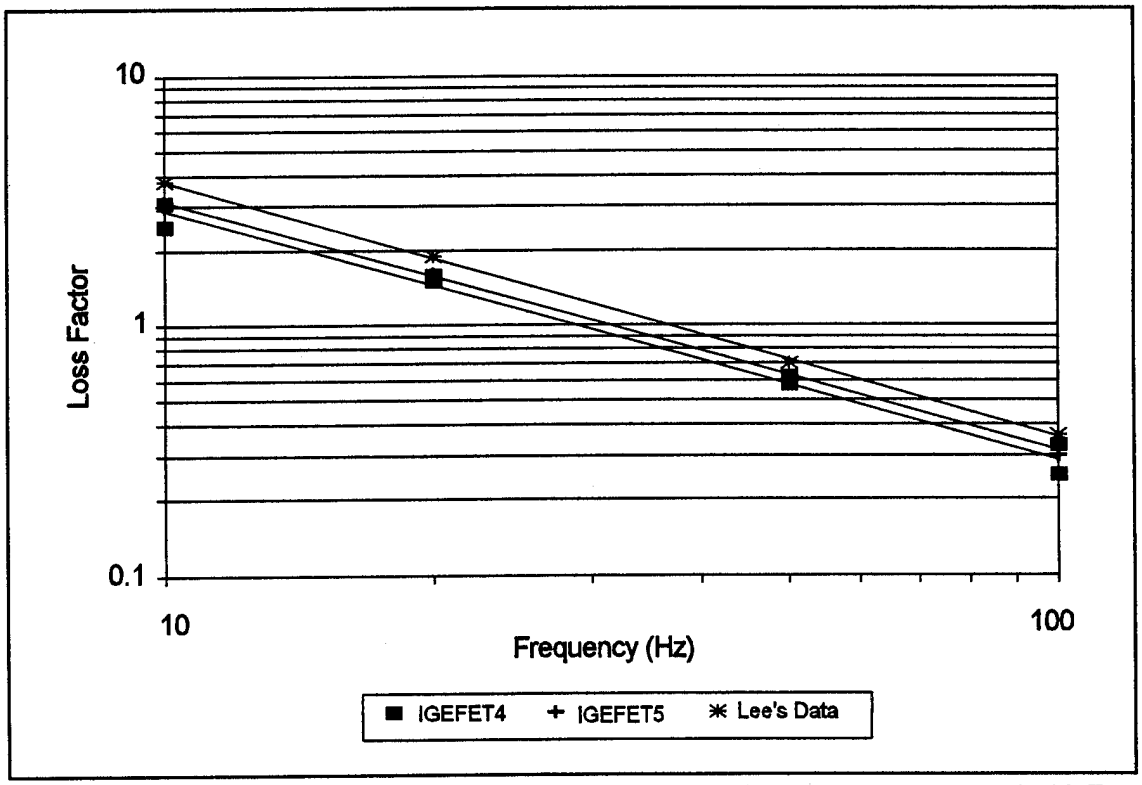


Figure V-50. Loss Factor Frequency Dependence of Uncured EPON 828 Epoxy Measured with Two Different IGEFETs along with Data Reported by Lee (190).

Table V-5. Comparison of EPON 828 Epoxy Material Parameters Extracted From the Finite-Difference Model and Data Reported By Lee (190).

	Lee	Measured	% Difference
Predicted Relative Permittivity	9.6	9.0	6.5
Predicted Bulk Conductivity (X1E-12 $(ohm\text{-}cm)^{-1}$)	3.1	2.6	17.5

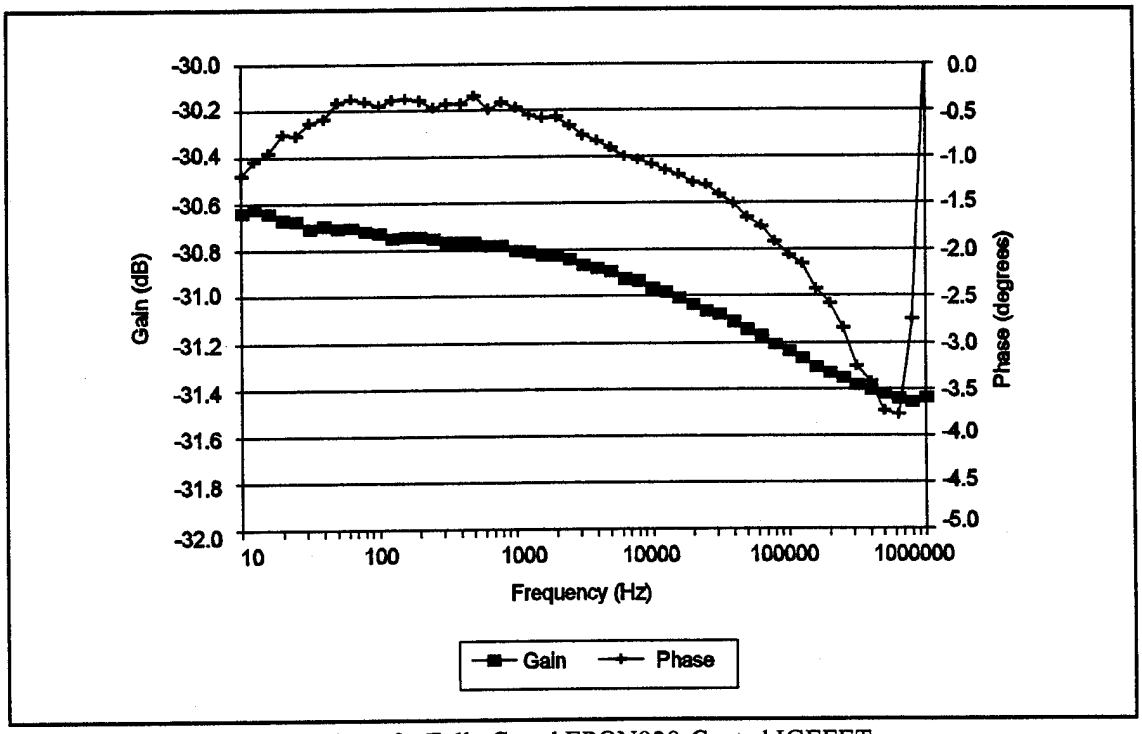


Figure V-51. Transfer Function of a Fully Cured EPON828-Coated IGEFET.

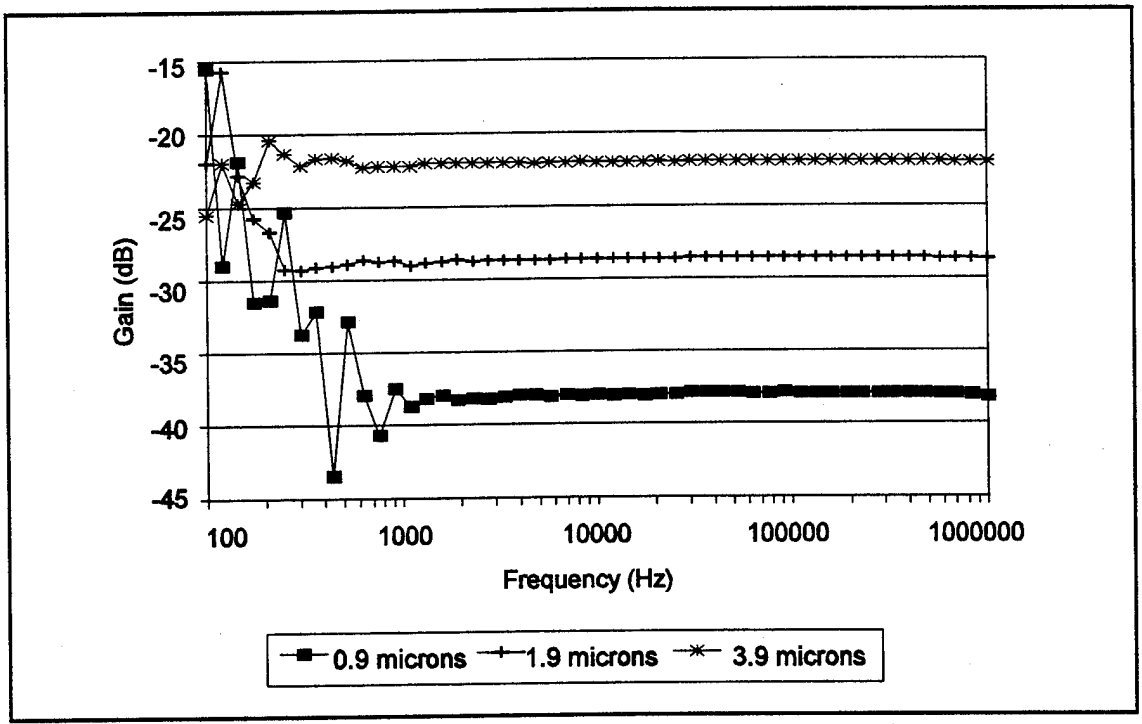


Figure V-52. Transfer Function Gain of the Tantalum Oxide Coated IGEFET Sensor.

measurements were performed in a dry nitrogen environment at room temperature. At frequencies below 1 KHz, the inter-electrode impedance exceeds the HP4192A's measurement capability (>10^9 ohms), and the computed gain became erratic. The IGEFET Revision 3 amplifiers were an open-loop design and, therefore, the amplifier's transfer function was sensitive to charge accumulation on the floating-gate. This situation caused unstable amplifier characteristics, which precluded reliable measurement of the transfer function gain with the HP4194A Gain/Phase Analyzer. Evidence of unstable amplifier performance was also observed during the moisture adsorption experiments described below. The gain response determined from the impedance measurements was compared with the gain response calculated with the IGEFET sensor's model for each film thickness, using a film relative permittivity of 18. This relative permittivity value was determined from the capacitance measurements associated with the parallel plate capacitors fabricated with sputtered tantalum oxide dielectrics. The published relative permittivity value for tantalum oxide is 22 (95). The measured and calculated sensor gain are shown in Table V-6.

Moisture adsorption experiments were conducted with the tantalum oxide coated IGEFETs to investigate the effect of dielectric loss on the sensor's transfer function. The sensor was baked at 150° C overnight to remove adsorbed moisture. The sensor was then inserted in the sample cell described in Chapter IV and flushed with dry, filtered laboratory air at a 100 ml/min flow rate. The initial (T=0) sensor transfer function measured with the HP4194A Gain/Phase Analyzer is shown in Figures V-53 and V-54. The decrease in gain and phase at high frequencies reflects the cutoff of the IGEFET amplifier, which had a -3 dB point at approximately 300 KHz. Since the amplifier was configured as an inverter, the initial phase was near 180°. These amplifier characteristics changed upon exposure to moisture. With moisture exposure, the dry air stream was diverted through a water bubbler prior to entry into the sample chamber. Following the introduction of the bubbled air stream into the sample chamber, the IGEFET sensor's transfer function was monitored with respect to time, as shown in Figures V-53 and V-54. The moisture exposure produced a large increase in the sensor gain over the entire frequency range. Also, a small decrease in phase was introduced at low frequencies. These changes are consistent with an increase in loss and/or permittivity of the tantalum oxide film, resulting from the adsorption of moisture. However, the data also suggests that the change in the IGEFET sensor's transfer function is, at least, in part, attributable to the change in the amplifier's characteristics. The -3 dB point was shifted towards 100 KHz, and the phase rotation, due to amplifier cut-off, shifted correspondingly to a lower frequency. Although the change in amplifier characteristics casts doubt over any quantitative analysis of the data, the qualitative behavior was consistent with an increase in the film's loss and/or permittivity.

Table V-6. Measured and Calculated Gain Response of IGEFET Sensors Coated with Tantalum Oxide Thin Films.

	Sensor Gain	
Film Thickness (μm)	Measured (dB)	Model (dB)
0.9	-38.0	-39.3
1.9	-28.7	-26.3
3.9	-22.0	-22.0

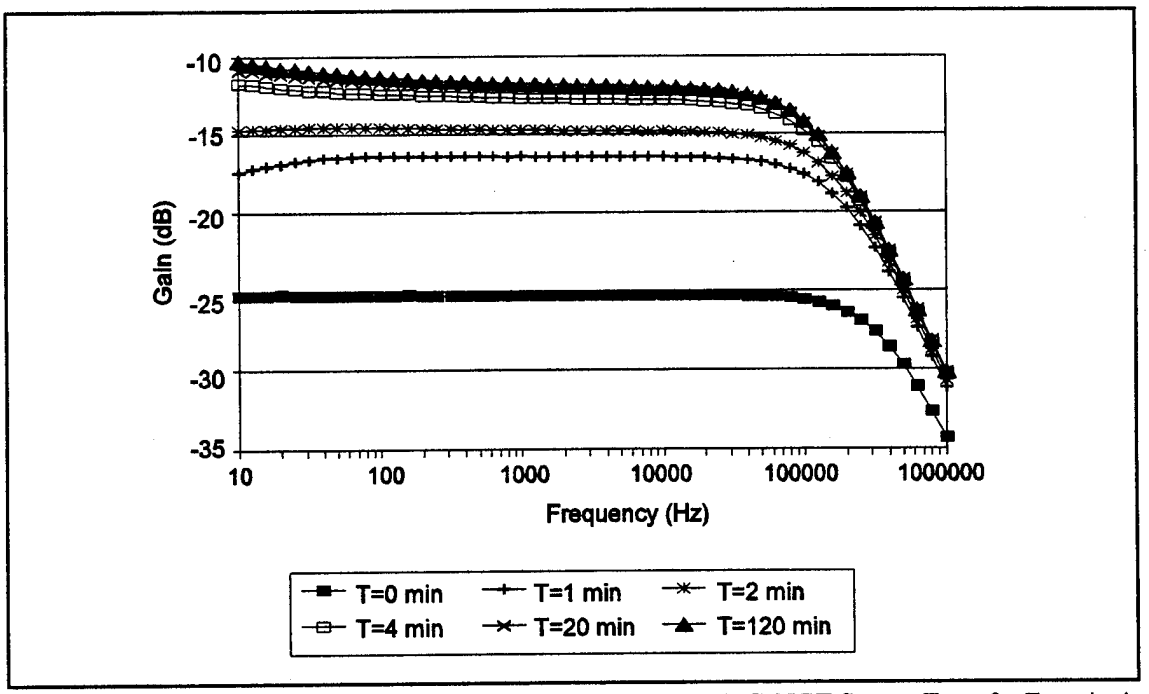


Figure V-53. Moisture Response of the Tantalum Oxide Coated IGEFET Sensor Transfer Function's Gain.

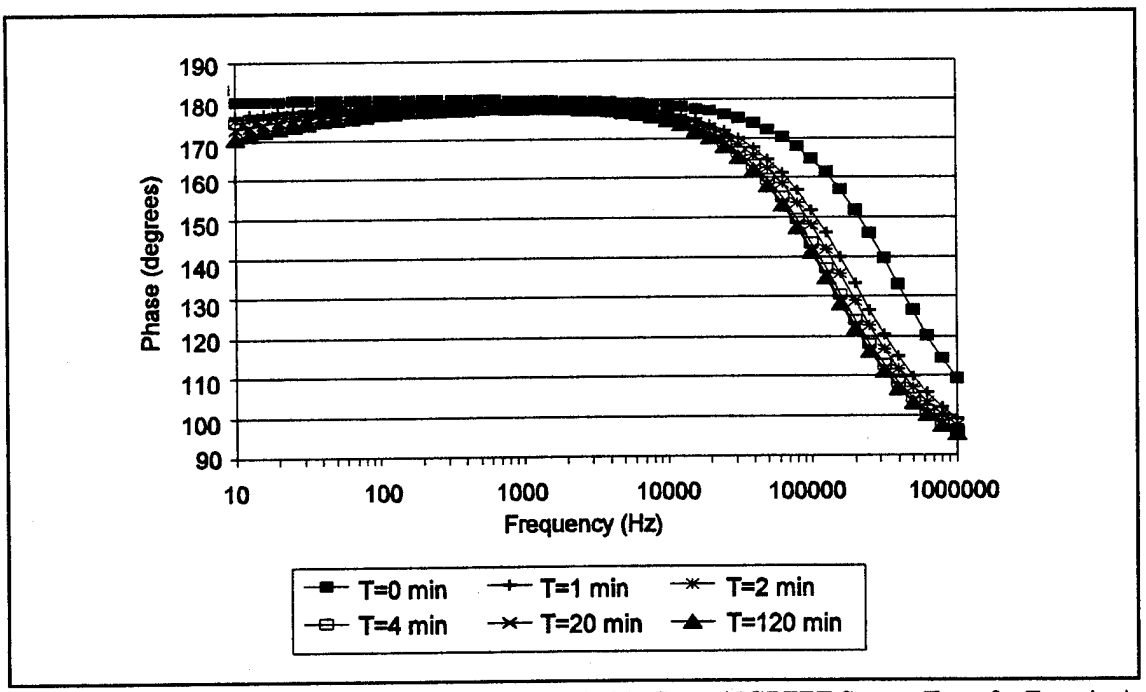


Figure V-54. Moisture Response of the Tantalum Oxide Coated IGEFET Sensor Transfer Function's Phase.

As a result of these experiments, the Revision 4 IGEFET design, which was used in subsequent experiments, was configured as a unity-gain, voltage-feedback amplifier to achieve stable operation. Capacitance measurements on the tantalum oxide parallel plate capacitors, conducted in the same manner as the IGEFET measurements, confirmed the increase in relative permittivity and loss, as shown in Figures V-55 and V-56. These Figures also show that the change in the parallel plate capacitance has substantially slower kinetics compared to the IGEFET sensor's transfer function response to moisture exposure.

Alternative Semi-Empirical Lumped-Element Circuit Model of the Interdigitated Gate Electrode Structure

The gain/phase contours produced by the finite-difference model (see Figures V-29 through V-39) were based on the assumption that the film coating on the interdigitated gate electrode structure is homogeneous, that contact effects are negligible, and that only the film's electrical characteristics are allowed to change. These assumptions produced the single semi-circular gain/phase arc that is characteristic of a single relaxation process. However, as shown in Chapter IV (see Figures IV-90 through IV-92), the measured gain/phase contours of the phthalocyanine coated IGEFET microsensors possessed two semi-circular arcs, indicating the presence of at least two separate relaxation processes. Contrary to the homogeneous assumption used in the finite-difference model, the SEM and TEM analysis discussed in Chapter IV demonstrated the polycrystalline nature of the deposited phthalocyanine films. Impedance spectroscopy studies of polycrystalline films have revealed the presence of two relaxation processes (manifested by two semi-circular arcs) (189). This data has been interpreted in terms of the relaxation processes occurring within the grain interiors and grain boundaries of the polycrystalline film (189). In conjunction with electrical studies, SEM/TEM analyses have also correlated the relaxation phenomenon with the degree of film crystallinity. Although the inhomogeneous morphology of the evaporated phthalocyanine films may result in two separate relaxation processes, contact effects between the phthalocyanine film and the metal electrodes, as discussed in Chapter IV, may also give rise to an additional relaxation process. Regardless of the specific mechanisms which contribute to the two observed relaxation processes, the finite-difference model could not be readily adapted to account for this behavior. Therefore, a semi-empirical, lumped-element circuit model was developed.

The measured gain and phase of the IGEFET sensor's transfer function was fitted to the analytical transfer function derived for the lumped-element circuit model shown in Figure V-57. In this

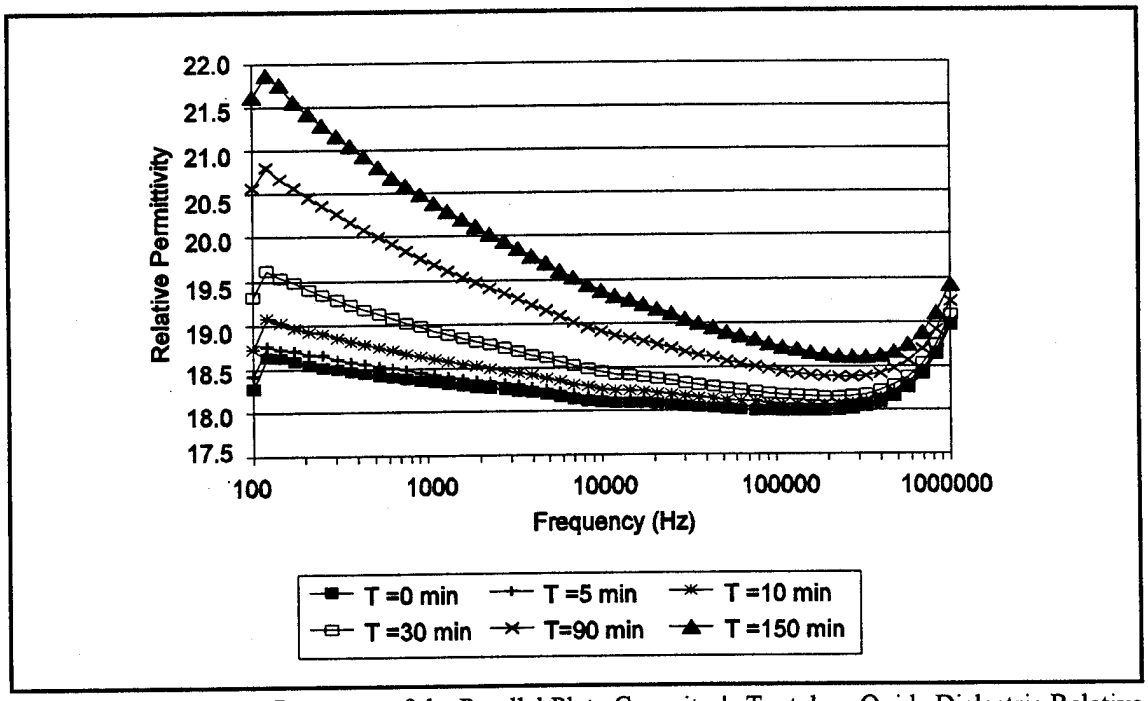


Figure V-55. Moisture Response of the Parallel Plate Capacitor's Tantalum Oxide Dielectric Relative Permittivity.

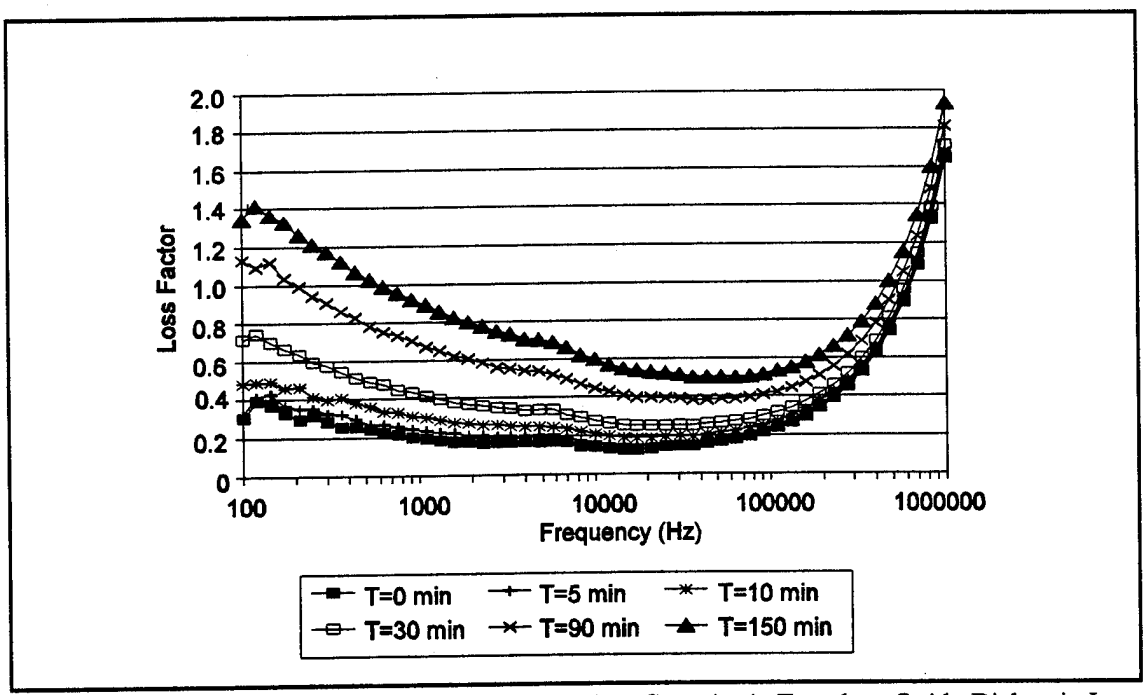


Figure V-56. Moisture Response of the Parallel Plate Capacitor's Tantalum Oxide Dielectric Loss Factor.

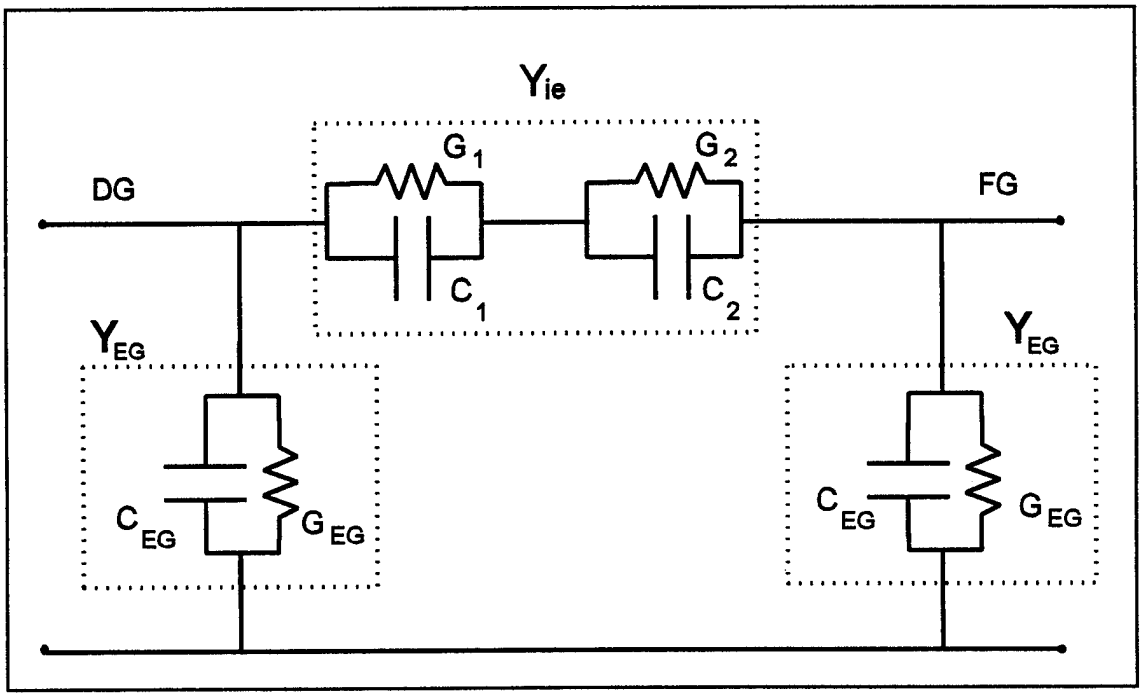


Figure V-57. Lumped-Element Circuit Model of the Interdigitated Gate Electrode Structure. Y_{IE} is the Inter-Electrode Admittance, Y_{EG} is the Electrode-to-Ground Admittance, G_1, G_2 are the Conductances and C_1, C_2 are the Capacitances, Associated with Two Separate Relaxation Processes which Combine to Form the Inter-Electrode Admittance, G_{EG} is the Electrode-to-Ground Conductance, and C_{EG} is the Electrode-to-Ground Capacitance.

model, the two relaxation processes are represented by two parallel admittances (G_1C_1 and G_2C_2) connected in series between the metal electrodes. The total series/parallel combination of these circuit elements represents the inter-electrode admittance, Y_{IE}. The electrode-to-ground admittance, Y_{EG}, is determined by the electrode-to-ground conductance, G_{EG}, and capacitance, C_{EG}. Using fundamental circuit analysis techniques, the transfer function's gain for the circuit depicted in Figure V-57 as a function of the ordinary frequency, $f = \omega/2\pi$, is given by:

$$\text{Gain} = 20 \cdot \log_{10}\left[\frac{|Y_{IE}|}{|Y_{IE} + Y_{EG}|}\right] \tag{V-31}$$

where

$$Y_{IE} = \frac{(G_1G_2 - 4\pi^2f^2C_1C_2) + j2\pi f(C_1G_2 + G_1C_2)}{(G_1 + G_2) + j2\pi f(C_1 + C_2)} \tag{V-32}$$

and

$$Y_{EG} = G_{EG} + j2\pi f C_{EG}. \tag{V-33}$$

Similarly, the transfer function's phase for the circuit in Figure V-57 is given by:

$$\text{Phase} = \phi_{Y_{IE}} - \phi_{(Y_{IE} + Y_{EG})} \tag{V-34}$$

where

$$\phi_{Y_{IE}} = \arctan\left[\frac{2\pi f(C_1G_2 + G_1C_2)}{G_1G_2 - 4\pi^2f^2C_1C_2}\right] - \arctan\left[\frac{2\pi f(C_1 + C_2)}{G_1 + G_2}\right], \tag{V-35}$$

$$\phi_{(Y_{IE} + Y_{EG})} = \arctan\left[\frac{(Y_{IE_{imag}} + Y_{EG_{imag}})}{(Y_{IE_{real}} + Y_{EG_{real}})}\right], \tag{V-36}$$

$$Y_{IE_{imag}} = \frac{2\pi f[G_1^2C_2 + G_2^2C_1 + 4\pi^2f^2C_1^2C_2 + C_1C_2^2)]}{(G_1 + G_2)^2 + 4\pi^2f^2(C_1 + C_2)^2}, \tag{V-37}$$

$$Y_{EG_{imag}} = 2\pi f C_{EG}, \tag{V-38}$$

$$Y_{IE_{real}} = \frac{G_1 G_2 (G_1 + G_2) + 4\pi^2 f^2 (C_1^2 G_2 + C_2^2 G_1)}{(G_1 + G_2)^2 + 4\pi^2 f^2 (C_1 + C_2)^2}, \tag{V-39}$$

and

$$Y_{EG_{real}} = G_{EG}. \tag{V-40}$$

The measured IGEFET gain/phase, as a function of frequency, was least-squares fitted to Equations V-31 through V-36. To facilitate the fitting process, the electrode-to-ground capacitance, C_{EG}, was assigned an initial value of 22 pF based upon the measured electrode-to-ground capacitance (see Table IV-8) and the finite-difference model calculations. Only slight variation of C_{EG} was permitted to fit the data ($< \pm 1$ pF adjustment). The conductance to ground was assigned an initial value of $1 \cdot 10^{-12}$ mhos since this represented the conductance through the oxide; the fit of the measured data was subsequently found to be independent of conductance to ground values less than $1 \cdot 10^{-11}$ mhos. Figures V-58 through V-60 show Bode and Nyquist plots of the measured gain/phase data of a CuPc coated IGEFET maintained at 170° C in air and the corresponding least-squares fit to the lumped-element circuit model. Similar results were obtained with the NiPc and CoPc thin films. The model parameters obtained by fitting the gain/phase data for each of the phthalocyanine coated IGEFET sensors measured at three different temperatures are provided in Tables V-7 through V-9. The model capacitances did not vary significantly with temperature; however, the model conductances were highly temperature dependent. Arrhenius plots of the two inter-electrode model conductances are shown in Figures V-61 and V-62. The activation energies for the inter-electrode conductances determined from these plots are shown in Table V-10. The activation energies corresponding to G_2, the model conductance associated with the longer time constant relaxation process, were consistently greater than the activation energies determined from the DC resistance measurements (Chapter IV). Although G_2 should dominate in the low-frequency regime, the activation energies corresponding to G_1 are in better agreement with the activation energies determined from DC resistance measurements. The differences between the experimental conditions to measure the DC resistance and the AC transfer function make it difficult to ascertain the cause of this apparent contradiction (see Chapter IV). A major difference in the experimental conditions for the two measurements was the applied voltage bias. While the DC resistance measurements were made with a

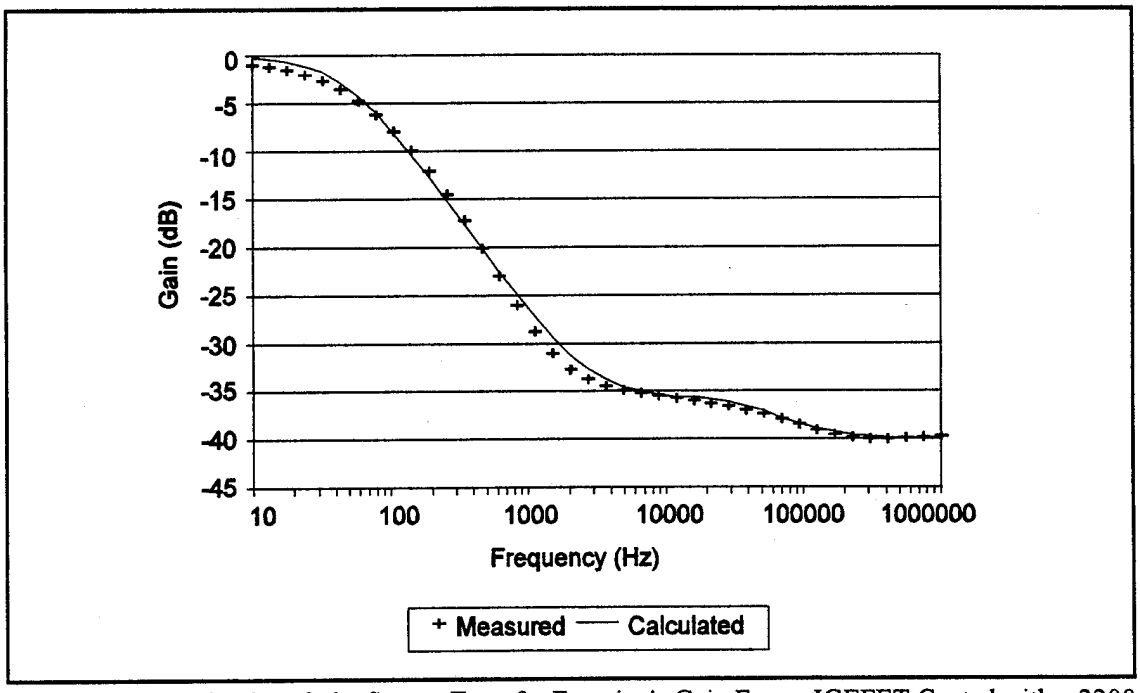


Figure V-58. Bode Plot of the Sensor Transfer Function's Gain For an IGEFET Coated with a 3200 Å Thick Copper Phthalocyanine (CuPc) Film at 170° C. Microsensor Maintained in a Dry Air Ambient.

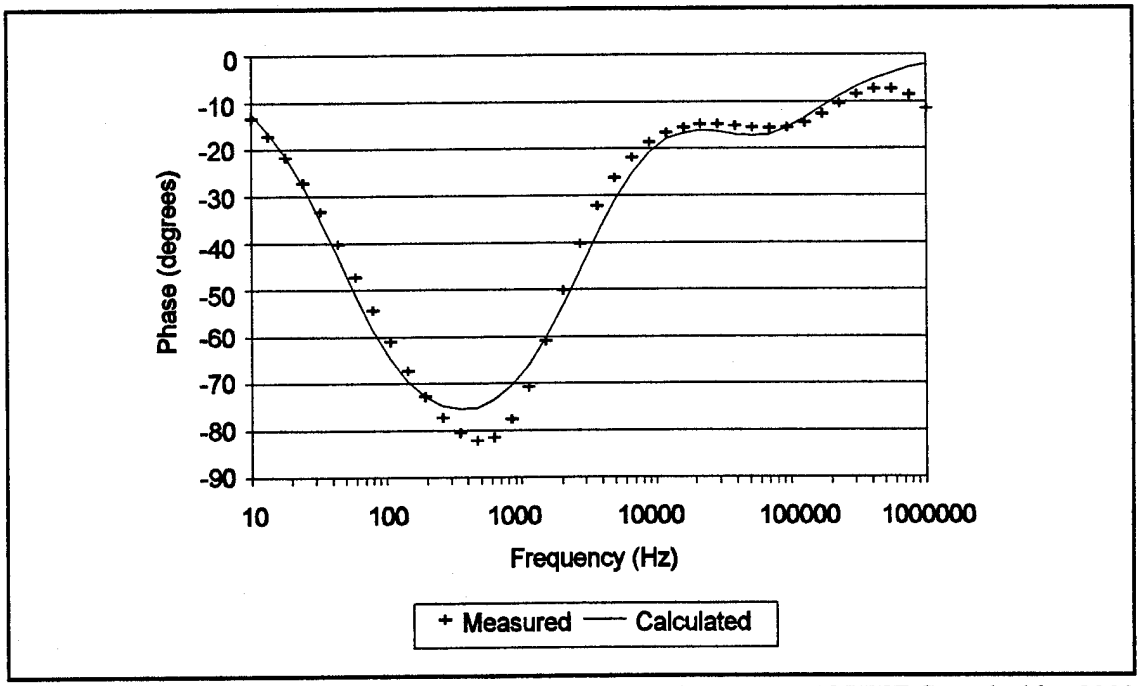


Figure V-59. Bode Plot of the Sensor Transfer Function's Phase For an IGEFET Coated with a 3200 Å Thick Copper Phthalocyanine (CuPc) Film at 170° C. Microsensor Maintained in a Dry Air Ambient.

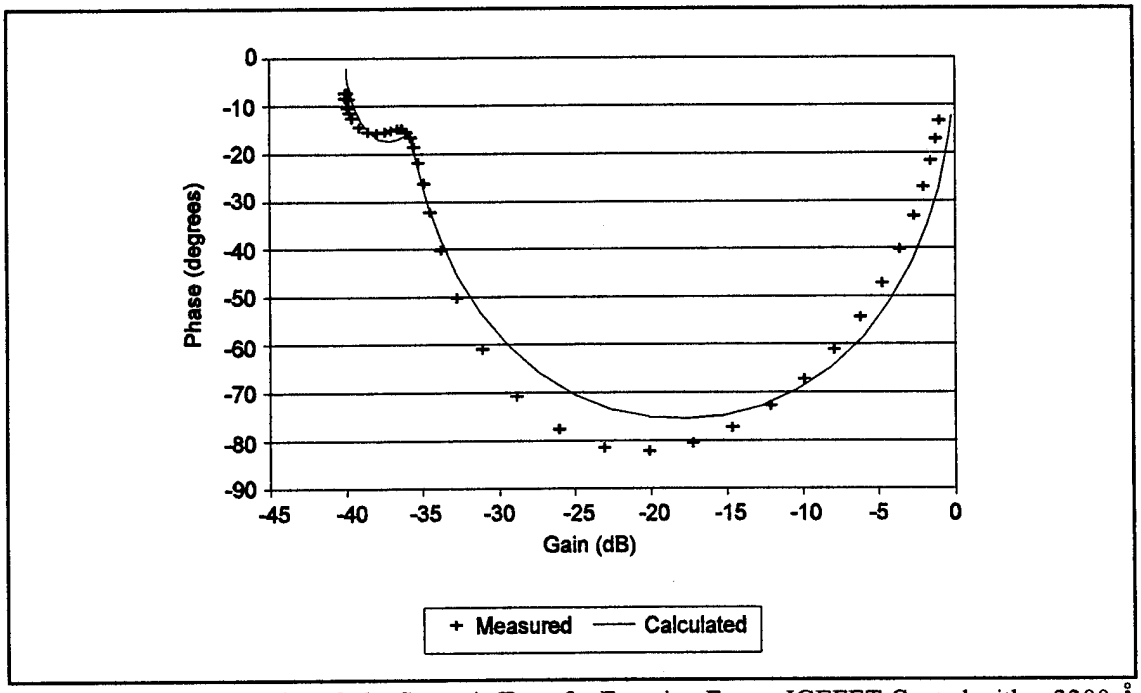


Figure V-60. Nyquist Plot of the Sensor's Transfer Function For an IGEFET Coated with a 3200 Å Thick Copper Phthalocyanine (CuPc) Film at 170 °C. Microsensor Maintained in a Dry Air Ambient.

Table V-7. Least-Squares Calculated Lumped-Element Circuit Model Parameters for a CuPc Coated IGEFET Sensor at Three Different Temperatures

Model Parameter	Temperature		
	30° C	80° C	170° C
G_1 (mhos)	$2.3 \cdot 10^{-9}$	$2.1 \cdot 10^{-8}$	$3 \cdot 10^{-7}$
C_1 (F)	$6.7 \cdot 10^{-13}$	$5.9 \cdot 10^{-13}$	$5.5 \cdot 10^{-13}$
G_2 (mhos)	$9 \cdot 10^{-12}$	$2.1 \cdot 10^{-10}$	$6.8 \cdot 10^{-9}$
C_2 (F)	$3.55 \cdot 10^{-13}$	$3.55 \cdot 10^{-13}$	$3.9 \cdot 10^{-13}$
G_{EG} (mhos)	$1 \cdot 10^{-12}$	$1 \cdot 10^{-12}$	$1 \cdot 10^{-12}$
C_{EG} (F)	$2.25 \cdot 10^{-11}$	$2.23 \cdot 10^{-11}$	$2.3 \cdot 10^{-11}$

Table V-8. Least-Squares Calculated Lumped-Element Circuit Model Parameters for a NiPc Coated IGEFET Sensor at Three Different Temperatures.

Model Parameter	Temperature		
	30° C	80° C	170° C
G_1 (mhos)	$3 \cdot 10^{-10}$	$3.3 \cdot 10^{-9}$	$1 \cdot 10^{-7}$
C_1 (F)	$6 \cdot 10^{-13}$	$6 \cdot 10^{-13}$	$5.5 \cdot 10^{-13}$
G_2 (mhos)	$3 \cdot 10^{-12}$	$6.9 \cdot 10^{-11}$	$5 \cdot 10^{-9}$
C_2 (F)	$3.45 \cdot 10^{-13}$	$3.8 \cdot 10^{-13}$	$3.6 \cdot 10^{-13}$
G_{EG} (mhos)	$1 \cdot 10^{-12}$	$1 \cdot 10^{-12}$	$1 \cdot 10^{-12}$
C_{EG} (F)	$2.2 \cdot 10^{-11}$	$2.25 \cdot 10^{-11}$	$2.25 \cdot 10^{-11}$

Table V-9. Least-Squares Calculated Lumped-Element Circuit Model Parameters for a CoPc Coated IGEFET Sensor at Three Different Temperatures.

Model Parameter	Temperature		
	30° C	80° C	170° C
G_1 (mhos)	$2.2 \cdot 10^{-9}$	$3. \cdot 10^{-8}$	$5.5 \cdot 10^{-7}$
C_1 (F)	$5.8 \cdot 10^{-13}$	$5.65 \cdot 10^{-13}$	$5.65 \cdot 10^{-13}$
G_2 (mhos)	$3 \cdot 10^{-12}$	$4 \cdot 10^{-11}$	$8 \cdot 10^{-10}$
C_2 (F)	$3.6 \cdot 10^{-13}$	$3.7 \cdot 10^{-13}$	$3.6 \cdot 10^{-13}$
G_{EG} (mhos)	$1 \cdot 10^{-12}$	$1 \cdot 10^{-12}$	$1 \cdot 10^{-12}$
C_{EG} (F)	$2.25 \cdot 10^{-11}$	$2.25 \cdot 10^{-11}$	$2.3 \cdot 10^{-11}$

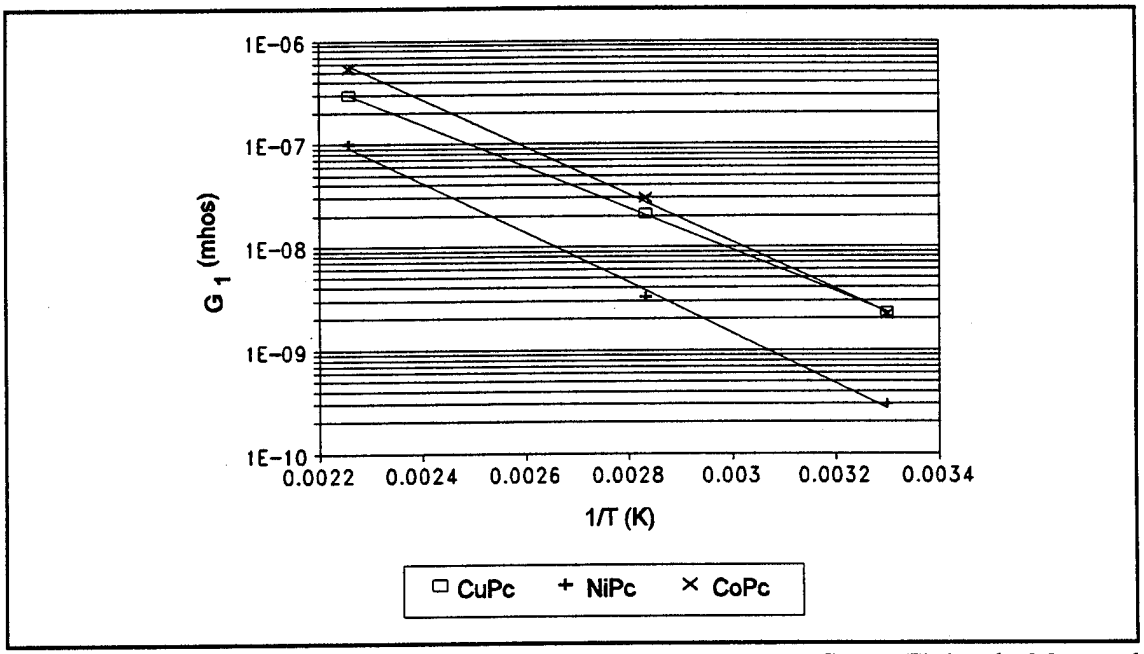


Figure V-61. Arrhenius Plot of the G_1 Conductance Obtained From Least-Square Fitting the Measured Gain/Phase of IGEFET Sensors Coated with 3200 Å Copper Phthalocyanine (CuPc), 4300 Å Nickel Phthalocyanine (NiPc), and 5100 Å Cobalt Phthalocyanine (CoPc) Thick Films. Microsensor Maintained in a Dry Air Ambient.

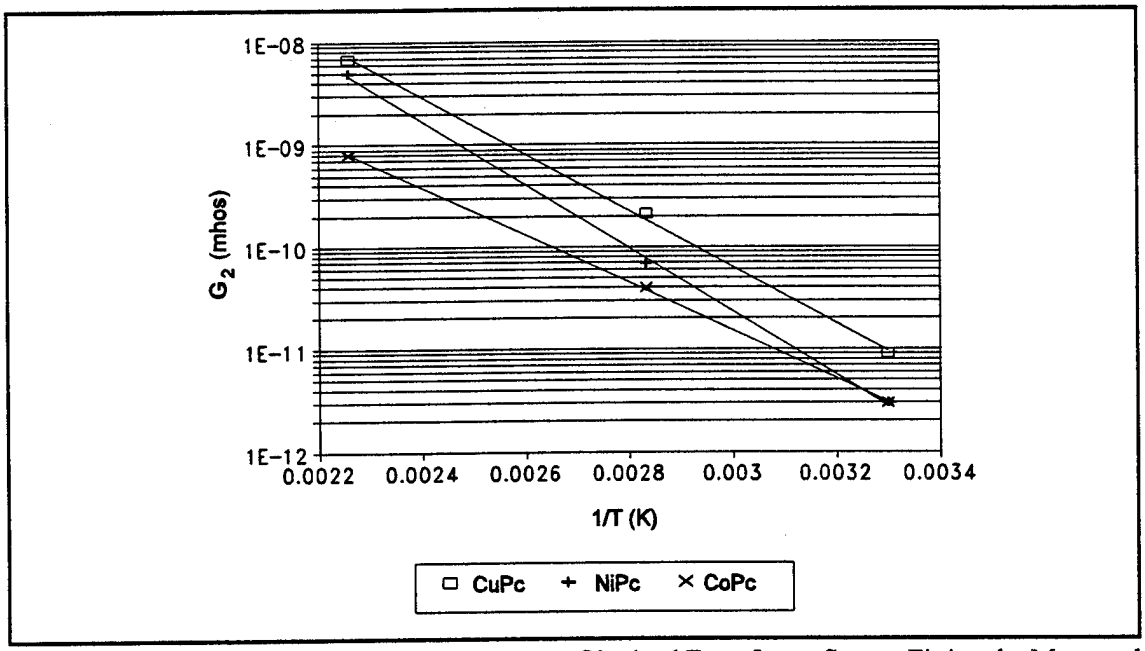


Figure V-62. Arrhenius Plot of the G_2 Conductance Obtained From Least-Square Fitting the Measured Gain/Phase of IGEFET Sensors Coated with 3200 Å Copper Phthalocyanine (CuPc), 4300 Å Nickel Phthalocyanine (NiPc), and 5100 Å Cobalt Phthalocyanine (CoPc) Thick Films. Microsensor Maintained in a Dry Air Ambient.

Table V-10. Activation Energies for the Inter-Electrode Model Conductances for the Three Different Phthalocyanine Thin Films.

	Activation Energy (eV)		
Model Parameter	CuPc	NiPc	CoPc
G_1	0.40	0.48	0.46
G_2	0.55	0.61	0.46

10 volt bias, the AC measurements were made with a small amplitude AC signal and zero DC bias. In Chapter IV, the DC resistance of the phthalocyanine coated IGE structure was shown to be highly dependent upon the applied bias, decreasing more than order of magnitude as the applied bias was increased from 1 to 10 volts. If G_2 was responsible for this observed voltage dependence, it may no longer dominate the inter-electrode DC resistance when measured with a 10 volt applied bias. Determination of the DC inter-electrode resistance thermal activation energy at different applied bias levels could be used to evaluate this hypothesis.

Summary

In this chapter, two models of the IGEFET sensor were developed: a finite-difference model and a lumped-element circuit model. The finite-difference model computes the transfer function of an interdigitated gate electrode (IGE) structure coated with a lossy dielectric film whose thickness spans 0.1 to 7.5 μm, or is considered to be semi-infinite. The model accounts for finite thickness electrodes and oxide overetch (undercut) within the inter-electrode space. The model also eliminates the assumption made in Garverick's model that requires the IGE structure capacitances to be independent of the film's conductance. The finite-difference model developed may serve in the future as a design tool for investigating the impact of geometrical parameter variations on the IGE structure's transfer function. The geometrical and material parameters that may be studied include the electrode (height/width) ratio, the oxide height, the width of the inter-electrode space, and the film's complex permittivity and thickness. The model results were verified experimentally and were confirmed by comparison with previously published data. The proposed finite-difference IGEFET sensor model results helped to identify the experimental configuration improvements, such as voltage feedback for stable amplifier operation, and the removal of the floating-gate bond wire to eliminate the effect of load capacitance on the measured transfer function. Due to the limited capability of the finite-difference approach for modeling multiple relaxation processes, the lumped-element circuit model was developed. This model permits the least-squares extraction of the values for the lumped-element circuit elements from the gain/phase data such that they adequately represent the measured transfer function of the IGEFET sensor. In Chapter VI, the change in the values for these circuit elements as a result of gas exposure are used as discriminant features in the analysis of binary gas mixtures.

VI. *IGEFET Gas Sensitivity and Selectivity Analysis*

This chapter describes the application of the metal phthalocyanine (MPc) coated IGEFET microsensor for gas detection and quantification of single component and binary gas mixtures. Two gases, nitrogen dioxide (NO_2) and ammonia (NH_3), were selected for this investigation from a set of six candidate gases. The selection of these two gases was based upon the known sensitivity and reversibility of the MPc-coated IGEFET electrical response upon exposure to each candidate gas. The screening of the candidate gases was accomplished in collaboration with Captain Clay Howe, and the results have been reported elsewhere (25). This chapter begins with a description of the experimental approach for the measurement and analysis of the MPc-coated IGEFET microsensor's electrical response to gas exposure. As discussed in Chapter IV, the electrical measurements used for gas analysis were limited to the interdigitated gate electrode (IGE) structure DC resistance, the IGEFET sensor transfer function gain, and the IGEFET sensor transfer function phase. Following the discussion of the experimental approach, the single component and binary gas mixture analyses utilizing the data collected with each type of measurement are presented. The discussions of the results are organized into separate sections corresponding to each measurement type.

Experimental Approach

The IGEFET gas analysis began with a series of experiments to identify a test protocol suitable for conducting binary gas mixture analysis. The experiments investigated the effect of temperature, challenge gas pre-conditioning, and the exposure and purge cycle durations relative to the sensor's sensitivity, the stability of the measurement baseline, and the overall experiment duration. The results of these preliminary experiments are presented in Appendix J. The test protocol selected on the basis of these preliminary experiments was applied to the measurement of the IGEFET electrical response to separate exposures of each of the challenge gases. The single component gas exposure data collected was analyzed using the ***P***-matrix method (165) and principal component analysis (161, 170) techniques described in Chapter III. After demonstrating the viability of the analysis of the IGEFET sensor response following exposure to single component gases, the binary gas mixture measurements and analysis were conducted in a similar manner. The implementation of this approach required the development of a gas generation and delivery system, definition of the test protocol, and establishment of the data reduction and analysis procedures. The details of each aspect of the implementation are discussed in the following sections.

Gas Generation and Delivery System. In order to generate reproducible concentrations of the two challenge gases and deliver them at a constant flow rate to the IGEFET microsensor for analysis, a gas generation and delivery system was designed that incorporated calibrated flowmeters and permeation tubes. A schematic of the gas generation and delivery system is shown in Figure VI-1.

The principal components of the gas generation and delivery system are the needle valves, the calibrated glass-bead flowmeters (Gilmont Instruments, Great Neck, NY), and the nitrogen dioxide and ammonia permeation tubes (model 23-7502 and model 23-7014, respectively, G.C. Industries, Fremont, CA). A permeation tube is a device calibrated to release the gas it contains at a specified rate at a given temperature. To insure a stable permeation rate, the permeation tubes were immersed in a thermostatically-controlled water bath (model RTE-88D, Neslab Corp., Newington, NH). When the gas released by the permeation tube is mixed with a carrier gas flowing across the tube at a known flow rate, the resulting concentration of the challenge gas present in the carrier gas can be calculated. The resulting challenge gas concentration (C) generated is given by the following expression:

$$C = \frac{KP}{F} \qquad \text{(VI-1)}$$

where P is the permeation rate in nanograms/min, F is the carrier gas flow rate in ml/min, and K is a constant specific to each gas. The permeation tube vendor supplied the permeation rate and the value of the constant, K, for each permeation tube.

Dehumidified room air was selected as the carrier gas. The room air was dehumidified using a desiccant vessel containing a bed of silica gel beads, and then it was filtered through a bed of activated charcoal to remove organic contaminants. The relative humidity of the carrier gas was monitored with an in-line digital display hygrometer (model HS-1CHDT-2A, Thunder Scientific Corp., Albuquerque, NM). With fresh desiccant, the hygrometer would typically indicate $0 \pm 2\%$ relative humidity. The desiccant was recharged whenever the relative humidity exceeded $+4\%$.

Independent control of the carrier gas flow rates across each permeation tube was required for independent control of the specific concentrations of each gas. To introduce both test gases into the same carrier gas stream and still provide independent control of the carrier gas flow rate across each tube, the permeation tubes were connected serially with the permeation tube requiring the highest flow rate located first in the carrier gas stream. A calibrated glass-bead flow meter controlled the carrier gas flow rate across the first permeation tube. The flow at the output of the first permeation tube in excess of that required to generate the appropriate concentration of the second gas component

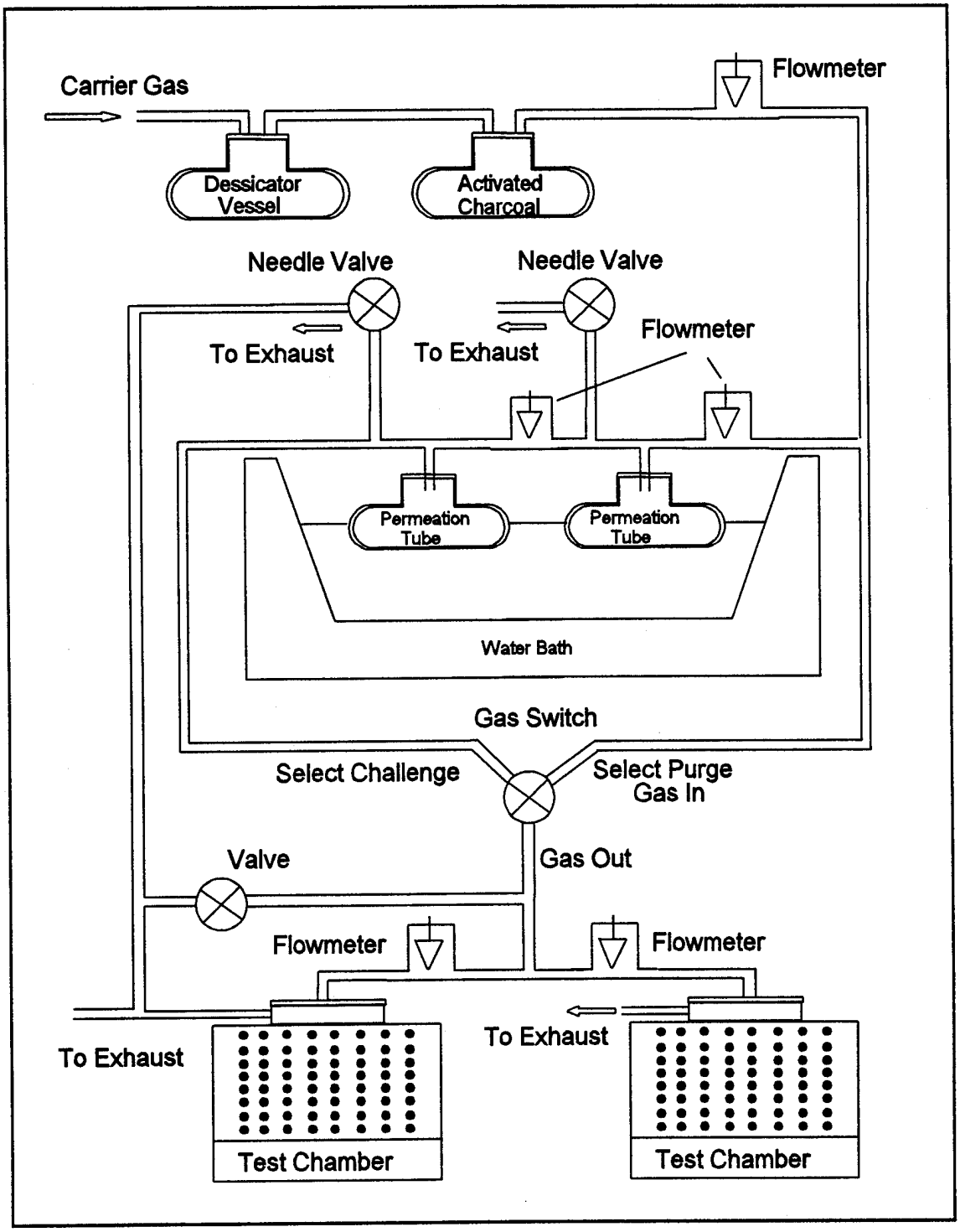


Figure VI-1. Gas Generation and Delivery System.

was vented to the exhaust through a needle valve. Since the needle valve actually controlled the flow, the glass-bead flow meter was used solely to monitor the carrier gas flow rate across the second permeation tube. The needle valve at the output of the second flow meter allowed continuous flow across the permeation tubes to permit adjustment and equilibration of the gas mixtures during the purge cycle. A three-way valve was used to select either the challenge gas or the purge (carrier) gas for delivery to the sample chambers. The challenge gas and the purge gas flow rates to each sample cell was monitored with a glass-bead flowmeter and maintained at a constant 100 ml/min value by venting the excess flow to the exhaust through a needle valve.

Test Protocol. The following test protocol was established to collect the MPc-coated IGEFET electrical response upon exposure to each of the individual challenge gases and their binary mixtures. As discussed earlier, these test conditions were defined as a result of several preliminary experiments (Appendix J) that confirmed these operating conditions afforded the best compromise between sensitivity, baseline stability, and experiment duration. The IGEFET electrical response during challenge gas exposure was collected from two microsensors located in the two sample chambers (Chapter IV). The IGE structure DC resistance was collected from one microsensor, while simultaneously, the IGEFET sensor transfer function gain/phase was measured from the other. The two IGEFET microsensors were coated with three different MPc thin films: copper phthalocyanine (CuPc), nickel phthalocyanine (NiPc), and cobalt phthalocyanine (CoPc). Each MPc film type had been simultaneously deposited upon both IGEFET microsensors to insure the two microsensors had identical film thicknesses. Table VI-1 specifies the MPc film coating type and thickness for each of the nine IGEFET sensing elements on the microsensors. To minimize the challenge gas exposure time, which adversely affects reversibility, and yet maintain an adequate sampling rate for each electrical measurement type, the DC resistance data was collected from a subset of six IGEFET sensing elements (elements 1, 2, 4, 5, 7, and 8).

The exposure cycle illustrated in Figure VI-2 was adopted for the IGEFET gas analysis. Following an overnight purge at 170° C, the temperature of the microsensors was automatically reduced (under software control) to the 100° C test temperature approximately two hours prior to the commencement of gas testing and data collection. At the end of the preceding day, the gas generation and delivery system was configured to generate the challenge gas mixture to be tested on the following day. After the instrumentation was recalibrated, data collection was initiated. After approximately 16 minutes, during which the baseline response was collected, the microsensors were exposed to the challenge gas for 16 minutes. Following the challenge gas exposure, the microsensors were purged

Table VI-1. IGEFET Sensing Element MPc Film Coating Type and Thickness.

IGEFET Element Number	MPc Film	Film Thickness (μm)
1	CuPc	0.32
2	CuPc	0.32
3	CuPc	0.32
4	NiPc	0.43
5	NiPc	0.43
6	NiPc	0.43
7	CoPc	0.51
8	CoPc	0.51
9	CoPc	0.51

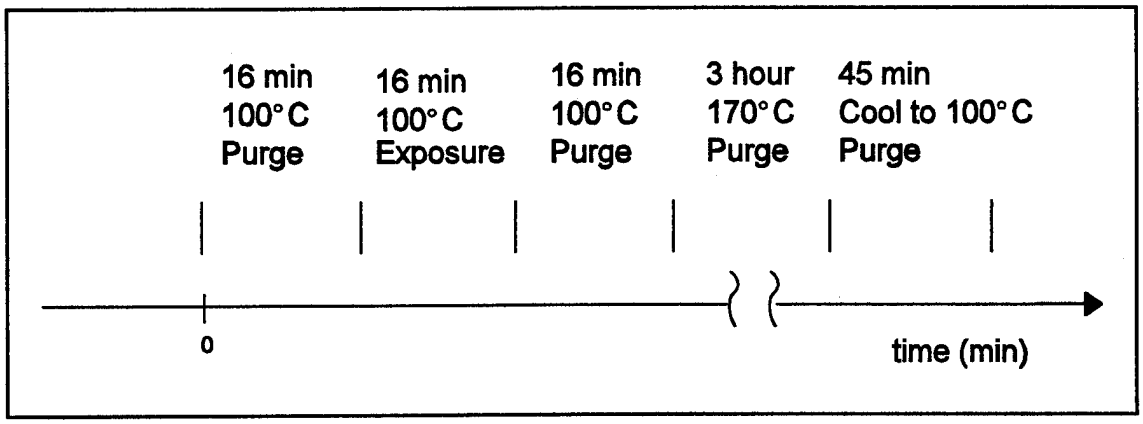


Figure VI-2. Challenge Gas Exposure Cycle for the IGEFET Microsensor Gas Analysis.

for 16 minutes at 100° C before the temperature was elevated to 170° C for approximately 3 hours. After the elevated temperature purge (170° C), the temperature was reduced to the test temperature (100° C) and allowed to stabilize prior to the next challenge gas exposure. This exposure cycle was repeated twice more with the same challenge gas concentration or mixture. The elevated temperature purge following the final exposure was continued overnight.

Data Reduction and Analysis Approach. The analysis of the IGEFET electrical response to the challenge gas exposure involved normalization of the measured data, formation of feature vectors representing the response of the three IGEFET electrical parameters (DC resistance, transfer function gain, and transfer function phase) measured during exposure to the challenge gas, and the application of the principal component analysis (PCA) technique with these feature vectors in an attempt to determine the individual challenge gas component concentrations. The feature vectors were formed from the characteristic discriminants identified by visually examining the IGEFET electrical response with respect to exposure duration, challenge gas species, and challenge gas concentrations. For the IGEFET transfer function gain and phase measurements, the response was also measured with respect to frequency. The lumped element circuit model developed in Chapter V permitted a second approach to the analysis of the IGEFET transfer function response upon gas exposure. In this second approach, the two inter-electrode conductance parameters derived from least-squares fitting the gain and phase measurements to Equations V-31 and V-34, respectively, were used as discriminant features in the PCA. This approach, which adds greater physical significance to the discriminant features extracted from the IGEFET transfer function response, was investigated to determine if enhanced predictive capability could be achieved with these features. However, this approach, which was first tested with the nitrogen dioxide analyses, had essentially the same predictive capability as the normalized DC resistance response. The results with the nitrogen dioxide analyses did not warrant the added complexity required to curve fit the data for the other analyses. The formation of the four categories of feature vectors (normalized DC resistance, gain response, phase response, and the conductance parameters) from the IGEFET electrical measurements and the implementation of the PCA technique are discussed in separate sections following the description of the IGEFET electrical response normalization process.

Normalization of the IGEFET Electrical Response. As indicated in the test protocol, the IGEFET electrical response to only a single challenge gas mixture (measured in triplicate) was collected each day. Consequently, the calibration data for the single component and binary gas mixture analyses was collected over a six-week period. Normalization of the IGEFET response was

accomplished to account for the sensor's baseline drift over the extended duration required to collect the IGEFET electrical response upon gas exposure. The IGEFET electrical response data collected for each challenge gas exposure was normalized with respect to the baseline electrical response measured just prior to the introduction of the challenge gas. The IGE structure DC resistance data was normalized by dividing the resistance measured at time t, R(t), by the baseline electrical resistance, R(t=0), measured just prior to gas exposure. The IGEFET transfer function gain, G(t), and phase, P(t), data was normalized by subtracting the baseline gain/phase, G(t=0) and P(t=0), from the gain and phase at time t, G(t) and P(t), respectively. The normalized gain and phase data will be referred to as the gain response and phase response, respectively. The conductance terms obtained from the least-squares fit of the transfer function measurements to Equations V-31 and V-34 are normalized in a manner similar to the resistance measurements. That is, the conductance terms at time t, $G_1(t)$ and $G_2(t)$, are divided by the baseline conductances, $G_1(t=0)$ and $G_2(t=0)$, measured just prior to each gas exposure. Examples of the baseline and gas exposed IGEFET electrical characteristics used to calculate the normalized response are shown in Figures VI-3 through VI-5 for a 400 ppb NO_2 challenge. Most of the analysis implemented to identify the characteristic features for the PCA gas analysis was performed with the average response that was formulated from each set of triplicate measurements.

Feature Vector Formation from the DC Resistance Measurements. Figures VI-6 through VI-8 depict the time response of the average normalized DC resistance of the MPc-coated IGE structure upon exposure to several NO_2 challenge gas concentrations. Each curve in these figures represents the average of the normalized DC resistance response observed from the triplicate exposures to each challenge gas concentration. The IGE resistance with all three MPc film types decreased monotonically with NO_2 exposure. The time response (particularly at high NO_2 concentrations) was characterized by an initial rapid decrease in the normalized resistance. After the first five minutes of the challenge gas exposure, the normalized resistance continued to decrease, but at a much slower rate. This two-stage time response of the MPc film's DC resistance to NO_2 has been interpreted by other investigators (154, 200) in terms of two different adsorption mechanisms. The initial response arises from adsorption on the MPc surface, while the slower response is postulated to be the result of surface heterogeneity, with the NO_2 diffusing into the MPc film at the intercrystallite interfaces, rather than being a true bulk diffusion mechanism (154). The decrease in the DC resistance is consistent with an increase in the effective hole concentration within the MPc film induced by the adsorption of the electron-accepting (electrophilic) nitrogen dioxide gas (26). In

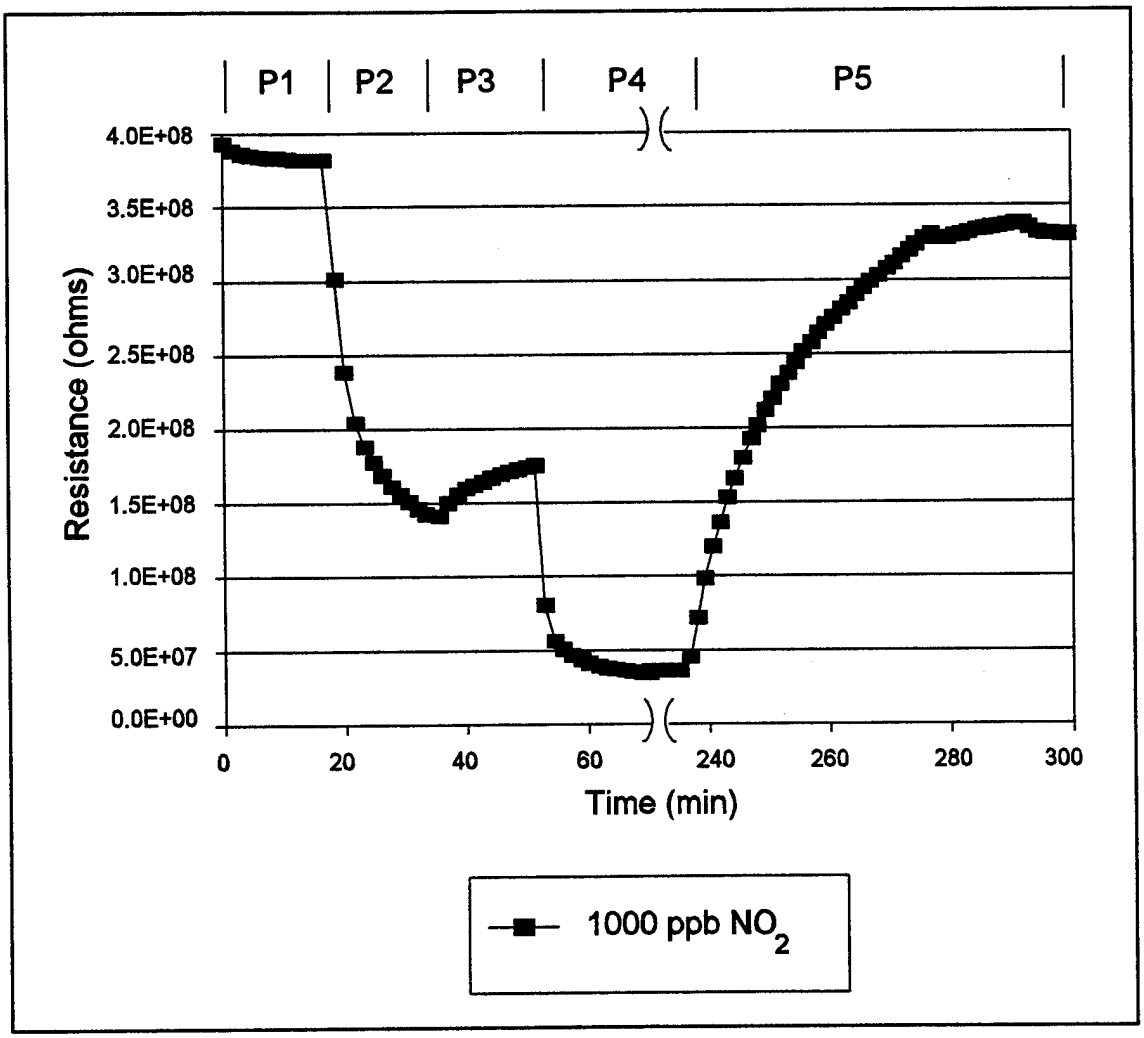


Figure VI-3. CuPc-Coated IGE Structure DC Resistance Before, During, and After Exposure to 1000 ppb NO_2 . P1 is a 16 minute (min), 100° C Purge , P2 is a 16 minute, 100° C Exposure, P3 is a 16 minute, 100° C Purge, P4 is a 3 hour, 170° C Purge, and P5 is a 45 minute Cool to 100° C Purge. (Film Thickness = 0.32 μm.)

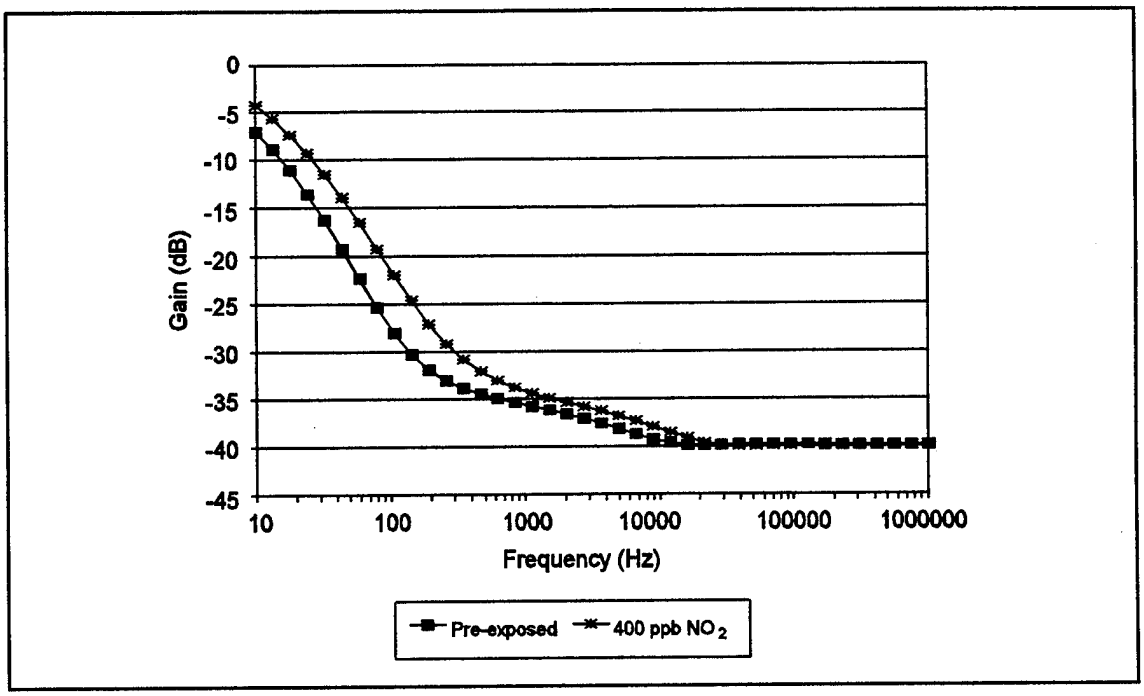


Figure VI-4. CuPc-Coated IGEFET Transfer Function Gain Before and After Exposure to 400 ppb NO_2. (Film Thickness = 0.32 μm. Temperature = 100° C.)

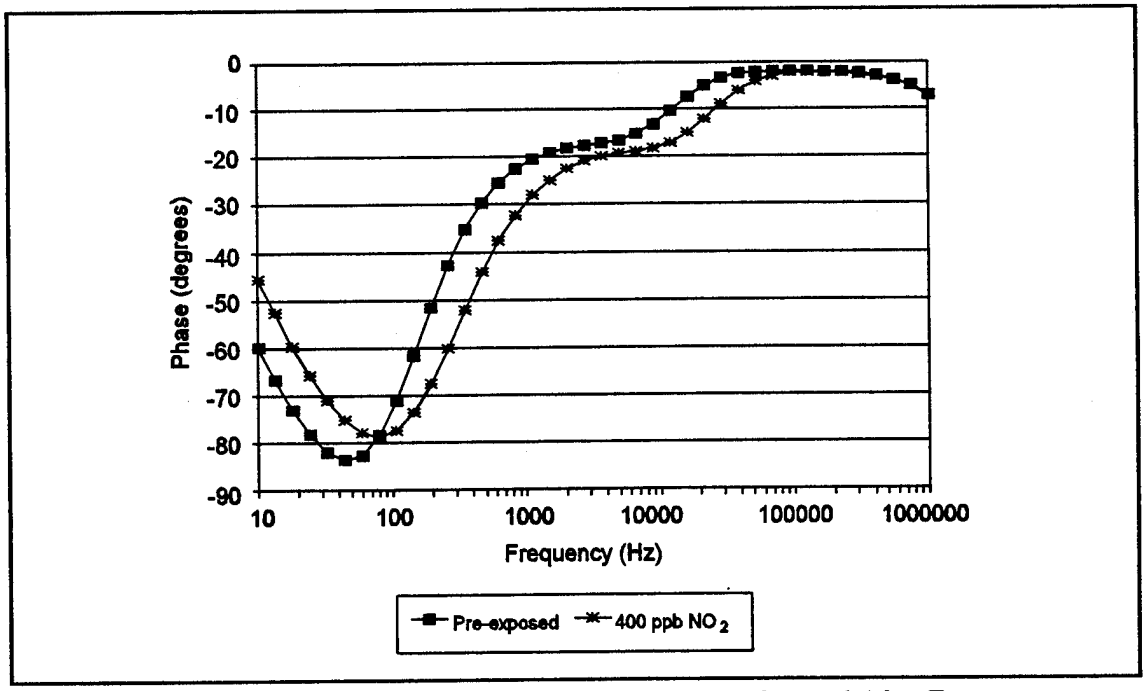


Figure VI-5. CuPc-Coated IGEFET Transfer Function Phase Before and After Exposure to 400 ppb NO_2. (Film Thickness = 0.32 μm. Temperature = 100° C.)

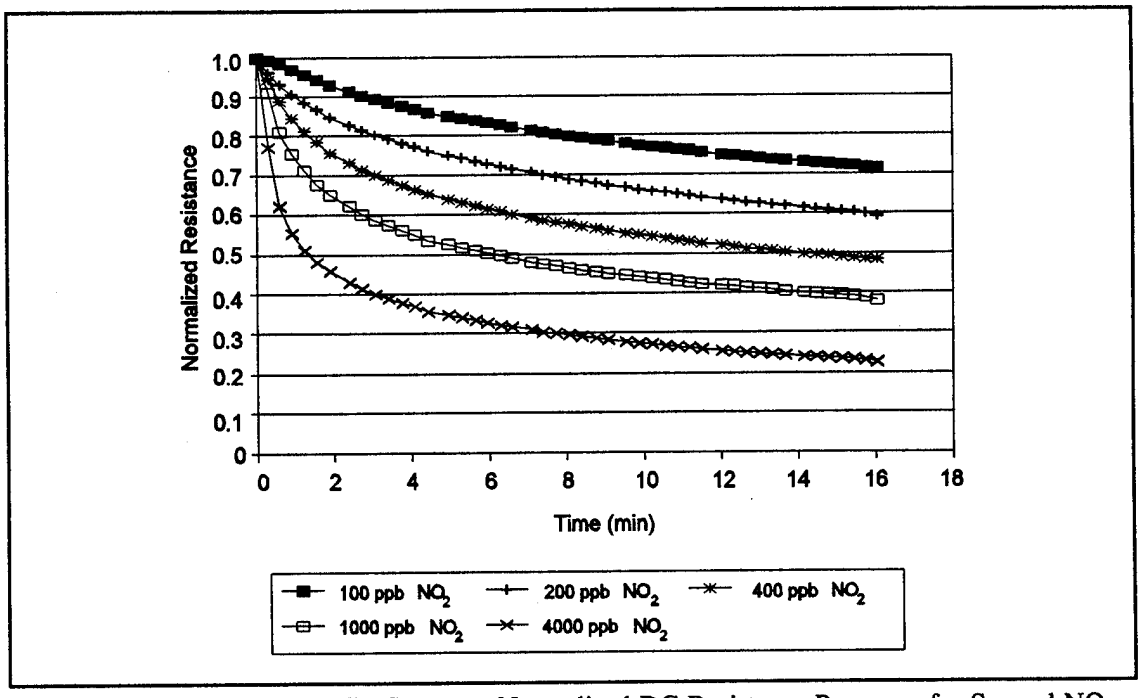


Figure VI-6. CuPc-Coated IGE Structure Normalized DC Resistance Response for Several NO_2 Exposures. (Film Thickness = 0.32 μm. Temperature = 100° C.)

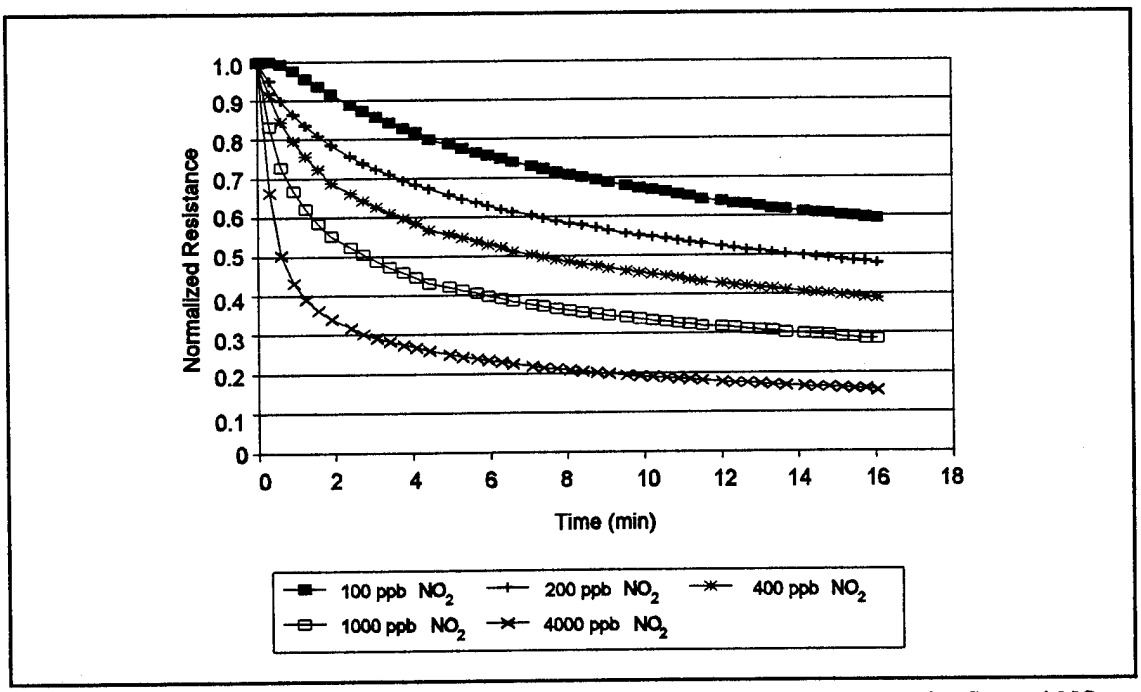


Figure VI-7. NiPc-Coated IGE Structure Normalized DC Resistance Response for Several NO_2 Exposures. (Film Thickness = 0.43 μm. Temperature = 100° C.)

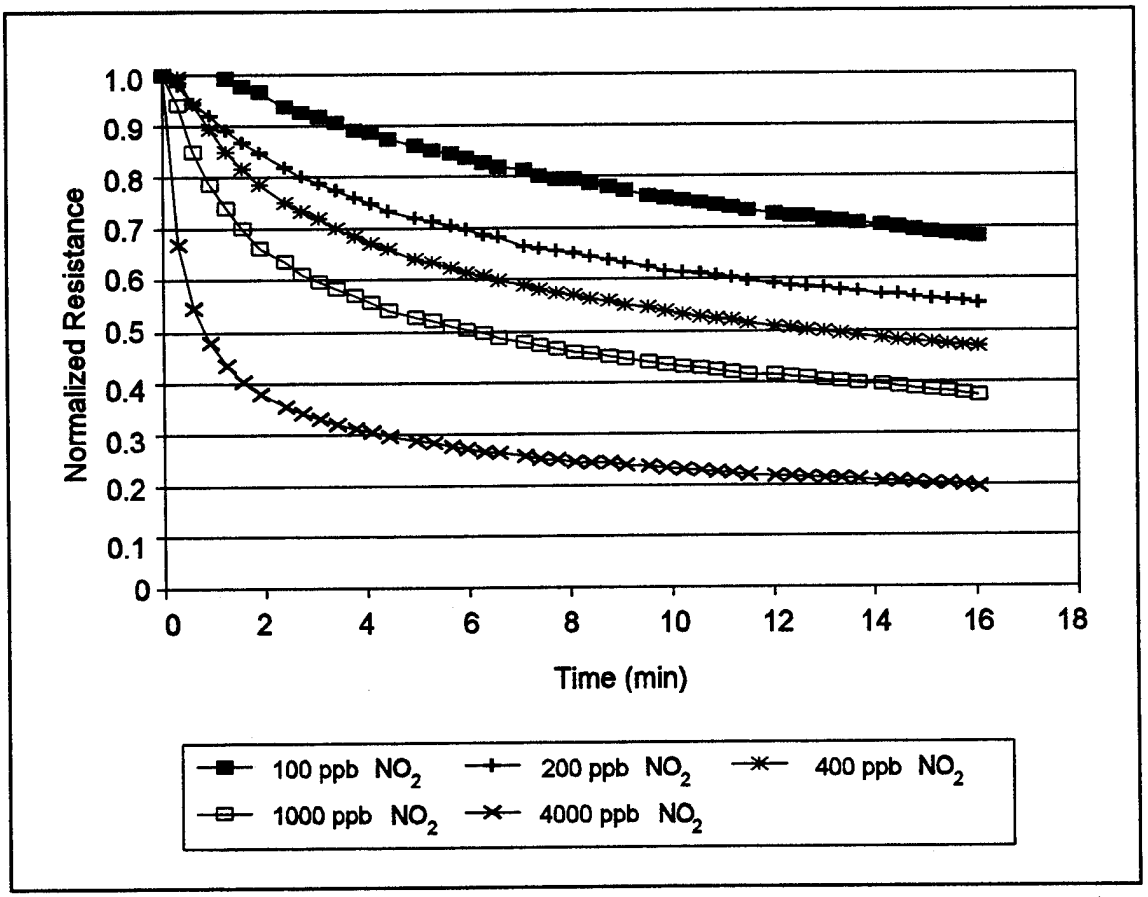


Figure VI-8. CoPc-Coated IGE Structure Normalized DC Resistance Response for Several NO_2 Exposures. (Film Thickness = 0.51 μm. Temperature = 100°C.)

contrast, the adsorption of an electron-donor (electrophobic) gas, such as ammonia, onto the surface of the MPc films decreases the effective hole concentration and, therefore, increases the MPc-coated IGE structure's normalized DC resistance. As shown in Figures VI-9 through VI-11, the normalized DC resistance response to each NH_3 challenge gas concentration increased monotonically with exposure time. The opposite conductivity changes induced in the MPc film upon gas exposure clearly identifies the presence of an electrophilic or electrophobic gas. However, an increase or decrease in the DC electrical conductance is not sufficient to identify both components of a binary gas mixture composed of both electrophilic and electrophobic gas species.

However, the identification of the binary gas mixture components can be accomplished if either a response feature unique to the mixture exists and/or the response of the MPc films differ with respect to their sensitivity to at least one gas component of the binary mixture. In this investigation, a unique time dependence was observed in the DC normalized resistance response of the MPc-coated IGE structures upon exposure to the binary gas mixtures. Figures VI-12 through VI-14 illustrate the average time response of the MPc-coated IGE structures to a binary gas mixture composed of 200 ppm NH_3 and various concentrations of NO_2. The time response of the MPc-coated IGE normalized DC resistance upon exposure to additional binary challenge gas mixtures are presented in Appendix K. In contrast to exposure with the single component gas challenges, the time dependence of the normalized IGE structure's DC resistance was non-monotonic, with an initial increase in the normalized DC resistance during the first few minutes (typically less than 5 minutes) of an exposure, followed by a slow decrease, as exposure to the mixture was continued. The initial increase in the normalized DC resistance indicates that the ammonia component, which, depending upon the mixture, was present at a concentration 50 to 4000 times the NO_2 concentration, adsorbs on the MPc-surface prior to significant adsorption of the NO_2 component. However, as the exposure continued, more NO_2 molecules were able to interact with the MPc's surface. As illustrated in Figure VI-15, this interaction may occur either at other adsorption sites, or at an NH_3 adsorption site through an exchange or reactive process. Both the exchange and reactive mechanisms are supported by the more rapid decrease in the normalized DC resistance observed with mixtures containing higher NO_2 concentrations. In support of a reactive process, a chemical reaction between ammonia and NO_2 has also been reported in the literature (201-204). At temperatures spanning 333-476°K, ppm concentrations of ammonia and nitrogen dioxide undergo chemical reaction in the gas phase (201, 202) to form nitrogen, water, nitric acid and ammonium nitrate. Furthermore, the chemical reaction between ammonia and nitrogen dioxide is reported to be catalyzed on p-type semiconductor catalysts

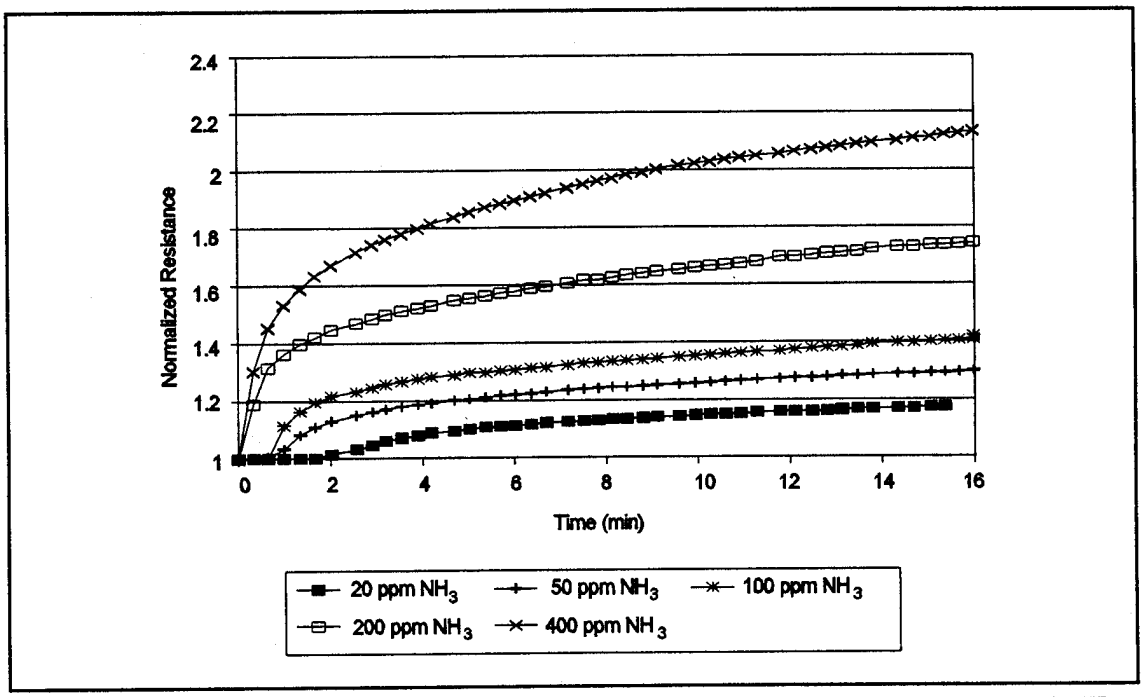


Figure VI-9. CuPc-Coated IGE Structure Normalized DC Resistance Response for Several NH_3 Exposures. (Film Thickness = 0.32 μm. Temperature = 100° C.)

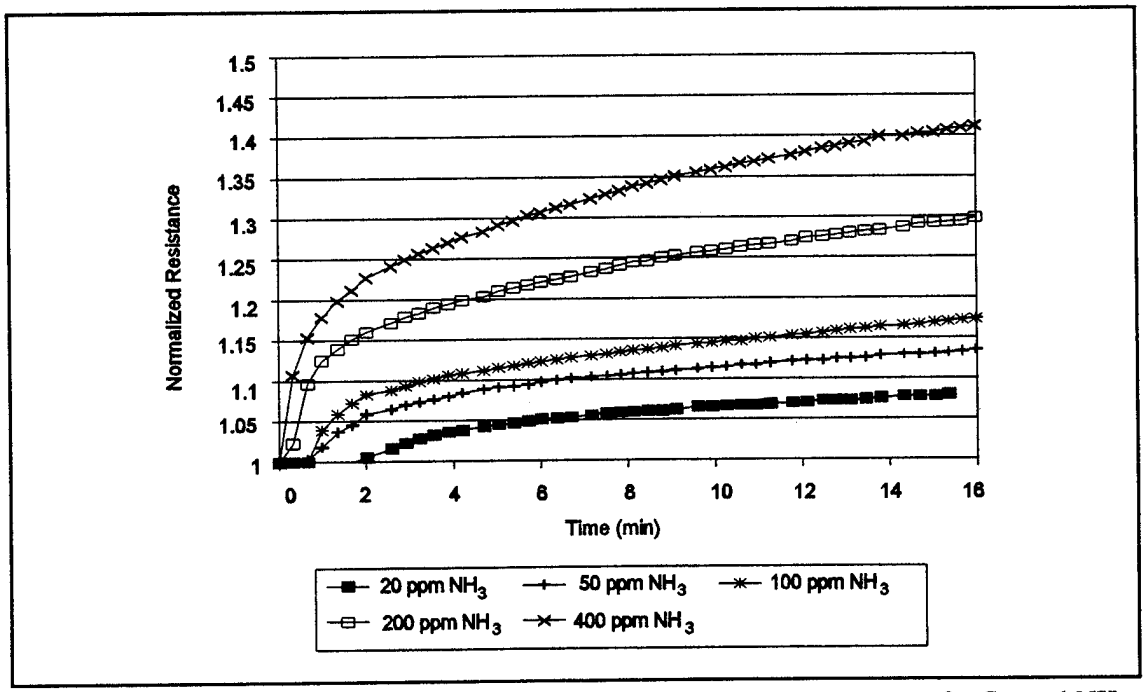


Figure VI-10. NiPc-Coated IGE Structure Normalized DC Resistance Response for Several NH_3 Exposures. (Film Thickness = 0.43 μm. Temperature = 100° C.)

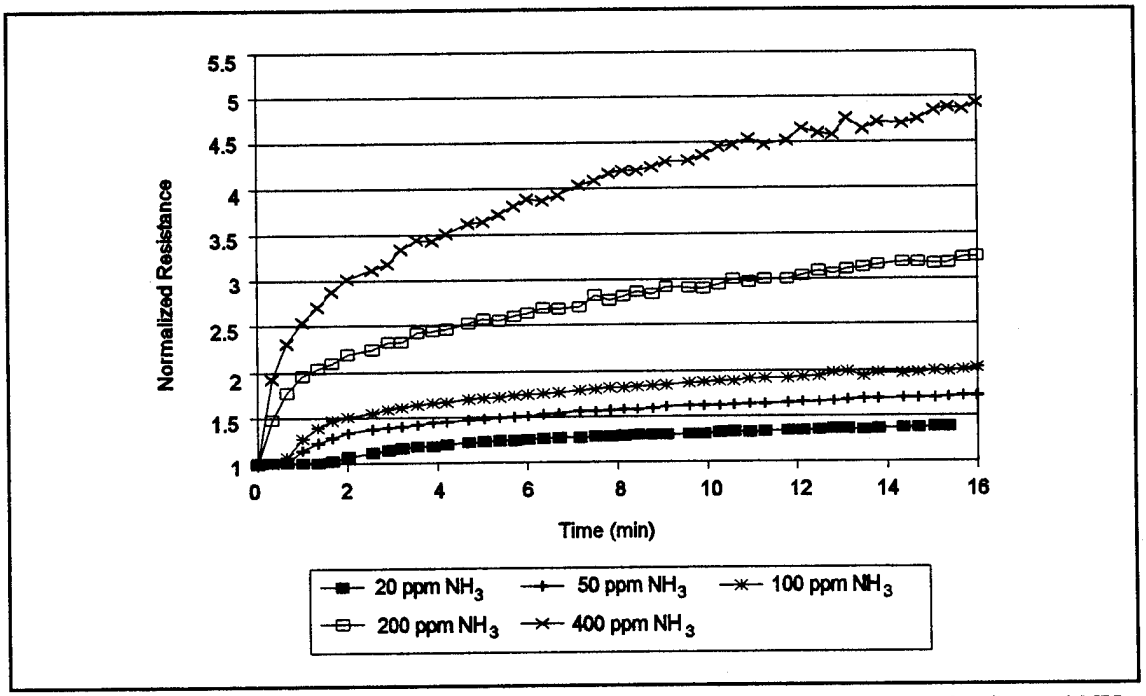


Figure VI-11. CoPc-Coated IGE Structure Normalized DC Resistance Response for Several NH_3 Exposures. (Film Thickness = 0.51 μm. Temperature = 100° C.)

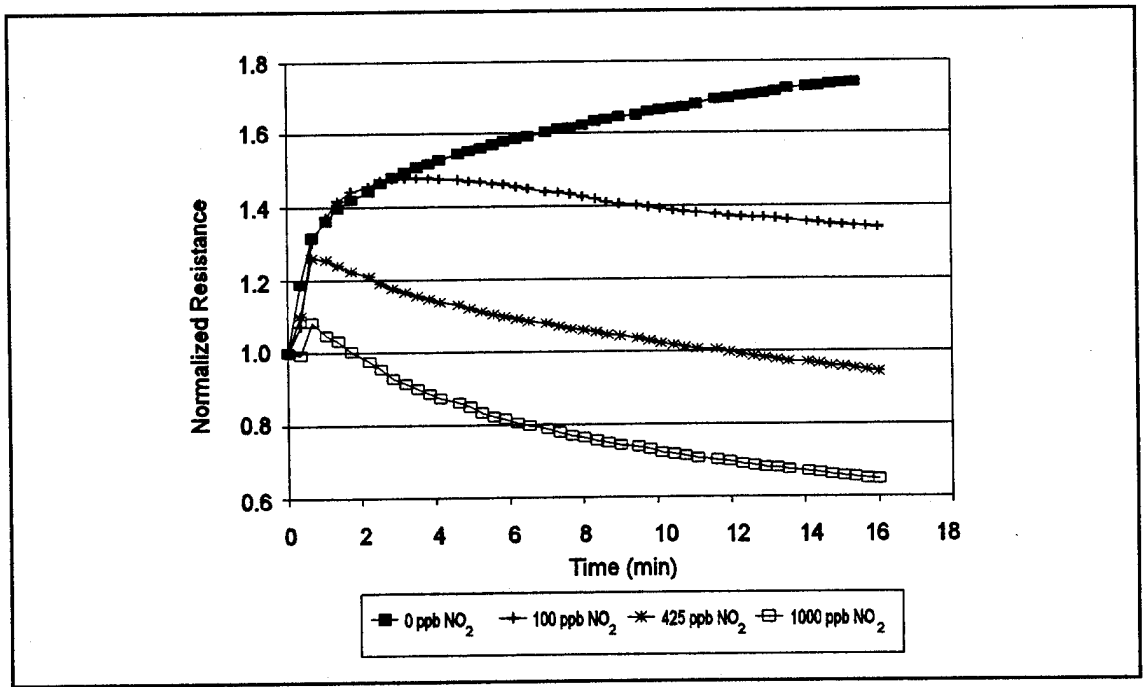


Figure VI-12. CuPc-Coated IGE Structure Normalized DC Resistance Response to Binary Gas Mixtures Containing 200 ppm NH_3 and Various NO_2 Concentrations. (Film Thickness = 0.32 μm. Temperature = 100° C.)

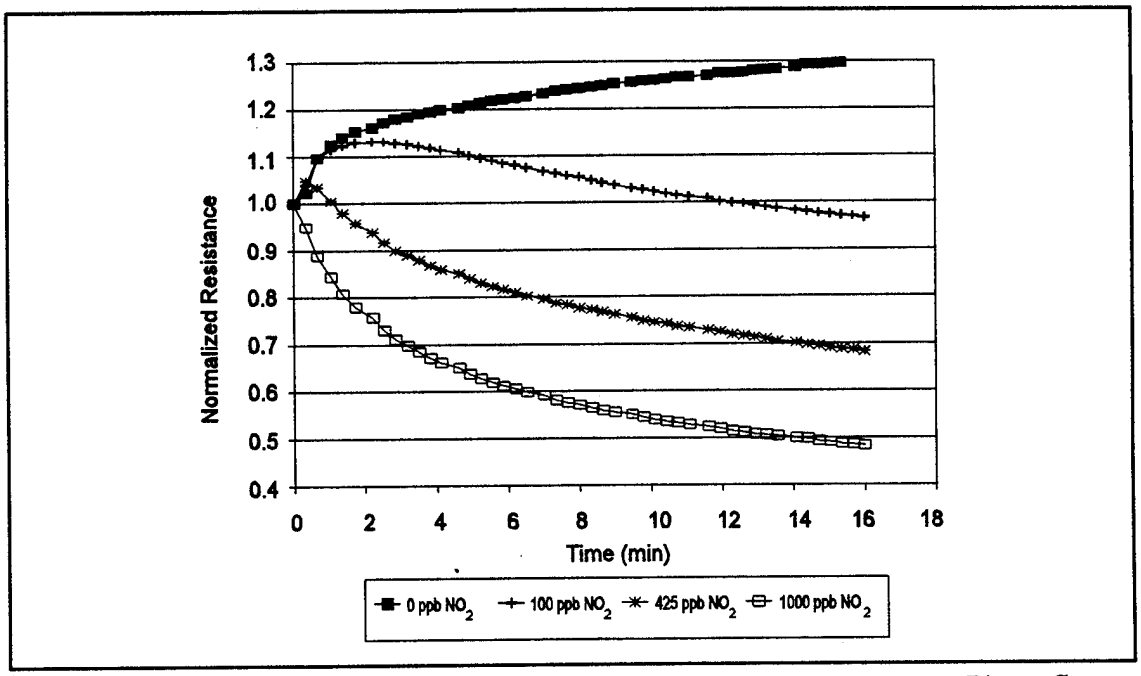


Figure VI-13. NiPc-Coated IGE Structure Normalized DC Resistance Response to Binary Gas Mixtures Containing 200 ppm NH_3 and Various NO_2 Concentrations. (Film Thickness = 0.43 μm. Temperature = 100°C.)

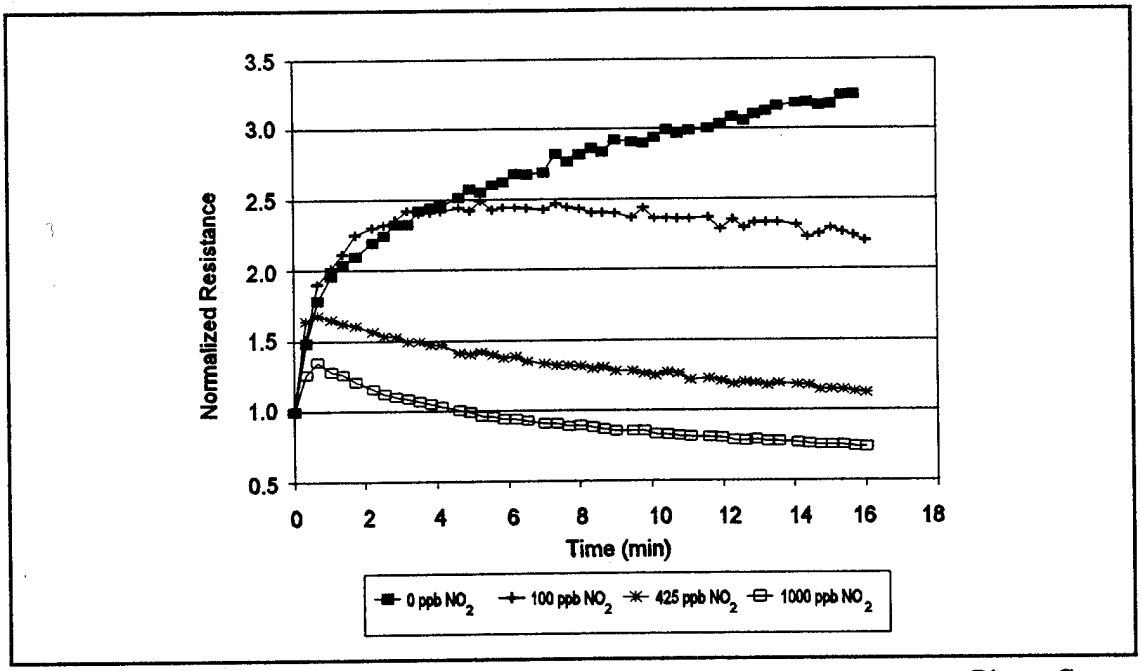


Figure VI-14. CoPc-Coated IGE Structure Normalized DC Resistance Response to Binary Gas Mixtures Containing 200 ppm NH_3 and Various NO_2 Concentrations. (Film Thickness = 0.51 μm. Temperature = 100°C.)

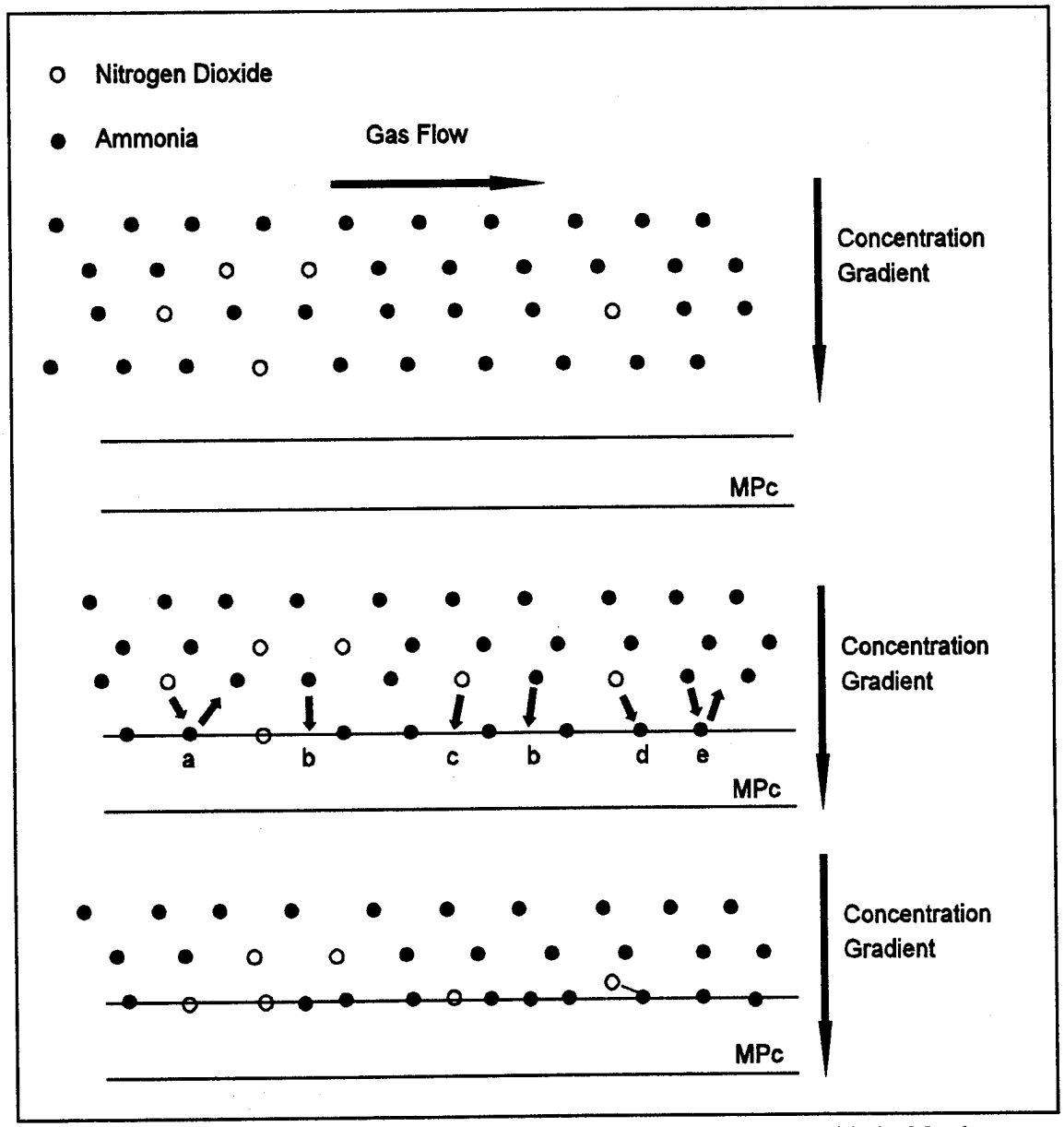


Figure VI-15. Possible Interactions of a NO_2 and NH_3 Binary Gas Mixture with the Metal-Phthalocyanine (MPc) Surface. a) NO_2 and NH_3 Exchange Process, b) NH_3 Adsorption on an Available Site, c) NO_2 Adsorption on an Available Site, d) Reactive Process, e) NH_3 Exchange Process.

(204). On a vanadia catalyst, nitrogen dioxide and ammonia react at 295°K to form nitrogen, water, and oxygen. The reaction mechanism proposed involves the adsorption of NO_2 and NH_3 at adjacent sites on the vanadia surface where they interact to form a vanadia-nitrous oxide complex (V-N_2O), water, and oxygen. The V-N_2O complex subsequently decomposes upon heating, or the nitrous oxide is displaced by the adsorption of NO_2. However, the vanadia-N_2O complex was stable in an excess of ammonia at ambient temperature. If NO_2 and NH_3 interact in a similar manner on the MPc surface, their interaction or their reaction product(s) may be more stable than either of the single component gases adsorbed on the MPc surface alone and, therefore, slow the desorption of the gas mixture during purge. The relatively repeatable electrical measurements collected with repeated exposure to the single component challenge gases compared to the considerable variation in the measured response observed upon repeated exposure (following the same test protocol used for the single component measurements) to the binary challenge gas mixtures (see Figures VI-16 through VI-18) support this hypothesis. To capture the information contained in the time response for the principal component analysis (PCA) of the challenge gas mixtures, a feature vector was constructed (discussed below) from the samples of the time response at six time points: 0.9, 1.6, 3.1, 6.3, 9.1, and 16.1 minutes. Since the time response variation is greatest during the fist few minutes of an exposure, more samples at shorter exposure times were chosen for this feature vector.

In addition to the information contained in the time response of the normalized IGE structure DC resistance upon gas exposure, the different sensitivities of each of the MPc films to each of the challenge gas species provided an additional discriminant to enhance the PCA of the gas mixtures. The sensitivity of the MPc-coated IGE structure normalized DC resistance to a challenge gas species was determined from the plots of the normalized DC resistance as functions of the single component challenge gas concentrations. Since the MPc film conductivity dependence on NO_2 adsorption has been widely reported to follow a Freundlich isotherm (Chapter II), the logarithm of the normalized DC resistance was plotted versus the logarithm of the NO_2 concentration (Figure VI-19) to evaluate the normalized IGE structure DC resistance dependence upon the NO_2 concentration. Consistent with the reported MPc film DC electrical conductance dependence upon NO_2 concentration (26), the log-log plots of the normalized IGE structure DC resistance as a function of the NO_2 challenge concentration were linear for the IGE structures coated with each of the three MPc film types. Although the spread in the normalized DC resistance of the IGE structures coated with the different MPc film types (triplicate exposures on two IGE elements for each film type) overlapped (Appendix K), a consistent pattern was observed in the relative sensitivity of the MPc-coated IGE

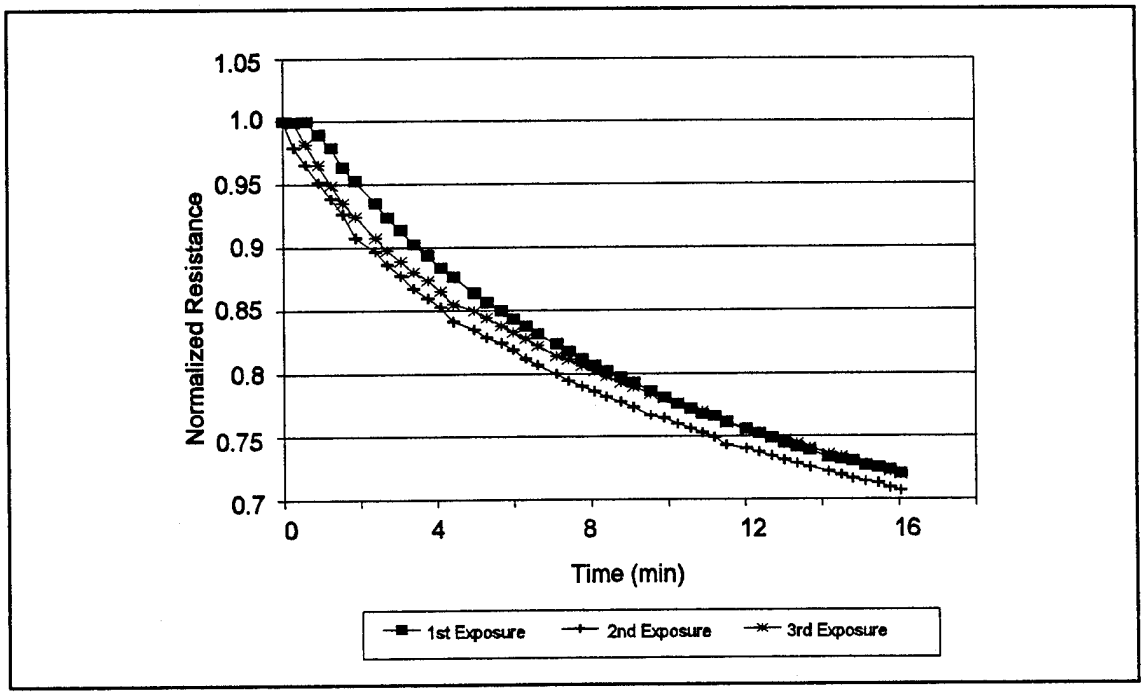


Figure VI-16. CuPc-Coated IGE Structure Normalized DC Resistance Response to Repeated 100 ppb NO_2 Exposures. (Film Thickness = 0.32 μm. Temperature = 100° C.)

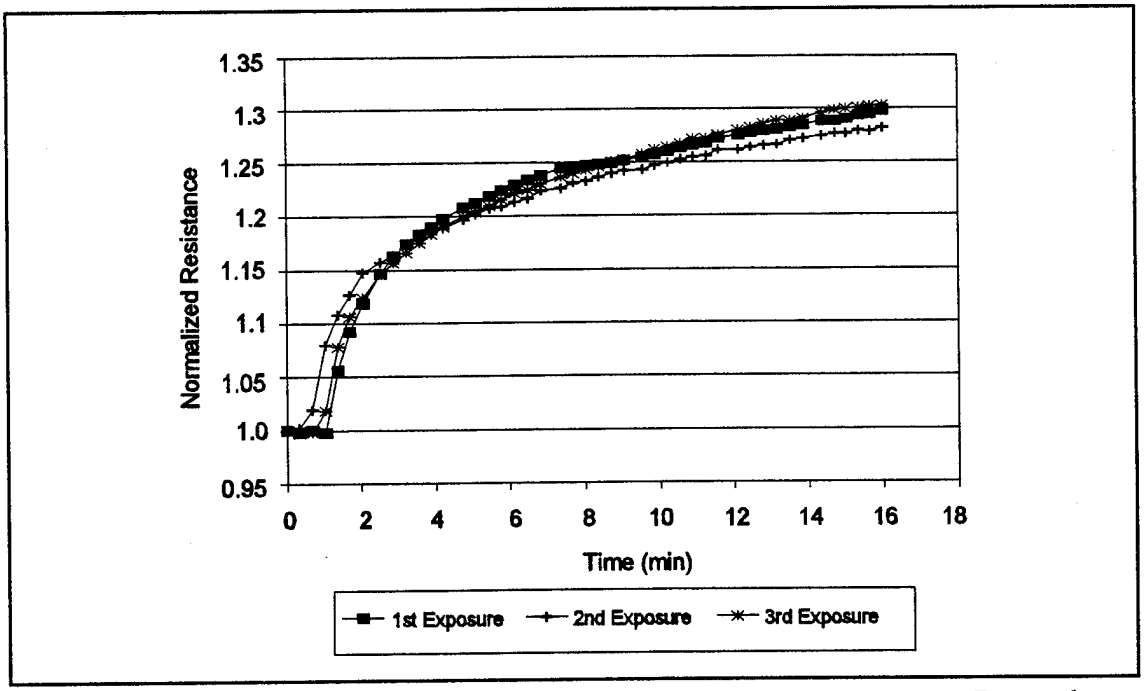


Figure VI-17. CuPc-Coated IGE Structure Normalized DC Resistance Response to Repeated 50 ppm NH_3 Exposures. (Film Thickness = 0.32 μm. Temperature = 100° C.)

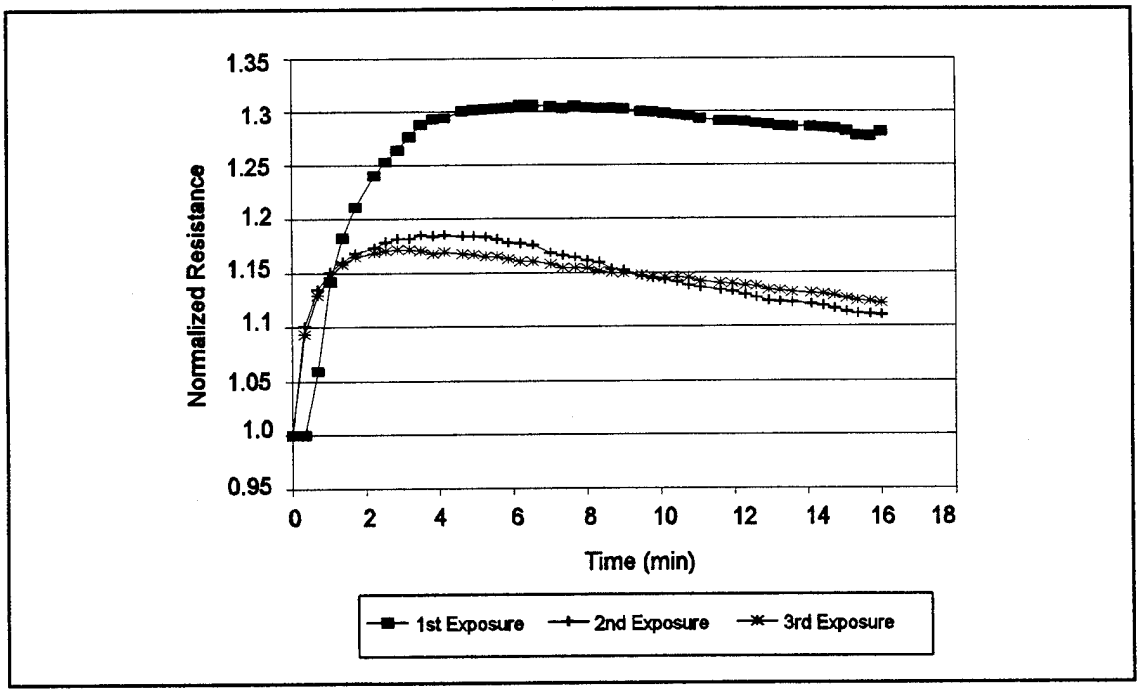


Figure VI-18. CuPc-Coated IGE Structure Normalized DC Resistance Response to Repeated Exposures to Binary Mixtures Containing 50 ppm NH_3 and 100 ppb NO_2. (Film Thickness = 0.32 μm. Temperature = 100° C.)

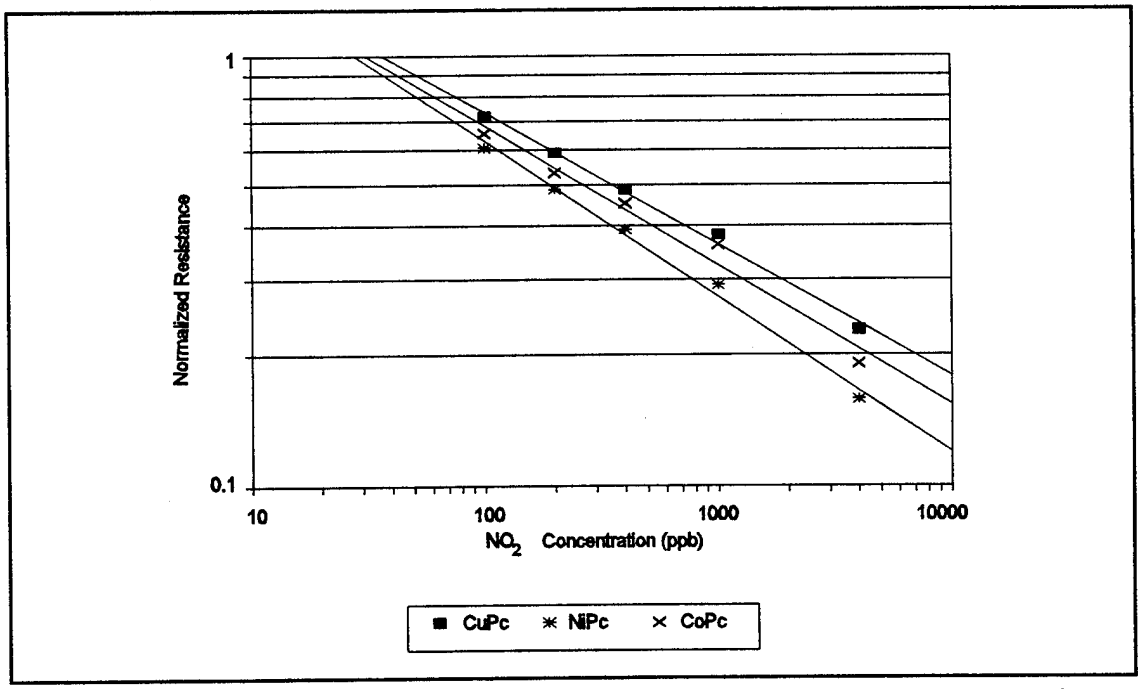


Figure VI-19. Concentration Dependence of the MPc-Coated IGE Structure Normalized DC Resistance Response to Nitrogen Dioxide. (Temperature = 100° C.)

structure DC resistance relative to the NO_2 exposure concentration. As indicated by the slope of these curves, the relative sensitivity of the normalized DC resistance upon NO_2 exposure decreased with respect to the MPc film type deposited upon the IGE structure in the following order: NiPc > CoPc > CuPc. Although the difference in NO_2 sensitivity between the different MPc-coated IGE structures was small, a much greater variation was observed in their NH_3 sensitivity. Figure VI-20 revealed that the linear decrease in the DC electrical conductivity upon exposure to NH_3 reported by Szczurek and Lorenz for CuPc (139) also occurs with the NiPc and CoPc films. Furthermore, Figure VI-6 reveals that the normalized DC resistance of the IGE structures coated with a CoPc film was significantly more sensitive to ammonia compared to the IGE structures coated with the other two MPc films. The relative sensitivity of the MPc film types to ammonia is also reflected in the normalized DC resistance response observed upon exposure to the binary challenge gas mixtures (see Figures VI-12 through VI-14 and Appendix K).

The normalized DC resistance response to each of the challenge gases suggested that the functional form in which to cast the normalized DC resistance data when formulating the gas analysis feature vectors. Since a Freundlich-type response was observed upon NO_2 exposure, the relationship between the challenge gas concentration (C) dependence and the average normalized resistance data (R_N) for a given time sample and MPc film type was least-squares fitted to an equation of the form:

$$C = AR_N^{\alpha} + B \qquad \text{(VI-2)}$$

where A, B, and α are constants. Similarly, the average normalized IGE DC resistance response to NH_3 exposure was least-squares fitted to a linear equation ($\alpha = 1$) of the form:

$$C = AR_N + B. \qquad \text{(VI-3)}$$

The value of the parameters obtained from least-squares fitting each of the six time samples collected from the sensors coated with each MPc film type during the NO_2 and NH_3 exposures are provided in Appendix L.

A column vector, called the sensor response vector, was formed to represent the normalized DC resistance response to the challenge gas for a sensor coated with a particular MPc film type. For the single component analyses, the sensor response vector was composed of the six normalized DC resistance time samples, collected from each sensor upon exposure to a particular challenge gas concentration, raised to the appropriate power, α, corresponding to the test gas and MPc film type.

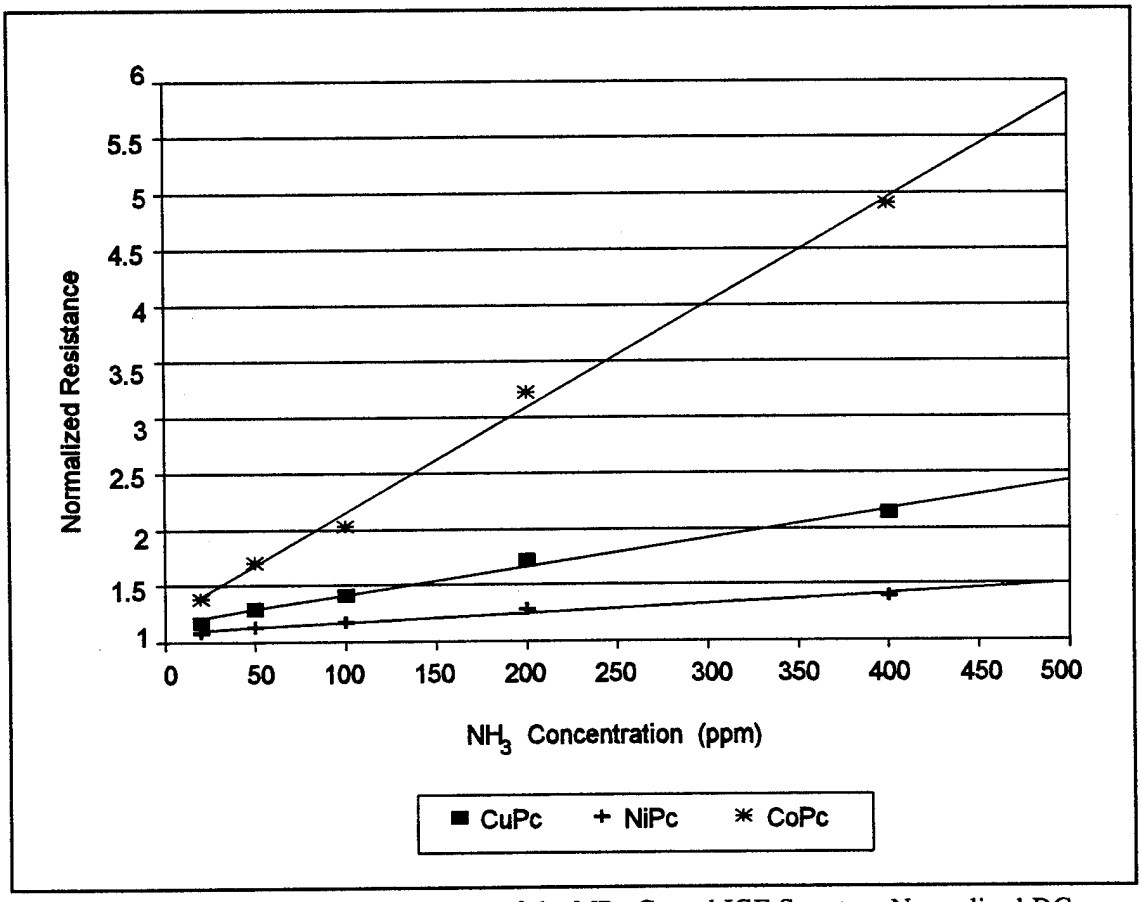


Figure VI-20. Concentration Dependence of the MPc-Coated IGE Structure Normalized DC Resistance Response to Ammonia. (Temperature = 100° C.)

For the binary gas mixtures, the sensor response vector was composed of twelve elements: six elements for each of the two component gases. Since the NH_3 response was linear, the first six elements were simply the six time samples of the normalized DC resistance. To represent the NO_2 response, the six time samples of the normalized DC resistance were raised to the appropriate power, α, as determined from the least-squares fit of the single component NO_2 response data. The feature vector for performing the gas analysis was then formed by combining the sensor response vectors corresponding to each MPc film type into a single column vector representing the response of all the MPc films to a particular challenge gas concentration. The entire process for generating the feature vectors from the DC resistance data is depicted in Figure VI-21. The calibration feature vectors and examples of the test feature vectors for each challenge gas concentration are provided in Appendix L.

Feature Vector Formation from the IGEFET Transfer Function Gain Measurements.

The analysis of the IGEFET transfer function gain, as well as the phase delay (discussed in the next section), is more complex compared to the analysis of the IGE structure DC resistance measurements. An obvious complication is that the IGEFET transfer function gain and phase are measured as a function of frequency. More importantly, the IGEFET transfer function is the product of a complex, nonlinear interaction between the inter-electrode and the electrode-to-ground resistances and capacitances (Chapter V). To accomplish principal component analysis with the transfer function data, the gas response data must be transformed to obtain a linear relationship with respect to the gas concentration. Unlike the normalized DC resistance data, a straightforward approach for manipulating the data is not apparent. Therefore, a set of functional forms, including logarithmic and power series relationships, were examined to establish a functional form which linearized the transfer function response and minimized the error in the predicted concentrations for a set of binary gas mixtures. Despite the difficulty of analyzing the gain and phase data, the complexity of the transfer function response possesses additional information that can be used to discriminate between the components of a binary gas mixture.

To identify these potential discriminants, Bode plots of the IGEFET transfer function gain response to gas exposure were examined. Figures VI-22 through VI-24 show the gain response of the MPc-coated IGEFET sensing elements to several NO_2 challenge gas concentrations. The gain response observed with the CuPc and NiPc-coated IGEFET sensors were similar and possessed two maxima located near 100 Hz and 8 KHz. However, the CoPc-coated IGEFET gain response possessed only a single maxima with a much smaller amplitude near 8 KHz. The dissimilarity between the CoPc-IGEFET transfer function gain response and the gain response measured with the

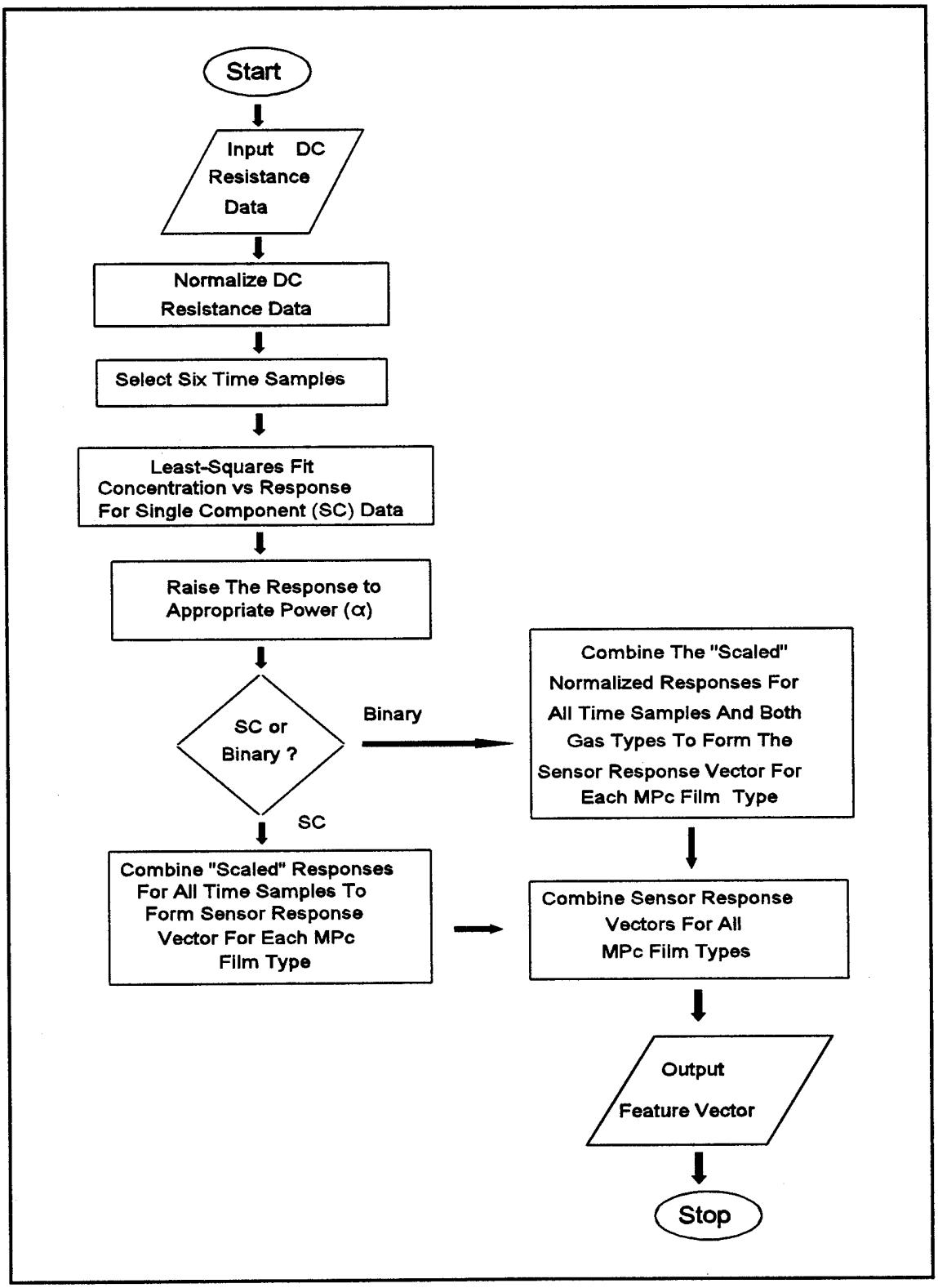


Figure VI-21. Normalized DC Resistance Feature Vector Formation Process.

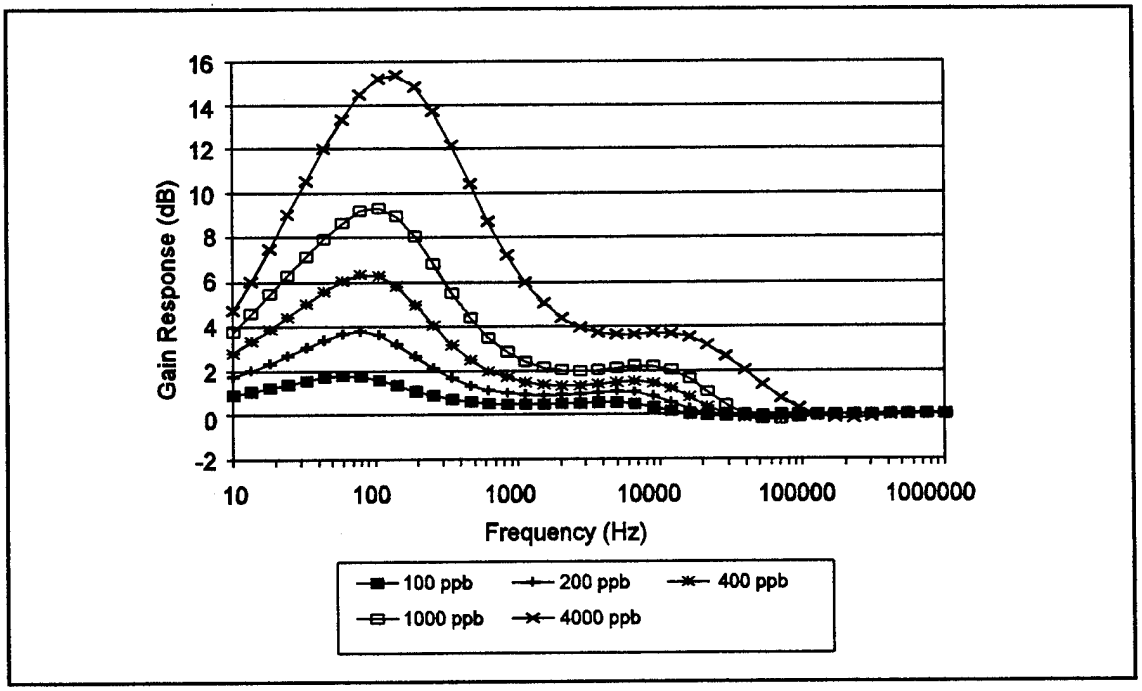


Figure VI-22. Bode Plots of the CuPc-Coated IGEFET Transfer Function Gain Response for Several NO_2 Exposures. (Film Thickness = 0.32 μm. Temperature = 100° C.)

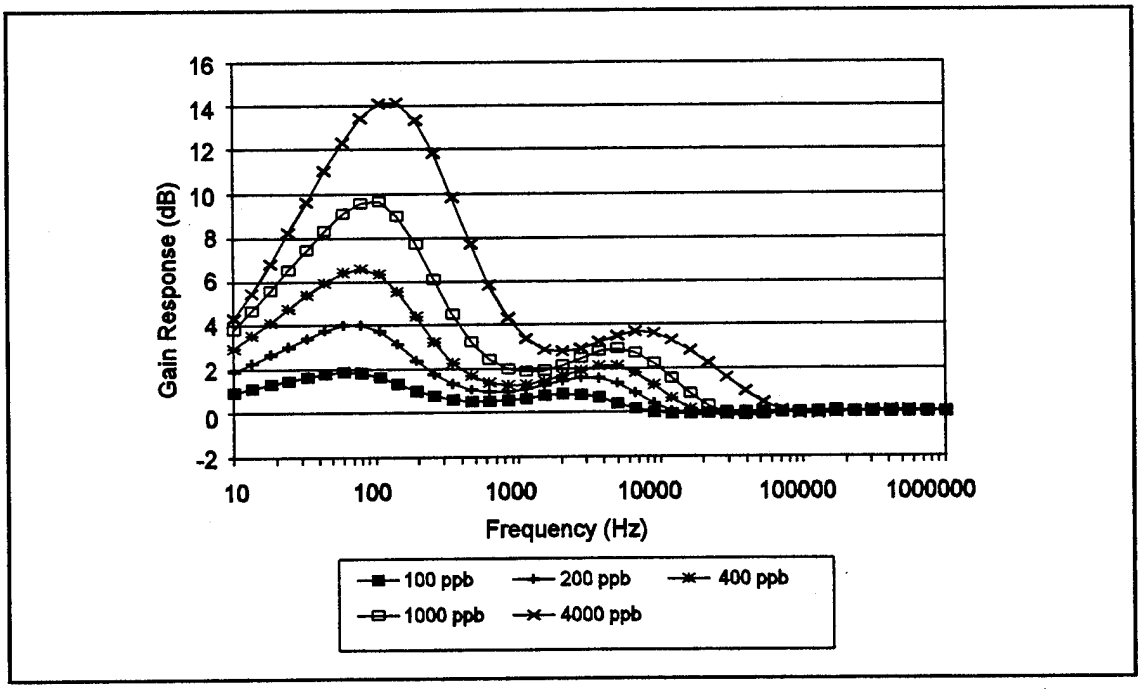


Figure VI-23. Bode Plots of the NiPc-Coated IGEFET Transfer Function Gain Response for Several NO_2 Exposures. (Film Thickness = 0.43 μm. Temperature = 100° C.)

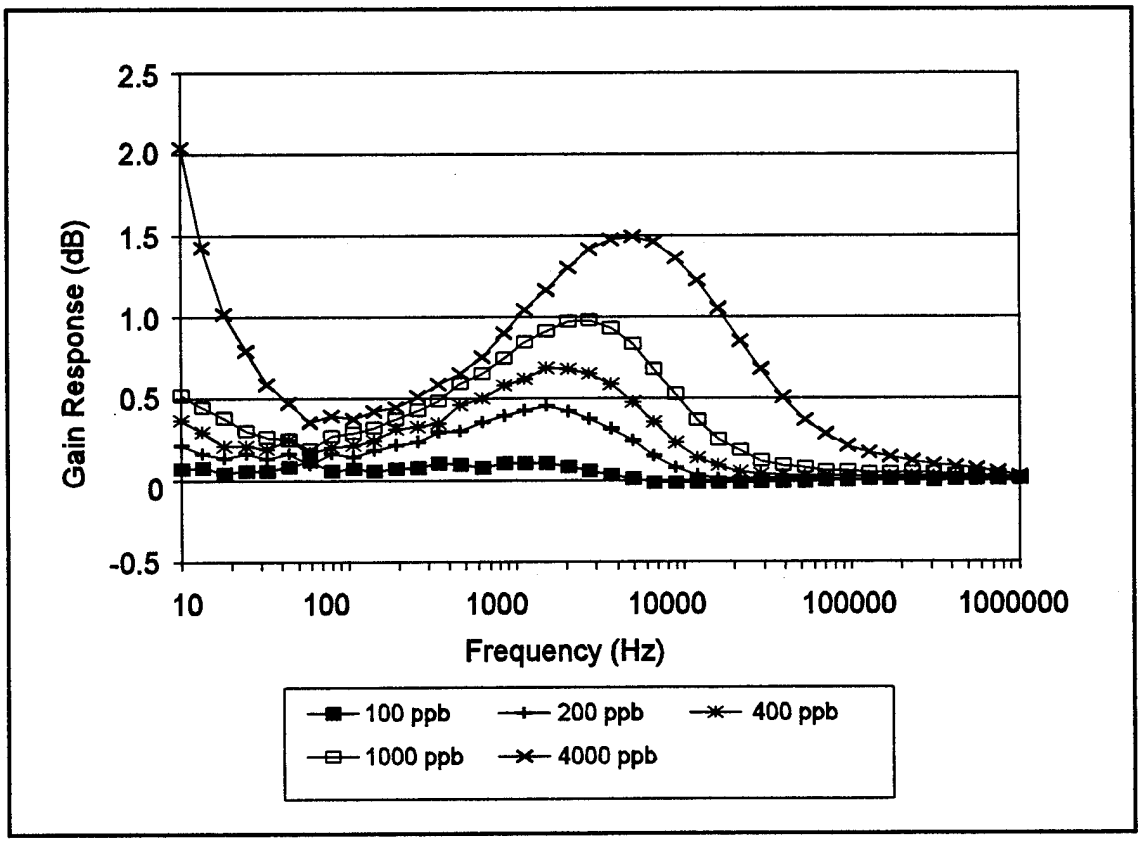


Figure VI-24. Bode Plots of the CoPc-Coated IGEFET Transfer Function Gain Response for Several NO_2 Exposures. (Film Thickness = 0.51 μm. Temperature = 100° C.)

CuPc and NiPc-coated IGEFET elements was the result of a significantly different baseline transfer function gain, as shown in Figure VI-25. At this temperature, only the smaller, high frequency relaxation process was observed in the CoPc-coated IGEFET transfer function gain. Additionally, the smaller gain of the CoPc-coated IGEFET sensor relative to the other MPc-coated IGEFET elements was also consistent with the DC resistance measurements. The CoPc-coated IGE resistance was at least an order of magnitude greater than the resistance of the other MPc-coated IGE elements. Since the small gain implies a smaller measured signal at the output of the IGEFET, and because the gain response to gas exposure was relatively small, the signal-to-noise ratio was much lower with the CoPc-IGEFET transfer function measurements (particularly, for the binary mixtures). Figure VI-26 shows the gain response of the three MPc-coated IGEFET sensing elements to a 100 ppb NO_2 challenge concentration, as well as the unexposed gain response. The unexposed gain response is the difference between the last two CoPc-coated IGEFET transfer function gain measurements collected prior to the gas exposure. Hence, the unexposed gain response is equivalent to the measurement noise. In contrast to the CuPc and NiPc-coated IGEFET gain responses, the CoPc-coated IGEFET gain response was barely above the noise level.

The negative gain response of the MPc-coated IGEFET sensors to the NH_3 challenge gas concentrations was, as expected, opposite to the positive gain response observed with the NO_2 challenge gas exposures. Figures VI-27 through VI-29 reveal that the low- and high-frequency gain response maxima (absolute value) occur near 44 Hz and 3 KHz. Similar to the NO_2 gain response measurements, only a single maxima (absolute value) was observed with the CoPc-coated IGEFET element near 500 Hz. The opposite gain response (sign change) behavior clearly distinguishes the NH_3 and NO_2 challenge gases.

Figures VI-30 through VI-32 show the response of the MPc-coated sensors upon exposure to the binary mixtures composed of a fixed 200 ppm NH_3 concentration and three different concentrations of NO_2 (Appendix M summarizes the gain response measured for the other binary mixtures). These plots, in general, reveal the same gain response maxima observed upon exposure to the single component gases with an NH_3-like response (negative gain response) observed with low NO_2 concentrations, and an NO_2-like response (positive gain response) observed with greater NO_2 concentrations. Interestingly, the CuPc-coated IGEFET gain response to the mixture containing 425 ppb NO_2 was missing the high frequency maxima (Figure VI-30) and, therefore, suggests that the relative amplitude of the two maxima may provide a discriminant for gas analysis.

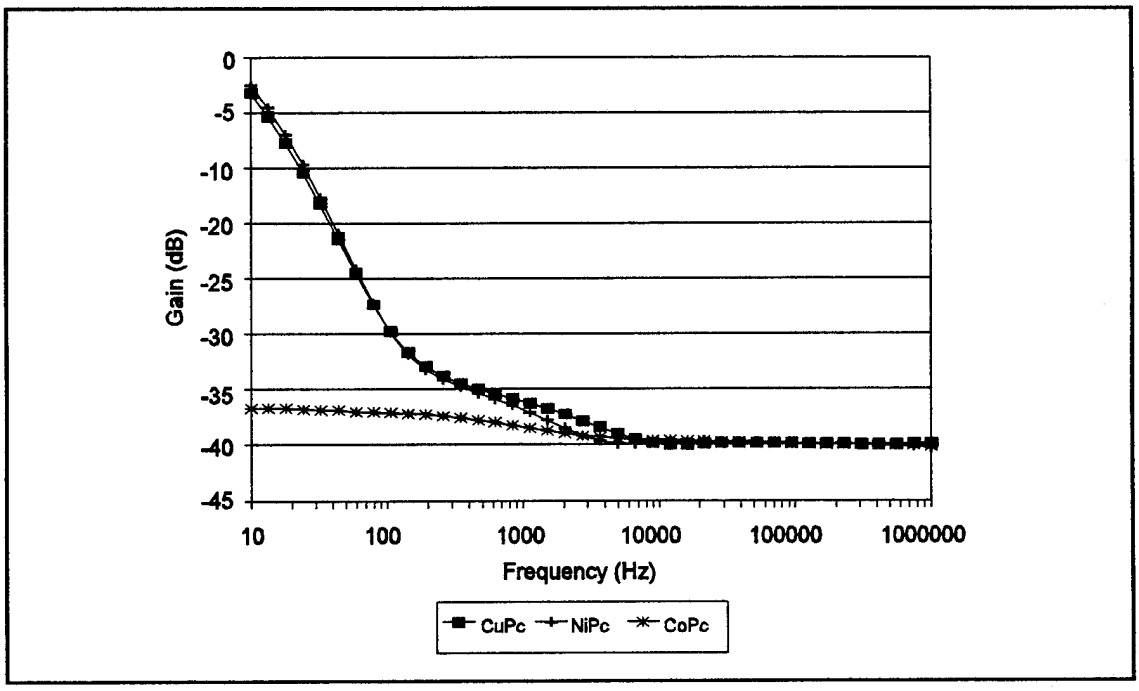


Figure VI-25. Bode Plots of the Baseline Transfer Function Gain of the MPc-Coated IGEFET Sensing Elements. (Temperature = 100°C.)

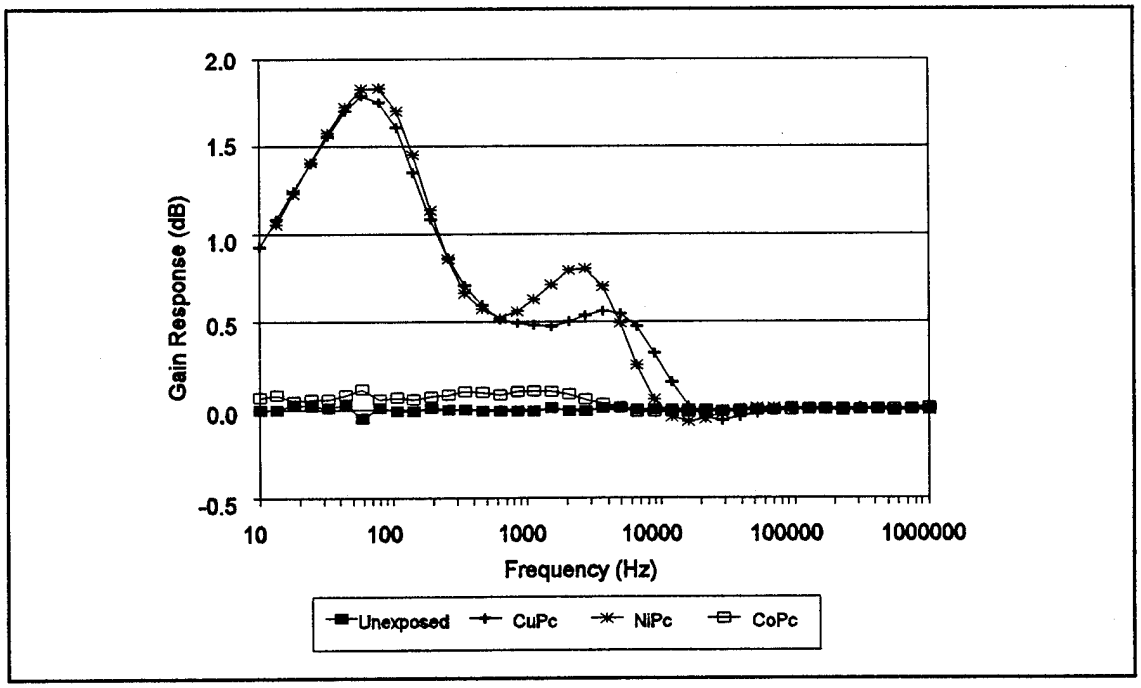


Figure VI-26. Comparison of the Transfer Function Gain Response of the Three MPc-Coated IGEFET Sensing Elements to a 100 ppb NO_2 Exposure. (Temperature = 100°C.)

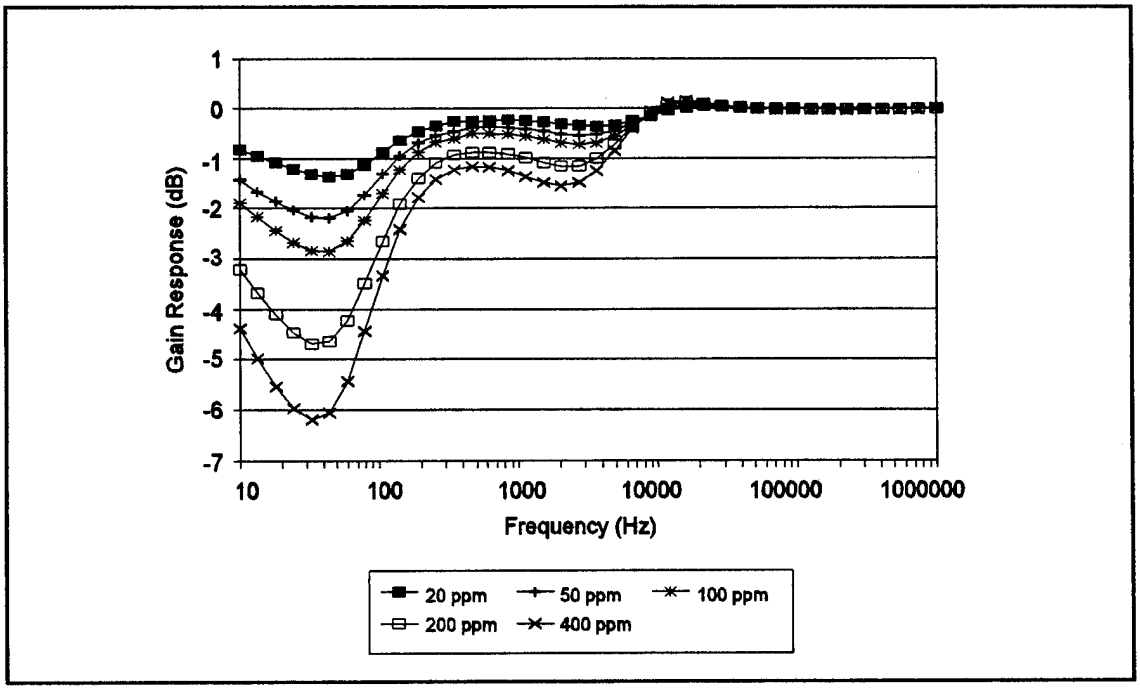


Figure VI-27. Bode Plots of the CuPc-Coated IGEFET Transfer Function Gain Response for Several NH_3 Exposures. (Film Thickness = 0.32 μm. Temperature = 100°C.)

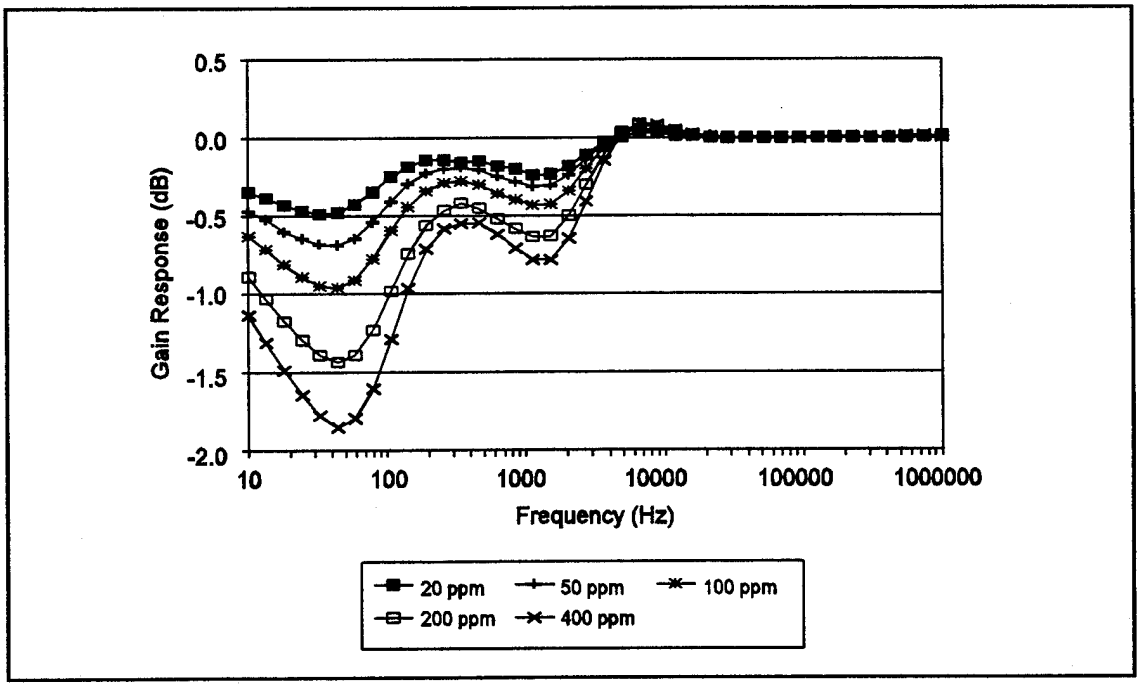


Figure VI-28. Bode Plots of the NiPc-Coated IGEFET Transfer Function Gain Response for Several NH_3 Exposures. (Film Thickness = 0.43 μm. Temperature = 100°C.)

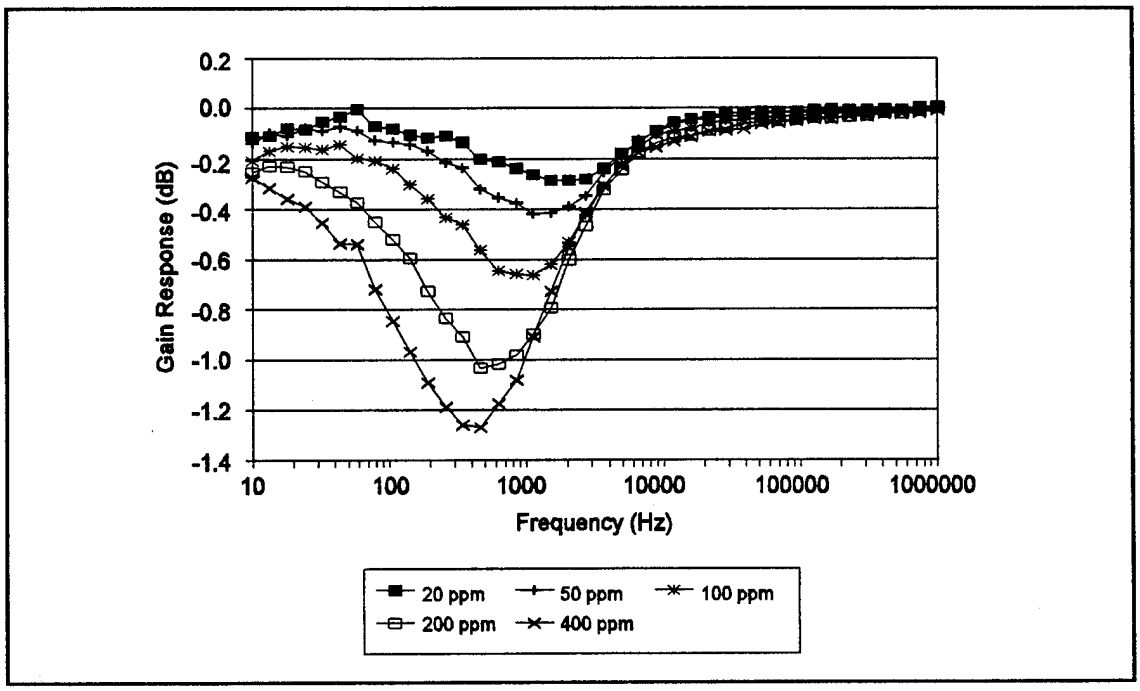


Figure VI-29. Bode Plots of the CoPc-Coated IGEFET Transfer Function Gain Response for Several NH_3 Exposures. (Film Thickness = 0.51 μm. Temperature = 100°C.)

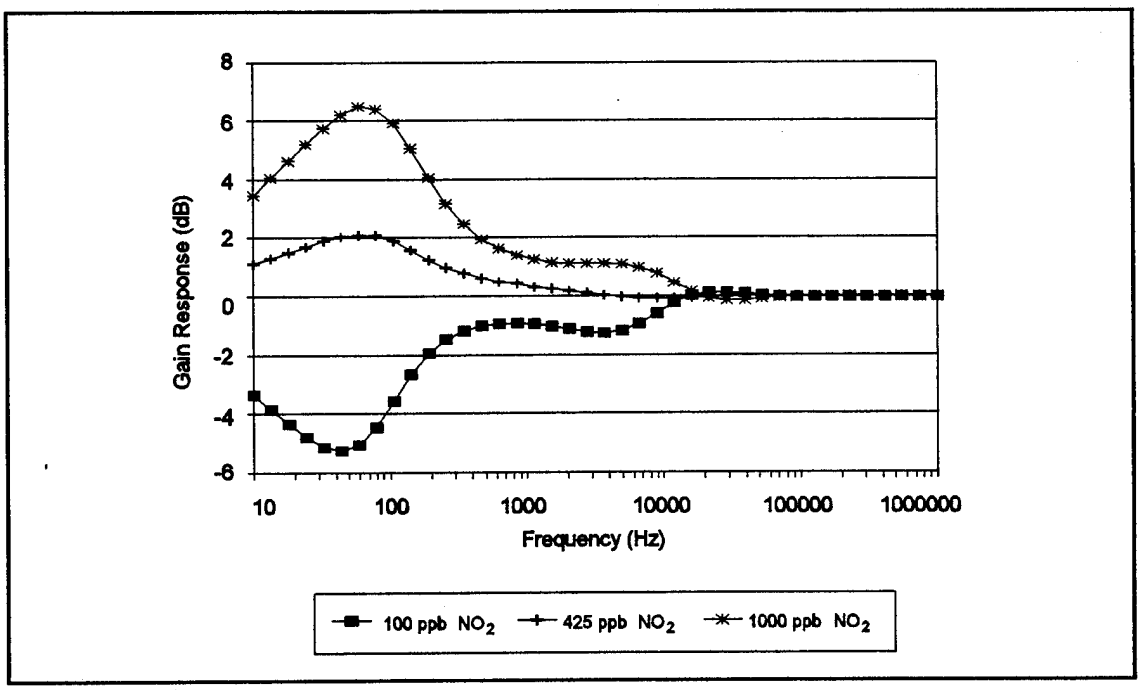


Figure VI-30. Bode Plots of the CuPc-Coated IGEFET Transfer Function Gain Response to a Binary Gas Mixture Containing 200 ppm NH_3 and Various NO_2 Concentrations. (Film Thickness = 0.32 μm. Temperature = 100°C.)

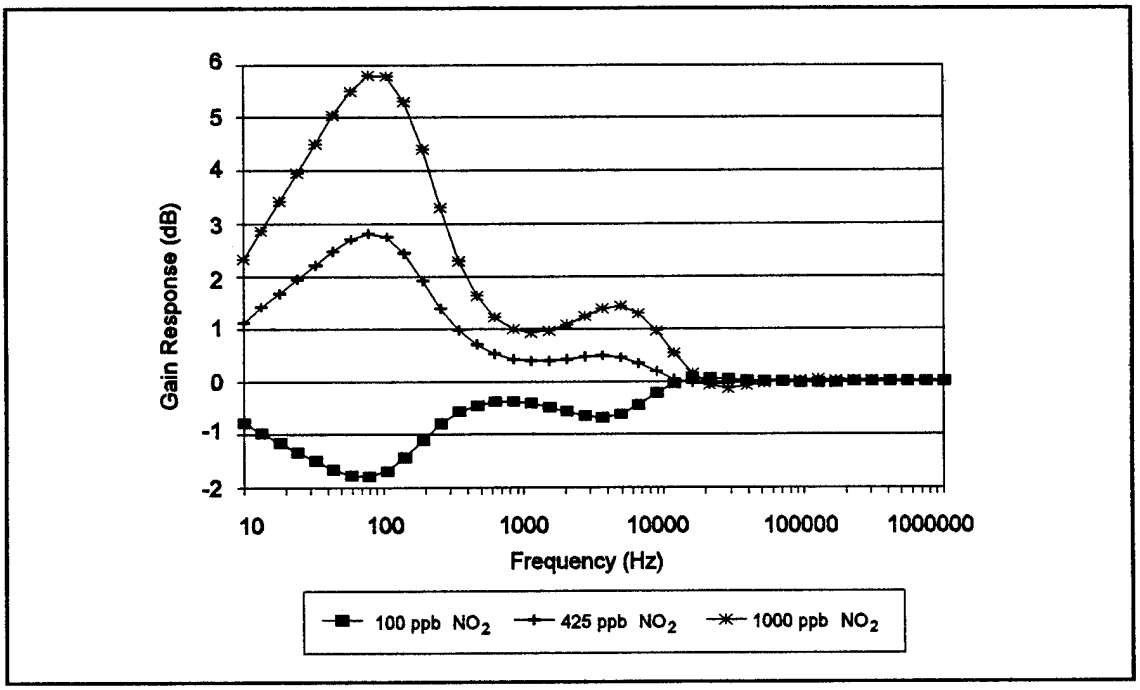


Figure VI-31. Bode Plots of the NiPc-Coated IGEFET Transfer Function Gain Response to a Binary Gas Mixture Containing 200 ppm NH_3 and Various NO_2 Concentrations. (Film Thickness = 0.43 μm. Temperature = 100°C.)

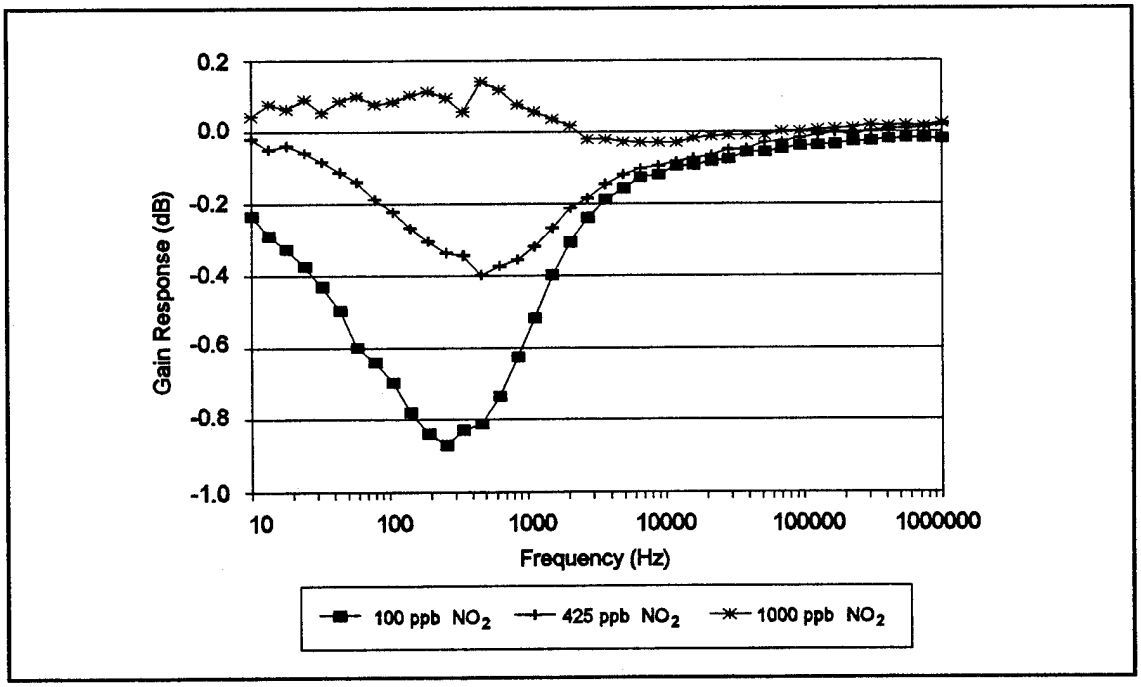


Figure VI-32. Bode Plots of the CoPc-Coated IGEFET Transfer Function Gain Response to a Binary Gas Mixture Containing 200 ppm NH_3 and Various NO_2 Concentrations. (Film Thickness = 0.51 μm. Temperature = 100°C.)

Based upon the above results, the gas analyses were conducted with the two gain response maxima observed in the CuPc- and NiPc-coated IGEFET transfer function gain responses. The gain response data collected from the CoPc-coated IGEFET elements, which lacked both maxima and possessed a lower measured signal-to-noise ratio, were not used in the subsequent gas analyses.

Since the time response of the IGE structure DC resistance to gas exposure had revealed features that could serve as discriminants in the analysis of the gas mixtures, the time dependence of the CuPc- and NiPc-coated IGEFET gain response at the two maxima were investigated. The time-dependent behavior of the two gain response maxima were found to be similar and, therefore, the results with the low-frequency maxima are discussed here, and the results obtained with the high-frequency maxima are provided in Appendix M. Similar to the IGE structure DC resistance response, the MPc-coated IGEFET gain response to NO_2 exposure (Figures VI-33 and VI-34) and NH_3 exposure (Figures VI-35 and VI-36) revealed a rapid response occurring within the initial two minutes of the exposure, followed by a slower increase with continued exposure. As was shown earlier, the gain response maxima were positive with NO_2 exposure and negative with NH_3 exposure. The time dependence of the gain response to binary mixtures was consistent with that observed in the IGE structure DC resistance response upon exposure to similar mixtures (Figures VI-37 through VI-38). That is, the gain response, which was initially NH_3-like (negative gain response), became NO_2-like (positive gain response) with continued exposure. Since the gain response changed most rapidly during the first few minutes of exposure, the feature vectors for gas analyses were generated using the gain response maxima measured from the first four time measurements (slices). These time slices occurred at approximately 2.4, 4.7, 7.1, and 9.5 minutes.

To determine the sensitivities of the IGEFET transfer function gain response relative to the challenge gas, the gain response for each time slice was plotted as a function of the challenge gas concentration. Figures VI-39 and VI-40 reveal that the low- and high-frequency gain response maxima of the CuPc- and NiPc-coated IGEFET elements varied linearly with the log of the NO_2 challenge concentration, and that the sensitivity (as indicated by the slope of the lines) of the CuPc- and NiPc-coated IGEFET elements were essentially the same. In contrast, the sensitivities of these two MPc-coated IGEFET sensors to NH_3 were significantly different (Figures VI-41 and VI-42). Although the gain responses of both the CuPc- and NiPc-coated IGEFET sensors also varied linearly with the logarithm of the NH_3 concentration, the CuPc-coated IGEFET gain response was much more sensitive to NH_3. The sensitivities of the CuPc-coated IGEFET gain response at the low- and high-

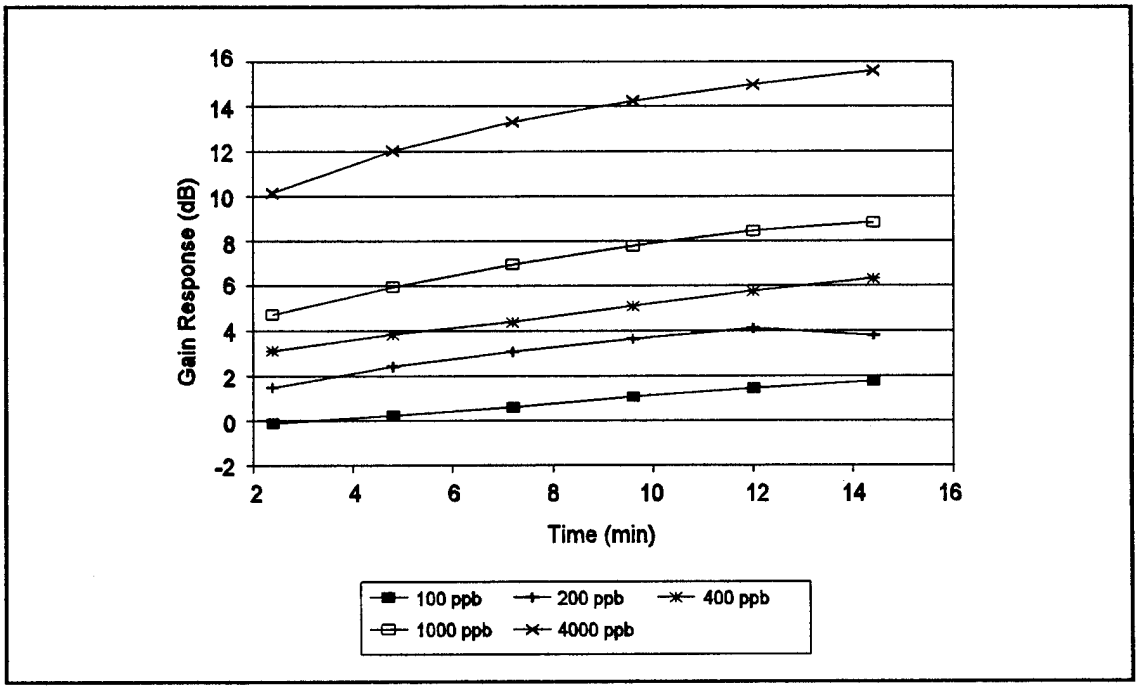


Figure VI-33. Time Dependence of the CuPc-Coated IGEFET Transfer Function Gain Response for Several NO_2 Exposures. (Approximate Frequency = 100 Hz. Film Thickness = 0.32 μm. Temperature = 100°C.)

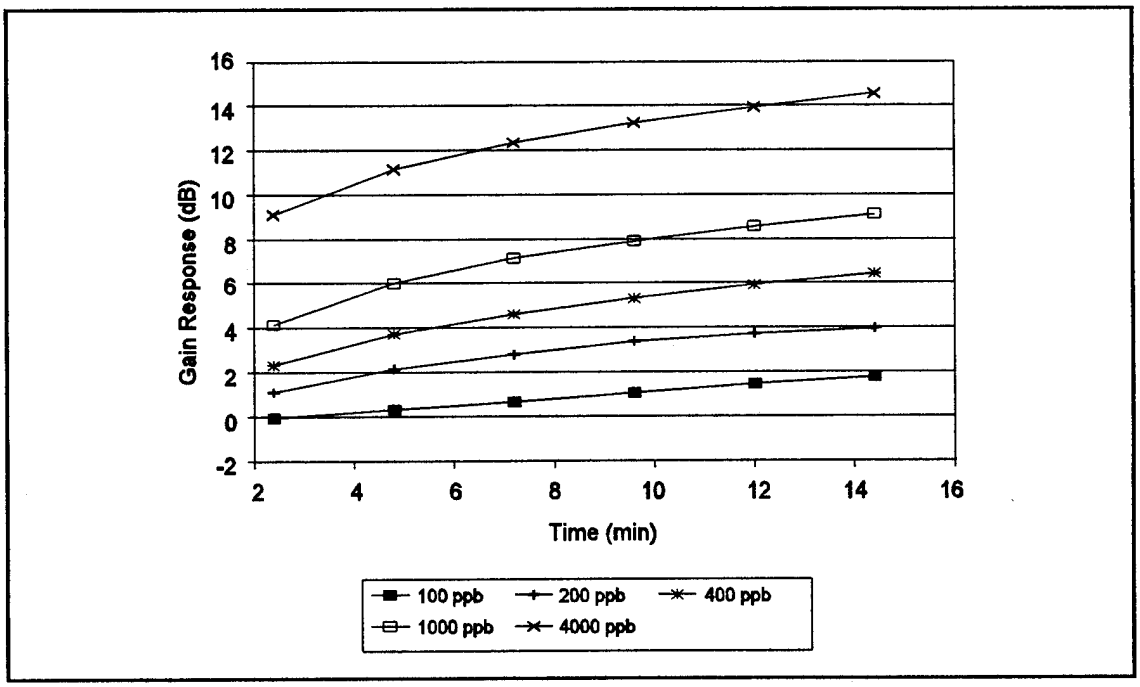


Figure VI-34. Time Dependence of the NiPc-Coated IGEFET Transfer Function Gain Response for Several NO_2 Exposures. (Approximate Frequency = 100 Hz. Film Thickness = 0.43 μm. Temperature = 100°C.)

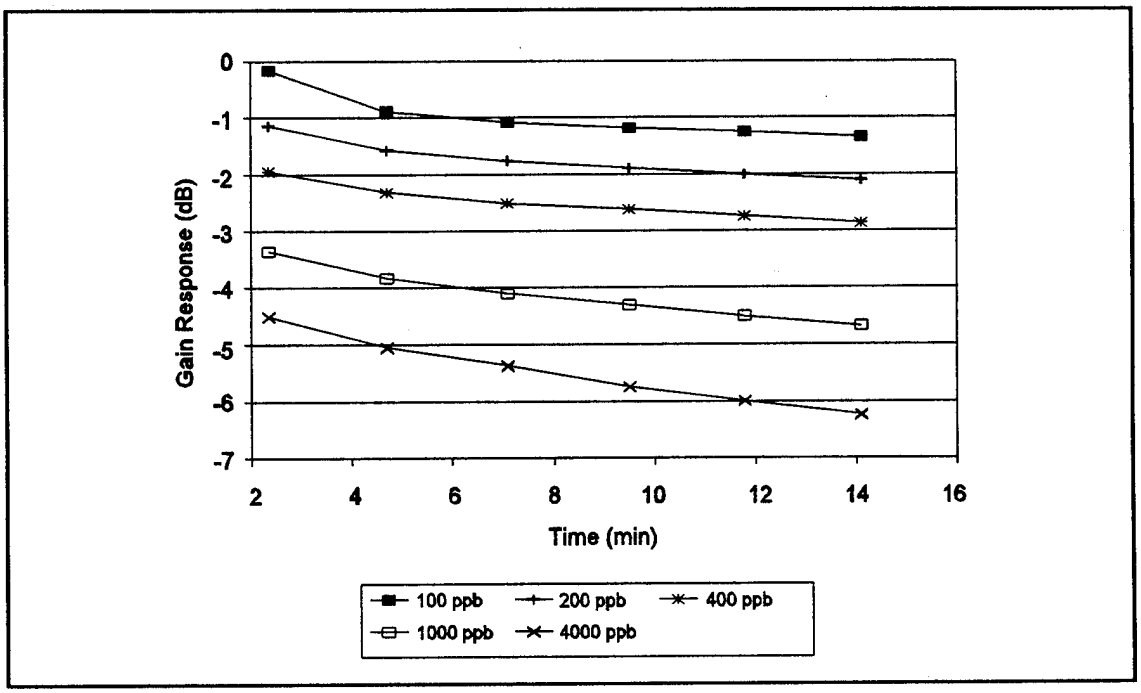


Figure VI-35. Time Dependence of the CuPc-Coated IGEFET Transfer Function Gain Response for Several NH_3 Exposures. (Approximate Frequency = 44 Hz. Film Thickness = 0.32 μm. Temperature = 100°C.)

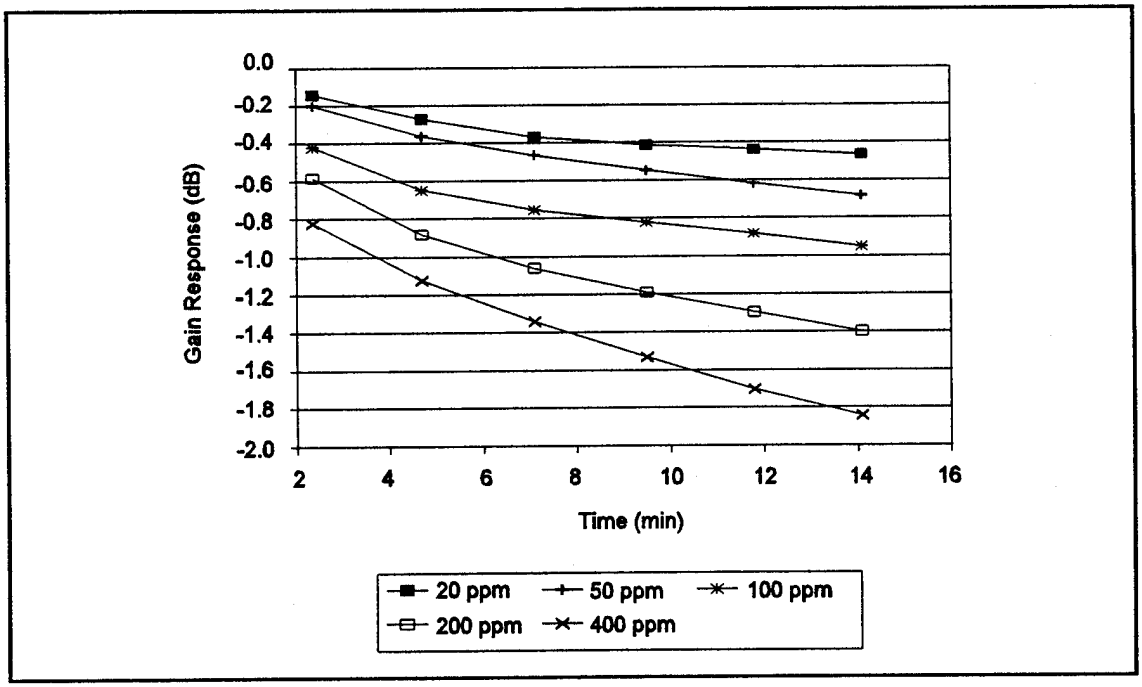


Figure VI-36. Time Dependence of the NiPc-Coated IGEFET Transfer Function Gain Response for Several NH_3 Exposures. (Approximate Frequency = 44 Hz. Film Thickness = 0.43 μm. Temperature = 100°C.)

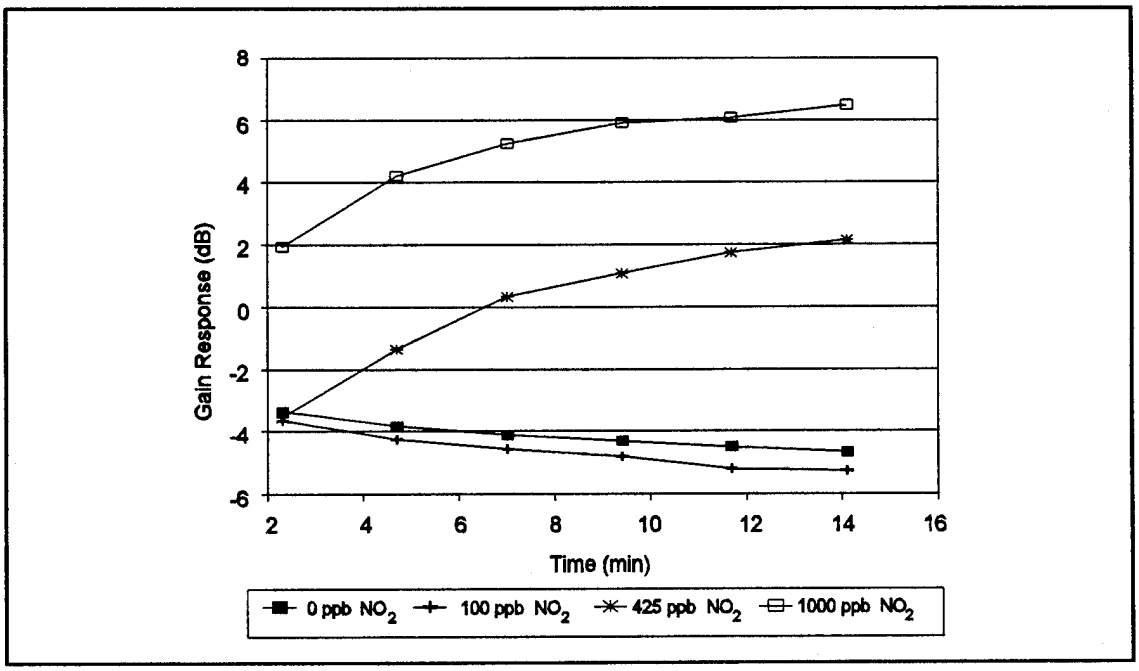


Figure VI-37. Time Dependence of the CuPc-Coated IGEFET Transfer Function Gain Response to Binary Gas Mixtures Composed of 200 ppm NH_3 and Various NO_2 Concentrations. (Approximate Frequency = 44 Hz. Film Thickness = 0.32 μm. Temperature = 100° C.)

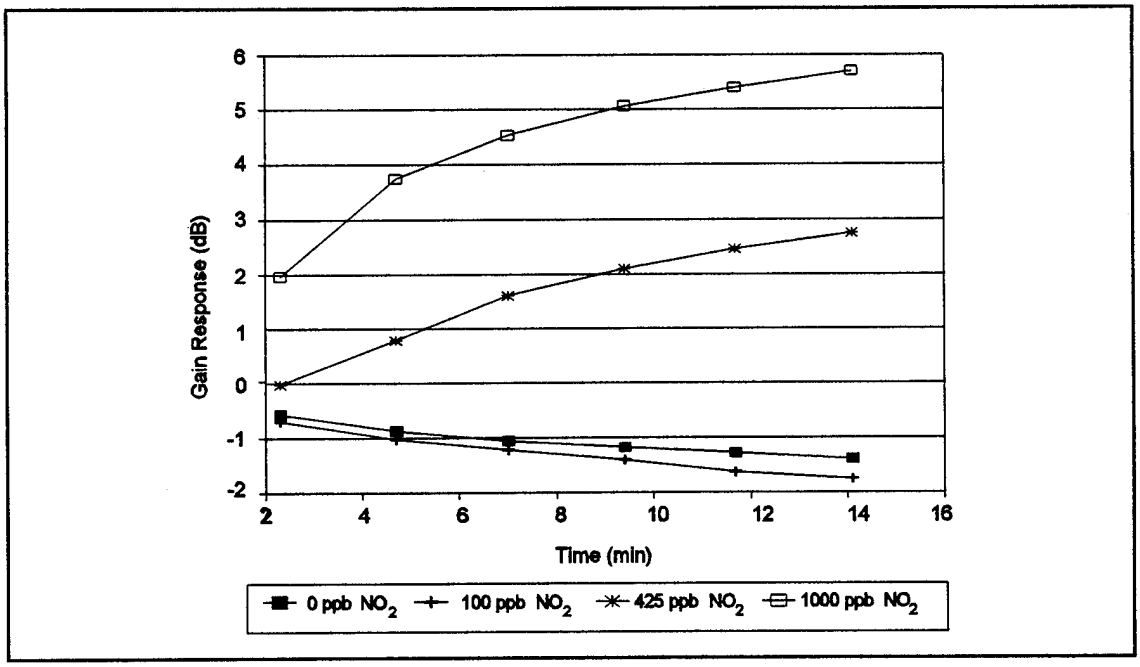


Figure VI-38. Time Dependence of the NiPc-Coated IGEFET Transfer Function Gain Response to Binary Gas Mixtures Composed of 200 ppm NH_3 and Various NO_2 Concentrations. (Approximate Frequency = 44 Hz. Film Thickness = 0.32 μm. Temperature = 100° C.)

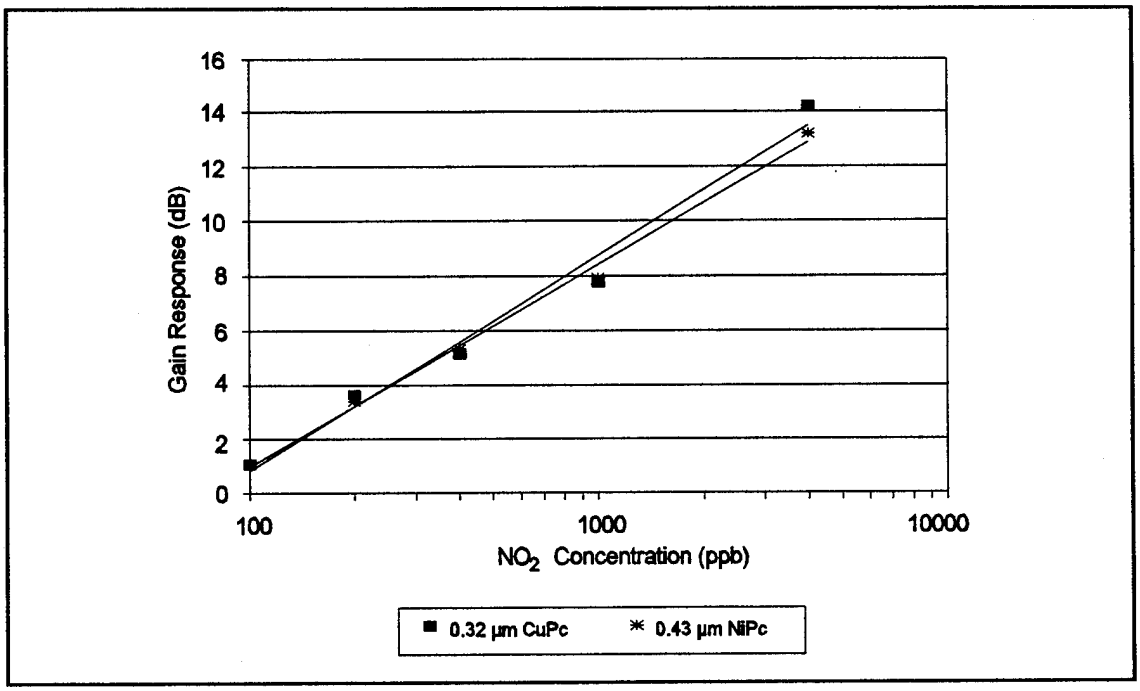


Figure VI-39. Concentration Dependence of the MPc-Coated IGEFET Transfer Function Gain Response for Several NO_2 Exposures. (Approximate Frequency = 100 Hz. Time Slice = 9.5 min. Temperature = 100°C.)

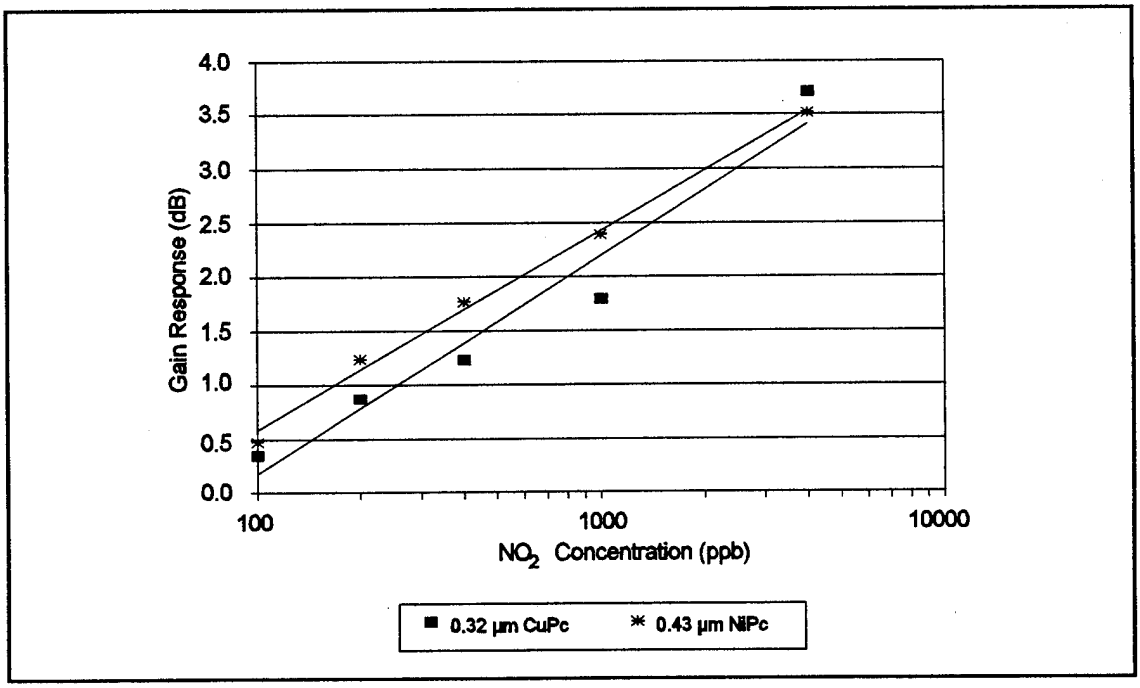


Figure VI-40. Concentration Dependence of the MPc-Coated IGEFET Transfer Function Gain Response for Several NO_2 Exposures. (Approximate Frequency Interval = 800 -12000 Hz. Time Slice = 9.5 min. Temperature = 100°C.)

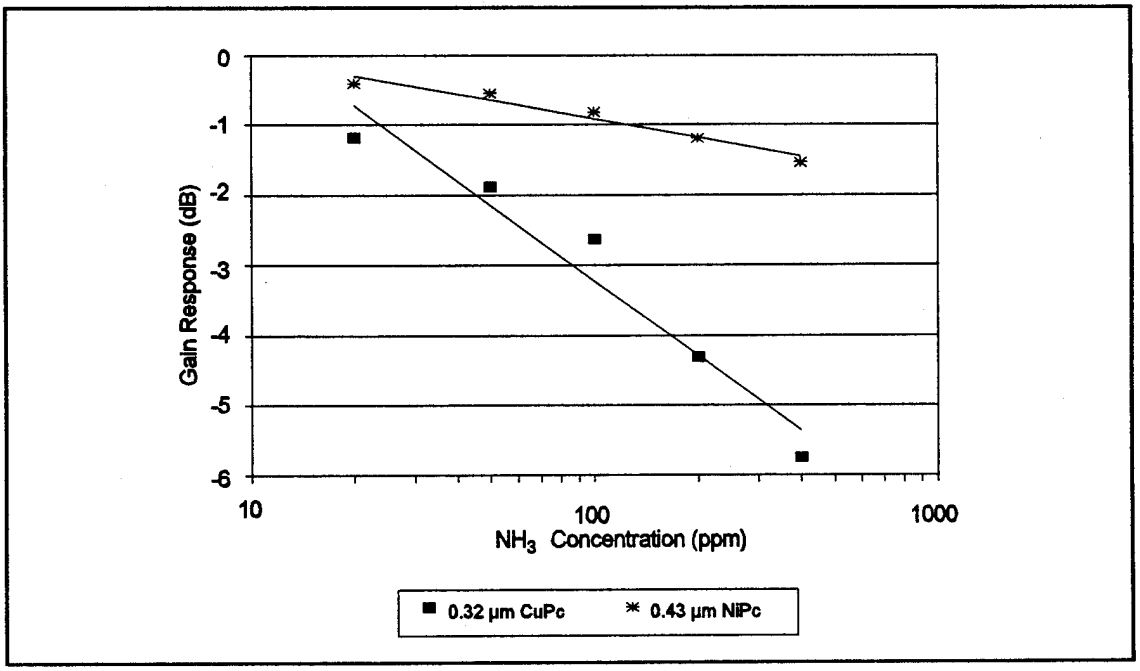


Figure VI-41. Concentration Dependence of the MPc-Coated IGEFET Transfer Function Gain Response for Several NH_3 Exposures. (Approximate Frequency = 44 Hz. Time Slice = 9.5 min. Temperature = 100°C.)

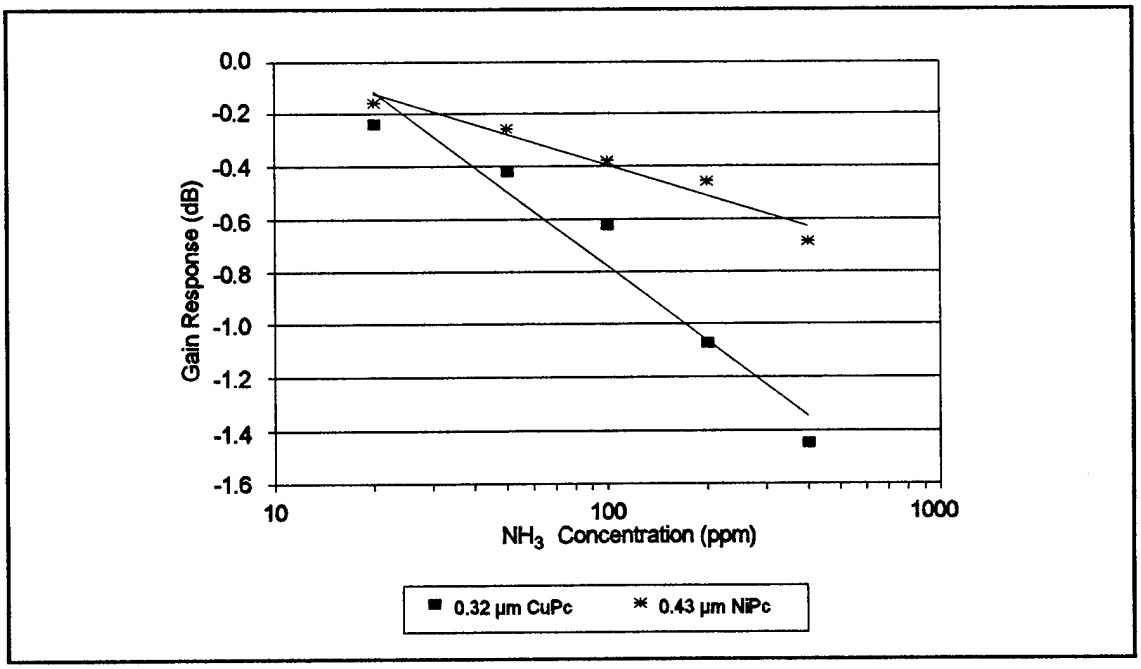


Figure VI-42. Concentration Dependence of the MPc-Coated IGEFET Transfer Function Gain Response for Several NH_3 Exposures. (Approximate Frequency Interval= 800-4000 Hz. Time Slice = 9.5 min. Temperature = 100°C.)

frequency maxima, as indicated by the slope of the lines, were approximately 4 times and 2.5 times greater than the corresponding sensitivities of the NiPc-coated IGEFET gain response.

Screening candidate functional forms in an attempt to linearize the gain response data and minimize the error in the predicted concentrations, revealed that a logarithmic functional form was valuable for performing the gas analysis with the gain response data. The normalized gain response maxima (G_N) were least-squares fitted to an equation of the form:

$$\log(C) = A G_N + B \qquad \text{(VI-4)}$$

where C is the challenge gas concentration, and A and B are constants. The value of the parameters obtained by least-squares fitting the data collected for the two challenge gases at the low- and high-frequency maxima are provided in Appendix L.

The feature vector for performing the gas analyses with the gain response data was formed in a manner similar to the construction of the feature vectors employed for the gas analyses accomplished with the normalized DC resistance data. The process for constructing the gain response feature vectors is illustrated in Figure VI-43. First, the sensor response vectors representing the gain response of an IGEFET sensor element coated with a particular MPc film type for each challenge gas, were formed. In contrast to the normalized DC resistance response, the gain response, upon exposure to each of the challenge gases, was least-squares fitted to the same functional form and, therefore, the sensor response vectors for the single component and binary mixture analyses could be formed in an identical fashion. That is, the gain sensor response vectors for both the single component and binary gas mixture analyses possessed eight elements representing the gain response of the four time samples at the low- and high-frequency maxima. The feature vector representing the gain response of the CuPc- and NiPc-coated IGEFET elements to a challenge gas exposure was then formed by combining the sensor response vectors for the two film types in a single column vector. The resulting feature vectors, including the complete calibration sets and limited test sets (one for each challenge gas concentration) for the single component and binary mixture analyses, are provided in Appendix L.

Feature Vector Formation from the IGEFET Transfer Function Phase Measurements.

The analysis of the IGEFET transfer function phase measurements and the formation of the feature vector for gas analysis was identical to the process used with the IGEFET transfer function gain measurements. First, Bode plots of the IGEFET transfer function phase were examined to identify features that could serve as discriminants in the analysis of the gas response. The time dependency of these features was then examined to identify additional characteristics that could be

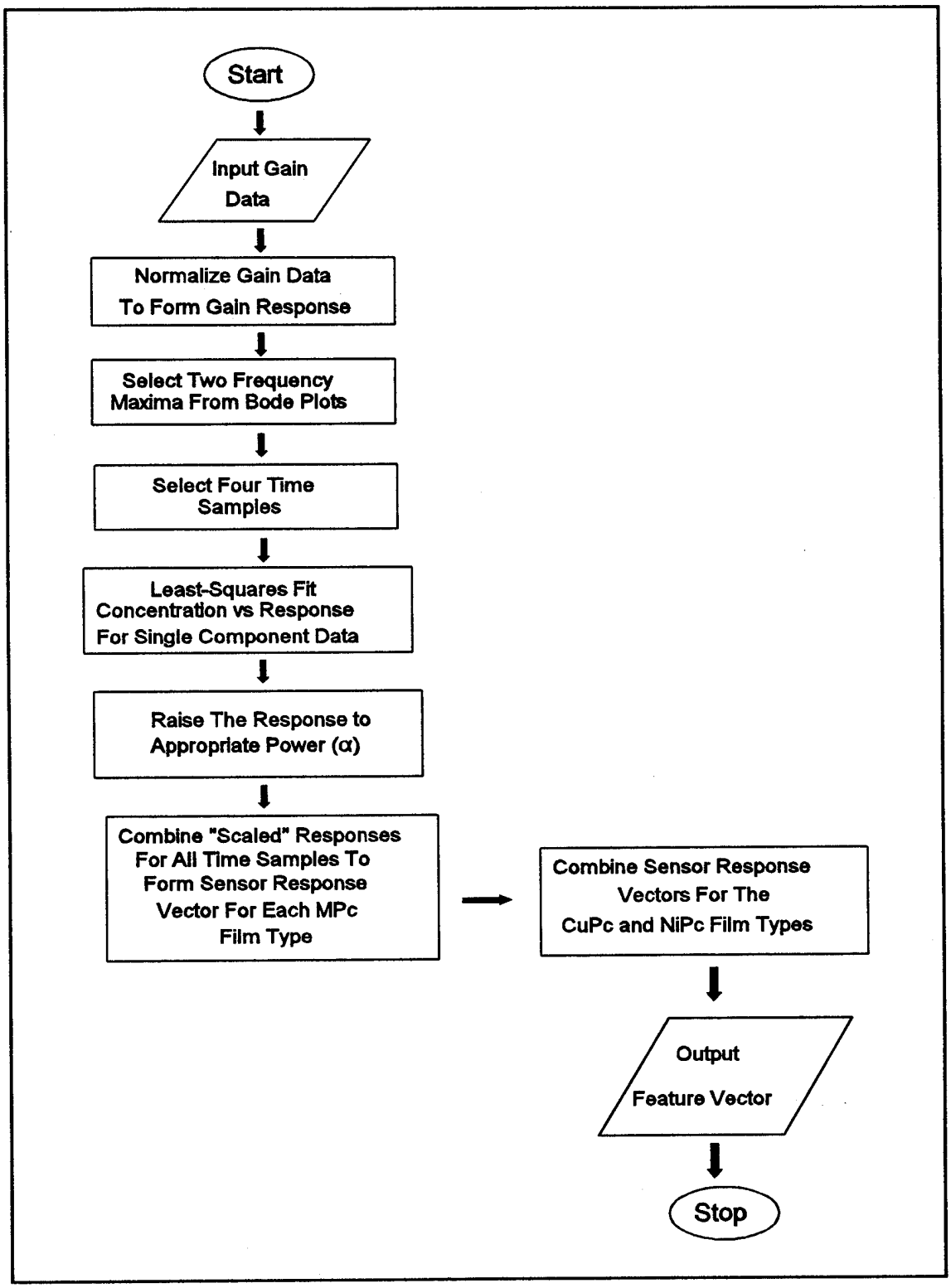


Figure VI-43. Gain Response Feature Vector Formation Process.

used in the gas response analysis. The sensitivity of the identified phase response features relative to each test gas was evaluated. That is, the phase response features were least-squares fitted to a functional form to provide, with the appropriate transformation of the data, a linear relationship between the concentration and the phase response features, while minimizing the error in the predicted concentrations obtained from the subsequent binary gas mixture analysis. Sensor response vectors were formed from the transformed phase response features derived from the measurements collected from the CuPc- and NiPc-coated IGEFET elements. Finally, the sensor response vectors corresponding to each MPc-coated IGEFET element were combined to form the feature vector for gas analysis.

Three potential features were identified after examining the IGEFET transfer function phase response to the challenge gases. Figures VI-44 through VI-46 show the phase response of the MPc-coated IGEFET sensing elements to several NO_2 challenge gas concentrations. Similiar to the gain response measurements, the phase response observed with the CuPc- and NiPc-coated IGEFET sensors were similar and possessed three maxima (absolute value) located near the frequency intervals of 10-20 Hz, 200-600 Hz, and 10-40 KHz. However, the CoPc-coated IGEFET transfer function phase response, similar to that observed with the gain response, was significantly different compared to the phase response measured with the IGEFET elements coated with the other MPc films. The CoPc-coated IGEFET phase response displays only two maxima: one near 0.5-1 KHz and the other in the vicinity of 8-20 KHz. As was concluded with the gain response measurements (Figure VI-25), the quiescent CoPc-coated IGEFET elements were operating with much less inter-electrode coupling compared to the other MPc-coated IGEFET elements. This difference in the baseline inter-electrode coupling results in the dissimilarity between the CoPc-coated IGEFET transfer function response and the transfer function responses of the other MPc-coated IGEFET elements. Despite this difference, the phase response maxima of all three MPc-coated IGEFET elements initially formed at the low end of the frequency intervals, discussed above, upon exposure to small NO_2 concentrations. As the NO_2 concentration was increased, the phase response maxima shifted to higher frequencies and increased in magnitude. The shift in the phase response maxima to higher frequency upon NO_2 exposure is consistent with a smaller inter-electrode RC time constant caused by the decrease in the DC resistance.

As expected, the phase response behavior of the MPc-coated IGEFET elements to the NH_3 challenge gas exposure was essentially the mirror image of the phase response to the NO_2 exposure (Figures VI-47 through VI-49). The phase response maxima near 10 Hz that was clearly revealed

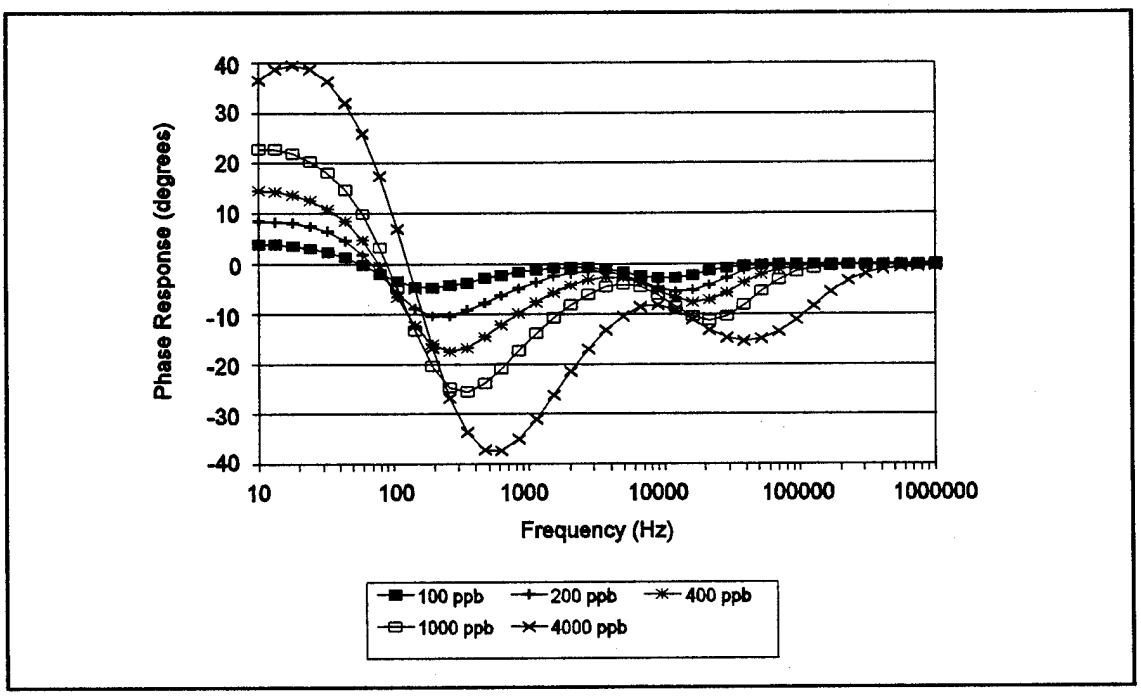


Figure VI-44. Bode Plots of the CuPc-Coated IGEFET Transfer Function Phase Response for Several NO_2 Exposures. (Film Thickness = 0.32 μm. Temperature = 100° C.)

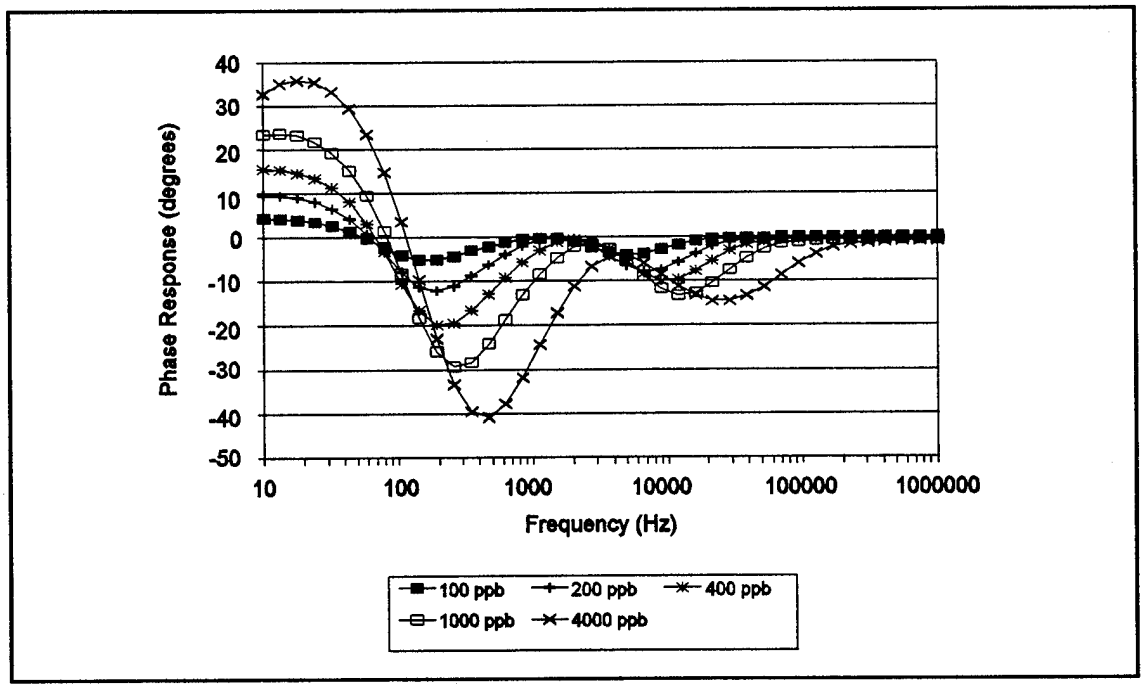


Figure VI-45. Bode Plots of the NiPc-Coated IGEFET Transfer Function Phase Response for Several NO_2 Exposures. (Film Thickness = 0.43 μm. Temperature = 100° C.)

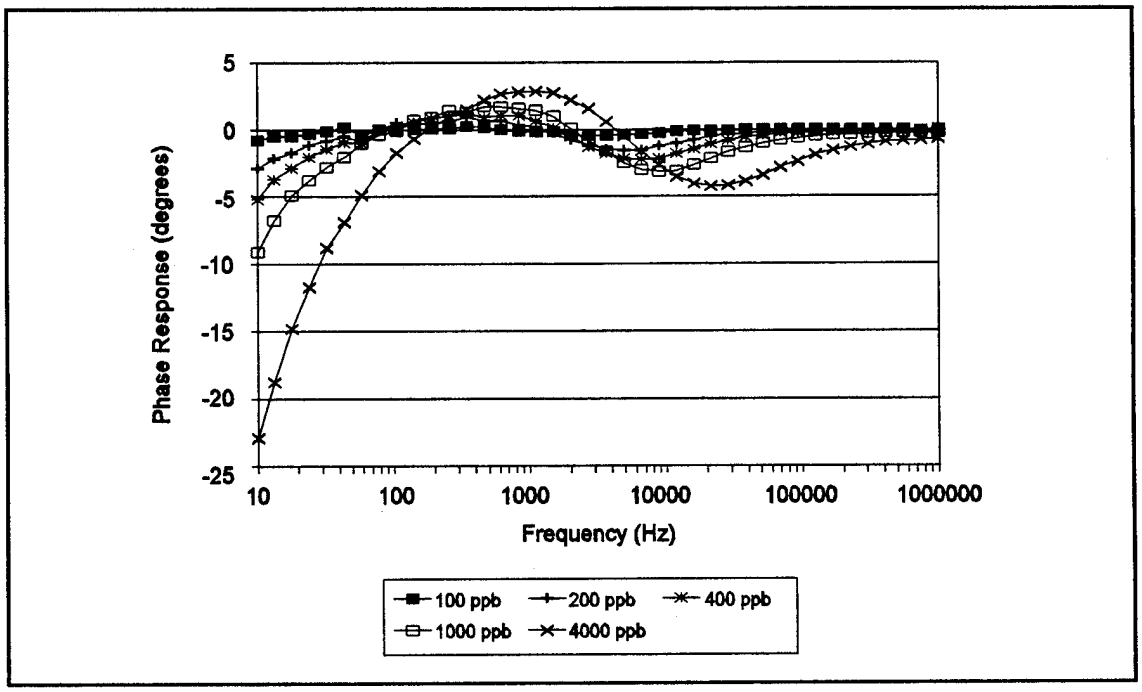


Figure VI-46. Bode Plots of the CoPc-Coated IGEFET Transfer Function Phase Response for Several NO_2 Exposures. (Film Thickness = 0.51 μm. Temperature = 100° C.)

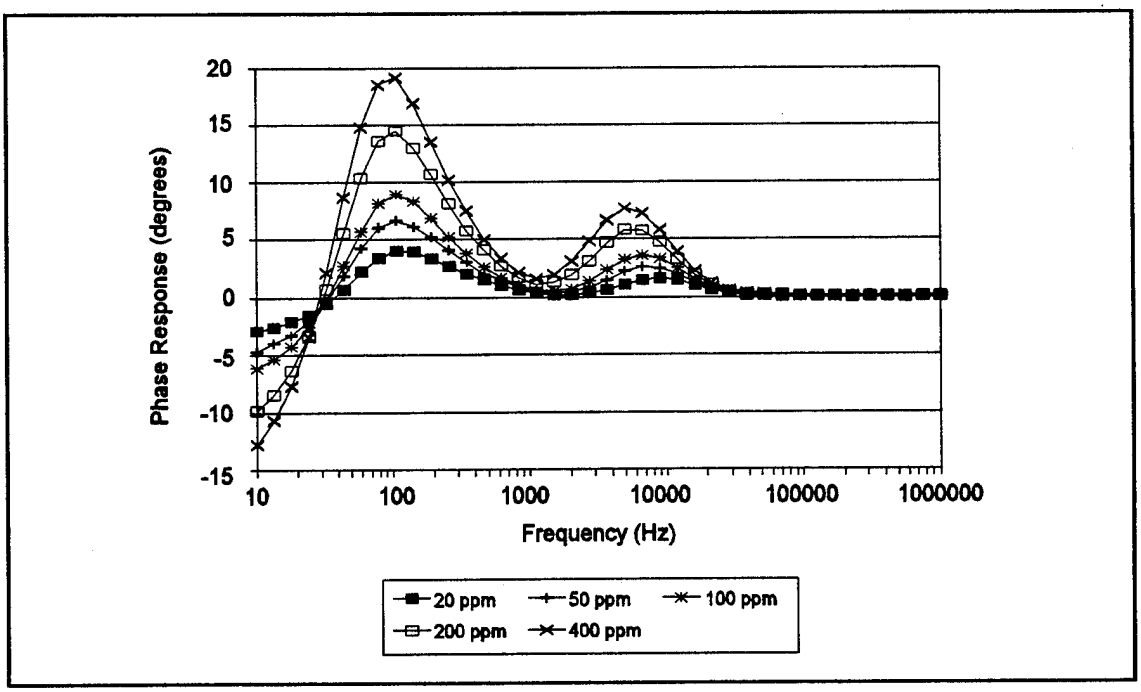


Figure VI-47. Bode Plots of the CuPc-Coated IGEFET Transfer Function Phase Response for Several NH_3 Exposures. (Film Thickness = 0.32 μm. Temperature = 100° C.)

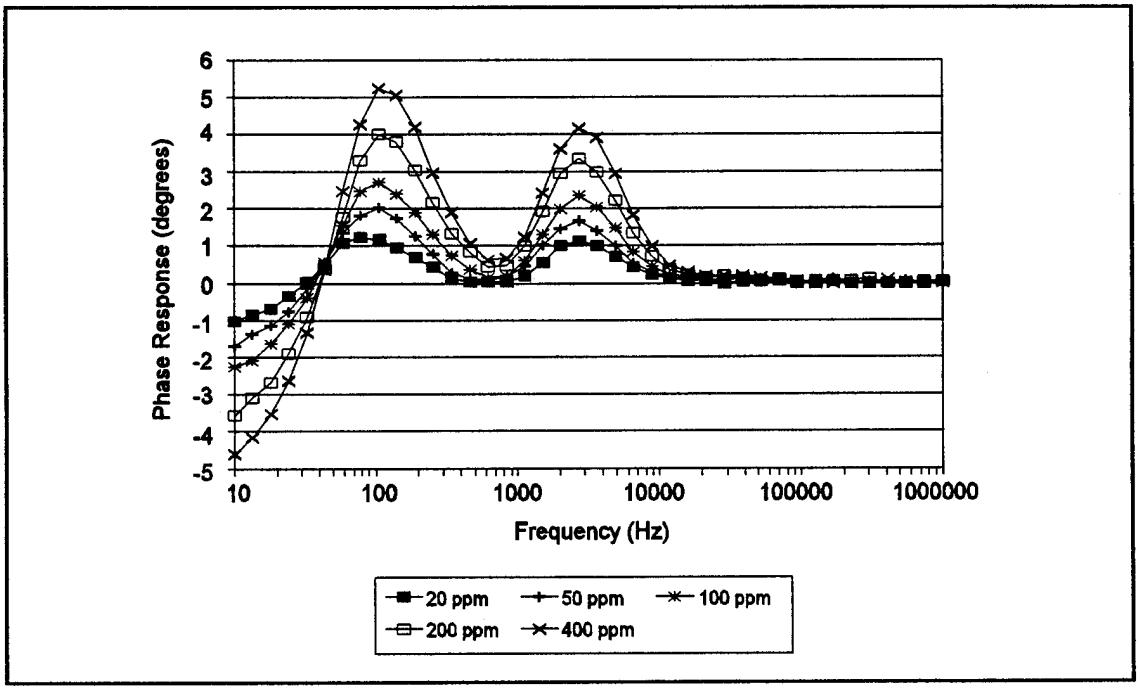


Figure VI-48. Bode Plots of the NiPc-Coated IGEFET Transfer Function Phase Response for Several NH_3 Exposures. (Film Thickness = 0.43 μm. Temperature = 100°C.)

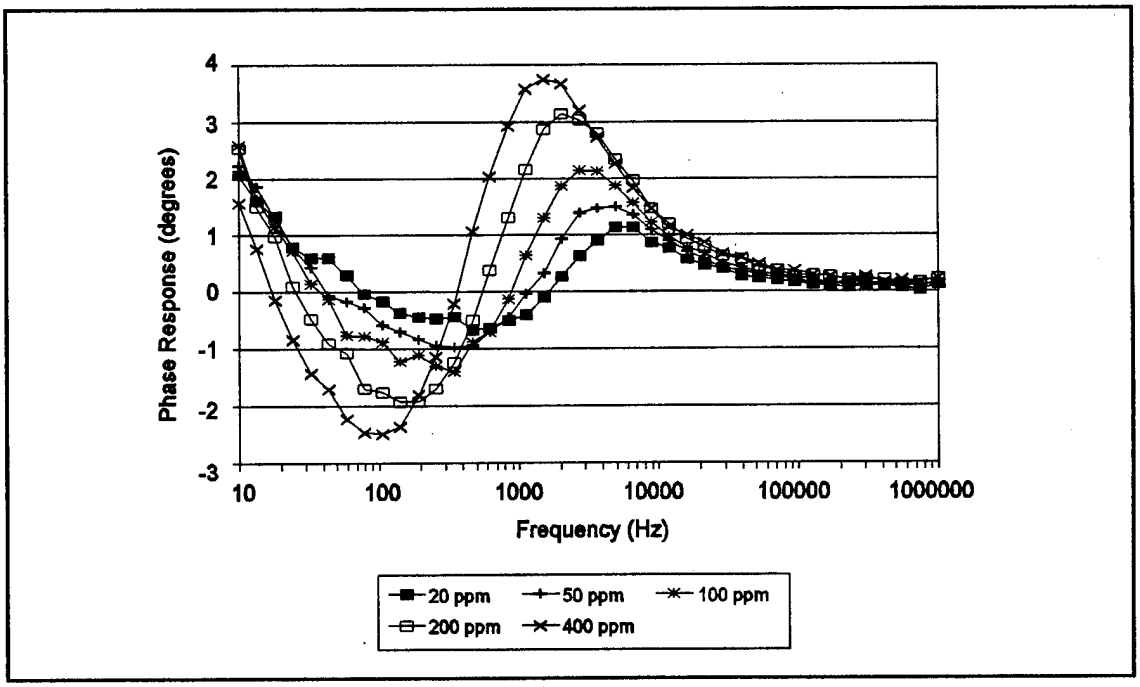


Figure VI-49. Bode Plots of the CoPc-Coated IGEFET Transfer Function Phase Response for Several NH_3 Exposures. (Film Thickness = 0.51 μm. Temperature = 100°C.)

with NO_2 exposure, was apparently shifted to a frequency less than the minimum measurable frequency during NH_3 exposure. With the CuPc-coated IGEFET elements, the other two phase response maxima were located near the 100-200 Hz and 4-9 KHz frequency intervals. For the NiPc-coated IGEFET elements, these phase response maxima were located near the 100-200 Hz frequency interval and at 2500 Hz. As would be expected from the relatively smaller increase in the DC resistance observed previously, the frequency shift in the phase response maxima, observed upon NO_2 exposure, was less pronounced with the NH_3 challenge gas exposures. For both the CuPc- and NiPc-coated IGEFET elements, the 100 Hz maxima did not shift significantly with increasing ammonia concentrations. This was also true for the 2500 Hz maxima observed in the NiPc phase response. However, the maxima which formed near 9 KHz in the phase response of the CuPc-coated IGEFET shifted to lower frequencies as the ammonia concentration was increased. A large shift in the phase response maxima to lower frequencies was also observed with the CoPc-coated IGEFET elements. The small sensitivity of the NiPc-coated IGEFET to NH_3 and a slight shift in the baseline transfer function gain/phase to higher frequency prevented the observation of the shift in the phase response maxima to lower frequency. The magnitude of the frequency shift observed with the three MPc films was consistent with the DC resistance data; that is, the NH_3 sensitivity manifested the following ascending order CoPc > CuPc > NiPc.

Figures VI-50 through VI-52 depict the phase response of the MPc-coated IGEFET sensors upon exposure to binary mixtures composed of a fixed 200 ppm NH_3 concentration and three different NO_2 concentrations (Appendix N details the phase response measured with other binary mixtures). Comparison of these plots with Figures VI-44 through VI-49, reveals that the phase response to the binary mixture containing a small NO_2 concentration (100 ppb) was NH_3-like. As the NO_2 concentration in the binary mixture was increased, the phase response became increasingly more like the phase response to single component NO_2 exposures. In general, the phase response to binary mixtures possessed the same response maxima observed upon exposure to the single component gases. Consistent with the absence of the high-frequency maxima in the gain response upon exposure to the intermediate 425 ppb NO_2 concentration, the high-frequency maxima in the phase response was also absent. The absence of the high-frequency maxima indicates that the relative amplitude of the phase response maxima may be used as a discriminant for gas analysis.

Based upon the above results, the gas analyses were conducted with the two higher frequency phase response maxima observed in the CuPc-and NiPc-coated IGEFET transfer function phase responses. Only the two higher phase response maxima were selected for the analysis since the low-

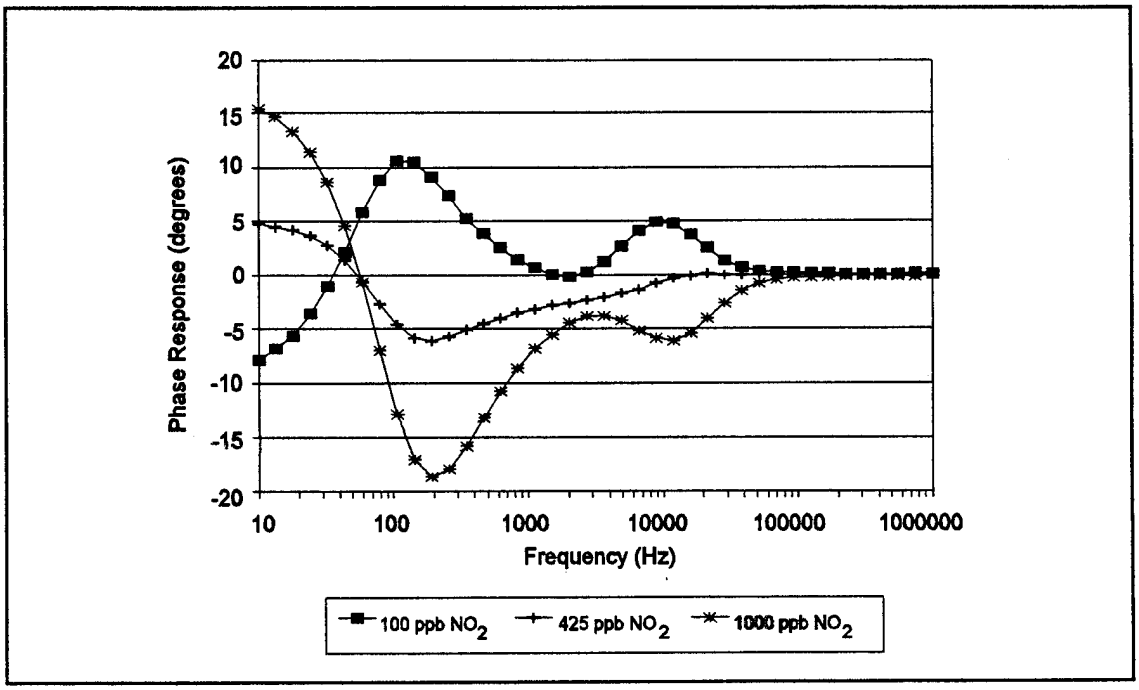


Figure VI-50. Bode Plots of the CuPc-Coated IGEFET Transfer Function Phase Response to a Binary Gas Mixture Containing 200 ppm NH_3 and Various NO_2 Concentrations. (Film Thickness = 0.32 μm. Temperature = 100°C.)

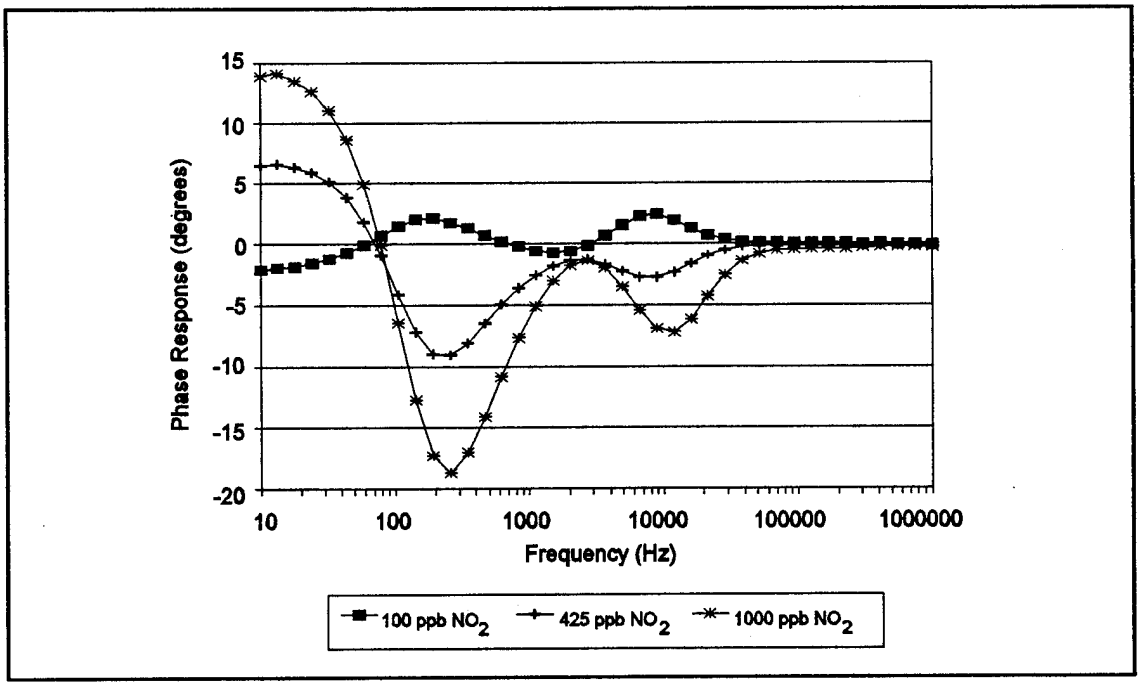


Figure VI-51. Bode Plots of the NiPc-Coated IGEFET Transfer Function Phase Response to a Binary Gas Mixture Containing 200 ppm NH_3 and Various NO_2 Concentrations. (Film Thickness = 0.43 μm. Temperature = 100°C.)

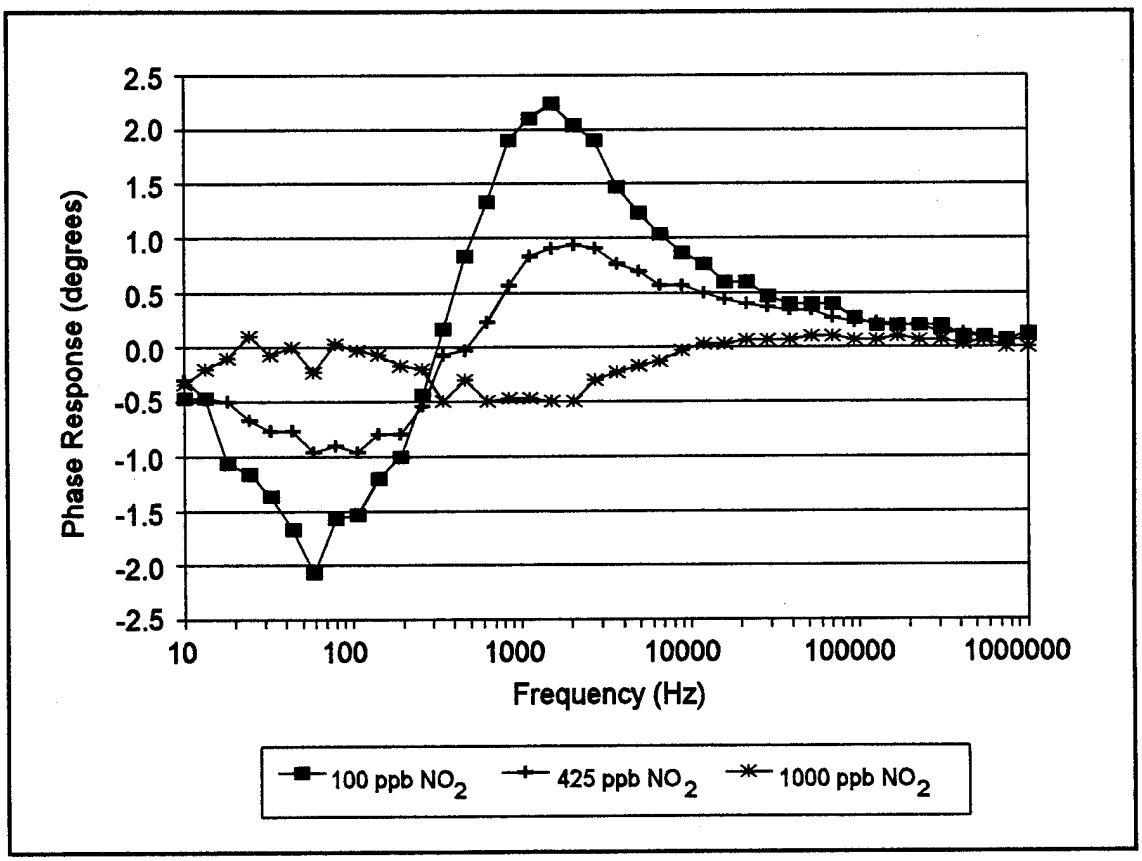


Figure VI-52. Bode Plots of the CoPc-Coated IGEFET Transfer Function Phase Response to a Binary Gas Mixture Containing 200 ppm NH_3 and Various NO_2 Concentrations. (Film Thickness = 0.51 μm. Temperature = 100° C.)

frequency maxima (near 10 Hz) was often shifted beyond the measurable frequency range and, therefore, was not present in the phase response measured with all gas mixtures. Furthermore, the phase response data collected from the CoPc-coated IGEFET elements, which lacked the two low-frequency maxima and exhibited a smaller response (smaller signal-to-noise ratio), was not used in the subsequent gas analyses.

Additional information for gas discrimination was extracted from the time dependence of the phase response maxima. The time-dependent behavior of the two phase response maxima were found to be similar and, therefore, the results with the low-frequency maxima are discussed here, and the results obtained with the high-frequency maxima are provided in Appendix N. However, one significant difference observed in the time dependence of the two phase response maxima was the saturation of the high-frequency maxima observed with a 4000 ppb NO_2 challenge (Appendix N). The saturation of the phase response was more pronounced with the NiPc-coated sensing elements, which are more sensitive to NO_2 compared to the CuPc-coated sensors. As shown earlier, the MPc-coated IGEFET transfer function's phase shifts with respect to frequency upon gas exposure (Figure VI-5). The high-frequency response maxima saturates at approximately 20° since the response maxima is primarily the result of the shift in the high-frequency relaxation process that has a phase peak of approximately 20°. Similar to the IGE structure DC resistance and the IGEFET gain response, the MPc-coated IGEFET's phase response to the NO_2 challenge gas exposure (Figures VI-53 and VI-54) and NH_3 exposure (Figures VI-55 and VI-56) revealed a rapid response occurring within the initial two minutes of exposure, followed by a slower increase with continued exposure. As was shown earlier, the phase response maxima were negative with NO_2 exposure and positive with NH_3 exposure. The time dependence in the phase response to binary mixtures was also consistent with that observed in the IGE structure DC resistance and the IGEFET gain response upon exposure to similar mixtures (Figures VI-57 and VI-58). That is, the phase response, which was initially NH_3-like (positive gain response), became NO_2-like (negative gain response) with continued exposure. Since the phase response changed most rapidly during the first few minutes of exposure, the feature vectors for gas analyses were constructed using the phase response maxima measured from the first four time measurements (slices). These time slices occurred at approximately 2.4, 4.7, 7.1, and 9.5 minutes.

The poor repeatability of the IGEFET's electrical response to binary mixtures, as discussed with respect to the normalized DC resistance response, was also observed with the phase measurements. The greatest variation in the IGEFET's phase response was observed in binary mixtures containing small NO_2 concentrations (100 ppb) (Figures VI-59 and VI-60). In these

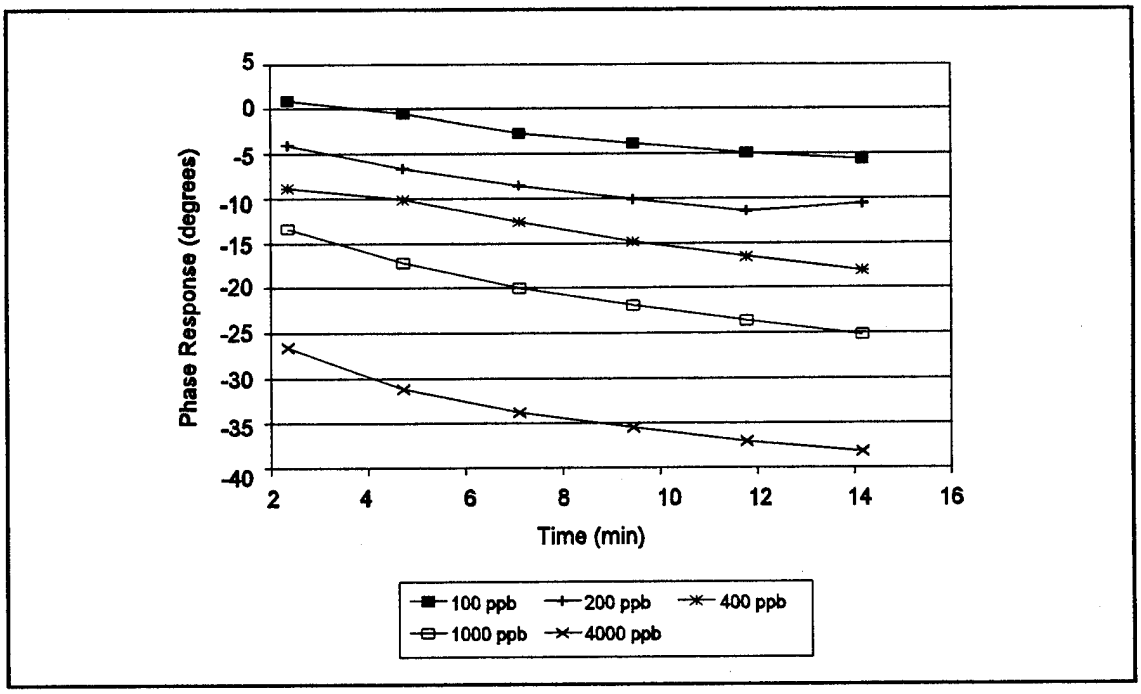


Figure VI-53. Time Dependence of the CuPc-Coated IGEFET Transfer Function Phase Response for Several NO_2 Exposures. (Approximate Frequency Interval = 100-500 Hz. Film Thickness = 0.32 μm. Temperature = 100° C.)

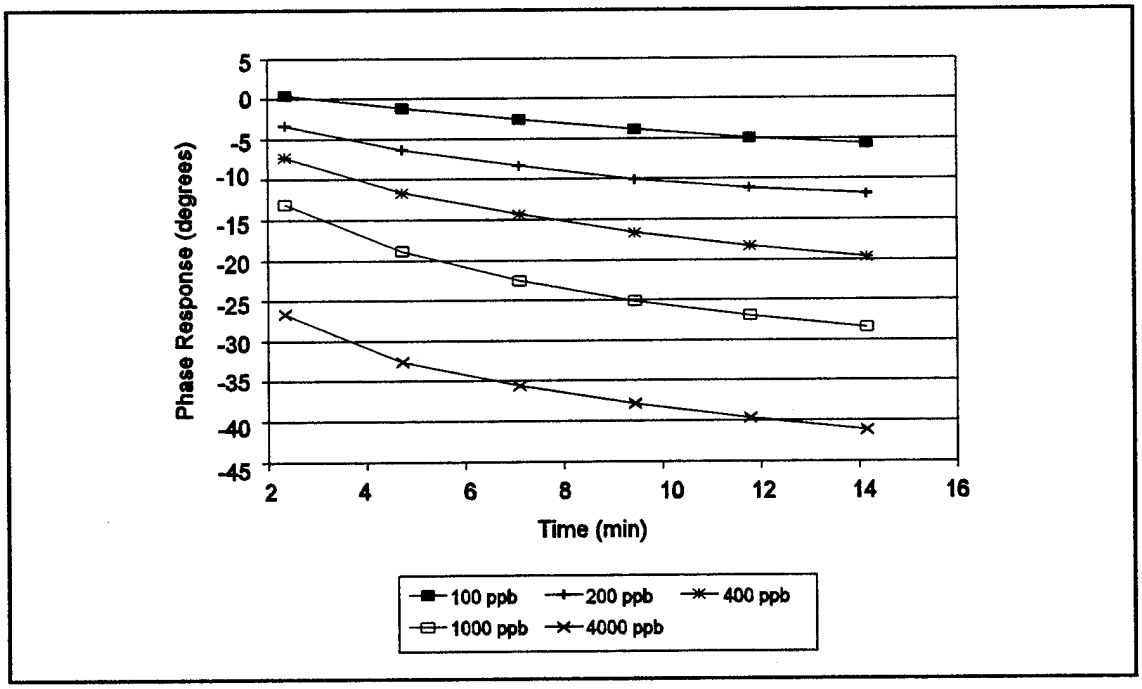


Figure VI-54. Time Dependence of the NiPc-Coated IGEFET Transfer Function Phase Response for Several NO_2 Exposures. (Approximate Frequency Interval = 100-500 Hz. Film Thickness = 0.43 μm. Temperature = 100° C.)

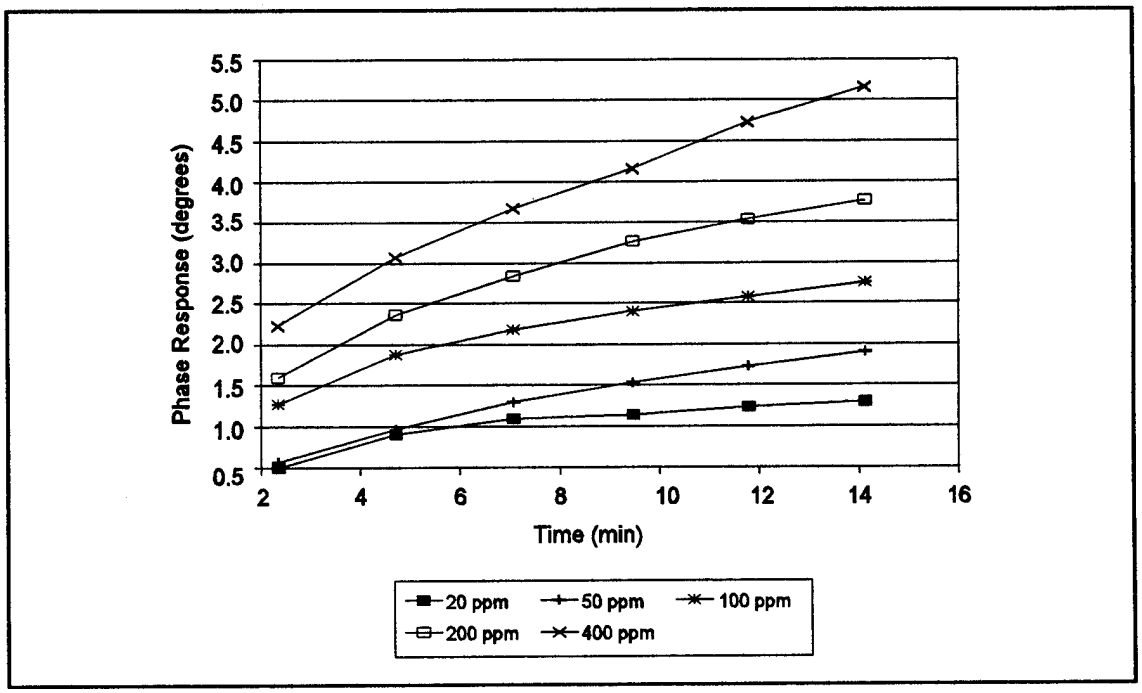


Figure VI-55. Time Dependence of the CuPc-Coated IGEFET Transfer Function Phase Response for Several NH_3 Exposures. (Approximate Frequency = 100 Hz. Film Thickness = 0.32 μm. Temperature = 100° C.)

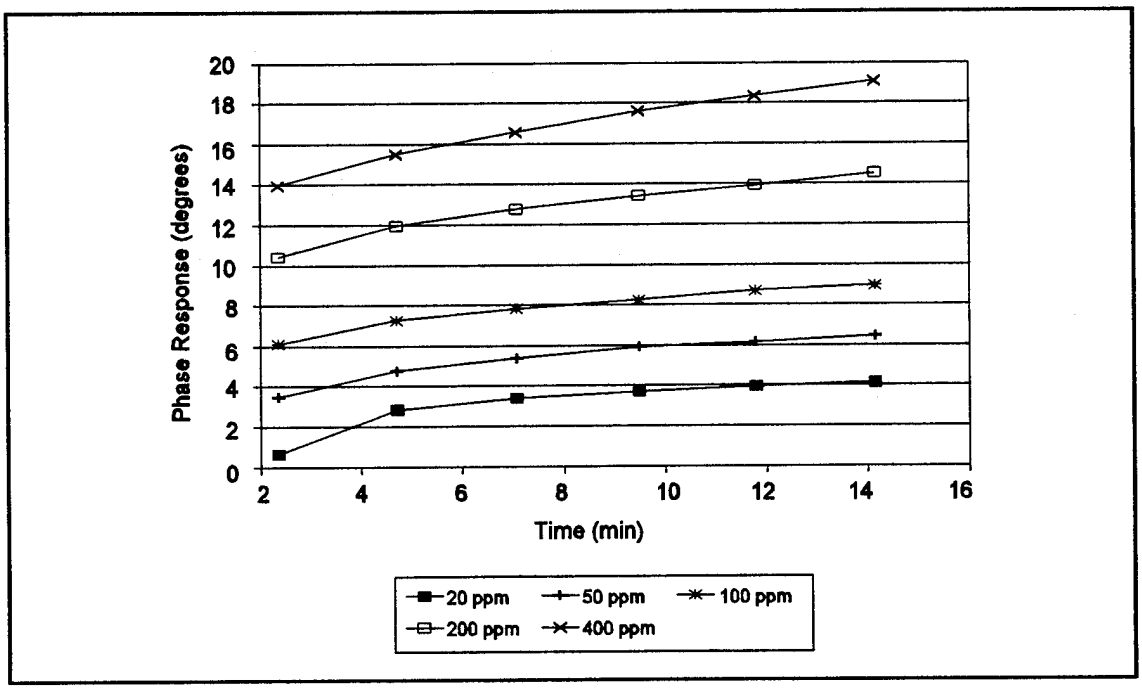


Figure VI-56. Time Dependence of the NiPc-Coated IGEFET Transfer Function Phase Response for Several NH_3 Exposures. (Approximate Frequency = 100 Hz. Film Thickness = 0.43 μm. Temperature = 100° C.)

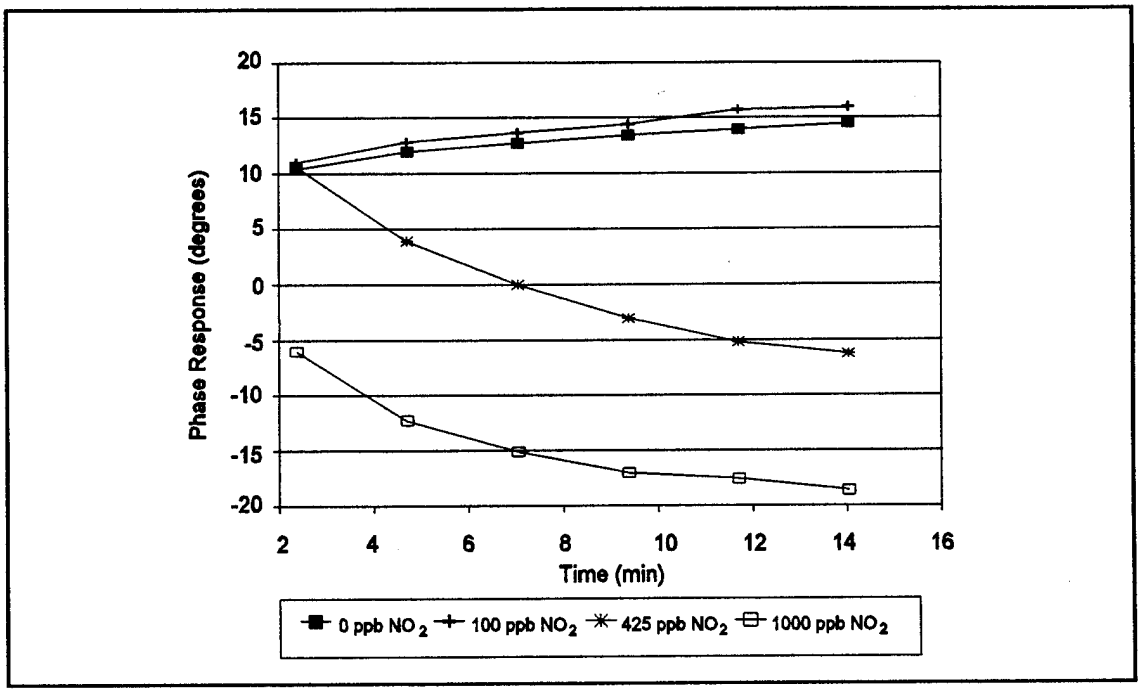


Figure VI-57. Time Dependence of the CuPc-Coated IGEFET Transfer Function Phase Response to Binary Gas Mixtures Composed of 200 ppm NH_3 and Various NO_2 Concentrations. (Approximate Frequency = 44 Hz. Film Thickness = 0.32 μm. Temperature = 100° C.)

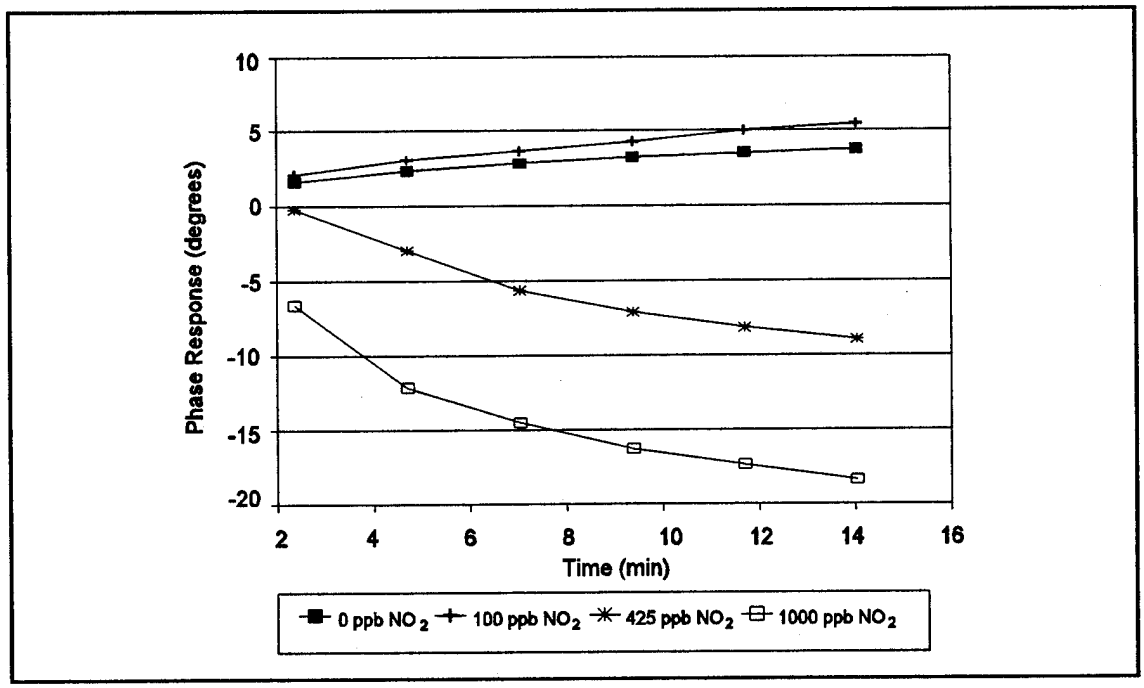


Figure VI-58. Time Dependence of the NiPc-Coated IGEFET Transfer Function Phase Response to Binary Gas Mixtures Composed of 200 ppm NH_3 and Various NO_2 Concentrations. (Approximate Frequency = 44 Hz. Film Thickness = 0.43 μm. Temperature = 100° C.)

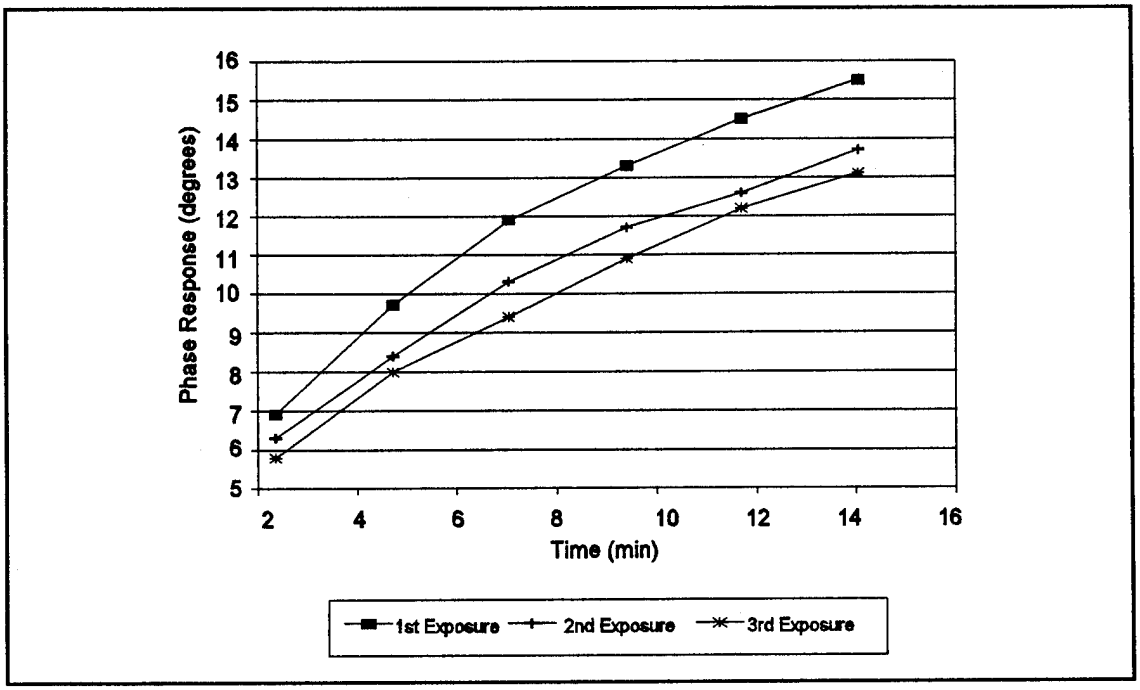


Figure VI-59. Time Dependence of the CuPc-Coated IGEFET Transfer Function Phase Response upon Repeated Exposure to a Binary Gas Mixture Composed of 50 ppm NH_3 and 100 ppb NO_2. (Approximate Frequency = 106 Hz. Film Thickness = 0.32 μm. Temperature = 100° C.)

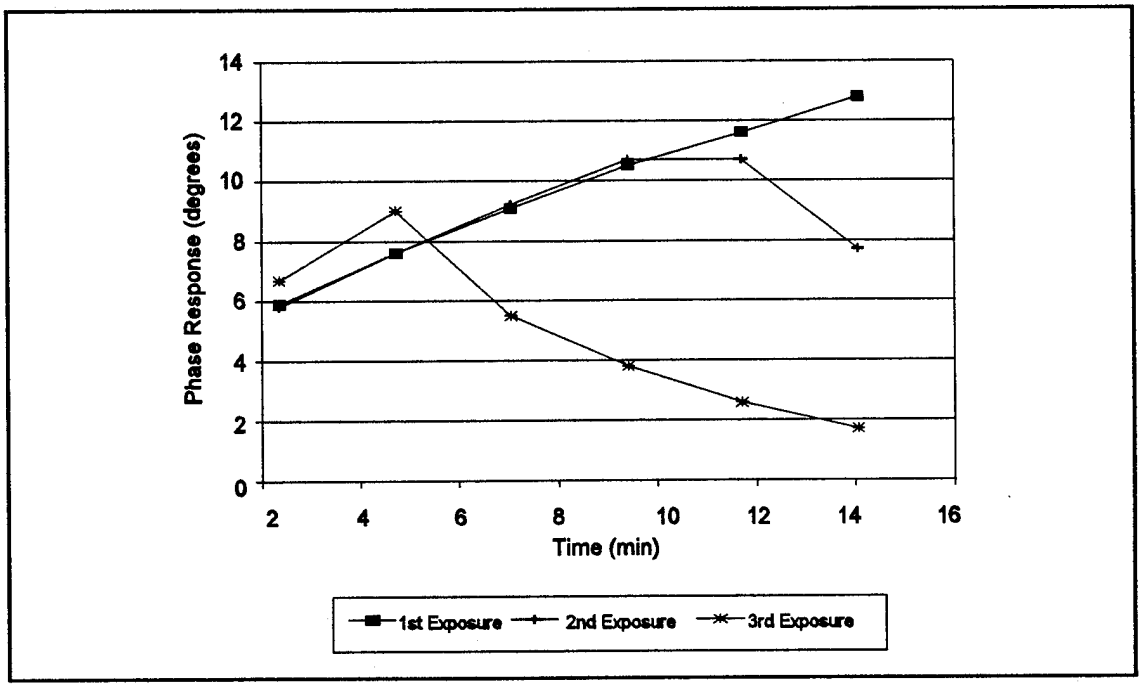


Figure VI-60. Time Dependence of the CuPc-Coated IGEFET Transfer Function Phase Response upon Repeated Exposure to a Binary Gas Mixture Composed of 50 ppm NH_3 and 100 ppb NO_2. (Measured in a Second Experiment One Month Later. Approximate Frequency = 106 Hz. Film Thickness = 0.32 μm. Temperature = 100° C.)

mixtures, variation in the final amplitude of the phase response maxima was accompanied by a significant change in the time dependence of the phase response between repeated exposures. In one experiment, the phase response maxima at 106 Hz increased monotonically with exposure time to repeated exposures with binary mixtures composed of 50 ppm NH_3 and 100 ppb NO_2 (Figure VI-59). The positive phase response at this frequency was indicative of the ammonia present in the mixture. With repeated exposure, the magnitude of the phase response decreased. The decrease in the phase response with repeated exposure is believed to be the result of incomplete desorption of the previous gas mixture. That is, the overnight elevated temperature (170° C) purge between each set of triplicate challenge gas exposures provided a "cleaner" MPc surface compared to the relatively short 3-hour heated purge (170° C) between exposures. Consequently, the first exposure elicits the largest change in the IGEFET electrical characteristics. The decision to use a 3-hour heated purge (170° C) between exposures was based on experiments with the single component gases. Figure VI-61 illustrates the repeatability of the IGEFET phase response to several 400 ppb NO_2 challenges. The poor repeatability is not likely to be caused by the slightly greater complexity of generating the binary mixtures, since the phase response decreased systematically with repeated exposure. Another possibility is that the two gases interact on the surface of the metal-substituted phthalocyanines, and the desorption of the individual gases and their intermediate products are inhibited. As discussed earlier with respect to the normalized DC resistance response, the chemical reaction between NH_3 and NO_2 on p-type semiconductor catalysts has been reported in the literature (204). Although the normalized DC resistance response, which was measured simultaneously with the transfer function response, manifested a similar decrease in the ammonia-like response, its time dependence was non-monotonic (Appendix K). In another experiment conducted a month later with the same IGEFET microsensors and gas mixture concentrations, the phase response during the first exposure was slightly less (-16%) than the phase response when compared to the first exposure in the earlier experiment, and it possessed essentially the same monotonically increasing time response characteristic (Figure VI-60). However, with subsequent exposures, the time response changed dramatically. That is, the phase response early in the exposure (first 5-10 min) in the second trial followed the same phase response as the initial exposure conducted in the first trial. However, as the exposure continued, the phase response, which was initially increasing, indicating the presence of ammonia, reversed and became more NO_2-like. Similar behavior was observed in the MPc-coated IGEFET phase response for several other exposures to the binary gas mixtures containing 100 ppb NO_2 and various ammonia concentrations. This non-monotonic time dependence was also evident in the phase response to binary

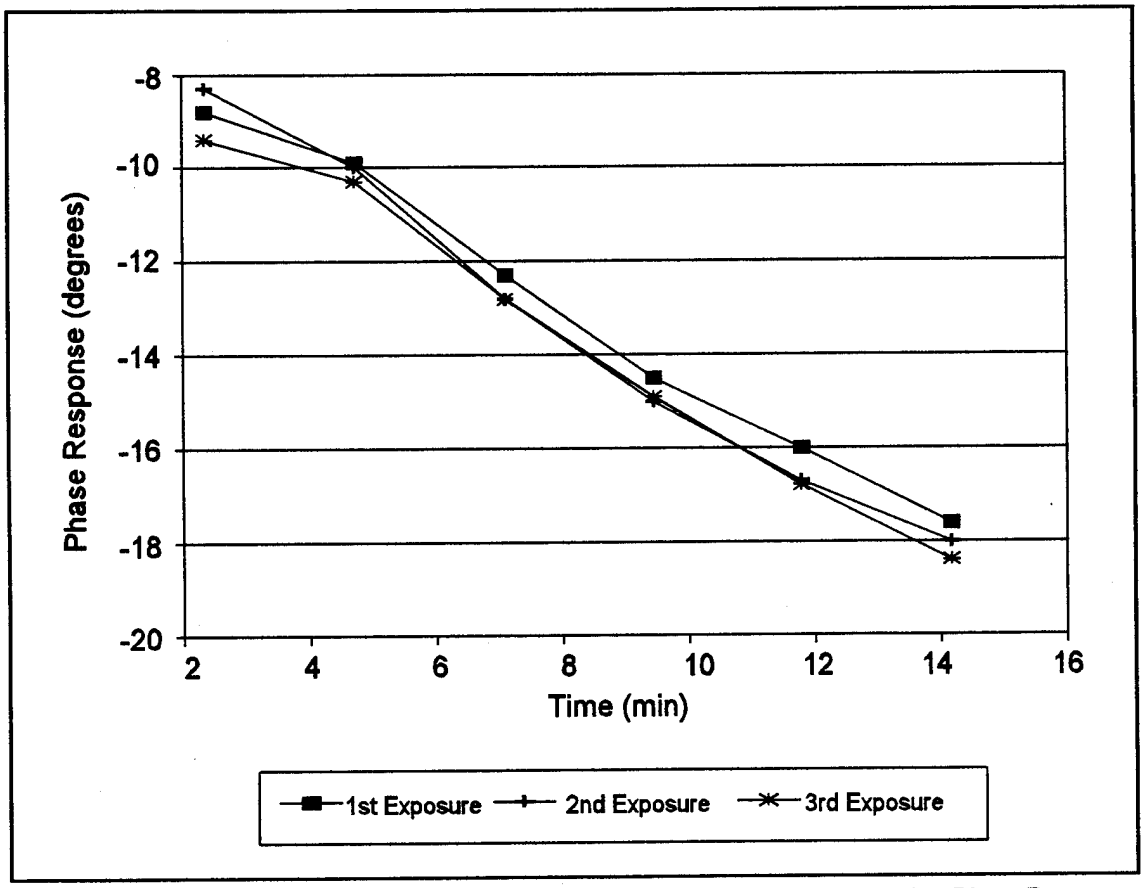


Figure VI-61. Time Dependence of the CuPc-Coated IGEFET Transfer Function Phase Response upon Repeated Exposure to a 400 ppb NO_2 Challenge Concentration. (Approximate Frequency = 200 Hz. Film Thickness = 0.32 μm. Temperature = 100° C.)

gas mixtures containing 425 ppb NO_2 and various ammonia concentrations. Upon exposure to these mixtures, only the first time slice (at 2.4 minutes) displayed an ammonia-like increase in the phase response. The phase response collected in subsequent time slices decreased (a NO_2-like response) monotonically. This non-monotonic time dependence was also observed in the normalized DC resistance response of the MPc-coated IGEFET sensors exposed to all the binary gas mixtures. As discussed earlier with respect to the non-monotonic time dependence of the normalized DC resistance response upon gas exposure, the ammonia component, which is present in much larger concentration compared to the NO_2 component, adsorbs on the MPc surface first. The adsorbed ammonia then exchanges or reacts with NO_2, resulting in the observed decrease in the ammonia response.

To investigate the phase response to binary mixtures containing small NO_2 concentrations in more detail, Bode plots of the phase response data collected at different exposure times were examined. Figures VI-62 through VI-64 illustrate the NiPc-coated IGEFET phase response to repeated exposures with binary mixtures composed of 200 ppm NH_3 and 100 ppb NO_2. For each exposure, the phase response data collected at three different times during each exposure are plotted. The phase response plot at 2.4 minutes represents the first measurement of the IGEFET transfer function after exposure to the challenge gas has been initiated. The second phase response plot represents the peak ammonia response to the challenge gas which occurred at the specific time indicated in the Figures. The third phase response plot represents the microsensor's response at the end of the exposure cycle. The striking feature revealed by these phase response plots is the difference in the time dependence of the phase response maxima located near the 100-200 Hz and 8-12 KHz frequency intervals. While the phase response maxima located near the 100-200 Hz frequency interval decreased significantly from the maximum ammonia-like response, the phase response at the 8-12 KHz frequency interval was constant. Assuming the phase response at these two frequency intervals is associated with surface and intercrystallite adsorption, respectively, these results imply that the surface is more readily accessible for an exchange or reactive process to proceed. Since the NH_3 molecules that have penetrated into the intercrystallite spaces, as illustrated in Figure VI-65, are less accessible to exchange or reaction with NO_2 molecules, the reversal of the phase response associated with the intercrystallite regions is impeded. Furthermore, the NH_3 molecules which desorb are more localized within the intercrystallite spaces and may more readily re-adsorb. Similar behavior was observed with the repeated exposure trials. However, the magnitude of the maximum ammonia-like phase response, and the time at which it was observed, decreased with repeated exposure trials. This difference in the time dependence of the phase response at these two

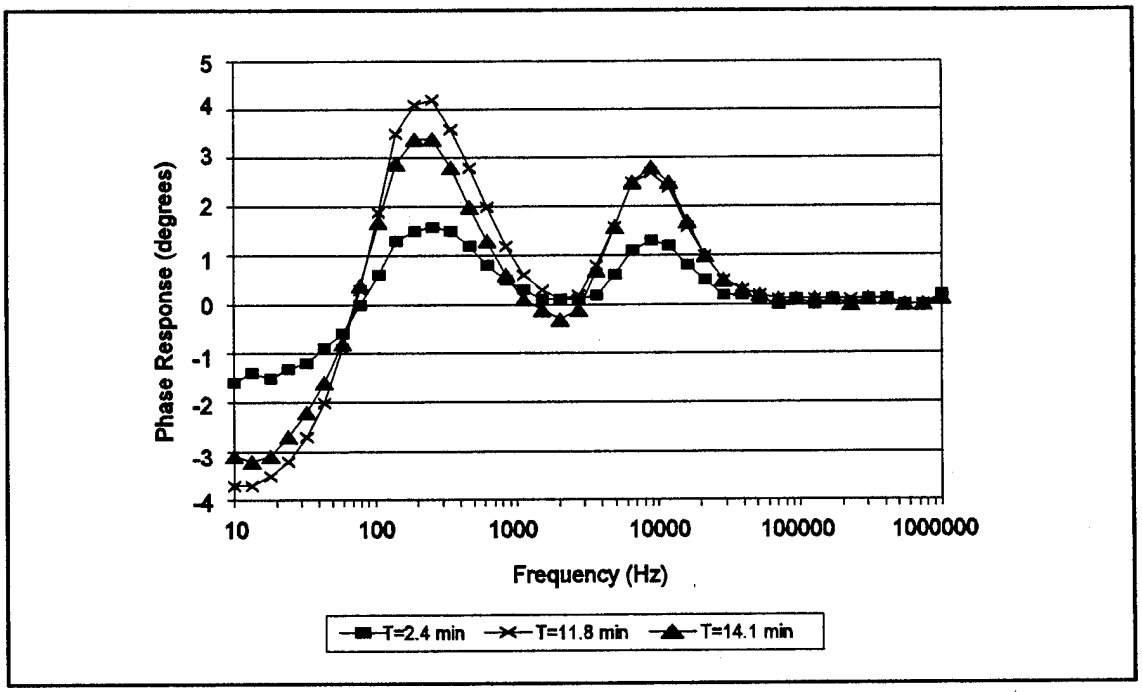


Figure VI-62. Bode Plots of the NiPc-Coated IGEFET Transfer Function Phase Response at Selected Time Intervals During the First Exposure to a Binary Gas Mixture Composed of 200 ppm NH_3 and 100 ppb NO_2. Film Thickness = 0.43 μm. Temperature = 100° C.

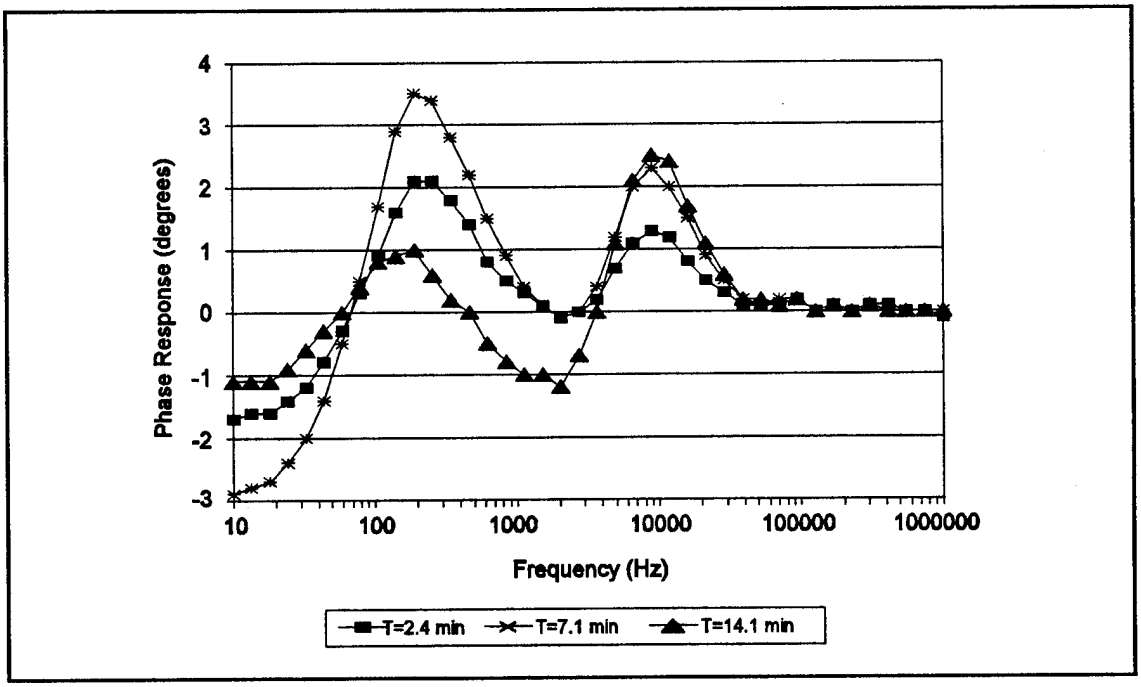


Figure VI-63. Bode Plots of the NiPc-Coated IGEFET Transfer Function Phase Response at Selected Time Intervals During the Second Exposure to a Binary Gas Mixture Composed of 200 ppm NH_3 and 100 ppb NO_2. (Film Thickness = 0.43μm. Temperature = 100° C.)

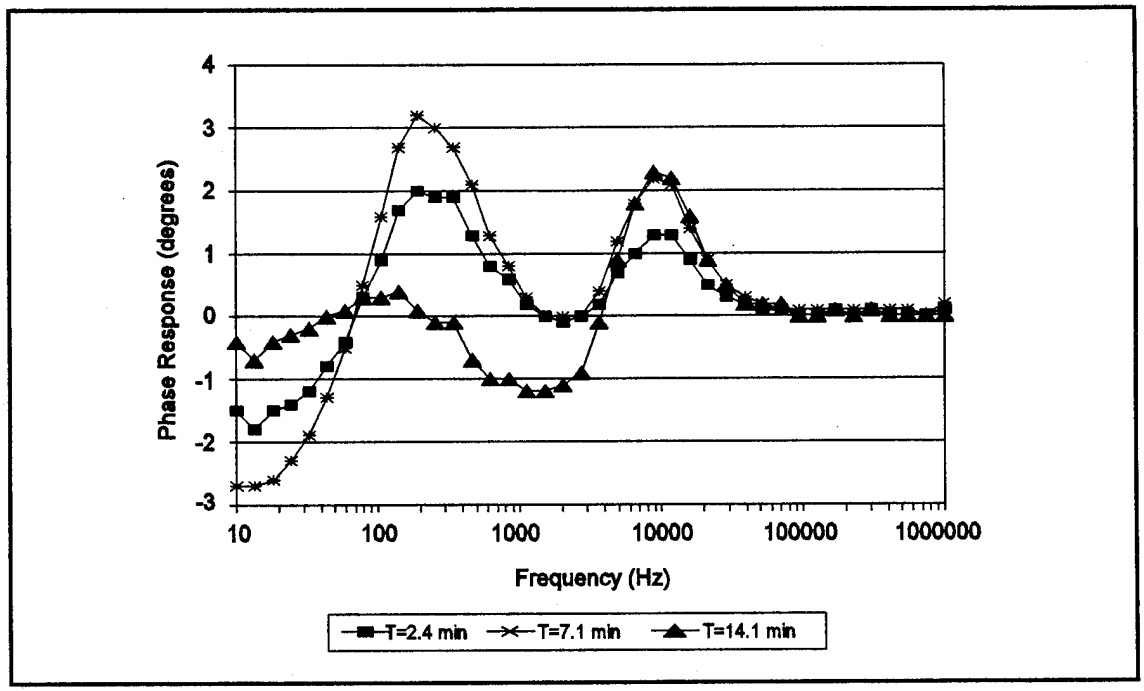


Figure VI-64. Bode Plots of the NiPc-Coated IGEFET Transfer Function Phase Response at Selected Time Intervals During the Third Exposure to a Binary Gas Mixture Composed of 200 ppm NH_3 and 100 ppb NO_2. (Film Thickness = 0.43μm. Temperature = 100°C.)

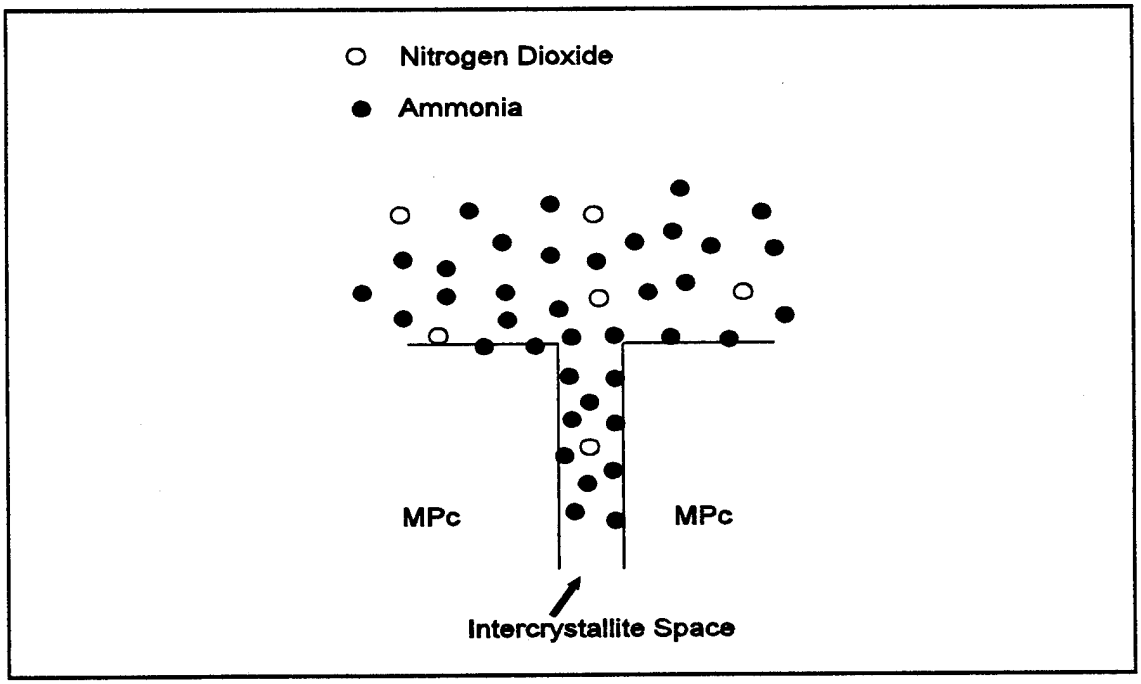


Figure VI-65. Interaction of an NO_2 and NH_3 Binary Gas Mixture with the Surface and Intercrystallite Space of an MPc Film.

frequency intervals provides information which may be useful in the analysis of a microsensor's gas mixture response. As mentioned earlier, the feature vectors for gas analysis were formulated from the phase response maxima measured from the first four time measurements (slices). However, the variability in the phase response upon repeated exposure, particularly the change from monotonic to non-monotonic time dependence, will likely limit the accuracy of the component concentrations determined from the IGEFET transfer function phase response (and gain response) measurements.

To determine the sensitivities of the IGEFET transfer function phase response relative to the challenge gas, the two phase response maxima for each time slice were plotted as a function of the challenge gas concentration. Since the behavior of the four time slices were similar, only the least-squares fitted data for the fourth time slice are presented to illustrate the results. Figures VI-66 and VI-67 reveal that the low- and high-frequency phase response maxima of the CuPc- and NiPc-coated IGEFET elements varied linearly with the logarithm of the NO_2 challenge concentration, and that the sensitivity (as indicated by the slope of the lines) of the CuPc- and NiPc-coated IGEFET elements were essentially the same. In contrast, the square of the phase response maxima varied linearly with the NH_3 concentration, and the sensitivities of the two MPc-coated IGEFET sensors to NH_3 were significantly different (Figures VI-68 and VI-69). The CuPc-coated IGEFET transfer function phase response at the low- and high-frequency maxima was 18.7 times and 4.2 times more sensitive to NH_3 compared to the NiPc-coated IGEFET sensors. The difference in the phase response sensitivity was much greater compared to the difference observed in the normalized DC resistance and gain response sensitivity of the two MPc-coated IGEFET elements.

The phase response to each of the test gases was least-squares fitted to two different functional forms. The NO_2 phase response data was least-squares fitted to the following equation:

$$C = AP^{\alpha} + B \qquad \text{(VI-5)}$$

where A, B, and α are constants, C is the challenge gas concentration in parts-per-billion (ppb), and P is the phase response in degrees. The NH_3 phase response data was least-squares fitted to an equation ($\alpha = 2$) of the form:

$$C = AP^2 + B. \qquad \text{(VI-6)}$$

The fit parameters obtained from the least-squares fit of the NO_2 and NH_3 phase response data to these functional forms are summarized in Appendix L. These particular functional forms were selected from a set of functional forms, including logarithmic and power series (of up to fourth order), that

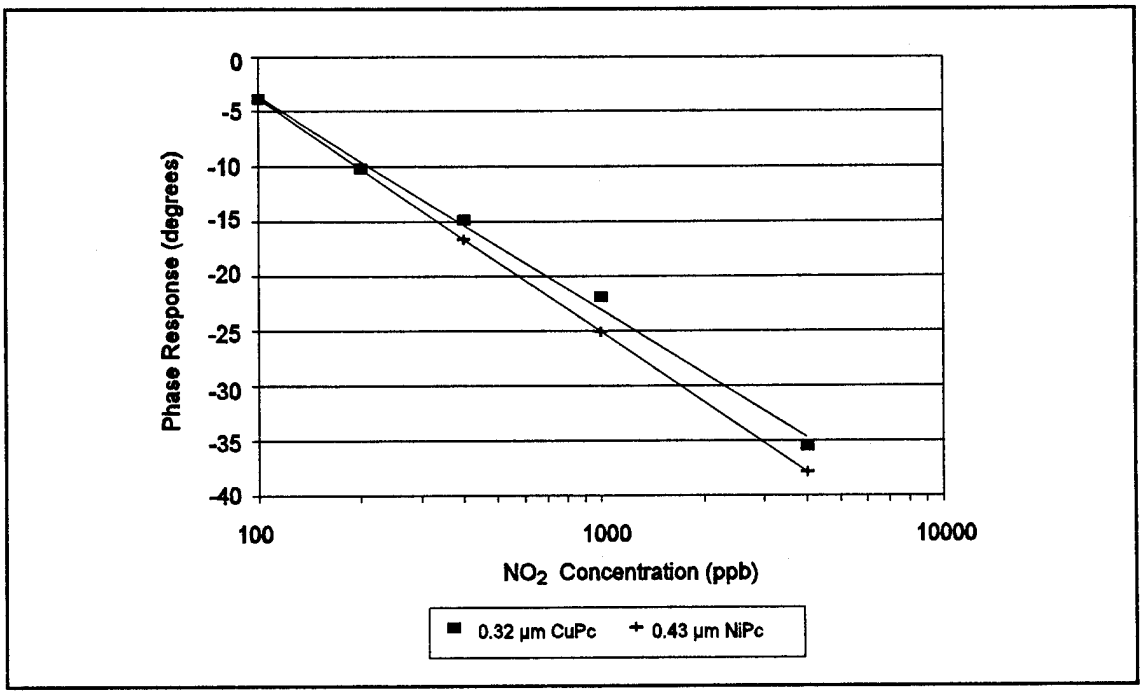


Figure VI-66. Concentration Dependence of the MPc-Coated IGEFET Transfer Function Phase Response to NO_2. (Approximate Frequency Interval = 200-600 Hz. Time Slice = 9.5 min. Temperature = 100° C.)

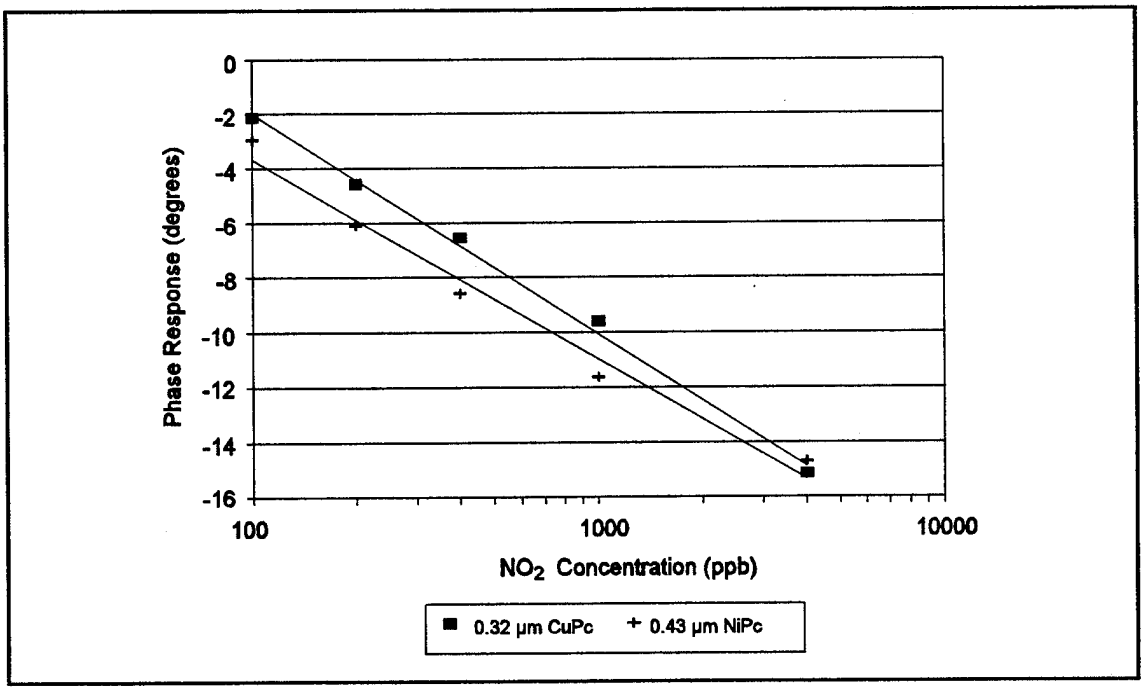


Figure VI-67. Concentration Dependence of the MPc-Coated IGEFET Transfer Function Phase Response to NO_2. (Approximate Frequency Interval = 10-38 KHz. Time Slice = 9.5 min. Temperature = 100° C.)

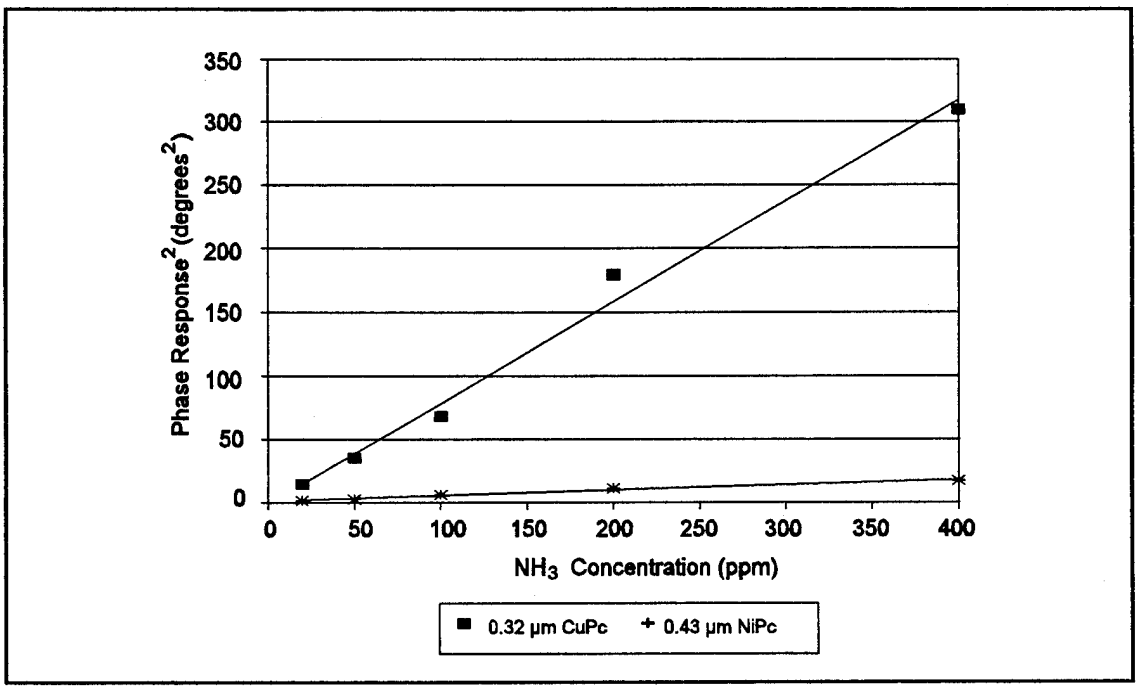


Figure VI-68. Concentration Dependence of the MPc-Coated IGEFET Transfer Function Phase Response upon NH_3. (Approximate Frequency = 106 Hz. Time Slice = 9.5 min. Temperature = 100° C.)

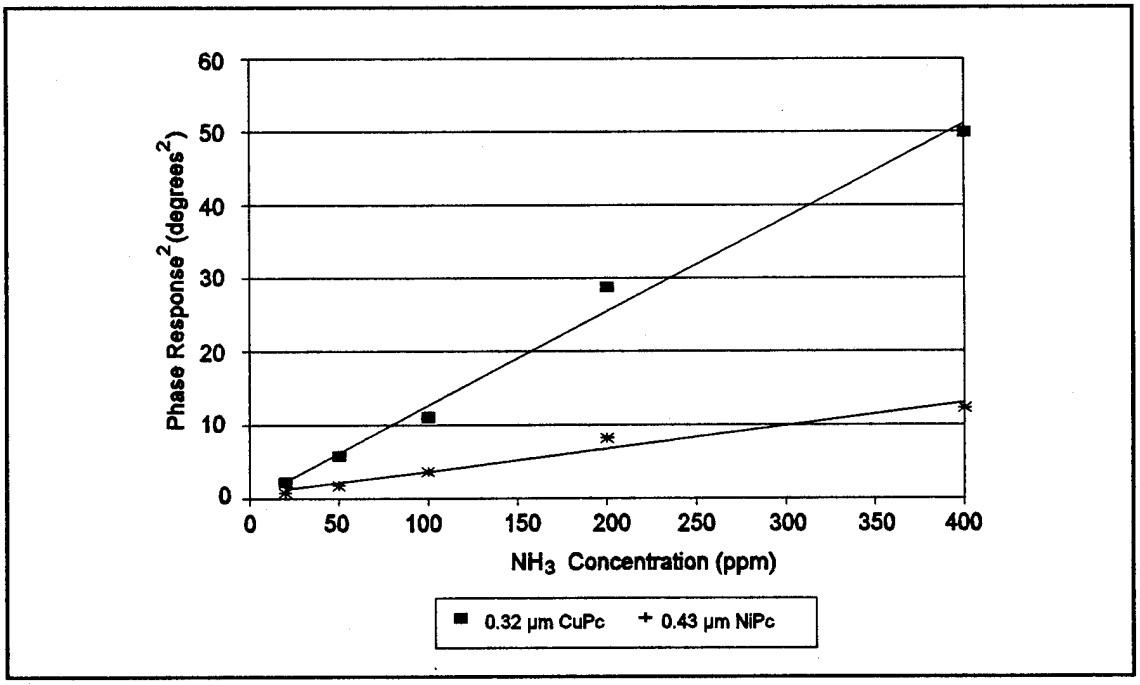


Figure VI-69. Concentration Dependence of the MPc-Coated IGEFET Transfer Function Phase Response upon NH_3. (Approximate Frequency Interval= 5-9 KHz. Time Slice = 9.5 min. Temperature = 100° C.)

were screened for their ability to linearize the phase response data and to minimize the error in the predicted concentrations.

The feature vector for performing the gas analyses with the phase response data was formed in a manner similar to the formulation of the feature vectors employed for the gas analyses accomplished with the normalized DC resistance data. The following procedure, which is illustrated in Figure VI-70, was used to formulate the phase response feature vector. First, the sensor response vectors, representing the phase response of an individual IGEFET sensor element coated with a particular MPc film type relative to a particular challenge gas, were formed. For the single component NO_2 analyses, the phase response maxima were transformed by raising the phase response maxima to the appropriate power (corresponding to the film type and time slice) determined from the least-squares fit to Equation VI-5. For the single component NH_3 analyses, the elements of the sensor response vector were simply the square of the phase response at the low- and high-frequency maxima for the first four time slices. Thus, the sensor response vectors for the single component analyses contained 8 elements (2 frequency maxima × 4 time slices). For the binary gas mixture analysis, the sensor response vectors were composed of 16 elements: 8 elements to represent each of the two component gases. The feature vectors for performing the PCA were then formed by combining the sensor response vectors corresponding to each film type into a single column vector representing the phase response of both the CuPc- and NiPc-coated IGEFET elements to a particular challenge gas mixture. The resulting feature vectors, including the complete calibration sets and limited test sets (one for each challenge gas concentration) for the single component and binary mixture analyses, are provided in Appendix L.

Feature Vector Formation with Conductance Parameters Extracted from the IGEFET Transfer Function Gain/Phase Measurements. A second, and somewhat limited approach to gas analysis with the IGEFET transfer function gain/phase measurements was evaluated to determine if characteristic features based upon the lumped element circuit model of the IGE structure developed in Chapter V could enhance the predictive capability relative to the visually identified features described in the previous two sections. Since the MPc films had greater sensitivity to NO_2 compared to NH_3, the evaluation of this alternative approach for analyzing the data was performed with NO_2 as the challenge gas. The formation of the feature vectors with this approach was more complicated since four non-linear curve fits (the gain and phase of the IGEFET before and after exposure) had to be performed for each challenge gas exposure to obtain the model's equivalent electrical circuit parameters. After extracting the model's equivalent electrical circuit parameters, the gas analysis

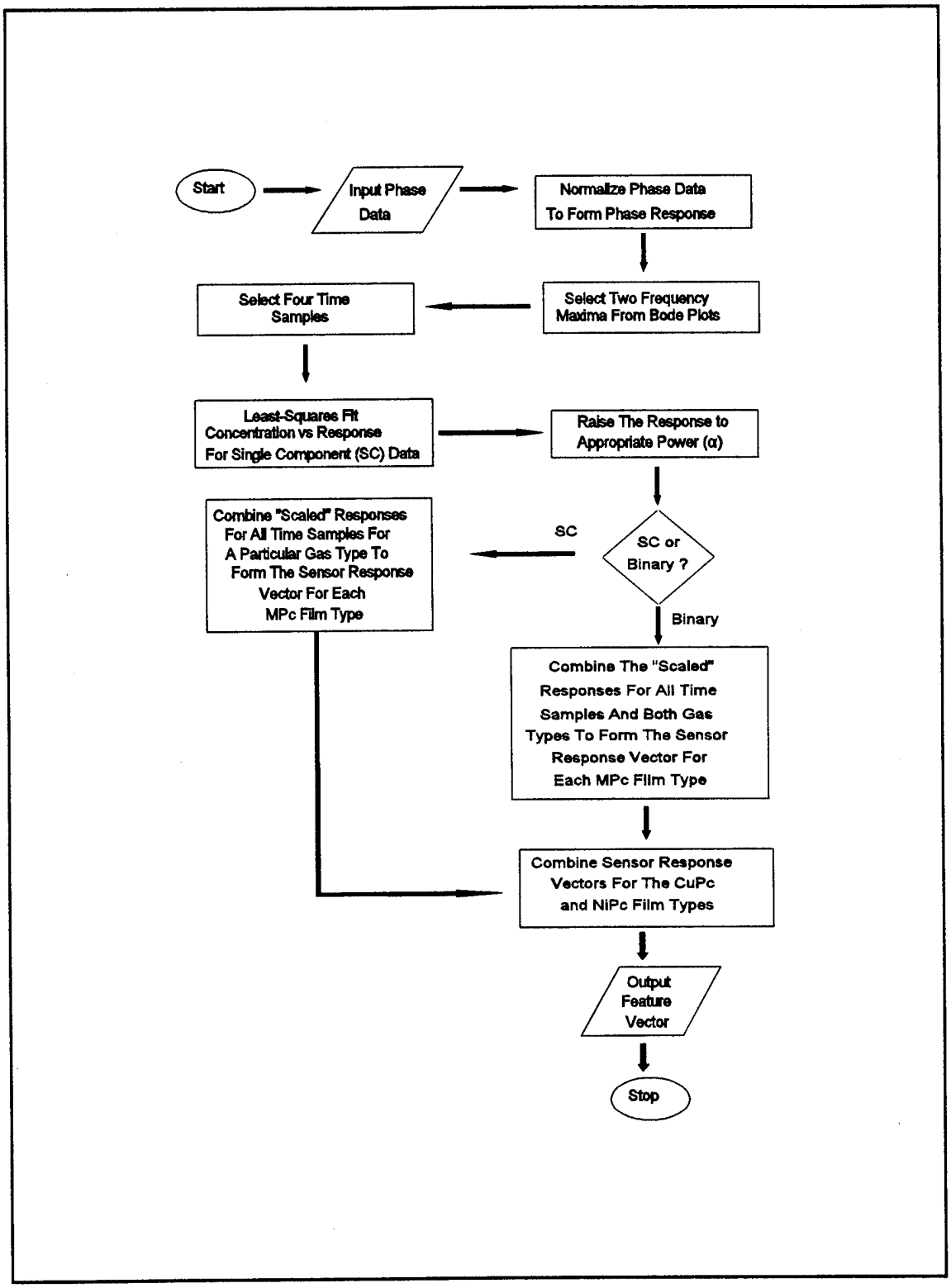


Figure VI-70. Phase Response Feature Vector Formation Process.

process was essentially identical to that described in the previous sections. The process for forming the extracted conductance parameter feature vectors is illustrated in Figure VI-71. In order to compare the results of this approach with the analysis of the DC resistance data, and since the conductivity was expected to possess a much greater sensitivity to the challenge gases compared to the capacitance parameters, the inter-electrode conductance parameters were selected as the characteristic features with which to conduct the gas analysis. The extracted inter-electrode conductance parameters were normalized as discussed earlier. The sensitivity of the normalized conductance parameter features to the challenge gas were then evaluated. The normalized conductance parameters were least-squares fitted to a functional form to provide, with the appropriate transformation of the data, a linear relationship between the normalized conductance parameters and the challenge gas concentration. Sensor response vectors were formed from the transformed normalized conductance parameters for each film type and then combined to form the feature vector used in the gas analysis. The resulting feature vectors, including the complete calibration sets and limited test sets (one for each challenge gas concentration) for the single component and binary mixture analyses, are provided in Appendix L.

As described in Chapter V, the IGE structure circuit model was composed of six elements to represent the inter-electrode (G_1, G_2, C_1, and C_2) and electrode-to-ground (G_{EG} and C_{EG}) conductances and capacitances. Applying circuit analysis to the model, the expressions for the transfer function gain (Equation V-31) and phase (Equation V-34) were developed. A spreadsheet model which implements these equations was developed to curve fit the measured IGEFET transfer function gain and phase data by manually adjusting the parameters to minimize the least-squares error for the two data sets. The validity of the spreadsheet model was confirmed by non-linear curve fitting a select set of test cases using an implementation (205) of the Levenberg-Marquardt algorithm (206) and a MathCad (207) non-linear curve fitting capability. In contrast to the Levenberg-Marquardt algorithm and the MathCad non-linear curve fitting capability, the spreadsheet model incorporated a greater flexibility for applying constraints and simultaneously evaluating the least-squares error for both the gain and phase curve fits.

In order to restrict the number of possible solutions, a number of electrical measurements and known physical properties of the IGE structure were used to limit, and in some cases, fix the values assigned to the parameters. From capacitance measurements of the uncoated IGE structure (Chapter IV), C_{EG} was approximately equal to 22 pF, and the inter-electrode capacitance (the parallel combination of C_1, and C_2) was approximately equal to 0.22 pF. Although not measured, the electrode-to-ground conductance was expected to be very small (less than 10^{-14} mhos) since the

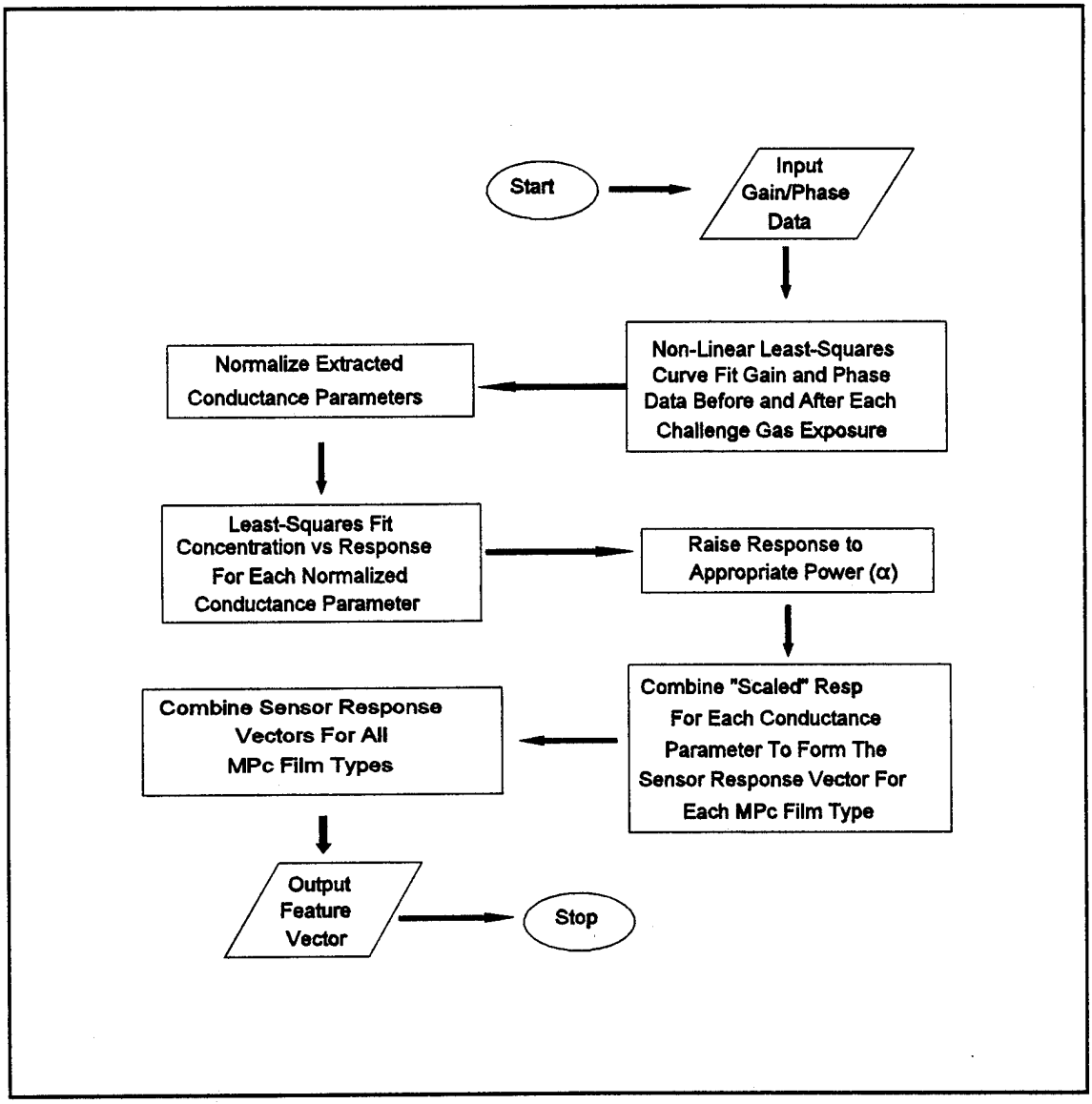


Figure VI-71. Conductance Parameter Feature Vector Formation Process.

electrodes were isolated from ground by a field oxide. Measurements of the inter-electrode resistance of the MPc-coated IGE structures following exposure to NO_2 revealed that the maximum inter-electrode conductance was on the order of 10^{-6} mhos. Several trials investigating the effect of C_{EG} on the solution revealed a similar least-squares error value when C_{EG} was changed over several orders of magnitude. Therefore, it was necessary to fix C_{EG} at a physically reasonable value. Since the value of the uncoated IGE structure C_{EG} was not expected to be significantly modified by the application of the MPc film or gas exposure, the value of C_{EG} was set equal to 22 pF. Given this value of C_{EG}, G_{EG} was found to have no effect on the solution when assigned any value less than 10^{-12} mhos. Since G_{EG} was expected to be small, and independent of the MPc film type and gas exposure, it was assigned the value of 10^{-12} mhos. The values for C_1 and C_2 were determined by performing the non-linear least-squares fit with the other parameters fixed, such that their parallel combination was approximately equal to the uncoated IGE structure's inter-electrode capacitance. For each MPc film type, the minimum least-squares error in the curve fits to the IGEFET transfer function gain and phase, before and after exposure to 4000 ppb NO_2, was determined over a limited range of C_1 and C_2 values which satisfied the parallel combination criteria. Table VI-2 reveals that the least-squares error was near its minimum for the CuPc- and NiPc-coated IGEFET transfer function data when C_1 was equal to 0.5 pF, and C_2 was equal to 0.38 pF. In contrast, the CoPc-coated IGEFET transfer function data required C_1 to be equal to 0.82 pF and C_2 to be equal to 0.31 pF. The capability to fit the data for all three MPc film types with values for C_1 and C_2 that satisfy the parallel combination criteria indicates that the high-frequency behavior of the MPc-coated IGEFET is primarily determined by its uncoated structure. The above approach for assigning values to C_1 and C_2 was compared to the solutions obtained with the Levenberg-Marquardt algorithm and the MathCad non-linear curve fitting capability. Figures VI-72 through VI-77 compare the curve fits to the MPc-coated IGEFET transfer function gain and phase after a 4000 ppb NO_2 exposure that was obtained with the spreadsheet model (C_1 and C_2 fixed to the specific values discussed above) and the Levenberg-Marquardt algorithm (C_1 and C_2 adjustable). Figures VI-78 and VI-79 compare the spreadsheet model and the MathCad curve fits to the transfer function gain and phase of a CuPc-coated IGEFET prior to a challenge gas exposure. These Figures reveal that the three methods produce essentially equivalent results. Table VI-3 reveals that the Levenberg-Marquardt algorithm solution was relatively independent of the initial guess assigned to the parameters. Furthermore, the values of C_1 and C_2 obtained with the Levenberg-Marquardt algorithm prior to exposure changed less than 30 percent upon exposure to 4000 ppb NO_2. In contrast, the values of G_1 and G_2 changed by

Table VI-2. Minimum Least-Squares Error Resulting from Fitting the MPc-Coated IGEFET Transfer Function Gain and Phase Data with the Spreadsheet Model using Fixed Values for the Inter-Electrode Capacitances (C_1 and C_2). (Challenge Gas Concentration = 4000 ppb NO_2. Temperature = 100° C.)

		C_1 (pF)	0.45	0.50	0.60	0.82	1.00
		C_2 (pF)	0.41	0.38	0.35	0.31	0.28
Film Type	Exposure Condition	Least-Squares Error					
CuPc	Before	Gain (dB)	0.31	0.45	0.33	0.60	0.98
		Phase (degrees)	12.2	14.5	13.4	22.4	31.3
	After	Gain (dB)	0.47	0.34	0.72	1.30	2.05
		Phase (degrees)	6.75	7.32	17.2	32.9	47.2
NiPc	Before	Gain (dB)	0.77	0.66	0.67	0.72	0.89
		Phase (degrees)	25.8	23.8	21.8	24.8	30.6
	After	Gain (dB)	0.50	0.40	0.40	0.59	1.01
		Phase (degrees)	17.8	16.9	15.3	22.5	32.6
CoPc	Before	Gain (dB)	2.61	1.40	0.58	0.06	0.37
		Phase (degrees)	25.8	16.8	7.22	1.57	1.86
	After	Gain (dB)	2.81	1.37	0.47	0.35	1.10
		Phase (degrees)	35.0	23.6	13.4	4.42	3.69
C_{EG} = 22 pF, G_{EG} = 10^{-12} mhos							

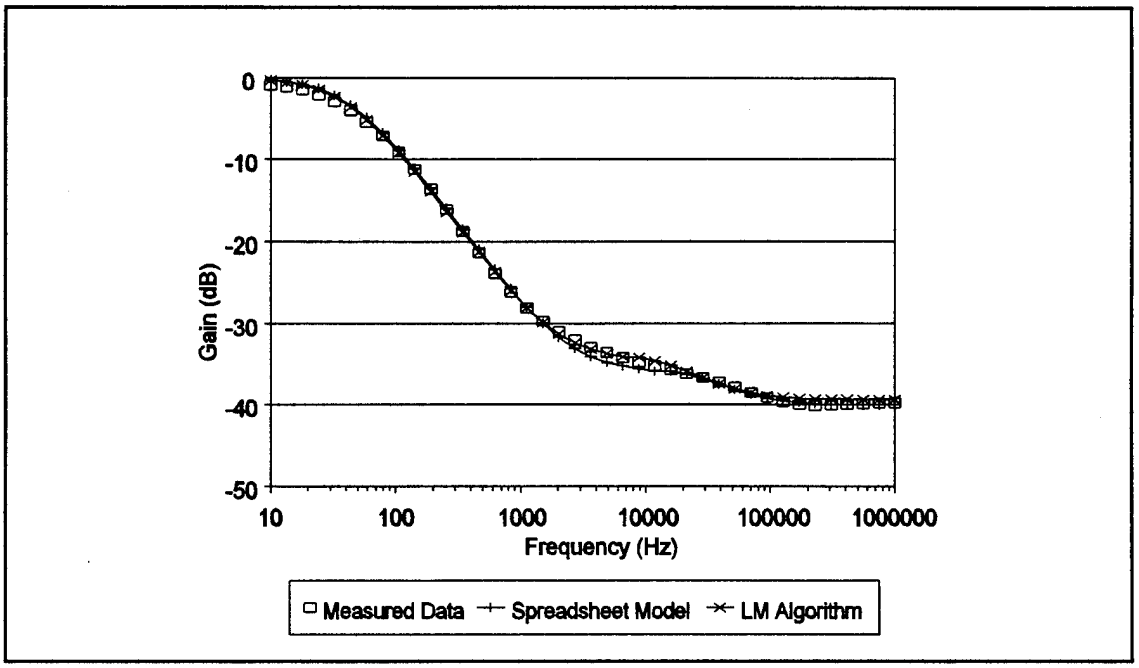


Figure VI-72. Comparison of the Spreadsheet Model and the Levenberg-Marquardt (LM) Non-Linear Least-Squares Curve Fit Methods for a Bode Plot of the CuPc-Coated IGEFET Transfer Function Gain After a 4000 ppb NO_2 Exposure. (Temperature = 100° C.)

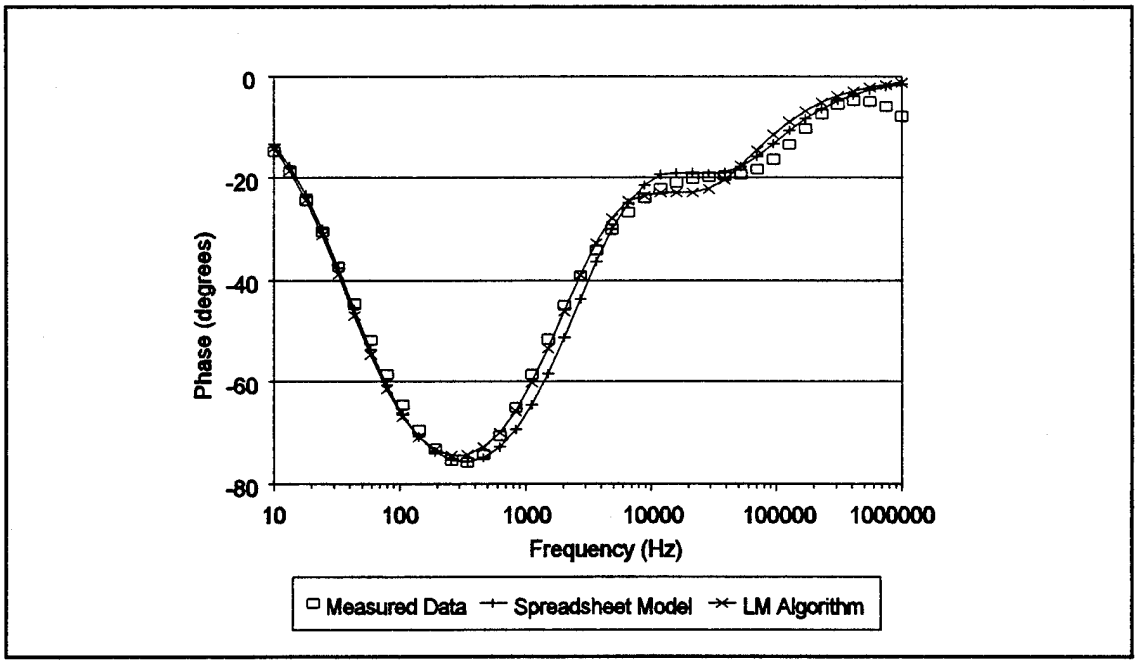


Figure VI-73. Comparison of the Spreadsheet Model and the Levenberg-Marquardt (LM) Non-Linear Least-Squares Curve Fit Methods for a Bode Plot of the CuPc-Coated IGEFET Transfer Function Phase After a 4000 ppb NO_2 Exposure. (Temperature = 100° C.)

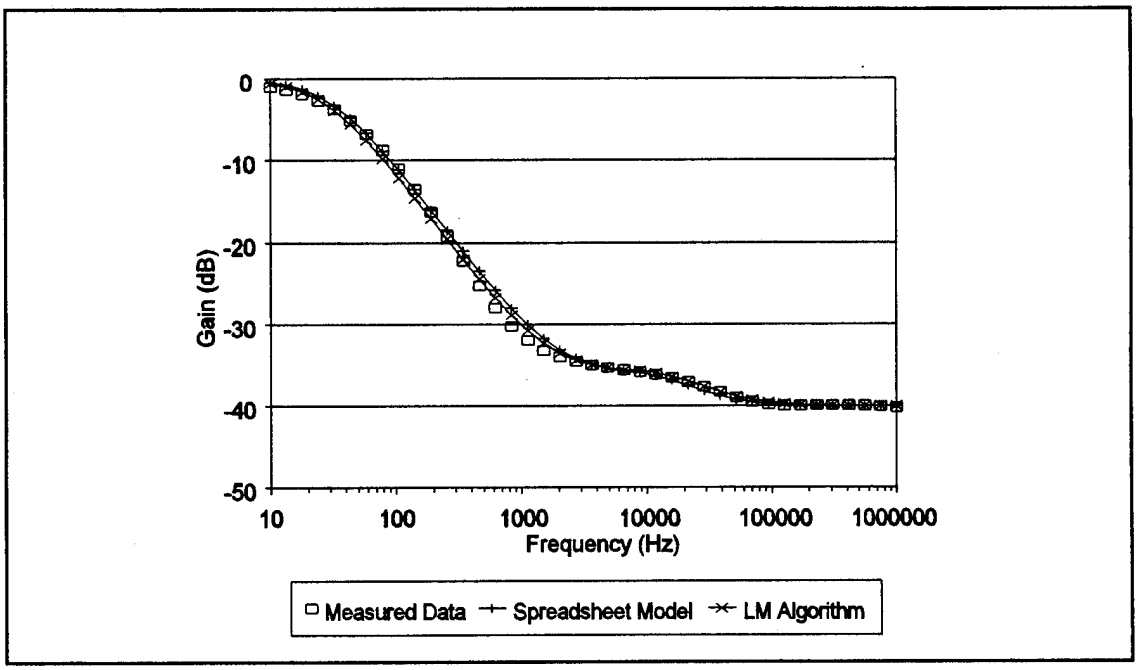


Figure VI-74. Comparison of the Spreadsheet Model and the Levenberg-Marquardt (LM) Non-Linear Least-Squares Curve Fit Methods for a Bode Plot of the NiPc-Coated IGEFET Transfer Function Gain After a 4000 ppb NO_2 Exposure. (Temperature = 100° C.)

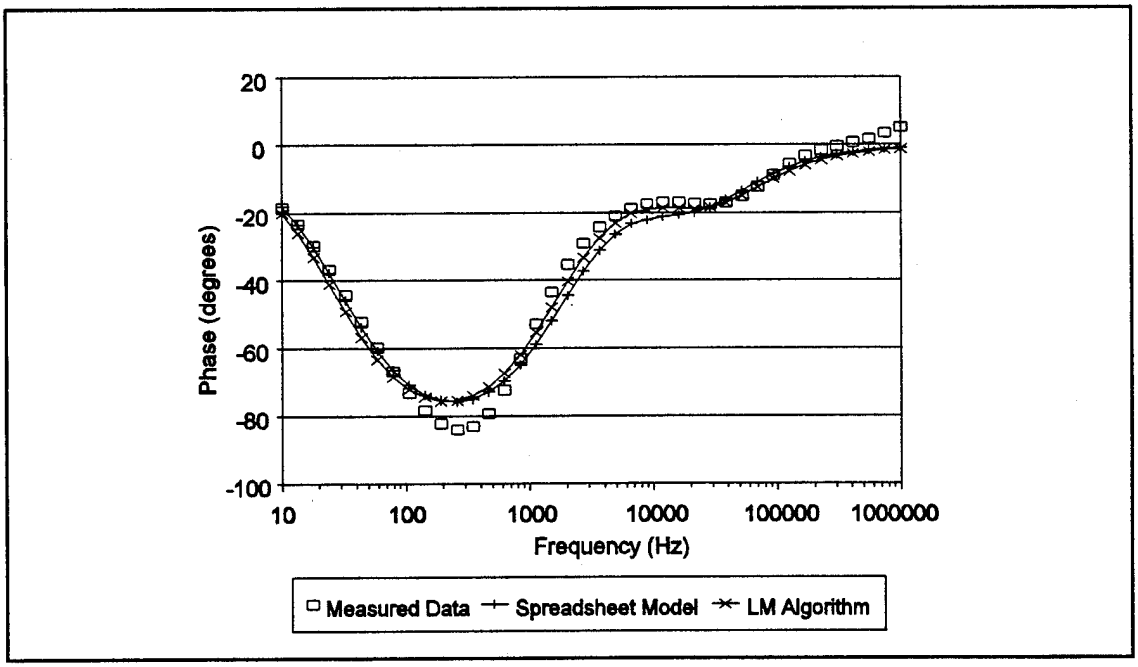


Figure VI-75. Comparison of the Spreadsheet Model and the Levenberg-Marquardt (LM) Non-Linear Least-Squares Curve Fit Methods for a Bode Plot of the NiPc-Coated IGEFET Transfer Function Phase After a 4000 ppb NO_2 Exposure. (Temperature = 100° C.)

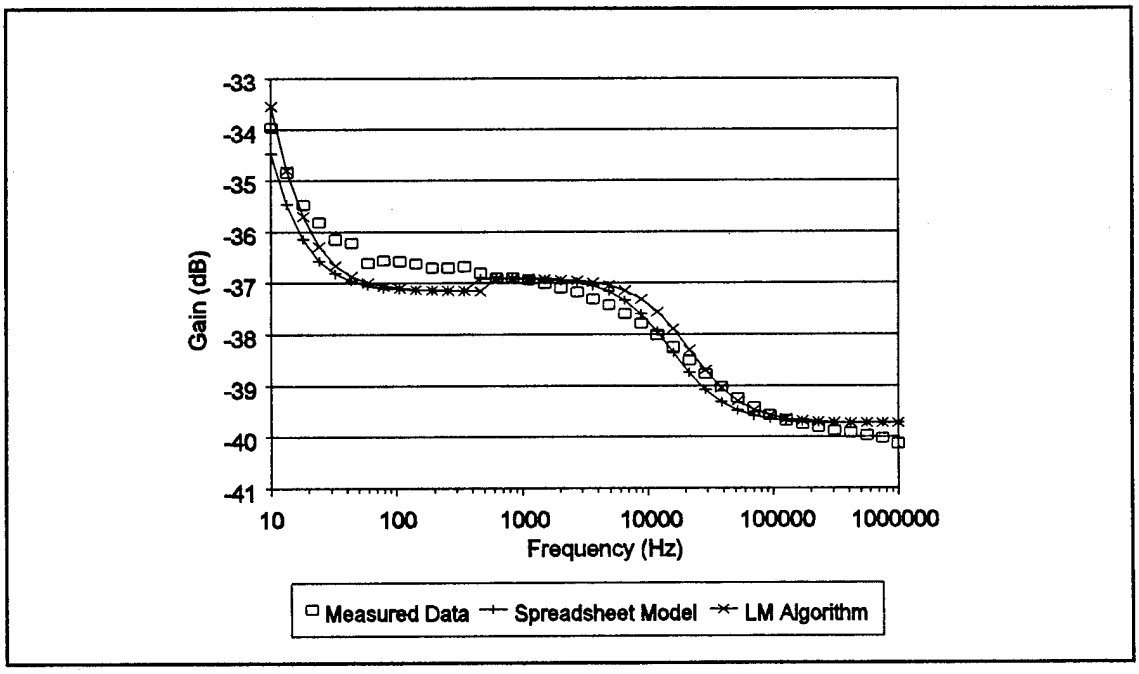


Figure VI-76. Comparison of the Spreadsheet Model and the Levenberg-Marquardt (LM) Non-Linear Least-Squares Curve Fit Methods for a Bode Plot of the CoPc-Coated IGEFET Transfer Function Gain After a 4000 ppb NO_2 Exposure. (Temperature = 100°C.)

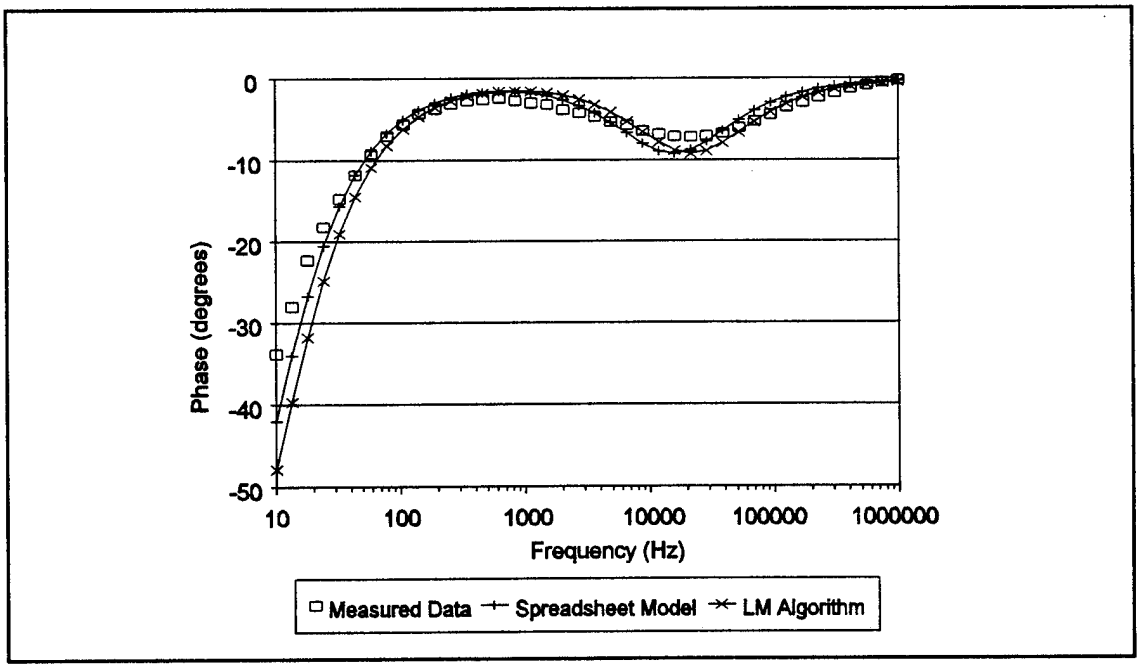


Figure VI-77. Comparison of the Spreadsheet Model and the Levenberg-Marquardt (LM) Non-Linear Least-Squares Curve Fit Methods for a Bode Plot of the CoPc-Coated IGEFET Transfer Function Phase After a 4000 ppb NO_2 Exposure. (Temperature = 100°C.)

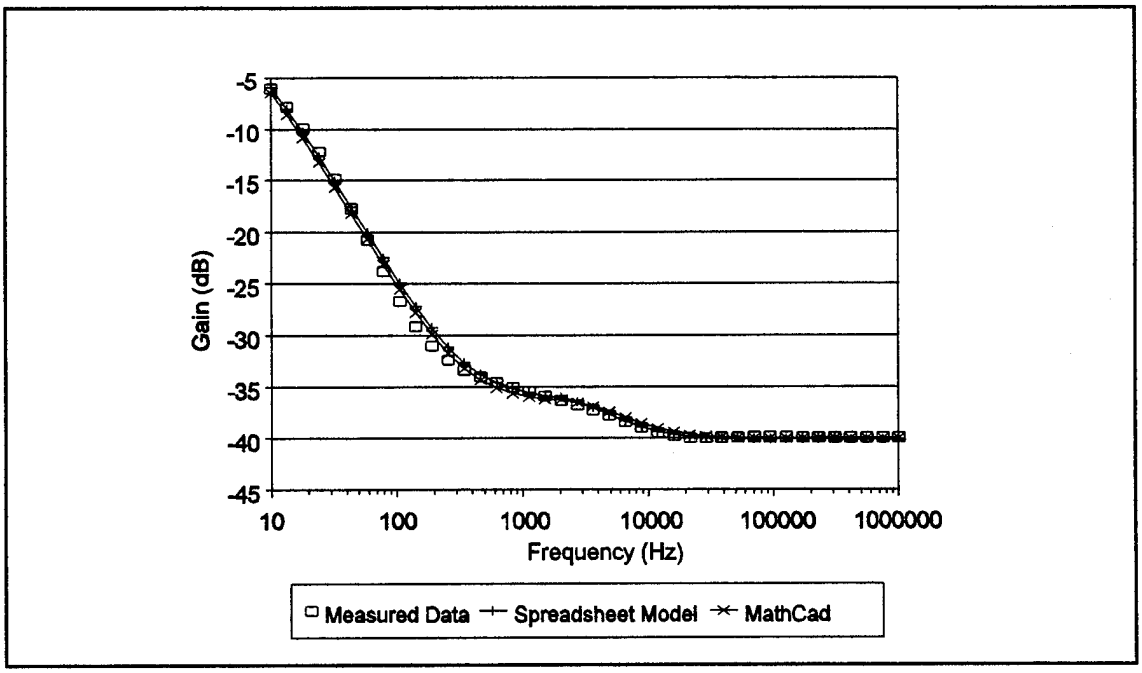


Figure VI-78. Comparison of the Spreadsheet Model and the MathCad Non-Linear Least-Squares Curve Fit Method for a Bode Plot of the CuPc-Coated IGEFET Transfer Function Gain Prior to Exposure. (Temperature = 100°C.)

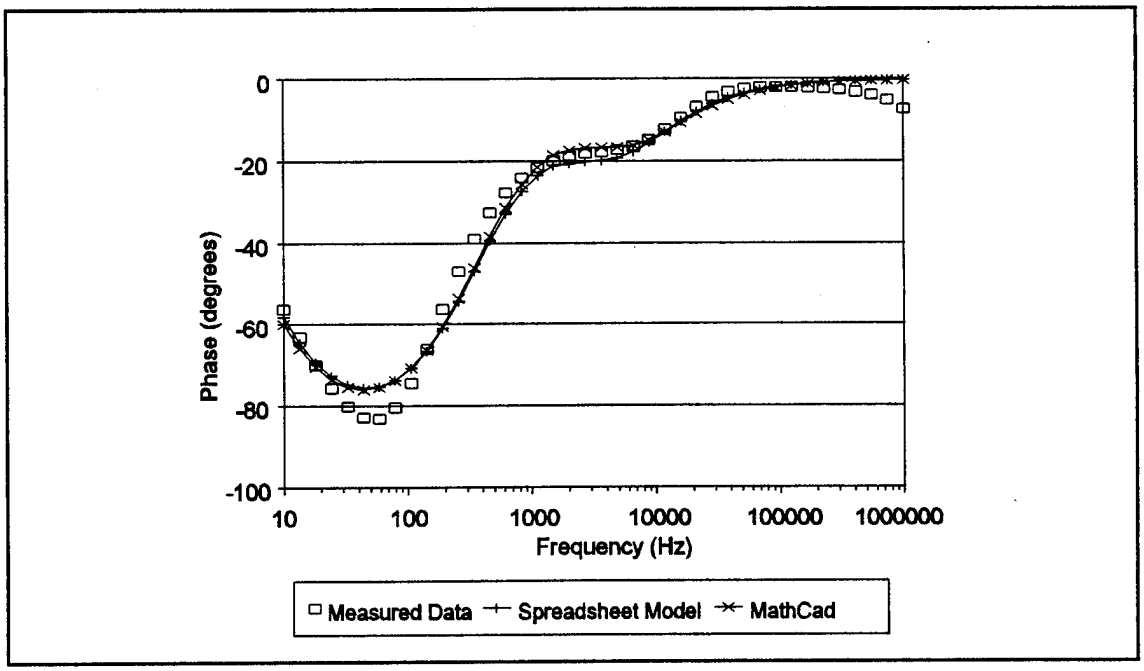


Figure VI-79. Comparison of the Spreadsheet Model and the MathCad Non-Linear Least-Squares Curve Fit Method for a Bode Plot of the CuPc-Coated IGEFET Transfer Function Phase Prior to Exposure. (Temperature = 100°C.)

Table VI-3. Dependence of the Levenberg-Marquardt Non-Linear Least-Squares Curve Fit Upon the Initial Guess for the Fit Parameters. (Data Fitted was the CuPc-Coated IGEFET Transfer Function Gain Measured Prior to Challenge Gas Exposure at 100° C.)

Fit Parameters	Trials				
Guess	1	2	3	4	5
G_1 (10^{-8} mhos)	2.7	27	260	27	2.8
G_2 (10^{-11} mhos)	78	7.8	7.8	78000	8
C_1 (pF)	0.57	0.057	5.7	0.057	0.5
C_2 (pF)	0.36	0.036	3.6	0.036	0.38
Solution					
G_1 (10^{-8} mhos)	2.70	3.39	0.729	2.77	3.13
G_2 (10^{-10} mhos)	7.80	7.82	8.80	7.74	7.82
C_1 (pF)	0.570	0.600	0.544	0.583	0.580
C_2 (pF)	0.360	0.349	0.277	0.359	0.354
χ^2 (10^{19})	3.00	3.26	15.8	3.03	3.15
C_{EG} = 22 pF, G_{EG} = 10^{-12} mhos					

nearly an order of magnitude. Therefore, the values of C_1 and C_2 were set equal to the values determined using the spreadsheet model. The spreadsheet model was then used to curve fit G_1 and G_2 to simultaneously minimize the least-squares error for both the gain and phase data. Figures VI-80 through VI-85 depict the curve fits to the IGEFET transfer function gain and phase measurements, before and after exposure to 4000 ppb NO_2. The corresponding gain and phase response curves are plotted in Figures VI-86 through VI-91. The gain and phase response plots have two advantages for examining the curve fits. First, the gain and phase response curves are plotted on expanded scales and better show the differences between the measured data and the curve fit. In addition, effects not included in the model which are independent of gas exposure (for example, amplifier cutoff at high frequency) are compensated for (subtracted out) in the formation of the gain and phase response. Tables VI-4 summarizes the parameters used to curve fit each exposure in the complete data set. The two conductance parameters, G_1 and G_2, were normalized and subsequently used to form the feature vectors for gas analysis.

The sensitivity of the MPc-coated IGEFET conductance response features to the NO_2 challenge gas was determined from the plots of the conductance response as a function of the challenge gas concentration. Similar to the DC resistance plots, the logarithm of the normalized conductance parameters were plotted versus the logarithm of the NO_2 concentration (Figures VI-92 and VI-93). Consistent with the earlier DC resistance plots, the log-log plots of the normalized conductance parameters as a function of the NO_2 concentration were linear for the IGEFETs coated with each of the three MPc film types. As indicated by the slope of these curves, the relative sensitivity of both normalized conductance parameters upon NO_2 exposure was similar for all three MPc film types. Although the CoPc curves had the steepest slopes, the error in the slope estimates indicates that the sensitivity of the conductance parameters to NO_2 was independent of the MPc film type. The small difference in sensitivity between the MPc film types was consistent with the normalized DC resistance data.

Since the response of the normalized conductance parameters to NO_2 were similar to the NO_2 response observed with the normalized DC resistance data, the relationship between the challenge gas concentration (C) and the average normalized conductance parameters (G_N) for each MPc film type was least-squares fitted to an equation of the form:

$$C = AG_N^{\alpha} + B \qquad \text{(VI-7)}$$

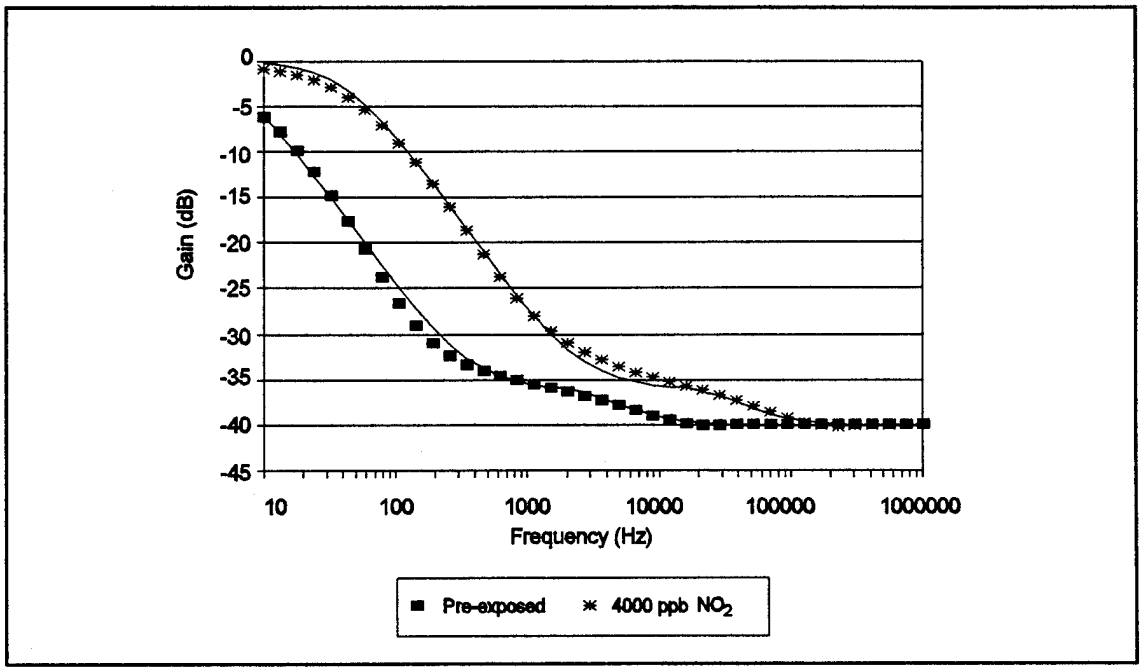


Figure VI-80. Bode Plots of the CuPc-Coated IGEFET Transfer Function Gain Before and After a 4000 ppb NO_2 Exposure. The Solid Lines Represent the Spreadsheet Model Curve Fits to Equation (V-31). (Temperature = 100° C.)

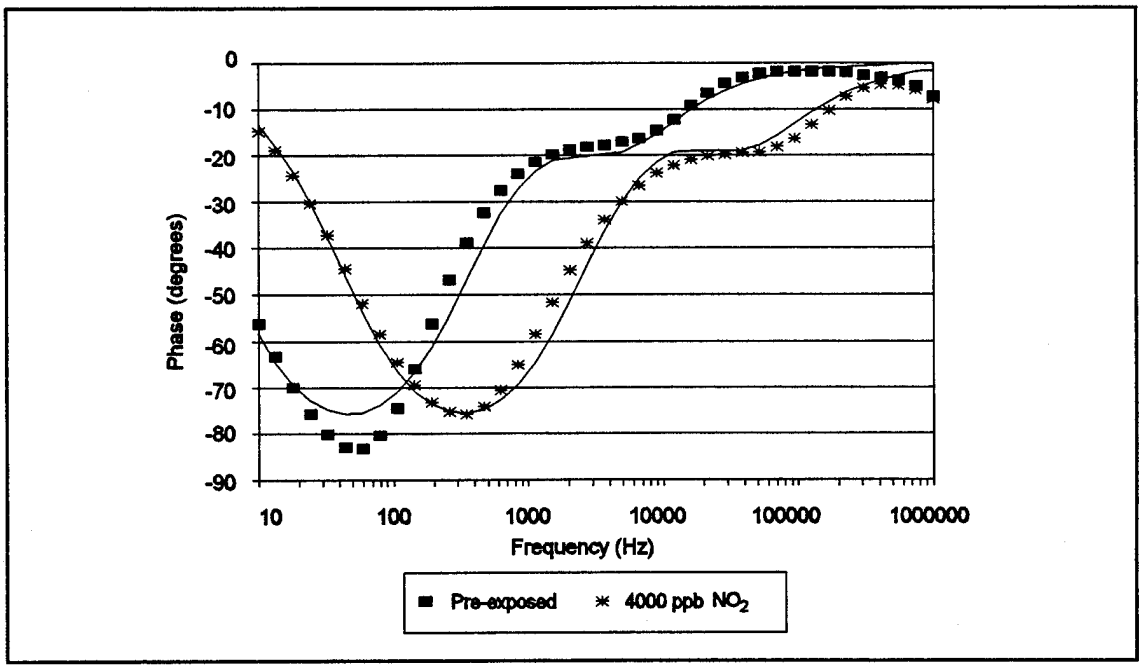


Figure VI-81. Bode Plots of the CuPc-Coated IGEFET Transfer Function Phase Before and After a 4000 ppb NO_2 Exposure. The Solid Lines Represent the Spreadsheet Model Curve Fits to Equation (V-34). (Temperature = 100° C.)

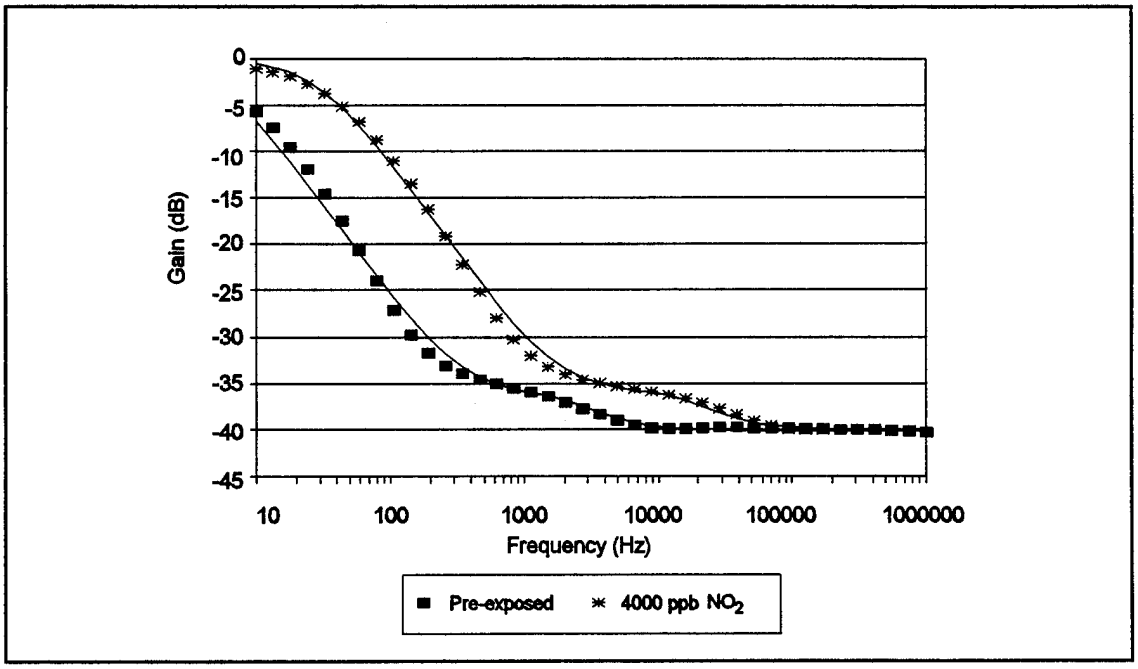


Figure VI-82. Bode Plots of the NiPc-Coated IGEFET Transfer Function Gain Before and After a 4000 ppb NO_2 Exposure. The Solid Lines Represent the Spreadsheet Model Curve Fits to Equation (V-31). (Temperature = 100°C.)

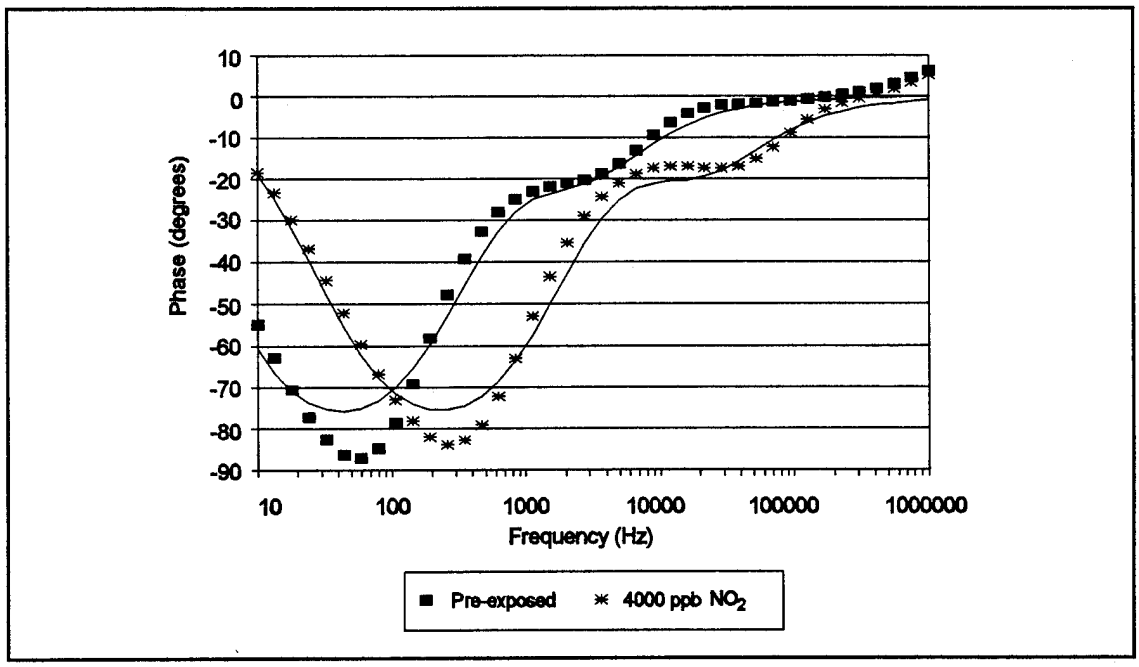


Figure VI-83. Bode Plots of the NiPc-Coated IGEFET Transfer Function Phase Before and After a 4000 ppb NO_2 Exposure. The Solid Lines Represent the Spreadsheet Model Curve Fits to Equation (V-34). (Temperature = 100°C.)

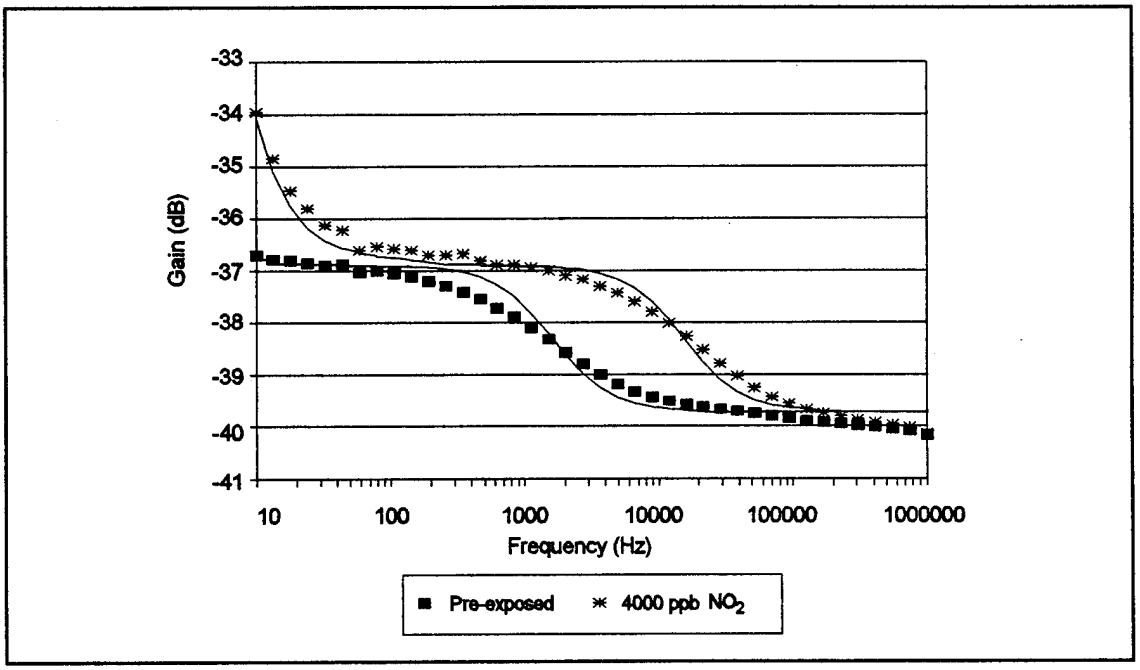


Figure VI-84. Bode Plots of the CoPc-Coated IGEFET Transfer Function Gain Before and After a 4000 ppb NO_2 Exposure. The Solid Lines Represent the Spreadsheet Model Curve Fits to Equation (V-31). (Temperature = 100° C.)

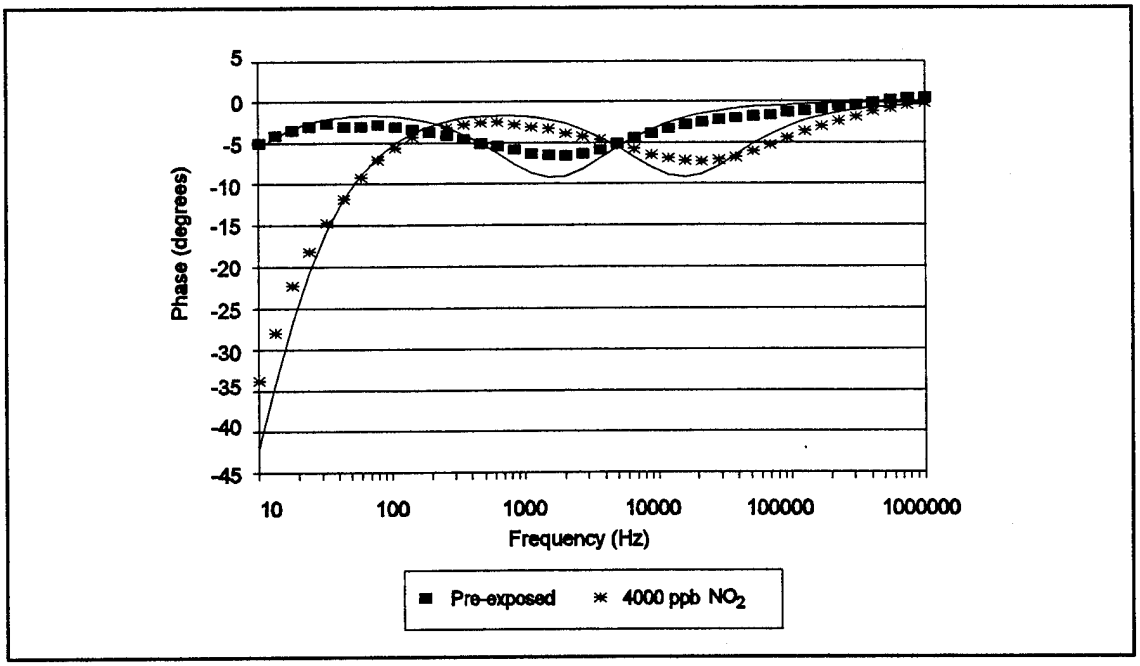


Figure VI-85. Bode Plots of the CoPc-Coated IGEFET Transfer Function Phase Before and After a 4000 ppb NO_2 Exposure. The Solid Lines Represent the Spreadsheet Model Curve Fits to Equation (V-34). (Temperature = 100° C.)

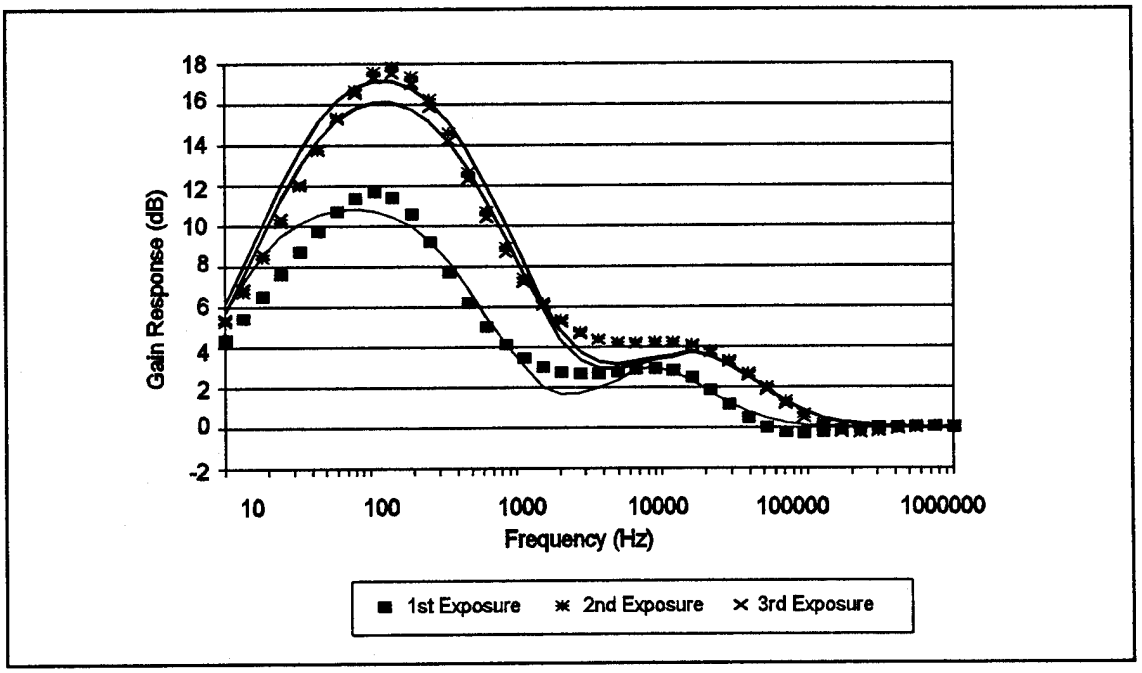


Figure VI-86. Bode Plots of the CuPc-Coated IGEFET Transfer Function Gain Response to Repeated 4000 ppb NO_2 Exposures. The Solid Lines Represent the Gain Response Derived from the Spreadsheet Model Curve Fits of the Pre-Exposed and Exposed CuPc-Coated IGEFET Transfer Function Gain Data to Equation (V-31). (Temperature = 100°C.)

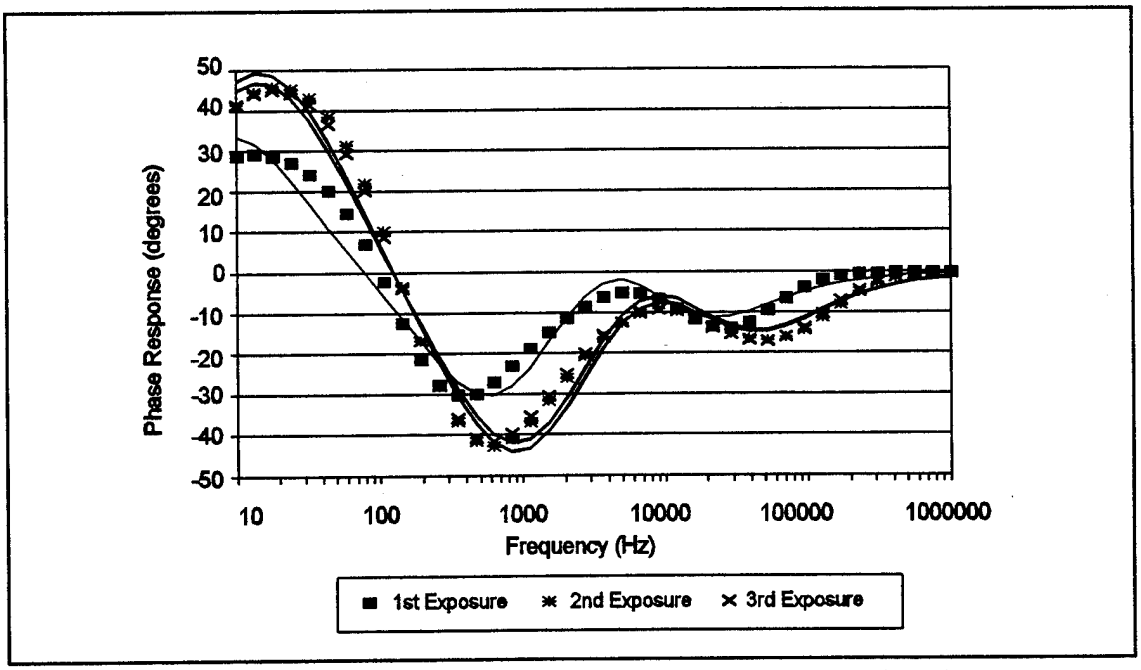


Figure VI-87. Bode Plots of the CuPc-Coated IGEFET Transfer Function Phase Response to Repeated 4000 ppb NO_2 Exposures. The Solid Lines Represent the Phase Response Derived from the Spreadsheet Model Curve Fits of the Pre-Exposed and Exposed CuPc-Coated IGEFET Transfer Function Gain Data to Equation (V-34). (Temperature = 100°C.)

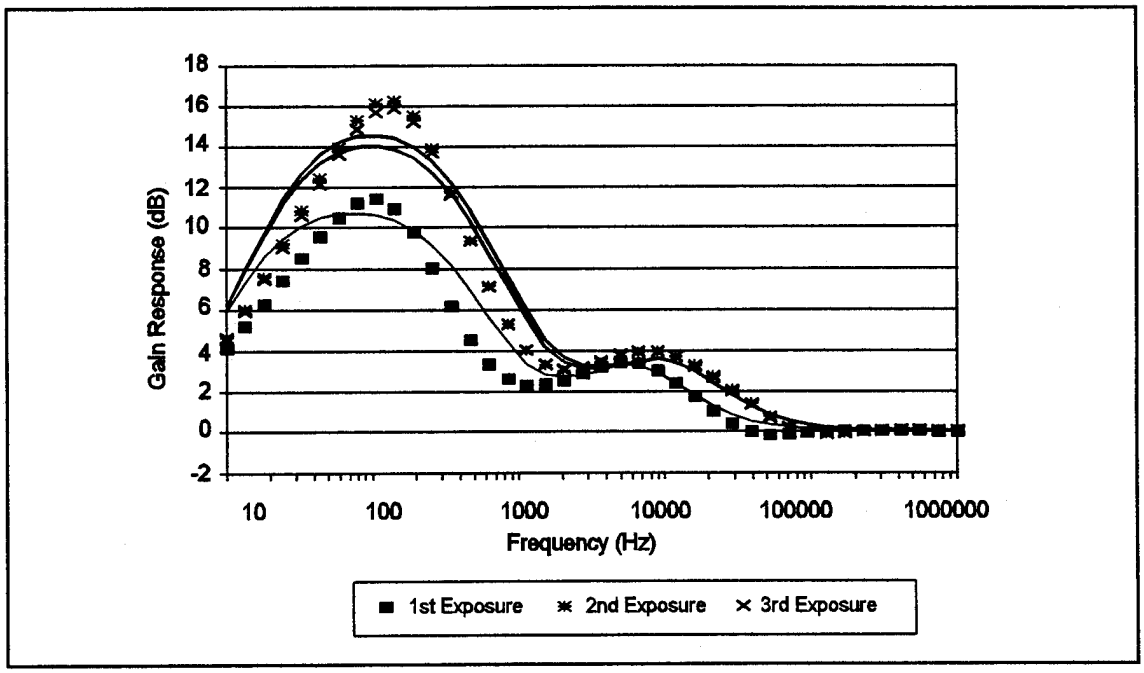


Figure VI-88. Bode Plots of the NiPc-Coated IGEFET Transfer Function Gain Response to Repeated 4000 ppb NO_2 Exposures. The Solid Lines Represent the Gain Response Derived from the Spreadsheet Model Curve Fits of the Pre-Exposed and Exposed NiPc-Coated IGEFET Transfer Function Gain Data to Equation (V-31). (Temperature = 100° C.)

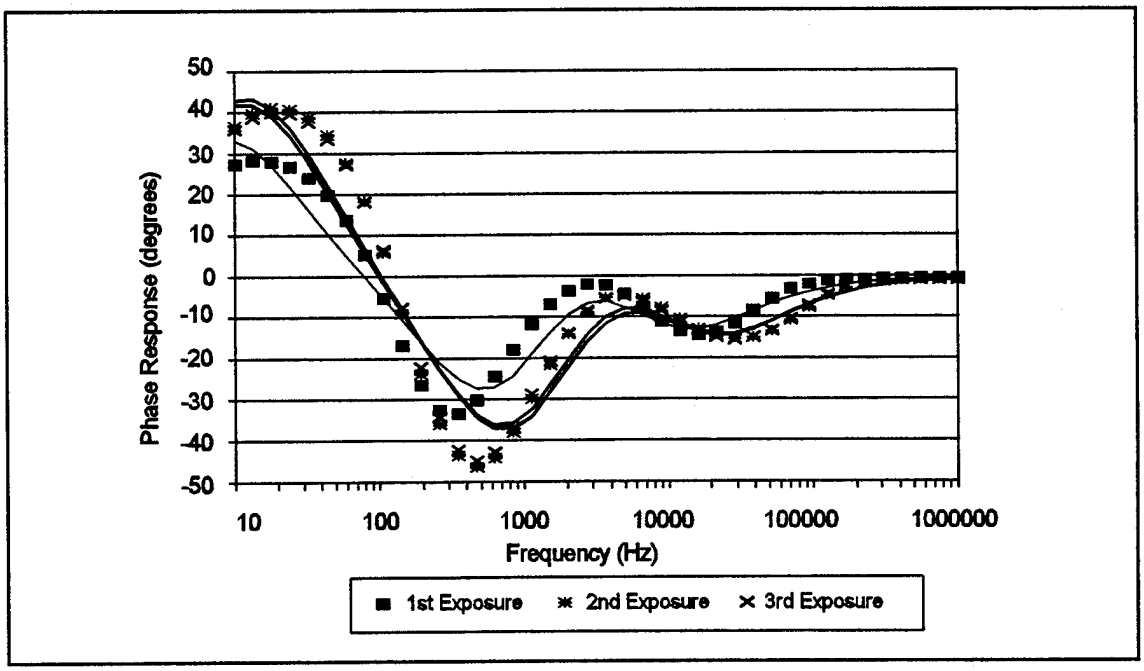


Figure VI-89. Bode Plots of the NiPc-Coated IGEFET Transfer Function Phase Response to Repeated 4000 ppb NO_2 Exposures. The Solid Lines Represent the Phase Response Derived from the Spreadsheet Model Curve Fits of the Pre-Exposed and Exposed NiPc-Coated IGEFET Transfer Function Gain Data to Equation (V-34). (Temperature = 100° C.)

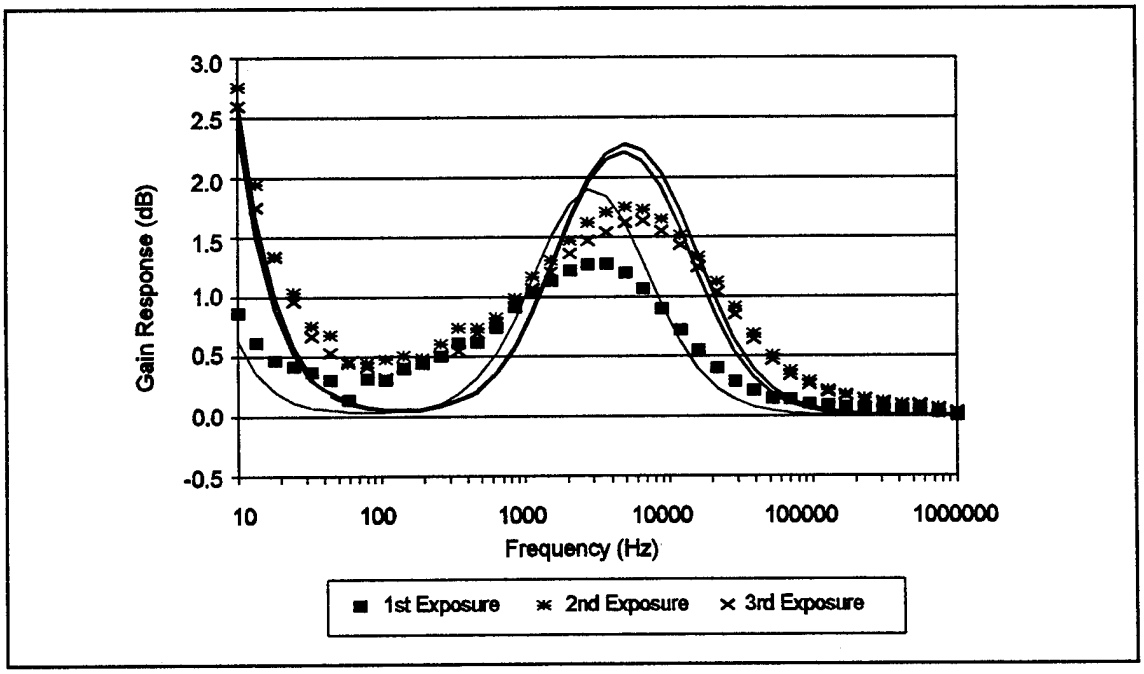


Figure VI-90. Bode Plots of the CoPc-Coated IGEFET Transfer Function Gain Response to Repeated 4000 ppb NO_2 Exposures. The Solid Lines Represent the Gain Response Derived from the Spreadsheet Model Curve Fits of the Pre-Exposed and Exposed CoPc-Coated IGEFET Transfer Function Gain Data to Equation (V-31). (Temperature = 100° C.)

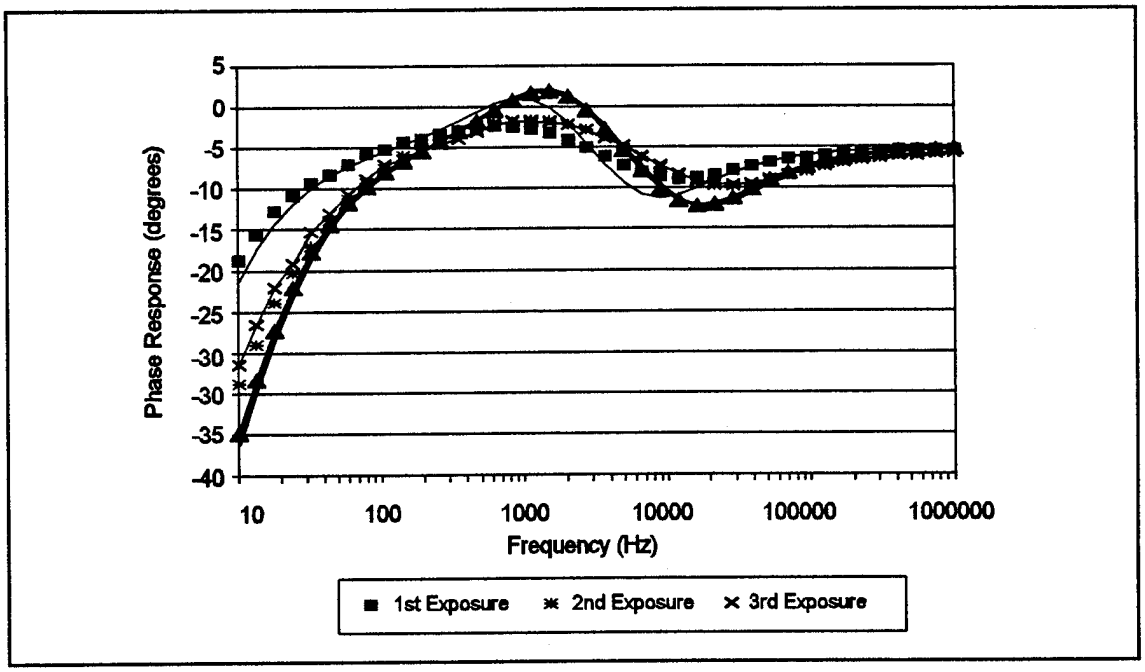


Figure VI-91. Bode Plots of the CoPc-Coated IGEFET Transfer Function Phase Response to Repeated 4000 ppb NO_2 Exposures. The Solid Lines Represent the Phase Response Derived from the Spreadsheet Model Curve Fits of the Pre-Exposed and Exposed CoPc-Coated IGEFET Transfer Function Gain Data to Equation (V-34). (Temperature = 100° C.)

Table VI-4. Spreadsheet Model Parameters used to Fit the MPc-Coated IGEFET Transfer Function Gain/Phase Data Before and After Exposure to Various NO_2 Challenge Gas Concentrations (Temperature = 100°C.)

Mixture Number	Conc. (ppb)	Fit Parameters											
		CuPc				NiPc				CoPc			
		G_1 (10^{-8} mhos)		G_2 (10^{-10} mhos)		G_1 (10^{-9} mhos)		G_2 (10^{-10} mhos)		G_1 (10^{-9} mhos)		G_2 (10^{-12} mhos)	
		Before	After	Before	After	Before	After	Before	After	Before	After	Before	After
1	100	1.1	1.5	6	6.8	6	9	7	8	5.75	6.25	2	2.25
2	100	1.2	1.6	6	7.3	6	9.2	7	8.4	5.75	6.3	2	2.45
3	100	1.2	1.65	6	7.7	7.3	9.8	7	8.9	6.3	7.1	2.3	2.85
4	200	1.35	2.4	6.2	10	8	14	6.8	10.5	7.75	12	2.5	4
5	200	1.35	2.4	6.2	9.1	7	14	6.9	10.5	7.75	12.5	2.5	4.2
6	200	1.5	2.6	6.9	10.1	9	17	7.5	11	7.75	12	2.5	4
7	400	1.7	3.4	6.6	13	10	24	7	13	8.9	16	3	5
8	400	1.5	3.2	6.6	13.5	8	24	7	14	7.1	16	2.6	5
9	400	1.8	3.5	6.8	14.5	8	26	7	13.5	8.4	16.5	2.6	5
10	1000	1.6	5	7.2	20	9	37	7.3	21	9	23	2.5	6.2
11	1000	1.7	4.5	7.6	20	10.5	38	7.5	21	9	22	2.5	6.2
12	1000	1.7	5	7.6	22	9	38	7.3	22	9	23	2.5	7
13	4000	1.7	7.5	7.4	27	9.5	55	7.4	26	7.7	40	1.9	8
14	4000	2.1	18	8.5	60	13	98	7.8	45	9.9	95	1.9	18
15	4000	2	18	8	65	13	98	7.8	42	10	85	1.9	17

CuPc and NiPc: C_1 = 0.5 pF, C_2 = 0.38 pF, C_{EG} = 22 pF, G_{EG} = 10^{-12} mhos
CoPc: C_1 = 0.82 pF, C_2 = 0.31 pF, C_{EG} = 22 pF, G_{EG} = 10^{-12} mhos

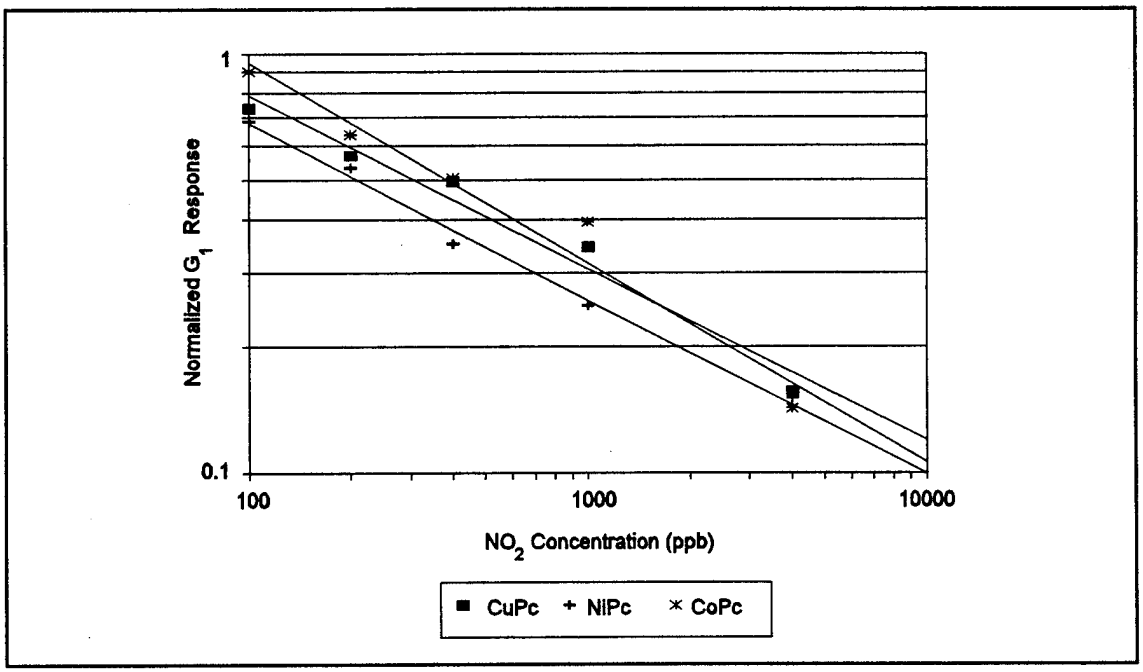


Figure VI-92. Concentration Dependence of the MPc-Coated IGEFET Normalized G_1 Conductance Parameter Response to Nitrogen Dioxide. (Temperature = 100°C.)

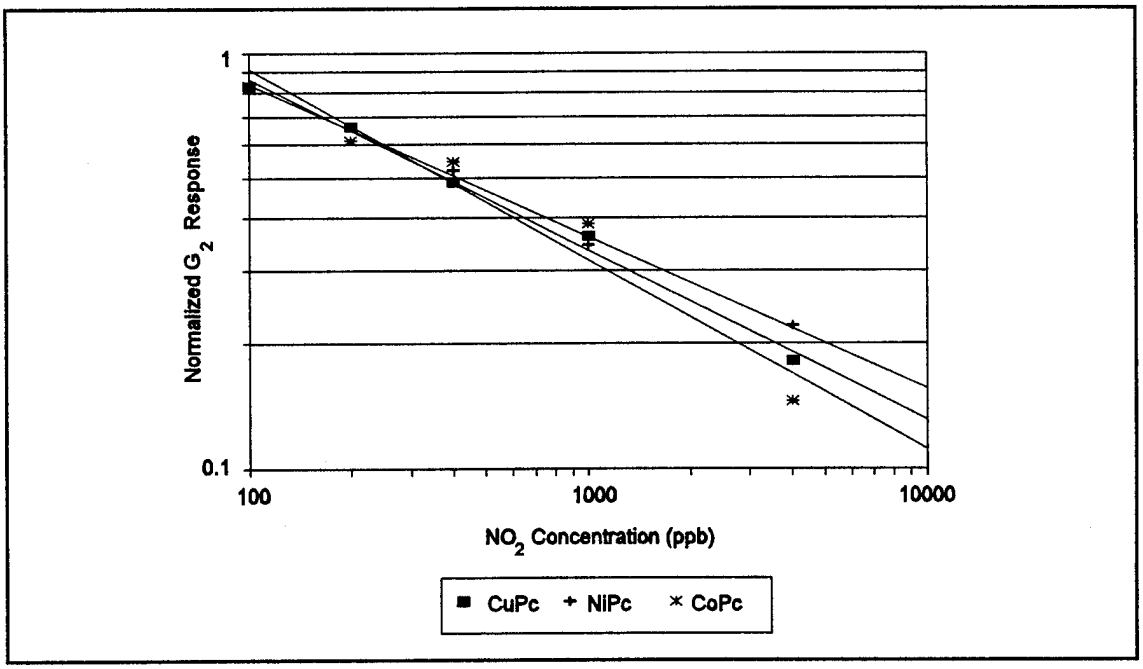


Figure VI-93. Concentration Dependence of the MPc-Coated IGEFET Normalized G_2 Conductance Parameter Response to Nitrogen Dioxide. (Temperature = 100°C.)

where A, B, and α are constants. The value of the parameters obtained from least-squares fitting each of the average normalized conductance parameters corresponding to each MPc film type are provided in Appendix L.

The feature vector for performing the gas analysis was formed by combining the sensor response vectors corresponding to each film type into a single column vector representing the response of all the MPc films to a particular challenge gas concentration. The sensor response vector was formed as a column vector whose elements were the two normalized conductance parameters raised to the corresponding power, α, required to linearize the conductance parameter response to NO_2 exposure. Appendix L provides examples of the calibration and test feature vectors for each challenge gas concentration examined in this analysis.

Principal Component Analysis and Multivariate Regression Implementation. To determine the component gas concentration(s), the IGEFET electrical response, upon exposure to the single component and binary gas mixtures, was analyzed using the principal component analysis (PCA) and ***P***-matrix multivariate regression techniques described in Chapter III. Separate analyses were conducted with the feature vectors formulated from the various IGEFET electrical response measurements: the IGE structure normalized DC resistance, the IGEFET transfer function gain response, the IGEFET transfer function phase response, and the IGEFET transfer function conductance parameters. As indicated in the previous sections, the feature vectors were formed by least-squares fitting the measured responses to a number of functional forms (Equations VI-2 through VI-6) that depended upon the electrical measurement and challenge gas species. Based upon these functional forms, the response to m-calibration samples containing i-components was expressed in one of two matrix forms for performing the multivariate regression. Regression analysis with the IGE structure normalized DC resistance, the IGEFET transfer function phase data, and the IGEFET transfer function conductance parameters was conducted assuming that the concentration was related to the electrical response features according to the following matrix equation:

$$\mathbf{C} = \mathbf{A}\,\mathbf{X} + \mathbf{B} \qquad \text{(VI-8)}$$

where **C** is a matrix containing i×m component concentrations, **X** is a matrix composed of m-feature vectors with j response elements, and **A** and **B** are i×j and i×m matrices, respectively, containing constants. The regression analyses conducted with the gain response feature vectors assumed a similar

matrix equation except that the concentration matrix, **C**, was replace by a matrix containing the logarithm of the component concentrations:

$$\log \mathbf{C} = \mathbf{A}\,\mathbf{X} + \mathbf{B} \qquad \text{(VI-9)}$$

Ideally, the gas calibration should be performed with a large number of gas mixture concentrations. However, the time required to measure the IGEFET electrical response to a single gas concentration precluded collecting the response with a large number of different gas concentrations. For the single component analyses, calibration was conducted with feature vectors formed from the average response to triplicate exposures with five different concentrations (m=5). Similarly, calibration for the binary mixture analyses was conducted with the feature vectors formed from the average response to triplicate exposures with nine calibration mixtures (m=9). The calibration concentrations are listed in Table VI-5 for the two test gases. For each analysis, the feature vectors for the concentrations listed in Table VI-5 were combined to form the calibration matrix, $\mathbf{X}_{cal}$.

The analyses were implemented using standard matrix formulations and procedures using the mathematical computation software, MathCad (Version 3.0, MathSoft Corp., Cambridge, MA). The MathCad code for performing the principal component analysis (PCA) and the multivariate regression is provided in Appendix O. In the principal component analysis (PCA) technique (Chapter III), the response features are projected onto a vector space whose orthogonal coordinate axes account for the maximum variation in the data. This vector space is given by the eigenvectors of the covariance matrix. Therefore, the first step in the analyses was to construct the covariance matrix, **Z**, by pre-multiplying the calibration matrix, $\mathbf{X}_{cal}$, with its transpose. Eigenanalysis was then performed to obtain the eigenvalues and eigenvectors of the covariance matrix. The eigenvectors were rank ordered in descending order according to the magnitude of the eigenvalue. The magnitude of an eigenvalue indicates the corresponding eigenvector's contribution to the variance in the data. The number of eigenvectors generated by eigenanalysis is limited to the number of mixtures in the calibration data set. Since a limited number of mixtures were used for calibration, it was feasible to test the predictive capabilities of the calibration starting with the most significant eigenvector and adding less significant eigenvectors one at a time. Figure VI-94 illustrates the test process. For each test, the calibration data was projected onto the vector space represented by the matrix, **L**, composed of a given number of eigenvectors. The resulting matrix, **F**, contains the factor loadings that indicate the relative contribution of each eigenvector necessary to reproduce the calibration matrix. Multiple regression

Table VI-5. Calibration Gas Concentrations for Single Component and Binary Gas Mixture Analyses.

Single Component NO_2 Analysis		Single Component NH_3 Analysis		Binary Gas Mixture Analysis	
$[NO_2]$ (ppb)	$[NH_3]$ (ppm)	$[NO_2]$ (ppb)	$[NH_3]$ (ppm)	$[NO_2]$ (ppb)	$[NH_3]$ (ppm)
100	-	-	20	100	50
200	-	-	50	425	50
400	-	-	100	1000	50
1000	-	-	200	100	200
4000	-	-	400	425	200
-	-	-	-	1000	200
-	-	-	-	100	400
-	-	-	-	425	400
-	-	-	-	1000	400

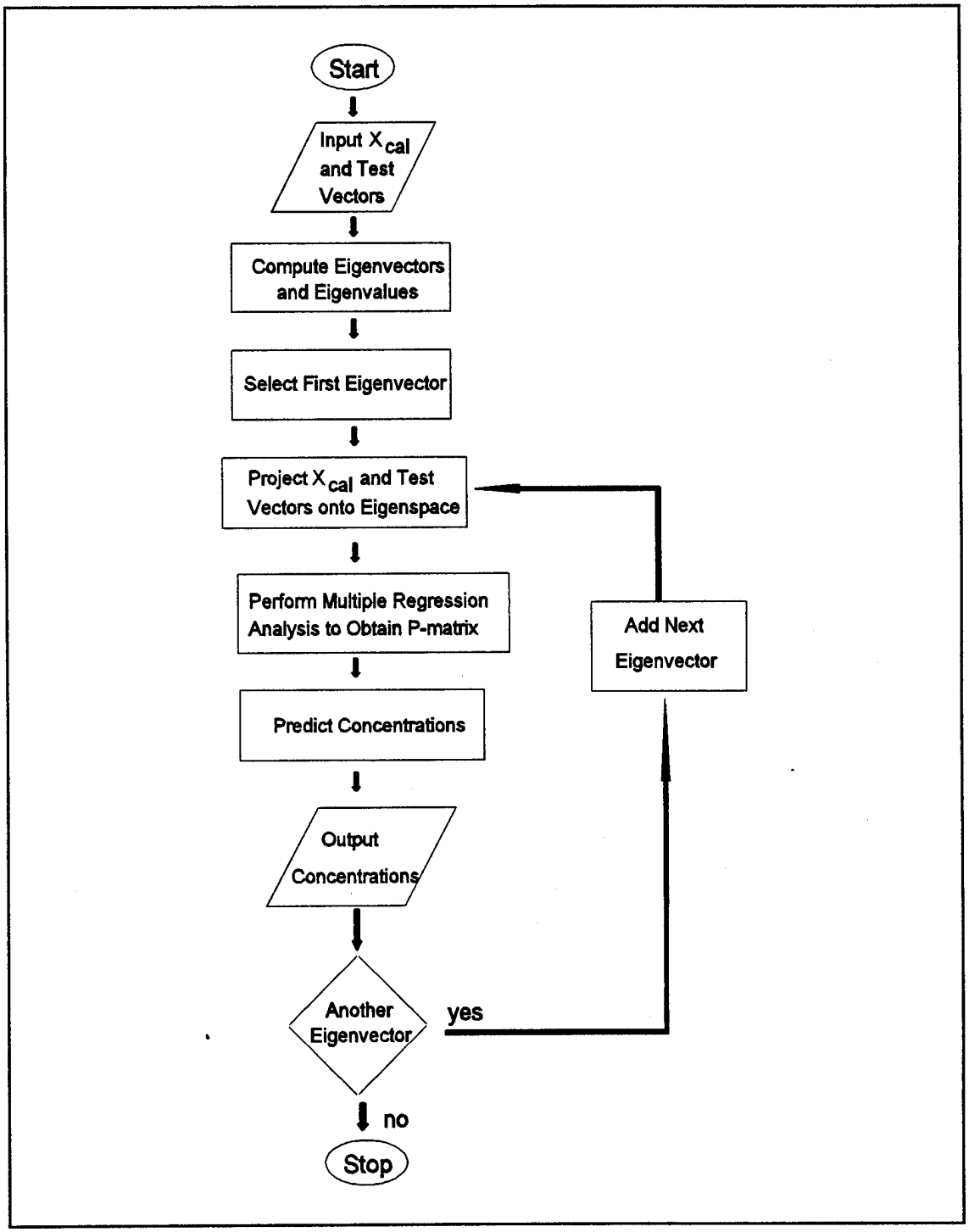


Figure VI-94. Principal Component Analysis Process.

analysis was then performed with the factor loading matrix, **F**, used in place of the original calibration response matrix, $\mathbf{X}_{cal}$. The fit parameters resulting from the regression analysis are contained in the **P**-matrix. To determine the gas concentrations within a test mixture, the test feature vector is first projected onto the eigenvector space, **L**, and then the resulting matrix is pre-multiplied by the fit parameter matrix, **P**.

As an internal check of the calibration process, the gas concentrations of the calibration set were predicted using the original calibration data as a test vector. As expected, when the eigenvector matrix, **L**, was composed of all the eigenvectors generated from the eigenanalysis of the covariance matrix, the predicted concentrations exactly matched the calibration concentrations. With a reduced number of eigenvectors, the predicted concentrations deviated from the calibration concentrations. The degradation in the predicted concentrations was a function of the relative importance (weight) of the eigenvector(s) not included in the calibration.

Two different tests (analyses) were performed to evaluate the ability of the calibrations to predict the component gas concentration(s) from the IGEFET electrical response upon exposure to a challenge gas. The calibration was initially tested with the feature vectors formed from the IGEFET electrical response to each of the triplicate gas challenges that had been averaged to produce the calibration feature vectors. A more rigorous test predicted the gas component concentrations from the IGEFET electrical response to 11 binary gas mixture challenges that were unrelated to the calibration set. Table VI-6 lists the NO_2 and NH_3 component concentrations for each mixture contained in the calibration and test sets used in the single component and binary gas mixture analyses. A metric, referred to as the prediction error (P.E.), was developed to indicate the accuracy of the predicted concentrations relative to the known concentrations (as generated from the calibrated permeation tubes). This metric was the root mean square (rms) error between the predicted and the known concentrations, and it is given by the following equation:

$$\text{Prediction Error} = \sqrt{\frac{\sum_{k=1}^{m}\left[\frac{PC_k - KC_k}{KC_k}\right]^2}{m}} \cdot 100\,\% \qquad \text{(VI-10)}$$

where PC and KC are the predicted and known concentrations for a given challenge gas, respectively, and m is the number of exposures (samples). The dependence of the prediction error on the number of eigenvectors included in the calibration set was also examined. The results of these tests are

Table VI-6. NO_2 and NH_3 Component Concentrations within the Single Component and Binary Mixture Calibration and Test Sets. (Brackets Indicate Concentration).

Single Component Analyses				Binary Mixture Analyses								
Calibration/Test Set		Calibration/Test Set		Calibration Set						Test Set		
Mixture Number	[NO_2] (ppb)	Mixture Number	[NH_3] (ppm)	Mixture Number	[NO_2] (ppb)	[NH_3] (ppm)	Mixture Number	[NO_2] (ppb)	[NH_3] (ppm)	Mixture Number	[NO_2] (ppb)	[NH_3] (ppm)
1	100	1	20	1	100	50	15	400	200	1	100	50
2	100	2	20	2	100	50	16	1000	200	2	100	50
3	100	3	20	3	100	50	17	1000	200	3	100	50
4	200	4	50	4	425	50	18	1000	200	4	100	50
5	200	5	50	5	425	50	19	100	400	5	100	50
6	200	6	50	6	425	50	20	100	400	6	100	200
7	400	7	100	7	1000	50	21	100	400	7	100	200
8	400	8	100	8	1000	50	22	425	400	8	100	200
9	400	9	100	9	1000	50	23	425	400	9	425	400
10	1000	10	200	10	100	200	24	425	400	10	425	400
11	1000	11	200	11	100	200	25	1000	400	11	425	400
12	1000	12	200	12	100	200	26	1000	400			
13	4000	13	400	13	425	200	27	1000	400			
14	4000	14	400	14	425	200						
15	4000	15	400									

discussed in the following sections according to the type of electrical measurement used to perform the analysis.

Gas Analysis Using the IGE Structure Normalized DC Resistance Response

Separate gas analyses were performed with the normalized resistance response collected during exposure to NO_2, NH_3, and the binary gas mixtures. The following paragraphs describe the results obtained from each analysis.

Figure VI-95 shows that the error between the predicted NO_2 concentrations and the known test concentrations decreased as the number of eigenvectors included in the calibration set increased. The minimum error (26%) was achieved when the calibration was performed with the maximum number of eigenvectors (five calibration concentrations). However, reducing the number of eigenvectors to four caused only a slight increase in the error (approximately 2%). A comparison of the predicted NO_2 concentrations (from the calibration with four eigenvectors) relative to the known concentrations for each gas challenge exposure is shown in Figure VI-96.

In contrast to the NO_2 gas analysis, the minimum prediction error (14%) in the analysis of the NH_3 single component exposures was achieved with only two eigenvectors (Figure VI-97). The prediction error increased significantly as the number of eigenvectors was increased beyond two. The minimum in the error analysis is typical in PCA, since the additional eigenvectors primarily represent noise, as well as components whose contribution to the measured response is small. A comparison of the predicted NH_3 concentrations (from the calibration with two eigenvectors) relative to the known concentrations for each challenge gas exposure is shown in Figure VI-98.

As indicated in the previous section, two different analyses were performed with the binary mixture calibration. The first analysis was similar to the single component gas analyses. Figure VI-99 shows the prediction error dependence for the component gases in 27 mixtures and the total error for the mixtures (the sum of the errors for each gas component). Initially, the error decreased rapidly as the number of eigenvectors used in the analysis was increased. After the first three eigenvectors, the error continued to decrease, but at a slower rate. The minimum error for both components was achieved with the maximum number (9 calibration mixtures) of eigenvectors. The NO_2 and NH_3 errors were 14% and 47%, respectively. A comparison of the predicted NO_2 and NH_3 concentrations (from the calibration with nine eigenvectors) relative to the known concentrations for each challenge gas exposure are shown in Figures VI-100 and VI-101. The second analysis evaluated the performance of the calibration with 11 binary mixtures outside the calibration set. In contrast to the

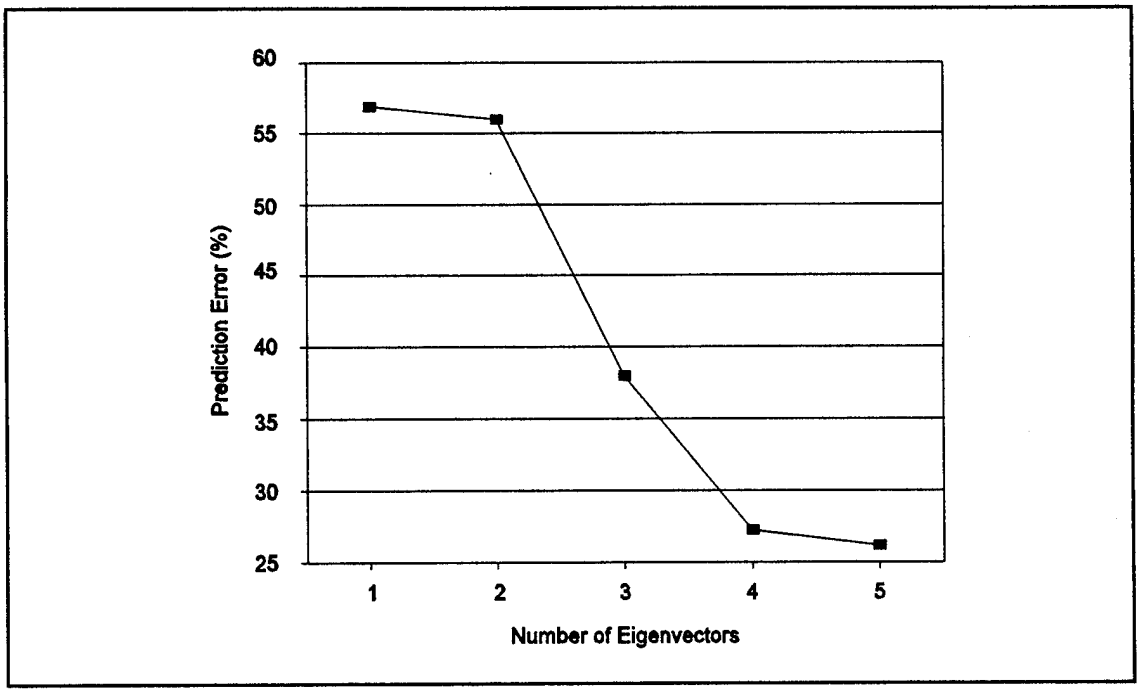


Figure VI-95. Prediction Error of the NO_2 Concentration for 15 Challenge Gas Exposures as a Function of the Number of Eigenvectors Used in the Calibration.

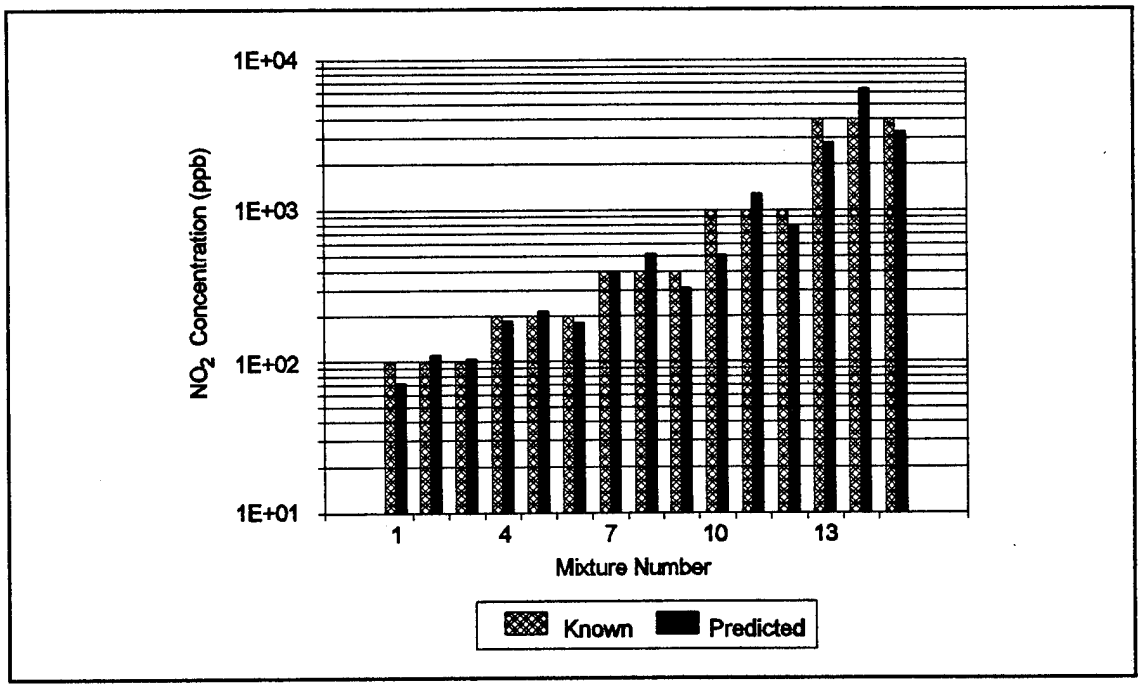


Figure VI-96. Comparison of the Known (as Generated) and Predicted NO_2 Concentration for 15 Challenge Gas Exposures. Analysis Performed with the Normalized DC Resistance Data Using 4 Eigenvectors in the Calibration.

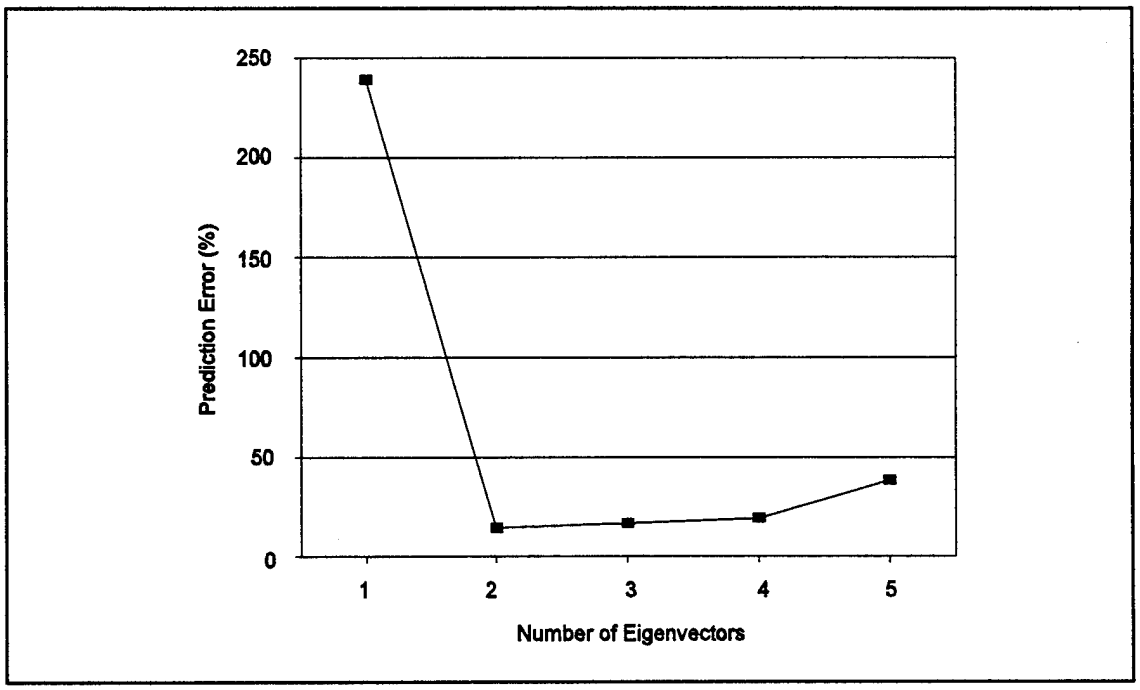


Figure VI-97. Prediction Error of the NH_3 Concentrations for 15 Challenge Gas Exposures as a Function of the Number of Eigenvectors Used in the Calibration.

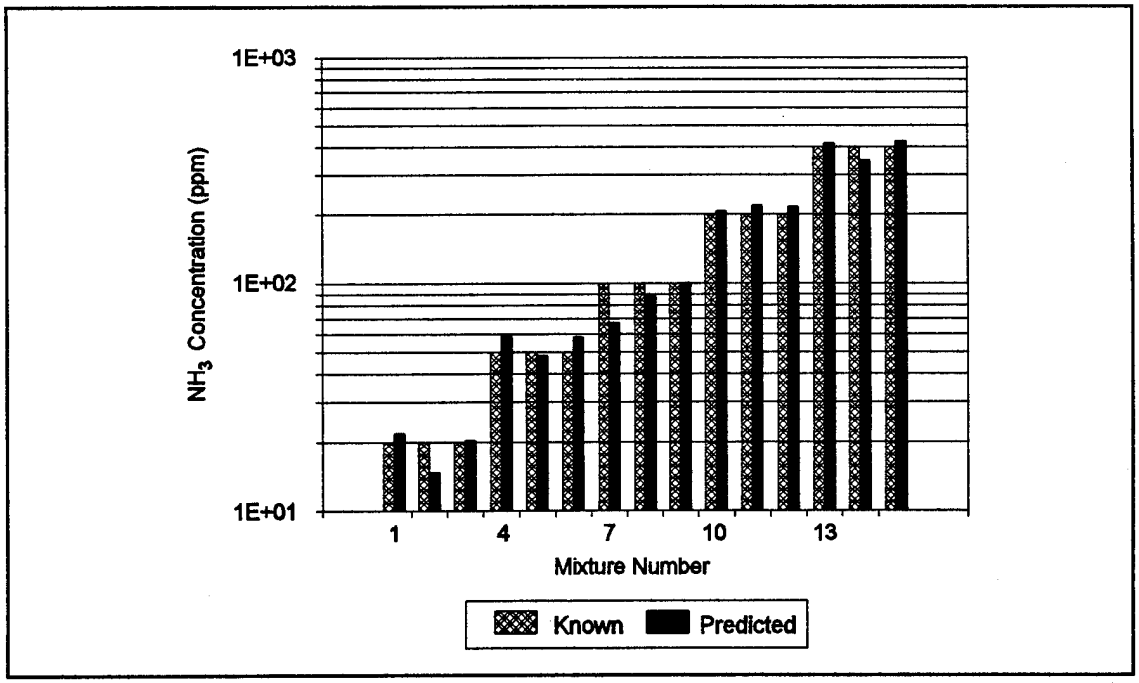


Figure VI-98. Comparison of the Known (as Generated) and Predicted NH_3 Concentration for 15 Challenge Gas Exposures. Analysis Performed with the Normalized DC Resistance Data Using 2 Eigenvectors in the Calibration.

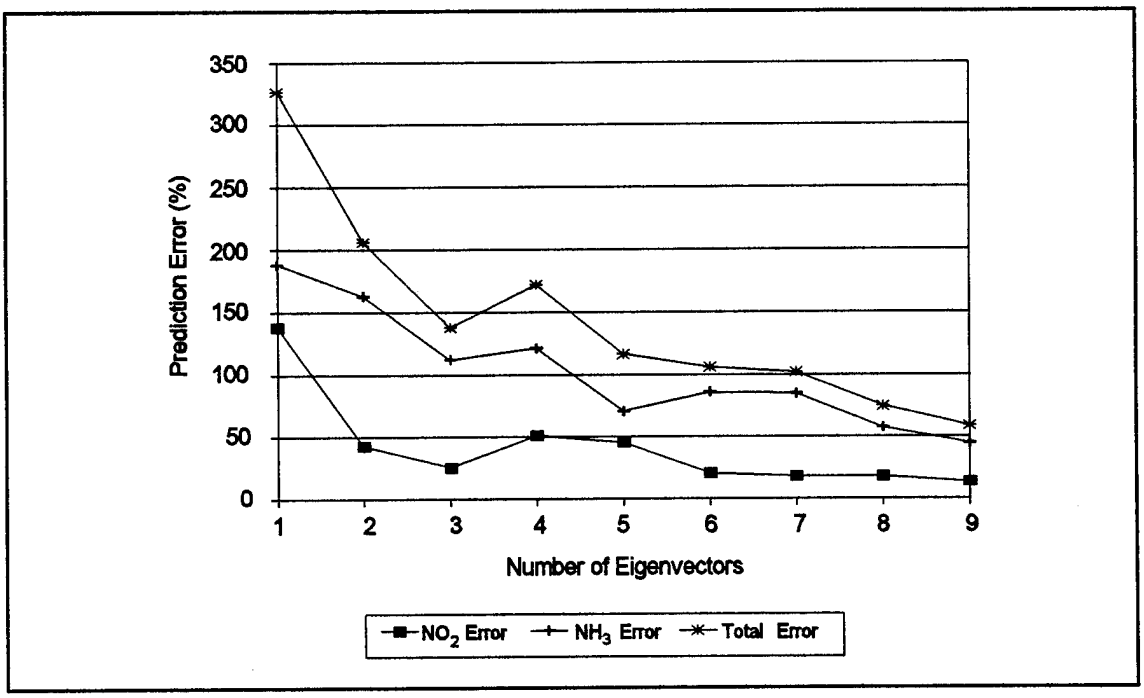


Figure VI-99. NO_2, NH_3, and Total Prediction Error For 27 Binary Gas Mixtures as a Function of the Number of Eigenvectors Used in the Calibration.

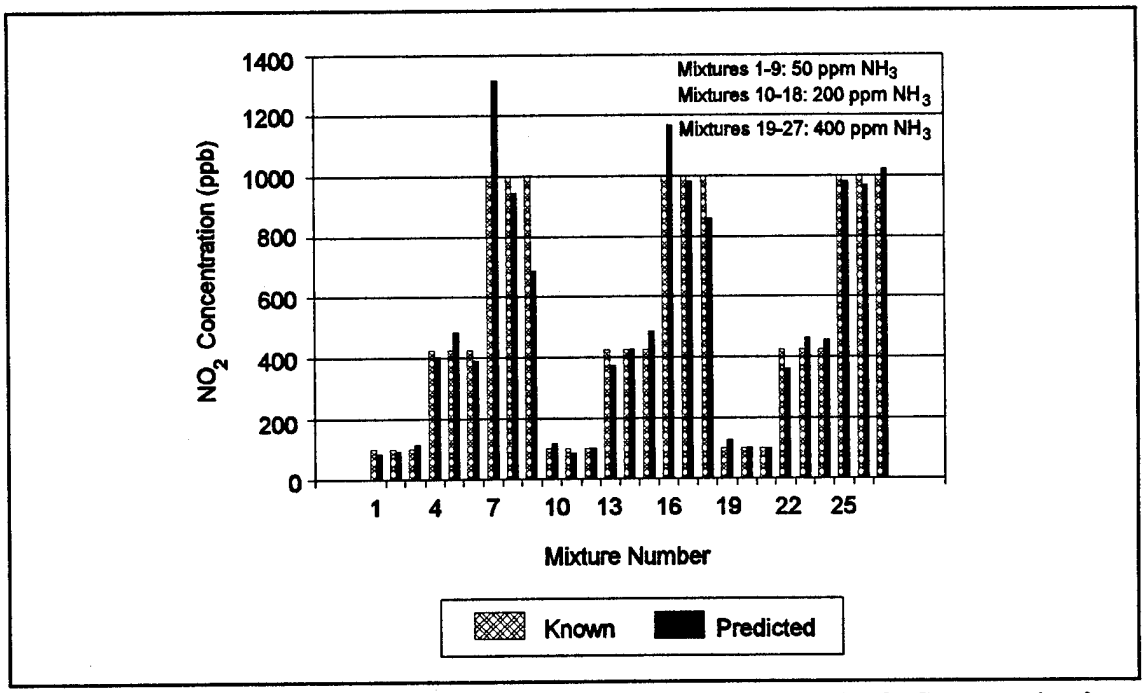


Figure VI-100. Comparison of the Known (as Generated) and Predicted NO_2 Concentration for 27 Binary Mixture Exposures. Analysis Performed with the Normalized DC Resistance Data Using 9 Eigenvectors in the Calibration.

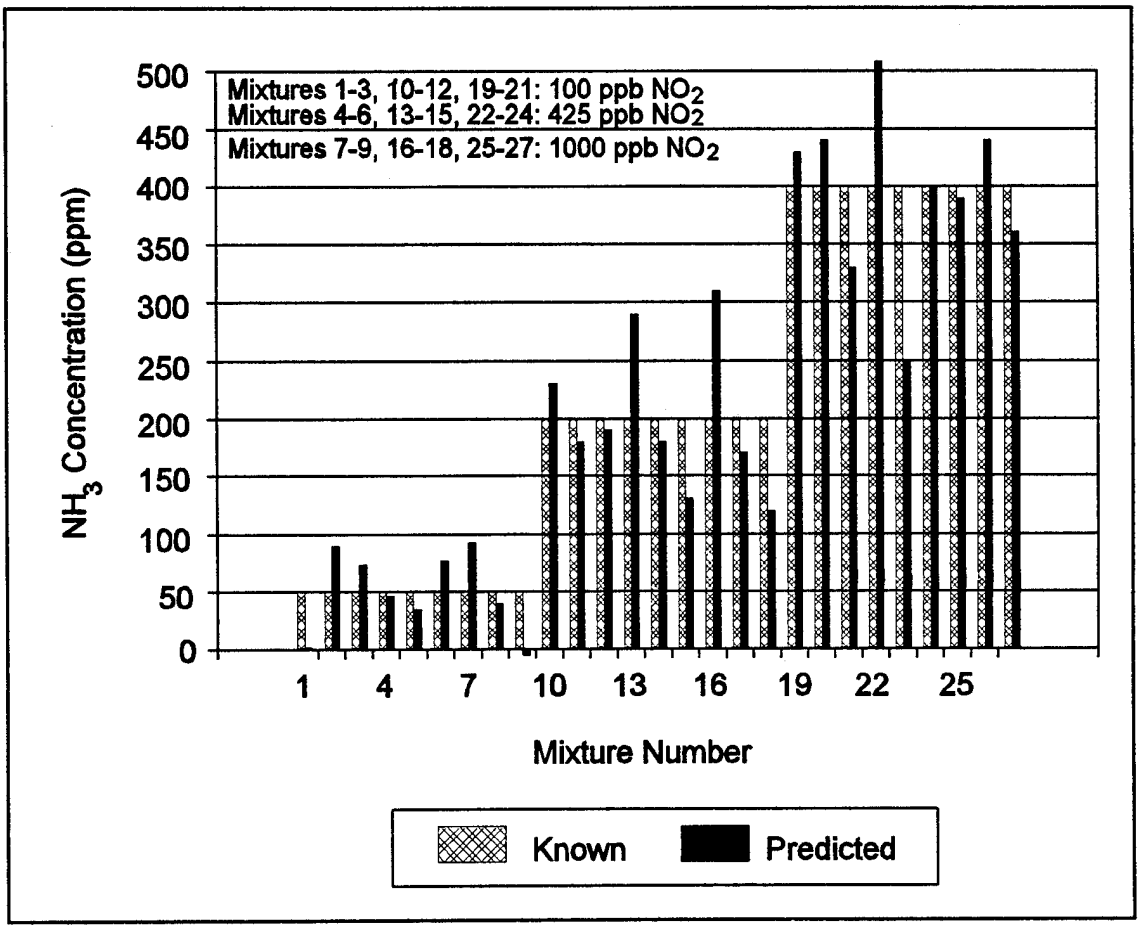


Figure VI-101. Comparison of the Known (as Generated) and Predicted NH_3 Concentration for 27 Binary Mixture Exposures. Analysis Performed with the Normalized DC Resistance Data Using 9 Eigenvectors in the Calibration.

first analysis, the error was minimized when seven eigenvectors were used to perform the calibration. Since this result disagreed with the results of the first analysis in which the error was minimized with nine eigenvectors, the results of the first analysis were re-examined using seven eigenvectors to perform the calibration, as shown in Figures VI-102 and VI-103. Comparing Figures VI-100 and VI-102 reveals that the predicted NO_2 concentrations are unchanged by decreasing the number of eigenvectors. However, a comparison of Figures VI-101 and VI-103 reveals that reducing the number of eigenvectors increased the error in the predicted NH_3 concentrations in the mixtures. The prediction error increased by the largest amount with mixtures containing small NH_3 concentrations. On the other hand, the prediction error decreased with mixtures containing large NH_3 concentrations. Figures VI-104 and VI-105 compare the predicted and known concentrations of the gas components in the 11 binary mixtures not included in the calibration set (7 eigenvectors). The prediction error was approximately 38% for both gas components. The largest error in the predicted NO_2 concentration was 100% for mixture 8. The largest error in the predicted NH_3 concentration was also 100% for mixture 2. Excluding these predicted concentrations, the prediction error was 27% for NO_2 and 24% for NH_3. This prediction error magnitude is on the order of the error observed in the predicted concentrations in the analysis of single component NO_2 exposures.

Gas Analysis Using the IGEFET Transfer Function Gain Response

Separate gas analyses were performed with the gain response collected during the exposures to NO_2, NH_3, and the binary gas mixtures. The following paragraphs describe the results obtained from each analysis.

Figure VI-106 shows that the error between the predicted NO_2 concentrations and the known test concentrations decreased as the number of eigenvectors included in the calibration set increased. The minimum error (42%) was achieved when the calibration set was established with the maximum number of eigenvectors (five calibration concentrations). Although reducing the number of eigenvectors to three caused only a slight increase in the error (approximately 6%); decreasing the number of eigenvectors to less than three significantly increased the prediction error. A comparison of the predicted NO_2 concentrations (from the calibration set with five eigenvectors) relative to the known concentrations for each challenge gas exposure is shown in Figure VI-107.

As shown in Figure VI-108, the minimum prediction error (40%) in the analysis of the NH_3 single component exposures was achieved with 4 eigenvectors. A small increase in the error (approximately 3%) was observed if the calibration was performed with 5 eigenvectors. However,

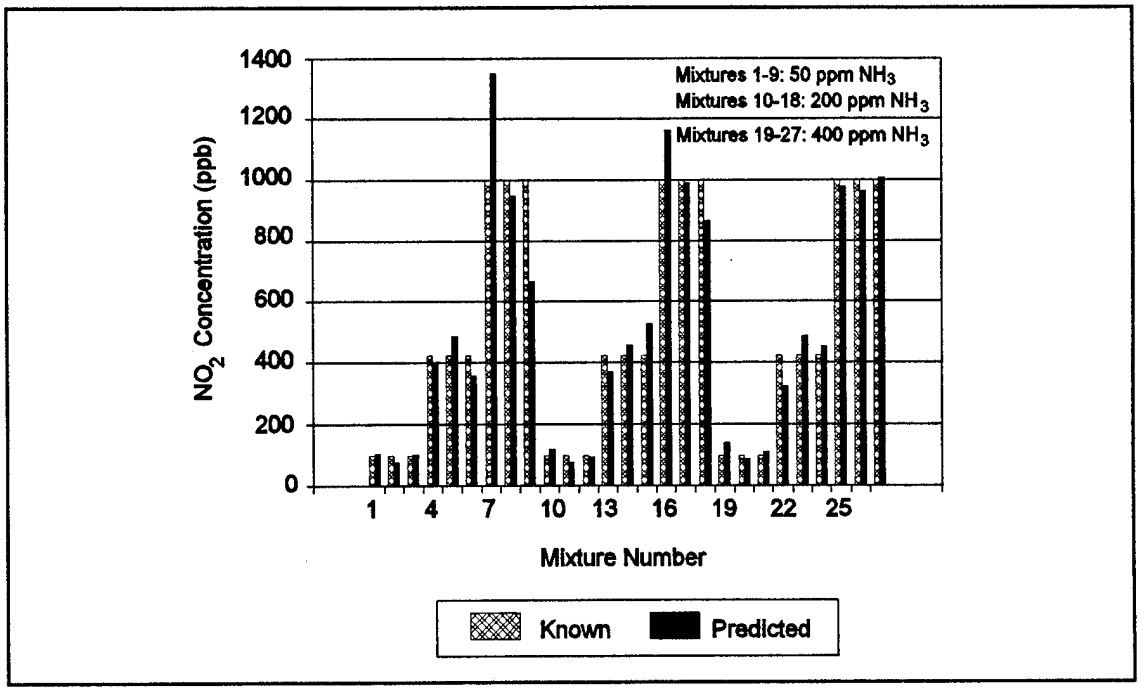


Figure VI-102. Comparison of the Known (as Generated) and Predicted NO_2 Concentration for 27 Binary Mixture Exposures. Analysis Performed with the Normalized DC Resistance Data Using 7 Eigenvectors in the Calibration.

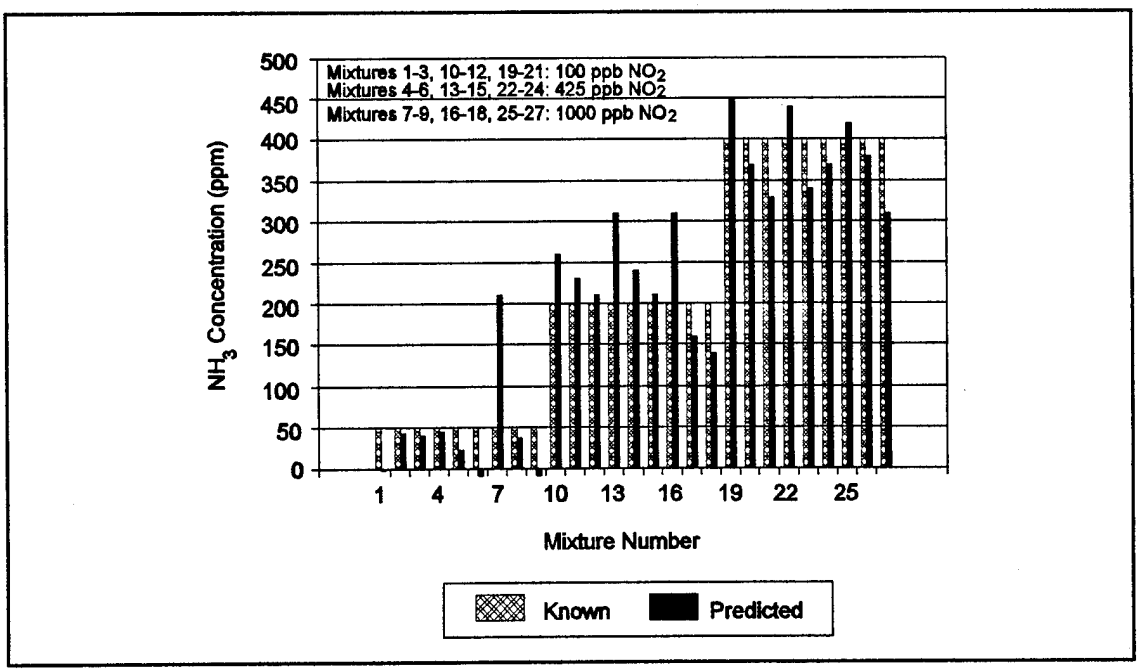


Figure VI-103. Comparison of the Known (as Generated) and Predicted NH_3 Concentration for 27 Binary Mixture Exposures. Analysis Performed with the Normalized DC Resistance Data Using 7 Eigenvectors in the Calibration.

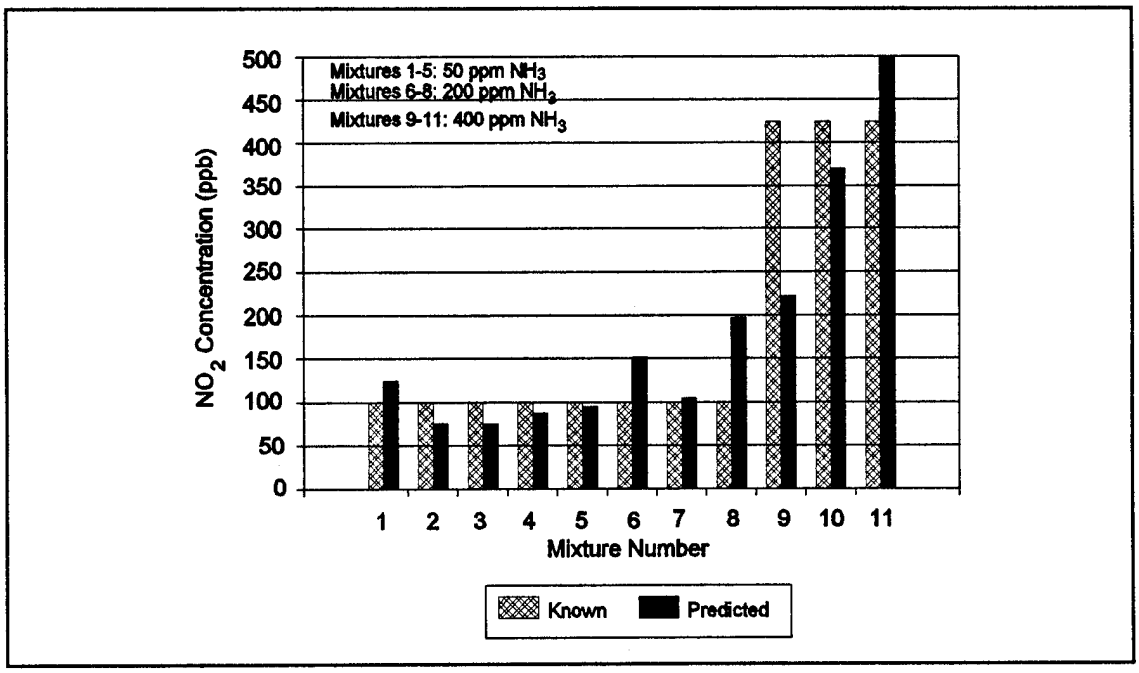


Figure VI-104. Comparison of the Known (as Generated) and Predicted NO_2 Concentration for 11 Binary Mixture Exposures. Analysis Performed with the Normalized DC Resistance Data Using 7 Eigenvectors in the Calibration.

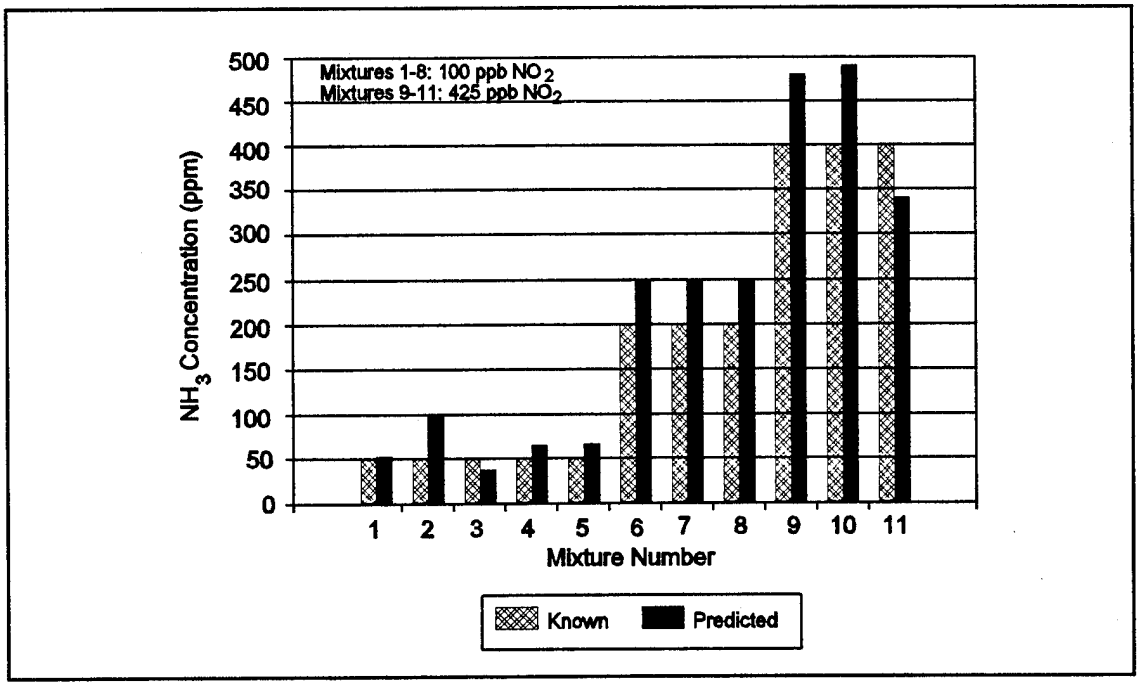


Figure VI-105. Comparison of the Known (as Generated) and Predicted NH_3 Concentration for 11 Binary Mixture Exposures. Analysis Performed with the Normalized DC Resistance Data Using 7 Eigenvectors in the Calibration.

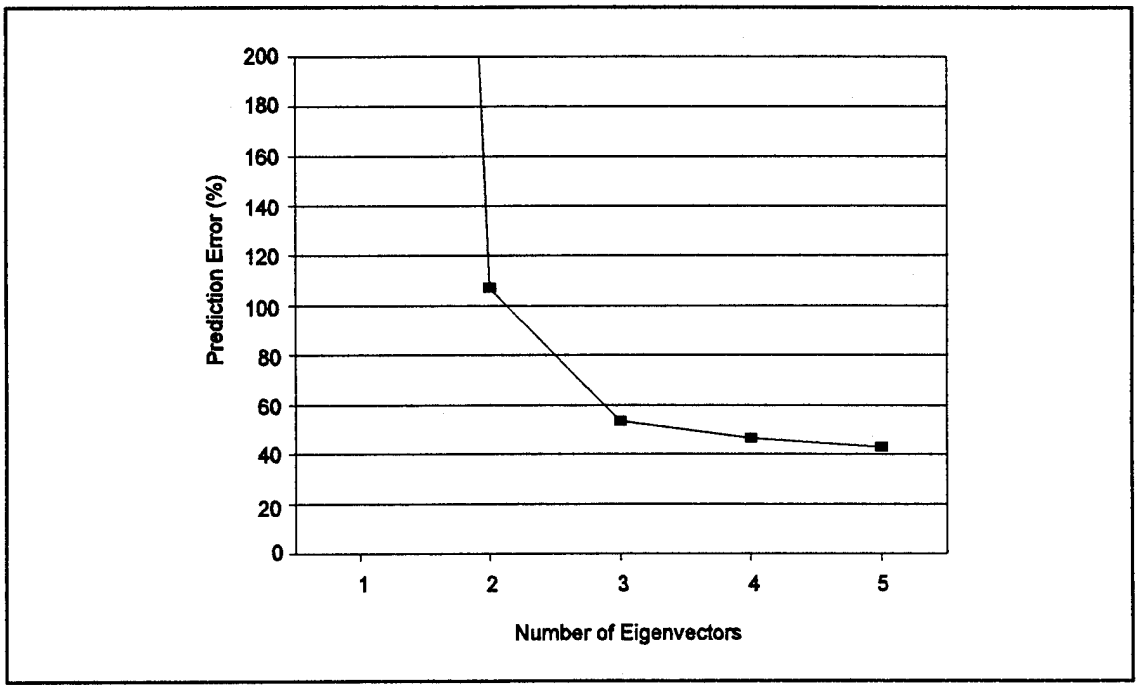


Figure VI-106. Prediction Error of the NO_2 Concentration for 15 Challenge Gas Exposures as a Function of the Number of Eigenvectors Used in the Calibration. Analysis Performed with the Gain Response Data.

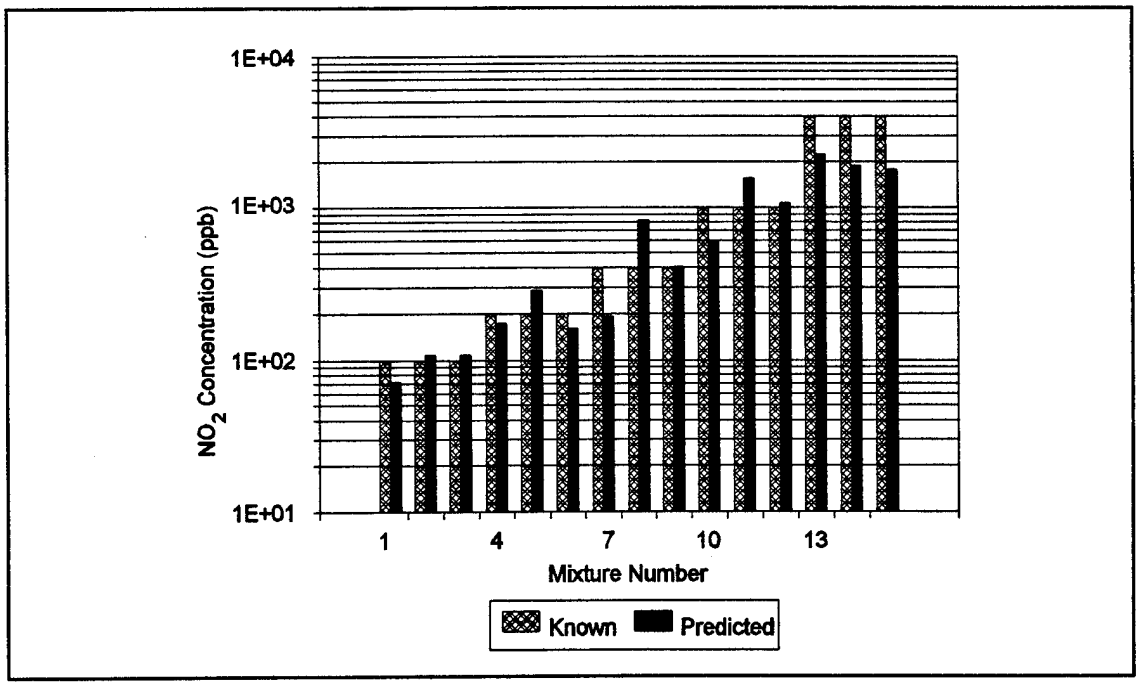


Figure VI-107. Comparison of the Known (as Generated) and Predicted NO_2 Concentration for 15 Challenge Gas Exposures. Analysis Performed with the Gain Response Data Using 5 Eigenvectors in the Calibration.

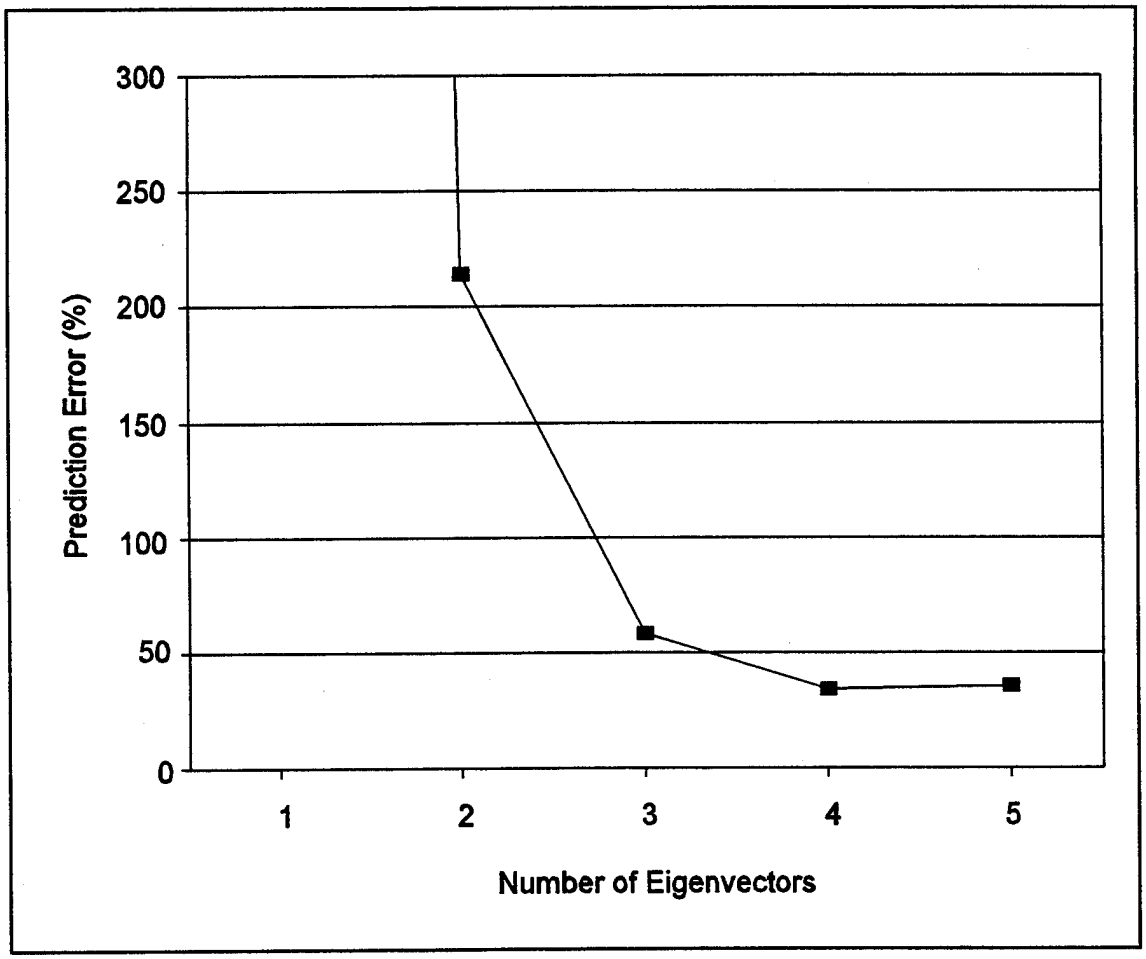


Figure VI-108. Prediction Error of the NH_3 Concentration for 15 Challenge Gas Exposures as a Function of the Number of Eigenvectors Used in the Calibration. Analysis Performed with the Gain Response Data.

the prediction error increased significantly for calibrations performed with less than 3 eigenvectors. A comparison of the predicted NH_3 concentrations (from the calibration set with four eigenvectors), relative to the known concentrations for each gas challenge exposure, is shown in Figure VI-109.

Figure VI-110 depicts the prediction error dependence on the number of eigenvectors for each component gas and the total error for both gases obtained from the analysis of 27 binary mixtures. As was observed with the single component analyses, the error decreased as the number of eigenvectors used in the analysis was increased. The minimum error for both components was achieved with the maximum number of eigenvectors (nine). The error in the predicted NO_2 and NH_3 concentrations were 25% and 27%, respectively. A comparison of the predicted NO_2 and NH_3 concentrations (from the calibration set with nine eigenvectors), relative to the known concentrations for each challenge gas exposure, are shown in Figures VI-111 and VI-112. In the analysis of the 11 binary mixtures not included in the calibration set, the error was also minimized with nine eigenvectors. Figures VI-113 and VI-114 show the predicted and known NO_2 and NH_3 concentrations for each of the mixtures. Excluding mixture number 6, the average error in the predicted NO_2 concentrations was 12%. In contrast, the average error in the predicted ammonia concentrations was 38%. Since mixture number 6 possessed a large error in the predicted NO_2 concentration, the gain response was re-examined in attempt to identify the gain response feature that contributed to the large error in the predicted NO_2 concentration. As was previously discussed with respect to the phase response of this particular mixture (Figure VI-60), the repeatability of the IGEFET electrical response was poor. Figure VI-115 shows the time dependence of the CuPc-coated IGEFET gain response at 44 Hz with respect to repeated exposure to 50 ppm NH_3 and 100 ppb NO_2. These exposures correspond to mixture numbers 3-5 in Figures VI-113 and VI-114. The gain response for the first two exposures were nearly identical for the first ten minutes of exposure. Since only the first ten minutes of data were used in the gas analyses, the divergence between the first and second exposure had no effect on the predicted concentrations. With the third exposure, the gain response was similar to the other two exposures for only two time slices. However, after the first five minutes, the gain response, which was initially decreasing, began to increase. An increase in the gain response is a NO_2-like response (Figure VI-19) and, therefore, may be the cause of the overestimate of the NO_2 concentration in mixture 5.

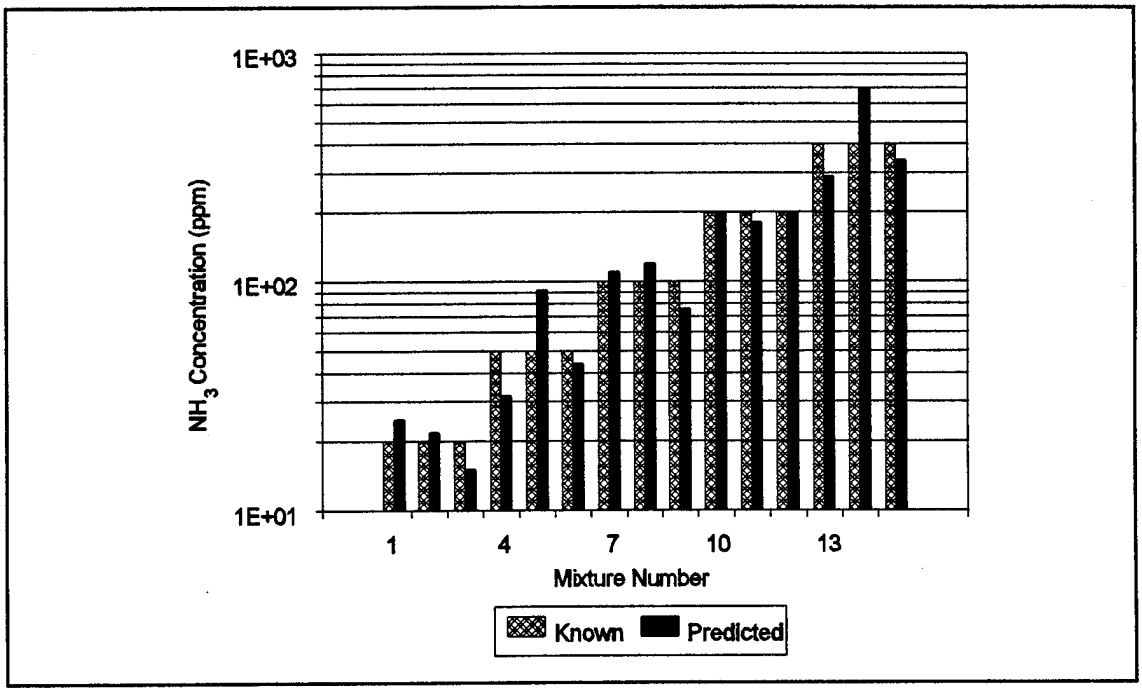


Figure VI-109. Comparison of the Known (as Generated) and Predicted NH_3 Concentrations for 15 Challenge Gas Exposures. Analysis Performed with the Gain Response Data Using 4 Eigenvectors in the Calibration.

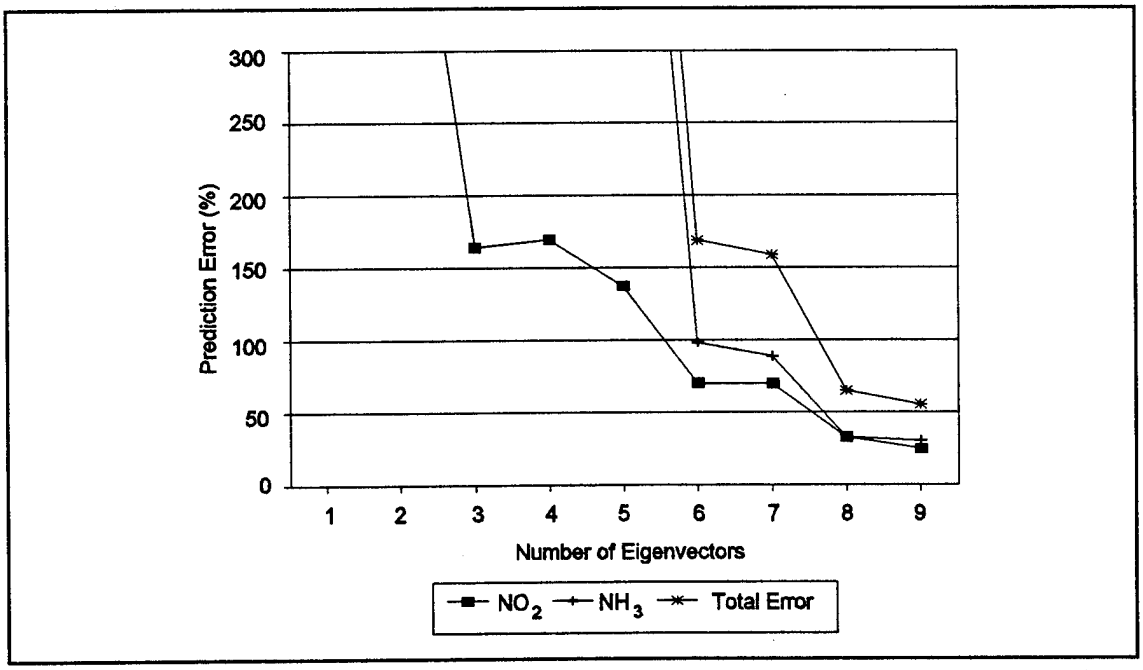


Figure VI-110. NO_2, NH_3, and Total Prediction Error for 27 Binary Gas Mixtures as a Function of the Number of Eigenvectors Used in the Calibration. Analysis Performed with the Gain Response Data.

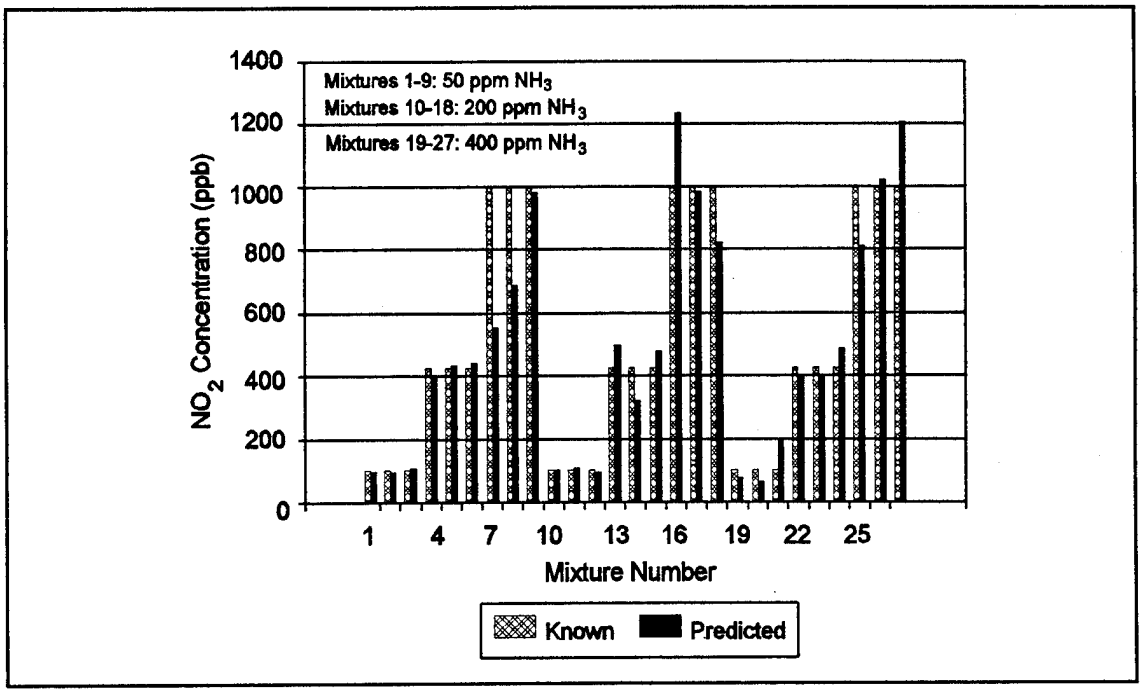


Figure VI-111. Comparison of the Known (as Generated) and Predicted NO_2 Concentration for 27 Binary Mixture Exposures. Analysis Performed with the Gain Response Data Using 9 Eigenvectors in the Calibration.

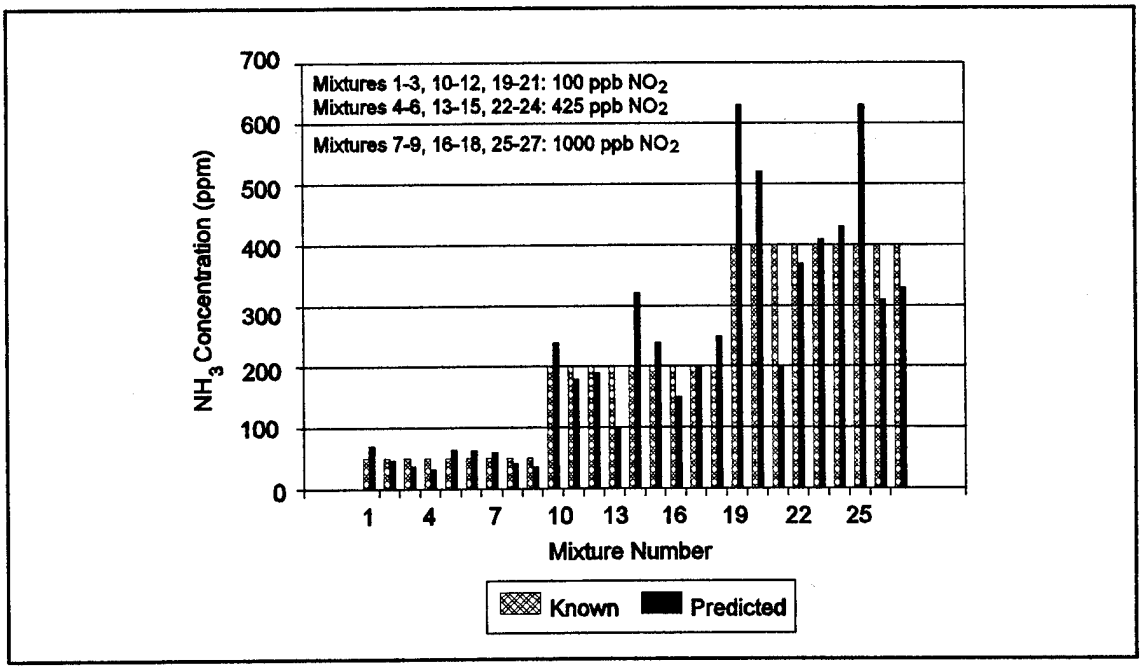


Figure VI-112. Comparison of the Known (as Generated) and Predicted NH_3 Concentration for 27 Binary Mixture Exposures. Analysis Performed with the Gain Response Data Using 9 Eigenvectors in the Calibration.

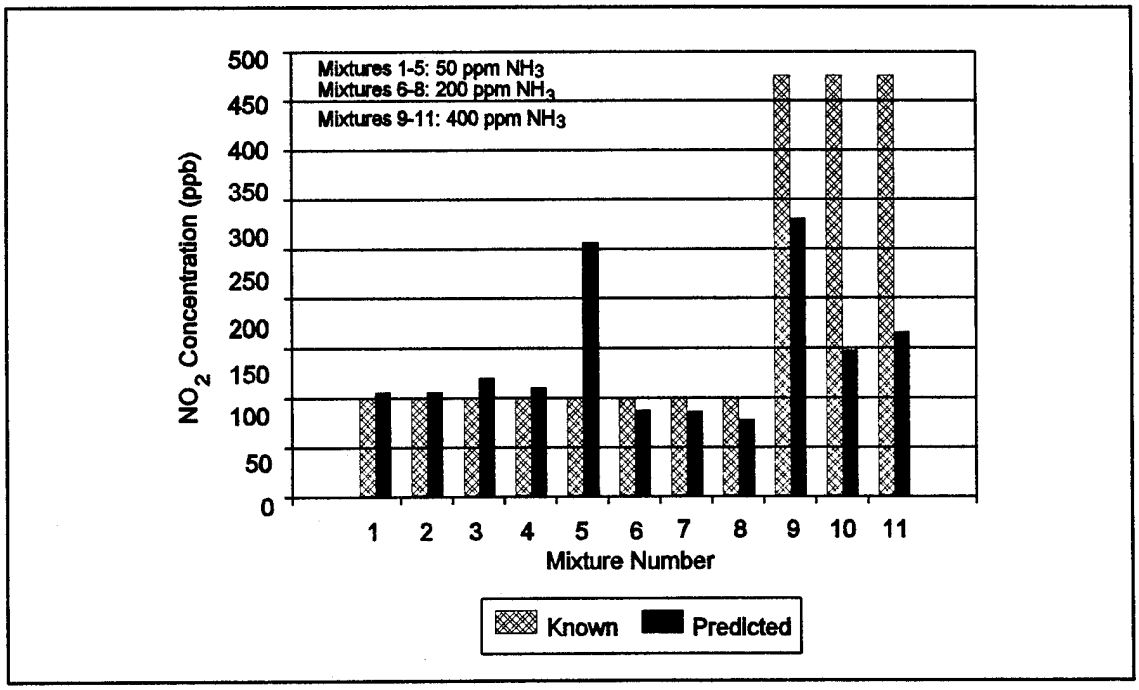


Figure VI-113. Comparison of the Known (as Generated) and Predicted NO_2 Concentration for 11 Binary Mixture Exposures. Analysis Performed with the Gain Response Data Using 9 Eigenvectors in the Calibration.

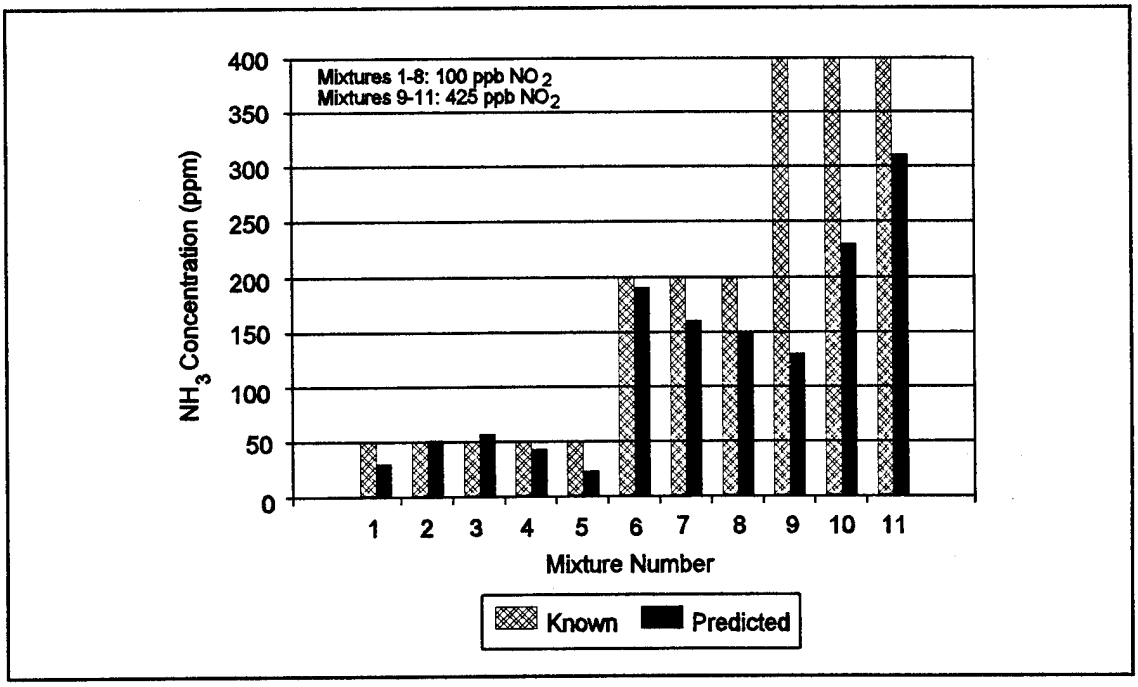


Figure VI-114. Comparison of the Known (as Generated) and Predicted NH_3 Concentration for 11 Binary Mixture Exposures. Analysis Performed with the Gain Response Data Using 9 Eigenvectors in the Calibration.

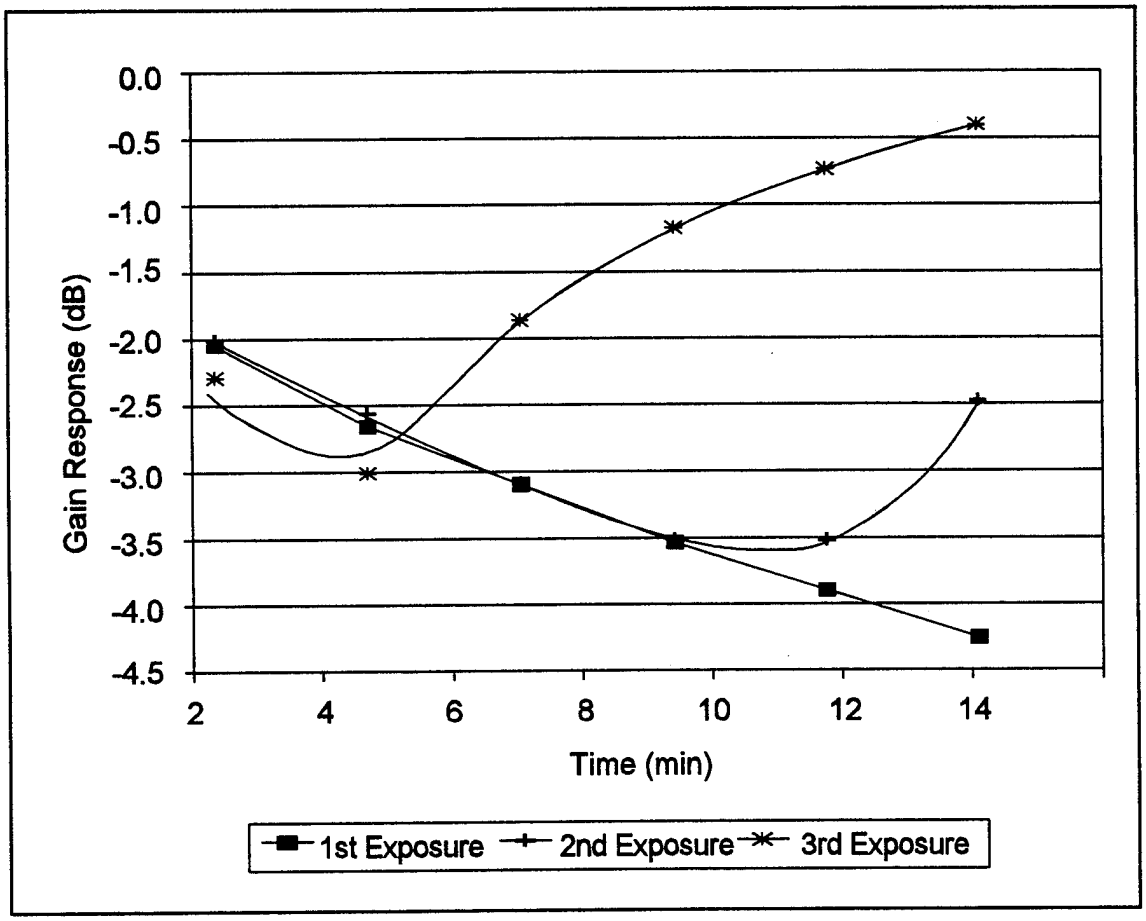


Figure VI-115. Time Dependence of the CuPc-Coated IGEFET Transfer Function Gain Response upon Repeated Exposure to the Binary Gas Mixture Composed of 50 ppm NH_3 and 100 ppb NO_2.

Gas Analysis Using the IGEFET Transfer Function Phase Response

Separate gas analyses were performed with the phase response data collected during exposure to NO_2, NH_3, and the binary gas mixtures. The following discussion describes the results obtained from each analysis.

Figure VI-116 shows that the error between the predicted NO_2 concentrations and the known test concentrations was minimized when the calibration was performed with three eigenvectors. The minimum error achieved was approximately 46%. A comparison of the predicted NO_2 concentrations (from the calibration set with three eigenvectors) relative to the known concentrations for each challenge gas exposure is shown in Figure VI-117. The known and predicted concentrations for mixture number 1 were not plotted since the predicted concentration was a negative quantity (physically unrealisitic). This Figure indicates that the predicted error was greatest for small NO_2 concentrations.

As shown in Figure VI-118, the minimum prediction error (18%) in the analysis of the NH_3 single component exposures was achieved with 2 eigenvectors. A large increase in the error was observed if the calibration was performed with more than 3 eigenvectors. A comparison of the predicted NH_3 concentrations (from the calibration set with two eigenvectors), relative to the known concentrations for each gas challenge exposure, is shown in Figure VI-119.

Figure VI-120 shows the prediction error dependence on the number of eigenvectors for each component gas along with the total error for both gases obtained from the analysis of 27 binary mixtures in the calibration set (Table VI-6). While the minimum error in the prediction of the NO_2 component was achieved with two eigenvectors, the minimum error in the predicted NH_3 concentrations was achieved with 4 eigenvectors. However, the error in the predicted NO_2 concentrations did not increase significantly until the number of eigenvectors used in the calibration set exceeded four eigenvectors. Thus, the minimum total error for both gas components was achieved with four eigenvectors. The resulting minimum errors in the predicted NO_2 and NH_3 concentrations were 72% and 28%, respectively. A comparison of the predicted NO_2 and NH_3 concentrations (from the calibration set with four eigenvectors), relative to the known concentrations for each challenge gas exposure, are shown in Figures VI-121 and VI-122. In the analysis of the 11 binary mixtures not included in the calibration set (Table VI-6), the prediction error was also minimized with four eigenvectors. For these 11 binary mixtures, the NO_2 and NH_3 prediction errors (as defined by Equation VI-9) were 57% and 42%, respectively. Figures VI-123 and VI-124 show the predicted and known NO_2 and NH_3 concentrations for each of these binary mixtures.

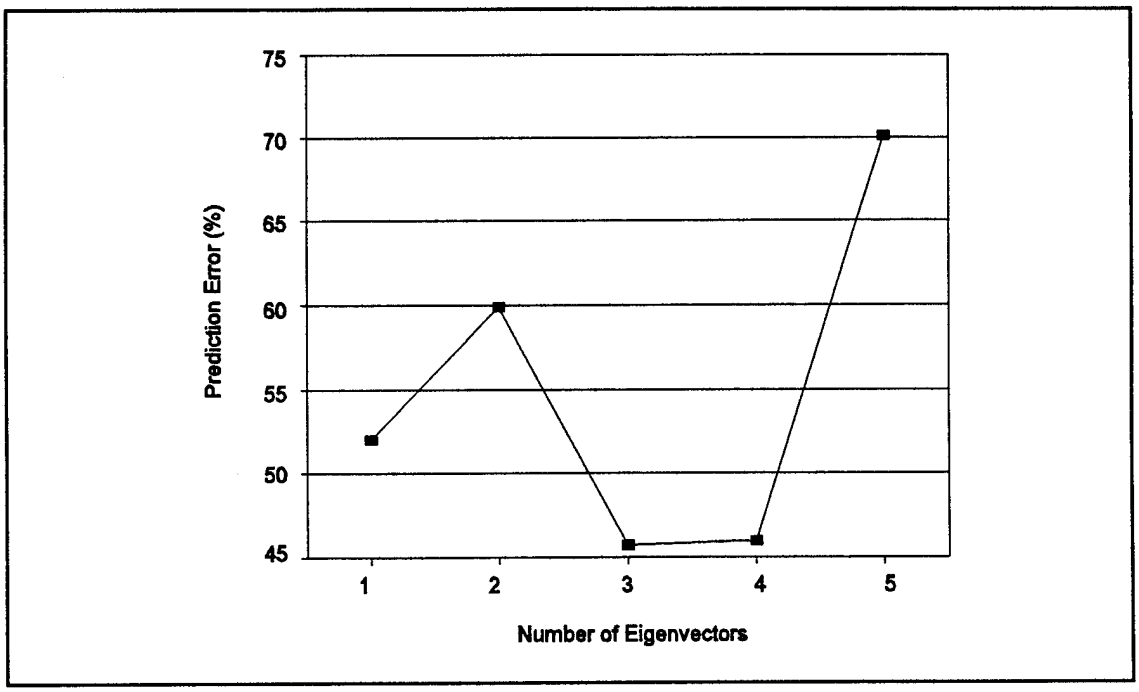


Figure VI-116. Prediction Error of the NO_2 Concentration for 15 Challenge Gas Exposures as a Function of the Number of Eigenvectors Used in the Calibration. Analysis Performed with the Phase Response Data.

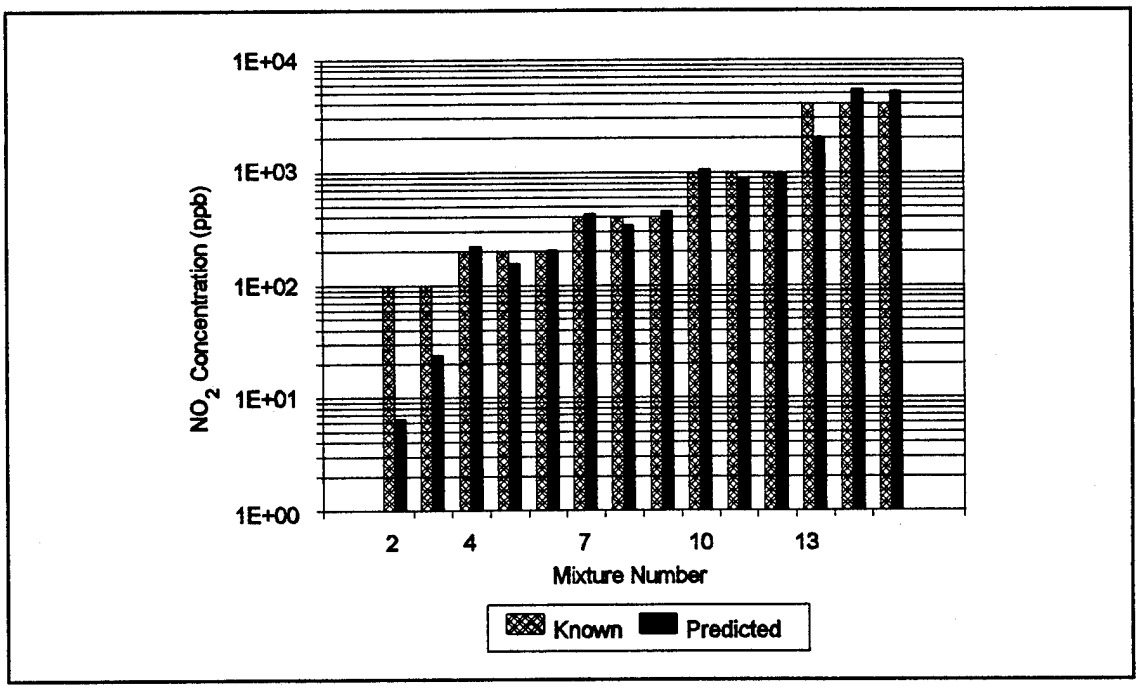


Figure VI-117. Comparison of the Known (as Generated) and Predicted NO_2 Concentration for 15 Challenge Gas Exposures. Analysis Performed with the Phase Response Data Using 3 Eigenvectors in the Calibration.

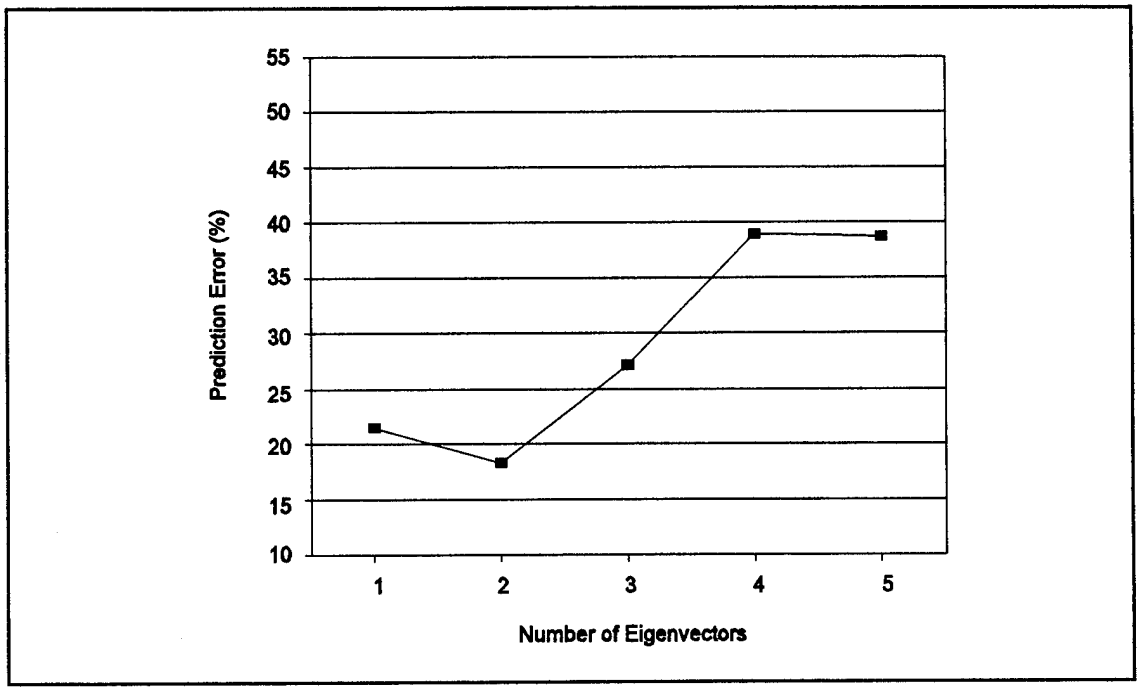


Figure VI-118. Prediction Error of the NH_3 Concentration for 15 Challenge Gas Exposures as a Function of the Number of Eigenvectors Used in the Calibration. Analysis Performed with the Phase Response Data.

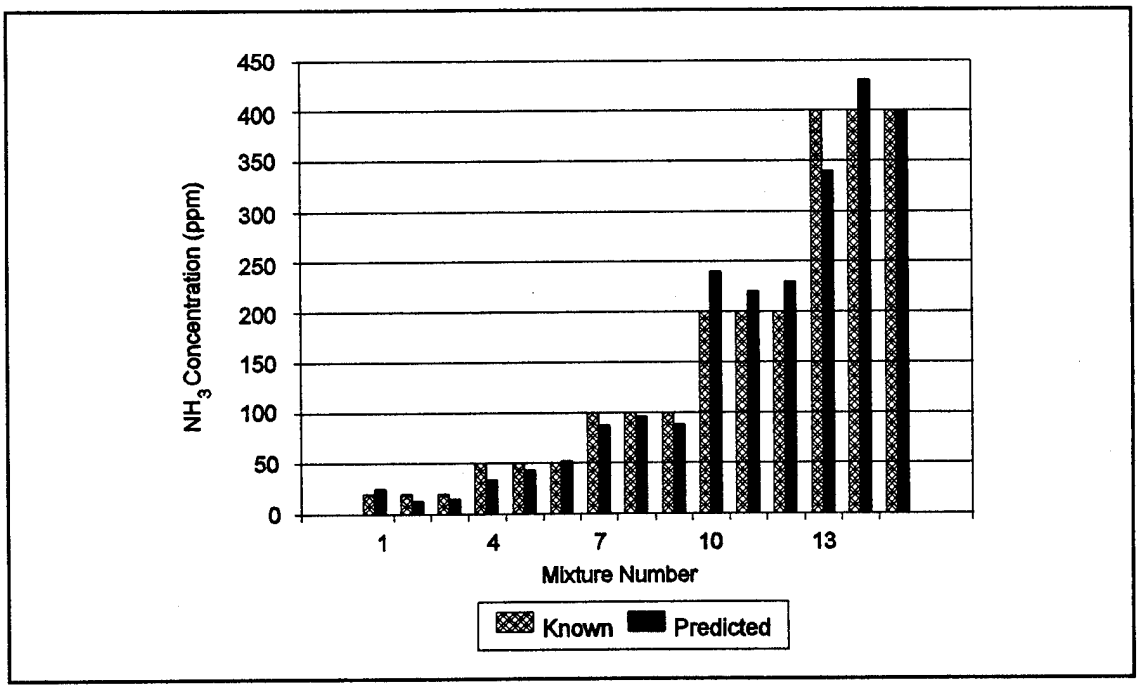


Figure VI-119. Comparison of the Known (as Generated) and Predicted NH_3 Concentrations for 15 Challenge Gas Exposures. Analysis Performed with the Phase Response Data Using 3 Eigenvectors in the Calibration.

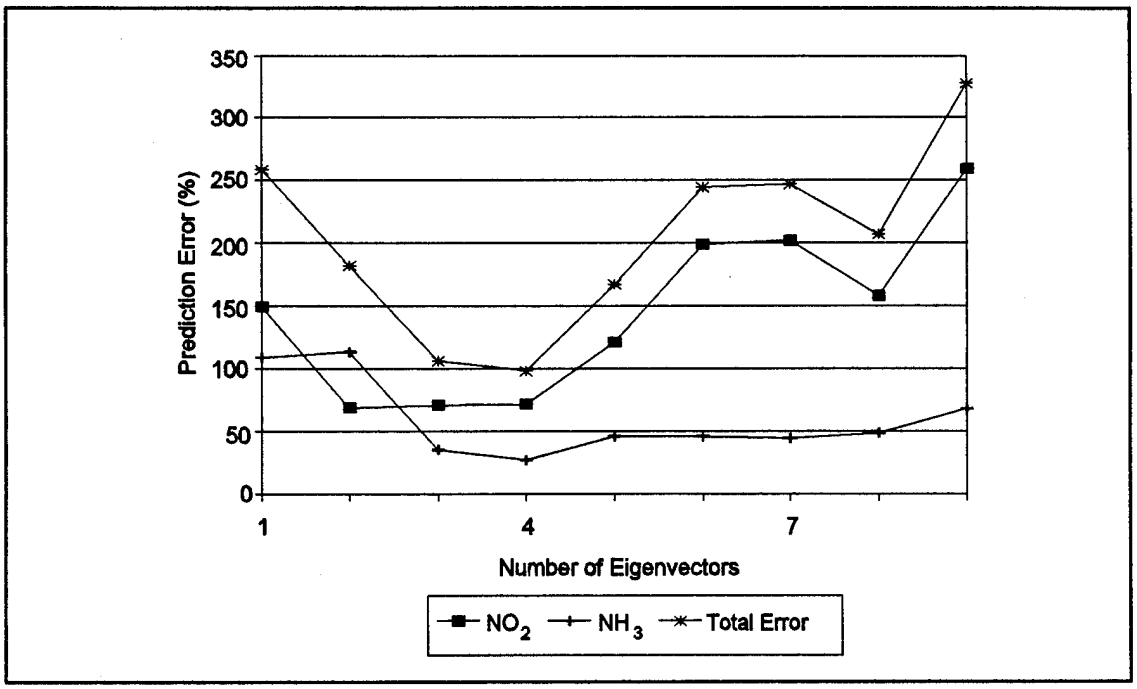


Figure VI-120. NO_2, NH_3, and Total Prediction Error for 27 Binary Gas Mixtures as a Function of the Number of Eigenvectors Used in the Calibration. Analysis Performed with the Phase Response Data.

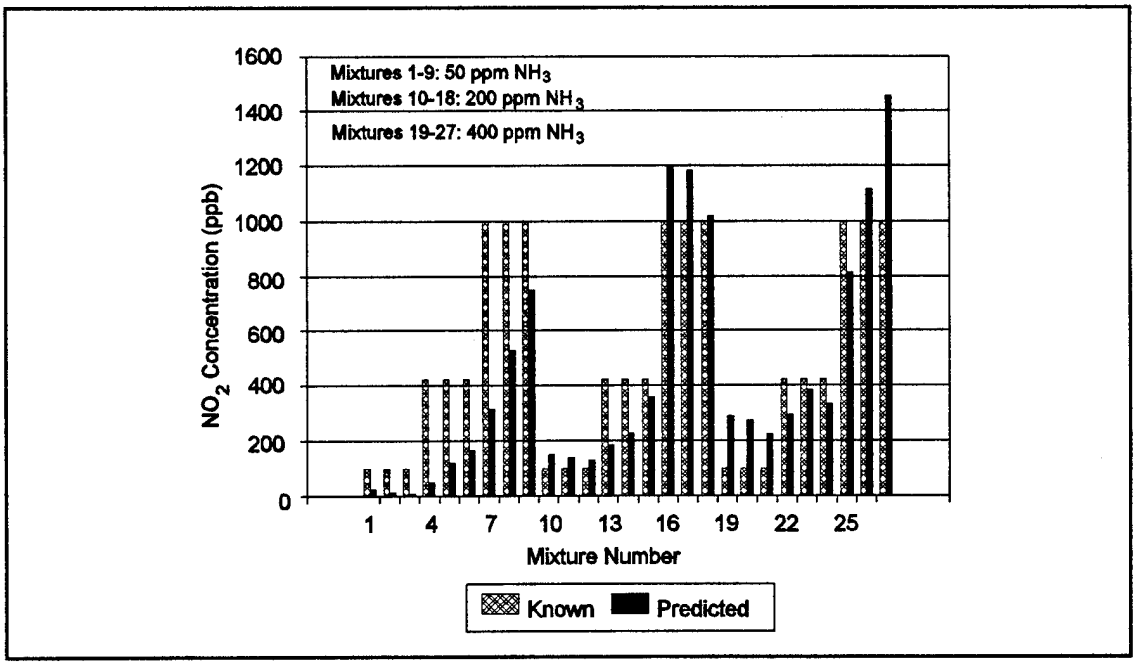


Figure VI-121. Comparison of the Known (as Generated) and Predicted NO_2 Concentration for 27 Binary Mixture Exposures. Analysis Performed with the Phase Response Data Using 4 Eigenvectors in the Calibration.

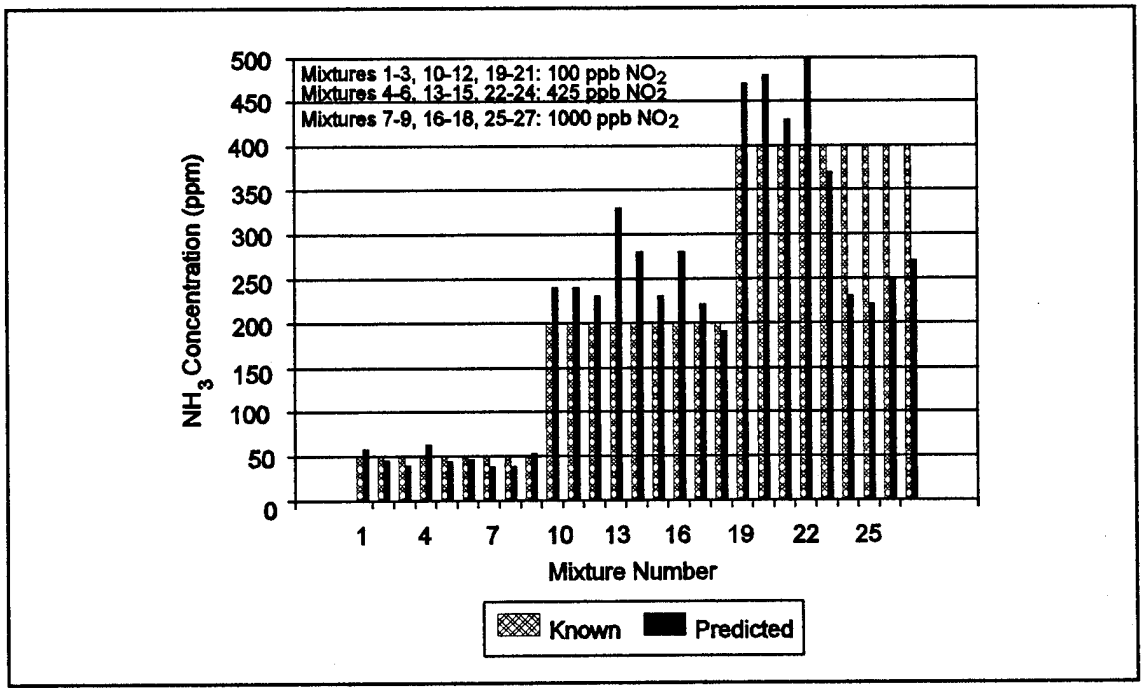


Figure VI-122. Comparison of the Known (as Generated) and Predicted NH_3 Concentration for 27 Binary Mixture Exposures. Analysis Performed with the Phase Response Data Using 4 Eigenvectors in the Calibration.

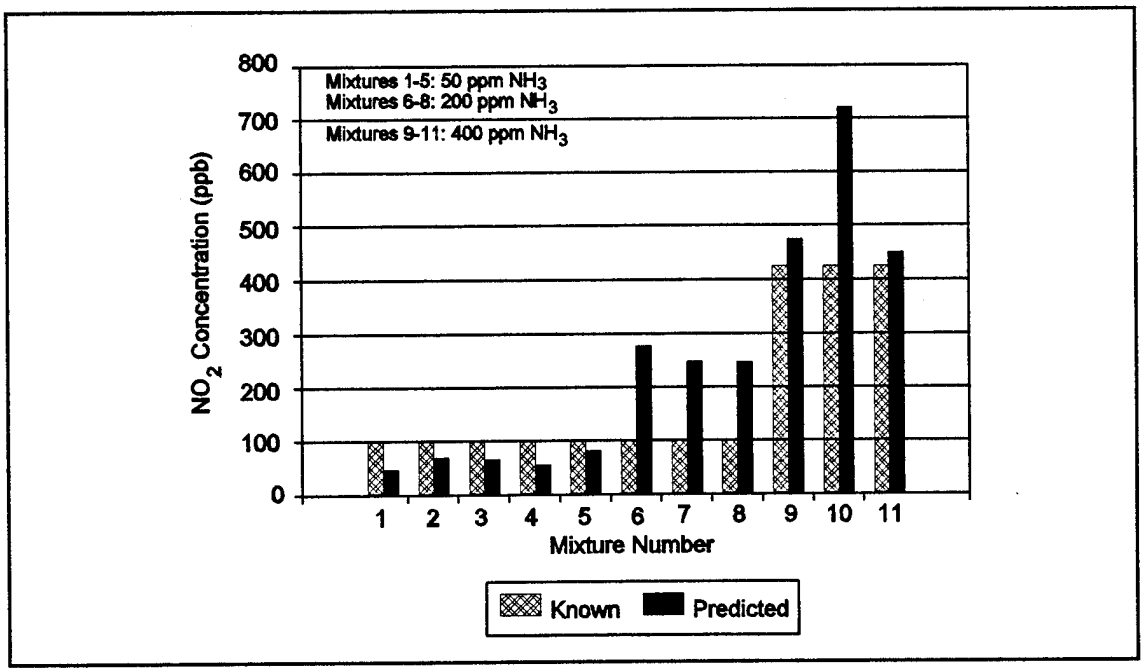


Figure VI-123. Comparison of the Known (as Generated) and Predicted NO_2 Concentration for 11 Binary Mixture Exposures. Analysis Performed with the Phase Response Data Using 4 Eigenvectors in the Calibration.

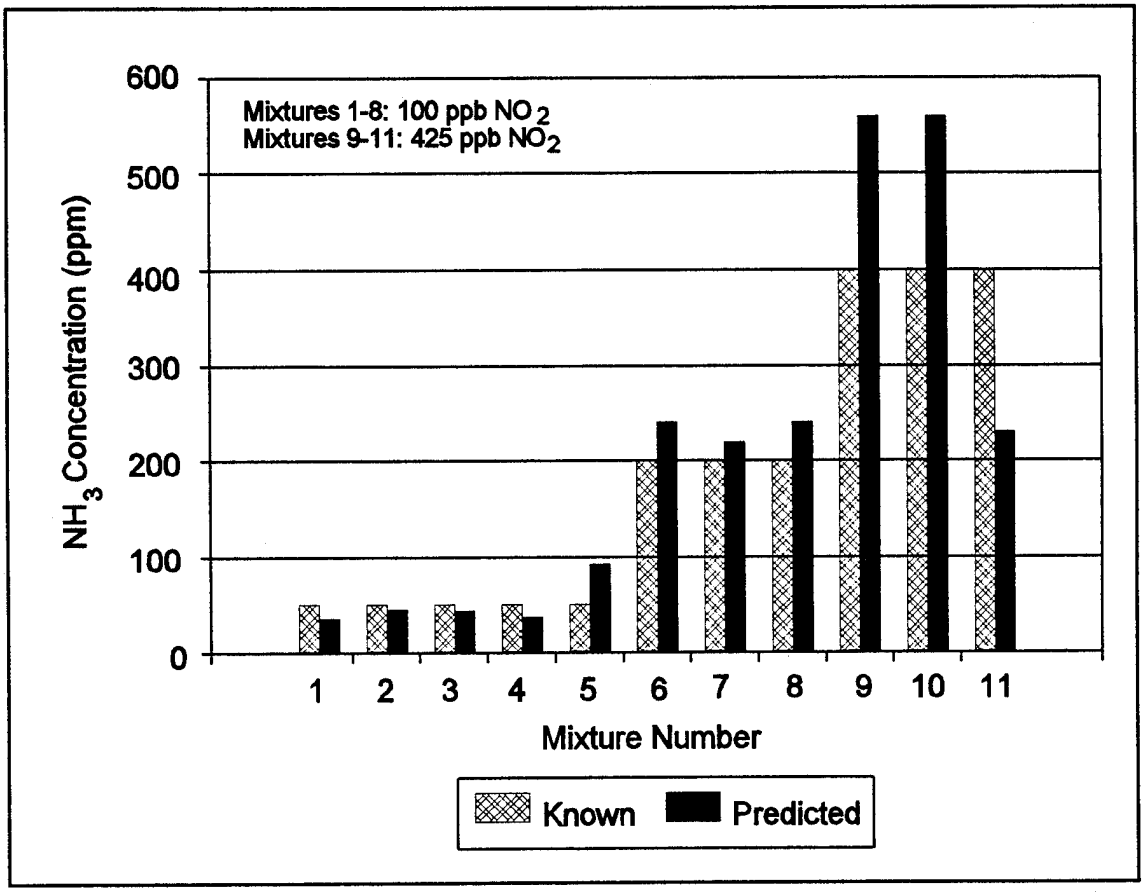


Figure VI-124. Comparison of the Known (as Generated) and Predicted NH_3 Concentration for 11 Binary Mixture Exposures. Analysis Performed with the Phase Response Data Using 4 Eigenvectors in the Calibration.

Gas Analysis Using the Conductance Parameters Extracted from the IGEFET Transfer Function Response

The extracted conductance parameters were only used for the single component NO_2 analysis. Figure VI-125 reveals that the error between the predicted NO_2 concentrations and the known test concentrations was minimized when the calibration was performed with four eigenvectors. The minimum error achieved was approximately 29%. This error was much less than the error achieved with the single component NO_2 analyses using the gain and phase response, and it was only slightly greater than the minimum error achieved in the analysis performed with the normalized DC resistance. The prediction error did not vary significantly with less than four eigenvectors, but it increased dramatically with five eigenvectors. A comparison of the predicted NO_2 concentrations (from the calibration set with four eigenvectors), relative to the known concentrations for each challenge gas exposure, is shown in Figure VI-126. This Figure indicates that the predicted error was dominated by the error associated with the 4000 ppb NO_2 concentrations.

Summary of the Gas Analyses

Three separate gas analyses were performed to demonstrate the ability to predict the gas concentrations in single component and binary gas mixtures of nitrogen dioxide and ammonia from the changes induced in the electrical properties of the MPc-coated IGEFET sensors. The analyses were conducted with the measured response of the IGE structure's DC resistance, as well as the IGEFET transfer function's gain and phase, upon gas exposure. A fourth gas analysis was performed using an equivalent electrical circuit model to evaluate the IGE inter-electrode conductance parameters as potential discriminant features for predicting the concentration of NO_2 within a challenge gas mixture. Each of the measured responses was normalized to account for baseline drift. The gas components in the binary mixtures were discriminated on the basis of the opposite changes (sign change) induced in the electrical properties of the MPc-coated IGEFET sensors upon exposure to each challenge gas, the different gas sensitivities manifested by the three MPc films, the time dependence of the electrical changes upon gas exposure, and the different gas sensitivities of the frequency components within the MPc-coated IGEFET transfer function. The prediction error calculated from the known (as generated) concentrations and the predicted concentrations was used to evaluate the predictive capability of the analyses performed with each measurement type.

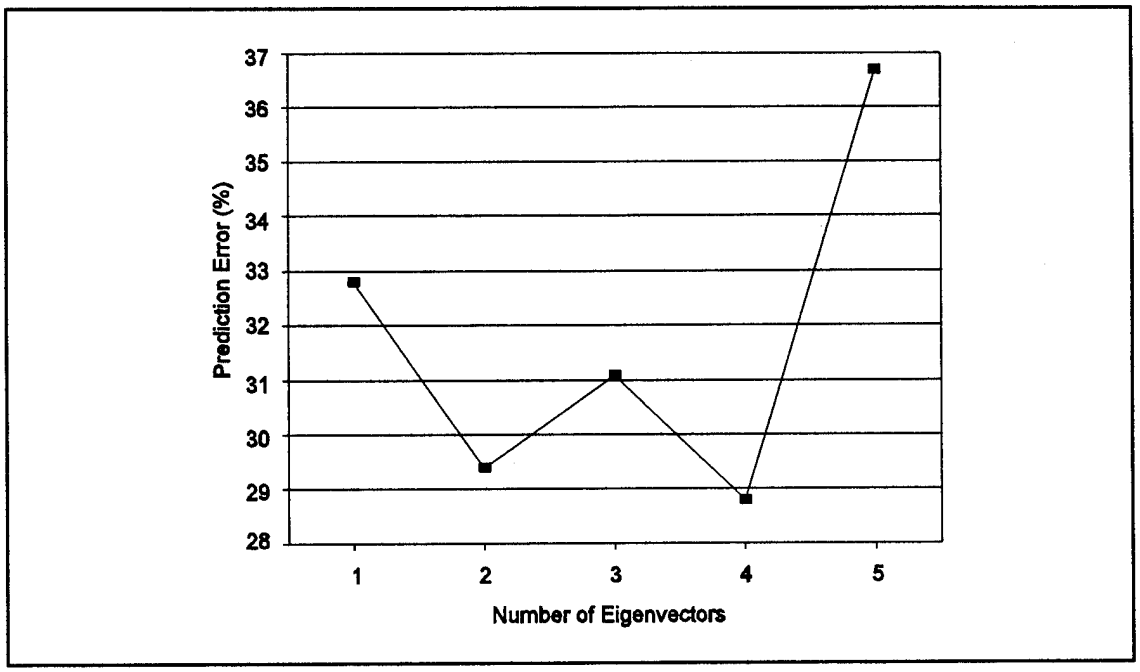


Figure VI-125. Prediction Error of the NO_2 Concentration for 15 Challenge Gas Exposures as a Function of the Number of Eigenvectors Used in the Calibration Set. Analysis Performed with the Conductance Parameters Extracted from the IGEFET Transfer Function Gain and Phase Data.

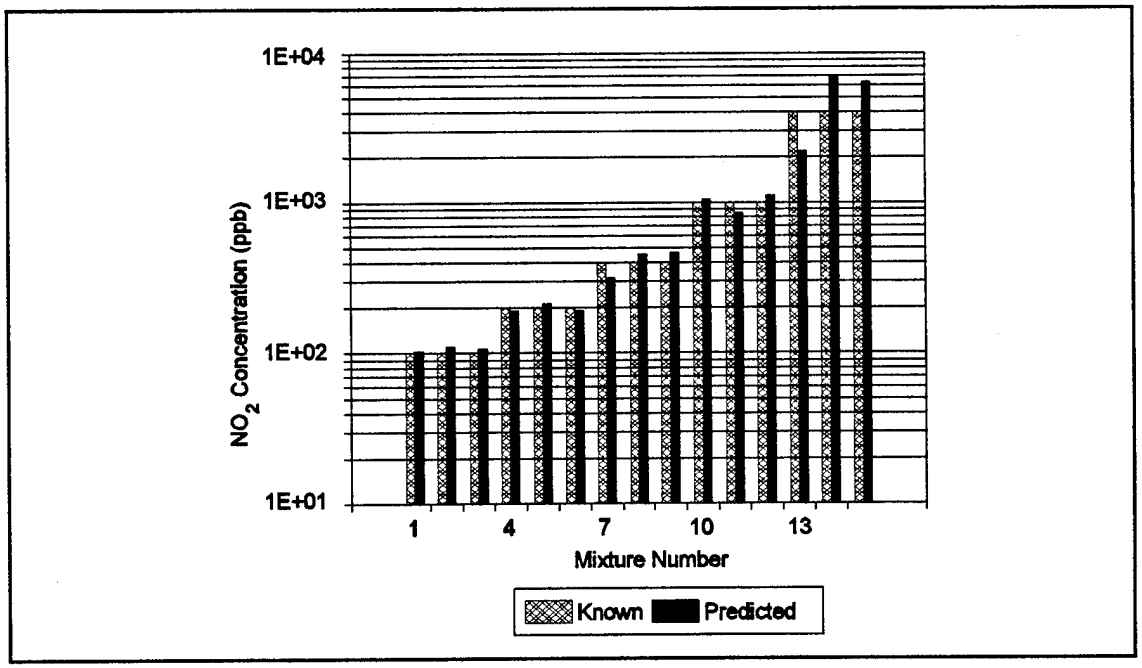


Figure VI-126. Comparison of the Known (as Generated) and Predicted NO_2 Concentration for 15 Challenge Gas Exposures. Analysis Performed with the Conductance Parameters Extracted from the IGEFET Transfer Function Gain and Phase Data Using 4 Eigenvectors in the Calibration.

Table VI-7 summarizes the results of the gas analyses conducted with each type of electrical measurement. The predicted gas concentrations were generally within 50% of the known concentrations for all analyses. The smallest error was achieved with the single component analysis of each test gas using the normalized DC resistance response data. As expected, the error increased for the binary gas mixture analyses using the normalized DC resistance response. This behavior is contrasted by the analyses conducted with the gain response data. With the gain response data, a larger error was observed in the predicted concentrations of the single component gases. Overall, the binary gas mixture analyses conducted with the gain response data yielded the least error in the predicted concentrations of the gas components. On the other hand, the phase response data was much less effective in predicting the gas component concentrations. Although the IGEFET gain and phase are derived from common electrical parameters, the analyses conducted with the gain and phase response data agreed poorly. The arbitrary visual selection of the discriminant features, as well as the non-linearities in the frequency response, likely contributed to the poor agreement. When the NO_2 analysis was conducted with the conductance parameters derived from an electrical model of the IGE structure, the prediction error was significantly less than the prediction error achieved with the gain and phase response features. Although the electrical model was unable to account for all of the variation in the gain and phase Bode plots, it did provide a consistent means for reducing the IGEFET transfer function non-linearities. However, the conductance parameters were no better at predicting the NO_2 concentrations compared to the normalized DC resistance technique.

Table VI-7. Prediction Error (%) Associated with the Gas Concentrations Obtained from the Four Analyses Conducted with each Type of Measured Data.

	Single Component Analysis		[1]Binary Mixture Analysis (27 mixtures)		[2]Binary Mixture Analysis (11 mixtures)	
Measurement Type	NO_2	NH_3	NO_2	NH_3	NO_2	NH_3
Normalized Resistance Response	26	14	14	47	38	38
Gain Response	42	40	25	27	12	38
Phase Response	46	18	72	28	57	42
Conductance Parameters	29	-	-	-	-	-

[1]Analysis of Binary Mixtures in Calibration Set
[2]Analysis of Binary Mixtures in Test Set (Not Included in Calibration Set)

VII. *Conclusions and Recommendations*

This research has demonstrated the analysis of single component and binary gas mixtures of NO_2 and NH_3 with a microsensor possessing an array of Interdigitated Gate Electrode Field Effect Transistor (IGEFET) sensor elements utilizing CuPc, NiPc, and CoPc thin films as the chemically-sensitive component. A finite-difference model of the interdigitated gate electrode structure confirmed the fundamental operation of the IGEFET microsensor. Direct current and alternating current electrical measurements were used to monitor the interaction of the challenge gas with the MPc-coated IGEFET microsensor. A unique time dependence in the IGEFET electrical response upon exposure to the binary gas mixture was revealed. The time dependence, as well as other features of the electrical response upon gas exposure, were extracted and analyzed with the mulitvariate statistical analysis techniques, principal component analysis (PCA) and multilinear regression, to determine the gas concentrations for the single component and binary challenge gas mixtures. The significant accomplishments derived from this research can be categorized into three areas: microsensor design and analysis, microsensor operation, and gas analysis.

The major accomplishments associated with the microsensor design and analysis was the implementation of several novel design features and the development of a finite-difference model to predict the IGEFET's electrical behavior. The key design features included the incorporation of a common ground plane, the isolation of IGEFET sensing elements, and the microsensor's associated amplifier design. The ground plane eliminated the parasitic metal-oxide-semiconductor capacitor beneath the interdigitated gate electrode structure which was present in the previous designs. Except for the ground plane, each IGEFET sensing element did not share any common connections, and therefore, failure of an individual sensing element could be isolated. The integration of an in-situ MOSFET operational amplifier with the interdigitated gate electrode structure permitted stable IGEFET operation at temperatures up to 170° C. To analyze the electrical behavior of the IGEFET design, a finite-difference model of the IGE structure was developed. The finite-difference model computes the transfer function gain and phase of an IGE structure coated with a lossy dielectric film whose thickness spans 0.1 to 7.5 μm, or is considered to be semi-infinite. This model eliminates the infinitely thin electrode approximation utilized in previously reported models of interdigitated electrode structures. The model also accounts for the previously unreported oxide overetch (undercut) within the inter-electrode space revealed in cross-sectional scanning electron microscopy images of the IGE structure. The model results were verified experimentally, and they were confirmed by comparing them with previously published

data. The finite-difference model helped to identify experimental configuration improvements, such as voltage feedback for stable amplifier operation, as well as the removal of the floating-gate bond wire to eliminate the effect of load capacitance on the measured transfer function. The uncoated IGE structure's input (electrode-to-ground) and through (inter-electrode) impedances were accurately predicted by the finite-difference model of the IGE structure. The impedance measurements were also shown to be consistent with the measured and computed transfer function of the uncoated IGEFET sensor. The development of the finite-difference model will facilitate the development of future IGEFET microsensors by providing a tool to predict the IGEFET transfer function for a wide range of geometries and material parameters.

With respect to the operational mode of the microsensor, the implementation of the IGEFET microsensor design facilitated an alternating current operating mode, in addition to the conventional direct current operating mode previously utilized with chemiresistor arrays. As was shown in this research, the large impedances of the interdigitated gate electrode structure (the chemiresistor portion) often exceed the dynamic range of the impedance analyzer instrumentation, and thus, limits the usefulness of this measurement. The integration of the IGE structure with the operational amplifier permits accurate measurement of the IGE AC transfer function, and indirectly, the measurement of the IGE impedances. By utilizing two IGEFET microsensors, the direct current and alternating current electrical response of the MPc thin films to challenge gas exposure can be measured simultaneously, and subsequently used for gas analysis. Another feature of the IGEFET electrical response that was subsequently used for gas analysis was revealed by operating the microsensor with a relatively long exposure duration (approximately 16 minutes). Over this time interval, the IGEFET electrical response exhibited a unique non-monotonic time dependence, with an initial electrical response corresponding to the ammonia component during the first 5 minutes, followed by a reversal of the electrical response attributed to the nitrogen dioxide component. This behavior indicates that the ammonia component, which was present at 50-4000 times the nitrogen dioxide concentration, adsorbs on the MPc-surface prior to significant adsorption of the NO_2 component.

In the area of gas analysis, the stated objective to analyze a binary gas mixture with an array of IGEFET sensing elements was accomplished. Utilizing principal component analysis (PCA) and multilinear regression of the features extracted from the DC and AC electrical response of an array of IGEFET sensing elements coated with CuPc, NiPc, and CoPc films, the gas concentrations in single component and binary gas mixtures of nitrogen dioxide and ammonia were determined. Gas analyses were conducted with features identified in the measured response of the IGE structure's DC resistance,

as well as the IGEFET transfer function's gain and phase, to challenge gas mixtures containing 100-4000 ppb NO_2 and 20-400 ppm NH_3. The gas components in the binary gas mixtures were discriminated on the basis of the opposite changes (sign change) induced in the electrical properties of the MPc-coated IGEFET sensors upon exposure to each challenge gas type, the different gas sensitivities manifested by the MPc films, the time dependence of the electrical changes upon gas exposure, and the different gas sensitivities of the frequency components within the MPc-coated IGEFET transfer function. The predicted concentrations were generally within 50% of the known concentrations for all of the gas analyses. The smallest error (14% for ammonia and 26% for nitrogen dioxide) was achieved with the single component analysis of each test gas using the normalized DC resistance response data. The error in the predicted single component gas concentrations were significantly larger (typically 40%) when the analyses were conducted with the IGEFET transfer function's gain and phase response. For the binary gas mixture analysis, the smallest error in the predicted concentrations of the gas components (approximately 25% for each component) was achieved with the gain response data. In contrast, the phase response data was the least effective measurement for predicting the gas component concentrations. The arbitrary visual selection of discriminant features, as well as nonlinearities in the frequency response likely contributed to the poor agreement. A lumped-element circuit model, which accounted for most of the variation observed in the gain and phase Bode plots, provided a consistent approach for selecting discriminant features. When the nitrogen dioxide analysis was performed with the conductance parameters extracted from the lumped-element circuit model, the predicted error in the gas concentration was significantly less than the prediction error achieved with the gain and phase response features, and was equivalent to the error obtained with the normalized DC resistance.

With respect to recommendations for further work, improvements can be made in the design and operation of the MPc-coated IGEFET microsensor to improve performance. The bond pad layout of the IGEFET microsensor design could be modified to provide additional separation between the corresponding driven- and floating-gate electrode bond pads to minimize electrical leakage paths . The redesign could also incorporate a guard ring around each interdigitated gate electrode structure. The gas exposure cycle needs to be modified to reduce the excessively long purge time required to re-establish the pre-exposure baseline. A shorter gas exposure period (on the order of five to ten minutes) would be sufficient to observe the time response of the MPc-coated IGEFET microsensor, and should correspondingly reduce the purge time. Computer controlled flowmeters and valves would facilitate the shorter gas exposure period and improve repeatability.

Perhaps the most important issue is the possible interaction of ammonia and nitrogen dioxide on the MPc surface. This research indicates that the reversibility of the IGEFET sensor response to a binary gas mixture of nitrogen dioxide and ammonia was much slower compared to the exposure response envelope associated with either of the single component gases. The gas exposure cycle should be established in consonance with the challenge gas mixture with the longest time response. Finally, the conductance parameters extracted from the lumped-element circuit model manifested significantly better predictive capability compared to the gain and phase response features, and they should be evaluated as discriminant features in the analysis of binary gas mixtures.

Bibliography

1. Department of Defense. Design and Acquisition of Nuclear, Biological, Chemical (NBC) Contamination-Survivable Systems. DoD Instruction 4245.13. Washington: Government Printing Office, 15 Jun 1987.

2. Ancman, 2Lt Eileen G. "Weapon System Vulnerability/Survivability in a Chemical Warfare Environment". Presented at the Air University's Symposium on Low Intensity Conflict. Maxwell AFB AL, 11-13 Mar 1985.

3. LaVoie, J., Senior Scientist. Personal Interview. EG&G Mound Applied Technologies, Inorganic Materials and Compatibility Group, Miamisburg, OH, 10 Feb 1988.

4. Carey, P. and B. Kowalski. "Monitoring a Dryer Operation Using an Array of Piezoelectric Crystals", Analytical Chemistry, 60: 541-544, 1988.

5. LaVoie, J., Senior Scientist. Personal Interview. EG&G Mound Applied Technologies, Inorganic Materials and Compatibility Group, Miamisburg OH, 10 April 1990.

6. Schiede, E. and G. Guilbault. "Piezoelectric Detectors for Organophosphorus Compounds and Pesticides", Analytical Chemistry, 44: 1764-1768, 1972.

7. Guilbault, G., Y. Tomita, and E. Kolesar. "A Coated Piezoelectric Crystal Coating for Detection of Organophosphorus Compounds and Pesticides", Sensors and Actuators, 2: 43-47, 1981.

8. Guilbault, G. et al. "Piezoelectric Crystal Coating for Detection of Organophosphorus Compounds", Analytical Chemistry, 53: 2057-2060, 1981.

9. King, W. "Piezoelectric Sorption Detector", Analytical Chemistry, 9: 1735-1739, 1984.

10. Nieuwenhuizen, M. and A. Barendsz. "Processes Involved at the Chemical Interface of a SAW Chemosensor", Sensors and Actuators, 11: 45-62, 1987.

11. Venema, A. et al. "NO_2 Gas-Concentration Measurement with a SAW-Chemosensor", IEEE Transactions on Ultrasonics, Ferroelectrics, and Frequency Control, UFFC-34: 148-154, 1987.

12. Rapp, M. et al. "A New High-Frequency High-Sensitivity SAW Device for NO_2 Gas-Detection in the Sub-ppm Range", Sensors and Actuators, B 4: 103-108, 1991.

13. Nieuwenhuizen, M., A. Nederlof, and A. Barendsz. "Metallo-phthalocyanines as Chemical Interfaces on a Surface Acoustic Wave Gas Sensor for Nitrogen Dioxide", Analytical Chemistry, 60: 230-235, 1988.

14. Kolesar, E. "Electronic Detection of Low Concentrations of Organophosphorus Compounds with a Solid State Device Utilizing Supported Copper and Cuprous Oxide Films, PhD Dissertation, University of Texas, Austin, Texas, 1985.

15. Jones, T. and B. Bott. "Gas-Induced Electrical Conductivity Changes in Metal Phthalocyanines", Sensors and Actuators, 9: 27-37, 1986.

16. Burr, P., et al. "A Gas-Sensitive Field Effect Transistor Utilizing a Thin Film of Lead Phthalocyanine as the Gate Material", Thin Solid Films, 151: L111-L113, 1987.

17. Kolesar, E., Associate Professor of Electrical and Computer Engineering. Personal Interview. Department of Electrical and Computer Engineering, Air Force Institute of Technology (AU), Wright-Patterson AFB, OH, 2 May 1988.

18. Kolesar, E. and J. Wiseman. "Interdigitated Gate Electrode Field Effect Transistor for the Selective Detection of Nitrogen Dioxide and Diisopropyl Methylphosphonate", Analytical Chemistry 61: 2355-2361, 1989.

19. Rose-Pehrsson, S., et al. "Detection of Hazardous Vapors Including Mixtures Using Pattern Recognition Analysis from Surface Acoustic Wave Devices", Analytical Chemistry, 60: 2801-2811, 1988.

20. Weimar, U. et al. "Pattern Recognition Methods for Gas Mixture Analysis: Applications to Sensor Arrays Based upon SnO_2", Sensors and Actuators, B 1: 93-96, 1990.

21. Jenkins, T. Evaluation of Doped Phthalocyanines and a Chemically-Sensitive Field-Effect Transistor for Detecting Nitrogen Dioxide. MS Thesis, AFIT/GE/89D-18. Department of Electrical and Computer Engineering, Air Force Institute of Technology (AU), Wright-Patterson AFB, OH, 1989.

22. Shin, J. Evaluation of Chemically-Sensitive Field Effect Transistors for Detection of Organophosphorus Compounds. MS Thesis, AFIT/GE/89D-47. Department of Electrical and Computer Engineering, Air Force Institute of Technology (AU), Wright-Patterson AFB, OH, 1989.

23. Graham, Thomas E. Evaluation of an Interdigitated Gate Electrode Field-Effect Transistor (IGEFET) for *In Situ* Resin Cure Monitoring. MS Thesis, AFIT/GE/90D-XX. Department of Electrical and Computer Engineering, Air Force Institute of Technology (AU), Wright-Patterson AFB, OH, 1990.

24. Jenkins, T. Unpublished Results. Department of Electrical and Computer Engineering, Air Force Institute of Technology (AU), Wright-Patterson AFB, OH, 1990.

25. Howe, C. Characterizing the Sensitivity, Selectivity, and Reversibility of the Metal-Doped Phthalocyanine Thin-Films Used with the Interdigitated Gate Electrode Field-Effect Transistor (IGEFET) to Detect Organophosphorus Compounds and Nitrogen Dioxide. MS Thesis, AFIT/GE/ENG/91D-26, Department of Electrical and Computer Engineering, Air Force Institute of Technology (AU), Wright-Patterson AFB, OH, 1991.

26. Wright, J. "Gas Adsorption on Phthalocyanines and Its Effect on Electrical Properties", Progress in Surface Science, 31: 1-60, 1989.

27. Moser, F. and A. Thomas. The Phthalocyanines. Vol II: Applications. Boca Raton, Florida: CRC Press, Inc., 1983.

28. Moser, F. and A. Thomas. Phthalocyanine Compounds. New York: Reinhold Publishing, Inc., 1963.

29. Lever, A. "The Phthalocyanines", Advances in Inorganic Chemistry and Radiochemistry, edited by H. Emeleus and A. Sharpe. New York: Academic Press, Inc., 1965.

30. Moser, F. and A. Thomas. The Phthalocyanines. Vol I: Properties. Boca Raton, Florida: CRC Press, Inc., 1983.

31. Garrett, C. "Organic Semiconductors", Semiconductors, edited by N. Hannay. New York: Reinhold Publishing Corp., 1959.

32. Wright, J. Molecular Crystals. Cambridge: Cambridge University Press, 1987.

33. Inokuchi, H. and H. Akamutu. "Electrical Conductivity of Organic Semiconductors", Solid State Physics: Advances in Research and Applications, edited by F. Seitz and D. Turnbull. New York: Academic Press, Inc., 1961.

34. Gutmann, F. and L. Lyons. Organic Semiconductors. New York: John Wiley and Sons, Inc., 1967.

35. Bolto, B. "Semiconducting Organic Polymers Containing Metal Groups", Organic Semiconducting Polymers, edited by J. Katon. New York: Marcel Dekker, Inc., 1968.

36. Gutmann, F. et al. Organic Semiconductors Part B. Malabar, Florida: Robert E. Kreiger Publishing Co., 1983.

37. Simon, J. and J. Andre. Molecular Semiconductors: Photoelectrical Properties and Solar Cells, edited by J. Lehn and C. Rees, Berlin: Springer - Verlag, 1985.

38. Brown, C. "Crystal Structure of β-Copper Phthalocyanine", Journal of the Chemical Society, A: 2488-2493, 1968.

39. Mason, R., G. Williams, and P. Fielding. "Structural Chemistry of Phthalocyaninato-Cobalt (II) and Manganese (II)", Journal of Chemical Society Dalton, 676-683, 1979.

40. Ukei, K. "Lead Phthalocyanine", Acta Crystallographica, B 29: 2290-2292, 1973.

41. Iyechika, Y. et al. "Structure of Lead Phthalocyanine (Triclinic Form)", Acta Cryst., B 38: 766-770, 1982.

42. Robertson, J. "An X-Ray Study of the Structure of the Phthalocyanines. Part I. The Metal-free, Nickel, Copper, and Platinum Compounds", Journal of the Chemical Society, Part I: 615-621, 1935.

43. Robertson, J. and I. Woodyard. "An X-Ray Study of the Structure of the Phthalocyanines. Part III. Quantitative Structure Determination of Nickel Phthalocyanines", Journal of the Chemical Society, Part I: 219-230, 1937.

44. Robertson, J. Organic Crystals and Molecules: Theory of X-Ray Structure Analysis with Applications to Organic Chemistry. Ithaca, New York: Cornell University Press, 1953.

45. Linstead, R. and J. Robertson. "The Stereochemistry of Metallic Phthalocyanines", Journal of the Chemical Society, Part II: 1736-1738, 1936.

46. Barrett, P., C. Dent, and R. Linstead. "Phthalocyanine as a Co-ordinating Group. A General Investigation of the Metallic Derivatives", Journal of the Chemical Society, Part II: 1719-1735, 1936.

47. Gould, R. "Dependence of the Mobility and Trap Concentration in Evaporated Copper Phthalocyanine Thin Films on Background Pressure and Evaporation Rate", J. Phys. D., 9: 1785-1790, 1986.

48. Snow, A. and W. Barger. "Phthalocyanine Films in Chemical Sensors". Phthalocyanines: Properties and Applications, edited by C. Leznoff and A. Lever, New York: VCH Publishers, Inc., 1989.

49. Sidorov, A. and I. Kotylar. "Infrared Spectra of Phthalocyanines. I. The Effect of Crystalline Structure and of the Central Metallic Atom on the Phthalocyanine Molecule in the Solid State", Optics and Spectroscopy, 11: 92 -96 (1961).

50. Mohammed, K. and R. Collins. "Phase Behavior of Copper and Zinc Phthalocyanines", Thermochimica Acta, 104: 377-381, 1986.

51. Collins, R. and K. Mohammed. "Phase Behavior of Cobalt, Nickel, and Zinc Phthalocyanines", Thermochimica Acta, 109: 397-402, 1987.

52. Schaffer, A., M. Gouterman, and E. Davidson. "Porphyrins XXVIII. Extended Hückel Calculations on Metal Phthalocyanines and Tetrazaporphins", Theoretica Chimica Acta, 30: 9-30, 1973.

53. Ashida, M. "The Orientation Overgrowth of Metal-Phthalocyanines on the Surface of Single Crystals. I. Vacuum-Condensed Films on Muscovite", Bulletin of the Chemical Society of Japan, 39: 2625-2631, 1966.

54. Fryer J. "Molecular Images of Thin-Film Polymorphs and Phase Transformations in Metal-Free Phthalocyanine", Acta Crystallographica, A 35: 327-332, 1979.

55. Ashida, M. "The Orientation Overgrowth of Metal-Phthalocyanines on the Surface of Single Crystals. II. Vacuum-Condensed Films of Copper-phthalocyanine on Alkali Halides", Bulletin of the Chemical Society of Japan, 39: 2632-2638, 1966.

56. Ashida, M., N. Uyeda, and E. Suito. "Unit Cell Metastable-Form Constants of Various Phthalocyanines", Bulletin of the Chemical Society of Japan, 39 : 2616-2624, 1966.

57. Buchholz, J. and G. Somorjai. "The Surface Structures of Phthalocyanine Monolayers and Vapor-Grown Films: A Low-Energy Electron Diffraction Study", The Journal of Chemical Physics, 66 : 573-580, 1977.

58. Fryer, J. "Annealing Processes in Organic Crystal Films", Proceedings of the 37th Annual Electron Microscopy Society of America (EMSA) Meeting, San Antonio, Texas, 616-617, August 13-17, 1979.

59. Hamm, F. and E. Van Norman. "Transformations in Organic Pigments", Journal of Applied Physics, 19: 1097-1109, 1948.

60. Kobayashi, T., Y. Fujiyoshi, and N. Uyeda. "The Observation of Molecular Orientations in Crystal Defects and the Growth Mechanism of Thin Phthalocyanine Films", Acta Cryst., A 38: 356-362, 1982.

61. Kobayashi, T., Y. Fujiyoshi, and N. Uyeda. " High-Resolution TEM Images of Zinc Phthalocyanine Polymorphs in Thin Films", Acta Cryst., A 37: 692-697, 1981.

62. Menter, J. "The Direct Study by Electron Microscopy of Crystal Lattices and Their Imperfections", Proceedings of the Royal Society of London, A 236: 119-135, 1956.

63. Murata, Y., J. Fryer, and T. Baird. "Molecular Image of Copper Phthalocyanine", Journal of Microscopy, 108: 261-275, 1976.

64. Suito, E., and N. Uyeda. "A Study of the Dimorphism and the Crystal Habit of Copper-Phthalocyanine by Electron Micro-Diffraction Method", Proceedings of Japan Academy, 32: 182-187, 1956.

65. Suito, E., and N. Uyeda. "The Relation Between the Crystal Habit and the Lattice Image of Copper-Phthalocyanine", Proceedings of Japan Academy, 33: 398-402, 1957.

66. Uyeda, N. "The Solvent Effect on Crystal Transformations of Metal Phthalocyanines in Organic Suspensions", Progress in Organic Coatings, 2: 131-157, 1973/74.

67. Uyeda, N. and K. Ishizuka. "Effects of Spherical Aberration and Accelerating Voltage on Atomic Resolution in Molecular Images", Journal of Electron Microscopy, 23: 79-88, 1974.

68. Schoch, K., J. Greggi, and T. Temofonte. "Morphology of Metal Phthalocyanine Thin Films", Journal of Vacuum Science and Technology, A 6: 155-158, 1988.

69. Vincett, P., Z. Popovic, and L. McIntyre. "A Novel Structural Singularity in Vacuum-Deposited Thin Films: The Mechanism of Critical Optimization of Thin Film Properties", Thin Solid Films, 82: 357-376, 1981.

70. Vincett, P., W. Barlow, and G. Roberts. "Structure and Properties of Vacuum-Deposited Thin Films: A New Basic Relationship", Journal of Applied Physics, 48: 3800-3806, 1977.

71. Karasek, F. and J. Decius. "Observations Concerning Polymorphic Crystalline Modifications of the Phthalocyanines", Journal of the American Chemical Society, 74: 4716-4717, 1952.

72. Mindorff, M. and D. Brodie. "Some Properties of Metal-Free Amorphous Phthalocyanine Vacuum Deposited Films", Canadian Journal of Physics, 59: 249-254, 1981.

73. Sadtler Index of Infrared Spectra. Technical Report. Sadtler Research Laboratories, Inc., 1967.

74. Sadtler Index of Infrared Spectra. Technical Report. Sadtler Research Laboratories, Inc., 1972.

75. Sammes, M. "The Infrared Spectrum of Phthalocyanine: Assignment of N-H Modes", The Journal of the Chemical Society, Perkin II, 2: 160-162, 1972.

76. Kobayashi, T., et al. "The Metal-Ligand Vibrations in the Infrared Spectra of Various Metal Phthalocyanines", Spectrochimica Acta, 26 A: 1305-1311, 1970.

77. Kobayashi, T. "The Far Infrared Spectra of Phthalocyanines and Its Metal Derivatives", Spectrochimica Acta, 26 A: 1313-1322, 1970.

78. Ebert, A. and H. Gottlieb. "Infrared Spectra of Organic Compounds Exhibiting Polymorphism", The Journal of the American Chemical Society, 74: 2806-2809, 1952.

79. Kendall, D. "Identification of Polymorphic Forms of Crystals by Infrared Spectroscopy", Analytical Chemistry, 25: 382-389, 1953.

80. Knudsen, B. "Copper Phthalocyanine: Infrared Absorption Spectra of Polymorphic Modifications", Acta Chemica Scandinavica, 20: 1344-1350, 1966.

81. Ogordonik, K. "Alpha-, Beta-Polymorphism and IR Spectra of a Sublimated Phthalocyanine Layer", Optics and Spectroscopy, 39: 223-224, 1975.

82. Tyler, J. and S. Ehrhardt. "Infrared Spectra of Evaporated Films", Analytical Chemistry, 25: 390-394, 1953.

83. Sidorov, A. "The Infrared Spectra of the Phthalocyanines III: Interaction of Sublimed Layers of Phthalocyanines with Water Vapor", Optics and Spectroscopy, 13: 379-382, 1961.

84. Terenin, A. and A. Sidorov. "Infra-red Spectra of Phthalocyanines with Different Central Metal Atoms", Spectrochimica Acta, 11 Sup.: 573-578, 1957.

85. Sidorov, A. and A. Terenin. "Infrared Spectra of Phthalocyanines. II. Interaction of Sublimed Layers of Phthalocyanines with Gaseous CH_3COOH, HCl, and HBr", Optics and Spectroscopy, 11: 175-179, 1961.

86. Sauvage, F., M. Backer, and B. Stymne. "An Infrared Study of the Complexing Ability of Manganese Phthalocyanine", Spectrochimica Acta, 38 A: 281-288, 1982.

87. Steinbach, F. and M. Zobel. "Infrared Spectroscopic Investigation of the Formation of Adducts of Fe-Phthalocyanine with Hydrazine and Ammonia", The Journal of Chemical Society, Faraday Transactions I, 75: 2587-2593, 1979.

88. Steinbach, F. and H. Joswig. "Infrared Spectroscopic Investigation of Sorption of Nitric Oxide by β-Metal Phthalocyanines of the First Transition Period", The Journal of Chemical Society, Faraday Transactions I, 75: 2594-2600, 1979.

89. Ercolani, C., C. Neri, and G. Sartori. "Phthalocyanines of Metals of the First Transition Series. Part II. Influence of the Crystal Features on the Interaction with Nitric Oxide and on the M-(NO) Moiety", The Journal of the Chemical Society, A: 2123-2127, 1968.

90. Honeybourne, C. and R. Ewen. "Dark DC Conductivity and Spectroscopy of Clean and Gas Doped Thin Films of Organic Semiconductors", Journal of Physics and Chemistry of Solids, 44: 215-223, 1983.

91. Sadaoka, Y. et al. "Effect of Adsorbed Oxidative Gases on Electrical Properties of Evaporated Films Of Phthalocyanines", Denki Kagaku, 50: 457-462, 1982.

92. Schoch, K. and T. Temofonte. "IR Response of Phthalocyanine Thin Films to Nitrogen Dioxide", Thin Solid Films, 165: 83-89, 1988.

93. McKelvey, J. Solid State and Semiconductor Physics, Malabar, Florida: Robert E. Krieger Publishing Company, 1986.

94. Kittel, C. Introduction to Solid State Physics, New York : John Wiley & Sons, Inc., 1971.

95. Sze, S. Semiconductor Devices: Physics and Technology, New York, John Wiley and Sons, 1985.

96. Cotts, D. and Z. Reyes. Electrically Conductive Organic Polymers for Advanced Applications. Park Ridge, New Jersey: Noyes Data Corporation, 1986.

97. Nagels, P. "Electronic Properties of Amorphous Semiconductors", Noncrystalline Semiconductors, Vol. 1, edited by M. Pollack. Boca Raton, Florida: CRC Press, Inc., 1987.

98. Austin, I. and N. Mott. "Polarons in Crystalline and Non-Crystalline Materials", Adv. Phys., 18: 41-102, 1969.

99. Johnsher, A. "Hopping Losses in Polarisable Dielectric Media", Nature, 250: 191-193, 1974.

100. Johnsher, A. "Physical Basis of Dielectric Loss", Nature, 253: 717-719, 1975.

101. Johnsher, A. "The Universal Dielectric Response", Nature, 267: 673-679, 1977.

102. Stremler F. Introduction to Communication Systems, 2nd Ed., Addison-Wesley Publishing Co. Reading, MA., 1982.

103. Mathur, S., J. Singh, and D. Singh. "Tight Binding Energy Band Structure Calculations for Phthalocyanines I. β-Hydrogen Phthalocyanine", J. Phys. C: Solid St. Phys., 4: 3122-3128, 1971.

104. Sukigara, M. and R. Nelson. "Band Structure and Transport of Charge in Metal-Free Phthalocyanine", Molecular Physics, 4: 387-396, 1969.

105. Singh, J. "Calculation of the Energy Band Structure and Carrier Mobilities in γ-Platinum Phthalocyanine Single Crystals", Phys. Stat. Sol. B 82: 263-268, 1977.

106. Devaux, P. and G. Delacote. "Charge Carrier Transfer Integrals Calculation in a Metal-Free Phthalocyanine Single Crystal", Journal of Chemical Physics, 52: 4922-4923, 1970.

107. Usov, N. and V. Benderskii. "Photoeffect in Metal-Free Phthalocyanine Crystals", Phys. Stat. Sol. 37: 535-543, 1970.

108. Westgate, C. and G. Warfield. "Drift Mobility Measurements in Metal-Free and Lead Phthalocyanine", The Journal of Chemical Physics, 46: 94-97, 1967.

109. Cox, G. and P. Knight. "The Temperature Dependence of Charge Carrier Drift Mobility in Single Crystals of Metal-Free Phthalocyanine in the β-Phase", Phys. Stat. Sol. B 50: K135-K137, 1972.

110. Kearns, D. and M. Calvin. "Electrical Properties of Organic Solids. IV. Charge Carrier Diffusivity in Metal-Free Phthalocyanine", The Journal of Chemical Physics, 11: 2022-2025, 1961.

111. Devaux, P. and P. Quedec. "Electron Drift Mobility in Copper Phthalocyanine Single Crystals", Physics Letters, 28 A: 537-538, 1969.

112. Cox, G. and P. Knight. " Drift Mobility, Trapping, and Photogeneration of Charge Carriers in β-Metal-Free Phthalocyanine Single Crystals", J. Phys. C: Solid State Phys., 7: 146-156, 1974.

113. Delacote, G., J. Fillard, and F. Marco. "Electron Injection in Thin Films of Copper Phthalocyanine", Solid State Communications, 2: 373-376, 1964.

114. Sussman, A. "Space-Charged-Limited Currents in Copper Phthalocyanine Thin Films", Journal of Applied Physics, 38: 2738-2748, 1967.

115. Heilmeier, G. and S. Harrison. "Charge Transport in Phthalocyanine Single Crystals", Physical Review, 132: 2010-2016, 1963.

116. Aoyagi, Y., K. Masuda, and S. Namba. "Electrical Conduction in Phthalocyanine Single Crystals", Journal of the Physical Society of Japan, 31: 164-170, 1971.

117. Fielding, P. and F. Gutman. "Electrical Properties of Phthalocyanines", The Journal of Chemical Physics, 26: 411-419, 1957.

118. Barbe, D. and C. Westgate. "Bulk Trapping States in β-Phthalocyanine Single Crystals", The Journal of Chemical Physics, 52: 4046-4054, 1970.

119. Laurs, H. and G. Heiland. "Electrical and Optical Properties of Phthalocyanine Films", Thin Solid Films, 149: 129-142, 1987.

120. Belghachi, A. and R. Collins. "Humidity Response of Phthalocyanine Gas Sensors", J. Phys. D: Appl. Phys., 21 : 1647-1651, 1988.

121. Westgate, C. and G. Warfield. "Thermally Stimulated Trap-Emptying Measurements in Phthalocyanine", The Journal of Chemical Physics, 46: 537-538, 1967.

122. Eley, D. and G. Parfitt. "The Semiconductivity of Organic Substances: Part 2", Trans. Faraday Soc., 51: 1529-1539, 1955

123. Huggins, C. and A. Sharbaugh. "Dielectric Properties of Some Powdered Orgainc Semiconductors", The Journal of Chemical Physics, 38: 393-397, 1963.

124. Abkowitz, M. and A. Lakatos. "Microwave Dielectric Constant and Conductivity Measurements in the Phthalocyanines", The Journal of Chemical Physics, 57: 5033-5036, 1972.

125. Sakai, Y. Y. Sadaoka, and H. Yokouchi. "Electrical Properties of Evaporated Thin Films of Copper Phthalocyanine", Bulletin of the Chemical Society of Japan, 47: 1886-1888, 1974.

126. Sadaoka, Y. and Y. Sakai. "Effect of Purification on Frequency Dependence of the Electrical Properties of Copper Phthalocyanine Discs", Trans, Faraday Soc. 2, 72: 379-382, 1976.

127. Fendley, J. and A. Johnsher. "Frequency Dependence of the Electrical Properties of Coordination Complexes of Transition Metals", Trans. Faraday Soc. 69: 1213-1217, 1973.

128. Vidadi, Y., et al. "Direct Current Conductivity of Copper Phthalocyanine Films in the Presence of Blocking Contacts", Phys. Stat. Sol. A 33: K67-K71, 1976.

129. Fan, F. and L. Faulkner. "Photovoltaic Effects of Metal-Free and Zinc Phthalocyanines. I. Dark Electrical Properties of Rectifying Cells", Journal of Chemical Physics, 69: 3334-3340, 1978.

130. Martin, M., J. Andre, and J. Simon. "Influence of Dioxygen on the Junction Properties of Metallophthalocyanine Based Devices", Journal of Applied Physics, 54: 2792-2794, 1983.

131. Vidadi, Y., et al. "Alternating Current Investigation of Copper Phthalocyanine Films in the Presence of Blocking Contacts", Phys. Stat. Sol. A 34: K77-K81, 1976.

132. Yasunaga, H. and H. Shintaku. "Effect of Schottky Barrier on Alternating Current Response of Lead Phthalocyanine", Journal of Applied Physics, 51: 2149-2152, 1980.

133. Boudjema, B., et al. "Characterization of Metallophthalocyanine-Metal Contacts: Electrical Properties in a Large Frequency Range", Journal of Applied Physics, 56: 2323-2329, 1984.

134. Nowroozi-Esfahani, R. and G. Maclay. "Complex Impedance Measurements of Capacitor Structures on Silicon with Copper Phthalocyanine Dielectric", Journal of Applied Physics, 67: 3409-3418, 1990.

135. van Ewyk, R., A. Chadwick, and J. Wright. "Electron Donor-Acceptor Interactions and Surface Semiconductivity in Molecular Crystals as a Function of Ambient Gas", Journal of the Chemical Society, Faraday Transactions I, 76: 2194-2205, 1980.

136. Bott, B. and T. Jones. "A Highly Sensitive NO_2 Sensor Based on Electrical Conductivity Changes in Phthalocyanine Films", Sensors and Actuators, 5: 43-53, 1984.

137. Sadaoka, Y., N. Yamazoe, and T. Seiyama. "A Gas Sensor Using Thin Films of Phthalocyanine", Denki Kagaku, 48: 597-602, 1978.

138. Temofonte, T. and K. Schoch. "Phthalocyanine Semiconductor Sensors for Room-Temperature PPB Level Detection of Toxic Gases", Journal of Applied Physics, 65: 1350-1355, 1989.

139. Szczurek, A. and K. Lorenz. "An Organic Semiconductor as a Gas Detector", Int. J. Environ. Anal. Chem., 23: 161-168, 1986.

140. Jones, T. and B. Bott. "Gas-Induced Electrical Conductivity Changes in Metal Phthalocyanines", Proc. Int. Conf. Solid State Sensors and Actuators - Transducers '85: 414-417, 1985.

141. Chadwick, A. et al. "Applications of Organic Solids to Chemical Sensing", Mol. Cryst. Liq. Cryst., 134: 137-153, 1986.

142. Sadaoka, Y. et al. "Relation Between Electrical Conductivity and Thermal Desorption Spectra for Cobalt Phthalocyanine-Oxidative Gas System", Chemistry Letters: 1263-1266, 1980.

143. Ionescu, N. and P. Banyai. "Influence of Oxygen on the Dark Conductivity of Copper Phthalocyanine", Revue Roumaine de Chimie, 24: 267-270, 1979.

144. Ionescu, N. and P. Banyai. "Influence of Oxygen on the Dark Conductivity of Metal-Free Phthalocyanine", Revue Roumaine de Chimie, 23: 1023-1027, 1978.

145. Ionescu, N. "Some Remarks Concerning the Logarithmic Law in Adsorption", Revue Roumaine de Chimie, 24: 399-401, 1979.

146. Langton, J. and P. Day. "Effect of Adsorbed Gases on the Dark and Photoconductivity of Fe^{II} Phthalocyanine Crystals", Journal of the Chemical Society, Faraday Transactions II, 78: 1675-1685, 1982.

147. Wilson, A. and R. Collins. "Gas-Surface Reactions on Phthalocyanine Thin Films", Phys. Stat. Sol. A 98: 633-644, 1986.

148. Wilson, A. and R. Collins. "Electrical Characteristics of Planar Phthalocyanine Thin Film Gas Sensors", Sensors and Actuators, 12: 389-403, 1987.

149. Collins, R. and K. Mohammed. "Electrical, Structural, and Gas Sensing Properties of Zinc Phthalocyanine Thin Films", Thin Solid Films, 145: 133-145, 1986.

150. Collins, R. and K. Mohammmed. "Gas Sensitivity of Some Metal Phthalocyanines", J. Phys. D., 21: 154-161, 1988.

151. Krutoyaova, O. et al. "Determination of Volatile Microcontaminants in Phthalocyanine of Copper with the Aid of Gas Chromatography", Bulletin, Institute of Higher Education of USSR, Chemistry and Chemical Technology, 14: 1379-1381, 1971.

152. Al'yanov, M. et al. "Determination of Volatile Organic Microcontaminants in Metal-Phthalocyanines of Different Value of Surface Finish", Bulletin, Institute of Higher Education of USSR, Chemistry and Chemical Technology, 16: 1604-1606, 1973.

153. Wright, J., et al. "Chemical and Structural Influences on Effects of Adsorbed Gases on Semiconductivity of Organic Films", Mol. Cryst. Liq. Cryst., 93: 315-325, 1983.

154. Archer, P. et al. "Kinetic Factors in the Response of Organometallic Semiconductor Gas Sensors", Sensors and Actuators, 16: 379-392, 1989.

155. Stetter, J. et al. "Sensor Array and Catalytic Filament for Chemical Analysis of Vapors and Mixtures", Sensors and Actuators, B 1: 43-47, 1990.

156. Stetter, J. et al. Sensor Array for Toxic Gas Detection, United States Patent Number 4,670,405. Washington, D.C.: United States Patent Office, 2 June 1987.

157. Schierbaum, K., U. Wiemar, and W. Gopel. "Multicomponent Gas Analysis: An Analytical Chemistry Approach to Modified SnO_2 Sensors", Sensors and Actuators, B 2: 71-78, 1990.

158. Clifford, P. Selective Gas Detection and Measurement System, United States Patent Number 4,542,640. Washington, D.C.: United States Patent Office, 24 September 1985.

159. Clifford, P. and D. Tuma. "Characteristics of Semiconductor Gas Sensors I. Steady State Gas Response", Sensors and Actuators, 3: 233-254, 1982/83.

160. Maris, M., C. Brown, and D. Lavery. "Non-linear Multicomponent Analysis by Infrared Spectrophotometry", Analytical Chemistry, 55: 1694-1703, 1983.

161. Fuller, M., G. Ritter, and C. Draper. "Partial Least-Squares Quantitative Analysis of Infrared Spectroscopic Data. Part I: Algorithm Implementation", Applied Spectroscopy, 42: 217-227, 1988.

162. Gardner, J. and P. Bartlett. "Pattern Recognition in Gas Sensing", Techniques and Mechanisms in Gas Sensing, edited by P. Moseley, J. Norris, and D. Williams. New York: Adam Higler, Inc., 1991.

163. Muller, R. "Multisensor Signal Processing", Sensors: A Comprehensive Survey, edited by W. Gopel, J. Hesse, and J. Zemel. Vol. 1 Fundamentals and General Aspects, edited by T. Grandke and W. Ko. New York: VCH Publishers, 1989.

164. Ballantine, D. et. al. "Correlation of Surface Acoustic Wave Device Coating Responses with Solubility Properties and Chemical Structure Using Pattern Recognition", Analytical Chemistry, 58: 3058-3066, 1986.

165. Haaland, D. and E. Thomas. "Partial Least-Squares Methods for Spectral Analyses. 1. Relation to Other Quantitative Calibration Methods and the Extraction of Qualitative Information", Analytical Chemistry, 60: 1193-1202, 1988

166. Fritz, J. and G. Schenk. Quantitative Analytical Chemistry, 3rd Edition. Boston: Allyn and Bacon, Inc., 1974.

167. Strang, G. Linear Algebra and Its Applications, 2nd Edition. Orlando: Academic Press, 1980.

168. Brown, C. and R. Obremski. "Multicomponent Quantitative Analysis", Applied Spectroscopy Review, 20: 373-418, 1984.

169. Fredericks, P., et al. "Materials Characterization Using Factor Analysis of FTIR Spectra. Part 2: Mathematical and Statistical Considerations", Applied Spectroscopy, 39: 311-316, 1985.

170. Malinowski, E. and D. Howery. Factor Analysis in Chemistry. New York: John Wiley & Sons, Inc., 1980.

171. Cahn, F. and S. Compton. "Multivariate Calibration of Infrared Spectra for Quantitative Analysis Using Designed Experiments", Applied Spectroscopy, 42: 865-872, 1988.

172. Devaux, M., et al. "Application of Multidimensional Analyses to the Extraction of Discriminant Spectral Patterns from NIR Spectra", Applied Spectroscopy, 42: 1015-1019, 1988.

173. Donahue, S., C. Brown, and R. Obremski. "Multicomponent Analysis Using Fourier Transform and UV Spectra", Applied Spectroscopy, 41: 353-359, 1988.

174. Nakamoto, T., K. Fukunishi, and T. Morizumi. "Identification Capability of Odor Sensor using Quartz-resonator Array and Neural Network Pattern Recognition", Sensors and Actuators B 1,: 473-476, 1990.

175. Gardner, J., E. Hines, and H. Tang. "Detection of Vapours and Odours From a Multisensor Array using Pattern Recognition Techniques. Part 2. Artificial Neural Networks", Sensors and Actuators B 9: 9-15, 1992.

176. Sommer V., P. Tobias, and D. Kohl. "Methane and Butane Concentrations in a Mixture with Air Determined by Microcalorimetric Sensors and Neural Networks", Sensors and Actuators B 12: 147-152, 1993.

177. Gemperline, P. J. Long, and V. Gregoriou. "Non-Linear Multivariate Calibration Using Principal Component Regression and Artificial Neural Networks", Analytical Chemistry, 63: 2313-2323, 1991.

178. Lippmann, R. "An Introduction to Computing with Neural Networks", Neural Networks: Theoretical Foundations and Analysis, edited by C. Lau, New York: IEEE Press, 1991.

179. Widrow, B. and M. Lehr. "30 Years of Adaptive Neural Networks: Perceptron, Madaline, and Backpropagation", Neural Networks: Theoretical Foundations and Analysis, edited by C. Lau, New York: IEEE Press, 1991.

180. Kreyszig, E. Advanced Engineering Mathematics, 6thEdition, New York: John Wiley and Sons, 1988.

181. Garverick, S. and S. Senturia. "A MOS Device for AC Measurement of Surface Impedance with Applications to Moisture Monitoring", IEEE Transactions on Electron Devices, ED-29: 90-94, 1982.

182. Cobalt Phthalocyanine (alpha form) Electron Diffraction Pattern. Index of Electron Diffraction Patterns. Card Number 22-1663.

183. Cobalt Phthalocyanine (beta form) Electron Diffraction Pattern. Index of Electron Diffraction Patterns. Card Number 14-948.

184. Brothers, C. Evaluation of an Interdigitated Gate Electrode Field-Effect Transistor for Detecting Organophosphorus Compounds. MS Thesis, AFIT/GE/ENG/90D-07, Department of Electrical and Computer Engineering, Air Force Institute of Technology (AU), Wright-Patterson AFB, OH, 1990.

185. Keithley Instruments, Inc. Model 7057A Thermocouple Scanner Card Instruction Manual. Document Number 7057A-901-01, Rev. C., Keithley Instruments, Inc. Cleveland, OH, December 1986.

186. Keithley Instruments, Inc. Model 617 Programmable Electrometer Instruction Manual. Document Number 617-901-01, Rev. C., Keithley Instruments, Inc. Cleveland, OH, June 1986.

187. Simmons, J., G. Nadkarni, and M. Lancaster. "Alternating Current Electrical Properties of Highly Doped Insulating Films", Journal of Applied Physics, 41: 538-544, 1970.

188. Mockert, H., D. Schmeisser, and W. Gopel. "Lead Phthalocyanine (PbPc) as a Prototype Organic Material for Gas Sensors: Comparative Electrical and Spectroscopic Studies to Optimize O_2 and NO_2 Sensing", Sensors and Actuators, 19: 159-176, 1989.

189. MacDonald, J. Impedance Spectroscopy. New York: John Wiley and Sons, Inc., 1987.

190. Lee, H. Optimization of a Resin Cure. MS thesis, Massachusetts Institute of Technology, Cambridge MA, 1982.

191. Dang R. and N. Shigyo. " Coupling Capacitances for Two-Dimensional Wires", IEEE Electron Device Letters, EDL-2: 196-197 ,1981.

192. Barksdale, H. Class Handout distributed in EENG 628, Electromagnetic Waves I. School of Engineering, Department of Electrical and Computer Engineering, Air Force Institute of Technology (AU), Wright-Patterson AFB OH, April 1989.

193. Lawrenson, P. "Numerical Methods", Field Analysis, edited by D. Vitokovich, London: D. Van Nostrand Company, 1966.

194. Leal, H. Rigorous Calculations of Lumped Electrical Parameters for a Microstrip Interdigitated Electrode Structure. MS Thesis, AFIT/GE/MA/89D-1. Department of Electrical and Computer Engineering and Department of Mathematics, Air Force Institute of Technology (AU), Wright-Patterson AFB, OH, 1989.

195. Wiseman, J. "Finite-Difference Modeling and Verification of Thin Film Coated Interdigitated Electrodes". EENG 899 Special Study under the direction of Lt Col Edward Kolesar. Department of Electrical and Computer Engineering, Air Force Institute of Technology (AU), Wright-Patterson AFB, OH, 1989.

196. Sheppard, N. Dielectric Analysis of the Cure of Thermosetting Epoxy/Amine Systems. PhD Dissertation. Massachusetts Institute Of Technology, Cambridge, MA, 1986.

197. Green, H. "The Numerical Solution of Some Important Transmission-Line Problems", IEEE Transactions on Microwave Theory and Techniques, MTT-13: 676-692, 1965.

198. Frankel, S. Multiconductor Transmission Line Analysis, Artech House Inc., 1977.

199. Shell Chemical Company. EPON Resin 828: Technical Bulletin SC:235-85.828. Houston, TX, 1985.

200. Pizzini, S. et al. "Influence of the Structure and Morphology on the Sensitivity to Nitrogen Dioxides of Phthalocyanine Thin-Film Resistivity Sensors", Sensors and Actuators, 17: 481-491, 1989.

201. Mearns, A. and K. Ofosu-Asiedu. "Kinetics of Reaction of Low Concentration Mixtures of Oxides of Nitrogen, Ammonia, and Water Vapor", J. Chem. Tech. Biotechnol., 34 A: 341-349, 1984.

202. Mearns, A. and K. Ofosu-Asiedu. "Ammonium Nitrate Formation in Low Concentration Mixtures of Oxides of Nitrogen and Ammonia", J. Chem. Tech. Biotechnol., 34 A: 350-354, 1984.

203. Ingemar, C. et al. "Catalytic Reduction of Nitrogen Oxides 2. The Reduction of NO_2", Applied Catalysis, 27: 363-377, 1986.

204. Dines, T., C. Rochester, and A. Ward. "Infrared Study of the Reaction between Nitrogen Oxides and Ammonia on Titania-supported Vanadia Catalysts", Journal of the Chemical Society, Faraday Transactions, 87: 1473-1477, 1991.

205. Reston, R. "Design and Performance of a Gas Chromatograph Micromachined in a Single Crystal Silicon Substrates", PhD Dissertation, AFIT/DS/ENG/93M-01. Department of Electrical Engineering and Computer Engineering, Air Force Institute of Technology (AU), Wright-Patterson AFB, OH, 1993.

206. Press, W., et al. Numerical recipes in C: The Art of Scientific Computing, Cambridge: Cambridge University Press, 1988.

207. MathSoft Corp. MathCad 5.0 Users Manual. Cambridge, MA, 1994.

Appendix A: Principal Component Analysis of a Multicomponent, Non-Linear System

This appendix illustrates the principal component analysis (PCA) technique for a hypothetical multicomponent, non-linear system. The non-linear system used in this example is based upon the quantitative analysis of a non-linear, multicomponent system by infrared spectrophotometry reported in the literature (160). The mixtures analyzed contain three components which contribute to the infrared absorbance measured at two different frequencies. To account for non-linearities in the measured data, the concentration, C, of a component is given by a power series of the absorbance, A, data. The cross-product term has been proposed to account for intermolecular interactions (160). The non-linear system of equations for a three-component mixture is given by:

$$\begin{aligned} C_1 &= P_{11}A_1 + P_{12}A_2 + P_{13}A_1^2 + P_{14}A_2^2 + P_{15}A_1A_2 \\ C_2 &= P_{21}A_1 + P_{22}A_2 + P_{23}A_1^2 + P_{24}A_2^2 + P_{25}A_1A_2 \\ C_3 &= P_{31}A_1 + P_{32}A_2 + P_{33}A_1^2 + P_{34}A_2^2 + P_{35}A_1A_2 \end{aligned} \tag{A-1}$$

or in matrix form:

$$\boldsymbol{C} = \begin{pmatrix} P_{11} & P_{12} & P_{13} & P_{14} & P_{15} \\ P_{21} & P_{22} & P_{23} & P_{24} & P_{25} \\ P_{31} & P_{32} & P_{33} & P_{34} & P_{35} \end{pmatrix} \begin{pmatrix} A_1 \\ A_2 \\ A_1^2 \\ A_2^2 \\ A_1A_2 \end{pmatrix} = \boldsymbol{PA} \quad , \tag{A-2}$$

where $\boldsymbol{P}$ is a matrix of proportionality constants. The A-matrix used in this example contains a randomly generated set of absorbance data (measured responses) for four different three-component mixtures, and therefore, the A-matrix is composed of four columns. The A-matrix is given by:

$$\boldsymbol{A} = \begin{pmatrix} 1 & 2 & 1.5 & 2 \\ 1 & 3 & 2 & 1.5 \\ 1 & 4 & 2.25 & 4 \\ 1 & 9 & 4 & 2.25 \\ 1 & 6 & 3 & 3 \end{pmatrix} \quad . \tag{A-3}$$

The C-matrix, which represents the component concentrations within the mixtures that give rise to the measured responses, was generated by pre-multiplying the A-matrix by a randomly generated matrix of proportionality constants, B, given by:

$$B = \begin{pmatrix} 0.5 & 0.3 & 0.2 & 0.1 & 0.0 \\ 0.0 & 0.1 & 0.4 & 0.2 & 0.1 \\ 0.1 & 0.2 & 0.0 & 0.3 & 0.2 \end{pmatrix}, \tag{A-4}$$

which yields:

$$C = \begin{pmatrix} 1.1 & 3.6 & 2.2 & 2.5 \\ 0.8 & 4.3 & 2.2 & 2.5 \\ 0.8 & 4.7 & 2.4 & 1.8 \end{pmatrix}. \tag{A-5}$$

Each column vector of C represents a single mixture with component concentrations given by its elements. To perform the principal component analysis with this system, A^t was substituted for D in Equation (III-10) to yield the covariance matrix, Z:

$$Z = (A^t)^t A^t = AA^t = \begin{pmatrix} 11.25 & 13.00 & 20.38 & 29.50 & 23.50 \\ 13.00 & 16.25 & 23.50 & 39.38 & 29.50 \\ 20.38 & 23.50 & 38.06 & 55.00 & 43.75 \\ 29.50 & 39.38 & 55.00 & 103.06 & 73.75 \\ 23.50 & 29.50 & 43.75 & 73.75 & 55.00 \end{pmatrix}. \tag{A-6}$$

From eigenanalysis of the covariance matrix, four eigenvalues were obtained with values of 215, 8.2, 0.63 and 0.0063. The L-matrix, whose rows are given by the four corresponding eigenvectors, is given by:

$$L = \begin{pmatrix} -0.22 & -0.27 & -0.40 & -0.68 & -0.51 \\ 0.38 & 0.08 & 0.69 & -0.61 & 0.08 \\ -0.50 & -0.73 & 0.43 & 0.09 & 0.14 \\ 0.72 & -0.55 & -0.06 & 0.27 & -0.53 \end{pmatrix}. \tag{A-7}$$

Projecting the transpose of the data matrix onto this eigenspace yields the abstract features which describe the data. This projection yields:

$$\boldsymbol{F} = \boldsymbol{A}^t\boldsymbol{L}^t \quad . \tag{A-8}$$

Using these abstract features, the least squares solution for $\boldsymbol{P}^t$ is given by:

$$\boldsymbol{P}^t = (\boldsymbol{F}^t\boldsymbol{F})^{-1}\boldsymbol{F}^t\boldsymbol{C}^t = \begin{pmatrix} -0.34 & -0.38 & -0.38 \\ 0.29 & 0.17 & -0.11 \\ -0.37 & 0.13 & -0.14 \\ 0.21 & -0.06 & -0.02 \end{pmatrix} \quad . \tag{A-9}$$

To test the prediction capability of the computed $\boldsymbol{P}$-matrix, the component concentrations were computed given one of the vectors used in the calibration, $\boldsymbol{X} = \{1,1,1,1,1\}^t$. To compute the component concentrations, the data vector was first projected into the eigenspace to obtain its abstract feature representation, and then it was pre-multiplied by the $\boldsymbol{P}$-matrix. That is,

$$\boldsymbol{C} = \boldsymbol{P}\,[\boldsymbol{X}\boldsymbol{U}^t] = \{1.1,\ 0.8,\ 0.8\}^t \quad . \tag{A-10}$$

Since there was no noise or error in the calibration data, the computed value obtained through PCA and multilinear regression produced exactly the same component concentrations as that found in the calibration matrix, $\boldsymbol{C}$. Performing the same analysis, except using only one, two or three eigenvectors, yielded predicted component concentrations of $\{0.70, 0.77, 0.79\}^t$, $\{0.88, 0.88, 0.72\}^t$, and $\{1.09, 0.80, 0.80\}^t$, respectively. Thus, these results demonstrate that only the first three eigenvectors are necessary to adequately describe the data.

Appendix B: The Design of an Active Microsensor Utilizing Conventional CMOS Processing and Phthalocyanine Thin-Films[1]

A new implementation of a microsensor based upon the Interdigitated Gate Electrode Field-Effect Transistor (IGEFET) was proposed to address the limitations of past designs. The proposed microsensor couples the interdigitated gate electrode (IGE) structure to a two-stage, complementary metal-oxide-semiconductor (CMOS) differential amplifier. As in the prior implementations of the IGEFET, the interdigitated gate electrode structure will be coated with a chemically-sensitive thin film, such as a metal-doped phthalocyanine compound. The floating gate portion of the interdigitated gate electrode structure (depicted in Figure V-11) is directly connected to the non-inverting input of the differential amplifier. This connection is designated as node V_{fg} in Figure B-1.

This design provides chemical sensitivity and active control of the electrical performance while maintaining compatibility with conventional CMOS integrated circuits. Electrical signals applied to the driven-gate electrode of the IGE structure are modulated by changes in the electrical properties of the thin films upon exposure to the detectants. The modulated signal is detected at the floating-gate electrode and subsequently amplified by the active network. The gate of the input metal-oxide-semiconductor field-effect transistor (MOSFET) provides the necessary impedance matching and electrical isolation between the thin-film coated IGE structure and the amplifier network. The amplified signal is made available for additional signal processing at the V_{out} node of the microsensor. The electrical performance of the microsensor's amplifier is controlled with two independent inputs, which are designated as the V_{bias} and V_{offset} nodes in Figure B-1.

The microsensor is designed to minimize its susceptibility to parasitic impedance effects. That is, a metal ground plane is provided directly under the interdigitated gate electrode structure to provide a common signal ground and to isolate the IGE structure from the parasitic metal-oxide-semiconductor (MOS) capacitance. Since non-inverting stages are incorporated within the amplifier design, the effects produced by network Miller capacitances are minimized. Also, the use of active loads and gain control provides a stable gain over a dynamic temperature range anticpated for operation of the IGEFET microsensor.

---

[1]This appendix is an excerpt from an unpublished report written by Capt Thomas Jenkins that describes the design of the IGEFET Revision 4 microsensor. The text has been edited to maintain consistency with the style of this document.

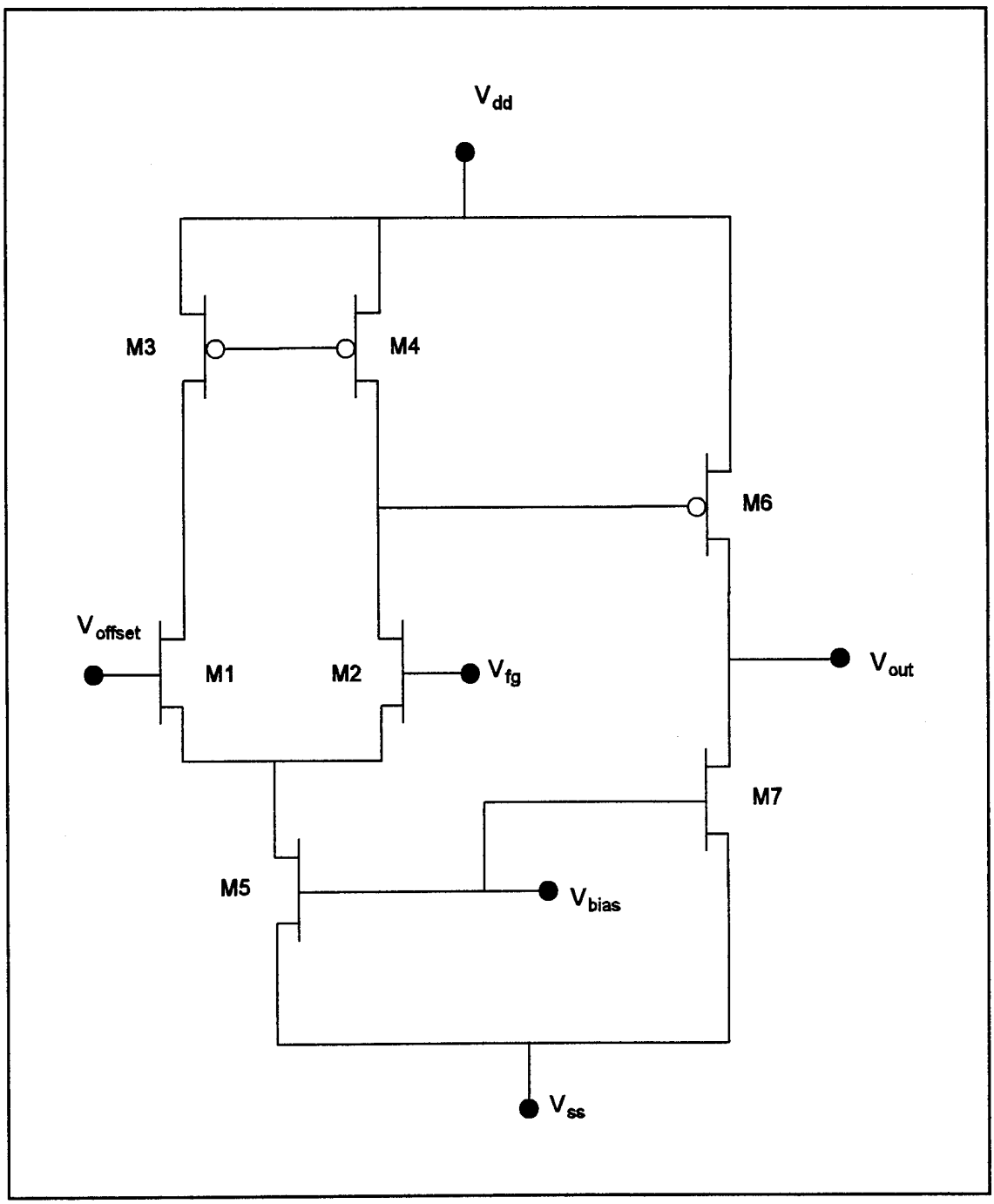


Figure B-1. Schematic of the IGEFET Two-Stage CMOS Differential Amplifier.

Theory of Operation

The active microsensor is operated in a simple manner which is amenable to external computer or future "on-chip" control. The operation of the device is also simple when it is used to characterize materials for consideration as the chemically-sensitive thin film. The operation can be described in terms of electrical ports.

The electrical stimuli are applied to the driven gate portion of the IGE structure. Thus, the driven-gate electrode functions as the input port with the underlying ground plane as the signal's ground terminal. The ground plane is used as the common signal terminal for all the other connections, as well. The driven gate electrode is also used when characterizing the electrical impedance of potential thin-film candidates. An external connection is provided to the floating-gate electrode to enable impedance measurements of the IGE structure. All impedance measurements of candidate thin-films should be completed before using the amplifier. When the impedance measurements are completed, the bond wire connection to the floating-gate electrode should be severed. This action permits the maximum isolation of the electrical signals, and reduces parasitic loading of the sensing thin-film coated IGE structure during conventional operation of the device.

The active microsensor's output port is located at the V_{out} node (Figure B-1). The ground plane establishes the output signal's ground terminal. For example, the V_{out} port is used to collect the IGEFET transfer function's gain and phase measurements. This port (V_{out}) may be connected to any subsequent signal processing instrumentation during normal operation of the device as a gas sensor.

The electrical gain of the active IGEFET amplifier is controlled by the V_{bias} node (Figure B-1). The voltage signal at this port provides control of the current source within the differential amplifier; hence, it controls the voltage gain. In practice, this control will determine the maximum possible gain that can be realized as the V_{offset} voltage is varied. In normal operation, the microsensor's V_{bias} signal (Figure B-1) is operated at a fixed, predetermined value.

The operating point of the IGEFET amplifier is determined by the V_{offset} node. This port compensates for a direct current (DC) voltage on the floating-gate electrode. The voltage at the V_{offset} node is coupled to the inverting input of the differential amplifier. Thus, by varying this voltage, the DC voltage difference between the inverting and non-inverting terminals can be canceled. Hence, the DC voltage can be offset. Therefore, the operating point of the active IGEFET amplifier can be effectively "tuned" to some maximum value of gain as the input port voltage drifts due to DC changes associated with the detector/detectant actions or parasitic effects. Simultaneously, the differences in the "tuned"

maximum gain at a fixed V_{bias} level provides an indication of the AC changes due to detector/detectant actions or parasitic effects.

The power for the active IGEFET amplifier is supplied at the V_{dd} (high) and V_{ss} (low) ports of the device. The circuit is designed for dual or single power supplies. The normal operating voltage is a ten volt difference between the V_{dd} and the V_{ss} ports, using the ground plane as a common reference. For example, positive five volts should be applied to V_{dd} and negative five volts should be applied to V_{ss}. However, the active microsensor will function with a supply voltage difference as small as six volts.

Design Implemented

The microsensor was designed using the AFIT very-large-scale-integration (VLSI) design tools. The microsensor, *sans* the chemically-sensitive thin-film coating , was fabricated using the Metal-Oxide-Semiconductor Implementation System (MOSIS) facilities (University of California, Berkeley, CA). The MOSIS, scalable, 2-micron, double-metal, double-polysilicon, p-well technology was used. The Spice simulation file which models the IGEFET amplifier operation is listed at the end of this appendix.

The transistor sizing is provided within the Spice simulation file, and the designation of transistors is consistent with Figure B-1. However, there is one exception. Within the output driver section (second stage) of the amplifier, the large gate width of transistor M6 was realized using a shunt combination of transistors designated M6 and M8 within the Spice file.

The active microsensor was implemented as a symmetric array of nine elements. The integrated circuit chip was designated as IGEFET91 by the AFIT VLSI administration for purposes of communication with the MOSIS. The chip was designed to minimize parasitic effects by configuring nine independently operated microsensors in the array. No two array elements share any pins on the chip. This approach also provides a level of redundancy to ensure that the failure of any one element will not render the entire array dysfunctional. Additionally, the routing of metal lines was accomplished using only a single metal layer with no cross-overs.

Another feature of the integrated circuit design is the layout of the bond pads. It was anticipated that pin-to-pin electrical coupling may pose a problem when attempting to use high-impedance thin-films, such as the metal-doped phthalocyanine compounds, as the chemically-sensitive coatings. Therefore, the amplifier input bond pads (floating-gate contacts) were isolated from the amplifier output bond pads using the power supply bond pads. Additionally, the driven- and floating-gate electrode contacts of interdigitated gate electrode structures #1 and #6 (Figure IV-1), were placed side-by-side.

This feature directly permits an empirical check of the package's parasitic effects that are in shunt with the thin films.

An additional feature of the integrated circuit design was the incorporation of three parallel plate capacitors using "metal-1" and "metal-2". The areas of the three capacitors were linearly related (by the standard parallel plate equation) and quite large (160,000-; 202,500-; and 250,000-square microns). The linear relationship permits fitting a linear solution to plots of capacitance versus capacitor area. The large metal areas used to form the capacitor structures yield large-valued capacitances which reduce the relative error in their electrical measurement. In addition, the large metal areas also reduce the error in the capacitor area resulting from fabrication variations. The slope of the fitted linear relation represents the ratio of the dielectric permittivity to the spacing between the "metal-1" ground plane and the "metal-2" interdigitated gate electrodes. Thus, the actual thickness of the field oxide beneath the interdigitated gate electrode structure can be determined and used in models of the IGE structure.

Spice Simulation File

```
* igefet amplifier extracted from MOSIS data (Vbias=0.0) *

.options dcon=1 relv=1e-4 relvar=0.01 acct nomod post=1
.width out=80

.param vdd=5 vss=-5
*.param voffset=-0.04775 vbias=-2.5
.param vbias=0.0
.param voffset=-.15
*.param dln=.358U dlp=.185U dwn=.217U dwp=.344U
.param dln=0U dlp=0U dwn=0U dwp=0U
.param xwide=1U

*set the circuit temperature
.temp 30

*.param  voffset=opt1(-.0167,-1,1)
*+       vbias=opt1(-1.94,-5,5)

*supply voltage
vdd vdd 0 vdd
vss vss 0 vss

*bias for current source
vbias vbias 0 vbias
```

```
*input signal on floating gate
*vfg fg 0 dc=0 ac=.1,0 PWL(0.0 0.0 1e-5 .01 .5e-3 .01 .501e-3 0 1e-3 0)
vfg fg 0 dc=0 ac=.1,0 sin(0 .005 1Khz)

*shunt signal through ige structure
*where cfg    = 2.07e-11
*     cseries = 2.2e-13
*     cdg     = 2.18e-11
cige fg 0 20.9e-12

*offset voltage
voff voff 0 voffset

** SPICE file created for circuit ampv4 using ext and ext2spice
** Technology: scmos
**

** NODE: 0 = GND
** NODE: vdd = Vdd
** NODE: vss = Vss within mosfets
** NODE: 100 = output of diff stage & input of output driver
** NODE: vout= output of amplifier circuit

*m6,m7,m8 are the output drivers
*m6 & m8 are shunted transistors to realize large width

M6 vout 100 vdd vdd pfet L='3.0U-dlp' W='24.0U-dwp'
+ AS='24.0U*6*xwide' AD='24.0U*8*xwide'

M8 vout 100 vdd vdd pfet L='3.0U-dlp' W='24.0U-dwp'
+ AS='24.0U*6*xwide' AD='24.0U*8*xwide'

M7 vout vbias vss vss nfet L='3.0U-dln' W='18.0U-dwn'
+ AS='18.0U*7*xwide' AD='18.0U*6*xwide'

*m1,m2 are the input differential pair

M2 100 fg 105 vss nfet L='3.0U-dln' W='6.0U-dwn'
+ AS='6.0U*6*xwide' AD='6.0U*5*xwide'

M1 103 voff 105 vss nfet L='3.0U-dln' W='6.0U-dwn'
+ AS='6.0U*6*xwide' AD='6.0U*5*xwide'

*m5 is the current source

M5 105 vbias vss vss nfet L='12.0U-dln' W='6.0U-dwn'
+ AS='6.0U*20*xwide' AD='6.0U*5*xwide'
```

```
*m3,m4 are the current mirrors

M4 100 103 vdd vdd pfet L='3.0U-dlp' W='18.0U-dwp'
+ AS='18.0U*5*xwide' AD='18.0U*5*xwide'

M3 103 103 vdd vdd pfet L='3.0U-dlp' W='18.0U-dwp'
+ AS='18.0U*5*xwide' AD='18.0U*5*xwide'

C0 voff 0 33F
** NODE: voff = voff
C1 105 0 31F
** NODE: 105 = 6_37_30#
C2 fg 0 31F
** NODE: fg = fg
C3 103 0 68F
** NODE: 103 = 6_105_27#
** NODE: 0 = GND!
C4 vbias 0 41F
** NODE: vbias = vbias
C5 vout 0 119F
** NODE: vout = vout
C6 100 0 72F
** NODE: 100 = 6_129_108#
C7 vdd 0 206F

*end of extracted amp data **********************

*load the amplifier
*hp4194 gain analyzer
cload vout 0 28Pf
rload vout 0 1e6
*cable from amp to input port of hp4194
ccable vout 0 100Pf


*perform the analysis


*.ac dec 5 1e3 1e7 sweep optimize=opt1
*+      results=dbgain model=optbias
*.model optbias opt close=10.0 cut=1.20 max=30000 itropt=50 relin=1e-6
*+      relout=1e-8 level=3

*.measure ac dbgain max vdb(vout,fg) from=1e3 to=1e5 goal=30.0

.dc voff -5 5 .1
*.ac dec 10 1e3 1e7
.ac dec 10 1e3 1e7 sweep voff poi 3 -.1 -.2 -.3
```

```
*.tran 1e-5 1e-3
.tran 1e-5 1e-3 sweep voff poi 5  -.160 -.155 -.150 -.145 -.140

.print ac vdb(vout,fg) vp(vout)
.print tran v(vout), v(fg)
.print dc v(voff), v(vout)

.plot ac vdb(vout,fg)
.plot ac vp(vout)
.plot tran v(vout), v(fg)
.plot dc v(vout), v(voff)


*bsim model parameters extracted using bsim2hsp
*
*PROCESS=orbit
*RUN=n11a
*WAFER=6
*Gate-oxide thickness= 415.0 angstroms
*Geometries (W-drawn/L-drawn, units are um/um) of transistors measured were:
* 3.0/2.0, 6.0/2.0, 18.0/2.0, 6.0/6.0, 6.0/18.0
*Bias range to perform the extraction (Vdd)=5 volts
*DATE=03-06-91
*
*NMOS PARAMETERS
*
.MODEL nfet NMOS LEVEL=13 VFB0=
+ -7.61643E-01, 1.83930E-02,-8.54158E-02
+  7.56356E-01,-3.89822E-24, 1.64402E-23
+  1.08178E+00, 6.07344E-02, 3.81455E-01
+ -1.51203E-02, 6.88994E-02, 5.94701E-02
+ -4.88512E-03, 8.62733E-03, 8.10981E-03
+  5.52720E+02,6.21705E-001,8.49763E-002
+  5.51328E-02, 3.79423E-02,-5.55550E-02
+ -9.76683E-03, 6.49082E-01,-6.71531E-02
+  1.48227E+01,-3.30939E+01, 4.23549E+01
+ -5.67026E-04,-3.38549E-03,-2.83701E-03
+  2.50835E-04,-2.21828E-04,-4.24785E-03
+  2.40917E-03,-1.56754E-02, 2.28772E-02
+  6.52793E-04,-4.22824E-03, 2.08583E-02
+  5.37954E+02, 3.42493E+02, 1.05729E+02
+  7.66667E+00,-4.35794E+01, 9.31587E+01
+ -2.75125E+00, 6.87539E+01,-4.86173E+00
+  7.99750E-04, 7.44753E-02,-9.89036E-03
+ 4.15000E-002, 2.70000E+01, 5.00000E+00
+ 3.87983E-010,3.87983E-010,6.75328E-010
+ 1.00000E+000,0.00000E+000,0.00000E+000
+ 1.00000E+000,0.00000E+000,0.00000E+000
```

```
+ 0.00000E+000,0.00000E+000,0.00000E+000
+ 0.00000E+000,0.00000E+000,0.00000E+000
+ 23.24,   4.103600e-04,   4.355700e-10,   0,   0.8
+ 0.8,   0.46577,   0.34806,   0,   0
*
* Gate Oxide Thickness is 414 Angstroms
*
*
*PMOS PARAMETERS
*
.MODEL pfet PMOS LEVEL=13 VFB0=
+ -2.63226E-01,-1.36187E-01, 5.73538E-01
+  6.25747E-01, 0.00000E+00, 8.51968E-24
+  4.45458E-01, 1.23914E-01,-5.49850E-01
+ -4.45401E-03, 7.57497E-02,-1.87714E-01
+ -1.03842E-02, 5.66745E-02, 3.57521E-02
+  2.39867E+02,3.17475E-001,-3.96475E-002
+  1.23063E-01, 3.28220E-02,-7.33741E-02
+  2.48326E-02, 3.41391E-01,-1.19113E-01
+  9.58626E+00,-4.34082E+00, 7.28166E+00
+ -4.84514E-04,-4.29358E-03, 2.97267E-03
+  7.37641E-04,-3.93047E-03,-3.12947E-03
+  5.46308E-03,-2.65983E-03, 5.49548E-03
+  2.00696E-03, 1.48921E-03,-9.94101E-04
+  2.42349E+02, 1.70751E+02,-1.01332E+02
+  8.47276E+00, 2.63702E+00, 4.45067E+00
+ -1.45916E+00, 1.59412E+01,-5.60290E+00
+ -1.85916E-02,-4.79766E-03, 1.16961E-02
+ 4.15000E-002, 2.70000E+01, 5.00000E+00
+ 1.98124E-010,1.98124E-010,6.45282E-010
+ 1.00000E+000,0.00000E+000,0.00000E+000
+ 1.00000E+000,0.00000E+000,0.00000E+000
+ 0.00000E+000,0.00000E+000,0.00000E+000
+ 0.00000E+000,0.00000E+000,0.00000E+000
+ 77.05,   1.925400e-04,   2.041100e-10,   0,   0.7
+ 0.7,   0.44436,   0.211587,   0,   0
*
*N+ diffusion::
*
.MODEL PC1_DU1 R
+ RSH=23.2 COX=0.00041 CAPSW=4.36e-10 W=0 DW=0
*
*P+ diffusion::
*
.MODEL PC1_DU2 R
+ RSH=77.1 COX=0.000193 CAPSW=2.04e-10 W=0 DW=0
*
*METAL LAYER -- 1
```

```
*
.MODEL PC1_ML1 R
+ RSH=0.048 COX=2.6e-05 CAPSW=0 W=0 DW=0
*
*METAL LAYER -- 2
*
.MODEL PC1_ML2 R
+ RSH=0.025 COX=0 CAPSW=0 W=0 DW=0

.end
```

Appendix C. Analysis of the MPc Infrared Absorption Spectra

This appendix provides an analysis of the metal-substituted phthalocyanine (MPc) infrared (IR) absorption spectra before and after exposure to nitrogen dioxide and ammonia. To examine reversibility, the IR spectra following the purge cycle of the adsorbed gases were also analyzed. To accomplish the analysis, the measured IR spectra were compared relative to the published spectra for each of the MPc film types. To account for differences in baseline, both the published spectra and the measured spectra were normalized to the 1120 cm^{-1} peak. The comparison was accomplished on the basis of the percent change (percent error) in the measured spectra relative to the published spectra.

Figures C-1 through C-3 depict the percent change in the IR spectra of the deposited CuPc, NiPc, and CoPc films relative to the published spectra (Figures II-8 through II-10). As discussed in Chapter IV, the limited bandwidth of the sodium chloride substrates likely contributes to the larger differences in the IR spectra observed at small wavenumbers. The average percent change (percent error) in the measured IR spectra relative to the published spectra at wavenumbers greater than 900 cm^{-1} are listed in Table C-1.

As discussed in Chapter IV, the IR absorption spectra of the MPc films was significantly modified upon exposure to nitrogen dioxide. The percent change in the pre-exposed, NO_2 exposed, and purged spectra relative to the reference spectra are shown in Figures C-4 through C-6 for the three MPc film types. These figures demonstrate that the large changes induced in the IR spectra as a result of adsorption of nitrogen dioxide are significantly reduced by the purge treatment. In contrast to the large changes observed upon nitrogen dioxide exposure, the IR spectra of the MPc films were not significantly affected by ammonia exposure, as shown in Figures C-7 through C-9.

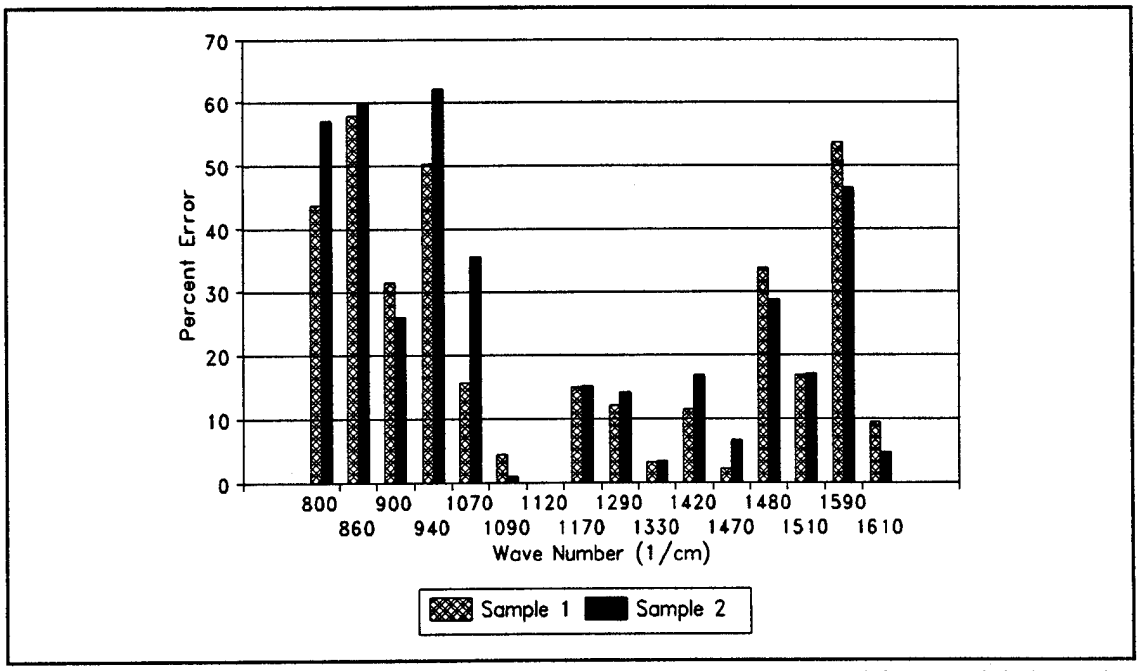


Figure C-1. Percent Error in the Infrared Absorption Spectra of the Deposited Copper Phthalocyanine Film Relative to the Sadtler Reference Spectra (73). (Sample 1: Film Thickness-6600 Å. Sample 2: Film Thickness-7700 Å. Infrared Spectra Normalized with Respect to the 1120 cm^{-1} Peak.)

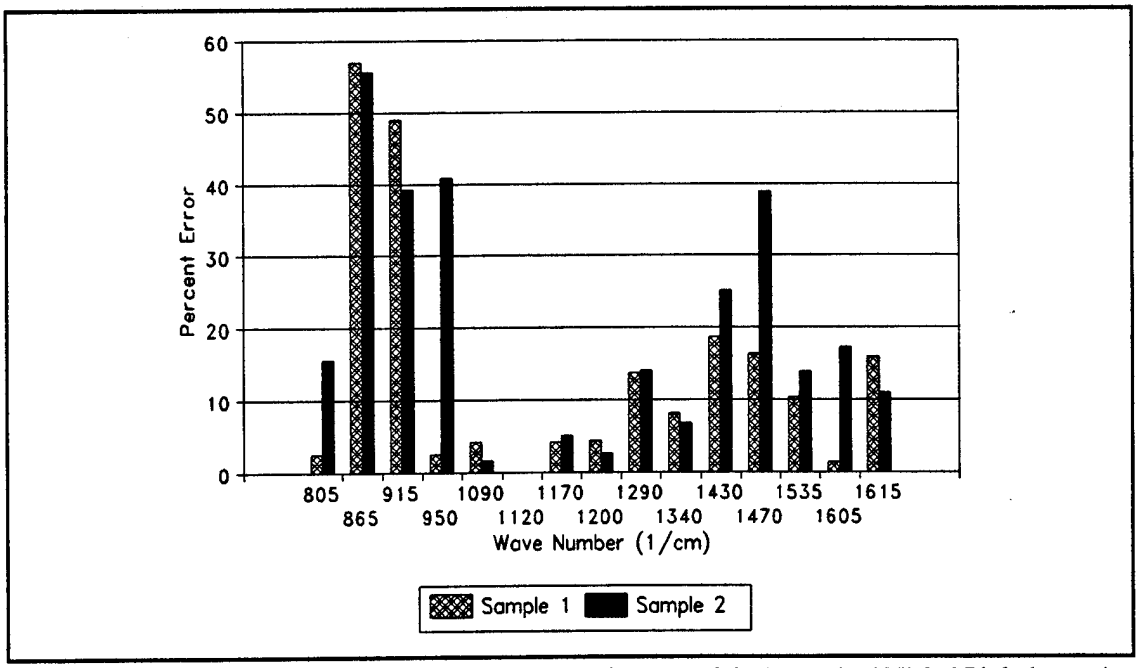


Figure C-2. Percent Error in the Infrared Absorption Spectra of the Deposited Nickel Phthalocyanine Film Relative to the Sadtler Reference Spectra (74). (Sample 1: Film Thickness-6500 Å. Sample 2: Film Thickness-7100 Å. Infrared Spectra Normalized with Respect to the 1120 cm^{-1} Peak.)

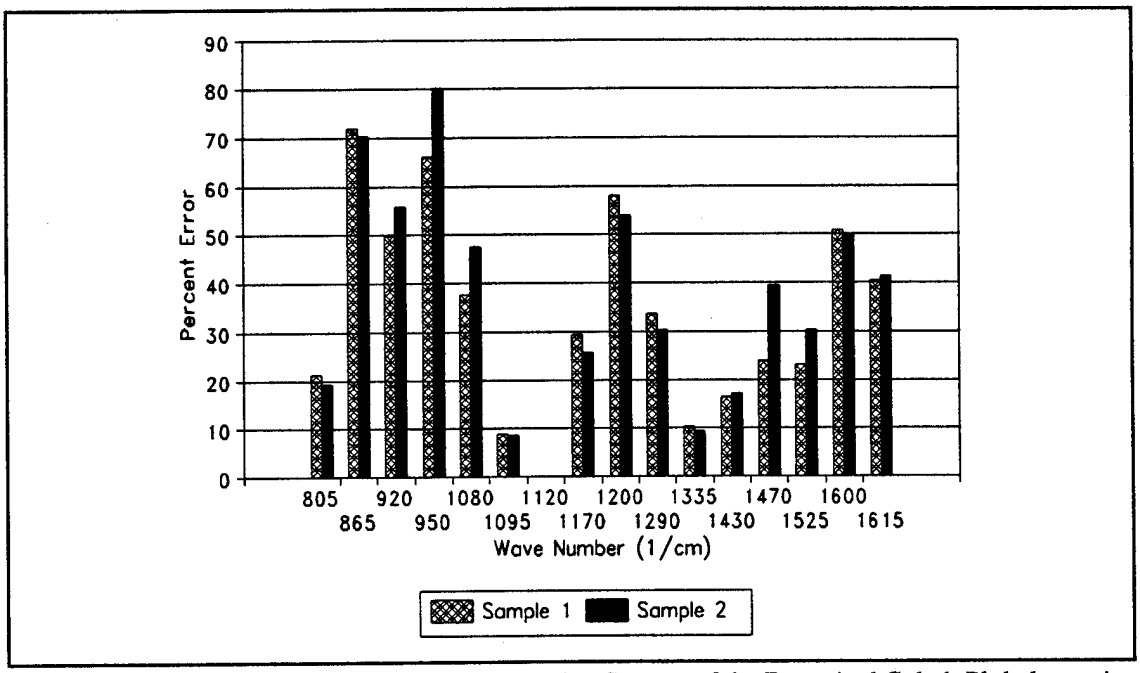


Figure C-3. Percent Error in the Infrared Absorption Spectra of the Deposited Cobalt Phthalocyanine Film Relative to the Published Reference Spectra (49). (Sample 1: Film Thickness-5300 Å. Sample 2: Film Thickness-5700 Å. Infrared Spectra Normalized with Respect to the 1120 cm^{-1} Peak.)

Table C-1. Percent Error in the Measured Infrared Absorption Spectra of the Metal-Substituted Phthalocyanine (MPc) Thin Films Relative to the Published Reference Spectra (73, 74, 49).

MPc Film Type	Film Thickness (Å)	Percent Error (%)
CuPc	6600	21.1
	7700	22.5
NiPc	6500	15.8
	7100	20.9
CoPc	5300	34.5
	5700	37.7

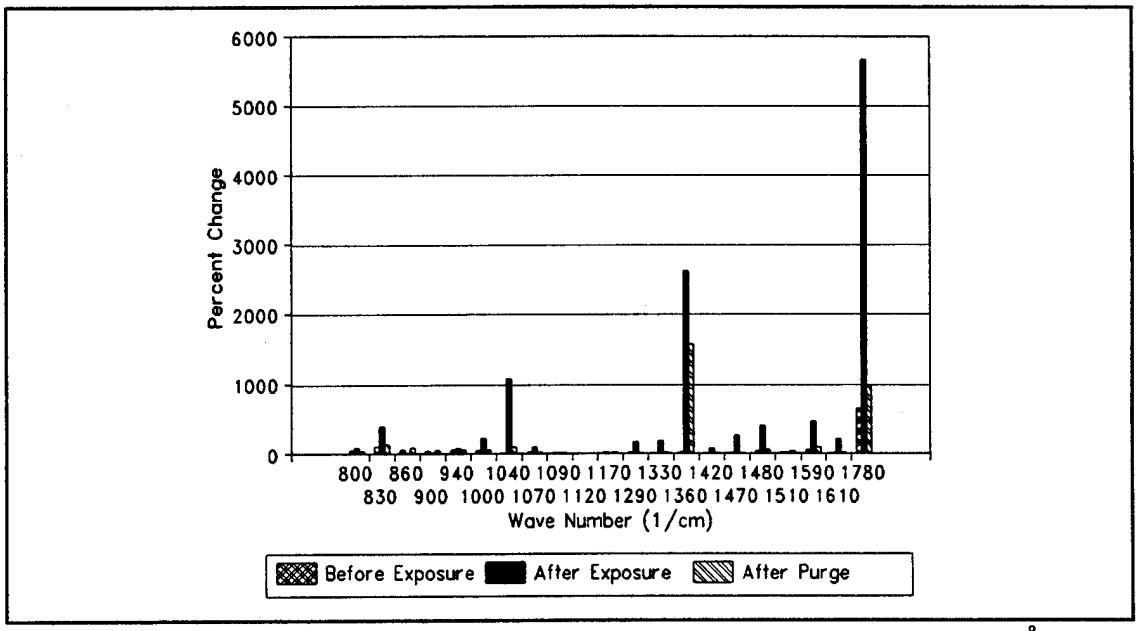


Figure C-4. Percent Change in the Infrared Absorption Spectra of the Deposited 6600 Å Copper Phthalocyanine Thin Film Relative to the Sadtler Reference Spectra (73) for the Pre-Exposed, 770 ppm NO_2 Exposed, and the Purged Conditions. (Infrared Spectra Normalized with Respect to the 1120 cm^{-1} Peak.)

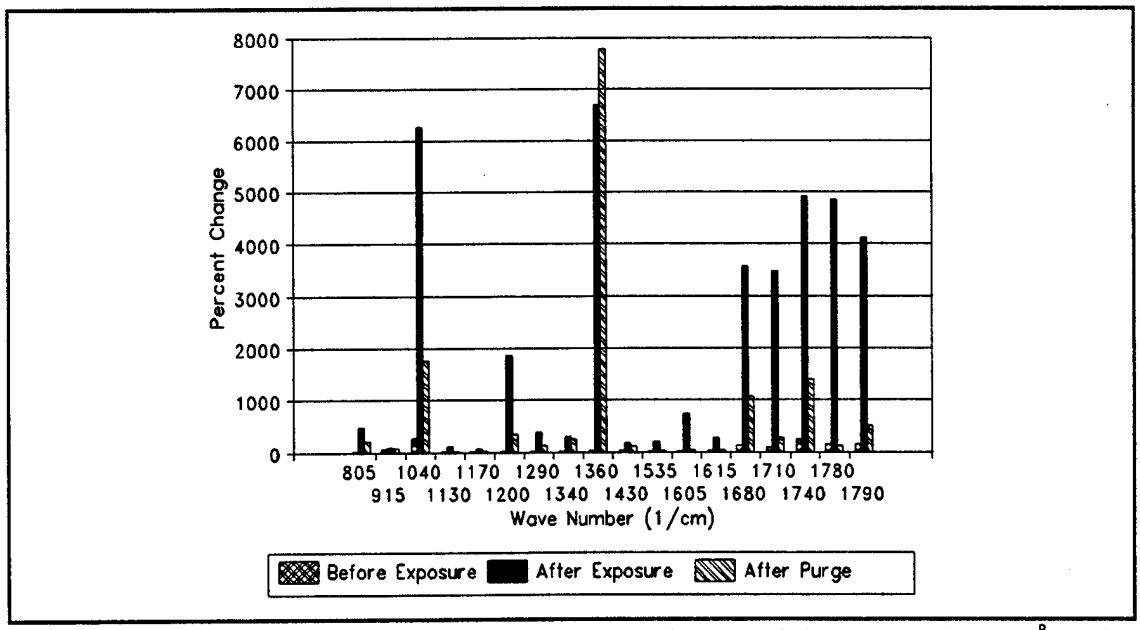


Figure C-5. Percent Change in the Infrared Absorption Spectra of the Deposited 7100 Å Nickel Phthalocyanine Thin Film Relative to the Sadtler Reference Spectra (74) for the Pre-Exposed, 770 ppm NO_2 Exposed, and the Purged Conditions. (Infrared Spectra Normalized with Respect to the 1120 cm^{-1} Peak.)

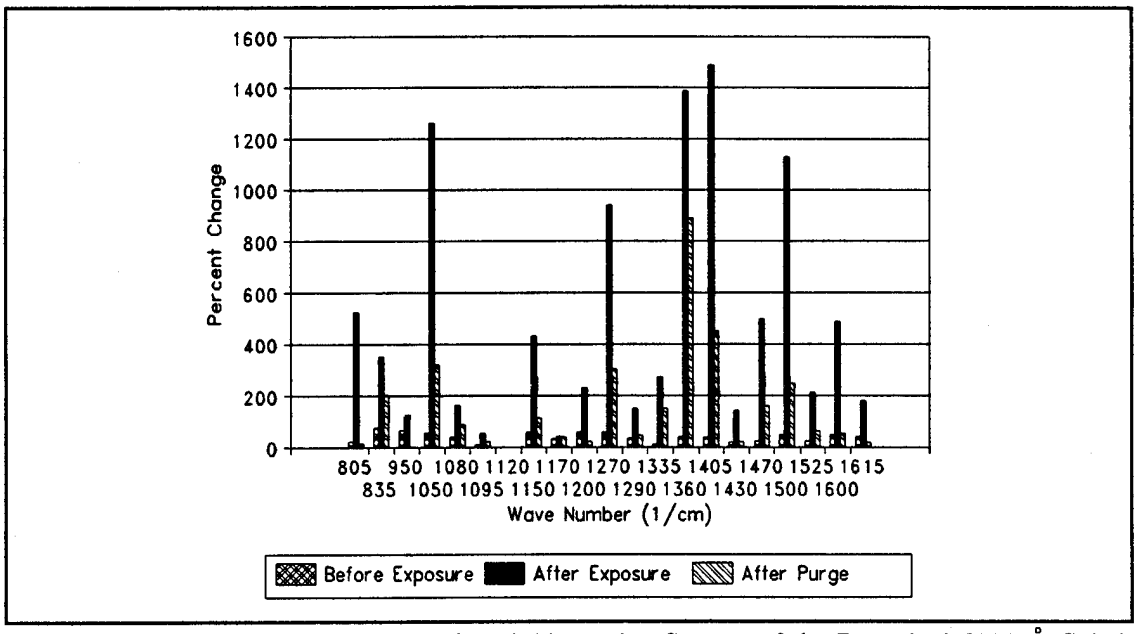


Figure C-6. Percent Change in the Infrared Absorption Spectra of the Deposited 5800 Å Cobalt Phthalocyanine Thin Film Relative to the Published Reference Spectra (49) for the Pre-Exposed, 770 ppm NO_2 Exposed, and the Purged Conditions. (Infrared Spectra Normalized with Respect to the 1120 cm^{-1} Peak.)

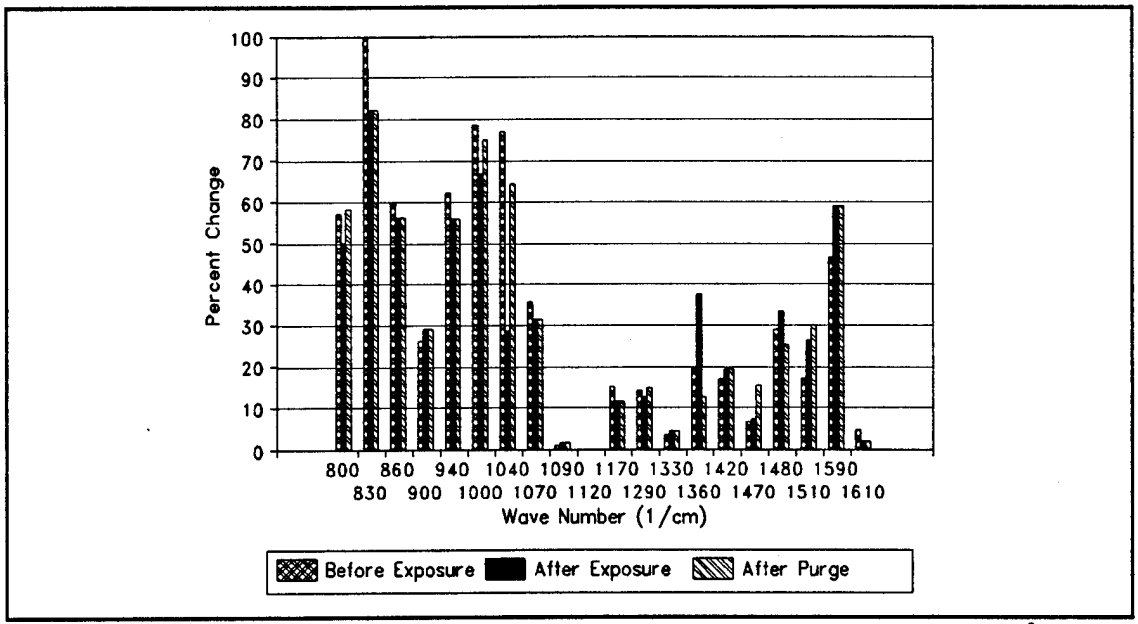


Figure C-7. Percent Change in the Infrared Absorption Spectra of the Deposited 7700 Å Copper Phthalocyanine Thin Film Relative to the Sadtler Reference Spectra (73) for the Pre-Exposed, 3700 ppm NH_3 Exposed, and the Purged Conditions. (Infrared Spectra Normalized with Respect to the 1120 cm^{-1} Peak.)

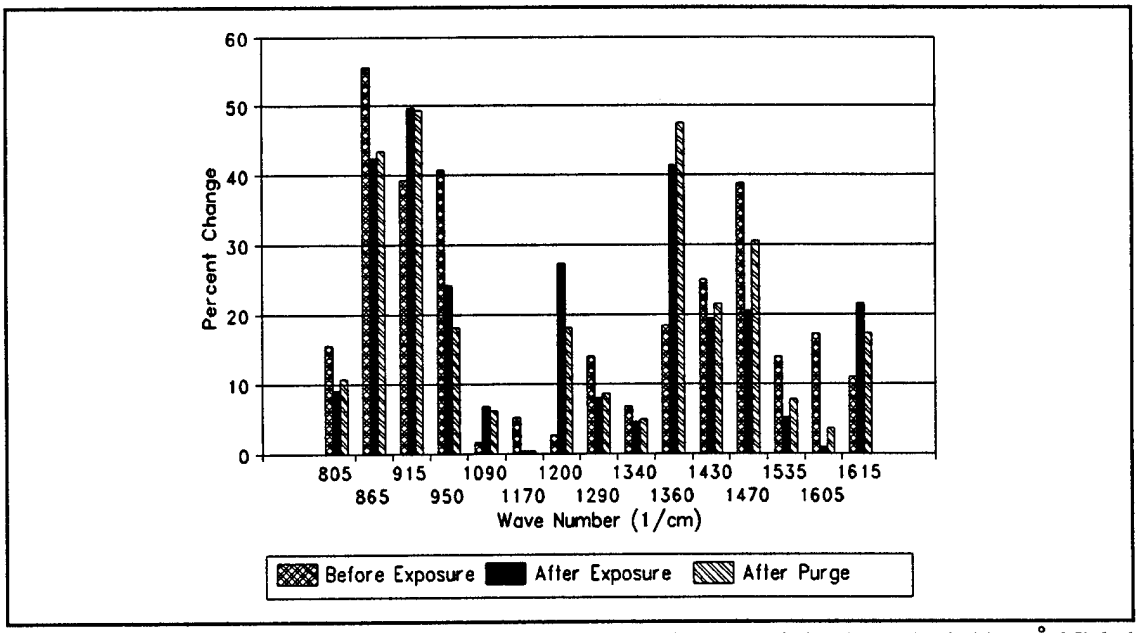


Figure C-8. Percent Change in the Infrared Absorption Spectra of the Deposited 6500 Å Nickel Phthalocyanine Thin Film Relative to the Sadtler Reference Spectra (74) for the Pre-Exposed, 3700 ppm NH_3 Exposed, and the Purged Conditions. (Infrared Spectra Normalized with Respect to the 1120 cm^{-1} Peak.)

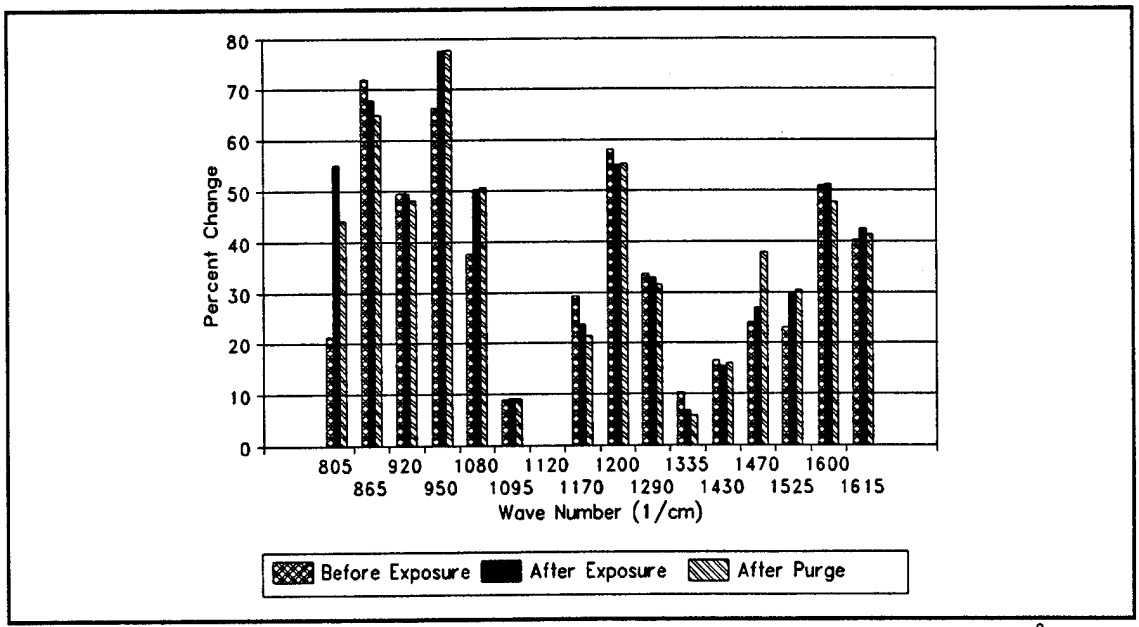


Figure C-9. Percent Change in the Infrared Absorption Spectra of the Deposited 5300 Å Cobalt Phthalocyanine Thin Film Relative to the Published Reference Spectra (49) for the Pre-Exposed, 3700 ppm NH_3 Exposed, and the Purged Conditions. (Infrared Spectra Normalized with Respect to the 1120 cm^{-1} Peak.)

Appendix D. Evaluation of Experimental Measurement Techniques

As discussed in Chapter IV, a large set of electrical measurements was initially considered for monitoring the IGEFET sensor's electrical response. This set included the IGE structure's DC resistance, the IGE structure's input (electrode-to-ground) and through (inter-electrode) AC impedances, the IGEFET sensor's time- and frequency-domain square-wave responses, and the IGEFET sensor's transfer function gain and phase. To facilitate a more rapid sampling period for each measurement type, while minimizing the duration of the challenge gas exposure, the DC resistance and transfer function measurements were selected to monitor the IGEFET's electrical behavior. This measurement subset was selected on the basis of the results from two separate experiments designed to: 1) evaluate the AC impedance measurements, and 2) evaluate the time- and frequency-domain square-wave response measurements.

Evaluation of the AC Impedance Measurements

The AC impedance measurements were evaluated by comparing the IGEFET sensor's transfer function gain computed from the AC impedance measurements with the actual measured IGEFET sensor's transfer function gain. For this evaluation, the IGE structure was coated with EPON 828 epoxy (Miller-Stephenson Chemical Company, Danbury, CT) that was mixed with the curing agent, Versamide V-40 (Miller Stephenson Chemical Company, Danbury CT). The electrical measurements were collected over time as the epoxy cured. The measurements were collected with the IGEFET sensors operating in the test chambers described in Chapter IV (nitrogen ambientwas provided). The sensor's temperature was maintained at 30° C. The epoxy, which is initially partially conductive, permits accurate AC impedance measurements with an impedance/gain-phase analyzer (model HP4194A, Hewlett Packard, Palo Alto, CA). However, as the epoxy cures, the conductivity decreases to a point that the AC impedance eventually exceeds the instrument's capability at low-frequency. To compute the IGEFET sensor's transfer function gain, both the through ($Z_{Through}$) and input (Z_{Input}) impedances were collected.

In Figures D-1 and D-2, the magnitude and phase of the input and through impedances, collected at 10, 20, and 30 minutes after the epoxy was mixed with the curing agent, are plotted. As the epoxy cured, the input impedance exhibited a small increase in its magnitude, while the phase slowly approached -90°. The variation in the input impedance's phase near 100 Hz reflects the limited capability of the instrument. The instrument limitation is even more apparent in the measurement of the through impedance. The initial through impedance's magnitude, which was greater than the largest input

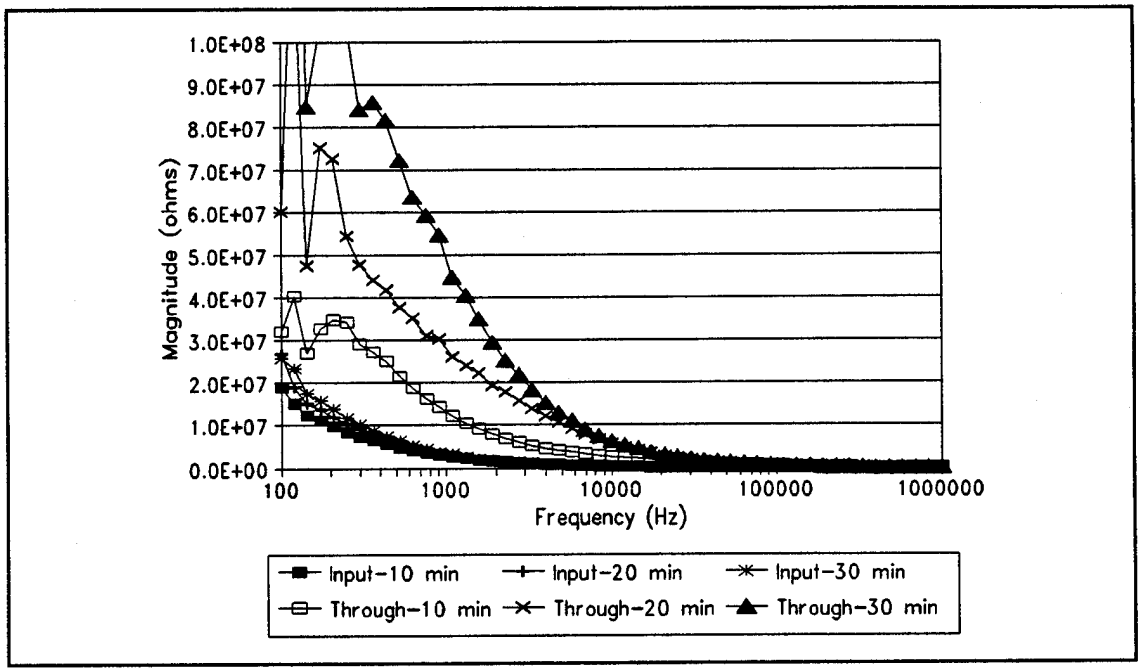


Figure D-1. Magnitude of the Input and Through Impedances as a Function of Frequency for an Epoxy-Coated Interdigtated Gate Electrode (IGE) Structure at Different Cure Times. (Temperature = 30° C, Nitrogen Ambient.)

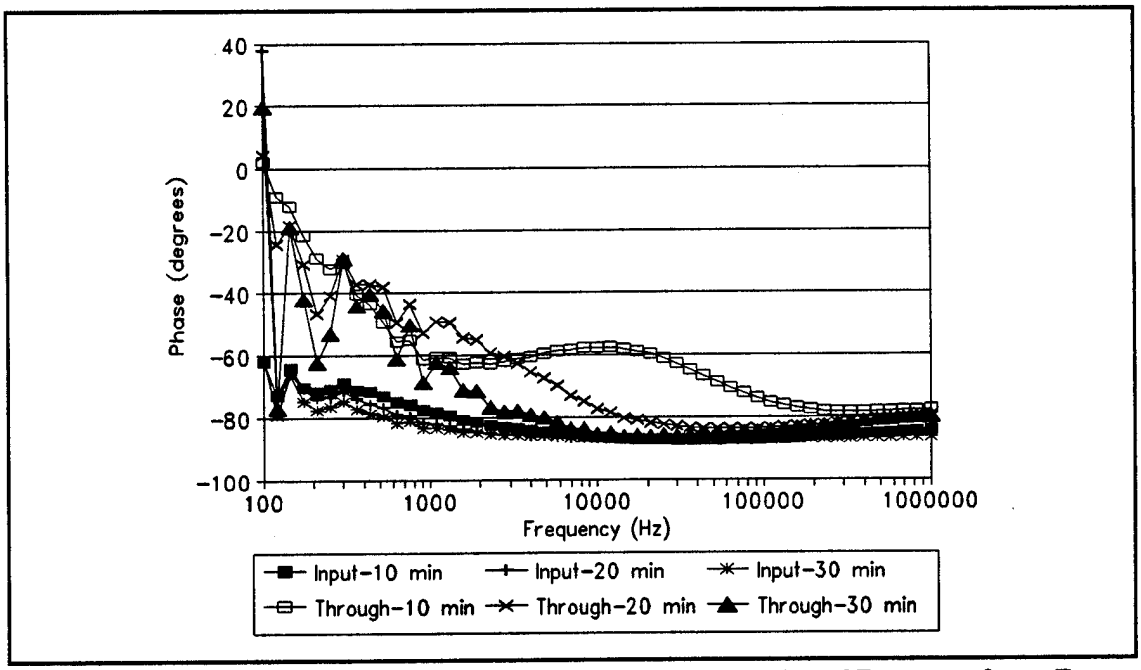


Figure D-2. Phase of the Input and Through Impedances as a Function of Frequency for an Epoxy-Coated Interdigtated Gate Electrode (IGE) Structure at Different Cure Times. (Temperature = 30° C, Nitrogen Ambient.)

impedance magnitude, increased rapidly as the epoxy cured. The instability in the through impedance's phase at frequencies less than 2 KHz reflect the limited capability of the instrument to measure impedances with magnitudes greater than approximately 30 Mohms.

Comparison of the IGEFET sensor's transfer function gain computed from the AC impedance measurements with the actual measured IGEFET sensor's transfer function gain was complicated by the fact that different electrical connections were required to accomplish the measurements. The AC through impedance was measured across the inter-electrode array, and this measurement required electrical connection to the floating-gate electrode. However, the measurement of the actual IGEFET sensor's transfer function gain required that the floating gate bond wire be removed to prevent capacitive loading (discussed in Chapter IV). Therefore, simultaneous measurement of the AC impedance and the IGEFET sensor's transfer function gain was precluded, and the evaluation was conducted with data collected in separate experiments from two different IGEFET sensor elements. In addition to the incompatibility between the AC impedance and the IGEFET sensor transfer function measurements, the electrical connections to measure the input impedance required manual modification to the automated system used to collect the DC resistance and through impedance.

Figures D-3 compares the IGEFET sensor's transfer function gain computed from the AC impedance measurements with that obtained from direct measurement with the gain/phase analyzer. The IGEFET sensor transfer function gain was computed from the AC impedance using the following equation:

$$\text{Gain} = 20 \log_{10}\left(\frac{Z_{Input}}{Z_{Input} + Z_{Through}}\right) \qquad \text{(D-1)}$$

Early in the epoxy cure (10 minutes) the conductivity decreases rapidly, and small differences in the cure time between the two samples significantly affected the measured electrical response. However, as the epoxy cured, and the conductivity changed more slowly, the difference between the measured IGEFET sensor's transfer function gain and the computed gain decreased. As expected from Kirchoff's Voltage Law, this comparison demonstrates that the IGEFET sensor's transfer function contains information reflecting the two AC impedance components. Although the AC impedance measurements provides information that is not available from the other measurements, its limited capability to measure large impedances was not suitable for impedance measurements over the operating frequency range of the MPc-coated IGEFET sensors. In addition, the modification to the electrical connections required to

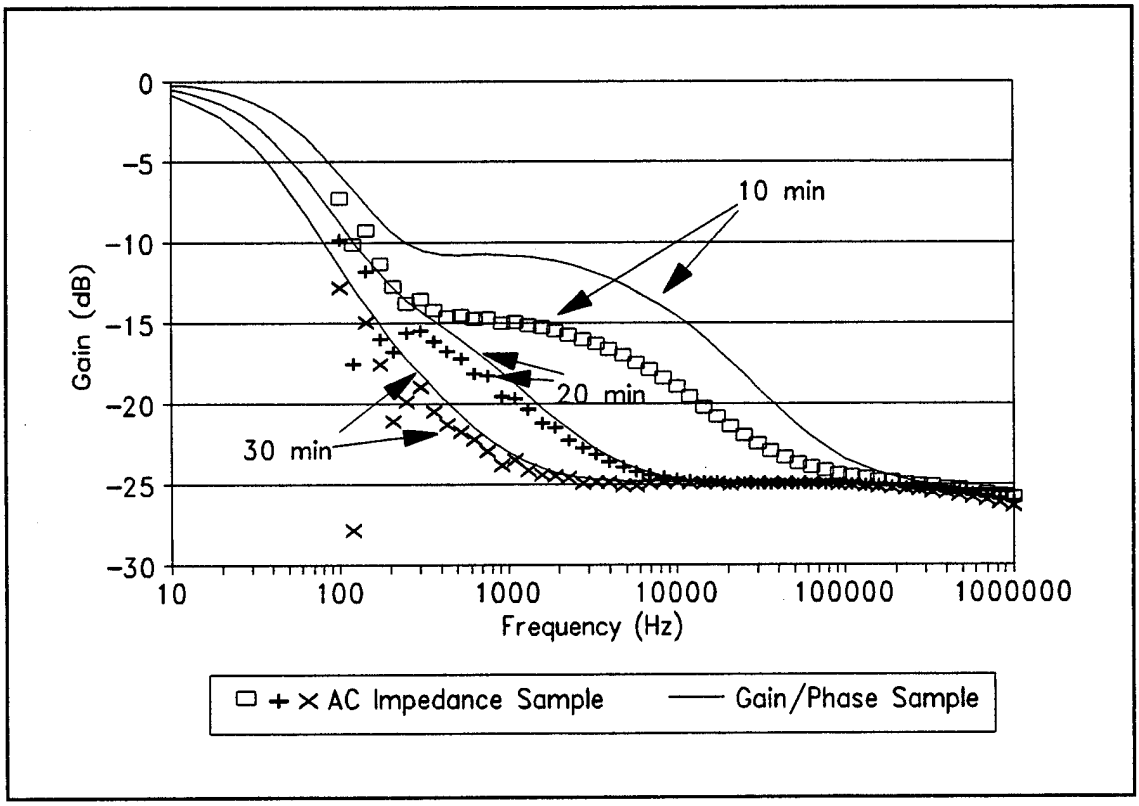


Figure D-3. Computed and Measured Transfer Function Gain for an Epoxy-Coated IGEFET at 10, 20, and 30 minute Cure Times. The Transfer Function Gain was Computed from the AC Impedance Measurements. The AC Impedance and the IGEFET Transfer Function Gain/Phase Measurements were Collected in Separate Experiments fromTwo Different Epoxy-Coated IGEFET Sensors. (Epoxy- EPON 828 Mixed with the Versamide V-40 Curing Agent, Temperature = 30° C, Nitrogen Ambient.)

measure the input impedance was cumbersome, and could not be effectively performed simultaneously with the other measurements.

Evaluation of the Time- and Frequency-Domain Square-wave Response Measurements

The evaluation of the time- and frequency-domain square-wave response measurements, like the evaluation of the AC impedance measurements, was accomplished by comparing the computed transfer function gain with the measured transfer function gain. For this evaluation, two sensor elements of the IGEFET microsensor were coated with 0.2 μm and 1 μm thick cobalt phthalocyanine (CoPc) films. The measurement of the time- and frequency-domain square-wave response and the IGEFET transfer function measurements were accomplished as described in Chapter IV. The MPc-coated IGEFET microsensor's temperature was maintained in air at 150° C within the test chamber. The electrical measurements were collected before and after a 1-hour, 1000 ppb nitrogen dioxide (NO_2) challenge gas exposure.

Figures D-4 and D-5 depict the time-domain square-wave response of the CoPc-coated IGEFET sensors before and after exposure to the NO_2 challenge gas. The applied input signal is provided as a reference. The output signal amplitude from the IGEFET sensor coated with 1 μm thick CoPc film indicates a flat 3 dB attenuation of the spectral content of the input signal. This unexpected behavior was the result of a minor problem with the experimental configuration. The input reference signal was measured once at the beginning of the experiment by applying the signal generator output directly to the high input impedance port of the oscilloscope. However, during the experiment, this signal was simultaneously applied to the channel-1 input port of the spectrum analyzer and to the driven gate of the IGEFET sensor element. The spectrum analyzer has a 50 ohm input impedance, and therefore, half the signal was dropped across the signal generator's 50 ohm output impedance. Thus, the actual applied signal level to the IGEFET sensor was reduced to 1 volt. Other than decreasing the signal-to-noise ratio, this problem did not affect the results. The time-domain square-wave response of the IGEFET sensor indicates a low-pass characteristic which is enhanced upon NO_2 exposure.

Figures D-6 and D-7 reveal the spectral energy content of the input and output signals of the IGEFET sensor. The spectrum of the input square-wave signal corresponds to the 1-volt signal level. The energy content of the output signal from the IGEFET sensor coated with the 0.2 μm CoPc film reveals that the input signal was attenuated at all harmonic frequencies. Although the input signal was attenuated less at low-frequency (frequencies less than 1 KHz), the attenuation at high frequency significantly decreased the harmonic energy content in the IGEFET output signal. As expected, the

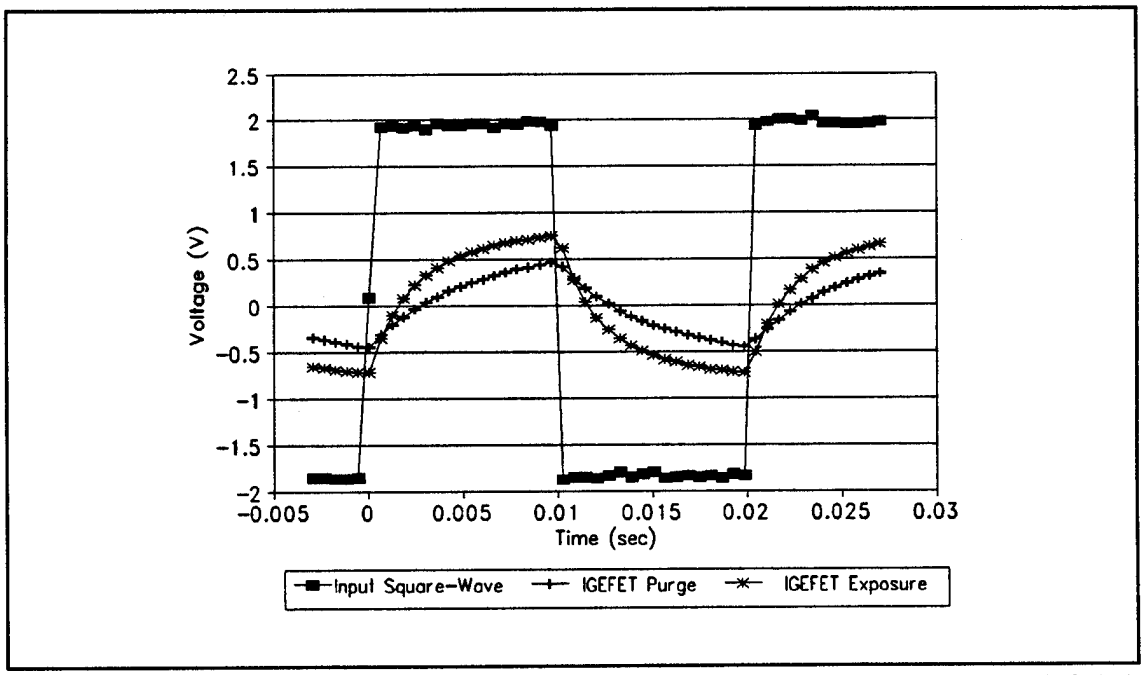


Figure D-4. Time-Domain Square-Wave Response of an IGEFET Coated with a 0.2 μm Thick Cobalt Phthalocyanine (CoPc) Thin Film Before (Purge) and After Exposure to 1000 ppb NO_2. The Input Square-Wave Signal is Provided as a Reference. (Temperature = 150° C)

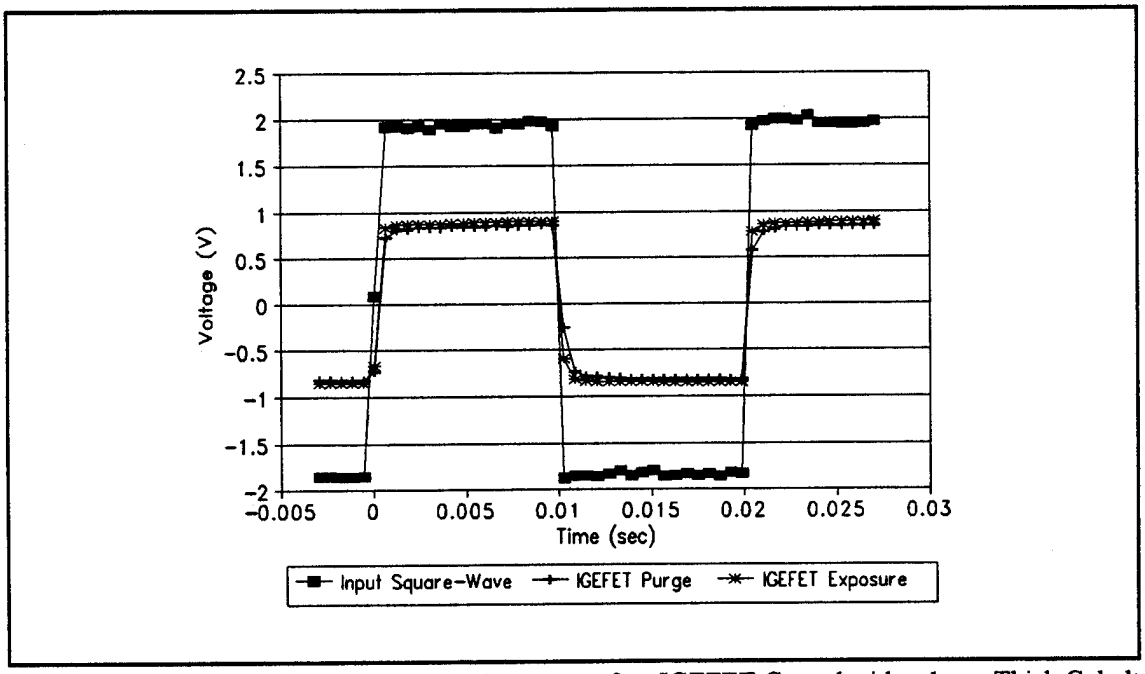


Figure D-5. Time-Domain Square-Wave Response of an IGEFET Coated with a 1 μm Thick Cobalt Phthalocyanine (CoPc) Thin Film Before (Purge) and After Exposure to 1000 ppb NO_2. The Input Square-Wave Signal is Provided as a Reference. (Temperature = 150° C)

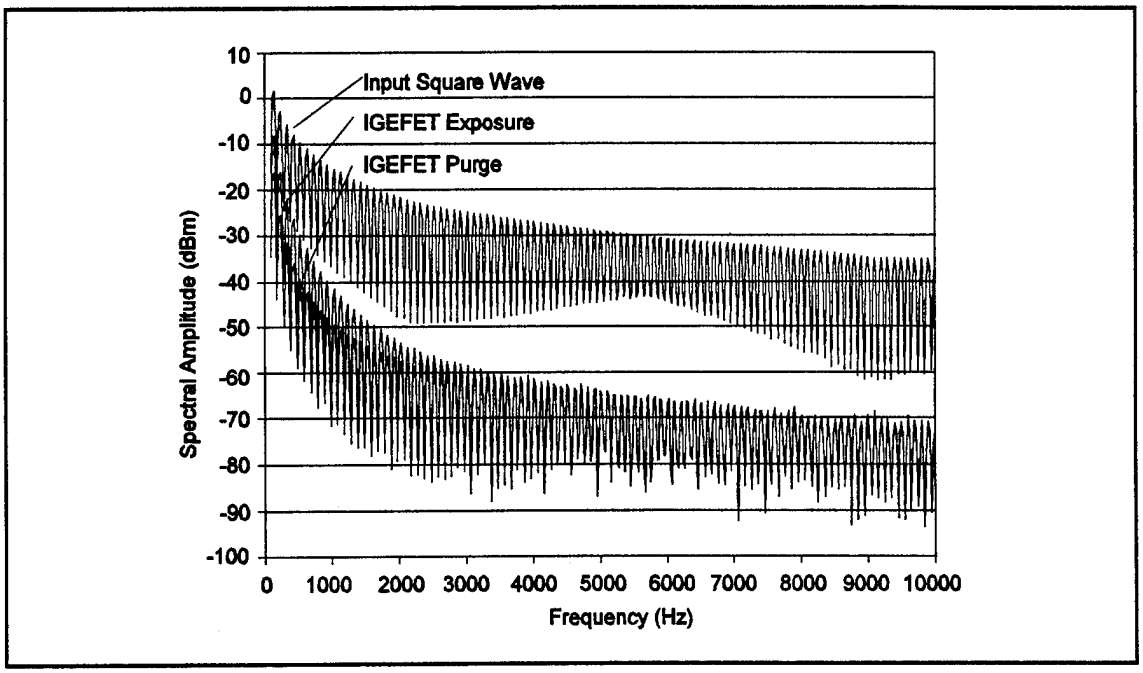


Figure D-6. Frequency-Domain Square-Wave Response of an IGEFET Coated with a 0.2 μm Thick Cobalt Phthalocyanine (CoPc) Thin Film Before (Purge) and After Exposure to 1000 ppb NO_2. The Harmonic Content of the Input Square-Wave Signal is Provided as a Reference. (Temperature = 150° C)

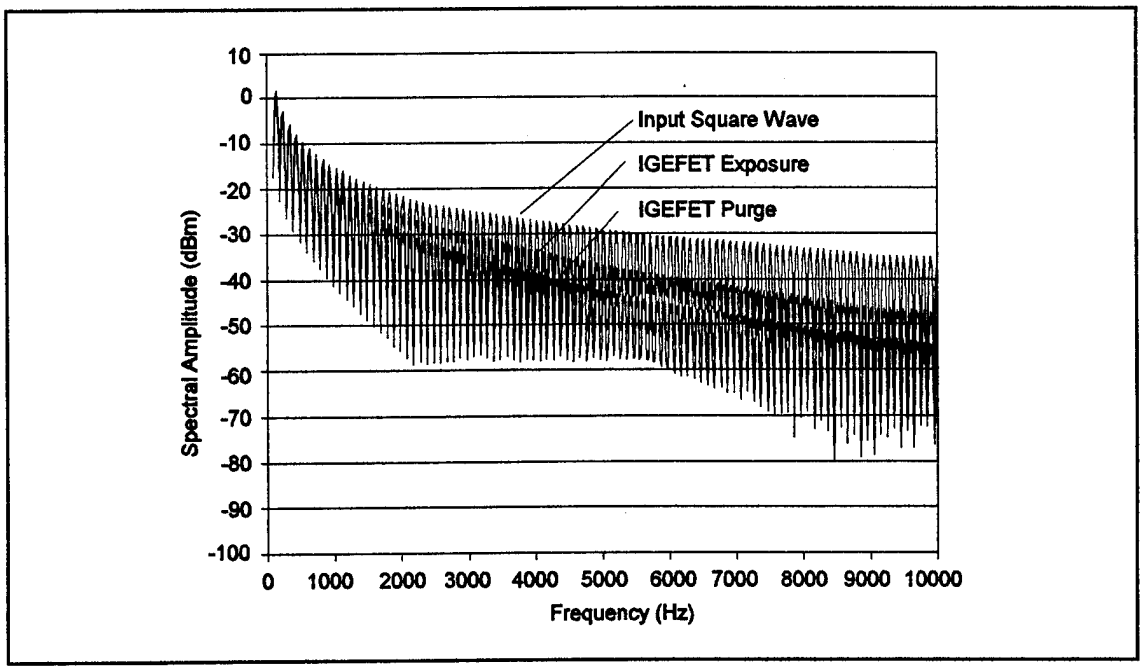


Figure D-7. Frequency-Domain Square-Wave Response of an IGEFET Coated with a 1 μm Thick Cobalt Phthalocyanine (CoPc) Thin Film Before (Purge) and After Exposure to 1000 ppb NO_2. The Harmonic Content of the Input Square-Wave Signal is Provided as a Reference. (Temperature = 150° C)

spectral attenuation of the IGEFET output signal was less when coated with the thicker 1 μm CoPc film and after NO_2 exposure.

To demonstrate that similar information is contained in the measured IGEFET sensor transfer function measurements, the transfer function gain was computed from the spectral content of the square-wave input and output signals. The transfer function gain was computed by subtracting the input spectrum from the output spectrum. Figures D-8 and D-9 demonstrate that the computed IGEFET transfer function was essentially identical to the measured IGEFET sensor's transfer function gain.

The noise present at high frequency in Figure D-8 illustrates a limitation of the square-wave response measurements. In the square-wave response measurements, the energy content of the signal is non-uniformly distributed across all harmonic frequencies; the harmonic content of the square-wave input signal is greatest at low frequency. The additional signal attenuation across the IGEFET sensor further reduces the signal level, and noise becomes a significant portion of the measured signal. In contrast, the gain/phase measurements are not limited in this way since the applied signal is a swept-frequency sine wave with the amplitude constant at all measurement frequencies. The distribution of the square-wave input signal's energy across its harmonic frequencies also limits the transfer function calculations to specific frequencies. The actual transfer function measurements are not limited in this manner.

One other factor in the evaluation of the time- and frequency-domain square-wave response measurements was the additional instrumentation required to collect this data. While the gain/phase measurements required only a single instrument, the time- and frequency-domain square-wave response measurements required a signal generator, an instrumentation amplifier, an oscilloscope, and a spectrum analyzer.

Summary

The AC impedance, as well as the time- and frequency-domain square-wave response measurements, were evaluated by comparing them with the actual IGEFET transfer function measurements. The relationship between the input and through impedances to the measured IGEFET transfer function was demonstrated. Although the AC impedance measurements yielded information that could not be obtained with the other measurements, instrument limitations restrict its applicability to the high impedance films studied in this research. Also, the measurement configuration required for the

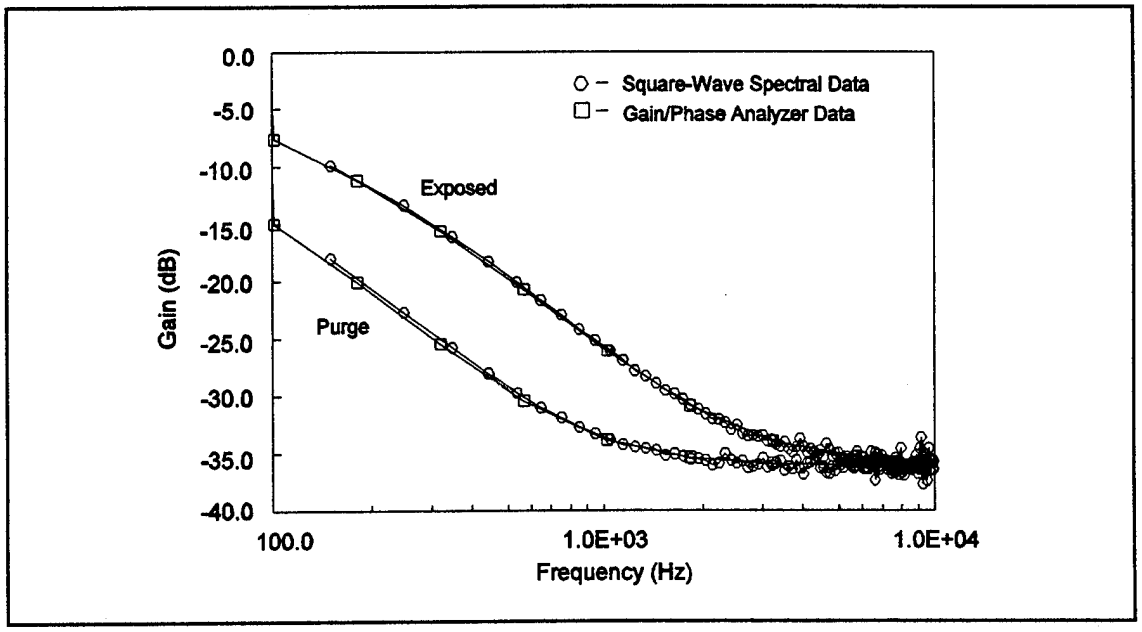


Figure D-8. Computed and Measured Transfer Function Gain of an IGEFET Coated with a 0.2 μm Thick Cobalt Phthalocyanine (CoPc) Thin Film Before (Purge) and After Exposure to 1000 ppb NO_2. The IGEFET Transfer Function Gain was Computed from the Frequency-Domain Square-Wave Response Data. (Temperature = 150° C)

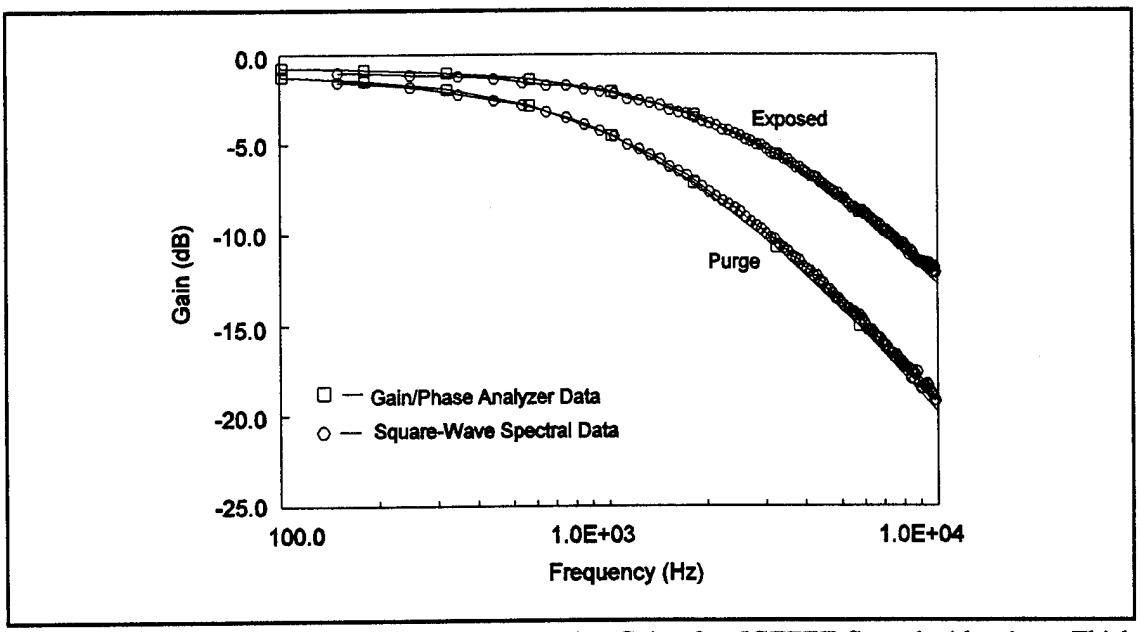


Figure D-9. Computed and Measured Transfer Function Gain of an IGEFET Coated with a 1 μm Thick Cobalt Phthalocyanine (CoPc) Thin Film Before (Purge) and After Exposure to 1000 ppb NO_2. The IGEFET Transfer Function Gain was Computed from the Frequency-Domain Square-Wave Response Data. (Temperature = 150° C)

input impedance was not compatible with the automated configuration for measuring the through impedance and the DC resistance. In the evaluation of the time- and frequency-domain square-response measurements, the computed transfer function gain was essentially identical to the measured IGEFET transfer function gain. Although similar information was obtained with the two approaches, the square-wave response measurements are more experimentally limited compared to the direct measure of the IGEFET sensor's transfer function.

Appendix E. Detailed Electrical Schematics of Test Configuration

The schematics on the following pages illustrate the electrical connections used for collecting data from the two test chambers and controlling the temperature of the microsensors. Figure E-1 shows the electrical connections for collecting data from the IGEFET microsensor where the electrical input signal was applied to the driven-gate (DG) electrode, and the output was measured at the output of the sensor amplifier (V_{out}). The floating-gate (FG) electrode bond wire was removed from each of the nine IGEFET elements prior to its insertion in test chamber #1. Figure E-2 shows the electrical connections for collecting data from the Interdigitated Gate Electrode (IGE) structure of the IGEFET microsensor elements. In this case, the FG bond wire was not removed. Figure E-3 shows the schematic of the closed-loop control circuit used to regulate the temperature of the microsensors within the test chambers.

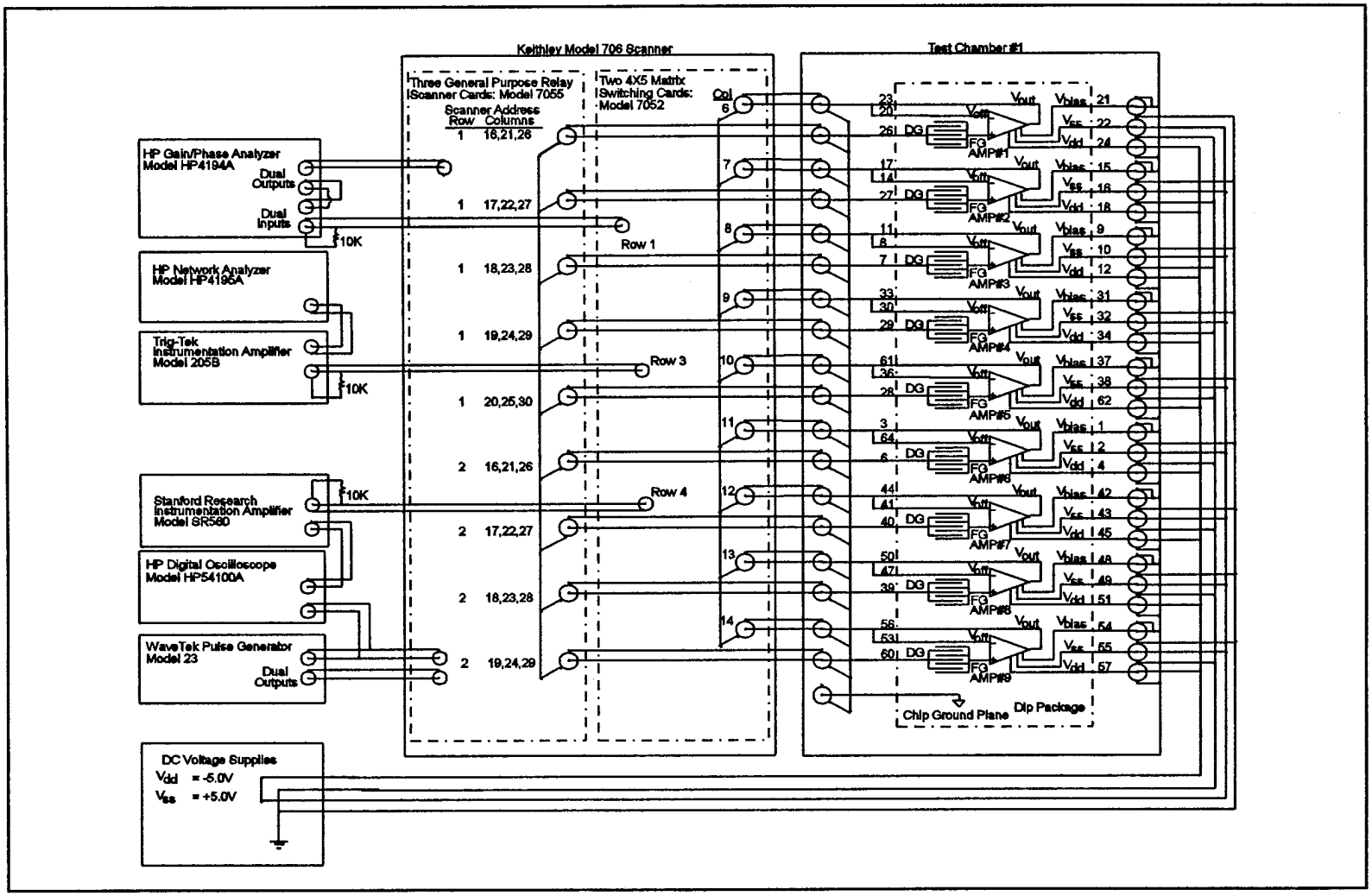


Figure E-1. Detailed Electrical Schematic for the IGEFET Microsensor Electrical Measurements. The Numbers within the Test Chamber are the IC Package Bond Pad Pin Numbers. DG - Driven Gate Electrode, FG - Floating Gate Electrode, V_{out} - Output Signal, V_{bias} - Bias Voltage, V_{ss} - Negative Supply Voltage, V_{dd} - Positive Supply Voltage, V_{off} - Offset Voltage, Col - Column, AMP - Sensor Amplifier.

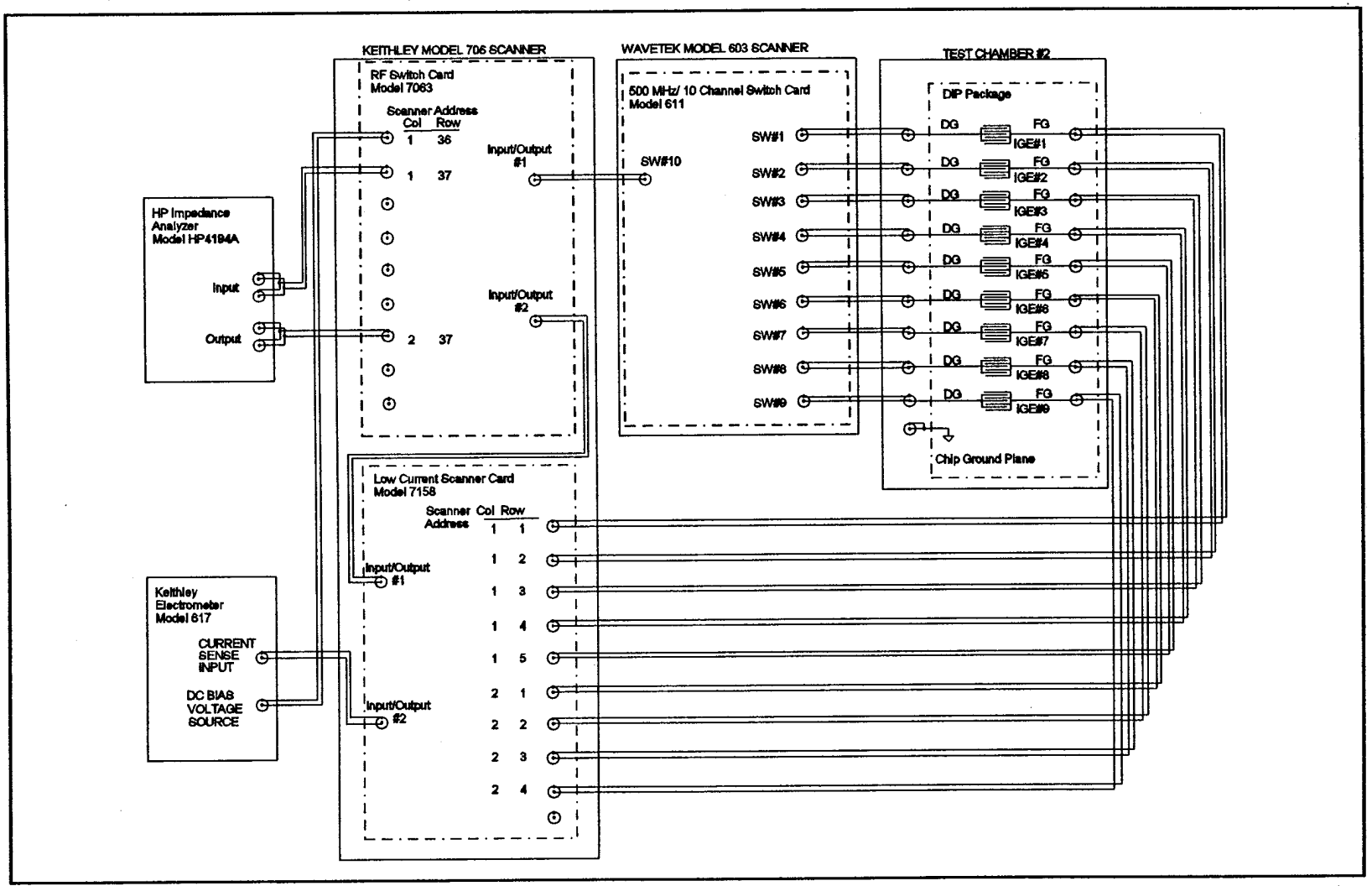


Figure E-2. Detailed Electrical Schematic for the Interdigitated Gate Electrode (IGE) Measurements. DG - Driven Gate Electrode, FG - Floating Gate Electrode, Col - Column, SW - Switch. All Unused Connections of Test Chamber #2 were Grounded.

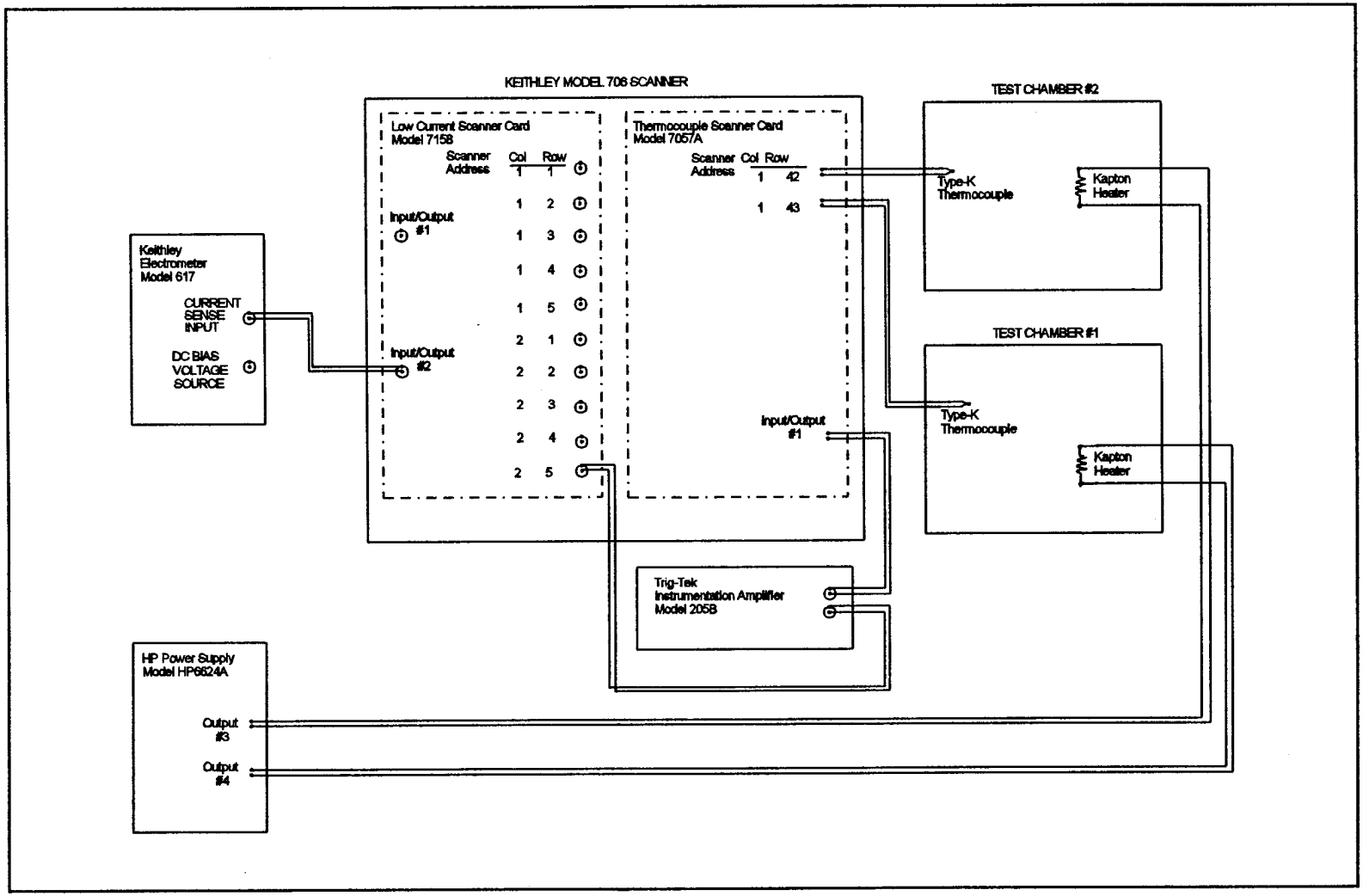


Figure E-3. Detailed Electrical Schematic for the Closed-Loop Temperature Regulation of the IGEFET Microsensors in both Test Chambers. Col - Column.

Appendix F. Supporting Data: Baseline Characterization of the MPc-Coated Microsensor

This appendix contains the DC resistance data collected during the baseline characterization of the nickel phthalocyanine (NiPc)- and cobalt phthalocyanine (CoPc)-coated interdigitated gate electrode field effect transistor (IGEFET) microsensors. The data presented in this appendix supports the baseline characterization of the copper phthalocyanine (CuPc)-coated IGEFET microsensor discussed in Chapter IV. Figures F-1 through F-6 present Arrhenius plots of the IGE structure's DC resistance when coated with 0.2, 0.5, and 1.0 μm thick NiPc and CoPc films. Figures F-7 and F-8 illustrate the dependence of the IGE structure's DC resistance upon the thickness of the MPc film coatings. Figures F-9 through F-20 depict the voltage dependence of the IGE structure's DC resistance when coated with 0.2, 0.5, and 1.0 μm thick NiPc and CoPc films.

Although the similarity in the DC resistance behavior of the three MPc-coated films are clearly demonstrated in the figures presented in this appendix and in Chapter IV, anomalous behavior was observed in the DC resistance behavior of IGEFET sensing elements 1 and 2 on the NiPc-coated microsensor. The IGE structure of IGEFET sensing element 2 was short-circuited (IC fabrication problem), and therefore, the data from this element was not presented. The DC resistance behavior of IGEFET sensing element 1 (Figures F-1, F-9, and F-15) indicates that the parasitic leakage path between the driven- and floating-gate electrodes, that was discussed in Chapter IV, dominates the measured resistance. Although not as pronounced, the effect of the parasitic leakage path was also observed in the DC resistance behavior of IGEFET sensing element 1 when it was coated with the CuPc and CoPc films (Figure IV-78 and F-12).

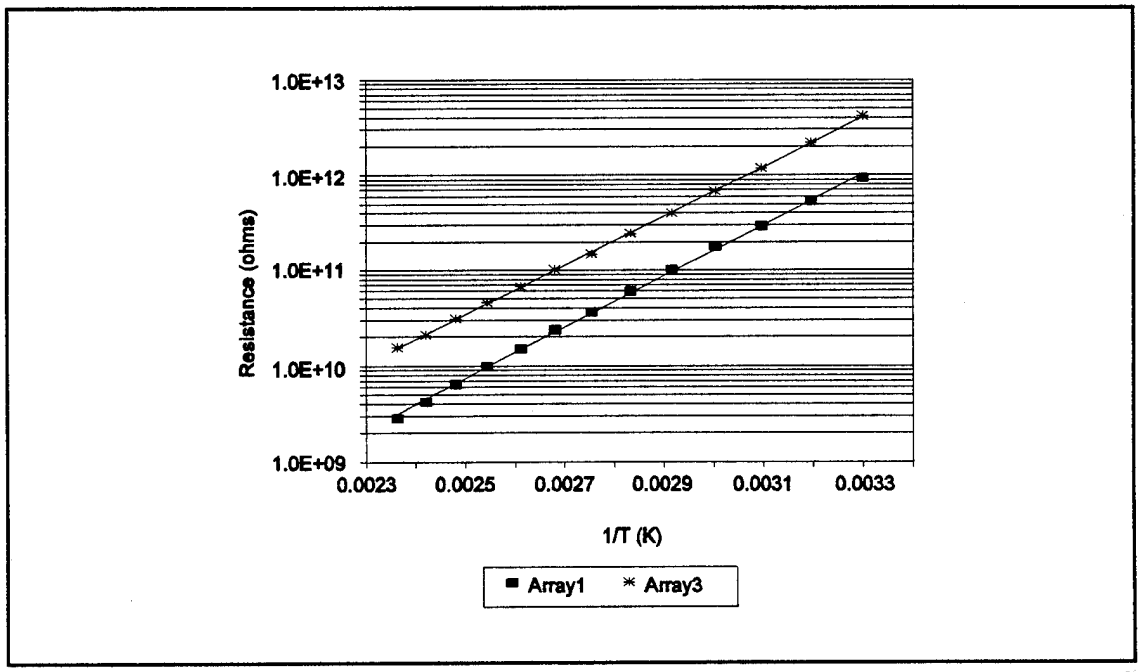


Figure F-1. Temperature Dependence of the Interdigitated Gate Electrode (IGE) Structure's DC Resistance for IGEFET Sensing Elements Coated with a 0.2 μm Thick Nickel Phthalocyanine (NiPc) Film. Microsensor Maintained in a Dry Air Ambient. Bias Voltage=10 V.

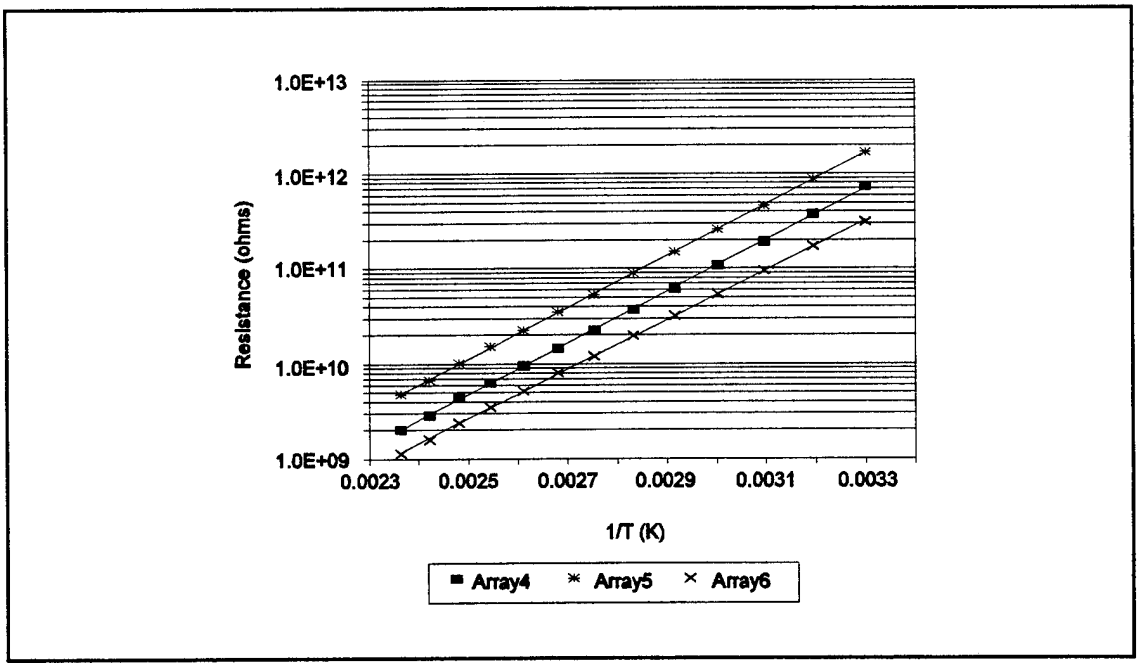


Figure F-2. Temperature Dependence of the Interdigitated Gate Electrode (IGE) Structure's DC Resistance for IGEFET Sensing Elements Coated with a 0.5 μm Thick Nickel Phthalocyanine (NiPc) Film. Microsensor Maintained in a Dry Air Ambient. Bias Voltage =10 V.

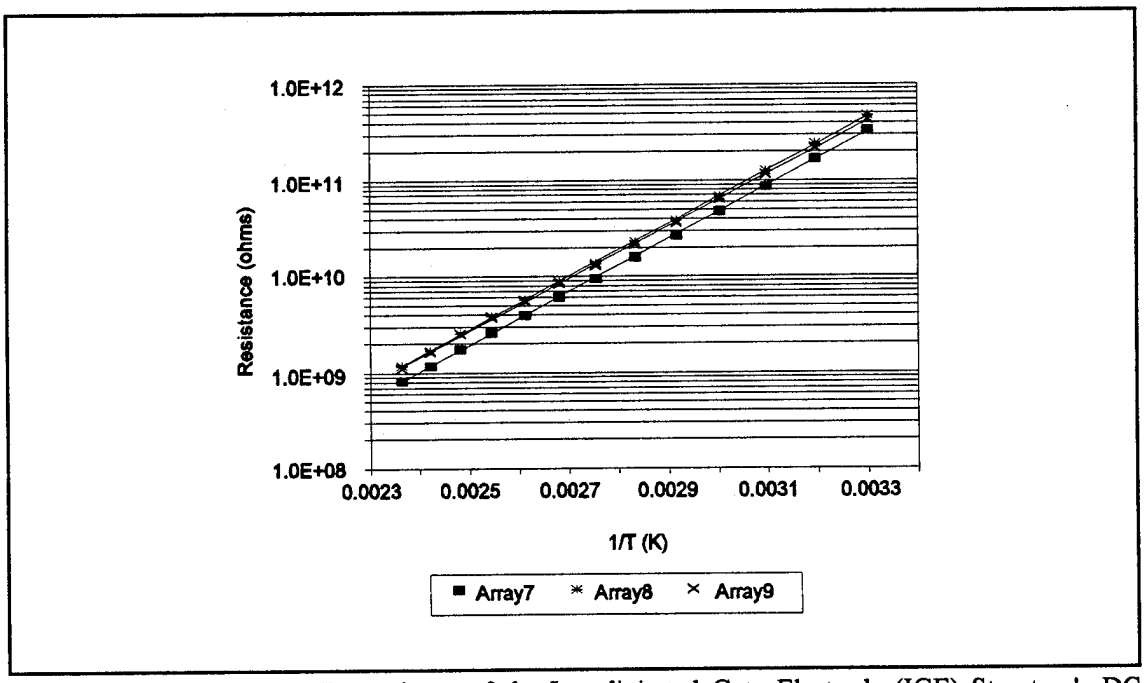


Figure F-3. Temperature Dependence of the Interdigitated Gate Electrode (IGE) Structure's DC Resistance for IGEFET Sensing Elements Coated with a 1.0 μm Nickel Phthalocyanine (NiPc) Film. Microsensor Maintained in a Dry Air Ambient. Bias Voltage=10 V.

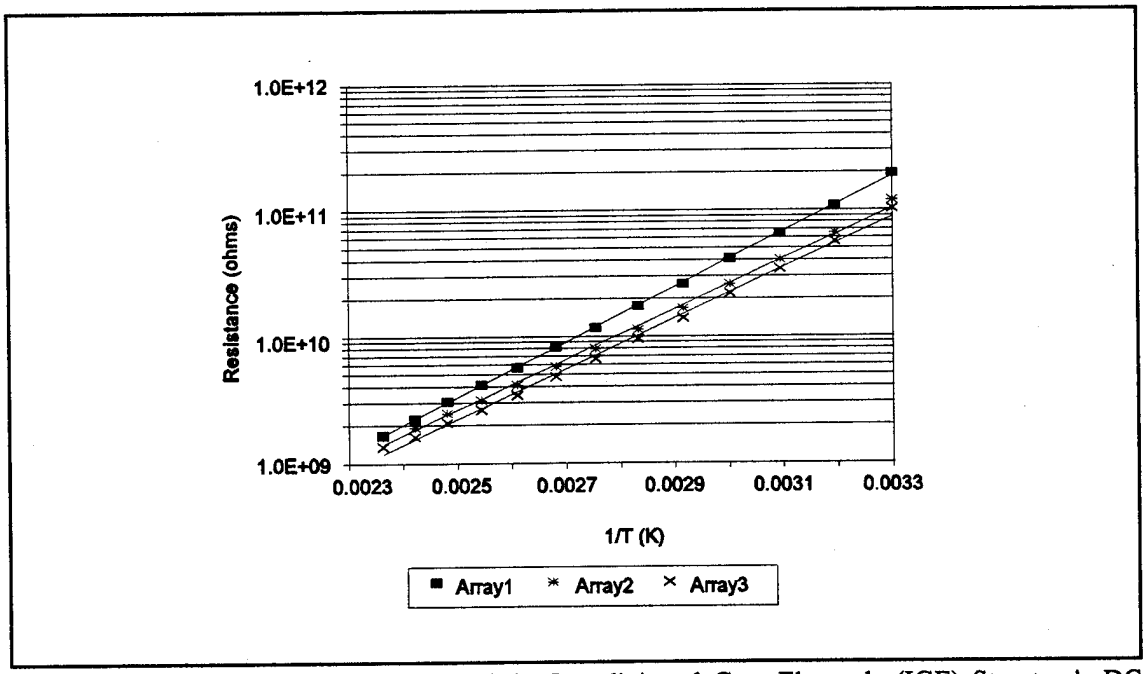


Figure F-4. Temperature Dependence of the Interdigitated Gate Electrode (IGE) Structure's DC Resistance for IGEFET Sensing Elements Coated with a 0.2 μm Cobalt Phthalocyanine (CoPc) Film. Microsensor Maintained in a Dry Air Ambient. Bias Voltage=10 V.

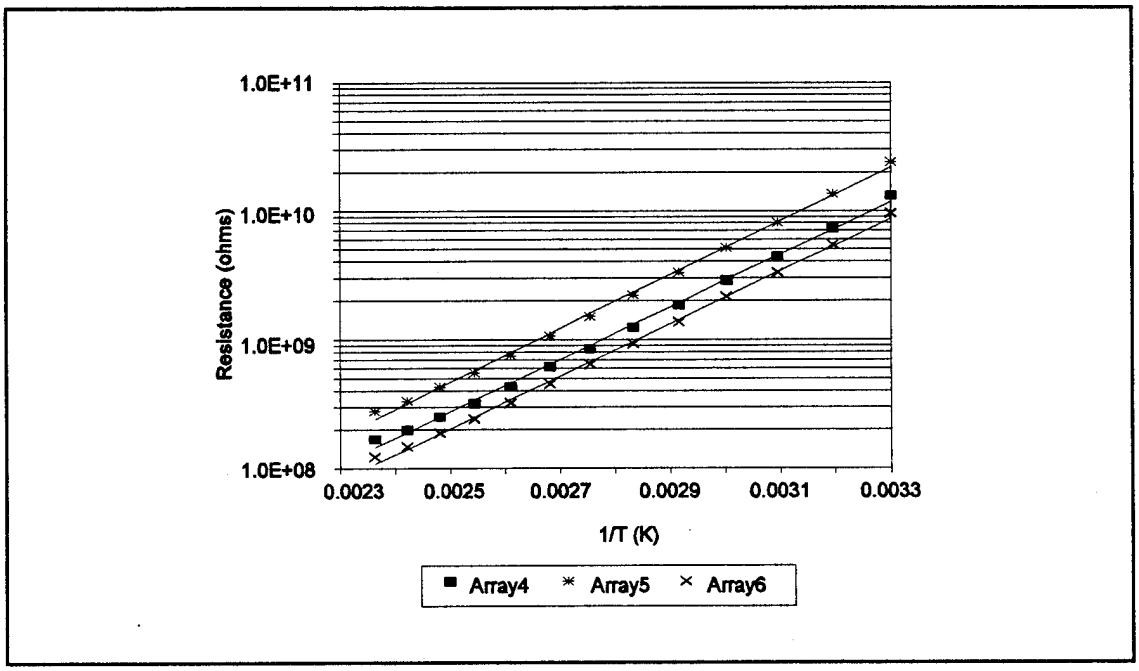


Figure F-5. Temperature Dependence of the Interdigitated Gate Electrode (IGE) Structure's DC Resistance for IGEFET Sensing Elements Coated with a 0.5 μm Cobalt Phthalocyanine (CoPc) Film. Microsensor Maintained in a Dry Air Ambient. Bias Voltage=10 V.

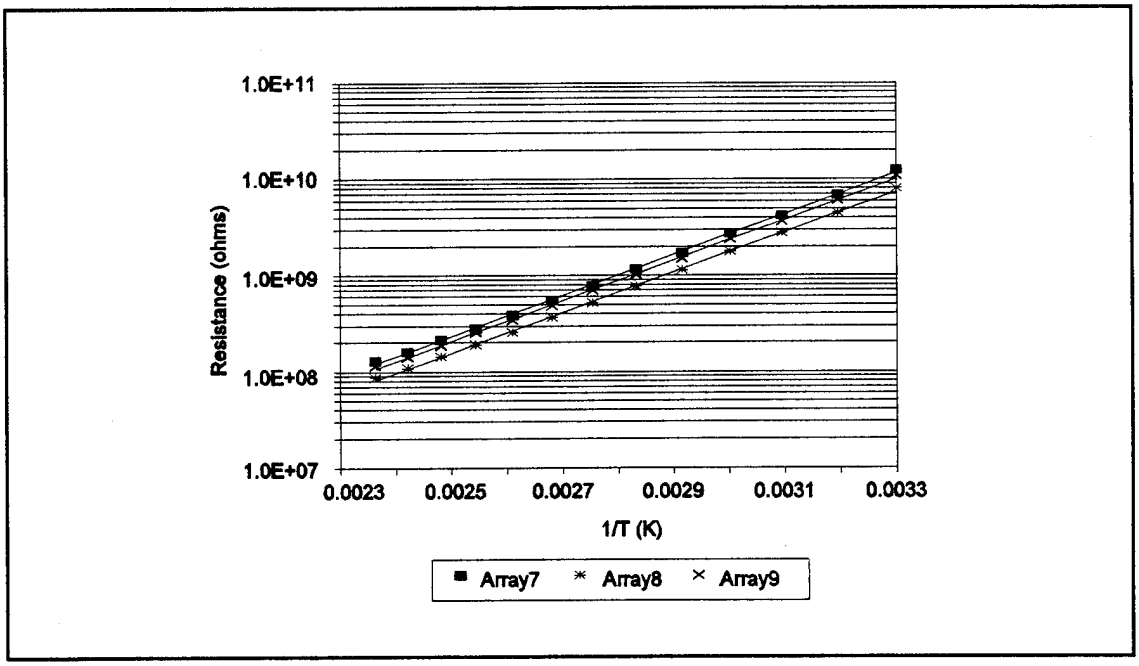


Figure F-6. Temperature Dependence of the Interdigitated Gate Electrode (IGE) Structure's DC Resistance for IGEFET Sensing Elements Coated with a 1.0 μm Cobalt Phthalocyanine (CoPc) Film. Microsensor Maintained in a Dry Air Ambient. Bias Voltage=10 V.

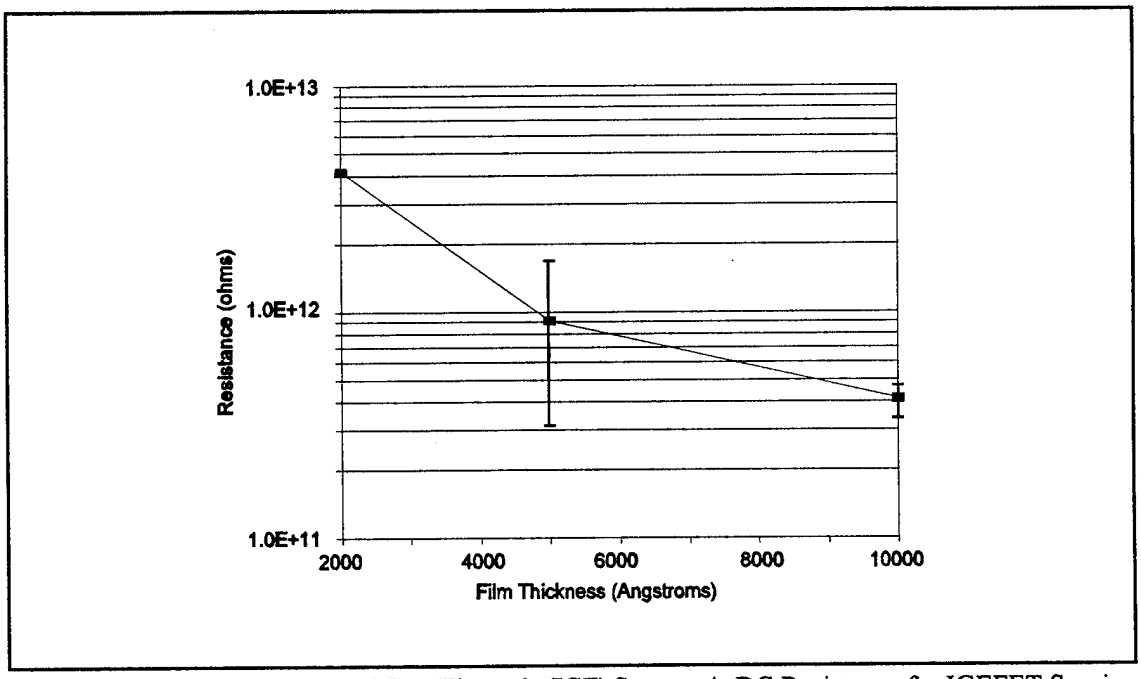


Figure F-7. Average Interdigitated Gate Electrode (IGE) Structure's DC Resistance for IGEFET Sensing Elements Coated with Nickel Phthalocyanine (NiPc) Films with Different Thicknesses. Microsensor Maintained at 30° C in a Dry Air Ambient. The Error Bars Represent the Maximum and Minimum Resistance of Three IGEFET Sensors Possessing the Same NiPc Film Thickness. No Error Bars are Plotted for the 0.2 μm Film Thickness, since only a Single Data Point was Available..

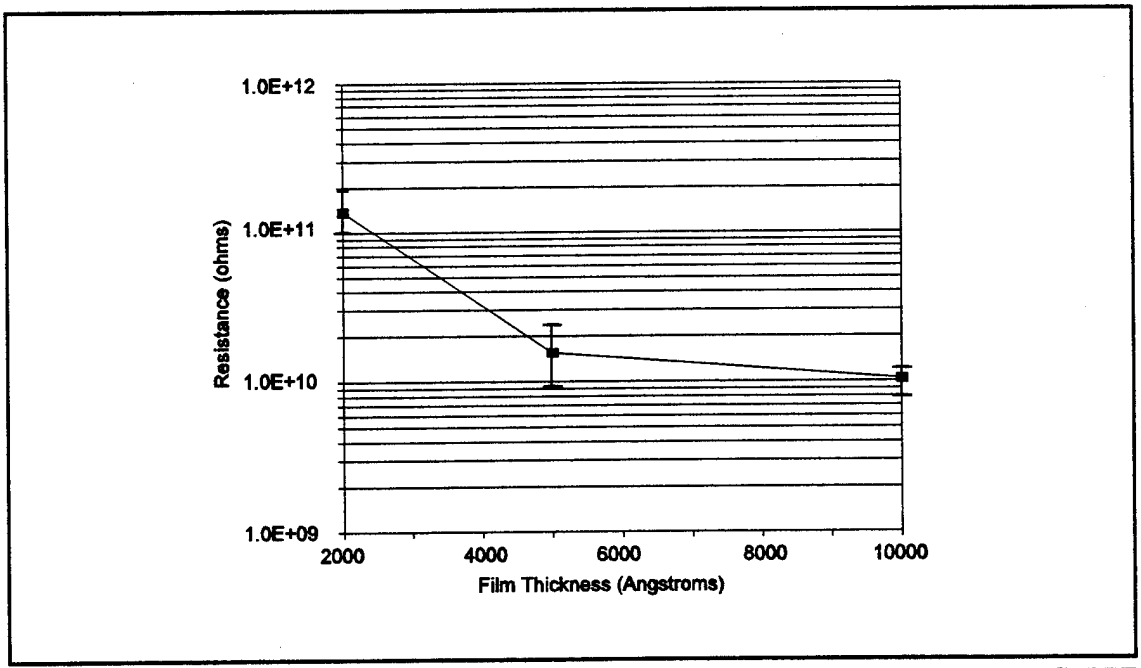


Figure F-8. Average Interdigitated Gate Electrode (IGE) Structure's DC Resistance for IGEFET Sensing Elements Coated with Cobalt Phthalocyanine (CoPc) Films with Different Thicknesses. Microsensor Maintained at 30° C in a Dry Air Ambient. The Horizontal Bars Represent the Maximum and Minimum Resistance of Three IGEFET Sensors Possessing the Same CoPc Film Thickness.

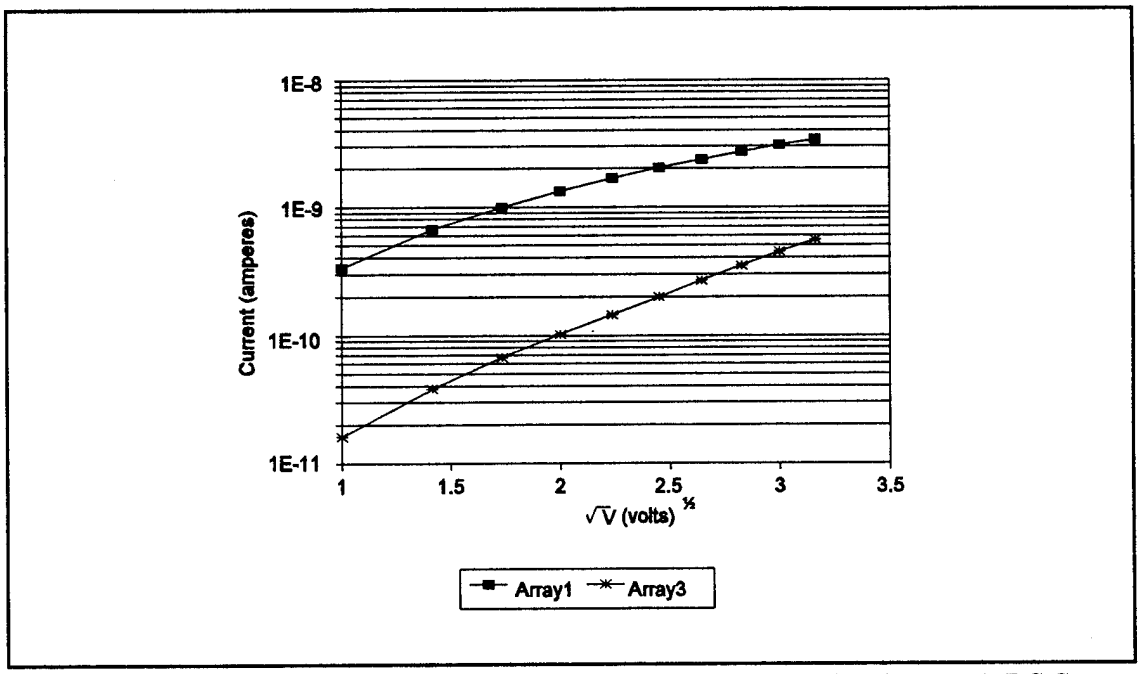


Figure F-9. Bias Voltage Dependence of the Interdigitated Gate Electrode (IGE) Structure's DC Current for IGEFET Sensing Elements Coated with a 0.2 μm Thick Nickel Phthalocyanine (NiPc) Film. Microsensor Maintained at 150° C in a Dry Air Ambient.

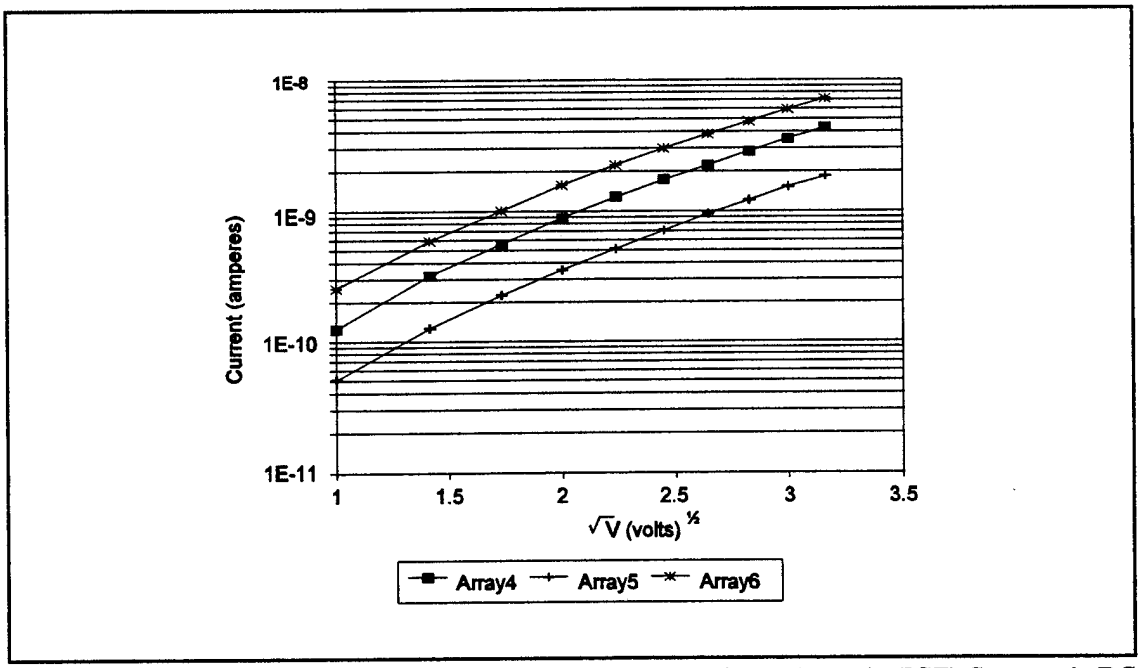


Figure F-10. Bias Voltage Dependence of the Interdigitated Gate Electrode (IGE) Structure's DC Current for IGEFET Sensing Elements Coated with a 0.5 μm Thick Nickel Phthalocyanine (NiPc) Film. Microsensor Maintained at 150° C in a Dry Air Ambient.

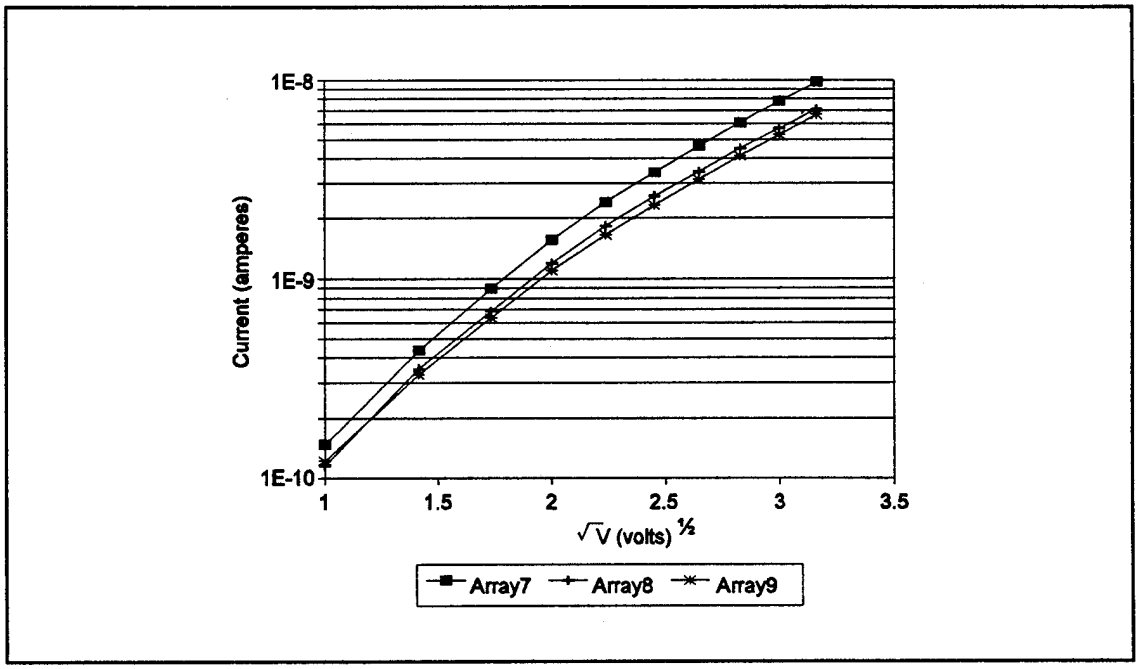


Figure F-11. Bias Voltage Dependence of the Interdigitated Gate Electrode (IGE) Structure's DC Current for IGEFET Sensing Elements Coated with a 1.0 μm Thick Nickel Phthalocyanine (NiPc) Film. Microsensor Maintained at 150° C in a Dry Air Ambient.

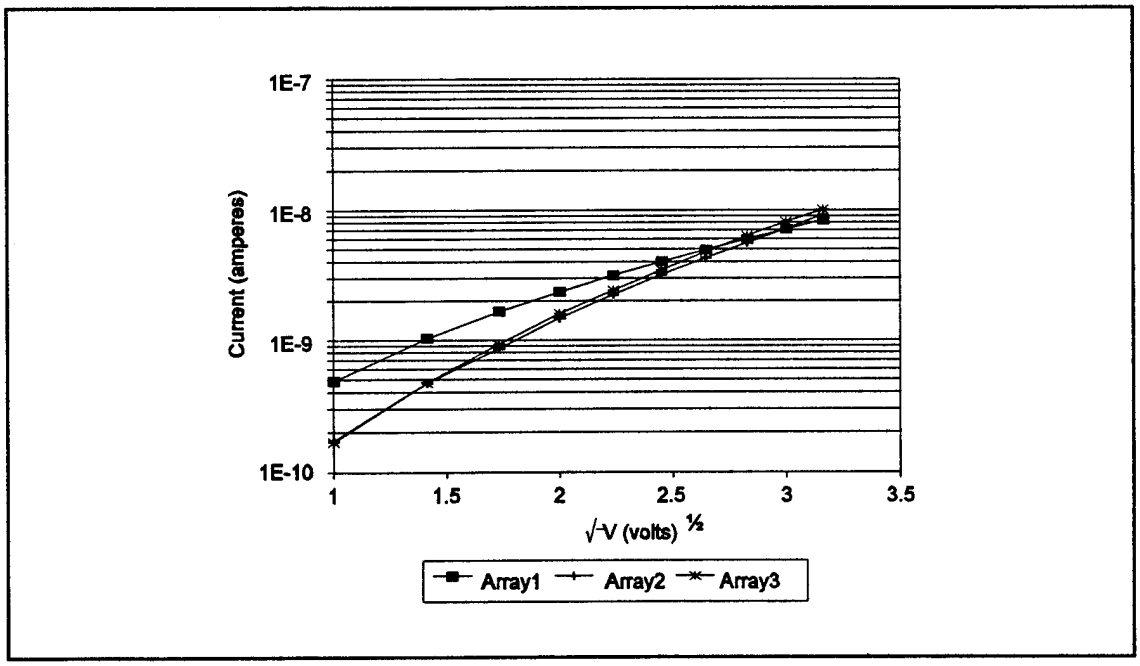


Figure F-12. Bias Voltage Dependence of the Interdigitated Gate Electrode (IGE) Structure's DC Current for IGEFET Sensing Elements Coated with a 0.2 μm Thick Cobalt Phthalocyanine (CoPc) Film. Microsensor Maintained at 150° C in a Dry Air Ambient.

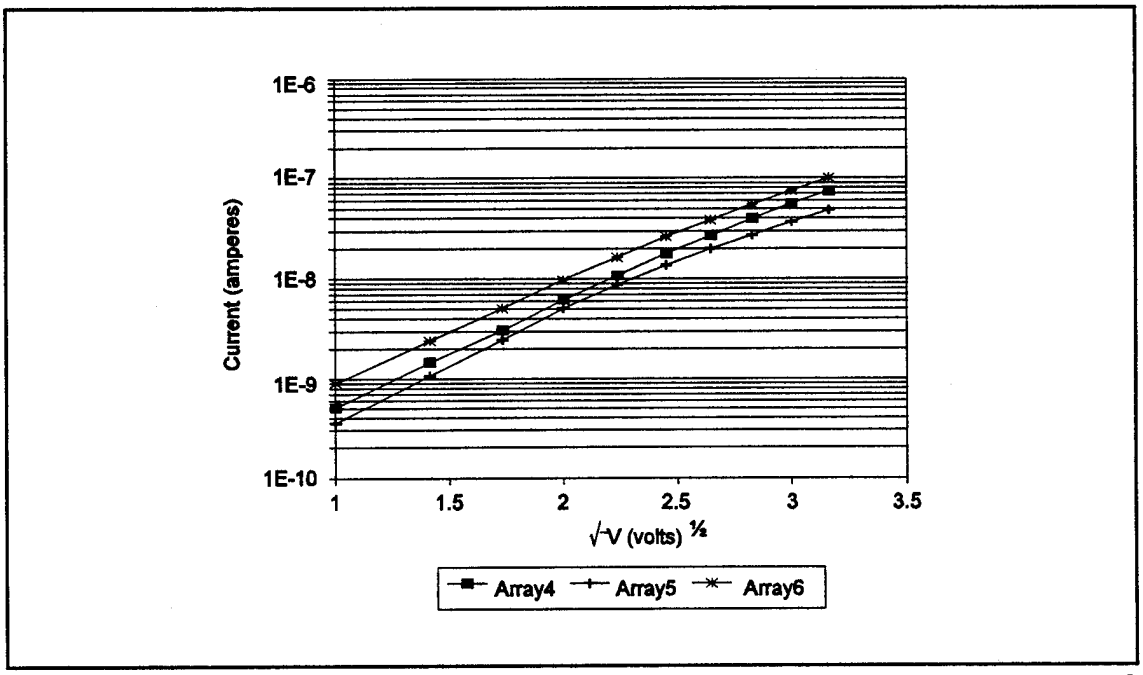


Figure F-13. Bias Voltage Dependence of the Interdigitated Gate Electrode (IGE) Structure's DC Current for IGEFET Sensing Elements Coated with a 0.5 μm Thick Cobalt Phthalocyanine (CoPc) Film. Microsensor Maintained at 150° C in a Dry Air Ambient.

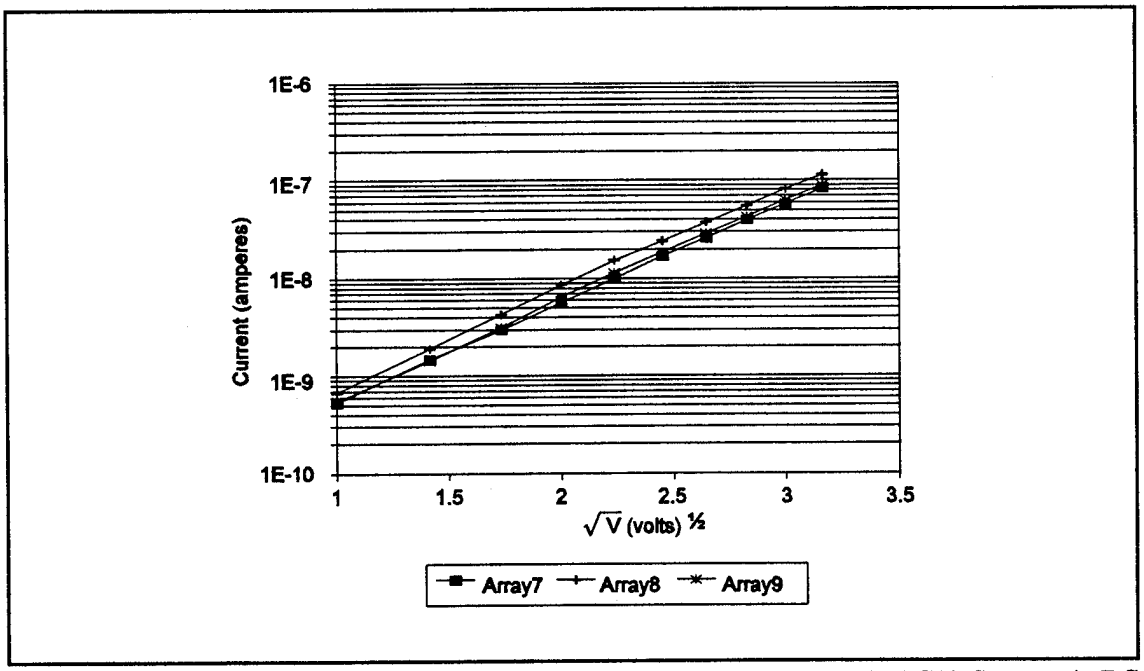


Figure F-14. Bias Voltage Dependence of the Interdigitated Gate Electrode (IGE) Structure's DC Current for IGEFET Sensing Elements Coated with a 1.0 μm Thick Cobalt Phthalocyanine (CoPc) Film. Microsensor Maintained at 150° C in a Dry Air Ambient.

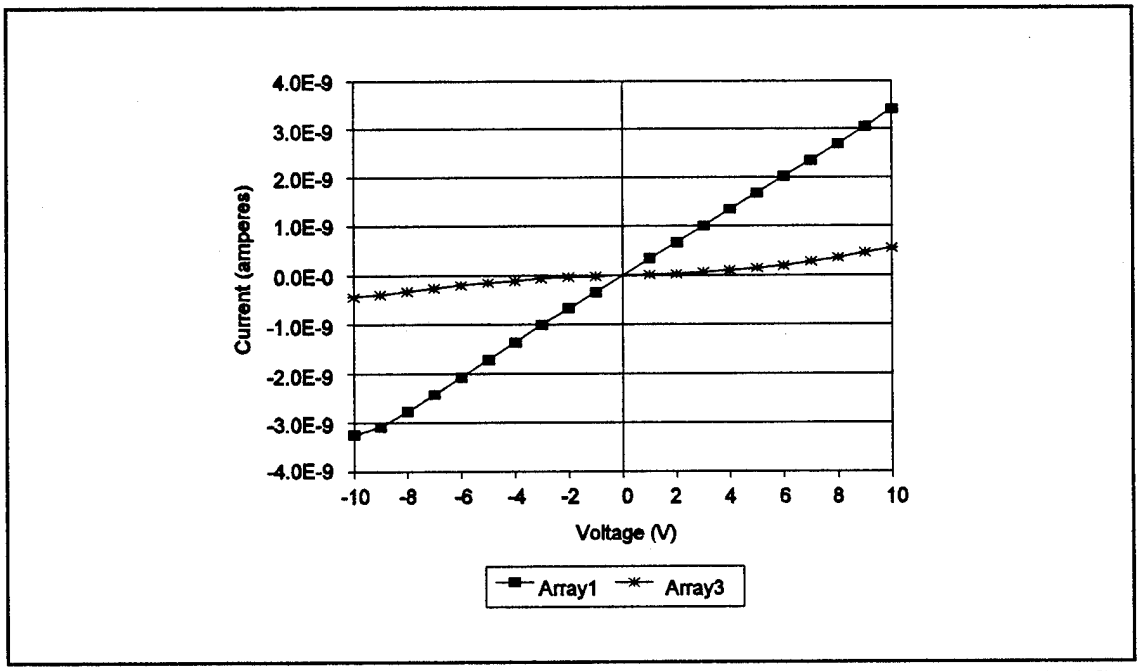


Figure F-15. Extended Range Bias Voltage Dependence of the Interdigitated Gate Electrode (IGE) Structure's DC Current for IGEFET Sensing Elements Coated with a 0.2 μm Thick Nickel Phthalocyanine (NiPc) Film. Microsensor Maintained at 150° C in a Dry Air Ambient.

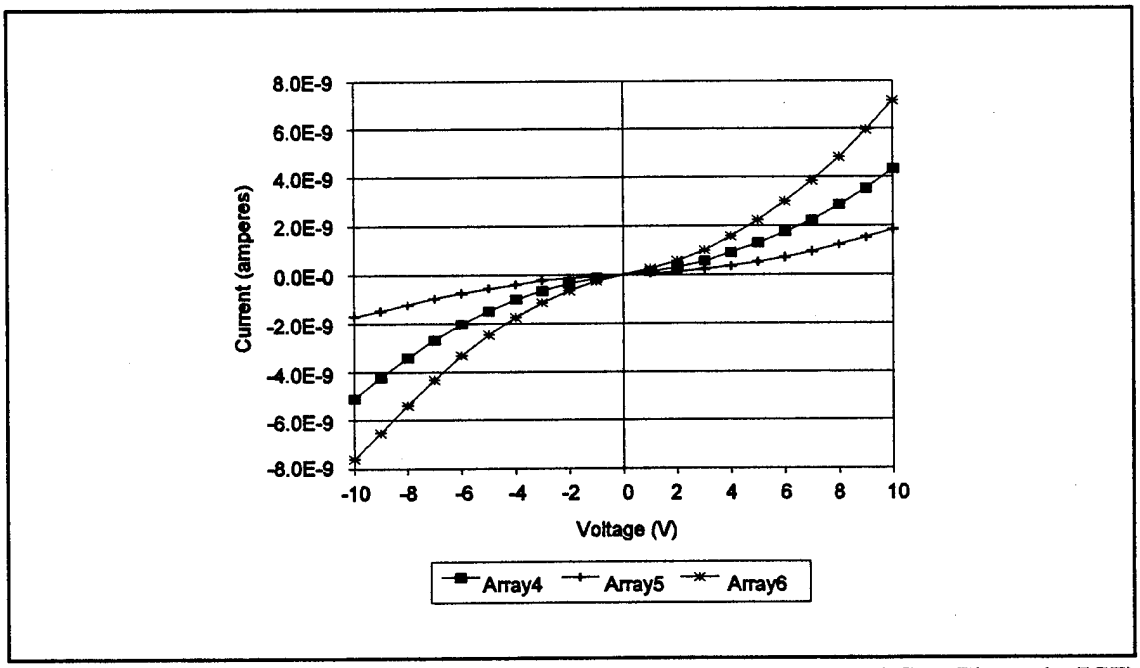


Figure F-16. Extended Range Bias Voltage Dependence of the Interdigitated Gate Electrode (IGE) Structure's DC Current for IGEFET Sensing Elements Coated with a 0.5 μm Thick Nickel Phthalocyanine (NiPc) Film. Microsensor Maintained at 150° C in a Dry Air Ambient.

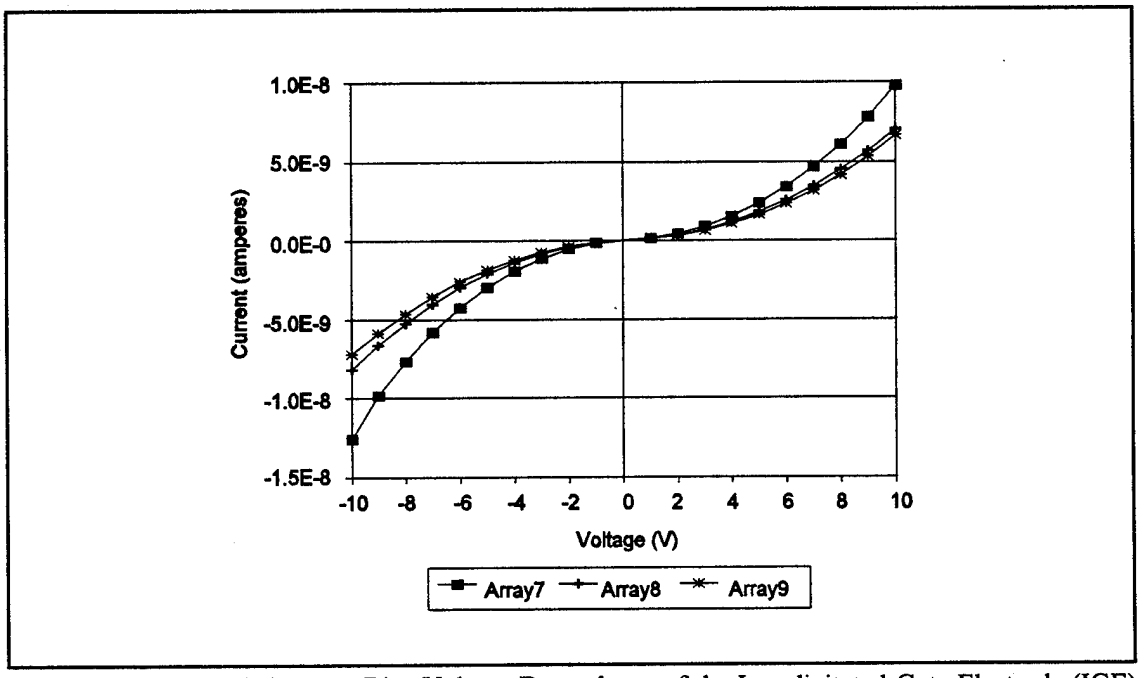


Figure F-17. Extended Range Bias Voltage Dependence of the Interdigitated Gate Electrode (IGE) Structure's DC Current for IGEFET Sensing Elements Coated with a 1.0 μm Thick Nickel Phthalocyanine (NiPc) Film. Microsensor Maintained at 150° C in a Dry Air Ambient.

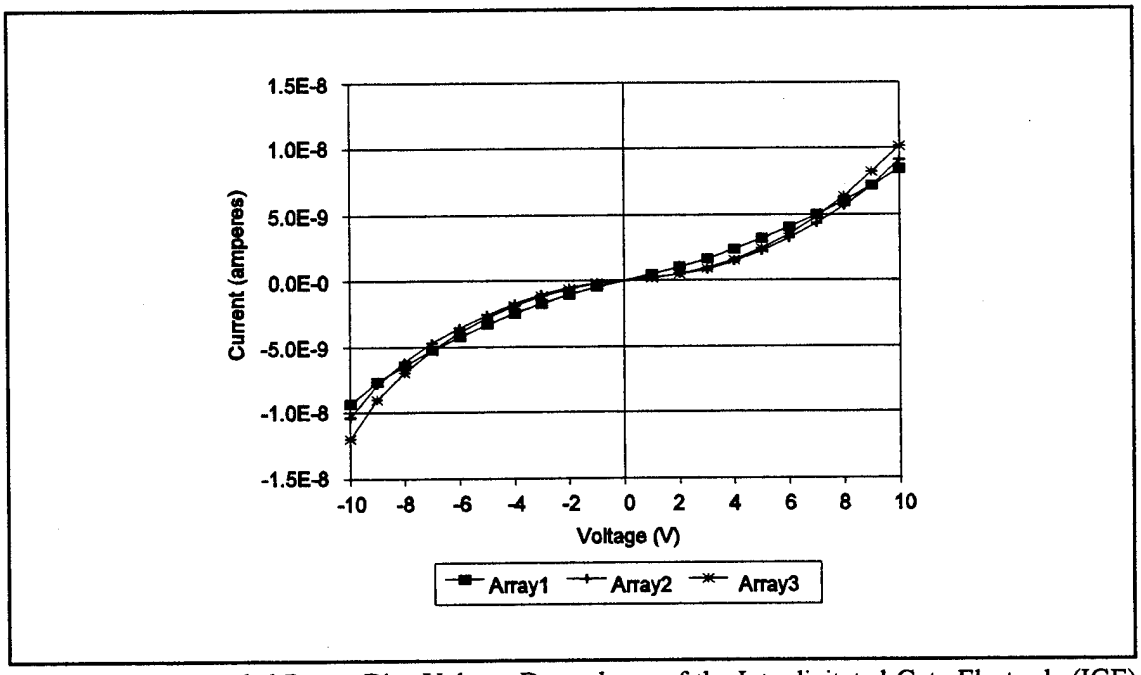


Figure F-18. Extended Range Bias Voltage Dependence of the Interdigitated Gate Electrode (IGE) Structure's DC Current for IGEFET Sensing Elements Coated with a 0.2 μm Thick Cobalt Phthalocyanine (CoPc) Film. Microsensor Maintained at 150° C in a Dry Air Ambient.

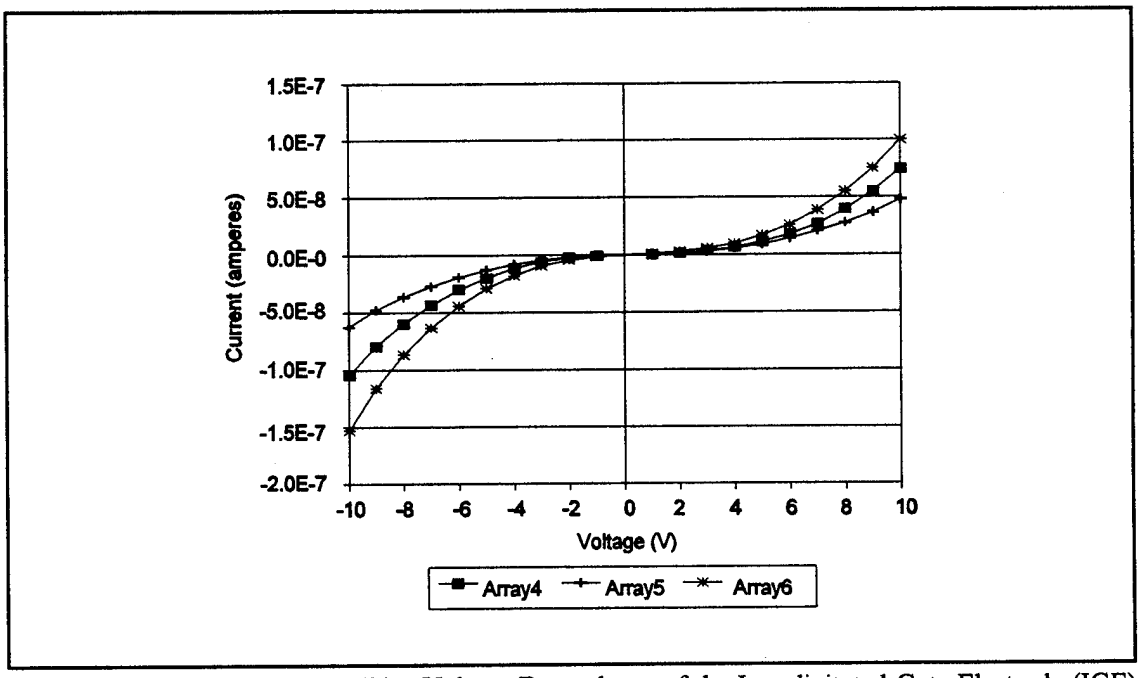


Figure F-19. Extended Range Bias Voltage Dependence of the Interdigitated Gate Electrode (IGE) Structure's DC Current for IGEFET Sensing Elements Coated with a 0.5 μm Thick Cobalt Phthalocyanine (CoPc) Film. Microsensor Maintained at 150° C in a Dry Air Ambient.

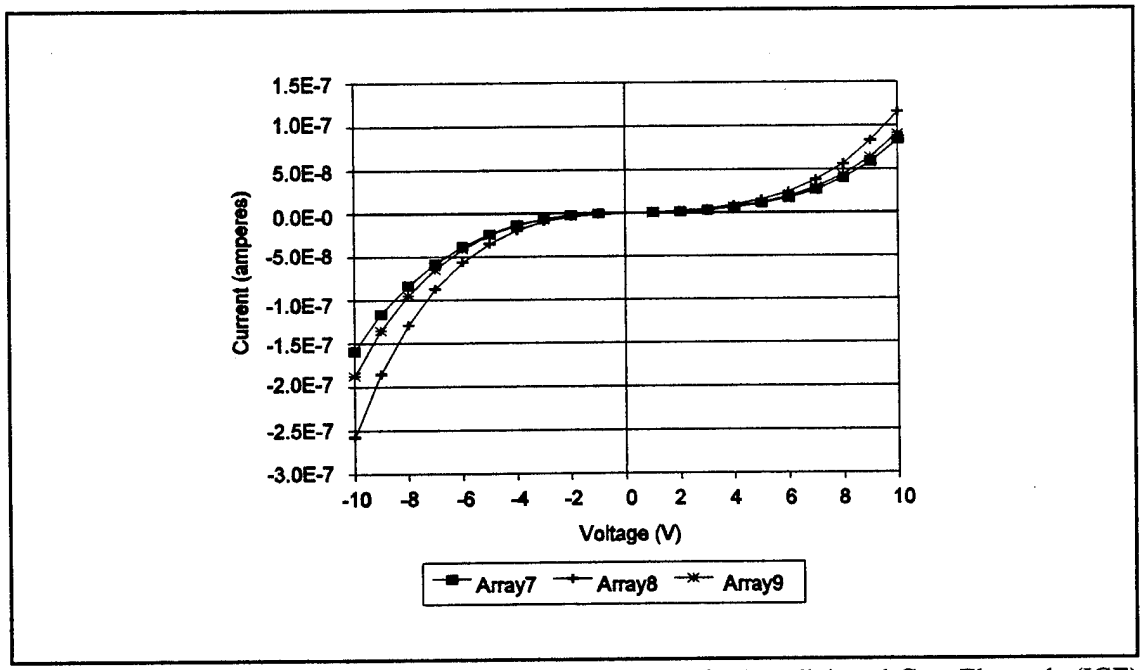


Figure F-20. Extended Range Bias Voltage Dependence of the Interdigitated Gate Electrode (IGE) Structure's DC Current for IGEFET Sensing Elements Coated with a 1.0 μm Thick Cobalt Phthalocyanine (CoPc) Film. Microsensor Maintained at 150° C in a Dry Air Ambient.

Appendix G. Derivation of the Equivalent Capacitance and Conductance of a Metal-Phthalocyanine-Metal Parallel Plate Capacitor with Schottky-Barrier Contacts

This appendix derives the frequency-dependent equivalent capacitance and conductance of a metal-phthalocyanine-metal parallel plate capacitor with a Schottky-barrier manifested at the contacts. Figure IV-97 illustrates the physical and electrical circuit model of the parallel plate capacitor. The electrical circuit in Figure IV-97b can be considered as three series admittances which combine in a manner equivalent to the parallel combination of impedances. First, the two Schottky-barrier capacitances, C_s, are combined to yield:

$$\frac{j\omega C_s \cdot j\omega C_s}{j\omega C_s + j\omega C_s} = \frac{1}{2} j\omega C_s . \tag{G-1}$$

This admittance is then combined in a similar manner with the thin film admittance to yield:

$$\frac{\frac{1}{2} j\omega C_s \cdot (G_b + j\omega C_b)}{\frac{1}{2} j\omega C_s + (G_b + j\omega C_b)} . \tag{G-2}$$

Multiplying the numerator and denominator of Equation G-2 by a factor of 2 yields:

$$\frac{j\omega C_s \cdot (G_b + j\omega C_b)}{j\omega C_s + 2(G_b + j\omega C_b)} = \frac{j\omega C_s G_b - \omega^2 C_s C_b}{j\omega C_s + 2(G_b + j\omega C_b)} \tag{G-3}$$

Multiplying the numerator and the denominator of Equation G-3 by the conjugate of the denominator, and simplifying the result, yields:

$$\frac{\omega^2 C_s^2 G_b + j\omega \left[2 G_b^2 C_s + \omega^2 C_s C_b (C_s + 2 C_b) \right]}{4 G_b^2 + \omega^2 (C_s + 2 C_b)^2} . \tag{G-4}$$

Thus, the electrical circuit of Figure IV-97b reduces to the equivalent circuit in Figure IV-97c whose

equivalent conductance, G_{eq}, and capacitance, C_{eq}, are given by:

$$G_{eq} = \frac{\omega^2 G_b C_s^2}{4G_b^2 + \omega^2 (C_s + 2C_b)^2} \tag{G-5}$$

and

$$C_{eq} = \frac{2G_b^2 C_s + \omega^2 C_s C_b (C_s + 2C_b)}{4G_b^2 + \omega^2 (C_s + 2C_b)^2}. \tag{G-6}$$

Appendix H. Finite-Difference Equations for Nodes Along Vertical Interfaces

A slight modification to the general finite-difference equation (Equation V-15) is required for the nodes along the vertical interfaces between the film coating the interdigitated electrodes and the adjacent dielectric (typically, air). These nodes are identified in Figure V-13. There are four special cases: two cases for the sets of nodes along the vertical interfaces above and below the driven-gate and floating-gate electrodes, and two cases for the nodes at the upper corners of each vertical interface associated with the driven-gate and floating-gate electrodes. The equations for the first two cases were developed with the same approach described in Chapter V, and they were simplified to a form similar to Equation V-15. The equations for the latter two cases were also developed in the same manner as described in Chapter V, but they can not be readily simplified.

General Finite-Difference Equation for Nodes Along the Vertical Interface Above and Below the Driven-Gate Electrode

The geometry for nodes along the vertical interface above and below the driven-gate electrode is shown in Figure H-1. As was shown in Chapter V, an admittance element connects node 0 to each of the adjacent nodes. The admittances of the elements connecting nodes 0-to-1, and 0-to-3, are given by:

$$Y_1 = \epsilon_1^* \left[\frac{(h_4/2 + h_2/2)}{h_1} \right] \cdot 1 \quad , \tag{H-1}$$

and

$$Y_3 = \epsilon_2^* \left[\frac{(h_4/2 + h_2/2)}{h_3} \right] \cdot 1 \quad . \tag{H-2}$$

Since an admittance element connecting either nodes 0-to-2, or nodes 0-to-4, spans across the interface, the admittances of these elements contain terms for each dielectric medium. The admittances for the elements connecting nodes 0-to-2, and 0-to-4, are given by:

$$Y_2 = \left[\frac{(\epsilon_1^* h_1/2 + \epsilon_2^* h_3/2)}{h_2} \right] \cdot 1 \quad , \tag{H-3}$$

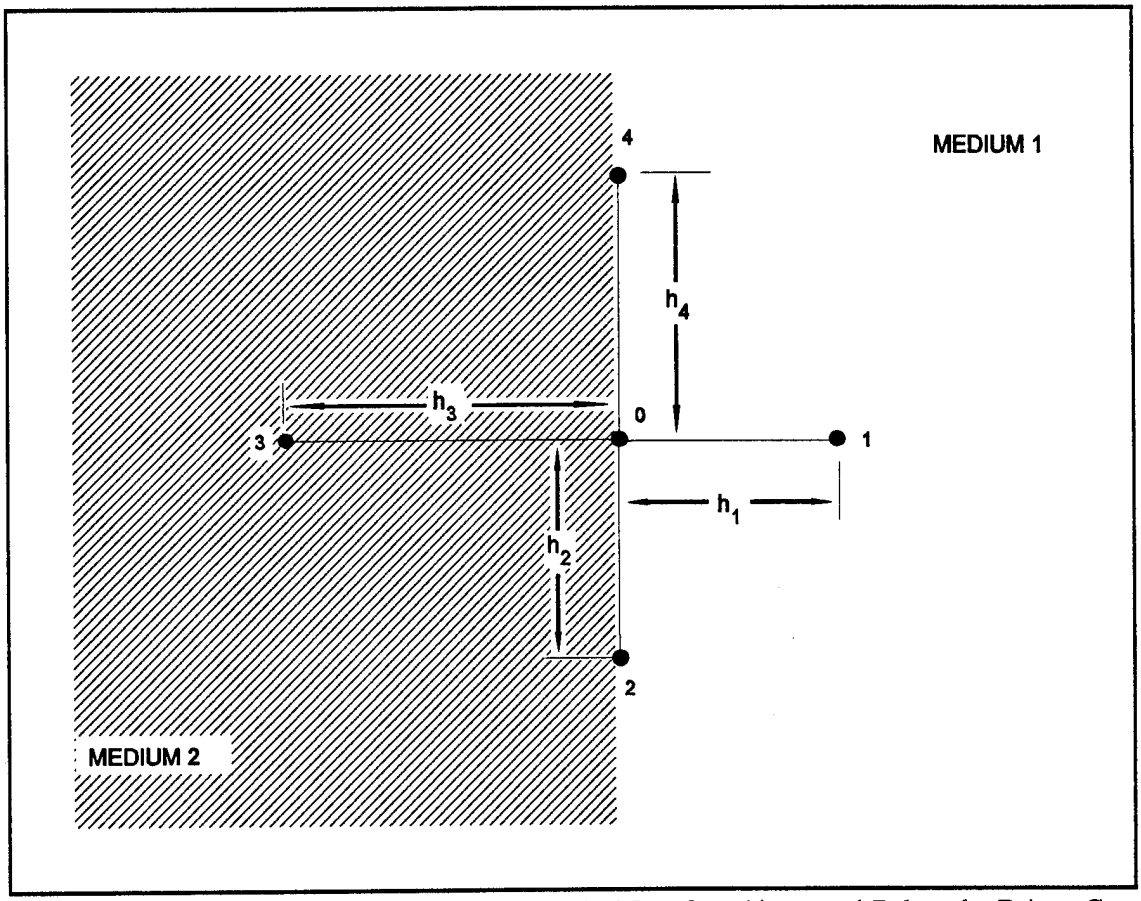


Figure H-1. Geometry of a Node Along the Vertical Interface Above and Below the Driven-Gate Electrode.

and

$$Y_4 = \left[\frac{(\epsilon_1^* h_1/2 + \epsilon_2^* h_3/2)}{h_4}\right] \cdot 1 \quad . \tag{H-4}$$

Applying Kirchoff's current law to node 0, using the current directions depicted in Figure V-3, implies:

$$I_1 + I_2 + I_3 + I_4 = 0 \tag{H-5}$$

where

$$I_n = Y_n (V_n - V_0). \tag{H-6}$$

Combining Equations (H-1) through (H-6), and rearranging the terms to isolate V_0, the voltage at the center node, is obtained as:

$$V_0 = \frac{\dfrac{V_1}{h_1\left(h_1+\dfrac{\epsilon_2^*}{\epsilon_1^*}h_3\right)} + \dfrac{V_2}{h_2(h_2+h_4)} + \dfrac{\dfrac{\epsilon_2^*}{\epsilon_1^*}V_3}{h_3\left(h_1+\dfrac{\epsilon_2^*}{\epsilon_1^*}h_3\right)} + \dfrac{V_4}{h_4(h_2+h_4)}}{\dfrac{1}{h_2h_4} + \dfrac{1}{h_1h_3}\left[\dfrac{\dfrac{\epsilon_2^*}{\epsilon_1^*}h_1+h_3}{h_1+\dfrac{\epsilon_2^*}{\epsilon_1^*}h_3}\right]} \quad . \tag{H-7}$$

General Finite-Difference Equation for Nodes Along the Vertical Interface Above and Below the Floating-Gate Electrode

The general finite-difference equation for nodes along the vertical interface above and below the floating-gate electrode may be derived in an identical manner(or it may be deduced by symmetry considerations) and is given by:

$$V_0 = \frac{\dfrac{\dfrac{\epsilon_2^*}{\epsilon_1^*}V_1}{h_1\left(h_3+\dfrac{\epsilon_2^*}{\epsilon_1^*}h_1\right)} + \dfrac{V_2}{h_2(h_2+h_4)} + \dfrac{V_3}{h_3\left(h_3+\dfrac{\epsilon_2^*}{\epsilon_1^*}h_1\right)} + \dfrac{V_4}{h_4(h_2+h_4)}}{\dfrac{1}{h_2h_4} + \dfrac{1}{h_1h_3}\left[\dfrac{\dfrac{\epsilon_2^*}{\epsilon_1^*}h_3+h_1}{h_3+\dfrac{\epsilon_2^*}{\epsilon_1^*}h_1}\right]} \quad . \tag{H-8}$$

General Finite-Difference Equation for the Node at the Upper Corner of the Vertical Interface Above the Driven Gate Electrode

The geometry for the node at the upper corner of the vertical interface above the driven-gate electrode is shown in Figure H-2. In this case, the admittances for the elements connecting node 0 to each of the adjacent nodes are given by:

$$Y_1 = \epsilon_1^*\left[\frac{(h_2/2 + h_4/2)}{h_4}\right]\cdot 1 \quad , \tag{H-9}$$

$$Y_2 = \left[\frac{(\epsilon_1^* h_1/2 + \epsilon_2^* h_3/2)}{h_2}\right]\cdot 1 \quad , \tag{H-10}$$

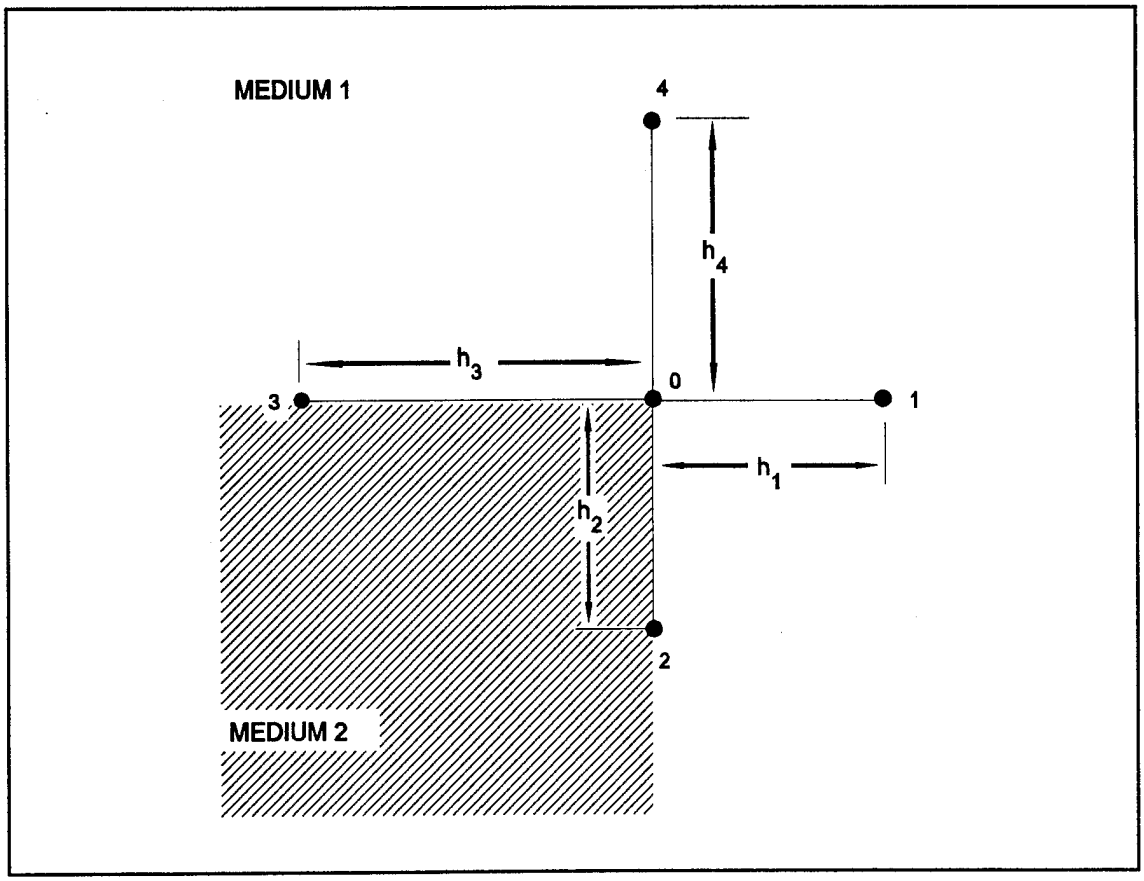


Figure H-2. Geometry of the Node At the Upper Corner of the Vertical Interface Above the Driven-Gate Electrode.

$$Y_3 = \left[\frac{(\epsilon_1^* h_4/2 + \epsilon_2^* h_2/2)}{h_3}\right] \cdot 1 \quad , \tag{H-11}$$

and

$$Y_4 = \epsilon_1^* \left[\frac{(h_1/2 + h_3/2)}{h_4}\right] \cdot 1 \quad . \tag{H-12}$$

Applying Kirchoff's current law to node 0, using the current directions depicted in Figure V-3, implies:

$$I_1 + I_2 + I_3 + I_4 = 0 \tag{H-13}$$

where

$$I_n = Y_n (V_n - V_0). \tag{H-14}$$

Combining Equations (H-9) through (H-14), and rearranging the terms to isolate V_0, the voltage at the center node, is obtained as:

$$V_0 = \frac{\dfrac{(h_2 + h_4) V_1}{h_1} + \dfrac{(\frac{\epsilon_2^*}{\epsilon_1^*} h_3 + h_1) V_2}{h_2} + \dfrac{(\frac{\epsilon_2^*}{\epsilon_1^*} h_2 + h_4) V_3}{h_3} + \dfrac{(h_1 + h_3) V_4}{h_4}}{\dfrac{(h_2 + h_4)}{h_1} + \dfrac{(\frac{\epsilon_2^*}{\epsilon_1^*} h_3 + h_1)}{h_2} + \dfrac{(\frac{\epsilon_2^*}{\epsilon_1^*} h_2 + h_4)}{h_3} + \dfrac{(h_1 + h_3)}{h_4}} \quad . \tag{H-15}$$

Equation H-15 can be rewritten as:

$$V_0 = \frac{A V_1 + B V_2 + C V_3 + D V_4}{A + B + C + D} \tag{H-16}$$

where

$$A = \frac{(h_2 + h_4)}{h_1}, \tag{H-17}$$

$$B = \frac{(\frac{\epsilon_2^*}{\epsilon_1^*} h_3 + h_1)}{h_2}, \tag{H-19}$$

$$C = \frac{(\frac{\epsilon_2^*}{\epsilon_1^*} h_2 + h_4)}{h_3}, \tag{H-18}$$

and

$$D = \frac{(h_1 + h_3)}{h_4} \quad . \tag{H-20}$$

General Finite-Difference Equation for the Node at the Upper Corner of the Vertical Interface Above the Floating-Gate Electrode

The general finite-difference equation for the node at the upper corner of the vertical interface above the floating-gate electrode may be derived in an identical manner(or it may be deduced by symmetry considerations) and is given by:.

$$V_0 = \frac{\frac{(\frac{\epsilon_2^*}{\epsilon_1^*} h_2 + h_4) V_1}{h_1} + \frac{(\frac{\epsilon_2^*}{\epsilon_1^*} h_1 + h_3) V_2}{h_2} + \frac{(h_2 + h_4) V_1}{h_3} + \frac{(h_1 + h_3) V_4}{h_4}}{\frac{(\frac{\epsilon_2^*}{\epsilon_1^*} h_2 + h_4)}{h_1} + \frac{(\frac{\epsilon_2^*}{\epsilon_1^*} h_1 + h_3)}{h_2} + \frac{(h_2 + h_4)}{h_3} + \frac{(h_1 + h_3)}{h_4}} \tag{H-21}$$

Equation H-21 can be rewritten as:

$$V_0 = \frac{A' V_1 + B' V_2 + C' V_3 + D' V_4}{A' + B' + C' + D'} \tag{H-22}$$

where

$$A' = \frac{(\frac{\epsilon_2^*}{\epsilon_1^*} h_4 + h_2)}{h_1}, \tag{H-23}$$

$$B' = \frac{(\frac{\epsilon_2^*}{\epsilon_1^*} h_3 + h_1)}{h_2}, \tag{H-24}$$

$$C' = \frac{(h_2 + h_4)}{h_3}, \tag{H-25}$$

and

$$D' = \frac{(h_1 + h_3)}{h_4} \quad . \tag{H-26}$$

When h_1 and h_3 are interchanged in Equations H-23 through H-26, Equations H-23 through J-26 may be used to define the coefficients for Equation H-16, where $A=C'$, $B=B$, $C=A'$ and $D=D'$.

Appendix I: Finite-Difference Model Source Code and Example Output

Two programs, named UCMODL.P and THCKMODL.P, were coded to implement the two finite-difference models of the interdigitated gate electrode structure developed in Chapter V. Both programs are coded in Turbo Pascal (Version 5.0, Borland International, Scotts Valley, CA). The two programs are similar in structure and use a number of "include" files. The "include" files unique to each program are listed after each main program source code listing. The unique "include" files for each program perform similar functions which 1) initialize the model (ucinit.i and thckinit.i), and 2) accomplish the two-port admittance calculation (ucprt.i and thckprt.i). The source code listings are divided into three sections. The first section lists the source code for the pseudo-planar model. The second section lists the source code for the planar model. The last section lists the "include" files which are common to both models (cmplxmth2.i, FNHANDL.PAS, and FDCALC.PAS).

An example of the output from the UCMODL.P program is provided in the final section following the source code listings. The initialization information, which is entered by the user interactively, and results in the listed program output, is provided. The output format from the THCKMODL.P program is similar to the UCMODL.P output. Both programs use fixed increments for adjusting the film's complex permittivity that can only be adjusted by editing and recompiling the source code. It also has some constants at the beginning of the main program source code listing that facilitate adjusting the model parameters and operating modes. Three operating modes are available: 1) voltage distribution calculation for a single film complex permittivity, 2) transfer function calculation for a number of film complex permittivities, and 3) calculation of the transfer function or voltage distribution for a semi-infinitely thick film. The example output is for the program operating in the second mode. The output from the first mode is an array of numbers representing the voltage distribution which are used to generate the contour plots shown in Chapter V.

Pseudo-Planar Model Source Code

```
(*************************************************************************)
(* Filename: UCMODL.P *)
(* This program is for semi-infinite films or for films less than 1.5 micron *)

program ucmodl1(input,output, outfile);
uses Dos, Crt;
(*    This program computes the potential distribution resulting   *)
(*    from the application of a 1V steady state sinusoidal voltage  *)
(*    on an interdigitated electrode structure ( could be viewed   *)
(*    as coupled microstrips). This program is an extension        *)
(*    of the algorithm developed by Huan Lee in his Master's       *)
(*    thesis,"Optimization of a Resin Cure", Massachusetts         *)
(*    Institute of Technology, 1982. This thesis is available      *)
(*    in the AFIT Library. The extension allows the calculation of  *)
(*    the IDE TF when coated with thin films (0.1-1.5 micron).     *)
(*    Variable electrode separation and undercutting the electrodes *)
(*    is also supported. The program computes the effect of an     *)
(*    arbitrary load capacitance connected to the floating         *)
(*    electrode on the IDE TF.          *)

 const
    ContourSw=1;        (* Switch=0: Transfer Function Output *)
                  (* Switch=1: Voltage Distribution Output *)
    SemiSw=0;           (* Switch=0: Thin Film *)
                  (* Switch=1: Semi-Infinite Film *)
    OxNodes = 10;              (* Number of oxide nodes *)
    Nodes6 = 15;              (* # vertical nodes in Region6 *)
    R6VertRes = 1.0;           (* Vertical Resolution in Region6 *)
    Horz = 33;                (* # horizontal nodes in entire grid *)
    EHeight = 1.2;          (* Electrode Height to nearest 0.1 microns *)
    OxHeight = 0.9;         (* Oxide Height in microns *)
    epsilon0 = 8.854e-14;       (* F/cm *)
    pi = 3.14159265358979323 85;

 type
  complex=record               (* define complex data type       *)
   x,y:real;
  end; (*complex Record*)

  GridArray =array[1.. 154, 1..33] of complex;
   (* GridArray is a new data type for the finite difference grid  *)
   (* with a max size of 100 vertical nodes and 40 horizontal nodes  *)

(*   outstring = packed array [1..20] of char; *)
  outstring = string[20];
                  (* outstring defines a file name data     *)
                  (* type, max size of 20 characters       *)

var
   Grid : GridArray;              (* finite difference grid *)
   FT : real;               (* Film Thickness To nearest .1 micron *)
   UC : real;               (* Undercut to nearest 0.1 micron *)
   ESep : real;                  (* Inter-Electrode Separation *)
   FNodes : integer;              (* Number of Film Nodes In 2a and 2c *)
   Nodes4 : integer;             (* Number of Nodes in Region 2b *)
   R1Vert, R2Vert, R3Vert, R4Vert,
    R5Vert, R6Vert             : integer; (* Top node in Each Region *)
   epsilon1, epsilonF, epsilon3 : complex; (* complex permittivities  *)
   MaxRelRes : real;           (* maximum relative residue/iteration  *)
   TotResA, TotResB,TotResC : real;  (* Total of relative residues    *)
                  (* for each grid per iteration    *)
   RelaxationParamA, RelaxationParamB, RelaxationParamC : real;
   OldTotResA, OldTotResB, OldTotResC : real;  (* Total relative      *)
   (* residues for each region from previous iteration              *)

   RelaxationUpdateCounter : integer;

  (* Multiplicative factors for averaging the nodes in each grid    *)
  R1V1, R1V2, R1V3, R1V4, R1V1C, R1V2C, R1V3C, R1V4C, R1V1LC, R1V2LC,
    R1V3LC, R1V4LC, R1V1RC, R1V2RC, R1V3RC, R1V4RC : complex;
  I12V1, I12V2, I12V3, I12V4 : complex;
  R2V1LC, R2V2LC, R2V3LC, R2V4LC, R2V1RC, R2V2RC, R2V3RC, R2V4RC,
    R2V1C, R2V2C, R2V3C, R2V4C  : complex;
  I23V1, I23V2,I23V3, I23V4 : complex;
  R3V1LC, R3V2LC, R3V3LC, R3V4LC, R3V1RC, R3V2RC, R3V3RC, R3V4RC,
    R3V1C, R3V2C, R3V3C, R3V4C : complex;
  R4V1, R4V2, R4V3, R4V4 : complex;
  I24V1, I24V2,I24V3, I24V4, I25V1, I25V2, I25V3, I25V4 : complex;
  R5V1, R5V2, R5V3, R5V4, R5V1C, R5V2C, R5V3C, R5V4C, R5V1LC,
    R5V2LC, R5V3LC, R5V4LC, R5V1RC, R5V2RC, R5V3RC, R5V4RC : complex;
  I56V1, I56V2, I56V3, I56V4, I56V1C, I56V2C, I56V3C, I56V4C, I56V1LC,
    I56V2LC, I56V3LC, I56V4LC, I56V1RC, I56V2RC,
    I56V3RC, I56V4RC : complex;
  R6V1, R6V2, R6V3, R6V4, R6V1C, R6V2C, R6V3C, R6V4C, R6V1LC, R6V2LC,
    R6V3LC, R6V4LC, R6V1RC, R6V2RC, R6V3RC, R6V4RC : complex;

  VCount, HCount : integer;
  RelaxUpdateSw : char;  (* Toggles variable/constant relax parameters *)
  ConvergenceValue : real; (* acceptable maximum relative           *)
                  (* residue/iteration              *)
  iterationctr, i, j : integer;
  Incy : real;
  Y1, Y2 : complex;      (* Two port admittance parameters          *)
  LoadCap, RedConverg : real;
  TransferFunction : complex;
  outfile, outfile2 : text;
  outname : outstring;    (* outname is the user specified output    *)
```

```
                (* file name                    *)
(*****************************************************************************)

(* #include "cplxmth2.i" *)      (* include complex math procedures *)
(* #include "newprt3b.i" *)
(* #include "mnewinit.i" *)
{$I cplxmth2.i}
{$I ucprt.i}
{$I ucinit.i}
{$I FDCALC.PAS}
{$I FNHANDL.PAS}

(*****************************************************************************)
begin (* main *)
 ReadConfig(epsilon3, ConvergenceValue, RelaxationParamA, RelaxationParamB,
       RelaxationParamC, LoadCap, FT, ESep, UC, FNodes, RelaxUpdateSw, outname);

 epsilonF.x := 105.0;
 R1Vert := OxNodes - round(UC/0.1);
 Nodes4 := round((EHeight -FT+UC)/0.1);
 R2Vert := FNodes + R1Vert;
 R3Vert := OxNodes;
 R4Vert := R2Vert + Nodes4;
 R5Vert := R4Vert + FNodes;
 R6Vert := R5Vert + Nodes6;

(* rewrite(outfile,outname); *) (* Sun Pascal Format *)
 assign(outfile,outname);
 rewrite(outfile);

 writeln(outfile, 'FNodes = ', FNodes, '  Electrode Separation = ', ESep);
 writeln(outfile, 'Film Thickness = ', FT, '  Variable Relaxation - ',
       RelaxUpdateSw);
 writeln(outfile, 'epsilon3.x = ', epsilon3.x, '  epsilon3.y = ', epsilon3.y);
 writeln(outfile, 'epsilon1.x = ', epsilon1.x, '  epsilon1.y = ', epsilon1.y);
 writeln(outfile, 'Nodes6 = ', Nodes6, '  Horz = ', Horz);
 writeln(outfile, 'R6VertRes = ', R6VertRes, '  Undercut = ', UC);

 RedConverg := 0.9 * ConvergenceValue;
 while epsilonF.x < 4000 do begin
  epsilonF.y:= -124.0;
  while epsilonF.y > -2000.0 do begin
   if(SemiSw = 1) then epsilon3 := epsilonF;  (* Used to Make Semi-Infinite Film *)
   RelaxationParamA := 1.8;
   RelaxationParamB := 1.8;
   RelaxationParamC := 1.8;
   Init;
   InitVCoeff;
   iterationctr := 0;
(*****************************************************************************)
   repeat
for RelaxationUpdateCounter := 1 to 3 do
 begin
 MaxRelRes := RedConverg;
 for VCount := 2 to R1Vert-1 do  (* Calculate new potentials over *)
  begin                  (* Region1 except at upper interface *)
   PtAvgR(VCount, 2, 6, R1V1, R1V2, R1V3, R1V4,
        TotResA, RelaxationParamA, MaxRelRes);
   PtAvgR(VCount, 7, 7, R1V1LC, R1V2LC, R1V3LC,
        R1V4LC, TotResA, RelaxationParamA, MaxRelRes);
   PtAvgR(VCount, 8, 26, R1V1C, R1V2C, R1V3C,
        R1V4C, TotResA, RelaxationParamA, MaxRelRes);
   PtAvgR(VCount, 27, 27, R1V1RC, R1V2RC, R1V3RC,
       R1V4RC, TotResA, RelaxationParamA, MaxRelRes);
   PtAvgR(VCount, 28, 32, R1V1, R1V2, R1V3,
        R1V4, TotResA, RelaxationParamA, MaxRelRes);
 end;
 if UC=0 then
  begin
   (* Calculate new potentials at Region1-Region2 interface *)
   PtAvg(R1Vert, 8, 26, I12V1, I12V2, I12V3, I12V4,
        TotResA, RelaxationParamA, MaxRelRes);
   (* Calculate new potentials in Region2 *)
   for VCount := R1Vert+1 to R2Vert-1 do
    PtAvgR(VCount, 8, 26, R2V1C, R2V2C, R2V3C, R2V4C,
      TotResB, RelaxationParamB, MaxRelRes);
   (* Calculate new potentials in Region4 (if it exists) *)
   if (Nodes4 > 0) then      (* Test for any Region4 *)
    begin
     PtAvg(R2Vert, 8, 26, I24V1, I24V2, I24V3,
       I24V4, TotResB, RelaxationParamB, MaxRelRes);
     for VCount := R2Vert+1 to R4Vert do
      PtAvgR(VCount, 8, 26, R4V1, R4V2, R4V3,
        R4V4, TotResB, RelaxationParamB, MaxRelRes);
    end
   else
  (* No Region4, calculate new potentials at Region2-5 interface *)
      PtAvg(R2Vert, 8, 26, I25V1, I25V2, I25V3,
        I25V4, TotResB, RelaxationParamB, MaxRelRes);
  end
 else
  begin
   PtAvgR(R1Vert, 2, 6, R1V1, R1V2, R1V3, R1V4,
      TotResA, RelaxationParamA, MaxRelRes);
   PtAvg(R1Vert, 7, 7, R2V1LC, R2V2LC, R2V3LC,
      R2V4LC, TotResA, RelaxationParamA, MaxRelRes);
   PtAvg(R1Vert, 8, 26, I12V1, I12V2, I12V3, I12V4,
      TotResA, RelaxationParamA, MaxRelRes);
   PtAvg(R1Vert, 27, 27, R2V1RC, R2V2RC, R2V3RC,
      R2V4RC, TotResA, RelaxationParamA, MaxRelRes);
   PtAvgR(R1Vert, 28, 32, R1V1, R1V2, R1V3,
      R1V4, TotResA, RelaxationParamA, MaxRelRes);
```

```
(* Check to see if film entirely fills undercut *)
if R2Vert < OxNodes then
  begin  (* yes, then R3 Exists *)
   for VCount := R1Vert+1 to R2Vert-1 do
    begin
     PtAvgR(VCount, 2, 6, R1V1, R1V2, R1V3, R1V4,
      TotResA, RelaxationParamA, MaxRelRes);
     PtAvg(VCount, 7, 7, R2V1LC, R2V2LC, R2V3LC,
      R2V4LC, TotResA, RelaxationParamA, MaxRelRes);
     PtAvg(VCount, 8, 26, R2V1C, R2V2C, R2V3C, R2V4C,
       TotResA, RelaxationParamA, MaxRelRes);
     PtAvg(VCount, 27, 27, R2V1RC, R2V2RC, R2V3RC,
      R2V4RC, TotResA, RelaxationParamA, MaxRelRes);
     PtAvgR(VCount, 28, 32, R1V1, R1V2, R1V3,
      R1V4, TotResA, RelaxationParamA, MaxRelRes);
    end;
   (* Calculate potential at R2-R3 Interface *)
   PtAvgR(R2Vert, 2, 6, R1V1, R1V2, R1V3, R1V4,
      TotResA, RelaxationParamA, MaxRelRes);
   PtAvg(R2Vert, 7, 7, R2V1LC, R2V2LC, R2V3LC,
      R2V4LC, TotResA, RelaxationParamA, MaxRelRes);
   PtAvg(R2Vert, 8, 26, I23V1, I23V2, I23V3, I23V4,
       TotResA, RelaxationParamA, MaxRelRes);
   PtAvg(R2Vert, 27, 27, R2V1RC, R2V2RC, R2V3RC,
      R2V4RC, TotResA, RelaxationParamA, MaxRelRes);
   PtAvgR(R2Vert, 28, 32, R1V1, R1V2, R1V3,
      R1V4, TotResA, RelaxationParamA, MaxRelRes);
   (* Calculate Potential in R3 *)
   for VCount := R2Vert+1 to R3Vert-1 do
    begin
     PtAvgR(VCount, 2, 6, R1V1, R1V2, R1V3, R1V4,
      TotResA, RelaxationParamA, MaxRelRes);
     PtAvg(VCount, 7, 7, R3V1LC, R3V2LC, R3V3LC,
      R2V4LC, TotResA, RelaxationParamA, MaxRelRes);
     PtAvg(VCount, 8, 26, R3V1C, R3V2C, R3V3C, R3V4C,
       TotResA, RelaxationParamA, MaxRelRes);
     PtAvg(VCount, 27, 27, R3V1RC, R3V2RC, R3V3RC,
      R3V4RC, TotResA, RelaxationParamA, MaxRelRes);
     PtAvgR(VCount, 28, 32, R1V1, R1V2, R1V3,
      R1V4, TotResA, RelaxationParamA, MaxRelRes);
    end;
   (* Compute potentials in R4 *)
   for VCount := R3Vert to R4Vert do
    PtAvgR(VCount,8,26,R4V1,R4V2, R4V3, R4V4, TotResB,
        RelaxationParamB, MaxRelRes);
   end
 else
  begin (* no, R3 does not exist *)
   (* Compute R2 up to bottom of electrodes *)
   for VCount := R1Vert+1 to OxNodes-1 do
    begin
     PtAvgR(VCount, 2, 6, R1V1, R1V2, R1V3, R1V4,
      TotResA, RelaxationParamA, MaxRelRes);
     PtAvg(VCount, 7, 7, R2V1LC, R2V2LC, R2V3LC,
      R2V4LC, TotResA, RelaxationParamA, MaxRelRes);
     PtAvg(VCount, 8, 26, R2V1C, R2V2C, R2V3C, R2V4C,
      TotResA, RelaxationParamA, MaxRelRes);
     PtAvg(VCount, 27, 27, R2V1RC, R2V2RC, R2V3RC,
      R2V4RC, TotResA, RelaxationParamA, MaxRelRes);
     PtAvgR(VCount, 28, 32, R1V1, R1V2, R1V3,
      R1V4, TotResA, RelaxationParamA, MaxRelRes);
    end;
  if R2Vert > OxNodes then
   begin
    (* Calculate new potentials in R2 Between Electrodes *)
    for VCount := OxNodes to R2Vert-1 do
     PtAvgR(VCount, 8, 26, R2V1C, R2V2C, R2V3C,
      R2V4C, TotResB, RelaxationParamB, MaxRelRes);

    (* Calculate new potentials in Region4 (if it exists) *)
    if (Nodes4 > 0) then      (* Test for any Region4 *)
     begin
      PtAvg(R2Vert, 8, 26, I24V1, I24V2, I24V3,
         I24V4, TotResB, RelaxationParamB, MaxRelRes);
       for VCount := R2Vert+1 to R4Vert do
        PtAvgR(VCount, 8, 26, R4V1, R4V2, R4V3,
         R4V4, TotResB, RelaxationParamB, MaxRelRes);
     end
    else
    (* No Region4, calculate new potentials at Region2-5 interface *)
      PtAvg(R2Vert, 8, 26, I25V1, I25V2, I25V3,
         I25V4, TotResB, RelaxationParamB, MaxRelRes);
    end
   else
    begin
     PtAvg(R2Vert, 8, 26, I24V1, I24V2, I24V3,
        I24V4, TotResB, RelaxationParamB, MaxRelRes);
     for VCount := R2Vert+1 to R4Vert do
       PtAvgR(VCount, 8, 26, R4V1, R4V2, R4V3,
        R4V4, TotResB, RelaxationParamB, MaxRelRes);
    end;
   end;
  end;
(* Calculate new potentials in Region5 *)
for VCount := R4Vert+1 to R5Vert-1 do
 begin
  PtAvgR(VCount, 2, 6, R5V1, R5V2, R5V3,
     R5V4, TotResB, RelaxationParamB, MaxRelRes);
  PtAvg(VCount, 7, 7, R5V1LC, R5V2LC, R5V3LC,
     R5V4LC, TotResB, RelaxationParamB, MaxRelRes);
  PtAvgR(VCount, 8, 26, R5V1C, R5V2C, R5V3C,
```

```
      R5V4C, TotResB, RelaxationParamB, MaxRelRes);
   PtAvg(VCount, 27, 27, R5V1RC, R5V2RC, R5V3RC,
      R5V4RC, TotResB, RelaxationParamB, MaxRelRes);
   PtAvgR(VCount, 28, 32, R5V1, R5V2, R5V3,
      R5V4, TotResB, RelaxationParamB, MaxRelRes);
  end;

(* Calculate new potentials at Region5-Region6 interface *)
 PtAvg(R5Vert, 2, 6, I56V1, I56V2, I56V3,
    I56V4, TotResB, RelaxationParamB, MaxRelRes);
 PtAvg(R5Vert, 7, 7, I56V1LC, I56V2LC, I56V3LC,
    I56V4LC, TotResB, RelaxationParamB, MaxRelRes);
 PtAvg(R5Vert, 8, 26, I56V1C, I56V2C, I56V3C,
     I56V4C, TotResB, RelaxationParamB, MaxRelRes);
 PtAvg(R5Vert, 27, 27, I56V1RC, I56V2RC, I56V3RC,
    I56V4RC, TotResB, RelaxationParamB, MaxRelRes);
 PtAvg(R5Vert, 28, 32, I56V1, I56V2, I56V3,
    I56V4, TotResB, RelaxationParamB, MaxRelRes);

 (* Calculate new potentials in Region6 *)
 for VCount := R5Vert+1 to R6Vert-1 do
  begin
   PtAvgR(VCount, 2, 6, R6V1, R6V2, R6V3, R6V4,
        TotResC, RelaxationParamC, MaxRelRes);
   PtAvgR(VCount, 7, 7, R6V1LC, R6V2LC, R6V3LC, R6V4LC,
     TotResC, RelaxationParamC, MaxRelRes);
   PtAvgR(VCount, 8, 26, R6V1C, R6V2C, R6V3C,
      R6V4C, TotResC, RelaxationParamC, MaxRelRes);
   PtAvgR(VCount, 27, 27, R6V1RC, R6V2RC, R6V3RC,
      R6V4RC, TotResC, RelaxationParamC, MaxRelRes);
   PtAvgR(VCount, 28, 32, R6V1, R6V2, R6V3, R6V4,
      TotResC, RelaxationParamC, MaxRelRes);
  end;

  (* apply side boundary conditions *)
  for VCount := 2 to R6Vert do
   begin
    Grid[VCount,1] := Grid[VCount,3];
    Grid[VCount,33] := Grid[VCount,31];
   end;

  (* apply upper boundary condition *)
  for HCount := 1 to Horz do
    Grid[R6Vert,HCount] := Grid[R6Vert-2,HCount];

  iterationctr := iterationctr + 1;
 end; (* Relaxation Update *)

 if RelaxUpdateSw in ['Y', 'y'] then
  begin
   UpdateRelaxParam(RelaxationParamA, TotResA, OldTotResA);
   UpdateRelaxParam(RelaxationParamB, TotResB, OldTotResB);
   UpdateRelaxParam(RelaxationParamC, TotResC, OldTotResC);
  end;
 writeln('iteration = ', iterationctr, '  MaxRelResidue = ',
     MaxRelRes);
 ChkKey;
until (MaxRelRes < ConvergenceValue);
(*****************************************************************************)

 if (ContourSw = 1) then begin
  assign(outfile2, outname + 'a');
  rewrite(outfile2);
  for i:= 1 to R6Vert do begin
   for j:=1 to Horz do
    write(outfile2,Grid[i,j].x:6:3, ',');
  writeln(outfile2);
  end;
  writeln(outfile2);
  for i:= 1 to R6Vert do begin
   for j:=1 to Horz do
    write(outfile2,Grid[i,j].y:6:3, ',');
   writeln(outfile2);
  end;
  Calculate_TF;
  close (outfile2);
  close (outfile);
  halt;
 end
 else begin
  writeln(outfile,' ');
  writeln(outfile, 'iteration = ',iterationctr, '   MaxRelResidue = ',
     MaxRelRes);
  Calculate_TF;
 end;
(*****************************************************************************)
 if epsilonF.y > -1.0 then Incy := -0.1
   else if epsilonF.y >-10.0 then Incy := -1.0
   else if epsilonF.y >-100.0 then Incy := -10.0;
  epsilonF.y := epsilonF.y + Incy;
 end; (* while epsilonF.y *)
 if epsilonF.x = 1.0 then epsilonF.x := 10.0
  else if epsilonF.x = 10.0 then epsilonF.x := 100.0
  else epsilonF.x := 110;
 end; (* while epsilonF.x *)

 close(outfile);
end.
```

```
(*************************************************************************)
(* Filename: UCINIT.I *)
(* Initialization Routines for the Thin Model with Undercut *)

procedure ReadConfig(var epsilon3 : complex; var ConvergenceValue,
                RelaxA, RelaxB, RelaxC, LoadCap, FT, ESep, UC:real;
                var FNodes : integer; var RelaxSw: char; var outname : outstring);

(* ReadConfig inputs the model paramters including the permittivities   *)
(* of each region, the convergence value, the relaxation parmaters for  *)
(* each region, the load capacitance, and the output filename. It also  *)
(* lets the user set whether variable or constant relaxation paramters  *)
(* will be used. If variable the initial setting is at 1.6 for all      *)
(* three grids.                                                         *)

var
  Sw : char;

begin
  write('Enter real part of complex permittivity of region 3 (Air) : ');
  readln(epsilon3.x);
  write('Enter imaginary part of complex permittivity of region 1 (Air): ');
  readln(epsilon3.y);
  epsilon3.y := -epsilon3.y;

  epsilon1.x := 3.9;
  epsilon1.y := 0.0;

  repeat
    write('Do you want variable relaxation parameters (Y/N) : ');
    readln(Sw);
    RelaxSw := Sw;
  until RelaxSw in ['Y', 'y', 'N', 'n'];

  if RelaxSw in ['Y', 'y'] then
    begin
      RelaxC := 1.8;
      RelaxB := 1.8;
      RelaxA := 1.8;
    end
  else
    begin
      write('Enter RegionA Relaxation Parameter between 1.2 and 1.9 : ');
      readln(RelaxA);
      write('Enter RegionB Relaxation Parameter between 1.2 and 1.9 : ');
      readln(RelaxB);
      write('Enter RegionC Relaxation Parameter between 1.2 and 1.9 : ');
      readln(RelaxC);
    end;

  write('Enter maximum residue value at convergence (usually 1e-3 - 1e-4) : ');
  readln(ConvergenceValue);

  write('Enter the Film Thickness in microns : ');
  readln(FT);
  FNodes := round(FT/0.1);

  write('Enter the Extent of Electrode Undercut in microns (Between 0 and 0.5) : ');
  readln(UC);

  write ('Enter Inter-Electrode Separation : ');
  readln(ESep);

  write('Enter load capacitance : ');
  readln(LoadCap);

  write('Enter name of output file : ');
  readln(outname);
(*  outname:= 'inttester5'; *)
end;
(*************************************************************************)

procedure InitGrid(VertDim, HorzDim : integer);
(* InitGrid initializes a grid of complex voltages to zero *)

var
  Zero : complex;
  VCount, HCount : integer;
begin
  Zero.x := 0.1;
  Zero.y := 0.0;
  for VCount := 1 to VertDim do
    begin
      for HCount := 1 to HorzDim do
        begin
          Grid[VCount,HCount] := Zero;
        end;
    end;
end; (* procedure InitGrid *)
(*************************************************************************)

procedure Init;
(* Init initializes the grid, inputs model parameters, applies input  *)
(* voltage, and initializes total relative residues *)

var
  DrivenGateVoltage : complex;
  VCount, HCount : integer;
begin
  InitGrid(R6Vert, Horz);

  DrivenGateVoltage.x := 1.0;
```

```
 DrivenGateVoltage.y := 0.0;
 for VCount := OxNodes to R4Vert do
  for HCount := 1 to 7 do
    Grid[VCount, HCount] := DrivenGateVoltage;
 for HCount := 1 to Horz do
    Grid[1,HCount].x := 0.0;

 TotResA := 0.0; TotResB := 0.0; TotResC := 0.0;
end; (* procedure Init *)
(*****************************************************************************)

procedure InitVCoeffC(var h1, h2, h3, h4 : real; var epsilonRatio, A, B, C,
            D : complex);
var Denom : complex;
begin
  A.x := (h2+h4)/h1;
  A.y := 0.0;
  D.x := (h1+h3)/h4;
  D.y := 0.0;
  B.x := epsilonRatio.x * (h3/h2);
  B.y := epsilonRatio.y * (h3/h2);
  B.x := B.x + (h1/h2);
  C.x := epsilonRatio.x * (h2/h3);
  C.y := epsilonRatio.y * (h2/h3);
  C.x := C.x + (h4/h3);
  Denom.x := A.x + B.x + C.x + D.x;
  Denom.y := A.y + B.y + C.y + D.y;
  DivideComplex(A, Denom, A);
  DivideComplex(B, Denom, B);
  DivideComplex(C, Denom, C);
  DivideComplex(D, Denom, D);

end; (* procedure InitVCoeffC *)
(*****************************************************************************)

procedure InitVCoeff2(var h1, h2, h3, h4, h1c, h3c : real; var epsilonRatio, V1Coeff,
            V2Coeff, V3Coeff, V4Coeff, V1C, V2C, V3C, V4C, V1LC, V2LC, V3LC,
            V4LC, V1RC, V2RC, V3RC, V4RC : complex);

 var
  temp, temp2, one : complex; Denom, DenomC, DenomLC : complex;

 begin
  Denom.x := 0.0;
  Denom.y := 0.0;
  V1Coeff.x := 1/(h1*(h1+h3));
  V1Coeff.y := 0.0;

  V1C.x := 1/(h1c*(h1c+h3c));
  V1C.y := 0.0;

  V3Coeff.x := 1/(h3*(h1+h3));
  V3Coeff.y := 0.0;

  V3C.x := 1/(h3c*(h1c+h3c));
  V3C.y := 0.0;

  DenomC.x := (1/(h1c*h3c)) + (1/(h2*h4));
  DenomC.y := 0.0;

  DenomLC.x := (1/(h1c*h3)) + (1/(h2*h4));
  DenomLC.y := 0.0;
  if Mag (epsilonRatio) = 1.0 then
   begin
    V1LC.x := 1/(h1c*(h1c+h3));
    V1LC.y := 0.0;

    V1RC.x := 1/(h1*(h1+h3c));
    V1RC.y := 0.0;

    V2Coeff.x := 1/(sqr(h2) + (h2*h4));
    V2Coeff.y := 0.0;

    V3LC.x := 1/(h3*(h1c+h3));
    V3LC.y := 0.0;

    V3RC.x := 1/(h3c*(h1+h3c));
    V3RC.y := 0.0;

    V4Coeff.x := 1/(sqr(h4)+(h2*h4));
    V4Coeff.y := 0.0;

    Denom.x := (1/(h1*h3)) + (1/(h2*h4));
    Denom.y := 0.0;

    DenomLC.x := (1/(h1c*h3)) + (1/(h2*h4));
    DenomLC.y := 0.0;
   end
  else
   begin

    temp.x := epsilonRatio.x * h2;
    temp.y := epsilonRatio.y * h2;
    temp.x := temp.x + h4;
    V2Coeff.x := temp.x * h2;
    V2Coeff.y := temp.y * h2;
    DivideComplex(epsilonRatio, V2Coeff, V2Coeff);
    one.x := 1.0;
    one.y := 0.0;
    V4Coeff.x := temp.x*h4;
    V4Coeff.y := temp.y*h4;
    DivideComplex(one, V4Coeff, V4Coeff);
```

```
    temp2 := epsilonRatio;
    temp2.x := temp2.x * (1/h2);
    temp2.y := temp2.y * (1/h2);
    temp2.x := temp2.x + (1/h4);
    DivideComplex(temp2, temp, Denom);
    Denom.x := Denom.x + (1/(h1*h3));
  end;

 DivideComplex(V2Coeff, DenomC, V2C);
 DivideComplex(V4Coeff, DenomC, V4C);
 DivideComplex(V2Coeff, DenomLC, V2LC);
 DivideComplex(V4Coeff, DenomLC, V4LC);
 DivideComplex(V1Coeff, Denom, V1Coeff);
 DivideComplex(V2Coeff, Denom, V2Coeff);
 DivideComplex(V3Coeff, Denom, V3Coeff);
 DivideComplex(V4Coeff, Denom, V4Coeff);
 DivideComplex(V1C, DenomC, V1C);
 DivideComplex(V3C, DenomC, V3C);
 DivideComplex(V1LC, DenomLC, V1LC);
 DivideComplex(V3LC, DenomLC, V3LC);
 DivideComplex(V1RC, DenomLC, V1RC);
 V2RC := V2LC;
 DivideComplex(V3RC, DenomLC, V3RC);
 V4RC := V4LC;
end; (* procedure InitVCoeff2 *)
(*****************************************************************************)

procedure InitVCoeff;
(* InitVCoeff computes the weighting values for adjacent nodes and the  *)
(* weighted denominator used for calculating the average at a given     *)
(* node in each grid. Within a grid the weighting values are            *)
(* independent of the permittivity, and weighting depends only on grid  *)
(* dimensions. The permittivites are required at the interface of the   *)
(* materials. *)

var
  epsilonRatio : complex;
  h1,h2,h3,h4, h1c, h3c  : real; (* h1,h2, h3 ,h4 correspond to the adjacent node *)
                (* separations clockwise starting with the node  *)
                (* to the right *)

  Dummyh : real;
  Dummy : complex;
begin
  Dummyh := 1.0;
  Dummy.x := 1.0;
  Dummy.y := 0.0;
  h1 := 1.0;  (* Region1 Weightings *)
  h4 := OxHeight/(OxNodes-1);
  h2 := h4;
  h3 := h1;
  h3c := ESep/20;
  h1c := h3c;
  epsilonRatio.x := 1.0;
  epsilonRatio.y := 0.0;
  InitVCoeff2(h1, h2, h3, h4, h1c, h3c, epsilonRatio, R1V1, R1V2, R1V3,
        R1V4, R1V1C, R1V2C, R1V3C, R1V4C, R1V1LC,
        R1V2LC, R1V3LC, R1V4LC, R1V1RC, R1V2RC, R1V3RC,
        R1V4RC);

  h4 := FT/FNodes;  (* Region2 Weightings *)
  h2 := h4;
  h1 := h1c;
  h3 := h3c;
  InitVCoeff2(h1, h2, h3, h4, Dummyh, Dummyh, epsilonRatio, R2V1C, R2V2C, R2V3C,
       R2V4C, Dummy, Dummy, Dummy, Dummy, Dummy, Dummy, Dummy, Dummy,
        Dummy, Dummy, Dummy, Dummy);

  h4 := 0.1;  (* Region3 Weightings *)
  h2 := h4;
  h1 := h1c;
  h3 := h3c;
  InitVCoeff2(h1, h2, h3, h4, Dummyh, Dummyh, epsilonRatio, R3V1C, R3V2C,
       R3V3C, R3V4C, Dummy, Dummy, Dummy, Dummy, Dummy, Dummy, Dummy,
Dummy,
        Dummy, Dummy, Dummy, Dummy);

  h4 := 0.1;  (* Region4 Weightings *)
  h2 := h4;
  h1 := h1c;
  h3 := h3c;
  InitVCoeff2(h1, h2, h3, h4, Dummyh, Dummyh, epsilonRatio, R4V1, R4V2,
         R4V3, R4V4, Dummy, Dummy, Dummy, Dummy, Dummy, Dummy, Dummy,
Dummy,
        Dummy, Dummy, Dummy, Dummy);

  h4 := FT/FNodes;  (* Region5 Weightings *)
  h2 := h4;
  h1 := 1.0;
  h3 := 1.0;

  InitVCoeff2(h1, h2, h3, h4, h1c, h3c, epsilonRatio, R5V1, R5V2,
        R5V3, R5V4, R5V1C, R5V2C, R5V3C, R5V4C,
        Dummy, Dummy, Dummy, Dummy, Dummy, Dummy, Dummy, Dummy);

  h1 := 1.0;  (* Region6 Weightings *)
  h4 := R6VertRes;
  h2 := h4;
  h3 := h1;
  epsilonRatio.x := 1.0;
  epsilonRatio.y := 0.0;
  InitVCoeff2(h1, h2, h3, h4, h1c, h3c, epsilonRatio, R6V1, R6V2, R6V3,
```

```
        R6V4, R6V1C, R6V2C, R6V3C, R6V4C, R6V1LC, R6V2LC, R6V3LC,
        R6V4LC, R6V1RC, R6V2RC, R6V3RC, R6V4RC);

          (* Region1-Region2 Interface Weightings *)
h2 := OxHeight/(OxNodes-1);
h4 := FT/FNodes;
h3 := h3c;
h1 := h1c;
DivideComplex(epsilon1, epsilonF, epsilonRatio);
InitVCoeff2(h1, h2, h3, h4, Dummyh, Dummyh, epsilonRatio, I12V1,
        I12V2, I12V3, I12V4, Dummy, Dummy, Dummy, Dummy, Dummy,
        Dummy, Dummy, Dummy, Dummy, Dummy, Dummy, Dummy);

        (* Region2-Region3 Interface  Weightings *)
h2 := h4;
h4 := 0.1;
DivideComplex(epsilonF, epsilon3, epsilonRatio);
InitVCoeff2(h1, h2, h3, h4, Dummyh, Dummyh, epsilonRatio, I23V1,
        I23V2, I23V3, I23V4, Dummy, Dummy, Dummy, Dummy,
        Dummy, Dummy, Dummy, Dummy, Dummy, Dummy, Dummy, Dummy);

        (* Region2-Region4 Interface  Weightings *)
h2 := h4;
h4 := 0.1;
DivideComplex(epsilonF, epsilon3, epsilonRatio);
InitVCoeff2(h1, h2, h3, h4, Dummyh, Dummyh, epsilonRatio, I24V1,
        I24V2, I24V3, I24V4, Dummy, Dummy, Dummy, Dummy,
        Dummy, Dummy, Dummy, Dummy, Dummy, Dummy, Dummy, Dummy);

       (* Region2-Region5 Interface  Weightings *)
h2 := FT/FNodes;
h4 := FT/FNodes;
h1 := h1c;
h3:= h3c;
DivideComplex(epsilonF, epsilon3, epsilonRatio);
InitVCoeff2(h1, h2, h3, h4, Dummyh, Dummyh, epsilonRatio, I25V1,
        I25V2, I25V3, I25V4, Dummy, Dummy, Dummy, Dummy,
        Dummy, Dummy, Dummy, Dummy, Dummy, Dummy, Dummy, Dummy);

        (* Region5-Region6 Interface  Weightings *)
h2 := FT/FNodes;
h4 := R6VertRes;
h1 := 1.0;
h3 := 1.0;
DivideComplex(epsilonF, epsilon3, epsilonRatio);
InitVCoeff2(h1, h2, h3, h4, h1c, h3c, epsilonRatio, I56V1, I56V2,
        I56V3, I56V4, Dummy, Dummy, Dummy, Dummy, Dummy, Dummy,
        Dummy, Dummy, Dummy, Dummy, Dummy, Dummy);

          (* Region5-Region6 Center Interface  Weightings *)
h2 := FT/FNodes;
h4 := R6VertRes;
h1 := ESep/20.0;
h3 := ESep/20.0;
epsilonRatio.x := 1.0;
epsilonRatio.y := 0.0;
InitVCoeff2(h1, h2, h3, h4, h1c, h3c, epsilonRatio, I56V1C, I56V2C,
        I56V3C, I56V4C, Dummy, Dummy, Dummy, Dummy, Dummy, Dummy,
        Dummy, Dummy, Dummy, Dummy, Dummy, Dummy);

        (* Region5-Region6 Interface Horizontal Weightings *)
h2 := FT/FNodes;
h4 := R6VertRes;
h1 := 1.0;
h3 := 1.0;
DivideComplex(epsilonF, epsilon3, epsilonRatio);
InitVCoeffC (h1c, h2, h3, h4, epsilonRatio, I56V1LC, I56V2LC,
        I56V3LC, I56V4LC);
InitVCoeffC (h3c, h2, h1, h4, epsilonRatio, I56V3RC, I56V2RC,
        I56V1RC, I56V4RC);

        (* Region5 Horizontal Interface  Weightings *)
h2 := FT/FNodes;
h4 := h2;

DivideComplex(epsilonF, epsilon3, epsilonRatio);
InitVCoeff2(h2, h3, h4, h1c, Dummyh, Dummyh, epsilonRatio, R5V2LC,
        R5V3LC, R5V4LC, R5V1LC, Dummy, Dummy, Dummy, Dummy,
        Dummy, Dummy, Dummy, Dummy, Dummy, Dummy, Dummy, Dummy);

DivideComplex(epsilon3, epsilonF, epsilonRatio);
InitVCoeff2(h2, h3c, h4, h1, Dummyh, Dummyh, epsilonRatio, R5V2RC, R5V3RC,
        R5V4RC, R5V1RC, Dummy, Dummy, Dummy, Dummy, Dummy, Dummy,
        Dummy, Dummy, Dummy, Dummy, Dummy, Dummy);

        (* Region3 Horizontal Interface  Weightings *)
h2 := OxHeight/(OxNodes-1);
h4 := h2;

DivideComplex(epsilon1, epsilon3, epsilonRatio);
InitVCoeff2(h2, h3, h4, h1c, Dummyh, Dummyh, epsilonRatio, R3V2LC,
        R3V3LC, R3V4LC, R3V1LC, Dummy, Dummy, Dummy, Dummy,
        Dummy, Dummy, Dummy, Dummy, Dummy, Dummy, Dummy, Dummy);

DivideComplex(epsilon3, epsilon1, epsilonRatio);
InitVCoeff2(h2, h3c, h4, h1, Dummyh, Dummyh, epsilonRatio, R3V2RC, R3V3RC,
        R3V4RC, R3V1RC, Dummy, Dummy, Dummy, Dummy, Dummy, Dummy,
        Dummy, Dummy, Dummy, Dummy, Dummy, Dummy);

        (* Region2 Horizontal Interface  Weightings *)
h2 := OxHeight/(OxNodes-1);
h4 := h2;
```

```
  DivideComplex(epsilon1, epsilonF, epsilonRatio);
  InitVCoeff2(h2, h3, h4, h1c, Dummyh, Dummyh, epsilonRatio, R2V2LC,
        R2V3LC, R2V4LC, R2V1LC, Dummy, Dummy, Dummy, Dummy,
        Dummy, Dummy, Dummy, Dummy, Dummy, Dummy, Dummy, Dummy);

  DivideComplex(epsilonF, epsilon1, epsilonRatio);
  InitVCoeff2(h2, h3c, h4, h1, Dummyh, Dummyh, epsilonRatio, R2V2RC, R2V3RC,
        R2V4RC, R2V1RC, Dummy, Dummy, Dummy, Dummy, Dummy, Dummy,
        Dummy, Dummy, Dummy, Dummy, Dummy, Dummy);

end; (* procedure InitVCoeff *)
(*************************************************************************)
```



```
(*************************************************************************)
(* Filename: UCPRT.I *)
(* Routines to Calculate Two-Port Admittances for Thin Model with Undercut *)

procedure CurrentElement (var Grid : GridArray; V1Pos, V2Pos,
      HPos :integer; Epsilon : complex; Coeff : real; var I : complex);
(* Computes the current elements between nodes in the vertical direction *)
var
  Temp : complex;
begin
   SubtractComplex(Grid[V1Pos,HPos], Grid[V2Pos,HPos], Temp);
   MultiplyComplex(Temp,Epsilon,Temp);
   Temp.x := Temp.x * Coeff;
   Temp.y := Temp.y * Coeff;
   AddComplex(I,Temp,I);
end; (* CurrentElement *)

procedure SideCurrentElement (var Grid : GridArray; VPos, H1Pos, H2Pos:
      integer; Epsilon : complex; Coeff : real; var I : complex);
(* Computes the currents elements between nodes in the horizontal  direction *)
var
  Temp : complex;
begin
   SubtractComplex(Grid[VPos,H1Pos], Grid[VPos,H2Pos], Temp);
   MultiplyComplex(Temp,Epsilon,Temp);
   Temp.x := Temp.x * Coeff;
   Temp.y := Temp.y * Coeff;
   AddComplex(I,Temp,I);
end; (* SideCurrentElement *)
(*************************************************************************)

procedure TwoPortAdmit;
(* Calculates the two port admittance parameters for the interdigitated *)
(* electrode structure. The current through each electrode is computed  *)
(* using surface integration around each electrode. Note that the nodes *)
(* along the interface at the outer boundaries do not contribute to the *)
(* to the current since the potential gradient is zero at these nodes.  *)
(* These currents are used to calculate the Y parameters. The Y         *)
(* parameters calculated here must be multiplied by the meander length  *)
(* to get total admittance. The total admittance is not calculated here *)
var
  Count : integer;
  SepCoeff : real;          (* SepCoeff := (h1/2 + h3/2)/h4 *)
  Temp1, Temp2, Temp3 : complex;
  SepCoeff2 : complex;
  I1, I2 : complex;
```

```
(* Add current elements along nodes above the electrodes and   *)
(* keep running sum in I1 and I2                               *)
(*SepCoeff := 1.0;*)          (* since h1=h3=h2=h4 *)
h1:=1.0;
h3:=1.0;
h4:=R6VertRes;
SepCoeff:=(h1/2 + h3/2)/h4;
CurrentElement(Grid, R5Vert+1, R5Vert+2, 2, epsilon3, 0.5*SepCoeff, I1);
CurrentElement(Grid, R5Vert+1, R5Vert+2, 32, epsilon3, 0.5*SepCoeff, I2);
for Count := 3 to 6 do
  CurrentElement(Grid, R5Vert+1, R5Vert+2, Count, epsilon3, SepCoeff, I1);
 for Count := 8 to 11 do
   CurrentElement(Grid, R5Vert+1, R5Vert+2, Count+20, epsilon3, SepCoeff, I2);

SepCoeff:= (ESep/20)/h4;
for Count := 8 to 14 do
   CurrentElement(Grid, R5Vert+1, R5Vert+2, Count, epsilon3, SepCoeff, I1);
for Count := 2 to 8 do
  CurrentElement(Grid, R5Vert+1, R5Vert+2, Count+18, epsilon3, SepCoeff, I2);

SepCoeff := (ESep/20 + 1.0)/(2.0*h4);
CurrentElement(Grid, R5Vert+1, R5Vert+2, 7, epsilon3, SepCoeff, I1);
CurrentElement(Grid, R5Vert+1, R5Vert+2, 27, epsilon3, SepCoeff, I2);

(* Add current elements along nodes on the medial sides of the  *)
(* electrodes in region3 to I1 and I2 *)
SepCoeff := (R6VertRes + R6VertRes)/(2*ESep/20);
SideCurrentElement(Grid, R5Vert+1, 14, 15, epsilon3, SepCoeff, I1);
SideCurrentElement(Grid, R5Vert+1, 20, 19, epsilon3, SepCoeff, I2);

(* Add current elements at interface between Region5 and Region6 *)
h2 := FT/FNodes;
h4 := R6VertRes;
h1 := ESep/20;
SepCoeff := (h2 + h4)/(2*h1);
SideCurrentElement(Grid, R5Vert, 14, 15, epsilon3, SepCoeff, I1);
SideCurrentElement(Grid, R5Vert, 20, 19, epsilon3, SepCoeff, I2);

(* Add current elements along nodes on the medial sides of the  *)
(* electrodes in region5 to I1 and I2 *)
h2 := FT/FNodes; (* h4 = h2 *)
h1 := ESep/20;
SepCoeff := h2/h1;
for Count := R4Vert+1 to R5Vert-1 do
 begin
   SideCurrentElement(Grid, Count, 14, 15, epsilon3, SepCoeff, I1);
   SideCurrentElement(Grid, Count, 20, 19, epsilon3, SepCoeff, I2);
 end;

(* Add current elements along nodes on the medial sides of the  *)
(* electrodes in region2 to I1 and I2 *)
for Count := R1Vert+1 to R2Vert-1 do
 begin
   SideCurrentElement(Grid, Count, 14, 15, epsilonF, SepCoeff, I1);
   SideCurrentElement(Grid, Count, 20, 19, epsilonF, SepCoeff, I2);
 end;

(* Add current elements along nodes on the medial sides of the  *)
(* electrodes in region4 to I1 and I2 *)
h4 := 0.1;
h2 := 0.1;
h1 := ESep/20;
SepCoeff := (h2 + h4)/(2*h1);
if Nodes4 > 0 then
 begin
  for Count := R2Vert+1 to R4Vert-1 do   (* will only execute if Nodes2b>1 *)
    begin
      SideCurrentElement(Grid, Count, 14, 15, epsilon3, SepCoeff, I1);
      SideCurrentElement(Grid, Count, 20, 19, epsilon3, SepCoeff, I2);
    end;
  (* Add current elements at interface of Region4 and Region5 *)
  h4 := FT/FNodes;
  SepCoeff := (h4+h2)/(2*h1);
  SideCurrentElement(Grid, R4Vert, 14, 15, epsilon3, SepCoeff, I1);
  SideCurrentElement(Grid, R4Vert, 20, 19, epsilon3, SepCoeff, I2);
 end;

(* Add current elements along nodes on the medial sides of the  *)
(* electrodes in region1 to I1 and I2 *)
h1 := ESep/20.0;
h4 := OxHeight/(OxNodes-1);
SepCoeff := h4/h1;  (* since h2=h4 and h1=h3 *)
for Count := 5 to R1Vert-1 do
 begin
   SideCurrentElement(Grid, Count, 14, 15, epsilon1, SepCoeff, I1);
   SideCurrentElement(Grid, Count, 20, 19, epsilon1, SepCoeff, I2);
 end;

(* Add current elements along nodes below the electrodes to I1 and I2  *)
h1:= 1.0;
h3 :=1.0;
h4:= OxHeight/(OxNodes-1);
SepCoeff := (h1+h3)/(2*h4);
CurrentElement(Grid, 5, 4, 2, epsilon1, 0.5*SepCoeff, I1);
CurrentElement(Grid, 5, 4, 32, epsilon1, 0.5*SepCoeff, I2);
for Count := 3 to 6 do
  CurrentElement(Grid, 5, 4, Count, epsilon1, SepCoeff, I1);
for Count := 8 to 11 do
   CurrentElement(Grid, 5, 4, Count+20, epsilon1, SepCoeff, I2);

SepCoeff:= (ESep/20)/h4;
for Count := 8 to 14 do
```

```
  CurrentElement(Grid, 5, 4, Count, epsilon1, SepCoeff, I1);
for Count := 2 to 8 do
  CurrentElement(Grid, 5 , 4, Count+18, epsilon1, SepCoeff, I2);

SepCoeff := (ESep/20 + 1.0)/(2.0*h4);
CurrentElement(Grid, 5 ,4, 7, epsilon1, SepCoeff, I1);
CurrentElement(Grid, 5, 4, 27, epsilon1, SepCoeff, I2);

V1 := Grid[R3Vert,2];
V2 := Grid[R3Vert,28];

(* Add currents due to nodes at the interface between Region1 and Region2 *)
(* along the medial sides of the electrodes. Here the Separation       *)
(* coeffcient becomes SepCoeff = [epsilonF*(h4/2) + epsilon1 * (h2/2)]/h1 *)

h2 := OxHeight/(OxNodes-1);  (* along interface h4 does not equal h2 *)
h4 := FT/FNodes;
h1 := ESep/20;
Temp2 := epsilon1;
Temp2.x := Temp2.x * (h2/(2*h1));
Temp2.y := Temp2.y * (h2/(2*h1));
Temp3 := epsilonF;
Temp3.x := Temp3.x * (h4/(2*h1));
Temp3.y := Temp3.y * (h4/(2*h1));
AddComplex(Temp2,Temp3,SepCoeff2);
SubtractComplex(Grid[R1Vert,14], Grid[R1Vert,15], Temp1);
MultiplyComplex(Temp1,SepCoeff2,Temp1);
AddComplex(I1,Temp1,I1);      (* Current element for driven electrode *)
SubtractComplex(Grid[R1Vert,20], Grid[R1Vert,19], Temp1);
MultiplyComplex(Temp1,SepCoeff2,Temp1);
AddComplex(I2,Temp1,I2);     (* Current element for floating electrode *)

(* Add currents due to nodes at the interface between Region2 and      *)
(* Region4 (or Region3) along the medial sides of the electrodes. Here
(* the Separation coeffcient becomes SepCoeff = [epsilon3*(h4/2) +     *)
(*  epsilonF * (h2/2)]/h1 *)
 h4 := 0.1;
 h2 := FT/FNodes;
 h1 := ESep/20;

 Temp2 := epsilon3;
 Temp2.x := Temp2.x * (h4/(2*h1));
 Temp2.y := Temp2.y * (h4/(2*h1));
 Temp3 := epsilonF;
 Temp3.x := Temp3.x * (h2/(2*h1));
 Temp3.y := Temp3.y * (h2/(2*h1));
 AddComplex(Temp2,Temp3,SepCoeff2);
 SubtractComplex(Grid[R2Vert,14], Grid[R2Vert,15], Temp1);
 MultiplyComplex(Temp1,SepCoeff2,Temp1);
 AddComplex(I1,Temp1,I1);      (* Current element for driven electrode *)
 SubtractComplex(Grid[R2Vert,20], Grid[R2Vert,19], Temp1);
 MultiplyComplex(Temp1,SepCoeff2,Temp1);
 AddComplex(I2,Temp1,I2);     (* Current element for floating electrode *)

 (* Calculate two port y parameters from currents and voltages. See     *)
 (* Lee, equations 3.10.3 and 3.10.4 *)
 MultiplyComplex(V1, V1, Temp1);
 MultiplyComplex(V2, V2, Temp2);
 SubtractComplex(Temp2,Temp1,Temp1); (* denominator of eqts. 3.10.3     *)
 MultiplyComplex(I2, V2, Temp3);
 MultiplyComplex(I1, V1, Temp2);
 SubtractComplex(Temp3, Temp2, Y1);
 DivideComplex(Y1,Temp1,Y1);        (* Calculate Y1 *)
 MultiplyComplex(I1, V2, Temp2);
 MultiplyComplex(I2, V1, Temp3);
 SubtractComplex(Temp3, Temp2, Y2);
 DivideComplex(Y2, Temp1, Y2);       (* Calculate Y2 *)
end; (* TwoPortAdmit *)
(*************************************************************************)
```

Planar Model Source Code

```
(*************************************************************************)
(* Filename: THCKMODL.P *)
(* Finite Diference Model Program for Thick Films (>1.5 micron *)

program thckmodl1(input,output, outfile);
uses dos, crt;
(*    This program computes the potential distribution resulting    *)
(*    from the application of a 1V steady state sinusoidal voltage  *)
(*    on an interdigitated electrode structure ( could be viewed    *)
(*    as coupled microstrips). This program is an extension         *)
(*    of the algorithm developed by Huan Lee in his Master's        *)
(*    thesis,"Optimization of a Resin Cure", Massachusetts          *)
(*    Institute of Technology, 1982. This thesis is available       *)
(*    in the AFIT Library. The extension allows the calculation of  *)
(*    the IDE TF when coated with thin films (>1.5 micron).         *)
(*    Variable electrode separation and undercutting the electrodes *)
(*    is also supported. The program computes the effect of an      *)
(*    arbitrary load capacitance connected to the floating          *)
(*    electrode on the IDE TF.          *)

 const
    ContourSw=0;       (* Switch=0: Transfer Function Output *)
                       (* Switch=1: Voltage Distribution Output *)
    SemiSw=0;          (* Switch=0: Thin Film *)
                       (* Switch=1: Semi-Infinite Film *)
    OxNodes = 10;              (* Number of oxide nodes *)
    Nodes7 = 11;               (* # vertical nodes in Region6 *)
    R6VertRes = 0.5;           (* Vertical Resolution in Region6 *)
    R7VertRes = 1.0;
    Horz = 33;                 (* # horizontal nodes in entire grid *)
```

```
    EHeight = 1.2;        (* Electrode Height to nearest 0.1 microns *)
    OxHeight = 0.9;       (* Oxide Height in microns *)
    epsilon0 = 8.854e-14;     (* F/cm *)
    pi = 3.1415926535897932385;

type
  complex=record              (* define complex data type      *)
    x,y:real;
  end; (*complex Record*)

  GridArray =array[1.. 155, 1..33] of complex;
    (* GridArray is a new data type for the finite difference grid *)
    (* with a max size of 100 vertical nodes and 40 horizontal nodes *)

(*   outstring = packed array [1..20] of char; *)
  outstring = string[20];
                (* outstring defines a file name data    *)
                (* type, max size of 20 characters      *)

var
    Grid : GridArray;           (* finite difference grid *)
    FT : real;             (* Film Thickness To nearest .1 micron *)
    UC : real;             (* Undercut to nearest 0.1 micron *)
    ESep : real;              (* Inter-Electrode Separation *)
    Nodes4 : integer;          (* Number of Nodes In Region4 *)
    Nodes5 : integer;          (* Number of Nodes in Region5 *)
    Nodes6 : integer;          (* Number of Nodes in Region6 *)
    R1Vert, R2Vert, R3Vert, R4Vert,
     R5Vert, R6Vert, R7Vert    : integer; (* Top node in Each Region *)
    epsilon1, epsilonF, epsilon3 : complex; (* complex permittivities *)
    MaxRelRes : real;         (* maximum relative residue/iteration *)
    TotResA, TotResB,TotResC : real; (* Total of relative residues   *)
                        (* for each grid per iteration   *)
    RelaxationParamA, RelaxationParamB, RelaxationParamC : real;
    OldTotResA, OldTotResB, OldTotResC : real; (* Total relative     *)
    (* residues for each region from previous iteration          *)

    RelaxationUpdateCounter : integer;

    (* Multiplicative factors for averaging the nodes in each grid   *)
    R1V1, R1V2, R1V3, R1V4, R1V1C, R1V2C, R1V3C, R1V4C, R1V1LC, R1V2LC,
      R1V3LC, R1V4LC, R1V1RC, R1V2RC, R1V3RC, R1V4RC : complex;
    I12V1, I12V2, I12V3, I12V4 : complex;
    R2V1LC, R2V2LC, R2V3LC, R2V4LC, R2V1RC, R2V2RC, R2V3RC, R2V4RC,
      R2V1C, R2V2C, R2V3C, R2V4C  : complex;
    I23V1, I23V2,I23V3, I23V4 : complex;
    R3V1LC, R3V2LC, R3V3LC, R3V4LC, R3V1RC, R3V2RC, R3V3RC, R3V4RC,
      R3V1C, R3V2C, R3V3C, R3V4C : complex;
    R4V1, R4V2, R4V3, R4V4 : complex;
    I24V1, I24V2,I24V3, I24V4, I25V1, I25V2, I25V3, I25V4 : complex;
    R5V1, R5V2, R5V3, R5V4, R5V1C, R5V2C, R5V3C, R5V4C, R5V1LC,
      R5V2LC, R5V3LC, R5V4LC, R5V1RC, R5V2RC, R5V3RC, R5V4RC : complex;
    I56V1, I56V2, I56V3, I56V4, I56V1C, I56V2C, I56V3C, I56V4C, I56V1LC,
      I56V2LC, I56V3LC, I56V4LC, I56V1RC, I56V2RC,
      I56V3RC, I56V4RC : complex;
    I57V1, I57V2, I57V3, I57V4, I57V1C, I57V2C, I57V3C, I57V4C, I57V1LC,
      I57V2LC, I57V3LC, I57V4LC, I57V1RC, I57V2RC,
      I57V3RC, I57V4RC : complex;
    I67V1, I67V2, I67V3, I67V4, I67V1C, I67V2C, I67V3C, I67V4C, I67V1LC,
      I67V2LC, I67V3LC, I67V4LC, I67V1RC, I67V2RC,
      I67V3RC, I67V4RC : complex;
    R6V1, R6V2, R6V3, R6V4, R6V1C, R6V2C, R6V3C, R6V4C, R6V1LC, R6V2LC,
      R6V3LC, R6V4LC, R6V1RC, R6V2RC, R6V3RC, R6V4RC : complex;
    R7V1, R7V2, R7V3, R7V4, R7V1C, R7V2C, R7V3C, R7V4C, R7V1LC, R7V2LC,
      R7V3LC, R7V4LC, R7V1RC, R7V2RC, R7V3RC, R7V4RC : complex;

    VCount, HCount : integer;
    RelaxUpdateSw : char;  (* Toggles variable/constant relax parameters *)
    ConvergenceValue : real; (* acceptable maximum relative          *)
                (* residue/iteration                  *)
    iterationctr : integer;
    Incy : real;
    Y1, Y2 : complex;      (* Two port admittance parameters         *)
    LoadCap, RedConverg : real;
    TransferFunction : complex;
    outfile, outfile2 : text;
    outname : outstring;    (* outname is the user specified output    *)
                (* file name                          *)
    i,j :integer;
(*****************************************************************************)

(* #include "cplxmth2.i" *)       (* include complex math procedures *)
(* #include "newprt3b.i" *)
(* #include "mnewinit.i" *)
{$I cplxmth2.i}
{$I thckprt.i}
{$I thckinit.i}
{$I FDCALC.PAS}
{$I FNHANDL.PAS}
(*****************************************************************************)

begin (* main *)
  ReadConfig(epsilon3, ConvergenceValue, RelaxationParamA, RelaxationParamB,
        RelaxationParamC, LoadCap, FT, ESep, UC, RelaxUpdateSw, outname);
  epsilonF.x := 1.0;
  R1Vert := OxNodes - round(UC/0.1);
  Nodes4 := round((EHeight-FT+UC)/0.1);
  if Nodes4 <= 0 then Nodes4 := 0;
  if (FT-(EHeight+UC) > (EHeight+UC)) then
    begin
      Nodes5 := round((EHeight+UC)/0.1);
      Nodes6 := round((FT-2*(EHeight+UC))/R6VertRes);
```

```
 end
else
 begin
  Nodes5 := round((FT-(EHeight+UC))/0.1);
  Nodes6 := 0;
 end;

R2Vert := round((EHeight+UC)/0.1) + R1Vert;
R3Vert := OxNodes;
R4Vert := R2Vert + Nodes4;
R5Vert := R4Vert + Nodes5;
R6Vert := R5Vert + Nodes6;
R7Vert := R6Vert + Nodes7;

(*  rewrite(outfile,outname); *)
assign(outfile,outname);
rewrite(outfile);

writeln(outfile, 'Electrode Separation = ', ESep);
writeln(outfile, 'Film Thickness = ', FT, '   Variable Relaxation - ',
      RelaxUpdateSw);
writeln(outfile, 'epsilon3.x = ', epsilon3.x, '  epsilon3.y = ', epsilon3.y);
writeln(outfile, 'epsilon1.x = ', epsilon1.x, '  epsilon1.y = ', epsilon1.y);
writeln(outfile, 'Nodes6 = ', Nodes6, '   Horz = ', Horz);
writeln(outfile, 'R6VertRes = ', R6VertRes, '    Undercut = ', UC);
writeln(outfile, 'R7VertRes = ', R7VertRes);

RedConverg := 0.9 * ConvergenceValue;
while epsilonF.x < 110.0 do
 begin
 epsilonF.y:= -2.0;
 while epsilonF.y > -1100.0 do
 begin
 if(SemiSw=1) then epsilon3 := epsilonF;  (* Switch=1: Semi-Infinite Film *)
 RelaxationParamA := 1.8;
 RelaxationParamB := 1.8;
 RelaxationParamC := 1.8;
 Init;
 InitVCoeff;
 iterationctr := 0;
 repeat
  for RelaxationUpdateCounter := 1 to 3 do
   begin
   MaxRelRes := RedConverg;
   for VCount := 2 to R1Vert-1 do   (* Calculate new potentials over *)
    begin                  (* Region1 except at upper interface *)
     PtAvgR(VCount, 2, 6, R1V1, R1V2, R1V3, R1V4,
          TotResA, RelaxationParamA, MaxRelRes);
     PtAvgR(VCount, 7, 7, R1V1LC, R1V2LC, R1V3LC,
          R1V4LC, TotResA, RelaxationParamA, MaxRelRes);
     PtAvgR(VCount, 8, 26, R1V1C, R1V2C, R1V3C,
          R1V4C, TotResA, RelaxationParamA, MaxRelRes);
    PtAvgR(VCount, 27, 27, R1V1RC, R1V2RC, R1V3RC,
         R1V4RC, TotResA, RelaxationParamA, MaxRelRes);
    PtAvgR(VCount, 28, 32, R1V1, R1V2, R1V3,
         R1V4, TotResA, RelaxationParamA, MaxRelRes);
end;
if UC=0 then
 begin
  (* Calculate new potentials at Region1-Region2 interface *)
  PtAvg(R1Vert, 8, 26, I12V1, I12V2, I12V3, I12V4,
       TotResA, RelaxationParamA, MaxRelRes);
  (* Calculate new potentials in Region2 *)
  for VCount := R1Vert+1 to R2Vert-1 do
   PtAvgR(VCount, 8, 26, R2V1C, R2V2C, R2V3C, R2V4C,
     TotResB, RelaxationParamB, MaxRelRes);
  (* Calculate new potentials in Region4 (if it exists) *)
  if (Nodes4 > 0) then      (* Test for any Region4 *)
    begin
     PtAvg(R2Vert, 8, 26, I24V1, I24V2, I24V3,
        I24V4, TotResB, RelaxationParamB, MaxRelRes);
     for VCount := R2Vert+1 to R4Vert do
       PtAvgR(VCount, 8, 26, R4V1, R4V2, R4V3,
         R4V4, TotResB, RelaxationParamB, MaxRelRes);
    end
   else
 (* No Region4, calculate new potentials at Region2-5 interface *)
      PtAvg(R2Vert, 8, 26, I25V1, I25V2, I25V3,
        I25V4, TotResB, RelaxationParamB, MaxRelRes);
 end
else
 begin
  PtAvgR(R1Vert, 2, 6, R1V1, R1V2, R1V3, R1V4,
      TotResA, RelaxationParamA, MaxRelRes);
  PtAvg(R1Vert, 7, 7, R2V1LC, R2V2LC, R2V3LC,
      R2V4LC, TotResA, RelaxationParamA, MaxRelRes);
  PtAvg(R1Vert, 8, 26, I12V1, I12V2, I12V3, I12V4,
      TotResA, RelaxationParamA, MaxRelRes);
  PtAvg(R1Vert, 27, 27, R2V1RC, R2V2RC, R2V3RC,
      R2V4RC, TotResA, RelaxationParamA, MaxRelRes);
  PtAvgR(R1Vert, 28, 32, R1V1, R1V2, R1V3,
      R1V4, TotResA, RelaxationParamA, MaxRelRes);


(* Check to see if film entirely fills undercut *)
if R2Vert < OxNodes then
  begin  (* yes, then R3 Exists *)
   for VCount := R1Vert+1 to R2Vert-1 do
    begin
     PtAvgR(VCount, 2, 6, R1V1, R1V2, R1V3, R1V4,
      TotResA, RelaxationParamA, MaxRelRes);
     PtAvg(VCount, 7, 7, R2V1LC, R2V2LC, R2V3LC,
```

```
      R2V4LC, TotResA, RelaxationParamA, MaxRelRes);
     PtAvg(VCount, 8, 26, R2V1C, R2V2C, R2V3C, R2V4C,
      TotResA, RelaxationParamA, MaxRelRes);
     PtAvg(VCount, 27, 27, R2V1RC, R2V2RC, R2V3RC,
      R2V4RC, TotResA, RelaxationParamA, MaxRelRes);
     PtAvgR(VCount, 28, 32, R1V1, R1V2, R1V3,
      R1V4, TotResA, RelaxationParamA, MaxRelRes);
    end;
   (* Calculate potential at R2-R3 Interface *)
   PtAvgR(R2Vert, 2, 6, R1V1, R1V2, R1V3, R1V4,
      TotResA, RelaxationParamA, MaxRelRes);
   PtAvg(R2Vert, 7, 7, R2V1LC, R2V2LC, R2V3LC,
      R2V4LC, TotResA, RelaxationParamA, MaxRelRes);
   PtAvg(R2Vert, 8, 26, I23V1, I23V2, I23V3, I23V4,
       TotResA, RelaxationParamA, MaxRelRes);
   PtAvg(R2Vert, 27, 27, R2V1RC, R2V2RC, R2V3RC,
      R2V4RC, TotResA, RelaxationParamA, MaxRelRes);
   PtAvgR(R2Vert, 28, 32, R1V1, R1V2, R1V3,
      R1V4, TotResA, RelaxationParamA, MaxRelRes);
   (* Calculate Potential in R3 *)
   for VCount := R2Vert+1 to R3Vert-1 do
    begin
     PtAvgR(VCount, 2, 6, R1V1, R1V2, R1V3, R1V4,
      TotResA, RelaxationParamA, MaxRelRes);
     PtAvg(VCount, 7, 7, R3V1LC, R3V2LC, R3V3LC,
      R2V4LC, TotResA, RelaxationParamA, MaxRelRes);
     PtAvg(VCount, 8, 26, R3V1C, R3V2C, R3V3C, R3V4C,
       TotResA, RelaxationParamA, MaxRelRes);
     PtAvg(VCount, 27, 27, R3V1RC, R3V2RC, R3V3RC,
      R3V4RC, TotResA, RelaxationParamA, MaxRelRes);
     PtAvgR(VCount, 28, 32, R1V1, R1V2, R1V3,
      R1V4, TotResA, RelaxationParamA, MaxRelRes);
    end;
   (* Compute potentials in R4 *)
   for VCount := R3Vert to R4Vert do
    PtAvgR(VCount,8,26,R4V1,R4V2, R4V3, R4V4, TotResB,
        RelaxationParamB, MaxRelRes);
   end
else
  begin (* no, R3 does not exist *)
   (* Compute R2 up to bottom of electrodes *)
   for VCount := R1Vert+1 to OxNodes-1 do
    begin
     PtAvgR(VCount, 2, 6, R1V1, R1V2, R1V3, R1V4,
      TotResA, RelaxationParamA, MaxRelRes);
     PtAvg(VCount, 7, 7, R2V1LC, R2V2LC, R2V3LC,
      R2V4LC, TotResA, RelaxationParamA, MaxRelRes);
     PtAvg(VCount, 8, 26, R2V1C, R2V2C, R2V3C, R2V4C,
      TotResA, RelaxationParamA, MaxRelRes);
     PtAvg(VCount, 27, 27, R2V1RC, R2V2RC, R2V3RC,
      R2V4RC, TotResA, RelaxationParamA, MaxRelRes);
     PtAvgR(VCount, 28, 32, R1V1, R1V2, R1V3,
      R1V4, TotResA, RelaxationParamA, MaxRelRes);
    end;
   if R2Vert > OxNodes then
    begin
     (* Calculate new potentials in R2 Between Electrodes *)
     for VCount := OxNodes to R2Vert-1 do
      PtAvgR(VCount, 8, 26, R2V1C, R2V2C, R2V3C,
       R2V4C, TotResB, RelaxationParamB, MaxRelRes);

     (* Calculate new potentials in Region4 (if it exists) *)
     if (Nodes4 > 0) then      (* Test for any Region4 *)
      begin
       PtAvg(R2Vert, 8, 26, I24V1, I24V2, I24V3,
          I24V4, TotResB, RelaxationParamB, MaxRelRes);
       for VCount := R2Vert+1 to R4Vert do
        PtAvgR(VCount, 8, 26, R4V1, R4V2, R4V3,
         R4V4, TotResB, RelaxationParamB, MaxRelRes);
      end
     else
     (* No Region4, calculate new potentials at Region2-5 interface *)
       PtAvg(R2Vert, 8, 26, I25V1, I25V2, I25V3,
          I25V4, TotResB, RelaxationParamB, MaxRelRes);
     end
    else
     begin
      PtAvg(R2Vert, 8, 26, I24V1, I24V2, I24V3,
         I24V4, TotResB, RelaxationParamB, MaxRelRes);
      for VCount := R2Vert+1 to R4Vert do
       PtAvgR(VCount, 8, 26, R4V1, R4V2, R4V3,
        R4V4, TotResB, RelaxationParamB, MaxRelRes);
     end;
   end;
  end;
 (* Calculate new potentials in Region5 *)
 for VCount := R4Vert+1 to R5Vert-1 do
  begin
   PtAvgR(VCount, 2, 6, R5V1, R5V2, R5V3,
      R5V4, TotResB, RelaxationParamB, MaxRelRes);
   PtAvg(VCount, 7, 7, R5V1LC, R5V2LC, R5V3LC,
      R5V4LC, TotResB, RelaxationParamB, MaxRelRes);
   PtAvgR(VCount, 8, 26, R5V1C, R5V2C, R5V3C,
      R5V4C, TotResB, RelaxationParamB, MaxRelRes);
   PtAvg(VCount, 27, 27, R5V1RC, R5V2RC, R5V3RC,
      R5V4RC, TotResB, RelaxationParamB, MaxRelRes);
   PtAvgR(VCount, 28, 32, R5V1, R5V2, R5V3,
      R5V4, TotResB, RelaxationParamB, MaxRelRes);
  end;

 if (Nodes6>0) then
  begin
```

```
(* Calculate new potentials at Region5-Region6 interface *)
 PtAvg(R5Vert, 2, 6, I56V1, I56V2, I56V3,
   I56V4, TotResB, RelaxationParamB, MaxRelRes);
 PtAvg(R5Vert, 7, 7, I56V1LC, I56V2LC, I56V3LC,
   I56V4LC, TotResB, RelaxationParamB, MaxRelRes);
 PtAvg(R5Vert, 8, 26, I56V1C, I56V2C, I56V3C,
   I56V4C, TotResB, RelaxationParamB, MaxRelRes);
 PtAvg(R5Vert, 27, 27, I56V1RC, I56V2RC, I56V3RC,
   I56V4RC, TotResB, RelaxationParamB, MaxRelRes);
 PtAvg(R5Vert, 28, 32, I56V1, I56V2, I56V3,
   I56V4, TotResB, RelaxationParamB, MaxRelRes);

 if (Nodes6>1) then
   begin
    (* Calculate new potentials in Region6 *)
    for VCount := R5Vert+1 to R6Vert-1 do
     begin
       PtAvgR(VCount, 2, 6, R6V1, R6V2, R6V3, R6V4,
         TotResC, RelaxationParamC, MaxRelRes);
       PtAvgR(VCount, 7, 7, R6V1LC, R6V2LC, R6V3LC, R6V4LC,
         TotResC, RelaxationParamC, MaxRelRes);
       PtAvgR(VCount, 8, 26, R6V1C, R6V2C, R6V3C,
         R6V4C, TotResC, RelaxationParamC, MaxRelRes);
       PtAvgR(VCount, 27, 27, R6V1RC, R6V2RC, R6V3RC,
         R6V4RC, TotResC, RelaxationParamC, MaxRelRes);
       PtAvgR(VCount, 28, 32, R6V1, R6V2, R6V3, R6V4,
         TotResC, RelaxationParamC, MaxRelRes);
     end;
    end;
    (* Calculate new potentials at Region6-Region7 interface *)
    PtAvg(R6Vert, 2, 6, I67V1, I67V2, I67V3,
      I67V4, TotResB, RelaxationParamB, MaxRelRes);
    PtAvg(R6Vert, 7, 7, I67V1LC, I67V2LC, I67V3LC,
      I67V4LC, TotResB, RelaxationParamB, MaxRelRes);
    PtAvg(R6Vert, 8, 26, I67V1C, I67V2C, I67V3C,
      I67V4C, TotResB, RelaxationParamB, MaxRelRes);
    PtAvg(R6Vert, 27, 27, I67V1RC, I67V2RC, I67V3RC,
      I67V4RC, TotResB, RelaxationParamB, MaxRelRes);
    PtAvg(R6Vert, 28, 32, I67V1, I67V2, I67V3,
      I67V4, TotResB, RelaxationParamB, MaxRelRes);

   end
 else
  (* Calculate new potentials at Region5-Region7 interface *)
  begin
   PtAvg(R5Vert, 2, 6, I57V1, I57V2, I57V3,
    I57V4, TotResB, RelaxationParamB, MaxRelRes);
   PtAvg(R5Vert, 7, 7, I57V1LC, I57V2LC, I57V3LC,
    I57V4LC, TotResB, RelaxationParamB, MaxRelRes);
   PtAvg(R5Vert, 8, 26, I57V1C, I57V2C, I57V3C,
    I57V4C, TotResB, RelaxationParamB, MaxRelRes);
   PtAvg(R5Vert, 27, 27, I57V1RC, I57V2RC, I57V3RC,
    I57V4RC, TotResB, RelaxationParamB, MaxRelRes);
   PtAvg(R5Vert, 28, 32, I57V1, I57V2, I57V3,
    I57V4, TotResB, RelaxationParamB, MaxRelRes);
  end;

  (* Calculate new potentials in Region7 *)
     for VCount := R6Vert+1 to R7Vert-1 do
      begin
       PtAvgR(VCount, 2, 6, R7V1, R7V2, R7V3, R7V4,
        TotResC, RelaxationParamC, MaxRelRes);
       PtAvgR(VCount, 7, 7, R7V1LC, R7V2LC, R7V3LC, R7V4LC,
        TotResC, RelaxationParamC, MaxRelRes);
       PtAvgR(VCount, 8, 26, R7V1C, R7V2C, R7V3C,
        R7V4C, TotResC, RelaxationParamC, MaxRelRes);
       PtAvgR(VCount, 27, 27, R7V1RC, R7V2RC, R7V3RC,
        R7V4RC, TotResC, RelaxationParamC, MaxRelRes);
       PtAvgR(VCount, 28, 32, R7V1, R7V2, R7V3, R7V4,
        TotResC, RelaxationParamC, MaxRelRes);
      end;

  (* apply side boundary conditions *)
  for VCount := 2 to R7Vert do
  begin
    Grid[VCount,1] := Grid[VCount,3];
    Grid[VCount,33] := Grid[VCount,31];
   end;

  (* apply upper boundary condition *)
  for HCount := 1 to Horz do
    Grid[R7Vert,HCount] := Grid[R7Vert-2,HCount];

  iterationctr := iterationctr + 1;
 end; (* Relaxation Update *)

 if RelaxUpdateSw in ['Y', 'y'] then
  begin
   UpdateRelaxParam(RelaxationParamA, TotResA, OldTotResA);
   UpdateRelaxParam(RelaxationParamB, TotResB, OldTotResB);
   UpdateRelaxParam(RelaxationParamC, TotResC, OldTotResC);
  end;
 writeln('iteration = ', iterationctr, '  MaxRelResidue = ',
     MaxRelRes);
 ChkKey;
until (MaxRelRes < ConvergenceValue);
(*****************************************************************************)

 if(ContourSw=1) then begin
  assign(outfile2, outname + 'a');
  rewrite(outfile2);
  for i:= 1 to R7Vert do begin
```

```
    for j:=1 to Horz do
      write(outfile2,Grid[i,j].x:6:3, ',');
     writeln(outfile2);
    end;
    writeln(outfile2);
    for i:= 1 to R7Vert do begin
     for j:=1 to Horz do
      write(outfile2,Grid[i,j].y:6:3, ',');
     writeln(outfile2);
    end;
    Calculate_TF;
    close(outfile2);
    close(outfile);
    halt;
   end
   else begin
    writeln(outfile,' ');
    writeln(outfile, 'iteration = ',iterationctr, '    MaxRelResidue = ',
          MaxRelRes);
    Calculate_TF;
   end;
(*************************************************************************)
   if epsilonF.y > -1.0 then Incy := -0.1
    else if epsilonF.y >-10.0 then Incy := -1.0
    else if epsilonF.y >-100.0 then Incy := -10.0;
   epsilonF.y := epsilonF.y + Incy;
   end; (* while epsilonF.y *)
   if epsilonF.x = 1.0 then epsilonF.x := 2.0
    else if epsilonF.x = 2.0 then epsilonF.x := 4.0
    else if epsilonF.x = 4.0 then epsilonF.x := 6.0
    else if epsilonF.x = 6.0 then epsilonF.x := 8.0
    else if epsilonF.x = 8.0 then epsilonF.x := 10.0
    else epsilonF.x := 110;
  end; (* while epsilonF.x *)
 close(outfile);
 end.
(*************************************************************************)
```



```
(*************************************************************************)
(* Filename: THCKINIT.I *)
(* Initialization Routines for Thick Model *)

procedure ReadConfig(var epsilon3 : complex; var ConvergenceValue,
                RelaxA, RelaxB, RelaxC, LoadCap, FT, ESep, UC:real;
                var RelaxSw: char; var outname : outstring);

(* ReadConfig inputs the model paramters including the permittivities  *)
(* of each region, the convergence value, the relaxation parmaters for  *)
(* each region, the load capacitance, and the output filename. It also  *)
(* lets the user set whether variable or constant relaxation paramters  *)
(* will be used. If variable the initial setting is at 1.6 for all     *)
(* three grids.                                                        *)

var
  Sw : char;

begin
  write('Enter real part of complex permittivity of region 3 (Air) : ');
  readln(epsilon3.x);
  write('Enter imaginary part of complex permittivity of region 1 (Air): ');
  readln(epsilon3.y);
  epsilon3.y := -epsilon3.y;

  epsilon1.x := 3.9;
  epsilon1.y := 0.0;

  repeat
   write('Do you want variable relaxation parameters (Y/N) : ');
   readln(Sw);
   RelaxSw := Sw;
  until RelaxSw in ['Y', 'y', 'N', 'n'];

  if RelaxSw in ['Y', 'y'] then
   begin
     RelaxC := 1.8;
     RelaxB := 1.8;
     RelaxA := 1.8;
    end
   else
    begin
       write('Enter RegionA Relaxation Parameter between 1.2 and 1.9 : ');
       readln(RelaxA);
       write('Enter RegionB Relaxation Parameter between 1.2 and 1.9 : ');
       readln(RelaxB);
       write('Enter RegionC Relaxation Parameter between 1.2 and 1.9 : ');
       readln(RelaxC);
    end;

   write('Enter maximum residue value at convergence (usually 1e-3 - 1e-4) : ');
```

```
  readln(ConvergenceValue);

  write('Enter the Film Thickness in microns : ');
  readln(FT);

  write('Enter the Extent of Electrode Undercut in microns (Between 0 and 0.5) : ');
  readln(UC);

  write ('Enter Inter-Electrode Separation : ');
  readln(ESep);

  write('Enter load capacitance : ');
  readln(LoadCap);

  write('Enter name of output file : ');
  readln(outname);
(*  outname:= 'inttester5'; *)
end;
(*************************************************************************)

procedure InitGrid(VertDim, HorzDim : integer);
(* InitGrid initializes a grid of complex voltages to zero *)

var
  Zero : complex;
  VCount, HCount : integer;
begin
  Zero.x := 0.1;
  Zero.y := 0.0;
  for VCount := 1 to VertDim do
    begin
      for HCount := 1 to HorzDim do
        begin
          Grid[VCount,HCount] := Zero;
        end;
    end;
end; (* procedure InitGrid *)
(*************************************************************************)

procedure Init;
(* Init initializes the grid, inputs model parameters, applies input  *)
(* voltage, and initializes total relative residues *)

var
  DrivenGateVoltage : complex;
  VCount, HCount : integer;
begin
  InitGrid(R7Vert, Horz);

  DrivenGateVoltage.x := 1.0;
  DrivenGateVoltage.y := 0.0;

  for VCount := OxNodes to R4Vert do
    for HCount := 1 to 7 do
      Grid[VCount, HCount] := DrivenGateVoltage;
  for HCount := 1 to Horz do
     Grid[1,HCount].x := 0.0;

  TotResA := 0.0; TotResB := 0.0; TotResC := 0.0;
end; (* procedure Init *)
(*************************************************************************)

procedure InitVCoeffC(var h1, h2, h3, h4 : real; var epsilonRatio, A, B, C,
                D : complex);
var Denom : complex;
begin
  A.x := (h2+h4)/h1;
  A.y := 0.0;
  D.x := (h1+h3)/h4;
  D.y := 0.0;
  B.x := epsilonRatio.x * (h3/h2);
  B.y := epsilonRatio.y * (h3/h2);
  B.x := B.x + (h1/h2);
  C.x := epsilonRatio.x * (h2/h3);
  C.y := epsilonRatio.y * (h2/h3);
  C.x := C.x + (h4/h3);
  Denom.x := A.x + B.x + C.x + D.x;
  Denom.y := A.y + B.y + C.y + D.y;
  DivideComplex(A, Denom, A);
  DivideComplex(B, Denom, B);
  DivideComplex(C, Denom, C);
  DivideComplex(D, Denom, D);

end; (* procedure InitVCoeffC *)
(*************************************************************************)

procedure InitVCoeff2(var h1, h2, h3, h4, h1c, h3c : real; var epsilonRatio, V1Coeff,
                V2Coeff, V3Coeff, V4Coeff, V1C, V2C, V3C, V4C, V1LC, V2LC, V3LC,
                V4LC, V1RC, V2RC, V3RC, V4RC : complex);

var
  temp, temp2, one : complex; Denom, DenomC, DenomLC : complex;

begin
  V1Coeff.x := 1/(h1*(h1+h3));
  V1Coeff.y := 0.0;

  V1LC.x := 1/(h1c*(h1c+h3));
  V1LC.y := 0.0;

  V1RC.x := 1/(h1*(h1+h3c));
  V1RC.y := 0.0;
```

```
V1C.x := 1/(h1c*(h1c+h3c));
V1C.y := 0.0;

V3Coeff.x := 1/(h3*(h1+h3));
V3Coeff.y := 0.0;

V3LC.x := 1/(h3*(h1c+h3));
V3LC.y := 0.0;

V3RC.x := 1/(h3c*(h1+h3c));
V3RC.y := 0.0;

V3C.x := 1/(h3c*(h1c+h3c));
V3C.y := 0.0;

Denom.x := (1/(h1*h3)) + (1/(h2*h4));
Denom.y := 0.0;

DenomC.x := (1/(h1c*h3c)) + (1/(h2*h4));
DenomC.y := 0.0;

DenomLC.x := (1/(h1c*h3)) + (1/(h2*h4));
DenomLC.y := 0.0;
if Mag (epsilonRatio) = 1.0 then
 begin

  V2Coeff.x := 1/(sqr(h2) + (h2*h4));
  V2Coeff.y := 0.0;

  V4Coeff.x := 1/(sqr(h4)+(h2*h4));
  V4Coeff.y := 0.0;

 end
else
 begin

  temp.x := epsilonRatio.x * h2;
  temp.y := epsilonRatio.y * h2;
  temp.x := temp.x + h4;
  V2Coeff.x := temp.x * h2;
  V2Coeff.y := temp.y * h2;
  DivideComplex(epsilonRatio, V2Coeff, V2Coeff);
  one.x := 1.0;
  one.y := 0.0;
  V4Coeff.x := temp.x*h4;
  V4Coeff.y := temp.y*h4;
  DivideComplex(one, V4Coeff, V4Coeff);

  temp2 := epsilonRatio;
  temp2.x := temp2.x * (1/h2);
  temp2.y := temp2.y * (1/h2);
  temp2.x := temp2.x + (1/h4);
  DivideComplex(temp2, temp, Denom);
  DenomLC := Denom;
  DenomC := Denom;
  if h2=h4 then
   begin
    Denom.y := 0.0;
    DenomLC.y := 0.0;
    DenomC.y := 0.0;
   end;
  Denom.x := Denom.x + (1/(h1*h3));
  DenomLC.x := DenomLC.x + (1/(h1c*h3));
  DenomC.x := DenomC.x + (1/(h1c*h3c));
 end;

DivideComplex(V2Coeff, DenomC, V2C);
DivideComplex(V4Coeff, DenomC, V4C);
DivideComplex(V2Coeff, DenomLC, V2LC);
DivideComplex(V4Coeff, DenomLC, V4LC);
DivideComplex(V1Coeff, Denom, V1Coeff);
DivideComplex(V2Coeff, Denom, V2Coeff);
DivideComplex(V3Coeff, Denom, V3Coeff);
DivideComplex(V4Coeff, Denom, V4Coeff);
DivideComplex(V1C, DenomC, V1C);
DivideComplex(V3C, DenomC, V3C);
DivideComplex(V1LC, DenomLC, V1LC);
DivideComplex(V3LC, DenomLC, V3LC);
DivideComplex(V1RC, DenomLC, V1RC);
V2RC := V2LC;
DivideComplex(V3RC, DenomLC, V3RC);
V4RC := V4LC;
end; (* procedure InitVCoeff2 *)
(*****************************************************************************)

procedure InitVCoeff;
(* InitVCoeff computes the weighting values for adjacent nodes and the  *)
(* weighted denominator used for calculating the average at a given     *)
(* node in each grid. Within a grid the weighting values are            *)
(* independent of the permittivity, and weighting depends only on grid  *)
(* dimensions. The permittivites are required at the interface of the   *)
(* materials. *)

var
 epsilonRatio : complex;
 h1,h2,h3,h4, h1c, h3c  : real; (* h1,h2, h3 ,h4 correspond to the adjacent node *)
            (* separations clockwise starting with the node  *)
            (* to the right *)

 Dummyh : real;
 Dummy : complex;
begin
```

```
Dummyh := 1.0;
Dummy.x := 1.0;
Dummy.y := 0.0;
h1 := 1.0;  (* Region1 Weightings *)
h4 := OxHeight/(OxNodes-1);
h2 := h4;
h3 := h1;
h3c := ESep/20;
h1c := h3c;
epsilonRatio.x := 1.0;
epsilonRatio.y := 0.0;
InitVCoeff2(h1, h2, h3, h4, h1c, h3c, epsilonRatio, R1V1, R1V2, R1V3,
      R1V4, R1V1C, R1V2C, R1V3C, R1V4C, R1V1LC,
      R1V2LC, R1V3LC, R1V4LC, R1V1RC, R1V2RC, R1V3RC,
      R1V4RC);

h4 := 0.1;  (* Region2 Weightings *)
h2 := h4;
h1 := h1c;
h3 := h3c;
InitVCoeff2(h1, h2, h3, h4, Dummyh, Dummyh, epsilonRatio, R2V1C, R2V2C, R2V3C,
      R2V4C, Dummy, Dummy, Dummy, Dummy, Dummy, Dummy, Dummy, Dummy,
       Dummy, Dummy, Dummy, Dummy);

h4 := 0.1;  (* Region3 Weightings *)
h2 := h4;
h1 := h1c;
h3 := h3c;
InitVCoeff2(h1, h2, h3, h4, Dummyh, Dummyh, epsilonRatio, R3V1C, R3V2C,
      R3V3C, R3V4C, Dummy, Dummy, Dummy, Dummy, Dummy, Dummy, Dummy,
Dummy,
       Dummy, Dummy, Dummy, Dummy);

h4 := 0.1;  (* Region4 Weightings *)
h2 := h4;
h1 := h1c;
h3 := h3c;
InitVCoeff2(h1, h2, h3, h4, Dummyh, Dummyh, epsilonRatio, R4V1, R4V2,
       R4V3, R4V4, Dummy, Dummy, Dummy, Dummy, Dummy, Dummy, Dummy,
Dummy,
       Dummy, Dummy, Dummy, Dummy);

h4 := 0.1;  (* Region5 Weightings *)
h2 := h4;
h1 := 1.0;
h3 := 1.0;

InitVCoeff2(h1, h2, h3, h4, h1c, h3c, epsilonRatio, R5V1, R5V2,
      R5V3, R5V4, R5V1C, R5V2C, R5V3C, R5V4C, R5V1LC, R5V2LC,
      R5V3LC, R5V4LC, R5V1RC, R5V2RC, R5V3RC, R5V4RC);

h1 := 1.0;  (* Region6 Weightings *)
h4 := R6VertRes;
h2 := h4;
h3 := h1;
epsilonRatio.x := 1.0;
epsilonRatio.y := 0.0;
InitVCoeff2(h1, h2, h3, h4, h1c, h3c, epsilonRatio, R6V1, R6V2, R6V3,
      R6V4, R6V1C, R6V2C, R6V3C, R6V4C, R6V1LC, R6V2LC, R6V3LC,
      R6V4LC, R6V1RC, R6V2RC, R6V3RC, R6V4RC);

h1 := 1.0;  (* Region7 Weightings *)
h4 := R7VertRes;
h2 := h4;
h3 := h1;
epsilonRatio.x := 1.0;
epsilonRatio.y := 0.0;
InitVCoeff2(h1, h2, h3, h4, h1c, h3c, epsilonRatio, R7V1, R7V2, R7V3,
      R7V4, R7V1C, R7V2C, R7V3C, R7V4C, R7V1LC, R7V2LC, R7V3LC,
      R7V4LC, R7V1RC, R7V2RC, R7V3RC, R7V4RC);

      (* Region1-Region2 Interface Weightings *)
h2 := OxHeight/(OxNodes-1);
h4 := 0.1;
h3 := h3c;
h1 := h1c;
DivideComplex(epsilon1, epsilonF, epsilonRatio);
InitVCoeff2(h1, h2, h3, h4, Dummyh, Dummyh, epsilonRatio, I12V1,
      I12V2, I12V3, I12V4, Dummy, Dummy, Dummy, Dummy, Dummy,
      Dummy, Dummy, Dummy, Dummy, Dummy, Dummy, Dummy);

      (* Region2-Region3 Interface  Weightings *)
h2 := h4;
h4 := 0.1;
epsilonRatio.x :=1.0;
epsilonRatio.y := 0.0;
InitVCoeff2(h1, h2, h3, h4, Dummyh, Dummyh, epsilonRatio, I23V1,
      I23V2, I23V3, I23V4, Dummy, Dummy, Dummy, Dummy,
      Dummy, Dummy, Dummy, Dummy, Dummy, Dummy, Dummy, Dummy);

      (* Region2-Region4 Interface  Weightings *)
h2 := h4;
h4 := 0.1;
epsilonRatio.x := 1.0;
epsilonRatio.y := 0.0;
InitVCoeff2(h1, h2, h3, h4, Dummyh, Dummyh, epsilonRatio, I24V1,
      I24V2, I24V3, I24V4, Dummy, Dummy, Dummy, Dummy,
      Dummy, Dummy, Dummy, Dummy, Dummy, Dummy, Dummy, Dummy);

     (* Region2-Region5 Interface  Weightings *)
h2 := 0.1;
h4 := 0.1;
```

```
h1 := h1c;
h3:= h3c;
epsilonRatio.x := 1.0;
epsilonRatio.y := 0.0;
InitVCoeff2(h1, h2, h3, h4, Dummyh, Dummyh, epsilonRatio, I25V1,
        I25V2, I25V3, I25V4, Dummy, Dummy, Dummy, Dummy,
        Dummy, Dummy, Dummy, Dummy, Dummy, Dummy, Dummy, Dummy);

        (* Region5-Region6 Interface  Weightings *)
h2 := 0.1;
h4 := R6VertRes;
h1 := 1.0;
h3 := 1.0;
epsilonRatio.x := 1.0;
epsilonRatio.y := 0.0;
InitVCoeff2(h1, h2, h3, h4, h1c, h3c, epsilonRatio, I56V1, I56V2,
        I56V3, I56V4, I56V1C, I56V2C, I56V3C, I56V4C, I56V1LC, I56V2LC,
        I56V3LC, I56V4LC, I56V1RC, I56V2RC, I56V3RC, I56V4RC);

        (* Region5-Region7 Interface  Weightings *)
h2 := 0.1;
h4 := R7VertRes;
h1 := 1.0;
h3 := 1.0;
DivideComplex(epsilonF, epsilon3, epsilonRatio);
InitVCoeff2(h1, h2, h3, h4, h1c, h3c, epsilonRatio, I57V1, I57V2,
        I57V3, I57V4, I57V1C, I57V2C, I57V3C, I57V4C, I57V1LC, I57V2LC,
        I57V3LC, I57V4LC, I57V1RC, I57V2RC, I57V3RC, I57V4RC);

        (* Region6-Region7 Interface  Weightings *)
h2 := R6VertRes;
h4 := R7VertRes;
h1 := 1.0;
h3 := 1.0;
DivideComplex(epsilonF, epsilon3, epsilonRatio);
InitVCoeff2(h1, h2, h3, h4, h1c, h3c, epsilonRatio, I67V1, I67V2,
        I67V3, I67V4, I67V1C, I67V2C, I67V3C, I67V4C, I67V1LC, I67V2LC,
        I67V3LC, I67V4LC, I67V1RC, I67V2RC, I67V3RC, I67V4RC);

        (* Region3 Horizontal Interface  Weightings *)
h2 := OxHeight/(OxNodes-1);
h4 := h2;

DivideComplex(epsilon1, epsilon3, epsilonRatio);
InitVCoeff2(h2, h3, h4, h1c, Dummyh, Dummyh, epsilonRatio, R3V2LC,
        R3V3LC, R3V4LC, R3V1LC, Dummy, Dummy, Dummy, Dummy,
        Dummy, Dummy, Dummy, Dummy, Dummy, Dummy, Dummy, Dummy);

DivideComplex(epsilon3, epsilon1, epsilonRatio);
InitVCoeff2(h2, h3c, h4, h1, Dummyh, Dummyh, epsilonRatio, R3V2RC, R3V3RC,
        R3V4RC, R3V1RC, Dummy, Dummy, Dummy, Dummy, Dummy, Dummy,
        Dummy, Dummy, Dummy, Dummy, Dummy, Dummy);

        (* Region2 Horizontal Interface  Weightings *)
h2 := OxHeight/(OxNodes-1);
h4 := h2;

DivideComplex(epsilon1, epsilonF, epsilonRatio);
InitVCoeff2(h2, h3, h4, h1c, Dummyh, Dummyh, epsilonRatio, R2V2LC,
        R2V3LC, R2V4LC, R2V1LC, Dummy, Dummy, Dummy, Dummy,
        Dummy, Dummy, Dummy, Dummy, Dummy, Dummy, Dummy, Dummy);

DivideComplex(epsilonF, epsilon1, epsilonRatio);
InitVCoeff2(h2, h3c, h4, h1, Dummyh, Dummyh, epsilonRatio, R2V2RC, R2V3RC,
        R2V4RC, R2V1RC, Dummy, Dummy, Dummy, Dummy, Dummy, Dummy,
        Dummy, Dummy, Dummy, Dummy, Dummy, Dummy);

end; (* procedure InitVCoeff *)
(*****************************************************************************)
```

```
(*****************************************************************************)
(* Filename: THCKPRT.I *)
(* Routines to Calculate Two-Port Admittances for Thick Model *)

procedure CurrentElement (var Grid : GridArray; V1Pos, V2Pos,
      HPos :integer; Epsilon : complex; Coeff : real; var I : complex);
(* Computes the current elements between nodes in the vertical direction *)
var
 Temp : complex;
begin
   SubtractComplex(Grid[V1Pos,HPos], Grid[V2Pos,HPos], Temp);
   MultiplyComplex(Temp,Epsilon,Temp);
   Temp.x := Temp.x * Coeff;
   Temp.y := Temp.y * Coeff;
   AddComplex(I,Temp,I);
end; (* CurrentElement *)

procedure SideCurrentElement (var Grid : GridArray; VPos, H1Pos, H2Pos:
      integer; Epsilon : complex; Coeff : real; var I : complex);
(* Computes the currents elements between nodes in the horizontal  direction *)
var
 Temp : complex;
begin
   SubtractComplex(Grid[VPos,H1Pos], Grid[VPos,H2Pos], Temp);
   MultiplyComplex(Temp,Epsilon,Temp);
   Temp.x := Temp.x * Coeff;
   Temp.y := Temp.y * Coeff;
   AddComplex(I,Temp,I);
end; (* SideCurrentElement *)
(*****************************************************************************)

procedure TwoPortAdmit;
(* Calculates the two port admittance parameters for the interdigitated *)
(* electrode structure. The current through each electrode is computed  *)
(* using surface integration around each electrode. Note that the nodes *)
(* along the interface at the outer boundaries do not contribute to the *)
(* to the current since the potential gradient is zero at these nodes.  *)
(* These currents are used to calculate the Y parameters. The Y         *)
(* parameters calculated here must be multiplied by the meander length  *)
(* to get total admittance. The total admittance is not calculated here *)
 var
  Count : integer;
  SepCoeff : real;          (* SepCoeff := (h1/2 + h3/2)/h4 *)
  Temp1, Temp2, Temp3 : complex;
  SepCoeff2 : complex;
  I1, I2 : complex;
  V1, V2 : complex;
  h1,h2, h3, h4 : real;
 begin
  I1.x := 0.0; I2.x := 0.0; I1.y := 0.0; I2.y := 0.0;

(* Add current elements along nodes above the electrodes and  *)
(* keep running sum in I1 and I2                              *)
(* SepCoeff := 1.0; *)          (* since h1=h3=h2=h4 *)
h1:=1.0;
h3:=1.0;
h4:=R7VertRes;
SepCoeff:=(h1/2 +h3/2)/h4;
CurrentElement(Grid, R6Vert+1, R6Vert+2, 2, epsilon3, 0.5*SepCoeff, I1);
CurrentElement(Grid, R6Vert+1, R6Vert+2, 32, epsilon3, 0.5*SepCoeff, I2);
for Count := 3 to 6 do
  CurrentElement(Grid, R6Vert+1, R6Vert+2, Count, epsilon3, SepCoeff, I1);
 for Count := 8 to 11 do
   CurrentElement(Grid, R6Vert+1, R6Vert+2, Count+20, epsilon3, SepCoeff, I2);

SepCoeff:= (ESep/20)/h4;
for Count := 8 to 14 do
   CurrentElement(Grid, R6Vert+1, R6Vert+2, Count, epsilon3, SepCoeff, I1);
for Count := 2 to 8 do
  CurrentElement(Grid, R6Vert+1, R6Vert+2, Count+18, epsilon3, SepCoeff, I2);

SepCoeff := (ESep/20 + 1.0)/(2.0*h4);
CurrentElement(Grid, R6Vert+1, R6Vert+2, 7, epsilon3, SepCoeff, I1);
CurrentElement(Grid, R6Vert+1, R6Vert+2, 27, epsilon3, SepCoeff, I2);

(* Add current elements along nodes on the medial sides of the  *)
(* electrodes in region7 to I1 and I2 *)
SepCoeff := (R7VertRes + R7VertRes)/(2*ESep/20);
SideCurrentElement(Grid, R6Vert+1, 14, 15, epsilon3, SepCoeff, I1);
SideCurrentElement(Grid, R6Vert+1, 20, 19, epsilon3, SepCoeff, I2);

(* Add current elements along nodes on the medial sides of the  *)
(* electrodes in region6 (if any) to I1 and I2 *)
if Nodes6 > 1 then
 begin
  h2 := R6VertRes; (* h4 = h2 *)
  h1 := ESep/20;
  SepCoeff := h2/h1;
  for Count := R5Vert+1 to R6Vert-1 do
   begin
    SideCurrentElement(Grid, Count, 14, 15, epsilonF, SepCoeff, I1);
    SideCurrentElement(Grid, Count, 20, 19, epsilonF, SepCoeff, I2);
   end;
 end;

(* Add current elements along nodes at the interface of Region5 *)
(* and Region6 along the medial side of electrodes *)
if Nodes6>0 then
 begin
  h2 := R6VertRes;
  h4 := 0.1;
  h1 := ESep/20;
```

```
  SepCoeff := (h2 + h4)/(2*h1);
  SideCurrentElement(Grid, R5Vert, 14, 15, epsilonF, SepCoeff, I1);
  SideCurrentElement(Grid, R5Vert, 20, 19, epsilonF, SepCoeff, I2);
 end;

(* Add current elements along nodes on the medial sides of the  *)
(* electrodes in region5 to I1 and I2 *)
h2 := 0.1; (* h4 = h2 *)
h1 := ESep/20;
SepCoeff := h2/h1;
for Count := R4Vert+1 to R5Vert-1 do
 begin
  SideCurrentElement(Grid, Count, 14, 15, epsilonF, SepCoeff, I1);
  SideCurrentElement(Grid, Count, 20, 19, epsilonF, SepCoeff, I2);
 end;

(* Add current elements along nodes on the medial sides of the  *)
(* electrodes in region2 to I1 and I2 *)
for Count := R1Vert+1 to R2Vert-1 do
 begin
  SideCurrentElement(Grid, Count, 14, 15, epsilonF, SepCoeff, I1);
  SideCurrentElement(Grid, Count, 20, 19, epsilonF, SepCoeff, I2);
 end;

(* Add current elements along nodes on the medial sides of the  *)
(* electrodes in region4 to I1 and I2 *)
h4 := 0.1;
h2 := 0.1;
h1 := ESep/20;
SepCoeff := (h2 + h4)/(2*h1);
if Nodes4 > 0 then
 begin
  for Count := R2Vert+1 to R4Vert-1 do  (* will only execute if Nodes2b>1 *)
   begin
    SideCurrentElement(Grid, Count, 14, 15, epsilonF, SepCoeff, I1);
    SideCurrentElement(Grid, Count, 20, 19, epsilonF, SepCoeff, I2);
   end;
 end;
 (* Add current elements at interface of Region4 and Region5 *)
 h4 := 0.1;
 SepCoeff := (h4+h2)/(2*h1);
 SideCurrentElement(Grid, R4Vert, 14, 15, epsilonF, SepCoeff, I1);
 SideCurrentElement(Grid, R4Vert, 20, 19, epsilonF, SepCoeff, I2);

(* Add current elements along nodes on the medial sides of the  *)
(* electrodes in region1 to I1 and I2 *)
h1 := ESep/20.0;
h4 := OxHeight/(OxNodes-1);
SepCoeff := h4/h1;  (* since h2=h4 and h1=h3 *)
for Count := 5 to R1Vert-1 do
 begin
  SideCurrentElement(Grid, Count, 14, 15, epsilon1, SepCoeff, I1);
  SideCurrentElement(Grid, Count, 20, 19, epsilon1, SepCoeff, I2);
 end;

(* Add current elements along nodes below the electrodes to I1 and I2  *)
h1:= 1.0;
h3 :=1.0;
h4:= OxHeight/(OxNodes-1);
SepCoeff := (h1+h3)/(2*h4);
CurrentElement(Grid, 5, 4, 2, epsilon1, 0.5*SepCoeff, I1);
CurrentElement(Grid, 5, 4, 32, epsilon1, 0.5*SepCoeff, I2);
for Count := 3 to 6 do
  CurrentElement(Grid, 5, 4, Count, epsilon1, SepCoeff, I1);
for Count := 8 to 11 do
  CurrentElement(Grid, 5, 4, Count+20, epsilon1, SepCoeff, I2);

SepCoeff:= (ESep/20)/h4;
for Count := 8 to 14 do
  CurrentElement(Grid, 5, 4, Count, epsilon1, SepCoeff, I1);
for Count := 2 to 8 do
  CurrentElement(Grid, 5 , 4, Count+18, epsilon1, SepCoeff, I2);

SepCoeff := (ESep/20 + 1.0)/(2.0*h4);
CurrentElement(Grid, 5 ,4, 7, epsilon1, SepCoeff, I1);
CurrentElement(Grid, 5, 4, 27, epsilon1, SepCoeff, I2);

V1 := Grid[R3Vert,2];
V2 := Grid[R3Vert,28];

(* Add currents due to nodes at the interface between Region1 and Region2 *)
(* along the medial sides of the electrodes. Here the Separation        *)
(* coeffcient becomes SepCoeff = [epsilonF*(h4/2) + epsilon1 * (h2/2)]/h1 *)

h2 := OxHeight/(OxNodes-1);  (* along interface h4 does not equal h2 *)
h4 := 0.1;
h1 := ESep/20;
Temp2 := epsilon1;
Temp2.x := Temp2.x * (h2/(2*h1));
Temp2.y := Temp2.y * (h2/(2*h1));
Temp3 := epsilonF;
Temp3.x := Temp3.x * (h4/(2*h1));
Temp3.y := Temp3.y * (h4/(2*h1));
AddComplex(Temp2,Temp3,SepCoeff2);
SubtractComplex(Grid[R1Vert,14], Grid[R1Vert,15], Temp1);
MultiplyComplex(Temp1,SepCoeff2,Temp1);
AddComplex(I1,Temp1,I1);      (* Current element for driven electrode *)
SubtractComplex(Grid[R1Vert,20], Grid[R1Vert,19], Temp1);
MultiplyComplex(Temp1,SepCoeff2,Temp1);
AddComplex(I2,Temp1,I2);      (* Current element for floating electrode *)

(* Add currents due to nodes at the interface between Region5 or       *)
```

```
(* Region6 and Region7 along the medial sides of the electrodes. Here   *)
(* the Separation coeffcient becomes SepCoeff = [epsilon3*(h4/2) +      *)
(* epsilonF * (h2/2)]/h1 *)
 h4 := R7VertRes;
 if Nodes6=0 then h2:=0.1 else h2:=R6VertRes;
 h1 := ESep/20;

 Temp2 := epsilon3;
 Temp2.x := Temp2.x * (h4/(2*h1));
 Temp2.y := Temp2.y * (h4/(2*h1));
 Temp3 := epsilonF;
 Temp3.x := Temp3.x * (h2/(2*h1));
 Temp3.y := Temp3.y * (h2/(2*h1));
 AddComplex(Temp2,Temp3,SepCoeff2);
 SubtractComplex(Grid[R6Vert,14], Grid[R6Vert,15], Temp1);
 MultiplyComplex(Temp1,SepCoeff2,Temp1);
 AddComplex(I1,Temp1,I1);      (* Current element for driven electrode *)
 SubtractComplex(Grid[R6Vert,20], Grid[R6Vert,19], Temp1);
 MultiplyComplex(Temp1,SepCoeff2,Temp1);
 AddComplex(I2,Temp1,I2);     (* Current element for floating electrode *)

 (* Calculate two port y parameters from currents and voltages. See     *)
 (* Lee, equations 3.10.3 and 3.10.4 *)
 MultiplyComplex(V1, V1, Temp1);
 MultiplyComplex(V2, V2, Temp2);
 SubtractComplex(Temp2,Temp1,Temp1); (* denominator of eqts. 3.10.3     *)
 MultiplyComplex(I2, V2, Temp3);
 MultiplyComplex(I1, V1, Temp2);
 SubtractComplex(Temp3, Temp2, Y1);
 DivideComplex(Y1,Temp1,Y1);        (* Calculate Y1 *)
 MultiplyComplex(I1, V2, Temp2);
 MultiplyComplex(I2, V1, Temp3);
 SubtractComplex(Temp3, Temp2, Y2);
 DivideComplex(Y2, Temp1, Y2);       (* Calculate Y2 *)
end; (* TwoPortAdmit *)
(*************************************************************************)
```


Source Code for Routines Common to Both Finite-Difference Models

```
(*************************************************************************)
(* Filename: CPLXMTH2.I *)
(* Complex Math Routines for THCKMODL and UCMODL *)

 procedure AddComplex (num1, num2: complex; var Z : complex);
 (*  AddComplex finds the sum of two complex numbers, num1 and num2   *)
 (*  in rectangular coorinates. The sum is returned in Z.  *)

 begin
   Z.x := num1.x + num2.x;
   Z.y := num1.y + num2.y;
end;  (* procedure AddComplex *)

procedure SubtractComplex (num1, num2 : complex; var Z : complex);
(*  This procedure finds the difference between two complex numbers,   *)
(*  num1 and num2, using rectangular coordinates. The difference is    *)
(*  returned in Z.                                                     *)

begin
  Z.x := num1.x - num2.x;
  Z.y := num1.y - num2.y;
end;  (* procedure SubtractComplex *)

procedure MultiplyComplex (num1, num2 : complex; var Z : complex);
(* MultiplyComplex finds the product of two complex numbers, num1      *)
(* and num2. The product is returned in Z.    *)

begin
  Z.x := (num1.x * num2.x) - (num1.y * num2.y);
  Z.y := (num1.x * num2.y) + (num1.y * num2.x);
end;  (* procedure MultiplyComplex *)

procedure DivideComplex (num1, num2 : complex; var Z : complex);
(*  DivideComplex finds the quotient of two complex numbers, num1      *)
(*  and num2. The quotient is returned in Z.    *)
var
  Denom : real;
  stop : char;
begin
  num2.y := -num2.y;
  MultiplyComplex(num1, num2, Z);
  Denom := sqr(num2.x) + sqr(num2.y);
  if Denom <1e-18 then
    begin
     writeln('Divide by zero attempted, control-c to interrupt');
     readln(stop);
    end
  else
   begin
```

```
  Z.x := Z.x/Denom;
  Z.y := Z.y/Denom;
 end;
end;  (* procedure DivideComplex *)

function Mag(Z:complex):real;
begin
 if (abs(Z.y) < 1E-18) then Mag := abs(Z.x)
  else Mag := sqrt(sqr(Z.x) + sqr(Z.y));
end;

function Angle(Z:complex): real;
const  small = 1.0e-18;    (* a real value close to small is        *)
                           (* to be equal to zero.                  *)
var
 Angle1 : real;
begin
 with Z do
  begin
   Angle1 := 0.0;          (* initialize Angle to zero; if y        *)
                           (* is less than small, theta will        *)
                           (* equal 0.0.                            *)

   if abs(x) > small then
                           (* if x is not close to zero, theta  *)
     Angle1 := arctan(y/x)  (* is the angle with tangent y/x     *)
    else
     if y > 0.0 then       (* otherwise theta is plus or minus  *)
       Angle1 := pi/2.0    (* 90 degrees, depending on the      *)
     else if y < 0.0 then  (* quadrant of the point.            *)
       Angle1 := -pi/2.0
     else Angle1 := 0.0;
    if x < 0.0  then         (* if x is negative, then theta is   *)
       Angle1 := Angle1 + pi; (* in the 2nd or 3rd quadrant.      *)
    if abs(Angle1)<1e-7 then Angle1:= 0.0;
   Angle := Angle1;
  end (* with Z do.*)
 end;
(*************************************************************************)
```

```
(*************************************************************************)
(* Filename: FDCALC.PAS *)
(* Finite Difference Calculation Routines Common to THCKMODL and UCMODL *)

procedure PtAvg(VCount, HS, HE : integer; V1C, V2C, V3C, V4C: complex;
          var TotRes, RelaxParam, MaxRelRes: real);
(* PtAvg adds the properly weighted complex node voltages V1,V2,V3, and  *)
(* V4, to obtain the node average. The residue is computed as the        *)
(* difference between the node average and its current value. If the     *)
(* node average value is not equal to zero, then the relative residue is *)
(* computed and added to the total relative residue for the iteration.   *)
(* The maximum relative residue is updated, if required.                 *)
(* The new node value is then computed and stored in the grid.           *)

const
 small = 1e-18;    (* Value considered equal to zero  *)

var
 V0 : complex;      (* Node Average *)
 Residue : complex;  (* Node Average - Curent Node Value *)
 RelResidue : real;  (* Residue/Node Average *)
 V0Mag :real;
 V1, V2, V3, V4 : complex;
 HCount : integer;
begin
 for HCount := HS to HE do
  begin
   MultiplyComplex(Grid[VCount, HCount+1],V1C,V1);
   MultiplyComplex(Grid[VCount-1, HCount],V2C,V2);
   MultiplyComplex(Grid[VCount, HCount-1],V3C,V3);
   MultiplyComplex(Grid[VCount+1, HCount],V4C,V4);

   V0.x := (V1.x + V2.x + V3.x + V4.x);
   V0.y := (V1.y + V2.y + V3.y + V4.y);
   SubtractComplex(V0,Grid[VCount,HCount],Residue);
   V0Mag := Mag(V0);
   if V0Mag > small then  (* check for division by zero *)
    begin
     RelResidue := Mag(Residue)/V0Mag;
     TotRes := TotRes + RelResidue;
    end
    else RelResidue := 0.0;
   if MaxRelRes < RelResidue then MaxRelRes := RelResidue;

  (* new node value = current node value + RelaxParam * residue *)
   Grid[VCount,HCount].x := Grid[VCount,HCount].x + Residue.x * RelaxParam;
   Grid[VCount,HCount].y := Grid[VCount,HCount].y + Residue.y * RelaxParam;
  end;
end; (* procedure PtAvg *)
(*************************************************************************)
```

```
procedure PtAvgR(VCount, HS, HE : integer; V1C, V2C, V3C, V4C: complex;
          var TotRes, RelaxParam, MaxRelRes: real);
(* PtAvgR adds the properly weighted real node voltages V1,V2,V3, and    *)
(* V4, to obtain the node average. The residue is computed as the        *)
(* difference between the node average and its current value. If the     *)
(* node average value is not equal to zero, then the relative residue is *)
(* computed and added to the total relative residue for the iteration.   *)
(* The maximum relative residue is updated, if required.                 *)
(* The new node value is then computed and stored in the grid.           *)

const
 small = 1e-18;    (* Value considered equal to zero  *)

var
 V0 : complex;      (* Node Average *)
 Residue : complex;  (* Node Average - Curent Node Value *)
 RelResidue : real;  (* Residue/Node Average *)
 V0Mag :real;
 HCount : integer;
begin
 for HCount := HS to HE do
  begin
   V0.x := Grid[VCount,HCount+1].x * V1C.x + Grid[VCount-1, HCount].x * V2C.x;
    V0.x := V0.x + Grid[VCount, HCount-1].x * V3C.x + Grid[VCount+1, HCount].x *
V4C.x;
   V0.y := Grid[VCount,HCount+1].y * V1C.x + Grid[VCount-1, HCount].y * V2C.x;
    V0.y := V0.y + Grid[VCount, HCount-1].y * V3C.x + Grid[VCount+1, HCount].y *
V4C.x;

   SubtractComplex(V0,Grid[VCount,HCount],Residue);
   V0Mag := Mag(V0);
   if V0Mag > small then  (* check for division by zero *)
    begin
     RelResidue := Mag(Residue)/V0Mag;
     TotRes := TotRes + RelResidue;
    end
    else RelResidue := 0.0;
   if MaxRelRes < RelResidue then MaxRelRes := RelResidue;

      (* new node value = current node value + RelaxParam * residue *)
   Grid[VCount,HCount].x := Grid[VCount,HCount].x + Residue.x * RelaxParam;
   Grid[VCount,HCount].y := Grid[VCount,HCount].y + Residue.y * RelaxParam;
  end;
end; (* procedure PtAvgR *)
(*************************************************************************)

procedure UpdateRelaxParam (var RelaxParam, NewTotRes, OldTotRes: real);
(* Updates the relaxation parameters. If the total relative residue is *)
(* increasing then the relaxation parameter is reduced. Otherwise, the *)
(* relaxation parameter is increased. The relaxation parameter is      *)
(* limited to values between 1.2 and 1.9 *)
begin

 if (NewTotRes > OldTotRes) then
  RelaxParam := RelaxParam - 0.02
 else
  RelaxParam := RelaxParam + 0.01;
 if (RelaxParam > 1.9) then
  RelaxParam := 1.9
 else if RelaxParam < 1.2 then
  RelaxParam := 1.2;
 OldTotRes := NewTotRes;
 NewTotRes := 0.0;
end; (* procedure UpdateRelaxParam *)
(*************************************************************************)

procedure Calculate_TF;
 begin
  TwoPortAdmit;  (* Calculate Y parameters for ID gate *)

   Y1.x := Y1.x + (LoadCap/epsilon0); (* Account for load capacitance *)
   DivideComplex(Y2, Y1, TransferFunction);
   writeln(outfile, 'Y1.x = ', Y1.x, '   Y1.y = ', Y1.y);
   writeln(outfile, 'Y2.x = ', Y2.x, '   Y2.y = ', Y2.y);
   writeln(outfile, 'epsilonF.x = ', epsilonF.x, '  epsilonF.y = ', epsilonF.y);
   writeln (outfile,'Gain = ', (20.0/2.30258) * (ln(Mag(TransferFunction))),
          '    Phase = ', Angle(TransferFunction)* 180/pi);
   writeln ('Gain = ', (20.0/2.30258) * (ln(Mag(TransferFunction))),
          '    Phase = ', Angle(TransferFunction)* 180/pi);
end; {Calculate_TF}
(*************************************************************************)
```

```
(*****************************************************************************)
(* Filename: FNHANDL.PAS *)
(* Function Key Handler for THCKMODL and UCMODL *)

procedure ChkKey;
{******************* Function Key Handler **********************}
var
PossFn, FnKey: char;

begin
 if KeyPressed then begin
   PossFn := ReadKey;
   if PossFn = #0 then begin
    FnKey:=ReadKey;
    case FnKey of
     ';': Calculate_TF;   (* If FnKey1 then Calculate_TF *)
(*     '<': FnKey2;
     '=': FnKey3;
     '>': FnKey4;
     '?': FnKey5;
     '@': FnKey6; *)
    end; {case}
   end;
 end;
end; {ChkFnKeys}
(*****************************************************************************)
```

Example of UCMODL.P Output

Interactive Input.

```
Enter real part of complex permittivity of region 3 (Air) : 1.0
Enter imaginary part of complex permittivity of region 3 (Air): 0.0
Do you want variable relaxation parameters (Y/N) : y
Enter maximum residue value at convergence (usually 1e-3 - 1e-4) : 1e-4
Enter the Extent of Electrode Undercut in microns (Between 0 and 0.5) : 0.3
Enter Inter-electrode Separation : 10.0
Enter load capacitance : 0.0
Enter name of output file : t3a
```

Program Output (limited to first few pages).

```
FNodes = 3   Electrode Separation =  1.00000000000000E+0001
Film Thickness =  3.00000000000182E-0001   Variable Relaxation - y
epsilon3.x =  1.00000000000000E+0000   epsilon3.y =  0.00000000000000E+0000
epsilon1.x =  3.90000000000146E+0000   epsilon1.y =  0.00000000000000E+0000
Nodes6 = 15   Horz = 33
R6VertRes =  1.00000000000000E+0000    Undercut =  3.00000000000182E-0001

iteration = 135    MaxRelResidue =  9.16514590096895E-0005
Y1.x =  2.50125495907851E+0001   Y1.y =  0.00000000000000E+0000
Y2.x =  2.61347167013810E-0001   Y2.y =  0.00000000000000E+0000
epsilonF.x =  1.00000000000000E+0000   epsilonF.y =  0.00000000000000E+0000
Gain = -3.96188909505548E+0001     Phase =  0.00000000000000E+0000

iteration = 135    MaxRelResidue =  9.13066149930142E-0005
Y1.x =  2.50138712220651E+0001   Y1.y = -3.33054134065947E-0002
Y2.x =  2.61291465144950E-0001   Y2.y =  1.07432003308650E-0004
epsilonF.x =  1.00000000000000E+0000   epsilonF.y = -1.00000000000023E-0001
Gain = -3.96212083124894E+0001     Phase =  9.98456122967410E-0002

iteration = 135    MaxRelResidue =  9.13002064375501E-0005
Y1.x =  2.50177353836189E+0001   Y1.y = -6.59981289305733E-0002
Y2.x =  2.61132808700495E-0001   Y2.y =  1.75922750539792E-0004
epsilonF.x =  1.00000000000000E+0000   epsilonF.y = -2.00000000000045E-0001
Gain = -3.96278469968500E+0001     Phase =  1.89748620697367E-0001

iteration = 135    MaxRelResidue =  9.19571306232658E-0005
Y1.x =  2.50238617145224E+0001   Y1.y = -9.75430549557359E-0002
Y2.x =  2.60893683324412E-0001   Y2.y =  1.74220948689019E-0004
epsilonF.x =  1.00000000000000E+0000   epsilonF.y = -3.00000000000182E-0001
Gain = -3.96379670686473E+0001     Phase =  2.61599183224092E-0001

iteration = 132    MaxRelResidue =  9.88440226402654E-0005
Y1.x =  2.50319479522586E+0001   Y1.y = -1.27542284747051E-0001
Y2.x =  2.60534557614847E-0001   Y2.y =  7.81589895727519E-0005
epsilonF.x =  1.00000000000000E+0000   epsilonF.y = -4.00000000000091E-0001
Gain = -3.96527862673771E+0001     Phase =  3.09118223551321E-0001
```

iteration = 138 MaxRelResidue = 9.00000000000345E-0005
Y1.x = 2.50411190974992E+0001 Y1.y = -1.55783342562245E-0001
Y2.x = 2.60360539279191E-0001 Y2.y = -1.00777852799605E-0004
epsilonF.x = 1.00000000000000E+0000 epsilonF.y = -5.00000000000000E-0001
Gain = -3.96618265805088E+0001 Phase = 3.34260761265488E-0001

iteration = 138 MaxRelResidue = 9.00000000000345E-0005
Y1.x = 2.50514554744586E+0001 Y1.y = -1.82088517084594E-0001
Y2.x = 2.60074359899590E-0001 Y2.y = -3.73392877502710E-0004
epsilonF.x = 1.00000000000000E+0000 epsilonF.y = -6.00000000000364E-0001
Gain = -3.96750167434126E+0001 Phase = 3.34191241811859E-0001

iteration = 222 MaxRelResidue = 9.95281909925705E-0005
Y1.x = 2.50616886043281E+0001 Y1.y = -2.06652842636686E-0001
Y2.x = 2.60201797223999E-0001 Y2.y = -6.77452892070995E-0004
epsilonF.x = 1.00000000000000E+0000 epsilonF.y = -7.00000000000728E-0001
Gain = -3.96743543451681E+0001 Phase = 3.23263854426736E-0001

iteration = 378 MaxRelResidue = 9.59584214975662E-0005
Y1.x = 2.50723209826683E+0001 Y1.y = -2.29524336364648E-0001
Y2.x = 2.59967511888590E-0001 Y2.y = -1.07739560110609E-0003
epsilonF.x = 1.00000000000000E+0000 epsilonF.y = -8.00000000001091E-0001
Gain = -3.96858863612048E+0001 Phase = 2.87046807852550E-0001

iteration = 765 MaxRelResidue = 9.91028224819335E-0005
Y1.x = 2.50832099010877E+0001 Y1.y = -2.50743803044770E-0001
Y2.x = 2.59821360356455E-0001 Y2.y = -1.51726163942811E-0003
epsilonF.x = 1.00000000000000E+0000 epsilonF.y = -9.00000000001455E-0001
Gain = -3.96945388708443E+0001 Phase = 2.38154453095167E-0001

iteration = 807 MaxRelResidue = 9.29296581545502E-0005
Y1.x = 2.50936398940976E+0001 Y1.y = -2.70691150289622E-0001
Y2.x = 2.59717955042106E-0001 Y2.y = -1.97956817035205E-0003
epsilonF.x = 1.00000000000000E+0000 epsilonF.y = -1.00000000000182E+0000
Gain = -3.97015745884752E+0001 Phase = 1.81339915566395E-0001

iteration = 813 MaxRelResidue = 9.85045534449558E-0005
Y1.x = 2.51682731881738E+0001 Y1.y = -4.32862354465215E-0001
Y2.x = 2.60743592739345E-0001 Y2.y = -5.94064264334548E-0003
epsilonF.x = 1.00000000000000E+0000 epsilonF.y = -2.00000000000364E+0000
Gain = -3.96919139327481E+0001 Phase = -3.19853071108129E-0001

iteration = 525 MaxRelResidue = 9.58934839176973E-0005
Y1.x = 2.52046943769092E+0001 Y1.y = -5.82903142482792E-0001
Y2.x = 2.62549442476029E-0001 Y2.y = -8.04243117067927E-0003
epsilonF.x = 1.00000000000000E+0000 epsilonF.y = -3.00000000000364E+0000
Gain = -3.96437434088136E+0001 Phase = -4.29709221067449E-0001

iteration = 861 MaxRelResidue = 9.40588431523892E-0005
Y1.x = 2.52291818718659E+0001 Y1.y = -7.40920049672241E-0001
Y2.x = 2.63813999448757E-0001 Y2.y = -9.20027315017080E-0003
epsilonF.x = 1.00000000000000E+0000 epsilonF.y = -4.00000000000728E+0000
Gain = -3.96106594949518E+0001 Phase = -3.15173733414641E-0001

iteration = 903 MaxRelResidue = 9.26248407987496E-0005
Y1.x = 2.52546910470701E+0001 Y1.y = -9.06444965635274E-0001
Y2.x = 2.64700530045047E-0001 Y2.y = -1.03192729426667E-0002
epsilonF.x = 1.00000000000000E+0000 epsilonF.y = -5.00000000000728E+0000
Gain = -3.95908283000334E+0001 Phase = -1.76942826435388E-0001

iteration = 1008 MaxRelResidue = 9.99237953774879E-0005
Y1.x = 2.52864694071177E+0001 Y1.y = -1.07520363400909E+0000
Y2.x = 2.65194517965483E-0001 Y2.y = -1.13340684611103E-0002
epsilonF.x = 1.00000000000000E+0000 epsilonF.y = -6.00000000000728E+0000
Gain = -3.95864801337590E+0001 Phase = -1.24558338351682E-0002

iteration = 1038 MaxRelResidue = 9.69951672062930E-0005
Y1.x = 2.53259855786455E+0001 Y1.y = -1.24360407695895E+0000
Y2.x = 2.65384567892852E-0001 Y2.y = -1.23081008867132E-0002
epsilonF.x = 1.00000000000000E+0000 epsilonF.y = -7.00000000000728E+0000
Gain = -3.95950290116702E+0001 Phase = 1.55805433485449E-0001

iteration = 1047 MaxRelResidue = 9.82029807186091E-0005
Y1.x = 2.53727499524830E+0001 Y1.y = -1.40952581400234E+0000
Y2.x = 2.65702760699241E-0001 Y2.y = -1.35169700960631E-0002
epsilonF.x = 1.00000000000000E+0000 epsilonF.y = -8.00000000001455E+0000
Gain = -3.96016741195761E+0001 Phase = 2.67399047062900E-0001

iteration = 1047 MaxRelResidue = 9.00000000000345E-0005
Y1.x = 2.54258914952516E+0001 Y1.y = -1.57069082424823E+0000
Y2.x = 2.65639362906768E-0001 Y2.y = -1.47170416528155E-0002
epsilonF.x = 1.00000000000000E+0000 epsilonF.y = -9.00000000001455E+0000
Gain = -3.96229948487812E+0001 Phase = 3.63890709587999E-0001

iteration = 1146 MaxRelResidue = 9.68653149259202E-0005
Y1.x = 2.54843962740852E+0001 Y1.y = -1.72693784206785E+0000
Y2.x = 2.65829467969525E-0001 Y2.y = -1.57802200961612E-0002
epsilonF.x = 1.00000000000000E+0000 epsilonF.y = -1.00000000000146E+0001
Gain = -3.96381324363393E+0001 Phase = 4.79477796605912E-0001

iteration = 1566 MaxRelResidue = 9.96519809505214E-0005
Y1.x = 2.61724315411702E+0001 Y1.y = -3.00689855486416E+0000
Y2.x = 2.67030925655035E-0001 Y2.y = -2.90190084880066E-0002
epsilonF.x = 1.00000000000000E+0000 epsilonF.y = -2.00000000000291E+0001
Gain = -3.98316981903074E+0001 Phase = 3.51707471806520E-0001

iteration = 954 MaxRelResidue = 9.58468090017650E-0005
Y1.x = 2.68466945379623E+0001 Y1.y = -3.95208179043038E+0000
Y2.x = 2.75104204047238E-0001 Y2.y = -3.93290882644806E-0002
epsilonF.x = 1.00000000000000E+0000 epsilonF.y = -3.00000000000291E+0001
Gain = -3.97932034990181E+0001 Phase = 2.38405623013630E-0001

iteration = 804 MaxRelResidue = 9.712674475370 61E-0005
Y1.x = 2.74573407880671E+0001 Y1.y = -4.72451183602971E+0000
Y2.x = 2.90939279578197E-0001 Y2.y = -3.03185721671468E-0002
epsilonF.x = 1.00000000000000E+0000 epsilonF.y = -4.00000000000582E+0001
Gain = -3.95770171450966E+0001 Phase = 3.81385088554736E+0000

iteration = 972 MaxRelResidue = 9.60087371343343E-0005
Y1.x = 2.80138513365237E+0001 Y1.y = -5.39044200324861E+0000
Y2.x = 2.97372939839534E-0001 Y2.y = 6.84598762194355E-0003
epsilonF.x = 1.00000000000000E+0000 epsilonF.y = -5.00000000000582E+0001
Gain = -3.96371091573627E+0001 Phase = 1.22105702033518E+0001

iteration = 690 MaxRelResidue = 9.20478797514779E-0005
Y1.x = 2.85233085463406E+0001 Y1.y = -5.98704150560661E+0000
Y2.x = 2.81187550960112E-0001 Y2.y = 6.93164613995805E-0002
epsilonF.x = 1.00000000000000E+0000 epsilonF.y = -6.00000000000582E+0001
Gain = -4.00552037126512E+0001 Phase = 2.57023556612083E+0001

iteration = 765 MaxRelResidue = 9.90828273225164E-0005
Y1.x = 2.90033602355688E+0001 Y1.y = -6.53270383636846E+0000
Y2.x = 2.25958273192873E-0001 Y2.y = 1.47656089071916E-0001
epsilonF.x = 1.00000000000000E+0000 epsilonF.y = -7.00000000001164E+0001
Gain = -4.08391201973998E+0001 Phase = 4.58567047200997E+0001

iteration = 642 MaxRelResidue = 9.00348228224379E-0005
Y1.x = 2.94498789085483E+0001 Y1.y = -7.04049376798503E+0000
Y2.x = 1.37243258296849E-0001 Y2.y = 2.27615328416050E-0001
epsilonF.x = 1.00000000000000E+0000 epsilonF.y = -8.00000000001164E+0001
Gain = -4.11323593460494E+0001 Phase = 7.23568209224595E+0001

iteration = 576 MaxRelResidue = 9.60046755962285E-0005
Y1.x = 2.98821946144744E+0001 Y1.y = -7.51664943498326E+0000
Y2.x = 5.87285652397185E-0003 Y2.y = 3.01378856376232E-0001
epsilonF.x = 1.00000000000000E+0000 epsilonF.y = -9.00000000001164E+0001
Gain = -4.01908852001128E+0001 Phase = 1.03003046704424E+0002

iteration = 540 MaxRelResidue = 9.72630045964484E-0005
Y1.x = 3.02907645690721E+0001 Y1.y = -7.94976165845583E+0000
Y2.x = -1.52772255912851E-0001 Y2.y = 3.46075066117919E-0001
epsilonF.x = 1.00000000000000E+0000 epsilonF.y = -1.00000000000116E+0002
Gain = -3.83589572977359E+0001 Phase = 1.28524239287593E+0002

iteration = 489 MaxRelResidue = 9.89515994205270E-0005
Y1.x = 3.06826830666396E+0001 Y1.y = -8.37389444714063E+0000
Y2.x = -3.35111762339693E-0001 Y2.y = 3.84263606161767E-0001
epsilonF.x = 1.00000000000000E+0000 epsilonF.y = -1.10000000000116E+0002
Gain = -3.59009105375678E+0001 Phase = 1.46356654707240E+0002

iteration = 450 MaxRelResidue = 9.91747767163931E-0005
Y1.x = 3.10559909775038E+0001 Y1.y = -8.78685645728547E+0000
Y2.x = -5.33844917061288E-0001 Y2.y = 4.05978203140421E-0001
epsilonF.x = 1.00000000000000E+0000 epsilonF.y = -1.20000000000116E+0002
Gain = -3.36471534674176E+0001 Phase = 1.58545865037233E+0002

iteration = 423 MaxRelResidue = 9.77810472918561E-0005
Y1.x = 3.14401766156370E+0001 Y1.y = -9.15773416965385E+0000
Y2.x = -7.66475644875754E-0001 Y2.y = 3.89801014207023E-0001
epsilonF.x = 1.00000000000000E+0000 epsilonF.y = -1.30000000000233E+0002
Gain = -3.16144614625606E+0001 Phase = 1.69283319503533E+0002

iteration = 402 MaxRelResidue = 9.81465099652024E-0005
Y1.x = 3.17862475030706E+0001 Y1.y = -9.50661191908875E+0000
Y2.x = -9.91106498185218E-0001 Y2.y = 3.46025975812154E-0001
epsilonF.x = 1.00000000000000E+0000 epsilonF.y = -1.40000000000233E+0002
Gain = -2.99949998961498E+0001 Phase = 1.77405164408463E+0002

iteration = 384 MaxRelResidue = 9.99673207212615E-0005
Y1.x = 3.21239271614468E+0001 Y1.y = -9.85954545675486E+0000
Y2.x = -1.22488421923481E+0000 Y2.y = 2.94898505156198E-0001
epsilonF.x = 1.00000000000000E+0000 epsilonF.y = -1.50000000000233E+0002
Gain = -2.85209997877447E+0001 Phase = 1.83525715772598E+0002

iteration = 372 MaxRelResidue = 9.75123863533600E-0005
Y1.x = 3.24691034781281E+0001 Y1.y = -1.01944397104380E+0001
Y2.x = -1.47708197107931E+0000 Y2.y = 2.20034963288072E-0001
epsilonF.x = 1.00000000000000E+0000 epsilonF.y = -1.60000000000233E+0002
Gain = -2.71543685878916E+0001 Phase = 1.88958093634507E+0002

iteration = 360 MaxRelResidue = 9.90520966979158E-0005
Y1.x = 3.28099730290705E+0001 Y1.y = -1.05006181530625E+0001
Y2.x = -1.73600542638997E+0000 Y2.y = 1.13282501437084E-0001
epsilonF.x = 1.00000000000000E+0000 epsilonF.y = -1.70000000000233E+0002
Gain = -2.59342011999722E+0001 Phase = 1.94013406556876E+0002

Appendix J. Preliminary Experiments to Establish the Challenge Gas Exposure Cycle

To establish the challenge gas exposure cycle used for the single component and binary gas mixture analyses, a series of experiments were performed to characterize the challenge gas response of the IGEFET microsensor when coated with copper-, nickel-, and cobalt-phthalocyanine films. The goal was to establish the exposure cycle conditions that would provide a reproducible gas response. The experiments investigated the affect of temperature, exposure duration, and a pre-conditioning process on the following performance characteristics of the IGEFET microsensor: response magnitude, time response, reversibility, and baseline drift. The electrical measurements performed on the IGEFET microsensors coated with the three metal-substituted phthalocyanine (MPc) films included the DC resistance, and the transfer function gain and phase delay. However, the reproducibility of the gas response can be obtained from either electrical measurement. Since the primary objective was to establish the challenge gas exposure cycle, and because similar results were observed with the three MPc films, the analysis concentrated on the CuPc-coated interdigitated gate electrode (IGE) structure's DC resistance response to nitrogen dioxide exposure.

The first experiment examined the IGEFET microsensor's response to a 100 ppb NO_2 challenge gas exposure at 150° C. The microsensor was purged for approximately one hour prior to introducing the challenge gas to demonstrate an initially stable response. The microsensor was exposed for one hour to the challenge gas, and subsequently purged with dry air for two hours (150° C). The microsensor was then re-exposed for 15 minutes to the 100 ppb NO_2 challenge gas, and again purged with dry air (150° C, 30 minutes). Figure J-1 depicts the IGE structure's normalized DC resistance over this time period for all three MPc film coatings. Despite the long initial exposure, the IGE structure's normalized DC resistance did not attain equilibrium, and the subsequent purge was also insufficient to completely reverse the gas response induced. Similar results were obtained with the short challenge gas exposure. These results indicate that equilibrium operation of the microsensor cannot be effectively accomplished under these conditions.

The second approach investigated the pre-conditioning of the MPc films by exposing them to a high concentration (1000 ppb) NO_2 challenge gas for one hour (150° C). As shown in Figure J-2, the normalized DC resistance of the MPc-coated IGE structures did not attain equilibrium following the long exposure. The high NO_2 concentration was purged for one hour with dry air (150° C). Consequently, the resistance of each MPc-coated IGE structure after this one-hour purge was selected as the baseline resistance for each particular sensor. The microsensor was then subjected to a series of challenge gas

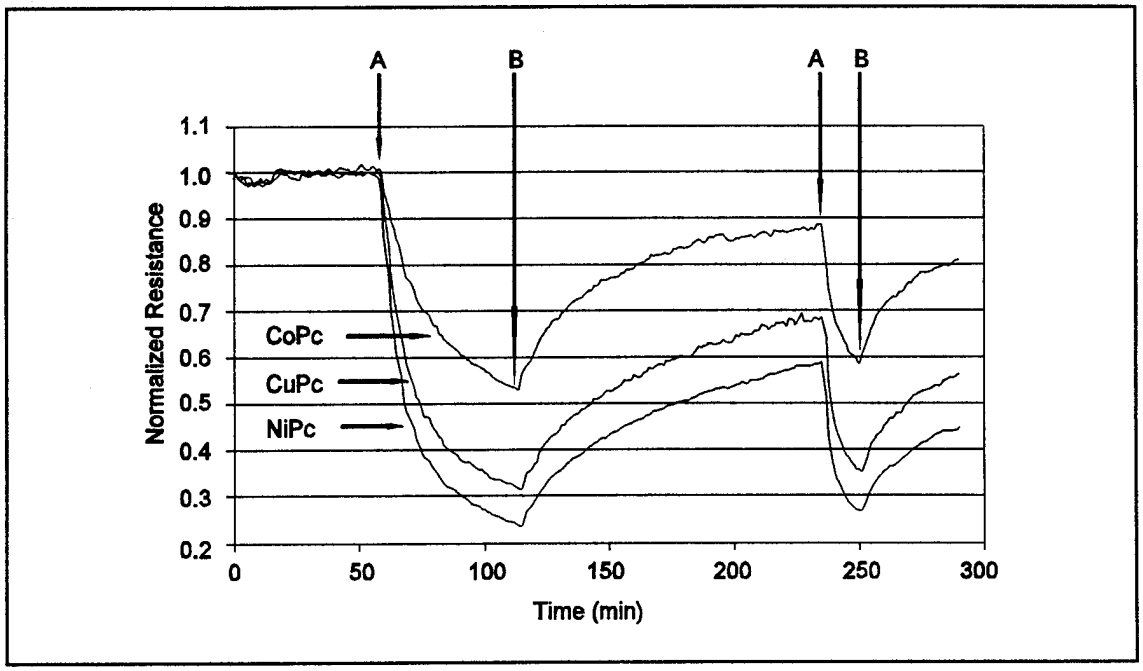


Figure J-1. MPc-Coated IGE Structure Normalized DC Resistance Response to a 100 ppb NO_2 Challenge Gas Exposure at 150° C. A- Begin 100 ppb NO_2 Exposure. B- Begin Dry Air Purge.

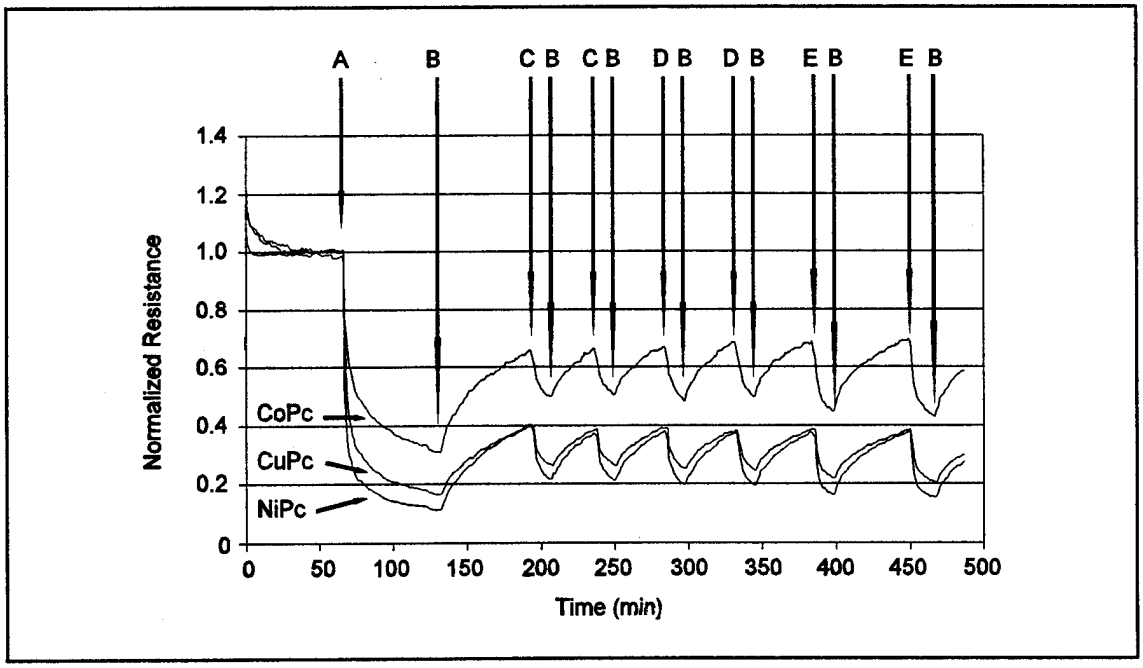


Figure J-2. MPc-Coated IGE Structure Normalized DC Resistance Response for Several NO_2 Challenge Gas Exposures Following Pre-conditioning of the Microsensor with a 1000 ppb NO_2 Exposure for 1 hour. A- Begin 1000 ppb NO_2 Exposure. B- Begin Dry Air Purge. C- Begin 15 minute, 100 ppb NO_2 Exposure. D- Begin 15 minute, 200 ppb NO_2 Exposure. E- Begin 15 minute, 400 ppb NO_2 Exposure. Temperature-150° C.

exposure cycles. During each cycle, the microsensor was exposed to the NO_2 challenge gas for 15 minutes, and then purged with dry air until the baseline resistance of the CuPc-coated IGE structure was re-established. Three NO_2 concentrations were tested: 100, 200, and 400 ppb. Based upon repeated exposure at each concentration, the normalized DC resistance response was shown to be reproducible. However, as the NO_2 concentration was increased, the time required to re-establish the baseline increased. The purge time required to re-establish the baseline resistance was approximately 50 minutes after exposure to 400 ppb NO_2. Another disadvantage with the pre-conditioning process is that the magnitude of the resistance change relative to the baseline resistance is much smaller than when the microsensor is thoroughly purged. Although the pre-conditioning process has less than ideal characteristics, it does satisfy the main objective of establishing a reproducible response.

To determine if increasing the operating temperature to 170° C would enhance the response characteristics of the pre-conditioning process, an experiment similar to that conducted at 150° C was implemented. In this experiment, the microsensor was exposed to four NO_2 concentrations: 100, 200, 300, and 400 ppb. Only the 100 ppb NO_2 exposure was repeated twice. As depicted in Figure J-3, the normalized DC resistance response was consistent with the reproducible behavior observed at 150° C. At 170° C, the pre-conditioned normalized DC resistance response was slightly less than that observed for the corresponding MPc film at 150° C. After purging the pre-conditioning challenge gas, the normalized DC resistance response was reversed to a greater extent at 170° C. The subsequent 15 minute challenge gas exposures elicited greater changes in the normalized DC resistance response, and the time required to reverse the elicited response increased. Despite the long recovery time, the pre-conditioning process yields reproducible results, and is acceptable for single component gas analyses. However, in the analysis of a binary gas mixture, and particularly when the two gases elicit opposite (sign change) conductivity changes, the pre-conditioning process is unacceptable. Figure J-4 illustrates the problem with pre-conditioning for analysis of a binary mixture of NO_2 and NH_3. After pre-conditioning, reproducible response to repeated 100 ppb NO_2 exposures was obtained. However, when a binary mixture of 100 ppb NO_2 and 100 ppm NH_3 was introduced, a small decrease in the normalized DC resistance was observed. When the binary gas mixture was purged, the normalized DC resistance rapidly increased beyond the baseline resistance established after the pre-conditioning process. This behavior forced establishing a new baseline resistance for subsequent exposures. From this new baseline resistance, a greater response to 100 ppb NO_2 exposures was observed.

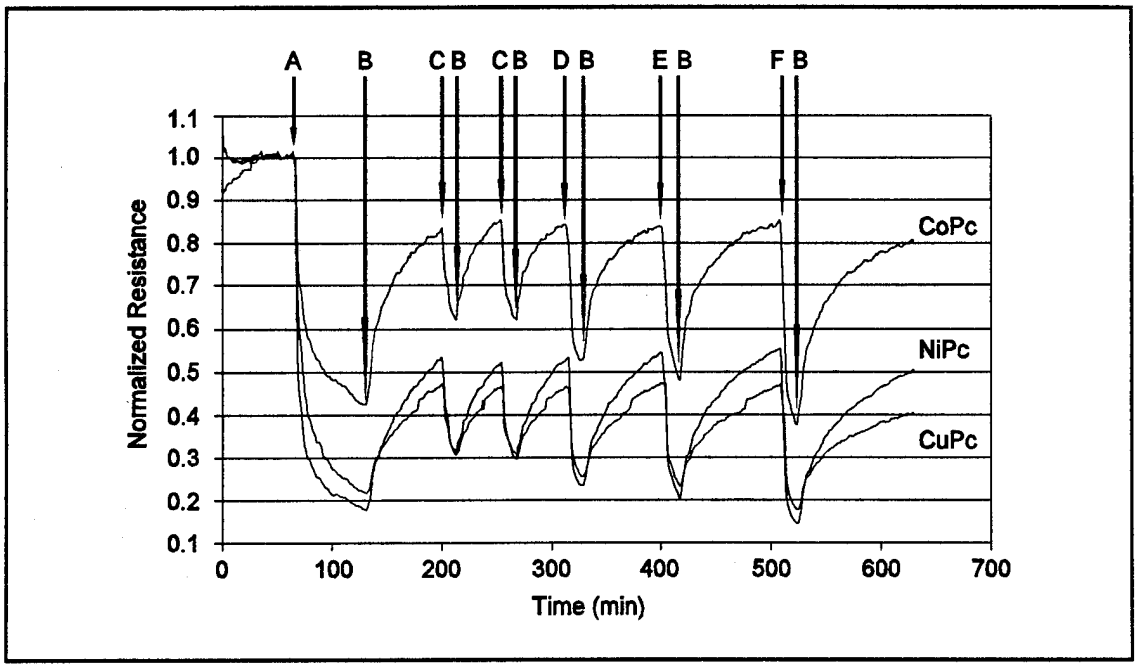


Figure J-3. MPc-Coated IGE Structure Normalized DC Resistance Response for Several NO_2 Challenge Gas Exposures Following Pre-conditioning of the Microsensor with a 1000 ppb NO_2 Exposure for 1 hour. A- Begin 1000 ppb NO_2 Exposure. B- Begin Dry Air Purge. C- Begin 15 minute, 100 ppb NO_2 Exposure. D- Begin 15 minute, 200 ppb NO_2 Exposure. E- Begin 15 minute, 300 ppb NO_2 Exposure. F- Begin 15 minute, 400 ppb NO_2 Exposure. Temperature-170° C.

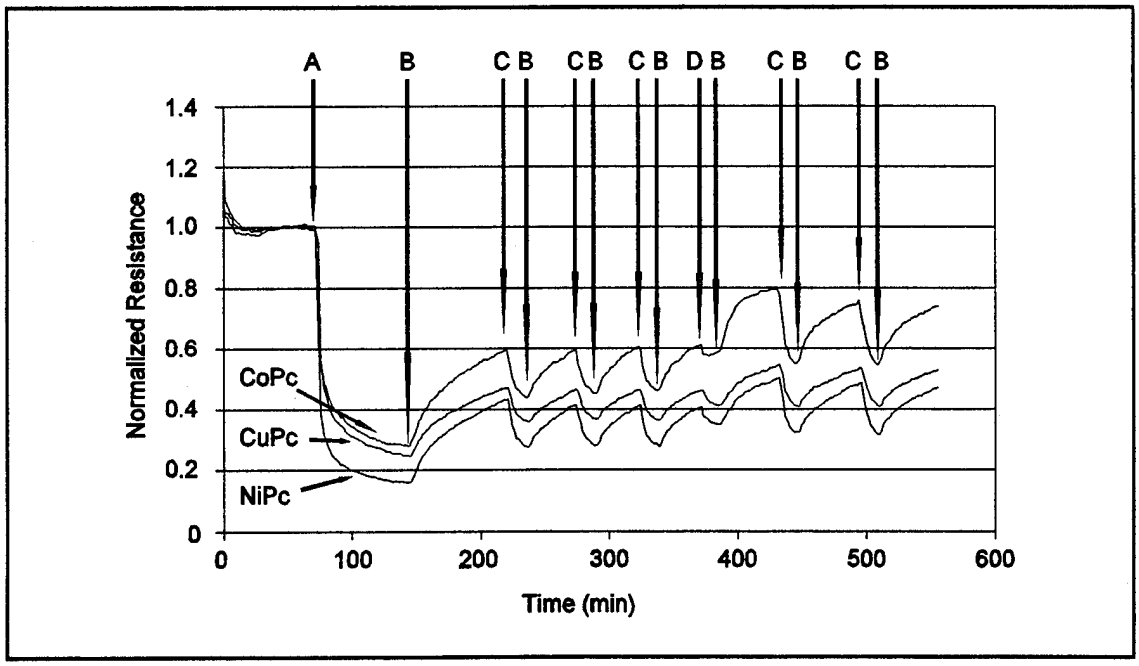


Figure J-4. MPc-Coated IGE Structure Normalized DC Resistance Response for Several NO_2 Challenge Gas Exposures Following Pre-conditioning of the Microsensor with 1000 ppb NO_2 for 1 hour. A- Begin 1000 ppb NO_2 Exposure. B- Begin Dry Air Purge. C- Begin 15 minute, 100 ppb NO_2 Exposure. D- Begin 15 minute, 100 ppb NO_2, 100ppm NH_3 Exposure. Temperature-170° C.

Since a pre-conditioning process was unacceptable for binary gas mixture analysis, the normalized DC resistance response to a short exposure period was investigated. As depicted in Figure J-5, after a thorough purge, the microsensor was exposed to a 15 minute, 100 ppb NO_2 challenge gas concentration at 170° C. Figure J-5 reveals a stable baseline resistance, a strong NO_2 response, and nearly complete reversibility. Although the recovery time was still long (3-4 hours), this exposure cycle was deemed promising for achieving reproducible results. The normalized DC resistance response to repeated NO_2 exposures was collected over several days. Figure J-6 reveals a significant long term drift in the baseline resistance for the CuPc-coated IGE. All the resistance data shown in Figure J-6 was normalized to a single resistance value measured near the beginning of this long experiment. Similar results were obtained with the other films. The instruments were recalibrated once each day during this experiment which extended over several days. As shown in Figure J-7, when the resistance data was re-normalized after each instrument re-calibration, a stable baseline was achieved and reproducible responses were measured. Table J-1 lists the normalized DC resistance response of the MPc-coated IGE structures for repeated NO_2 challenge gas exposures.

The last two experiments investigated a dual-temperature mode of operation for the microsensor. The results from the experiments described above indicated that a stronger response may be elicited at lower temperature. Therefore, the microsensor was exposed at 40° C for 15 minutes to a 100 ppb NO_2 challenge gas. The gas was purged for 30 minutes at 40° C before increasing the temperature to 170° C for extended purging. Figure J-8 reveals a much stronger NO_2 response at 40° C compared to that measured at the higher temperatures. The gas response was not reversed by an isothermal (40° C) purge. However, following an extended purge at 170° C, the baseline resistance was re-established. In an attempt to reduce the exposure/purge temperature differential, the extended purge temperature was evaluated at 85° C. Figure J-9 reveals that this temperature differential was insufficient for reversing the gas response.

Although these results indicate that a low exposure temperature (30-40° C) yields the greatest response, the two relaxation processes observed in the IGEFET transfer function occur at frequencies less than the minimum measurement frequency of the instrumentation at this temperature (see Chapter IV). Therefore, the dual-temperature exposure cycle described in Chapter VI was adopted with the exposure temperature at 100° C and the purge temperature at 170° C. The exposure duration was set at 16 minutes, and the measured resistance was normalized to the resistance just prior to each exposure.

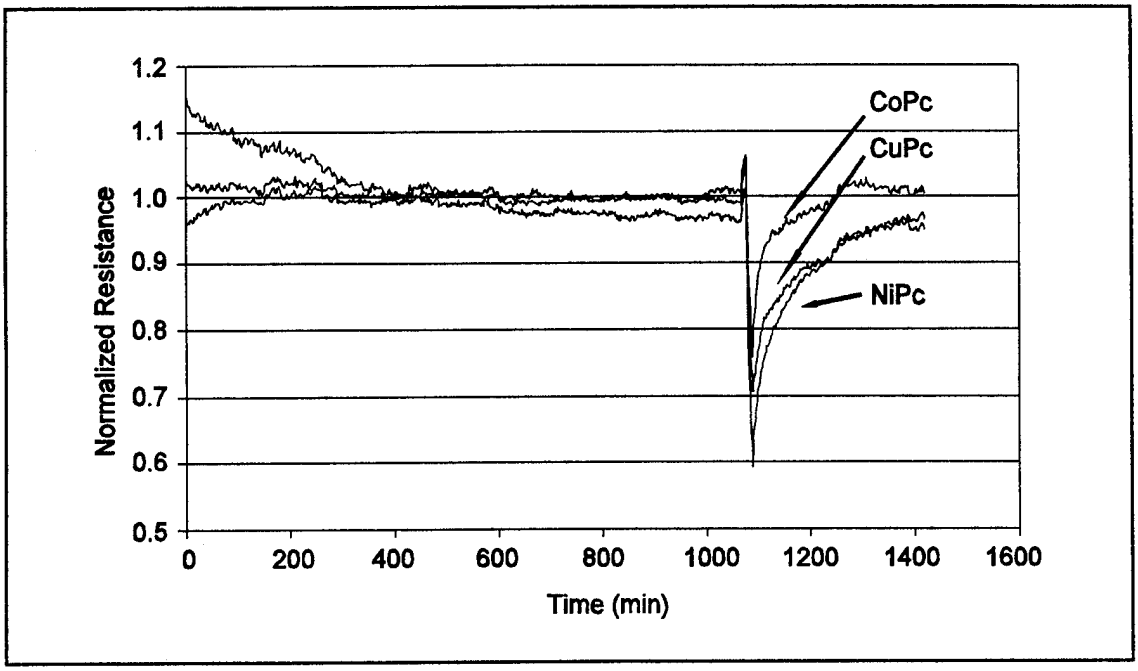


Figure J-5. MPc-Coated IGE Structure Normalized DC Resistance Response to a 15 minute, 100 ppb NO_2 Challenge Gas Exposure at170° C.

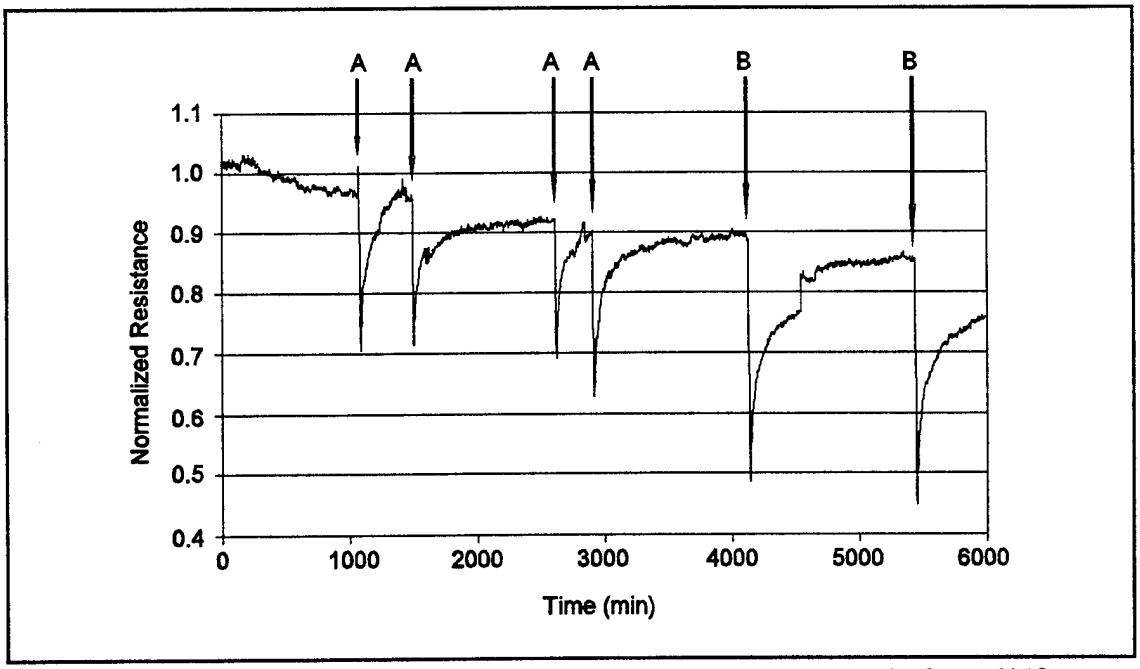


Figure J-6. CuPc-Coated IGE Structure Normalized DC Resistance Response for Several NO_2 Challenge Gas Exposures. A- Begin 15 minute, 100 ppb NO_2 Exposure with Subsequent Dry Air Purge. B- Begin 15 minute, 400 ppb NO_2 Exposure with Subsequent Dry Air Purge. Temperature-170° C.

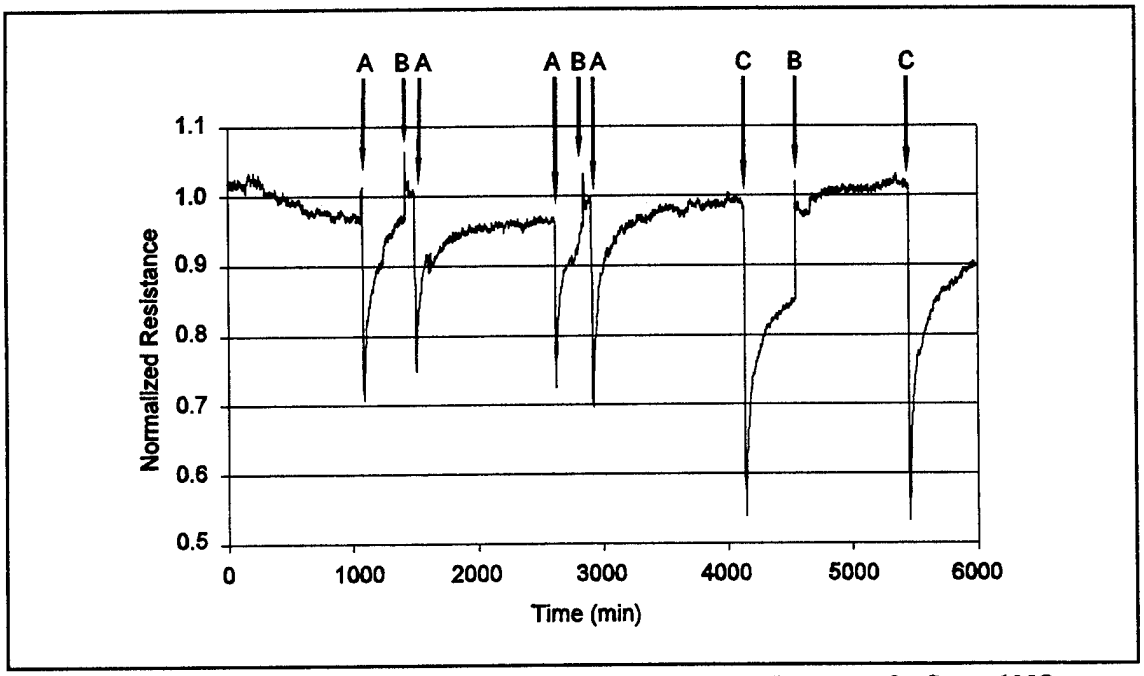


Figure J-7. CuPc-Coated IGE Structure Normalized DC Resistance Response for Several NO_2 Challenge Gas Exposures. A- Begin 15 minute, 100 ppb NO_2 Exposure with Subsequent Dry Air Purge. B- Instrument Re-calibration and Response Re-normalization. C- Begin 15 minute, 400 ppb NO_2 Exposure with Subsequent Dry Air Purge. Temperature-170° C.

Table J-1. MPc-Coated IGE Structure Normalized DC Resistance Response to the Nitrogen Dioxide (NO_2) Challenge Gas Exposures when Re-normalized after Instrument Re-calibration.

NO_2 Concentration (ppb)	CuPc	NiPc	CoPc
100	0.71	0.59	0.76
100	0.75	0.61	0.75
100	0.70	0.58	0.76
100	0.70	0.58	0.77
400	0.54	0.43	0.60
400	0.53	0.39	0.56

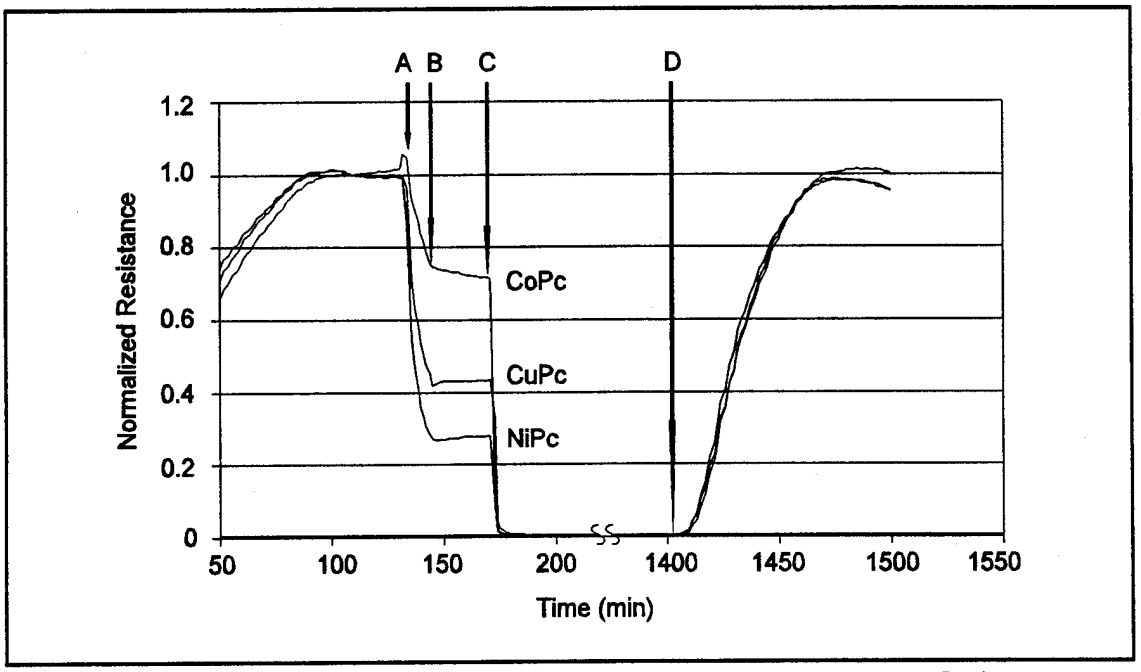


Figure J-8. MPc-Coated IGE Structure Normalized DC Resistance Response to a 15 minute, 100 ppb NO_2 Challenge Gas Exposure at 40° C with a Subsequent Dual-Temperature Dry Air Purge. A-Begin 100 ppb NO_2 Challenge Gas Exposure. B- Begin 30 minute, Dry Air Purge at 40° C. C- Begin Approximately 13 hour, Dry Air Purge at 170° C. D- Begin Cooling to 40° C.

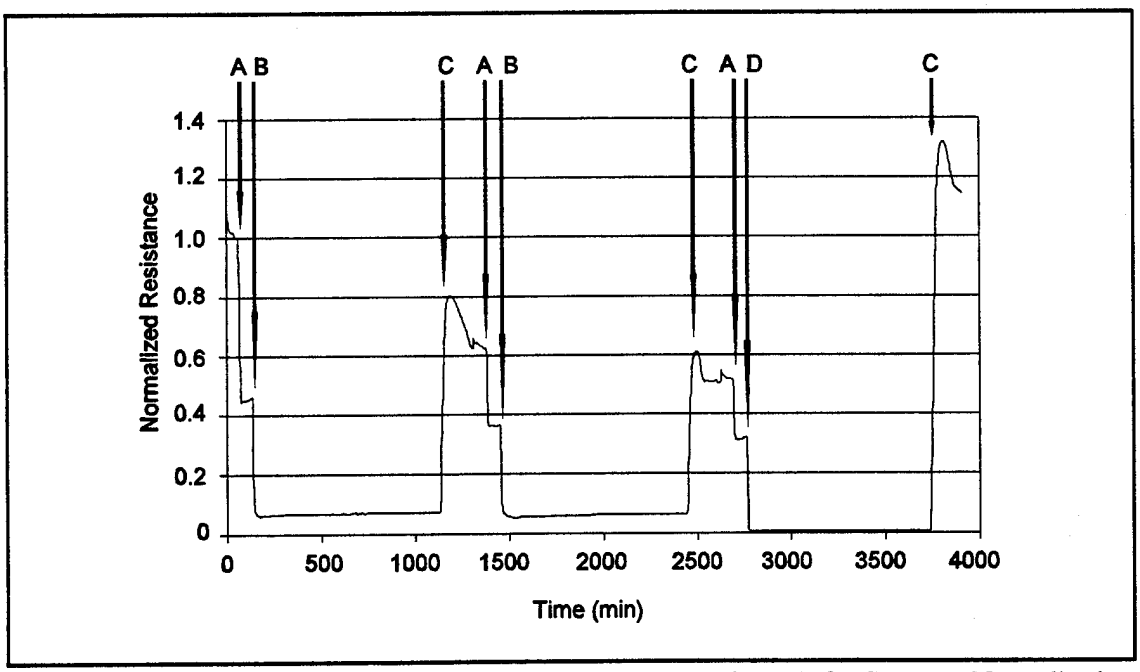


Figure J-9. Effect of Different Purge Temperatures on the MPc-Coated IGE Structure Normalized DC Resistance Response to a 15 minute, 100 ppb NO_2 Challenge Gas Exposures at 40° C. A-Begin 100 ppb NO_2 Challenge Gas Exposure with a 60 minute, Dry Air Purge at 40° C. B- Begin Approximately 15 hour, Dry Air Purge at 85° C. C- Begin Cooling to 40° C. D- Begin Approximately 15 hour, Dry Air Purge at 170° C.

Appendix K. Supporting Data: Normalized DC Resistance Response of the MPc-Coated Microsensor to Challenge Gas Exposure

This appendix contains the normalized DC resistance response of the copper phthalocyanine (CuPc)-, nickel phthalocyanine (NiPc)-, and cobalt phthalocyanine (CoPc)-coated interdigitated gate electrode field effect transistor (IGEFET) microsensors as a result of challenge gas exposure. The data presented in this appendix supports the normalized DC resistance response data presented in Chapter VI. Figures K-1 through K-9 present the normalized DC resistance response of the MPc-coated IGEFET microsensor to binary gas mixtures containing a fixed nitrogen dioxide concentration and various concentrations of ammonia. Similarly, Figures K-10 through K-15 depict the normalized DC resistance response of the MPc-coated microsensor to binary gas mixtures containing a fixed ammonia concentration and various concentrations of nitrogen dioxide. Figures K-16 through K-18 illustrate the dependence of the MPc-coated IGE structure's normalized DC resistance response as a result of exposure to the nitrogen dioxide challenge gas. The normalized DC resistance response for each MPc film type was calculated as the average of the responses determined from the DC resistance measurements of two IGE structures as a result of repeated exposure to the challenge gas. Although the spread in the normalized resistance responses overlapped, the average response indicates that the relative sensitivity of the three MPc films to nitrogen dioxide was in the following order: NiPc>CoPc>CuPc. In contrast to the similar sensitivity of the MPc films to nitrogen dioxide, the MPc films manifested a significantly different sensitivity to ammonia, as shown in Figures K-19 through K-21. The relative sensitivity of the three MPc films to ammonia was in the following order: CoPc>CuPc>NiPc.

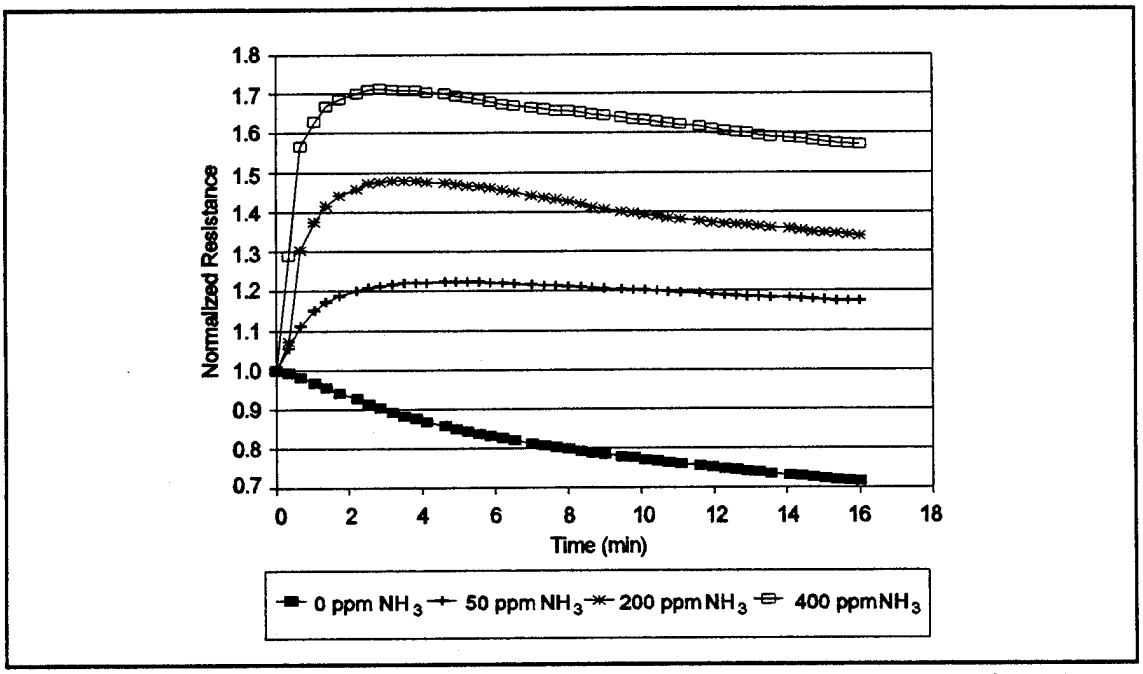


Figure K-1. CuPc-Coated IGE Structure Normalized DC Resistance Response to Binary Gas Mixtures Containing 100 ppb NO_2 and Various NH_3 Concentrations. (Film Thickness = 0.32 μm. Temperature = 100° C.)

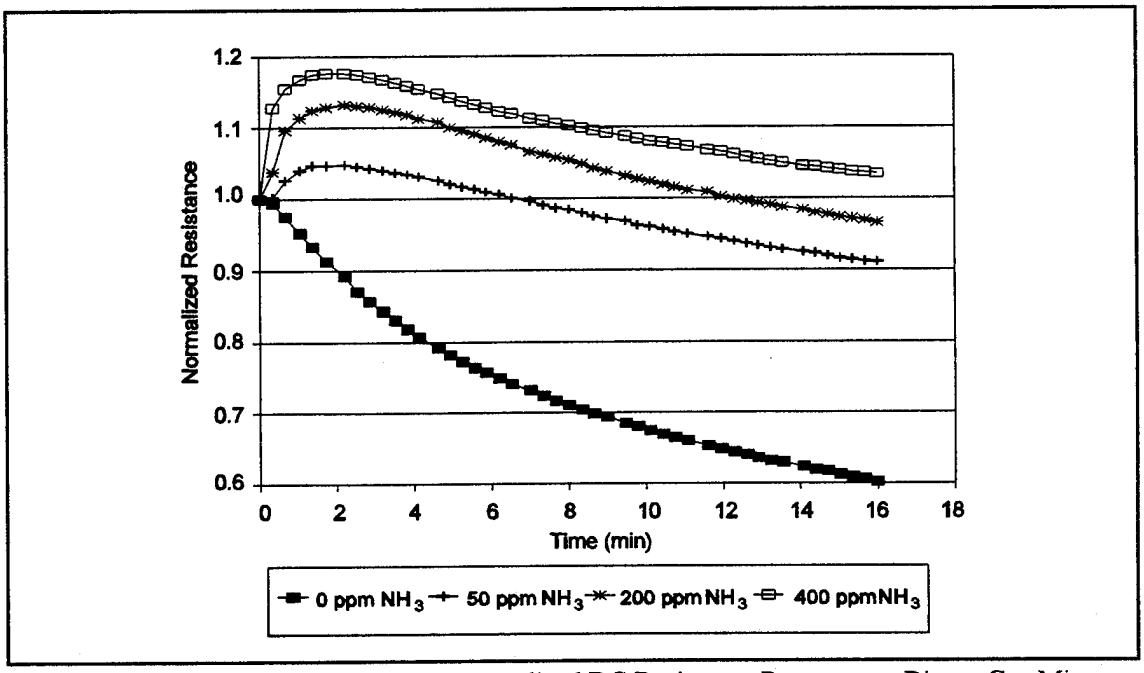


Figure K-2. NiPc-Coated IGE Structure Normalized DC Resistance Response to Binary Gas Mixtures Containing 100 ppb NO_2 and Various NH_3 Concentrations. (Film Thickness = 0.43 μm. Temperature = 100° C.)

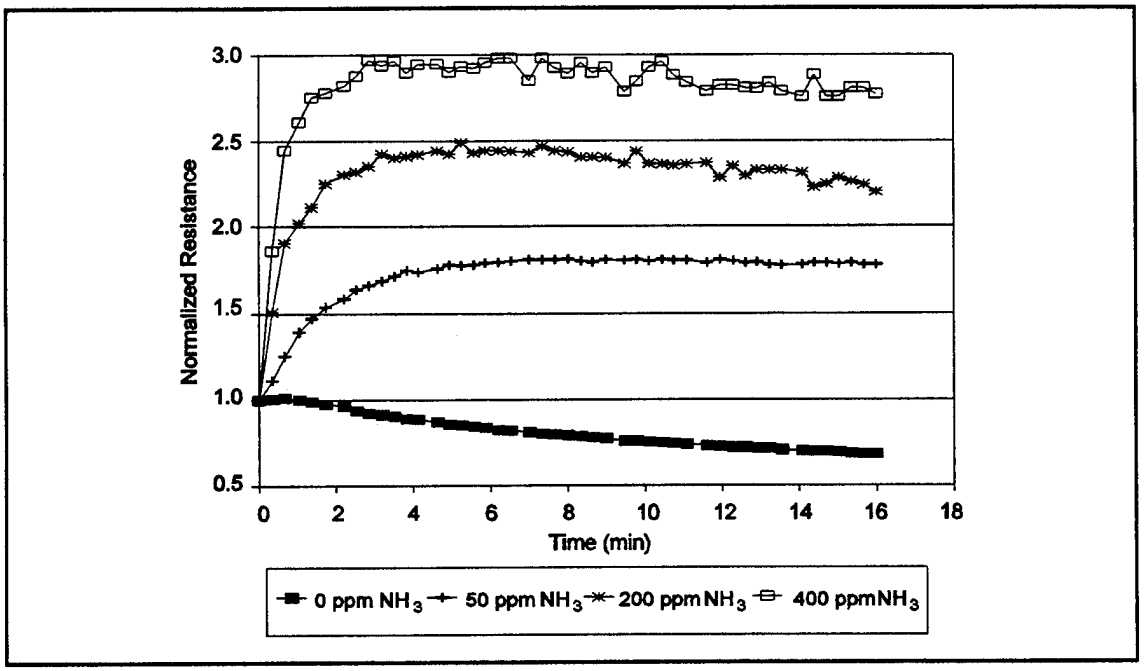


Figure K-3. CoPc-Coated IGE Structure Normalized DC Resistance Response to Binary Gas Mixtures Containing 100 ppb NO_2 and Various NH_3 Concentrations. (Film Thickness = 0.51 μm. Temperature = 100° C.)

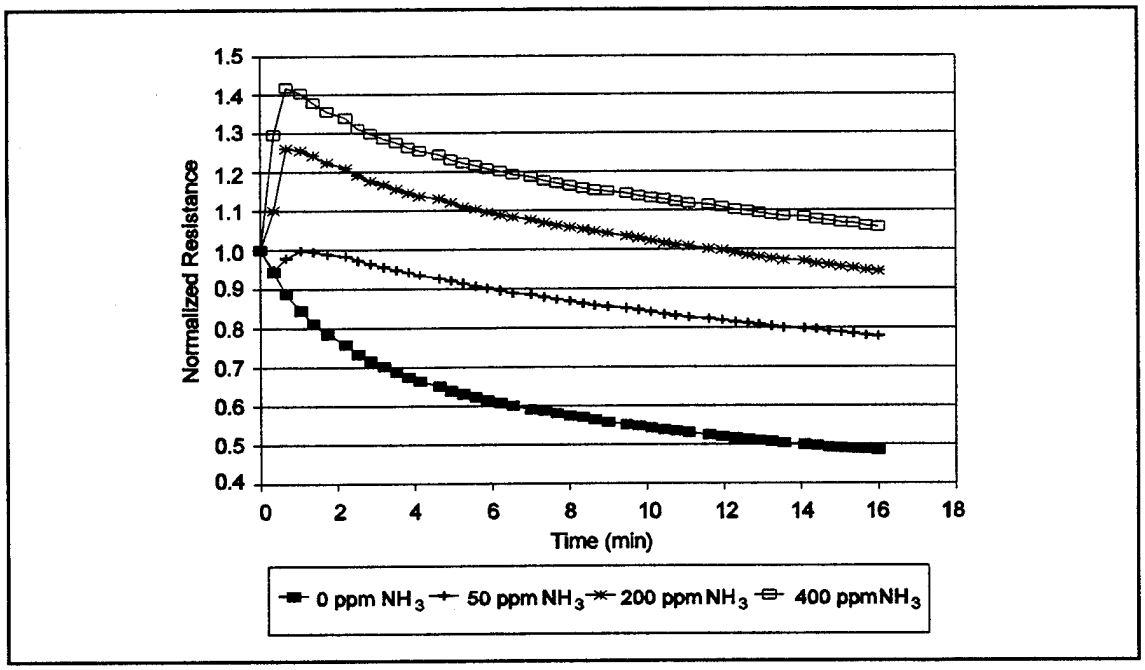


Figure K-4. CuPc-Coated IGE Structure Normalized DC Resistance Response to Binary Gas Mixtures Containing 425 ppb NO_2 and Various NH_3 Concentrations. (Film Thickness = 0.32 μm. Temperature = 100° C.)

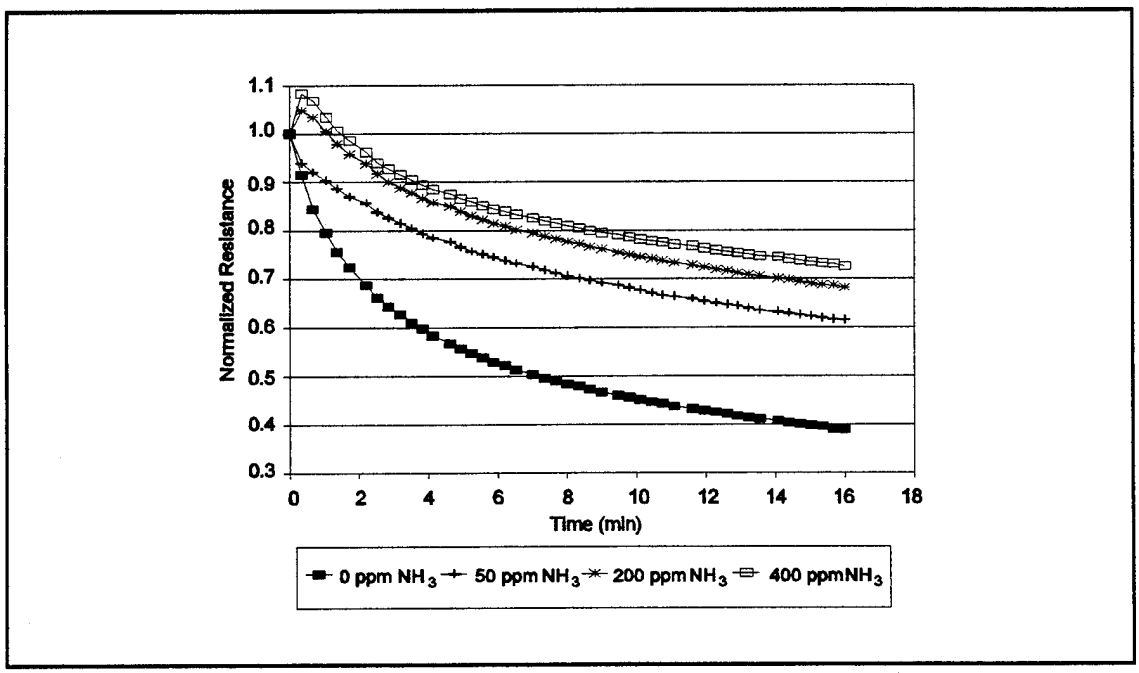


Figure K-5. NiPc-Coated IGE Structure Normalized DC Resistance Response to Binary Gas Mixtures Containing 425 ppb NO_2 and Various NH_3 Concentrations. (Film Thickness = 0.43 μm. Temperature = 100° C.)

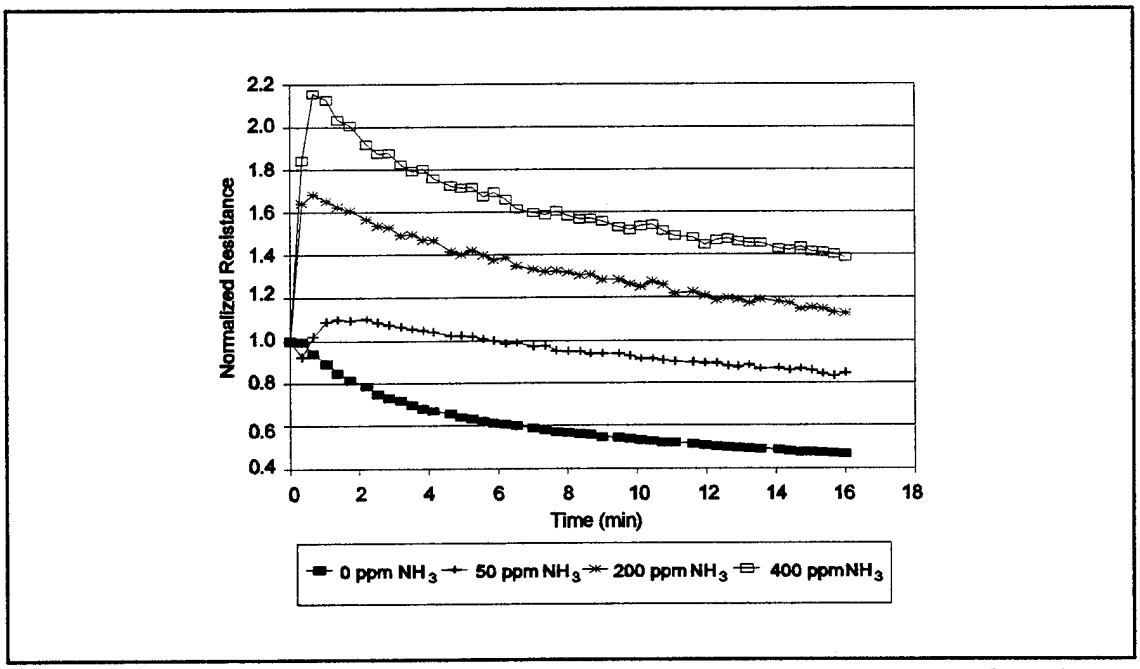


Figure K-6. CoPc-Coated IGE Structure Normalized DC Resistance Response to Binary Gas Mixtures Containing 425 ppb NO_2 and Various NH_3 Concentrations. (Film Thickness = 0.51 μm. Temperature = 100° C.)

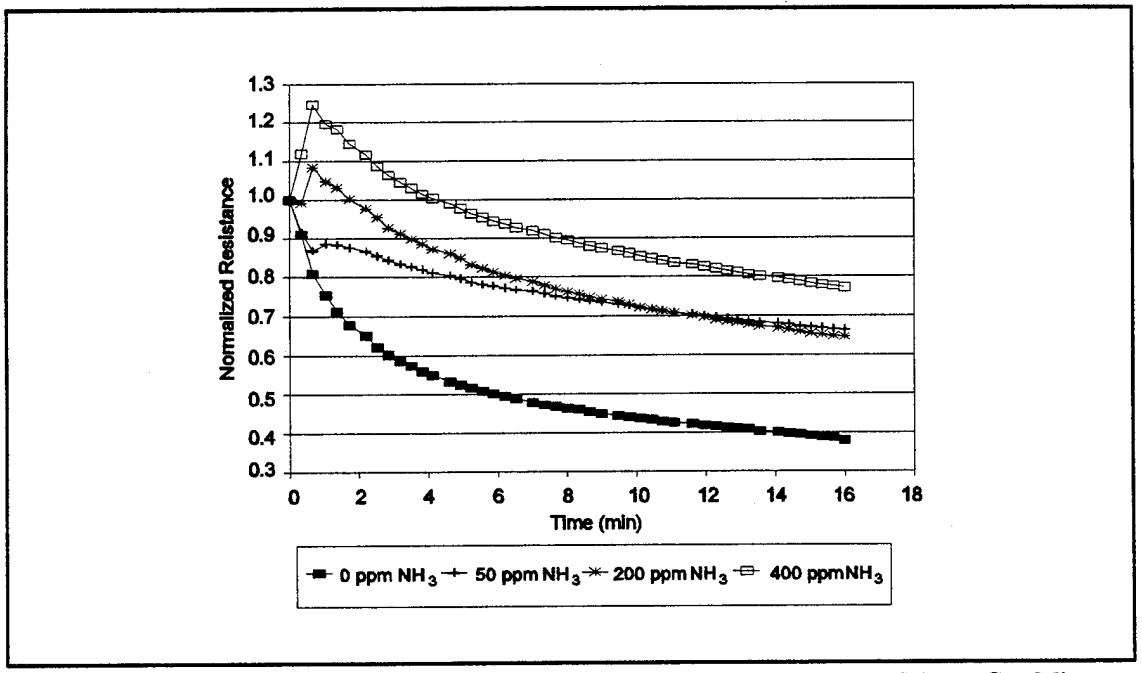


Figure K-7. CuPc-Coated IGE Structure Normalized DC Resistance Response to Binary Gas Mixtures Containing 1000 ppb NO_2 and Various NH_3 Concentrations. (Film Thickness = 0.32 μm. Temperature = 100° C.)

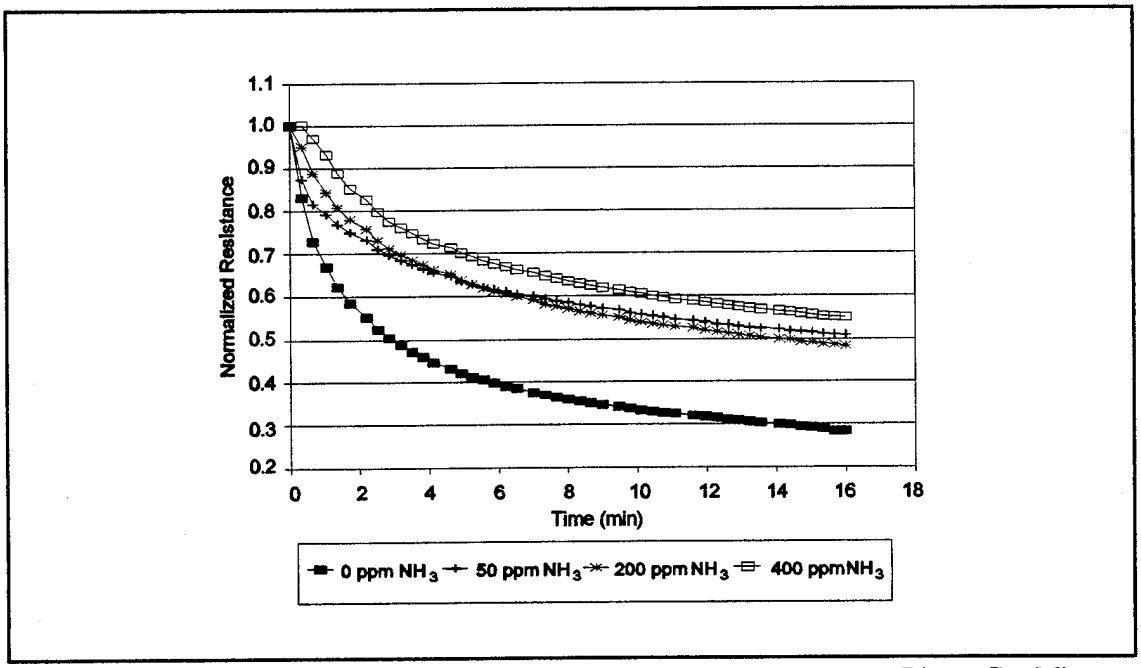


Figure K-8. NiPc-Coated IGE Structure Normalized DC Resistance Response to Binary Gas Mixtures Containing 1000 ppb NO_2 and Various NH_3 Concentrations. (Film Thickness = 0.43 μm. Temperature = 100° C.)

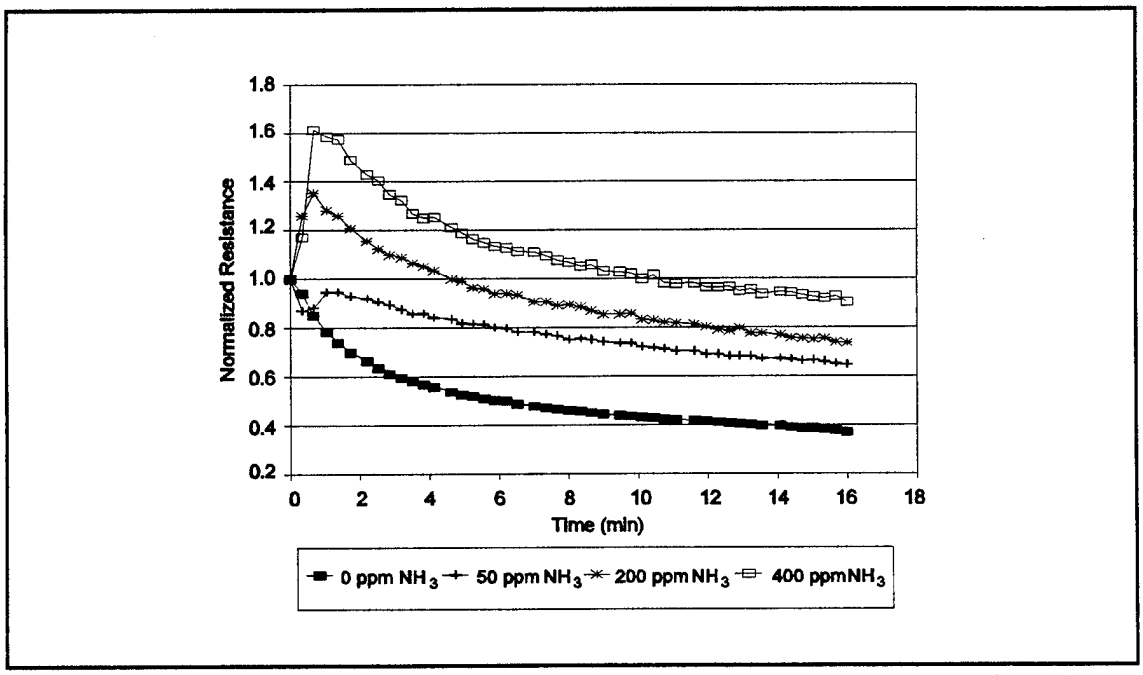


Figure K-9. CoPc-Coated IGE Structure Normalized DC Resistance Response to Binary Gas Mixtures Containing 1000 ppb NO_2 and Various NH_3 Concentrations. (Film Thickness = 0.51 µm. Temperature = 100° C.)

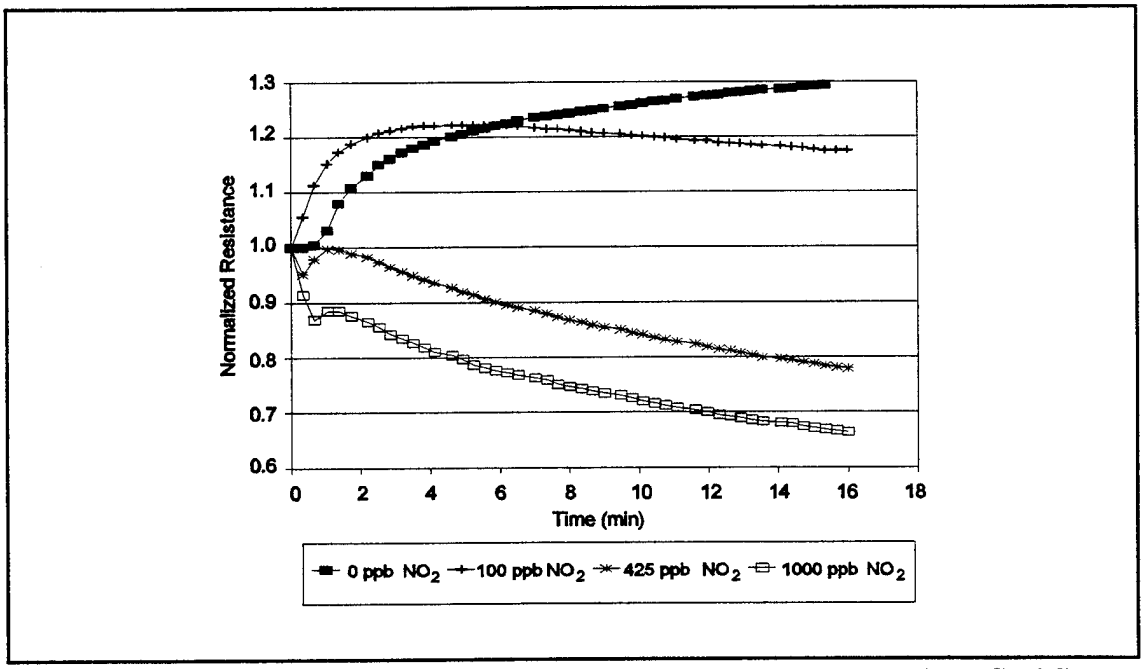


Figure K-10. CuPc-Coated IGE Structure Normalized DC Resistance Response to Binary Gas Mixtures Containing 50 ppm NH_3 and Various NO_2 Concentrations. (Film Thickness = 0.32 µm. Temperature = 100° C.)

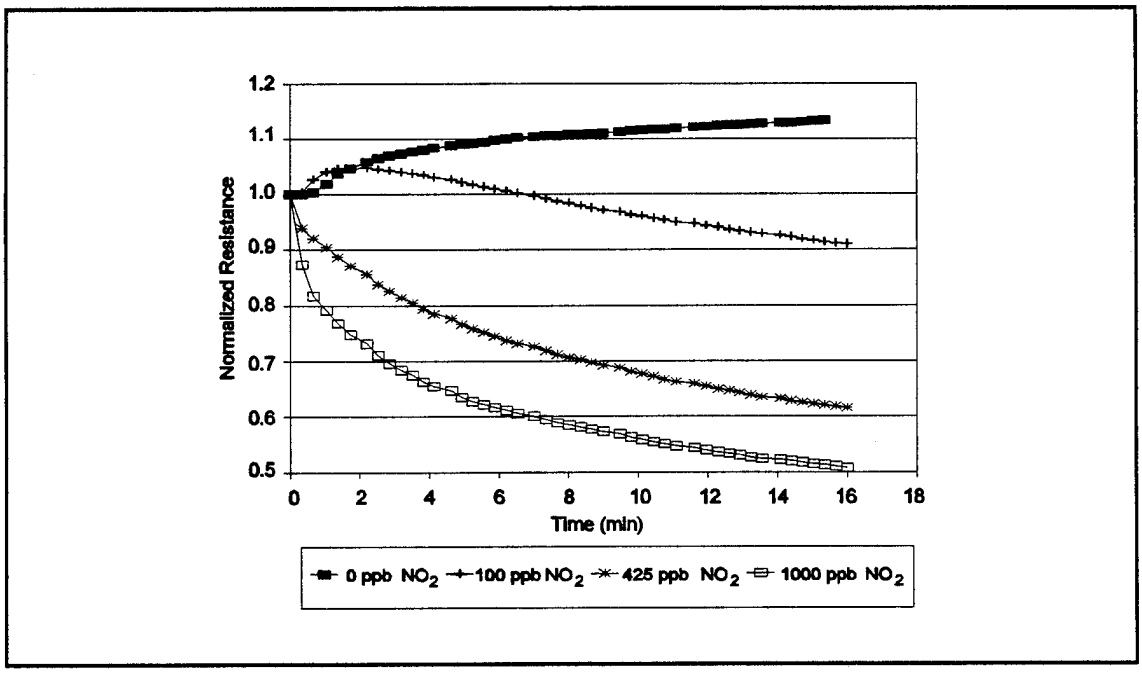


Figure K-11. NiPc-Coated IGE Structure Normalized DC Resistance Response to Binary Gas Mixtures Containing 50 ppm NH_3 and Various NO_2 Concentrations. (Film Thickness = 0.43 μm. Temperature = 100° C.)

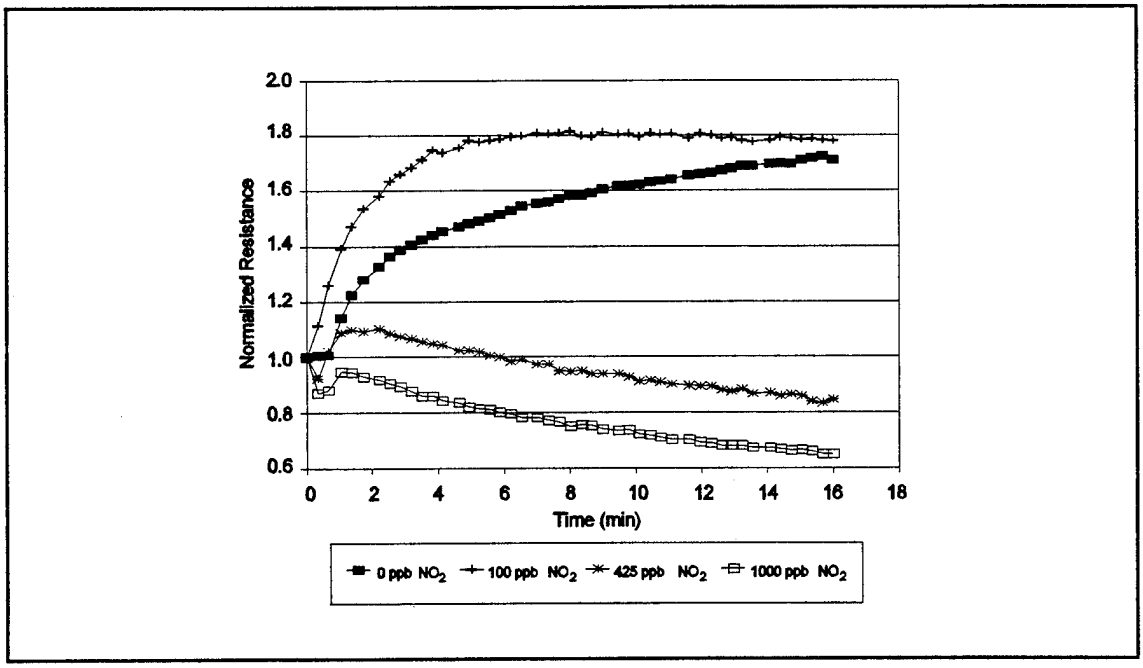


Figure K-12. CoPc-Coated IGE Structure Normalized DC Resistance Response to Binary Gas Mixtures Containing 50 ppm NH_3 and Various NO_2 Concentrations. (Film Thickness = 0.51 μm. Temperature = 100° C.)

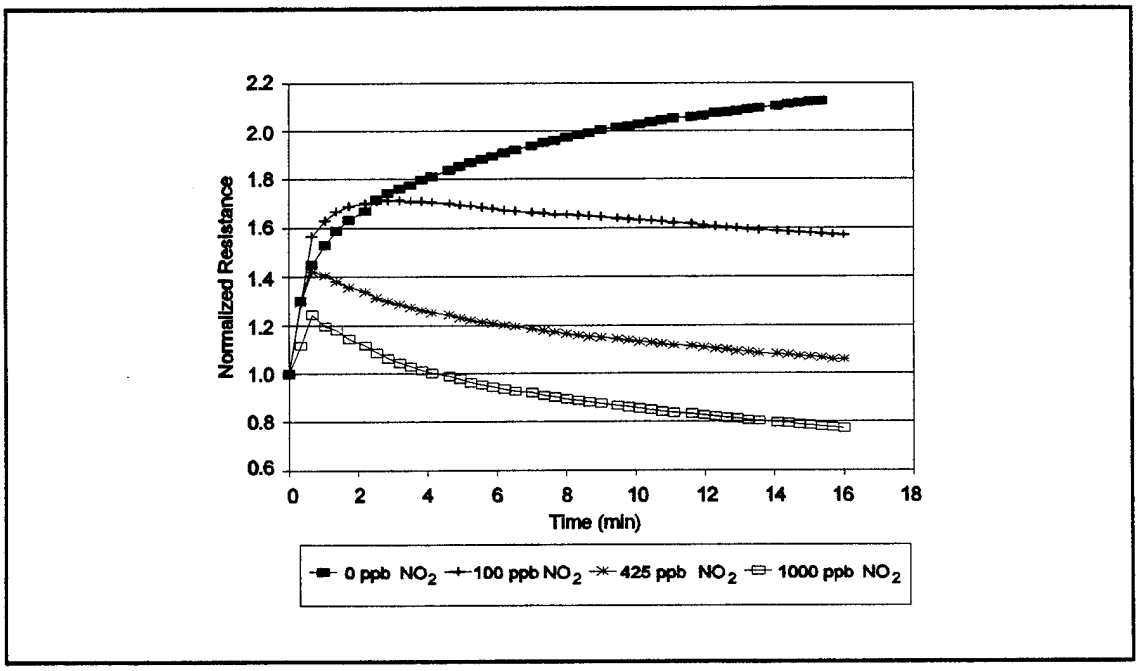


Figure K-13. CuPc-Coated IGE Structure Normalized DC Resistance Response to Binary Gas Mixtures Containing 400 ppm NH_3 and Various NO_2 Concentrations. (Film Thickness = 0.32 μm. Temperature = 100° C.)

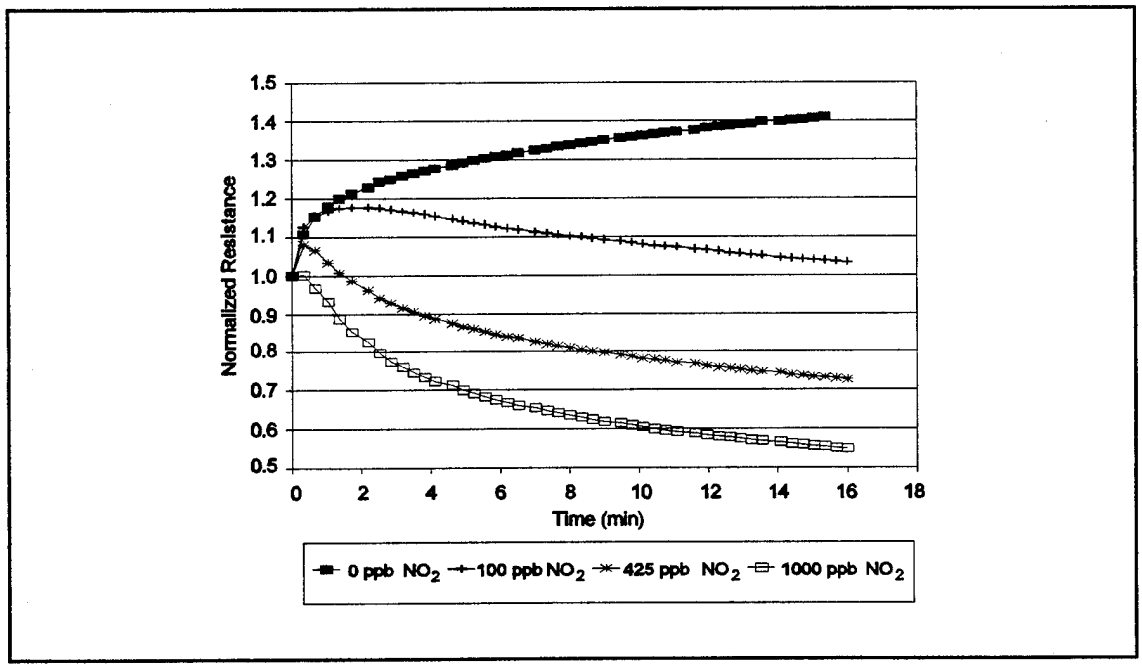


Figure K-14. NiPc-Coated IGE Structure Normalized DC Resistance Response to Binary Gas Mixtures Containing 400 ppm NH_3 and Various NO_2 Concentrations. (Film Thickness = 0.43 μm. Temperature = 100° C.)

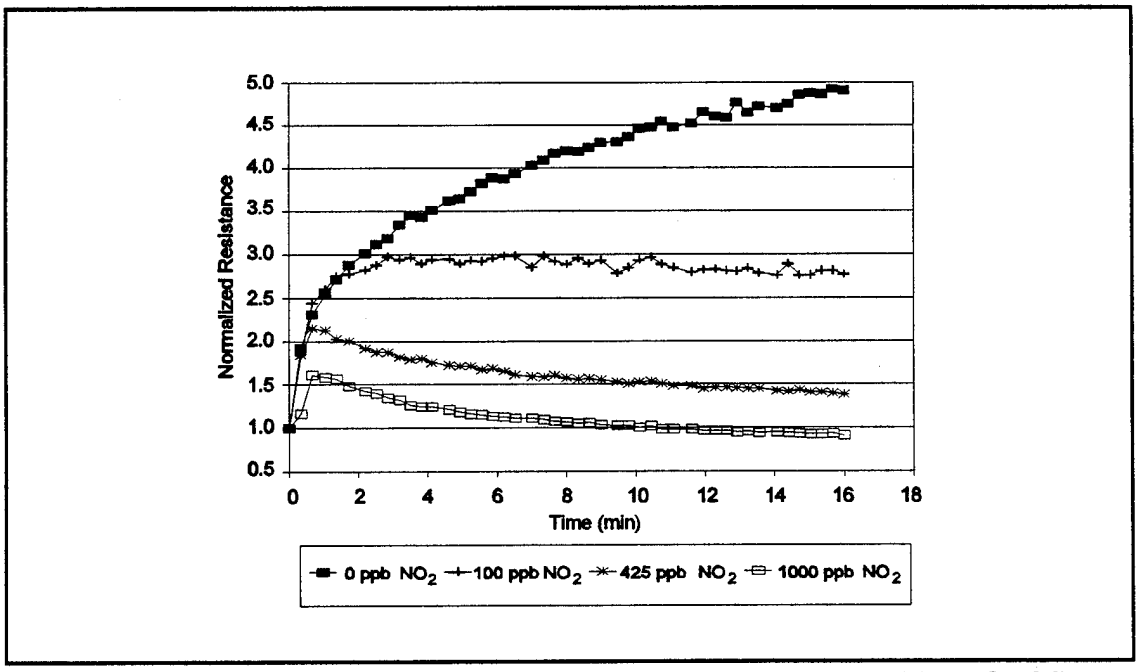


Figure K-15. CoPc-Coated IGE Structure Normalized DC Resistance Response to Binary Gas Mixtures Containing 400 ppm NH_3 and Various NO_2 Concentrations. (Film Thickness = 0.51 μm. Temperature = 100° C.)

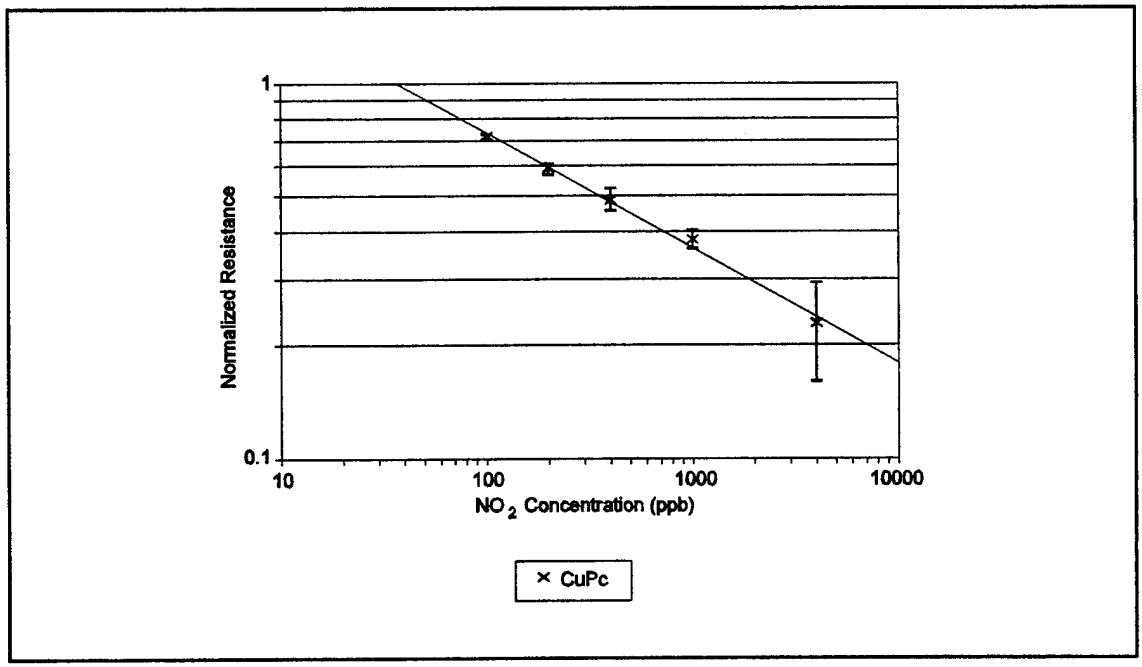


Figure K-16. Concentration Dependence of the CuPc-Coated IGE Structure Normalized DC Resistance Response to Nitrogen Dioxide (NO_2). Error Bars Indicate the Maximum and Minimum Normalized Resistances in a Data Set which Included the Responses Measured From Two IGEFET Sensor Elements After Triplicate Exposures to the Challenge Gas. (Film Thickness = 0.32 μm. Temperature = 100 ° C.)

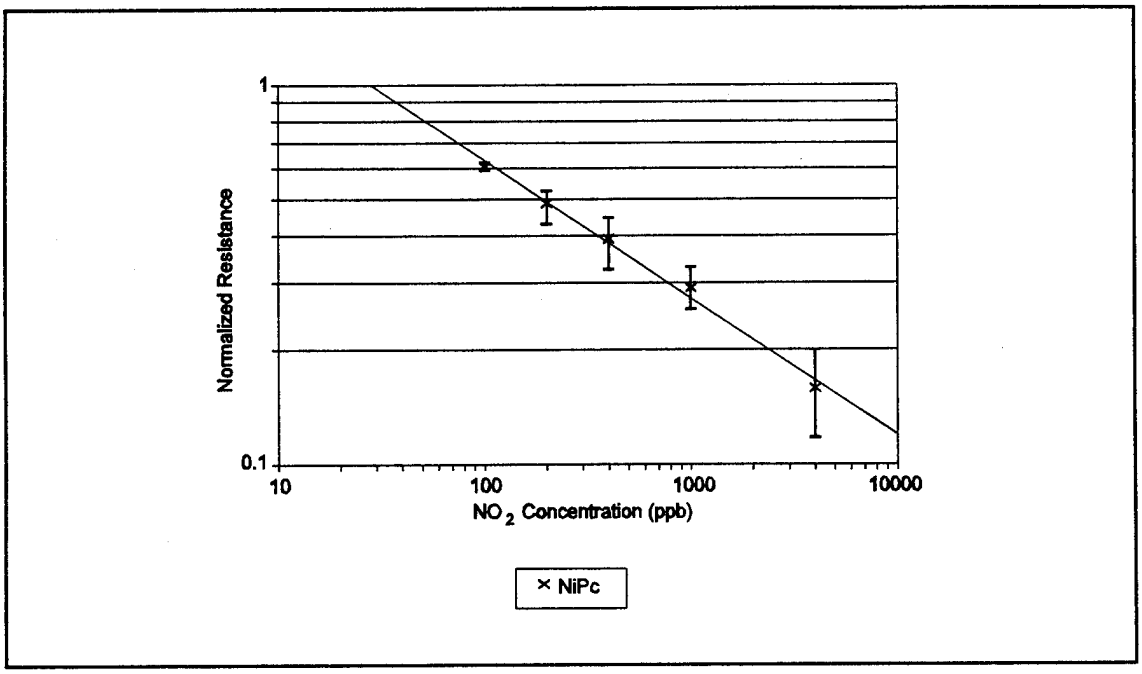


Figure K-17. Concentration Dependence of the NiPc-Coated IGE Structure Normalized DC Resistance Response to Nitrogen Dioxide (NO_2). Error Bars Indicate the Maximum and Minimum Normalized Resistances in a Data Set which Included the Responses Measured From Two IGEFET Sensor Elements After Triplicate Exposures to the Challenge Gas. (Film Thickness = 0.43 μm. Temperature = 100 °C.)

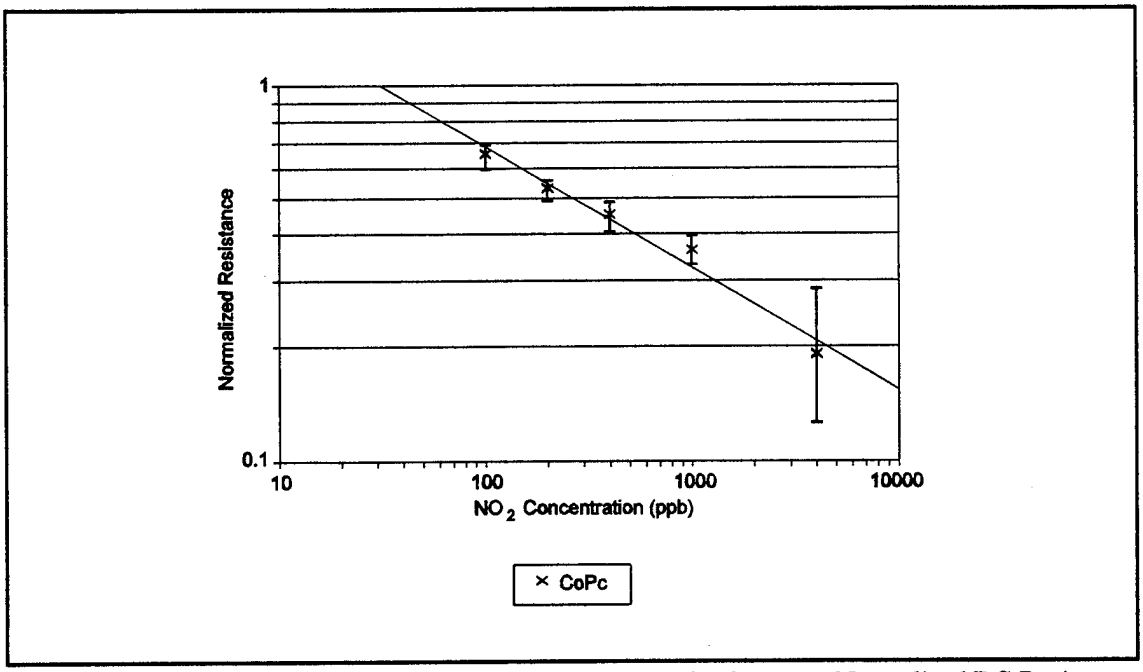


Figure K-18. Concentration Dependence of the CoPc-Coated IGE Structure Normalized DC Resistance Response to Nitrogen Dioxide (NO_2). Error Bars Indicate the Maximum and Minimum Normalized Resistances in a Data Set which Included the Responses Measured From Two IGEFET Sensor Elements After Triplicate Exposures to the Challenge Gas. (Film Thickness = 0.51 μm. Temperature = 100 °C.)

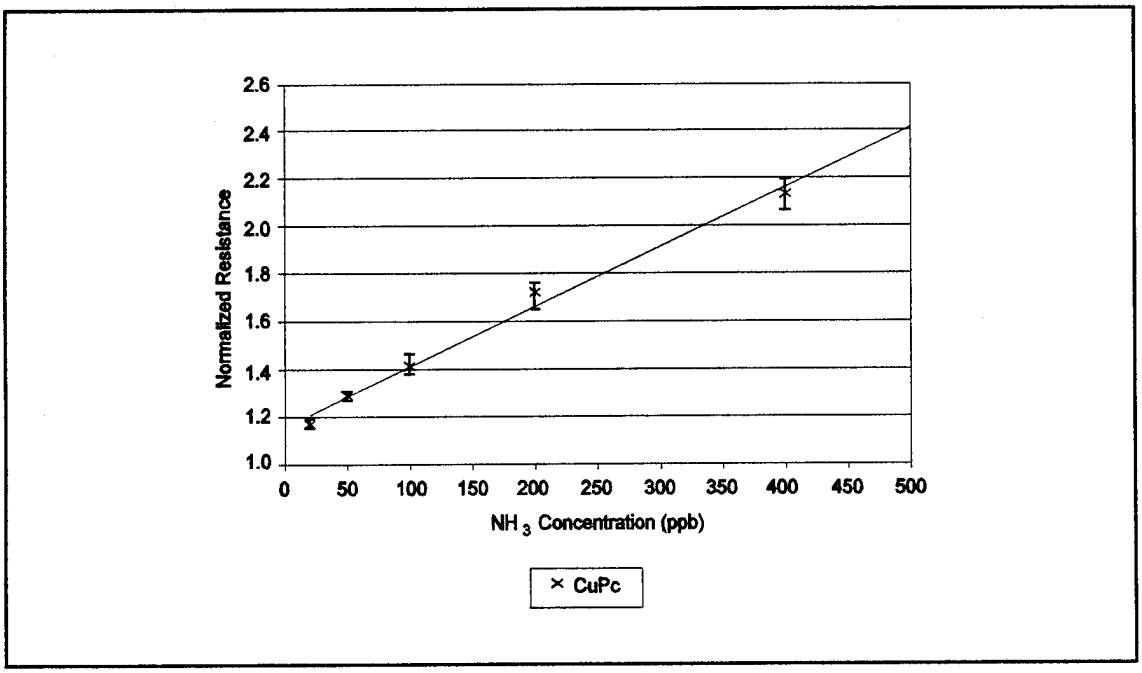


Figure K-19. Concentration Dependence of the CuPc-Coated IGE Structure Normalized DC Resistance Response to Ammonia (NH_3). Error Bars Indicate the Maximum and Minimum Normalized Resistances in a Data Set which Included the Responses Measured From Two IGEFET Sensor Elements After Triplicate Exposures to the Challenge Gas. (Film Thickness = 0.32 μm. Temperature = 100 °C.)

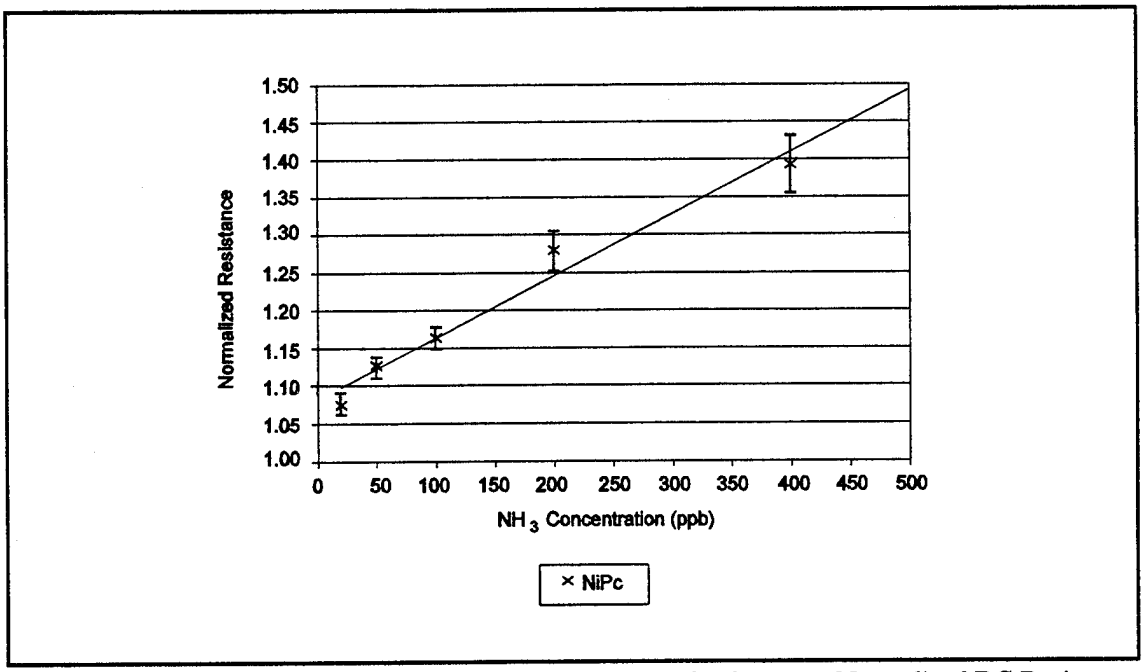


Figure K-20. Concentration Dependence of the NiPc-Coated IGE Structure Normalized DC Resistance Response to Ammonia (NH_3). Error Bars Indicate the Maximum and Minimum Normalized Resistances in a Data Set which Included the Responses Measured From Two IGEFET Sensor Elements After Triplicate Exposures to the Challenge Gas. (Film Thickness = 0.43 μm. Temperature = 100 °C.)

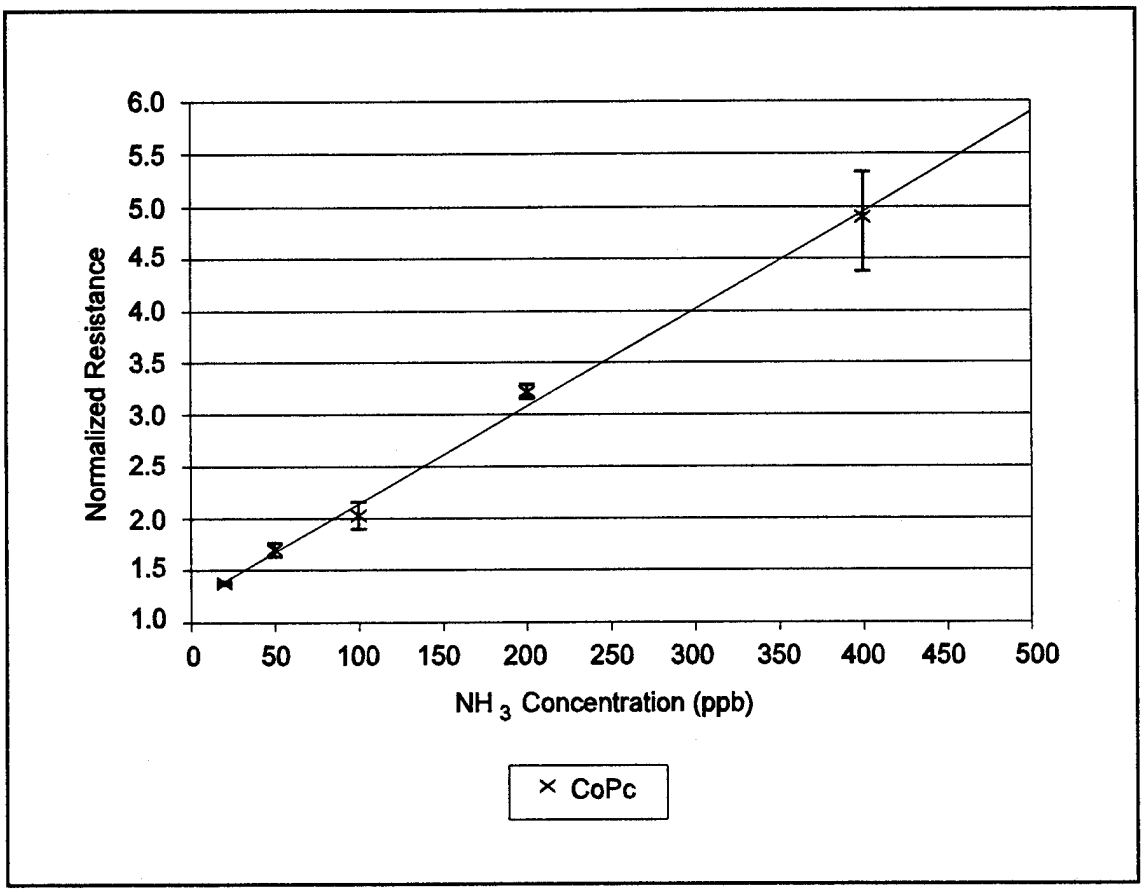


Figure K-21. Concentration Dependence of the CoPc-Coated IGE Structure Normalized DC Resistance Response to Ammonia (NH_3). Horizontal Bars Indicate the Maximum and Minimum Normalized Resistances in a Data Set which Included the Responses Measured From Two IGEFET Sensor Elements After Triplicate Exposures to the Challenge Gas. (Film Thickness = 0.51 μm. Temperature = 100 °C.)

Appendix L: Least-Squares Curve Fit Parameters Used to Form Feature Vectors and Examples of Feature Vectors Used for the Gas Analyses

This appendix presents the least-squares parameters used to curve fit the electrical response data to functions of each single component gas concentration. With the appropriate mathematical transformation of the electrical response data, the functional forms utilized were fit using linear least-squares analysis. As discussed in Chapter VI, different functional forms were used to linearize the different electrical response measurements. In addition to the least-squares curve fit parameters, examples of the resulting calibration and test feature vectors that are based upon these functional forms are provided. Tables L-1 through L-12, L-13 through L-22, L-23 through L-32, and L-33 through L-34 correspond to the gas analyses conducted with the normalized resistance data, gain response data, phase response data, and the conductance parameters extracted from the transfer function measurements, respectively.

Table L-1. Least-Squares Fit Parameters for the CuPc-Coated IGE Structure's Normalized DC Resistance Response as a Function of the NO_2 Challenge Gas Concentration. (Data Fitted to an Equation of the Form: $C=AR_N^{\alpha} + B$. R^2-Correlation Coefficient)

	Time (min)					
	1	1.5	3	6	9	16
α	-3.37	-3.37	-3.37	-3.37	-3.37	-3.37
A	640	376	191	88	57	26
B	-670	-404	-192	-40	21	120
R^2	.9993	.9995	.9996	.9988	.9978	.9942

Table L-2. Least-Squares Fit Parameters for the NiPc-Coated IGE Structure's Normalized DC Resistance Response as a Function of the NO_2 Challenge Gas Concentration. (Data Fitted to an Equation of the Form: $C=AR_N^{\alpha} + B$. R^2-Correlation Coefficient)

	Time (min)					
	1	1.5	3	6	9	16
α	-3.14	-3.14	-3.14	-3.14	-3.14	-3.14
A	303	167	83	39	25	11
B	-212	-60	38	91	121	173
R^2	.9976	.9968	.9962	.9962	.9953	.9922

Table L-3. Least-Squares Fit Parameters for the CoPc-Coated IGE Structure's Normalized DC Resistance Response as a Function of the NO_2 Challenge Gas Concentration. (Data Fitted to an Equation of the Form: $C=AR_N^{\alpha} + B$. R^2-Correlation Coefficient)

	Time (min)					
	1	1.5	3	6	9	16
α	-1.73	-1.73	-1.73	-1.73	-1.73	-1.73
A	1523	1060	710	471	385	267
B	-1441	-1061	-801	-639	-599	-502
R^2	.9971	.9978	.9983	.9980	.9980	.9982

Table L-4. Calibration Vectors Formed From the Normalized DC Resistance Data for Single Component Nitrogen Dioxide Challenge Gas Exposures.

MPc Film Type	Time Slice (min)	Nitrogen Dioxide Concentration (ppb)				
		100	200	400	1000	4000
CuPc	1	1.11	1.39	1.76	2.59	7.30
	1.5	1.22	1.62	2.27	3.71	11.70
	3	1.46	2.10	3.32	6.01	21.99
	6	1.90	3.00	5.34	10.65	46.01
	9	2.26	3.80	7.15	14.81	70.41
	16	3.10	5.81	11.51	25.97	152.44
NiPc	1	1.16	1.58	2.05	3.55	14.00
	1.5	1.33	1.95	2.76	5.39	24.41
	3	1.71	2.76	4.33	9.55	48.15
	6	2.49	4.49	7.71	19.17	101.94
	9	3.16	6.01	10.94	28.17	158.92
	16	4.93	10.18	19.38	52.11	342.93
CoPc	1	1.00	1.16	1.22	1.52	3.58
	1.5	1.04	1.28	1.42	1.86	4.79
	3	1.16	1.51	1.77	2.46	6.76
	6	1.39	1.92	2.37	3.34	9.85
	9	1.57	2.21	2.82	4.04	11.92
	16	1.94	2.80	3.73	5.51	16.85

Table L-5. Typical Test Vectors Formed From the Normalized DC Resistance Data for Single Component Nitrogen Dioxide Challenge Gas Exposures.

MPc Film Type	Time Slice (min)	Nitrogen Dioxide Concentration (ppb)				
		100	200	400	1000	4000
CuPc	1	1.04	1.41	1.95	2.21	4.60
	1.5	1.13	1.64	2.51	2.86	7.13
	3	1.35	2.14	3.65	4.27	12.66
	6	1.81	3.07	5.84	7.06	23.84
	9	2.19	3.84	7.83	9.29	33.19
	16	3.03	5.74	12.41	15.73	61.86
NiPc	1	1.02	1.51	1.95	2.34	9.02
	1.5	1.11	1.83	2.55	3.14	15.35
	3	1.32	2.55	3.90	4.99	29.51
	6	1.72	4.04	6.79	8.98	57.09
	9	2.05	5.34	9.44	12.55	83.57
	16	2.77	8.77	16.10	21.73	157.92
CoPc	1	0.92	1.18	1.32	1.44	2.42
	1.5	0.88	1.29	1.55	1.63	3.09
	3	1.17	1.53	1.93	2.04	4.17
	6	1.42	1.92	2.54	2.72	5.90
	9	1.64	2.17	3.02	3.20	7.02
	16	2.06	2.74	3.91	4.10	9.57

Table L-6. Least-Squares Fit Parameters for the CuPc-Coated IGE Structure's Normalized DC Resistance Response as a Function of the NH_3 Challenge Gas Concentration. (Data Fitted to an Equation of the Form: $C=AR_N + B$. R^2-Correlation Coefficient)

	Time (min)					
	1	1.5	3	6	9	16
α	1	1	1	1	1	1
A	652	590	541	477	442	395
B	-634	-596	-576	-528	-496	-458
R^2	.952	.960	.976	.985	.987	.985

Table L-7. Least-Squares Fit Parameters for the NiPc-Coated IGE Structure's Normalized DC Resistance Response as a Function of the NH_3 Challenge Gas Concentration. (Data Fitted to an Equation of the Form: $C=AR_N + B$. R^2-Correlation Coefficient)

	Time (min)					
	1	1.5	3	6	9	16
α	1	1	1	1	1	1
A	1945	1743	1610	1435	1304	1131
B	-1931	-1756	-1662	-1514	-1389	-1223
R^2	.949	.934	.950	.961	.962	.967

Table L-8. Least-Squares Fit Parameters for the CoPc-Coated IGE Structure's Normalized DC Resistance Response as a Function of the NH_3 Challenge Gas Concentration. (Data Fitted to an Equation of the Form: $C=AR_N + B$. R^2-Correlation Coefficient)

	Time (min)					
	1	1.5	3	6	9	16
α	1	1	1	1	1	1
A	233	204	173	143	128	108
B	-215	-203	-187	-164	-148	-130
R^2	.972	.987	.995	.992	.995	.994

Table L-9. Calibration Vectors Formed From the Normalized DC Resistance Data for Single Component Ammonia Challenge Gas Exposures.

MPc Film Type	Time Slice (min)	Nitrogen Dioxide Concentration (ppm)				
		20	50	100	200	400
CuPc	1	1.00	1.03	1.12	1.36	1.53
	1.5	1.00	1.11	1.20	1.42	1.63
	3	1.06	1.17	1.26	1.50	1.76
	6	1.12	1.23	1.31	1.59	1.91
	9	1.14	1.25	1.34	1.64	1.99
	16	1.18	1.29	1.41	1.74	2.13
NiPc	1	1.00	1.02	1.04	1.13	1.18
	1.5	1.00	1.05	1.07	1.15	1.21
	3	1.02	1.07	1.10	1.18	1.26
	6	1.05	1.10	1.13	1.22	1.31
	9	1.06	1.11	1.14	1.25	1.35
	16	1.08	1.13	1.17	1.30	1.41
CoPc	1	1.00	1.14	1.27	1.96	2.54
	1.5	1.04	1.28	1.47	2.10	2.88
	3	1.15	1.41	1.61	2.33	3.34
	6	1.26	1.53	1.76	2.69	3.87
	9	1.30	1.59	1.84	2.84	4.24
	16	1.38	1.72	2.01	3.24	4.86

Table L-10. Typical Test Vectors Formed From the Normalized DC Resistance Data for Single Component Ammonia Challenge Gas Exposures.

MPc Film Type	Time Slice (min)	Ammonia Concentration (ppm)				
		20	50	100	200	400
CuPc	1	1.00	1.00	1.08	1.37	1.54
	1.5	1.00	1.09	1.19	1.42	1.65
	3	1.05	1.17	1.24	1.50	1.79
	6	1.12	1.23	1.30	1.59	1.95
	9	1.15	1.25	1.33	1.63	2.03
	16	1.19	1.30	1.39	1.74	2.18
NiPc	1	1.00	1.00	1.04	1.13	1.17
	1.5	1.00	1.04	1.08	1.16	1.20
	3	1.02	1.08	1.10	1.19	1.26
	6	1.05	1.11	1.13	1.23	1.32
	9	1.06	1.11	1.14	1.26	1.35
	16	1.08	1.14	1.17	1.30	1.42
CoPc	1	1.00	1.10	1.11	1.92	2.54
	1.5	1.00	1.26	1.39	2.09	2.84
	3	1.17	1.42	1.51	2.32	3.42
	6	1.28	1.56	1.65	2.73	4.02
	9	1.31	1.63	1.73	2.79	4.39
	16	1.40	1.75	1.88	3.13	5.08

Table L-11. Calibration Vectors Formed From the IGE Structure's Normalized DC Resistance Response to Binary Gas Mixtures of Ammonia and Nitrogen Dioxide.

MPc Film Type	Time Slice (min)	50 ppm NH_3			200 ppm NH_3			400 ppm NH_3		
		Nitrogen Dioxide Concentration (ppb)			Nitrogen Dioxide Concentration (ppb)			Nitrogen Dioxide Concentration (ppb)		
		100	425	1000	100	425	1000	100	425	1000
CuPc	1	1.15	0.99	0.88	1.37	1.25	1.04	1.63	1.40	1.19
	1.5	1.18	0.98	0.87	1.44	1.22	1.00	1.68	1.35	1.14
	3	1.21	0.95	0.83	1.47	1.16	0.91	1.71	1.28	1.04
	6	1.22	0.89	0.77	1.45	1.09	0.80	1.67	1.20	0.93
	9	1.20	0.85	0.73	1.40	1.04	0.74	1.64	1.15	0.87
	16	1.17	0.77	0.66	1.34	0.94	0.64	1.57	1.05	0.77
NiPc	1	1.03	0.90	0.79	1.11	1.00	0.84	1.16	1.03	0.93
	1.5	1.04	0.87	0.74	1.12	0.95	0.77	1.17	0.98	0.85
	3	1.04	0.81	0.68	1.12	0.88	0.69	1.16	0.91	0.76
	6	1.00	0.73	0.61	1.08	0.80	0.60	1.12	0.83	0.66
	9	0.97	0.69	0.57	1.03	0.76	0.55	1.09	0.79	0.61
	16	0.91	0.61	0.50	0.96	0.68	0.48	1.03	0.72	0.54
CoPc	1	1.39	1.08	0.94	2.01	1.65	1.28	2.60	2.12	1.58
	1.5	1.53	1.09	0.92	2.25	1.60	1.20	2.77	2.00	1.49
	3	1.68	1.06	0.87	2.42	1.49	1.08	2.93	1.82	1.32
	6	1.79	0.98	0.79	2.44	1.38	0.93	2.98	1.65	1.12
	9	1.80	0.93	0.74	2.40	1.28	0.85	2.92	1.55	1.03
	16	1.77	0.84	0.64	2.20	1.12	0.73	2.76	1.38	0.90
CuPc	1	0.62	1.00	1.50	0.34	0.46	0.85	0.19	0.31	0.54
	1.5	0.55	1.03	1.56	0.29	0.50	0.99	0.17	0.35	0.63
	3	0.51	1.16	1.84	0.26	0.59	1.36	0.16	0.42	0.86
	6	0.51	1.44	2.38	0.28	0.74	2.08	0.17	0.53	1.24
	9	0.53	1.69	2.81	0.31	0.87	2.72	0.18	0.62	1.57
	16	0.58	2.32	3.99	0.37	1.21	4.36	0.21	0.82	2.38
NiPc	1	0.88	1.37	2.08	0.71	0.98	1.71	0.61	0.89	1.25
	1.5	0.86	1.54	2.48	0.68	1.14	2.18	0.59	1.04	1.65
	3	0.88	1.90	3.29	0.68	1.44	3.09	0.61	1.32	2.36
	6	0.98	2.59	4.69	0.78	1.94	4.83	0.69	1.73	3.54
	9	1.09	3.17	5.77	0.88	2.34	6.32	0.75	2.04	4.50
	16	1.34	4.60	8.39	1.11	3.31	9.80	0.90	2.73	6.56
CoPc	1	0.56	0.86	1.09	0.29	0.42	0.65	0.19	0.27	0.45
	1.5	0.47	0.85	1.14	0.24	0.44	0.72	0.17	0.29	0.50
	3	0.40	0.89	1.25	0.21	0.49	0.86	0.15	0.35	0.61
	6	0.36	1.02	1.48	0.21	0.56	1.11	0.15	0.41	0.81
	9	0.35	1.11	1.68	0.21	0.64	1.31	0.15	0.46	0.95
	16	0.36	1.33	2.11	0.25	0.81	1.69	0.17	0.56	1.19

Table L-12. Typical Test Vectors Formed From the IGE Structure's Normalized DC Resistance Response to Binary Gas Mixtures of Ammonia and Nitrogen Dioxide.

MPc Film Type	Time Slice (min)	50 ppm NH_3			200 ppm NH_3			400 ppm NH_3		
		Nitrogen Dioxide Concentration (ppb)			Nitrogen Dioxide Concentration (ppb)			Nitrogen Dioxide Concentration (ppb)		
		100	425	1000	100	425	1000	100	425	1000
CuPc	1	1.14	1.02	0.89	1.39	1.34	1.08	1.67	1.52	1.20
	1.5	1.21	1.01	0.91	1.49	1.32	1.07	1.78	1.46	1.20
	3	1.27	0.98	0.89	1.57	1.26	0.97	1.88	1.39	1.11
	6	1.30	0.92	0.83	1.55	1.18	0.84	1.88	1.30	1.00
	9	1.30	0.88	0.78	1.51	1.13	0.77	1.84	1.24	0.94
	16	1.28	0.80	0.70	1.44	1.02	0.65	1.76	1.15	0.83
NiPc	1	1.05	0.92	0.79	1.12	1.06	0.87	1.17	1.10	0.91
	1.5	1.07	0.88	0.75	1.14	1.01	0.80	1.20	1.05	0.86
	3	1.08	0.83	0.69	1.16	0.94	0.71	1.23	0.97	0.78
	6	1.06	0.75	0.61	1.12	0.85	0.60	1.21	0.88	0.69
	9	1.02	0.70	0.56	1.07	0.80	0.55	1.17	0.84	0.63
	16	0.96	0.62	0.49	0.99	0.71	0.46	1.11	0.76	0.56
CoPc	1	1.32	1.16	1.01	2.13	1.88	1.46	2.90	2.46	1.69
	1.5	1.52	1.17	1.03	2.42	1.90	1.40	3.22	2.29	1.72
	3	1.77	1.16	1.00	2.73	1.78	1.26	3.63	2.12	1.52
	6	2.00	1.06	0.91	2.79	1.65	1.07	3.91	1.95	1.33
	9	2.04	1.00	0.83	2.83	1.52	0.97	3.70	1.83	1.22
	16	2.08	0.89	0.73	2.65	1.33	0.82	3.64	1.65	1.06
CuPc	1	0.63	0.92	1.46	0.32	0.36	0.74	0.17	0.24	0.53
	1.5	0.52	0.95	1.33	0.26	0.39	0.79	0.14	0.27	0.53
	3	0.43	1.06	1.47	0.21	0.45	1.10	0.11	0.32	0.68
	6	0.40	1.30	1.86	0.22	0.56	1.75	0.11	0.41	0.97
	9	0.40	1.52	2.24	0.24	0.65	2.38	0.12	0.47	1.22
	16	0.43	2.10	3.29	0.28	0.93	4.08	0.14	0.61	1.85
NiPc	1	0.85	1.28	2.08	0.70	0.81	1.54	0.59	0.73	1.31
	1.5	0.80	1.45	2.42	0.65	0.94	1.98	0.55	0.85	1.59
	3	0.77	1.78	3.17	0.61	1.20	2.90	0.51	1.09	2.17
	6	0.82	2.41	4.64	0.69	1.63	4.78	0.54	1.45	3.19
	9	0.91	2.98	5.94	0.78	1.98	6.50	0.59	1.72	4.06
	16	1.10	4.41	9.27	1.00	2.88	10.7	0.71	2.29	6.02
CoPc	1	0.61	0.76	0.97	0.26	0.33	0.51	0.15	0.20	0.40
	1.5	0.48	0.76	0.93	0.21	0.32	0.55	0.13	0.23	0.39
	3	0.37	0.76	0.99	0.17	0.36	0.66	0.10	0.27	0.48
	6	0.30	0.89	1.17	0.16	0.41	0.88	0.09	0.31	0.60
	9	0.28	0.98	1.36	0.16	0.48	1.04	0.10	0.34	0.70
	16	0.28	1.20	1.70	0.18	0.60	1.40	0.10	0.41	0.89

Table L-13. Least-Squares Fit Parameters for the CuPc-Coated IGEFET Transfer Function Gain Response as a Function of the NO_2 Challenge Gas Concentration. (Data Fitted to an Equation of the Form: $\log(C) = AG_N + B$)

	Time Slice					
	1 (2.4 min)	2 (4.7 min)	3 (7.1 min)	4 (9.5 min)	5 (12 min)	6 (14 min)
Low Frequency Gain Response Maxima						
A	0.16	0.14	0.13	0.12	0.12	0.12
B	2.10	2.03	1.98	1.91	1.87	1.86
R^2	0.97	0.98	0.98	0.98	0.98	0.99
High Frequency Gain Response Maxima						
A	0.54	0.51	0.48	0.47	0.46	0.45
B	2.22	2.08	2.01	1.95	1.90	1.89
R^2	0.88	0.94	0.95	0.95	0.95	0.95

Table L-14. Least-Squares Fit Parameters for the NiPc-Coated IGEFET Transfer Function Gain Response as a Function of the NO_2 Challenge Gas Concentration. (Data Fitted to an Equation of the Form: $\log(C)=AG_N + B$)

	Time Slice					
	1 (2.4 min)	2 (4.7 min)	3 (7.1 min)	4 (9.5 min)	5 (12 min)	6 (14 min)
Low Frequency Gain Response Maxima						
A	0.17	0.15	0.14	0.13	0.13	0.13
B	2.13	2.01	1.94	1.87	1.83	1.80
R^2	0.97	0.99	0.99	1.00	1.00	1.00
High Frequency Gain Response Maxima						
A	0.58	0.53	0.53	0.54	0.53	0.55
B	2.12	1.94	1.81	1.69	1.62	1.52
R^2	0.96	1.00	1.00	0.99	0.99	0.99

Table L-15. Calibration Vectors Formed From the IGEFET Transfer Function Gain Response Data for Single Component Nitrogen Dioxide Challenge Gas Exposures.

MPc Film Type	Time Slice (min)	Nitrogen Dioxide Concentration (ppb)				
		100	200	400	1000	4000
CuPc	2.4	-0.14	1.48	3.12	4.74	10.15
	4.7	0.24	2.42	3.87	5.98	12.04
	7.1	0.60	3.09	4.38	7.00	13.31
	9.5	1.08	3.65	5.14	7.79	14.23
	2.4	0.08	0.31	0.33	0.96	2.72
	4.7	0.15	0.54	0.84	1.36	3.20
	7.1	0.25	0.72	1.06	1.61	3.49
	9.5	0.35	0.87	1.23	1.80	3.71
NiPc	2.4	-0.05	1.13	2.36	4.17	9.09
	4.7	0.29	2.14	3.73	6.00	11.14
	7.1	0.64	2.83	4.61	7.12	12.35
	9.5	1.08	3.38	5.34	7.92	13.22
	2.4	-0.02	0.39	0.69	1.23	2.72
	4.7	0.12	0.74	1.21	1.87	3.17
	7.1	0.30	1.01	1.53	2.20	3.38
	9.5	0.48	1.24	1.77	2.40	3.52

Table L-16. Typical Test Vectors Formed From the IGEFET Transfer Function Gain Response Data for Single Component Nitrogen Dioxide Challenge Gas Exposures.

MPc Film Type	Time Slice (min)	Nitrogen Dioxide Concentration (ppb)				
		100	200	400	1000	4000
CuPc	2.4	-0.16	1.52	3.11	4.40	5.42
	4.7	-0.30	2.43	4.54	5.84	6.14
	7.1	-0.13	3.10	4.27	6.78	7.19
	9.5	0.41	3.66	4.99	7.52	8.02
	2.4	0.06	0.32	0.52	0.89	1.05
	4.7	0.07	0.55	0.79	1.24	1.50
	7.1	0.17	0.71	1.01	1.47	1.76
	9.5	0.27	0.85	1.16	1.65	1.96
NiPc	2.4	-0.07	1.12	2.36	4.11	4.23
	4.7	-0.09	2.07	3.59	5.70	6.35
	7.1	0.05	2.73	4.40	6.72	7.57
	9.5	0.51	3.25	5.10	7.46	8.43
	2.4	-0.10	0.38	0.62	1.12	1.35
	4.7	-0.12	0.72	1.10	1.67	2.11
	7.1	0.17	0.99	1.40	1.97	2.45
	9.5	0.48	1.21	1.62	2.16	2.66

Table L-17. Least-Squares Fit Parameters for the CuPc-Coated IGEFET Transfer Function Gain Response as a Function of the NH_3 Challenge Gas Concentration. (Data Fitted to an Equation of the Form: $\log(C) = AG_N + B$)

	Time Slice					
	1 (2.4 min)	2 (4.7 min)	3 (7.1 min)	4 (9.5 min)	5 (12 min)	6 (14 min)
Low Frequency Gain Response Maxima						
A	-0.29	-0.29	-0.28	-0.27	-0.26	-0.25
B	1.34	1.18	1.15	1.15	1.14	1.13
R^2	0.98	0.96	0.95	0.94	0.94	0.94
High Frequency Gain Response Maxima						
A	-1.16	-1.11	-1.05	-1.00	-1.00	-0.95
B	1.38	1.26	1.23	1.22	1.16	1.18
R^2	0.98	0.95	0.93	0.94	0.95	0.95

Table L-18. Least-Squares Fit Parameters for the NiPc-Coated IGEFET Transfer Function Gain Response as a Function of the NH_3 Challenge Gas Concentration. (Data Fitted to an Equation of the Form: $\log(C)=AG_N + B$)

	Time Slice					
	1 (2.4 min)	2 (4.7 min)	3 (7.1 min)	4 (9.5 min)	5 (12 min)	6 (14 min)
Low Frequency Gain Response Maxima						
A	-1.76	-1.40	-1.22	-1.08	-0.97	-0.89
B	1.21	1.06	1.01	1.01	1.03	1.02
R^2	0.95	0.96	0.95	0.96	0.95	0.96
High Frequency Gain Response Maxima						
A	-4.16	-2.94	-2.70	-2.45	-2.07	-2.39
B	1.19	1.10	1.06	1.04	1.10	0.88
R^2	0.89	0.93	0.95	0.95	0.94	0.93

Table L-19. Calibration Vectors Formed From the IGEFET Transfer Function Gain Response Data for Single Component Ammonia Challenge Gas Exposures.

MPc Film Type	Time Slice (min)	Ammonia Concentration (ppm)				
		20	50	100	200	400
CuPc	2.4	-0.17	-1.14	-1.93	-3.35	-4.51
	4.7	-0.88	-1.56	-2.31	-3.83	-5.04
	7.1	-1.08	-1.75	-2.50	-4.12	-5.37
	9.5	-1.18	-1.88	-2.62	-4.30	-5.75
	2.4	-0.01	-0.24	-0.44	-0.80	-1.09
	4.7	-0.17	-0.33	-0.54	-0.95	-1.26
	7.1	-0.25	-0.35	-0.59	-1.01	-1.35
	9.5	-0.24	-0.42	-0.62	-1.07	-1.45
NiPc	2.4	-0.14	-0.20	-0.42	-0.58	-0.82
	4.7	-0.27	-0.36	-0.65	-0.88	-1.13
	7.1	-0.37	-0.46	-0.76	-1.06	-1.34
	9.5	-0.41	-0.55	-0.82	-1.19	-1.53
	2.4	-0.09	-0.07	-0.19	-0.27	-0.34
	4.7	-0.13	-0.16	-0.29	-0.38	-0.54
	7.1	-0.13	-0.22	-0.34	-0.40	-0.61
	9.5	-0.16	-0.26	-0.38	-0.45	-0.68

Table L-20. Typical Test Vectors Formed From the IGEFET Transfer Function Gain Response Data for Single Component Ammonia Challenge Gas Exposures.

MPc Film Type	Time Slice (min)	Ammonia Concentration (ppm)				
		20	50	100	200	400
CuPc	2.4	-0.20	-0.97	-1.85	-3.43	-4.22
	4.7	-1.10	-1.38	-2.22	-3.95	-4.63
	7.1	-1.30	-1.58	-2.39	-4.25	-4.91
	9.5	-1.44	-1.69	-2.47	-4.45	-5.50
	2.4	-0.03	-0.18	-0.34	-0.80	-1.03
	4.7	-0.24	-0.34	-0.53	-0.95	-1.16
	7.1	-0.30	-0.30	-0.45	-1.02	-1.24
	9.5	-0.33	-0.44	-0.46	-1.07	-1.39
NiPc	2.4	-0.26	-0.07	-0.33	-0.54	-0.73
	4.7	-0.43	-0.22	-0.56	-0.86	-1.00
	7.1	-0.52	-0.30	-0.64	-1.06	-1.18
	9.5	-0.55	-0.39	-0.69	-1.22	-1.38
	2.4	-0.06	-0.06	-0.14	-0.29	-0.28
	4.7	-0.14	-0.14	-0.25	-0.31	-0.53
	7.1	-0.19	-0.18	-0.30	-0.37	-0.59
	9.5	-0.22	-0.22	-0.32	-0.42	-0.67

Table L-21. Calibration Vectors Formed From the IGEFET Transfer Function Gain Response to Binary Mixtures of Ammonia and Nitrogen Dioxide.

MPc Film Type	Time Slice (min)	50 ppm NH_3			200 ppm NH_3			400 ppm NH_3		
		Nitrogen Dioxide Concentration (ppb)			Nitrogen Dioxide Concentration (ppb)			Nitrogen Dioxide Concentration (ppb)		
		100	425	1000	100	425	1000	100	425	1000
CuPc	2.4	-2.10	-0.98	1.92	-3.65	-3.53	1.92	-4.88	-4.18	1.63
	4.7	-2.87	0.19	2.93	-4.26	-1.34	4.20	-5.43	-0.41	4.04
	7.1	-3.43	1.02	3.42	-4.58	0.32	5.26	-5.20	0.91	5.02
	9.5	-3.83	1.66	3.86	-4.81	1.09	5.91	-4.39	1.69	5.62
	2.4	-0.53	0.14	1.91	-0.70	-0.04	1.98	-0.83	-0.05	1.93
	4.7	-0.92	0.80	2.92	-1.03	0.79	3.75	-1.15	1.15	3.72
	7.1	-1.27	1.47	3.46	-1.23	1.60	4.53	-1.13	2.00	4.43
	9.5	-1.55	1.98	3.89	-1.42	2.11	5.07	-0.81	2.44	4.90
NiPc	2.4	-0.46	-0.30	0.00	-0.89	-0.87	-0.21	-1.16	-1.13	-0.43
	4.7	-0.61	-0.16	0.32	-1.05	-0.73	0.39	-1.30	-0.86	0.14
	7.1	-0.70	0.04	0.48	-1.13	-0.50	0.70	-1.38	-0.63	0.48
	9.5	-0.75	0.20	0.61	-1.17	-0.33	0.89	-1.36	-0.47	0.68
	2.4	-0.17	-0.03	0.46	-0.28	-0.22	0.22	-0.29	-0.30	0.12
	4.7	-0.30	0.08	0.87	-0.40	-0.17	0.68	-0.47	-0.20	0.53
	7.1	-0.39	0.29	1.13	-0.47	0.01	1.00	-0.53	-0.03	0.81
	9.5	-0.44	0.49	1.31	-0.53	0.19	1.20	-0.55	0.14	0.99

Table L-22. Typical Test Vectors Formed From the IGEFET Transfer Function Gain Response to Binary Mixtures of Ammonia and Nitrogen Dioxide.

MPc Film Type	Time Slice (min)	50 ppm NH_3			200 ppm NH_3			400 ppm NH_3		
		Nitrogen Dioxide Concentration (ppb)			Nitrogen Dioxide Concentration (ppb)			Nitrogen Dioxide Concentration (ppb)		
		100	425	1000	100	425	1000	100	425	1000
CuPc	2.4	-2.30	-1.78	0.44	-3.67	-3.95	0.52	-5.20	-5.15	-0.26
	4.7	-3.22	-1.29	1.74	-4.39	-4.18	3.73	-5.88	-2.19	2.58
	7.1	-3.83	-0.14	2.28	-4.85	-1.49	5.10	-6.23	-0.46	3.57
	9.5	-4.33	0.76	2.76	-5.18	-0.44	5.99	-6.51	0.53	4.17
	2.4	-0.55	-0.42	1.08	-0.62	-0.62	1.74	-0.89	-0.95	1.46
	4.7	-1.03	-0.12	2.24	-1.03	-0.33	3.68	-1.29	0.26	3.13
	7.1	-1.38	0.66	2.90	-1.29	0.61	4.70	-1.55	1.38	3.87
	9.5	-1.66	1.27	3.38	-1.47	1.28	5.38	-1.75	1.87	4.36
NiPc	2.4	-0.52	-0.37	-0.11	-0.91	-0.91	-0.43	-1.27	-1.24	-0.65
	4.7	-0.70	-0.37	0.35	-1.09	-1.02	0.32	-1.42	-1.12	-0.22
	7.1	-0.79	-0.18	0.56	-1.18	-0.73	0.74	-1.53	-0.81	0.21
	9.5	-0.85	0.03	0.71	-1.26	-0.49	1.01	-1.60	-0.63	0.43
	2.4	-0.20	-0.11	0.28	-0.26	-0.26	0.25	-0.22	-0.38	0.01
	4.7	-0.36	-0.11	0.72	-0.39	-0.29	0.84	-0.52	-0.31	0.40
	7.1	-0.44	0.08	1.08	-0.46	-0.12	1.30	-0.60	-0.13	0.68
	9.5	-0.49	0.30	1.33	-0.52	0.09	1.60	-0.67	0.06	0.89

Table L-23. Least-Squares Fit Parameters for the CuPc-Coated IGEFET Transfer Function Phase Response as a Function of the NO_2 Challenge Gas Concentration. (Data Fitted to an Equation of the Form: $C = AP^{\alpha} + B$. R^2-Correlation Coefficient)

	Time Slice					
	1 (2.4 min)	2 (4.7 min)	3 (7.1 min)	4 (9.5 min)	5 (12 min)	6 (14 min)
Low Frequency Phase Response Maxima						
α	2.20	2.20	2.20	2.40	2.60	2.80
A	-2.88	-2.03	-1.72	-0.76	-0.33	-0.15
B	105.49	51.99	-36.73	-45.56	-42.66	-14.20
R^2	1.00	1.00	0.99	0.99	0.99	0.99
High Frequency Phase Response Maxima						
α	2.00	2.00	2.20	2.40	2.60	2.90
A	-26.58	-21.08	-10.92	-5.89	-1.83	-1.29
B	134.70	-26.79	-60.57	-93.65	-42.65	-67.08
R^2	1.00	1.00	0.99	0.99	0.99	0.99

Table L-24. Least-Squares Fit Parameters for the NiPc-Coated IGEFET Transfer Function Phase Response as a Function of the NO_2 Challenge Gas Concentration. (Data Fitted to an Equation of the Form: $C=AP^{\alpha} + B$. R^2-Correlation Coefficient)

	Time Slice					
	1 (2.4 min)	2 (4.7 min)	3 (7.1 min)	4 (9.5 min)	5 (12 min)	6 (14 min)
Low Frequency Phase Response Maxima						
α	2.00	2.20	2.60	2.80	3.00	3.20
A	-5.49	-1.84	-0.36	-0.15	-0.06	-0.03
B	103.77	16.41	28.87	14.12	19.39	29.55
R^2	1.00	1.00	0.99	0.99	0.99	0.99
High Frequency Phase Response Maxima						
α	2.00	2.00	2.40	2.80	3.00	3.00
A	-21.50	-10.62	-3.06	-0.97	-0.52	-0.48
B	111.36	48.89	49.07	50.27	31.98	6.30
R^2	1.00	0.99	0.99	0.99	0.99	0.97

Table L-25. Calibration Vectors Formed From the IGEFET Transfer Function Phase Response Data for Single Component Nitrogen Dioxide Challenge Gas Exposures.

MPc Film Type	Time Slice (min)	Nitrogen Dioxide Concentration (ppb)				
		100	200	400	1000	4000
CuPc	2.4	0.70	-21.50	-120.64	-301.74	-1352.51
	4.7	-0.33	-64.95	-160.82	-522.59	-1930.22
	7.1	-8.89	-113.74	-265.06	-722.23	-2306.27
	9.5	-25.42	-257.26	-643.62	-1648.41	-5263.59
	2.4	0.00	-2.89	-9.40	-30.80	-145.81
	4.7	-0.81	-8.60	-20.85	-57.38	-188.38
	7.1	-2.81	-19.23	-46.02	-115.93	-365.77
	9.5	-5.93	-38.29	-90.43	-226.33	-680.75
NiPc	2.4	0.16	-10.67	-53.78	-171.61	-707.56
	4.7	-1.36	-58.02	-221.08	-641.14	-2137.03
	7.1	-11.40	-250.40	-1015.09	-3278.50	-10808.61
	9.5	-43.58	-642.81	-2593.33	-8253.95	-26265.60
	2.4	0.00	-4.27	-12.48	-41.60	-147.02
	4.7	-1.96	-14.95	-36.80	-87.89	-191.13
	7.1	-7.00	-49.91	-130.00	-303.83	-590.18
	9.5	-20.68	-158.10	-409.14	-961.83	-1855.62

Table L-26. Typical Test Vectors Formed From the IGEFET Transfer Function Phase Response Data for Single Component Nitrogen Dioxide Challenge Gas.

MPc Film Type	Time Slice (min)	Nitrogen Dioxide Concentration (ppb)				
		100	200	400	1000	4000
CuPc	2.4	1.00	-23.50	-119.64	-263.52	-606.18
	4.7	2.44	-67.85	-155.02	-489.75	-990.38
	7.1	1.23	-116.67	-249.91	-673.33	-1275.16
	9.5	-0.42	-269.66	-612.75	-1524.78	-2947.47
	2.4	-0.16	-2.89	-8.41	-25.00	-84.64
	4.7	-0.49	-8.41	-18.49	-46.24	-125.44
	7.1	-1.00	-18.86	-40.86	-89.18	-241.06
	9.5	-3.57	-36.96	-82.87	-174.90	-454.26
NiPc	2.4	0.49	-10.24	-51.84	-166.41	-353.44
	4.7	1.23	-53.42	-195.46	-591.78	-1179.34
	7.1	0.27	-222.86	-868.70	-2948.35	-5789.10
	9.5	-0.54	-562.81	-2231.10	-7151.80	-13675.38
	2.4	-0.16	-4.00	-10.89	-31.36	-106.09
	4.7	-0.81	-13.69	-30.25	-65.61	-166.41
	7.1	-3.09	-45.34	-110.41	-222.09	-507.05
	9.5	-10.30	-150.95	-349.75	-666.93	-1618.67

Table L-27. Least-Squares Fit Parameters for the CuPc-Coated IGEFET Transfer Function Phase Response as a Function of the NH_3 Challenge Gas Concentration. (Data Fitted to an Equation of the Form: $C = AP^{\alpha} + B$. R^2-Correlation Coefficient)

	Time Slice					
	1 (2.4 min)	2 (4.7 min)	3 (7.1 min)	4 (9.5 min)	5 (12 min)	6 (14 min)
Low Frequency Phase Response Maxima						
α	2.00	2.00	2.00	2.00	2.00	2.00
A	0.53	0.63	0.71	0.80	0.86	0.93
B	-10.39	-3.76	-1.51	-1.45	-1.19	-1.23
R^2	0.99	0.99	0.99	0.99	0.99	0.99
High Frequency Phase Response Maxima						
α	2.00	2.00	2.00	2.00	2.00	2.00
A	0.08	0.10	0.11	0.13	0.14	0.15
B	-1.74	-0.84	-0.26	-0.26	-0.42	-0.15
R^2	0.99	0.99	0.98	0.99	0.99	0.99

Table L-28. Least-Squares Fit Parameters for the NiPc-Coated IGEFET Transfer Function Phase Response as a Function of the NH_3 Challenge Gas Concentration. (Data Fitted to an Equation of the Form: $C=AP^{\alpha}+B$. R^2-Correlation Coefficient)

	Time Slice					
	1 (2.4 min)	2 (4.7 min)	3 (7.1 min)	4 (9.5 min)	5 (12 min)	6 (14 min)
Low Frequency Phase Response Maxima						
α	2.00	2.00	2.00	2.00	2.00	2.00
A	0.01	0.02	0.03	0.04	0.06	0.07
B	0.01	0.50	0.82	0.93	0.74	0.65
R^2	0.98	0.97	0.98	0.98	1.00	1.00
High Frequency Phase Response Maxima						
α	2.00	2.00	2.00	2.00	2.00	2.00
A	0.01	0.02	0.03	0.03	0.04	0.04
B	-0.20	0.10	0.34	0.59	0.73	0.96
R^2	0.99	0.97	0.97	0.97	0.98	0.98

Table L-29. Calibration Vectors Formed From the IGEFET Transfer Function Phase Response Data for Single Component Ammonia Challenge Gas Exposures.

MPc Film Type	Time Slice (min)	Ammonia Concentration (ppm)				
		20	50	100	200	400
CuPc	2.4	0.44	12.25	37.21	108.16	195.07
	4.7	8.03	22.72	52.93	143.20	241.28
	7.1	11.79	29.16	61.62	162.99	274.45
	9.5	13.94	35.20	68.48	179.56	309.76
	2.4	0.04	1.87	5.41	16.81	30.25
	4.7	1.07	3.48	8.12	22.72	38.44
	7.1	1.87	4.55	9.77	26.69	44.00
	9.5	2.15	5.76	11.06	28.80	49.94
NiPc	2.4	0.25	0.32	1.63	2.56	4.99
	4.7	0.81	0.93	3.52	5.60	9.40
	7.1	1.28	1.69	4.73	8.03	13.44
	9.5	1.36	2.35	5.76	10.67	17.36
	2.4	0.05	0.16	1.00	2.35	4.27
	4.7	0.28	0.64	2.25	4.84	7.47
	7.1	0.54	1.28	2.98	6.76	10.24
	9.5	0.81	1.78	3.61	8.22	12.25

Table L-30. Typical Test Vectors Formed From the IGEFET Transfer Function Phase Response Data for Single Component Ammonia Challenge Gas Exposures.

MPc Film Type	Time Slice (min)	Ammonia Concentration (ppm)				
		20	50	100	200	400
CuPc	2.4	0.64	8.41	42.25	112.36	171.61
	4.7	11.56	17.64	56.25	151.29	207.36
	7.1	16.81	23.04	62.41	169.00	231.04
	9.5	20.25	28.09	67.24	190.44	285.61
	2.4	0.09	1.69	5.76	17.64	27.04
	4.7	1.44	2.89	8.41	24.01	33.64
	7.1	2.56	4.00	9.61	28.09	37.21
	9.5	3.24	5.29	10.24	30.25	44.89
NiPc	2.4	0.81	0.09	2.25	2.25	3.61
	4.7	1.96	0.16	4.41	5.29	6.76
	7.1	2.56	0.64	5.76	8.41	9.61
	9.5	2.56	1.00	6.76	11.56	12.96
	2.4	0.09	-0.01	1.21	2.25	4.00
	4.7	0.49	0.16	2.25	4.84	6.76
	7.1	0.81	0.81	2.89	6.76	9.61
	9.5	1.21	1.44	3.24	8.41	11.56

Table L-31. Calibration Vectors Formed From the IGEFET Transfer Function Phase Response to Binary Mixtures of Ammonia and Nitrogen Dioxide.

MPc Film Type/ Condition	Time Slice (min)	50 ppm NH_3			200 ppm NH_3			400 ppm NH_3		
		Nitrogen Dioxide Concentration (ppb)			Nitrogen Dioxide Concentration (ppb)			Nitrogen Dioxide Concentration (ppb)		
		100	425	1000	100	425	1000	100	425	1000
CuPc/ Low Frequency NO_2 Fit	2.4	58.00	12.3	-28.7	195.5	180.2	-51.5	239.6	-35.5	358.9
	4.7	116.7	0.7	-97.9	272.8	20.3	-248.4	2.2	-233.8	453.9
	7.1	177.7	-7.5	-140.5	316.8	-0.0	-396.2	-9.4	-364.4	413.7
	9.5	386.5	-37.6	-293.3	606.0	-14.0	-906.1	-31.3	-807.5	462.8
CuPc/ High Frequency NO_2 Fit	2.4	5.3	2.0	-3.5	20.0	18.8	0.0	32.5	29.9	1.6
	4.7	9.6	0.3	-8.2	27.7	11.1	-7.8	41.4	15.0	-1.9
	7.1	15.7	-0.1	-18.1	44.3	5.1	-23.1	65.7	8.0	-14.8
	9.5	24.1	-1.5	-33.1	68.9	1.4	-48.4	90.4	3.7	-32.50
NiPc/ Low Frequency NO_2 Fit	2.4	2.8	0.0	-4.4	4.4	-0.1	-43.6	1.7	-43.1	5.8
	4.7	10.9	-8.0	-129.8	11.8	-10.9	-241.1	-17.1	-249.9	14.4
	7.1	40.0	-28.6	-494.1	29.3	-88.2	-1046.	-157.5	-1046.	21.1
	9.5	94.0	-178.2	-1126.	58.1	-241.8	-2464.	-378.7	-2366.	13.0
NiPc/ High Frequency NO_2 Fit	2.4	0.8	0.0	-2.5	1.9	1.1	-2.1	2.9	1.9	-0.8
	4.7	2.2	-0.3	-19.1	3.9	0.0	-13.7	5.3	0.6	-9.2
	7.1	4.9	-3.1	-59.8	7.9	-0.3	-52.3	10.2	-0.0	-35.0
	9.5	9.9	-13.5	-173.0	15.6	-2.4	-165.5	16.1	-1.0	-104.8
CuPc/ Low Frequency NH_3 Fit	2.4	40.10	9.8	-21.2	121.0	112.4	-36.0	145.6	-25.7	210.3
	4.7	75.7	0.8	-64.5	163.8	15.5	-150.5	2.1	-142.4	260.3
	7.1	111.0	-6.3	-89.6	187.7	-0.0	-230.0	-7.7	-213.2	239.2
	9.5	143.2	-20.6	-113.8	208.3	-9.0	-291.3	-17.6	-264.6	166.4
CuPc/ High Frequency NH_3 Fit	2.4	5.3	2.0	-3.5	20.0	18.8	0.0	32.5	29.9	1.6
	4.7	9.6	0.3	-8.2	27.7	11.1	-7.8	41.4	15.0	-1.9
	7.1	12.3	-0.1	-13.9	31.4	4.4	-17.4	44.9	6.6	-11.6
	9.5	14.2	-1.4	-18.5	34.0	1.3	-25.3	42.7	3.0	-18.20
NiPc/ Low Frequency NH_3 Fit	2.4	2.8	0.0	-4.4	4.4	-0.1	-43.6	1.7	-43.1	5.8
	4.7	8.8	-6.6	-83.4	9.4	-8.8	-146.4	-13.2	-151.3	11.3
	7.1	17.1	-13.2	-118.1	13.4	-31.4	-210.3	-49.0	-210.3	10.5
	9.5	25.7	-40.5	-151.3	18.2	-50.4	-264.6	-69.4	-257.1	6.3
NiPc/ High Frequency NH_3 Fit	2.4	0.8	0.0	-2.5	1.9	1.1	-2.1	2.9	1.9	-0.8
	4.7	2.2	-0.3	-19.1	3.9	0.0	-13.7	5.3	0.6	-9.2
	7.1	3.7	-2.6	-30.3	5.6	-0.4	-27.0	6.9	-0.0	-19.4
	9.5	5.1	-6.4	-39.7	7.1	-1.9	-38.4	7.3	-1.0	-27.7

Table L-32. Typical Test Vectors Formed From the IGEFET Transfer Function Phase Response to Binary Mixtures of Ammonia and Nitrogen Dioxide.

MPc Film Type/ Condition	Time Slice (min)	50 ppm NH_3			200 ppm NH_3			400 ppm NH_3		
		Nitrogen Dioxide Concentration (ppb)			Nitrogen Dioxide Concentration (ppb)			Nitrogen Dioxide Concentration (ppb)		
		100	425	1000	100	425	1000	100	425	1000
CuPc/ Low Frequency NO_2 Fit	2.4	70.10	42.5	1.0	199.4	241.1	-4.6	403.9	398.2	0.6
	4.7	148.2	24.8	-27.4	296.8	258.9	-183.9	529.3	51.5	-91.8
	7.1	232.4	1.8	-49.6	364.4	31.5	-358.9	628.1	3.6	-169.1
	9.5	498.0	-5.3	-114.2	719.1	7.4	-897.6	1217.1	1.9	-389.1
CuPc/ High Frequency NO_2 Fit	2.4	6.8	3.2	-2.3	21.2	21.2	2.6	38.4	37.2	8.4
	4.7	13.0	2.9	-4.4	30.3	26.0	-5.3	50.4	27.0	0.2
	7.1	21.1	0.5	-12.1	51.5	13.8	-27.4	86.7	15.7	-6.2
	9.5	33.1	-0.0	-23.1	82.9	5.9	-68.0	138.4	9.9	-15.1
NiPc/ Low Frequency NO_2 Fit	2.4	3.2	2.6	-11.6	3.2	2.9	-32.5	6.3	7.3	-26.0
	4.7	13.8	0.3	-65.7	11.2	0.6	-211.4	17.8	0.2	-176.4
	7.1	44.4	-8.7	-269.0	32.2	-9.7	-1027.	52.9	-62.3	-726.0
	9.5	106.7	-52.0	-666.9	59.4	-63.3	-2564.	95.8	-173.0	-1651.
NiPc/ High Frequency NO_2 Fit	2.4	1.0	0.4	-2.3	1.4	1.7	-2.6	2.9	3.6	-0.0
	4.7	3.2	0.4	-13.7	3.6	0.2	-21.2	6.3	2.3	-5.8
	7.1	6.6	-0.2	-52.3	7.4	-0.0	-92.7	12.9	0.1	-24.6
	9.5	13.0	-3.7	-180.8	14.5	-0.7	-337.8	28.3	-0.1	-80.8
CuPc/ Low Frequency NH_3 Fit	2.4	47.60	30.3	1.0	123.2	146.4	-4.0	234.1	231.0	0.6
	4.7	94.1	18.5	-20.3	176.9	156.3	-114.5	299.3	36.0	-60.8
	7.1	141.6	1.7	-34.8	213.2	23.0	-210.3	349.7	3.2	-106.1
	9.5	176.9	-4.0	-51.8	240.3	5.3	-289.0	372.5	1.7	-144.0
CuPc/ High Frequency NH_3 Fit	2.4	6.8	3.2	-2.3	21.2	21.2	2.6	38.4	37.2	8.4
	4.7	13.0	2.9	-4.4	30.3	26.0	-5.3	50.4	27.0	0.2
	7.1	16.0	0.5	-9.6	36.0	10.9	-20.3	57.8	12.3	-5.3
	9.5	18.5	-0.0	-13.7	39.7	4.4	-33.6	60.8	6.8	-9.6
NiPc/ Low Frequency NH_3 Fit	2.4	3.2	2.6	-11.6	3.2	2.9	-32.5	6.3	7.3	-26.0
	4.7	10.9	0.4	-44.9	9.0	0.6	-130.0	13.7	0.3	-110.3
	7.1	18.5	-5.3	-74.0	14.4	-5.8	-207.4	21.2	-24.0	-158.8
	9.5	28.1	-16.8	-104.0	18.5	-19.4	-272.3	26.0	-39.7	-198.8
NiPc/ High Frequency NH_3 Fit	2.4	1.0	0.4	-2.3	1.4	1.7	-2.6	2.9	3.6	-0.0
	4.7	3.2	0.4	-13.7	3.6	0.2	-21.2	6.3	2.3	-5.8
	7.1	4.8	-0.3	-27.0	5.3	-0.0	-43.6	8.4	0.2	-14.4
	9.5	6.3	-2.6	-41.0	6.8	-0.8	-64.0	10.9	-0.2	-23.0

Table L-33. Least-Squares Fit Parameters for the Conductance Parameters Extracted From the MPc-Coated IGEFET Transfer Function Gain/Phase Measurements as a Function of the NO_2 Challenge Gas Concentration. (Data Fitted to an Equation of the Form: $C = AG_N^{\alpha} + B$. R^2-Correlation Coefficient)

	CuPc		NiPc		CoPc	
	G_1	G_2	G_1	G_2	G_1	G_2
α	-2.37	-2.43	-2.38	-2.72	-2.02	-2.08
A	48.44	63.12	44.68	66.29	77.84	70.02
B	131.10	73.60	-73.16	-40.64	143.35	156.45
R^2	0.99	1.00	1.00	1.00	0.98	0.98

Table L-34. Calibration Vectors Formed From the Conductance Parameters Extracted From the MPc-Coated IGEFET Transfer Function Gain/Phase Measurements for Single Component Nitrogen Dioxide Challenge Gas Exposures.

MPc Film Type	Conductance Parameter	Nitrogen Dioxide Concentration (ppb)				
		100	200	400	1000	4000
CuPc	G_1	2.06	3.83	5.31	12.38	80.55
	G_2	1.58	2.73	5.70	11.83	62.64
NiPc	G_1	2.44	4.46	11.96	26.55	90.36
	G_2	1.65	3.07	5.95	18.00	60.38
CoPc	G_1	1.22	2.47	3.98	6.40	49.95
	G_2	1.45	2.75	3.51	7.17	55.36

Table L-35. Typical Test Vectors Formed From the Conductance Parameters Extracted From the MPc-Coated IGEFET Transfer Function Gain/Phase Measurements for Single Component Nitrogen Dioxide Challenge Gas Exposures.

MPc Film Type	Conductance Parameter	Nitrogen Dioxide Concentration (ppb)				
		100	200	400	1000	4000
CuPc	G_1	2.09	3.91	5.17	14.89	33.71
	G_2	1.36	3.20	5.19	11.97	23.23
NiPc	G_1	2.62	3.79	8.03	28.92	65.33
	G_2	1.44	3.26	5.39	17.71	30.51
CoPc	G_1	1.18	2.41	3.25	6.59	27.43
	G_2	1.28	2.66	2.89	6.61	19.89

Appendix M. Supporting Data: Gain Response of the MPc-Coated Microsensor to Challenge Gas Exposure

This appendix contains the gain response of the copper phthalocyanine (CuPc)-, nickel phthalocyanine (NiPc)- and cobalt phthalocyanine (CoPc)-coated interdigitated gate electrode field-effect transistor (IGEFET) microsensors as a result of exposure to the challenge gas. The data presented in this appendix supports the gain response data presented in Chapter VI. Figures M-1 through M-9 present the gain response of the MPc-coated IGEFET microsensor to binary gas mixtures containing a fixed nitrogen dioxide concentration and various concentrations of ammonia. Similarly, Figures M-10 through M-15 depict the gain response of the MPc-coated microsensor to binary gas mixtures containing a fixed ammonia concentration and various concentrations of nitrogen dioxide. Figures M-16 through M-20 illustrate the time dependence of the CuPc- and NiPc-coated IGEFET transfer function's high-frequency (800-12000 Hz) gain response maxima upon exposure to various nitrogen dioxide and ammonia challenge gas concentrations. As a result of the significantly different baseline transfer function (discussed in Chapter VI), the time dependence of the CoPc-coated IGEFET transfer function gain response maxima was not investigated.

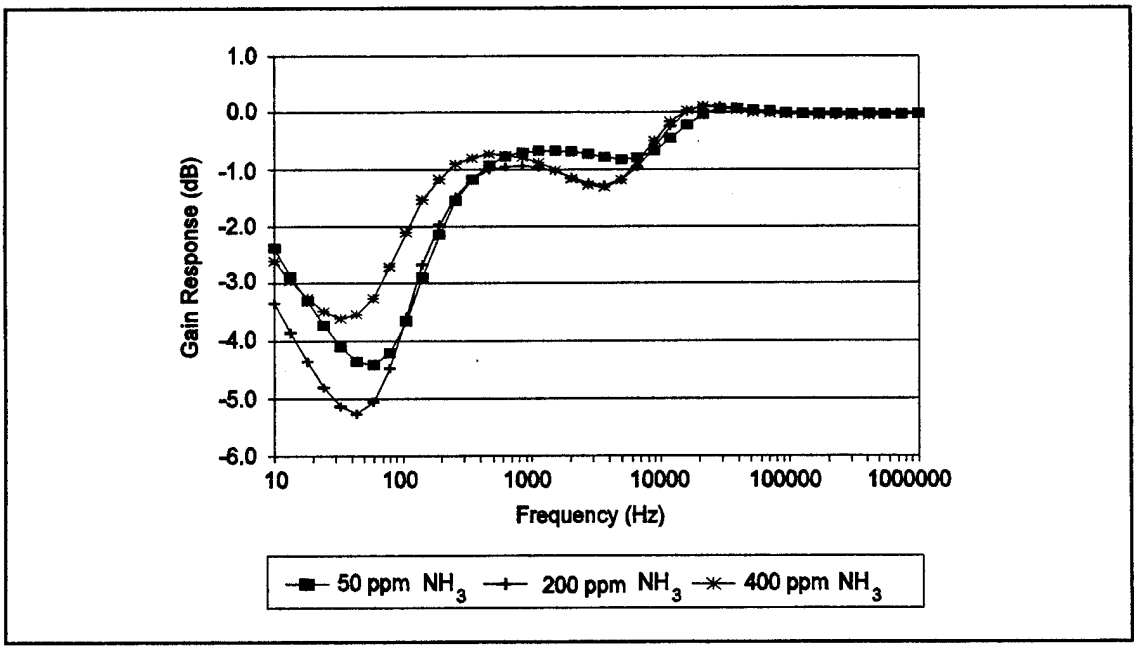


Figure M-1. Bode Plots of the CuPc-Coated IGEFET Transfer Function Gain Response After a 16 minute Exposure to a Binary Gas Mixture Containing 100 ppb NO_2 and Various NH_3 Concentrations. (Film Thickness = 0.32 μm. Temperature = 100° C.)

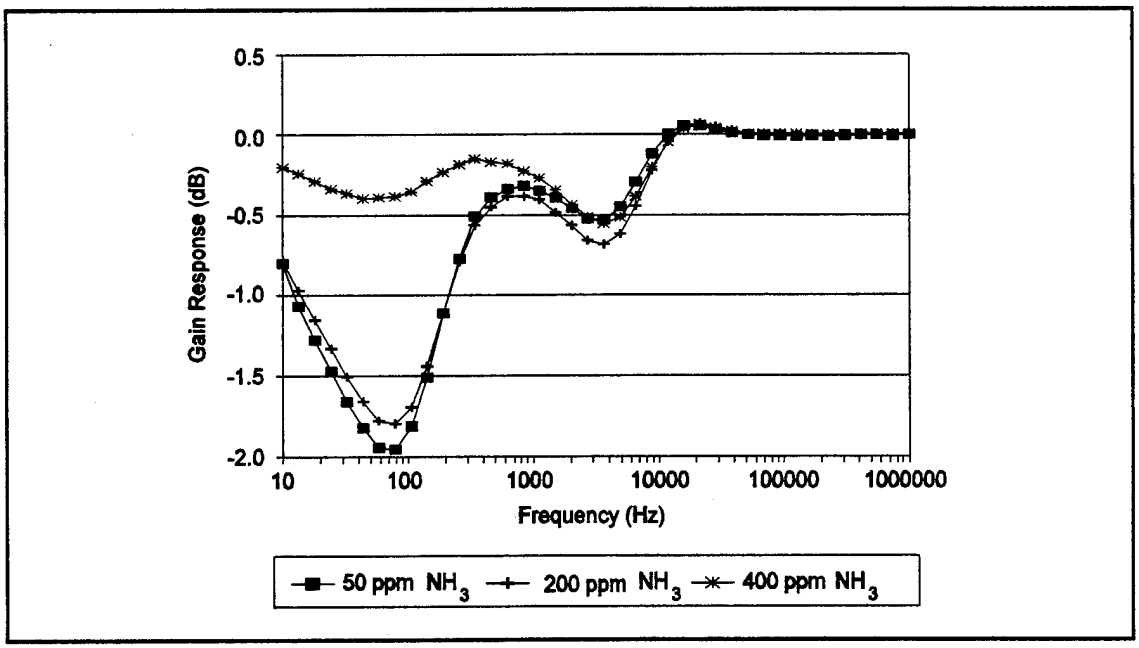


Figure M-2. Bode Plots of the NiPc-Coated IGEFET Transfer Function Gain Response After a 16 minute Exposure to a Binary Gas Mixture Containing 100 ppb NO_2 and Various NH_3 Concentrations. (Film Thickness = 0.43 μm. Temperature = 100° C.)

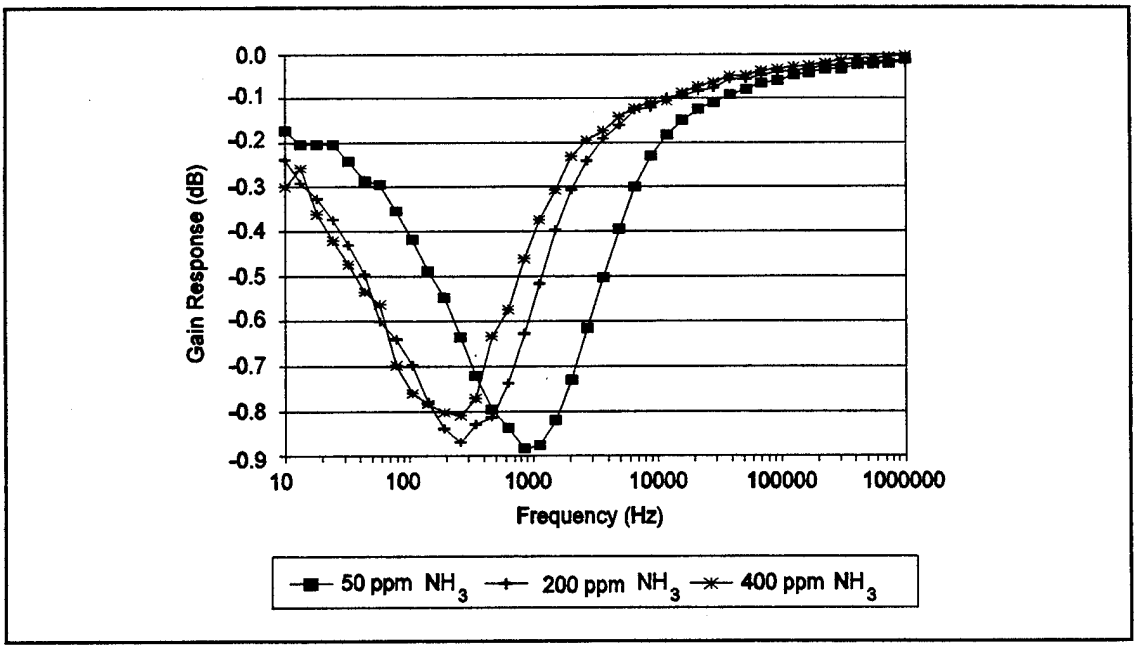


Figure M-3. Bode Plots of the CoPc-Coated IGEFET Transfer Function Gain Response After a 16 minute Exposure to a Binary Gas Mixture Containing 100 ppb NO_2 and Various NH_3 Concentrations. (Film Thickness = 0.51 μm. Temperature = 100° C.)

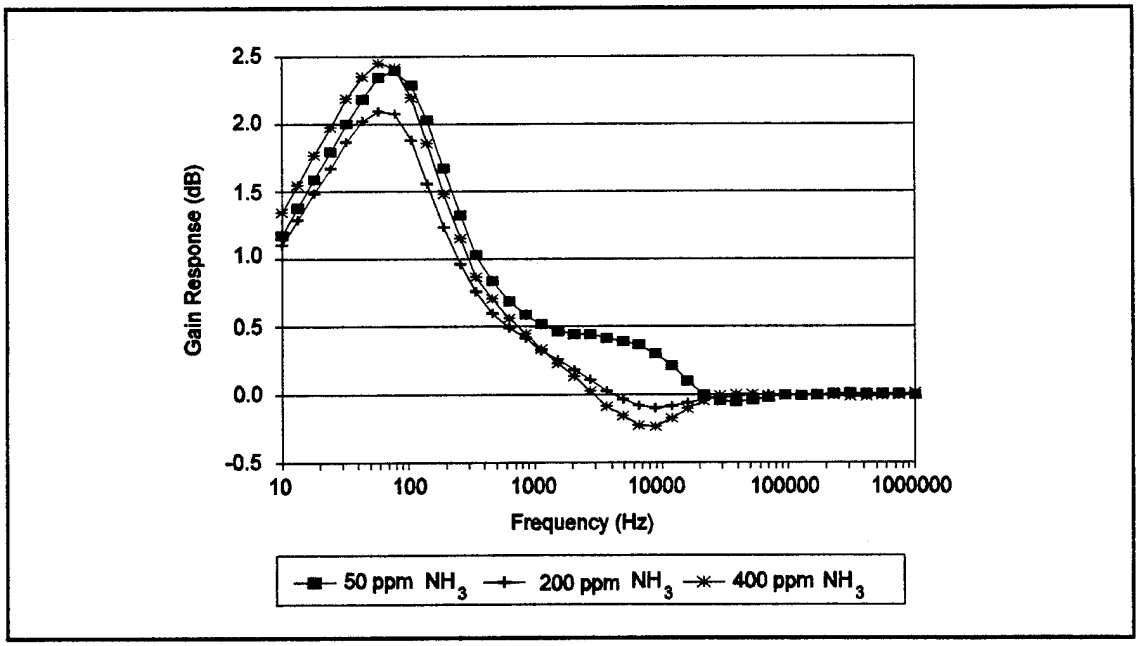


Figure M-4. Bode Plots of the CuPc-Coated IGEFET Transfer Function Gain Response After a 16 minute Exposure to a Binary Gas Mixture Containing 425 ppb NO_2 and Various NH_3 Concentrations. (Film Thickness = 0.32 μm. Temperature = 100° C.)

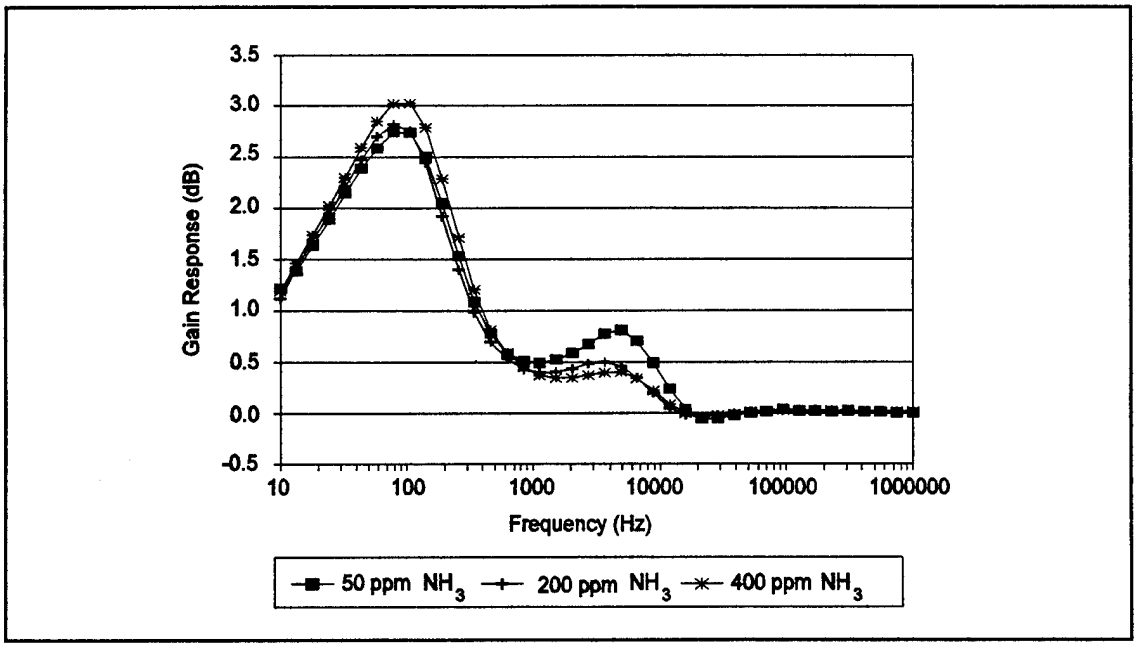


Figure M-5. Bode Plots of the NiPc-Coated IGEFET Transfer Function Gain Response After a 16 minute Exposure to a Binary Gas Mixture Containing 425 ppb NO_2 and Various NH_3 Concentrations. (Film Thickness = 0.43 μm. Temperature = 100° C.)

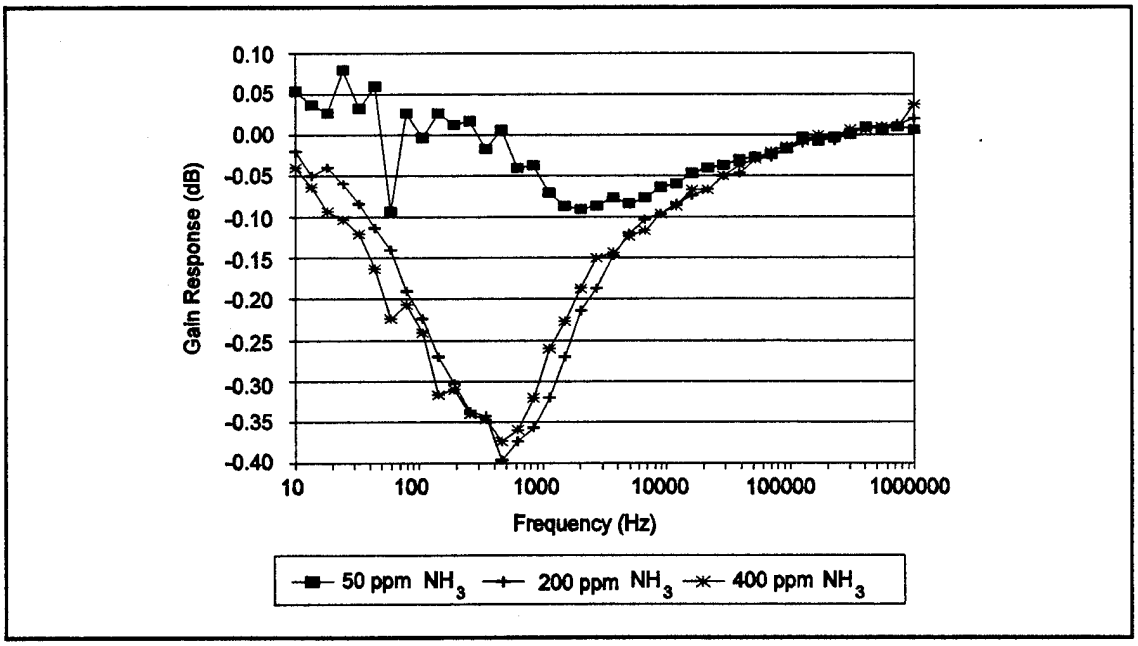


Figure M-6. Bode Plots of the CoPc-Coated IGEFET Transfer Function Gain Response After a 16 minute Exposure to a Binary Gas Mixture Containing 425 ppb NO_2 and Various NH_3 Concentrations. (Film Thickness = 0.51 μm. Temperature = 100° C.)

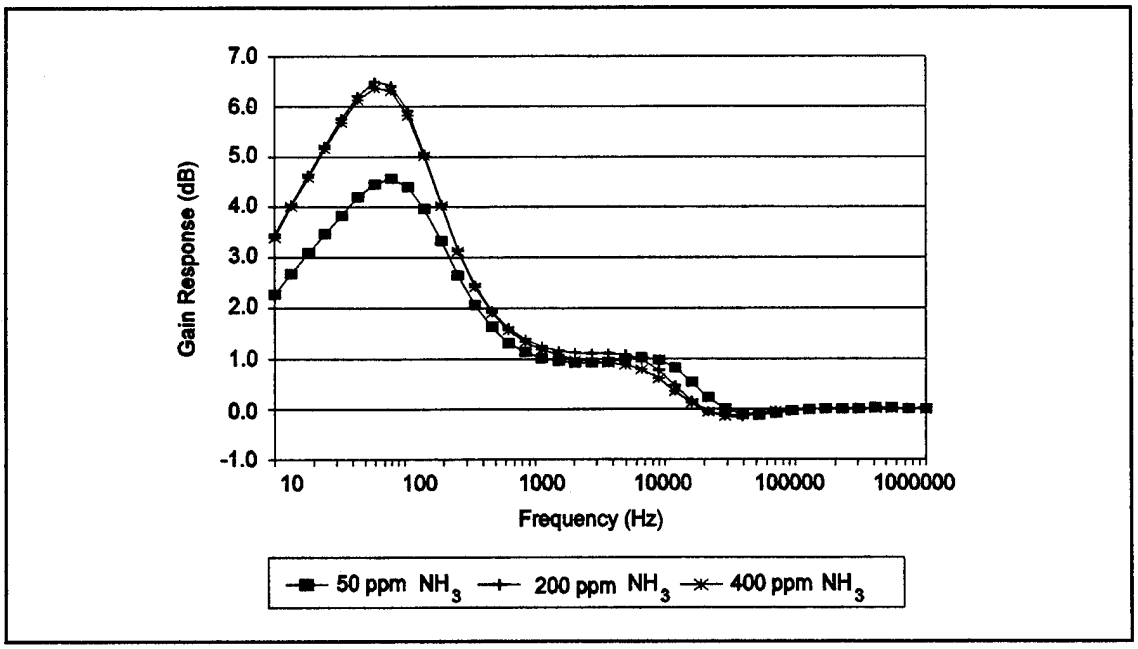


Figure M-7. Bode Plots of the CuPc-Coated IGEFET Transfer Function Gain ResponseAfter a 16 minute Exposure to a Binary Gas Mixture Containing 1000 ppb NO_2 and Various NH_3 Concentrations. (Film Thickness = 0.32 μm. Temperature = 100° C.)

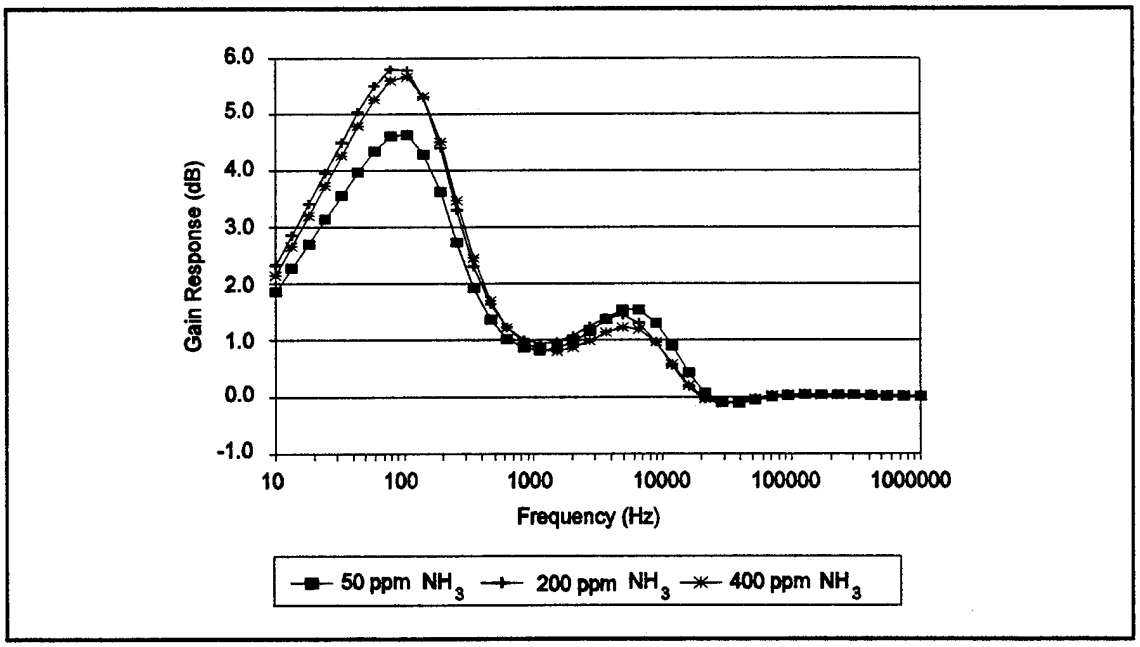


Figure M-8. Bode Plots of the NiPc-Coated IGEFET Transfer Function Gain Response After a 16 minute Exposure to a Binary Gas Mixture Containing 1000 ppb NO_2 and Various NH_3 Concentrations. (Film Thickness = 0.43 μm. Temperature = 100° C.)

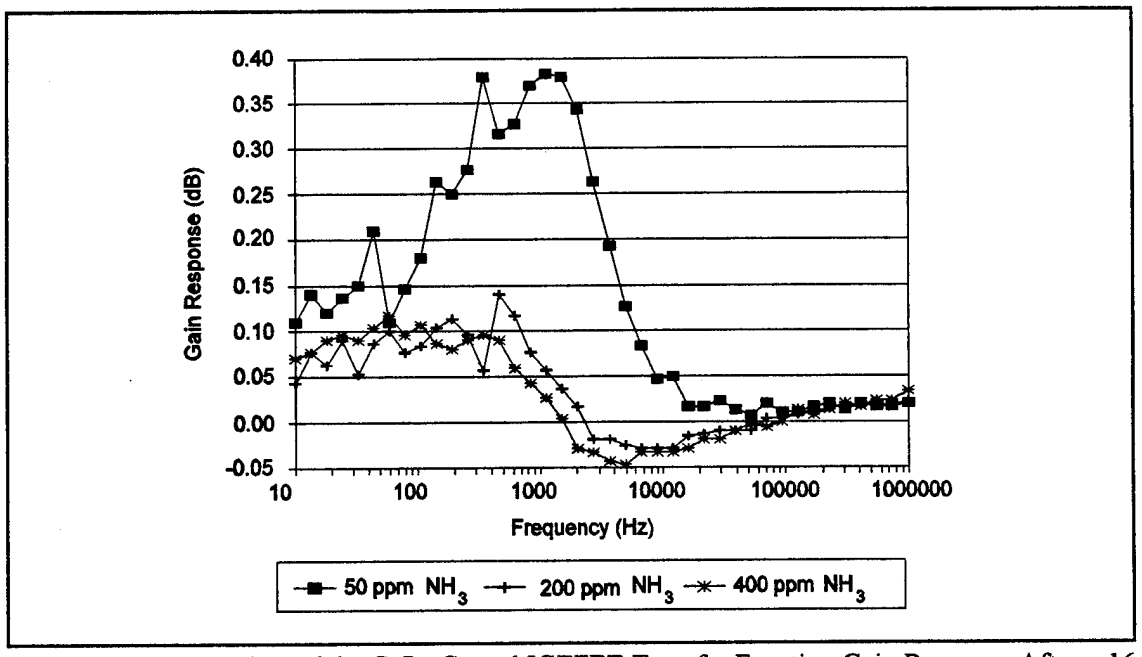


Figure M-9. Bode Plots of the CoPc-Coated IGEFET Transfer Function Gain Response After a 16 minute Exposure to a Binary Gas Mixture Containing 1000 ppb NO_2 and Various NH_3 Concentrations. (Film Thickness = 0.51 μm. Temperature = 100° C.)

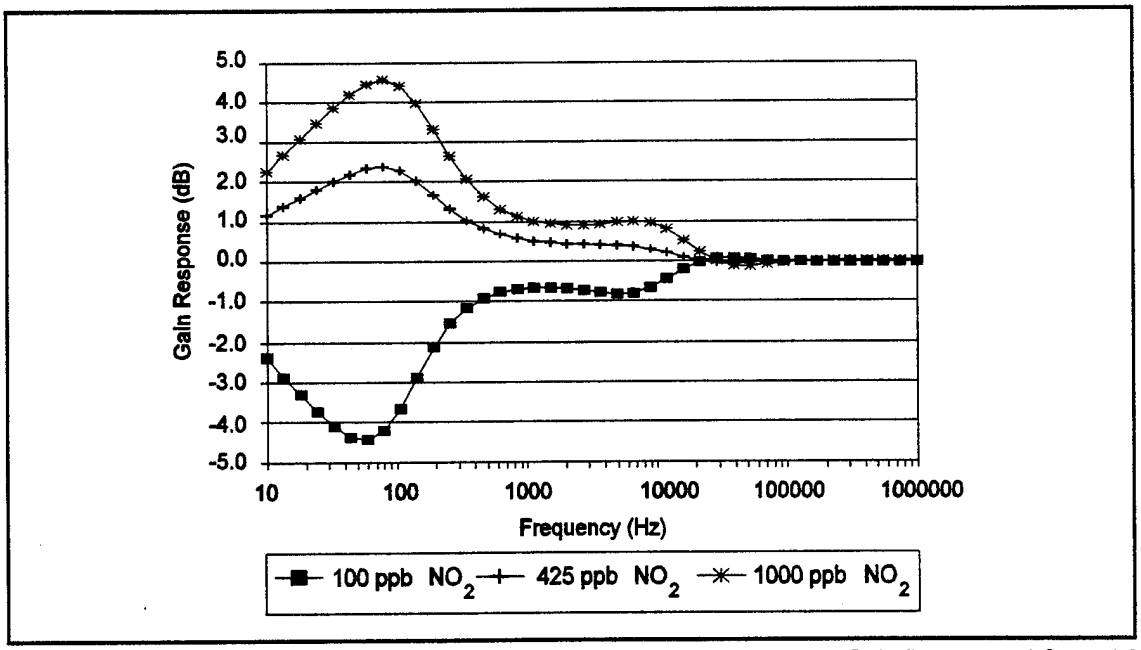


Figure M-10. Bode Plots of the CuPc-Coated IGEFET Transfer Function Gain Response After a 16 minute Exposure to a Binary Gas Mixture Containing 50 ppm NH_3 and Various NO_2 Concentrations. (Film Thickness = 0.32 μm. Temperature = 100° C.)

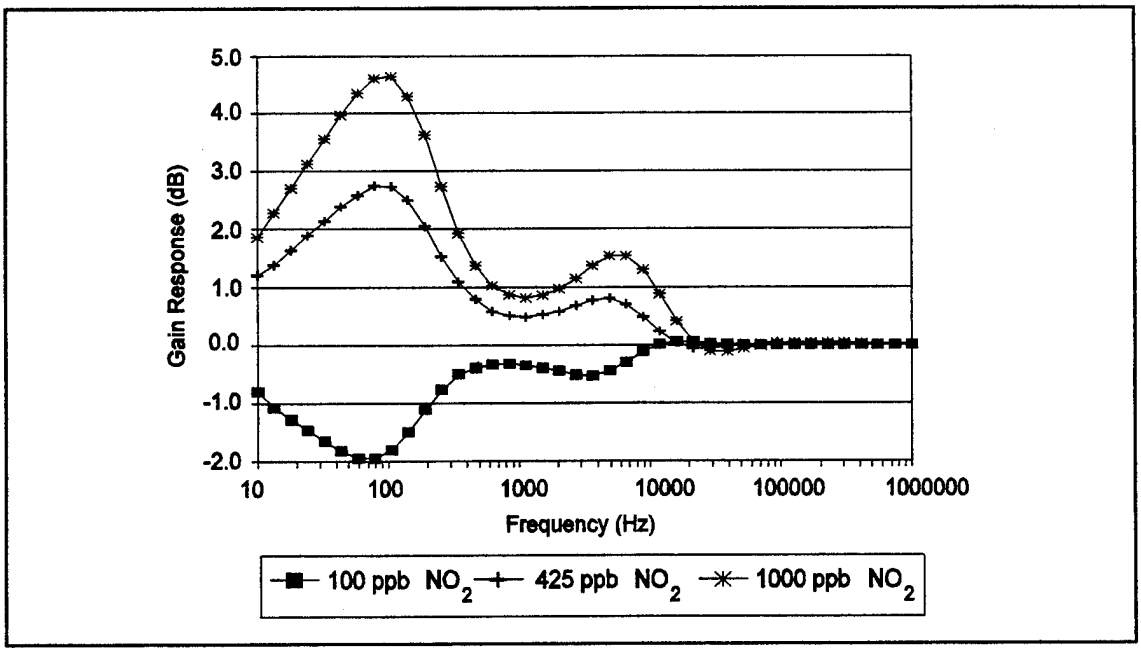


Figure M-11. Bode Plots of the NiPc-Coated IGEFET Transfer Function Gain Response After a 16 minute Exposure to a Binary Gas Mixture Containing 50 ppm NH_3 and Various NO_2 Concentrations. (Film Thickness = 0.43 μm. Temperature = 100° C.)

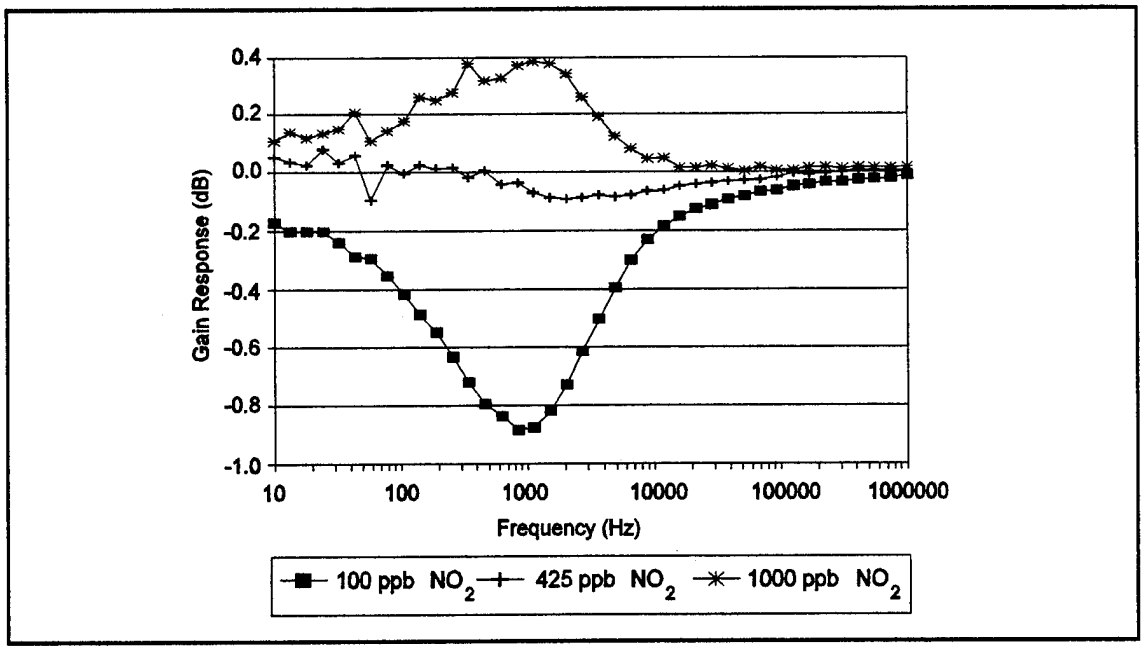


Figure M-12. Bode Plots of the CoPc-Coated IGEFET Transfer Function Gain Response After a 16 minute Exposure to a Binary Gas Mixture Containing 50 ppm NH_3 and Various NO_2 Concentrations. (Film Thickness = 0.51 μm. Temperature = 100° C.)

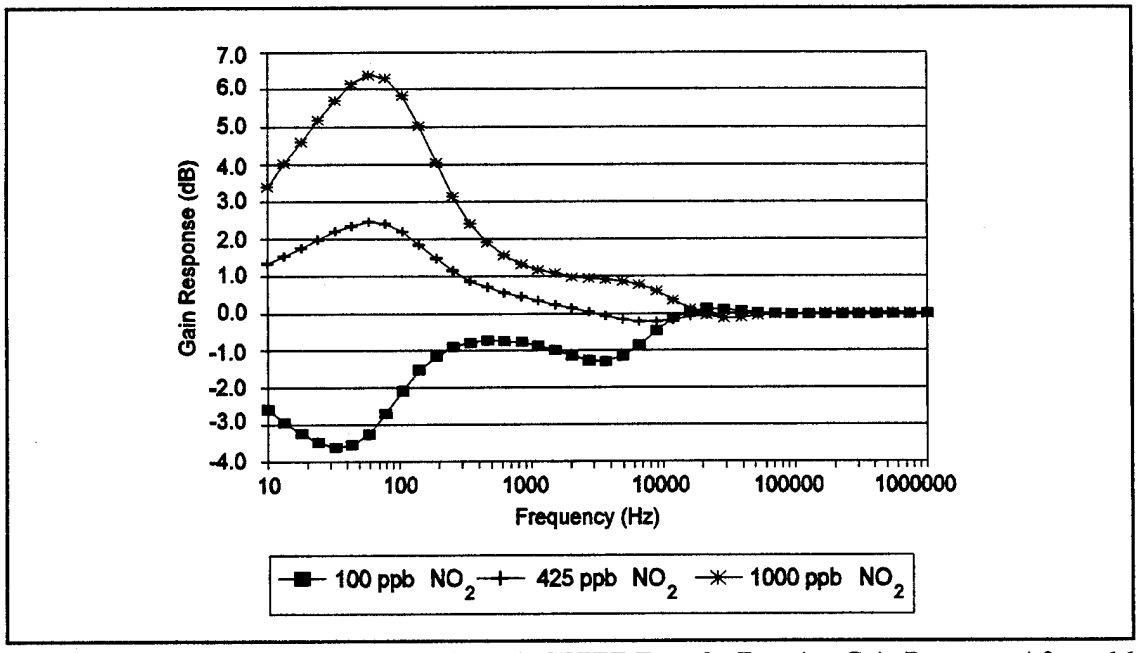


Figure M-13. Bode Plots of the CuPc-Coated IGEFET Transfer Function Gain Response After a 16 minute Exposure to a Binary Gas Mixture Containing 400 ppm NH_3 and Various NO_2 Concentrations. (Film Thickness = 0.32 μm. Temperature = 100° C.)

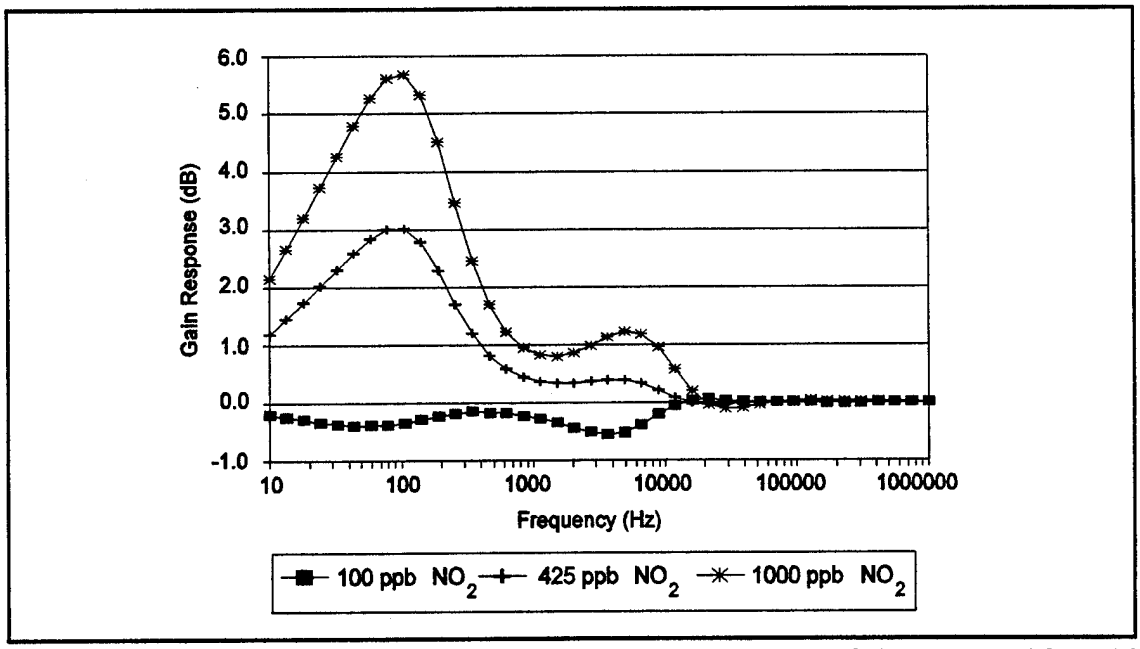


Figure M-14. Bode Plots of the NiPc-Coated IGEFET Transfer Function Gain Response After a 16 minute Exposure to a Binary Gas Mixture Containing 400 ppm NH_3 and Various NO_2 Concentrations. (Film Thickness = 0.43 μm. Temperature = 100° C.)

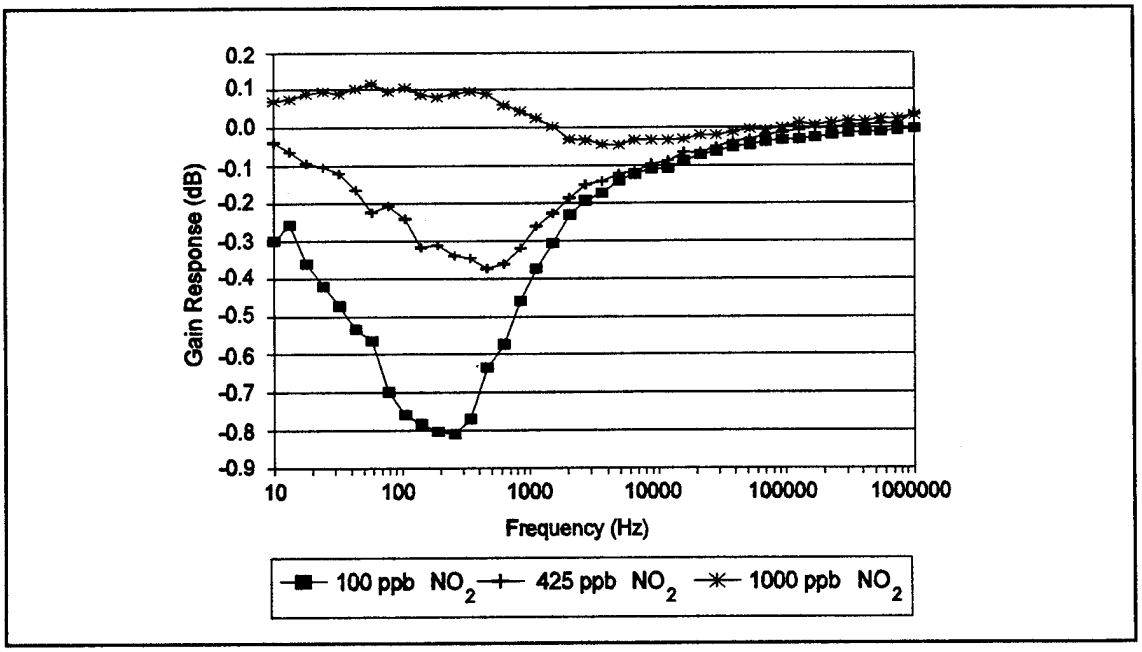


Figure M-15. Bode Plots of the CoPc-Coated IGEFET Transfer Function Gain Response After a 16 minute Exposure to a Binary Gas Mixture Containing 400 ppm NH_3 and Various NO_2 Concentrations. (Film Thickness = 0.51 μm. Temperature = 100° C.)

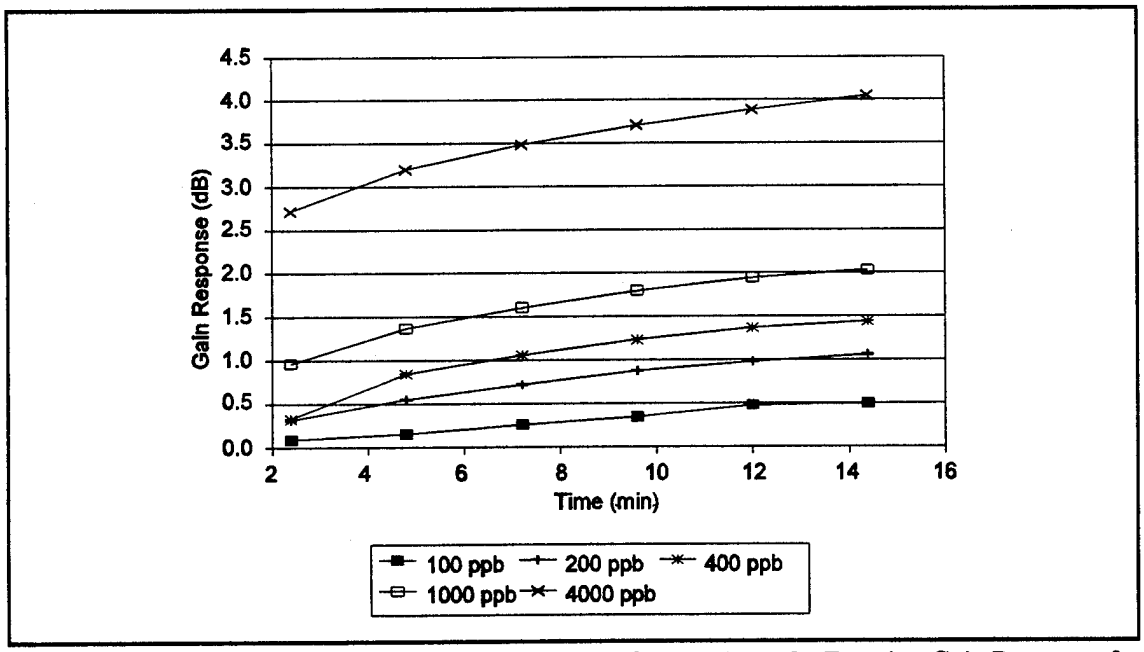


Figure M-16. Time Dependence of the CuPc-Coated IGEFET Transfer Function Gain Response for Several NO_2 Concentrations. (Approximate Frequency = 800-12000 Hz. Film Thickness = 0.32 μm. Temperature = 100° C.)

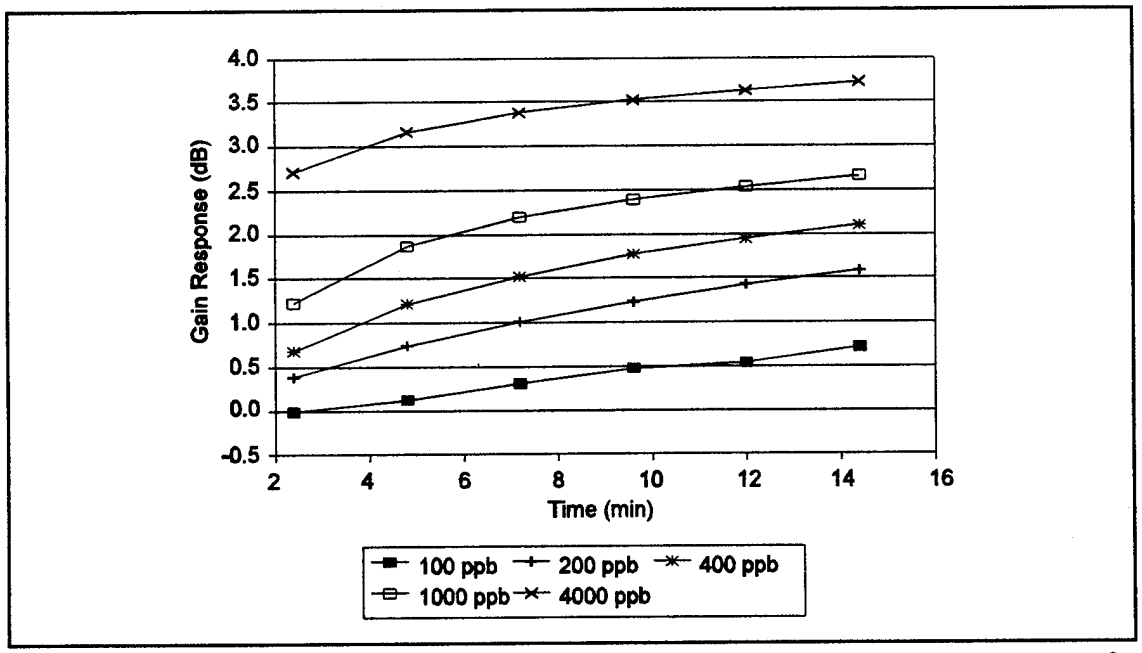


Figure M-17. Time Dependence of the NiPc-Coated IGEFET Transfer Function Gain Response for Several NO_2 Concentrations. (Approximate Frequency = 800-12000 Hz. Film Thickness = 0.43 μm. Temperature = 100° C.)

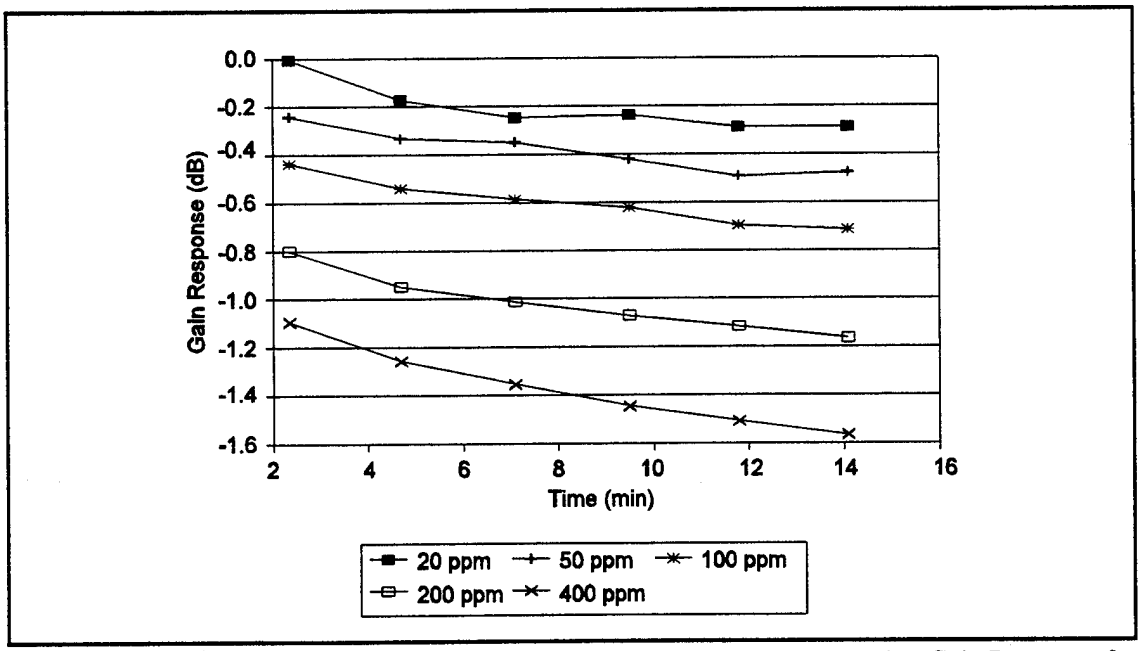


Figure M-18. Time Dependence of the CuPc-Coated IGEFET Transfer Function Gain Response for Several NH_3 Concentrations. (Approximate Frequency = 800-12000 Hz. Film Thickness = 0.32 μm. Temperature = 100° C.)

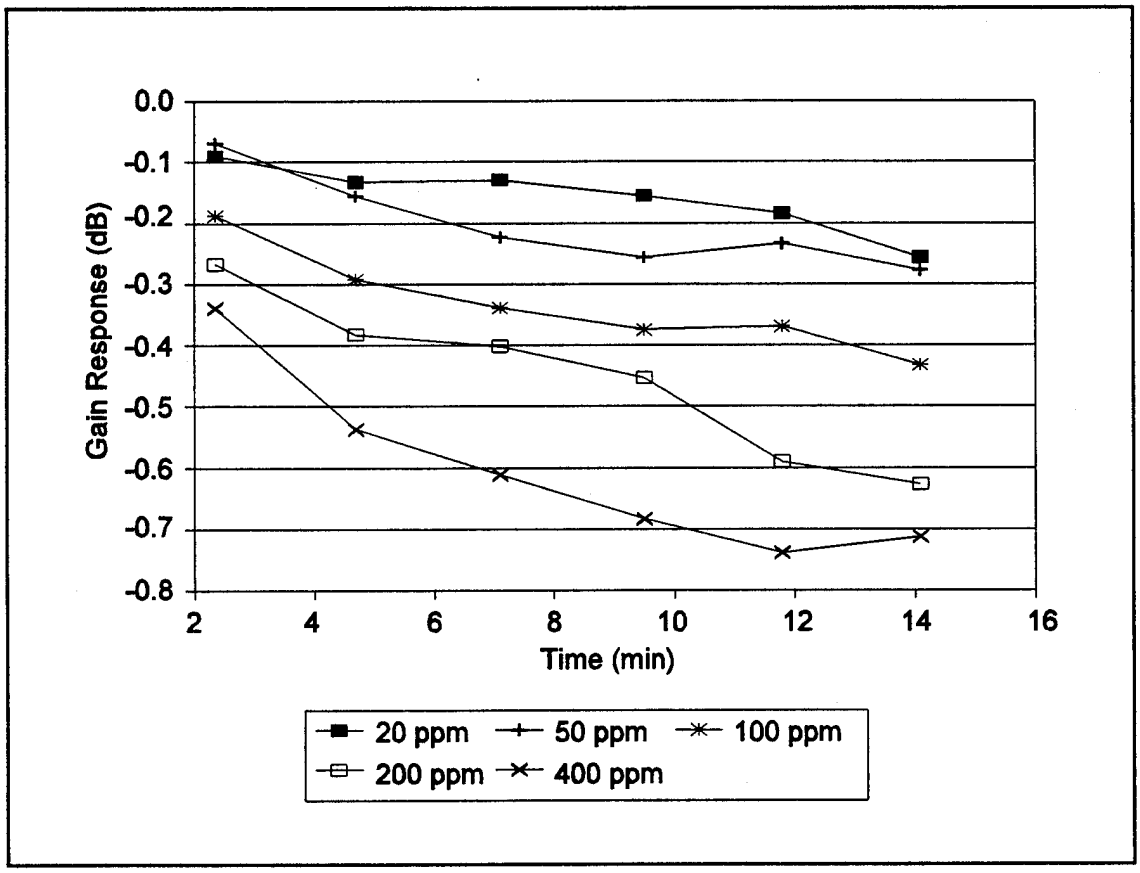


Figure M-19. Time Dependence of the NiPc-Coated IGEFET Transfer Function Gain Response for Several NH_3 Concentrations. (Approximate Frequency = 800-12000 Hz. Film Thickness = 0.43 μm. Temperature = 100° C.)

Appendix N. Supporting Data: Phase Response of the MPc-Coated Microsensor to Challenge Gas Exposure

This appendix contains the phase response of the copper phthalocyanine (CuPc)-, nickel phthalocyanine (NiPc)- and cobalt phthalocyanine (CoPc)-coated interdigitated gate electrode field effect transistor (IGEFET) microsensors as a result of exposure to the challenge gases. The data presented in this appendix supports the phase response data presented in Chapter VI. Figures N-1 through N-9 present the phase response of the MPc-coated IGEFET microsensor after a 16 minute exposure to binary gas mixtures containing a fixed nitrogen dioxide concentration and various concentrations of ammonia. Similarly, Figures N-10 through N-15 depict the phase response of the MPc-coated microsensor after a 16 minute exposure to binary gas mixtures containing a fixed ammonia concentration and various concentrations of nitrogen dioxide. Figures N-16 through N-20 illustrate the time dependence of the CuPc- and NiPc-coated IGEFET transfer function's high-frequency (10-38 KHz for NO_2 and 5-9 KHz for NH_3) phase response maxima upon exposure to various nitrogen dioxide and ammonia challenge gas concentrations. As a result of the significantly different baseline transfer function (discussed in Chapter VI), the time dependence of the CoPc-coated IGEFET transfer function phase response maxima was not investigated.

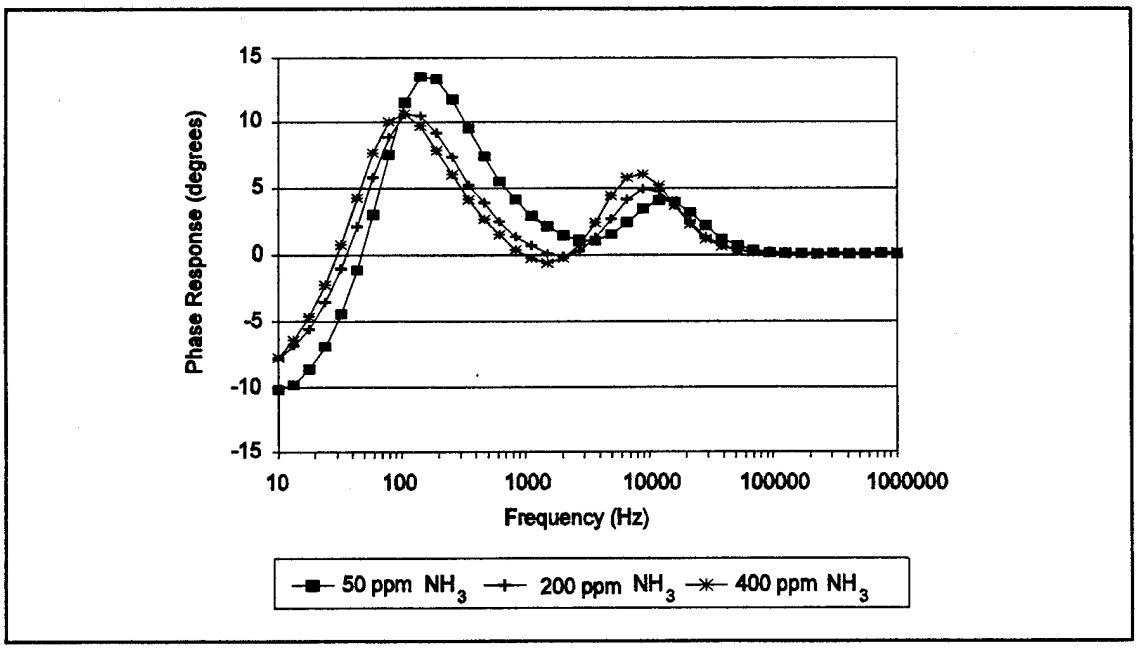


Figure N-1. Bode Plots of the CuPc-Coated IGEFET Transfer Function Phase Response After a 16 minute Exposure to a Binary Gas Mixture Containing 100 ppb NO_2 and Various NH_3 Concentrations. (Film Thickness = 0.32 μm. Temperature = 100° C.)

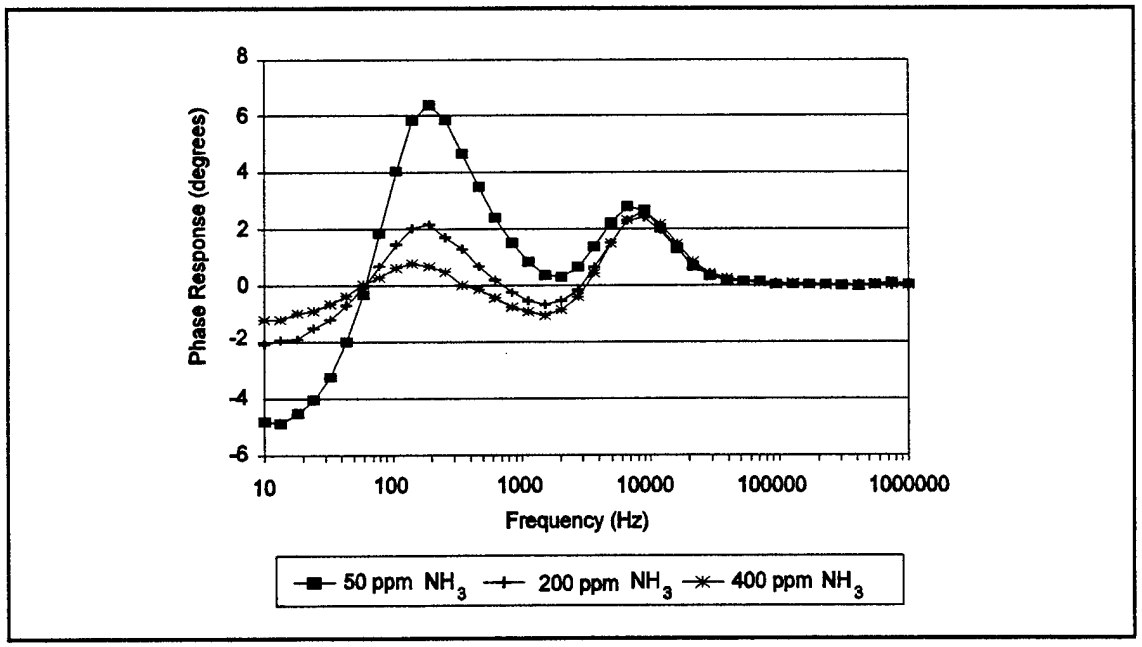


Figure N-2. Bode Plots of the NiPc-Coated IGEFET Transfer Function Phase Response After a 16 minute Exposure to a Binary Gas Mixture Containing 100 ppb NO_2 and Various NH_3 Concentrations. (Film Thickness = 0.43 μm. Temperature = 100° C.)

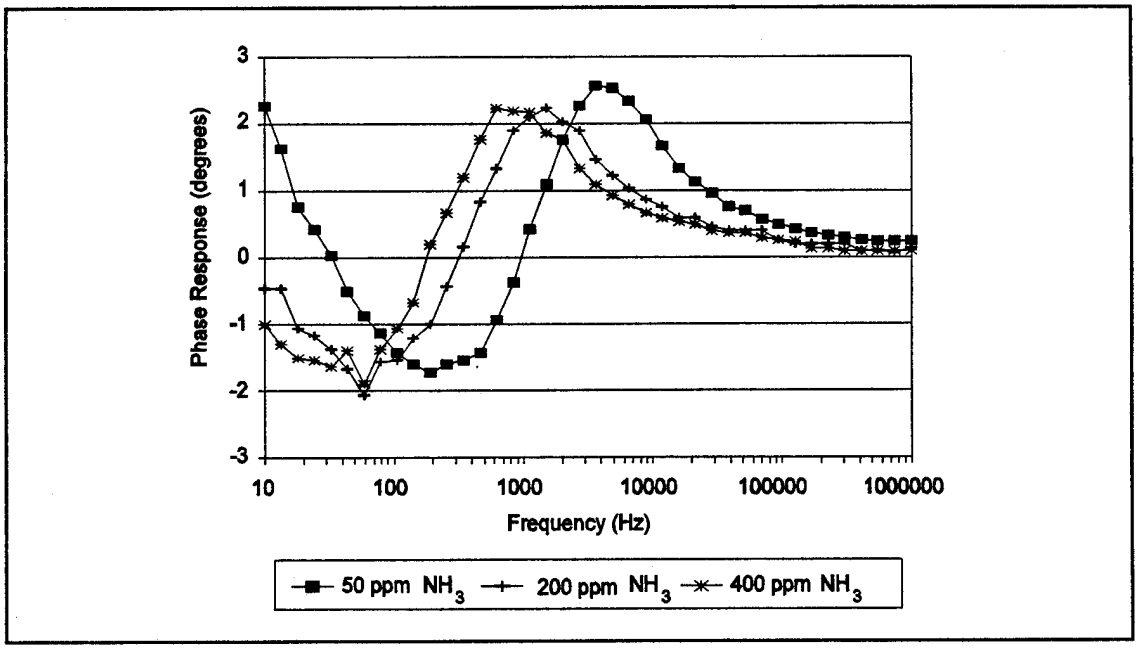


Figure N-3. Bode Plots of the CoPc-Coated IGEFET Transfer Function Phase Response After a 16 minute Exposure to a Binary Gas Mixture Containing 100 ppb NO_2 and Various NH_3 Concentrations. (Film Thickness = 0.51 μm. Temperature = 100° C.)

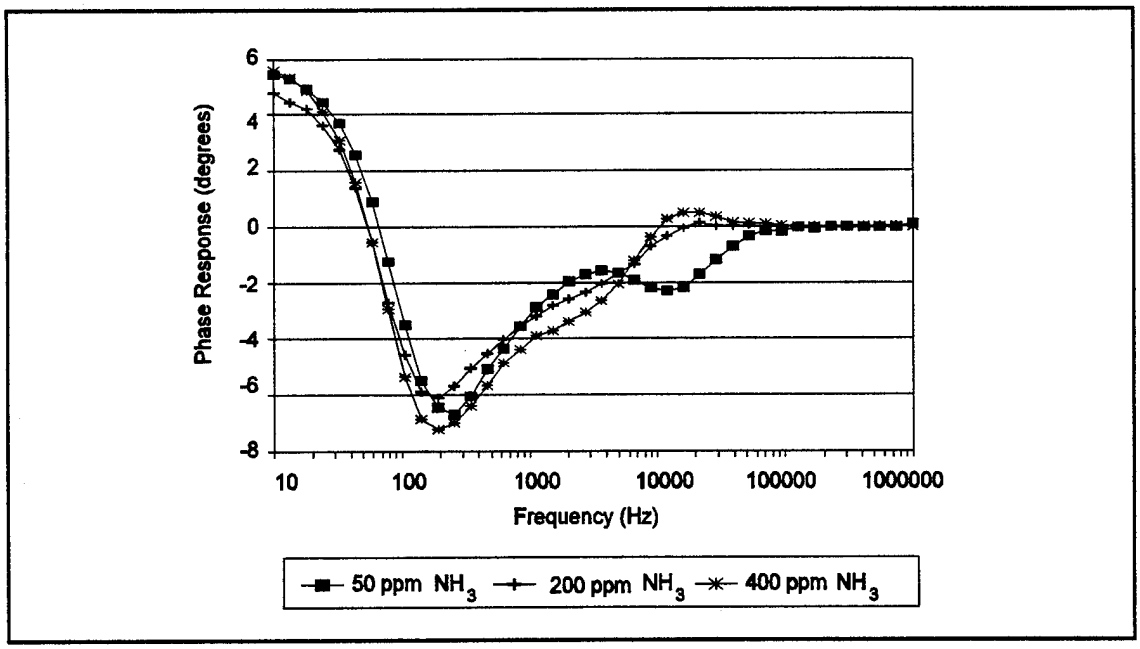


Figure N-4. Bode Plots of the CuPc-Coated IGEFET Transfer Function Phase Response After a 16 minute Exposure to a Binary Gas Mixture Containing 425 ppb NO_2 and Various NH_3 Concentrations. (Film Thickness = 0.32 μm. Temperature = 100° C.)

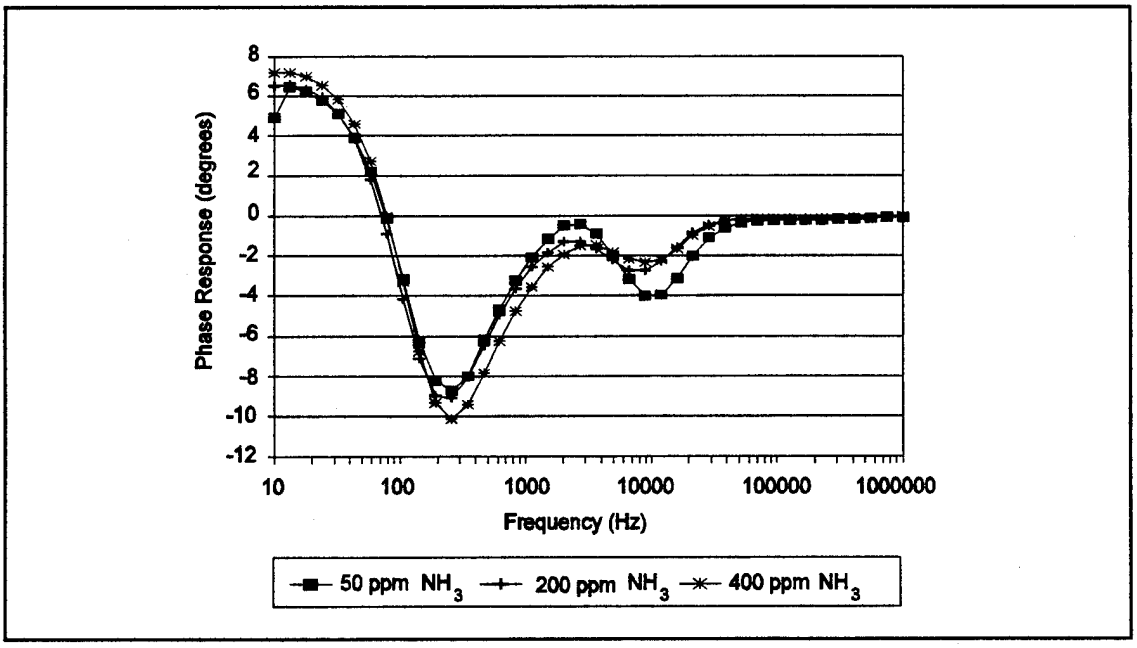


Figure N-5. Bode Plots of the NiPc-Coated IGEFET Transfer Function Phase Response After a 16 minute Exposure to a Binary Gas Mixture Containing 425 ppb NO_2 and Various NH_3 Concentrations. (Film Thickness = 0.43 μm. Temperature = 100° C.)

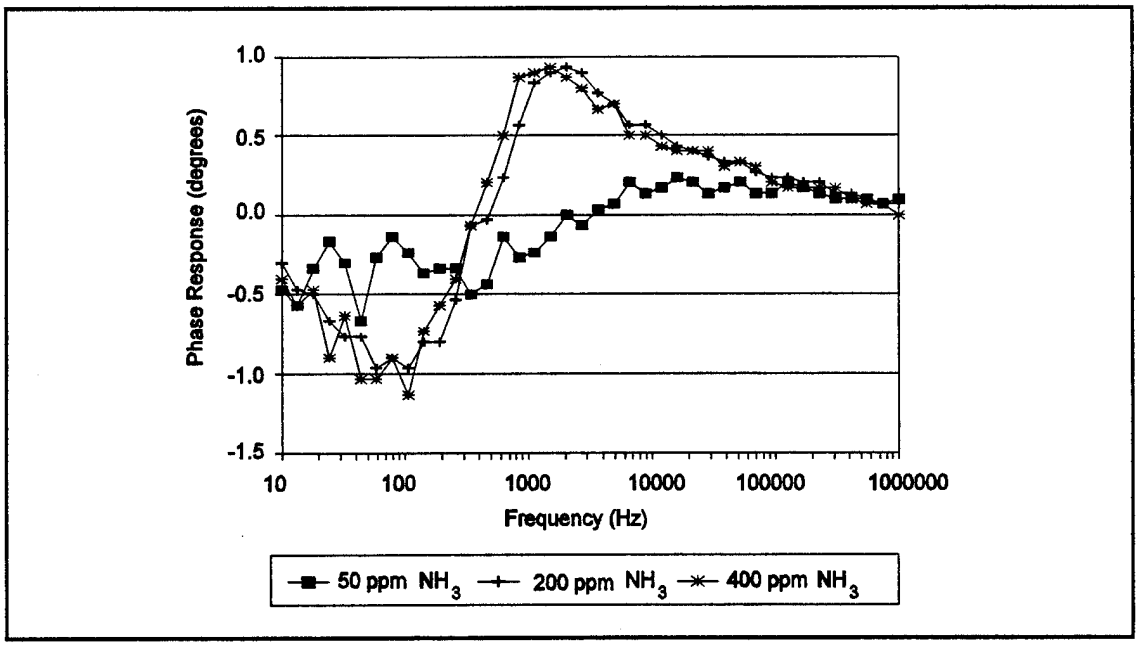


Figure N-6. Bode Plots of the CoPc-Coated IGEFET Transfer Function Phase Response After a 16 minute Exposure to a Binary Gas Mixture Containing 425 ppb NO_2 and Various NH_3 Concentrations. (Film Thickness = 0.51 μm. Temperature = 100° C.)

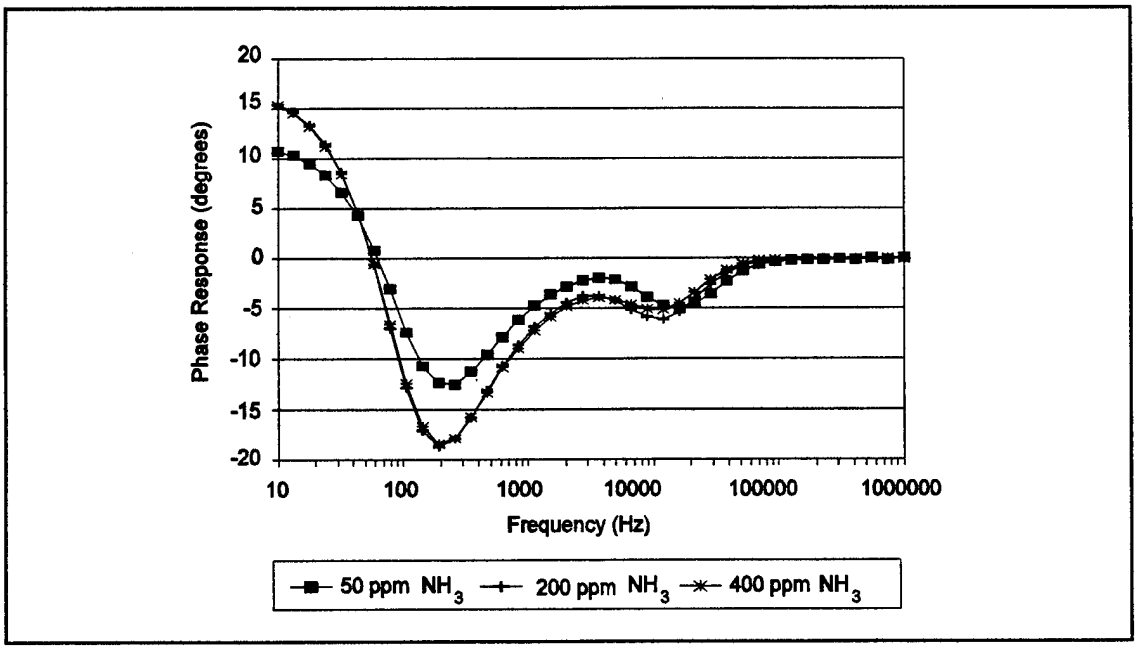


Figure N-7. Bode Plots of the CuPc-Coated IGEFET Transfer Function Phase Response After a 16 minute Exposure to a Binary Gas Mixture Containing 1000 ppb NO_2 and Various NH_3 Concentrations. (Film Thickness = 0.32 μm. Temperature = 100° C.)

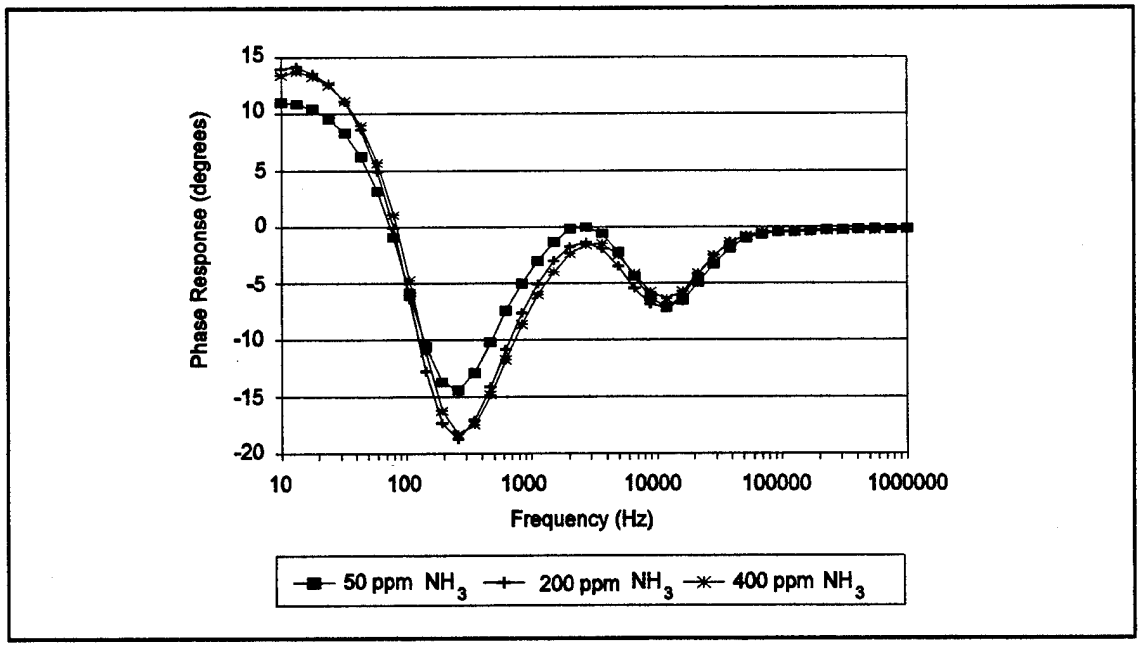


Figure N-8. Bode Plots of the NiPc-Coated IGEFET Transfer Function Phase Response After a 16 minute Exposure to a Binary Gas Mixture Containing 1000 ppb NO_2 and Various NH_3 Concentrations. (Film Thickness = 0.43 μm. Temperature = 100° C.)

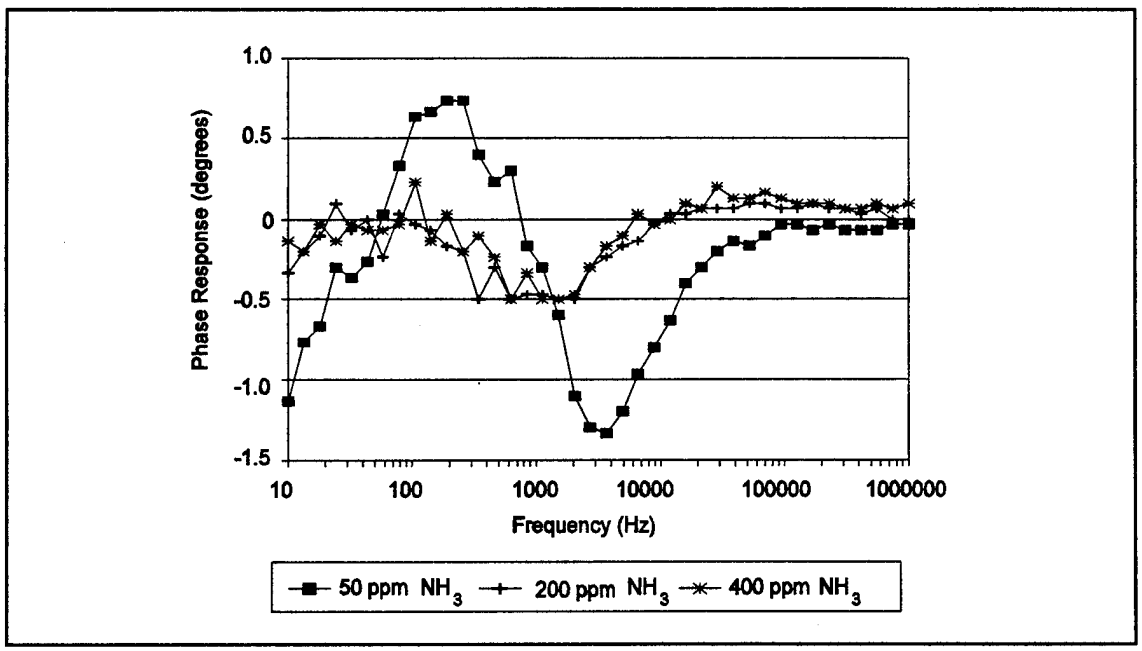


Figure N-9. Bode Plots of the CoPc-Coated IGEFET Transfer Function Phase Response After a 16 minute Exposure to a Binary Gas Mixture Containing 1000 ppb NO_2 and Various NH_3 Concentrations. (Film Thickness = 0.51 μm. Temperature = 100° C.)

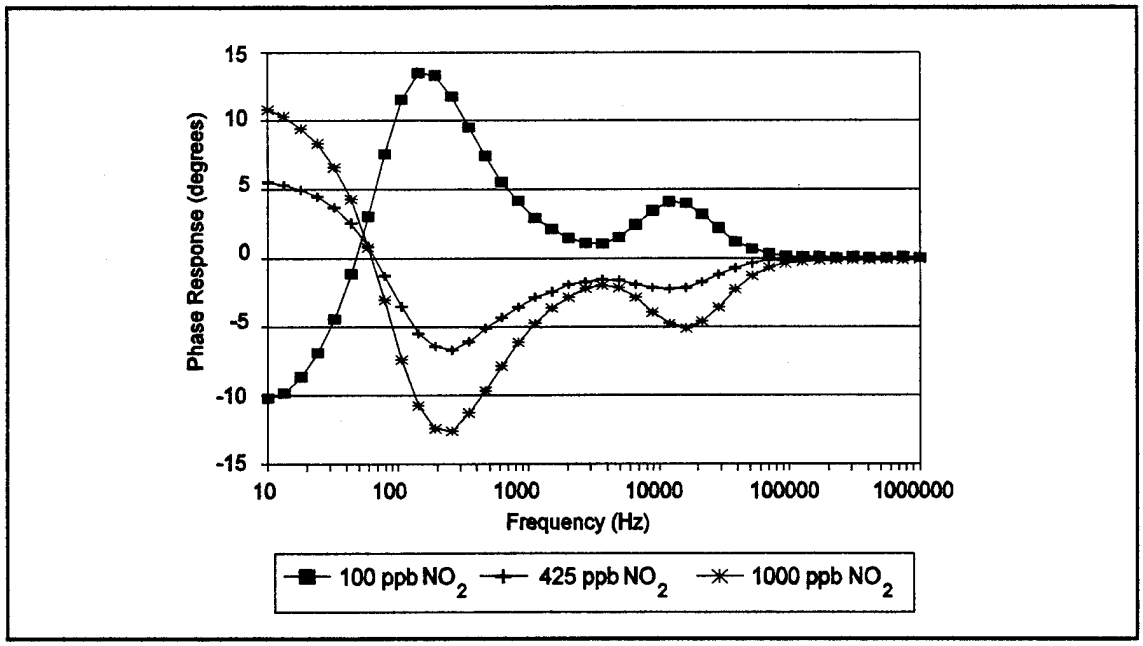


Figure N-10. Bode Plots of the CuPc-Coated IGEFET Transfer Function Phase Response After a 16 minute Exposure to a Binary Gas Mixture Containing 50 ppm NH_3 and Various NO_2 Concentrations. (Film Thickness = 0.32 μm. Temperature = 100° C.)

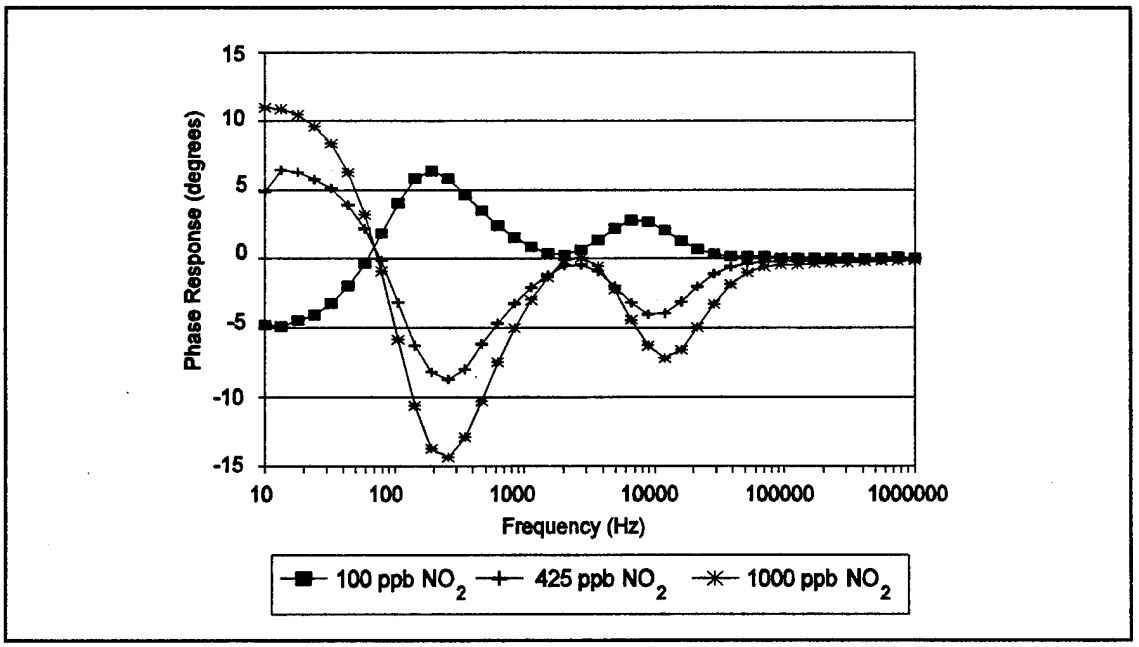


Figure N-11. Bode Plots of the NiPc-Coated IGEFET Transfer Function Phase Response After a 16 minute Exposure to a Binary Gas Mixture Containing 50 ppm NH_3 and Various NO_2 Concentrations. (Film Thickness = 0.43 μm. Temperature = 100° C.)

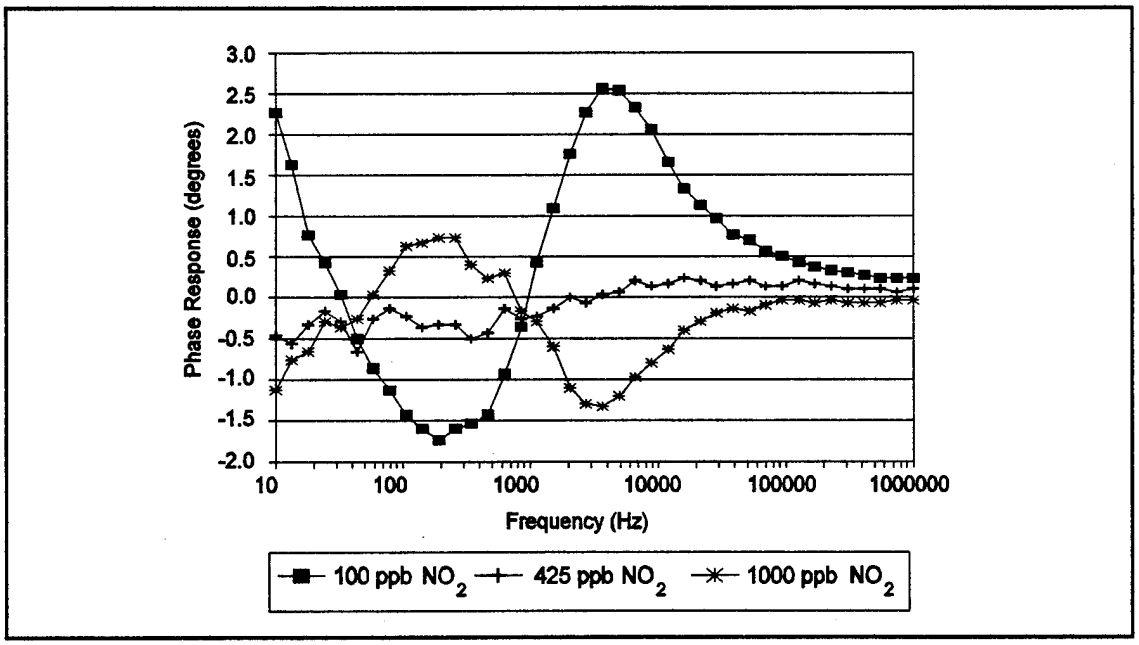


Figure N-12. Bode Plots of the CoPc-Coated IGEFET Transfer Function Phase Response After a 16 minute Exposure to a Binary Gas Mixture Containing 50 ppm NH_3 and Various NO_2 Concentrations. (Film Thickness = 0.51 μm. Temperature = 100° C.)

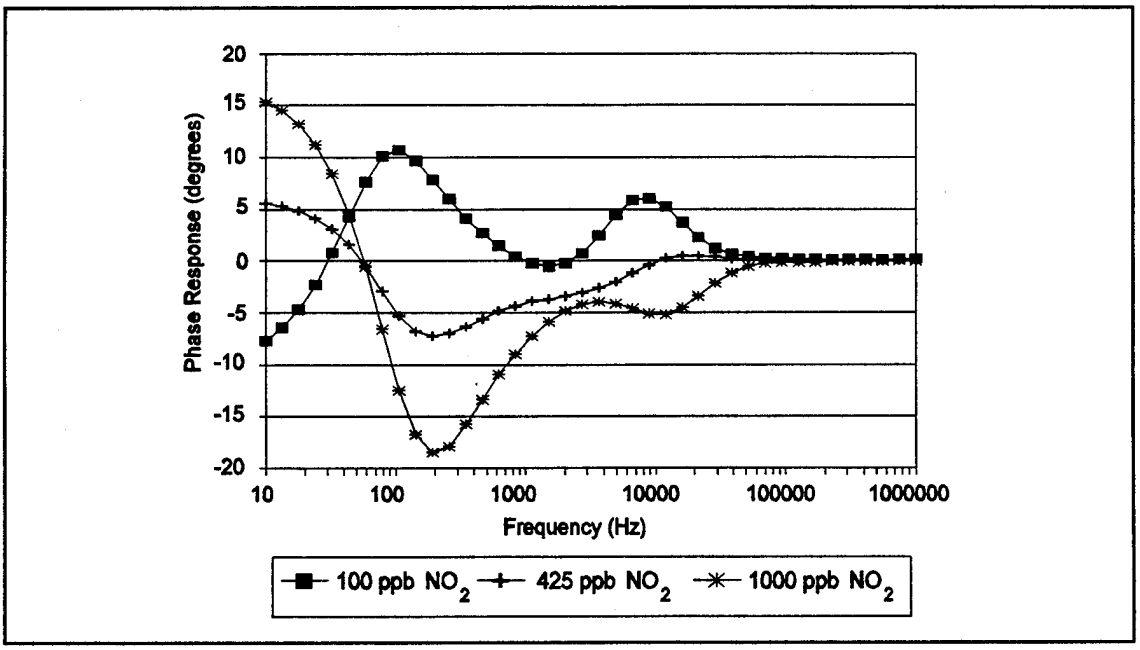


Figure N-13. Bode Plots of the CuPc-Coated IGEFET Transfer Function Phase Response After a 16 minute Exposure to a Binary Gas Mixture Containing 400 ppm NH_3 and Various NO_2 Concentrations. (Film Thickness = 0.32 μm. Temperature = 100° C.)

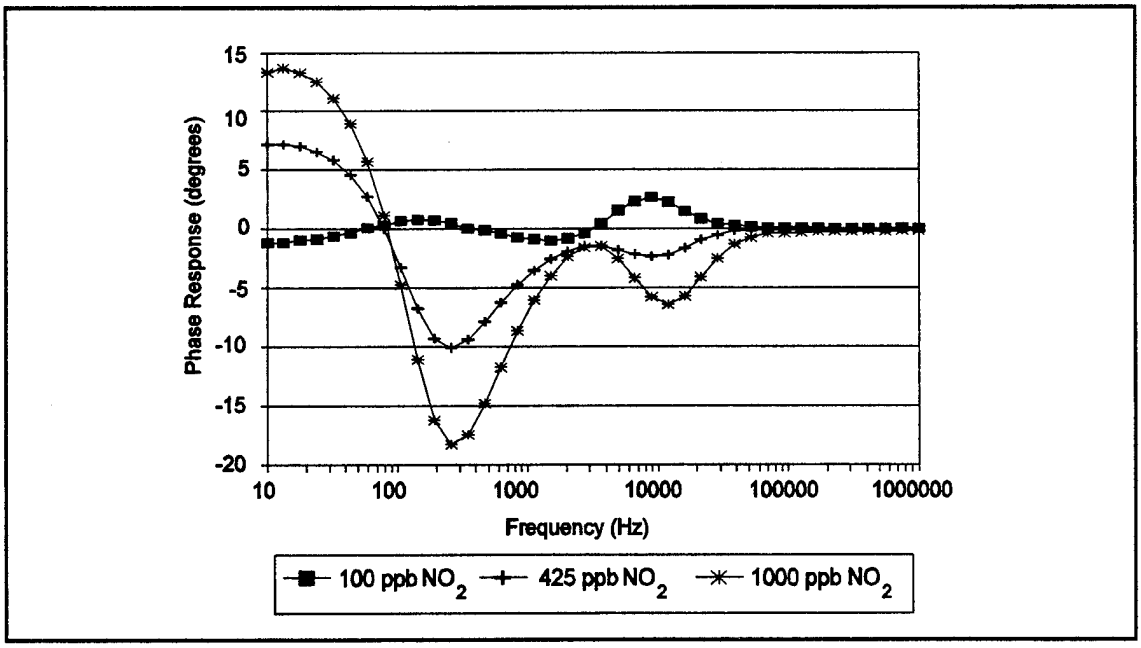


Figure N-14. Bode Plots of the NiPc-Coated IGEFET Transfer Function Phase Response After a 16 minute Exposure to a Binary Gas Mixture Containing 400 ppm NH_3 and Various NO_2 Concentrations. (Film Thickness = 0.43 μm. Temperature = 100° C.)

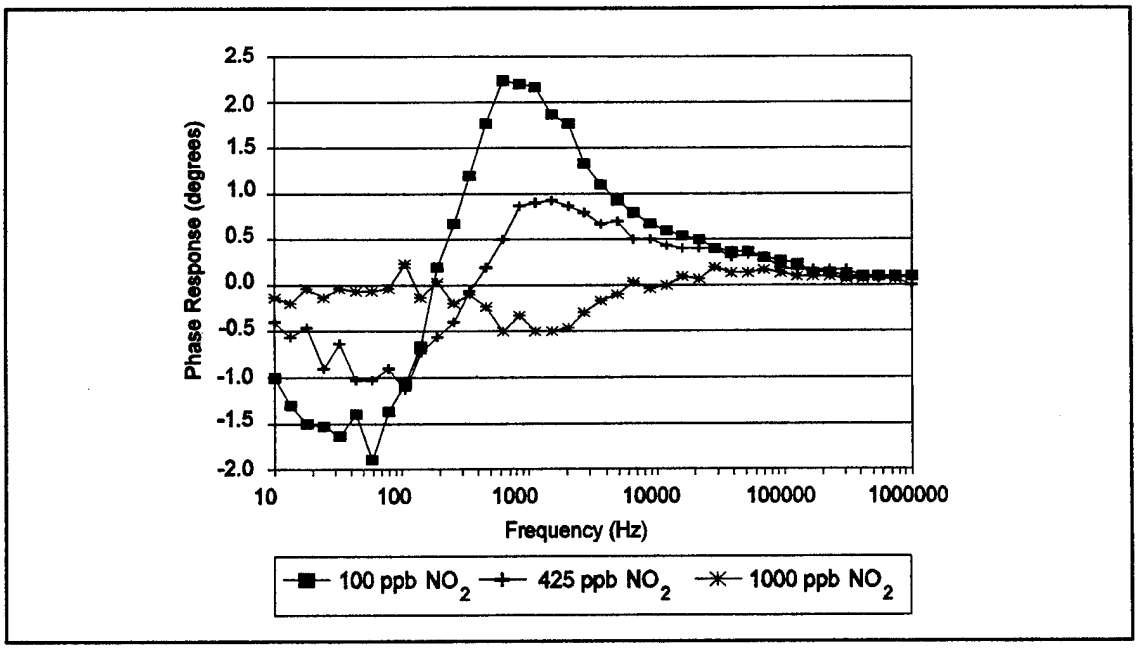


Figure N-15. Bode Plots of the CoPc-Coated IGEFET Transfer Function Phase Response After a 16 minute Exposure to a Binary Gas Mixture Containing 400 ppm NH_3 and Various NO_2 Concentrations. (Film Thickness = 0.51 μm. Temperature = 100° C.)

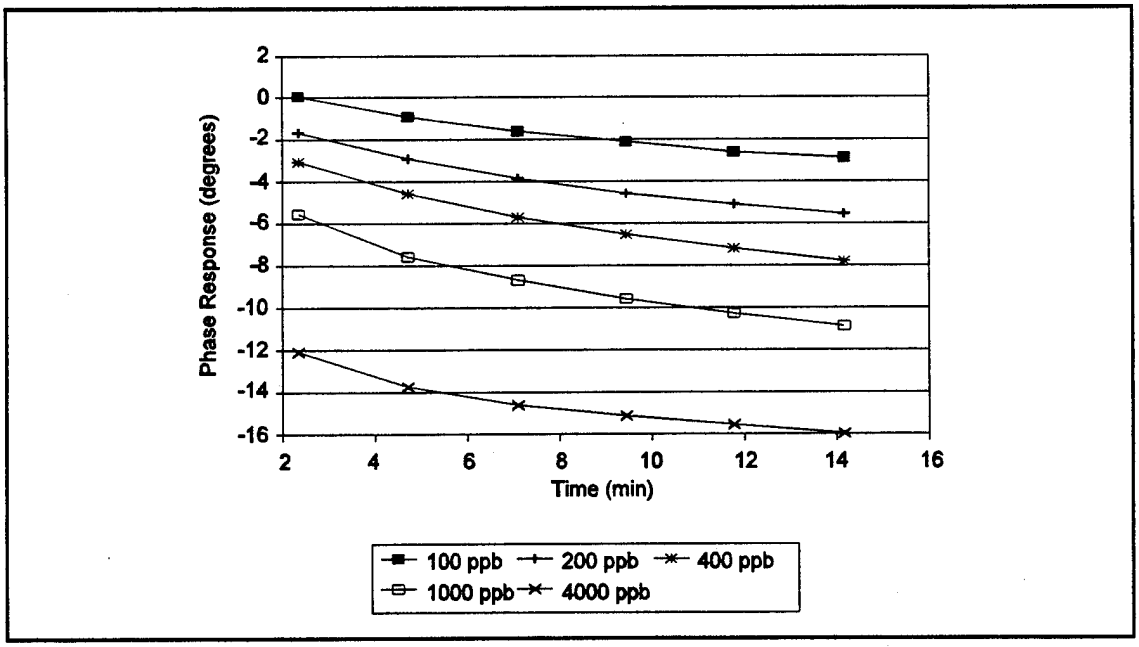


Figure N-16. Time Dependence of the CuPc-Coated IGEFET Transfer Function Phase Response for Several NO_2 Concentrations. (Approximate Frequency = 10-38 KHz. Film Thickness = 0.32 μm. Temperature = 100° C.)

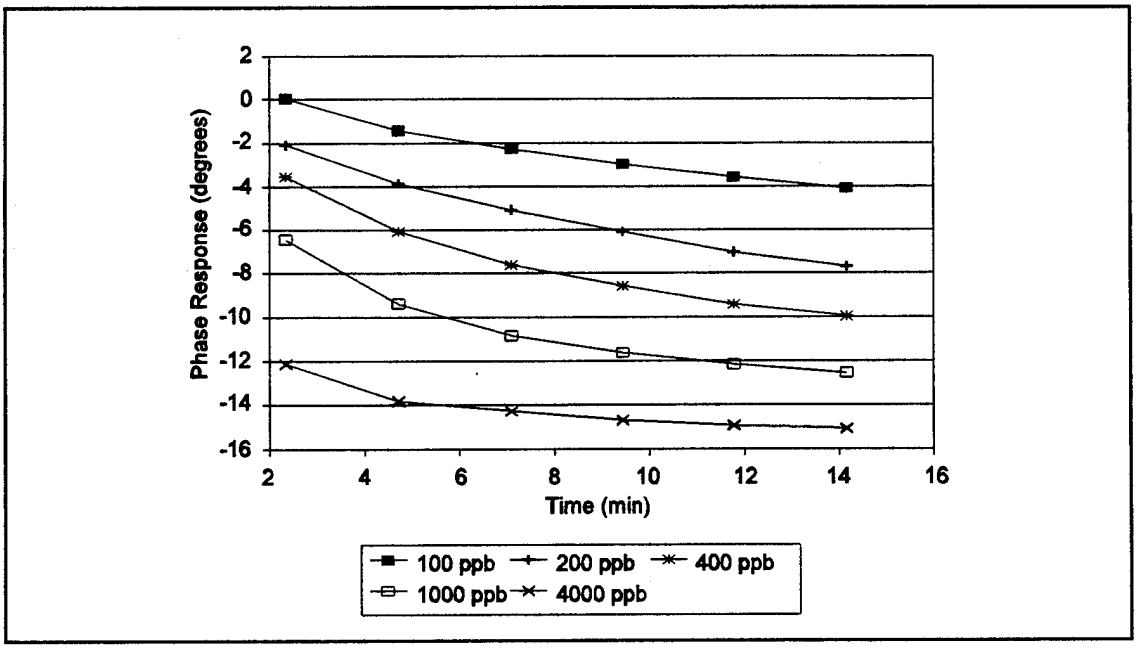


Figure N-17. Time Dependence of the NiPc-Coated IGEFET Transfer Function Phase Response for Several NO_2 Concentrations. (Approximate Frequency = 10-38 KHz. Film Thickness = 0.43 μm. Temperature = 100° C.)

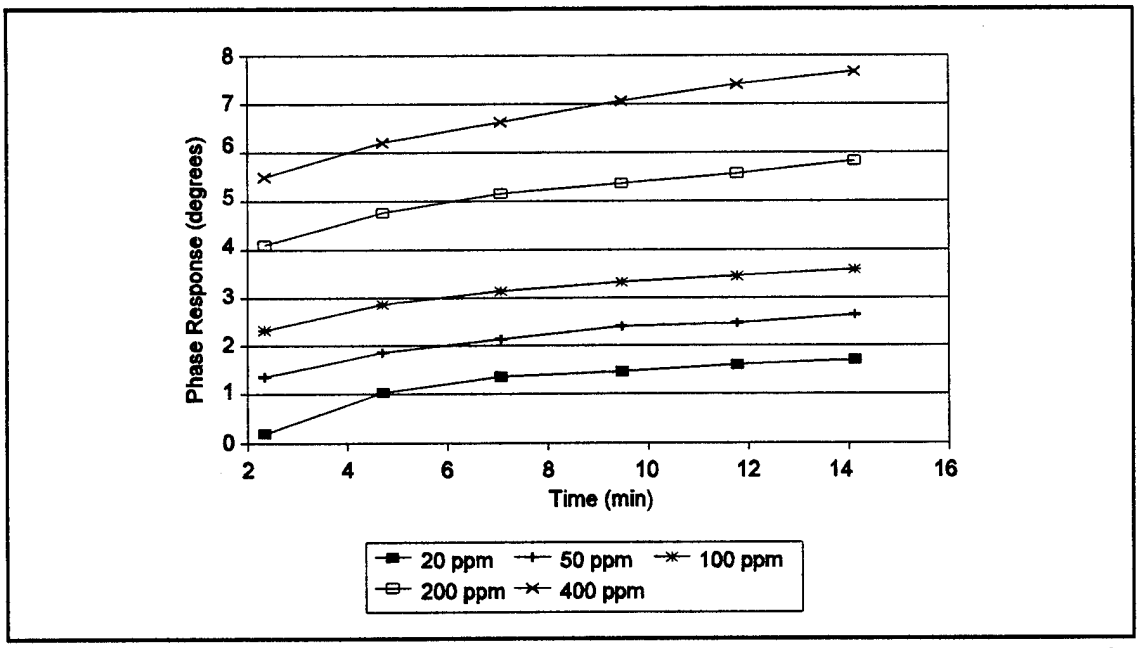


Figure N-18. Time Dependence of the CuPc-Coated IGEFET Transfer Function Phase Response for Several NH_3 Concentrations. (Approximate Frequency = 5-9 KHz. Film Thickness = 0.32 μm. Temperature = 100° C.)

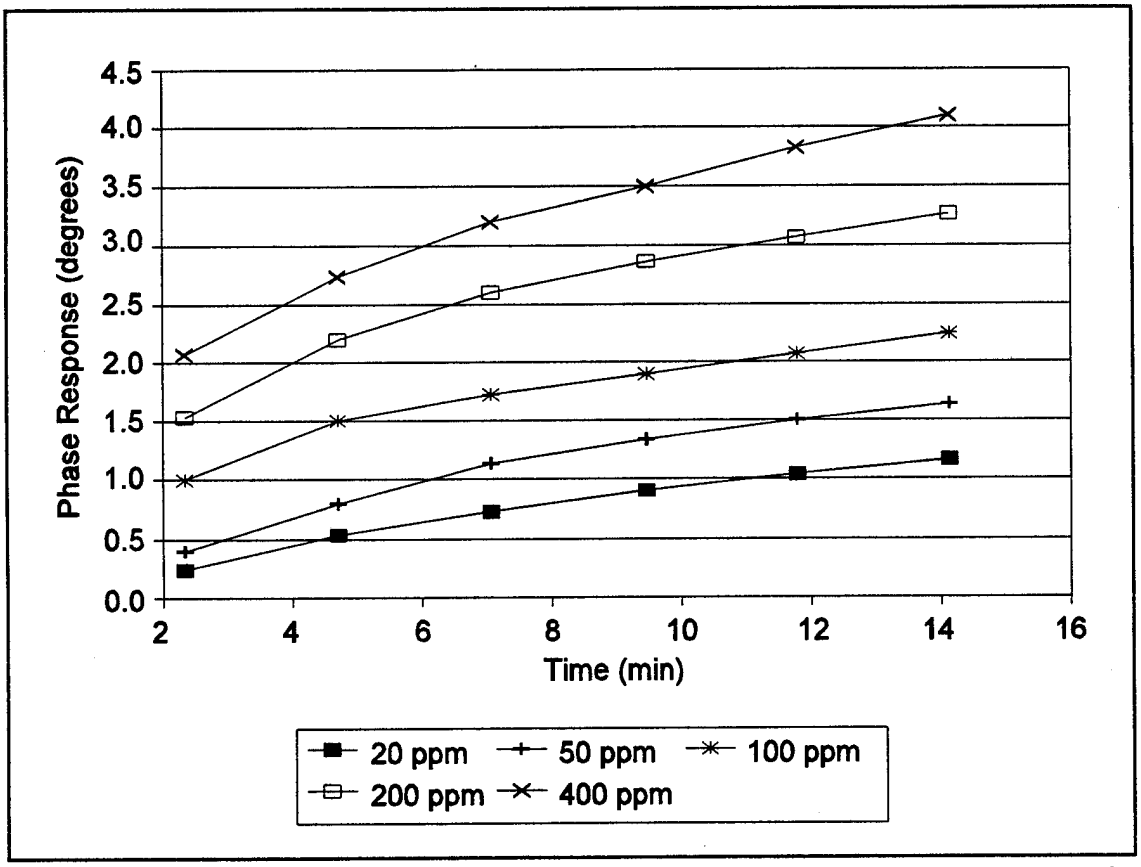


Figure N-19. Time Dependence of the NiPc-Coated IGEFET Transfer Function Phase Response for Several NH_3 Concentrations. (Approximate Frequency = 5-9 KHz. Film Thickness = 0.43 μm. Temperature = 100° C.)

Appendix O: PCA and Multivariate MathCad Code

The following MathCad code was used to perform the principal component analysis (PCA) and multivariate regression.

$$ORIGIN := 1$$

$$DCR := READPRN(MIXMTRA)$$

$$C := \begin{pmatrix} 100 & 425 & 1000 & 100 & 425 & 1000 & 425 & 1000 & 100 \\ 5\cdot10^{4} & 5\cdot10^{4} & 5\cdot10^{4} & 2\cdot10^{5} & 2\cdot10^{5} & 2\cdot10^{5} & 4\cdot10^{5} & 4\cdot10^{5} & 4\cdot10^{5} \end{pmatrix}$$

$$j := 1..9 \qquad i := 1..9$$

$$Z := DCR \cdot DCR^{T}$$

$$EIGENS := eigenvals(Z)$$

$$L^{<i>} := eigenvec(Z, EIGENS_i)$$

$$F := DCR^{T} \cdot L$$

$$P := \left[\left(F^{T} \cdot F \right)^{-1} \cdot F^{T} \cdot C^{T} \right]^{T}$$

$$C1 := \left(P \cdot \left((DCR)^{T} \cdot L \right)^{T} \right)$$

$$DCR := READPRN(MIXMTR1)$$

$$C1 := \left(P \cdot \left((DCR)^{T} \cdot L\right)^{T}\right)$$

$$j := 1 .. 27$$

$$KC := \begin{bmatrix} 100 & 5\cdot10^{4} \\ 100 & 5\cdot10^{4} \\ 100 & 5\cdot10^{4} \\ 425 & 5\cdot10^{4} \\ 425 & 5\cdot10^{4} \\ 425 & 5\cdot10^{4} \\ 1000 & 5\cdot10^{4} \\ 1000 & 5\cdot10^{4} \\ 1000 & 5\cdot10^{4} \\ 100 & 2\cdot10^{5} \\ 100 & 2\cdot10^{5} \\ 100 & 2\cdot10^{5} \\ 425 & 2\cdot10^{5} \\ 425 & 2\cdot10^{5} \\ 425 & 2\cdot10^{5} \\ 1000 & 2\cdot10^{5} \\ 1000 & 2\cdot10^{5} \\ 1000 & 2\cdot10^{5} \\ 100 & 4\cdot10^{5} \\ 100 & 4\cdot10^{5} \\ 100 & 4\cdot10^{5} \\ 425 & 4\cdot10^{5} \\ 425 & 4\cdot10^{5} \\ 425 & 4\cdot10^{5} \\ 1000 & 4\cdot10^{5} \\ 1000 & 4\cdot10^{5} \\ 1000 & 4\cdot10^{5} \end{bmatrix}$$

$$Err := \sqrt{\frac{\sum_{j}\left[\frac{\left(C1^{T}\right)_{(j,1)} - KC_{(j,1)}}{KC_{(j,1)}}\right]^{2}}{27}}$$

$$Err := \sqrt{\frac{\sum_{j}\left[\frac{\left(C1^{T}\right)_{(j,2)} - KC_{(j,2)}}{KC_{(j,2)}}\right]^{2}}{27}}$$

REPORT DOCUMENTATION PAGE

Form Approved
OMB No. 0704-0188

Public reporting burden for this collection of information is estimated to average 1 hour per response, including the time for reviewing instructions, searching existing data sources, gathering and maintaining the data needed, and completing and reviewing the collection of information. Send comments regarding this burden estimate or any other aspect of this collection of information, including suggestions for reducing this burden, to Washington Headquarters Services, Directorate for Information Operations and Reports, 1215 Jefferson Davis Highway, Suite 1204, Arlington, VA 22202-4302, and to the Office of Management and Budget, Paperwork Reduction Project (0704-0188), Washington, DC 20503.

1. AGENCY USE ONLY (Leave blank)	2. REPORT DATE	3. REPORT TYPE AND DATES COVERED
	December, 1995	PHD DISSERTATION

4. TITLE AND SUBTITLE
Binary Gas Mixture Analysis with an Interdigitated Gate Electrode Field Effect Transistor (IGEFET) Microsensor

5. FUNDING NUMBERS

6. AUTHOR(S)
John Michael Wiseman

7. PERFORMING ORGANIZATION NAME(S) AND ADDRESS(ES)
AFIT/ENG
Wright-Patterson AFB, OH 45433

8. PERFORMING ORGANIZATION REPORT NUMBER
AFIT/DS/ENG/95-07

9. SPONSORING / MONITORING AGENCY NAME(S) AND ADDRESS(ES)
AL/OEDR, Brooks AFB. TX 78235-5301
EG&G Mound Applied Technologies, Miamisburg, OH, 45343-0987

10. SPONSORING / MONITORING AGENCY REPORT NUMBER

11. SUPPLEMENTARY NOTES

12a. DISTRIBUTION / AVAILABILITY STATEMENT
Approved for public release; Distribution Unlimited

12b. DISTRIBUTION CODE

13. ABSTRACT *(Maximum 200 words)*

Single component and binary gas mixtures of nitrogen dioxide (NO_2) and ammonia (NH_3) were analyzed with a microsensor composed of an array of Interdigitated Gate Electrode Field Effect Transistor (IGEFET) sensor elements coated with copper-, nickel-, and cobalt-phthalocyanine thin films. Improvements in the IGEFET microsensor design and operation facilitated simultaneous measurement of the direct current (DC) and alternating current (AC) electrical response of the metal-substituted phthalocyanine (MPc) films to challenge gas exposure. A finite-difference model of the interdigitated gate electrode (IGE) structure confirmed the fundamental operation of the IGEFET microsensor. Principal component analysis (PCA) and multilinear regression were applied to features identified in the IGE structure's normalized DC resistance response, aswell as the IGEFET transfer function's gain and phase response, to gas mixtures containing parts-per-billion (ppb) NO_2 and parts-per-million (ppm) NH_3. The predicted concentrations were generally within 50% of the known concentrations for all gas analyses. The single component analysis of each test gas using the normalized DC resistance data yielded the smallest error (14% for NH_3 and 26% for NO_2). For the binary gas mixture analysis, the smallest error was achieved with the gain response data (approximately 25% for each component).

14. SUBJECT TERMS
GAS ANALYSIS, DIRECT CURRENT, ALTERNATING CURRENT, CONDUCTIVITY, MOSFET, CUPC, NIPC, COPC, PHTHALOCYANINE, AMMONIA, NITROGEN DIOXIDE MULTICOMPONENT, PRINCIPAL COMPONENT ANALYSIS, CHEMIRESISTOR

15. NUMBER OF PAGES
604

16. PRICE CODE

17. SECURITY CLASSIFICATION OF REPORT	18. SECURITY CLASSIFICATION OF THIS PAGE	19. SECURITY CLASSIFICATION OF ABSTRACT	20. LIMITATION OF ABSTRACT
UNCLASSIFIED	UNCLASSIFIED	UNCLASSIFIED	UL